DTIC FILE COPY

20030206040

GC-TR-90-1947

RESEARCH AND DEVELOPMENT

IN SUPPORT OF THE

SURFACE CHEMISTRY BRANCH

AD-A223 838

DTIC
ELECTE
JUL 06 1990
S B D

DISTRIBUTION STATEMENT A
Approved for public release;
Distribution Unlimited

90 07 5 068

(4)

GC-TR-90-1947

RESEARCH AND DEVELOPMENT

IN SUPPORT OF THE

SURFACE CHEMISTRY BRANCH

DTIC
ELECTE
JUL 06 1990
S B D

Final Report

Prepared for
Naval Research Laboratory
4555 Overlook Avenue, S.W.
Washington, DC 20375-5000
Under Contract Number N00014-88-C-2247

Prepared by
GEO-CENTERS, INC.
7 Wells Avenue
Newton Centre, MA 02159

January 1990

DISTRIBUTION STATEMENT A
Approved for public release;
Distribution Unlimited

GEO-CENTERS, INC.

UNCLASSIFIED
SECURITY CLASSIFICATION OF THIS PAGE

REPORT DOCUMENTATION PAGE

1a REPORT SECURITY CLASSIFICATION	1b RESTRICTIVE MARKINGS
2a SECURITY CLASSIFICATION AUTHORITY	3 DISTRIBUTION/AVAILABILITY OF REPORT Approved for public release; distribution unlimited.
2b DECLASSIFICATION/DOWNGRADING SCHEDULE	
4 PERFORMING ORGANIZATION REPORT NUMBER(S) GC-TR-90-1947	5 MONITORING ORGANIZATION REPORT NUMBER(S)
6a NAME OF PERFORMING ORGANIZATION GEO-CENTERS, INC. — 6b OFFICE SYMBOL (If applicable)	7a NAME OF MONITORING ORGANIZATION
6c ADDRESS (City, State, and ZIP Code) 7 Wells Avenue Newton Centre, MA 02159	7b ADDRESS (City, State, and ZIP Code)
8a NAME OF FUNDING/SPONSORING ORGANIZATION Naval Research Laboratory — 8b OFFICE SYMBOL (If applicable) Code 6170	9 PROCUREMENT INSTRUMENT IDENTIFICATION NUMBER Contract No. N00014-88-C-2247
8c ADDRESS (City, State, and ZIP Code) 4555 Overlook Avenue, S.W. Washington, DC 20375-5000	10 SOURCE OF FUNDING NUMBERS PROGRAM ELEMENT NO — PROJECT NO — TASK NO — WORK UNIT ACCESSION NO

11 TITLE (Include Security Classification)
Research and Development in Support of the Surface Chemistry Branch(U)

12 PERSONAL AUTHOR(S)
L. Isaacson, R. Binstead, M. Twigg, D. Ballantine, F. Hutson

13a TYPE OF REPORT	13b TIME COVERED	14 DATE OF REPORT (Year, Month, Day)	15 PAGE COUNT
Final	FROM 5/88 TO 11/89	January 1990	687

16 SUPPLEMENTARY NOTATION

17 COSATI CODES			18 SUBJECT TERMS (Continue on reverse if necessary and identify by block number)
FIELD	GROUP	SUB-GROUP	Surface analysis, surface modification, tribological characterization, air purification, chemical microsensors, detection, interface modification & analysis (continued on reverse)

19 ABSTRACT (Continue on reverse if necessary and identify by block number)

This report summarizes GEO-CENTERS' programs in support of the Naval Research Laboratory's Surface Chemistry Branch of the Chemistry Division. These programs deal with the properties and chemistry on/at/near surfaces and interfaces. Of particular interest to the Navy are the advances and studies summarized as follows: Friction/Wear Testing & Surface Analysis: Examined & studied were the effects caused by chemistry & wear debris on the friction/wear of ion-implanted metals and ceramics, & the friction/wear of solid lubricating films. Air Purification: Emphasis centered on predicting the breakthrough behavior of high humidity air streams on activated carbon & the effect of relative humidity on the breakthrough of chemical challenges on impregnated carbon. Chemical Microsensors: Testing & analyzing data from Surface Acoustic Wave (SAW) devices were investigated as were the elastic properties & transition temperatures of thin polymer films. Continued on reverse

20 DISTRIBUTION/AVAILABILITY OF ABSTRACT	21 ABSTRACT SECURITY CLASSIFICATION
☒ UNCLASSIFIED/UNLIMITED ☐ SAME AS RPT ☐ DTIC USERS	UNCLASSIFIED
22a NAME OF RESPONSIBLE INDIVIDUAL Dr. David Venezky	22b TELEPHONE (Include Area Code) 202-767-3550 — 22c OFFICE SYMBOL Code 6170

DD FORM 1473, 84 MAR — 83 APR edition may be used until exhausted. All other editions are obsolete.

SECURITY CLASSIFICATION OF THIS PAGE

GPO: 1988-607-047

UNCLASSIFIED

18. Intermodulation Interference, electrochemical kinetics, and transition metal complexes.

19. A 4-SAW array was tested on-board a Naval platform. Interface Modification and Analysis: Defects were characterized in silicon/insulator interfaces and EXAFS spectral data processing programs were modified so they could be performed on a PC. Solution Kinetics and Mechanisms: Intermodulation interference (IMI) was investigated and electron transfer reactions and kinetics were examined for metal-organic complexes in solution. Programs were written for PC control of the Varian 2390.

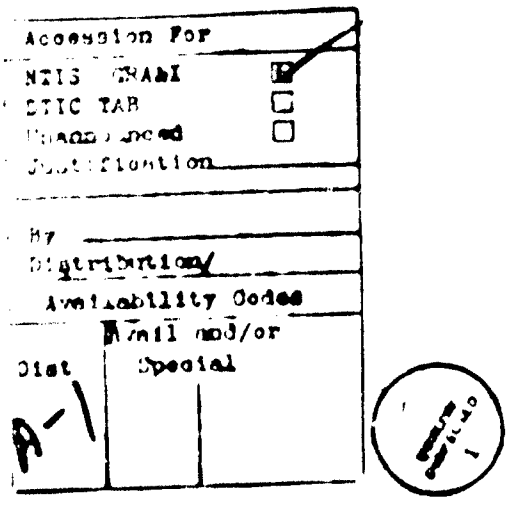


TABLE OF CONTENTS

Section			Page
INTRODUCTION			1
I.	FRICTION/WEAR TESTING AND SURFACE ANALYSIS.		4
	A.	Oxidation and Implantation of Metals	4
	B.	High Temperature Implantation of Ceramics.	7
	C.	Solid Films Deposited on Metals and Ceramics	8
II.	AIR PURIFICATION		14
III.	CHEMICAL MICROSENSORS		15
	A.	Signal/Data Processing Software	15
	B.	Elastic Properties of Thin Polymer Films	16
	C.	Field Evaluation of SAW Sensor Performance	16
IV.	INTERFACE MODIFICATION AND ANALYSIS.		17
	A.	Interface Characterization of Silicon on Insulator Substrates	18
	B.	X-ray Absorption Fine Structure (EXAFS)	23
V.	SOLUTION KINETICS AND MECHANISMS		33
	A.	Intermodulation Interference Studies	33
	B.	Electron Transfer in Transition Metal Complexes	33
	C.	Software Programs for the CARY 2390	33
APPENDICES			35

INTRODUCTION

In support of Naval Research Laboratory (NRL) Contract Number N00014-88-C-2247, GEO-CENTERS, INC. has met all technical requirements and summarizes results in this report. During the period of performance, May, 1988 through November, 1989, work was carried out at the Naval Research Laboratory in the Chemistry Division and the Electronics Technology Division. The majority of this work has subsequently been the subject of numerous publications, reports and presentations at scientific meetings. Work was also carried out under subcontract with Microsensor Systems, Inc., Fairfax, VA, and Locus, Inc., Alexandria, VA. Their final reports are submitted under separate cover.

The individual research projects in which GEO-CENTERS' technical staff members have been involved under this contract can be organized into five (5) general areas, which are described below. More detailed discussions relating to progress and accomplishments, as well as listings of relevant publications and presentations are included in the body of this report.

(1) Friction/Wear Testing and Surface Analysis. Work in the Chemistry Division centered on studying the effects caused by chemistry and wear debris on the friction/wear of ion-implanted metals and ceramics, and the friction/wear of solid lubricating films. The friction/wear studies of ion-implanted metals and ceramics included titanium, nitrogen, nickel and neon implanted in stainless and bearing steels and aluminum and titanium implanted in silicon carbide and silicon nitride. The friction/wear studies of solid lubricating films included films of molybdenum disulfide and diamond.

(2) Air Purification. The behavior of vapor challenges to carbon filters was investigated. Emphasis was centered on predicting the breakthrough behavior of high humidity air streams (50 to 80% RH) on activated carbon (BPL) and the effect of relative humidity on the breakthrough of chemical challenges on ASC-TEDA impregnated carbon.

(3) Chemical Microsensors. Various aspects of testing and analyzing data from Surface Acoustic Wave (SAW) devices were investigated. Pattern recognition techniques were applied and used to distinguish and characterize single or combination vapor challenges to SAW device arrays containing combinations of different selective sorbent coatings. SAW devices were used to investigate the elastic properties and transition temperature (T_m, T_g) of thin polymer films. A 4-SAW array was tested aboard a Naval platform under field conditions to compare field performance with laboratory performance. Under subcontract with Microsensor Systems, a program to investigate SAW device characterization and performance was carried out. The contractor's report and documentation is included under separate cover.

(4) Interface Modification and Analysis. For the Electronics Technology Division, transmission electron microscopy (TEM) was used to characterize defects in silicon/insulator interfaces that are being investigated for integrated circuit applications. These defects are generated during epitaxial growth, ion implantation and/or materials processing. Specific silicon/insulator systems studied include silicon on sapphire (SOS) and germanium on sapphire (GOS). The use of a silicon-germanium layer as an etch stop in the bond and etch back process was also examined.

For the Chemistry Division, programs were modified so X-ray absorption fine structure (EXAFS) spectral data processing could

be performed on a PC rather than the mainframe computer originally used to process data.

(5) Solution Kinetics and Mechanisms. Intermodulation interference (IMI) represents a serious cause of communications problems onboard Navy ships. Under subcontract with Locus, a program to investigate IMI effects was carried out. The results of these studies are briefly discussed. The contractor's report and documentation are included under separate cover.

Electrochemically active transition metal complexes are useful for catalytic conversion and/or decomposition of dissolved gases such as CO_2. Electron transfer reactions and kinetics were studied for metal-organic complexes in solution. Particular emphasis was placed on studying the electron transfer reactions of metal acetylacetonate complexes.

I. FRICTION/WEAR TESTING AND SURFACE ANALYSIS

The friction and wear properties of modified tribological materials are being studied by the U.S. Navy to allow the development of bearing assemblies for use in harsh environments. Present interests have concentrated on modifying surfaces by ion-implantation of metals and ceramics and the study of strong adhering solid lubricating films.

GEO-CENTERS, INC. has been involved in the preparation, testing and evaluation of ion modified materials. Also, GEO-CENTERS has tested and analyzed diamond, titanium nitride and molybdenum-disulfide solid lubricating coatings. The results are summarized in this section and the details are found in the articles in the Appendices.

A. The Oxidation and Implantation of Metals

Three separate studies in this area were performed:

- The effects of oxidation on the friction and wear of 52100 bearing steel (both unimplanted and implanted with titanium) (1); see Appendix A1.
- How wear debris affects the friction of unimplanted and titanium implanted 52100 bearing steel (2); see Appendix A2.
- The effects of implanted nitrogen, nickel and neon ions on the wear resistance and microstructure of 304 stainless steel (3); see Appendix A3.

1. The friction and wear behavior and the composition of oxidized (at temperatures 300 to 600°C) titanium implanted 52100 bearing steel was studied. The friction of the oxidized Ti+ 52100 increased from 0.2 to 0.6; whereas, the friction of unimplanted

and Ti-implanted 52100 were constant at 0.6 and 0.3, respectively. The wear of the oxidized substrates occurred within the oxide layer only. The wear rate showed a behavioral dependence on oxide thickness.

Auger analysis of the wear tracks on the oxidized Ti-implanted samples indicated failure at the Fe-oxide Ti-oxide interface. Compared to the oxidized and nonimplanted 52100, the oxide films greater than 1 μm thick on Ti-implanted steel buckled and cracked.

The heat treatment not only oxidized the Ti-implanted 52100 bearing steel but also fully carburized the implanted layer. The carburization phenomenon was caused by carbon migrating from the bulk substrate at temperatures greater than 400°C.

Heating and oxidizing Ti-implanted 52100 does not improve its frictional behavior, but carburization of the implanted layer may improve wear resistance of Ti-implanted tested at intermediate temperatures (300-400 C).

2 The frictional behavior and the formation of debris were examined for nonimplanted, Ti-implanted, Ti+C-implanted and TiC coated 52100 bearing steel. Tests were performed using a pin-on-disk or Bowden-Leben tester. Correlations of the test data were made between debris and friction.

TEM and Auger studies showed that wear debris consisted mainly of iron oxides, titanium oxides with some metallic iron. Whereas, a mixture of Fe_3O_4 and TiO_2 developed from Ti-implanted surfaces, only Fe_3O_4 was formed on nonimplanted 52100. Debris morphology seemed highly dependent on implantation conditions.

Low friction coefficients, exhibited by Ti- and Ti+C-implanted and TiC coated 52100, were associated with very thin flake debris. The nonimplanted and oxidized implanted substrates formed spherical debris particles and had high friction coefficients.

The friction and wear behavior was successfully related to the debris chemistry, the adhesion of the debris to the surface and the tribomechanical behavior of surface layers.

3. The wear resistance of implanted AISI-304 was studied. Various ions (N^+, Ni^+ or Ne^+) were implanted at $2x10^{17}/cm^2$ dose. The implanted samples wore 20% to 40% less than nonimplanted AISI-304. Auger analysis of the implanted surfaces showed:

- the N-implanted layer has a Gaussian-like profile with enhanced oxidation of the surface;
- the Ni-implanted layer has a sputter-limited implantation profile (due to sputter removal) and some vacuum carburization;
- the Ne-implanted layer profile was also Gaussian-like.

Transmission electron microscopy showed that the initial surface preparation produced a martensite layer in the AISI-304 (mainly austenitic). Implantation of nitrogen changed the martensite into austenite at the surface with an iron-nitride layer beneath. The nitrogen also prevented the austenite to martensite wear transformation.

The martensite layer was sputtered away during nickel implantation. The neon implanted region remained predominantly martensite.

The changes in wear rates and microstructure were limited to depths commensurate with the ion range in the implanted layer.

Varying microstructure of the implanted layers limits the possibility of a specific implantation-induced phase caused by the decrease in abrasion resistance. Therefore, the reduced wear rates may be due to a decrease in ductility of the AISI-304 caused by implanted solutes and irradiation defects.

High Temperature Implantation of Ceramics

The solute redistribution of aluminum and titanium implanted at high fluences and high temperatures into silicon carbide and silicon nitride was studied. Ternary phase diagrams were calculated that were designed to predict complicated compositions from high temperature implantation and ion mixing of metals in ceramics (4), see Appendix A4.

Polished commercial silicon nitride and silicon carbide were implanted with titanium (190 keV) and aluminum (110 keV) at a fluence of 4×10^{17} ions/cm^2, in both room and ~ 600°C (hot) temperatures. X-ray photoelectron spectroscopy (XPS), scanning electron microscopy and energy-dispersive X-ray analysis were employed to investigate near surface composition.

The hot Al-implanted SiC had submicron-size spherical particles, composed mostly of Al, distributed uniformly over the substrate (from SEM and EDX). XPS profiles of hot and room temperature Al-implanted SiC are quite different. The hot implant, after etching of Al spheres, had a uniform Al concentration of 17% to 200 nm depth. The room temperature implant profile was Gaussian-like with a peak concentration of 40% at 110 nm. In contrast, the Al implanted Si_3N_4 had nearly Gaussian profiles for both hot and room temperatures.

The hot Ti-implanted profile in SiC is Gaussian-like; whereas, the hot implant profile in Si_3N_4 showed migration of Si to the surface with TiN formation at two depths.

Ternary phase diagrams were developed from thermochemical data for binary compounds. These ternary phase diagrams were more reliable than the enthalpy rule for predicting ion mixing of metal-insulator pairs.

C. Solid Films Deposited on Metal and Ceramics

Two topics of interest were explored:

- comparison of ion beam assisted to reactive magnetron sputtered deposition;
- behavior of solid lubricating films (molybdenum-disulfide and diamond/diamond-like carbon).

1. Ion Beam Assisted Deposition. Reactive magnetron sputtered (RS) and ion beam assisted (IBAD) titanium nitride films were investigated (5), see Appendix A5. Surface composition, adhesion, and fric-tion/wear were examined. IBAD TiN films were softer and less abrasion resistant than RS TiN films. IBAD films adhered to both steel and ceramic substrates well. Also, IBAD films decreased the friction coefficient by a factor of three.

2. Solid Lubricating Films. Test equipment had to be developed before friction and wear analyses of the solid lubricating films could be performed. GEO-CENTERS modified and automated/computerized the present generation of tribotesters (both data acquisition and control). The enhancements to the testers included writing software (plotting and control/input) and the design of systems that integrated electronic switches, electronic devices and environmental control chambers.

a. Molybdenum-Disulfide. The molybdenum-disulfide research can be divided into three parts:

- SDIO Tribomaterials group round-robin testing for ultra-low friction, high endurance films;
- reproducing Kuwano and Nagai's results (1986) for dual layer MoS_2 films;
- modeling of the load dependency of MoS_2.

SDIO Tribomaterial's round-robin program was to test three differing methods for depositing MoS_2 (Table 1). A series of MoS_2 specimens from each company were supplied to the test locations (each location using its own test) (Table 2). Film friction and endurance were measured. The film with best overall performance would determine the film standard used for SDI program.

The SDIO Tribomaterial program was further divided into two phases. Phase I studied the effects of thickness on friction and endurance. Phase II examined the role of storage time on friction and endurance (note all films were of the same thickness and had experienced similar storage conditions and time).

The data are still being collected and analyzed. The testing summary and overall SDIO Tribomaterial program summary/film handbook is being compiled.

TABLE 1. Films Involved in SDIO Tribomaterial Program

DEPOSITION LOCATION	FILM AND DEPOSITION METHOD
National Centre of Tribology Risley, UK	MoS_2 (rf magnetron sputtered)
Hohman Plating Dayton, OH	MoS_2:Ni (dc triode sputtered)
Aerospace, Los Angeles, CA	MoS_2 (rf diode sputtered)

TABLE 2. SDIO Tribotesting Locations

TESTING LOCATION	TESTER USED
NCT, Risley, UK	Pin-on-disk (three ball) in vacuum
Hohman Plating, Dayton, OH	A-6 tester in air and vacuum
Aerospace, Los Angeles, CA	Flat-on-flat (dry nitrogen)
Naval Research Laboratory Washington, DC	4-ball tester in dry and ambient air; A-6 tester in ambient air; pin-on-disk (one ball) in dry air

One segment of the present program was to reproduce Kuwano and Nagai's dual layer MoS_2 film results. The program involved the deposition and testing of dual layer films formed using NRL's new dual ion-assisted deposition system (DIAD).

These DIAD films are expected, from Kuwano's data, to yield friction values less than 0.01 with long endurance in both low and high humidities. The DIAD films (MoS_2 with a hard interlayer material) have been deposited on metal and ceramic materials at thin film thicknesses ($\leq$ 1 μm).

Preliminary results indicate very good friction ($\leq$ 0.02) and endurance for NRL DIAD films on steel, sapphire and silicon carbide.

Based on data collected from a literature search, MoS_2 exhibits a frictional load dependency (contrary to Amonton's Law). From an analysis of the literature data, a theoretical model for the friction load dependency was developed that had the form:

$$\mu \alpha S_o/L^{\beta} + \alpha.$$

where μ = friction coefficient, S_o = film sheer strength, L = normal load, β is dependent on test geometry, and α is a constant. The literature data and the load dependency model were presented at the 1988 Gordon Tribology Conference (6), see Appendix A6.

Additional data have been collected for MoS_2:Ni films supplied by Hohman Plating (Dayton, OH). The final results are to be presented later.

b. Diamond Films. Diamond promises to be an excellent tribological coating, especially in corrosive environments and in

applications where liquid lubricants cannot be used. Current chemical vapor deposition (CVD) techniques tend to produce coatings with an appreciable amount of non-diamond material (graphite, etc.), and relatively rough surfaces (typically Ra = 0.1 μm). The consequences of this on the tribological behavior have been investigated (7), see Appendix A7.

The coatings generally have a higher friction coefficient than natural diamond. This decreases with continued sliding to a steady value (0.1 - 0.2) by a "run-in" process. The "run-in" can be artificially performed before the tests by mechanical polishing. When this is accomplished, the coatings maintain a steady friction value from the outset of the tests.

The coatings are relatively rough, leading to high wear rates of materials in contact with them, including the diamond styli used in the majority of the GEO-CENTERS tests. The wear can be reduced by polishing or by altering the coating growth conditions.

The coatings contain an appreciable quantity of non-diamond material. Tests have shown that coatings with large amounts of graphite, etc., have higher friction coefficients than their counterparts without non-diamond material.

Experiments have been performed on coatings grown by the oxyacetylene torch method (grown by TA&T personnel). These contain large quantities of non-diamond material, and are very non-uniform. Again, the composition with the greatest proportion of diamond yields the lowest friction coefficient.

Coating surfaces have also been covered with long-chain organic acid which reduces the friction coefficient. Chemical

alteration of the diamond coating's surface should enable low friction coefficients to be achieved without resorting to the organic acid.

REFERENCES

1. S. Fayeulle, I.L. Singer, "Friction Behavior and Debris Formation of Titanium Implanted 52100 Steel," presented at SM2IB Riva, Italy, September, 1988.

2. I.L. Singer, R.A. Jeffries, "Composition and Sliding Contact Behavior of Oxidized Ti-Implanted 52100 Steel," SM2IB Riva, Italy, September, 1988.

3. I.L. Singer, R.G. Vardiman, R.N. Bolster, "Polishing Wear Resistance of Ion-Implanted 304 Steel," J. Mat. Res. 3 (6), Nov./Dec. 1988.

4. I.L. Singer, J.H. Wandass, "Ion-Beam Alloying and Thermochemistry of Ceramics at High Temperatures," presented at NATO-ASI Conference, August 1988.

5. R.N. Bolster, I.L. Singer, R.A. Kant, B.D. Sartwell, C.R. Gossett, "Tribological Behavior of TiN Films Deposited by High Energy Ion Beam Assisted Deposition," April, 1988.

6. I.L. Singer, R.N. Bolster, J. Wegand, S. Fayeulle, "Friction Coefficients-How Low Can They Go?," poster board presentation, Gordon Tribology Conference, June, 1988.

7. I.P. Hayward, I.L. Singer, "Friction and Wear Behavior of Diamond Films on Si," presentation at SDIO Diamond Technology Conference, July, 1989.

II. AIR PURIFICATION

Water vapor is present in all Naval environments involving platforms at sea. The quantity of water vapor in the air varies as a function of temperature. This important fact is reflected in the ever-changing water vapor concentration as a function of geographical location of the ship, time of day/night and season. Reported here is the development of an approach to predict the dynamic behavior of water vapor on an activated carbon adsorbent. A heat balance has been included to account for behavior in high relative humidity environments. Two mathematical models were developed to predict and/or analyze the experimental results. These two models use either a non-isothermal stage model with a fluid phase mass transfer resistance or an adiabatic equilibrium theory model. Water vapor isotherms were measured for BPL carbon at three temperatures and breakthrough experiments were performed at two relative humidities and two bed conditions. The three types of waves (e.g., gradual, abrupt or constant pattern and combined) that can be formed in and passed through an adsorption bed were demonstrated both mathematically and experimentally. The stage model seemed to fairly represent the breakthrough using equilibrium data and a priori calculated rate parameters. Equilibrium theory allowed the exact nature of the transitions to be explored. The inability of equilibrium theory to be used with heat and mass transfer resistances leads to some discrepancy between this method and the experimental results. The details of the development of the two models and the correlation with the experimental results are given in Appendix B1.

The effect of relative humidity on the breakthrough behavior of a particular vapor challenge on ASC-TEDA carbon was examined for



a classified application. The cover sheet of the report and the Table of Contents are included in Appendix B2.

III. CHEMICAL MICROSENSORS

Surface Acoustic Wave (SAW) detectors show great potential as microsensors, which are low power, low cost, rapid and sensitive response and small size. These sensors are being investigated for the detection of and/or discrimination among hazardous, noxious and toxic vapors and liquids. Applications include their use as personnel safety and area monitors. The work on this task has emphasized the development of signal/data processing software for interpretation of results, the investigation of elastic properties of thin polymer films using SAW devices and the field evaluation of SAW sensor array performance.

A. Signal/Data Processing Software

Ten SAW devices were each coated with one of ten polymer materials which were designed to interact with different vapor properties. The ten different coated sensors were exposed to nine different individual vapors and two-component mixtures consisting of combinations of five of the individual vapors with other test vapors (eg. 33 different two component mixtures). The resulting data matrix was examined using pattern recognition techniques. The responses of four of the coatings, common to a previous study, to the single vapors were used as a prediction set to test the classification capacity of the linear discriminant previously developed. All of the vapors were correctly identified except water. Principal components analysis and clustering methods were applied to the responses of the coatings to all the vapors, including mixtures. The individual vapor responses cluster into

specific regions in space, and the mixtures lie in the areas between the clusters. Supervised learning techniques were used to reduce to eight the number of sensors necessary to identify the hazardous vapors in the presence of mixtures. Details of the data acquisition and data reduction and processing methods are found in the article by Rose-Pehrrson, Grate, Ballantine and Jurs in Appendix C1.

B. Elastic Properties of Thin Polymer Films

The responses of thin polymer film coatings on SAW devices have been used to investigate the changes in the elastic properties of the coating materials. The preliminary data indicate that the observed glass transition temperatures (T_g) of several of the thin polymer films (e.g., fluoropolyol, poly(ethylene maleate), ethyl cellulose and poly(caprolactone)) on the surface of the SAW devices were increased by 50-60°C relative to T_g results reported for methods such as differential scanning calorimetry (DSC). These results demonstrate the sensitivity of the SAW device to the elastic properties of polymer coatings. Parameters and effects that can be studied using the SAW are thermal expansion coefficients, glass transition temperatures (T_g), melting temperatures (T_m), thermal activation energies, elastic moduli and plasticization effects. Details of the investigation of elastic property effects are found in the report by Ballantine and Wohltjen in Appendix C2.

C. Field Evaluation of SAW Sensor Performance

Field tests have been conducted to evaluate the performance of SAW devices under shipboard conditions and verify/compare the field results with results obtained in the laboratory. The field tests were performed onboard the ex-USS Shadwell, a decommissioned Navy LSD, moored at Little Sand Island in Mobile Bay, Alabama. The SAW field tests were performed concurrent with simulant dispersal

tests. The simulant used in the tests was diethyl malonate (DEM). The SAW package tested was a 4-SAW array each containing a different coating (i.e. fluoropolyol, ethyl cellulose, poly(isobutylene) and a soluble extract of TENAX-GC). The dispersal tests were monitored using Miniature Infra-Red Analyzers (MIRAN) that sense a minimum detectable concentration of 0.05 ppm. The fluoropolyol sensor gave the best response to the DEM challenge. The performance of the 4-SAW array during field tests closely matched the performance under laboratory conditions. Details of the field tests and the data reduction and comparison process are found in the report by Ballantine, Wohltjen, Thomas and Venezky in Appendix C3.

IV. INTERFACE MODIFICATION AND ANALYSIS

The Navy is vitally interested in utilizing integrated circuit technology that employs a thin (500 nm or less) silicon layer supported by an insulator layer or substrate. The advantage to this approach is the potential to isolate each electronic device from adjacent devices as well as from radiation-induced charging of the substrate. Since defects are generated during material growth and/or processing, the nature of the defects must be identified and characterized. The transmission electron microscope (TEM) is a useful tool for studying defects at the silicon/insulator interface. GEO-CENTERS has used the TEM to study this interface for silicon on sapphire, germanium on sapphire and the bond and etch back process.

X-ray absorption fine structure (EXAFS) spectroscopy is used to examine thin metal films on substrates. The acquired X-ray absorption data has normally been processed using mainframe

computers. The availability of PCs allows the examination of these computer systems to be used to analyze EXAFS data. GEO-CENTERS has converted and/or modified EXAFS data processing and analysis algorithms so they can be employed with a PC.

A. Interface Characterization of Silicon on Insulator Substrates

Silicon on insulator (SOI) substrates are in use for the fabrication of devices that are high speed, resistant to latch up, and radiation hard. The performance of these devices is strongly influenced by the nature of the silicon/insulator interface. Carrier densities, carrier mobilities, defect nucleation, and epitaxial relationships are all effected by the structure of the silicon/insulator interface. GEO-CENTERS' scientists have used their expertise in the structure and chemistry of interfaces in order to characterize these interface effects and to develop new strategies for reducing some of the potentially deleterious effects of heteroepitaxial interfaces on device performance.

One extremely useful technique for studying interfaces is transmission electron microscopy (TEM). Using the ability of the TEM to image the crystallographic details of interfaces and defects on a subnanometer scale, GEO-CENTERS' scientists have made significant progress in understanding and controlling crystalline defects associated with the silicon/insulator interface.

1. Silicon on Sapphire (SOS). Since the inception of silicon on sapphire (SOS) technology, a number of investigations have pursued the deposition of the silicon epilayer by vapor deposition. Only a limited number of these have used molecular beam epitaxy (MBE) as the mode of vapor deposition in SOS. In addition, little attention has been paid to the analysis of the microstructural defects, crystallinity, and the crystalline quality of the resulting silicon epilayer. In collaboration with the NRL

Silicon MBE effort, GEO-CENTERS' scientists have explored this new approach to the growth of SOS.

The most familiar technique for growing SOS is chemical vapor deposition (CVD); the epitaxial silicon grown on sapphire via CVD contains a large volume fraction of microtwins (1-4%). One of the most important measures of microtwins in SOS, the distribution of microtwins as a function of the distance from the silicon/sapphire interface, had not been accurately quantified prior to our efforts. GEO-CENTERS and NRL scientists had developed a new method, based on TEM, for determining the volume fraction of microtwins as a function of distance from the silicon/sapphire interface (1), see Appendix D1. Using this new technique, we have succeeded in defining some of the differences between MBE-grown and CVD-grown SOS. In MBE SOS the volume fraction of microtwins falls off very quickly with the distance from the interface, whereas in CVD SOS, the volume fraction falls off much less rapidly with distance. We have also found that microtwins are more stable in CVD SOS than in MBE SOS (2,3), see Appendices D2, D3. It is our conjecture that the less steep volume fraction profile contributes to microtwin stability in CVD SOS.

Our determination of the volume fraction profile in SOS has also contributed to the understanding of the silicon/sapphire interface. From the volume fraction profile, we have shown how to calculate the amount of strain relief that can be ascribed to microtwins. The most closely matched spacings at the interface differ by 10%, which dwarfs the figure of 0.7% that we have calculated for the maximum strain relief attributable to microtwins (4), see Appendix D4. Therefore, these large strains must be accommodated by a different defect network at the interface, such as a dislocation network. We are currently using TEM to uncover

the structure of such a network, and in so doing arrive at a better understanding of the electronic properties of the interface.

It is clear from our study that the defect structure of MBE SOS is very different from that of CVD SOS. It appears that dislocations in the silicon epilayer are more prevalent in MBE SOS than in CVD SOS (5), see Appendix D5. The difference in the defect distributions between these two different materials may have a profound effect on the electrical properties of these two materials. Indeed, preliminary Hall measurements indicate that MBE SOS has greater carrier mobility than CVD SOS (6). see Appendix D6. A higher mobility is, of course, a desirable parameter in an electronic material.

2. Germanium on Sapphire (GOS). The growth of SOS, at least by CVD, is well established and has played an important role in semiconductor applications. Although the growth of germanium on sapphire has been reported in the past, details regarding the orientation and quality of the film were completely lacking. GEO-CENTERS and NRL scientists, however, have successfully developed and characterized single crystal, MBE-grown germanium on sapphire. The single crystal nature of the film has been confirmed by both TEM and X-ray diffraction observations. In addition, X-ray diffraction measurements indicate that germanium epitaxial layer in GOS is remarkably unstrained (7), see Appendix D7.

3. Bond and Etch Back. We have already indicated that one of the challenges in growing SOS for electronic device applications is in the control of crystalline defects. There is, however, an intrinsic problem in the control of defects in a heteroepitaxial system such as silicon on sapphire. Due to the great difference between the substrate and the epilayer, layer by layer growth is not possible. Indeed, equilibrium thermodynamics dictates that



island growth must be favored over layer by layer growth. A number of studies indicate that microtwin and dislocation nucleation can be ultimately traced to islanding acting as the predominant growth mode. Given these problems associated with the heteroepitaxial growth strategies such as SOS and GOS, one is tempted to consider other approaches to achieving good silicon on insulator growth.

One process that does not rely on heteroepitaxial growth is that of SIMOX (Silicon IMplanted with OXygen). This material is fabricated by oxygen implantation and annealing to generate a buried oxide. Although SIMOX is a promising technology, threading dislocations generated by the implantation in the active device region limit the performance of the material. In addition, the buried oxide is of poor quality and results in back channel leakage.

Bond and etch back technology as an alternative to SIMOX for SOI has the advantage of a cleaner oxide/silicon interface at the buried oxide. This material is generated by oxidizing two silicon wafers, followed by bonding the two wafers. The active device region is exposed on one of the wafers by precision machining and etching to the desired film thickness. Although this technology is suitable for the fabrication of a 600 nm thick silicon layer, the presence of an etch stop is essential to fabricating SOI wafers with a silicon film thickness of 250 nm or less. Heavily doped boron regions, placed by diffusion or implantation into the silicon, have been reported to make an effective etch stop, although not without the generation of threading dislocations in the device region. In addition, both diffusion and implantation result in residual p-doping. A potential solution to these problems is through the use of an as-grown silicon-germanium alloy strained layer as an etch stop. Indeed, we have recently shown



that a silicon-germanium layer functions very well as an etch stop for the bond and etch back process (8), see Appendix D8.

GEO-CENTERS contributed to this program via a TEM-based study of the silicon-germanium etch stop. In our analysis of the etch stop, we observed that the generation of dislocations was confined to the 50 nm thick strained layer. We were not able to observe any dislocations generated in the silicon cap. This is an especially important observation, since this silicon cap will ultimately become the surface layer (and therefore the device region) of the bond and etch back material.

REFERENCES

1. M.E. Twigg and E.D. Richmond, J. Appl. Phys. 64, 3042 (1988).

2. M.E. Twigg, E.D. Richmond, and J.G. Pellegrino, Mat. Res. Soc. Symp. Proc. 138, 409 (1989).

3. M.E. Twigg, E.D. Richmond, and J.G. Pellegrino, Appl. Phys. Lett. 54, 1766 (1989).

4. M.E. Twigg, E.D. Richmond, and J.G. Pellegrino, submitted to J. Appl. Phys.

5. E.D. Richmond, M.E. Twigg, A.R. Knudson, S. Qadri, and N. Green, submitted to Thin Solid Films.

6. E.D. Richmond, J.G. Pellegrino, M.E. Twigg, B. Mrstik, and M.T. Duffy, submitted to Appl. Phys. Lett.

7. D.J. Godbey, S.B. Qadri, M.E. Twigg, and E.D. Richmond, Appl. Phys. Lett. 54, 2449 (1989).

8. D. Godbey, H. Hughes, F. Kub, M. Twigg, L. Palkuti, P. Leonov, and J. Wang, submitted to Appl. Phys. Lett.

B. X-ray Absorption Fine Structure (EXAFS)

EXAFS spectral data processing has normally been performed using mainframe computers. The advent of fully 32-bit 25MHz PCs with 4 megabytes of core memory and more allows for down-loading of long Fortran codes (5000 lines and more of code). The EXAFS mainframe data processing/plotting/analysis program was modified to operate on an American "micro"-Frame Technologies PC using the Lahey F771-EM/32 Fortran compiler (ANSI-77 standard) and HGRAPH plotting software.

Modifying the mainframe EXAFS Fortran code to run on a PC proceeded in three steps: 1) recompiling the mainframe Fortran EXAFS code using the Lahey F771-EM32 Fortran compiler; 2) acquiring Fortran for several IMSL subroutines; and, 3) replacing all graphics commands in the plotting subroutines.

Recompiling the mainframe EXAFS program was a simple task because of the Lahey PC compiler. The original program was written for a VAX 700 series computer. The programmers did not stray from the ANSI-77 standard into VAX specific commands with the exception of three options related to file open and close statements. The incorrect Fortran statements were presented on the screen by the compiler during the first attempt to recompile. Simply changing DISP to STATUS in close commands and removing ORGANIZATION = 'RELATIVE' and RECORDTYPE = 'FTXED' from the open commands allowed the program to compile without error. A fourth problem was encountered when the three (EXAFS code, IMSL, and Graphics) parts of the code were linked to create an executable module. When writing format statements for the VAX, one may use as a spacer either X or 1X. The Lahey compiler/linker package requires the use of 1X.



Before linking the compiled PC code we needed Fortran code for several IMSL subroutines required by the EXAFS program. Fortran code was extracted from a 1982 version of the IMSL library stored on a VAX at NRL and available for public use. A list of the required programs appears in Table 1. The IMSL Fortran code compiled errors in the UERSET, UERTST, UGETIO, and USPKD subroutines. The errors related to use of character strings in ways which the Lahey compiler could not process. It was determined that the tasks these subroutines performed were unnecessary and could be eliminated. These programs performed internal IMSL "bookkeeping" that in no way affected the computations provided by the required IMSL subroutines.

Table 1. Required IMSL Subroutines

ICSSCU.FOR;1	LUREFN.FOR;1
LEQT1P.FOR;1	UERSET.FOR;1
LEQT2F.FOR;1	UERTST.FOR;1
LINV2F.FOR;1	UGETIO.FOR;1
LUDATN.FOR;1	USPKD.FOR;1
LUDECP.FOR;1	VCVTSF.FOR;1
LUELMN.FOR;1	VXAAD.FOR;1
LUELMP.FOR;1	VXMUL.FOR;1
	VXSTO.FOR;1

The changes to the graphics associated with EXAFS code were dictated by the Lahey compiler/linker package. At the beginning of this project, Heartland Software, Inc. provided the only second party graphics software compatible with Lahey's EM/32 system. The modification to the plotting routines was extensive. We started with a working knowledge of the plots which could be generated by the mainframe program. Five examples of plots used in the determination of the final chi plot for the EXAFS program are shown in Figures 1-5. These figures were generated by the new PC version of the EXAFS program. Figures 6 and 7 are examples of plots from the original mainframe program as presented on a Tektronics 4014

screen or from Tektronics PC emulator, respectively. The essential information presented in Figures 6 and 7 can be compared to that in Figure 4.

The original graphics code was separated into two parts: 1) code which determined labels and axis max and min ranges, etc., and 2) any code which was dependent on GINO mainframe graphics object library. The latter code was completely removed and replaced by graphics calls provided by Heartland's HGRAPH software. HGRAPH documentation allowed easy reconstruction of all on-line graphics. The command GRAPHBOUNDARY (2000, 8000, 1000, 5200) creates the box around the graph within the bounds of the HGRAPH "screen". SCALE (XMIN, XMAX, YMIN, YMAX) (note the use of variables from mainframe code) determined the X and Y range of the data. Each of the commands required has a sensible name and can be easily incorporated into a Fortran plotting subroutine. Appendix E1 includes a copy of each of the subroutines as written to operate in the PC environment using the HGRAPH software. An example of the mainframe code is included as Appendix E2 for comparison.

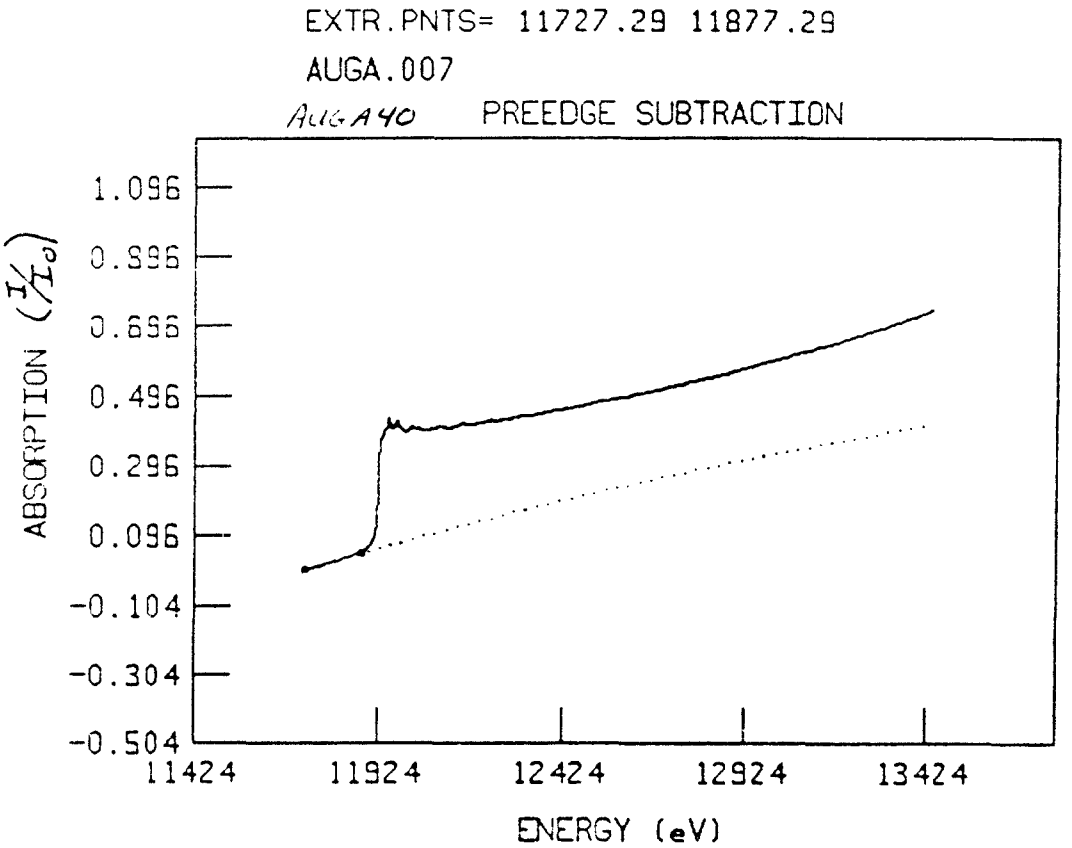


FIGURE 1: Experimental EXAFS data and background extrapolation from the pre-edge.

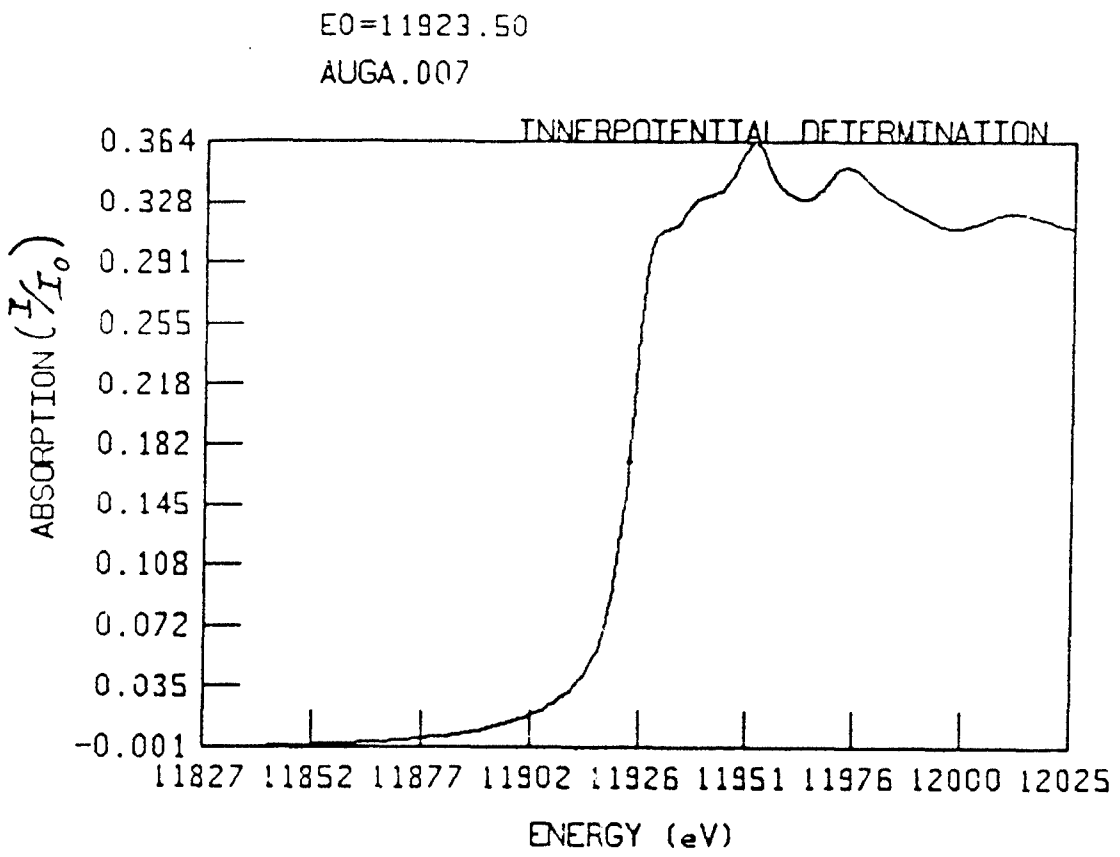


FIGURE 2: EXAFS data after pre-edge subtraction.

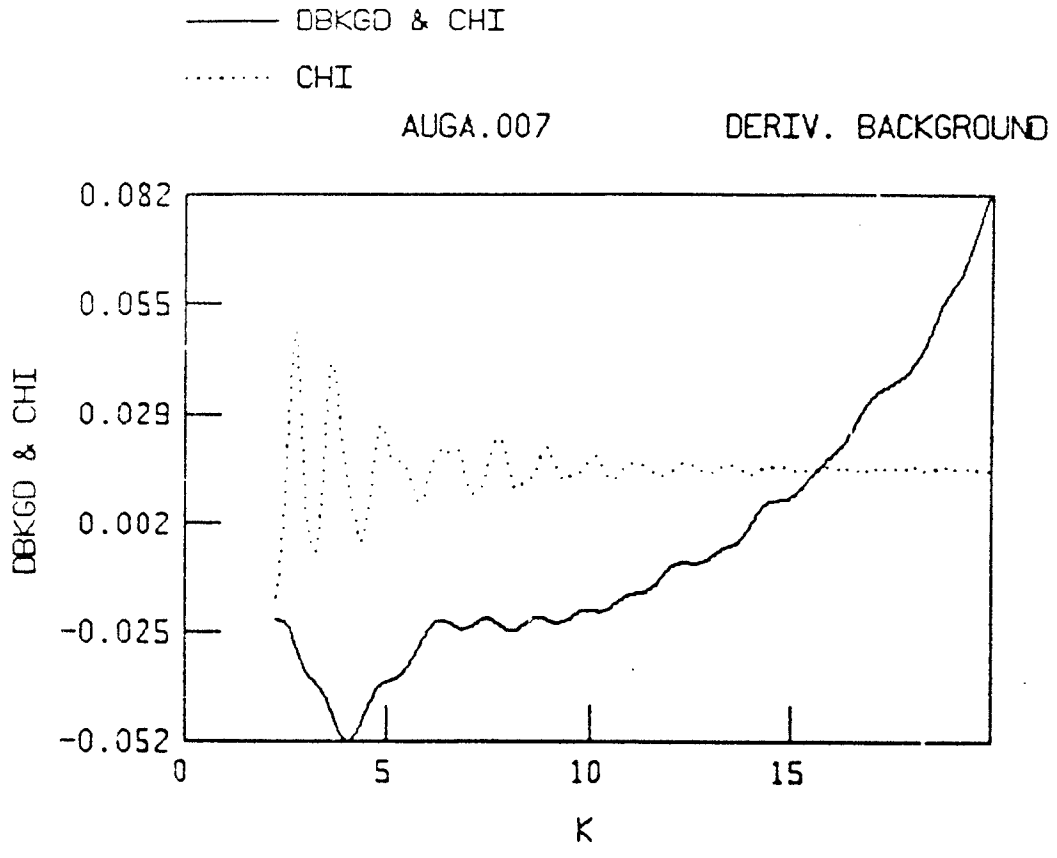


FIGURE 3: EXAF's Chi file (now in phase space) and the derivative of the background.

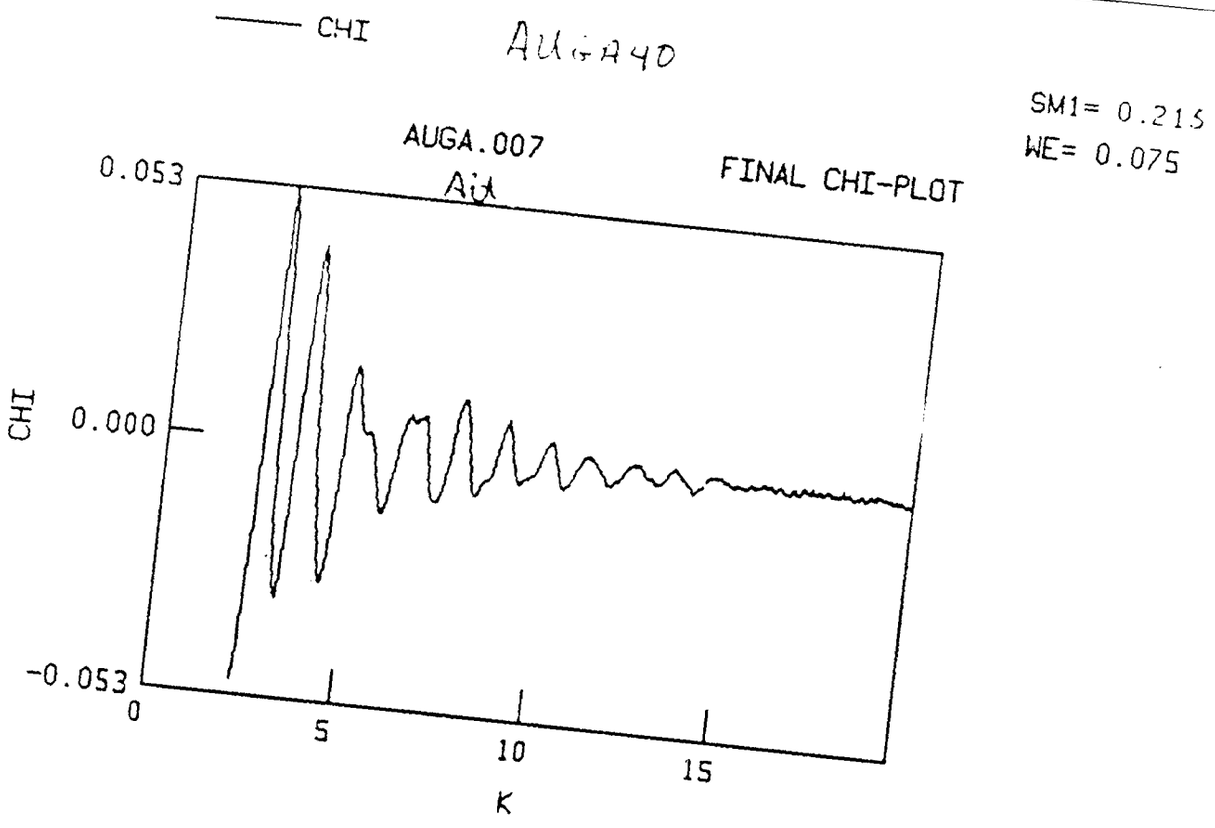


FIGURE 4: Final Chi plot.

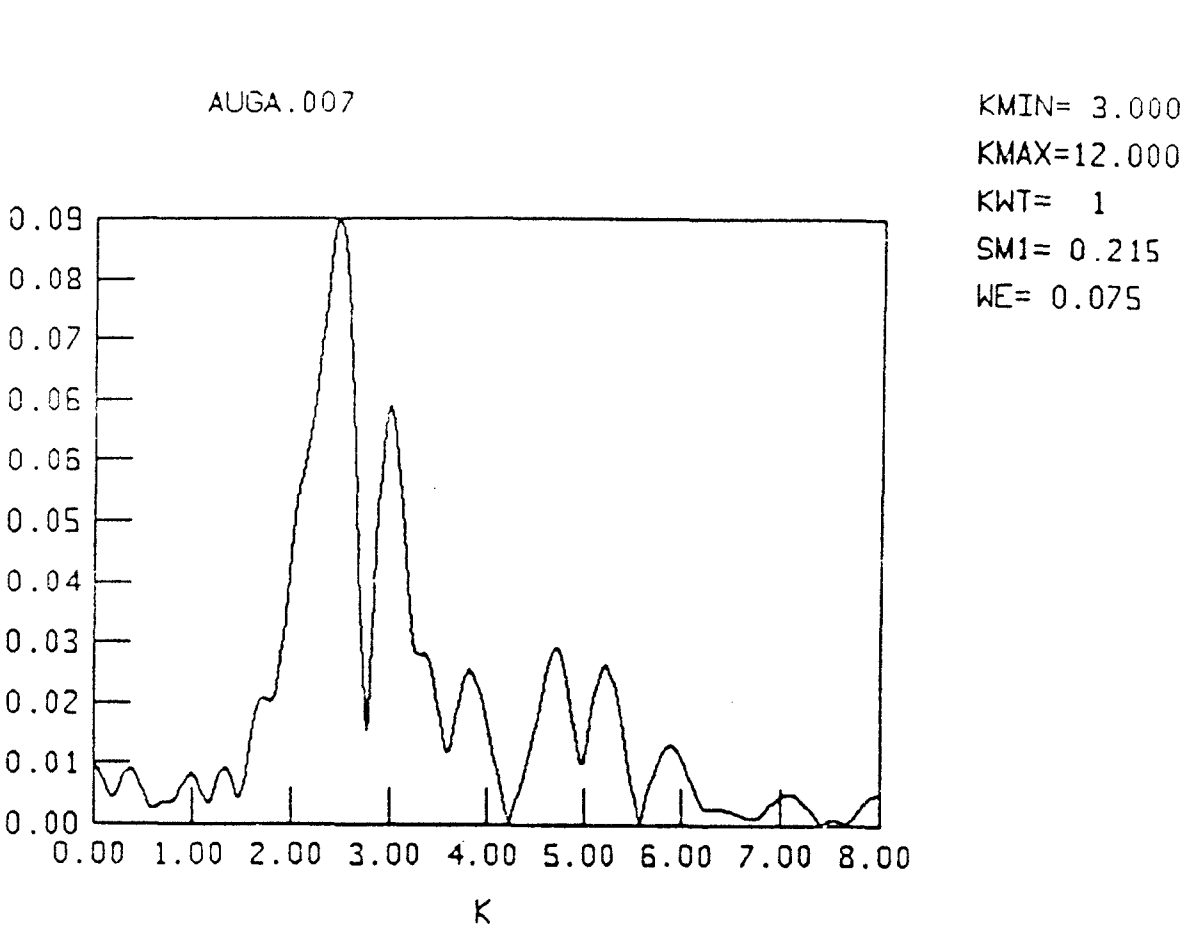


FIGURE 5: Fourier Transform of background subtracted EXAFS data.

GEO-CENTERS, INC.

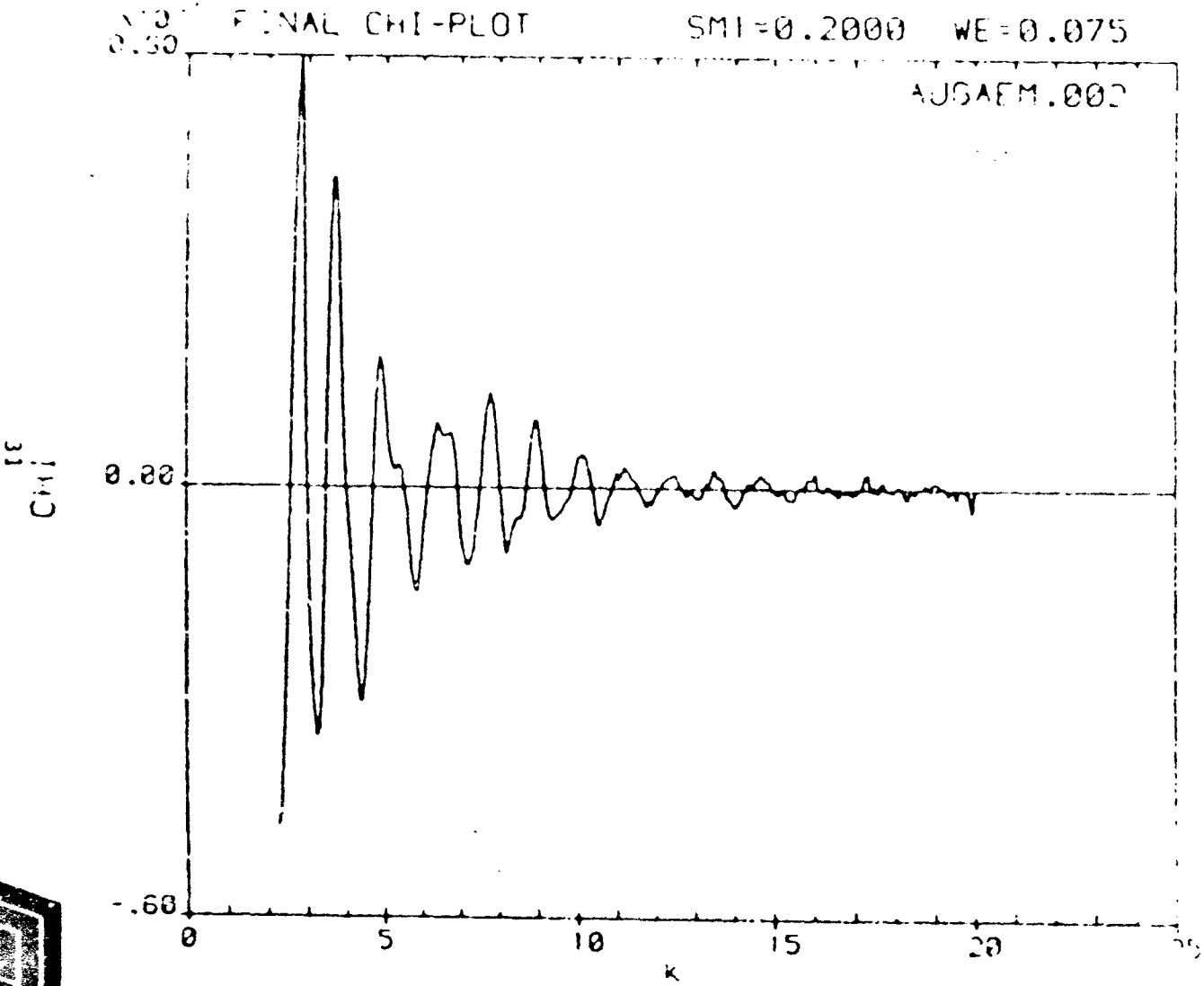


FIGURE 6: Plot generated for Tektronics 4014 scope.
Compare to Figure 4.

GEO-CENTERS, INC.

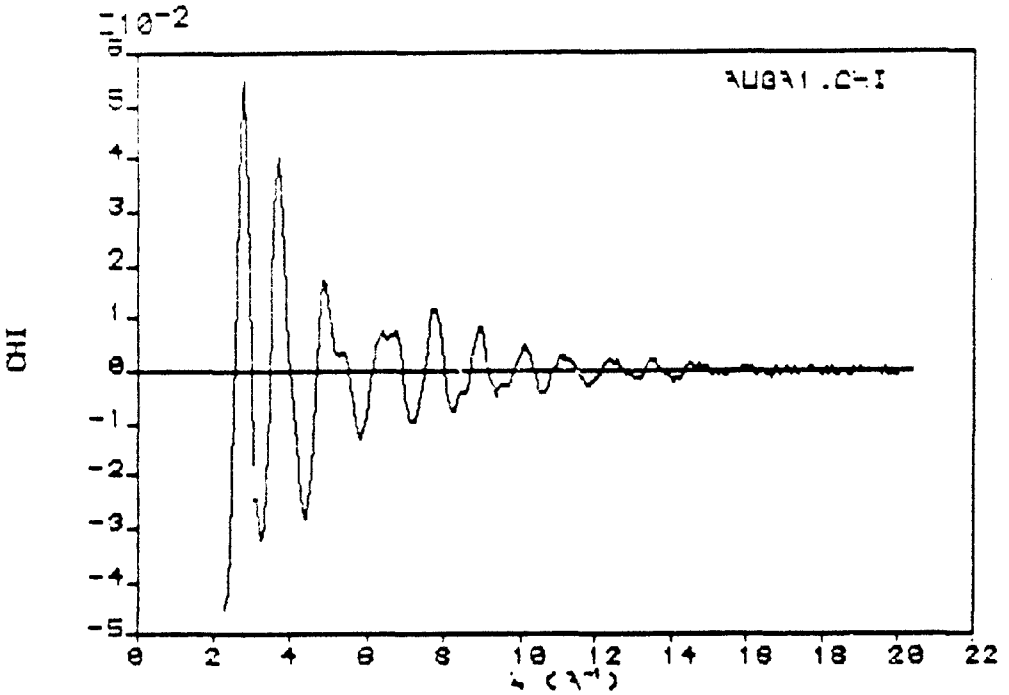


FIGURE 7: Plot generator by Tektronic PC emulator. Compare to Figure 4.

GEO-CENTERS, INC.

V. SOLUTION KINETICS AND MECHANISMS

Work on this task has concentrated on identifying and characterizing the cause(s) of and finding methods/techniques for suppressing intermodulation interference (IMI) onboard Navy surface ships, studying electrochemically active transition metal complexes that can be employed as catalysts for the conversion and/or decomposition of dissolves gases (CO_2, NO) and other small molecules, and developing/writing of programs for analytical instruments such as the Varian CARY 2390.

A. Intermodulation Interference Studies

See Appendix F.

B. Electron Transfer in Transition Metal Complexes

See Appendix F.

C. Software Programs for the CARY 2390

The Varian CARY 2390 spectrophotometer is a high quality, microprocessor controlled analytical instrument intended for measurements of the UV-Visible-Near IR absorption spectra of solids, liquids and gases. When equipped with an optional IEEE-488 standard interface, these instruments and their accessories are programmable and accessible by an external computer system. The use of an external computer capability enables instrument control and acquisition of spectra measurements in digital form, the editing and manipulation of spectral data and provides flexible plotting facility, plot documentation and the production of presentation material.

Three (3) programs have been written and implemented for external computer control and manipulation of data from the CARY

2390. These three programs are referenced as CARYSPEC, EDITSPEC, AND PLOTSPEC and are included as Appendices G1, G2 and G3, respectively.

APPENDIX A1

Friction Behavior and Debris Formation of Titanium-implanted 52100 Steel*

S. FAYEULLE†

Geo-Centers, Inc., 10903 Indian Head Hwy, Ft. Washington, MD 20744 (U.S.A.)

I. L. SINGER

Code 6170, U.S. Naval Research Laboratory, Washington DC 20375 (U.S.A.)

(Received September 16, 1988)

Abstract

The friction and wear behavior of titanium-implanted bearing steel (AISI-52100) has been shown to depend critically on the near-surface composition, as determined by the implantation conditions. Friction, in turn, is believed to be controlled by wear debris, which have been found to consist mainly of oxides. In order to investigate the role of oxides, transfer films formed on non-implanted, titanium-implanted and oxidized substrates have been characterized by transmission electron microscopy and by Auger spectroscopy. Wear debris contained mainly iron oxides and titanium oxides and, occasionally, metallic iron. A mixture of $Fe_2O_3 + Ti_2O_3$ was obtained from a Ti^+-implanted surface. Fe_3O_4 debris also developed in non-implanted substrates, but not in titanium-implanted substrates. The morphology of wear debris was highly dependent on the implantation conditions. Very thin flake debris were seen after Ti^+ and $(Ti^+ + C^+)$ implantation (and on TiC-coated steel) and are associated with low friction coefficients. Spherical debris were formed from non-implanted substrates and oxidized implanted substrates. Friction coefficients and wear behavior will be discussed in terms of chemistry of debris, adhesion between surface and debris, and the tribomechanical behavior of superficial layers.

1. Introduction

Titanium implantation into steels, under special processing conditions, can produce an unusually low friction surface with very low wear [1-5]. Singer has shown that the low friction on these optimally processed surfaces of type 52100 steel correlates with the presence of a high carbon concentration at the oxide-metal interface [6, 7], brought about by vacuum carburization during implantation [8]. Earlier studies revealed that insufficient carbon at the surface led to adhesive-type wear and high friction [2]. Recent studies have indicated that oxidation of these low friction surfaces leads to higher friction, without loss of the titanium-implanted layer [9].

In this paper we attempt to explain the role of the vacuum-carburized layer in the origins of low friction. We do this by determining the composition and structure of debris formed during low and high friction sliding contact and identifying the wear modes that produce the debris.

2. Experimental details

Disks of hardened 52100 steel were polished and implanted in NRL's modified Varian Extrion implanter. During implantation, disks were kept near room temperature owing to a water-cooled holder. The target chamber was cryogenically pumped to a base pressure of 5×10^{-7} Torr. Samples were implanted with a $^{48}Ti^+$ beam (at current densities of 10-20 $\mu A\ cm^{-2}$) to a fluence of 5×10^{17} Ti cm^{-2} at an energy of 190 keV. One Ti^+-implanted sample was also implanted with carbon (3×10^{17} C cm^{-2} at 50 keV) and another was oxidized at 300 °C for 1 h.

Friction measurements were carried out in air (30% relative humidity, room temperature) on a Bowden-Leben type tester (sliding speed, 0.1 mm s^{-1}) or on a pin-on-disk machine (sliding speed 8 mm s^{-1}). Bowden-Leben tests consisted of repeated, unidirectional sliding on a

*Paper presented at the Sixth International Conference on Surface Modification of Metals by Ion Beams, Riva del Garda, Italy, September 12-16, 1988.

†Visiting Scientist at NRL from Laboratoire de Metallurgie UA CNRS 447; Ecole Centrale de Lyon BP 63, 69131 Ecully Cedex (France).

0921-5093/89/$3.50

© Elsevier Sequoia/Printed in The Netherlands

single track 5 mm long, whereas pin-on-disk tests produced continuous contact along a circular track. Hardened 52100 steel balls (12.3 mm in diameter) were loaded to 9.8 N (mean Hertzian stress of 0.54 GPa) and slid against non-implanted and implanted disks as well as a TiC-coated M2 steel disk.

At the end of the friction tests, wear scars and the debris generated during sliding contact were examined by optical (Nomarski) and electron microscopy. Wear scars were analyzed by Auger sputter depth profiling, using the techniques described previously [2, 10]. Wear debris on the balls were removed with cellulose acetate film, softened by acetone, then stripped from the surface. The film plus debris was coated with carbon and placed on copper grids. The cellulose acetate film was then dissolved in acetone, leaving the debris in a carbon frame on the copper grids. Debris were examined in a 200 CX scanning transmission electron microscope and characterized by electron diffraction and energy dispersive X-ray (EDX) analysis.

3. Results

3.1. Friction and wear behavior

Two types of friction and wear behavior were observed. With the TiC coating and the $(Ti^+ + C^+)$- and Ti^+-implanted disks, the friction coefficients remained low (0.15–0.3) and the "wear" was limited to debris particles attached to the ball. Very little or no debris particles were found in the wear track. With the oxidized Ti^+-implanted disk and the non-implanted disk, steady state friction coefficients were high (0.5–0.6) and "wear" was observed as debris particles attached to both ball and wear track (initially, the friction coefficient of the oxidized implanted disk was low but rose steadily to 0.5 after 5–7 passes). Figure 1 shows optical micrographs of debris on ball and in the wear track for selected cases of the two types: Fig. 1(a) was taken after 1000 passes (pin-on-disk) against a $(Ti^+ + C^+)$-implanted disk and shows that virtually no debris accumulated in the wear track. Figure 1(b) was taken after 15 passes

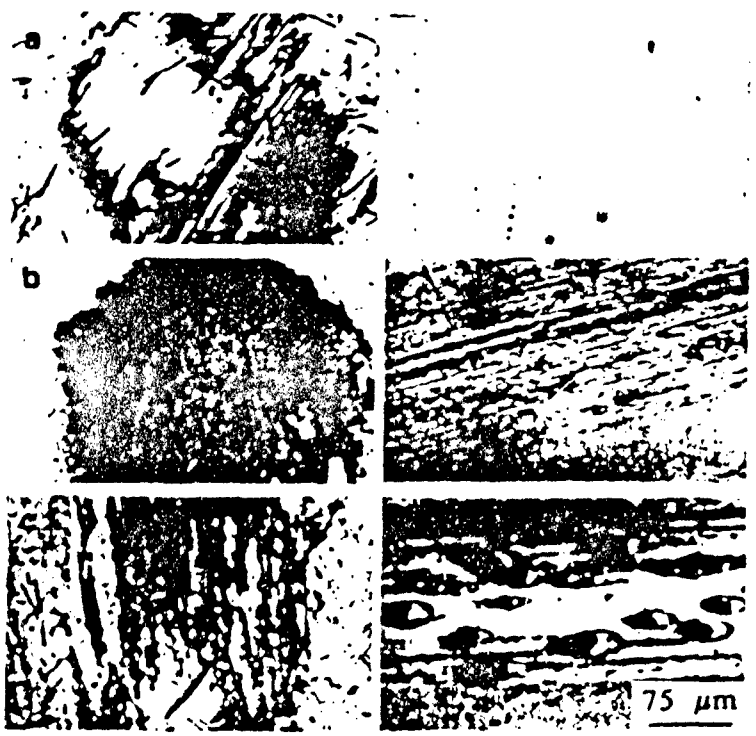


Fig. 1. Optical (Nomarski) micrograph of wear scars on ball (left) and track (right) for: a) $(Ti^+ + C^+)$-implanted 52100 steel after 1000 passes; b) non-implanted 52100 steel after 15 passes; and c) oxidized Ti^+-implanted 52100 steel after 15 passes.

(Bowden–Leben) against a non-implanted disk and illustrates that debris covered most of the wear track. Figure 1(c) shows debris after 15 passes (Bowden–Leben) against oxidized Ti^+-implanted steel. The debris formed only after the friction coefficient exceeded 0.4. Nomarski microscopy revealed that each of the rather large debris flakes consisted of a rough (dark) patch of material at back and a smooth (light) area in front.

3.2. *Morphology of debris*

Flakes of debris stripped from the contact spot on ball sliders were examined by transmission electron microscopy (TEM). In each case, flakes consisted of an agglomeration of submicron-sized particles. However, the morphologies of the flakes from the low-friction surfaces were different from those of the high-friction surfaces. Flakes from the three low-friction substrates appear to be made of stacks of angular-shaped platelets, several micrometers in diameter. Examples of this morphology for Ti^+- and ($Ti^+ + C^+$)-implanted disks at intermediate magnification are seen in Figs. 2(a) and 2(b), respectively. At higher magnification (Fig. 2(c)), the flakes appear rather uniformly transparent and have no boundaries or interfaces, suggesting that they are made up of thin, uniformly thick platelets. These platelets, in turn, are an agglomeration of nanometer-sized particles, as seen in the dark-field micrograph of Fig. 2(d). Flakes obtained from the TiC-coated disk had the same morphology as implanted-disk debris.

Flakes from the high friction surfaces showed nanometer-sized particles, similar to those described above. TEM also revealed that these very fine particles agglomerate to form an intermediate structure, not seen in the low-friction flakes. The intermediate structure, presented in Fig. 3(a), consists of spherical particles 0.1 μm in diameter. Collection of these balls, in turn, gives the very irregular flakes shown in Fig. 3(b) (debris from the non-implanted surface) and Fig. 3(c) (debris from the oxidized implanted surface).

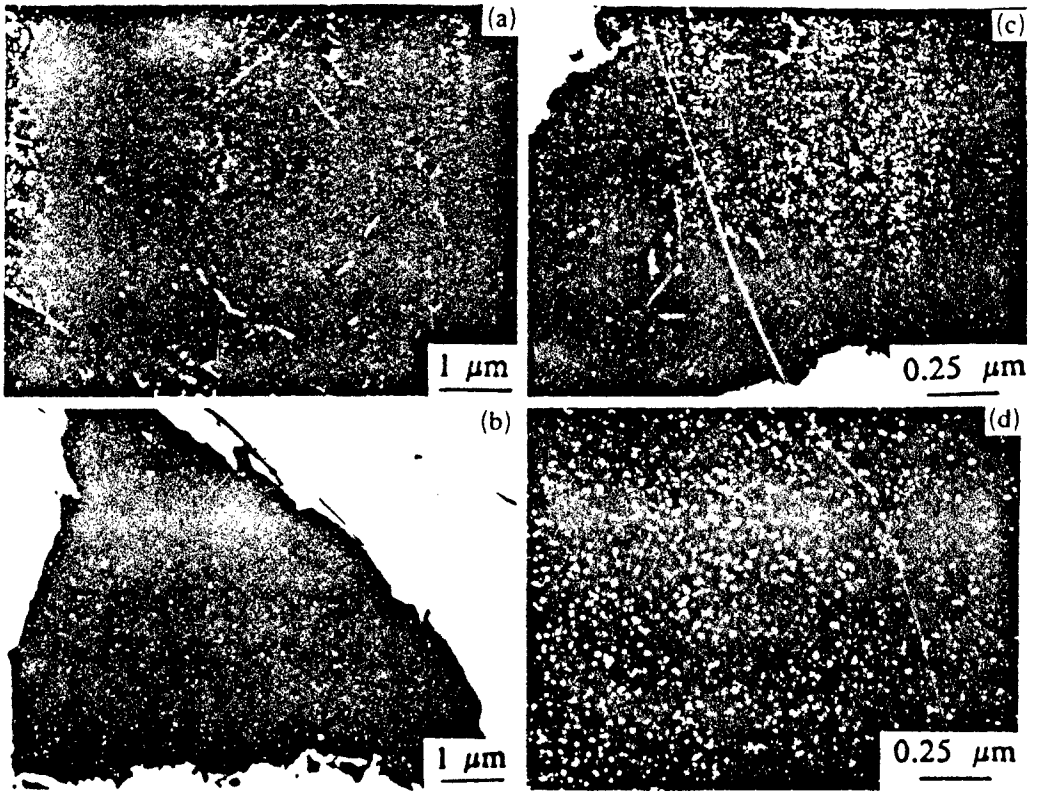


Fig. 2. TEM micrographs of debris flakes stripped from balls worn against low-friction implanted surfaces: (a) Ti^+-implanted; (b), (c), (d) ($Ti^+ + C^+$)-implanted.

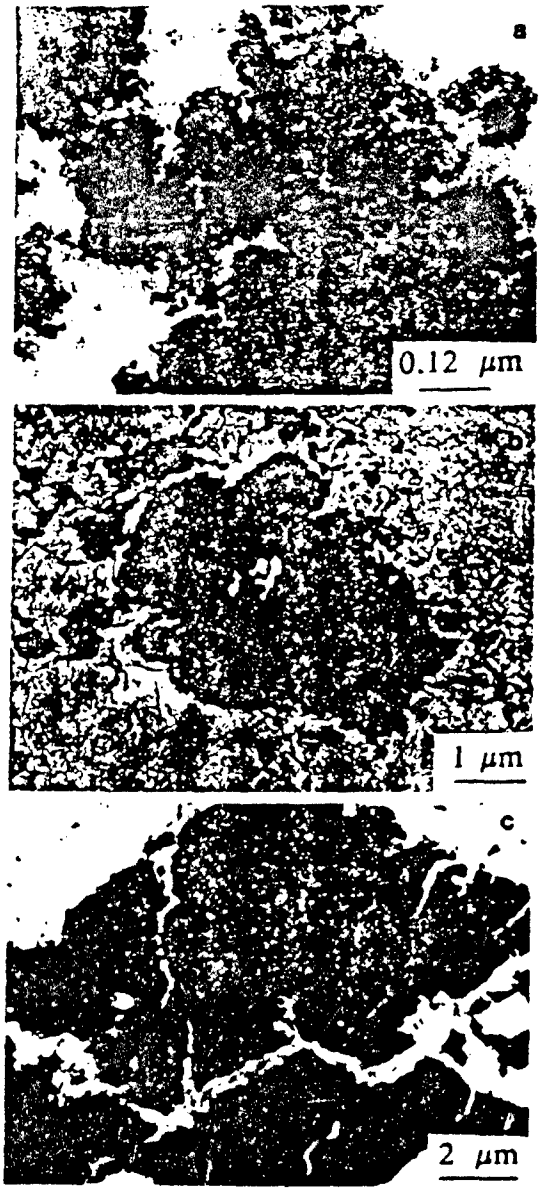


Fig. 3. TEM micrograph of debris flakes stripped from balls worn against high-friction surfaces: (a), (b) non-implanted; (c) oxidized Ti^+-implanted.

3.3. Composition of the wear debris

Electron diffraction of debris flakes from the low-friction titanium-implanted samples revealed an Fe_2O_3 structure, and EDX analysis showed a considerable amount of titanium. The debris was probably a mixture of Fe_2O_3 and Ti_2O_3 (which have very close lattice spacings) or $(FeTi)_2O_3$. The same mixed structure is seen in the debris from the $(Ti^+ + C^+)$-implanted disks. In addition, after longer tests (1000 passes per 25 m) other rings were detected, corresponding to a Fe_2O_3 or Fe_2TiO_5 structure. Diffraction patterns of the flakes obtained from the TiC-coated sample showed mainly Fe_2O_3 plus small amount of non-oxidized iron, but again EDX analysis revealed some amount of titanium, indicating that the debris came not only from wear of the ball but also from wear of the coating.

Electron diffraction patterns from the high-friction non-implanted steel showed that wear debris were predominantly iron oxide having the Fe_3O_4 structure with varying amounts of Fe_2O_3 (the rings of Fe_3O_4 were always more intense). Addition spot patterns having an hexagonal structure ($a = 0.275$ nm, $c = 0.435$ nm) were seen and attributed to the ε carbide phase in 52100 steel. Debris obtained from the oxidized titanium-implanted sample also contained mixtures of Fe_2O_3 and Fe_3O_4.

Auger analysis of the wear track on the oxidized Ti-implanted disk are presented in Fig. 4. Depth profiles were taken at the spots designated by letters (a–d) shown in the scanning electron photograph. The rougher, black part (Fig. 4(a)) was mainly iron oxide (plus a little bit of titanium oxide) whereas the smoother, gray part (Fig. 4(d)) had a composition similar to the unworn, oxidized layer (Fig. 4(b)). Comparison of the profiles inside (Fig. 4(c)) and outside (Fig. 4(b)) the track indicates that only the oxide layer was removed during sliding, which resulted in titanium enrichment of the surface. (The composition of the oxidized titanium-implanted layer is discussed more fully in [9].)

4. Discussion

TEM analysis of debris generated during high-friction sliding contact is consistent with the oxidative wear behavior of 52100 steel. Steel surfaces undergo accelerated oxidation under sliding contact [11, 12]. At a critical thickness, depending on the model used, oxidized flakes break free from the surface, creating a debris particle. Because there exists a gradient in the oxygen concentration from the surface into the bulk, one expects these particles to have a substoichiometric composition. In addition, since the outermost oxides occupy a larger volume than the metal below (Fe_2O_3 has twice the molecular volume of iron [13]), flakes will be under stress,

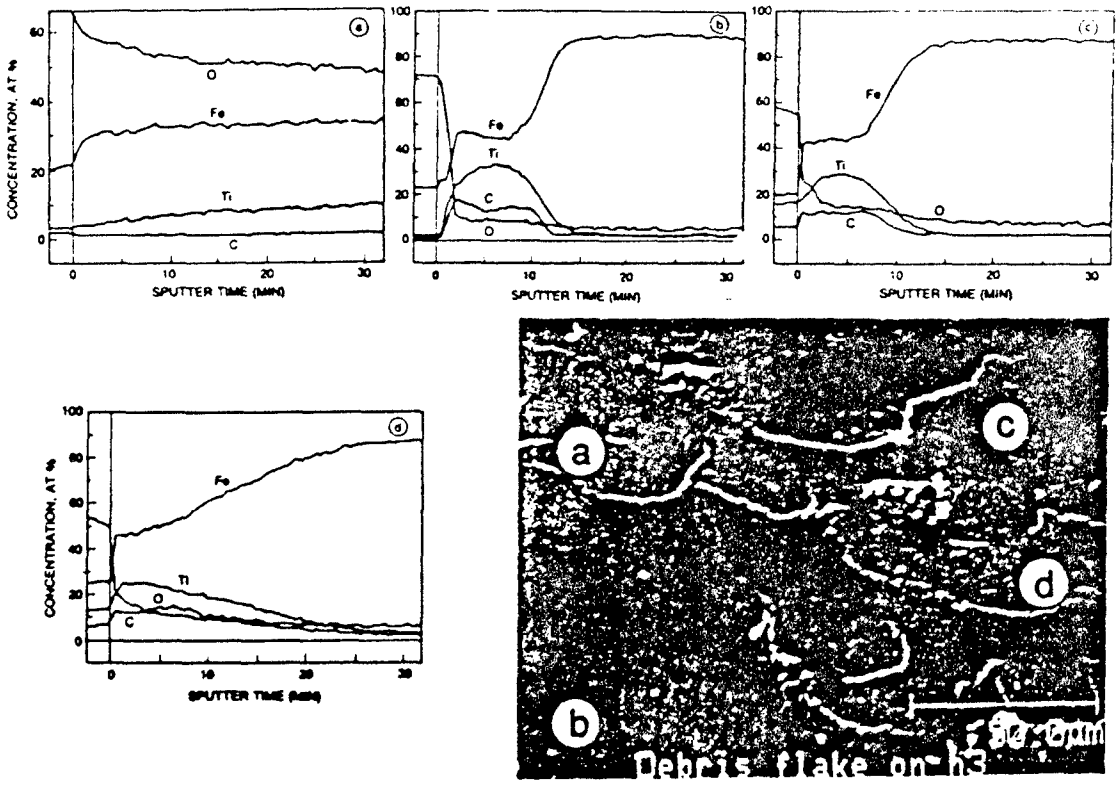


Fig. 4. Scanning electron micrograph and Auger analysis of selected areas of a fifteenth pass wear scar on oxidized, Ti^+-implanted steel: (a) Auger profile on the black part of the debris; (b) Auger profile in the wear scar; (c) Auger profile on the unworn surface; (d) Auger profile on the gray part of the debris.

causing them to curl. Both these features, substoichiometric Fe_3O_4 phase and spherical morphology, were demonstrated in the TEM studies.

TEM analysis of debris from TiC-coated and Ti^+ or $(Ti^+ + C^+)$-implanted steel suggests the following wear mode for low-friction surfaces. The thin outermost iron oxide layer of titanium-implanted steel, shown by Auger analysis to have the same Fe_2O_3 composition [1] found on air exposed steel [14], is sheared at the Fe-Ti-C interface during sliding contact. These very thin oxide platelets (approximately 1-2 nm thick [15]) collect on the ball and form a debris particle. TEM analysis of these debris stripped from the ball showed Fe_2O_3 particles having platelet morphology. These debris did not transfer to the wear track during subsequent passes probably because of the ease with which shear occurs at the Fe-Ti-C layer.

After oxidation of the titanium-implanted surface, sliding contact produced oxidative wear, generating spherical Fe_3O_4 debris, as determined by TEM. But the friction coefficient was initially low, which means that the easily sheared plane achieved by implantation was not completely eliminated by oxidation. The transition from easy shear and low-friction coefficients to oxidative wear and high-friction coefficients was accompanied by debris accumulation in the wear track. This accumulation can be described by a three-step process: first, a subtle change in chemistry at the Fe-Ti-C interface—the titanium level was enriched, compared with the carbon level (Fig. 4(c)); second, enhanced adhesion—we know from earlier studies that oxide particles adhere more strongly to a titanium-rich layer [2, 16]; and third, ploughing—once adhered, the oxide debris transmit higher stresses locally to the surface, ploughing the implanted layer and causing the surface to bulge in front. This ploughing action is evident in the Nomarski micrograph of the wear track (Fig. 1(c) right).

The correlations obtained between the wear modes and friction coefficients suggest a model for the friction and wear behavior of steel sur-

faces. The friction coefficient is the sum of two terms. The first term corresponds to the shearing of the superficial oxide films and is probably similar for all substrates since the primary wear particles are always the very small oxide crystallites. This term has a value around 0.2, the value predicted by Bowden and Tabor [17] for the interfacial shear of weakly adhering junctions. The second term accounts for the adhesion of wear debris to the ball and the track and the mechanical resistance (deformation and ploughing) produced by the adherent wear debris. This last term is in the process of being modelled.

5. Summary and conclusions

The friction behavior of titanium-implanted (and TiC-coated) steel surfaces has been correlated to the morphology and chemistry of the debris flakes produced during dry sliding. Low-friction surfaces (Ti^+- or ($Ti^+ + C^+$)-implanted and TiC-coated steel) produced platelets of $(FeTi)_2O_3$ debris; high-friction surfaces (non-implanted and oxidized titanium-implanted steel) generated agglomerates of mainly Fe_3O_4, compacted ball debris. The platelet debris tended not to transfer to the wear track during low-friction sliding, whereas the ball debris adhered to the track when the friction coefficient exceeded 0.4. Higher friction coefficients observed with oxidized titanium-implanted steel were attributed to titanium-enrichment of the surface. These observations provide evidence, in place of earlier speculations, that the low-friction coefficients obtained with high-fluence titanium implantation are related to easy shear and low adhesion at the Fe–Ti–C interface in the implanted surface.

References

1 I. L. Singer, C. A. Carosella and J. R. Reed, *Nucl. Instrum. Methods, B2/B3* (1984) 923.
2 I. L. Singer and R. A. Jeffries, *J. Vacuum Sci. Technol. A, 1* (1983) 317.
3 L. E. Pope, F. G. Yost, D. M. Follstaedt, J. A. Knapp and S. T. Picraux, in K. C. Ludema (ed.), *Wear of Materials*, ASME, New York, 1983, p. 280.
4 T. E. Fischer, M. J. Luton, J. M. Williams, C. W. White and B. R. Appleton, *ASLE. Trans., 26* (1983) 466.
5 F. M. Kustas and M. S. Misra, *Thin Solid Films, 122* (1984) 279.
6 I. L. Singer and R. A. Jeffries, *ASLE Trans., 28* (1985) 134.
7 I. L. Singer and R. A. Jeffries, *Appl. Phys. Lett., 43* (1983) 925.
8 I. L. Singer, *J. Vacuum Sci. Technol. A, 1* (1983) 419.
I. L. Singer and T. M. Barlak, *Appl. Phys. Lett., 43* (1983) 457.
9 I. L. Singer and R. A. Jeffries, *Mater. Sci. Eng., A114* (1989).
10 I. L. Singer, *Appl. Surf. Sci., 18* (1984) 28.
11 T. F. J. Quinn, in N. P. Suh and N. Saka (eds.), *Fundamentals of Tribology*, MIT Press, Cambridge, Mass., 1980, p. 477.
12 T. E. Fisher and M. D. Sexton, in P. Lacombe (ed.), *Physical Chemistry of the Solid State: Applications to Metals and their Compounds*, Elsevier, Amsterdam, 1981, p. 391.
13 O. Kubaschewski and B. E. Hopkins, *Oxidation of Metals and Alloys*, 2nd edn, Butterworths, London, 1962, p. 10.
14 M. Seo, J. B. Lumsden and R. W. Staehle, *Surf. Sci., 50* (1975) 541.
15 G. Hultquist, M. Seo and N. Sato, *Oxid. Metall., 25, 5/6* (1986) 363.
16 D. H. Buckley, *Surface Effects on Adhesion, Friction, Wear and Lubrication*, Elsevier, Amsterdam, 1980, p. 391.
17 F. P. Bowden and D. Tabor, *The Friction and Lubrication of Solids*, Part II, Clarendon Press, Oxford, 1964, pp. 53, 77.

APPENDIX A2

COMPOSITION AND SLIDING CONTACT BEHAVIOR OF OXIDIZED Ti-IMPLANTED 52100 STEEL.

by

I.L. Singer
Code 6170, U.S. Naval Research Laboratory
Washington DC 20375

and

R.A. Jeffries
Geo-Centers, Inc., 10903 Indian Head Hwy.
Ft. Washington MD 20744

ABSTRACT

Ti-implanted 52100 bearing steel was oxidized at temperatures from 300 to 600°C. Friction and wear tests were performed using low speed, high stress sliding contact in air. Auger depth profiling and SIMS were used to investigate changes in composition. Friction coefficients of oxidized implanted surfaces rose from low values of 0.2 to 0.6; nonimplanted steel measured 0.6 whereas non-oxidized Ti-implanted steel gave 0.3. Wear was confined to the oxide layer, but the behavior changed with oxide thickness. Relatively thin oxide layers (ca. 10 nm) resulted in transfer of oxide wear debris to the wear track. Thicker oxides ($\gtrsim$ 100 nm) sheared from the implanted layer on the first pass; Auger analysis of the wear track indicated that failure occurred at the Fe oxide/ Ti oxide interface. Very thick oxides (1 um) buckled and cracked, unlike those on oxidized, nonimplanted steel. In addition to generating oxides, the heat treatment caused carbon from the bulk to migrate into the Ti-implanted layer, leading to full carburization of the implanted layer at temperatures above 400°C. The influence of oxide films on tribological behavior was illustrated by removing an oxide film with ion-milling and demonstrating reduced friction and wear.

Presented at 5th I2IB, Riva, Italy, Sept. 1988

INTRODUCTION

Ti implantation has been shown to dramatically improve the friction and wear behavior of a wide variety of engineering steels [Ref.1,2,3]. Optimal processing parameters for obtaining low friction and wear resistant layers have been established for both single ion implants of Ti [Ref. 4] and dual implants of Ti + C [Ref. 5]. In both cases, the low friction coefficients [Ref. 6] and the increased wear resistance [Ref.7] have been linked strongly to the Fe-Ti-C alloy layer formed in the surface. However, the stability of these low-friction, wear resistant surfaces has not been fully explored. Singer and Jeffries [Ref. 6] observed increased friction coefficients in Ti-implanted substrates which did not receive sufficient "vacuum carburization" [Ref. 8] of the near surface layer . Follstaedt, et al [Ref. 9] saw increased friction coefficients, albeit decreased wear, in a (Ti + C)-implanted austenitic steel annealed at 650°C.

The purpose of this paper is to examine the influence of oxide formation on the friction and wear behavior of Ti implanted steel. Oxidation is the most pervasive surface modification facing all metals in sliding contact, in air [Ref. 10], in lubricants [Ref. 11] and even in modest high vacuum environments [Ref. 12]. In this study, bearing steel substrates were given an "optimal" Ti implantation treatment then oxidized at temperatures from about 300 to 600°C. Oxidation not only produced oxide films with thickness from less than 10 nm to greater than 1 μm but also altered the composition of the implanted layer. Friction coefficients and initiation of wear were investigated and correlated with changes in composition of the oxidized and worn oxidized substrates.

EXPERIMENTAL

Polished disks of hardened 52100 bearing steel were implanted with Ti ions to a dose of $4.6 \times 10^{17}/cm^2$ at 190 keV. The chamber was intentionally backfilled with ^{13}CO gas to a pressure of 1×10^{-5} Torr, in order to obtain ^{13}C species in the vacuum carburized layer. Substrates were mounted on a water-cooled holder to prevent temperatures from rising above about 40°C during implantation. One of each implanted disk was then heat treated in an 80% Ar + 20% O_2 gas mixture for one hour at temperatures 298°C, 412°C and 596°C (+ 3°C). One of the oxidized substrates was later ion milled in a commercial ion milling machine. The substrate was bombarded with 1 keV Ar ions impinging at 45° to a rotating, water-cooled substrate holder. For the remainder of the paper, we will use the sample designations listed in Table 1 to identify the substrates and their treatments.

Friction tests were performed on a Bowden-Leben type tester. A 12.7 mm (1/2") diameter ball, also made of bearing quality 52100 steel, was loaded to 1 kgf (mean Hertzian pressure = 0.54 GPa) against the moving substrate. Speed was maintained at 0.1 mm/sec and from one to 20 unidirectional passes were made over the same track. Tests were performed in air (Relative humidity 30 - 40 %), without lubrication. Friction coefficients are reported to two place accuracy (+ 0.03). Wear tracks were examined optically with Nomarski and Michelson interferometry. Knoop hardness measurements (at 2 kgf) were also taken.

Composition analyses were performed by scanning Auger electron spectroscopy (SAM) in conjunction with sputter depth profiling (2 keV Ar ions), secondary ion mass spectrometry (SIMS), using 5.5 keV Ar ions, and energy dispersive X-ray analysis (EDX). Auger data were converted to concentrations using sensitivity factors established from reference compounds [Ref. 8], and depth scales were obtained from interferometric measurements of sputtered craters. SIMS was

particularly useful in identifying the isotopic ^{12}C and ^{13}C species in the implanted layer [Ref. 13].

RESULTS

Hardness and color changes accompanying oxidation of the 52100 steel substrates are listed in Table 1. The bulk hardness of the substrate decreased with temperature, as expected for a fine-grained 1 wt. % carbon steel [Ref. 14]. Implanted surfaces that were oxidized up to 412C were nearly as smooth as polished surfaces, as determined visually in reflecting light and by the relative sharpness of interference bands seen in a Michelson interferometer. While not as specular, the oxidized I596 substrate was smooth enough to reflect uniform interference bands in the interferometer. By contrast, the oxidized nonimplanted substrate N596 was rough. Table 1 also summarizes the friction coefficients measured on the oxidized substrates and the two reference (room temperature) substrates. Compositions and tribological behavior associated with each of the oxidized substrates are described in more detail below:

Substrate I298. The oxide film on the I298 substrate had the same composition as the non-oxidized I25 substrate [Ref. 1], but the film was 2 to 3 times thicker. Auger lineshapes of the oxide constituents showed the outermost layer to be Fe_2O_3, followed by a TiO_2-Ti_2O_3 layer with metallic Fe, then a Ti(OC) layer merged with the Fe-Ti-C interface. The subsurface layer of I298 showed a broad Ti profile and a near-surface carbon peak, similar to that found in the I25 substrate (see Fig. 1). In addition, it had a deeper carbon peak, depicted by the cross-hatched area of Fig. 1. SIMS analysis of the substrate before and after oxidation (Fig. 2) showed that the near-surface carbon profile was predominantly ^{13}C, therefore derived from vacuum carburization, whereas the

deeper carbon profile was predominantly ^{12}C. The full I298 profile, with the two carbon distributions distinguished, is shown in Fig. 1.

The friction coefficient on substrate I298 started low (0.22) then gradually increased to a steady-state value of 0.62 after the tenth pass. Debris generated on the first pass was redeposited at the outside edges of, but not inside, the track. With subsequent passes, as the friction coefficient rose to 0.4 and above, debris accumulated inside the track. No wear of the track could be detected by interferometry, but SAM analysis showed that the debris in the track were composed mainly of Fe oxide. (The wear behavior of this substrate is discussed more fully in a companion paper [Ref.15].)

Substrate I298IM. As a means of assessing the role of the oxide film in debris generation and friction increase, the oxide layer of substrate I298 was removed by ion milling then friction tests and surface analyses were repeated. The ion milled area of the substrate (I298IM) gave friction coefficients ranging from 0.30 on the first pass to 0.39 after 15 passes. No measurable wear and very little debris were detected after 15 passes.

EDX analysis established that the ion-milled surface had lost approx 20% of the implanted Ti. Auger analysis of I298IM was identical to that of substrate I298, except that all of the oxide and a small portion of the implanted layer had been removed by ion-milling. The depth profile of I298IM is indicated in Fig. 1, where the outermost surface after ion milling begins at the thin vertical line.

Substrate I412. An Auger sputter depth profile of the implanted layer of substrate I412 is shown in Fig. 3a with an expanded scale for the oxide layer. The surface layer had a substantially thicker oxide film (around 120 nm) than the as-implanted surface. The oxide film was made up of an Fe oxide layer,

whose stoichiometry was roughly Fe_2O_3, on top of a mixed layer consisting of 3 parts Ti_2O_3, as indicated by the Ti(LMM) lineshape [Ref. 16], and 2 parts metallic Fe. The presence of a carbon peak at the Fe oxide/Ti oxide interface suggests that this was the location of the original carbon-contaminated surface, and that Fe oxide grew on top of it. Below the oxide layer, a Ti(OC) interface merged gradually with the subsurface Ti-implanted layer. The subsurface Ti layer was fully carburized, i.e., C/Ti ratio of 1 throughout the layer.

As with substrate I298, the friction coefficient of substrate I412 began low (0.23) then rose gradually to a steady-state value of 0.62 after the tenth pass. Again, debris accumulated at the edges of the track on the first pass, then inside the track as the friction coefficient rose above 0.4. On the first pass, however, the I412 track was sheared uniformly to a depth of 55 ± 10 nm. Over the next 14 passes, very little further wear took place. Interferograms of the sheared wear track can be seen in Fig. 4, which shows the 1st to 7th pass, and 15th pass region of two different tracks.

Scanning Auger microscopy (SAM) performed on the first pass wear track of substrate I412 is shown in Fig. 3b. Auger lineshape analysis indicates that TiO_2 was the predominant oxide on the surface of the track. A comparison of Figs. 3a and 3b shows that an Fe oxide film 30 to 60 nm thick was sheared off the wear track, consistent with the interferometry measurements.

Substrate I596. The SIMS depth profile of I596 in Fig. 5 indicates a complicated multilayer composition, consisting of an Fe-rich (Ti-depleted) surface oxide, followed by a C-lean Ti oxide, then a broad oxide/metal interface incorporating piled-up C from the decarburization process. Auger analysis (not shown) detected only Fe oxide (no Ti) during a 20 minute sputtering period

(approximately 100 nm deep). After a few minutes, the O/Fe(650 eV) ratio reached a steady state value of 1.9. Sputter depth profiles under identical conditions on substrate N596 and Fe_2O_3 powders gave O/Fe(650 eV) ratios of 2.7 and 3.3 + 0.2, respectively. Recognizing that substoichiometric compounds can undergo substantial ion-beam reduction, we nevertheless infer that the surface of substrate N596 had an Fe_3O_4 oxide film, whereas substrate I596 had an FeO film.

Friction coefficients for substrate I596 displayed stick-slip for nearly every pass. Stick-slip excursions were small on the first pass (0.4-0.5) but increased to 0.2-0.6 after 5 passes. The track began to buckle on the first pass, then these buckled areas fractured and accumulated debris with subsequent passes. Interferometry at areas where the track fractured gave depths greater than 1 um (not shown), suggesting that the oxide film was at least 1 um thick.

Substrate N596. The friction coefficient for substrate N596 began at 0.5 with slight stick-slip, then rose to 0.8 with increasing amounts of stick-slip after 8 passes. Unlike the I596 track, the N596 track did not buckle and fracture, but it did accumulate wear debris.

DISCUSSION

High temperatures (300 - 600°C) and oxygen exposure altered the chemistry of the implanted layer in two distinct ways: by thickening the oxide film and by promoting full carburization of the Ti-rich implanted layer. The oxide film, as it thickened, maintained an Fe oxide/Ti oxide multilayer composition. One rather unique aspect of the oxide formation was that the oxidized surface remained smooth, as revealed by interferometry. We attribute reduced roughness to uniform oxide growth on the amorphous surface of Ti-implanted steel [Ref. 1].

Carburization of the Ti-implanted layer occurred in conjunction with decarburization of the bulk steel, i.e., as solute C atoms from the bulk migrated towards the surface, they were gettered by Ti atoms to form the very stable TiC compound. Similar precipitation behavior was reported by Follstaedt, who observed TiC precipitates in heat treated Ti-implanted Fe [Ref. 17].

Although not investigated in this paper, the long-term wear behavior of Ti-implanted steel may benefit from the TiC formation accompanying heat treatment. Follstaedt et al [Ref. 9] have observed the same excellent wear resistance in 650°C vacuum annealed Ti + C implanted steels as in the as-implanted steel, despite the loss of low friction. The enhanced wear resistance was attributed to the added subsurface strengthening achieved by TiC precipitate formation. As for the friction increase, we suspect that oxides may have formed during the "vacuum annealing", causing the higher friction coefficients. Increased wear resistance was also obtained by Ti implantation into steel heated to 600°C by beam heating, where a TiC precipitate layer was formed [Ref. 18].

Despite potential benefits of subsurface carburization, the tribological properties of the oxidized Ti-implanted 52100 steel appeared to degrade in two ways: First, the multilayer oxide "failed" under the stress transmitted during dry sliding contact. In the thin (<100 nm) oxide formed at 412°C, the outermost Fe oxide layer exhibited shear failure at the Fe oxide/Ti oxide interface. This easy shear may be linked to changes in the subsurface chemistry: 1) due to the subsurface carbon layer retained from the original surface, or 2) to the sharp gradient in composition at the Fe oxide/Ti oxide

interface. In the thicker oxides (1 μm), the oxide film fractured. Here too, one sees gradients in the composition of the oxidized layer.

Secondly, debris that formed from the oxide layer during the first few traverses of the slider were later redeposited in the track, causing the friction to increase from about 0.2 to 0.6, the value of nonimplanted steel on steel. Direct evidence that the oxide layer promoted debris transfer and an increase in the friction coefficient was given in the ion milling study of substrate I298. These results suggest that the reduced friction and low wear behavior of Ti-implanted steel is diminished by oxidation. In a companion paper detailing investigations of debris formation and friction behavior, we suggested that low friction coefficients require the Fe-Ti-C interface obtained on the implanted surface [Ref. 15].

SUMMARY AND CONCLUSIONS

Heating and oxidation bring about considerable changes in the composition of the surface and subsurface layers. Hultilayer oxides that form on top of the Ti-implanted layer ultimately contribute to the demise of a low friction surface by a two step process: First, the outermost Fe oxide films are wiped off the track during sliding and collect as debris on the slider. Second, fragments of the debris are redeposited on the track with subsequent passes. Heating, however, promotes full carburization of the implanted layer, which may contribute to added wear resistance at intermediate temperatures (300 - 400°C).

ACKNOWLEDGEMENTS

We thank George Ramsayer for providing the SIMS profiles and John Wegand for assistance with the wear scar analysis.

REFERENCES

1. I.L. Singer, C.A. Carosella, and J.R. Reed, Nucl. Instrum. Methods 182/183 (1981) 923.

2. L.E. Pope, F.G. Yost, D.M. Follstaedt, J.A. Knapp, S.T. Picraux, in Wear of Materials , Ed. K.C. Ludema (ASME, NY, 1983) 280.

3. F.M. Kustas and M.S. Misra, Thin Solid Films 122 (1984) 279.

4. I.L. Singer and R.A. Jeffries, ASLE Trans. 28 (1985) 134.

5. D.M. Follstaedt, J.A. Knapp, L.E. Pope, F.G. Yost and S.T. Picraux, Appl. Phys. Lett. 45 (1984) 529.

6. I.L. Singer and R.A. Jeffries, Appl. Phys. Letts. 43 (1983) 925.

7. D.M. Follstaedt, F.G. Yost, L.E. Pope, S.T. Picraux, and J.A. Knapp, Appl. Phys. Lett. 43 (1983) 358.

8. I.L. Singer, J. Vac. Sci. Technol. A1 (1983) 419.

9. D.M. Follstaedt, L.E. Pope, J.A. Knapp, S.T. Picraux and F.G. Yost, Thin Solid Films 107 (1983) 259.

10. F.P. Bowden and D. Tabor, The Friction and Lubrication of Solids, (Clarendon Press, Oxford, 1950) p. 145.

11. T.E. Fischer and M.J. Luton, ASLE Trans., 26 (1982) 31.

12. D.H. Buckley, Friction Wear, and Lubrication in Vacuum, NASA SP-277 (NASA, Washington, DC, 1971).

13. I.L. Singer and T.M. Barlak, Appl. Phys. Letts. 43 (1983) 457.

14. S.L. Hoyt, Metal Data (Reinhold, New York, 1952) p. 107

15. S. Fayeulle and I.L. Singer, these proceedings.

16. G.D. Davis, M. Natan and K.A. Anderson, Appl. Surf. Science 15 (1983) 321.

17. D.M. Follstaedt, J. Appl. Phys., 51 (1980) 1001.

18. I.L. Singer, R.N. Bolster, J.A. Sprague, K. Kim, S. Ramalingam, R.A. Jeffries and G.O. Ramseyer, J. Appl. Phys. 58 (1985) 1255.

TABLE 1. OXIDATION TEMPERATURE, BULK HARDNESS, VISUAL APPEARANCE AND FRICTION COEFFICIENT FOR OXIDIZED AND REFERENCE SUBSTRATES. [DESIGNATORS: N-NONIMPLANTED; I-IMPLANTED; IM-ION-MILLED.]

SUBSTRATE DESIGNATION	OXIDATION TEMP.,°C	HARDNESS (KNOOP)	VISUAL	FRICTION COEFFICIENT vs PASS NUMBER 1	5	10	15
N25	25	660	mirror-like	0.2-0.3	0.62	0.62	0.62
I25	25	660	mirror-like	0.18	0.26	0.30	0.30
I298	298	600	golden yellow	0.22	0.44	0.62	0.62
I298IM	298	600	mirror-like	0.30	0.36	0.37	0.39
I412	412	520	blue-to-gray	0.23	0.35	0.60	0.60
I596	596	280	black	0.4-0.5*	0.2-0.6*	0.2-0.6*	0.2-0.6*
N596	596	280	black	0.5	0.7	0.6-0.8*	0.6-0.8*

* stick-slip behavior.

FIGURE CAPTIONS

Fig. 1. Concentration vs depth profile of Ti-implanted 52100 steel oxidized at 298°C (substrate I298). The near surface carbon originated from vacuum carburization and the subsurface carbon, from the bulk carbon. The thin vertical line indicates position of surface after ion milling.

Fig. 2. SIMS depth profiles of 52100 steel implanted with Ti in the presence of ^{13}CO. (left) before oxidation and (right) after oxidation at 298°C.

Fig. 3. Auger sputter depth profiles of Ti-implanted 52100 steel oxidized at 412°C (substrate I412). a) as-oxidized surface, with expanded scale for the oxide layer; b) oxide film inside the first pass wear track. Note: sputtering rates in two profiles were not the same.

Fig. 4. Michelson interferograms of a wear track on Ti-implanted 52100 steel oxidized at 412°C.

Fig. 5. SIMS depth profile of the Ti-implanted 52100 steel oxidized at 596°C.

AUGER COMPOSITION PROFILE

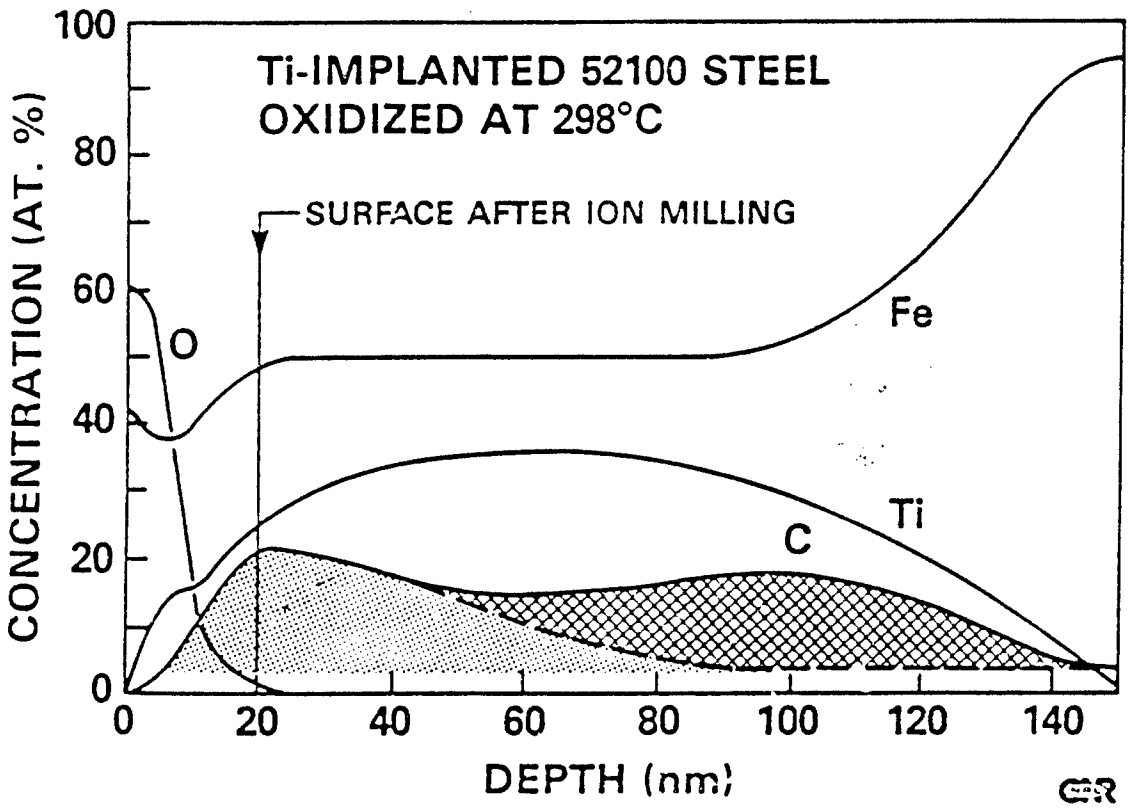


Fig 1

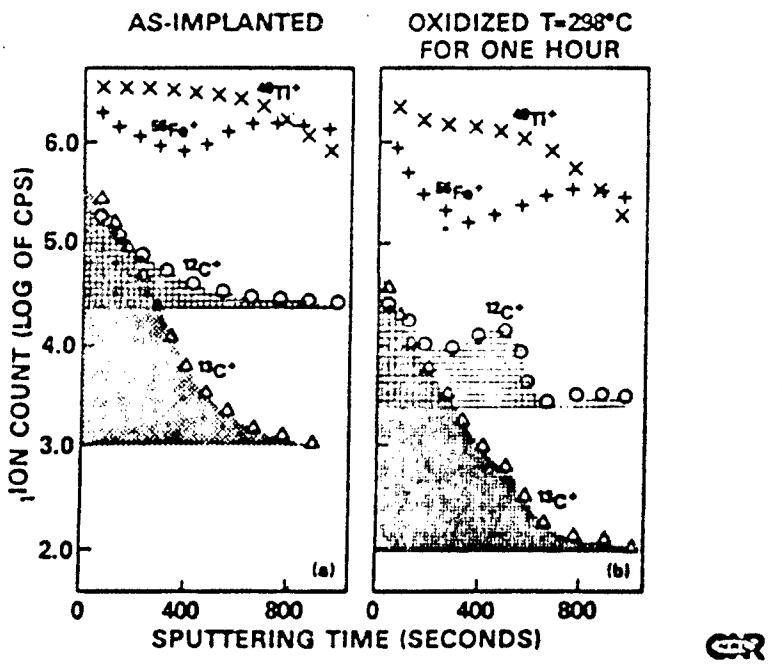
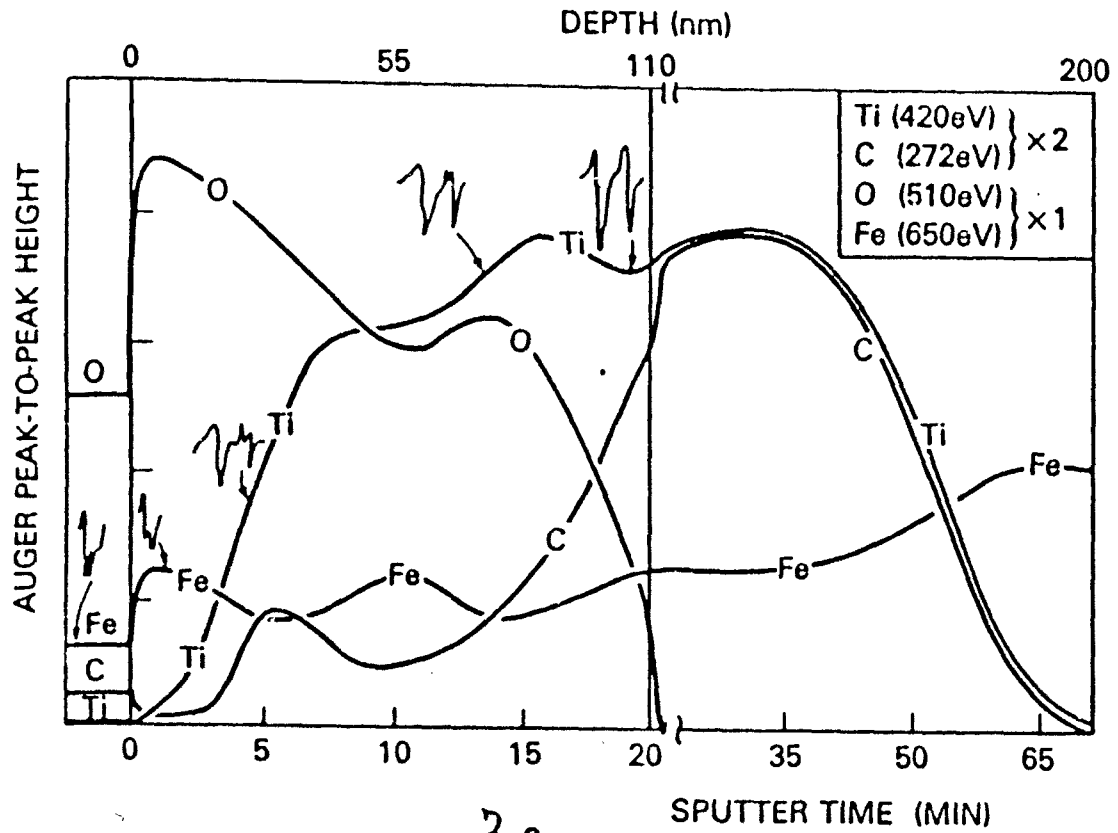
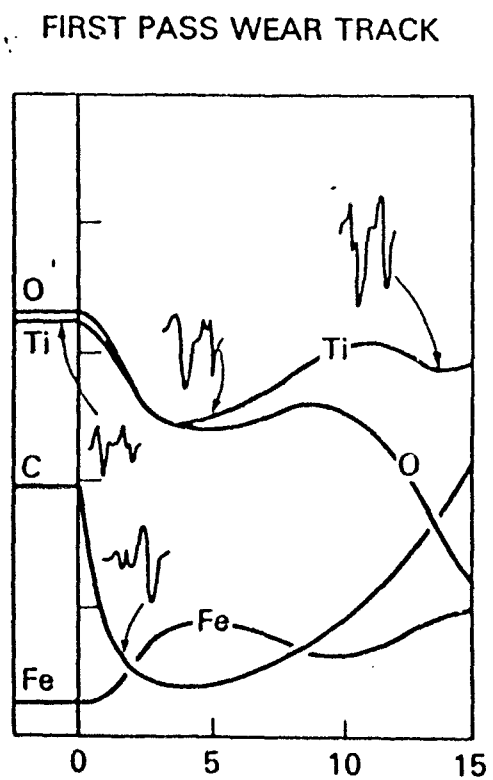


Fig 2

AUGER SPUTTER DEPTH PROFILE
52100:Ti+ OXIDIZED AT 412°C



3a.



3b.

Fig 3

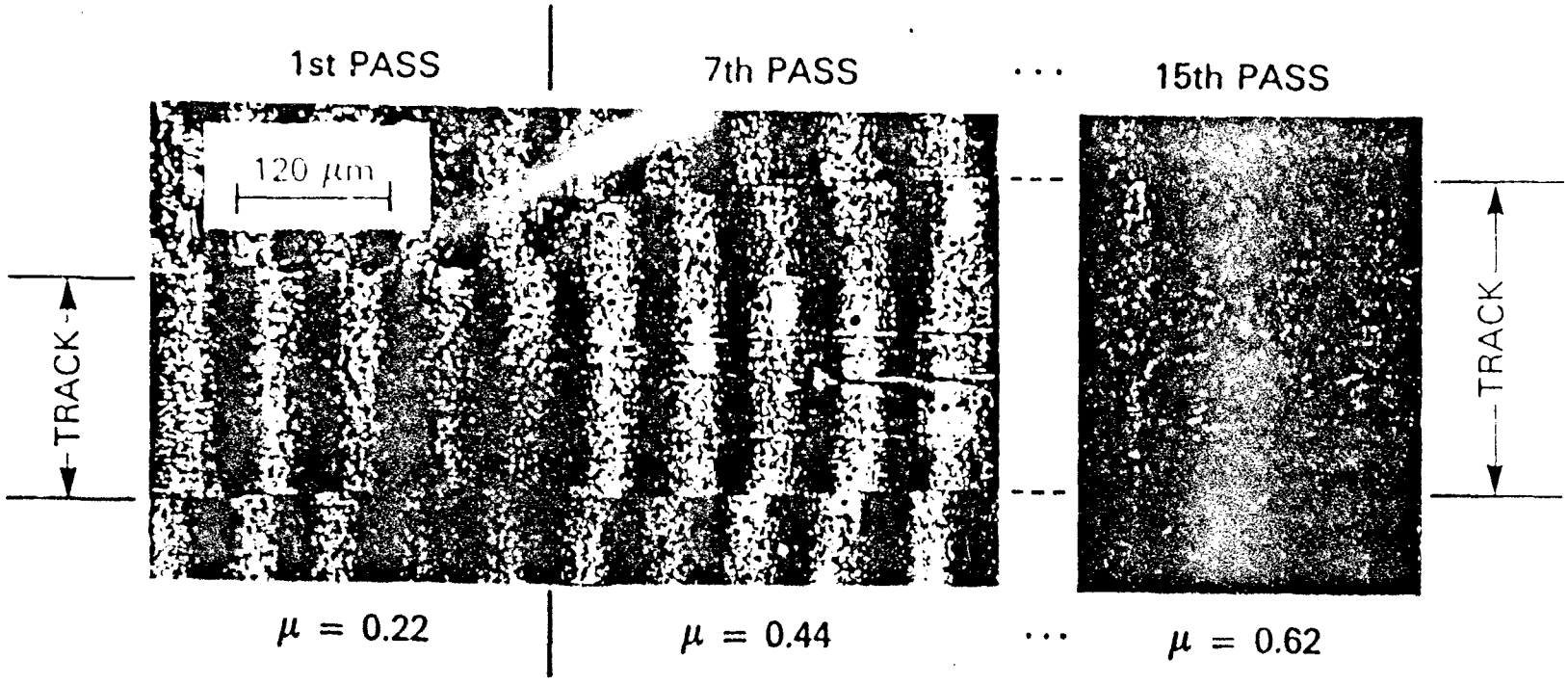


Fig. 4

SIMS SPUTTER DEPTH PROFILE

OXIDIZED Ti-IMPLANTED STEEL (596°C)

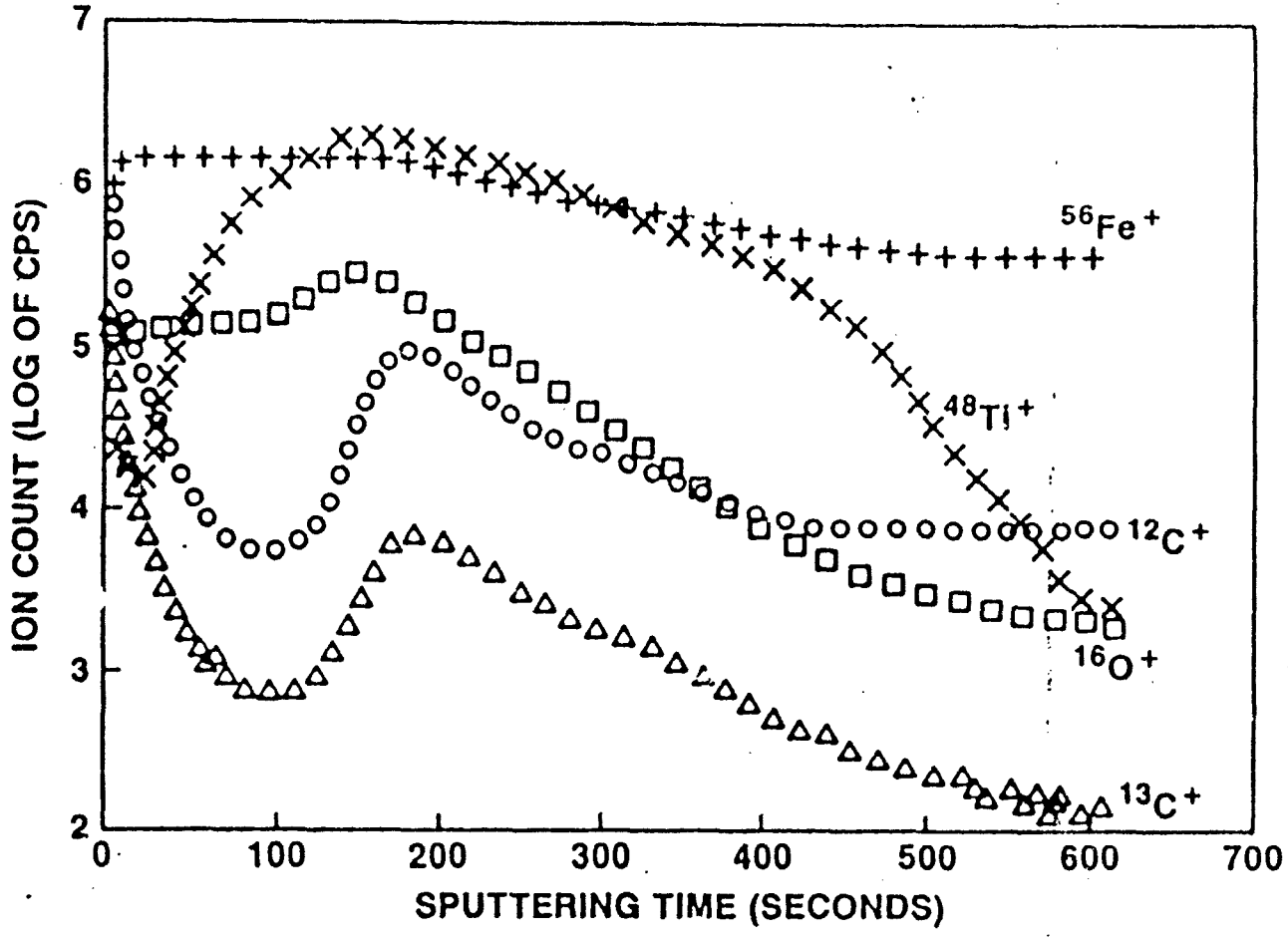


Fig. 5.

APPENDIX A3

A2

Polishing wear resistance of ion-implanted 304 steel

I. L. Singer,[a] R. G. Vardiman,[b] and R. N. Bolster[a]
U.S. Naval Research Laboratory, Washington, DC 20375

(Received 27 May 1988; accepted 2 August 1988)

Steel (AISI-304) disks, polished to a 3 μm diamond finish, were implanted to doses of about 2×10^{17}/cm^2 with N^+, Ni^+, or Ne^+ ions. Polishing wear rates, measured to a depth resolution of about 20 nm, showed that each of the implanted disks wore 20% to 40% faster than nonimplanted layers. Auger analysis showed (1) Gaussian-like profiles of the N-implanted layer, but with somewhat enhanced oxidation of the surface, and (2) a sputter-limited implantation profile in the Ni-implanted layer, with some vacuum carburization. Transmission electron microscope analysis indicated that polishing produced an α'-martensite layer in the mainly austenitic 304 surface, but that implantation of N transformed the martensite to austenite at the outermost layers and produced iron nitrides below. In addition, Ni implantation stabilized the austenite against martensite transformation during subsequent wear. Martensite vanished after Ni implantation because of sputter removal, not phase transformation, during Ni bombardment. The Ne-implanted layer remained predominantly martensite. Changes in wear rates and microstructures were confined to depths commensurate with the range of ions in the implanted layer. Several hypotheses on the effects of ion implantation on microstructure and wear are discussed.

I. INTRODUCTION

The wear resistance of steel is very sensitive to surface chemistry and microstructure,[1,2] as witnessed by the numerous thermochemical and thermomechanical treatments available for improving wear behavior.[3] Austenitic stainless steels are a particularly pathological class of steels in wear situations: their wear resistance is high in abrasion[4,5] but low in sliding contact.[6] This dichotomy can also be seen in ion-implanted 304 steel, where N implantation has dramatically increased the sliding wear resistance[7–9] but caused a decrease in the abrasion resistance.[10,11]

In order to explain the large effects found in N-implanted 304 steel, many compositional[10,12,13] and microstructural[14–17] studies have been performed, but there is still no agreement on the microstructures attained. While sliding wear tests are simple to perform, the resulting wear surfaces are too irregular and inhomogeneous to be studied easily by transmission electron microscopy (TEM),[18] thus leaving a large gap in our understanding of the microstructural basis for wear behavior. Polishing wear tests, by contrast, produce flat, smooth surfaces, thereby making polished surfaces very amenable to surface analytical techniques.[10,19,20] Moreover, wear rates in polishing tests can be obtained with a depth resolution of about 20 nm.[21]

The purpose of this study is to provide a chemical and microstructural basis for the polishing wear behavior of 304 steel. Guided by previous studies in which the decrease in wear resistance of N-implanted 304 was accompanied by an α'-martensite to austenite transformation,[14] we elected to investigate disks implanted with austenitic stabilizers (N and Ni) as well as an inert gas (Ne). An implantation dose of 2×10^{17}/cm^2 was chosen, as this dose produces the optimum sliding wear resistance in many steels.[9,22,23]

At these high fluences, ion implantation alters not only the subsurface microstructure but also the surface composition by sputtering, bombardment-induced surface chemistry, and solute redistribution.[13] Therefore, in addition to investigating wear behavior, we attempt to properly account for these high-fluence effects.

In Sec. II, experimental techniques are described for obtaining abrasive (polishing) rates and sputtering yields by weight loss measurements, as well as compositions and microstructures by Auger analysis and transmission electron microscopy (TEM), respectively. In Sec. III, wear behavior and materials characterization are presented for polished, implanted, and implanted-then-polished surfaces. We begin Sec. IV by discussing factors contributing to the variety of phases obtained in ion-implanted steel, then attempt to identify the mechanisms controlling the polishing wear behavior of ion-implanted 304 steel.

II. EXPERIMENTAL

Disks, 12.7 mm in diameter and 2.8 mm thick, were machined from 304 steel alloy bar stock, ground, fine ground, and polished with 3 μm diamond to a steady-state finish on the polishing machine to be used for the abrasive wear studies.

[a] Code 6170
[b] Code 6320

Ion implantation was performed in a high-current Varian/Extrion implanter. Polished disks were mounted on a water-cooled holder and the target chamber was cryogenically pumped to pressures 2×10^{-6} Torr or better. Ions were implanted to doses around $2 \times 10^{17}/cm^2$ and at energies that gave projected range values of about 50 nm, that of 40 keV N^+ ions in steel. Implantation parameters and sputtering rates were computed using TRIM,[24] a Monte Carlo simulation program. For range and straggling data, a target composition of 72% Fe, 20% Cr, and 8% Ni (in at. %), hereafter designated Fe20Cr8Ni, was assumed. For sputter yield data, the metal atom-to-ion yield was computed for both the metal target (as above) and an oxide-covered metal target. Predicted concentrations at peak depth, calculated from range straggling data (see Table I and Appendix for details), varied from 30 to 50 at. %.

Wear tests were performed by polishing implanted and reference (nonimplanted) disks in a vibratory polisher charged with 3 μm diamond paste.[11,25] In this procedure, two reference disks were polished in the same holder as the implanted disk at a mean pressure of 6400 Pa. Wear rates and wear depths were determined by weighing disks with microgram precision after periods of polishing. The relative wear resistance (RWR) of an implanted disk was calculated as the inverse of the wear rate of the implanted disk normalized to that of the nonimplanted disks. The number of implanted sample disks used were: 6 with N, 9 with Ne, and 2 with Ni. Weight changes were also measured before and after implantation, in order to determine sputter yields during implantation.

Auger sputter depth profiles were performed on N- and Ni-implanted 304 steel using 2 keV Ar^+ ion milling. Compositions were computed by normalizing derivative data, using sensitivity factors acquired from bulk 304 steel, from Cr carbides and Fe oxide powders, and by nuclear reaction analysis for N implantation.[13] Implanted Ni concentrations were obtained by subtracting the bulk Ni concentration, assumed to be 8/72 = 0.11 times the Fe concentration, from the total Ni concentration. Depth scales were determined from depths of ion-milled craters measured interferometrically; uniform sputtering rates were assumed.

TABLE I. Range (R_p), range straggling (δR_p), and concentration at peak depth for implanted 304 steel.

Ion	Energy (keV)	Dose ($10^{17}/cm^2$)	Range (nm)	Straggling (nm)	Concentration (at. %)
N^{+a}	40	2.0	47	21	31[c]
Ni^{+a}	175	2.0	52	22	43[b]
Ne^{+a}	55	2.4	48	22	51[b]

[a] As interstitial solute.
[b] As substitutional solute (see Appendix).

Foils for TEM examination were prepared by slicing a layer, roughly 0.4 mm thick, from polished or implanted substrates, mechanically polishing the cut side to a thickness of 0.1 mm, punching out 3 mm diam disks, and electrolytically thinning from the back side. Several disks, prior to thinning, had their front sides Ar^+-ion milled to preselected depths in the Auger spectrometer in order to examine the structure beneath the surface. Electron diffraction patterns were usually taken with the largest aperture, giving a selected area of 11.6 μm.

III. RESULTS

A. Relative wear resistance

Relative wear resistance (RWR) versus depth data for the three implantation treatments are shown in Fig. 1. The individual data points exhibit considerable scatter due to the short polishing intervals and very small mass losses (typically tens of micrograms) required for obtaining the depth resolution shown. The dashed lines are smooth curves drawn through moving averages, which are particularly effective in reducing the oscillations due to weighing errors. Integrated mass losses were less subject to error, as they were derived from the starting weights minus the final, values which were large compared to the weighing errors.

In all cases, the RWR decreased in the implanted layer. The smoothed RWR curves had minima at depths corresponding to the calculated mean range, then returned to 1, indicating that the decreased wear resistance was confined to the implanted layer. Integrated mass losses over the depths affected by the implantation showed that implanted N caused the largest loss, followed by Ni then Ne. These results are summarized in Table II.

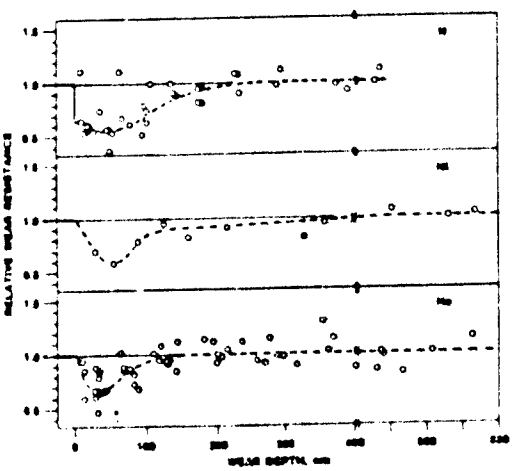


FIG. 1. Relative wear resistance versus depth for N-, Ni-, and Ne-implanted 304.

TABLE II. Minimum values of RWR curves and integrated mass losses (relative to N implanted) for implanted 304 steel.

Implant species	N	Ni	Ne
Minimum RWR values	0.55	0.6	0.65
Relative mass loss	1.0	0.85	0.42

B. Composition

1. Weight change on implantation

Disks were weighed before and after implantation in order to determine the thickness of material removed by sputtering. Disks implanted with Ni lost weight, whereas those implanted with N or Ne gained (see Table III). Weight change data were converted to sputter yields according to[26]

$$Y = (-\delta M \times N_0)/(M_2 \times N_1) + M_1/M_2,$$

where δM is the change in mass, N_0 is Avogadro's number, M_1 and M_2 are the mass of the ion and target atom, respectively, and N_1 is the number of ions. Results are given in Table III, along with two sets of yields calculated using TRIM.[24] Because atoms are sputtered mainly from the outermost atomic layers and metals are usually covered with an oxide layer, TRIM yields were calculated for two different surface conditions: a metallic surface of composition Fe20Cr8Ni and an oxide-covered metal composed of 1 nm Fe_2O_3 on 1 nm Cr_2O_3 on Fe20Cr8Ni. Parameters used in the TRIM yield calculations were: surface binding energy = 5.1 eV [Ref. 27] and densities of 8.2 $g \cdot cm^{-3}$ for the metal and 5.2 $g \cdot cm^{-3}$ for the oxide.

As seen in Table III, the sputter yields were less than 1 for N and Ne but greater than 1 for Ni. The measured yields for N and Ne lie between the calculated values of the metal and an oxide-covered metal, suggesting that an oxide layer was retained on the 304 surface throughout the implantation period. The calculated sputter yield for Ni, however, is closer to that of the metal surface, indicating that the oxide layer was rapidly sputtered away and then considerable sputtering of the metal occurred.

TABLE III. Measured and calculated sputter yields of ion-implanted 304 steel

Implant species	N	Ni	Ne
Number of disks	3	2	9
Weight change (μg)	$+0.3 \pm 3$	-27 ± 5	$+3 \pm 6$
Measured yield	0.25 ± 0.1	2.2 ± 0.2	0.2 ± 0.2
Calculated yield:			
Metal surface[a]	0.33	2.4	0.56
Oxide surface[b]	0.11	0.69	0.19

[a] Fe20Cr8Ni target.
[b] Oxide-covered Fe20Cr8Ni target (see text).

2. Auger analysis

An Auger sputter depth profile for N atoms in polished 304 steel is shown in Fig. 2. At this fluence, the N profile is similar to the predicted TRIM profile (also shown) and the peak concentration of approximately 33 at. % is consistent with the calculated concentration for N as an interstitial species (see Appendix). (More detailed presentations of the dose dependence and chemical state of the N atoms implanted into polished 304 steel disks can be found in Refs. 10, 12, and 13.)

Auger analysis also showed that the oxide layers on N-implanted disks were from one to three times thicker than on nonimplanted polished disks, estimated to be approximately 1 nm [Ref.28]. Figure 3 presents Auger depth profiles of a polished surface and of one of the thicker oxide films examined. (The broader lines depict Fe and Cr in an oxidized state, as determined from the LVV Auger spectra.[29]) These oxides, which grew in the high-vacuum chamber (1×10^{-6} Torr base pressure) during implantation, probably contributed to the low sputter yield (Table III) during N (and probably Ne) implantation. The oxides, however, did not significantly affect wear resistance; after a short period of polishing, the oxides on N-implanted disks attained the same thickness as on nonimplanted disks.[10]

Unlike N, Ni implantation resulted in a depth profile (shown in Fig. 4) that was not Gaussian-like; rather, it resembled a sputter-limited profile with the maximum Ni concentration close to the surface. We estimate the thickness of the layer removed by sputtering during Ni implantation (dose = $2 \times 10^{17}/cm^2$) to be about 50 nm,

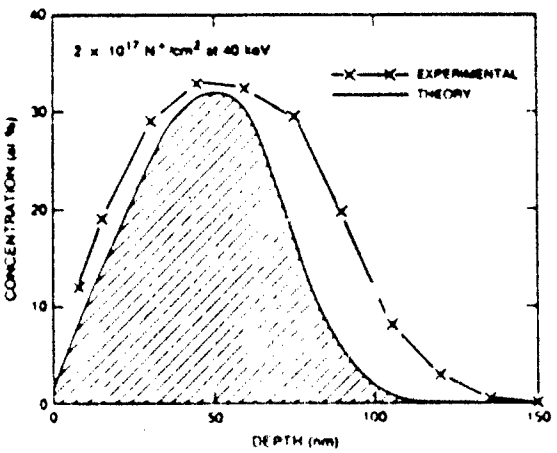


FIG. 2. Auger sputter depth profile and calculated (by TRIM) depth profile of N-implanted 304 steel.

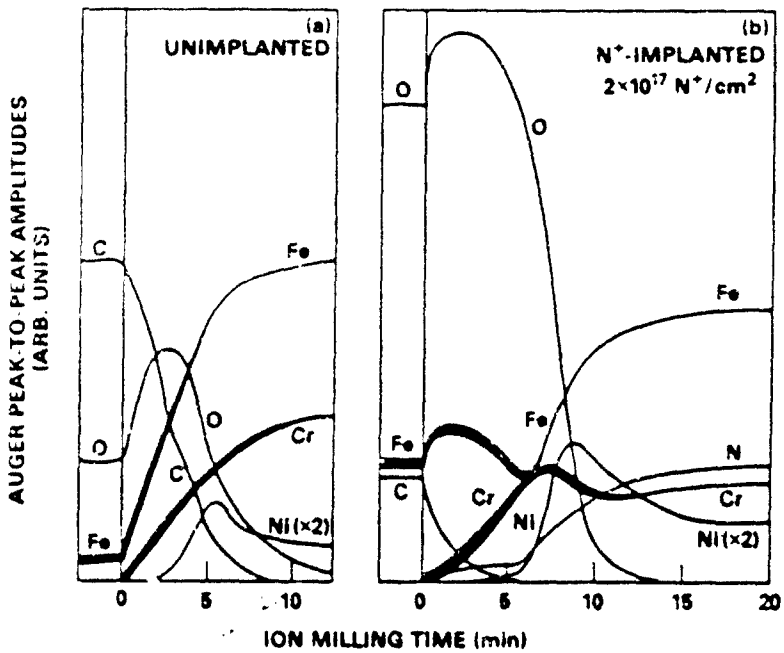


FIG. 3. Auger sputter depth profiles of oxide layers on (a) nonimplanted and (b) N-implanted 304 steel. The broader lines depict Fe and Cr in an oxidized state, as determined from the LVV Auger spectra.

using the yield data in Table III and an atomic density for 304 steel of 8.6×10^{22} atoms/cm^3. Both N and Ni profiles, however, were commensurate with the depth over which the RWR data showed decreases in Fig. 1. A second difference was that the oxide layers on Ni-implanted 304 steel were no thicker than those found on polished surfaces. Finally, a carbon profile extended to a depth of about 45 nm below the oxide layer. This type of profile, indicative of vacuum carburization, is common in steels whose surfaces are sputter eroded during implantation, exposing carbide-forming elements like Cr.[11,20,30]

Elemental Ne profiles could not be obtained by Auger sputter depth profiling. However, Ne retention in disks implanted to 2×10^{17}/cm^2 at 55 keV was confirmed by both electron microprobe and nuclear reaction analysis. Oxide films on Ne-implanted 304 steel were similar in composition and thickness to N-implanted steels (Fig. 3).

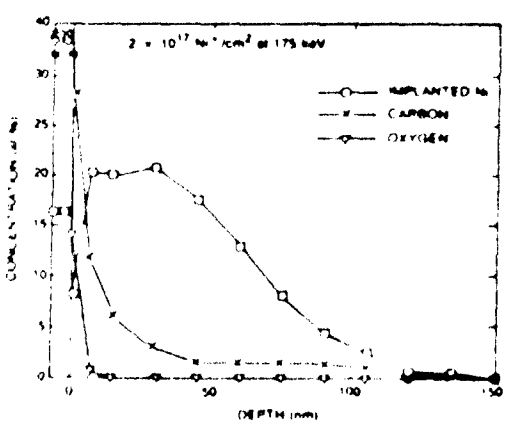


FIG. 4. Auger sputter depth profile of Ni-implanted 304 steel.

C. Microstructure

Microstructures of surfaces have been characterized by electron diffraction patterns from back-thinned surface layers. In Fig. 5, patterns taken after different treatments are arranged to show the changes in austenitic and martensitic reflections. Most reflections were circular or nearly so, and those shown here are characteristic of the overall pattern. A few reflections, from deeper material or from a phase present in very small amount, were more isolated or segmented, and may appear stronger or weaker than their overall pattern showed. Because the (110) α'-martensite and (111) γ-austenite reflections lie so close together, the phases are best identified by the (200) and (220) for the austenite and the (200) and especially the (211) for the martensite.

The diffraction pattern of the nonimplanted, polished surface, shown in Fig. 5(a), displayed strong α'-martensite reflections as well as the austenite rings. A small amount of ϵ-martensite was also found. After removing (by ion milling) 50 nm from the surface of a similarly polished disk, the martensite reflections were weak and difficult to find, as seen in Fig. 5(b). Hence, the polish-induced martensite layer was less than 50 nm deep. The presence of a thin (10 nm) α'-martensite phase on a "mechanically polished" 304 steel disk has also been detected by Arnaud *et al.*,[31] using grazing incidence x-ray diffraction.

After implantation with N, martensite was almost completely eliminated from the polished surface, as seen

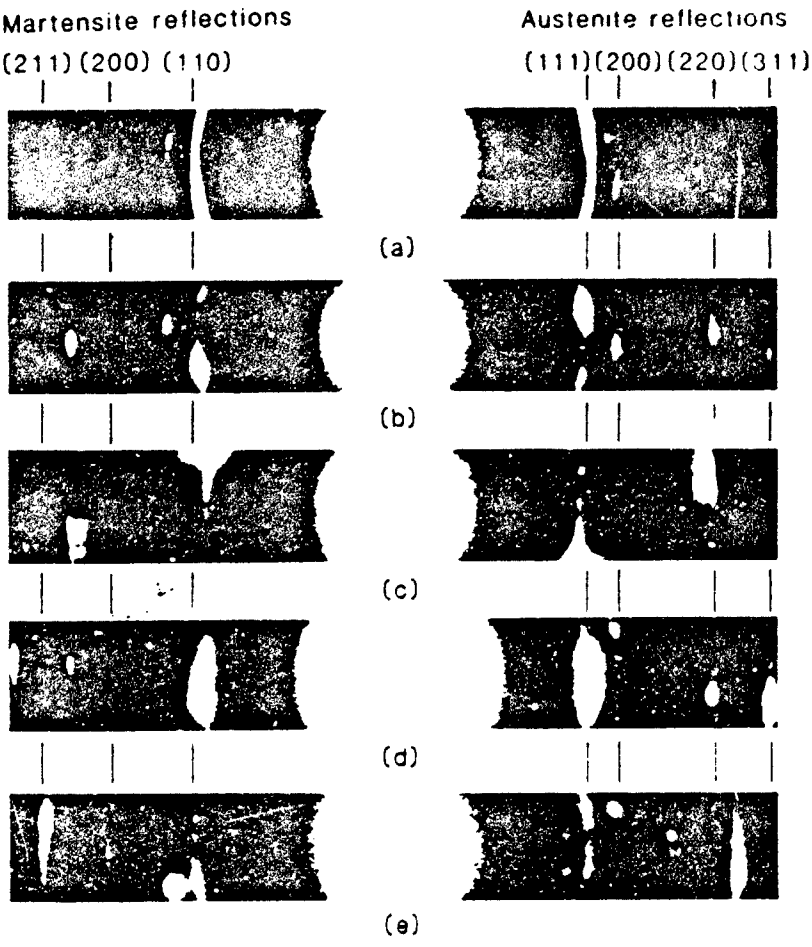


FIG. 5. Large aperture electron diffraction patterns from polished 304 steel surfaces: (a) nonimplanted; (b) nonimplanted but ion milled 50 nm; (c) implanted 2×10^{17} N^+/cm^2, 40 keV; (d) implanted 2×10^{17} Ni^+/cm, 175 keV; (e) implanted 2.4×10^{17} Ne^+/cm^2, 55 keV.

in Fig. 5(c). The diffraction pattern is reproduced in Fig. 6 to allow a clear labeling of all reflections. Three phases can be distinguished: the short arcs belong to austenite (γ) lying beneath the implanted layer while the remaining continuous lines can be indexed to ϵ-Fe_2N_{1-x} and to austenite expanded by N atoms in solid solution (γ_N). The lattice parameter for this dilated austenite is 0.370 ± 0.001 nm. This dilation would correspond to 13 at. % N in solid solution, based on the lattice expansion coefficient found for austenite at low-N concentrations (0.84 fm per at. % N).[32] These line identifications represent a reinterpretation of previous work, in which some ϵ-nitride reflections had been identified as dilated austenite.[15] As shown in an earlier study, the dilated austenite phase must reside near the surface, since it was not detectable after 37 nm of the implanted layer was removed by ion milling.[15] The nitride reflections, however, were still present at this point.

After implantation with Ni, austenite again became the predominant phase and martensite was almost completely eliminated [Fig. 5(d)]. The diffraction pattern of Ni-implanted 304 showed no lattice dilation, as expected, since Ni atoms occupy substitutional lattice sites. As presented earlier, sputtering during Ni implantation removed 50 nm of the polished surface layer. Therefore, it is likely that most of the polishing-induced martensite, which resided in the outermost 50 nm, was sputtered away. Nonetheless, it should be pointed out that earlier studies showed that Ni implantation into the bulk 304 martensite specimens did transform martensite to austenite,[15] suggesting that the Ni-induced transformation could also have occurred in polished surfaces.

Unlike N and Ni implantation, Ne implantation did not remove martensite from the surface, as shown by the strong martensite reflections in Fig. 5(e). In addition, austenite reflections in the Ne-implanted surface were about as intense as those in the polished surface [Fig. 5(a)]. Ne implantation, therefore, did not cause significant martensite-to-austenite or austenite-to-martensite transformations.

Microstructures of polished and implanted surface

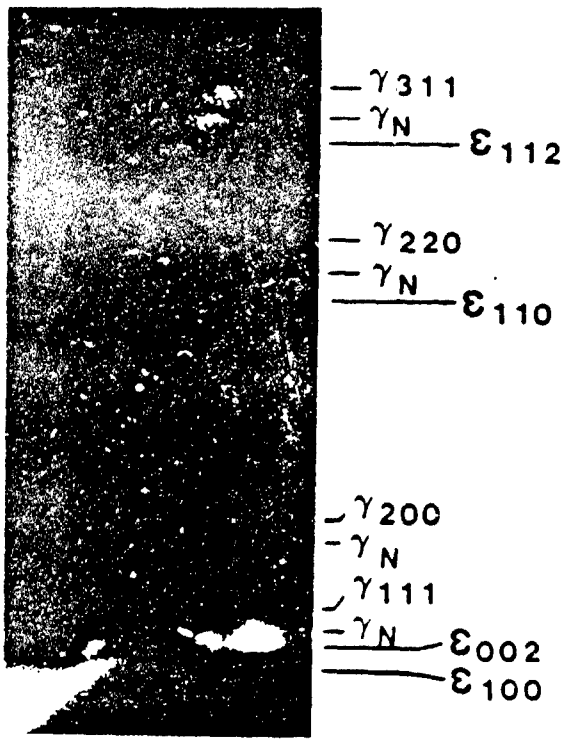


FIG. 6. Portion of an electron diffraction pattern from nitrogen implanted, polished 304 steel surfaces, as in Fig. 5(c), showing reflections for underlying austenite (γ), implanted austenite (γ_N), and hexagonal ϵ-nitride. The γ_{311} reflection does not appear in this part of the pattern.

layers are presented in the transmission electron micrographs of Fig. 7. The polished surface [Figs. 7(a)–7(c)] showed a dense dislocation structure, with the austenite a largely continuous phase and the martensite a smaller and more discrete phase. Because of high strain, only a portion of the austenite present actually appeared "bright" in the dark-field micrograph, Fig. 7(b). Similarly, more martensite was present than is visible in Fig. 7(c). In the implanted surface, the fine-scale implantation damage is difficult to observe against the high dislocation density already present. In the cases of Ni and Ne implantation, no new phases are present and the implanted layer looks similar to Fig. 7(a). For N implantation, nitride precipitates formed and can be seen [Fig. 7(d)] as dark features 10–80 nm in diameter. Table IV summarizes the microstructures observed in polished and ion-implanted polished 304 steel surfaces.

The phase stability of the N-implanted surface under the stress of wear has been investigated by TEM studies of a surface worn part way through the implanted layer. A polished surface, whose diffraction pattern is shown in Fig. 8(a), was subsequently implanted with N (2×10^{17}/cm^2 at 75 keV to produce a deeper and thicker implanted layer) and then worn an additional 70 nm (just short of the N concentration peak). Diffraction patterns of the as-implanted surface (not shown) indicated that, at this dose/energy condition (i.e., lower N concentration), the γ_N phase was strong whereas the ϵ-nitride phase was not detected in the implanted layer. The diffraction pattern of the implanted then polished surface [Fig. 8(b)] displayed strong austenite reflections, again showing the γ_N phase, but only weak martensite reflections, in contrast to the strong martensite reflections of the as-polished surface [Fig. 8(a)]. The weak martensitic reflections from the implanted-then-polished layer may have arisen from material below the implanted layer. Thus, N implantation not only transformed the martensite, it also stabilized the surface against reversion to martensite during subsequent polishing wear. Wang *et al.*[33] have reported that N implantation stabilized the austenitic 304 steel phase from transforming to martensite during fatigue deformation.

IV. DISCUSSION

A. Factors contributing to ion-implanted microstructures

There is, at present, no consensus on what phases should form in N-implanted stainless steel. A number of nitride phases, usually containing chromium or chromiumiron-iron nitrides, have been detected,[16,17,31,34,35] and their occurrence is N concentration dependent.[34] The iron nitride found in the present study undoubtedly contains some chromium and is a phase that should be relatively stable under irradiation.[36] Martensite has also been found in austenitic stainless steels implanted with N^+ ions as well as other ions.[9,16,37,38] As martensite forms in response to stress, implantation-induced martensite has been attributed to the stresses produced by interstitial atoms, precipitates, or the presence of gas bubbles (e.g., with Kr and Ar implantation).[37,38] N implantation has also been shown to form and stabilize austenite in both 304 steel, as shown by a previous study of heavily martensitic 304 steel,[15] as well as in ferritic iron[39] and steel.[40]

This variety of phases in N-implanted steels may be due to differences in the initial surface microstructure. In the present study, the 304 steel surface was heavily deformed and martensitic to begin with, in contrast to the more commonly used electropolished, austenitic surface. The high dislocation density of this heavily deformed surface may serve to trap the N atoms, reducing the resultant stress and changing the conditions for the nucleation of nitrides. Thus the implantation-induced phases may depend on the starting microstructure, whether annealed austenite, deformed austenite, or martensite.

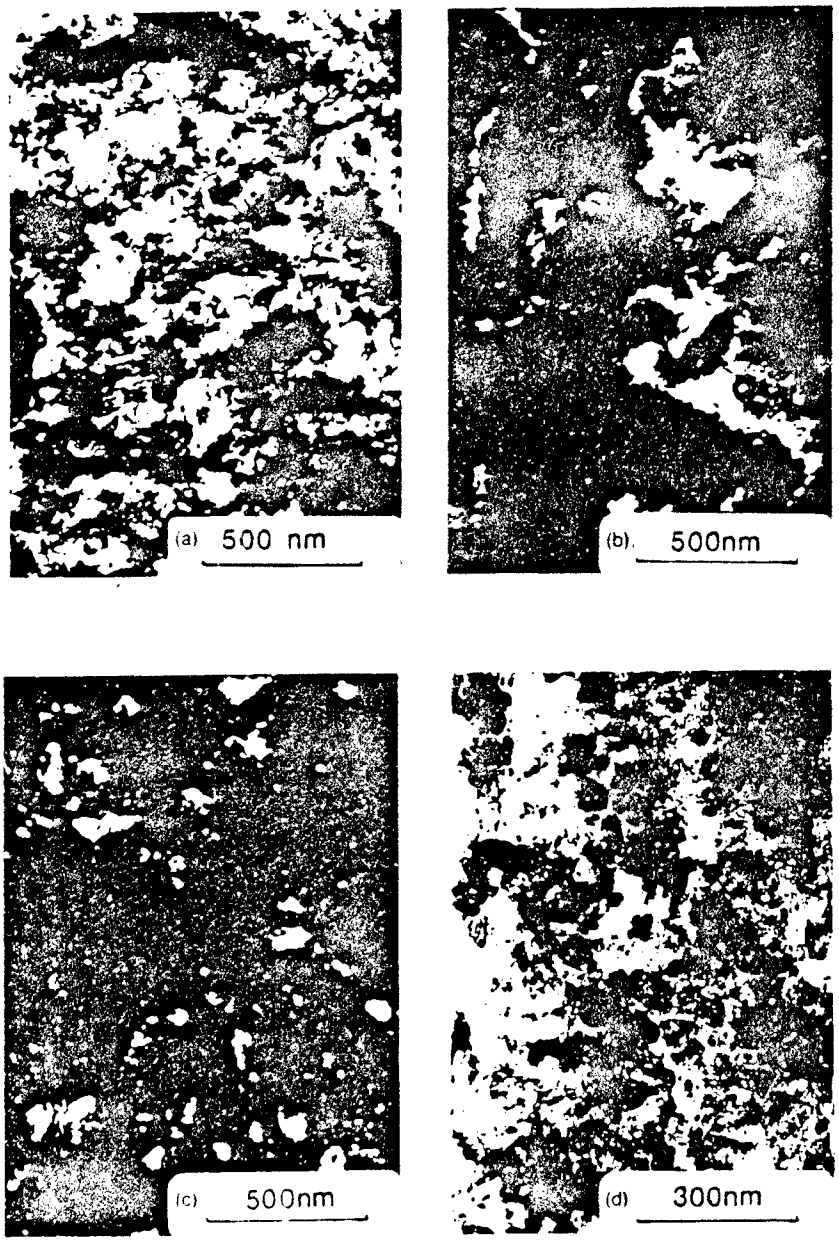


FIG. 7. The TEM micrographs of polished 304 steel surfaces. (a)–(c) nonimplanted, (d) implanted 2×10^{17} N^+/cm^2 at 40 keV; (a) and (d) bright field, (b) dark field, $g=(220)$ γ, (c) dark field, $g=(211)$ α'.

TABLE IV. Near-surface microstructures of implanted and/or polished 304 steel.

Surface preparation	Microstructures: Martensite (α')	Austenite (γ)
Polished	discrete grains in layer ~50 nm thick	continuous but dislocated
then ion milled	none	same
then N implanted	very little	bulk γ and N-dilated γ
then Ne implanted	same	same
then Ne implanted	very little	bulk γ

[illegible]

B. Polishing wear mechanisms of ion-implanted 304 steel

The task of identifying a mechanism that controls the abrasion behavior of implanted 304 steel is particularly difficult because the mechanisms of polishing wear are not well understood.[41] One property, hardness, is commonly associated with abrasion resistance[42] and, specifically, with low-stress, three-body abrasion expected of polishing.[43] However, preliminary studies of 304 steels have shown that N implantation increased the surface hardness,[44,45] which would predict increased

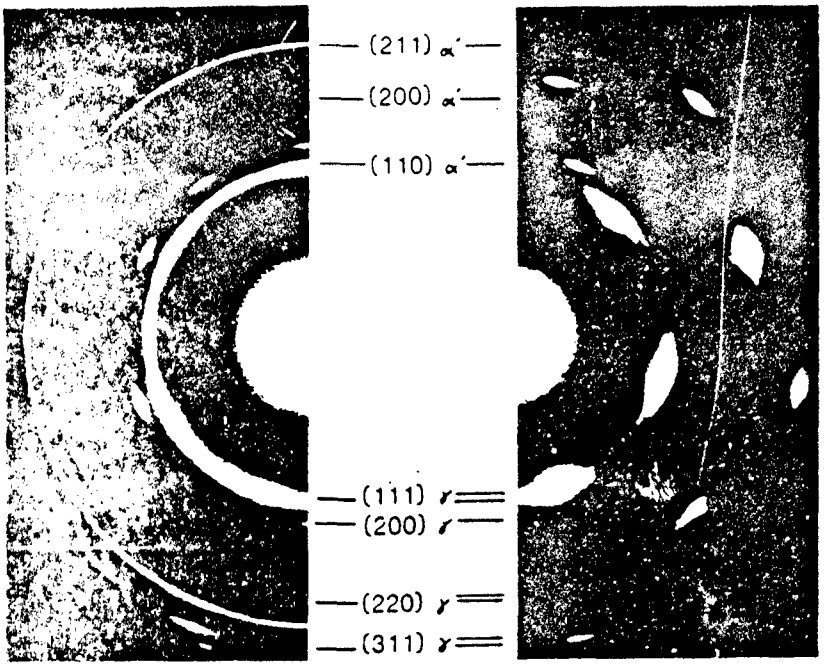


FIG. 8. Large aperture electron diffraction patterns from polished 304 steel surfaces: (a) nonimplanted, (b) implanted 2×10^{17} N^+/cm^2, 75 keV then polished 70 nm.

[illegible] RWR values. Thus changes in the surface [illegible] account for the decrease in RWR. For [illegible], generally, the wear-induced surface [illegible] than the bulk hardness appears to correlate with abrasion resistance.[4,46] This finding led [illegible] that the high abrasion resistance [illegible] austenitic steels was due to the [illegible] formed during abrasion.

Richardson's proposal, we suggested [illegible] that the decrease in RWR after N implantation is due to the transformation of the surface [illegible] austenite. In the present study, this hypothesis is supported by two correlations: first, the decrease in austenite stabilization during polishing of implanted surface and, second, the [illegible] and removal of martensite after Ni implantation. At the same time, the hypothesis is contradicted by implantation results where the RWR [illegible] the retention of surface martensite. [illegible] that weakens this surface phase hypothesis has recently been obtained[47] from polishing wear measurements on heat-treated, cold-worked, and annealed steel specimens. The RWR values for [illegible] remained constant (± 10%) despite widely different surface microstructures before wear. It is necessary to conclude, therefore, that presence or absence of martensite on the 304 steel surface before wear is not a [illegible] controlling the wear resistance.

[illegible] that can influence wear is fracture [illegible] has described how wear resistance can decrease, despite an increase in hardness, when fracture toughness becomes a dominant factor. Moore *et al.*,[49] investigating the strength of alloy surfaces strained by wear, found that ductile fracture limits their strength and thereby controls wear. They showed that pure metals, although relatively soft, attained high wear resistance because of their high ductility. In alloys where solid solution and second phase strengthening reduce ductility, fracture occurred at lower strain levels. Interstitial solid solutions were found to be most effective in reducing ductility whereas dispersed precipitates were the least effective.

The mechanical behavior of metals alloyed by ion implantation can be affected in a similar manner. Spitznagel *et al.*[50] measured the stress–strain behavior of thin, implanted 304 steel foils and found that while N and He implants increased the yield strength, they drastically reduced the strain to failure (ductility). We suggest that in the present experiment, implantation of N, Ni, or Ne decreased the ductility of 304 steel for the following reasons. It is well known that implantation produces defect clusters and small dislocation loops in metals and that these defects decrease ductility.[51] Moreover, implanted atoms themselves further diminish ductility by solid solution strengthening: N, demonstrated by TEM diffraction to be an interstitial, would be the most effective of the three; Ni, a substitutional solute in 304, would have less effect; and least effective would be Ne, which, at the dose used here, is expected to come out of solution and precipitate as a dispersion of gas bub-

bles.[52] As shown in Table II, this is the order of effectiveness for the three implants. We speculate, therefore, that implantation-induced defects and the implanted solute atoms cause decreased ductility and fracture toughness, thereby reducing the intrinsically high abrasive wear resistance of 304 steel.

V. SUMMARY AND CONCLUSIONS

We have identified the near-surface composition and microstructure of polished 304 steel whose wear resistance was reduced by ion implantation. Oxide formation appears to keep the already low sputtering yield of N- and Ne-implanted 304 steel even lower. Sputtering during Ni implantation removed most of the martensite layer formed during polishing (approximately 50 nm) and resulted in a sputter-limited Ni profile and a vacuum-carburized implanted layer. Implantation of the austenite-stabilizing element N into martensitic surfaces brought about a martensite-to-austenite phase transformation and formed a two-phase austenite–nitride structure that was stable under wear. The Ni-implanted surfaces were austenitic, due mainly to removal of the martensite by sputtering. The Ne-implanted surfaces appeared to have retained the martensite of the polished surface.

The three implanted species generated qualitatively similar polishing wear behavior, each reducing the RWR over depths commensurate with the implanted layer's thickness, despite producing different compositions and microstructures. This diversity in microstructure makes it unlikely that a specific implantation-induced phase could have decreased the abrasion resistance. A quantitative ranking of the three species puts N as the most effective followed by Ni then Ne in reducing the wear resistance. After demonstrating that this ranking was consistent with solute-controlled reductions of ductility, we suggested that the decrease in abrasion resistance is due to a decrease in ductility of 304 steel brought about by implanted solutes and irradiation defects.

ACKNOWLEDGMENT

The authors thank Serge Fayeulle for critical comments on the manuscript and for assistance in interpreting several TEM features.

APPENDIX

The maximum concentration of implanted ions, assuming a Gaussian distribution, occurs at a depth given by the mean, or projected, range. This "peak" (i.e., at peak depth) concentration, N_p (atoms/cm^3), depends only on the range straggling, δR_p (cm), and dose, F (atoms/cm^2), and is calculated as

$$N_p = 0.4 \times F/\delta R_p .$$

The peak concentration for ions I, which enter a lattice interstitially, can be calculated (in at. %) as

$$[I] = 100 \times N_p/(N_p + \rho)$$

and for ions that enter the lattice substitutionally as

$$[I] = 100 \times N_p/\rho ,$$

where ρ is the atomic density of the nonimplanted lattice. For 304 steel, having an atomic composition of Fe20Cr8Ni, the atomic density is $\rho = 8.6 \times 10^{22}$ atoms/cm^3.

REFERENCES

[1] *Fundamentals of Friction and Wear of Materials*, edited by D. A. Rigney (ASM, Metals Park, OH, 1981).
[2] K. H. Zum Gahr, Met. Prog. 116(3), 46 (September 1979).
[3] R. F. Smart, Tribol. Int. 11, 97 (1978); J. C. Gregory, Tribol. Int. 11, 105 (1978); T. L. Elliott, Tribol. Int. 11, 121 (1978).
[4] R. C. D. Richardson, Wear 10, 353 (1967).
[5] C. Allen, A. Ball, and B. E. Protheroe, Wear 74, 287 (1981–1982).
[6] K.-L. Hsu, T. M. Ahn, and D. A. Rigney, Wear 60, 13 (1980).
[7] N. E. W. Hartley, Thin Solid Films 64, 177 (1979).
[8] L. E. Pope, F. G. Yost, D. M. Follstaedt, S. T. Picraux, and J. A. Knapp, in *Ion Implantation and Ion Beam Processing of Materials*, edited by G. K. Hubler, O. W. Holland, C. R. Clayton, and C. W. White (North-Holland, New York, 1984), p. 661.
[9] S. Fayeulle and D. Treheux, Nucl. Instrum. Methods B 19/20, 216 (1987).
[10] R. N. Bolster and I. L. Singer, Appl. Phys. Lett. 36, 208 (1980); I. L. Singer and R. N. Bolster, in *Ion Implantation Metallurgy*, edited by C. M. Preece and J. K. Hirvonen (AIME, Warrendale, PA, 1980), p. 116.
[11] R. N. Bolster and I. L. Singer, ASLE Trans. 24, 526 (1981).
[12] I. L. Singer and J. S. Murday, J. Vac. Sci. Technol. 17, 327 (1980)
[13] I. L. Singer, Vacuum 34, 853 (1984).
[14] R. G. Vardiman, I. L. Singer and R. N. Bolster, in *Metastable Materials Formation by Ion Implantation*, edited by S. T. Picraux and W. J. Choyke (Elsevier, New York, 1982), p. 269.
[15] R. G. Vardiman and I. L. Singer, Mater. Lett. 2, 150 (1983).
[16] J. L. Whitton, G. T. Ewan, M. M. Fergusson, T. Laursen, I. V. Mitchell, H. H. Plattner, M. L. Swanson, A. V. Drigo, G. Celotti, and W. A. Grant, Mater. Sci. Eng. 69, 111 (1985).
[17] F. G. Yost, S. T. Picraux, D. M. Follstaedt, L. E. Pope, and J. A. Knapp, Thin Solid Films 107, 287 (1983).
[18] S. Fayeulle, in *Wear of Materials 1987*, edited by K. C. Ludema (ASME, New York, 1987), p. 13.
[19] J. L. Whitton, J. Appl. Phys. 36, 3917 (1965).
[20] I. L. Singer, Appl. Surf. Sci. 18, 28 (1984).
[21] I. L. Singer, R. N. Bolster, and C. A. Carosella, Thin Solid Films 73, 283 (1980).
[22] N. E. W. Hartley, Wear 34, 427 (1975).
[23] F.-Z. Cui, H.-D. Li, and X.-Z. Zhang, Nucl. Instrum. Methods 209/210, 881 (1983).
[24] J. F. Ziegler, J. P. Biersack, and U. Littmark, *The Stopping and Range of Ions in Solids* (Pergamon, New York, 1985) (TRIM Version 2.1).
[25] R. N. Bolster and I. L. Singer, in *Mechanical Properties, Performance, and Failure Mode of Coatings*, edited by T. R. Shives and M. B. Peterson (Cambridge U. P., Cambridge, 1984), p. 201.
[26] H. H. Anderson and H. L. Bay, in *Sputtering by Particle Bombardment I*, edited by R. Behrisch (Springer, Berlin, 1981), p. 151.
[27] R. Kelly, Nucl. Instrum. Methods B 18, 388 (1987); W. Husinsky, P. Worz, B. Strehl, and G. Betz, Nucl. Instrum. Methods B 18, 452 (1987)

[28]G. Hultquist, M. Seo, and N. Sato, Oxid. Met. **25**, 363 (1986).
[29]M. Seo, J. B. Lumsden, and R. W. Staehle, Surf. Sci. **50**, 541 (1975).
[30]I. L. Singer and T. M. Barlak, Appl. Phys. Lett. **43**, 457 (1983).
[31]Y. Arnaud, M. Brunel, A. M. Debecdelievre, M. Romand, P. Thevenard, and M. Robelet, Appl. Surf. Sci. **26**, 12 (1986).
[32]K. J. Irvine, T. Gladman, and F. B. Pickering, J. Iron Steel Inst. **207**, 1017 (1969).
[33]J. J. Wang, G. Welsch, H. Bakhru, A. Mashayekhi, and W. Gibson, Nucl. Instrum. Methods B **7/8**, 228 (1985).
[34]S. Fayeulle, D. Treheux, and C. Esnouf, Appl. Surf. Sci. **25**, 288 (1986).
[35]M. Baron, A. L. Chang, J. Schreurs, and R. Kossowsky, Nucl. Instrum. Methods **182/183**, 531 (1981).
[36]D. M. Follstaedt, Nucl. Instrum. Methods B **7/8**, 11 (1985).
[37]E. Johnson, U. Littmark, A. Johansen, and C. Christoloudiles, Philos. Mag. A **45**, 803 (1982).
[38]E. Johnson, A. Johansen, L. Sarholt-Kristensen, L. Graabaeck, N. Hayashi, and I. Sakamoto, Nucl. Instrum. Methods B **19/20**, 171 (1987).
[39]B. Rauschenbach and A. Kolitsch, Phys. Status Solidi A **80**, 211 (1983).
[40]M. Carbucicchio, L. Bardana, and S. Tosto, J. Appl. Phys. **52**, 4589 (1981).
[41]L. E. Samuels, *Metallographic Polishing by Mechanical Methods* (ASM, Metals Park, OH, 1982), 3rd ed., p. 187.
[42]M. M. Khruschov, Wear **28**, 69 (1974).
[43]A. Misra and I. Finnie, Trans. ASME **104**, 94 (1982).
[44]W. C. Oliver, R. Hutchings, J. B. Pethica, I. L. Singer, and G. K. Hubler, in Ref. 8, p. 603.
[45]H. M. Pollock, D. Maugis, and M. Barquins, in *Microindentation Techniques in Materials Science and Engineering*, ASTM Spec. Tech. Pub. 889 (ASTM, Philadelphia, PA, 1986), p. 47.
[46]P. J. Mutton and J. D. Watson, Wear **48**, 385 (1978).
[47]R. N. Bolster, I. L. Singer, and R. G. Vardiman, unpublished results.
[48]E. Hornbogen, Wear **33**, 251 (1975).
[49]M. A. Moore, R. C. D. Richardson, and D. G. Atwood, Metall. Trans. **3**, 2485 (1972).
[50]J. A. Spitznagel, B. O. Hall, N. J. Doyle, R. Jayram, R. W. Wallace, J. R. Townsend, and M. Miller, in Ref. 8, p. 597.
[51]M. A. Meyers and K. K. Chawla, *Mechanical Metallurgy*, (Prentice-Hall, Englewood Cliffs, NJ, 1984), p. 531.
[52]R. S. Nelson, in *Ion Implantation*, edited by G. Dearnaley, J. H. Freeman, R. S.Nelson, and J. Stephen (North-Holland, Amsterdam, 1973), p. 246.

APPENDIX A4

A4

ION-BEAM ALLOYING AND THERMOCHEMISTRY OF CERAMICS AT HIGH TEMPERATURES.

I.L. Singer and J.H. Wandass[1] .

U.S. Naval Research Lab. Code 6170. Wash.D.C. 20375.

1. INTRODUCTION

High fluence ion implantation affords the possibilities of creating unique materials by overcoming chemical or physical processing limitations. Recently there has been considerable interest in high-fluence implantation into heated substrates in the semiconductor industry, where this "hot" implantation process has been shown to produce buried dielectric layers in Si [Ref. 1]. Hot implantation into metals [Ref. 2] and ceramics [Ref. 3] has also been investigated for producing graded interfaces with improved surface mechanical properties. Unlike "low" temperature implantation, which sustains only athermal mechanisms for solute redistribution and usually produces metastable phase formation [Ref. 4,5,6], hot implantation should be controlled by thermal processes (e.g., thermochemical reactions, diffusion, and defect annealing) leading to stable-phase formation. Hot implantation metallurgy, however, is expected to be more complicated in engineering materials than in Si because three or more elements are generally involved.

This paper has two goals. The first is to show the type of solute redistribution that can occur during high fluence implantation of Al^+ and Ti^+ into two ceramics, SiC and Si_3N_4, at high temperatures. The second is to demonstrate how simple calculated ternary phase diagrams can provide guidelines for interpreting the rather complicated compositions obtained during "hot" implantation and ion mixing of metals in ceramics.

2. EXPERIMENTAL

2.1 Substrate Preparation and Ion Implantation

Commercial SiC and Si_3N_4 substrates (SiC: ESK high-density sintered alpha; Si_3N_4: Norton NC132, MgO hot-pressed and Ceradyne 147, Y_2O_3 hot-pressed) were polished to a 3-μm diamond finish. Ion implantation was performed at NRL in a Varian/Extrion high current implanter. Base pressures before implantation were in the 10^{-7} Torr range. Ti^+ ions were implanted at and energy of 190 keV and Al^+ ions at 110 keV, both to a fluences of 4 x 10^{17} ions/cm^2, in order to achieve approximately 45 at. % peak concentration at the same depth in both SiC and Si_3N_4. The predicted range and range straggling values for the four combinations are about 116 nm and 36 nm, respectively [Ref. 7].

During implantation, substrates were either held at room temperature or implanted "hot." "Hot" implantation denotes direct heating of the substrates by the intense ion beam (up to 40 μA/cm^2) and was achieved by suspending the substrates in a Mo sheet basket during implantation. An optical pyrometer, calibrated by a thermocouple, was used to monitor the substrate temperature. A few minutes after implantation commenced, substrates reached temperatures of 900 °C. For both cold and hot implantation conditions, substrates were partially masked in order to retain a nonimplanted area of each surface.

---

[1] present address: AKZO Chemie America, Dobbs Ferry, NY

2.2. Surface Analysis

The near surface composition was investigated by X-ray Photoelectron Spectroscopy (XPS). XPS was performed with monochromatized Al X-rays in a Surface Science Instrument (SSI) small-spot analyzer. Sputter depth profiling was accomplished using 3 keV Ar^+ ion bombardment. Depths of the ion-milled craters were measured by Michelson interferometry. Data analysis was performed using SSI software routines. Composition vs depth profiles were quantified by integrating the photoelectron spectra and normalizing them using SSI's modified Scofield cross sections. Scanning electron microscopy (SEM) and energy-dispersive X-ray analysis (EDX) were performed in a commercial instrument.

3. RESULTS

3.1. Al-implantation. Scanning electron microscopy of implanted SiC showed submicron-size spherical particles distributed uniformly over the implanted surface. These particles can be seen in the SEM micrograph in Fig. 1, surrounding the Vickers' indentation in the hot-implanted surface. EDX analysis (V_e = 5 keV) on a sphere, between the spheres and over wide areas gave Al/Si ratios of 2.5, 0.4, and 0.5 respectively, indicating that the spheres were composed mainly of Al.

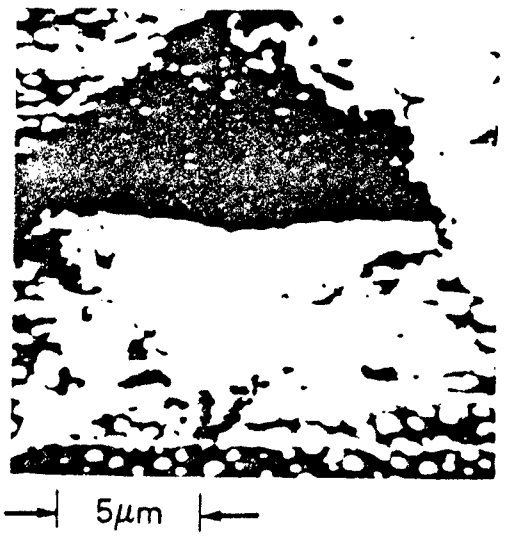


FIGURE 1. Scanning electron micrograph of Al-implanted (hot) SiC surface, showing Al-rich spheres.

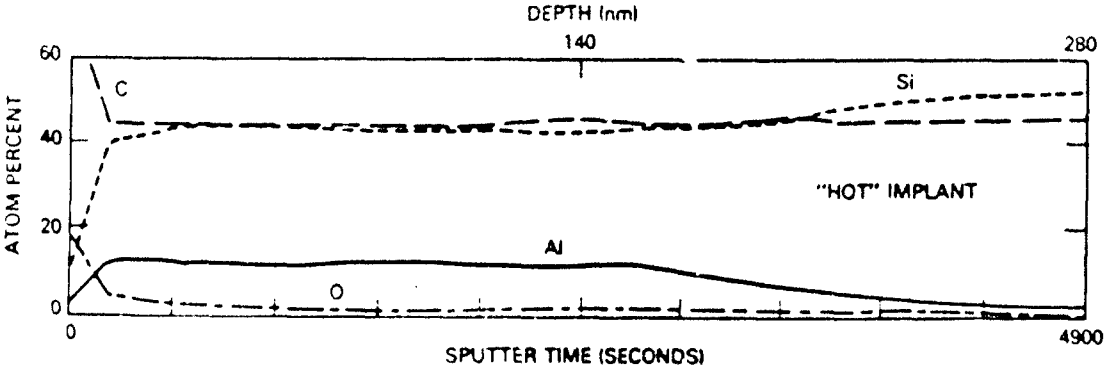


FIGURE 2. XPS sputter-depth profile of Al-implanted (hot) SiC.

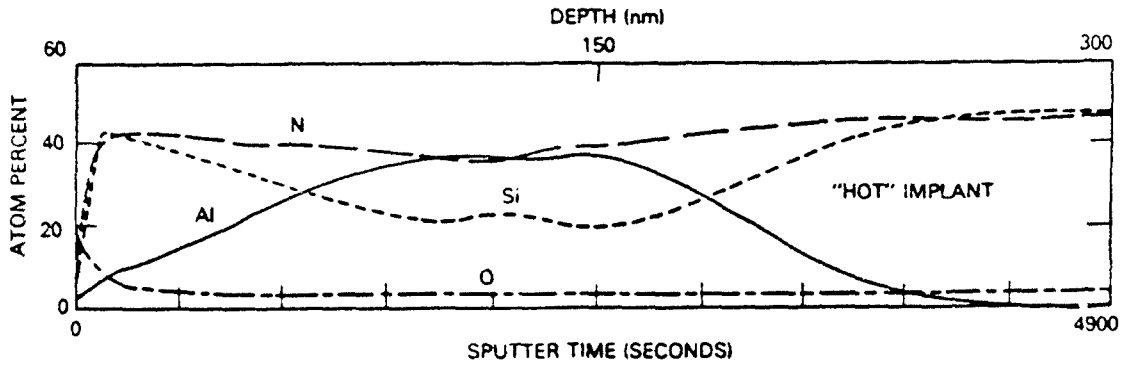


FIGURE 3. XPS sputter-depth profile of Al-implanted (hot) Si_3N_4.

In order to obtain reliable XPS depth profiles of the hot implanted SiC layer, the Al spheres were etched off the surface with a 20% aqueous sodium hydroxide solution. The XPS depth profile, displayed in Fig. 2, shows a flat Al concentration of 17% to a depth of about 200 nm. Room temperature implantation profiles (not shown), by contrast, showed a Gaussian-like distribution, with a peak concentration at 110 nm of around 40 at. %. Apparently, in the hot-implanted substrate, Al moved to the surface during implantation and, because the temperature was above the melting point of Al (ca. 660°C in bulk), it melted and formed droplets of Al.

An XPS depth profile of the hot implanted Si_3N_4 layer is shown in Fig. 3. This profile was more nearly Gaussian, although it too displayed a somewhat flat top, leveling out at a concentration of about 40 at. %. Room temperature Al implantation showed a more sharply peaked Gaussian profile (not shown).

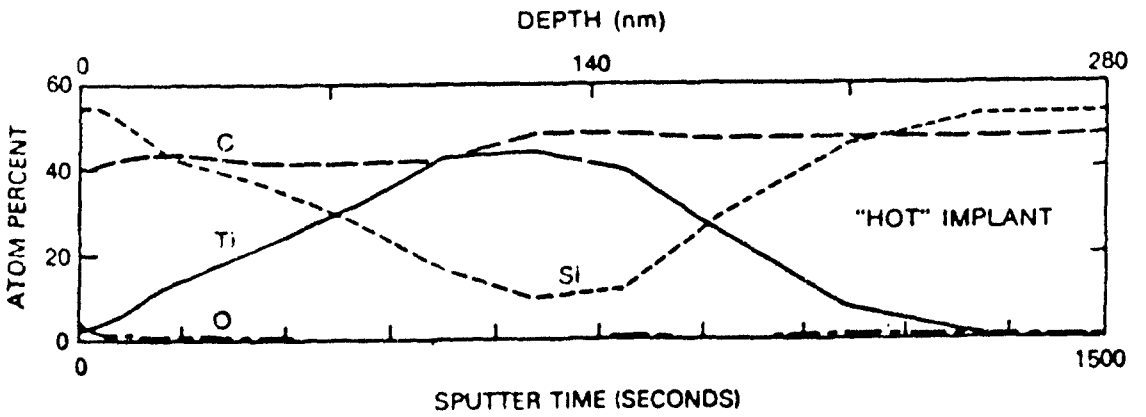


FIGURE 4. XPS sputter-depth profile of Ti-implanted (hot) SiC.

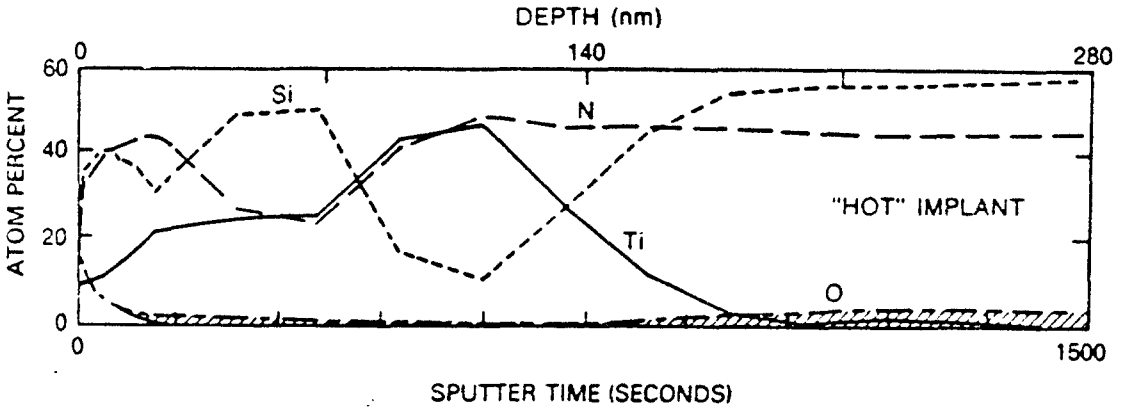


FIGURE 5. XPS sputter-depth profile of Ti-implanted (hot) Si_3N_4.

3.2. Ti-implantation. XPS depth profiles of Ti implanted (hot) into SiC and Si_3N_4 are shown in Figs. 4 and 5, respectively. These profiles, reported and discussed elsewhere [Ref. 3], are presented here for comparison with the hot Al implantation profiles. The Ti depth profile in the SiC substrate shows a Gaussian-like distribution, similar to that found in the room temperature Ti-implanted SiC. By contrast, in the hot-implanted Si_3N_4 substrate, the profile shows considerable Si outmigration combined with TiN formation at two depths. These features have also been confirmed by TEM and RBS analysis [Ref.8], the latter a profiling technique which does not suffer from preferential sputtering and the resultant composition changes often found in XPS profiles.

4. DISCUSSION

In order to understand the compositions achieved by high fluence, hot implantation into compounds, both thermdynamic and kinetic factors should be considered. In this paper, however, we focus only on thermodynamics; in particular, on a simple method for predicting possible solute redistribution and phase formation. The method relies on calculated ternary phase diagrams, or more accurately, on isothermal sections of calculated ternary phase diagrams. Similar diagrams have been used recently to rationalize interfacial reactions in a number of metal-Si-O systems [Ref. 9] and ternary semiconductor systems [Ref. 10].

Ternary or higher order phase diagrams provide the correct description of competing phases where three or more components are in thermodynamic equilibrium [Ref. 11]. Unfortunately, complete ternary phase diagrams are not available for most materials at all temperatures of interest. For the purpose of assessing possible compositions in the highly nonequilibrium environment of the implanted layer, one may use readily available (albeit of variable quality) thermochemical data to calculate ternary phase diagrams for the elements of interest. In practice, one computes the stable "tie-lines" of the ternary system, i.e., lines joining binary compounds that do not react with one another. In the present treatment, we limit ourselves to ternary phase diagrams incorporating binary compounds. (see Appendix for more details.)

Calculated ternary phase diagrams for Al-Si-C and Al-Si-N are shown in Figs. 6 and 7. For Al-Si-C, two diagrams are shown because calculations showed that the tie lines may have switched from Si-Al_4C_3 to Al-SiC at 570°C or 900°C, depending on the thermochemical data used (see Appendix). The two tie lines for the Al-Si-N diagram, however, were found to be stable at all temperatures.

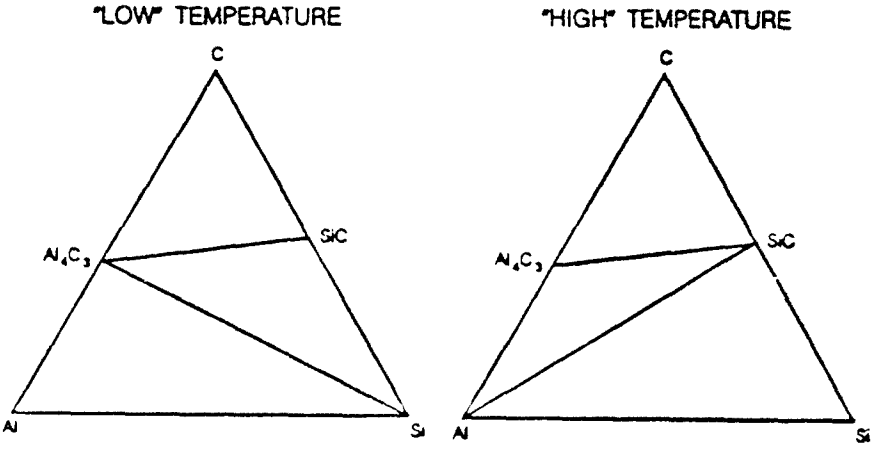


FIGURE 6. Calculated ternary phase diagrams for the Al-Si-C system at "low" and "high" temperatures. (see Appendix for details.)

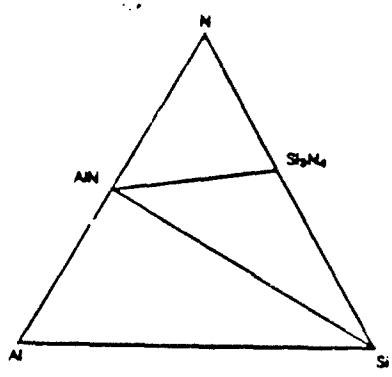


FIGURE 7. Calculated ternary phase diagrams for the Al-Si-N system.

According to the "low" temperature Al-Si-C diagram, Al initially reacts with SiC to form Al_4C_3, plus elemental Si. By constructing a reaction line from Al to SiC, one finds that no elemental Al is produced until the concentration of Al reaches 42 at. %. However, in the "high" temperature Al-Si-C system, elemental Al is the stable product at all concentrations. Considering the experimental data in Fig. 2, we suggest that at this temperature (900°C), implanted Al remained a solute species and was able to diffuse out of the implanted layer. On reaching the surface whose temperature far exceeded the melting point of Al (660°C), the Al agglomerated into the droplets seen in Fig. 1.

By contrast, Fig. 3 shows that very little Al migrated out of the hot-implanted Si_3N_4 layer because most of the Al, according to Fig. 7, tends towards compound AlN, not elemental Al, formation. At Al concentrations above 36 at. %, however, free Al should form, which could account for the flattening of the hot-implanted Al profile at peak concentrations about 40 at. %.

To more easily visualize and better quantify compound formation in implanted layers, we have constructed hypothetical phase distribution vs depth profiles for the two ternary systems. These profiles were calculated from the Al-Si-C and Al-Si-N ternary diagrams in Figs. 6 and 7, using the lever rule applied to the Gaussian depth distributions predicted for the energy/fluence conditions used. The phase profiles for Si_3N_4 implanted with Al to a fluence of $4 \times 10^{17}/cm^2$ at 110 keV are shown in Fig. 8. One observes the reaction products AlN and Si throughout the implanted layer and elemental Al from a depth of 100 to 140 nm. This is the depth range where the measured Al profile in Fig. 3 flattened out. The phase profiles for SiC implanted with Al to $4 \times 10^{17}/cm^2$ at 110 keV

are shown in Fig. 9. As expected, the profiles give a Gaussian profile of elemental Al in a diluted SiC matrix. These profiles are particularly useful for a systems like Al-Si-N or even the more complex Ti-Si-N ternary [Ref. 8] where mixtures of compounds and elements are present.

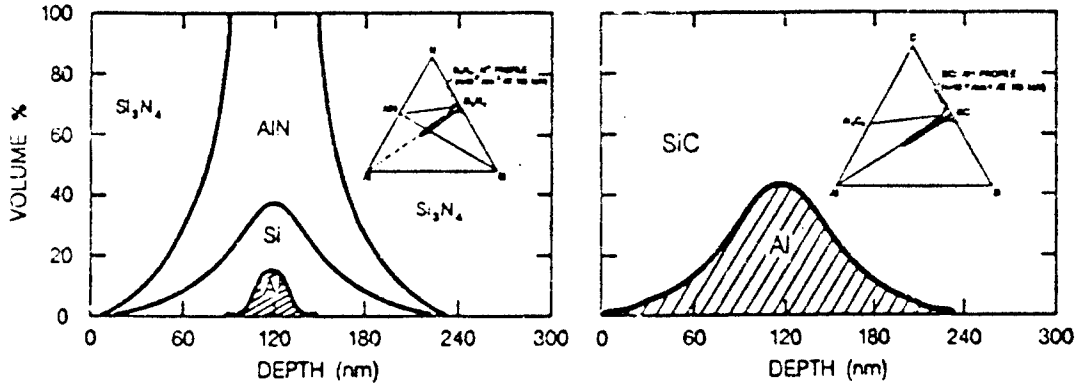


FIGURE 8. Calculated phase distributions vs depth distribution for Al implanted at 110 keV to a fluence of 4 x $10^{17}/cm^2$ into Si_3N_4. (left)

FIGURE 9. Calculated phase distributions vs depth distribution for Al implanted at 110 keV to a fluence of 4 x $10^{17}/cm^2$ into SiC. (right)

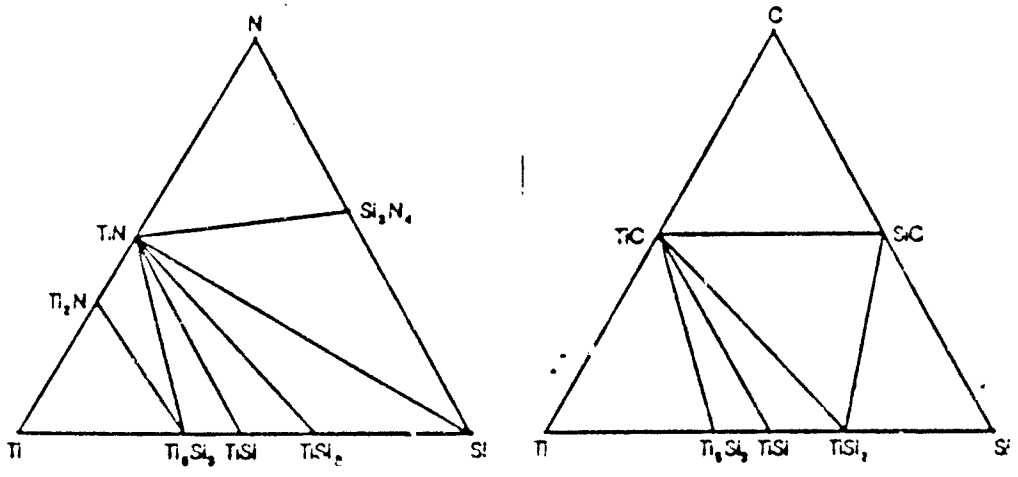


FIGURE 10. Calculated ternary phase diagrams for the Ti-Si-N system.

FIGURE 11. Ternary phase diagrams for the Ti-Si-C system, adapted from Ref. 13.

Calculated ternary phase diagrams have been used in a similar fashion to explain the concentration vs depth profiles of Ti implanted into Si_3N_4 and SiC (Figs. 4 and 5). The calculated Ti-Si-N diagram [Ref. 12] is shown in Fig. 10. In the reaction of Ti with Si_3N_4, elemental Si is produced at all concentrations of Ti up to about 44 at. % because of the tie line that joins TiN to Si. Again, we suggest that the redistribution of Si in Ti-implanted Si_3N_4, presented in Fig. 5, is possible because of the presence of free Si [Refs.3,8]. By contrast, there is no tie-line joining either Si or Ti in the Ti-Si-C ternary diagram (see Fig. 11) [Ref. 13], and the reaction of Ti with SiC up to elemental Ti concentrations of 45 at. % produces only compounds (carbides and silicides). A phase distribution vs depth profile for SiC implanted with Ti to 4 x $10^{17}/cm^2$ at 190 keV is

illustrated in Fig. 12. Hence, while many reactions should occur as the Ti implantation concentration increases, elemental Si is not expected to be one of the products therefore no solute redistribution of Si is predicted.

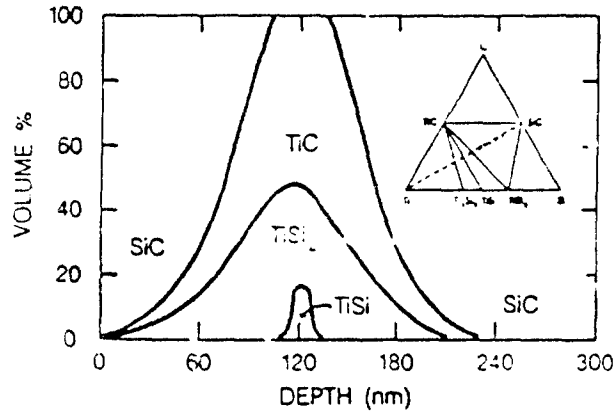


FIGURE 12. Calculated phase distributions vs depth distribution for Ti implanted at 190 keV to a fluence of 4 x $10^{17}/cm^2$ into SiC.

Ternary phase diagrams may also be used to assess thermochemical factors influencing ion mixing of metals on insulators. Previous considerations of thermochemical factors in ion-mixing studies have been based on "the enthalpy rule of metal-insulator mixing," which holds that mixing occurs only if the reaction enthalpy is negative [Ref. 14,15,16]. The reaction enthalpy is determined by writing the balanced equation for reactants of a metal-insulator system against known reaction products. Reaction enthalpies are then calculated using standard heats of formation data as found in e.g. Ref. 17. For example, in the Zr-Al_2O_3 system, one calculates enthalpies for the equation

$$3Zr + 2Al_2O_3 = 3ZrO_2 + 4Al. \qquad (1)$$

Farlow et al [Ref. 15] recently ion mixed and analyzed more than 20 metal-insulator pairs and found the rule held for most, but could not account for mixing in the Zr-Al_2O_3 system, whose reaction enthalpy was nearly zero. This apparent ambiguity of the enthalpy rule, however, can be understood by examining the calculated Zr-Al-O ternary phase diagram, illustrated in Fig. 13. If one draws a reaction line (shown as a dashed line) between Zr and Al_2O_3, it is clear that Al_2O_3 is reduce (initially) to ZrO_2 and Al_2Zr, not to the reaction products given in eqn. 1. The problem with applying the enthalpy rule in this case was that the reaction enthalpy was calculated for the obvious product, but it was the wrong product. In calculating the ternary diagram in Fig. 13, all reactions products were considered.

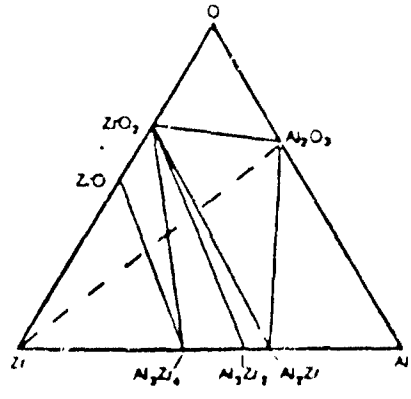


FIGURE 13. Calculated ternary phase diagrams for the Zr-Al-O system (T < 1400°C). The dashed line is a reaction line that depicts compositions obtained by reacting Zr with Al_2O_3.

A second example of the ambiguity inherent in the enthalpy rule is found in Ref. 16, where the authors attempted to use the rule to explain results of ion mixing Ti on Si_3N_4. They computed a positive enthalpy assuming TiSi or $TiSi_2$ products but a negative enthalpy assuming a TiN product and had to conclude that the reaction could go "...either way, depending on the assumed reaction product." The ternary phases diagram in Fig. 10 shows explicitly which reaction products are expected (e.g. TiN and Si) and predicts mixing if thermodynamics were the controlling factor. (In fact, although the authors in Ref. 16 did not observe mixing in the Ti-Si_3N_4 system, Noda et al [Ref. 18] have presented clear evidence for mixing at room temperature.) Ternary phase diagrams, therefore, should be used in place of the enthalpy rule of mixing because they perform the same function as the enthalpy rule but take into account all possible reactions. And, as discussed in the appendix, the calculated diagrams also include entropy contributions ignored by the enthalpy rule.

5. SUMMARY AND CONCLUSIONS

Surface analysis performed on Al^+ and Ti^+ implanted "hot" into SiC and Si_3N_4 indicated "anomalous" redistribution of Al in SiC and Ti in Si_3N_4. Thermochemical reactions expected in these ternary systems were explained with ternary phase diagrams calculated from thermochemical data for binary compounds. The calculated ternary phase diagrams indicated that elemental Al and elemental Si are favored in the two cases where these species were found to redistribute, but Al and Si compounds were favored in the two other cases where no solute redistribution was seen. Ternary phase diagrams were also shown to be more reliable than the enthalpy rule for predicting ion mixing of metal-insulator pairs. Thus, calculated ternary diagrams appear to be easy to use and useful tools for assessing and perhaps predicting compositions achieved in ion implanted and ion mixed ceramics.

ACKNOWLEDGEMENTS

ILS is indebted to M. Colette Einloth who, with the help of Ensign Tom Smith and Dr. Peter Ehni, developed the programs to calculate and plot the ternary diagrams; Mr. John Wegand for technical assistance; Mr. Dan Buntman, of Surface Science Laboratories, for several XPS analyses and DARPA for funding. JHW wishes to acknowledge the support of a National Research Council-Naval Research Laboratory Fellowship.

APPENDIX

Ternary phase diagrams provide a complete description of phase equilibria in three component systems. In such systems at equilibrium, Gibbs phase rule must be satisfied, i.e., $P = C - F + 2$, where P is the number of phases, C is the number of components, and F is the number of degrees of freedom. For a solid solution of 3 components at constant temperature and pressure, only 2 degrees of freedom are possible, i.e., the concentration of 2 of the 3 components; hence, the number of phases equals the number of components. In such an isobaric, isothermal section of a ternary phase diagram, a region of three phases in equilibrium is represented by a triangular area whose vertices are the three equilibrium phases; the sides of the triangle are tie lines and the vertices specify the compositions of the three co-existing phases. For simplicity (and, in part, out of ignorance) we ignore ternary phases (invariant points) and assume that binary compounds are stoichiometric (no bivariant lines).

An equilateral triangle provides a convenient framework for constructing this simplified ternary phase diagram and determining compositions. The three elements are placed at the vertices of the triangle. Binary compounds, known to exist at the specified temperature/pressure conditions, are placed according to some scale, e.g. at. %, at points on the sides of the triangle. The larger triangle is then subdivided into $n + 1$ tie triangles (where n is the number of binary compounds) whose vertices define, according to the phase rule, the three phases that determine the composition of any point within

the triangle, or two phases if the point lies on a tie line. Tie lines, in other words, connect phases that are stable when brought in contact.

Tie lines are established by calculating the Gibbs free energy of reaction between competing reactions at the point where the two possible tie lines would cross. This is performed by writing balanced equations for all the possible reaction products, such as those given in eqns. (1) and (2) above and (A1) and (A2) below. Tie lines are then chosen by a process of elimination from those reactions which give the lowest negative free energy. Since free energies vary with temperature, tie lines may switch as the temperature changes. Once the ternary diagram is established, the amounts of each phase present at a point in the diagram can be computed by the lever rule [Ref. 11].

In this work, several methods for determining tie lines and their switching temperatures were used because the necessary thermochemical data were either inaccurate or contradictory. Calculations were performed for temperatures from 25°C to 1500°C. In the Si-N-Al case, the reaction

$$4Al + Si_3N_4 = 4AlN + 3Si \qquad (A1)$$

gave $\Delta G°_{298K}$ = -120 kcal/mole, and a tie-line switch would not be expected. However, in the Si-C-Al case, $\Delta G°_{298K}$ values for the reaction

$$4Al + 3SiC = Al_4C_3 + 3Si \qquad (A2)$$

varied from -9 to +3 kcal/mole, depending on the method of calculation, so we had to consider that the tie lines might switch at some temperature between 25°C and the implantation temperature, 900°C.

The first method used room temperature $\Delta H°_{298K}$ and $S°_{298K}$ values to approximated $\Delta G_T = \Delta H°_{298K} - \Delta S°_{298K}(T - 298K)$ [Ref. 17]. The limitations of this approach are obvious, as it does not take into account the temperature dependence of $\Delta H°_{298K}$. This method predicted an Al_4C_3 - Si tie line up to about 570°C, then a switch to an Al - SiC tie line at higher temperatures. The second method used an algebraic representation for the Gibbs energies of reaction: $\Delta G°_T = A + BT \log T + CT$ [Ref.19]. The solution of these equations indicated the same tie lines but a switch temperature of about 900°C. A third method used tabulated values of the Gibbs function for the various reactants [Ref.20]. This method predicted that the Al - SiC tie line is stable over the temperature range 25 to 1500°C. We suggest, therefore, that the Al - SiC tie line should exist at temperatures above 600 to 900°C, or, perhaps, as low as 25°C.

REFERENCES

1. Wilson I.H., Nucl. Instrum and Meth. B1 (1984) 331; also, in "Ion Beam Modification of Insulators," Eds. P. Mazzoldi and G.W. Arnold (Elsevier, Amsterdam, 1987) p. 245.
2. Singer I.L., R.N. Bolster, J.A. Sprague, K. Kim, S. Ramalingam, R.A. Jeffries and G.O. Ramseyer, J. Appl. Phys. 58 (1985) 1255.
3. Singer I.L., Surf. Coat. and Technol. 31 (1987) 487.
4. "Metastable Materials Formation by Ion Implantation," edited by S.T. Picraux and W.J. Choyke (North Holland, N.Y. 1982).
5. Singer I.L., Vacuum 34 (1984) 853.
6. Follstaedt D.M., Nucl. Instrum. Meth., B7/8 (1985) 11.
7. Manning I., and G.P. Mueller, Computer Phys. Commun. 7 (1974) 85.
8. Singer I.L., R.G. Vardiman and C.R. Gossett, in "Fundamentals of Beam-Solid Interactions," ed. M.J. Aziz and L.E. Rehn (MRS, Pgh PA, 1988) 201-206.
9. Beyers R., J. Applied Physics 56 (1984) 147.
10. Lin J.-C., K.-C. Hsieh, K.J. Schulz, and Y.A. Chang, J. Mater. Res., 3 (1988) 148.
11. West D.R.F., "Ternary Equilibrium Diagrams," (Macmillan, New York, 1965).

12. Beyers R., R. Sinclair and M.E. Thomas, J. Vac. Sci. Technol. B2 (1984) 781. [Note an error in the Ti-Si-N drawing in Fig. 4. The position of Si_3N_4 along the N-Si line was incorrectly placed at 33% Si and actually belongs at 43% Si.]; also, verified by the present authors.
13. Adapted from the Ti-Si-C ternary phase diagram in E. Rudy, "Ternary Phase Equilibria in Transition Metal-B-C-Si Systems, Part V," Technical Report AFML-TR-65-2 (Air Force Materials Lab, Wright-Patterson Air Force Base, OH, May 1969), p. 522.; the calculated diagram is similar, except that a tie line connects SiC to TiSi, not $TiSi_2$.
14. Banwell T., B.X. Liu, I. Golecki, M.-A. Nicolet, Nucl. Instrum. Methods 209/210 (1983) 125.
15. Farlow G.C., B.R. Appleton, L.A. Boatner, C.J. McHargue, C.W. White, G.J. Clark, and J.E.E. Baglin, Mater. Res. Soc. Symp. Proc. 45 (1985) 137.
16. Bhattacharya R.S., A.K. Rai, and P.P. Pronko, J. Mater. Res. 2 (1987) 211.
17. Kubaschewski O., and C.B. Alcock, "Metallurgical Thermochemistry," 5th edition (Pergamon Press, Oxford, 1979) Table A.
18. Noda, S., H. Doi, N. Yamamoto, T. Hioki, H. Kawamoto, O. Kamigaito, J. Mater. Sci. Letts. 5 (1986) 381.
19. Kubaschewski O., and C.B. Alcock, "Metallurgical Thermochemistry," 5th edition (Pergamon Press, Oxford, 1979) Table E.
20. Barin I., and O. Knacke, "Thermochemical Properties of Inorganic Substances," (Springer, Berlin, 1973 and 1977).

APPENDIX A5

TRIBOLOGICAL BEHAVIOR OF TiN FILMS DEPOSITED BY HIGH ENERGY ION BEAM ASSISTED DEPOSITION

R.N. Bolster[1], I.L. Singer[1], R.A. Kant[2], B.D. Sartwell[2] and C.R. Gossett[2]
Naval Research Laboratory, Washington, DC 20375-5000 (U.S.A)

SUMMARY

Hardness measurements and abrasive and sliding wear tests were performed on TiN films deposited on metal and ceramic substrates by reactive magnetron sputtering (RS) and by ion beam assisted deposition (IBAD) using 30 keV N^+_2 or 40 keV Ti^+ ions. Composition depth profiles obtained by Rutherford backscattering depicted significant intermixing of film and substrate at the interface. IBAD TiN films were found to be considerably softer and about 1/30 as abrasion resistant as RS TiN films. The IBAD films were extremely adherent to either steel or ceramic substrates and reduced the dry sliding friction coefficient for steel/steel and ceramic/ceramic couples from roughly 0.7 to 0.2. The intermixing of film and substrate atoms can account for the excellent adherence of the IBAD films to otherwise incompatible ceramic substrates such as SiC. Based on these and previous studies, the tribomechanical properties of high energy IBAD TiN films appear to be relatively insensitive to processing parameters such as ion species, ion/atom arrival ratio, and high vacuum conditions--an advantage in commercial film preparation.

---

[1]Code 6170; telephone: (202) 767 2920; telefax: (202) 767 1716

[2]Code 4670; telephone: (202) 767 4800

International Conference on Metallurgical Coatings, April 11 - 15, 1988, San Diego, California

1. INTRODUCTION

Physical vapor deposition (PVD)[1,2] and ion-implantation[3,4] are relatively low temperature processes that can improve surface mechanical properties without significantly changing the geometry or degrading bulk mechanical properties, as do diffusion coatings. But each of these techniques has a major drawback. PVD films often suffer from poor adhesion on certain substrates[5]; this lack of adhesion can restrict the use of films as coatings to improve the tribological properties of bearing elements. In ion implantation, the depth of the modified layer is generally limited to less than 1 μm, the depth that ions with several hundred keV of energy can penetrate solids. The depth limitation also applies to ion beam mixing, a potentially attractive hybrid of coatings and ion implantation that produces an extremely adherent surface layer that, in certain applications, has been shown to improve the tribological properties of materials[6,7]. Another promising new technology that combines the benefits of coatings (e.g., independent control of elemental deposition and film thickness) with those of ion implantation (e.g., independent control of ion beam energy and species) is ion-beam assisted deposition (IBAD), which combines vapor deposition with a directed ion beam [8]. IBAD (which should not be confused with the ion assisted deposition (IAD) process that plays an integral role in film formation through application of a bias voltage to the substrate in the presence of a plasma[1]) is having a major impact in optical technology [9] and is increasingly being investigated with respect to tribological applications [10,11,12,13,14,15].

Previous NRL investigations showed that (N^+)IBAD TiN films deposited on

steel substrates were extremely adherent and ductile and reduced the dry-sliding friction coefficient [12,13]. These IBAD films were analyzed by Auger spectroscopy and were shown to contain significant O and C contamination. In this paper, we have extended the study to investigate both (N^+) and (Ti^+)IBAD TiN films on ceramic as well as metallic substrates. The ductility of the films was investigated directly through Knoop microindentation hardness measurements and indirectly using a polishing wear technique developed for abrasive wear measurements of thin (ca. 100 nm) surface layers [16,17]. Comparisons of IBAD with reactively sputtered (RS) TiN films and N^+-implanted RS TiN films were also made. Friction and wear behavior of IBAD films in dry sliding at high contact stress (ca. 1 GPa) against steel and Si_3N_4 sliders were also determined. Finally, Rutherford backscattering analysis (RBS) was performed in order to provide a more quantitative analysis of the TiN film and the film/substrate interface than previously obtained with Auger sputter depth profiling [12].

2. EXPERIMENTAL

2.1 Substrates and films.

Most of the substrates used were disks 12.7 mm in diameter and about 2.8 mm thick. Nickel disks were machined from electrodeposited nickel, ground, fine ground, and polished with 3-μm diamond. Single-crystal sapphire disks were received with polished faces, which were repolished similarly. Hot-pressed B_4C and SiC disks and hardened M2 and 52100 steel substrates were fine ground and similarly polished.

The RS TiN films were produced by reactive magnetron sputtering on Ni and M2 tool steel substrates. The properties of the films were typical of those

obtained from hard, bright gold colored TiN [18].

The IBAD TiN films were produced by electron beam evaporation of titanium to form a PVD film and simultaneous bombardment with either 30 keV N^+_2 or 40 keV Ti^+ ions generated by a medium-current Varian/Extrion ion implanter. Prior to initiating film deposition, each substrate was "presputtered" with 1 x 10^{16} ions/cm^2 of either N^+ or Ti^+. During film deposition, the IBAD chamber was backfilled with ultra-high-purity nitrogen gas from a base pressure of 2 x 10^{-7} torr to 1 x 10^{-6} torr. The ion/atom arrival ratio, R, ranged from 0.002 to 0.2. The substrates were attached to a heat sink that maintained the processing temperature below 50°C. Areas on these films that were outside of the ion beam will be referred to as "PVD", and the N^+ and Ti^+ bombarded areas as (N^+)IBAD and (Ti^+)IBAD, respectively.

In addition, 70 keV ^{14}N ions were implanted to a dose of 5 x 10^{16} ions/cm^2 into a 5 μm thick RS TiN film. This was done to produce a peak damage distribution (approx. 25 displacements per atom) equivalent to that for an IBAD film deposited with R = 0.1. Predicted range and range straggling values as calculated using TRIM [19] for 70 keV N^+ in TiN and for ion/energy/substrate combinations associated with the IBAD films are given in Table 1.

2.2 RBS analysis.

Composition depth profiles were obtained by Rutherford backscattering spectrometry (RBS) with a 2 MeV beam of the ions impinging the target at normal incidence. The scattered ions were detected at 165° to the beam with a surface barrier detector of about 15 keV energy resolution and subtending a solid angle of about 6 msr. Samples were surrounded by surfaces at liquid nitrogen temperatures to reduce carbon surface contamination.

2.3 Hardness and abrasive wear measurements.

Microhardness measurements were made with a Knoop diamond indenter on a Tukon microhardness tester capable of applying loads down to 0.01 N (1 g).

Abrasive relative wear resistances (RWRs) were determined by mass loss during simultaneous polishing of coated disks and reference disks with 3-μm diamond paste under controlled conditions [16,17]. A wheel polisher was used, with a pressure of 10 kPa for the RS and (N+)IBAD films, and 6.4 kPa for the (Ti+)IBAD and RS:N+ films. The reference surfaces were hardened M2 steel or previously polished RS TiN films.

2.4 Friction and wear measurements.

Friction and wear measurements were performed in air under dry sliding conditions with two different tribotesters. The first was a "stick-slip" machine, in which a ball loaded to 1 kgf slid at low speeds against a coated flat, making unidirectional but multipass tracks. The second tribotester was a ball-on-disk machine, in which a stationary ball wore a circular track on a flat rotating at a speed of approximately 20 mm/s. Peak Hertzian contact stresses ranged from 0.85 GPa to 1.1 GPa for a 12.7 mm (1/2 inch) 52100 steel ball and 1.7 GPa to 2.3 GPa for a 5.56 mm (7/32 inch) Si_3N_4 ball.

3. RESULTS AND DISCUSSION

3.1 Composition.

Quantitative composition depth profiles of (Ti+) and (N+)IBAD films were obtained from the RBS data by fitting the spectra with the simulation program RUMP[20]. The (Ti+)IBAD films had compositions typically 45% Ti, 40% N and about 15 + 5% (O+C). The (N+)IBAD films had similar contamination levels while the PVD (non-IBAD) portions of the films showed considerably higher

levels of (O+C) contamination[13].

Depth profiles of (Ti⁺)IBAD films on Al_2O_3 and B_4C from the RBS data are shown in Figs. 1a and 1b. The film/substrate interface is taken to be the depth where the Ti concentration is reduced to 50% of its level in the film. Depth scales have been constructed at the top of the figures using the atomic densities of 1.05×10^{23} atoms/cm³ TiN, 1.37×10^{23} for B_4C and 1.18×10^{23} for Al_2O_3. The intermixing evident in Fig. 1 at the film/substrate interface was quantified by comparing the slope (12 to 88%) for the experimental data to a simulation for an unmixed film of the same thickness; the simulation utilized the fitted detector resolution and the Bohr straggling value for that thickness. The (Ti⁺)IBAD film on Al_2O_3 showed a slope of 62 keV and that on B_4C 96 keV compared to an unmixed slope of 31 keV. The added slope in the latter case may be in part due to the presence of small pits in the otherwise smooth flat surface of the B_4C substrate, not present in the Al_2O_3. In either case, however, it is clear that significant interfacial mixing has occurred during IBAD.

3.2 Hardness and Abrasive Wear Resistance.

Shown in Fig. 2 are the results of microhardness measurements of (N+)IBAD films approximately 1 μm thick on hardened 52100 steel substrates. The composite hardnesses were lower than those for the substrate, especially at low loads. This clearly indicates that these films were softer than the steel, as noted by Kant and Sartwell [13]. At the lowest loads the indent depths were approaching 1/10 of the film thickness, so that the effect of the substrate was becoming negligible. The true film hardness was thus 1/2 to 1/3 that of the steel. RBS analyses of these two films showed that the one

having the lowest hardness at 0.01 N had an excessive carbon concentration (near 50%) in the outermost 150 nm, which may have been responsible for the flatter curve.

The results of microhardness measurements of films on nickel substrates are shown in Fig. 3. The composite hardness of an (N+)IBAD film was only slightly higher than that of the nickel. A (Ti+)IBAD film showed greater hardness, even though it was thinner. The thin RS film was harder than the (N+)IBAD film of the same thickness. It was also harder than the (Ti+) IBAD film, but not as much as the data indicate, since this film was only 0.13 μm thick rather than 0.2 μm. Thus the (N+)IBAD films were the softest, the (Ti+)IBAD films appeared to be intermediate, and the RS films were hardest. The thickest RS films showed much higher composite hardness, since, at the lowest loads, the effect of the soft substrate was becoming negligible. When the thick RS film was implanted with nitrogen, no substantial decrease in hardness was detected. Even though the implanted layer was quite thin (0.1 to 0.2 μm), a softer implanted layer should have been detected at the lowest loads.

When the various TiN films were subjected to abrasion by 3 μm diamond particles, large differences in their wear resistances were found. As shown in Table 2, the (N+)IBAD and (Ti+)IBAD films were less resistant to abrasion than hardened M2 steel reference surfaces. Both films quickly wore through, exposing the substrate.

The changes in RWR with mass loss of the RS films are shown in Fig. 4. Initially 4 times as resistant as the M2 steel, the films showed an increase with depth over 20 to 30 nm to a steady state wear resistance of 25 times that of the M2 steel. The thinnest (0.2 μm) films, after rising to a RWR of 25,

were soon penetrated by a few deep scratches. Thereafter, even though the exposed area was still small, the mass losses increased rapidly and the RWR dropped as the soft, dense nickel began to erode. The four points in the lower right of Fig. 4 thus represent composite wear of film and substrate and not that of the RS film.

The abrasion resistance of RS films was not reduced by implantation with nitrogen. In fact, the abrasion resistance of the first 50 nm of the film had been slightly increased.

Hardness and abrasive wear measurements give a consistent picture that the IBAD TiN films were considerably softer and less wear resistant that RS TiN films. Moreover, the softening obtained in the IBAD films cannot be attributed solely to implantation damage, since no evidence for softening was seen in the N^+ implanted RS films. In contrast to these findings, Sato et al [14] have measured hardness on thick (1 to 10 μm) IBAD films approaching that of bulk TiN. Their films, were also prepared at room temperature using high energy N^+ beams, and also showed ca. 15 at. % (O + C) contamination. No explanation for the differences in hardness are offered, at present.

3.3 Friction and Durability.

Summarized in Table 3 are the "stick-slip" friction and wear behavior of IBAD and RS films on steel and ceramic substrates in sliding contact with both steel and Si_3N_4 balls. Steady state friction coefficients were between 0.15 and 0.20 for the thick TiN films and for nearly all combinations of IBAD films (N^+ and Ti^+), on steel or ceramic substrates, independent of ion/atom arrival rate or backfill gas (N_2 or NH_3). We attribute this material-independent, low friction coefficient to a transfer film (oxidized Ti nitride) that began to form during the first pass and remained interposed between the ball and wear

track during subsequent passes. First pass friction coefficients for many of the IBAD and the TiN films was also about 0.2. The higher friction coefficients obtained during the first pass against (Ti$^+$)IBAD films on the ceramic substrates may be due to the relatively higher shear strength (hardness) of the (Ti$^+$)IBAD films with respect to the 52100 steel (HK = 8.3 GPa). For reference, substrates without coatings had high friction coefficients, ranging from 0.6 to 0.8.

Microscopy of wear tracks indicated that the IBAD films suffered only mild wear. By contrast, non-implanted (PVD) portions of these films were wiped off during the first pass. The thick RS film showed no signs of wear, whereas part of a thin RS film pulled free of the SiC substrate on the first pass, indicative of poor adherence of TiN films to ceramic substrates.

The wear behavior of coated ceramics contributed to the friction in the following way: A relatively thick transfer layer formed along the center of the Si_3N_4 wear tracks on (Ti$^+$)IBAD and RS films on SiC and on (Ti$^+$)IBAD films on B_4C. The transfer layer was a mixture of oxidized Ti nitride and wear debris from polishing pits and Hertzian cracks in the substrate surface and Si_3N_4 debris from the ball slider, worn flat at these high contact stresses. This debris caused ceramic-to-ceramic contact during sliding, which in turn increased the friction coefficient.

Ball-on-disk tests were performed with the Si_3N_4 ball against the three (Ti$^+$)IBAD coated ceramic flats. Steady state friction coefficients were the same as in the stick-slip test (see Table 3) until film failure. Failure usually occurred at a scratch along the track where the film appeared to be abraded. The Si_3N_4 balls, at the time of failure, had been worn flat at the contact spot, which suggests that Si_3N_4 debris might have contributed to the

failure of the coating. Before the coating failed, debris had transferred to the track, but the IBAD film remained intact across the track. On one sample, film was removed almost immediately (probably during the first pass, as suggested by the friction spikes during each revolution). Fig. 5 shows a portion of this (Ti^+)IBAD film on SiC after 240 revolutions: film failure can be seen in the PVD film where the wear track crossed the boundary into the intact IBAD film.

In general, IBAD films showed impressive endurance and low friction at contact stresses greater than 1 GPa (140 ksi). The adherence of the films, particularly on ceramic substrates, makes the IBAD process worthy of further wear testing.

4. SUMMARY AND CONCLUSIONS

IBAD TiN films prepared with N^+ and Ti^+ ions were found to be considerably softer and much less abrasion resistant than hardcoat-quality RS TiN films. The IBAD films demonstrated high adherence and reduced dry sliding friction when deposited on metal as well as ceramic substrates. The intermixing of film and substrate atoms was clearly depicted by RBS depth profiles and can account for the excellent adherence of IBAD films to otherwise incompatible ceramic substrates such as SiC. Based on these and previous studies, the tribomechanical properties of high energy IBAD TiN films appear to be relatively independent of major processing parameters such as ion species, ion/atom ratio, and high vacuum conditions--an advantage in commercial film preparation.

ACKNOWLEDGEMENT

We would like to thank Kristen Hafterson, Catherine Pollock and John Wegand of Geo-Centers, Inc. for assistance with the hardness, friction and wear studies; Bill Sproul (BIRL) and Tom Thorpe (NRL) for providing TiN films; and DARPA for partial financial support.

REFERENCES

1. R.F. Bunshah et al, Deposition Technologies for Films and Coatings, Noyes, Park Ridge, N.J., 1982.
2. W.D. Sproul, J.E. Greene and J.A. Thornton (eds), Physics and Chemistry of Protective Coatings (CP no. 149), AIP, New York, 1986.
3. J.K. Hirvonen (ed), Ion Implantation, Academic Press, New York, 1980.
4. G.K. Hubler, O.W. Holland, C.R. Clayton and C.W. White (eds), Ion Implantation and Ion Beam Processing of Materials, North-Holland, NY, 1984.
5. D.M. Mattox, Chapter 3 in Ref. 1.
6. K.R. Padmanabhan, Y.F. Hsieh, J. Chevallier, and G. Sorensen, J. Vac. Sci. Technol. A1 (1983) 279.
7. M. Kohzaki, S. Noda, H. Doi, and O. Kamigaito, Mater. Letts., 6 (1987) 64.
8. J.M.E. Harper, J.J. Cuomo, R.J. Gambino and H.R. Kaufman in in O. Auciello and R. Kelly (eds), Ion Bombardment Modification of Surfaces: Fundamentals and Applications, Elsevier, Amsterdam, 1984, p. 127.
9. P.J. Martin, R.P. Netterfield, W.G. Sainty and C.G.Pacey, J. Vac. Sci. Technol. A2 (1984) 341
10. I.N. Evdokimov and G. Fischer, J. Mater. Sci. 15 (1980) 854.
11. J.S. Colligon, A.E. Hill, and H. Kheyrandish, Vacuum, 34 (1984) 843.
12. R.A. Kant, B.D. Sartwell, I.L. Singer and R.G. Vardiman, Nucl. Instrum. Methods B7/8 (1985) 915.
13. R.A. Kant and B.D. Sartwell, Mat. Sci. & Engineering, 90 (1987) 357.
14. T. Sato, K. Ohata, N. Asahi, Y. Ono, Y. Oka, I. Hashimoto and K. Arimatsu, Nucl. Instrum. Methods, B19/20 (1987) 644.
15. G. Dearnaley, Surf. Coat. Technol., 33 (1987) 453.

16. R.N. Bolster, and I.L. Singer, ASLE Trans., 24 (1981) 526.

17. R.N. Bolster and I.L. Singer in T.R. Shives and M.B. Peterson (eds.), Mechanical Properties, Performance, and Failure Modes of Coatings, Cambridge University Press, Cambridge, 1984, p. 201.

18. W.D. Sproul in Ref. 2, p. 157.

19. J.F. Ziegler, J.P. Biersack and U. Littmark, The Stopping and Range of Ions in Solids, Pergamon Press, NY, 1985, (TRIM Version 2.1).

20. L.R Doolittle, Nucl. Instrum. and Methods, B9 (1985) 344.

TABLES

Table 1. Range and range straggling values for IBAD TiN films and implanted TiN[19].

ION (Energy)	N^+ (15 keV)		Ti^+ (40 keV)		N^+ (70 keV)
SUBSTRATE	B_4C	TiN	Al_2O_3	TiN	TiN
RANGE(nm)	31	22	23	21	90
RANGE STRAGGLING(nm)	8.2	10	8.2	8.8	31

Table 2. Composite hardness and relative wear resistance of TiN films

	KNOOP HARDNESS* (GPa)	Rel. Wear Resistance (referenced to M2 steel)
(N^+)IBAD	5	0.8
(Ti^+)IBAD	6.4	0.9
Reactive Sputtered	8.5	25

* 0.1-0.2 μm thick films on Ni at 0.15 μm indent depth.

Table 3. Friction coefficients of IBAD and RS films on steel and ceramic substrates.

		FILM TYPE	IBAD					RS	
		ION	N^+	Ti^+	Ti^+	Ti^+	Ti^+	—	—
BALL	PASS No.	SUBSTRATE	52100	52100	B_4C	SiC	Al_2O_3	H_2	SiC
52100	1st		0.18	0.16	0.52	0.47	0.35	0.20	—
52100	10th		0.20	0.17	0.16	0.20	0.22	0.18	—
Si_3N_4	1st		0.16	—	0.25	0.26	0.29	0.16	0.63
Si_3N_4	10th		0.16	—	0.24	0.43	0.14	0.15	0.42

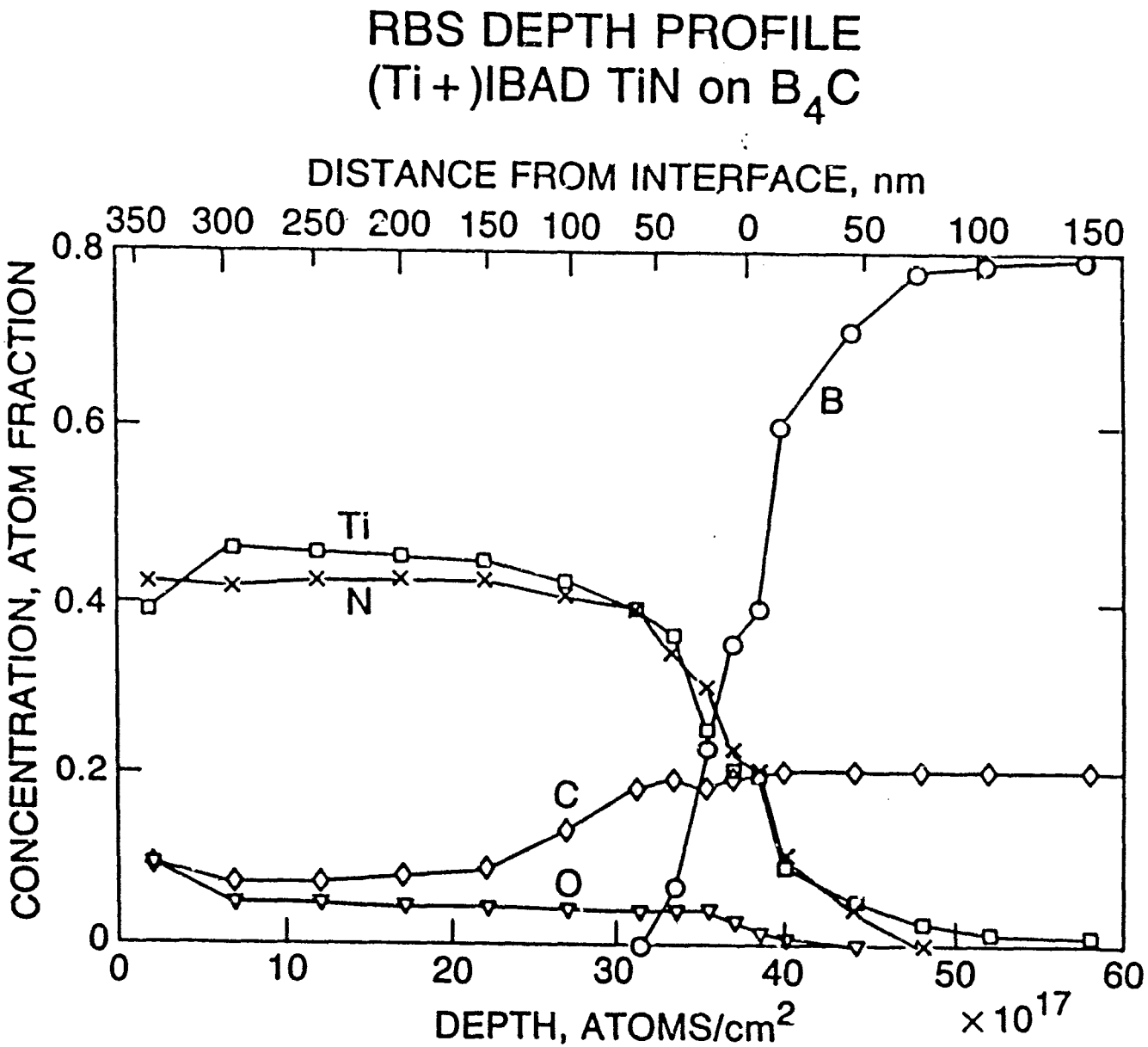


Fig. 1 a. RBS depth profiles of (Ti+)IBAD TiN on B_4C

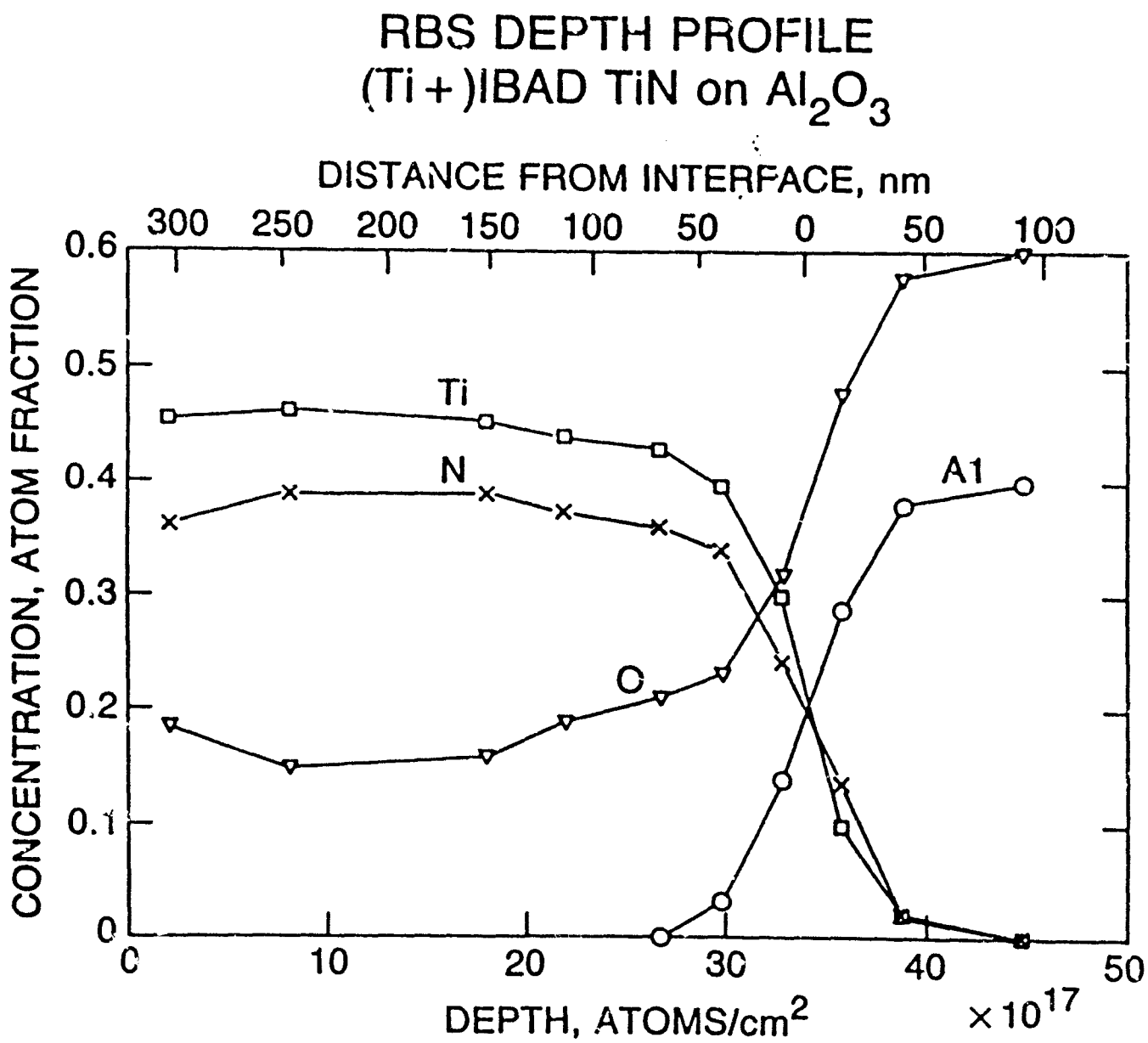


Fig. 1 b. RBS depth profiles of (Ti⁺)IBAD TiN on Al_2O_3.

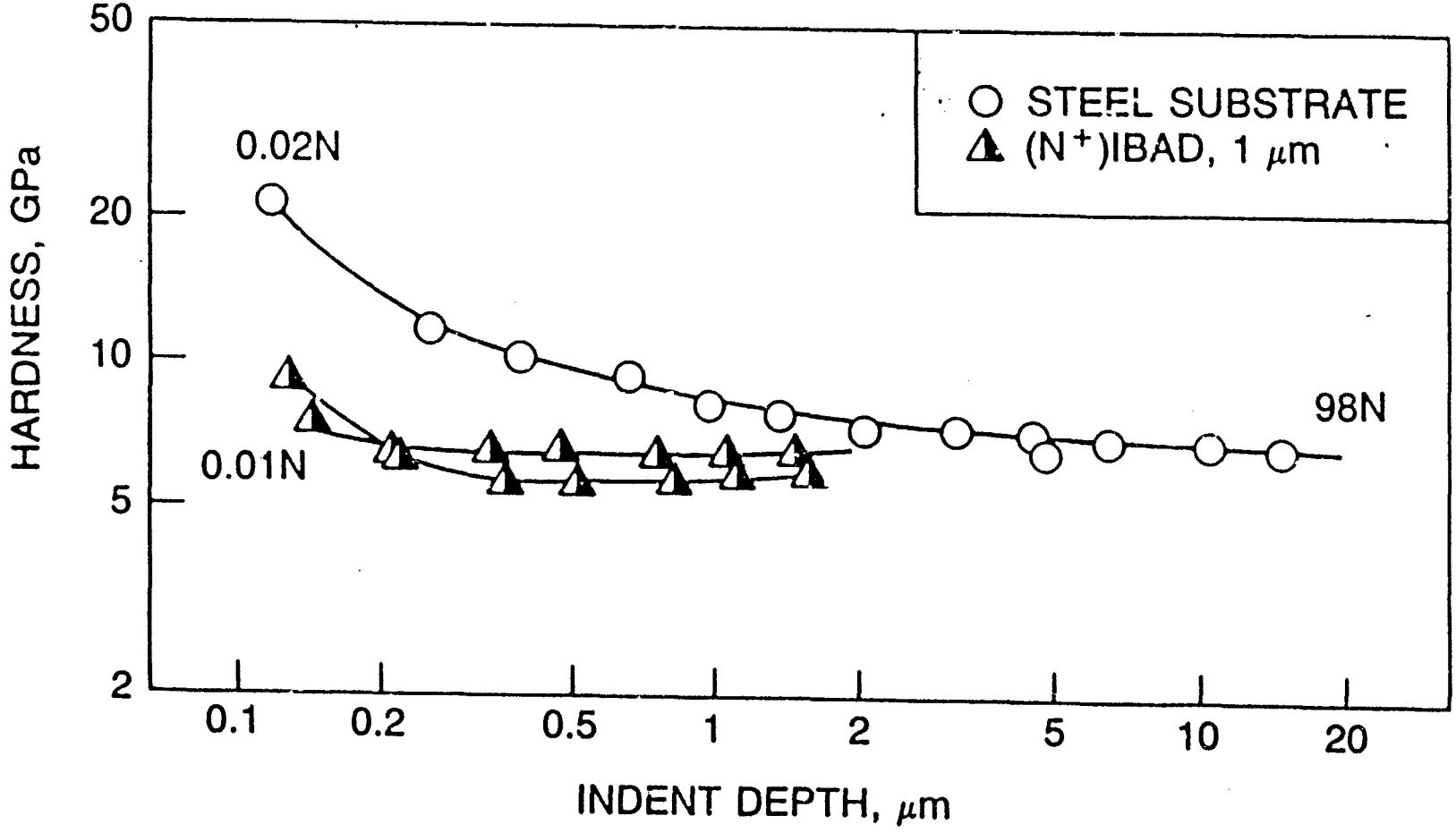


Fig. 2. Composite Knoop hardness vs. indentation depth of thick (N^+)IBAD TiN films on 52100 steel.

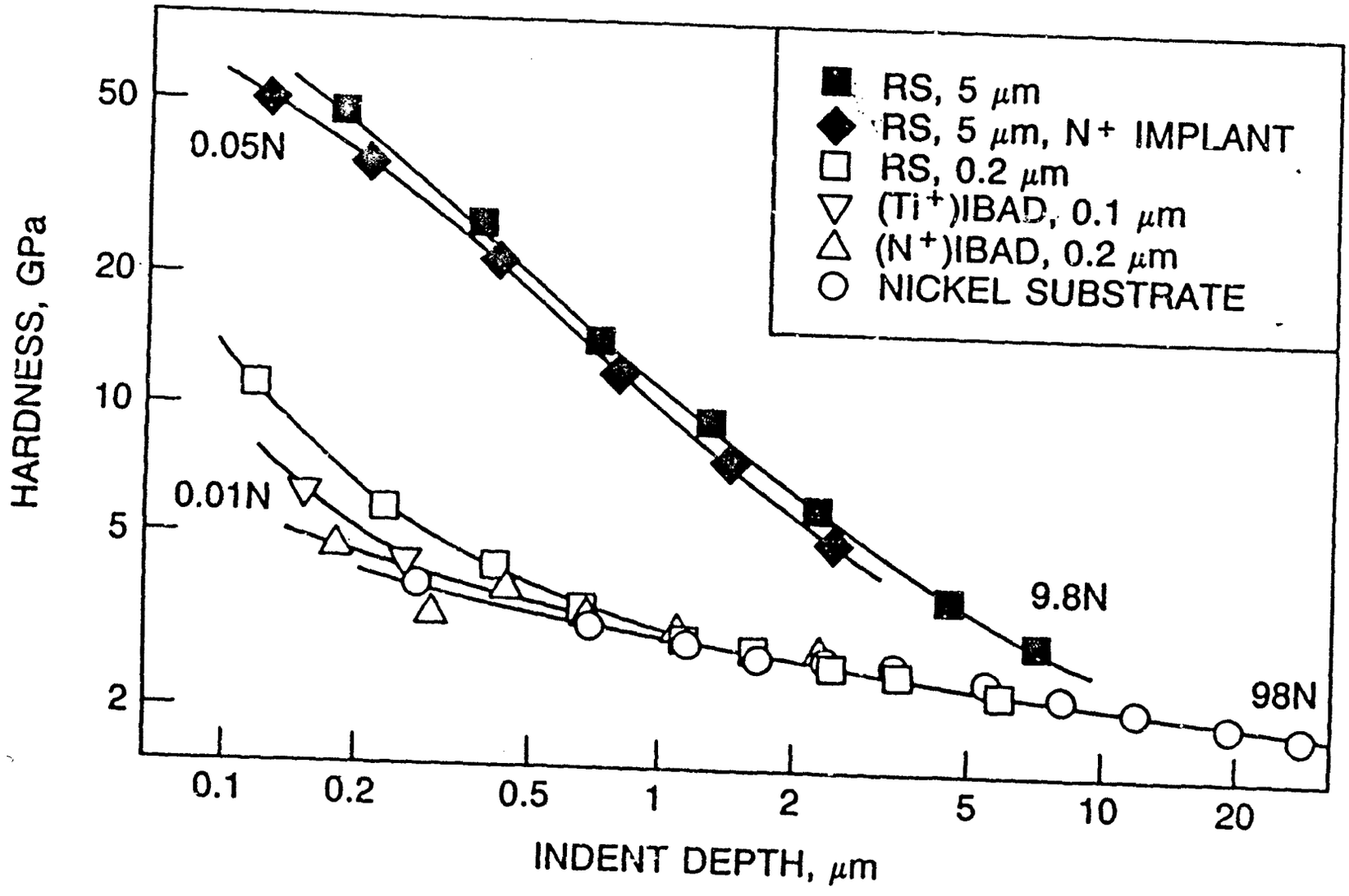


Fig. 3. Composite Knoop hardness vs. indentation depth of IBAD and RS TiN films on nickel.

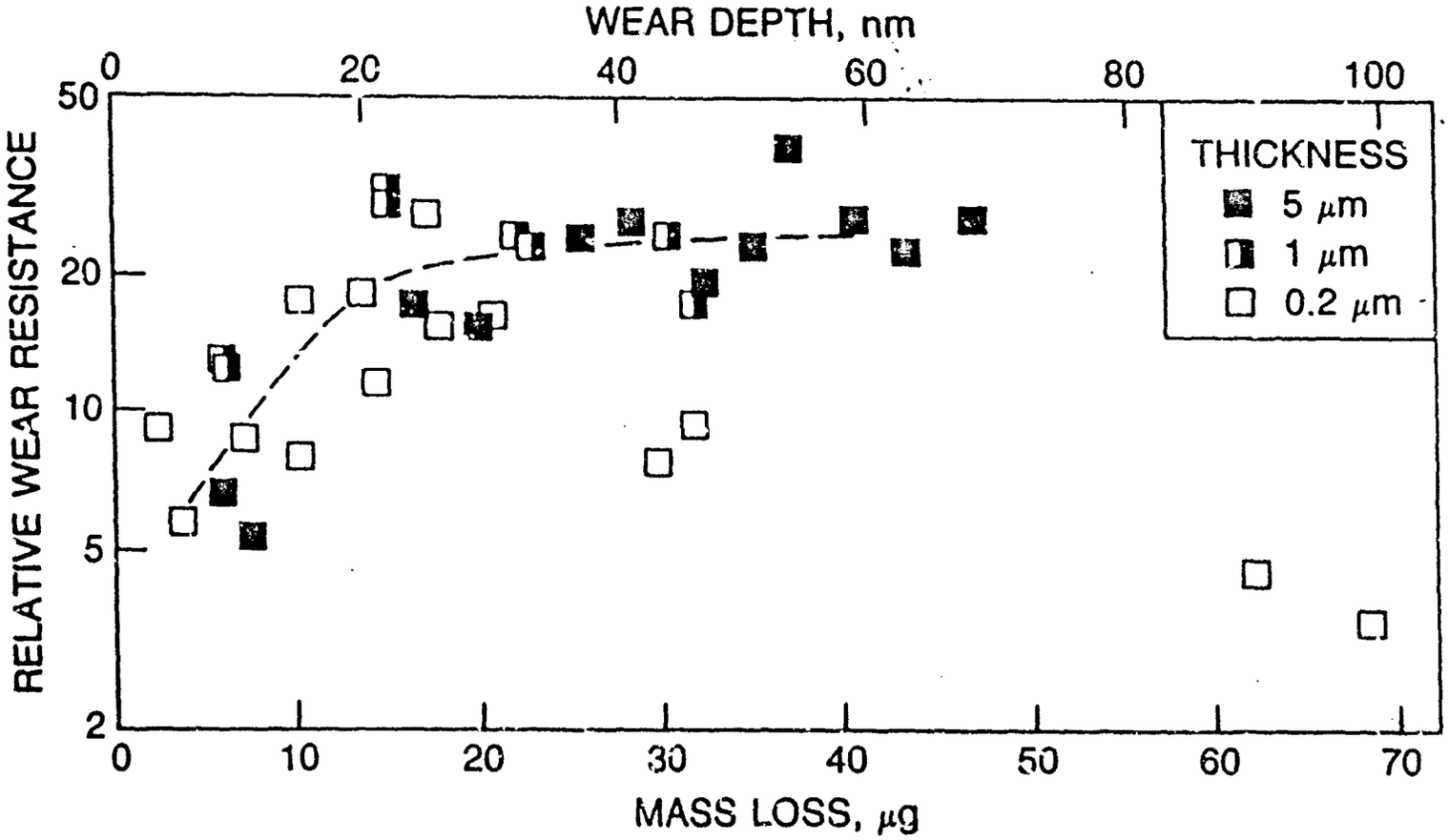
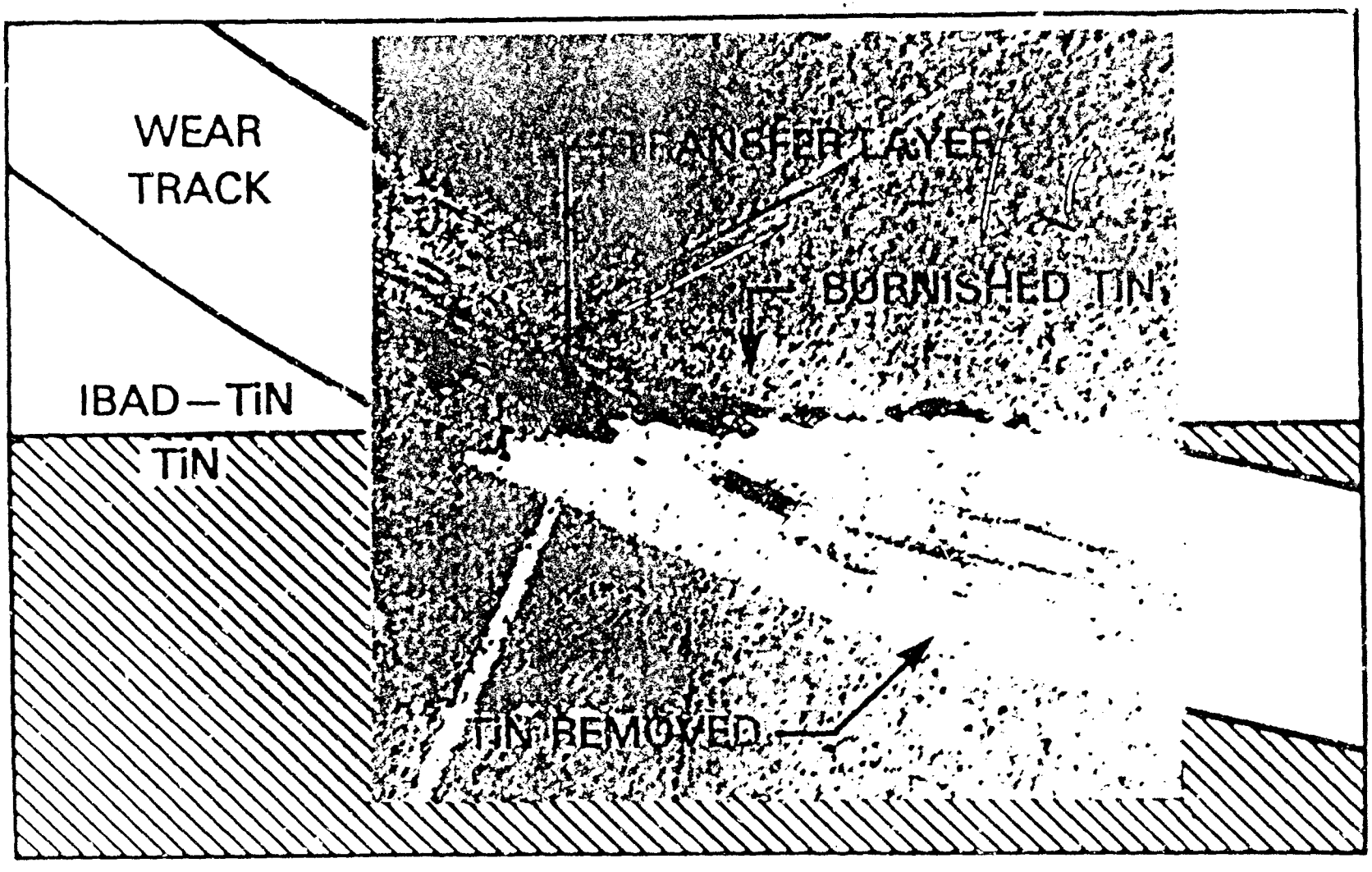


Fig. 4. Relative abrasive wear resistance vs. mass loss of RS TiN films of several thicknesses on nickel substrates referenced to M2 tool steel.

Fig. 5. Ball-on-disk wear track crossing (Ti⁺)IBAD into non-implanted PVD film on SiC substrate (after 240 passes.)



APPENDIX A6

June 1988 Gordon Conference

FRICTION COEFFICIENTS - HOW LOW CAN THEY GO?

I.L. SINGER, R.N. BOLSTER, J. WEGAND[a], S. FAYEULLE[a,b]
NAVAL RESEARCH LABORATORY. WASHINGTON D.C.
[a] GEO-CENTERS, WASHINGTON D.C.
[b] ECOLE CENTRAL de LYON, ECULLY FRANCE

INTRODUCTION

Friction coefficients of low friction films generally do not obey Amonton's law, which finds that the friction coefficient is independent of load. Investigations of thin films of organic, metallic and dichalcogenide materials tend to show decreasing friction coefficients with increasing loads.

This paper examines the load dependence of the friction coefficients of MoS_2 films. Several explanations for this behavior have been proposed:

a. FRICTION TEXTURING - High loads orient MoS_2 grains with (0002) planes parallel to the substrate;

b. HEATING EFFECTS - High loads generate heat, which drives off moisture (known to increase the friction coefficient);

c. FILM SHEARING UNDER HERTZIAN CONTACT - High loads on elastically deformed substrates result in a friction coefficient, u, given by:

$$u \propto S/L^{\beta},$$

where S is the SHEAR STRENGTH of the film, and $1/3 < \beta < 1/2$, depending on nature of contact (point to line). The above relationship follows directly from the interpretation of friction coefficient as the shearing pressure divided by the normal pressure. For elastic (Hertzian) contact, the normal pressure varies as L^{β}, as seen below.

Data taken from the literature and in our laboratory has been analyzed according to the Hertzian contact model for the friction coefficient of a thin easily sheared film on a hard substrate. Applicability of the model and its implications on the lower limits of friction coefficients are discussed.

DEFORMATION OF METALS BY SPHERICAL INDENTERS (TABOR, 1951)

NOMENCLATURE:

L	load	P_m	mean pressure
a	radius of contact	E	Elastic (Young's) modulus
A	Contact area	S	shear strength
R	Radius of sphere		

THE PRESSURE EXERTED BY A SPHERE ON A FLAT IS GIVEN BY:

$$P_m = L/[\pi a^2] \qquad (1)$$

CONTACT AREA UNDER ELASTIC DEFORMATION:

$$A = \pi a^2 = \pi[(3LR)/(4E)]^{2/3} \qquad (2)$$

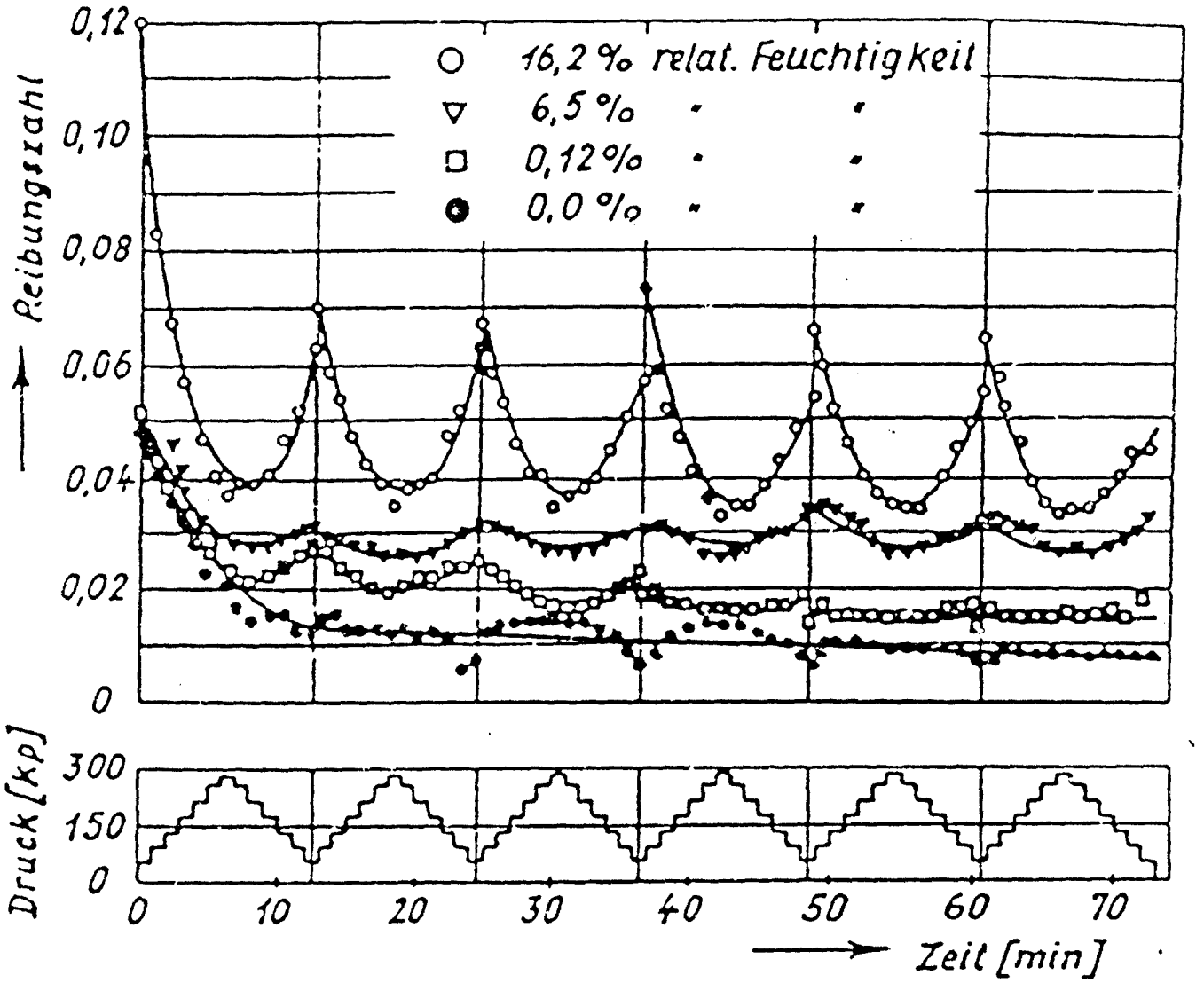
HENCE,

$$P_m = L/[\pi a^2] = 1/\pi * [(4E)/(3R)]^{2/3} * (1/L)^{1/3} \qquad (3)$$

A SIMILAR ANALYSIS FOR CYLINDER VS FLAT GIVES:

$$P_m \propto (1/L)^{1/2} \qquad (4)$$

Gänsheimer (1964)



ild 14: Einfluß von Feuchtigkeit und Belastung auf die Reibungszahl von Molybdändisulfidschichten bei Versuchen mit der LFW-1-Prüfmaschine.

ig 14: Influence de l'humidité et de la charge sur le coefficient de frottement de couches de bisulfure de molybdène lors d'essais faits avec la machine d'essai LFW-1.

14: Influsso dell'umidità e del carico sull'indice d'attrito, negli esperimenti colla macchina di prova LFW-1

Salomon and de Gee (1965)

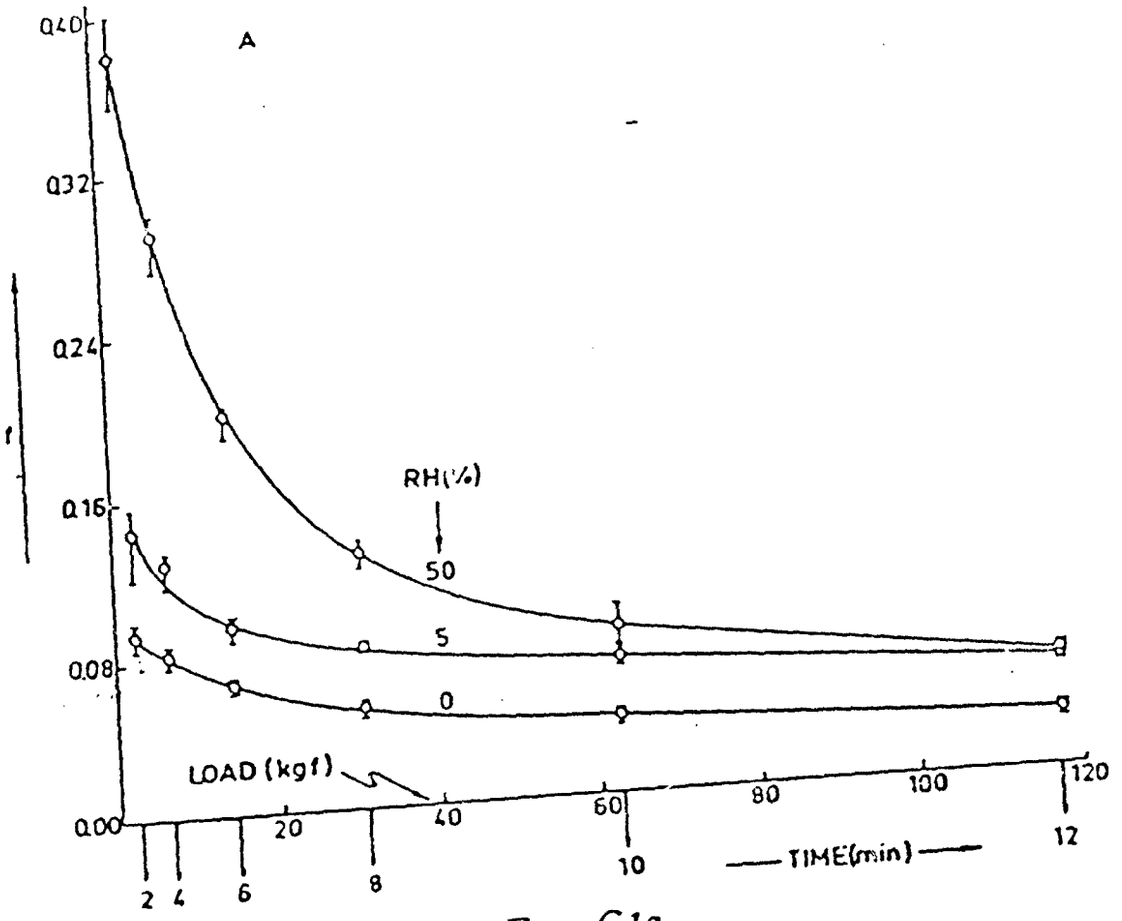
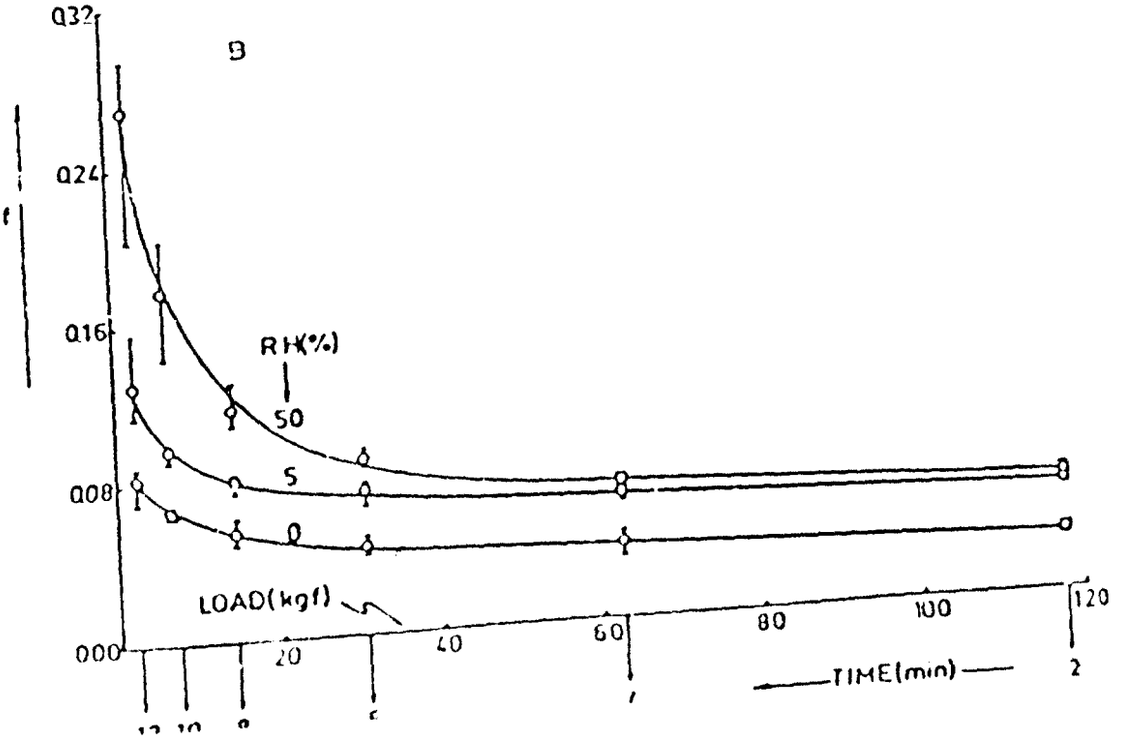
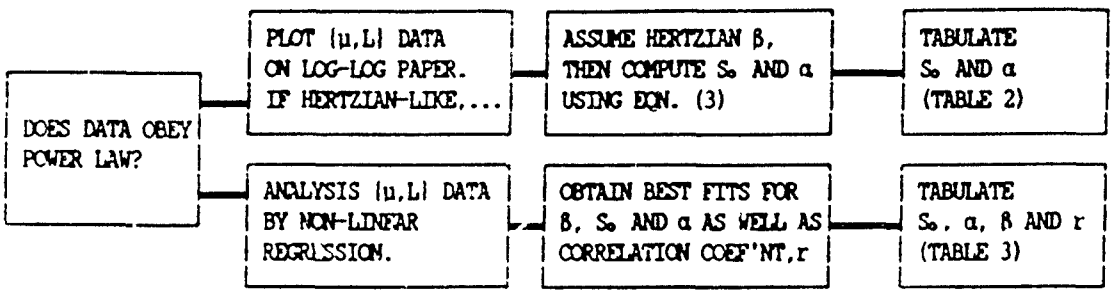
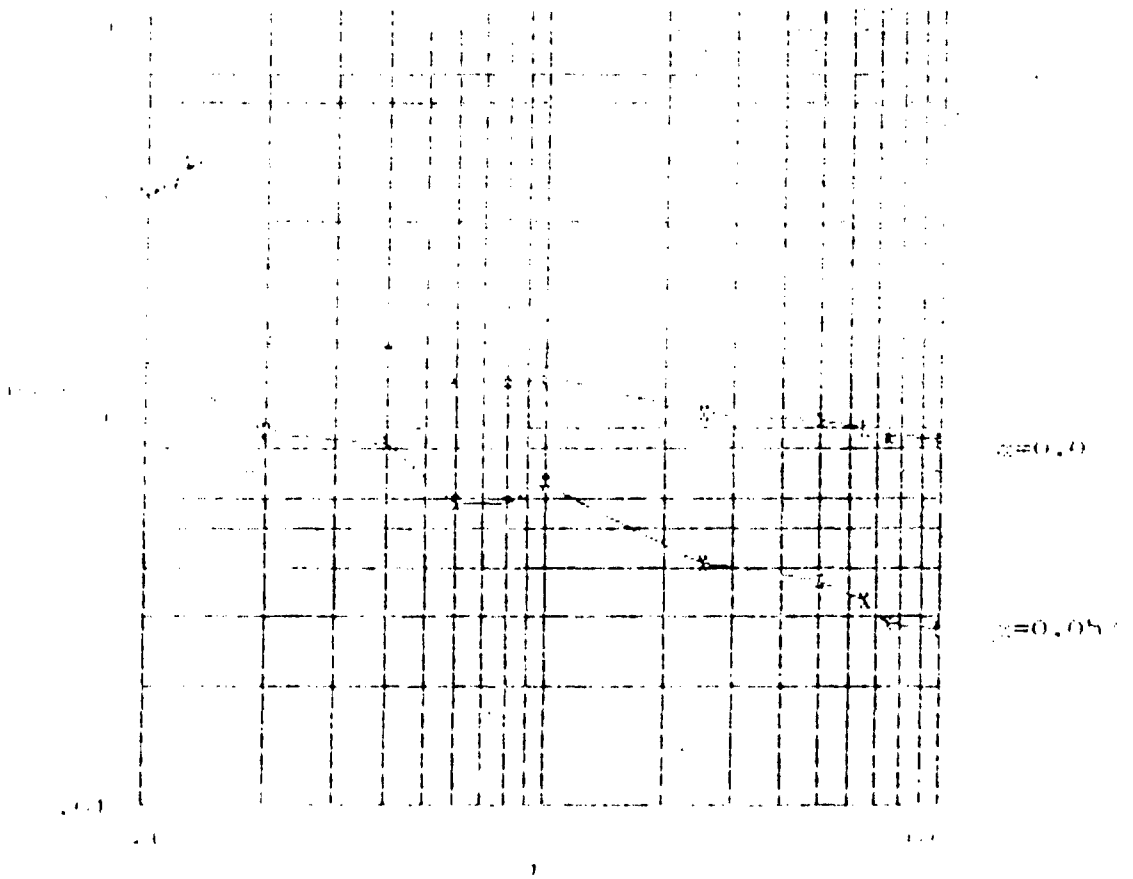


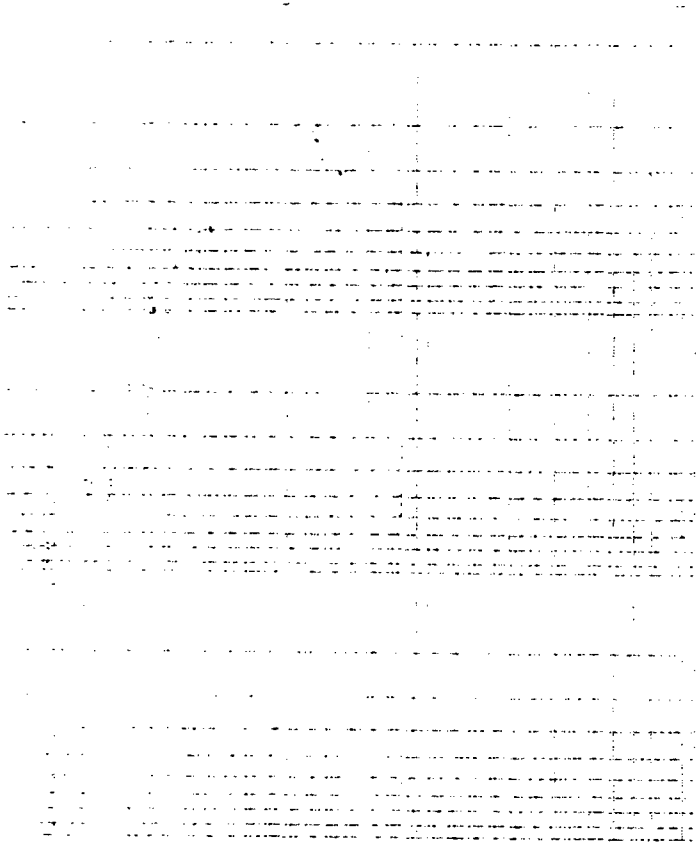
FIG. C1a



ANALYSIS OF μ vs LOAD FOR MoS_2.




=0,0
=0,05



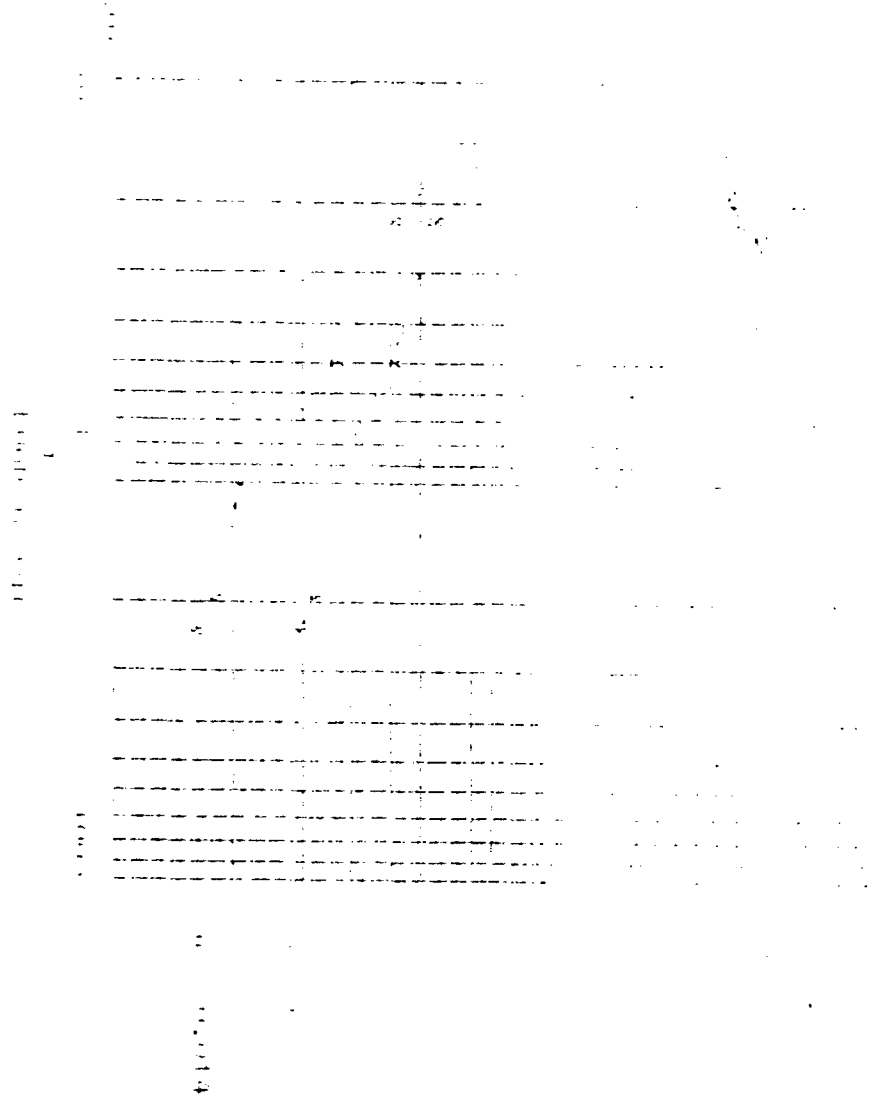


TABLE 3: β, S_o AND α VALUES AND CORRELATION COEFFICIENT BY NON-LINEAR REGRESSION.

INVESTIGATOR	β	α	S_o (MPa)	$\lvert r \rvert$
GANSHEIMER				
best fit				
RH=16.2	0.002-0.08	-0.3-(-11)	7-100	0.99
RH=6.5	0.001	-4-(-10)	50-100	0.95
α=0 fit				
RH=16.2	0.43-0.50	"0"	10-20	0.98-0.99
RH=6.5	0.12	"0"	10	0.95
KARPE				
best fit	0.2-0.4	0.04-0.07	25-40	0.96-0.99
α=0 fit	-0.15	"0"	60-70	0.95-0.97
SALOMON AND DeGEE				
best fit				
RH=50	0.26	-0.13	20	0.998
RH=5	0.19	-0.02	5	0.990
α=0 fit				
RH=50	0.48	"0"	20	0.992
RH=5	0.23	"0"	5	0.990
ROBERTS				
best fit	0.39	0.001	6.2	0.962
α=0 fit	0.33	"0"	6.6	0.962
NRL				
best fit	0.7	0.22	47	0.988
α=0 fit	0.33	"0"	5	0.985

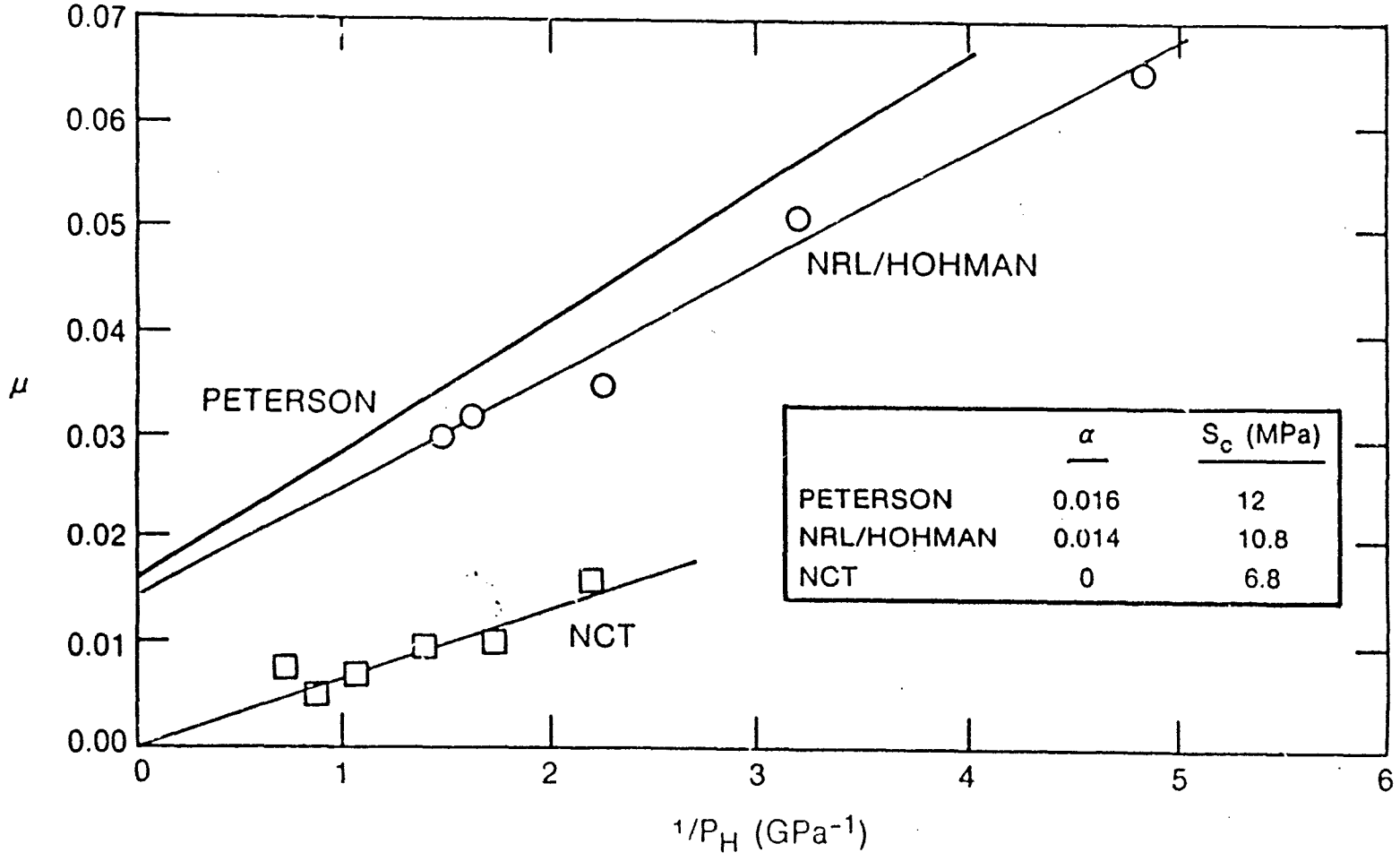
β, α, S_o and r obtained from:

$$\mu = C\, S_o / L^{\beta} + \alpha$$

and C is a geometrical constant.

FRICTION BEHAVIOR OF M_oS_2

$$\mu = \frac{S_o}{P_H} + \alpha$$



	α	S_c (MPa)
PETERSON	0.016	12
NRL/HOHMAN	0.014	10.8
NCT	0	6.8

BIBLIOGRAPHY

1. Kanakia, M.D. and Peterson, M.B., "Literature Review of Solid Lubrication Mechanisms," Interim Report BFLRF No. 213 (AD A185010), Defense Tech Info. Center, Washington DC, November 1986.

2. Gansheimer, J. "Neue Erkenntnisse Uber Dei Wirkungsweise von Molybdandisulfid als Schmierstoffe," Schmiertechnik, 11 (1964) 271-280.

3. Karpe, S.A., "The Effects of Load on the Frictional Properties of Molybdenum Disulfide," Trans. ASLE, 8, (1965) 156-178 .

4. Salomon, G. and DeGee, A.W.J., discussion to Karpe above.

5. Roberts, E.W., "The tribology of sputtered Molybdenum Disulphide films," Proc. Inst. Mech. Eng., Tribology - Friction, Lubrication and Wear, Fifty Years On, Vol. 1, London, (1987) 503-510.

APPENDIX A7

FRICTION & WEAR BEHAVIOUR OF DIAMOND FILMS ON Si

Ian P. Hayward - GeoCenters, Inc.

Irwin L. Singer - Naval Research Lab

13 July 1989

A71

DIAMOND COATING TRIBOLOGY : Key Issues

How slippery are the coatings (in air and vacuum)?

How hard and tough are the coatings?

How well do the coatings adhere to their substrates?

FRICTION OF DIAMOND AND DLC

	DIAMOND	DLC
IN VACUUM	0.05 TO >1 0.1 (H PRESENT)*	0.005 TO 0.01
IN AIR	0.05	0.1 TO 0.5
TEMPS (<800°C)	0.1	DEGRADES

*I. HAYWARD, CAMBRIDGE UNIV. (1987)

TEST CONFIGURATION

Apparatus	Reciprocating sliding
	Bidirectional, pin-on-flat.
Pin	Diamond. 200 um radius spherical tip
	with 100 um diameter wear flat.
Flats	Diamond coated silicon
Load	100 - 300 g (1 - 3 N).
Contact pressure	1 GPa.
Sliding speed	1 mm s^{-1}.
Track lengths	1 mm.
Atmosphere	Air (2% - 70% RH).

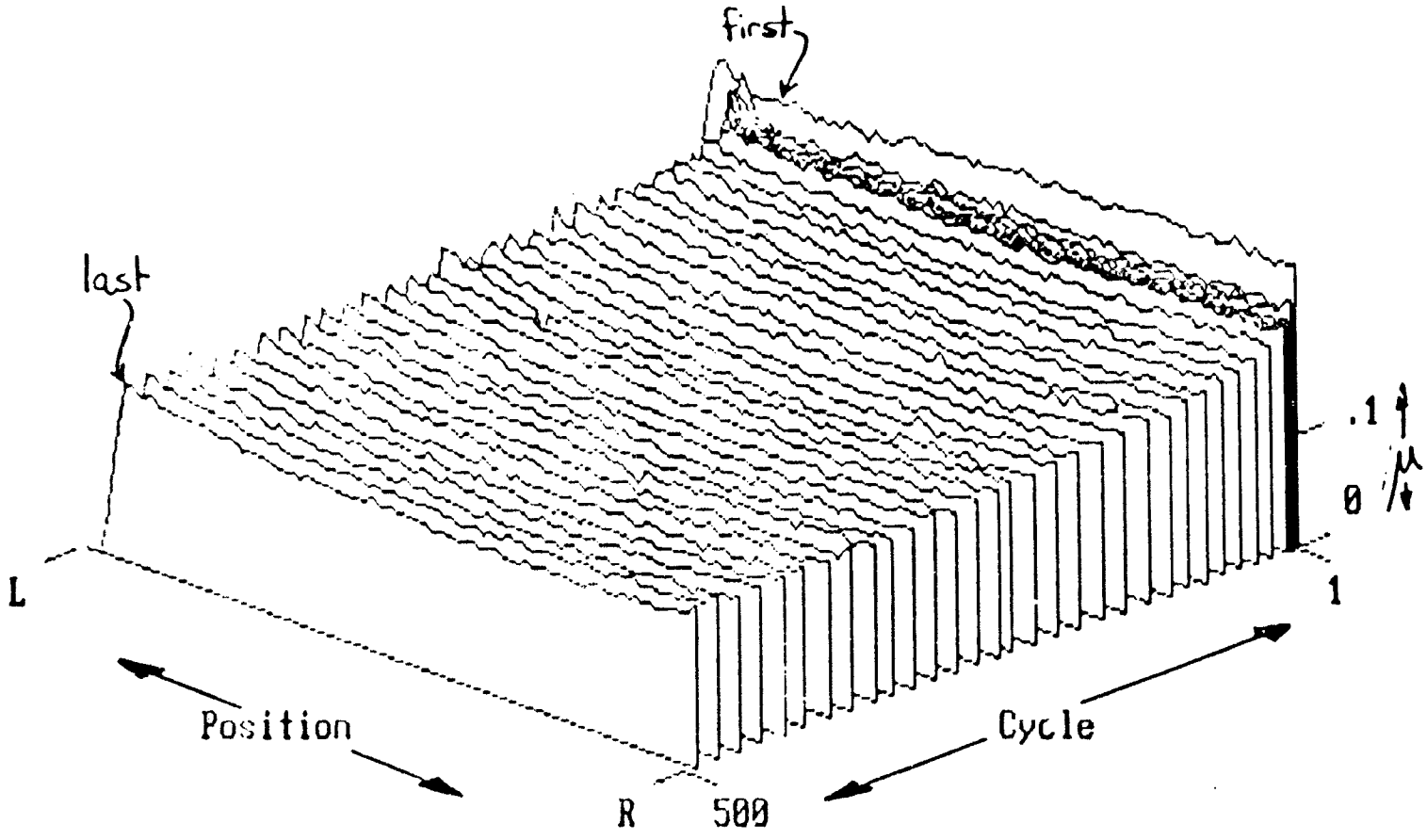
ANALYTICAL TECHNIQUES

Micro Raman.

Infra-red spectroscopy (transmission FTIR).

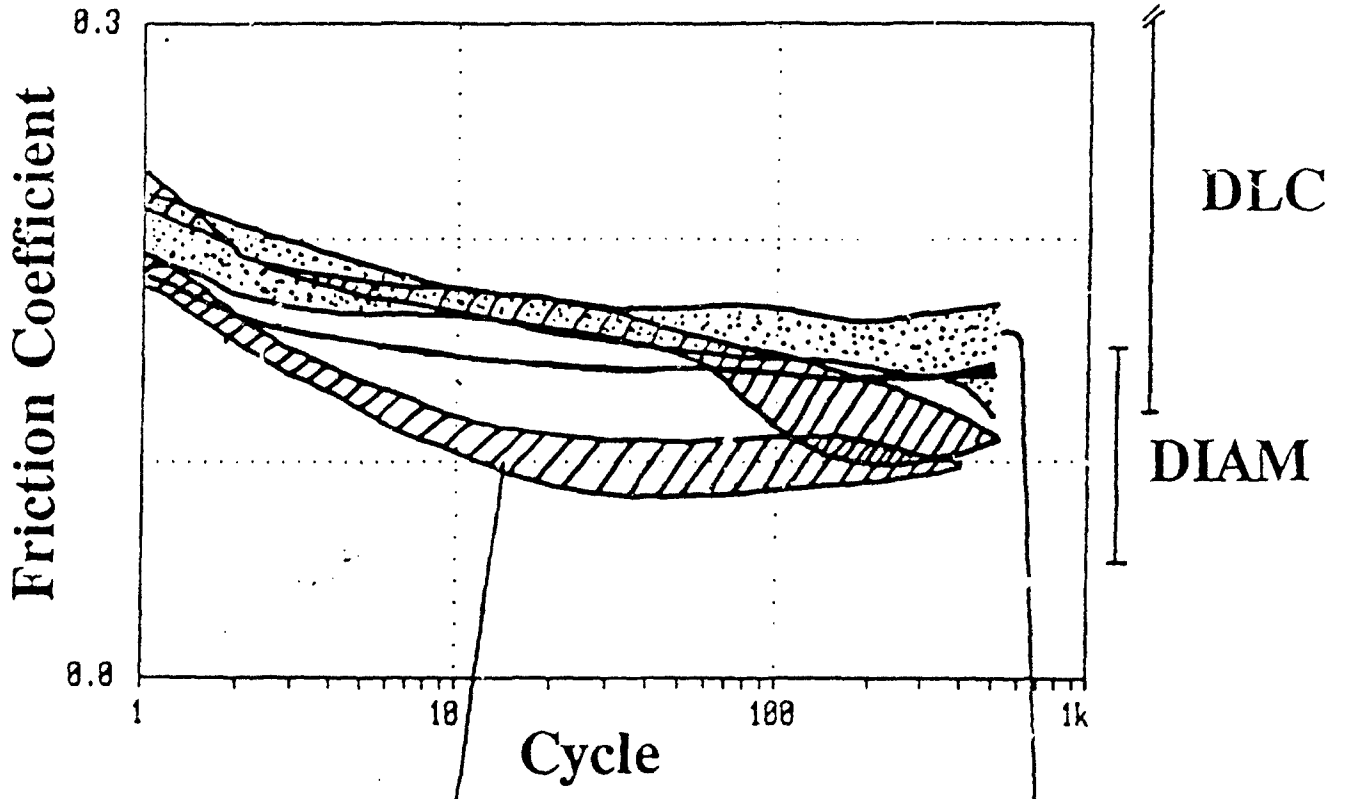
Surface profilometry.

Optical microscopy.



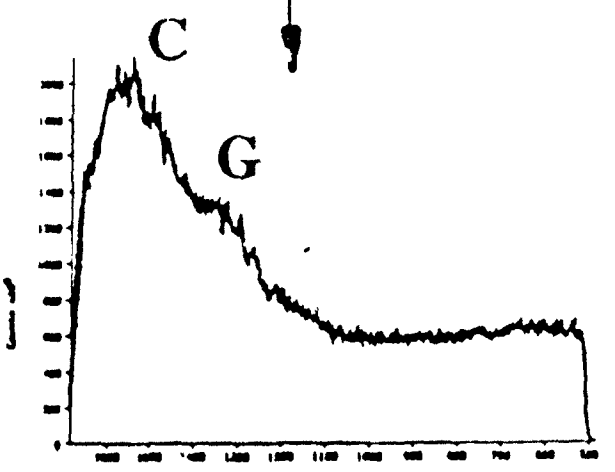
Forward friction coeffic ent (0-100)
XL12B

DIAMOND FILMS DC PLASMA



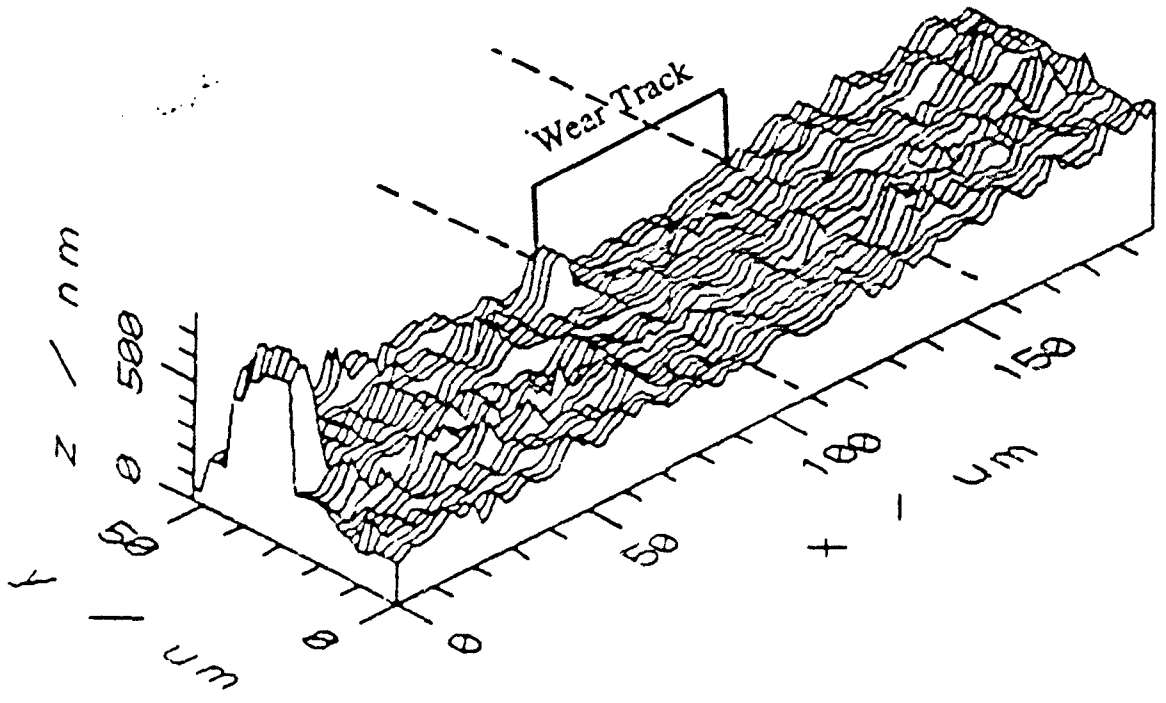
RAMAN





3-D Surface Profile of Crystallume Diamond Film

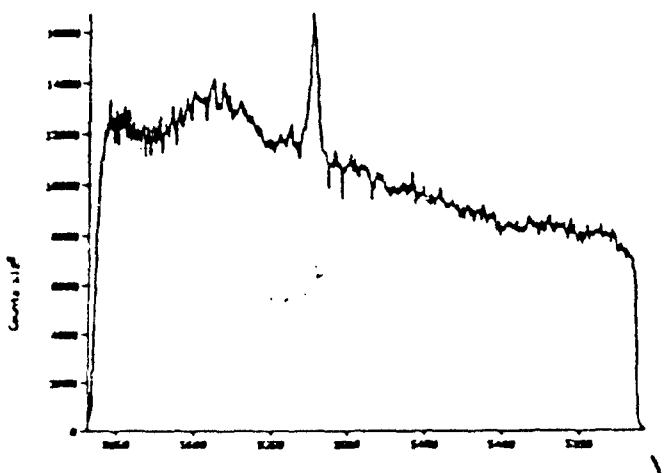
Crystallume specimen 13-Y-2



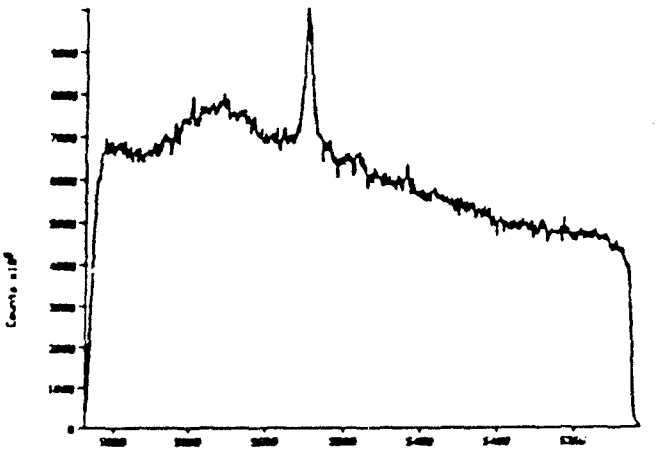
RA 0.07 µm

MICRORAMAN SPECTRA FROM CRYSTALLUME DIAMOND FILM

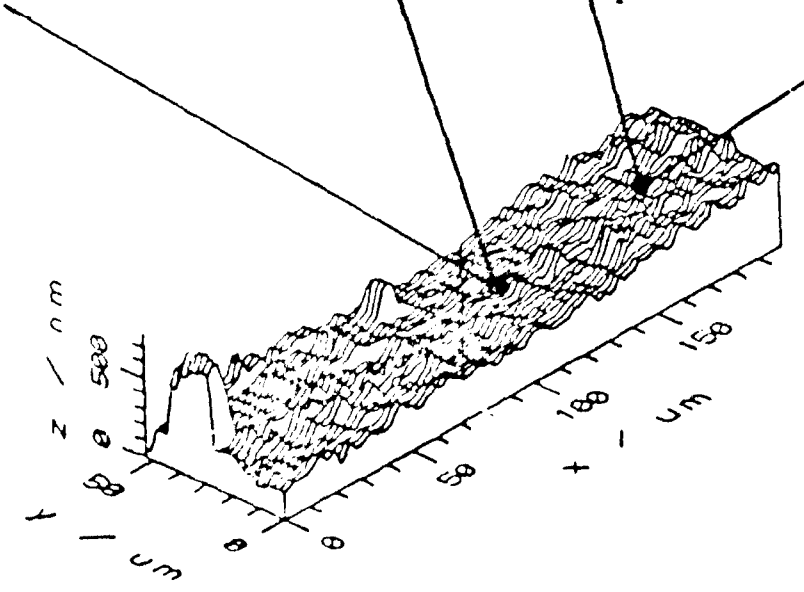
Crystallume specimen 13-Y-2



Spectrum from within wear track



Spectrum from outside wear track



Lower final friction:

- bigger diamond peak in Raman
- less C-H stretching in FTIR
- rougher coating surface before sliding
- rougher wear track (frictional mechanism)

No effect of humidity on friction and wear.

- Diamond friction independent of humidity.
- DLC friction 0.01 at 1% RH or less.

MECHANISM

DIAMOND SLIDING ON (DIAMOND + DLC)

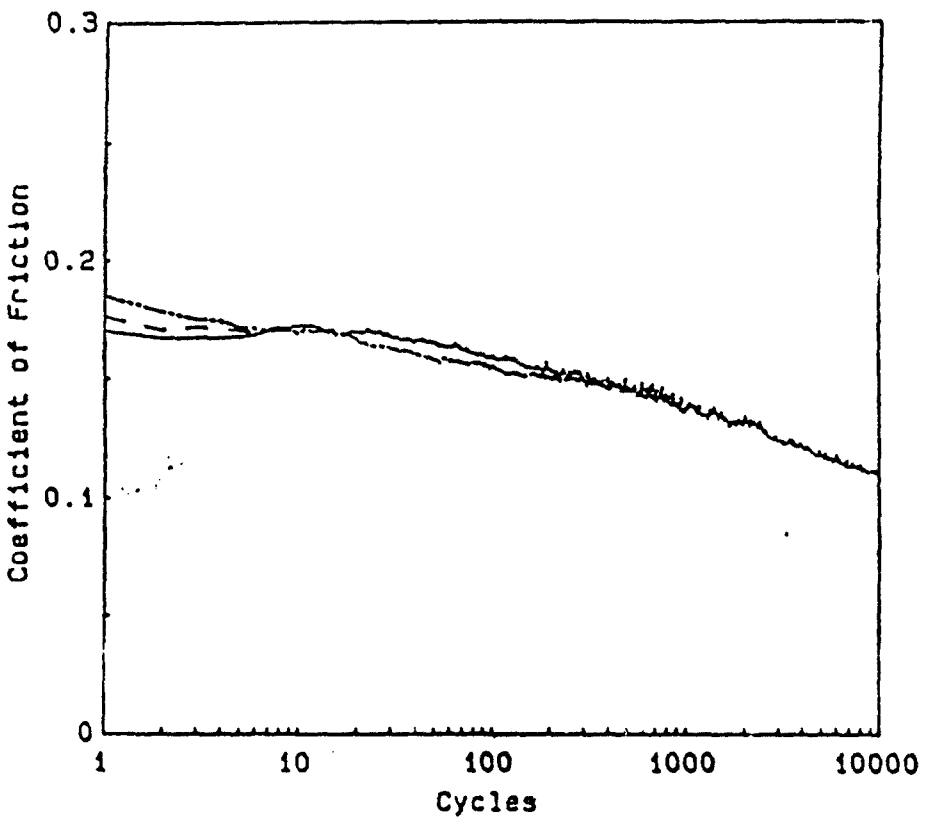
DLC deforms/wears

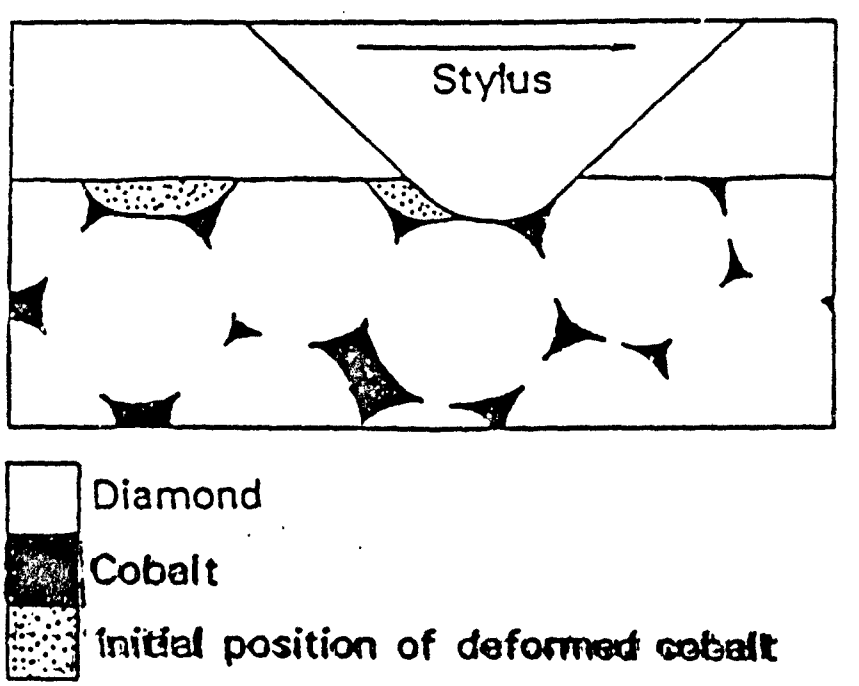
faster than diamond

DIAMOND SLIDING ON DIAMOND

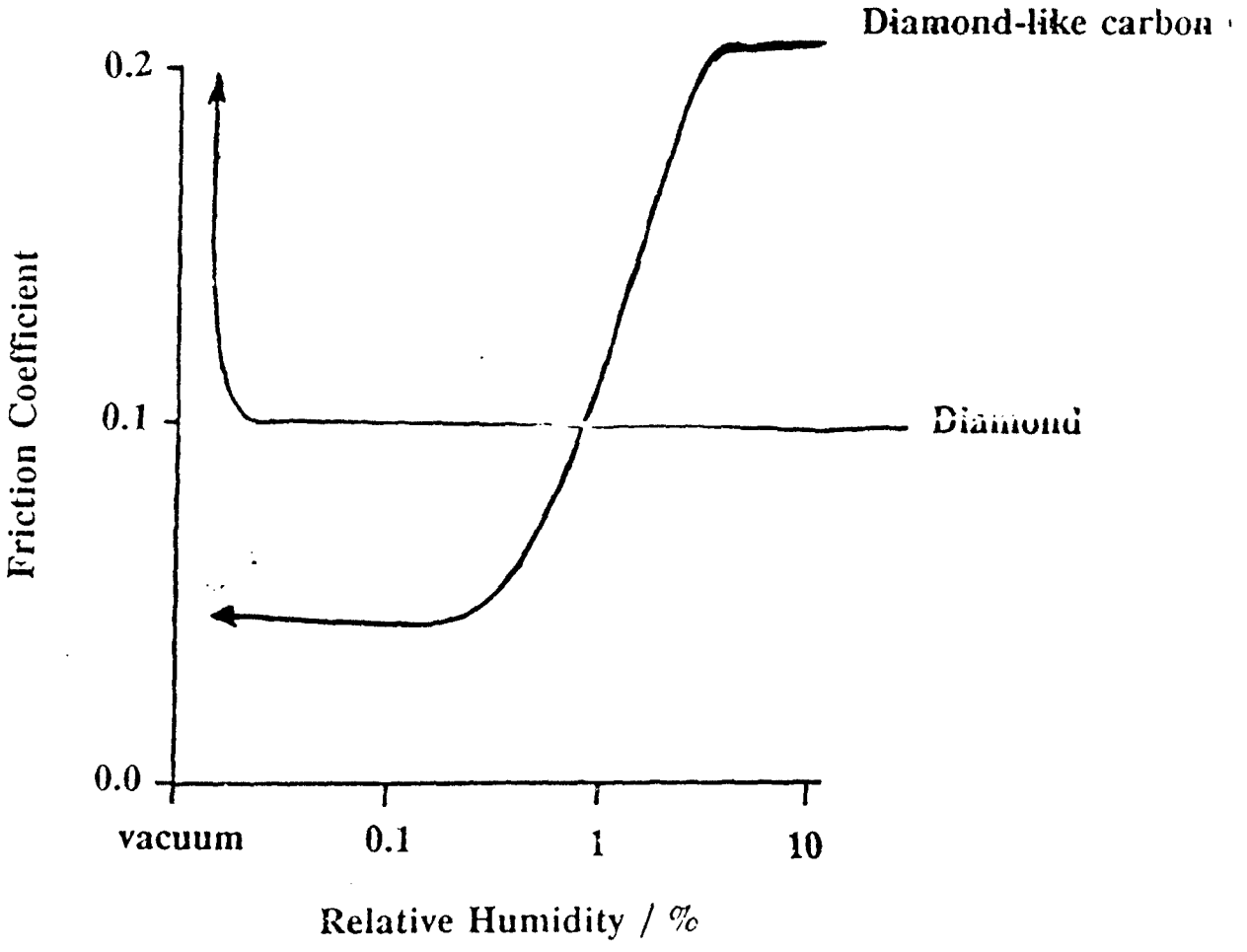
DIAMOND SLIDING ON SYNDITE. (Hayward, 1987).

(Small diamond grits sintered in a cobalt matrix).





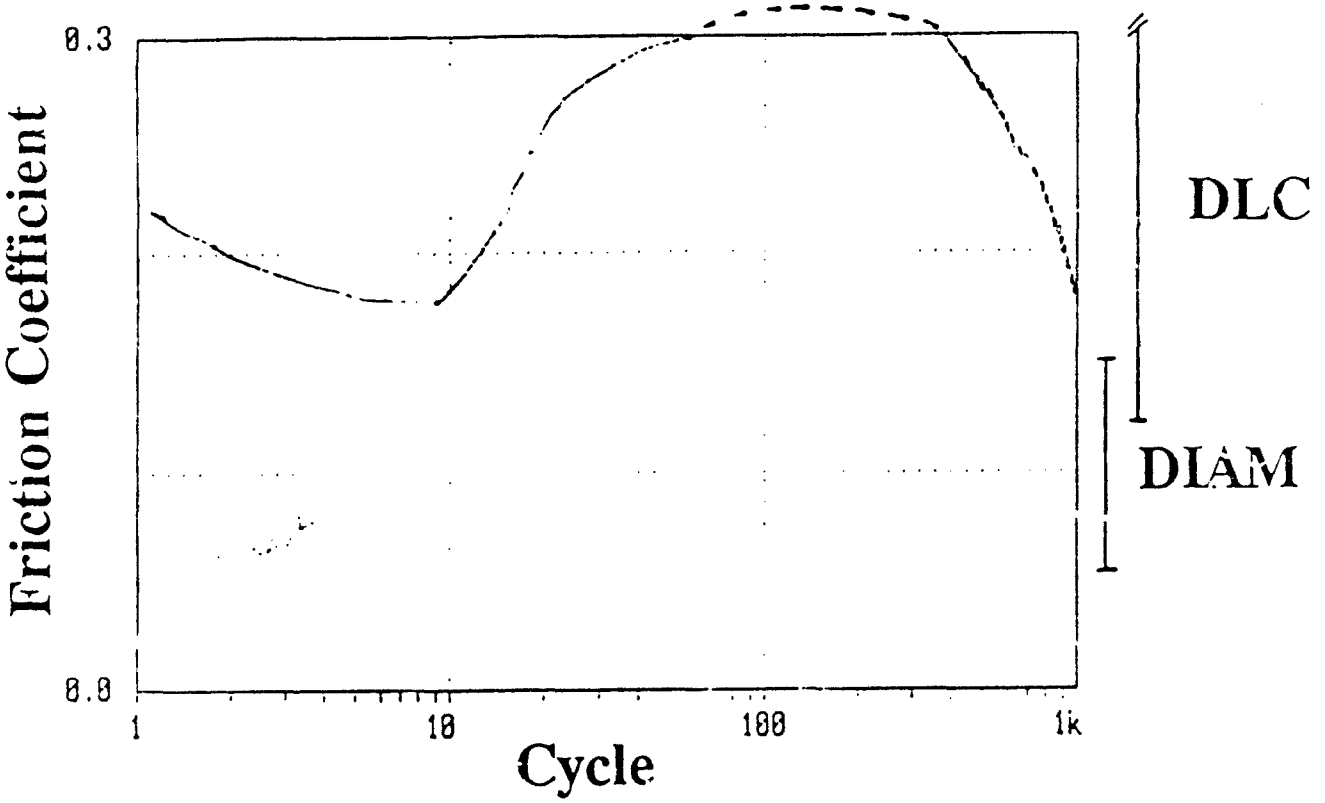
BENEFICIAL EFFECTS OF DLC



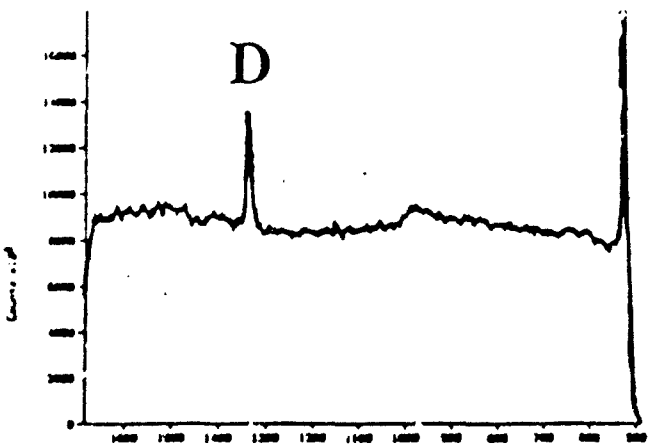
DLC : Weissmantel et al., Thin Solid Films 96, 31 (1982).

Diamond : Bowden & Hanwell, Proc. R. Soc. A295, (1966).

DIAMOND FILMS
MICROWAVE DEPOSITED



RAMAN



FRICTION OF DIAMOND ON DIAMOND FILMS COATED WITH ORGANIC ACID

Minimum friction coefficient	
without C20 acid	with C20 acid
0.1	0.03

SIGNIFICANCE

If the "proper" surface chemical configuration can be achieved then ultralow friction coefficients are possible on diamond films.

CONCLUSIONS

- Tribological behaviour correlates with Raman and FTIR.

  More diamond... lower final friction.

- Coatings need "running in" to achieve lowest friction values.

- Microwave deposited films appear to have a lower cohesive strength than DC plasma films.

- Surface chemistry modifications may allow very low friction coefficients to be achieved.

PLANS

- FTIR studies of wear tracks.
- Extend studies to harder substrates / higher contact pressures.
- Vacuum Tribotester.
  - Testing in simulated space conditions.
  - Surface analytical techniques (Scanning Auger etc.).
- Non-diamond styli.

DIAMOND FILM TRIBOLOGY (NRL)

- Correlation of friction coefficient with % diamond in film
- Evidence for reduced friction of diamond films with "proper" surface treatment
- Potential of Diamond-like carbon (DLC) components in space applications (vacuum environments)

APPENDIX B1

P1

CHEMICAL
RESEARCH,
DEVELOPMENT &
ENGINEERING
CENTER

CRDEC-TR-045

THE DYNAMIC BEHAVIOR OF WATER VAPOR ON ACTIVATED CARBON

John J. Mahle
RESEARCH DIRECTORATE

David K. Friday
GEO-CENTERS, INC.
Ft. Washington, MD 20744

February 1989

U.S. ARMY
ARMAMENT
MUNITIONS
CHEMICAL COMMAND

Aberdeen Proving Ground, Maryland 21010-5423

Disclaimer

The findings in this report are not to be construed as an official Department of the Army position unless so designated by other authorizing documents.

Distribution Statement

Approved for public release; distribution is unlimited.

UNCLASSIFIED
SECURITY CLASSIFICATION OF THIS PAGE

REPORT DOCUMENTATION PAGE

Form Approved
OMB No. 0704-0188

1a REPORT SECURITY CLASSIFICATION UNCLASSIFIED	1b. RESTRICTIVE MARKINGS
2a SECURITY CLASSIFICATION AUTHORITY	3. DISTRIBUTION/AVAILABILITY OF REPORT Approved for public release; distribution is unlimited.
2b DECLASSIFICATION/DOWNGRADING SCHEDULE	
4 PERFORMING ORGANIZATION REPORT NUMBER(S) CRDEC-TR-045	5. MONITORING ORGANIZATION REPORT NUMBER(S)
6a. NAME OF PERFORMING ORGANIZATION See Reverse 6b. OFFICE SYMBOL (If applicable)	7a. NAME OF MONITORING ORGANIZATION
6c. ADDRESS (City, State, and ZIP Code)	7b. ADDRESS (City, State, and ZIP Code)
8a NAME OF FUNDING/SPONSORING ORGANIZATION CRDEC 8b. OFFICE SYMBOL (If applicable) SMCCR-RSC-A	9. PROCUREMENT INSTRUMENT IDENTIFICATION NUMBER DAAA15-87-D-0007
8c. ADDRESS (City, State, and ZIP Code) Aberdeen Proving Ground, MD 21010-5423	10. SOURCE OF FUNDING NUMBERS PROGRAM ELEMENT NO. / PROJECT NO. 1C161102 / TASK NO. A71A / WORK UNIT ACCESSION NO.

11 TITLE (Include Security Classification)
The Dynamic Behavior of Water Vapor on Activated Carbon

12. PERSONAL AUTHOR(S)
Mahle, John J. (CRDEC); and Friday, David K. (GEO-Centers, Inc.)

13a. TYPE OF REPORT	13b TIME COVERED	14. DATE OF REPORT (Year, Month, Day)	15. PAGE COUNT
Technical	FROM 87 Feb TO 88 Jul	1989 February	30

16 SUPPLEMENTARY NOTATION

17 COSATI CODES			18. SUBJECT TERMS (Continue on reverse if necessary and identify by block number)
FIELD	GROUP	SUB-GROUP	Breakthrough, Simulation, Water vapor, Stage model, Activated carbon, Equilibrium theory
15	06	03	

19. ABSTRACT (Continue on reverse if necessary and identify by block number)

Water vapor is present, usually in relatively large concentrations, in many adsorption systems of industrial and military interest. This work develops an approach to predict the dynamic behavior of water vapor on an activated carbon adsorbent. Prior studies have neglected the importance of including the heat balance to account for behavior to high relative humidities.

Water vapor isotherms were measured for BPL carbon at 15, 25, and 35 °C, and the data were correlated using a modified version of the Antoine Equation first suggested by LeVan. Breakthrough experiments were performed using the following initial bed and feed conditions: (1) 50% RH feed to a dry bed, (2) 80% RH feed to a bed initially equilibrated at 50% RH, and (3) 80% RH feed to a dry bed. Two mathematical models were developed to analyze the values predicted using a non-isothermal stage model with a fluid phase mass transfer resistance and an adiabatic equilibrium theory model.

20 DISTRIBUTION/AVAILABILITY OF ABSTRACT ☐ UNCLASSIFIED/UNLIMITED ☐ SAME AS RPT ☐ DTIC USERS	21 ABSTRACT SECURITY CLASSIFICATION UNCLASSIFIED
22a NAME OF RESPONSIBLE INDIVIDUAL SANDRA J. JOHNSON	22b TELEPHONE (Include Area Code) (301) 671-2 4
	22c OFFICE SYMBOL SMCCR-SPS-T

DD Form 1473, JUN 86 Previous editions are obsolete. SECURITY CLASSIFICATION OF THIS PAGE
UNCLASSIFIED

6. NAME AND ADDRESS OF PERFORMING ORGANIZATION (Continued)

U.S. Army Chemical Research, Development and Engineering Center
ATTN: SMCCR-RSC-A
Aberdeen Proving Ground, MD 21010-5423

GEO-Centers, Inc.
10903 Indian Head Highway
Ft. Washington, MD 20744

PREFACE

The work described in this report was authorized under Project No. 1C161102A71A, Research in CW/CB Defense, and Contract No. DAAA15-87-D-0007. This work was started in February 1987 and completed in July 1988.

The use of trade names or manufacturers' names in this report does not constitute an official endorsement of any commercial products. This report may not be cited for purposes of advertisement.

Reproduction of this document in whole or in part is prohibited except with permission of the Commander, U.S. Army Chemical Research, Development and Engineering Center, ATTN: SMCCR-SPS-T, Aberdeen Proving Ground, Maryland 21010-5423. However, the Defense Technical Information Center and the National Technical Information Service are authorized to reproduce the document for U.S. Government purposes.

This report has been approved for release to the public.

Blank

CONTENTS

		Page
1.	INTRODUCTION	7
2.	THEORY	7
2.1	Material and Energy Balances	7
2.2	Stage Model Approach	10
2.3	Equilibrium Theory	11
3.	MATERIALS AND METHODS	13
4.	RESULTS AND DISCUSSION	14
4.1	Water on Activated Carbon	14
4.2	Breakthrough of 50% RH Feed To A Clean Bed	16
4.3	Breakthrough of 80% RH Feed To Bed Equilibrated At 50% RH	18
4.4	Breakthrough of 80% RH Feed To A Clean Bed	18
5.	CONCLUSIONS	19
	NOTATION	21
	LITERATURE CITED	29

LIST OF FIGURES

		Page
1.	Schematic of Breakthrough Apparatus	22
2.	Path In Modified Isotherm Plane 50%RH, 80%RH Feed To Clean Bed And 80%RH Feed to 50%RH Bed of BPL	23
3.	Enlargement of Path In Modified Isotherm Plane 50%RH, 80%RH Feed To Clean Bed Of BPL	24
4.	Breakthrough of Water Vapor On BPL Carbon 50%RH Feed To Clean Bed	25
5.	Breakthrough Of Water Vapor On BPL Carbon 80%RH Feed To Bed Equilibrated To 50%RH	26
6.	Breakthrough Of Water Vapor On BPL Carbon 80%RH Feed To Clean Bed	27

LIST OF TABLES

		Page
1.	Breakthrough Experiment Conditions	15
2.	Heat Capacities	15

THE DYNAMIC BEHAVIOR OF WATER VAPOR ON ACTIVATED CARBON

1. INTRODUCTION

Water adsorption on activated carbon is of particular interest for air purification applications where contaminants must be removed from humid air. Water vapor adsorption can limit filter performance against challenges of light gases by displacing previously adsorbed contaminants or by reducing the available adsorption space. A complete understanding of the single component adsorption behavior of water vapor on activated carbon can serve as a basis to develop a theory for multicomponent behavior. This study considers in detail the adsorption of water on BPL activated carbon.

The adsorption behavior of any vapor on an adsorbent can be understood through the adsorption equilibrium relationship and the material and energy balances. Water adsorption on activated carbon exhibits a pronounced hysteresis that complicates the analysis of desorption. Doong and Yang[1] present a model for multicomponent adsorption of water and hydrocarbons on activated carbon including equilibrium and adsorber dynamics. Their work, however, neglects the energy balance and does not present data on breakthrough runs. The purpose of this paper is to develop and solve the material and energy balance equations so the results can be compared to actual breakthrough experiments. The results presented here for adsorption dynamics can be extended to desorption dynamics. Two approaches to analyzing the water adsorption process on activated carbons are considered. These are the stage model approach and the equilibrium theory approach. In both cases a mathematical model is used to describe the dynamic behavior of water vapor challenging a bed of activated carbon. Three breakthrough experiments are performed that result in three different types of waves. The characteristics of each wave type and their impact on filter performance are discussed.

2. THEORY

2.1 Material and Energy Balances.

The equations to describe water adsorption on activated carbon should include material and energy balances as well as the equilibrium relationship. The easiest way to develop these equations is to describe the bed as consisting of a solid phase and a vapor phase. The stationary(solid) phase consists of the solid porous

particles and the adsorbate. The vapor phase consists of the inert carrier gas and the adsorbable vapor in both the intersticies of the bed and the pores of the particles.

The governing differential equations for the conservation of mass and energy respectively, neglecting dispersion and channeling, of a fixed-bed adsorber can be written as follows:

$$\epsilon \frac{\partial vc}{\partial z} + \epsilon \frac{\partial c}{\partial t} + \rho_b \frac{\partial q}{\partial t} = 0 \tag{1}$$

$$\epsilon \frac{\partial (v \rho_f h_f)}{\partial z} + \epsilon \frac{\partial (\rho_f h_f)}{\partial t} + \rho_b \frac{\partial h_s}{\partial t} = -U \Delta T \tag{2}$$

The fluid phase and stationary phase enthalpies are defined by:

$$h_f = c_f (T - T_{ref}) \tag{3}$$

$$h_s = (c_s + c_a q)(T - T_{ref}) - \int_0^q \lambda \, dq \tag{4}$$

Here c is the vapor concentration, q, the adsorbed phase concentration in moles of adsorbate per unit mass of adsorbent, T, the temperature, z, the distance down the tube length, t, the time, ϵ, the void fraction of the bed, and U, the overall heat transfer coefficient of the filter tube.

The rate at which material is transferred from the passing vapor stream to the surface of the carbon is governed by a film mass transfer resistance which can be written as follows:

$$\rho_b \frac{\partial q}{\partial t} = (k_v a)(c - c^*) \tag{5}$$

Equation 5 assumes Glueckauf's linear driving force, where c^* is the vapor phase concentration at the surface of the particle.

Dimensionless variables can be introduced to simplify equations 1, 2, 5:

$$\tau = \frac{\epsilon v_o t}{L} \qquad \zeta = \frac{z}{L} \qquad v^* = \frac{v}{v_o} \tag{6,7,8}$$

$$U' = \frac{2\,U\,L}{\epsilon\, v_o\, r_i} \tag{9}$$

$$(k_v a)' = k_v a \frac{L}{\epsilon\, v_o} \tag{10}$$

The choice of the dimensionless parameter τ has special physical significance. It represents the number of superficial column volumes that have been fed to the bed at any given time.

In evaluating solutions, parameters appearing in equations 1, 2, and 5 can be treated as functions of concentration and temperature. However, to simplify the development, several assumptions can be made, namely:

(a) all heat capacities are constant with mean values taken.

(b) the vapor phase is ideal and the effect of composition on the vapor-phase density and velocity is small.

(c) the adsorption process considered here occurs at low gas phase concentrations so that the effect on velocity and density is negligible.

Thus, the dimensionless velocity and the fluid density can be written as:

$$v^* = \frac{T}{T_o} \qquad \rho_f = \rho_{fo} \frac{T_o}{T} \tag{11,12}$$

For adsorption processes involving gases at low to moderate pressures (which would be typical of all air purification applications) the rate of accumulation in the vapor phase is small compared to the accumulation in the solid phase. This leads to the elimination of the second term in equations 1 and 2. The system of governing differential equations may then be expressed as:

$$\frac{\partial(v^* c)}{\partial \zeta} + \rho_b \frac{\partial q}{\partial \tau} = 0 \tag{13}$$

$$\frac{\partial(v^{*}\rho_f h_f)}{\partial \zeta} + \rho_b \frac{\partial h_s}{\partial \tau} = -U'\Delta T \qquad (14)$$

$$\rho_b \frac{\partial q}{\partial \tau} = (k_v a)' (c - c^{*}) \qquad (15)$$

Equations 13, 14, and 15 are three independent equations with four dependent variables (c, c^{*}, q, T). Another equation is required in order to specify the system, namely the adsorption equilibrium relationship:

$$q = f(c^{*}, T) \qquad (16)$$

The solution to equations 13 - 15 with 16 requires the imposition of appropriate initial and boundary conditions. For systems considered here the initial bed state and the feed concentration are constant throughout the experiment. Mathematically this can be expressed as:

$$\begin{aligned} c &= c_o \quad \text{and} \quad T = T_o \quad \text{at } \tau = 0 \quad \text{for } 0 < \zeta < 1 \\ c &= c_{feed} \quad \text{and} \quad T = T_{feed} \quad \text{at } \zeta = 0 \quad \text{for all } \tau > 0 \end{aligned} \qquad (17)$$

Two approaches are taken to solve the governing set of differential equations, 13 - 15, with 16: the stage model and equilibrium theory. The stage model is more flexible and can easily treat systems with non-constant initial and boundary conditions. Generally, equilibrium theory is more insightful about the nature of the adsorption waves, however, it cannot be used where mass and heat transfer effects must be considered. Both techniques are presented here in order to gain a complete understanding of the process.

2.2 Stage Model Approach.

Equations 13 - 15 when coupled with the equilibrium relationship 16 can be reduced to a set of ordinary differential equations using a stage model approach.[2,3] Each stage is considered to be well mixed with the effluent concentration and temperature of stage i used as the feed concentration of stage i+1. Friday and LeVan[4] have reported a successful method for reducing the partial differential equations 13 - 15 to ordinary differential equations by writing the spatial derivatives in equations 13 and 14 in finite difference form using backward differences.

$$\frac{dq_i}{d\tau} = \frac{1}{\rho_b \Delta\zeta}\left[(v^* c)_{i-1} - (v^* c)_i\right] \tag{18}$$

$$\frac{dT_i}{d\tau} = \frac{1}{\rho_b(c_s + c_a q_i)}\left\{\frac{\rho_{fo} c_f}{\Delta\zeta}(T_{i-1} - T_i) - \rho_b[c_a(T_i - T_{ref}) - \lambda_i]\frac{dq_i}{d\tau} - U'\Delta T\right\} \tag{19}$$

The resulting equations 18 and 19 are solved using a Runge-Kutta 4th order integration algorithm with twenty stages.

2.3 Equilibrium Theory.

The development of the equilibrium theory solution requires the mass and heat transfer resistances to be negligible. Therefore, the driving force terms on the right side of equations 14 and 15 are set to zero.

The equilibrium theory solution to 13, 14 and 16 requires the use of the method of characteristics that has been presented by numerous authors.[5-10] If concentration of the material in the bed can be expressed as a function of distance and time by,

$$c = f(\zeta, \tau) \tag{20}$$

then the total differential of c can be written as:

$$dc = \frac{\partial c}{\partial \zeta} d\zeta + \frac{\partial c}{\partial \tau} d\tau \tag{21}$$

The solution along regions of constant concentration require that $dc = 0$ so that equation 19 can be rearranged.

$$\frac{d\zeta}{d\tau} = -\frac{\partial c/\partial \tau}{\partial c/\partial \zeta} \tag{22}$$

Now the material balance equation 13 can be rewritten when the equilibrium relationship 16 is substituted for the partial of q with respect to time.

$$\frac{\partial c}{\partial \zeta} + \rho_b \frac{dq}{d(v^* c)} \frac{\partial c}{\partial \tau} = 0 \qquad (23)$$

Equation 23 can be rearranged into a form compatible with the right hand side of equation 22.

$$-\frac{dc/d\tau}{dc/d\zeta} = \frac{1}{\rho_b} \frac{d(v^* c)}{dq} \qquad (24)$$

When equation 24 is substituted into equation 22 the following expression for the characteristic direction is obtained.

$$\frac{d\zeta}{d\tau} = \frac{1}{\rho_b} \frac{d(v^* c)}{dq} \qquad (25)$$

The left hand side of equation 25 represents the speed with which a given concentration travels down the bed, while the right hand side of equation 25 is the slope of the equilibrium relationship.

The energy balance when written without the heat transfer resistance takes the following form:

$$\frac{\partial(v^* \rho_f h_f)}{\partial \zeta} + \rho_b \frac{\partial h_s}{\partial \tau} = 0 \qquad (26)$$

Using the same procedure as for the material balance, the characteristic equation takes the following form:

$$\frac{d\zeta}{d\tau} = \frac{1}{\rho_b} \frac{d(v^* \rho_f h_f)}{dh_s} \qquad (27)$$

The material and energy balances can be combined for the initial value problem to provide:

$$\frac{r}{\varsigma} = \rho_b \frac{dq}{d(v^* c)} = \rho_b \frac{dh_s}{d(v^* \rho_f h_f)} \tag{28}$$

The two enthalpy terms on the right of equation 28 can be written as functions of q and T. Thus equation 28 can be rearranged in terms of the directional derivative dq/dT to take the following form:

$$\left[\frac{\partial(v^* c)}{\partial q}\frac{\partial h_s}{\partial q}\right]\left(\frac{dq}{dT}\right)^2 + \left[\frac{\partial(v^* c)}{\partial q}\frac{\partial h_s}{\partial T} + \frac{\partial(v^* c)}{\partial T}\frac{\partial h_s}{\partial q} - \frac{d(v^* \rho_f h_f)}{dT}\right]\frac{dq}{dT} + \frac{\partial(v^* c)}{\partial T}\frac{\partial h_s}{\partial T} = 0 \tag{29}$$

Equation 29 is a quadratic in dq/dT. The two solutions correspond to the characteristics emanating from a given point of c, q, and T. By starting from the initial and feed conditions the solution to equation 29 is obtained. The resulting slopes are then plotted in the hodograph planes of q versus T and the q versus $v^* c$ until the characteristics intersect. Implementation of equilibrium theory to obtain the breakthrough curves requires adherence to two rules. A wave must be gradual if possible. Slopes in the $v^* c$ plane must increase from initial bed condition to feed condition. If the slope of the characteristic does not increase continuously in going from initial to feed conditions then the larger concentrations would overrun the smaller concentrations. This is an impossible situation. Earlier studies by Devault[11] and Lax[12] showed that these conditions result in the formation of a shock. The shock path must satisfy the material and energy balances as given by the following relationship:

$$\frac{r}{\varsigma} = \rho_b \frac{\Delta q}{\Delta(v^* c)} = \rho_b \frac{\Delta h_s}{\Delta(v^* \rho_f h_f)} \tag{30}$$

This is similar to equation 28 except that here a chord, rather than the slope of the characteristic, is used to determine the speed of the wave in the bed.

3. MATERIALS AND METHODS

The apparatus used for the breakthrough experiments is shown in Figure 1. Air, used as the carrier gas, passes through a molecular sieve dryer and a carbon filter to remove water and organics. The main metering valve regulates the flow. After the clean air passes through the flowmeter, a portion of the stream is

saturated in a water bath. The desired relative humidity is achieved in the following manner. The metering valve and the bypass valve are set such that the ratio of the their flows produces a relative humidity near the desired value. The humidity analyzer and controller (EG&G 911 Digital Humidity Analyzer) measures the relative humidity of the feed stream based on the temperature of the feed stream. If the relative humidity is below the setpoint, the water bath heater is activated. Since, it is a simple on-off controller with no cooling action, the initial setting of the bypass flow must produce a lower than desired RH. The humidified air flows through the carbon bed and the effluent relative humidity is measured by a second EG&G humidity analyzer. Periodically during each breakthrough run the bed was removed from the flowing air stream in order to weigh it.

The carbon sample used was 12x30 mesh BPL Lot #7502. Calgon literature states that the bulk density of the carbon is 480 kg/m^3. The particle diameter is taken to be 0.001 m. The sample for each experiment is dried for at least two days at 110 °C. The carbon is then poured into a 0.0415 m diameter plexiglass tube to give a bed depth of approximately 4 cm. The overall heat transfer coefficient of the plexiglass is taken to be 0.093 kJ/m^2 K s.

4. RESULTS AND DISCUSSION

4.1 Water On Activated Carbon.

The breakthrough concentration and temperature have been measured using the following feed and initial bed conditions: 50% RH feed to a clean bed, 80% RH feed to a bed equilibrated at 50% RH, 80% RH feed to a clean bed. These conditions have been chosen to illustrate the three different wave types that can be formed in an adsorption bed. Rhee et al.[6] describe the three wave types as gradual, abrupt and combined in their equilibrium theory analysis. The important features of each are discussed as each experiment is analyzed. Table 1 is a summary of the operating conditions for each experiment. Table 2 lists the heat capacity values used in this study.

TABLE 1. Breakthrough Experiment Conditions

Experiment	Feed		Initial Bed Conditions			v	T_{amb}
	RH%	T(K)	RH%	T(K)	Carbon(g)	(m/sec)	(K)
1	50	298	0	297.5	23.96	.0616	297.5
2	80	297	50	297	23.96	.0616	297
3	80	298	0	298	25.85	.123	298

TABLE 2. Heat Capacities

c_a	= 1.04 kJ/kg K
c_s	= 2.7 kJ/kg K
c_f	= 0.075 kJ/kg K
T_{ref}	= 298^{o} K

In order to implement the stage model and the equilibrium theory model the form of the equilibrium relationship must be established. It is proposed that a modification to the Hacskaylo-LeVan isotherm[13] would give a reasonable fit to the data. The form of the equation is as follows:

$$\ln(p) = A' - \frac{B'}{C' + T} \tag{31}$$

where

$$A' = A + (K1\theta + 1)\ln(\theta) \quad B' = B \quad C' = C + K2(1 - \theta) \tag{32}$$

and

$$\theta = \frac{q}{q_{sat}} \tag{33}$$

$$\lambda = RT^2 \left(\frac{\partial \ln (p)}{\partial T} \right)_q = RT^2 \frac{B'}{(C' + T)^2} \tag{34}$$

The following values are used for water adsorption on BPL:

$A = 18.3036$ $B = 3816.44$ $C = -46.13$

$K1 = 2.56$ $K2 = 37.9$ $q_{sat} = 0.0217$

The Antoine parameters, taken from Reid et al.,[14] give the vapor pressure in millimeters of mercury. The isotherms of water on BPL have been measured previously by Mahle and Friday[15] over the temperature range 15 - 35 °C. Only adsorption data is considered here; desorption is not considered. The result of correlating the adsorption data using equations 31 - 33 is presented in Figures 2 and 3 in the modified isotherm plane of q versus v^*c. Figure 3 is an enlargement of Figure 2 in the low loading region.

The value of k_y, the mass transfer coefficient, can be calculated using the Sherwood number correlation of Rans and Marshall.[16] Calgon literature indicates that an appropriate value for a, the surface to volume ratio, is 3400 m^{-1}.

4.2 Breakthrough of 50% RH Feed To A Clean Bed.

The breakthrough results for a challenge of 50% RH(0.628 mol/m^3 at 298 °K) air to clean bed correspond to a region of the isotherm that is unfavorable for adsorption. The effluent concentration and temperature are plotted as a function of time in Figure 4. The effluent concentration versus time curve is typical of a gradual wave. The breakthrough curve is concave downward to the time axis. After a short period of time, an appreciable percentage of the feed concentration is seen in the effluent. The temperature response is also typical of a gradual wave. The temperature quickly rises to a maximum (in this case about 305 °K) and then falls gradually back to the feed temperature.

Construction of solutions using equilibrium theory requires the use of the two rules stated earlier. A wave will be gradual if possible. Slopes in the q versus v^*c plane must increase from initial to feed conditions. There are two sets of characteristics corresponding to two roots of the equation 29. The two

characteristic curves are required in order to obtain the path that connect any initial condition to any feed condition. The 1 wave is the first wave to leave the bed, therefore it must be the wave connected to the initial condition while the 2 wave is connected to the feed.

The slope of the 1 characteristic on the q versus $v^* c$ plane is decreasing from the initial condition, a clean bed. This means there will be a shock path that leaves this point. This is shown as the bottom dotted line in Figure 2 and the upper dotted line in Figure 3 emanating from the origin. The 2 wave that connects the feed condition, 50% RH, has a constantly increasing slope from initial to feed condition corresponding to a gradual wave represented by the bold solid line in Figures 2 and 3. The point where the shock from the initial condition and gradual wave meet can be found by stepping out in temperature along each path using equations 29 and 30 until they intersect. This corresponds to a plateau concentration. Figures 2 and 3 make it easy to visualize how the solution path cuts across isotherms producing a temperature wave.

There is very close agreement between the stage model, the equilibrium theory model, and the data as seen in Figure 4. The equilibrium theory solution does predicts a larger temperature rise than the stage model. This is expected because equilibrium theory assumes adiabatic behavior. The actual recorded temperature does not reach as high as the prediction because during the first minutes of the run the sample tube was periodically taken off line so that the water uptake could be recorded. Note that both the concentration and the temperature wave travel with the same velocity as seen in Figure 4. This is predicted by equilibrium theory using equation 28.

A preliminary study, using only isothermal equilibrium theory, did not fit the data indicating that the effect of temperature is very important to this process. There is a gradual wave associated with the low RH for the isothermal case. However, the shock associated with temperature tends to overrun these gradual wave characteristics in the adiabatic case leading to a shock in temperature and concentration. Note that because the water isotherm is unfavorable at lower RH these low concentrations tend to run out of the column quickly. The large temperature rise associated with the 1 wave has the effect of removing water from the bed that was just adsorbed at the lower temperature. This increases the required time for complete saturation of the bed. It appears that isothermal adsorption would provide a faster means of achieving saturation.

4.3 Breakthrough of 80% RH Feed To Bed Equilibrated At 50% RH.

The water isotherm is favorable between 50% RH(0.628 mol/m^3 at 298°K) and 80% RH(1.001 mol/m^3 at 298°K) as seen in Figure 2. This is the typical shape of an adsorption isotherm, and one could expect the standard S-shaped breakthrough curve. Figure 5 shows the results of an 80% RH feed to a bed initially equilibrated at 50% RH. Although the shape of this curve is not very sharp, the breakthrough behavior does follow an S-shaped pattern.

This S-shaped pattern is called an abrupt wave or a constant pattern wave. This means that at a certain distance into the bed, the shape of the concentration front does not change as the wave is transmitted down the bed. There is also an initial shock characterized primarily by a temperature rise.

Referring back to Figure 2, the 2 characteristic emanating from the feed of 80% RH and the 1 characteristic from the initial concentration of 50% RH both violate the gradual wave criterion. The slopes of these waves decrease from initial to feed conditions, therefore each of these waves must start as a shock. The equilibrium theory solution then requires that equation 30 be solved from both the initial and feed conditions until they intersect, while at each increment checking to see whether the slope of the gradual wave is continuing to violate the gradual wave criterion. The intersection point leads to a plateau condition. This path is close to having a gradual portion because it is so close to the inflection point of the isotherm. However, the adiabatic nature of this system results in the formation of two shocks.

The simulation provided by the stage model and equilibrium theory represent the data well for this run. The resulting breakthrough behavior is shown in Figure 5. Equilibrium theory provides a very accurate measure of the center of both the concentration and temperature waves. The plateau region between the two shock fronts is apparent in the data. Again the temperature rise measured in the experiment is reduced due to sampling of the uptake weight of the bed. The effect of the mass and heat transfer resistances in the stagemodel becomes obvious in the shock portion of the breakthrough curves. These resistances tend to spread out the shock wave in an actual experiment.

4.4 Breakthrough of 80% RH Feed To A Clean Bed.

The water isotherm changes from unfavorable to favorable between 50% RH and 80% RH. The effect of this inflection in the isotherm should be apparent on the breakthrough behavior. Figure 6 shows the breakthrough data measured for 80% RH feed to a clean bed. Notice that the resulting breakthrough curves of both

temperature and concentration are essentially a combination of the first two experiments. The only difference is the faster flow rate (10 l/min as opposed to 5 l/min).

The equilibrium theory solution path is characterized by an initial 1 wave shock as in the run with 50% RH feed to a clean bed, the lower dotted line in Figure 3. There is also a shock emanating from the feed as in the run with 80% RH feed to a bed equilibrated to 50% RH. However there is a third transition. As the isotherm changes from favorable to unfavorable a combined wave is formed that shows both shock and gradual wave behavior, Figure 2. It is possible to identify this as a combined transition because it does not have a plateau region where the two waves unite. There is a portion of the gradual wave for 80% RH feed to clean bed that parallels the shock path for 80% RH feed to a bed equilibrated at 50%RH. The two runs are not identical over the same range of RH. This result only becomes apparent in the adiabatic analysis.

The shape of both the concentration and temperature profiles agrees with the stage model and equilibrium theory predictions. The subtle shape of the combined transition is not obvious from the data. Equilibrium theory allows this combined transition to be identified.

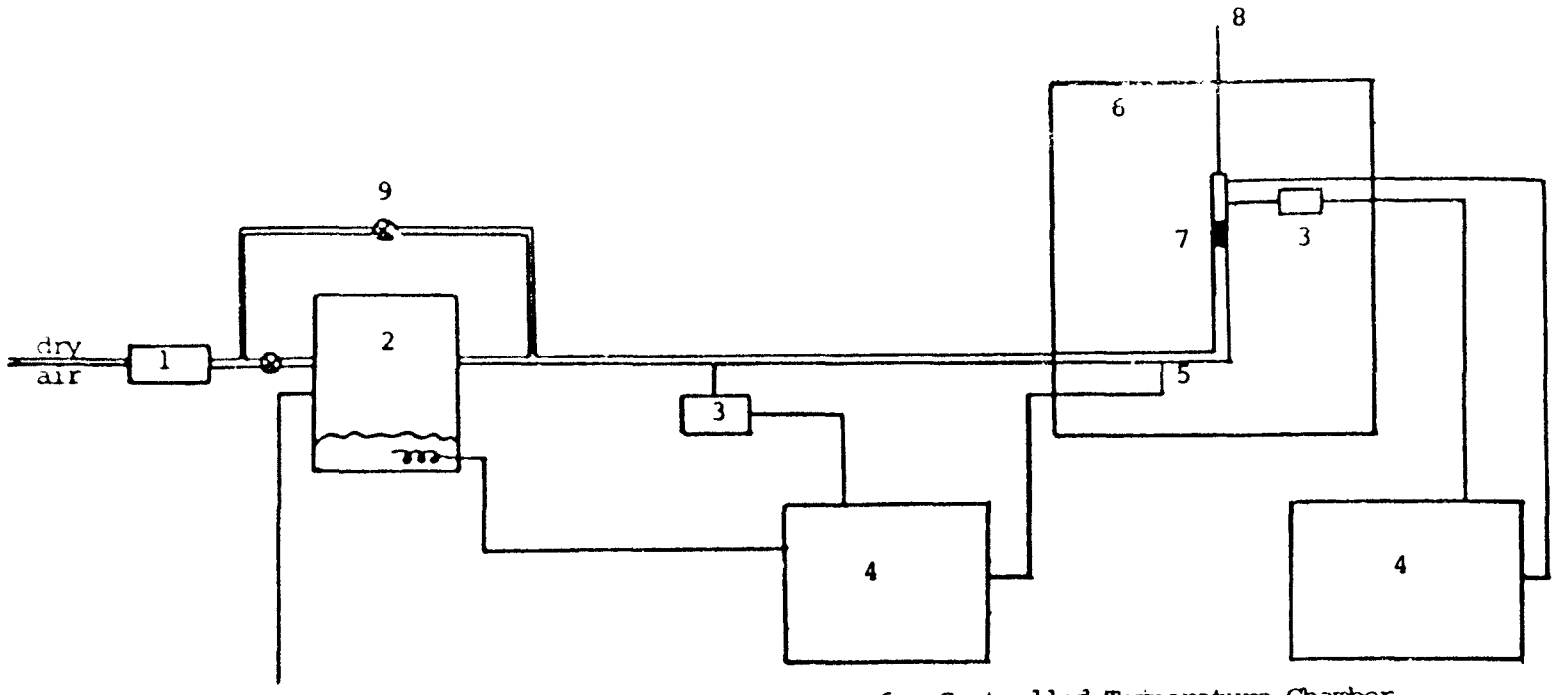
5. CONCLUSIONS

- The three types of waves that can be formed in and passed through an adsorption bed are demonstrated both mathematically and experimentally.
- The stage model seems to fairly represent the breakthrough using correlated equilibrium data and *a priori* calculated rate parameters.
- Equilibrium theory allows the exact nature of the transitions to be explored.
- The inability of equilibrium theory to be used with heat and mass transfer resistances leads to some discrepancy between this method and the experimental results.

Blank

NOTATION

a	= surface to volume ratio(m^{-1})
A, B, C	= Antoine equation parameters(p_{sat} in mm Hg)
c_*	= gas phase concentration of water(mol/m^3)
c	= gas phase concentration of water in the pellet(mol/m^3)
c_a	= heat capacity of adsorbed phase(kJ/kgK)
c_f	= heat capacity of gas phase(kJ/kgK)
c_s	= heat capacity of solid phase(kJ/kgK)
h_f	= enthalpy of gas phase(kJ/kg)
h_s	= enthalpy of solid phase(kJ/kg)
k_v	= mass transfer coefficient(m/s Ref. 16)
K1, K2	= coefficients of water adsorption isotherm, Eq. (32)
L	= length of bed(m)
p	= partial pressure of water(Torr)
q	= solid phase concentration(mol/kg)
q_{sat}	= solid phase concentration at saturation(mol/kg)
r_i	= inner radius of filter tube(m)
R	= gas constant
t	= time
T	= temperature(K)
T_o	= temperature of feed gas(K)
T_{ref}	= heat capacity reference temperature(K)
U	= overall heat transfer coefficient of filter tube(kJ/m^2Ks)
v	= interstitial velocity(m/s)
v_o	= interstitial velocity of feed(m/s)
z	= axial distance coordinate(m)
ϵ	= void fraction of packing
ζ	= dimensionless axial coordinate, Eq. (7)
θ	= fractional saturation of the bed
λ	= heat of adsorption(kJ/mol)
ρ_b	= bulk density of packing(kg/m^3)
ρ_f	= density of gas phase(kg/m^3)
ρ_{fo}	= density of inlet gas (kg/m^3)
τ	= dimensionless time, Eq. (6)



1. Flow meter
2. Water bath
3. Humidity Sensor
4. Humidity Analyzer and Controller
5. Temperature probe
6. Controlled Temperature Chamber
7. Carbon Bed
8. Effluent Air
9. By-pass Valve

Figure 1. Schematic of Breakthrough Apparatus

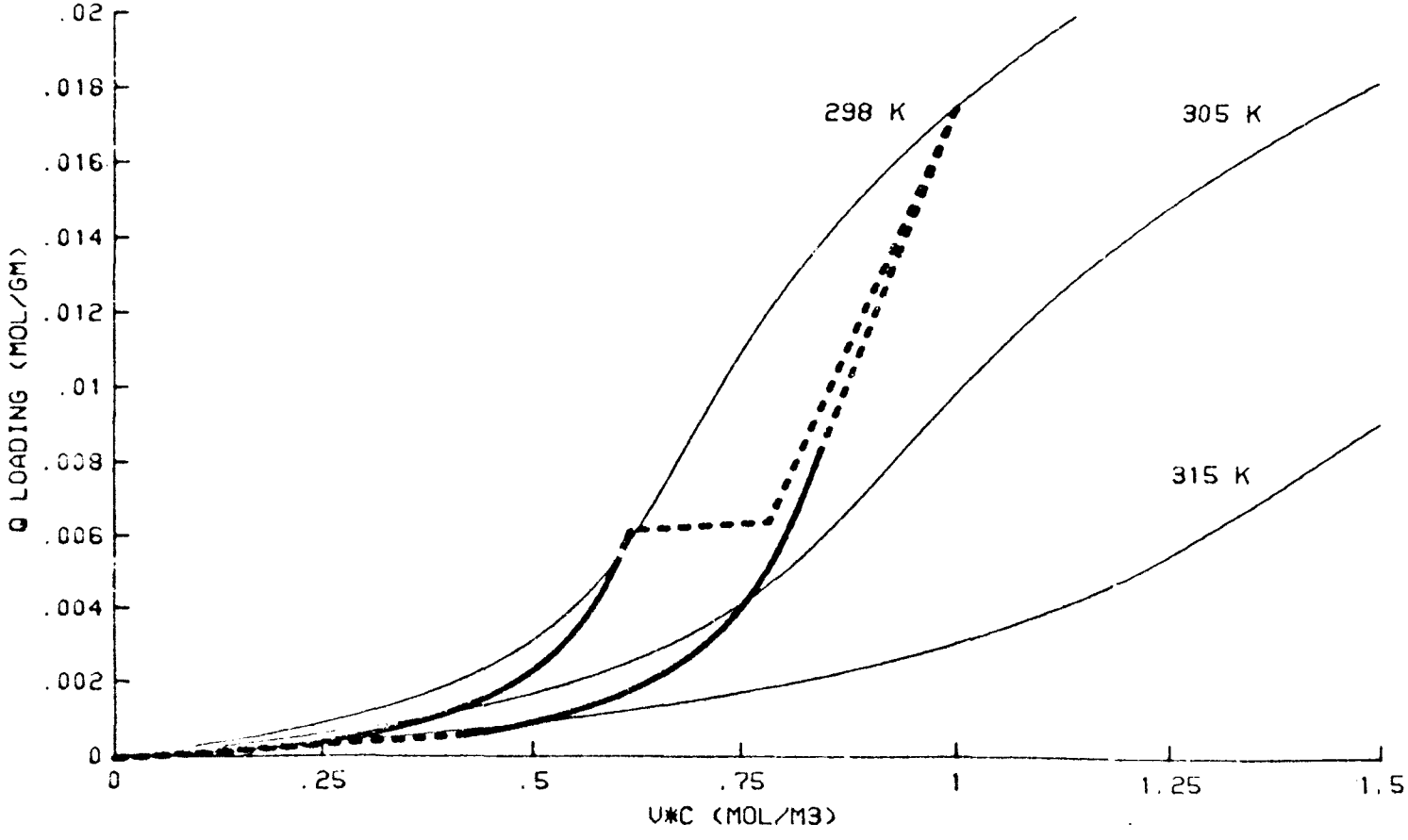


Figure 2. Path In Modified Isotherm Plane 50%RH, 80%RH Feed To Clean Bed And 80%RH Feed To 50%RH Bed Of BPL

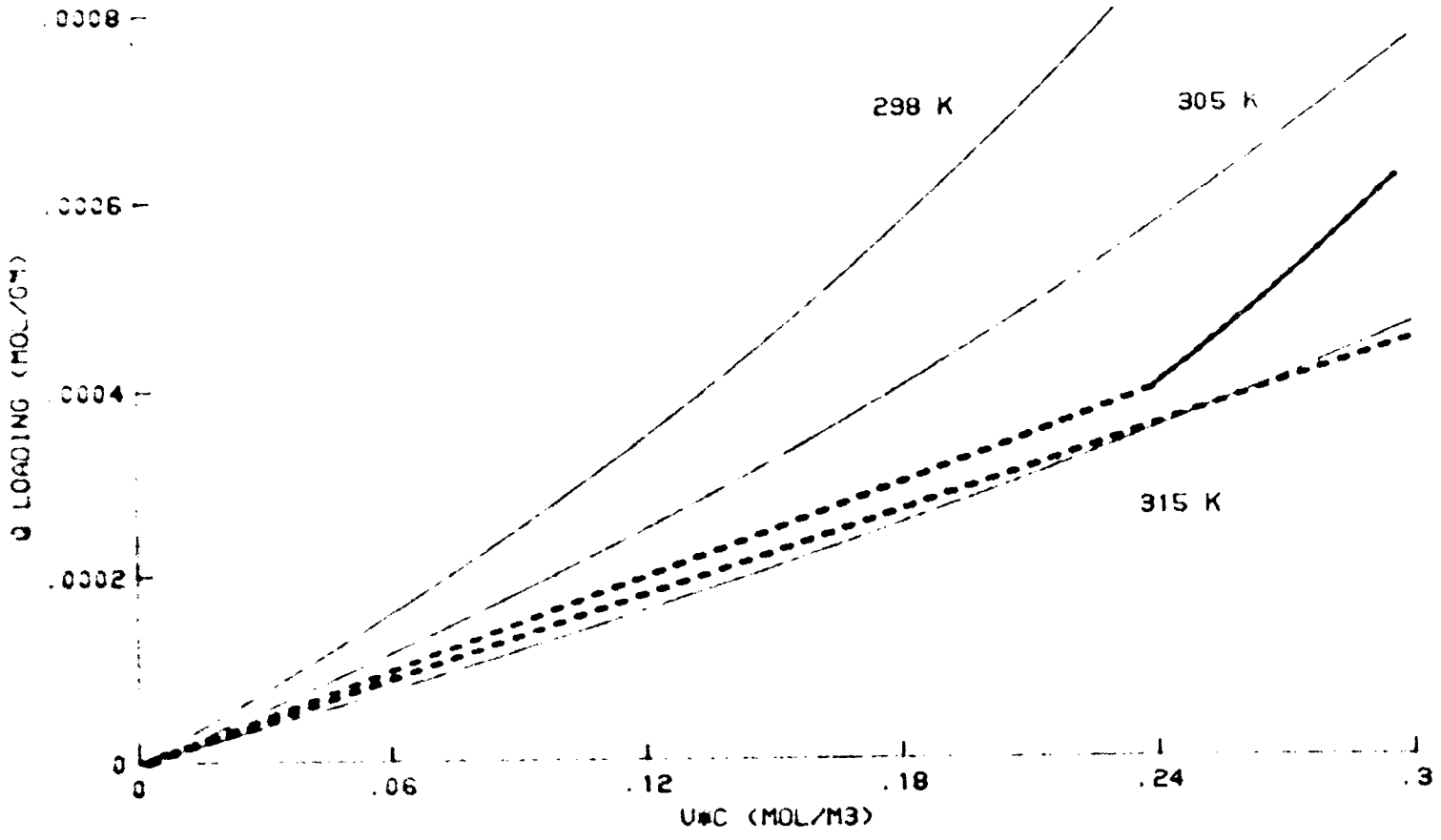


Figure 3. Enlargement Of Path In Modified Isotherm Plane 50%RH, 80%RH Feed To Clean Bed Of BPL

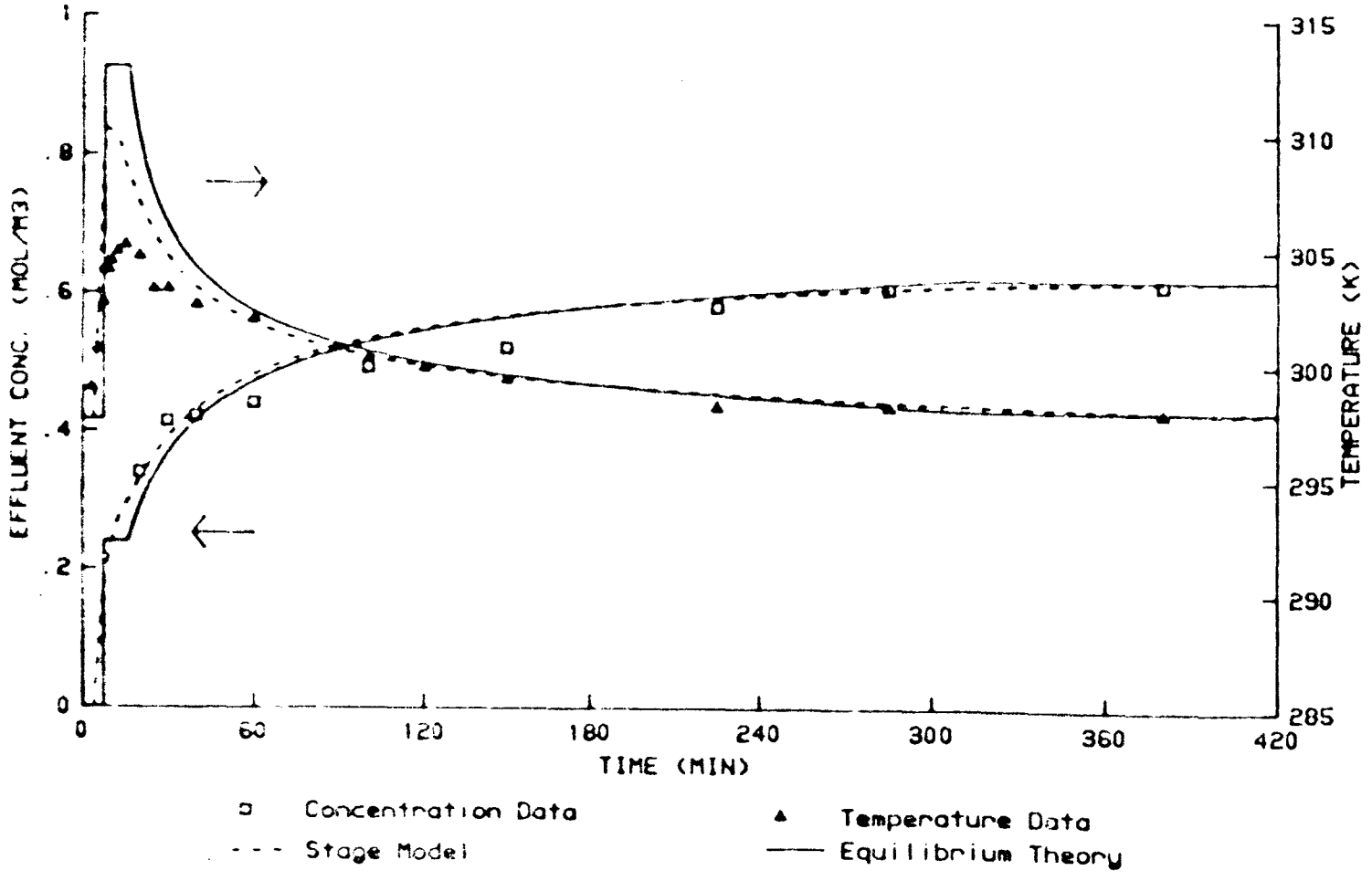


Figure 4. Breakthrough Of Water Vapor On BPL Carbon 50%RH Feed To Clean Bed

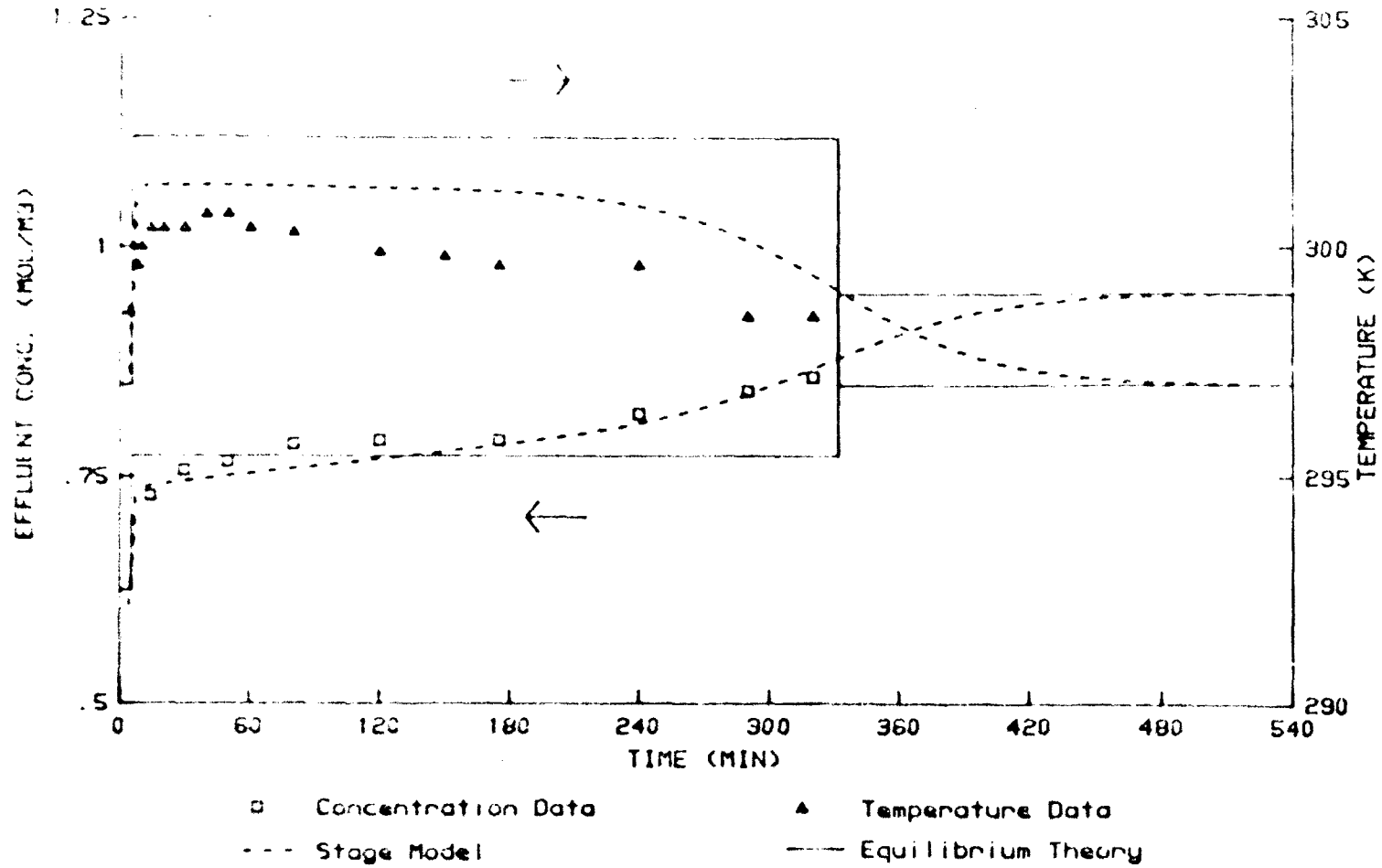


Figure 5. Breakthrough Of Water Vapor On BPL Carbon 80%RH Feed To Bed Equilibrated To 50%RH

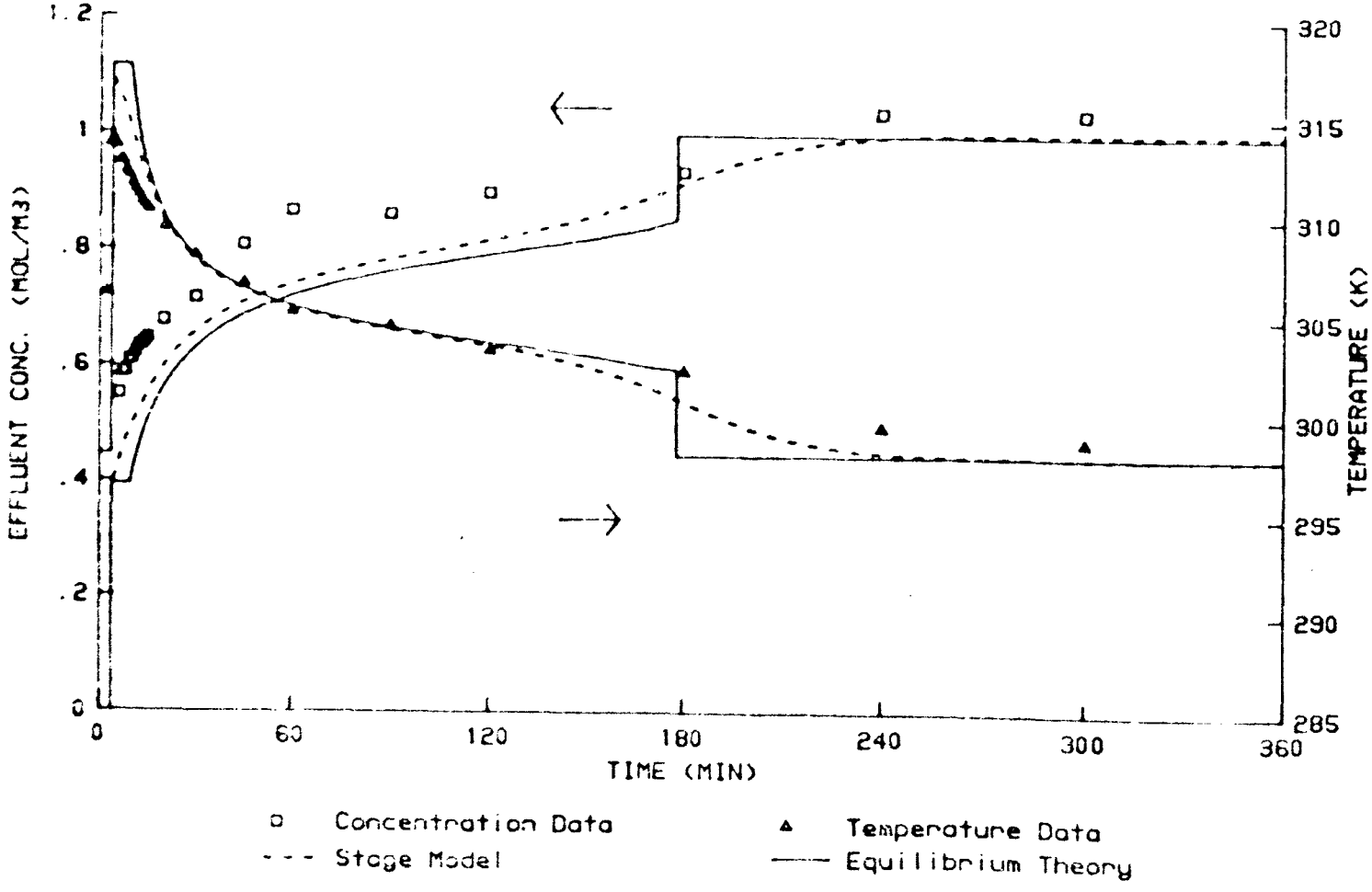


Figure 6. Breakthrough Of Water Vapor On BPL Carbon 80%RH Feed To Clean Bed

Blank

LITERATURE CITED

1. Doong,S.J., and Yang,R.T., "Adsorption of Mixtures of Water Vapor and Hydrocarbons By Activated Carbon Beds: Thermodynamic Model for Adsorption Equilibrium and Adsorber Dynamics," *AIChE Symposium Series: Adsorption and Ion Exchange* vol. 259(83), p. 87 (1987).

2. Rodrigues, A.E. and Beira, E.C., "Staged Approach of Percolation Processes," *AIChE J.* vol. 25, p. 416 (1976).

3. Ikeda, K., "Performance of the Nonisothermal Fixed-Bed Adsorption Column with Nonlinear Isotherms," *Chem. Eng. Sci.* vol. 34, p. 941 (1981).

4. Friday, D.K., and LeVan, D., "Solute Condensation in Adsorption Beds During Thermal Regeneration," *AIChE. J.* vol. 28, p. 86 (1982).

5. Friday, D.K., and LeVan, D., "Thermal Regeneration of Adsorption Beds: Equilibrium Theory for Solute Condensation," *AIChE J.* vol. 30, p. 679 (1984).

6. Acrivos, A., "Method of Characteristics Technique: Application to Heat and Mass Transfer Problems," *Ind. Eng. Chem.* vol. 48, p. 703 (1956).

7. Pan, C. Y., and Basmadjian, D., "Constant Pattern Adiabatic Fixed-Bed Adsorption," *Chem. Eng. Sci.* vol. 22, p. 285 (1967).

8. Pan, C.Y., and Basmadjian, D., "An Analysis of Adiabatic Sorption of Single Solutes in Fixed Beds: Equilibrium Theory," *Chem. Eng. Sci.* vol. 26, p. 45 (1971).

9. Rhee, H.K., Aris, R. and Amundson, N.R., *First Order Partial Differential Equations: Volume I, Theory and Applications of Single Equations*, pp. 188-410, Prentice-Hall, Englewood Cliffs, NJ, 1986.

10. Ruthven, D M., *Principles of Adsorption and Adsorption Processes*, pp. 274-323, John Wiley and Sons, New York, NY 1984.

11. DeVault, D., "The Theory of Chromatography," *J. Amer. Chem. Soc.* vol. 65, p. 532 (1943).

12. Lax, P.D., "The Formation and Decay of Shock Waves," *Amer. Math. Monthly* vol. 79, p. 227 (1972).

13. Hacskaylo, J.J., and LeVan, M.D., "Correlation of Adsorption Equilibrium Data Using a Modified Antoine Equation: A New Approach for Pore-Filling Models," *Langmuir* vol. 1, p. 97 (1987).

14. Reid, R.C., Prausnitz, J.M., and Sherwood,T.K., *The Properties of Gases And Liquids*, 3rd ed., p. 634, McGraw-Hill, New York, NY, 1977.

15. Mahle, J.J., and Friday, D.K., *Water Adsorption Equilibria On Microporous Carbons*, CRDEC-TR-018, U.S. Army Chemical Research, Development and Engineering Center, Aberdeen Proving Ground, MD, November 1988, UNCLASSIFIED REPORT.

16. Ranz, W.E. and Marshall, W.R., "Evaporation From Drops Part II," *Chem. Eng. Prog.* vol. 48, p. 173 (1952).

APPENDIX B2

THE EFFECT OF RELATIVE HUMIDITY ON THE BREAKTHROUGH BEHAVIOR OF EA____ ON ASC-TEDA, PART 1. EXPERIMENTAL STUDIES. (U)

by

Leonard C. Buettner

John J. Mahle

Research Directorate

David K. Friday

GEO - CENTERS Inc.

CONTENTS (U)

		Page
1.	INTRODUCTION	5
2.	MATERIALS AND METHODS	6
2.1	Charcoal Pretreatment and Conditioning	6
2.2	Test Apparatus and Data Collection	7
2.3	Generation of Challenge Gas Concentration ..	7
3.	PROCEDURE	8
4.	RESULTS AND DISCUSSION	9
4.1	Analysis of Breakthrough Data	9
4.2	Related Observations and Additional Experimental Findings.....	11
5.	CONCLUSIONS	12
	LITERATURE CITED	22
	DISTRIBUTION LIST	23

APPENDIX C1

(2) Recent Advances in Capillary Gas Chromatography; Bartsch, W., Jennings, W., Kaiser, R., Eds.; Huthing: Heidelberg, 1981.
(3) White, C.; Houck, R. HRC CC. J. High Resolut. Chromatogr. Chromatogr. Commun. 1986, 9, 4.
(4) Knox, J.; Gilbert, M. J. Chromatogr. 1979, 186, 405.
(5) Mikkers, F.; Everaerts, F.; Verheggen, Th. J. Chromatogr. 1979, 169, 11.
(6) Jorgenson, J.; Lukac, K. Science (Washington, D.C.) 1983, 222, 266.
(7) Jorgenson, J. Science (Washington, D.C.) 1984, 226, 254.
(8) Yeung, E. In Advances in Chromatography; Giddings, J., Ed.; Marcel Dekker: New York, 1984; Vol. 23.
(9) Meyer, V. J. Chromatogr. 1986, 334, 197.
(10) Bomhop, D.; Dovichi, N. Anal. Chem. 1986, 58, 504.
(11) Bomhop, D.; Nolan, T.; Dovichi, N. J. Chromatogr. 1987, 384, 161.
(12) Munk, M. In Liquid Chromatographic Detectors; Vickers, T., Ed.; Marcel Dekker: New York, 1983.
(13) Yeung, Edward In Liquid Chromatography Detectors; Yeung, E., Ed.; Marcel Dekker: New York, 1987.
(14) Woodruff, S.; Yeung, E. J. Chromatogr. 1983, 280, 383.
(15) Bogoslovskii, Y.; Razin, V. Zh. Fiz. Khim. 1971, 40, 1410.
(16) Banerjee, S.; Pack, E., Jr. Anal. Chem. 1982, 54, 326.
(17) Pawliszyn, J. Anal. Chem. 1986, 58, 243.
(18) Pawliszyn, J. Anal. Chem. 1986, 58, 3207.
(19) Pawliszyn, J. J. Liq. Chromatogr. 1987, 10, 3377.
(20) Pawliszyn, J. Rev. Sci. Instrum. 1987, 58, 245.
(21) Sa, A. Principles of Electronic Instrumentation; Arnold: East Kilbridge, Scotland, 1981; p 227.
(22) Lapherdt, J. In Transform Techniques in Chemistry; Griffiths, P., Ed.; Plenum: New York, 1979; p 294.
(23) Pawliszyn, J.; Weber, M.; Dignam, M. Rev. Sci. Instrum. 1985, 56, 1740.
(24) Pawliszyn, J. Anal. Chem. 1988, 60, 766.
(25) Ruzicka, J.; Hansen, E. Flow Injection Analysis; Wiley: New York, 1981.
(26) CRC Handbook of Chemistry and Physics, 64th ed.; CRC: Boca Raton, FL, 1985; p E 365.

RECEIVED for review June 13, 1988. Accepted September 13, 1988.

Detection of Hazardous Vapors Including Mixtures Using Pattern Recognition Analysis of Responses from Surface Acoustic Wave Devices

Susan L. Rose-Pehrsson* and Jay W. Grate

Chemistry Division, Naval Research Laboratory, Washington, D.C. 20375-5000

David S. Ballantine, Jr.

GEO-Centers, Inc., 10903 Indian Head Highway, Ft. Washington, Maryland 20744

Peter C. Jurs

152 Davey Laboratory, Pennsylvania State University, University Park, Pennsylvania 16802

Surface acoustic wave (SAW) devices coated with selectively sorbent materials are being investigated as monitors for personnel safety where detection of hazardous vapors is required at sub-part-per-million concentrations in ambient air that can contain interferences at much higher concentrations. A set of ten SAW devices coated with polymer materials designed to interact with different vapor properties has been used to detect hazardous vapors by producing unique fingerprints to represent a given vapor. The coatings were exposed to nine individual vapors and two-component mixtures of the vapors representing different chemical classes and concentrations, and the resulting data matrix was studied by using pattern recognition methods. Four of the coatings were common to a previous study, and their responses to the single vapors were used as a prediction set to test the classification capacity of a linear discriminant developed in that study. All of the vapors were correctly identified, except water. Principal components analysis and clustering methods were applied to the responses of the coatings to all the vapors, including mixtures. The individual vapors cluster into specific regions in space, and the mixtures lie in the areas between the clusters. Supervised learning techniques were used to reduce to eight the number of sensors necessary to identify the hazardous vapors in the presence of mixtures.

INTRODUCTION

Great demands have been placed on toxic vapor detectors because detection of sub-part-per-million concentrations is required in ambient conditions where interferences can be present at much higher concentrations. In addition, field instruments should be small, portable, and inexpensive. It would also be advantageous to have an instrument that could be adapted to many detection problems. Few instruments have the necessary sensitivity and selectivity, while maintaining the small size needed in the field. Microelectronic chemical sensors meet the size requirement, can be very sensitive, and can show 3 to 4 orders of magnitude selectivity between toxic vapors of interest and common interferents. Nevertheless, these capabilities may be insufficient if the interferent concentrations are orders of magnitude greater than the vapor concentrations that must be detected.

Pattern recognition techniques in conjunction with an array of sensors is a promising approach to this type of analytical problem. This approach has been applied to vapor response data from electrochemical sensors (*1*), to the selection of coatings for piezoelectric crystal sensors (*2*), and to the study of coatings and identification of vapors using surface acoustic wave (SAW) devices (*3*). In the latter study, the clustering of vapors demonstrated that vapor solubility properties, such as hydrogen bonding, were important in determining how the sensors respond. In a recent paper by Carey and co-workers, multiple linear regression and partial least-squares calibration techniques were used to measure the concentration of two- and three-component mixtures by an array of nine piezoelectric crystal sensors (*4*). The goal of our present work is the detection of a single vapor or class of vapors in a complex environment, rather than the identification of the different components of the large number of mixtures possible in the environment. Our specific objective is the detection of toxic organophosphorus compounds.

Several research groups are investigating SAW devices for toxic vapor detection because of their small size and excellent sensitivity (*3*, *5*-*21*). These planar microsensors consist of

0003-2700/88/0360-2801$01.50/0 © 1988 American Chemical Society

interdigital transducers that are microfabricated onto the surface of a piezoelectric substrate, such as quartz. The transducers convert an applied radio frequency (rf) voltage into a Rayleigh surface wave when placed in an oscillator circuit. Chemical sensitivity is provided by a thin film coating of a selectively sorbent material. Vapors sorbed into the coating increase its mass and perturb the Rayleigh wave. This perturbation is detected electronically as a shift in the frequency of the oscillator circuit. The principles of operation are described in detail in ref 7. The sensitivity and selectivity of the response are dependent upon the vapor/coating interactions. The sorption of vapors by a SAW sensor coating and the solubility interactions between the vapor and the coating are discussed in detail in ref 5.

An instrument comprised of an array of SAW sensors would be designed with a different coating on each sensor, and each coating would be selected to respond differently to a set of vapors. The combination of sensors selected to interact with different chemical properties would produce a unique fingerprint for each vapor. The sensors encode chemical information about the vapors in a numerical form, which can be analyzed with pattern recognition methods. Each sensor defines an axis in a multidimensional space. Vapors can be represented as points positioned in this space according to sensor responses. Vapors that produce similar responses from the set of coatings will tend to be represented by points that cluster near one another in the multidimensional space. Pattern recognition uses multivariate statistics and numerical analysis to investigate such clustering and to elucidate relationships in multidimensional data sets. By use of supervised learning techniques, a discriminant can be developed to distinguish between toxic vapors of interest and interferents. This type of instrument can be adapted to specific detection problems by the choice of the discriminant developed or by selecting different coatings for the array and developing the appropriate discriminant.

In a previous study conducted in our laboratory, a large data set was generated by using 112-MHz SAW vapor sensors. Pattern recognition techniques were used to analyze the responses of 12 SAW coatings to 11 vapors at various concentrations (3). The vapors were divided into two classes: class 1, vapors of interest; class 2, potential interferences. The number of sensors needed to discriminate between vapors of interest and the interferences was reduced from the original 12 to 4 by pattern recognition data analysis. Several combinations of coatings were successful in the classification.

In the present study, 158-MHz SAW devices were used to generate another large data set. These higher frequency devices have a greater mass sensitivity and are smaller. Each sensor is wire bonded on a conventional 12-pin gold TO-8 header, for ease of handling. Ten coatings were examined, including four used in the previous study. The data set includes exposures to nine single vapors at various concentrations, plus several two-component mixtures of the vapors. The objectives were 2-fold. First, we wanted to test the classification capability of the discriminant generated in the previous study. The responses of the sensors coated with the same materials tested 2 years earlier were used as a prediction set. Second, we wanted to investigate the clustering of sensor responses in a data set including both single vapors and mixtures. These data served as a training set for a new discriminant able to identify hazardous vapors when present in mixtures containing an interference vapor at a much higher concentration.

EXPERIMENTAL SECTION

This study was conducted in two stages: (a) collection of the data and (b) application of pattern recognition analysis methods to the collected data.

Table I. Test Vapors and Mixtures

Class 1
dimethyl methylphosphonate (DMMP)
N,N-dimethylacetamide (DMAC)
mixtures of each class 1 vapor with each class 2 vapor
Class 2
1,2-dichloroethane (DCE)
water
isooctane (ISO)
toluene (TOLN)
diethyl sulfide (DES)
2-butanone (BTN)
1-butanol (BTL)
mixtures of water with each class 2 vapor
isooctane with each class 2 vapor
2-butanone with each class 2 vapor

Table II. Coatings

FPOL	fluoropolyol
PEM	poly(ethylene maleate)
PECH	poly(epichlorohydrin)
PVP	poly(vinylpyrrolidone)
ECEL	ethyl cellulose
PBOH	poly(butadiene) hydroxylated
PEI	poly(ethylenimine)
PEPH	poly(ethylene phthalate)
PFA	poly(isoprene/fluoro alcohol)
PIB	poly(isobutylene)

Materials. The vapors used are listed in Table I. Solvents for the vapor generation were commercial materials of 99% or greater purity, except diethyl sulfide (98%, Aldrich) and dimethyl methylphosphonate (97%, Aldrich).

A list of the coating materials and the abbreviations used in this study is given in Table II. The coating materials poly(epichlorohydrin) and poly(isobutylene) were obtained from Aldrich. Poly(vinylpyrrolidone) was purchased from Alltech. Poly(ethylenimine) and ethyl cellulose were acquired from Polysciences. Poly(ethylene maleate) was prepared as described by Snow and Wohltjen (8). Fluoropolyol was prepared by using methods described by Field (22). Poly(ethylene phthalate) was prepared from phthalic anhydride and ethylene glycol as described in ref 23. The poly(isoprene/fluoro alcohol) was prepared from poly(3,4-isoprene) and excess hexafluoroacetone as described in ref 24, where it is referred to as PIPFA1. Poly(butadiene)-hydroxylated was prepared by hydrolyzing epoxidized poly(butadiene) with aqueous HCl in dioxane. The poly(butadiene) used was from Polysciences.

SAW Sensors. The 158-MHz dual SAW delay lines (Microsensor System, Inc., of Fairfax, VA, part number SD-158-A) have been described (5) and are depicted in Figure 1. The rf electronics modules that operated the devices were described in the same reference. One delay line of each dual device was spray coated with a dilute solution of the coating material in a volatile solvent (usually chloroform, tetrahydrofuran, or a methanol/chloroform mixture) as described in ref 3 and 5. Coating deposition produced frequency shifts of 200–250 kHz, which were recorded and used as a measure of the amount of coating material for normalization and comparison of data (7). The uncoated delay line acted as a reference oscillator to provide compensation for ambient temperature and pressure fluctuations. The low frequency difference signal between the uncoated reference delay line and the coated delay line was monitored during the vapor exposures (3, 5).

Data Collection. Vapor streams were generated by using an automated gas handler system interfaced with an Apple IIe microcomputer. The test vapors were generated from bubblers or permeation tubes and diluted to known concentrations. The gas flow rate to the sensors was 200 mL/min. This experimental system is described in detail in ref 25.

The temperature at the sensors was monitored and was typically 35 ± 2 °C. The sensors were tested in arrays of four connected to the vapor stream in series. Each array included one fluoropolyol-coated sensor and three other coatings. The fluoropolyol-coated sensor provided a check for consistency from one array to another. Each array was exposed to nine single vapors.

Each vapor was measured at four concentrations, with each concentration repeated four times. Two-component mixtures were generated at a single combination of concentrations and the sensor responses were again measured four times. Typical experiments consisted of repeated exposures of air/vapor/air/vapor/air. Sensor exposures were 3 min long with at least 6 min of recovery time between exposures. The difference frequency output was usually recorded every 6 s at 1-Hz resolution. Dimethyl methylphosphonate exposures were repeated periodically throughout each vapor test set to check for consistent sensor performance. Some of the sensors were repeated in more than one array. Poly(vinylpyrrolidone) demonstrated poor reproducibility, and a good data set including mixtures was not generated with that coating. This coating was used only for comparison with the pattern recognition study reported in 1986 (3).

Responses were determined from the equilibrium vapor sorption at the end of the exposure, as described in detail in ref 5. Each sensor was coated with slightly different amounts of material. To enable comparisons of one coating response to another, the responses were normalized for coating thickness by dividing by the kilohertz frequency shift observed when each sensor was coated.

Pattern Recognition. The normalized sensor responses were organized into two data matrices for analysis. The two exposures within a vapor exposure experiment were averaged. A 104 × 4 matrix included data for four coatings exposed to the nine single vapors. The results of all the single vapor exposure experiments at the different concentrations were included. These four coatings were common to our previous study; this matrix was used as a set of unknowns (a prediction set) to test the linear discriminant developed in that study. The second matrix, 172 × 9, included all the coatings tested in this study, except poly(vinylpyrrolidone), tested against both the individual vapors and the mixtures. At least two vapor exposures at each concentration were included in the data set. This matrix was first examined by using the normalized data as collected. It was also examined after correcting for variations observed in the fluoropolyol responses between test arrays.

These data were analyzed on a VAX 11-750 computer using pattern recognition routines included in the ADAPT software system (26). Each row in each matrix is a pattern vector, representing responses of the coatings to a given vapor/concentration experiment. The pattern vectors were normalized by dividing each sensor response by the square root of the sum of the squared sensor responses in a given vapor experiment because dividing the sensor responses by concentration is not possible for a field instrument measuring unknowns. This closure method is pattern normalization as described previously (1). Sensor responses can vary by orders of magnitude; it is important to make them more compatible. Autoscaling, a preprocessing method that scales and normalizes the data, is useful for correcting the imbalance between sensors and does not alter the basic geometry of the clustering (26). Each response for a coating was then autoscaled to a mean of zero and a standard deviation of unity.

Because many of the available sensor coatings encode similar information, collinearities between sensors may cause numerical instabilities in the analysis phase. Multiple linear regression analysis was used to uncover multicollinear relationships among the detector responses in order to identify the smallest set of sensors providing the largest amount of relevant information. Once a set of sensors is found that contributes unique information, pattern recognition techniques for display, mapping, clustering, and classification were employed. the methods used have been described in ref 1 and 3.

RESULTS AND DISCUSSION

SAW Sensor Testing. A schematic diagram of the dual delay line SAW device is given in Figure 1. Sensor response data were collected by monitoring the difference frequency between the coated delay line and the uncoated reference delay line. When the gas stream over the sensor is changed from clean air to vapor-containing air, the frequency of the coated delay line shifts to a lower value. This negative frequency shift is related to the mass of the vapor sorbed by the coating (7). Ideally, the reference signal does not change, and the positive difference signal is also related to the mass of vapor sorbed.

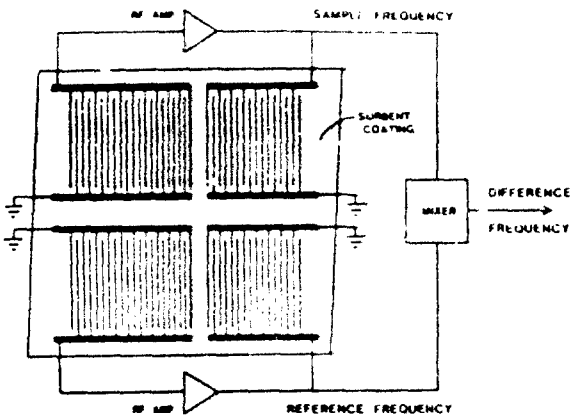


Figure 1. 158-MHz SAW device and associated electronic circuit diagram.

However, in practice, the reference signal can change significantly in response to vapor exposures (5). Therefore, the difference signal accurately represents vapor sorption only when the signal change on the coated side is much greater than the change on the reference side. This condition is true for the sorption of DMMP by fluoropolyol-coated sensors (5), for example, but not for all the vapors and sensor coating materials reported here.

The sensor testing results are presented in Table III as the frequency shift observed divided by the kilohertz of coating on the sensor. Each number is the average of (usually) four measurements at that vapor concentration. Negative difference signals were observed in a minority of cases. These occurred most frequently for the coating poly(isobutylene), which does not sorb most vapors very strongly. The vapor most frequently associated with negative difference signals is water, which can sorb strongly to the glass surface on the reference side.

Our specific objective is the detection of toxic organophosphorus compounds. These strongly hydrogen bond accepting vapors are simulated by using less toxic dimethyl methylphosphonate (DMMP) and *N,N*-dimethylacetamide. DMMP is an organophosphorus compound, and both simulants are strong hydrogen bond acceptors. DMMP vapor streams were generated at low concentrations with a permeation tube, and at higher concentrations with a bubbler. Thus sensors were tested against this vapor over a much wider concentration range than in previous studies (3). The seven vapors that are not simulants represent a variety of potential interferents.

Most coating materials respond similarly to the two simulant vapors and statements about DMMP will usually also apply to *N,N*-dimethylacetamide. The most sensitive coatings for these vapors are fluoropolyol and poly(isoprene/fluoro alcohol). The latter material has been designed to be highly sensitive to these vapors by incorporating the strongly hydrogen bond donating hexafluoro-2-propanol functionality (24, 27, 28). Fluoropolyol has been reported in previous studies (3, 6) and the sorption of vapors by this material has recently been examined in detail (5). Individual fluoropolyol-coated sensors are reproducible for repeated vapor exposures, and separate sensors are comparable to one another. The responses of a single fluoropolyol-coated sensor to repeated exposures of DMMP are reported in Table IV. The range of variation at any given concentration is ca. ±10%. Fluoropolyol-coated sensors were included in each array of four sensors tested simultaneously to provide a check for consistency from one four sensor array to another. The responses of the fluoropolyol sensor in the first test array were used in the data set described here for the pattern recognition analysis.

Table III Frequency Shifts (Hz/kHz)

vapor	concn, μg/L	FPOL	PEM	ECEL	PEI	PEPH	PECH	TFA	PIB	PBOH	PVP
DMAC	91	67.10	9.10	3.97	−0.58	2.60	3.32	158.80	−4.58	2.57	0.47
	40	57.00	7.00	2.37	−0.39	1.26	1.91	124.99	−3.81	1.34	0.39
	20	33.94	3.27	1.54	0.24	0.55	0.93	92.21	−2.74	0.62	0.22
	11	18.83	1.69	0.81	−0.17	0.28	0.54	69.54	−1.96	0.34	0.17
DMMP	2290	257.62	90.66	54.34	−2.64	45.25	44.84	933.92	−8.46	39.53	4.30
	1100	207.48	56.64	25.25	−2.25	24.92	24.07	414.63	−6.24	21.42	2.72
	569	160.90	31.39	14.44	−1.88	14.11	11.48	346.16	−7.07	10.32	1.69
	372	142.23	24.28	10.84	−2.01	11.48	8.01	321.69	−6.09	6.73	0.74
	137	128.81	20.50	8.31	−1.45	7.02	3.90	228.80	−5.95	2.95	1.13
	84	102.79	13.44	5.53	−1.15	4.97	2.32	183.50	−4.90	1.63	1.70
	52	83.89	8.51	4.02	−0.84	3.62	1.53	157.92	−4.27	0.93	0.44
	29	58.70	4.54	2.33	−0.62	2.44	0.80	124.49	−3.18	0.44	0.40
ICE	176000	35.59	56.62	113.18	16.99	47.49	115.79	69.05	52.82	122.03	22.27
	84600	19.35	30.51	72.07	8.05	23.44	56.64	29.07	21.96	54.86	15.5
	45700	8.98	14.34	39.72	3.80	11.03	27.12	11.59	8.86	23.42	7.78
	30500	6.05	9.04	24.75	2.49	7.75	18.45	8.19	5.97	16.54	5.76
DES	137000	20.45	13.02	48.54	5.86	17.02	66.28	133.40	72.88	35.56	5.33
	68700	26.68	6.99	33.85	2.14	8.50	32.46	69.59	32.56	34.51	3.85
	35400	11.83	3.14	18.40	0.85	4.13	15.63	32.91	13.55	14.84	1.85
	23600	6.29	2.31	12.94	0.32	2.80	10.96	22.75	8.39	9.81	1.21
water	7190	9.71	3.22	2.44	35.23	1.99	1.95	20.49	−2.20	1.35	24.44
	3550	4.86	5.41	0.46	12.55	0.32	0.28	7.57	−1.46	0.72	5.79
	1820	2.51	3.63	0.02	4.91	−0.28	−0.01	4.04	−1.20	0.52	−0.40
	1210	1.69	2.93	−0.03	2.86	−0.38	−0.13	1.58	−1.49	0.24	−2.31
ISO	129000	13.43	0.54	7.33	0.82	1.48	21.25	35.17	78.95	25.22	0.54
	64300	5.90	0.06	4.78	0.61	0.74	10.78	14.88	33.49	11.63	1.02
	33100	2.52	0.24	2.67	0.45	0.38	5.10	6.20	13.84	4.30	0.62
	22000	1.77	0.16	1.98	0.13	0.29	3.57	3.76	9.19	3.42	0.56
TOL	57900	22.07	11.73	40.07	3.22	17.94	93.59	56.83	77.31	77.83	4.07
	28400	14.53	7.41	29.82	1.28	8.67	33.95	29.35	37.10	40.68	3.29
	14500	7.68	3.81	17.24	0.56	4.11	16.52	13.32	15.66	17.89	1.95
	9680	5.11	2.48	12.11	0.17	2.91	11.58	7.84	9.36	11.15	1.25
1HTL	8030	31.20	8.06	19.37	3.46	8.92	13.68	104.22	−4.65	13.26	7.90
	4040	15.45	3.26	11.29	1.64	5.25	6.71	62.13	−4.60	7.01	4.78
	2020	7.46	2.04	6.06	0.91	2.98	4.29	52.67	−3.63	5.36	2.61
	1400	5.42	1.63	4.43	0.50	2.37	2.84	29.02	−3.04	2.87	2.33
2BTN	149000	185.31	45.37	55.67	10.36	41.18	87.73	325.67	17.58	66.37	11.15
	74400	113.02	22.27	35.06	5.69	19.57	35.52	199.64	5.81	30.60	9.33
	37100	65.33	11.27	18.91	2.90	9.68	15.83	136.41	1.32	15.22	4.48
	25400	45.78	7.51	12.62	1.49	6.88	9.73	111.75	−0.13	10.30	3.81

Table IV. Fluoropolyol Responses to DMMP in Array I

concn, μg/L	response, Hz/kHz						av	% error
137	121	132	130	132	120	117	126	7
	123	134	132	131	122	117		
84	98	91	89	108	100	95	98	12
	90	90	89	107	99	93		
52	77			86	80	74	79	9
	81			85	78	73		
29	53			63	58	52	57	16
	58			66	56	52		

Two common interferents in many environments are water and hydrocarbon fuels. Poly(ethyleneimine), a coating material that we have not reported previously, was the most water-sensitive coating in this study (Table III). Poly(vinylpyrrolidone) coated sensors are also water sensitive but were not as sensitive in these tests as had been observed previously (7). Indeed, repeated experiments on this material indicated poor reproducibility from sensor to sensor, and on repeated testing of individual sensors. Data from the most consistently behaved poly(vinylpyrrolidone) coated sensor were selected for use in the prediction set below. Both poly(ethyleneimine) functionalities that can interact with water. They are among the most water-sensitive coatings in this data set but are much less sensitive to DMMP than the two DMMP sensitive coatings noted above. (The DMMP sensitive coatings also respond to water, but their water sensitivities are much less than their DMMP sensitivities.)

The properties of hydrocarbon fuels are represented in the set of vapors by isooctane and toluene. In our previous study, poly(isoprene) was the most sensitive coating material for isooctane. However, the high reactivity of unsaturated hydrocarbon polymers to ozone (29) prompted us to replace it with another elastomeric hydrocarbon polymer, poly(isobutylene). As expected, this material was the most sensitive coating for isooctane among those tested.

The patterns observed in response to DMMP, dimethylacetamide, water, and isooctane are illustrated in Figure 2. These graphs are normalized to the highest response. The patterns for DMMP and dimethylacetamide are quite similar, while those for water and isooctane are strikingly different from these and from each other.

Two-component mixtures were also included in the sensor test sequence. The vapors in these mixtures and their concentrations are given in Table V. Simulants at low concentrations were mixed with interferents at much higher con-

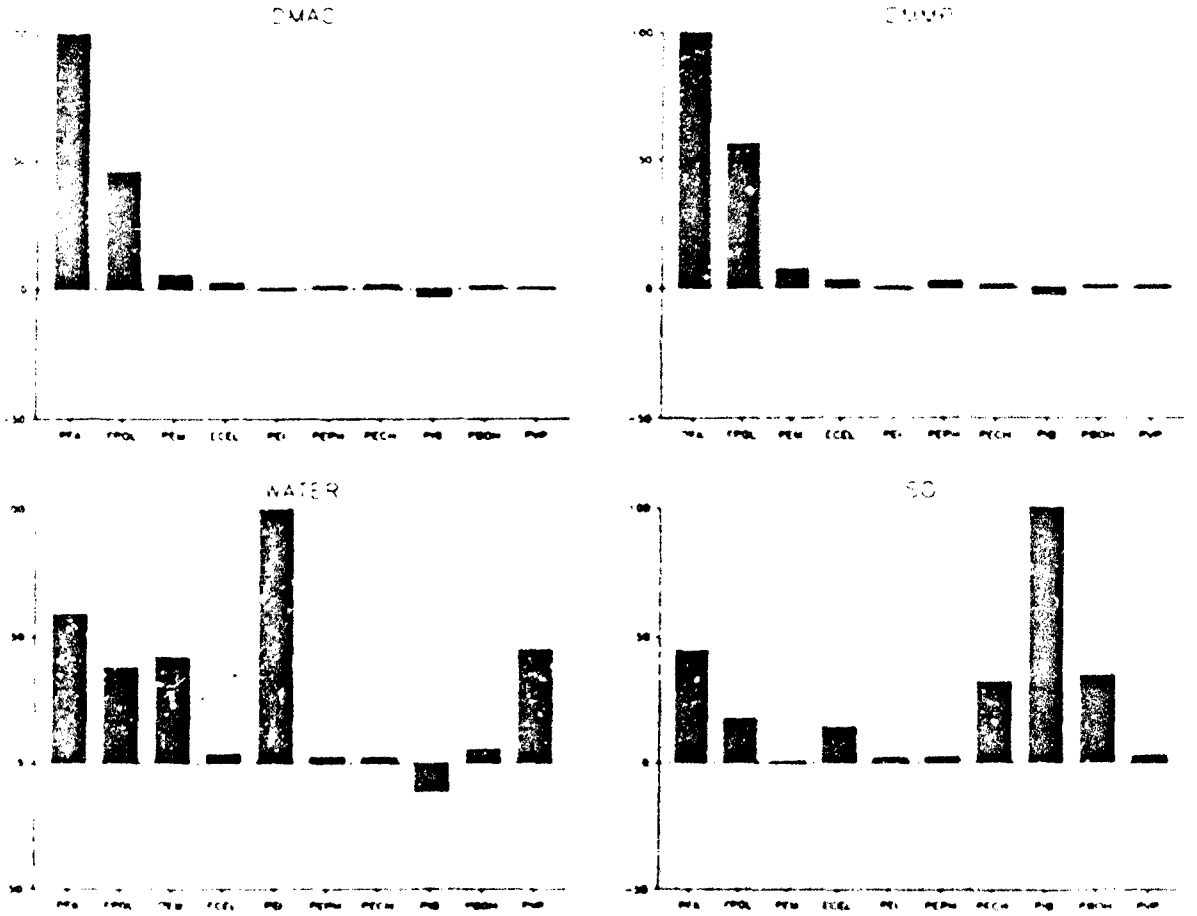


Figure 2. Bar graphs showing relative response patterns using all the coatings tested for four of the test vapors

Table V. Vapor Mixture Components and Concentrations

		vapor 2 concentration, μg/L							
vapor 1	concn, μg/L	water 1940	I-SO 32480	2-BTN 35310	TCE 44630	DES 14450	1-BTL 2845	T-CL 15330	DMMP-B 809
DMMP	66	•	•	•	•	•	•	•	
DMAC	21	•	•	•	•	•	•	•	•
water	1940		•	•	•	•	•	•	•
I-SO	32480			•	•	•	•	•	•
2-BTN	35310				•	•	•	•	•

mixtures of two components. The observed sensor responses, Δf_{obs}, were examined to see if they were comparable to the responses expected from a linear combination of responses to the single vapors where

$$\Delta f_{mix} = \Delta f_{vapor\,1} + \Delta f_{vapor\,2} \qquad (1)$$

In the vast majority of cases, the observed responses were within 30% of the calculated combination. For nonspecific but reasonably sorbent coatings such as poly(epichlorohydrin) and poly(butadiene) hydroxylated, the agreement was particularly good, typically within 10%. The DMMP sensitive coatings, fluoropolyol and poly(isoprene/fluoro alcohol), gave responses to mixtures containing DMMP (at low concentration) and interferent that ranged from 10% to 30% less than the calculated additive response. In each of these cases, the largest deviations were mixtures of DMMP and 2-butanone. This observation is interesting since these two vapors are both hydrogen bond acceptors and will compete with one another for the hydrogen bond donating sites in the coating material. Notable exceptions to linearly additive responses occurred in frequency shift. This result was most frequent with poly(isobutylene) but also occurred for poly(ethylenimine) in response to mixtures of DMMP (low concentration) with toluene, diethyl sulfide, 2-butanone, and 1-butanol. Significantly, responses to mixtures including water, for which poly(ethylenimine) gives important information, were generally within 10–20% of the expected value. Other exceptions to linearly additive responses include the responses of poly(ethylenimine) to mixtures of isooctane and 2-butanone with other interferents and responses of poly(ethylene maleate) to mixtures of water with isooctane, diethyl sulfide, and 1-butanol.

Pattern Recognition Analysis. The vapors and two-component mixtures tested in this study were divided into two classes as shown in Table I. An earlier paper by Stouch and Jurs (30, 31) outlined the precautions that should be used to avoid chance or random results when nonparametric classifiers are applied to data. Balanced data sets containing about the same number of observations in each class is one way to minimize chance classifications. Therefore, we collected mixture data for both classes. Class 1 mixtures contain

Table VI. Correlation Matrix for Eight Sensors

	FPOL	PEM	ECEL	PEI	PEPH	PECH	PFA	PIB	PBOH
FPOL	1	−0.134	−0.612	−0.189	−0.444	−0.711	0.601	−0.625	−0.724
PEM		1	0.258	0.706	0.165	0.156	−0.456	−0.241	0.193
ECEL			1	−0.072	0.877	0.917	−0.665	0.456	0.856
PEI				1	−0.186	−0.092	−0.352	−0.181	−0.051
PEPH					1	0.801	−0.427	0.274	0.758
PECH						1	−0.725	0.714	0.989
PFA							1	−0.611	−0.754
PIB								1	0.727
PBOH									1

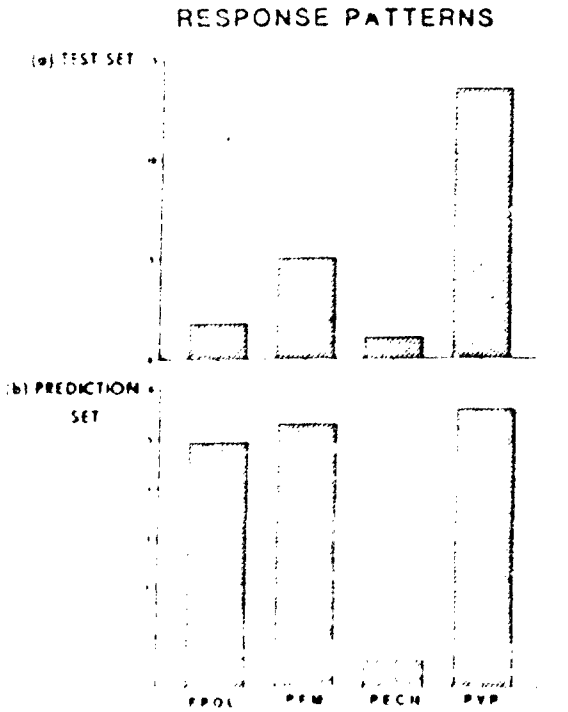


Figure 3. Response patterns for water from (a) the previous test set and (b) the prediction set.

Class 2 mixtures contain two interferents.

The responses to the single vapors for the four coatings common to the previous study, fluoropolyol, poly(ethylene maleate), poly(epichlorohydrin), and poly(vinylpyrrolidone), were used as a prediction set. The prediction set measured the ability of the linear discriminant developed in our previous study (*3*) to classify the vapors in an unknown set into the appropriate classes. All of the vapors in the data matrix (104 × 4) were identified correctly, except water. Figure 3 shows the relative responses to water of the four coatings for both studies. The largest difference is observed from poly(vinylpyrrolidone) (PVP). As noted above, devices coated with poly(vinylpyrrolidone) gave inconsistent responses during the data collection stage. Following the prediction, a supervised learning pattern recognition method called the adaptive least-squares algorithm (*37*) was employed using the prediction set. A new discriminant, developed from the previous weight vector, produced a completely separable data set. In other words, water was no longer misclassified, and the discriminant recognized the new pattern for water.

The larger data matrix (172 × 9) collected for this study was used as a training set to investigate the clustering of mixtures. Regression analysis revealed a strong pairwise correlation between poly(butadiene) hydroxylated and poly(epichlorohydrin) and some correlation between poly(ethylene phthalate), ethyl cellulose, poly(epichlorohydrin), and poly(butadiene) hydroxylated as shown by the correlation matrix in Table VI. A hierarchical cluster analysis routine using the Euclidean distance metric and flexible fusion (*33*, *34*) was employed to compare the responses of the coatings to all the vapors in the data set. The hierarchical cluster analysis of the coatings demonstrated similar results to the regression analysis. The dendrogram produced from the results of the cluster routine are shown in Figure 4. The y axis on the dendrogram is a measure of dissimilarity; coatings that are fused together lower on the y axis are similar, while coatings fused higher are different. Four large divisions are observed. The coatings correlated in the regression analysis make up one group. Poly(isobutylene) is significantly different from all the other coatings. Poly(ethylene maleate) and poly(ethyleneimine) are similar to each other and are very different from all the other coatings. The two DMMP-sensitive coatings, fluoropolyol and poly(isoprene/fluoro alcohol), are similar to one another and significantly different from all the other coatings. Due to the strong correlation with the other coatings, poly(butadiene) hydroxylated was removed from the data set for further analysis.

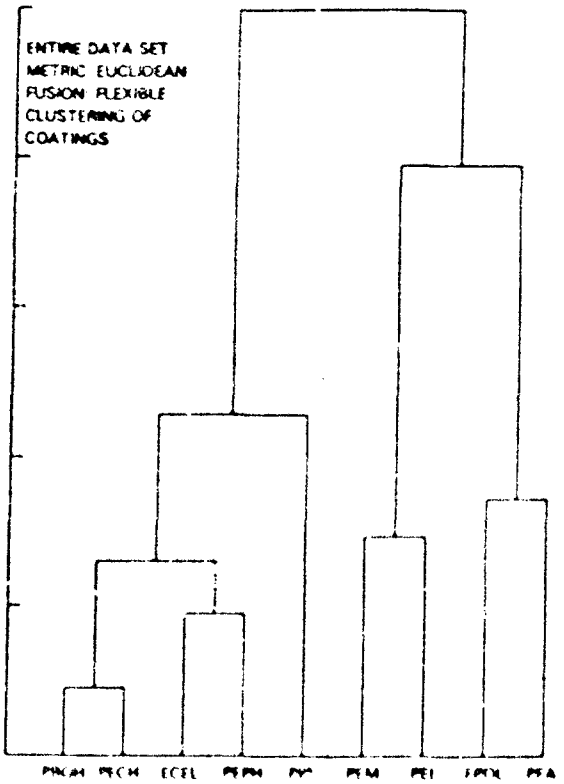


Figure 4. Hierarchical cluster results of coatings based on the responses to nine individual vapors and mixtures.

A graphical means of displaying the large data matrix is through the use of circular profiles. Each pattern vector for a given vapor is drawn in as a polygonal figure, consisting of lines connecting points placed on axes that radiate from the

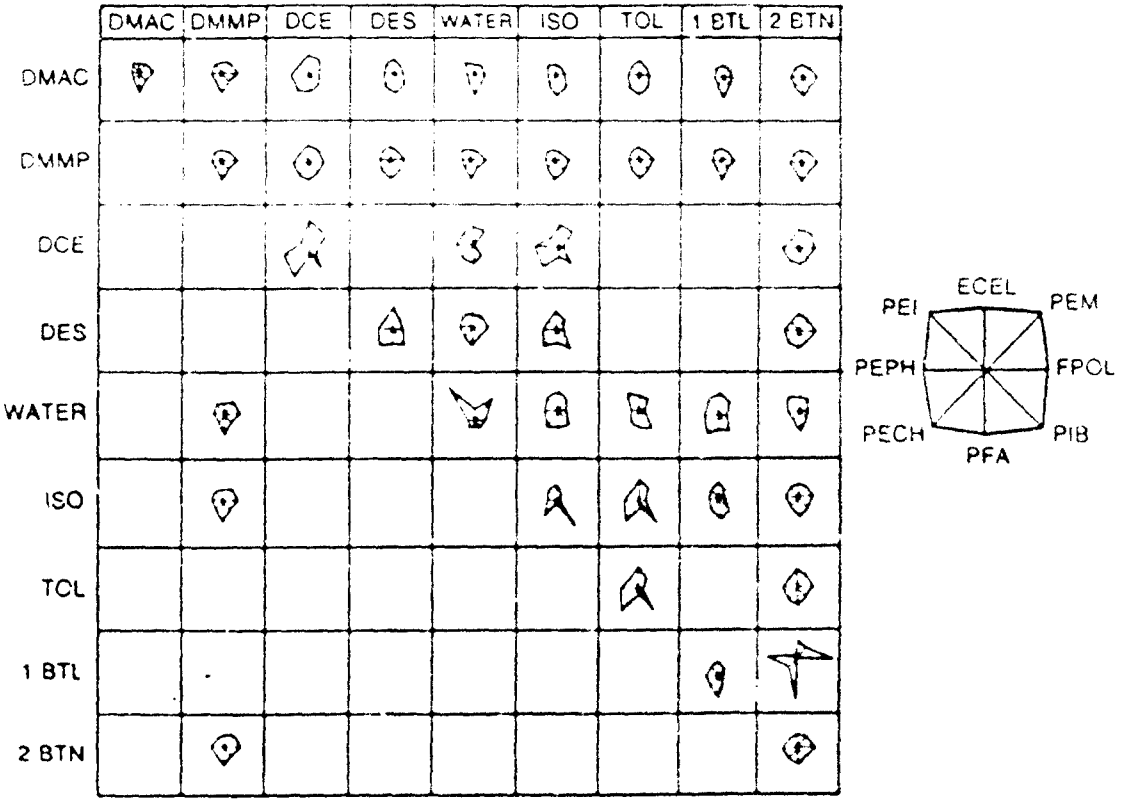


Figure 6. Circular profiles of the individual vapors and each of the mixtures tested and a diagram showing the coating responsible for each of the observed responses.

center like spokes on a wheel. The distance of each point from the center or the length of the spoke depends on the response of the sensor to the vapor. This visual display of the eight sensor responses to each of the vapors and mixtures is shown in Figure 5. A diagram defining the position of each coating represented by each spoke is also drawn. The profiles in each row are the result of the combination of the entry on the left with the vapors listed above each column. For example, the profiles in the top row of the figure are the response of the eight sensors to dimethylacetamide and dimethylacetamide mixed with each of the vapors listed across the columns. The profiles in the second row and in the second column are examples of the responses to DMMP and mixtures containing DMMP. These profiles do change when a class 2 vapor is mixed with the class 1 vapor, although they do maintain a certain character that is not observed among the class 2 vapors. The DMMP in the mixtures listed in the column labeled DMMP was generated from a bubbler and is present at much higher concentrations than in the entries in the row labeled DMMP (generated from a permeation tube).

The first two principal components, found using principal component analysis, were used to initialize a nonlinear mapping routine. The two-principal component plot describes the plane that best represents the data, although misrepresentation of the position of some of the points exists when points are projected from the eight dimensional space of the sensors to 2-space. The nonlinear mapping routine adjusts the position of the points in the two-space defined by the principal component by minimizing an error function so that the resulting plot most closely reflects the relative positions of the points in the 8-space. Thus, the nonlinear mapping routine in combination with principal component analysis transforms a set of points from 8-space to 2-space by maintaining the similarities and dissimilarities between the points. The resulting plot is shown in Figure 6. Only half of the data set [illegible] the plot to reduce its complexity. One example of each concentration for each the vapors is included. A boundary is drawn around each of the single vapors. Most of the data for each individual vapor cluster in discrete sectors. Water, isooctane, toluene, dichloroethane, and diethyl sulfide are well separated from DMMP and dimethylacetamide. All of the mixtures containing a toxic vapor (class 1 vapor) cluster close to the individual class 1 vapors even though the class 2 component is much more concentrated. Butanone and butanol and some of the class 2 mixtures cluster close to the class 1 vapors and could lead to misclassification.

Hierarchical cluster analysis produced similar results. A Euclidean distance metric with flexible fusion (33, 34) was selected to display the data set and the resulting dendrogram is shown in Figure 7. One third of the original data matrix is shown to simplify visualization. Most of the class 2 vapors are grouped together on the right, most of the class 1 vapors are grouped together in the center, and the some of the mixtures are grouped together on the left. The best clustering is among the class 1 vapors and mixtures containing them; these vapors have much similarity as shown by their fusion low on the y axis. Water, isooctane, toluene, dichloroethane, and diethyl sulfide are all located in the block labeled class 2 and they are the least similar to the class 1 vapors. A mixture of dimethylacetamide and dichloroethane clusters with the class 2 vapors. Butanone and butanol and most of the mixtures containing butanone are located on the left side of the dendrogram and appear to be similar to the class 1 vapors because they cluster lower on the y axis.

The data set was divided into two classes as defined in Table I. Each class contained 86 vapor experiments for the eight remaining sensors. The data and the correct classification results were given to several supervised learning techniques in the ADAPT software package. The classifiers were designed to generate a discriminant in one classifier and to allow that discriminant to be passed to another. A typical study used a statistically based classifier (35) to generate the

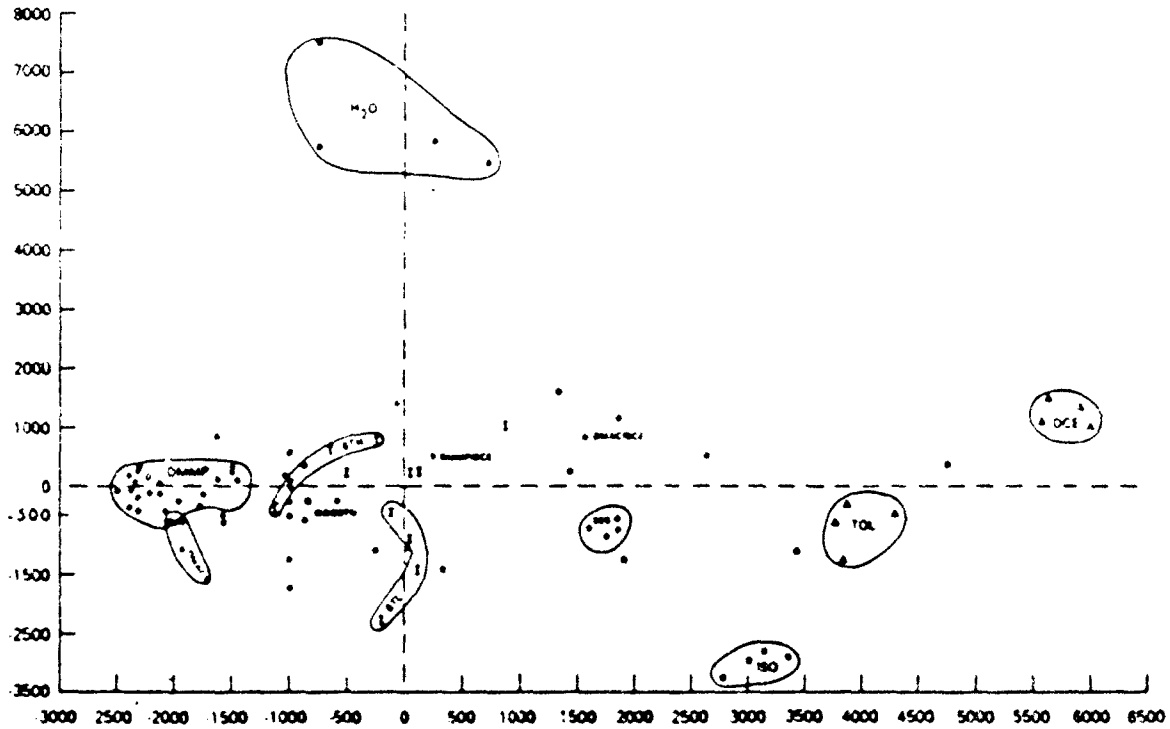


Figure 6. Principal component plot obtained by using results from eight coatings. Each vapor is represented by a symbol. Each of the mixtures is represented by the symbol of vapor 1 in Table V, except the mixtures including DMMP from the bubbler, which have the same symbol as DMMP. The three mixtures misclassified in the discriminate analysis are individually labeled.

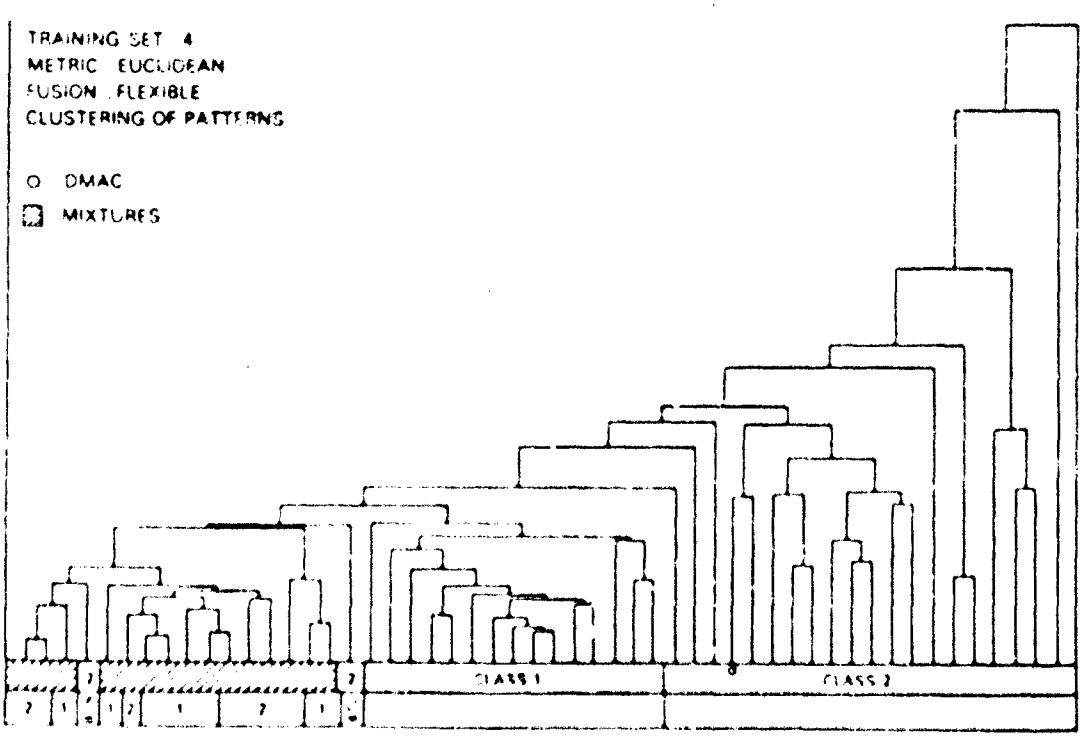


Figure 7. Hierarchical cluster results of the test vapors and mixtures based on eight coatings.

initial discriminant, which was then passed to the adaptive least-squares algorithm (J2). Several iterations and several combinations of classifiers were used to train the data set. All of the vapors and mixtures were correctly classified except three mixtures, dimethylacetamide and dichloroethane, DMMP and dichloroethane, and isooctane and butanone. They were consistently misclassified. This is not surprising when the position of these mixtures are identified in the principal-component plot (Figure 7).

The data set was reexamined considering the usually slight variations in the responses of the fluoropolyol-coated sensor in each of the four sensor test arrays. The responses of the fluoropolyol-coated sensor in the first test array served as the standard, and data for each vapor or mixture were examined separately. If the response of the fluoropolyol-coated sensor in a subsequent test array was significantly different from the corresponding response in the first test array (i.e. the difference in the average response between the two test arrays

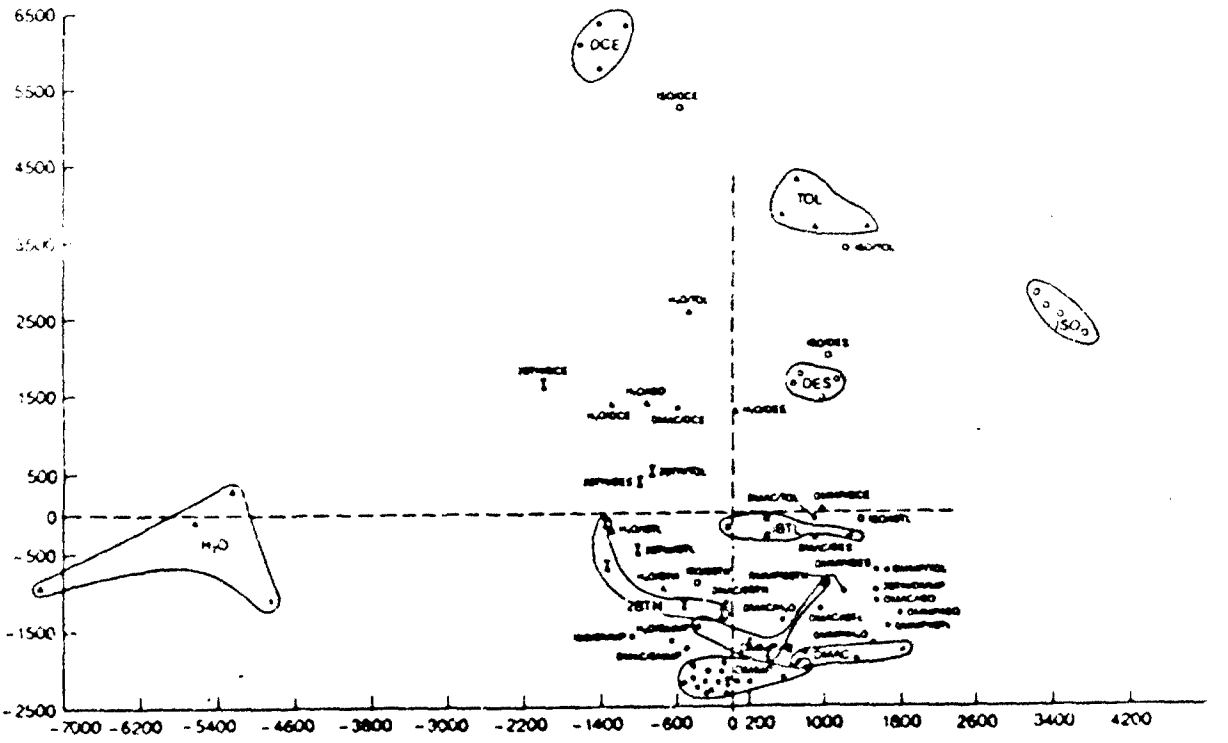


Figure 8. Principal component plot for the corrected data using eight coatings. All of the mixtures are labeled and the individual vapors are enclosed in discrete boundaries.

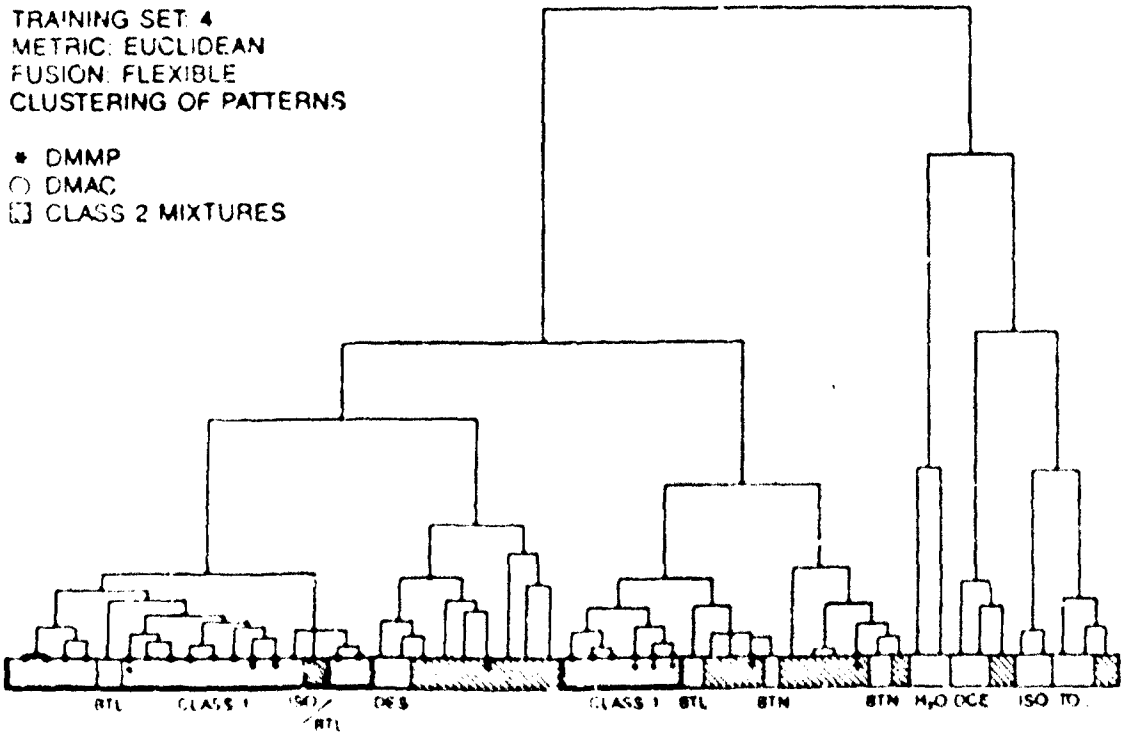


Figure 9. Hierarchical cluster results for the corrected data using eight coatings. The class 2 vapors are labeled, and most of the class 1 vapors are in the bold blocks, the ones that are not are marked.

was greater than the variation in response within the first array), then a linear correction factor was determined. The sensor responses of all the coatings in the subsequent test array to that particular vapor were then multiplied by the correction factor. These factors are given in Table VII.

The regression results indicated the same correlation between the poly(butadiene) hydroxylated and poly(epichlorohydrin) responses. Poly(butadiene) hydroxylated was deleted and the remaining eight coatings were reexamined by the cluster and display methods. The results of principal component analysis are similar to the uncorrected results for the individual vapors, as shown in Figure 8. The corrected data does improve the clustering of the mixtures. The mixtures do not crowd the class 1 vapors as much as in the previous plot, especially for butanone. The hierarchical cluster analysis supports this observation. As seen in Figure 9, most

Table VII. Correction to the Conditions of the First Array

vapor	FPOL, PEM ECEL	PEI, PEPH	PECH, PFA PIB, PBOH
DMMP	1.00	1.20	1.50
DMAC	1.00	1.30	1.60
DCE	1.00	1.00	1.00
water	1.00	1.50	2.50
ISO	1.00	1.00	1.30
TOL	1.00	1.00	1.30
DES	1.00	1.00	1.30
2BTN	1.00	1.00	1.00
1BTL	1.00	1.00	1.00
DMAC/DCE	1.00	1.00	1.00
DMAC/H_2O	1.00	1.00	1.30
DMAC/ISO	1.00	1.00	1.30
DMAC/TOL	1.00	1.00	1.30
DMAC/DES	1.00	1.00	1.50
DMAC/DMMP	1.00	1.00	1.30
DMAC/2BTN	1.00	1.00	1.30
DMAC/1BTL	1.00	1.00	1.30
DMMP/DCE	1.00	1.00	2.50
DMMP/H_2O	1.00	1.00	2.50
DMMP/ISO	1.00	1.00	2.50
DMMP/TOL	1.00	1.00	2.50
DMMP/DES	1.00	1.00	2.50
DMMP/2BTN	1.00	1.00	2.50
DMMP/1BTL	1.00	1.00	2.50
water/DCE	1.00	1.00	1.30
water/ISO	1.00	1.00	1.30
water/TOL	1.00	1.00	1.30
water/DES	1.00	1.00	1.30
water/DMMP	1.00	1.00	1.30
water/2BTN	1.00	1.00	1.30
water/1BTL	1.00	1.00	1.30
ISO/DCE	1.00	1.10	1.10
ISO/TOL	1.00	1.10	1.10
ISO/DES	1.00	1.10	1.10
ISO/DMMP	1.00	1.10	1.10
ISO/2BTN	1.00	1.10	1.10
ISO/1BTL	1.00	1.10	1.10
2BTN/DCE	1.00	1.10	1.10
2BTN/TOL	1.00	1.10	1.10
2BTN/DES	1.00	1.10	1.10
2BTN/DMMP	1.00	1.10	1.10
2BTN/1BTL	1.00	1.10	1.10

of the class 1 vapors are on the left side of dendrogram and are positioned lower on the y axis relative to the class 2 vapors, indicating less similarity between the two groups. Even the class 1 vapors in the center of the dendrogram are positioned lower on the y axis compared to the class 2 vapors and mixtures containing class 2 vapors. Water, isooctane, toluene, and diethylsebacate, shown on the right of the dendrogram, are well-separated from all the other vapors and are very dissimilar as indicated by the higher level of fusion on the y axis. Most of the class 2 mixtures are closer to the class 1 vapors than the single class 2 vapors, although the mixtures appear in discrete regions in the dendrogram.

The Bayes classifier was used to generate the initial discriminant for the new 172 × 8 data matrix, and the results of that supervised learning technique were used to initialize the adaptive least-squares algorithm. After several iterations, all of the vapors were correctly classified including those mixtures previously misclassified. The resulting discriminant was passed to a classifier called the linear learning machine (35), and the data set was trained further adding thickness to the discriminant hyperplane between the two classes. A deadzone or linear discriminant thickness 200 times greater than the standard generated by the routines was obtained, which indicates that the classes are well separated. A summary of the results is given in Table VIII. The new discriminant was examined by using another routine designed to test the importance of each coating to the classification. In this routine, several classifications were made by using the new discriminant and for each classification one sensor was left out of the analysis. The percentage correctly classified was measured. The lower the percentage correct, the more important the sensor for the discriminant evaluated. The list of sensors is sorted and given in Table VIII from least important to most important. The most important coatings in this linear discriminant are ethyl cellulose, poly(ethylene phthalate), poly(ethylenimine), and poly(isoprene/fluoropolyol). Fluoropolyol is the least important because the removal of this coating from the set would only reduce the classification results to 97%. In the previous study, fluoropolyol was the most important coating based on the classification results. In this study, fluoropolyol has been supplanted by poly(isoprene/fluoro alcohol), which provides much the same information and has greater DMMP sensitivity.

Table VIII. Weight Vector Components for Best Coatings

coating	discriminant function values	no. wrong 1	no. wrong 2	% recognition
	+0.13	0	0	100
FPOL	−0.03	2	3	97
PEM	+0.24	4	7	94
PIB	−0.11	3	7	91
PECH	+0.60	2	15	90
PFA	+0.22	36	15	70
PEI	−0.40	40	17	67
PEPH	−0.32	56	25	55
ECEL	−0.49	72	38	36

CONCLUSIONS

Pattern recognition techniques can readily distinguish between the class 1 vapors and the class 2 vapors when the SAW sensors are exposed to single vapors. The linear discriminant developed in our previous study was 100% successful in distinguishing class 1 from class 2 vapors in the previous data set (3). The same discriminant applied to the single vapors in this data set correctly classified all vapors, except water. This discrepancy arose due to the poor reproducibility of the water-sensitive coating poly(vinylpyrrolidone). A new discriminant was developed to achieve 100% correct classification, and a better water-sensitive, poly(ethylenimine), has been identified.

The single vapors that cluster nearest to DMMP are 2-butanone and 1-butanol. Like DMMP, 2-butanone can accept hydrogen bonds. It differs by being a weaker acceptor and by having a much higher saturation vapor pressure. 1-Butanol is also a hydrogen bond acceptor of comparable strength to 2-butanone, but differs in its ability as a hydrogen bond donor. The saturation vapor pressure of 1-butanol is closer to that of DMMP than that of 2-butanone.

Single vapors could be correctly classified by using as few as four sensors. When two-component mixtures were included in the data set, eight sensors were required to obtain the best classification results. The responses of mixtures were generally close to those expected from a linear combination of the single vapor responses. This result is encouraging because it simplifies the correct classification of mixtures. It is particularly notable in the context of the detection problem discussed here that the responses of the DMMP-sensitive coatings to mixtures containing DMMP were well-behaved.

The clustering results for mixtures were similar to those for single vapors. All of the class 1 mixtures clustered close to the class 1 vapors. The class 2 mixtures clustering closest to the class 1 vapors were usually those containing 2-butanone or 1-butanol. By use of the experimental data as collected, all mixtures could be correctly classified, except three. When correction factors were applied to the data as explained in the

Results, 100% correct classification could be achieved. The mixtures were successfully analyzed even with large concentration differences between the vapors of interest and the potential interferents.

Variations in fluoropolyol-coated sensor responses from one test array to another are likely to arise from three factors. Changes in the actual vapor concentrations generated by the test apparatus will cause linear changes in the responses of the sensors. Variations in the sensor temperature will change sensor response because the sorption of vapors into the coating material varies exponentially with temperature. Hysteresis due to previous vapor exposures might also cause sensor response variations. This is expected to be minimal for sensors whose behavior is based on simple reversible absorption, but it cannot be summarily ruled out.

The ability of pattern recognition techniques to discriminate between vapors is expected to improve as the sensor technology matures and testing procedures are more rigorously controlled. SAW coating materials whose responses are consistent and reproducible, and which provide greater sensitivity, will offer obvious advantages. A set of materials with more widely varying responses to key vapors will enhance the information to be analyzed. Rigorous control of sensor temperature and a truly inert reference on the SAW sensor will improve performance. Finally, it may be useful to examine mixtures where the concentration ratio of the two components is varied.

ACKNOWLEDGMENT

The authors wish to thank Arthur Snow for all his efforts, particularly in materials support and syntheses, Jim Griffith for providing the fluoropolyol, and Hank Wohltjen for his efforts. The authors gratefully acknowledge the support of the coating testing work by Army/CRDEC, Aberdeen Proving Ground, MD, and of the pattern recognition work by HQ RDSX, Brooks Air Force Base, TX.

LITERATURE CITED

(1) Stetter, J.; Jurs, J. P.; Rose, S. L. *Anal. Chem.* **1986**, *58*, 860.
(2) Carey, W. P.; Beebe, K. R.; Kowalski, B. R.; Illman, D. L.; Hirschfeld, T. *Anal. Chem.* **1986**, *58*, 149.
(3) Ballantine, D.; Rose, S. L.; Grate, J. W.; Wohltjen, H. *Anal. Chem.* **1986**, *58*, 3058.
(4) Carey, W. P.; Beebe, K. R.; Kowalski, B. R. *Anal. Chem.* **1987**, *59*, 1529.
(5) Grate, J. W.; Snow, A.; Ballantine, D. S., Jr.; Wohltjen, H.; Abraham, M. H.; McGill, R. A.; Sasson, P. *Anal. Chem.* **1988**, *60*, 869–875.
(6) Wohltjen, H.; Snow, A. W.; Barger, W. R.; Ballantine, D. S. *IEEE Trans. Ultrason., Ferroelectrics, Freq. Contr.* **1987**, *UFFC-34*, 172–178.
(7) Wohltjen, H. *Sens. Actuators* **1984**, *5*, 307–325.
(8) Snow, A.; Wohltjen, H. *Anal. Chem.* **1984**, *56*, 1411–1416.
(9) Nieuwenhuizen, M. S.; Nederlof, A. J.; Barendsz, A. W. *Anal. Chem.* **1988**, *60*, 230–235.
(10) Nieuwenhuizen, M. S.; Nederlof, A. J. *Anal. Chem.* **1988**, *60*, 236–240.
(11) Venema, A.; Nieuwkoop, E.; Vellekoop, M. J.; Ghijsen, W. J.; Barendsz, A. W.; Nieuwenhuizen, M. S. *IEEE Trans. Ultrason., Ferroelectrics, Freq. Contr.* **1987**, *UFFC-34*, 148–155.
(12) Nieuwenhuizen, M. S.; Barendsz, A. W. *Sens. Actuators* **1987**, *11*, 45–62.
(13) Nieuwenhuizen, M. S.; Barendsz, A. W.; Nieuwkoop, E.; Vellekoop, M. J.; Venema, A. *Electron. Lett.* **1988**, *22*, 184–185.
(14) Venema, A.; Nieuwkoop, E.; Vellekoop, M. J.; Nieuwenhuizen, M. S.; Barendsz, A. W. *Sens. Actuators* **1986**, *10*, 47–64.
(15) Martin, S. J.; Ricco, A. J.; Ginley, D. S.; Zipperian, T. J. *IEEE Trans. Ultrason., Ferroelectrics, Freq. Contr.* **1987**, *UFFC-34*, 142–147.
(16) Ricco, A. J.; Martin, S. J.; Zipperian, T. E. *Sens. Actuators* **1985**, *8*, 319–333.
(17) Martin, S. J.; Schweitzer, K. S.; Ricco, A. J.; Zipperian, T. E. Proceedings of the 3rd Int. Conf. on Solid-State Sensors and Actuators-Transducers, Philadelphia, PA, June 11–14, 1985, IEEE Cat. No. CH2127-9/85/0000-0066, pp. 71–73.
(18) Vetelino, J. F.; Lade, R. K.; Falconer, R. S. *IEEE Trans. Ultrason., Ferroelectrics, Freq. Contr.* **1987**, *UFFC-34*, 156–161.
(19) Bryant, A.; Potter, M.; Riley, G.; Lee, D. L.; Vetelino, J. F. *Sens. Actuators* **1982**, *4*, 105.
(20) D'Amico, A.; Palma, A.; Verona, E. *Sens. Actuators* **1982/1983**, *3*, 31–39.
(21) Chuang, C. T.; White, R. M.; Bernstein, J. J. *IEEE Electron Device Lett.* **1982**, *EDL-3*, 145–148.
(22) Field, D. E. *J. Paint Technol.* **1970**, *48*, 43.
(23) Snow, A. W.; Ballantine, D. S.; Whitney, T.; Barger, W. R.; Klusty, M.; Wohltjen, H.; Grate, J.; Chaput, D. Proceedings of the 1986 U.S. Army Chemical Research, Development, and Engineering Center Scientific Conference on Chemical Defense Research, CRDEC-SP-87006, Rausa, M. D. eds., U.S. Army, 1987; pp 695–703.
(24) Sprague, L. G.; Snow, A. W.; Soulen, R. L.; Lint, J.; Wohltjen, H.; Ballantine, D. S.; Grate, J. W. Proceedings of the 1987 U.S. Army Chemical Research, Development and Engineering Center Scientific Conference on Chemical Defense Research, U.S. Army, in press.
(25) Grate, J. W.; Ballantine, D. S.; Wohltjen, H. *Sens. Actuators* **1987**, *11*, 173.
(26) Stuper, A. J.; Brugger, W. E.; Jurs, P. C. *Computer Assisted Studies of Chemical Structure and Biological Function*; Wiley-Interscience: New York, 1979.
(27) Chang, Y.; Nortyen, J.; Lloyd, D. R.; Barlow, J. W. *Polym. Eng. Sci.* **1987**, *27*, 693.
(28) Barlow, J. W.; Cassidy, P. E.; Lloyd, D. R.; You, C. J.; Chang, Y.; Wong, P. C.; Nortyen, J. *Polym. Eng. Sci.* **1987**, *27*, 703.
(29) Fog, H. M.; Rietz, B. *Anal. Chem.* **1985**, *57*, 2634.
(30) Stouch, T. R.; Jurs, P. C. *J. Chem. Inf. Comput. Sci.* **1985**, *25*, 45.
(31) Stouch, T. R.; Jurs, P. C. *J. Chem. Inf. Comput. Sci.* **1985**, *25*, 92.
(32) Moriguchi, I.; Komatsu, K.; Matsushita, Y. *J. Med. Chem.* **1980**, *23*, 20.
(33) Williams, W. T.; Lance, G. N. *Statistical Methods for Digital Computers*; Enslein, K., Ralston, A., Jr., R., Ed.; Wiley-Interscience: New York, 1975.
(34) Massart, D. L.; Kaufman, L. *The Interpretation of Analytical Chemical Data by the Use of Cluster Analysis*; Wiley: New York, 1983.
(35) Tou, J. T.; Gonzalez, R. C. *Pattern Recognition Principles*; Addison-Wesley: Reading, MA, 1974.

RECEIVED for review April 20, 1988. Accepted July 18, 1988.

APPENDIX C2

INVESTIGATION OF ELASTIC PROPERTIES OF THIN POLYMER FILMS USING SURFACE ACOUSTIC WAVE DEVICES

David S. Ballantine, Jr.[1] and Henry Wohltjen[2]

[1]GEO-CENTERS, Inc., 10903 Indian Head Hwy
Ft. Washington, MD 20744

[2]MicroSensor Systems, Inc., P. O. Box 90
Fairfax, VA 22030

The observed glass transition temperatures (T_g) of several thin polymer films on the surface of SAW devices were increased by 50-60 °C relative to T_g results reported for other methods such as DSC. The increase in the onset of T_g is the result of interaction of the high frequency surface acoustic wave with the polymer film, consistent with the time-temperature superposition principle. The T_g were identified as localized minimum in the frequency curves, or by changes in the slope of the curves, as the coated sensors were heated between 35-110 °C. Potential applications of SAWs for the characterization of polymeric materials and the implication of these findings on the interpretation of SAW sensor data are discussed.

Polymeric materials are being employed in an increasing number of novel applications in our technological society. No doubt, as stronger, more flexible and more durable materials are discovered the demand for these materials will continue to grow. The chemical and physical properties of these materials will determine the types of applications for which they may be employed. Thus, the rapid and reliable characterization of these properties will be crucial.

In the area of chemical sensors, thin polymer films are routinely used as coatings for the semi-selective sorption of chemical vapors. One such sensor technology, the surface acoustic wave (SAW) device, has demonstrated excellent sensitivity as a vapor sensor when coated with films having appropriate solubility properties (1). To date, most sensor applications have taken advantage of the extreme mass sensitivity of the devices. In this paper, we will examine the response mechanisms of the SAW sensor and demonstrate the sensitivity of these devices to changes in elastic properties of the coating

[1]Current address: Department of Chemistry, Northern Illinois University
DeKalb, IL 60115

materials. Finally, we will discuss the significance of these results in terms of current sensor applications, and the applicability and advantages of the SAW for the characterization of polymeric materials.

Background

Since its introduction in the early 1970's, the SAW has seen increasing utilization as a chemical sensor due to its sensitivity, potentially rapid response, and low cost. A brief description of the operating principles of the SAW will aid in understanding the basis of this study and in the interpretation of the results. Typically, a SAW device consists of a set of interdigital transducers which have been microlithographically deposited on the surface of a piezoelectric substrate. The application of a time-varying electric potential to the transducer causes a mechanical deformation of the substrate, resulting in the generation of a surface acoustic wave. The properties of this wave (amplitude, frequency, phase) are sensitive to perturbations occurring on or near the surface of the substrate. A more detailed discussion of the SAW operation can be found in reference (2). The generation of different types of surface waves is possible (3); for the purposes of this work, when we refer to the surface acoustic wave we specifically mean Rayleigh-type surface waves.

In general, the response of the SAW is the combined result of changes in the mass loading, conductivity, or elastic properties of the surface film. Equations describing the effects of changes in these properties on the frequency of the device have been derived previously (2,4). For many sensor studies, non-conducting polymer films are usually employed. One equation, given below, describes the response behavior for a SAW device coated with a thin, lossless, isotropic, non-conducting film,

$$\Delta f = (k_1+k_2)\rho h f_c^2 - k_2 h f_o^2 (4\mu/V_R^2)[(\lambda+\mu)/(\lambda+2\mu)] \qquad (1)$$

where k_1 and k_2 are material constants for the quartz substrate, V_R is the Rayleigh wave velocity, h is the film thickness, ρ is the density, μ is the shear modulus, λ is the Lame constant, and f_o is the fundamental frequency of the device. The first half of the equation yields the frequency shift resulting from mass loading, while the second half describes the effect of changes in the elastic properties of the film on the resonant frequency.

To date, the selection of coatings for vapor sensor applications has been mostly empirical, requiring the screening of a large number of candidate materials to identify coatings with sufficient sensitivity to the vapor of interest. To address this problem, recent work has focused on characterizing the observed sensor responses in terms of solubility interactions (1,5). The sorption of a solute vapor into a solvent coating can be quantitatively defined as a partition coefficient, K. A modified version of Equation 1 has been used to predict the frequency response of coated SAWs to predict the frequency response of these sensors to specific vapors utilizing partition coefficients calculated from GLC data (5). The inherent assumptions in that work are that (1) the polymer coating is a lossless film (that is, there is no significant attenuation of the surface wave resulting from interactions with the surface film), and (2) the contributions to

the observed response from elastic properties of the film are negligible. To justify the second assumption, care was taken to select polymer films that would be above their glass transition temperatures (T_g) at the operating temperature of the device.

In order to assess the validity of the second assumption, a brief discussion of the elastic properties of polymers is needed. The viscoelastic behavior of a polymer is depicted schematically in Figure 1. The parameter of interest in the case of SAWs is the shear modulus, denoted as G in Figure 1 and as μ in Equation 1. Simply stated, the modulus is a measure of the rigidity of the polymer. The regions of interest are the glassy region (where the polymer is a hard, rigid material) and the elastomeric region (where the polymer is a rubber). Rigid, glassy polymers typically have high modulus values on the order of 10^9 - 10^{10} dyne/cm^2. In this region, the polymer chains are locked into the lowest energy conformations and there is insufficient energy in the system to allow free rotation around the polymer backbone. As the temperature increases the polymer becomes an elastomer. In this region, there is sufficient energy in the system for free rotation to occur. This additional rotational freedom is manifested as a 'softening' of the polymer, with a corresponding decrease in the modulus to 10^4 - 10^7 dyne/cm^2. The temperature at which this softening occurs is the T_g. Other changes occur at this temperature that can be monitored experimentally to identify the T_g. These include changes in the specific volume of the polymer, the index of refraction, the gas diffusion coefficient, the thermal expansion coefficient (measured by dilatometry), and specific heat (measured by differential scanning calorimetry (DSC) or by differential thermal analysis (DTA)). Good general discussions of the elastic properties of polymers can be found in references (6,7).

The T_g of a polymer increases as a function of frequency. This phenomenon was first described by Williams, Landel and Ferry in 1955, and became the basis of the time-temperature superposition principle (8). Previous work by Wohltjen and Dessy demonstrated that the SAW could be used to characterize polymeric materials (9). In that work, both thin films and bulk samples were characterized by monitoring changes in the amplitude of the surface wave as the temperature of the polymer samples was increased. Their results indicated that, for thin polymer films, there is significant interaction of the polymer film with the high frequency surface wave, resulting in an increase in the T_g of the polymer. This observation is consistent with the time-temperature superposition principle.

The work to be presented here was motivated by two factors. First, it had been assumed that polymer films used in previous sensor applications were above their T_g at the SAW operating temperature. If the T_g of a given polymer film is significantly increased due to the effects of the high frequency surface wave, then the elastic properties of the film must be taken into consideration when interpreting sensor responses. Second, since the frequency mode of the SAW device represents a more sensitive measurement than the amplitude, these devices have tremendous potential in the area of materials characterization. The following experiments were performed to verify this potential and to investigate the possible effect of elastic properties on sensor responses.

Experimental

The polymer coatings studied are given in Table I, along with pertinent physical parameters. These coatings were selected based on availability, since they are among coatings previously used for chemical sensor studies at NRL. In addition, the transition temperatures (T_g, T_m) are within the range that could be easily investigated using our experimental apparatus. Of these coatings, fluoropolyol (FPOL) and poly(ethylene maleate) (PEM) were provided by the Polymeric Materials Branch, Chemistry Division, of the Naval Research Laboratory in Washington D.C. They are both linear polymers with no observed crystallinity. PEM is a polyester material with a repeating monomer unit of 35-50. FPOL is a highly viscous epoxy pre-polymer with a repeating monomer of 8-10. Densities were measured using a float technique, and T_g were measured by DSC at the NRL Chemistry Division. Additional information regarding the structure and properties of these materials can be found in reference (1).

TABLE I. POLYMER COATINGS AND PHYSICAL PARAMETERS

polymer	T_g (°C)	T_m (°C)	n	ρ (g/cm^3)
fluoropolyol (FPOL)	10	---	8-10	1.653 (25 °C) 1.563 (90 °C)
poly(ethylene maleate) (PEM)	-10	---	35-50	1.353 (25 °C)
ethyl cellulose (ECEL)	43	157-165	---	1.14 (at T_m)
poly(caprolactone)	<-40	60	---	---

Poly(caprolactone) and ethyl cellulose were obtained from Aldrich, and were used as received. They are semi-crystalline materials and would be expected to exhibit localized changes in elastic properties at both T_g and the melting point, T_m. Physical parameters for these polymers were obtained from the Aldrich catalog. No value was available for the T_g of PCAP; the value in Table I is estimated using the relationship

$$T_m = K\, T_g \qquad (2)$$

where K = 1.4 - 2 (2).

The 158 MHz dual SAW devices were obtained from MicroSensor Systems, Inc. (MSI part # SD-158A). They consisted of two individual delay lines manufactured on a single quartz chip. Electrical connections to the transducers were established by wire bonding to a T-08 plug-in

package. Additional information regarding the dimensions and geometry of the devices can be obtained from MSI.

Dilute solutions of the coating materials were prepared in chloroform. These solutions were then aspirated using an airbrush to generate a finely dispersed aerosol, which was deposited on one side of the dual SAW device. The other delay line remained uncoated, acting as a reference to correct for frequency deviations due to fluctuations in ambient temperature and pressure.

The coated devices were then placed in the heating chamber illustrated in Figure 2. The chamber consisted of a 3/4" brass Swagelok union fitting which was wrapped with heating tape. The temperature of the heating tape was controlled by a Variac, and the temperature of the chamber was monitored using a YSI Series 400 thermistor. This thermistor was incorporated in a circuit to convert the thermistor resistance into a voltage that could be read directly by the computer-controlled data acquisition system. A dry air stream was heated via a coiled tube located within the chamber prior to introduction to the sensor. A constant flow rate of 40-50 ml/min was maintained during the experiments to minimize the effects of temperature gradients and localized heating near the sensor surface.

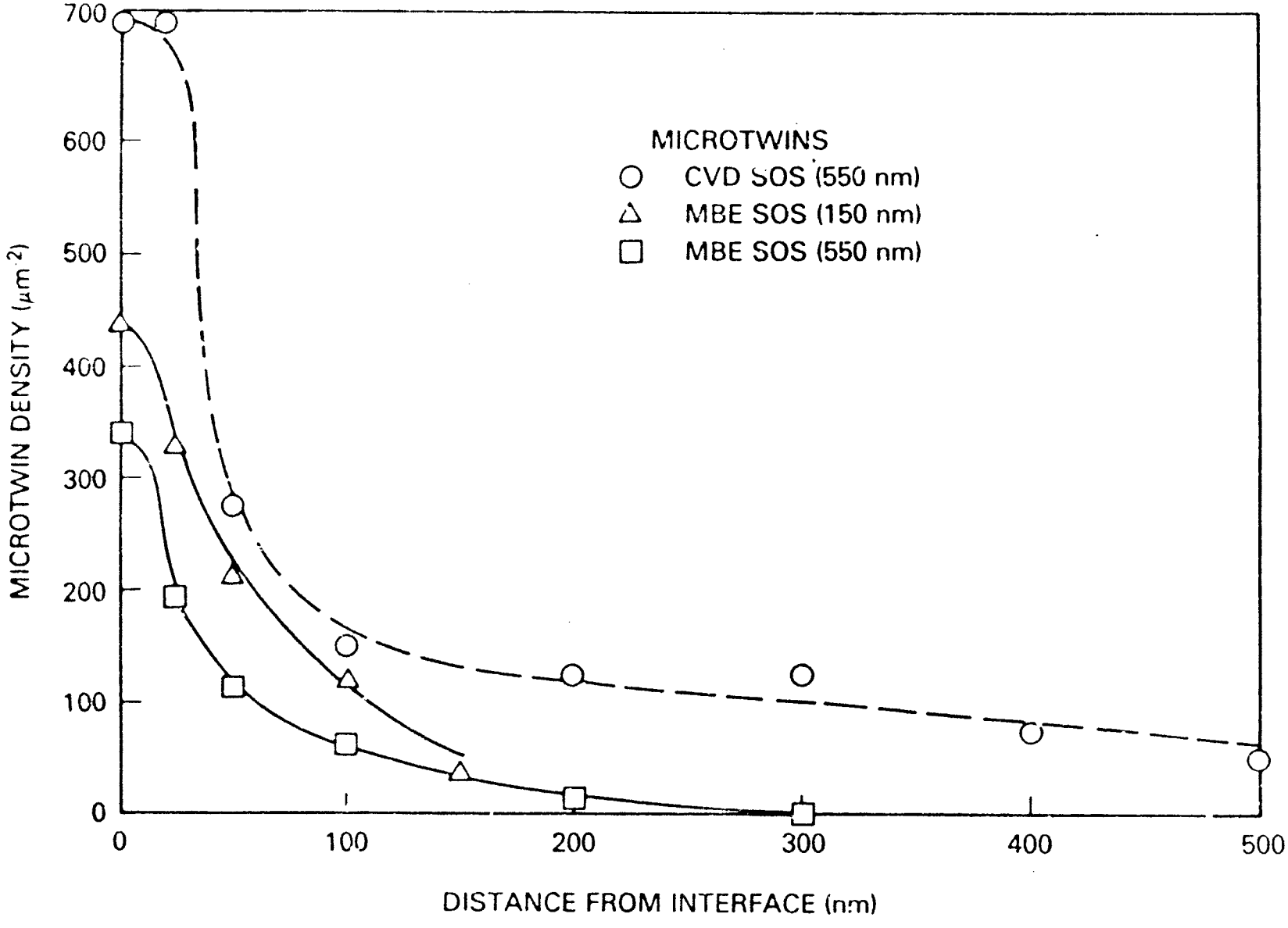
The frequencies of the individual delay lines were monitored independently, and the difference frequency of the two sides of the device was obtained as output from an electronic mixer. These frequencies were recorded as the devices were first heated from 35 °C to 110 °C, and as they were subsequently cooled to room temperature. Each device was subjected to repeated heating/cooling cycles, with frequencies being recorded continuously as a function of temperature. The coatings were then removed, as the SAWs were washed in chloroform in an ultrasonic cleaner. The bare devices were once again placed in the heating chamber and subjected to successive heating/cooling cycles. The frequency curves of the bare devices were recorded for use as blanks.

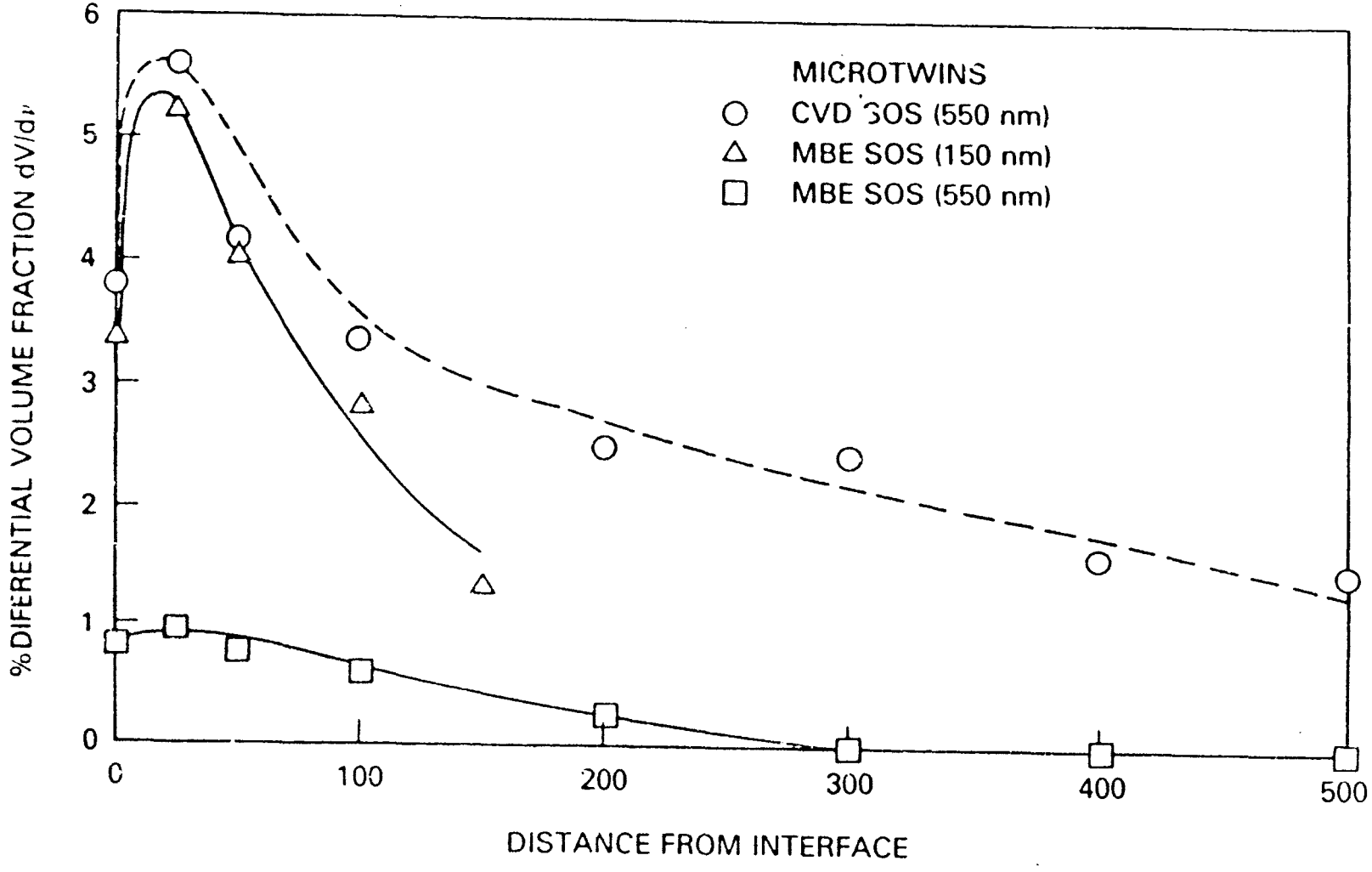
Results and Discussion

Once the effect of temperature on the frequency of a bare device was known, the effect of temperature on the coatings could be determined by subtracting the results for the bare devices from the frequency-temperature curves for the coated devices. The frequency shifts recorded during these temperature studies are reported in parts per million (ppm), which is defined as the observed frequency shift, in Hz, divided by the resonant frequency of the device, in MHz. For the devices used in this study, 1 ppm is equivalent to 158 Hz. In order for several related curves to be easily viewed on the same plot, individual curves are offset from one another by several hundred ppm.

Examples of the frequency-temperature curves for a bare device are given in Figure 3. Channel 1 and channel 2 refer to the two delay lines of the dual device. When used as a sensor, channel 1 would be coated and channel 2 would remain uncoated to act as a reference. The difference curve is the output from the mixer, and represents the frequency difference between the two delay lines.

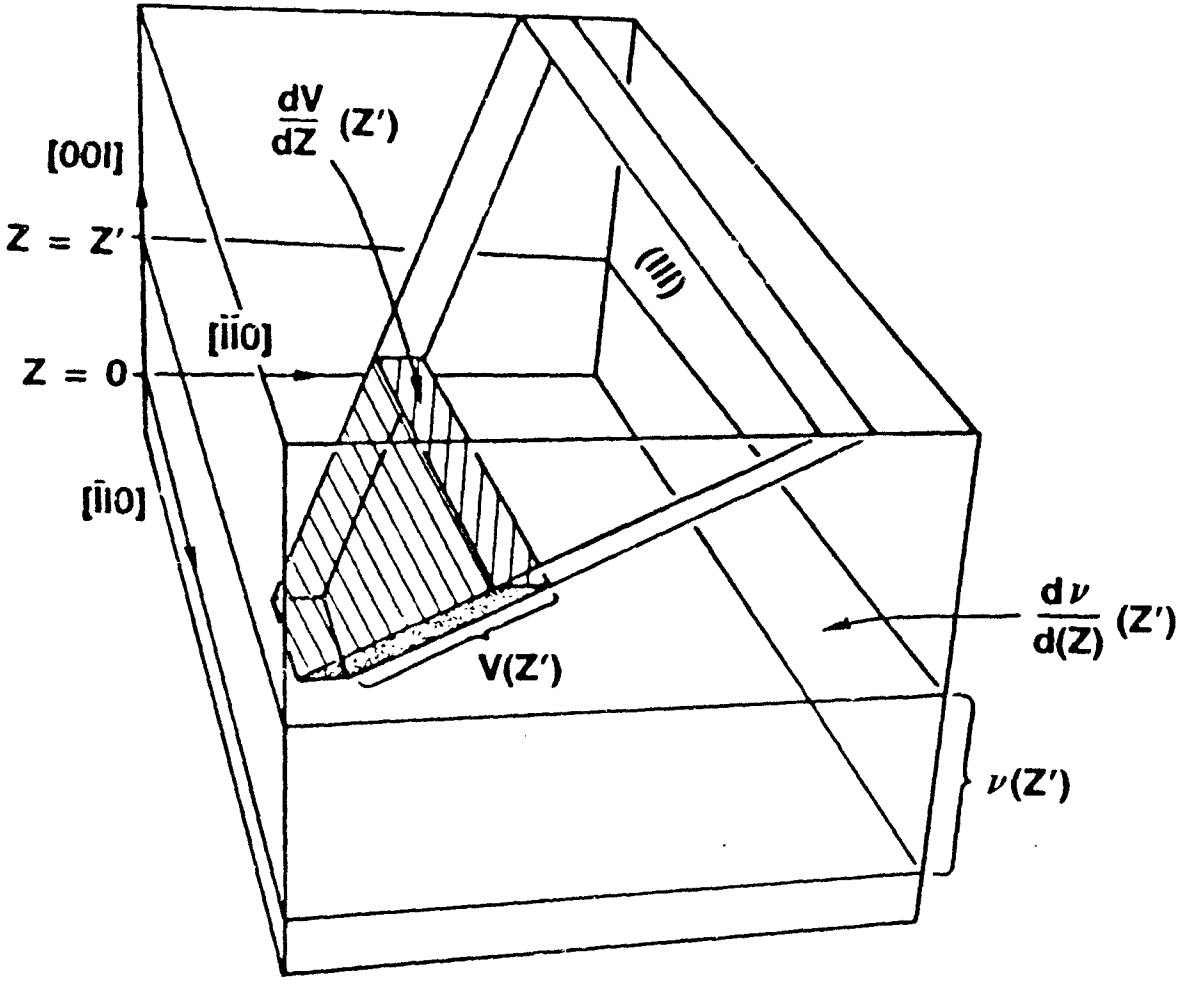
It is worth noting that there is substantial frequency shift for both delay lines resulting from temperature changes, on the order of 3-6 ppm/°C. This is the result of thermal stresses arising in the

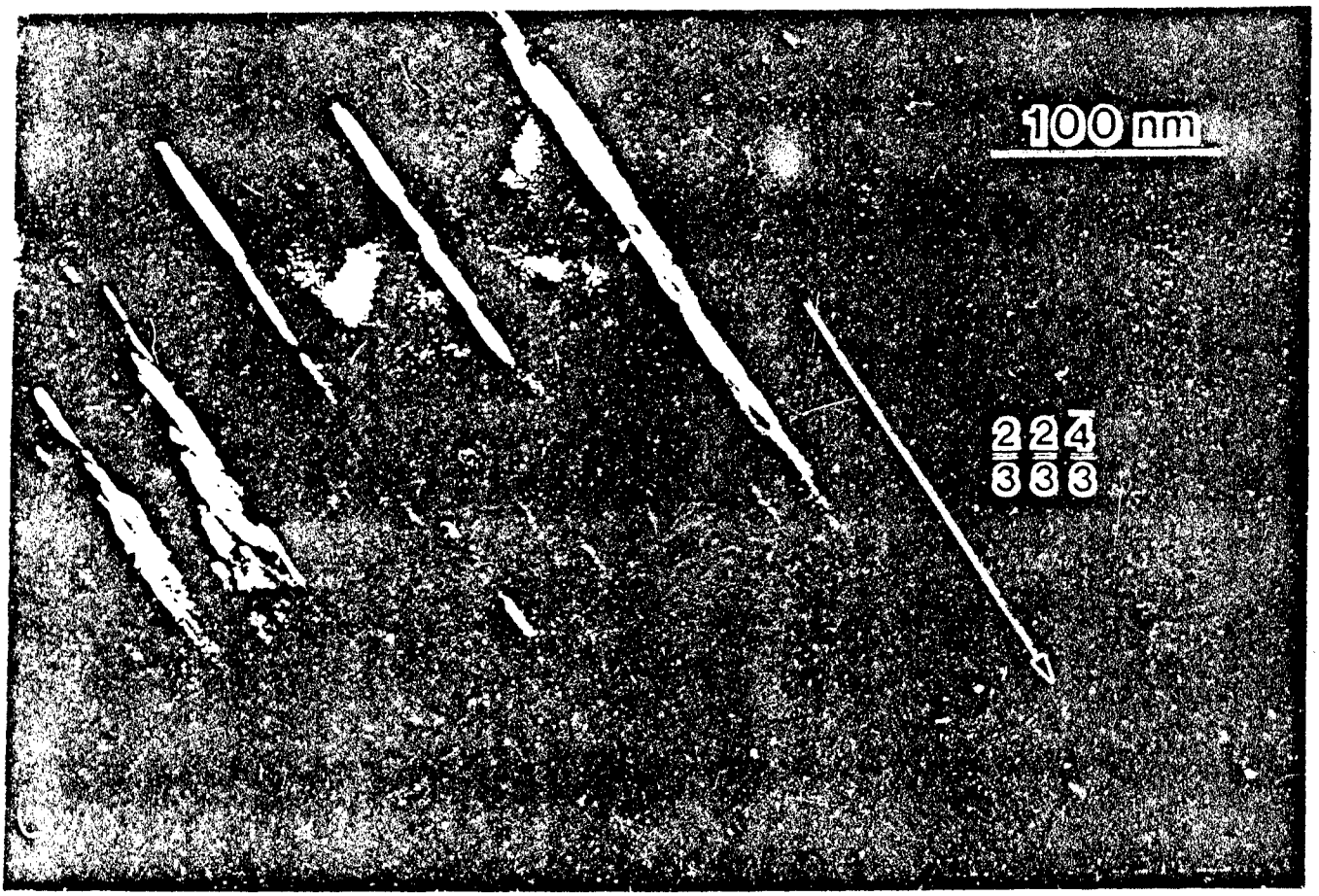

MICROTWINS
CVD SOS (550 nm)
MBE SOS (150 nm)
MBE SOS (550 nm)
MICROTWIN DENSITY (μm⁻²)
DISTANCE FROM INTERFACE (nm)
0
100
200
300
400
500
600
700


MICROTWINS
CVD SOS (550 nm)
MBE SOS (150 nm)
MBE SOS (550 nm)
%DIFERENTIAL VOLUME FRACTION dV/dx
DISTANCE FROM INTERFACE
0
1
2
3
4
5
6
0
100
200
300
400
500

DEFINITION OF DIFFERENTIAL VOLUME FRACTION:

$$\frac{dV}{d\nu} = \frac{dV}{dZ} \Big/ \frac{d\nu}{dZ}$$




100 nm
$\frac{2}{3}\frac{2}{3}\frac{\bar{4}}{3}$

SURFACE
W
3/8 Z
INTERFACE
1 μm

Fig.7 Given the normal to the microtwin habit plane $\underline{n}$ and the Burgers vector $\underline{b}$ for the twinning partial dislocation, it can be determined whether a twinning system responds to compression or tension when loaded along an axis parallel to $\underline{r}$. If $(\underline{b}\cdot\underline{r})(\underline{n}\cdot\underline{r})$ is negative, the twinning system responds to tension; for a positive value, the twinning system responds to tension.

FIGURE CAPTIONS

Fig.1 Illustration of method for measuring the microtwin width "w" at a particular distance z' from the interface. Note that the projected distance from the interface is actually $3/\sqrt{8}z'$ for a [114] beam direction and a microtwin with a (111) habit plane.

Fig.2 A Dark-field TEM image presents an edge-on view of microtwins associated with the majority (111) twinning system.

Fig.3 Schematic definition of the differential volume fraction, dV/dv, for microtwins. V(z) is the total volume of microtwins measured from the interface. v(z) is the total volume of the silicon film measured from the interface.

Fig.4 Plot of microtwin differential volume fraction as a function of distance from the interface for 150nm and 550nm MBE SOS, and 550nm CVD SOS.

Fig.5 Plot of the microtwin density as the number of microtwins per unit area as a function of distance from the silicon/sapphire interface.

Fig.6 Plot of the differential microtwin area, dA/dv, as a function of distance from the silicon/sapphire interface.

Pittsburgh, PA, 1988), in press.

15. K. Yasutake, J.D. Stephenson, M. Umeno, and H. Kawabe, J. Appl. Phys. 61, 940; 947 (1987).

16. F. C. Frank and N. Thompson, Acta Metall. 3, 30 (1954).

17. J. J. Gilman, Micromechanics of Flow in Solids (New York, McGraw--Hill, 1969), p.73.

REFERENCES

1. R. Lihl, H. Oppolzer, P. Pongranz, P. Skalicky, and W. Svanda, J. Micros. 118, 89 (1980).

2. F. A. Ponce and J. Aranovich, Appl. Phys. Lett. 38, 439 (1981).

3. M. S. Abrahams and C. J. Buiocchi, Appl. Phys. Lett. 27, 325 (1975).

4. M. S. Abrahams, J. C. Hutchinson, and G. R. Booker, Phys. Stat. Sol. 63, K3 (1981).

5. J. L. Hutchingson, G. R. Booker, and M. S. Abrahams, Inst. Phys. Conf. Ser. 60, 139 (1981).

6. R. C. Pond, M. Aindow, C. Dineen, and T. Peterns, Inst. Phys. Conf. Ser. 87, 181 (1987).

7. M. Aindow, J. L. Batstone, L. Pfeiffer, J. M. Phillips, and R. C. Pond, Proc. Mater. Res. Soc. 138, (1989), in press.

8. M. Aindow, D. Phil. Thesis, University of Liverpool (1989).

9. P. Pirouz, F. Ernst, and T. T. Cheng, Proc. Mater. Res. Soc. 116, 57 (1988).

10. F. Ernst and P. Pirouz, J. Appl. Phys. 64, 4526 (1988).

11. M. E. Twigg and E. D. Richmond, J. Appl. Phys. 64, 3037 (1988).

12. M. E. Twigg, E. D. Richmond, and J. G. Pellegrino, Proc. Mater. Res. Soc. 138, (1989), in press.

13. M. E. Twigg ~~and~~ E. D. Richmond and J. G. Pellegrino, Appl. Phys. Lett. 54 1764 (1989) ~~in press~~.

14. J. G. Pellegrino, M. E. Twigg, and E. D. Richmond, Silicon-on-Insulator and Buried Metals in Semiconductors, edited by C. K. Chen, P. L. F. Hemment, J. C. Sturm, and L. Pfeiffer (Mater. Res. So. Proc. 107,

1012°, differ by 10%, which clearly dwarfs any contribution to strain relaxation that can be attributed to microtwins. Therefore these large strains must be accommodated by a different defect network at the interface or by an incoherent interface. Aindow, Pond, and coworkers have observed dislocations at the interface of a SOS sample processed by rapid thermal annealing (RTA) using weak beam TEM; they have also observed that the misorientation of the silicon film can be accurately expressed in terms of vicinal angle from an analysis of the postulated dislocation network. The assessment of the interface as incoherent comes from essentially null measurements: in high-resolution TEM (HRTEM) a number of studies have noted the apparent absence of a dislocation network at the interface. In light of the difficulty in interpreting HRTEM measurements in the absence of proper image simulations, however, it would seem that the interfacial dislocation network theory proposed by Aindow, Pond, and coworkers, has been more successfully tested than the incoherent interface conjecture.

ACKNOWLEDGEMENTS

We would like to thank the Defence Nuclear Agency for partial funding this research effort. We would also like to thank Dr. Chandra Pande of the Materials Science Division of the Naval Research Laboratory for access to the transmission electron microscope.

can use Eqs. 6 and 7 to calculate the strain relief for a silicon film grown on sapphire. Let us first consider the possibility that the microtwins act as plastic deformation twins acting to relieve compressive strains in the silicon film. The configuration of a deformation twin is such that it is bounded by an array of partial dislocations with parallel Burgers vectors. Each {111} plane of the twin is separated from the matrix by one of these partial dislocations so that the magnitude of the displacement vector equals the number of {111} planes (i.e. p=m). The factor $\sqrt{2}/12$ equals 0.12 and the greatest value of dV/dv is less than 6%, so that from Fig.2 it is clear that the strain relief due to microtwins in SOS is always less than 0.7%.

According to Pirouz et al., however, the structure of growth twins in heteroepitaxial systems does not resemble that of deformation twins. In this model, a microtwin could provide as little strain relief as a stacking fault (i.e. p=1), and one third of all microtwins (those in which m is divisible by three) might provide no strain relief. The contribution of microtwins to strain relief in 550nm CVD SOS can be found by assuming dA/dv=6/um, and assuming that only 2/3 of all microtwins are active in strain relief. For this case, the strain relief would only be 0.02% For 150nm MBE SOS, dA/dv=13/um so that strain relief would be 0.05%. For 550nm MBE SOS, dA/dv=7/um, giving a strain relief of 0.02%.

The most closely matched lattice spacings at the silicon (001)/-sapphire ($\bar{1}012$) heteroepitaxial interface, silicon {220} and sapphire

twinning systems are acting to relieve [100] compression and four other twinning systems are acting to relieve [010] compression, we need to consider the sum of two strain relief vectors. For [010] compression, the active twinning system are $a/6[1\bar{2}1]/(111)$, $a/6[121]/(1\bar{1}1)$, $a/6[\bar{1}21]/(\bar{1}\bar{1}1)$, $a/6(\bar{1}\bar{2}1)/(\bar{1}11)$. From Eqs.(1-3) the displacement vector is

$$\underline{d}^{[100]} = (p/m)'2/6[1\bar{2}1]dV/dv \quad . \tag{5}$$

If we assume that half of the microtwins are relieving [100] compression while the other half are relieving [010] compression. The total strain relief is then,

$$\begin{aligned} \underline{d} &= \underline{d}^{[100]}/2 + \underline{d}^{[010]}/2 \qquad (6) \\ &= (p/m)(1/2)(\sqrt{2}/6)\{\,[\bar{2}11] + [1\bar{2}1]\,\}dV/dv \\ &= (p/m)'2/12[\bar{1}\bar{1}2]dV/dv \quad . \end{aligned}$$

Therefore, for both [100] and [010], the strain relief for compression is $(p/m)\sqrt{2}/12$ dV/dv. Because $dV/dv = ma/\sqrt{2}$ dA/dv, the strain relief for compression is also equal to pa/12 dA/dv. The expression analogous to Eq.(6) is,

$$\underline{d} = pa/2[\bar{1}\bar{1}2]dA/dv \quad . \tag{7}$$

Because we know the differential volume fraction and the differential area as functions of the distance from the interface, we

compression of a (001) film. Corresponding to the scalar quantity $\underline{d}_r$ is what we define are the strain relief vector $\underline{d}$, which we define as

$$\underline{d} = [\underline{d}_x, \underline{d}_y, \underline{d}_z] \quad , \tag{3}$$

where $\underline{x}$, $\underline{y}$, and $\underline{z}$ are unit vectors along the x, y, and z axes. For the twinning systems that correspond to [100] compression, {a/6[$\bar{2}$11]/(111), a/6[$\bar{2}\bar{1}$1]/(1$\bar{1}$1), a/6[2$\bar{1}$1]/($\bar{1}\bar{1}$1), and a/6[211]/($\bar{1}$11)} the strain relief vector is

$$\underline{d}[100] = (p/m)\sqrt{2}/6[\bar{2}11]dV/dv \quad , \tag{4}$$

and this contribution to the strain relief is valid for each of the four twinning systems that relieve [100] compression. Therefore, for the case of [100] uniaxial compression of a (001) film, dV/dv in Eq.(4) is the sum of the differential volume fractions of the four twinning systems. It is also clear from this expression that the strain relief vector $\underline{d}$[100] acts to relieve compressive stress along the [100] axis by bringing any two parts of the matrix, separated by a microtwin, closer together. Along the [010] and [001] directions, however, the two parts of the matrix separated by a microtwin are pushed apart.

For the case that we are interested in, which is biaxial compression, we have to consider the fact that some of microtwins are involved in accommodating [100] compression, while others would be relieve [010] compression in a (001) film. If we assume that four

relative displacement of the crystal halves to the differential volume fraction. dV/dv is proportional to the projected microtwin thickness $ma/\sqrt{2}$ and the microtwin displacement is equal to $pa/3$ in the [100] direction, where m is the number of $(\bar{1}\bar{1}1)$ planes that compose the microtwin and p is defined so that the displacement vector of the microtwin in $pa/6[2\bar{1}1]$. If we assume the sum of the widths of all of the microtwins in the film, as they intersect the z=z' plane, is W, and that the total film area is A, then the strain relief due to the microtwins is $paW/3/A$ and the differential volume fraction of microtwins is $maW/\sqrt{2}/A$. Therefore, the ratio of the strain relief to the differential volume fraction for the [100] axis and the $[2\bar{1}1]/(\bar{1}\bar{1}1)$ twinning system is $(p/m)\sqrt{2}/3$.

In general, the strain relief $\underline{d}_r$ along a given axis, for a given twinning system will be $pW\underline{b}_r/A$, where $\underline{b}_r$ is defined as

$$\underline{b}_r = |\underline{b}\cdot\underline{r}| \quad \text{for} \quad (\underline{b}\cdot\underline{r})(\underline{n}\cdot\underline{r}) > 0 \qquad (1)$$

$$\underline{b}_r = -|\underline{b}\cdot\underline{r}| \quad \text{for} \quad (\underline{b}\cdot\underline{r})(\underline{n}\cdot\underline{r}) < 0$$

$$\underline{b}_r = 0 \quad \text{for} \quad (\underline{b}\cdot\underline{r})(\underline{n}\cdot\underline{r}) = 0$$

and the differential volume fraction dV/dv is $maW/\sqrt{2}/A$. The strain relief can be expressed in terms of the differential volume fraction as

$$\underline{d}_r = (p/m)\underline{b}_r\sqrt{2}/a \; dV/dv. \qquad (2)$$

This expression is valid for the case of uniaxial strain, such as [100]

ystals into two halves, and that one half of the crystal is anslated by the vector $a/6[2\bar{1}1]$. Along the [100] axis, the glide of single $a/6[2\bar{1}1]$ twinning partial dislocation causes the two halves of e crystal to draw closer by $a/3$. Along the [010] and [001] axes, wever, the two halves of the crystal are displaced from one another $a/6$.

One can determine whether a given twinning syster is compressive tensile along a given direction $\underline{r}$ from the sign of the product $\underline{r}\cdot(\underline{n}\cdot\underline{r})$, where $\underline{b}$ is the Burgers vector of the twinning partial and $\underline{n}$ the normal to the twinning plane directed from the substrate to the itaxial layer (as shown in Fig.7). We arrive at this condition by nsidering the distance between points on opposite sides of the undary and initially separated by the vector $c\underline{n}$ (which is, of course, rallel to $\underline{n}$). After the displacement due to the twinning partial, e two points are separated by the vector $c\underline{n}+\underline{b}$. The direction of terest is $\underline{r}$ so that the distance between the initial and final sitions in the $\underline{r}$ direction are $|c\underline{n}\cdot\underline{r}|$ and $|(c\underline{n}+\underline{b})\cdot\underline{r}|$ respectively. e difference between the final and initial distances, $|(cn+\underline{b}).\underline{r}|-|\underline{n}\cdot\underline{r}|$, to the first order in $(\underline{b}\cdot\underline{r})$, is $(\underline{b}\cdot\underline{r})(\underline{n}\cdot\underline{r})$. This is identical the conditions outlined by Frank and Thompson[16] for determining ether a microtwin will respond to compression or tension. The oduct is positive for tension and negative for compression.[17]

For a given uniaxial strain and twinning system, such as [100] in mpression for $[2\bar{1}1]/(\bar{1}\bar{1}1)$, we can compare the magnitude of the

the distance from the interface. From Fig.5 it is obvious that the microtwin area is much larger for 150nm MBE SOS than for 550nm CVD SOS.

DISCUSSION

The configuration of microtwins in plastically deformed silicon have been examined in detail by Yasutake et al.,[15] who have confirmed the presence of the $\langle 112\rangle/\{111\}$ twinning systems first proposed for the analogous fcc metals. In particular, Yasutake et al. have studied the twinning systems active in uniaxial in-plain compression. Assuming that the stresses relieved in SOS are compressive, we can ascribe four twinning systems to [100] compression and four to [010] compression. The twinning systems corresponding to [100] compression are $a/6[\bar{2}11]/(111)$, $a/6[\bar{2}\bar{1}1]/(\bar{1}\bar{1}1)$, $a/6[2\bar{1}1]/(\bar{1}\bar{1}1)$, and $a/6[211]/(\bar{1}11)$. For [010] compression, the twinning systems are $a/6[1\bar{2}1]/(111)$, $a/6[121]/(\bar{1}\bar{1}1)$, $a/6[\bar{1}21]/(\bar{1}11)$, and $a/6[\bar{1}\bar{2}1]/(\bar{1}\bar{1}1)$

The thickness of a microtwin projected onto the plane z=z' is equal to the product of the microtwin thickness t divided by the cosine of the angle between the plane and the microtwin normal. This cosine is equal to $2/\sqrt{6}$ and the distance between two silicon (111) planes is $a/\sqrt{3}$ (where a is the lattice constant for silicon), so that the projected distance between two adjacent {111} planes must be $a/\sqrt{2}$. If we consider the $a/6[2\bar{1}1]/(\bar{1}\bar{1}1)$ twinning system activated by [010] compression, we know that the $(\bar{1}\bar{1}1)$ plane separates the silicon

efined as dv(z'), leading to the definition of the microtwin ifferential volume fraction as dV/dv.

ESULTS

Since it is possible to assess the microtwin volume fraction as a unction of distance from the interface in a quantitative manner, we ave determined the microtwin differential volume fraction, as a unction of distance from the interface, for 150nm and 550nm MBE SOS, s well as for 550nm CVD SOS. From these data, shown in Fig.4, it is lear that the differential volume fraction of microtwins is less, at very point, for the MBE 550nm film than for the 550nm CVD film. For he first 150nm of the 550nm CVD film, the microtwin differential olume fraction is greater than for the 150nm MBE film. We can also se PVTEM observations to determine the number of microtwins per unit rea, as shown in Fig.5. Microtwins in 550nm CVD SOS are greater in umber for all distances from the interface, than for the MBE SOS amples.

The differential volume fraction can be regarded as proportional o the average microtwin width and thickness, as well as the number of icrotwins per unit area. A measurement of only the microtwin width an be used to define a new quantity, the differential area, dA/dv, hich is equivalent to the differential volume fraction divided by the verage microtwin thickness. In Fig.6, we plot dA/dv as a function of

an annealing treatment at 1415-1450°C in the ultra high vacuum (UHV) environment of the MBE system. After the annealing procedure, silicon was deposited, on the sapphire substrate held at 750°C, at a rate of 0.05nm per second for a 150nm film and 0.1nm per second for a 550nm film.[14] We also examined a 550nm SOS sample grown by chemical vapor deposition (CVD) at a growth temperature of 910°C and a deposition rate of 30nm per second. Material from each of the three samples was made into a cross-sectional transmission electron microscopy (XTEM) specimen as well as a plan-view TEM (PVTEM) specimen.

Using the TEM-based technique of Twigg and Richmon [11], we have examined PVTEM and XTEM specimens from each SOS sample in order to measure the differential volume fraction, dV/dv, of microtwins as a function of the distance from the silicon/sapphire interface. PVTEM measurements provide an estimate of the width of an individual microtwin as a function of distance z' from the interface, as shown in Fig.1. XTEM measurements give the average microtwin thickness, as shown in Fig.2. In Fig.3 we see how combining measurements of thickness and width allows a complete assessment of the volume of a microtwin as a function of distance from the silicon/sapphire interface. Over a given area in a PVTEM specimen, the integrated width of the microtwins, for a differential volume of the film ranging from a distance z' to a distance z'+dz from the interface, can be multiplied by the average microtwin thickness and the differential volume thickness, dz, in order to give the differential contribution, dV(z'), to the total microtwin volume. The differential volume of the film is

INTRODUCTION

It has been observed by a number of authors that microtwins occur in great abundance in (001) silicon on ($\bar{1}012$) sapphire (SOS).[1,2] The role that microtwins play in accommodating the large misfit that exists between the silicon lattice and the sapphire lattice has also been considered in the literature.[3-5] A recent study, however, conducted by Aindow, Pond, and others suggests that the role of accommodating the misfit between silicon and sapphire can be assigned to a dislocation network at the interface.[6-8] The conclusions are in agreement with the conjecture of Pirouz, Ernst, and coworkers[9,10] that growth twins do not make a large contribution to strain relief in heteroepitaxial systems.

In order to assess the contribution of microtwins in the strain relief of thin films, one must begin with microtwin quantification. A new procedure for microtwin quantification in SOS was recently developed by Twigg and Richmond;[11-13] it is our intention to utilize this approach in determining the strain relief due to microtwins in this system.

EXPERIMENTAL DETAILS

Silicon was grown on sapphire substrates using the NRL Vacuum Generators V80 MBE/SA System. Each sapphire substrate was subjected to

RELIEF OF COMPRESSIVE BIAXIAL STRAINS IN THIN FILMS VIA MICROTWINS

M. E. Twigg

GEO-Centers, Inc., Prospect Square Building, 10903 Indian Head Highway, Suite 502, Fort Washington, MD 20744

E. D. Richmond and J. G. Pellegrino[1]

Naval Research Laboratory, Code 6816, Washington, D. C. 20375-5000

ABSTRACT

For heteroepitaxial systems, such as silicon on sapphire, microtwins can usually be observed in the epitaxial layer. It has also been suggested that microtwins also play a significant role in strain relief in these systems. From a knowledge of the differential volume fraction of microtwins occurring in a heteroepitaxial systems, it is possible to estimate the greatest possible strain relief due to microtwins. Measurements of the differential volume fraction of microtwins in silicon on sapphire, however, indicate the strain relief due to microtwins cannot be greater than 0.7%, even though the lattice mismatch between silicon and sapphire is an order of magnitude larger. Therefore, if the silicon/sapphire interface is coherent, the misfit strain must be relieved by another mechanism.

---

[1]Present address: National Institute of Standards and Technology, Building 225, Gaithersburg, MD 20889

APPENDIX D4

growth time, and microtwin contribution to strain relief) allow a degree of strain relaxation, due to plastic flow, in MBE-grown SOS that does not occur in CVD-grown SOS. Strain relaxation in the silicon thin film eliminates residual stresses responsible for microtwin stability in MBE-grown SOS, whereas incomplete strain relaxation acts to preserve microtwins in CVD-grown SOS.

We would like to thank the Defense Nuclear Agency for partial funding of this research effort. Access to the transmission electron microscope was graciously provided by Chandra Pande of the Materials Science Division of the U.S. Naval Research Laboratory. We would also like to thank Jeffrey Tsao of Sandia National Laboratory for helpful comments and for providing us with several preprints.

[1]L. Pfeiffer, J. M. Phillips, K. E. Luther, K. W. West, J. L. Batstone, F. A. Stevie, and J. E. A. Maurits, Appl. Phys. Lett. **50**, 466 (1987).
[2]E. D. Richmond, G. Campisi, and M. E. Twigg, in *Silicon on Insulator and Buried Metals in Semiconductors*, edited by C. K. Chen, P. L. F. Hemment, J. C. Sturm, and L. Pfeiffer (Materials Research Society, Pittsburgh, PA, 1988), Mater. Res. Soc. Symp. Proc. Vol. 107, p. 377.
[3]E. D. Richmond, A. R. Knudson, T. J. Magee, H. Kawayoshi, and C. Leung, J. Vac. Sci. Technol. A **2**, 569 (1984).
[4]J. C. Bean, Appl. Phys. Lett. **36**, 741 (1980).
[5]A. Christou, E. D. Richmond, B. R. Wilkins, and A. R. Knudson, Appl. Phys. Lett. **44**, 796 (1984).
[6]J. G. Pellegrino, M. E. Twigg, and E. D. Richmond, Mater. Res. Soc. Proc. **107**, 383 (1988).
[7]J. G. Pellegrino, E. D. Richmond, and M. E. Twigg, in *Heteroepitaxy in Silicon: Fundamentals, Structures and Devices*, edited by H. K. Choi, R. Hull, H. Ishiwara, and R. J. Nemanich (Materials Research Society, Pittsburgh, PA, 1988), Mater. Res. Soc. Symp. Proc. Vol. 116, p. 389.
[8]M. S. Abrahams and C. J. Buiocchi, Appl. Phys. Lett. **27**, 325 (1975).
[9]M. E. Twigg and E. D. Richmond, J. Appl. Phys. **64**, 3037 (1988).
[10]J. C. Bean, L. C. Feldman, A. T. Fiory, S. Nakahara, and I. K. Robinson, J. Vac. Sci. Technol. A **2**, 436 (1984).
[11]J. Y. Tsao, B. W. Dodson, S. T. Picraux, and D. M. Cornelison, Phys. Rev. Lett. **59**, 848 (1987).
[12]J. Y. Tsao and B. W. Dodson, Appl. Phys. Lett. **53**, 848 (1988).
[13]J. W. Matthews and A. E. Blakeslee, J. Cryst. Growth **27**, 118 (1974).
[14]B. W. Dodson and J. Y. Tsao, Appl. Phys. Lett. **51**, 1325 (1987).
[15]B. W. Dodson and J. Y. Tsao, Appl. Phys. Lett. **52**, 852 (1988).
[16]B. W. Dodson and J. Y. Tsao, Appl. Phys. Lett. **53**, 2498 (1988).
[17]M. E. Twigg, E. D. Richmond, and J. G. Pellegrino, in *Characterization of the Structure and Chemistry of Defects in Materials*, edited by B. C. Larson, M. Ruhle, and D. N. Seidman (Materials Research Society, Pittsburgh, PA) (in press).
[18]R. C. Pond, D. J. Bacon, and A. M. Bastaweesy, Int. Phys. Conf. Ser. **67**, 253 (1983).
[19]M. J. Stowell and T. J. Law, Philos. Mag. **19**, 1257 (1969).
[20]J. P. Hirth and J. Lothe, *Theory of Dislocations* (McGraw-Hill, New York, 1968), p. 87.
[21]K. Yasutake, S. Shimizu, M. Umeno, and H. Kawabe, J. Appl. Phys. **61**, 940 (1987).

in Fig. 1(d), it is clear that the density of microtwins in 700 nm (001) silicon films grown on ($\bar{1}012$) sapphire is much less than for 550 nm films. It also appears that dislocations are the predominant defect in the 700 and 4000 nm films. The elimination of microtwins in thick MBE SOS films stands in contrast to observations of thick CVD SOS films in which microtwins occur in significant numbers for even 4000 nm films.[8]

It is also possible to assess the microtwin volume fraction as a function of distance from the interface in a quantitative manner. Using the TEM-based technique of Twigg and Richmond,[9] we have determined the microtwin differential volume fraction, as a function of distance from the interface, for 150 and 550 nm MBE SOS, as well as for 550 nm CVD SOS. The CVD SOS was grown at a measured temperature of 910 °C at a rate of 2 μm/min. From these data shown in Fig. 2, it is clear that the differential volume fraction of microtwins is less, at every point, for the MBE 550 nm film than for the 550 nm CVD film. For the first 150 nm of the 550 nm CVD film, the microtwin differential volume fraction is greater than for the 150 nm MBE film. It would also seem that the elimination of microtwins in 700 nm MBE SOS results from the same decrease in the microtwin density as a function of film thickness.

The change in the quantity of microtwins at a particular value of film thickness is reminiscent of the onset of dislocation generation and extension in germanium-silicon thin films (grown by MBE upon germanium or silicon substrates) at a critical value of the film thickness.[10] According to the model of Tsao *et al.*,[11,12] the driving force for plastic deformation in thin films is the difference between the stress due to lattice mismatch and the stress associated with the creation or extension of dislocations. This difference is defined by Tsao *et al.* as the "excess stress" and corresponds to the deviation from mechanical equilibrium that was formulated earlier by Matthews and Blakeslee.[13] In their plastic flow model, Dodson and Tsao regard the critical stress as the driving force in strain relief of an initially coherent metastable strained layer.[14–16]

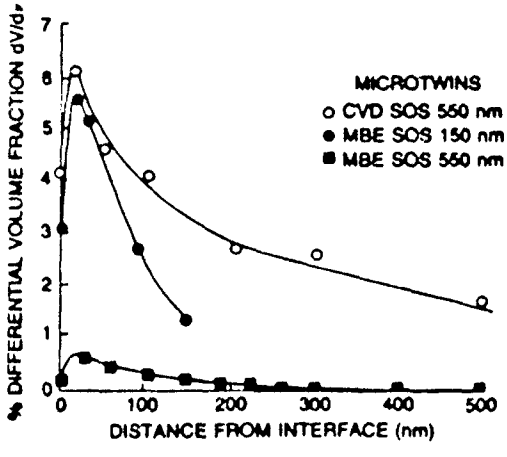


FIG. 2. Plot of microtwin differential volume fraction as a function of distance from the interface for 0.15 μm and 0.55 μm MBE SOS, and 0.55 μm CVD SOS. The extended growth time and rapid attenuation of microtwin growth beyond the interfacial region contribute to dislocations replacing microtwins as the predominant defect for relieving residual strains in MBE SOS.

From Fig. 2 it is apparent that microtwins are more prevalent and stable in SOS grown by CVD techniques than in SOS grown by MBE techniques. Consequently, greater relief of compressive strains is achieved by microtwins in CVD SOS than in MBE SOS. For 150 nm MBE SOS, the differential volume fraction of microtwins has dropped to 2% at 100 nm from the interface, whereas in CVD SOS, the differential volume fraction falls to 4% at the same distance. For the thicker (55 nm) MBE SOS film, the process by which the microtwins collapse has reduced the differential volume fraction to 0.3% at 100 nm from the interface. The volume fraction of microtwins in MBE SOS falls off rapidly with the distance from the silicon/sapphire interface, so that microtwins play a greater role in strain relief for thinner (150 nm) films than in thicker (550 nm) films. In CVD SOS, the volume fraction of microtwins falls off less rapidly than in MBE SOS, so that for relatively thick (550 nm) silicon films, microtwins relieve more strain in CVD SOS than in MBE SOS.

Because the excess stress increases linearly with the strain in the film, in MBE SOS the excess stress is greater in thicker films than in thinner films. Similarly, the excess stress is greater for 550 nm MBE SOS than in 550 nm CVD SOS. The 150 and 550 nm MBE SOS films were grown at the same temperature and similar growth rates, and therefore one would expect for the greater excess stress associated with the 550 nm film to generate more plastic flow than in the 150 nm film. CVD SOS is grown much more quickly and at much higher temperatures than MBE SOS, so that an evaluation of excess stress is not the only consideration in estimating the plastic flow of CVD SOS with respect to MBE SOS. From a knowledge of the excess stress, deposition rate, and growth temperature, however, Dodson and Tsao's model can calculate plastic flow in such epitaxial overlayers[16]; using this approach, we have estimated for the MBE growth process that dislocation generation and extension within the silicon epitaxial layer achieves 0.1% strain relief during the growth of a 100 nm film.[17] The same model predicts only a 0.05% strain relief, however, for 500 nm CVD-grown SOS.

Microtwins in thicker MBE SOS films would be expected to collapse owing to the relief of compressive strains that is a product of dislocation generation and extension. The surface energies associated with microtwin/matrix interfaces in silicon[18] favor the contraction of microtwins[19]; only the Peach–Koehler forces[20] (due to compressive stresses) acting on twinning partial dislocations, prevent microtwin collapse, and these forces only exist while the film is under compression.[21] For 150 nm MBE SOS films and 550 nm CVD SOS films, our application of the Tsao and Dodson model calls for less plastic flow and strain relaxation than for 550 nm MBE SOS. Because the silicon film is still under considerable strain in 150 nm MBE SOS and 550 nm CVD SOS, large enough compressive stresses are present to ensure microtwin stability.

In conclusion, it is our conjecture that the combined effects of the principal quantifiable differences between MBE-grown SOS and CVD-grown SOS (temperature,

Elimination of microtwins in silicon grown on sapphire by molecular beam epitaxy

M. E. Twigg
GEO-Centers, Incorporated, 10903 Indian Head Highway No. 502, Fort Washington, Maryland 20744

E. D. Richmond and J. G. Pellegrino[a)]
Naval Research Laboratory, Code 6816, Washington, DC 20375-5000

(Received 31 October 1988; accepted for publication 16 February 1989)

Using transmission electron microscopy, we have examined a number of (001) silicon thin films grown on ($\bar{1}012$) sapphire substrates by molecular beam epitaxy (MBE). We have found that for silicon films less than 0.55 μm thick, microtwins are very much in evidence. For silicon films greater than 700 nm thick, however, dislocations, rather than microtwins, are the predominant defect. It is our conjecture that dislocation extension, and the associated disappearance of microtwins in thicker MBE-grown SOS films, is analogous to the generation of misfit dislocations in silicon-germanium films grown on silicon or germanium substrates by MBE; furthermore, these observations can be understood via the concept of excess stress that has been recently formulated by Tsao, Dodson, and others. The persistence of microtwins in SOS grown by chemical vapor deposition, as opposed to MBE-grown SOS, can be understood in terms of Dodson and Tsao's formulation of plastic deformation kinetics in thin films.

A number of techniques have been advanced for reducing the microtwin density for (001) silicon grown on ($\bar{1}012$) sapphire (SOS), including rapid thermal annealing (RTA)[1,2] and ion implantation followed by solid phase epitaxy (SPE).[3] These techniques have been implemented only on SOS grown by chemical vapor deposition (CVD). It is also possible, however, to grow SOS by molecular beam epitaxy (MBE).[4–7] In this study we have chosen to focus on the MBE growth of SOS[6,7] rather than on subsequent processing of the as-grown material. In order to better understand the behavior of crystal defects in SOS, we have used transmission electron microscopy (TEM) to study these defects in MBE-grown SOS for a wide range of silicon thin-film thicknesses.

Silicon was grown on sapphire substrates using the NRL vacuum generators V80 MBE/SA system. Each sapphire substrate was subjected to an annealing treatment at 1415–1450 °C in the ultrahigh vacuum (UHV) environment of the MBE system. After the annealing procedure, silicon was deposited on the sapphire substrate held at 750 °C using a rate of 0.05 nm/s for thinner films and 0.1 nm/s for the thicker films (550 nm or thicker). SOS samples with silicon film thicknesses 6, 150, 550, 700, and 4000 nm were grown using this procedure.[6] Material from each of these samples was made into a cross-sectional transmission electron microscopy (XTEM) specimen and analyzed in the TEM. For the 150 and 550 nm samples, plan-view TEM specimens were also prepared.

By studying 6-nm-thick silicon films grown on sapphire, we can investigate the genesis of defects in SOS. For the islands visible in XTEM images of 6-nm-thick SOS films, microtwins appear to be the predominant defect. For 150 and 550 nm films, microtwins are also very much in evidence. A bright field XTEM micrograph of the 550 nm film is shown in Fig. 1(a). From the corresponding transmission electron diffraction pattern in Fig. 1(b), diffraction spots due to microtwins are clearly visible. For XTEM specimens made from 700 and 4000 nm SOS films, however, microtwins are not visible. A bright field micrograph of a 700 nm film and the corresponding diffraction pattern are shown in Figs. 1(c) and 1(d), respectively. Because diffraction spots for twinned silicon are absent in the diffraction pattern

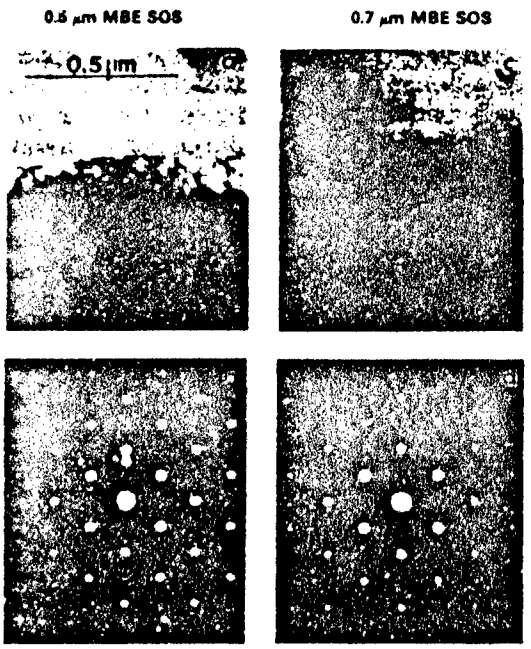


FIG. 1. (a) Bright field XTEM image of 550 nm MBE-grown SOS. Visible defects are both microtwins and dislocations. (b) [110] diffraction pattern from 550 nm MBE-grown SOS. Diffraction spots corresponding to microtwins are clearly visible. (c) Bright field XTEM image of 700 nm MBE-grown SOS. Dislocations are the only visible defects. (d) [110] diffraction pattern from 700 nm MBE-grown SOS. Diffraction spots due to microtwins do not appear in the [110] diffraction pattern of the 700 nm SOS.

a) Present address: National Institute of Standards and Technology, Bldg. 225, Gaithersburg, MD 20889.

 0003-6951/89/181766-03$01.00 © 1989 American Institute of Physics

APPENDIX D3

relief. Because smaller values of excess stress are combined with a shorter growth time in CVD SOS, dislocation generation is retarded and microtwins in the silicon film are preserved.

ACKNOWLEDGEMENTS

We would like to thank the Defence Nuclear Agency for partial funding of this research effort. We would also like to thank Chandra Pande of the Materials Science Division of the Naval Research Laboratory for access to the transmission electron microscope. Thanks are also due to Jeffrey Tsao of Sandia National Laboratory for helpful comments and for providing us with several preprints.

REFERENCES

1. J. C. Bean, L. C. Feldman, A. T. Fiory, S. Nakahara, and I. K. Robinson, J. Vac. Sci. Technol. A 2, 436 (1984).
2. R. People and J. C. Bean, Appl. Phys. Lett. 47, 322 (1985).
3. J. Y. Tsao, B. W. Dodson, S. T. Picraux, and D. M. Cornelison, Phys. Rev. Lett. 59, 848 (1987).
4. J. Y. Tsao and B. W. Dodson, Appl. Phys. Lett. 53, 848 (1988).
5. J. W. Matthews and A. E. Blakeslee, J. Cryst. Growth, 27, 118 (1974).
6. B. W. Dodson and J. Y. Tsao, Appl. Phys. Lett. 51, 1325 (1987); 52, 852 (1988).
7. J. G. Pellegrino, M. E. Twigg, and E. D. Richmond in Silicon on Insulator and Burried Metals in Semiconductors, edited by C. K. Chen, P. L. F. Hemment, J. C. Sturm, and L. Pfeiffer (Mater. Res. Soc. Proc. 107, Pittsburgh, PA 1988) pp. 383-388.
8. J. G. Pellegrino, E. D. Richmond, and M. E. Twigg in Heteroepitaxy in Silicon: Fundamentals, Structures, and Devices, edited by H. K. Choi, R. Hull, H. Ishiwara, and R. J. Nemanich (Mater. Res. Soc. Proc. 116, Pittsburgh, PA 1988) pp. 389-395; J. G. Pellegrino, S. Qadri, M. E. Twigg, E. D. Richmond, and C. L. Vold, ibid., pp. 395-400.
9. M. E. Twigg, E. D. Richmond, and J. G. Pellegrino, submitted to Appl. Phys. Lett.
10. M. S. Abrahams and C. J. Buiocchi, Appl. Phys. Lett. 27, 325 (1975).
11. M. E. Twigg and E. D. Richmond, J. Appl. Phys. 64, 3037 (1988).
12. K. Yasutake, S. Shimizu, M. Umeno, and H. Kawabe, J. Appl. Phys. 61, 940 (1987); 61, 947 (1987).
13. B. W. Dodson and J. Y. Tsao, Phys. Rev., to be published
14. B. W. Dodson and I. J. Fritz, in Compound Semiconductor Strained-Layer Superlattices, edited by R. M. Biefeld, to be published.
15. M. E. Twigg, E. D. Richmond, and J. G. Pellegrino, to be published.
16. R. L. Nolder and I. B. Cadoff, Trans. Metall. Soc. AIME 233, 549 (1965).
17. M. Aindow, J. L. Batstone, L. Pfeiffer, J. M. Phillips, and R. C. Pond, these proceedings.
18. F. A. Ponce, Appl. Phys. Lett. 41, 371 (1982).

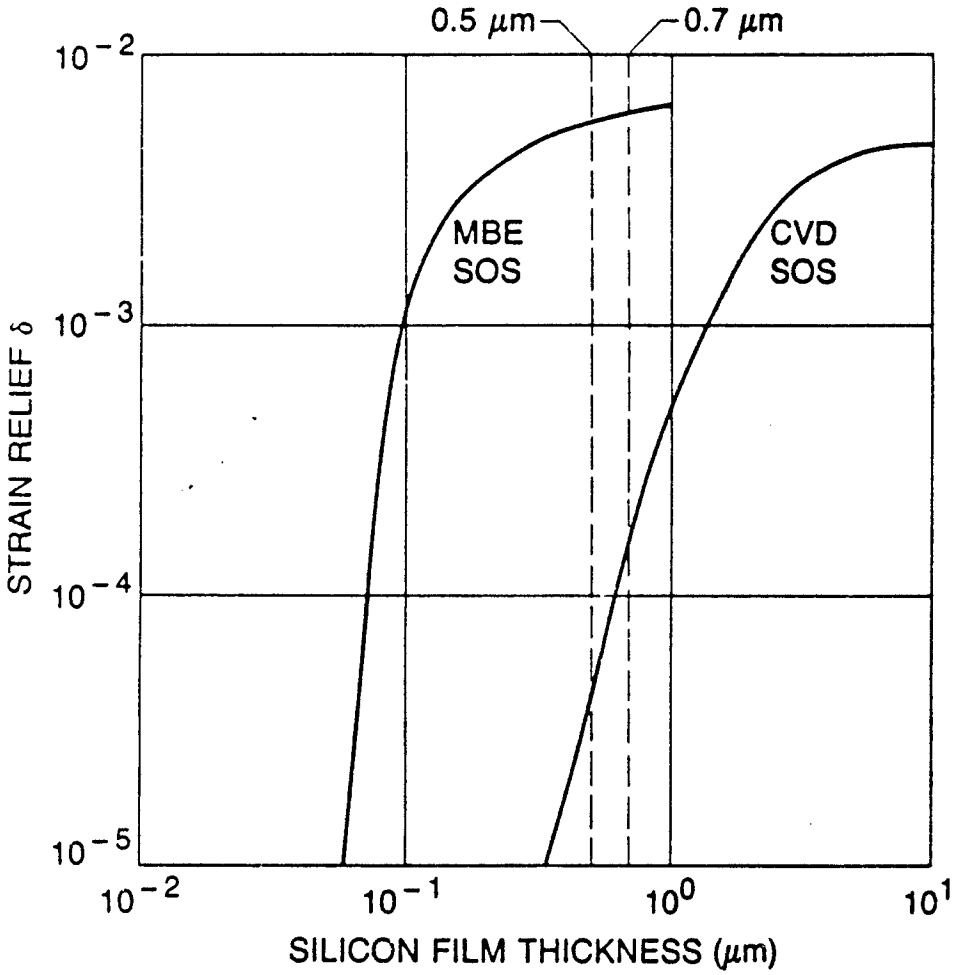


Fig.3 Log-log plot of the strain relief δ as a function of film thickness for MBE and CVD SOS.

CONCLUSIONS

The MBE growth process for SOS, which includes a different substrate preparation, reduced growth temperatures, and longer growth times, compared to the CVD growth process, favors dislocation nucleation and growth to a greater degree than in CVD-grown SOS. The strain relief that results from greater dislocation densities leads, in turn, to the collapse of microtwins. For CVD-grown SOS, the values of excess stress are smaller than for MBE-grown SOS, due to a greater volume fraction of microtwins and the associated greater strain

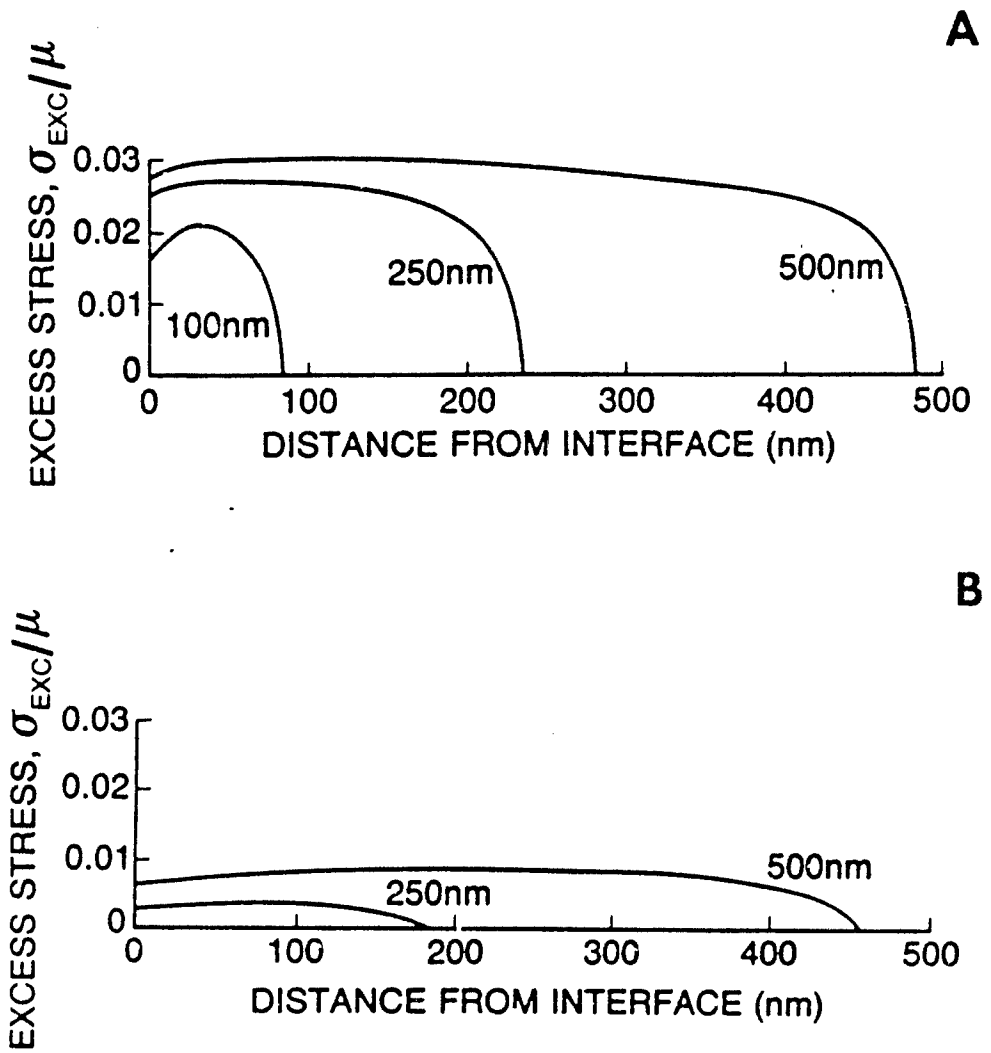


Fig.2 Plot of the reduced excess stress as a function of kink position. (a) MBE-grown SOS. (b) CVD-grown SOS. μ is equal to the shear modulus of silicon.

computations are shown in Fig.3. From this log-log plot of the strain relief δ as a function of film thickness, it is apparent that the strain relief saturates (with a saturation value of approximately 0.5%) at less than 1um for MBE SOS, and less than 10um for CVD SOS. Microtwins would be expected to collapse owing to the relief of compressive strains that is a product of dislocation generation. The surface energies associated with microtwin/matrix interfaces favor the contraction of microtwins; only the Peach-Koehler forces on twinning partial dislocations prevent microtwin collapse, and these forces only exist while the film is under compressio[illegible] [12]

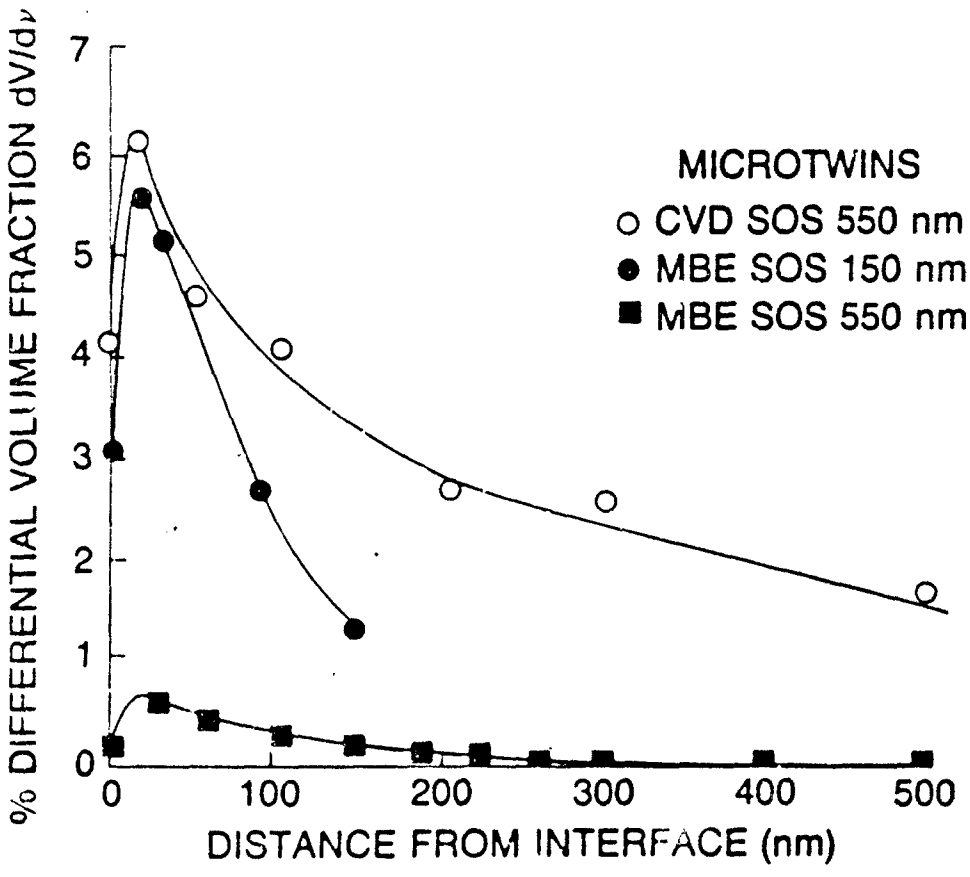


Fig.1 Plot of microtwin differential volume fraction as a function of distance from the interface for 0.15μm and 0.55μm MBE SOS, and 0.55μm CVD SOS.

In Figs.2a and 2b we plot the excess stress (for MBE and CVD SOS respectively) as a function of the distance of a single kink in a threading dislocation from the silicon/sapphire interface. Because there is clearly a smaller volume fraction of microtwins in 150nm MBE SOS as compared to 550nm CVD SOS, the strain profile e(z) is greater in MBE SOS than in CVD SOS. The excess stress, which increases monotonically with the strain profile, is greater in the MBE film than in the CVD film. The strain relief o due to plastic flow can be calculated from Dodson and Tsao's expression for the rate of strain relief, $d\delta/dt$, which is a function of growth temperature, excess stress, and the current value of δ. We calculated the strain relief, for a silicon thin film of given thickness grown upon sapphire, by numerically integrating the rate of strain relief over the growth time for the film. The results of these

specimen and analyzed in the TEM. For the 150nm and 550nm samples, plan-view TEM specimens were also prepared.

RESULTS

For the islands visible in XTEM images of 6nm thick SOS films, microtwins appear to be the predominant defect. Microtwins are also very much in evidence in 150nm and 550nm films. For 700nm and 4000nm films, however, microtwins are not visible in XTEM and have been replaced by dislocations [9]. The elimination of microtwins in thick MBE SOS films stands in contrast to observations of thick CVD SOS films in which microtwins occur in significant numbers for even 4000nm films [10].

Using the TEM-based technique of Twigg and Richmond [11], we have determined the microtwin differential volume fraction, dV/dv, as a function of distance from the interface, for 150nm and 550nm MBE SOS, as well as for 550nm CVD SOS. The CVD SOS was grown at a measured temperature of 910°C at a rate of 30nm per second. From these data, shown in Fig.1, it is clear that the differential volume fraction of microtwins is less, at every point, for the MBE 150nm and 550nm films than for the 550nm CVD film. It is also apparent that, during the MBE growth process, dV/dv falls by an order of magnitude as the silicon film thickness increases from 150nm to 550nm. The drop in dV/dv continues for thicker films to such an extent that in 700nm MBE SOS no microtwins are observable in XTEM.

DISCUSSION

Microtwins are sustained by and grow in response to stresses within the crystal matrix. In a thin film, these stresses result from misfit strains between the substrate and the epitaxial layer, and can be relieved by plastic flow. Of course, the reduction of such stresses leads to the elimination of the microtwins [12]. In the model of Dodson and Tsao [13-14], the driving force for plastic flow is the excess stress. The excess stress can calculated from the biaxial strain profile $e(z)$ [4], which can be expressed in terms of the differential volume fraction $V'(z)$. That is [15],

$$e(z) = \sqrt{2}/12 \, [\, V'(z_0) - V'(z) \,] \, , \quad (1)$$

where $V'(z_0)$, the maximum value of $V'(z)$, is assumed to relieve a misfit strain of $\sqrt{2}/12 \; V'(z_0)$. Because $\sqrt{2}/12 \; V'(z_0)$ is approximately 0.5% and the misfit strain associated with a coherent silicon/sapphire interface is an order of magnitude larger [16], either defects other than microtwins act to relieve most of the strain at the interface [17] or the silicon/sapphire interface is not coherent in the conventional sense. The possibility that the heteroepitaxial interface in SOS is not a series of aligned planes separated by defects has been suggested by Ponce, who conjectured that silicon might be bonded to sapphire using aluminosilicate bonding configurations [18].

ELIMINATION OF MICROTWINS IN MBE-GROWN SILICON ON SAPPHIRE

M. E. TWIGG*, E. D. RICHMOND**, AND J. G. PELLEGRINO**
*GEO-Centers, Inc., Prospect Square Building, 10903 Indian Head Highway, Suite 502, Fort Washington, MD 20744
**Naval Research Laboratory, Code 6816, Washington, D. C. 20375-5000

ABSTRACT

We have examined a number of MBE-grown (001) silicon thin films grown on ($\bar{1}012$) sapphire substrates using transmission electron microscopy. We have found that for silicon films less than 0.55μm thick, microtwins are very much in evidence. For silicon films greater than 700nm thick, however, dislocations, rather than microtwins, are the predominant defect. It is our conjecture that the generation of dislocations, and the associated disappearance of microtwins in thicker MBE-grown SOS films, is analogous to the generation of misfit dislocations in silicon-germanium films grown on silicon or germanium substrates by MBE. The persistence of microtwins in CVD-grown SOS, as opposed to MBE-grown SOS, can be understood in terms of Dodson and Tsao's formulation of the kinetics of plastic flow in thin germanium-silicon films.

INTRODUCTION

For germanium-silicon thin films grown upon germanium or silicon substrates, the onset of plastic flow at a particular value of film thickness has been attributed to dislocation generation [1,2]. According to the model of Tsao, Dodson, and others [3,4], the driving force for plastic deformation in thin films is the difference between the stress due to lattice mismatch and the stress required for the formation of extended kinks in threading dislocations. This difference is defined by Tsao et al. as the "excess stress" and corresponds to the deviation from mechanical equilibrium that was formulated earlier by Matthews and Blakeslee [5]. In their plastic flow model, Dodson and Tsao regard the excess stress as the driving force in the strain relief of an initially coherent metastable strained layer [6]. It is our intention to show that Dodson and Tsao's plastic flow model can be applied to strain relief in silicon on sapphire (SOS).

EXPERIMENTAL DETAILS

Silicon was grown on sapphire substrates using the NRL Vacuum Generators V80 MBE/SA System. Each sapphire substrate was subjected to an annealing treatment at 1415-1450°C in the ultra high vacuum (UHV) environment of the MBE system. After the annealing procedure, silicon was deposited on the sapphire substrate held at 750°C using a rate of 0.05nm per second for thinner films and 0.1nm per second for the thicker films (550nm or thicker). SOS samples with silicon film thicknesses 6nm, 150nm, 550nm, 700nm and 4000nm were grown using this procedure [7,8]. Material from each of these samples was made into a cross-sectional transmission electron microscopy (XTEM)

Mat. Res. Soc. Symp. Proc. Vol. 138. ©1989 Materials Research Society

APPENDIX D2

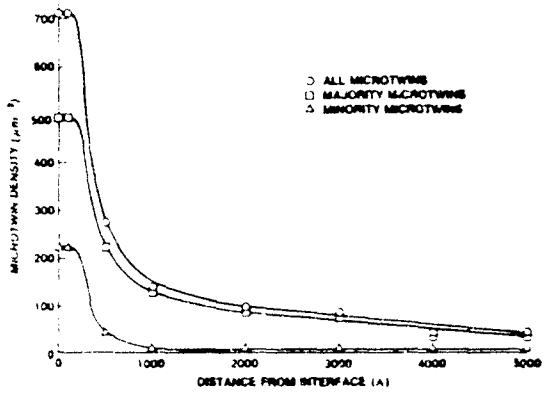


FIG. 10. Plot of the microtwin density as the number of microtwins per unit area as a function of distance from the silicon/sapphire interface.

the interface, but these studies only measured the microtwin density for distances greater than 300 Å from the interface. Although Parker and co-workers[2] also began their measurements 300 Å from the interface, they found that the microtwin density was greatest 1000 Å from the interface. Of course, these studies were measuring density rather than volume fraction. For the sake of completeness, we have developed our own measurement of microtwin density as a function of distance from the interface. In Fig. 10, we display the microtwin density as the number of microtwins per unit area that survive to a given distance from the silicon/sapphire interface. As in other measurements of microtwin density, we found that the number of microtwins per unit area decreases monotonically with the distance from the interface.

It is our contention that the microtwin differential volume fraction is not greatest at the interface because over the first several hundred angstroms from the interface, the volume of an individual microtwin increases markedly. There are a large number of microtwins that extend only a few hundred angstroms from the interface, however, so that the loss of these small microtwins in the calculation of the volume fraction eventually brings about a decrease in the differential volume fraction. Nevertheless, the continuing volume increase for some microtwins with distance from the interface prevents a drastic decrease in dV/dv. For this reason the quantity dV/dv shows a less marked decrease with thickness than measurements[1-3] of microtwin density.

In this study, as well as in previous studies, it is apparent that of the four twinning systems for silicon, two produce a relatively large number of microtwins (the majority twinning systems) and two produce a relatively small number of microtwins (the minority twinning systems),[1] when the (001) plane of silicon is parallel to the $(\bar{1}012)$ plane of sapphire. From transmission electron diffraction experiments, we found that the vertical misorientation of the silicon [001] direction was $+0.5°$ from normal to the $(\bar{1}012)$ sapphire plane and the horizontal misorientation was effectively zero (using the definitions for misorientation in the silicon/sapphire system established by Smith and Weitzel[9]). For such a small misorientation, the volume fraction of majority microtwins should be greater than the volume fraction of minority microtwins.[9] We have found that the number of majority microtwins is greater than that of minority twins for all distances from the interface. This dominance of the majority twinning system is in force at the interface with the majority microtwin differential volume fraction of the interface assuming a value more than twice that of minority microtwins. That the majority value of dV/dv at the interface is clearly greater than the minority value argues well for the contention that majority microtwins nucleate on the sapphire surface more easily than minority microtwins. This point of view is supported by the observation of Lihl *et al.* that the lattice of majority microtwins is in closer coincidence with the sapphire surface than the lattice of minority microtwins.[3] If our observations had indicated that majority and minority value of dV/dv were the same at the interface, then the difference between majority and minority concentration profiles might be ascribed to anisotropic stresses set up by growing a cubic crystal onto the face of a rhombohedral substrate. On the basis of the observations of this study, however, nothing can be said regarding the role of anisotropic stresses in the growth of microtwins.

CONCLUSIONS

The results of this study indicate that microtwin differential volume fraction does not decrease monotonically from the interface. The volume fraction of silicon occurring as microtwins does not abruptly decrease away from the interface; instead there is a tendency for the volume fraction of individual microtwins to increase over the first several hundred angstroms away from the interface due to an increase in the average microtwin volume. PVTEM observations also indicate that the microtwins are heavily faceted and grow from nucleation sites at the interface.

ACKNOWLEDGMENTS

We would like to thank Dr. Chandra Pande for access to the electron microscope facility at the Materials Science and Technology Division of the U. S. Naval Research Laboratory. We would also like to thank the Defense Nuclear Agency for funding this project.

[1] M. S. Abrahams and C. J. Buiocchi, Appl. Phys. Lett. 27, 327 (1975).
[2] M. A. Parker, R. Sinclair, and T. W. Sigmon, Mater. Res. Soc. Symp. 37, 211 (1985).
[3] R. Lihl, H. Oppolzer, P. Pongratz, P. Skalicky, and W. Svanda, J. Microsc. 118, 89 (1980).
[4] G. W. Cullen, M. T. Duffy, and R. K. Smeltzer, Proc. Electro. Chem. Soc. 84, 230 (1984).
[5] G. Foti, L. Csepregi, E. F. Kennedy, J. W. Mayer, P. P. Pronko, and M. D. Rechtin, Philos. Mag. 37A, 591 (1978).
[6] P. Hirsh, A. Howie, R. B. Nicholson, D. W. Pashley, and M. J. Whelan, *Electron Microscopy of Thin Crystals* (Krieger, Huntington, NY, 1977), pp. 310–311.
[7] J. Brayman and R. Sinclair, J. Electron Microsc. Technol. 1, 53 (1984).
[8] M. H. Loretto and R. E. Smallman, *Defect Analysis in Electron Microscopy* (Wiley, New York, 1975), pp. 15–16.
[9] R. T. Smith and C. E. Weitzel, J. Cryst. Growth 58, 61 (1982).

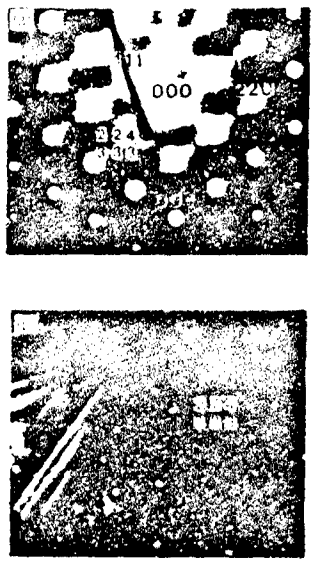


FIG. 8. (a) Electron diffraction condition for DF imaging configuration with a [110] beam direction and a $(\bar{2}\bar{2}4)$ diffracted beam. (b) Using this diffracting condition, a DF TEM image presents an edge-on view of microtwins associated with the minority $(\bar{1}\bar{1}1)$ twinning system.

flection. From the DF image in Fig. 8(b), the median thickness of the minority twins appears to be 50 Å, which gives a value of 60 Å for the projected width along the (001) plane.

In order to obtain a DF image of a microtwin edge-on, one need only require that the diffraction vector is parallel to the habit plane of the microtwin, and that the systematic reflections $\pm g$ corresponding to the habit plane are equally excited. Orienting a TEM specimen so $\pm g$ are equally excited can usually be done very easily with the aid of Kikuchi lines. Unfortunately, in the SOS samples examined in this study, the strain fields associated with the large microtwin density prevented the appearance of Kikuchi lines. Without Kikuchi lines, specimen alignment must rely on the intensity of diffraction spots. We therefore decided to assure that the microtwins were being imaged edge on by directing the undiffracted beam down the $[1\bar{1}0]$ zone axis.

Because the differential volume fraction of twinned silicon, dV/dv, is defined over a specific area, it is important to consider that the area corresponding to a TEM micrograph is also altered by projection effects. Any plane defining an area used for calculating the defect density in a plan-view sample must be parallel to the (001) plane. When viewing some portion of the (001) plane using the [114] beam direction, the area of such a region must appear in the projected image to be reduced by a factor equal to the cosine of the angle between the [114] and [001] directions. In this case the projected area is equal to the actual area multiplied by $4/\sqrt{18}$. The area used for calculating the defect density can then be determined by multiplying the projected area by $\sqrt{18}/4$.

The differential volume fraction of twinned material, dV/dv, is plotted as a function of distance from the silicon/sapphire interface in Fig. 9. As indicated above, one begins the calculation of dV/dv for a specific distance z' from the interface by determining the cross-sectional area of a microtwin defined by its intersection with the $z = z'$ plane, which is, of course, parallel to the plane of the substrate. The value for z' is determined by multiplying the distance along a microtwin facet up from the interface by $\sqrt{8}/3$, as indicated in Fig. 6. The cross-sectional area of the microtwin for the distance z' is the product of the width (defined as "w" in Fig. 4) of the microtwin parallel to the substrate by the thickness of the substrate in the $z = z'$ plane. For minority and majority microtwins these thicknesses are 60 and 90 Å, respectively, as measured from Figs. 7(b) and 8(b). The cross-sectional area for all microtwins are summed for a specific region; this sum is then divided by the area of the region in question. Due to projection effects, the true area of the defined region is greater than that calculated directly from the micrograph by a factor of $\sqrt{18}/4$.

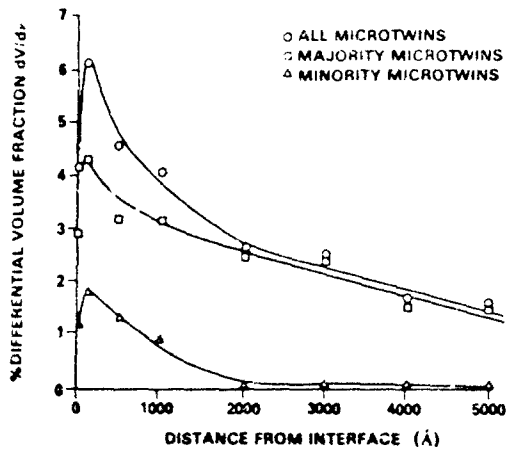


FIG. 9. Plot of the differential volume fraction dV/dv as a function of distance from the silicon/sapphire interface.

A useful check for the differential volume fraction profile measurement technique is performed by integrating dV/dv over the distance from the interface in order to estimate the total microtwin volume fraction of the sample. This number for the total microtwin volume fraction can then be compared with a value obtained by a reliable macroscopic technique. For the measurement of the volume fraction of microtwins in a macroscopic sample, x-ray pole figure analysis is an appropriate technique. According to Cullen, Duffy, and Smeltzer,[4] x-ray pole figure analysis measurements indicate that device-grade SOS contains from 1% to 4% twinned silicon by volume. Integration of our differential volume fraction measurements over silicon film thickness indicate that the total volume fraction for microtwins is 3%.

DISCUSSION

One of the most interesting features evident in the microtwin volume fraction profiles is that dV/dv does not appear to be greatest at the interface. In general, the differential microtwin volume fraction is greatest 100 Å from the interface and does not drop significantly below the interface value for distances from the interface that are less than 1000 Å. The studies of Abrahams and Buiocchi[1] and Lihl *et al.*[3] showed density dropping monotonically with distance from

dv/dz of the volume $v(z)$ of a silicon film of thickness z. Dividing dV/dz by dv/dz yields the quantity $(dV/dv)z = z'$ which can be measured by dividing the area of the microtwins in the plane $z = z'$ by the total area of the substrate plane. In practice, the quantity $(dV/dv)z = z'$ can be estimated by marking off a representative area of the sample and dividing it into the area of the microtwins intersecting the plane $z = z'$. The area used for our measurement is marked by the diamond in Fig. 2. The volume fraction of twinned material for the whole thickness of the silicon film can be determined from dV/dv by integrating it over the film thickness and then dividing by the total film thickness.

In Fig. 6 we illustrate this procedure for a single microtwin. In this case the electron beam is parallel to the [114] direction of the silicon epitaxial layer. We are interested in the width of the microtwin parallel to the interface. For a microtwin in the (111) plane that direction is $[\bar{1}10]$. Because $[\bar{1}10]$ lies in both the (111) and (114) planes, the silicon crystal can be viewed as rotating about a stationary $[\bar{1}10]$ axis as the electron beam direction passes from [111] to [114]. Any measurement made from a projected TEM image along the $[\bar{1}10]$ direction cannot be distorted by this rotation and thus one need only account for the effect of magnification in measuring the microtwin width. Measuring the distance of a given point of the microtwin from the interface, however, requires a more detailed consideration of the geometry.

The TEM image is a two-dimensional projection of a three-dimensional object. Therefore, when imaging a microtwin lying on the (111) plane via a [11- beam direction, the lines that lie in the (111) plane and are not parallel to $[\bar{1}10]$ will appear shorter than their actual length. In this case, the projected lengths of $[0\bar{1}1]$ and $[10\bar{1}]$ are $\frac{1}{2}$ of their corresponding actual lengths. The distance from the interface can be measured along these two $\langle 110 \rangle$ directions by simply dividing the distance along the line by $\sqrt{2}$. Therefore, from a TEM image with a [114] beam direction, the distance from the interface can be calculated by multiplying the distance along $[10\bar{1}]$ or $[0\bar{1}1]$ by $\sqrt{8}/3$ (which is the product of $\frac{1}{2}$ and $1/\sqrt{2}$).

If SOS were not such a highly strained material, microtwin thickness might be obtained by examining fringes within the microtwins. This type of thickness measurement is very difficult for even relatively unstrained material, however, due to the possibility that each microtwin is actually a sandwich of twinned and untwinned silicon.[3] Due to these complications, we have chosen to determine microtwin thickness by DF imaging of XTEM samples oriented so that the microtwins are viewed edge-on.

The thickness of microtwins can be measured from a properly oriented XTEM sample imaged in DF. An electron diffraction pattern for the $[1\bar{1}0]$ beam direction of an XTEM sample is shown in Fig. 7(a). This is the diffraction configuration we have chosen for imaging the majority set of microtwins. The diffraction vector marked for DF imaging is the $\frac{1}{2}(22\bar{4})$, which is parallel to the (111) habit plane of the microtwins. Under this imaging condition, the DF coils have deflected the $\frac{1}{2}(22\bar{4})$ beam so that it is parallel to the optical axis and the specimen has been tilted clockwise about the $[\bar{1}\bar{1}\bar{1}]$ axis in order to make the main beam once again parallel to the $[1\bar{1}0]$ axis. For this configuration, (111) microtwins are imaged edge-on, as in Fig. 7(b). The median thickness of the majority microtwins appears to be approximately 75 Å, which translates into a 90-Å projected width along the (001) plane of the substrate.

Using an analogous diffracting condition, shown in Fig. 8(a), the minority microtwins corresponding to the $(\bar{1}\bar{1}1)$ habit plane are imaged edge-on in DF using the $\frac{1}{2}(\bar{2}\bar{2}\bar{4})$ re-



FIG. 6. Illustration of method for measuring the microtwin width "w" at a particular distance z' from the interface. Note that the projected distance from the interface is actually $\sqrt{8}/3\,z$ for a [114] beam direction and a microtwin with a (111) habit plane.

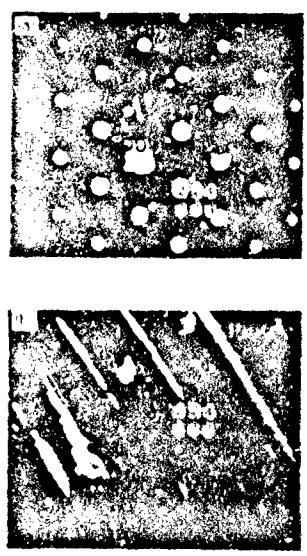


FIG. 7. (a) Electron diffraction condition for DF imaging configuration with a [110] beam direction and a $\frac{1}{2}(22\bar{4})$ diffracted beam. (b) Using this diffracting condition, a DF TEM image presents an edge-on view of microtwins associated with the majority (111) twinning system.

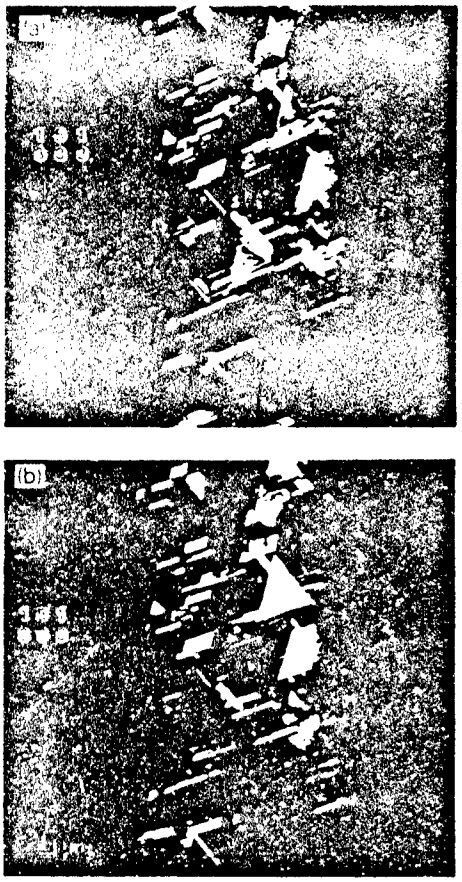


FIG. 3. Stereopair TEM micrographs showing the morphology of microtwins in SOS. From this pair of micrographs, it is apparent that microtwins grow as contiguous structures from the interface.

the four ⟨114⟩ beam directions considered here, we found that the microtwins in every twinning system are bounded by facets corresponding to ⟨110⟩ directions in the plane of the microtwin. In Fig. 4 the facets of a microtwin associated with the (111) twinning system are indexed. Though trace analysis provides the direction of microtwin features, a complete understanding of the microtwin morphology is still greatly assisted by the three-dimensional view of the microtwins provided by stereomicroscopy. The results of the DF stereomicroscopy experiment for the [114] pole is shown in Fig. 3. It is apparent from this stereomicrograph and from stereomicrographs corresponding to the other ⟨114⟩ beam directions, that all microtwins are contiguous and grow from the interface. The point where the sapphire substrate is milled away and only the silicon epitaxial layer remains is also more obvious when viewed in stereo. Futhermore, it is apparent from Fig. 3 that many twins are in contact with the interface for only a few hundred angstroms. A large microtwin has a tendency to begin at the interface as only a very small feature and then grow rapidly in area as it propagates through the film.

MICROTWIN VOLUME FRACTION

Rather than focusing on the number of microtwins seen to occur within some distance, area, or volume, it is the aim

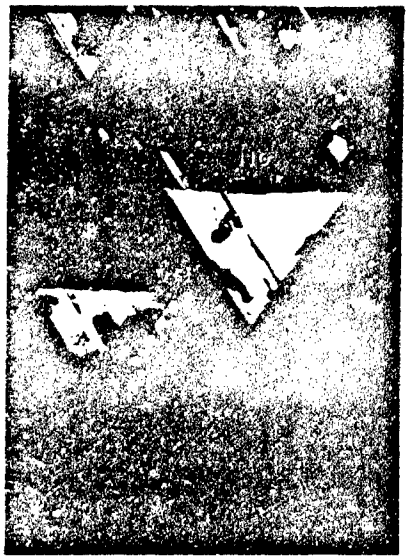


FIG. 4. Indexing of facets for a microtwin occurring in silicon grown on sapphire. The "facet" parallel to the [$\bar{1}$10] direction is actually the top of the microtwin as it intersects the surface of the silicon film.

of this study to determine the volume fraction of twinned silicon as a function of the distance from the silicon/sapphire interface. In discussing the volume fraction of microtwins as a function of the distance from the interface, we are considering a differential quantity. Let us imagine a function that corresponds to the total volume $V(z)$ of twinned material up to a specific distance z from the interface, as in Fig. 5. When we evaluate the derivative dV/dz at a distance z' from the interface, the contribution to this quantity from a single microtwin is given by the cross-sectional area defined by the intersection of the microtwin and the plane defined by $z = z'$. The value of dV/dz at z' corresponds to the sum of these areas marked off in the $z = z'$ plane. The total area of the plane a distance z' from the interface equals the derivative

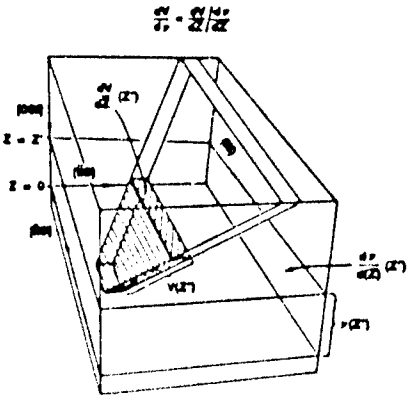


FIG. 5. Schematic definition of the differential volume fraction, dV/dv, for microtwins. $V(z)$ is the total volume of microtwins measured from the interface. $v(z)$ is the total volume of the silicon film, measured from the interface.

down on a piece of sapphire. After perforating the sample during the first stage of ion milling, we further reduced the overall thickness of the plan-view sample by milling it at a 15° angle on both sides at 6 kV and 1 mA for 6 min. XTEM samples are glued together in the usual way[7] and then mechanically dimpled to a thickness of 30 μm or less. Ion milling of XTEM samples is carried out at a 10° angle with a voltage of 5 kV and a current of 1 mA. Using the parameters described here, sapphire appears to mill away at about 1 μm/h for both PVTEM and XTEM samples.

CRYSTALLOGRAPHIC CONSIDERATIONS

In order to obtain the detailed geometrical information required for a determination of the microtwin density profile, it is necessary to find a number of beam directions with strong and distinct reflections for the DF TEM imaging of microtwins. The smallest extinction distance for silicon corresponds to the {111} reflection and the only poles containing as many as two of these reflections are the ⟨110⟩ poles. It is relatively easy to determine which poles in the original crystal system correspond to the ⟨110⟩ poles after the twinning operation, because twinning can be viewed as the result of a 60° rotation about the normal to the twin plane. This operation corresponds to a simple rotation matrix and from the application of these transformations, it is apparent that all ⟨110⟩ directions transform to other ⟨110⟩ directions or to ⟨114⟩ directions. We prefer the poles used in our imaging experiments to be in close angular proximity to one another. Four of the ⟨114⟩ poles (i.e., [114], [$1\bar{1}4$], [$\bar{1}14$], and [$\bar{1}\bar{1}4$]) meet this criterion. Each of these four poles is 19.47° from the [001] pole. There is a simple relationship between a given ⟨114⟩ zone axis pattern, Fig. 1, and the {111} habit plane of the microtwin giving rise to the twinned diffraction spots. The first two indices of the habit plane match the first two indices of the zone axis (e.g., ($\bar{1}\bar{1}1$) corresponds to [$\bar{1}\bar{1}4$]).

MICROTWIN MORPHOLOGY

We begin our study of microtwin morphology by identifying the principle features of TEM images for plan-view SOS samples. The PVTEM sample is ion milled from the sapphire side until a small hole develops in the center of the sample. The part of the sample nearest the edge of the hole is devoid of sapphire, so that only the silicon epitaxial layer remains. The foil edge consisting only of silicon is clearly visible in Fig. 2 as the leftmost part of the specimen image.

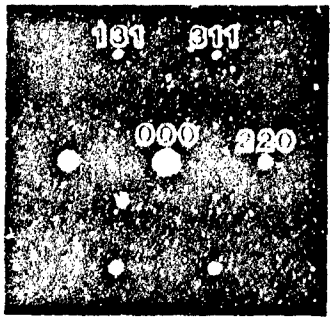


FIG. 1. Zone axis diffraction pattern for the [114] beam direction.

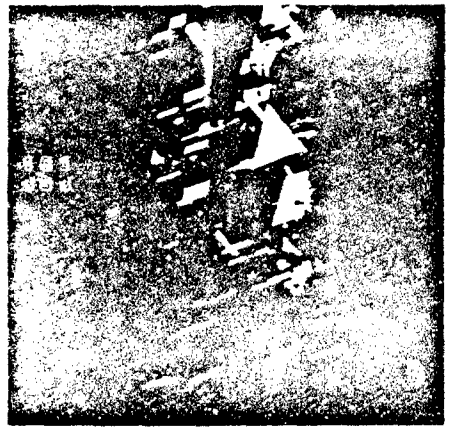


FIG. 2. Dark-field TEM micrograph of plan-view specimen. This region of the specimen is bounded on the left by the hole made by the ion milling process, and bounded to the right by the increasingly thick sapphire substrate. The boundary marked by arrows corresponds to the elimination of the sapphire substrate by ion milling; hence, the specimen to the left of the boundary is composed only of silicon. To the right of the boundary silicon on sapphire is imaged. The diamond circumscribes the area used in the microtwin density measurements.

Within the silicon edge of the thin-foil specimen, microtwins with a white appearance are visible. This image was obtained using a dark-field imaging condition set up so that the objective aperture only admitted diffracted intensity associated with one of the Bragg reflections of the twinned silicon lattice. As we follow the sample features from right to left, it is apparent that the image contrast undergoes a marked change at a boundary marked by arrows in Fig. 2. This boundary identifies the point where ion milling has completely removed the sapphire substrate and revealed the silicon eptitaxial layer. Near this boundary the sapphire is sufficiently thin to allow the study of microtwins growing from the silicon/sapphire interface via TEM.

In order to study the microtwins growing from the interface towards the silicon surface, a three-dimensional observation of microtwin morphology is extremely helpful. One can study features in a thin foil in three dimensions via stereomicroscopy. As in any other form of microscopy or photography, the observer obtains a stereoimage by viewing the object from two slightly different directions. The only significant difference between stereoimaging in the TEM and in conventional photography is the constraint that the diffraction conditions must be similar for each of the two TEM stereoimages.[6] In Fig. 3 we show such a pair of stereomicrographs (known as a stereopair) corresponding to beam directions that are about 5° apart. Each TEM image was obtained in dark field using the 1/3 ($1\bar{5}1$) diffraction vector.

From the DF PVTEM stereopair in Fig. 3, it is apparent that microtwins in SOS are faceted. For microtwins imaged with one of the twin refections of the [114] zone axis diffraction pattern, the direction of the facet must lie in the (111) plane. The projected direction of a given facet can be determined for the [114] beam direction and analyzed subject to the constraint that the direction remains in the (111) plane and the actual direction of the facet can be determined via trace analysis.[8] After performing such an analysis for each of

Microtwin morphology and volume fraction for silicon on sapphire

M. E. Twigg
GEO-Centers Inc., Prospect Square Building, 10903 Indian Head Highway, Suite 502, Fort Washington, Maryland 20744

E. D. Richmond
Code 6816, Naval Research Laboratory, Washington, DC 20375

(Received 3 March 1988; accepted for publication 26 May 1988)

In order to understand the influence of various growth and processing procedures on the quality of silicon grown on sapphire (SOS), one needs a way to measure microtwin density as a function of distance from the interface. In previous studies, however, the technique best suited for determining such a density profile, transmission electron microscopy (TEM), has been applied to this problem in a relatively qualitative manner. We have chosen to apply TEM in a more quantitative fashion to this problem by keying our observations to microtwin morphology. These observations indicate that the microtwins occurring in SOS grown by chemical vapor deposition are faceted and grow contiguously from the interface. The volume fraction of silicon occurring as microtwins does not decrease away from the interface at as large a rate as indicated by previous TEM studies. Instead, the decrease in the number of twins away from the interface appears to be balanced by an increase in twin size. It also appears that the greatest volume fraction of twinned material occurs at least several hundred angstroms away from the interface rather that at the interface.

INTRODUCTION

It is well established that microtwins play an important role in accommodating stresses that accompany growth of silicon on sapphire (SOS) for the (001) silicon/($\bar{1}012$) sapphire heteroepitaxial system.[1] Despite the importance of microtwins in SOS growth, few investigations have addressed their actual morphology. Some of the previous studies on thicker (>1000 Å) silicon films grown on sapphire by chemical vapor deposition (CVD) have relied on transmission electron microscopy (TEM) of cross-section TEM (XTEM) samples.[1,2] The XTEM geometry is useful for studying the silicon/sapphire interface and for quickly arriving at a qualitative estimate of the defect density as a function of distance from the interface. From XTEM, however, it is difficult to assess microtwin morphology because most microtwins imaged in an XTEM sample are artificially terminated by the sample preparation process. Lihl *et al.*[3] used plan-view TEM (PVTEM) for determining microtwin density profiles in SOS, but did not associate density measurements with microtwin morphology. It appears that the aim of most previous studies has been to calculate a quantity that resembles the number of microtwins per unit volume rather than the volume fraction. Furthermore, these previous studies have not addressed microtwin morphology in SOS. It is our view that the volume fraction of twinned material is a particularly useful quantity for describing crystal perfection in SOS. The overall volume fraction of twinned silicon can be easily measured by x-ray pole figure analysis[4] and the effect of the volume fraction on crystalline quality can be profiled by MeV He^+ ion dechanneling effect measurements.[5] The twinned volume fraction profile determined via TEM and the properties determined by these other characterization techniques allows for a more systematic study of the defects in SOS. There are problems associated with deciding on a logically consistent approach to counting the number of twins in a given volume. This difficulty arises because a particular twin might either fill a small fraction of that volume or continue outside the boundaries of the given volume. On the other hand, the definition for the volume fraction of twinned material is unambiguous.

If one had a geometric description of each microtwin in the area marked for microtwin density measurement, the differential microtwin volume fraction could be measured. It is our aim to arrive at such a geometric description by a detailed study of microtwin morphology via dark field (DF) TEM. In a highly strained material such as SOS, it is easier to analyze TEM micrographs that have been obtained via an imaging procedure that is not overly sensitive to strain. From DF images of PVTEM samples, most of the details of microtwin morphology can be obtained. In addition, stereoimaging of PVTEM samples in DF has been used to provide details of microtwin morphology that are not always evident in a two-dimensional micrograph.[6]

EXPERIMENTAL DETAILS

Union Carbide Corportion grew the sample material analyzed in this study via chemical vapor deposition. The 0.5-μm silicon film was grown at a measured temperature of 910 °C at a rate of 2 μm/min.

In order to determine the volume fraction of twinned silicon on sapphire as a function of distance from the interface, both PVTEM and XTEM samples must be prepared. The thinning procedure for the plan-view samples begins with mechanically dimpling to a thickness of 30 μm. The sample is then ion milled at a 20° angle from the plane of the sample with the ion beam directed at the sapphire side using a voltage of 6 kV and a current of 0.5 mA. During ion milling, the silicon side of the SOS sample is positioned face

 0021-8979/88/183037-06$02.40 © 1988 American Institute of Physics

APPENDIX D1

Shipboard Contamination Flow Test
Mobile, Alabama

Trial No.: 04-NH-09
Z Time: 10:10:00

Date: 27 May 1988

Miran Data µg/L

Z Time	Pos 08 1-55	Pos 09 1-56	Pos 10 01-55	Pos 12 1-49	Pos 13 1-44	Pos 14 02-49
38.00	4.5	8.5	8.5	3.4	3.2	3.7
39.00	4.3	8.4	8.3	3.5	3.2	3.9
40.00	4.2	8.1	8.0	3.5	3.2	4.0
41.00	4.0	8.0	7.8	6.2	3.2	4.1
42.00	3.8	7.8	7.6	5.5	3.1	4.2
43.00	3.8	7.6	7.4	4.1	3.1	4.4
44.00	3.5	7.5	7.2	6.8	3.1	4.4
45.00	3.4	7.3	7.1	6.4	3.0	4.6
46.00	3.3	7.2	6.9	6.4	3.0	4.7
47.00	3.2	7.0	6.8	4.3	2.9	4.8
48.00	3.1	6.8	6.6	4.0	2.9	5.0
49.00	3.0	6.7	6.4	4.2	2.8	5.1
50.00	3.0	6.6	6.3	4.0	2.8	5.2
51.00	2.9	6.5	6.1	4.2	2.8	5.4
52.00	2.8	6.4	6.0	4.8	2.8	5.5
53.00	2.7	6.3	5.9	6.7	2.8	5.7
54.00	2.6	6.2	5.8	5.1	2.8	5.9
55.00	2.6	6.1	5.7	4.3	2.8	5.9
56.00	2.5	6.0	5.6	4.5	2.8	6.1
57.00	2.3	6.0	5.6	6.2	2.7	6.2
58.00	2.4	5.9	5.5	5.9	2.8	6.4
59.00	2.4	5.9	5.4	4.8	2.7	6.6
60.00	2.4	5.8	5.4	4.6	2.7	6.7
61.00	2.3	5.8	5.3	4.6	2.7	6.8
62.00	2.2	5.7	5.2	4.6	2.7	6.9
63.00	2.2	5.7	5.1	4.5	2.7	7.0
64.00	2.2	5.6	5.1	4.6	2.7	7.0
65.00	2.1	5.6	5.1	4.7	2.7	7.1
66.00	2.2	5.5	5.0	4.5	2.6	7.3
67.00	2.0	5.5	4.9	4.8	2.6	7.5
68.00	2.1	5.4	4.8	4.8	2.7	7.7
69.00	1.9	5.4	4.8	4.9	2.7	8.0
70.00	2.0	5.4	4.8	5.0	2.7	8.2
71.00	1.9	5.4	4.7	5.6	2.8	8.3
72.00	1.9	5.4	4.8	5.7	2.8	8.4
73.00	2.0	5.4	4.7	5.8	2.8	8.5
74.00	2.0	5.3	4.7	6.4	2.7	8.5
75.00	1.9	5.4	4.7	7.1	2.7	8.4
76.00	1.9	5.3	4.7	6.1	2.7	8.4
77.00	1.7	5.3	4.6	7.8	2.7	8.4
78.00	1.7	5.3	4.6	6.8	2.7	8.3
79.00	1.9	5.3	4.5	6.1	2.7	8.3
80.00	1.7	5.3	4.5	5.3	2.8	8.3

Shipboard Contamination Flow Test
Mobile, Alabama

Trial No.: 04-NH-09
Z Time: 10:10:00

Date: 27 May 1988

Miran Data μg/L

Z Time	Pos 08 1-55	Pos 09 1-56	Pos 10 01-55	Pos 12 1-49	Pos 13 1-44	Pos 14 02-49
-5.00	0.0	0.0	0.0	0.6	0.5	0.0
-4.00	0.0	0.0	0.0	0.6	0.6	0.2
-3.00	0.0	0.0	0.0	0.5	0.6	0.0
-2.00	0.0	0.0	0.0	0.8	0.7	0.0
-1.00	0.0	0.0	0.0	0.9	0.7	0.1
0.00	0.0	0.0	0.0	0.7	0.8	0.2
1.00	0.0	0.0	0.0	0.9	0.8	0.3
2.00	0.3	0.0	0.5	1.0	0.9	0.3
3.00	5.8	0.9	5.6	1.2	2.2	0.6
4.00	14.2	4.8	14.5	1.2	4.3	0.7
5.00	19.6	9.7	20.9	1.3	5.6	0.8
6.00	21.7	13.5	23.9	1.4	6.3	0.8
7.00	22.3	16.4	25.1	1.7	6.7	0.9
8.00	22.6	18.4	25.8	1.7	6.9	1.0
9.00	21.4	19.5	25.6	3.1	7.0	1.2
10.00	20.4	19.9	24.8	3.9	6.9	1.4
11.00	19.5	20.1	24.1	2.4	6.9	1.6
12.00	18.1	19.8	23.1	3.4	6.7	1.7
13.00	17.1	19.4	22.2	3.7	6.5	1.8
14.00	16.0	18.9	21.2	2.4	6.3	1.9
15.00	14.9	18.4	20.3	2.1	6.1	2.0
16.00	13.8	17.7	19.4	3.0	6.0	2.2
17.00	12.9	17.0	18.6	4.8	5.7	2.2
18.00	12.0	16.5	17.9	4.6	5.5	2.3
19.00	11.4	15.9	17.2	4.8	5.4	2.5
20.00	10.6	15.3	16.5	3.5	5.2	2.5
21.00	10.0	14.8	16.0	2.5	5.1	2.4
22.00	9.6	14.3	15.3	2.9	4.8	2.5
23.00	9.1	13.8	14.7	3.8	4.6	2.6
24.00	8.3	13.4	14.1	5.4	4.5	2.6
25.00	8.0	12.9	13.6	4.9	4.3	2.7
26.00	7.5	12.5	13.1	4.7	4.2	2.8
27.00	7.3	12.1	12.5	3.1	4.1	2.8
28.00	6.9	11.7	12.1	4.5	4.0	2.9
29.00	6.6	11.3	11.7	3.2	4.0	3.0
30.00	6.5	11.0	11.3	3.2	3.8	3.1
31.00	6.1	10.6	10.9	3.2	3.8	3.1
32.00	5.6	10.3	10.5	4.0	3.7	3.0
33.00	5.4	9.9	10.0	4.0	3.6	3.2
34.00	5.1	9.6	9.7	4.0	3.5	3.3
35.00	4.8	9.3	9.4	3.4	3.4	3.4
36.00	4.9	9.0	9.0	3.4	3.3	3.5
37.00	4.7	8.8	8.7	3.5	3.3	3.6

Shipboard Contamination Flow Test
Mobile, Alabama

Trial No.: 04-NH-09
Z Time: 10:10:00

Date: 27 May 1988

Miran Data μg/L

Z Time	Pos 01 1-37	Pos 02 1-40	Pos 03 1-44	Pos 04 1-46	Pos 05 01-49	Pos 06 01-51	Pos 07 01-53
38.00	20.8	25.5	4.3	0.3	4.3	7.9	7.4
39.00	20.2	24.5	4.6	0.3	4.5	7.4	7.2
40.00	19.7	23.5	4.4	0.3	4.7	7.4	6.9
41.00	18.5	22.0	3.8	0.3	4.5	7.6	6.7
42.00	18.1	21.6	3.8	0.3	4.6	6.7	6.5
43.00	17.7	20.6	3.4	0.3	4.6	6.8	6.3
44.00	16.6	19.5	2.9	0.3	4.6	6.1	6.1
45.00	16.0	18.7	3.0	0.3	4.7	6.1	6.0
46.00	15.6	18.0	3.1	0.2	4.9	5.9	5.8
47.00	15.2	17.2	3.2	0.2	4.8	5.6	5.5
48.00	14.5	16.6	2.3	0.2	5.0	5.6	5.4
49.00	14.2	15.9	2.4	0.2	5.0	5.4	5.2
50.00	13.8	15.2	2.4	0.2	5.0	5.2	5.1
51.00	13.2	14.6	1.6	0.2	5.1	5.0	4.9
52.00	12.7	13.7	1.6	0.2	5.2	4.7	4.8
53.00	12.5	13.5	1.5	0.2	5.2	4.6	4.7
54.00	11.9	12.8	1.6	0.2	5.4	4.2	4.6
55.00	11.7	12.5	1.3	0.3	5.2	4.2	4.5
56.00	11.6	12.1	1.7	0.2	5.5	4.2	4.3
57.00	11.0	11.5	1.5	0.2	5.4	4.3	4.2
58.00	10.9	11.1	1.2	0.2	5.4	3.8	4.2
59.00	10.5	10.9	1.0	0.2	5.6	3.6	4.1
60.00	10.3	10.4	0.9	0.2	5.5	3.4	4.0
61.00	10.1	9.9	1.0	0.3	5.7	3.5	4.0
62.00	9.7	9.7	0.8	0.3	5.8	3.7	3.9
63.00	9.5	9.4	1.0	0.3	5.7	3.4	3.8
64.00	9.3	8.9	0.7	0.3	5.8	3.4	3.7
65.00	9.2	8.8	0.5	0.3	5.8	3.1	3.6
66.00	8.8	8.3	0.4	0.3	5.8	3.2	3.5
67.00	8.7	8.1	0.6	0.3	6.1	3.1	3.4
68.00	8.6	7.7	0.4	0.4	5.9	3.1	3.3
69.00	8.5	7.5	0.4	0.4	6.3	2.7	3.3
70.00	8.4	7.2	0.3	0.5	6.5	2.5	3.3
71.00	8.3	7.0	0.4	0.5	6.2	2.8	3.2
72.00	8.0	6.9	0.3	0.5	6.2	2.6	3.2
73.00	8.1	6.6	0.4	0.5	6.2	2.4	3.1
74.00	8.0	6.4	0.3	0.5	6.4	2.5	3.1
75.00	7.9	6.1	0.5	0.5	6.5	2.5	3.0
76.00	7.6	6.1	0.3	0.6	6.3	2.2	2.9
77.00	7.5	6.0	0.3	0.6	6.5	2.2	2.9
78.00	7.3	5.6	0.2	0.6	6.6	2.2	2.8
79.00	7.2	5.6	0.4	0.7	6.7	2.2	2.8
80.00	7.1	5.5	0.1	0.7	6.8	1.9	2.8

Shipboard Contamination Flow Test
Mobile, Alabama

Trial No.: 04-NH-09
Z Time: 10:10:00

Date: 27 May 1988

Miran Data µg/L

Z Time	Pos 01 1-37	Pos 02 1-40	Pos 03 1-44	Pos 04 1-46	Pos 05 01-49	Pos 06 01-51	Pos 07 01-53
-5.00	0.0	0.0	0.0	0.0	0.0	0.0	0.0
-4.00	0.0	0.0	0.0	0.0	0.0	0.0	0.0
-3.00	0.0	0.0	0.0	0.0	0.0	0.0	0.0
-2.00	0.0	0.0	0.0	0.0	0.0	0.0	0.0
-1.00	0.0	0.0	0.0	0.0	0.0	0.0	0.0
0.00	0.0	0.0	0.0	0.0	0.0	0.0	0.0
1.00	97.0	101.3	0.0	0.0	0.0	0.0	0.0
2.00	123.6	117.0	2.3	0.0	0.0	2.8	0.3
3.00	123.6	117.0	11.4	0.1	0.0	17.4	5.3
4.00	123.6	117.0	18.8	0.8	0.0	31.3	13.1
5.00	123.6	117.0	28.8	1.6	0.0	36.2	18.8
6.00	123.6	117.0	34.3	2.0	0.1	35.8	22.9
7.00	123.6	117.0	31.6	2.0	0.1	36.2	24.0
8.00	117.7	117.0	33.2	2.0	0.2	37.6	24.6
9.00	108.9	117.0	33.3	2.0	0.2	34.5	24.3
10.00	99.1	117.0	31.8	2.0	0.3	31.7	23.6
11.00	91.1	113.5	29.2	2.0	0.4	29.9	22.8
12.00	82.9	106.2	26.3	1.8	0.4	27.4	21.9
13.00	77.3	98.8	24.4	1.7	0.6	27.3	20.8
14.00	72.8	91.5	23.1	1.6	0.5	25.6	19.7
15.00	66.1	85.9	21.1	1.5	0.7	23.8	18.9
16.00	62.2	80.9	19.6	1.4	0.6	21.5	18.0
17.00	58.1	76.0	17.4	1.3	0.6	20.9	17.3
18.00	54.5	70.9	16.6	1.2	0.8	20.1	16.4
19.00	50.8	67.4	15.5	1.1	0.8	19.3	15.6
20.00	48.4	63.5	15.8	1.0	0.8	18.0	15.0
21.00	45.5	59.2	13.7	1.0	0.8	16.7	14.3
22.00	43.3	55.7	12.7	0.9	0.7	16.8	13.7
23.00	41.0	53.0	11.8	0.8	0.8	15.5	13.2
24.00	38.0	50.2	11.9	0.8	1.0	14.6	12.5
25.00	36.2	48.0	10.5	0.7	3.1	14.3	12.1
26.00	34.6	45.3	11.5	0.6	3.6	13.0	11.8
27.00	33.0	42.9	9.4	0.7	3.8	12.6	11.1
28.00	31.8	40.7	9.1	0.6	3.8	12.0	10.7
29.00	30.3	38.9	8.5	0.6	3.9	11.1	10.5
30.00	29.3	36.8	7.1	0.6	4.0	11.5	10.0
31.00	28.2	35.3	6.6	0.5	3.9	10.9	9.6
32.00	26.6	33.4	6.3	0.5	4.1	10.6	9.1
33.00	25.5	32.2	6.0	0.4	4.0	9.9	8.8
34.00	24.8	30.6	6.2	0.4	4.2	9.4	8.4
35.00	23.8	29.1	6.3	0.4	4.2	8.6	8.1
36.00	22.7	28.1	5.7	0.3	4.2	8.3	7.9
37.00	21.7	26.7	5.6	0.3	4.3	8.2	7.6

Shipboard Contamination Flow Test
Mobile, Alabama

Trial No.: 03-NH-08
Z Time: 13:26:00

Date: 26 May 1988

Miran Data µg/L

Z Time	Pos 08 1-55	Pos 09 1-56	Pos 10 01-55	Pos 12 02-43	Pos 13 02-47	Pos 14 02-49	Pos 15 01-51
-4.00	0.0	0.0	0.0	0.0	0.7	0.0	0.0
-3.00	0.0	0.0	0.0	0.0	0.7	0.0	0.1
-2.00	0.1	0.0	0.0	0.0	0.5	0.0	0.0
-1.00	0.1	0.0	0.0	0.0	0.5	0.1	0.1
0.00	0.1	0.0	0.0	0.0	0.6	0.1	0.2
1.00	3.0	0.8	1.8	4.9	7.9	19.2	29..
2.00	7.1	4.2	6.3	7.5	8.8	15.5	20.3
3.00	7.3	6.0	7.5	1.7	3.6	6.6	10.2
4.00	6.7	6.1	7.0	0.0	1.5	3.3	8.2
5.00	5.8	5.6	6.0	0.0	0.7	1.6	7.1
6.00	5.1	5.1	5.1	0.0	0.9	0.7	1.9
7.00	4.2	4.4	4.1	0.0	1.0	0.2	0.8
8.00	3.3	3.7	3.2	0.0	0.9	0.3	1.4
9.00	3.0	3.1	2.5	0.0	0.6	0.2	1.1
10.00	2.6	2.6	1.9	0.0	0.7	0.4	1.1
11.00	2.2	2.2	1.5	0.0	0.7	0.2	0.5
12.00	1.9	1.8	1.1	0.0	0.7	0.2	0.8
13.00	1.7	1.5	0.9	0.0	0.9	0.2	0.3
14.00	1.6	1.3	0.6	0.0	0.6	0.1	0.6
15.00	1.4	1.1	0.3	0.0	0.5	0.0	2.5
16.00	1.3	1.0	0.1	0.0	0.6	0.1	1.5
17.00	1.2	0.8	0.0	0.0	0.6	0.1	1.5
18.00	1.2	0.8	0.0	0.0	0.7	0.1	1.6
19.00	1.1	0.8	0.0	0.0	1.0	0.3	0.7
20.00	1.1	0.8	0.0	0.0	0.9	0.3	0.1
21.00	1.1	0.7	0.0	0.0	0.7	.2	0.4
22.00	1.1	0.7	0.0	0.0	0.5	0.1	0.1
23.00	1.0	0.6	0.0	0.0	0.2	0.0	0.0
24.00	0.9	0.6	0.0	0.0	0.3	0.1	0.1
25.00	0.9	0.6	0.0	0.0	0.3	0.0	0.0
26.00	1.0	0.5	0.0	0.0	0.3	0.0	0.3
27.00	1.0	0.6	0.0	0.0	0.4	0.0	0.0
28.00	0.9	0.5	0.0	0.0	0.5	0.0	0.2
29.00	1.0	0.6	0.0	0.0	0.7	0.1	0.3

Shipboard Contamination Flow Test
Mobile, Alabama

Trial No.: 03-NH-08 Date: 26 May 1988
Z Time: 13:26:00

Miran Data μg/L

Z Time	Pos 01 1-37	Pos 02 1-40	Pos 03 1-44	Pos 04 1-46	Pos 05 01-49	Pos 06 01-51	Pos 07 01-53
-4.00	0.0	0.0	0.0	0.0	0.0	0.2	0.0
-3.00	0.0	0.0	0.0	0.0	0.0	0.3	0.0
-2.00	0.0	0.0	0.0	0.0	0.0	0.3	0.0
-1.00	0.0	0.0	0.0	0.0	0.1	0.4	0.0
0.00	0.0	0.0	0.0	0.0	0.1	0.3	0.0
1.00	0.7	1.8	0.0	3.4	42.1	1.5	1.1
2.00	5.3	6.8	0.9	13.7	37.1	8.5	5.1
3.00	8.7	8.7	5.3	14.6	17.5	12.4	6.7
4.00	8.7	8.2	8.5	10.9	9.0	12.5	6.9
5.00	7.9	7.1	8.7	7.7	5.6	11.2	6.5
6.00	6.8	6.0	7.9	5.3	3.3	9.4	5.9
7.00	5.7	4.9	6.8	3.4	2.1	7.6	5.1
8.00	4.6	4.0	5.5	2.2	2.2	6.3	4.2
9.00	3.9	3.3	4.3	1.4	1.9	5.4	3.5
10.00	3.2	2.7	3.4	1.0	2.4	4.4	2.9
11.00	2.7	2.3	2.8	0.7	2.0	3.7	2.5
12.00	2.2	1.9	2.2	0.5	1.8	3.2	2.1
13.00	1.9	1.5	1.8	0.3	1.9	2.9	1.8
14.00	1.6	1.2	1.5	0.1	1.6	2.5	1.5
15.00	1.3	0.9	1.2	0.0	1.7	2.2	1.3
16.00	1.0	0.8	0.9	0.0	1.9	2.0	1.1
17.00	0.9	0.6	0.8	0.0	1.9	1.8	1.0
18.00	0.7	0.5	0.6	0.0	2.1	1.7	0.9
19.00	0.7	0.5	0.7	0.0	2.3	1.4	0.8
20.00	0.7	0.4	0.6	0.0	2.3	1.4	0.8
21.00	0.6	0.4	0.6	0.0	2.3	1.3	0.7
22.00	0.5	0.3	0.6	0.0	2.0	1.2	0.6
23.00	0.4	0.2	0.5	0.0	2.1	1.3	0.6
24.00	0.3	0.2	0.5	0.0	2.4	1.3	0.5
25.00	0.3	0.1	0.4	0.0	2.2	1.1	0.5
26.00	0.2	0.1	0.4	0.0	2.3	1.1	0.5
27.00	0.2	0.1	0.3	0.0	2.6	1.1	0.4
28.00	0.2	0.1	0.3	0.0	2.7	1.0	0.4
29.00	0.2	0.0	0.3	0.0	2.9	1.0	0.4

Shipboard Contamination Flow Test
Mobile, Alabama

Trial No.: 03-NH-07
Z Time: 11:53:00

Date: 26 May 1988

Miran Data µg/L

Z Time	Pos 08 1-55	Pos 09 1-56	Pos 10 01-55	Pos 12 02-43	Pos 13 02-47	Pos 14 02-49	Pos 15 01-51
38.00	2.0	3.5	1.1	0.0	0.0	4.1	7.5
39.00	1.9	3.5	1.1	0.0	0.0	4.0	8.2
40.00	1.8	3.5	1.0	0.0	0.0	4.1	12.1
41.00	1.9	3.5	1.0	0.0	0.0	4.5	19.6
42.00	2.1	3.7	1.2	0.0	0.0	4.7	21.1
43.00	2.1	3.7	1.2	0.0	0.0	4.4	10.2
44.00	2.1	3.7	1.2	0.0	0.0	4.2	5.9
45.00	2.1	3.7	1.1	0.0	0.0	4.2	5.6
46.00	1.9	3.7	1.0	0.0	0.0	4.1	4.8
47.00	1.9	3.6	1.0	0.0	0.0	4.1	6.2
48.00	2.0	3.7	0.9	0.0	0.0	4.0	16.0
49.00	1.9	3.7	0.8	0.0	0.0	3.9	11.0
50.00	2.0	3.6	0.8	0.0	0.0	4.0	4.5
51.00	1.9	3.7	0.8	0.0	0.0	4.0	5.9
52.00	2.1	3.8	0.7	0.0	0.0	3.9	5.6
53.00	2.1	3.8	0.8	0.0	0.0	4.0	7.6
54.00	2.0	3.8	0.8	0.0	0.0	4.0	6.0

Shipboard Contamination Flow Test
Mobile, Alabama

Trial No.: 03-NH-07
Z Time: 11:53:00

Date: 26 May 1988

Miran Data µg/L

Z Time	Pos 08 1-55	Pos 09 1-56	Pos 10 01-55	Pos 12 02-43	Pos 13 02-47	Pos 14 02-49	Pos 15 01-51
-4.00	0.2	0.3	0.2	0.0	0.7	1.9	2.5
-3.00	0.3	0.4	0.2	0.0	0.5	1.9	1.2
-2.00	0.2	0.5	0.2	0.0	0.6	2.1	2.3
-1.00	0.2	0.5	0.2	0.0	0.7	2.3	3.5
0.00	0.2	0.6	0.2	0.0	0.8	2.4	1.3
1.00	0.3	0.6	0.2	0.0	0.7	2.6	1.2
2.00	0.3	0.7	0.2	0.0	0.8	2.9	47.9
3.00	3.1	2.1	2.0	0.0	1.2	20.1	113.3
4.00	3.8	3.8	4.0	0.0	1.0	7.5	113.3
5.00	3.5	4.0	3.9	0.0	1.2	5.0	113.3
6.00	3.4	4.1	3.7	0.0	1.3	6.1	112.7
7.00	3.4	4.2	3.6	0.0	1.3	8.3	108.9
8.00	4.2	4.7	4.2	0.0	1.3	8.6	98.1
9.00	3.9	4.9	4.2	0.0	1.4	6.5	88.9
10.00	4.2	5.1	4.3	0.0	1.8	8.8	106.4
11.00	4.2	5.3	4.4	0.0	2.7	8.1	75.3
12.00	4.1	5.3	4.3	1.1	5.9	7.4	75.8
13.00	3.8	5.2	4.1	0.6	4.7	6.3	67.3
14.00	3.6	5.0	3.7	1.0	5.2	6.0	57.5
15.00	3.1	4.7	3.3	1.0	3.9	5.6	52.5
16.00	2.9	4.4	2.9	1.3	3.7	5.5	49.4
17.00	2.7	4.2	2.7	0.2	3.4	5.5	50.6
18.00	2.7	4.1	2.6	0.3	3.6	5.4	51.2
19.00	2.7	4.1	2.6	0.0	1.8	6.0	64.4
20.00	2.6	4.1	2.6	0.0	0.2	4.9	113.3
21.00	2.5	4.0	2.3	0.0	0.1	4.2	113.3
22.00	2.2	3.8	2.1	0.0	0.0	4.4	92.4
23.00	2.2	3.7	2.0	0.0	0.4	4.6	50.6
24.00	2.1	3.6	1.8	0.0	2.3	4.7	44.9
25.00	2.2	3.6	1.8	0.2	2.4	4.8	43.9
26.00	2.0	3.5	1.7	0.4	1.6	5.0	44.5
27.00	2.0	3.4	1.6	0.9	1.6	5.0	36.1
28.00	1.9	3.4	1.5	0.7	1.5	4.8	30.6
29.00	1.8	3.3	1.4	0.2	1.0	4.6	29.8
30.00	1.7	3.3	1.3	0.1	0.3	4.5	33.6
31.00	1.8	3.2	1.3	0.1	0.0	4.5	28.5
32.00	1.9	3.3	1.3	0.1	0.0	4.5	23.8
33.00	2.0	3.3	1.3	0.1	0.1	4.9	32.5
34.00	2.0	3.5	1.3	0.0	0.0	4.6	33.8
35.00	2.0	3.5	1.3	0.0	0.0	3.9	38.1
36.00	2.0	3.5	1.2	0.0	0.0	3.9	9.8
37.00	1.9	3.5	1.1	0.0	0.0	3.9	7.4

Shipboard Contamination Flow Test
Mobile, Alabama

Trial No.: 03-NH-07 Date: 26 May 1988
Z Time: 11:53:00

Miran Data µg/L

Z Time	Pos 01 1-37	Pos 02 1-40	Pos 03 1-44	Pos 04 1-46	Pos 05 01-49	Pos 06 01-51	Pos 07 01-53
38.00	0.5	0.0	0.7	0.8	4.1	1.0	1.5
39.00	0.4	0.0	0.7	0.8	3.9	1.2	1.5
40.00	0.4	0.0	0.6	0.8	3.9	1.0	1.4
41.00	0.4	0.0	0.6	0.8	4.6	1.1	1.4
42.00	0.5	0.0	0.6	1.2	5.0	1.3	1.5
43.00	0.6	0.0	0.6	1.1	4.2	1.3	1.5
44.00	0.5	0.0	0.7	1.0	4.0	1.2	1.5
45.00	0.5	0.0	0.6	0.9	4.0	1.2	1.5
46.00	0.4	0.0	0.5	0.8	4.0	1.2	1.4
47.00	0.3	0.0	0.5	0.8	4.1	0.9	1.4
48.00	0.3	0.0	0.5	0.8	4.2	0.8	1.4
49.00	0.3	0.0	0.5	0.7	4.5	1.0	1.4
50.00	0.3	0.0	0.4	0.8	4.4	0.9	1.3
51.00	0.3	0.0	0.4	0.9	4.6	0.9	1.3
52.00	0.3	0.0	0.4	0.9	4.6	0.9	1.3
53.00	0.3	0.0	0.5	0.9	4.6	0.9	1.3
54.00	0.4	0.0	0.5	0.9	4.9	1.0	1.4

Shipboard Contamination Flow Test
Mobile, Alabama

Trial No.: 03-NH-07 Date: 26 May 1988
Z Time: 11:53:00

Miran Data μg/L

Z Time	Pos 01 1-37	Pos 02 1-40	Pos 03 1-44	Pos 04 1-46	Pos 05 01-49	Pos 06 01-51	Pos 07 01-53
-4.00	0.0	0.0	0.0	0.0	0.1	0.1	0.1
-3.00	0.0	0.0	0.0	0.0	0.1	0.2	0.2
-2.00	0.0	0.0	0.0	0.0	0.1	0.2	0.2
-1.00	0.0	0.0	0.0	0.0	0.1	0.1	0.2
0.00	0.0	0.0	0.0	0.0	0.1	0.2	0.2
1.00	0.0	0.0	0.0	0.0	0.1	0.2	0.2
2.00	0.0	0.0	0.0	0.0	0.3	0.2	0.2
3.00	0.2	0.0	0.0	3.6	30.3	1.0	1.7
4.00	2.3	0.0	0.5	7.8	9.9	5.2	3.6
5.00	3.1	0.0	2.6	5.6	4.8	6.0	3.6
6.00	2.9	0.0	3.1	4.2	5.6	5.5	3.6
7.00	2.8	0.0	3.1	3.8	8.2	4.9	3.6
8.00	3.2	0.0	3.1	5.3	11.4	5.4	4.2
9.00	3.6	0.0	3.3	4.8	6.7	5.6	4.2
10.00	3.6	0.0	3.5	4.8	9.7	5.6	4.3
11.00	3.9	0.0	3.7	5.1	8.7	6.0	4.5
12.00	4.0	0.0	3.9	4.6	6.9	6.1	4.4
13.00	3.8	0.0	3.9	4.0	5.0	5.7	4.2
14.00	3.4	0.0	3.8	3.2	4.0	5.2	3.9
15.00	3.0	0.0	3.3	2.5	3.6	4.4	3.6
16.00	2.7	0.0	2.9	2.1	3.7	3.9	3.3
17.00	2.3	0.0	2.5	1.9	4.0	3.6	3.0
18.00	2.1	0.0	2.1	1.8	4.2	3.3	2.8
19.00	2.0	0.0	2.0	2.1	5.7	3.2	2.8
20.00	1.9	0.0	1.9	2.1	4.6	3.2	2.7
21.00	1.9	0.0	1.9	1.7	2.9	3.1	2.6
22.00	1.5	0.0	1.6	1.3	3.3	2.6	2.3
23.00	1.3	0.0	1.4	1.3	3.4	2.2	2.2
24.00	1.2	0.0	1.3	1.1	3.6	2.1	2.1
25.00	1.1	0.0	1.1	1.1	3.5	2.1	2.0
26.00	0.9	0.0	1.1	1.0	3.3	2.0	1.9
27.00	0.9	0.0	0.9	1.0	3.4	1.7	1.8
28.00	0.7	0.0	0.8	0.9	3.2	1.9	1.7
29.00	0.7	0.0	0.8	0.8	3.0	1.7	1.6
30.00	0.6	0.0	0.7	0.7	3.2	1.3	1.6
31.00	0.5	0.0	0.6	0.7	3.4	1.3	1.5
32.00	0.5	0.0	0.5	0.8	3.8	1.3	1.5
33.00	0.5	0.0	0.5	0.9	4.5	1.5	1.6
34.00	0.6	0.0	0.7	1.1	4.4	1.3	1.6
35.00	0.7	0.0	0.6	1.1	3.5	1.6	1.6
36.00	0.6	0.0	0.7	1.0	3.4	1.4	1.5
37.00	0.5	0.0	0.8	0.8	3.6	1.2	1.5

Shipboard Contamination Flow Test
Mobile, Alabama

Trial No.: 03-NH-06
Z Time: 10:40:00

Date: 26 May 1988

Miran Data µg/L

Z Time	Pos 08 1-55	Pos 09 1-56	Pos 10 01-55	Pos 12 02-43	Pos 13 02-47	Pos 14 02-49	Pos 15 01-51
39.00	0.3	2.5	4.3	6.4	3.0	6.8	0.1
[illegible].00	0.4	2.6	4.4	6.4	3.0	6.9	0.1
40.00	0.4	2.6	4.5	6.6	3.0	7.3	0.1
41.00	0.3	2.6	4.6	6.6	2.9	7.1	0.1
42.00	0.4	2.6	4.6	7.3	3.1	7.2	0.2
43.00	0.3	2.7	4.7	7.5	3.2	7.6	0.2
44.00	0.4	2.7	4.8	7.4	3.3	7.6	0.2
45.00	0.4	2.7	4.8	7.3	3.4	7.7	0.2
46.00	0.4	2.7	4.9	7.5	3.5	7.9	0.1
47.00	0.3	2.8	5.0	7.9	3.7	8.0	0.2
48.00	0.4	2.8	5.0	8.2	3.7	8.1	0.2
49.00	0.5	2.8	5.1	8.3	3.8	8.2	0.2
50.00	0.4	2.8	5.1	8.6	3.9	8.4	0.2
51.00	0.3	2.9	5.2	8.8	4.0	8.5	0.2
52.00	0.3	2.9	5.3	8.9	4.0	8.6	0.2
53.00	0.3	2.9	5.3	9.0	4.1	8.6	0.2
54.00	0.4	2.9	5.4	9.0	4.1	8.7	0.2
55.00	0.4	2.9	5.4	9.3	4.2	8.9	0.3
56.00	0.4	2.9	5.5	9.5	4.4	9.0	0.2
57.00	0.4	3.0	5.5	10.0	4.6	9.3	0.3
58.00	0.4	3.0	5.6	10.1	4.8	9.5	0.3
59.00	0.4	3.1	5.7	10.4	5.2	9.6	0.3
60.00	0.5	3.1	5.8	10.8	5.4	9.8	0.3

Shipboard Contamination Flow Test
Mobile, Alabama

Trial No.: 03-NH-06
Z Time: 10:40:00

Date: 26 May 1988

Miran Data μg/L

Z Time	Pos 08 1-55	Pos 09 1-56	Pos 10 01-55	Pos 12 02-43	Pos 13 02-47	Pos 14 02-49	Pos 15 01-51
-4.00	0.0	0.0	1.0	0.0	0.5	1.0	0.0
-3.00	0.0	0.0	1.1	0.0	0.4	1.0	0.0
-2.00	0.0	0.1	1.2	0.0	0.6	1.2	0.0
-1.00	0.0	0.1	1.3	0.0	0.6	1.3	0.0
0.00	0.0	0.1	1.3	0.0	0.6	1.4	0.0
1.00	0.0	0.2	1.6	0.0	0.5	3.3	0.0
2.00	0.2	0.6	2.1	0.2	0.4	4.0	0.0
3.00	0.8	1.2	2.8	0.5	0.6	6.9	0.0
4.00	1.1	1.7	3.5	0.0	0.7	5.2	3.6
5.00	1.4	2.2	3.9	1.9	1.0	5.2	2.1
6.00	1.7	2.5	4.3	5.6	3.0	5.1	1.4
7.00	1.6	2.7	4.5	5.6	2.6	5.3	0.8
8.00	1.9	3.0	4.7	3.1	1.2	5.2	0.6
9.00	1.8	3.1	4.8	2.1	1.0	4.9	0.5
10.00	1.8	3.2	4.8	1.1	1.0	4.5	0.5
11.00	1.5	3.1	4.6	0.7	0.9	3.4	0.5
12.00	1.2	2.9	4.3	0.9	0.9	3.9	0.5
13.00	1.1	2.8	4.2	1.4	1.0	5.1	0.3
14.00	1.5	2.9	4.3	1.9	1.0	5.9	0.2
15.00	1.4	3.1	4.4	1.7	1.1	5.6	0.2
16.00	1.6	3.2	4.6	1.7	1.2	5.6	0.2
17.00	1.3	3.1	4.6	2.2	1.2	4.2	0.3
18.00	1.1	2.9	4.3	2.5	1.2	4.0	0.3
19.00	1.0	2.7	4.1	4.3	1.3	4.2	0.3
20.00	0.9	2.7	4.0	5.3	1.4	5.6	0.2
21.00	1.0	2.8	4.1	4.3	1.4	6.0	0.2
22.00	1.1	2.9	4.3	3.4	1.4	5.9	0.2
23.00	1.0	2.9	4.3	3.0	1.6	5.3	0.1
24.00	1.0	2.9	4.3	3.3	1.7	5.1	0.2
25.00	0.8	2.8	4.1	3.5	1.7	4.9	0.2
26.00	0.6	2.7	4.0	3.9	1.8	5.1	0.2
27.00	0.6	2.6	4.0	4.1	1.9	5.5	0.2
28.00	0.6	2.6	4.0	4.9	2.0	5.4	0.2
29.00	0.5	2.5	4.0	7.2	2.1	5.6	0.2
30.00	0.4	2.6	4.0	7.1	2.2	5.7	0.2
31.00	0.4	2.5	4.0	5.5	2.4	6.1	0.2
32.00	0.5	2.6	4.1	6.1	2.5	6.3	0.1
33.00	0.5	2.6	4.2	7.8	2.5	6.2	0.2
34.00	0.5	2.6	4.2	6.0	2.6	6.2	0.2
35.00	0.4	2.6	4.2	5.8	2.7	6.4	0.2
36.00	0.4	2.6	4.3	6.1	2.8	6.5	0.1
37.00	0.4	2.6	4.3	6.1	2.8	6.6	0.1

Shipboard Contamination Flow Test
Mobile, Alabama

Trial No.: 03-NH-06
Z Time: 10:40:00

Date: 26 May 1988

Miran Data $\mu g/L$

Z Time	Pos 01 1-37	Pos 02 1-40	Pos 03 1-44	Pos 04 1-46	Pos 05 01-49	Pos 06 01-51	Pos 07 01-53
38.00	1.1	0.5	0.6	0.7	2.9	0.5	0.9
39.00	1.1	0.5	0.6	0.7	3.0	0.4	0.8
40.00	1.0	0.4	0.6	0.8	3.3	0.5	0.8
41.00	1.1	0.4	0.5	0.8	3.0	0.4	0.9
42.00	1.0	0.4	0.6	0.8	3.1	0.5	0.8
43.00	1.0	0.4	0.5	0.8	3.5	0.4	0.8
44.00	1.0	0.4	0.5	0.9	3.4	0.5	0.8
45.00	1.0	0.4	0.5	0.8	3.4	0.5	0.8
46.00	1.0	0.4	0.5	0.8	3.5	0.5	0.8
47.00	1.0	0.3	0.5	0.9	3.5	0.4	0.8
48.00	1.0	0.3	0.4	0.8	3.5	0.3	0.8
49.00	1.0	0.3	0.4	0.9	3.5	0.4	0.8
50.00	0.9	0.3	0.4	0.9	3.6	0.4	0.8
51.00	0.9	0.3	0.5	0.9	3.6	0.4	0.8
52.00	0.9	0.3	0.5	0.9	3.7	0.5	0.8
53.00	1.0	0.3	0.4	0.9	3.5	0.3	0.8
54.00	0.9	0.3	0.4	0.8	3.6	0.3	0.8
55.00	0.9	0.2	0.5	0.8	3.6	0.4	0.8
56.00	0.9	0.2	0.4	0.8	3.8	0.2	0.7
57.00	0.8	0.2	0.4	0.9	4.0	0.3	0.7
58.00	0.9	0.2	0.4	1.0	4.3	0.3	0.8
59.00	0.9	0.3	0.4	1.0	4.2	0.4	0.8
60.00	0.9	0.2	0.3	1.0	4.3	0.4	0.8

Shipboard Contamination Flow Test
Mobile, Alabama

Trial No.: 03-NH-06 Date: 26 May 1988
Z Time: 10:40:00

Miran Data μg/L

Z Time	Pos 01 1-37	Pos 02 1-40	Pos 03 1-44	Pos 04 1-46	Pos 05 01-49	Pos 06 01-51	Pos 07 01-53
-4.00	0.0	0.0	0.0	0.0	0.6	0.1	0.0
-3.00	0.0	0.0	0.0	0.0	0.4	0.0	0.0
-2.00	0.0	0.0	0.0	0.0	0.7	0.1	0.0
-1.00	0.0	0.0	0.0	0.0	0.7	0.2	0.0
0.00	0.0	0.0	0.0	0.0	0.6	0.1	0.0
1.00	0.0	0.1	0.0	0.2	3.5	0.1	0.1
2.00	0.2	0.3	0.0	1.0	5.4	0.4	0.5
3.00	0.8	1.0	0.0	2.5	10.4	1.0	1.2
4.00	1.7	1.5	0.3	3.3	7.2	2.3	1.8
5.00	2.2	2.0	0.9	3.5	7.3	2.7	2.2
6.00	2.5	2.2	1.2	3.5	7.1	3.2	2.5
7.00	2.8	2.4	1.6	3.4	7.2	3.4	2.7
8.00	3.0	2.6	1.8	3.5	7.0	3.5	2.8
9.00	3.1	2.8	2.0	3.5	6.0	3.6	3.0
10.00	3.2	2.6	2.2	3.1	4.9	3.5	2.9
11.00	3.0	2.3	2.2	2.4	2.7	2.9	2.6
12.00	2.6	2.0	2.0	1.8	2.9	2.6	2.3
13.00	2.4	1.9	1.6	1.8	4.7	2.4	2.1
14.00	2.5	2.0	1.6	2.4	6.6	2.3	2.3
15.00	2.6	2.2	1.6	2.6	5.6	2.7	2.4
16.00	2.8	2.3	1.7	2.8	5.9	2.8	2.5
17.00	2.7	2.1	1.9	2.3	3.0	2.9	2.3
18.00	2.5	1.8	1.8	1.7	2.3	2.4	2.1
19.00	2.2	1.5	1.6	1.3	2.2	2.1	1.8
20.00	1.9	1.4	1.3	1.3	4.8	1.6	1.7
21.00	2.0	1.6	1.2	1.8	5.1	1.8	1.8
22.00	2.3	1.7	1.2	2.0	4.8	2.1	1.9
23.00	2.2	1.7	1.3	1.8	3.7	2.1	1.8
24.00	2.2	1.5	1.3	1.6	3.1	1.9	1.8
25.00	2.0	1.3	1.4	1.3	2.4	1.7	1.6
26.00	1.7	1.1	1.2	1.0	2.4	1.2	1.4
27.00	1.6	1.1	1.0	1.0	2.9	1.0	1.3
28.00	1.5	0.9	0.9	0.9	2.6	1.0	1.2
29.00	1.4	0.8	0.8	0.8	2.5	0.9	1.2
30.00	1.3	0.7	0.8	0.8	2.6	0.8	1.1
31.00	1.3	0.7	0.7	0.8	3.3	0.7	1.1
32.00	1.3	0.8	0.6	1.0	3.3	0.7	1.1
33.00	1.4	0.8	0.6	1.0	2.9	0.9	1.0
34.00	1.3	0.7	0.7	0.9	2.7	0.7	1.0
35.00	1.2	0.6	0.7	0.8	2.8	0.7	0.9
36.00	1.2	0.6	0.6	0.8	2.9	0.6	0.9
37.00	1.1	0.5	0.6	0.7	2.6	0.5	0.9

Shipboard Contamination Flow Test
Mobile, Alabama

Trial No.: 02-NH-05
Z Time: 13:00:00

Date: 25 May 1988

Miran Data μg/L

Z Time	Pos 06 1-51	Pos 07 1-53	Pos 08 1-55	Pos 09 1-56	Pos 10 01-55	Pos 11 02-34	Pos 12 02-43
-4.00	0.1	0.0	0.0	0.0	0.0	0.0	0.0
-3.00	0.0	0.0	0.1	0.0	0.0	0.0	0.0
-2.00	0.0	0.0	0.0	0.0	0.1	0.0	0.0
-1.00	0.1	0.0	0.0	0.0	0.1	0.0	0.0
0.00	0.0	0.0	0.0	0.0	0.1	0.0	0.0
1.00	0.8	2.2	4.9	3.2	2.3	0.0	0.0
2.00	12.6	7.8	8.3	7.7	9.8	0.0	0.0
3.00	12.8	8.0	7.2	7.4	9.1	0.0	0.0
4.00	11.8	8.0	6.7	7.2	8.4	0.0	0.0
5.00	10.9	7.8	6.3	6.9	8.1	0.0	0.0
6.00	9.4	7.0	5.1	6.1	7.0	0.0	0.0
7.00	7.4	5.9	4.2	5.1	5.8	0.0	0.0
8.00	6.0	5.2	3.7	4.4	5.1	0.0	0.0
9.00	5.2	4.5	3.1	3.8	4.4	0.0	0.0
10.00	4.3	3.8	2.6	3.1	3.8	0.0	0.0
11.00	3.6	3.2	2.3	2.6	3.3	0.0	0.0
12.00	2.8	2.8	1.9	2.2	2.8	0.0	0.0
13.00	2.3	2.4	1.5	1.9	2.5	0.0	0.0
14.00	2.0	2.1	1.4	1.7	2.2	0.0	0.0
15.00	1.8	1.9	1.3	1.4	1.7	0.0	0.0
16.00	1.6	1.7	1.1	1.3	1.6	0.0	0.0
17.00	1.3	1.5	0.9	1.1	1.6	0.0	0.0
18.00	1.1	1.4	0.9	1.0	1.6	0.0	0.0
19.00	0.9	1.3	0.8	0.9	1.4	0.0	0.2
20.00	0.9	1.2	0.7	0.8	1.2	0.0	0.0
21.00	0.7	1.1	0.8	0.7	1.1	0.0	0.0
22.00	0.7	1.1	0.6	0.7	1.0	0.0	0.0
23.00	0.5	1.0	0.7	0.6	0.7	0.0	0.0
24.00	0.4	0.9	0.7	0.6	0.9	0.0	0.0
25.00	0.4	0.9	0.6	0.5	0.7	0.0	0.0
26.00	0.5	0.8	0.7	0.5	0.6	0.0	0.0
27.00	0.3	0.8	0.6	0.5	0.6	0.0	0.0
28.00	0.4	0.8	0.7	0.5	0.4	0.0	0.0
29.00	0.4	0.8	0.5	0.4	0.4	0.0	1.3
30.00	0.3	0.8	0.7	0.5	0.3	0.0	1.0

Shipboard Contamination Flow Test
Mobile, Alabama

Trial No.: 02-NH-04
Z Time: 11:40:00

Date: 25 May 1988

Miran Data ug/L

Z Time	Pos 06 1-51	Pos 07 1-53	Pos 08 1-55	Pos 09 1-56	Pos 10 01-55	Pos 11 02-34	Pos 12 02-43
38.00	1.1	1.3	0.8	1.6	1.6	1.3	2.2
39.00	1.0	1.3	0.8	1.5	1.6	1.4	2.2
40.00	1.0	1.2	0.8	1.5	1.6	1.7	2.3
41.00	1.1	1.2	0.8	1.5	1.6	1.9	2.8
42.00	0.9	1.2	0.8	1.5	1.6	1.8	2.6
43.00	0.9	1.2	0.8	1.5	1.7	1.9	2.6
44.00	0.8	1.2	0.9	1.5	1.6	1.7	2.5
45.00	0.8	1.2	0.8	1.5	1.7	1.9	2.5
46.00	0.8	1.2	0.9	1.5	1.7	2.0	2.8
47.00	0.9	1.2	0.8	1.5	1.7	1.9	2.8
48.00	0.9	1.1	0.9	1.5	1.7	2.0	2.8
49.00	0.7	1.2	0.9	1.5	1.7	1.9	2.9
50.00	0.8	1.1	0.9	1.5	1.6	1.9	2.9

Chipboard Contamination Flow Test
Mobile, Alabama

Trial No.: 02-NH-04 Date: 25 May 1988
Z Time: 11:40:00

Miran Data ug/L

Z Time	Pos 06 1-51	Pos 07 1-53	Pos 08 1-55	Pos 09 1-56	Pos 10 01-55	Pos 11 02-34	Pos 12 02-43
-4.00	0.2	0.1	0.0	0.0	0.0	0.1	0.6
-3.00	0.1	0.1	0.0	0.0	0.0	0.2	0.6
-2.00	0.2	0.1	0.0	0.0	0.0	0.4	0.9
-1.00	0.2	0.1	0.0	0.0	0.0	0.2	0.8
0.00	0.2	0.1	0.0	0.0	0.0	0.2	0.8
1.00	1.1	2.3	4.0	2.5	2.1	0.3	1.1
2.00	12.6	10.1	12.6	9.9	11.4	0.4	1.3
3.00	20.3	13.3	12.7	12.1	14.3	0.5	1.5
4.00	20.9	14.3	12.5	12.8	14.8	0.4	1.5
5.00	19.5	13.9	11.6	12.6	13.8	0.4	1.2
6.00	17.8	13.2	10.7	12.3	13.1	0.7	1.4
7.00	15.8	11.9	9.0	11.1	11.5	0.6	1.4
8.00	13.5	10.7	8.3	10.1	10.1	0.7	1.6
9.00	12.0	9.7	7.4	9.3	9.2	0.8	1.8
10.00	11.0	8.8	6.7	8.5	8.4	0.8	1.8
11.00	9.6	7.7	5.7	7.5	7.4	0.9	1.9
12.00	8.3	6.8	4.9	6.7	6.5	1.1	2.1
13.00	7.3	6.0	4.2	5.9	5.7	1.1	2.1
14.00	6.3	5.3	3.7	5.3	5.0	1.0	1.9
15.00	5.6	4.7	3.2	4.8	4.4	1.0	1.9
16.00	4.9	4.2	2.9	4.3	4.0	1.2	2.1
17.00	4.5	3.8	2.6	3.9	3.6	1.2	2.2
18.00	4.0	3.4	2.3	3.5	3.3	1.2	2.3
19.00	3.5	3.1	2.1	3.3	3.0	1.2	2.4
20.00	3.3	2.9	1.9	3.1	2.8	1.0	2.3
21.00	3.2	2.7	1.7	2.8	2.6	1.1	2.4
22.00	2.7	2.5	1.6	2.6	2.4	1.2	2.4
23.00	2.4	2.3	1.4	2.5	2.2	1.3	2.7
24.00	2.5	2.2	1.5	2.4	2.1	1.6	2.8
25.00	2.1	2.1	1.4	2.3	2.0	1.6	2.9
26.00	2.1	2.0	1.3	2.2	2.0	1.8	2.8
27.00	2.1	1.9	1.2	2.1	1.9	1.9	2.7
28.00	1.8	1.9	1.2	2.1	1.8	2.0	2.8
29.00	1.8	1.8	1.1	2.0	1.7	1.7	2.6
30.00	1.7	1.7	1.1	2.0	1.7	1.4	2.5
31.00	1.8	1.7	1.2	1.9	1.7	1.4	2.3
32.00	1.7	1.7	1.1	1.9	1.7	1.5	2.3
33.00	1.3	1.5	1.0	1.8	1.7	1.6	2.4
34.00	1.4	1.5	1.0	1.7	1.7	1.7	2.4
35.00	1.2	1.4	1.0	1.7	1.7	1.5	2.3
36.00	0.9	1.4	0.8	1.7	1.6	1.5	2.2
37.00	1.1	1.3	0.9	1.6	1.6	1.4	2.1

ADDENDA: MIRAN DATA FOR SHADWELL FIELD TESTS

REFERENCES

1. NRL Publication 0076-6180, October 1986.

2. H. Wohltjen, Sens. & Actuators 5, 307 (1984).

3. Details of MIRAN settings and detection limits were obtained from Foxboro promotional literature (PUB-522, 1981).

response to the simulant vapor. It is not surprising, then, that some of the coatings gave little or no response to DEM during these tests. By the selection of coatings with adequate sensitivity to the vapor(s) of interest, the array response can be maximized.

3. Noise/drift reduction. As noted in the discussion, significant drift in the frequency baseline will present problems in the accurate determination of frequency responses. The use of temperature controlled devices will minimize this drift. As environmental conditions change during the day, the sensor baseline can be re-zeroed to compensate for drift arising from changes in the ambient conditions.

The use of a SAW device configuration with lower noise, such as the resonator, will serve to reduce the detection limit of each sensor and the array as a whole.

SUMMARY

The SAW device has been demonstrated as a reliable sensor technology suitable for detection of vapor phase chemicals in field and shipboard applications. Performance of the 4-SAW array during field tests closely matched the performance under laboratory conditions. Comparison of SAW performance with the MIRANs indicates that the SAW is a viable alternative sensor technology for this type of environmental monitoring. The 4-SAW array has the potential for detection and identification of target vapors at low concentration. Although the absolute detection limit of the 4-SAW array was slightly higher than that of the MIRANs, the detection limit could be further improved by implementing some or all of the recommendations listed in this report. The advantages of the SAW technology include:

- rapid, sensitive response
- ruggedness, reliable performance
- small size, portability
- low cost
- versatility (detection capabilities can be customized for a given application by the selection of appropriate coatings).

ACKNOWLEDGEMENTS

The authors wish to thank the NRL personnel assigned to the Shadwell facility, Brad Havlevik and Terry Toomey, and the US Coast Guard for their cooperation and outstanding efforts on our behalf during these tests. We are grateful to Dr. Fred Williams of the NRL Chemistry Division for alerting us to this opportunity and allowing us to participate in the field tests. This work was funded under NRL contract N-00014-88-C-2247.

RECOMMENDATIONS

The SAW sensors used in this study performed well , and the observed responses were in keeping with expectations based on lab results. The devices did not appear to be adversely affected by environmental conditions enccuntered during thes shipboard tests. Based on the results presented here, the following reccmmendations are offered to enhance the performance of the SAW array in the field.

1. Continuous monitoring vs. purge/sample methods. Under the current configuration, a baseline response to a purged air stream is subtracted from the ambient response. This requires the use of a trap, a programmed purge/sample cycle, and a data reduction algorithm to calculate frequency differences. Previous discussions have indicated the problems inherent in this approach, specifically the effects of vapor breakthrough from the charcoal trap and errors arising from the data reduction algorithm. In addition, use of the purge/sample cycle configuration significantly reduces the time resolution that can be realized, with only 1 data point acquired every 2-4 minutes.

   By employing a continuous monitoring configuration, the frequency can be recorded every 2 seconds, significantly improving the time resolution. This configuration also eliminates the need for a charcoal trap, a purge/sample cycle, and the problems inherent in their use. When used as an environmental monitor, the sensitivity and selectivity of the SAW response will be determined by the coatings, but some response to interferences would be expected. Since most interferences (such as water vapor, exhaust fumes, etc.) are present in small or relatively constant concentrations, the response to these vapors will change very little over time. The introduction of a challenge vapor will appear as a frequency shift superimposed on the normal ambient background.

   In addition, continuous monitoring will simplify the detection algorithm. Under the current purge/sample configuration, the response pattern for the 4 SAW array would be compared to response patterns representing various vapors stored in a library. In a shipboard environment, this response pattern would represent the array response to **all** vapors present, making definitive identification of a target vapor more difficult. In the continuous mode, those interferences which are normally present would become part of the ambient background response or baseline. The introduction of a target vapor would result in an array response pattern that more closely matches the library response pattern. By eliminating the need for multicomponent interference corrections, the pattern recognition/detection algorithm can be greatly simplified and made more reliable.

2. Selection of coatings. For the purposes of these tests, 4 coated sensors were selected based on past performance and availablity. No attempt was made to maximize the array

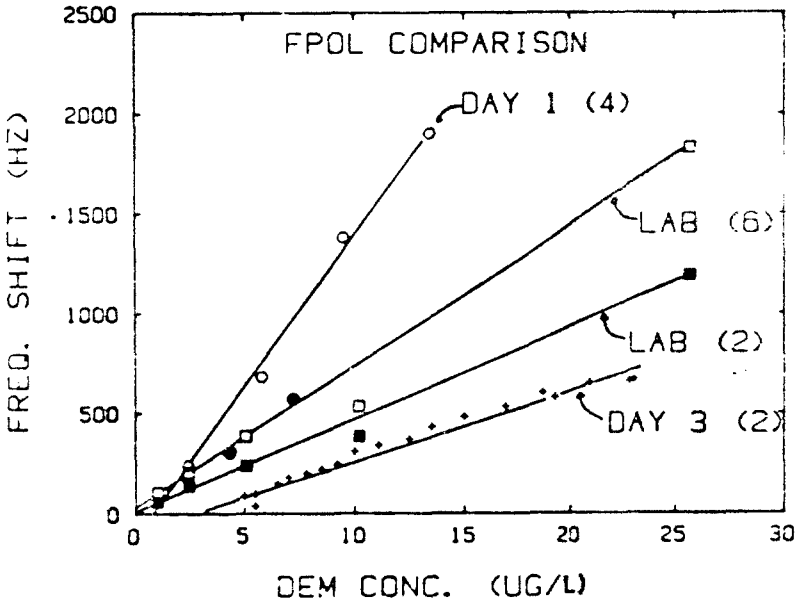


FIGURE 19. Comparison of FPOL response sensitivities for field data and lab data. Sampling cycle times for individual curves are in parentheses.

between the two sets of data. The relative errors associated with data from the field tests have been discussed previously.

The sensitivity of the FPOL sensor decreased to 46.3 Hz/μg/L in the lab when a 2 minute cycle was used. In the field, sensitivities of 39.7 Hz/μg/L (day 2) and 37.3 Hz/μg/L (day 3) were observed, which also indicates good agreement with the lab data. Even though the total responses decreased on day 3, probably as a result of saturation and breakthrough of the charcoal traps, the sensitivity of the device did not change significantly.

These results indicate that the performance during the field tests compares well with the observed response performance in the laboratory. There is a significant decrease in calculated frequency shifts when the 2 minute cycle is used. It is possible that, even though steady sensor responses are achievable in 1 minute or less, idiosyncracies in the data reduction algorithm result in lower calculated responses. This would be the case if the algorithm takes a 1 minute average to determine the peak maximum frequency and baseline frequency to calculate a frequency difference. Even though sensor responses stabilized in less than 1 minute, a longer cycle would be needed to obtain a representative average for the peak maximum and the baseline frequency.

Field results also indicate that charcoal traps would require continuous maintenance if this array configuration is to provide reliable data. Under conditions of high humidity or continuous vapor challenges, the traps could saturate in a relatively short period of time. The use of larger volume traps would strech the usable time frame, but may significantly affect the amount of air flow which could be sent to the sensor.

TABLE III. SENSOR/ARRAY SENSITIVITY AND DETECTION LIMITS

SAW Coating		Sensitivity[a] (Hz/μg/L)	Detection Limit[b] (μg/L)
LAB STUDIES:			
FPOL (2 min.)		46.3	1.1
(6 min.)		71.2	0.7
TENAX (2 min.)		7.5	6.7
(6 min.)		14.0	3.6
ECEL (2 min.)		16.5	3.0
(6 min.)		26.9	1.9
PIB (2 min.)		0.75	67
(6 min.)		1.3	38
Σ (2 min.)		70.0	2.9
(6 min.)	(<10 μg/L)	77.8	2.6
	(>10 μg/L)	120.3	---
FIELD TESTS:			
FPOL (tests #1/2 - 4 min.)		142/83[c] (day 1)	---
(tests #4/5 - 2 min.)		39.7 (day 2)	---
(test #6 - 2 min.)		37.3 (day 3)	---

[a]Assumes an average noise level of 25 Hz for individual coated SAW devices, and 100 Hz for Σ.
[b]Assumes a signal to noise ratio (S/N) of 2.
[c]Calculated sensitivities from the slopes of curves a and b in Figure 11. Slope for curve b assumes a zero x-intercept.

DISCUSSION

The FPOL sensor sensitivities for the field tests are summarized in Table III. These calibration curves are compared with calibration curves for lab tests, using a 2 minute and a 6 minute cycle, in Figure 19. It can be seen that while the results for test 1 are significantly higher, the responses for test 2 (signified by • in Figure 19) are in line with the lab results using the 6 minute cycle. The sensitivity of the FPOL sensor was 83 Hz/μg/L for field test 2 (4 min. cycle) and 71.2 Hz/μg/L for the lab test (6 min. cycle). Considering the differences in ambient conditions between the field tests and lab studies, such as temperature and relative humidity, there is very good agreement

In all cases, the frequency shifts determined for the 2 minute cycle were 25-50% lower than frequency shifts determined for the 6 minute cycle. It also appears that the sensitivity decreased when the cycle was increased to 8 minutes for the FPOL sensor. For the other sensors, however, the data in Table II indicate reasonably good agreement between the 6 and 8 minute cycles. The discrepancies noted for the FPOL sensor may be the result of large errors associated with some of the calculated shifts, and errors resulting from insufficient time resolution for the 8 minute cycle.

The relative sensitivities of the sensors is displayed in Figure 18. FPOL exhibited the highest sensitivity to DEM, followed by ECEL and TENAX. The sensitivities of the individual sensors, calculated as the slopes of the calibration curves, are given in Table III along with estimated detection limits for the 2 and 6 minute cycles. It should be noted that the FPOL response dominates the cumulative array (SUM or Σ) response at low DEM concentrations. For this reason, the slopes of the response curves for FPOL and Σ are comparable below 10 μg/L, being 71.2 Hz/μg/L and 77.8 Hz/μg/L respectively. Above 10 μg/L, the cumulative response curve increased dramatically to 120 Hz/μg/L due to increased responses from the other sensors, including PIB at 25.7 μg/L.

For all the sensors in the array the calibration curves had zero x-intercepts, indicating that vapor breakthrough of the charcoal traps did not occur during the lab tests. Thus, the calculated sensitivities for these sensors from the lab tests can be used to gauge the performance of the array in the field.

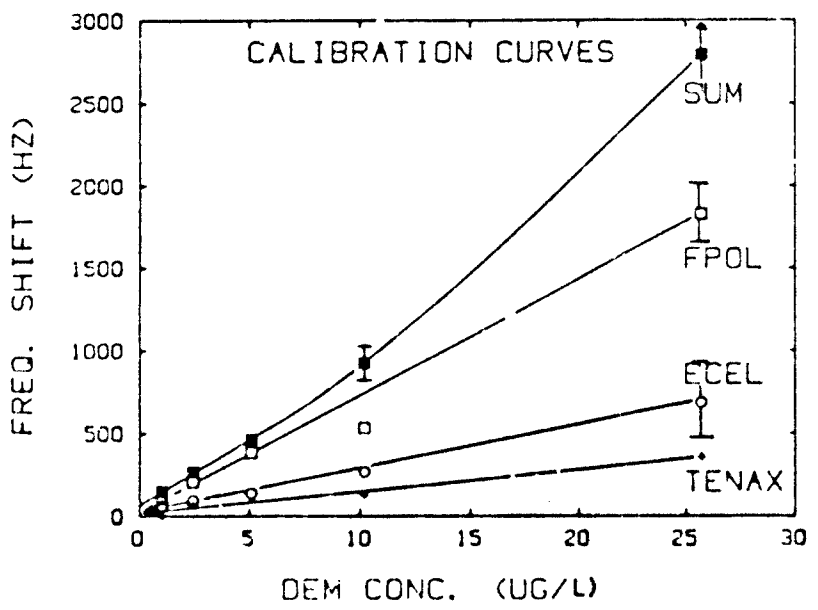


FIGURE 18. Comparison of sensor sensitivities to DEM from lab results.

curves were too noisy to allow accurate assessments of frequency shifts. In other cases, usually for the 8 minute cycle, there was insufficient resolution to calculate an accurate shift. This problem was exascerbated for the 8 minute cycle because of the running smooth performed during data reduction, since only 3 points (at most) were available for each 25 minute vapor exposure. For the PIB coated devices, frequency responses were negligible for all DEM concentrations below 25.7 μg/L, so there are no entries in the table for this sensor, and no calibration curve among the figures.

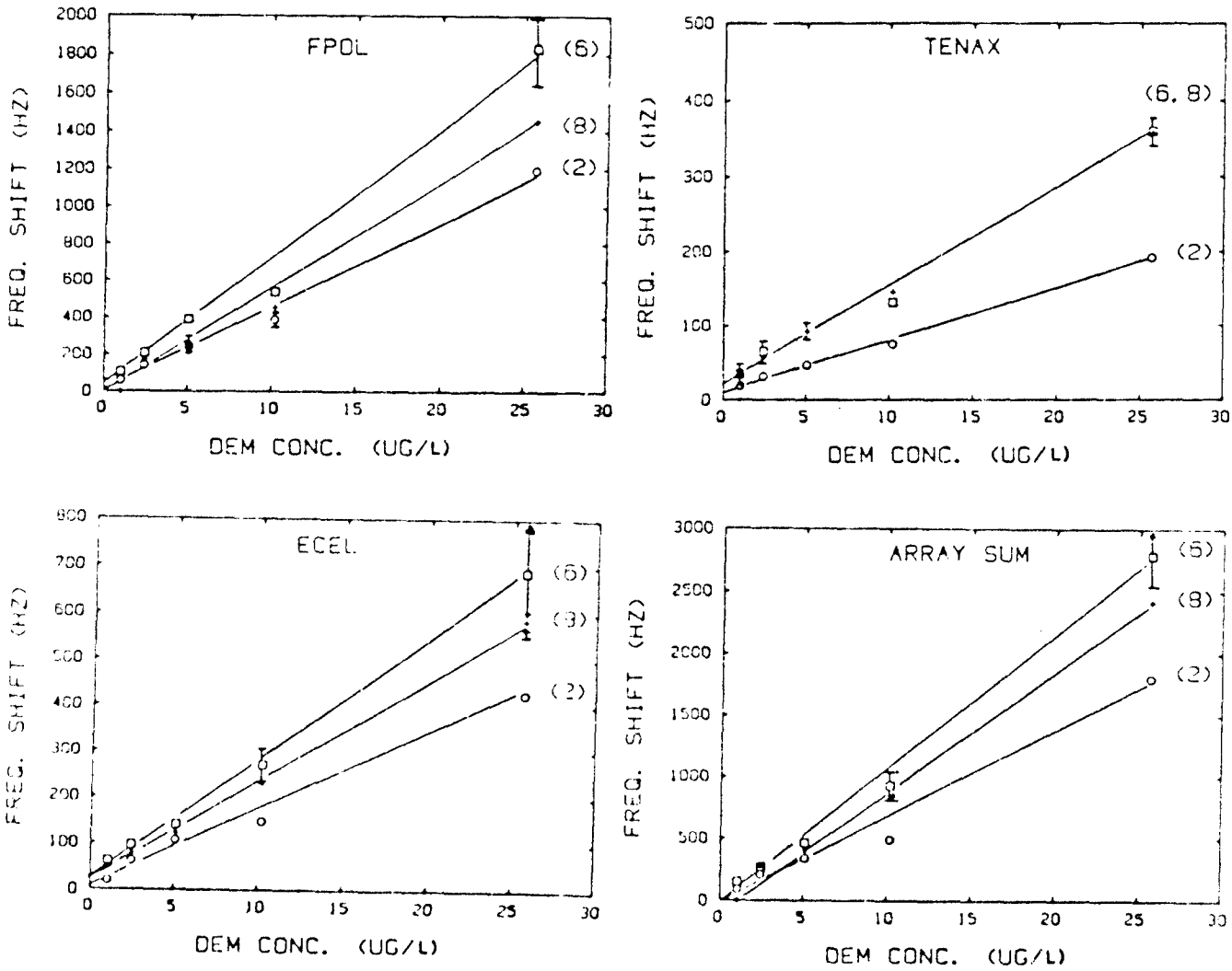


FIGURE 17. Calibration curves for sensor array from lab studies - a) FPOL, b) TENAX, c) ECEL, d) SUM. Sampling cycle times for each curve are in parentheses.

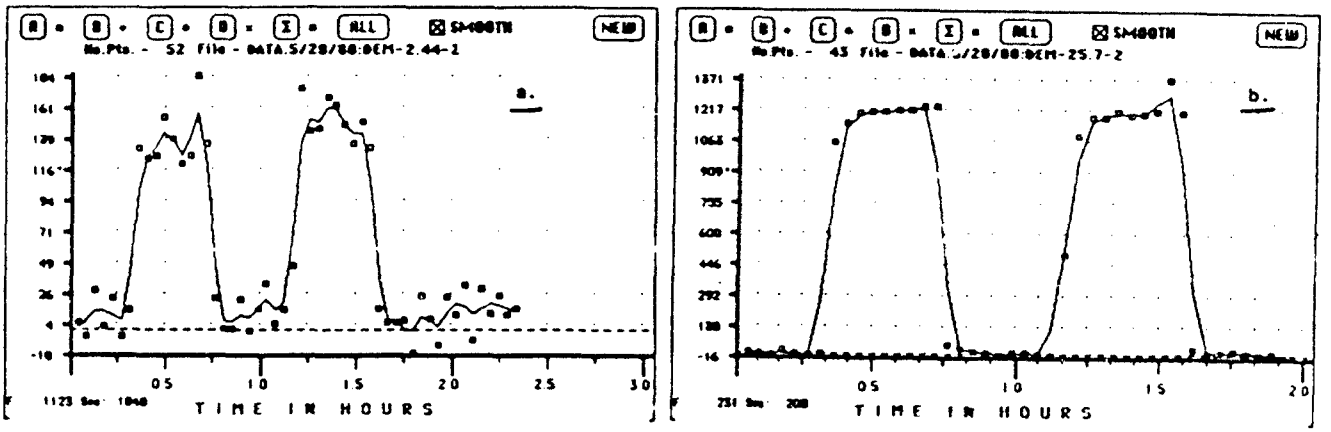


FIGURE 14. Examples of 4-SAW array response curves for lab test using 2 min. sample cycle. DEM exposures of a) 2.44 μg/L, and b) 25.7 μg/L.

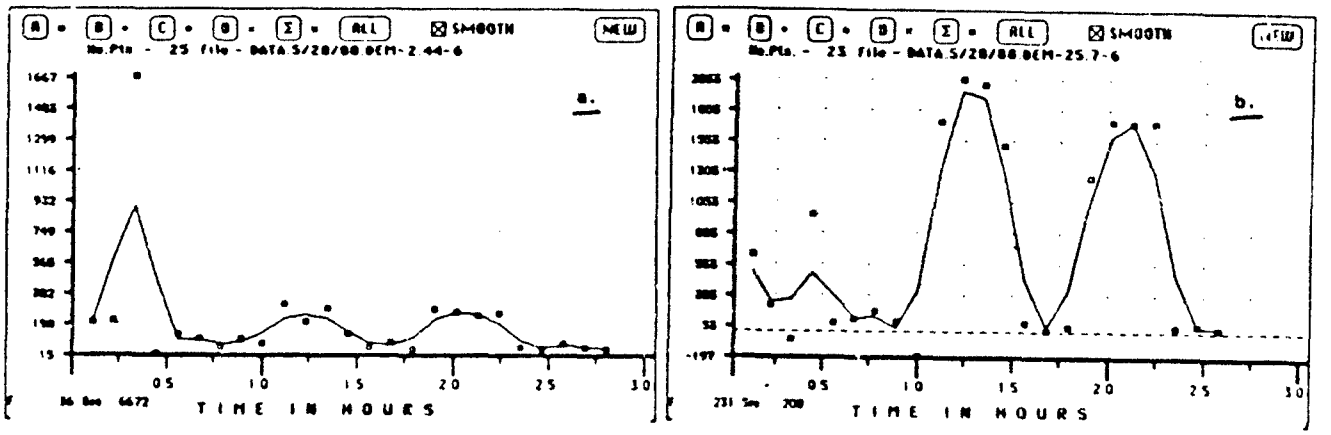


FIGURE 15. Response curves for lab tests using 6 min. cycle.

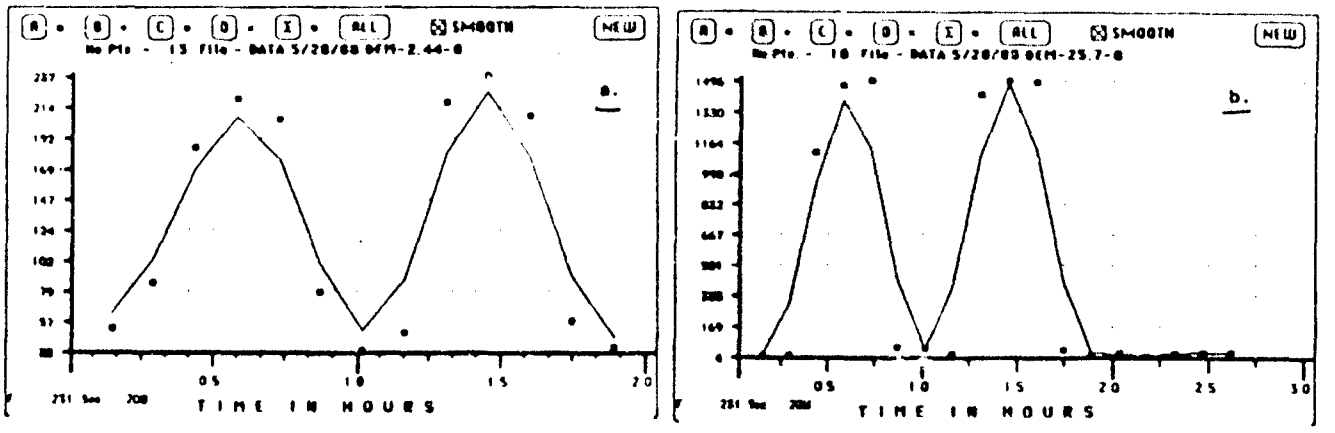


FIGURE 16. Response curves for lab tests using 8 min. cycle. data are plotted in Figure 17 (a-d). In some cases, the response

6-min., and an 8-min. cycle. By varying the cycling time, the effect of cycle time on calculated responses could be determined.

At the beginning of each day of testing, charcoal traps were replaced with charcoal and mol. sieve which had been regenerated in an oven at 180 ° C for 24 hr. Thus, problems associated with trap saturation and subsequent vapor breakthrough were avoided.

B. Results

Typical frequency response curves are seen in Figures 14-16. These curves represent the responses of the FPOL sensor to 2.44 μg/L and 25.7 μg/L for the 2 min., 6 min., and 8 min. cycles respectively. The curves plotted on these Figures represent a running smooth, where the line represents a boxcar average of the actual plotted data points. These curves were analyzed, and frequency shifts were calculated for each of the sensors in the array. The frequency shifts calculated for the 2, 6, and 8 minute cycles are tabulated in Table II. Calibration curves for these

TABLE II. LAB TEST RESULTS: SAW ARRAY RESPONSES

[DEM] (μg/L)	Cycle (min.)	Array Channel* FPOL (255 kHz)	TENAX (kHz)	ECEL (kHz)	Σ
1.03	2	60 ± 16	19 ± 2	20 ± -	90 ± 2
	6	106 ± 12	33 ± -	62 ± 2	150 ± 25
	8	--------	35 ± 5	51 ± -	--------
2.44	2	140 ± 20	32 ± -	62 ± 2	220 ± 10
	6	207 ± 15	65 ± 15	96 ± 15	270 ± 10
	8	170 ± 8	57 ± 7	78 ± 23	280 ± 20
5.08	2	240 ± 6	47 ± 2	107 ± 4	340 ± -
	6	386 ± 33	------	140 ± -	465 ± 50
	8	260 ± 50	92 ± 13	123 ± -	403 ± --
10.2	2	385 ± 45	75 ± 2	149 ± 8	490 ± 50
	6	535 ± 2	130 ± -	270 ± 37	930 ± 120
	8	450 ± -	145 ± -	230 ± -	820 ± --
25.7	2	1193 ± 17	192 ± 2	425 ± 3	1800 ± 20
	6	1830 ± 200	360 ± 20	690 ± 140	2790 ± 260
	8	1450 ± 13	358 ± 7	585 ± 20	2420 ± 20

* Responses for the PIB coated device were below noise levels. Other blanks in the table correspond to curves which could not be quantified either due to insufficient resolution and/or excessive baseline/signal noise or drift.

re-examine the sampling cycle. During the average cycle, air is scrubbed by passage thorugh a trap containing activated charcoal and molecular sieve. The charcoal purges the air stream of volatile organics, and the mol. seive removed water vapor. After the purge cycle, ambient air is then sent to the sensors. The plotted frequency difference represents the difference between the sensors responses to the ambient and scrubbed air streams.

The traps used during these tests were relatively clean at the beginning of the tests, having seen only occasional use in the MSI labs prior to the field tests. During the field tests, these traps were subjected to prolonged periods of high humidity and periodic challenges from the simulant and other ambient vapors. These traps were not replaced or regenerated during the field tests, so the possibility of saturation and/or breakthrough is likely. If the traps became saturated, there would be a fairly constant release of water vapor and adsorbed volatiles from the exhaust end of the trap. Calculated sensor responses would then be due to the change in concentration of these vapors between the ambient air and the purged air bleeding from the trap. The net result would be a decrease in observed responses and a shift in the x-intercept. The x-intercept, in fact, would correspond to the concentration of vapors eluting from the saturated trap.

To verify these hypotheses and more fully evaluate the performance of these sensors in the field, the 4-SAW array was returned to NRL and an extensive evaluation under controlled lab conditions was performed.

LABORATORY TESTS

A. Instrumentation

The 4-SAW array was calibrated in the Chemical Microsensor labs of the Surface Chemistry Branch at NRL, using the same data acquisition software that was used in the field. The sensor vapor input port was connected to the output port of a VG-7000 vapor generation system designed by MSI. The VG-7000 is capable of delivering a controlled, reproducible, pre-calibrated concentration of vapor to the sensor. During normal operation, the VG-7000 will switch back and forth between the vapor stream and a dry carrier gas stream. The duration of each vapor exposure and the number of vapor/carrier gas cycles is programmable.

For these lab tests, the DEM concentration was varied between 1 and 25 $\mu g/L$, which spanned the concentration range observed during the field tests. The lab temperature was fairly constant between 25-28 $^{\circ}C$ during the tests, which is comparable to some of the field tests. The relative humidity during these tests was not a factor, since the carrier gas sent to the sensors had been dried by Drierite and molecular sieve. The VG-7000 was programmed to send a vapor stream of 25 min. duration, followed by 25 min of carrier gas, and to repeat this cycle 2-3 times during a given test. The vapor generator was allowed to warmup for 1 hr at the beginning of each day to ensure the generation of an equilibrated vapor stream for sensor testing. The sensor array responses to these vapor streams were recorded while operating with a 2-min.,

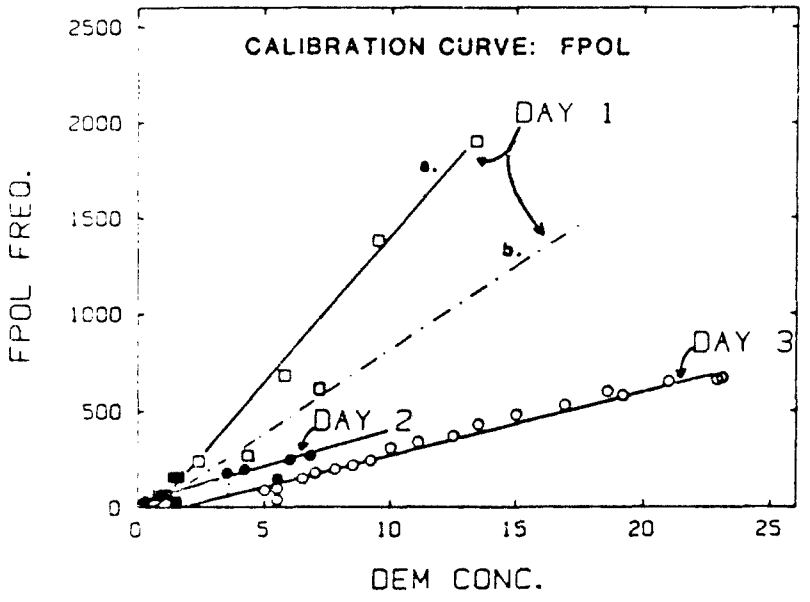


FIGURE 12. Calibration curves for FPOL sensor, calculated from MIRAN data. For Day 1, curve a. corresponds to test 1 and curve b. corresponds to test 2.

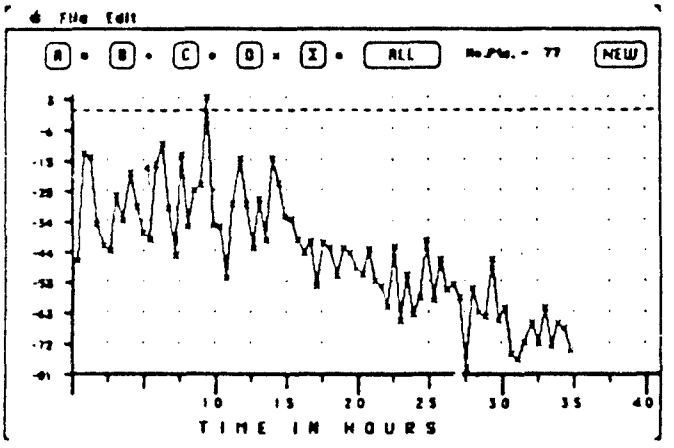


FIGURE 13. Example of typical noise levels for SAW sensors.

considerable amount of drift in the sensor baseline from the beginning to the end of the run. In addition, noise levels for the devices is relatively high when the sensors are first turned on, and generally decrease to 20-25 Hz after the first hour. Typical noise levels can be seen in Figure 13. This combination of increased noise and large initial drift may be responsible for the difference in the two calibration curves for the day 1 tests.

To explain the trend toward a positive x-intercept, we must

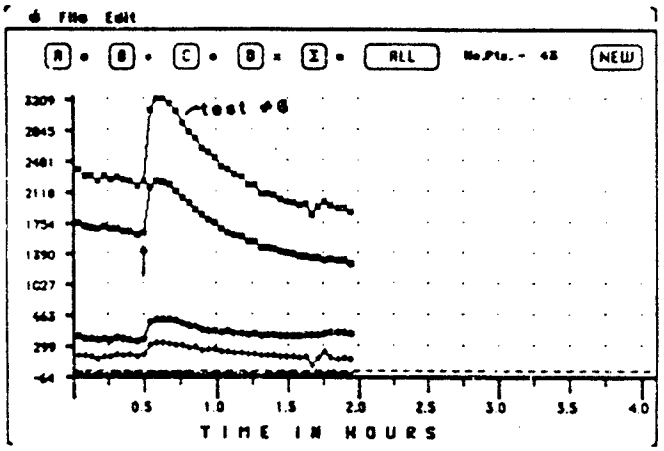


FIGURE 10. Plot of 4-SAW array responses for test 6, Day 3.

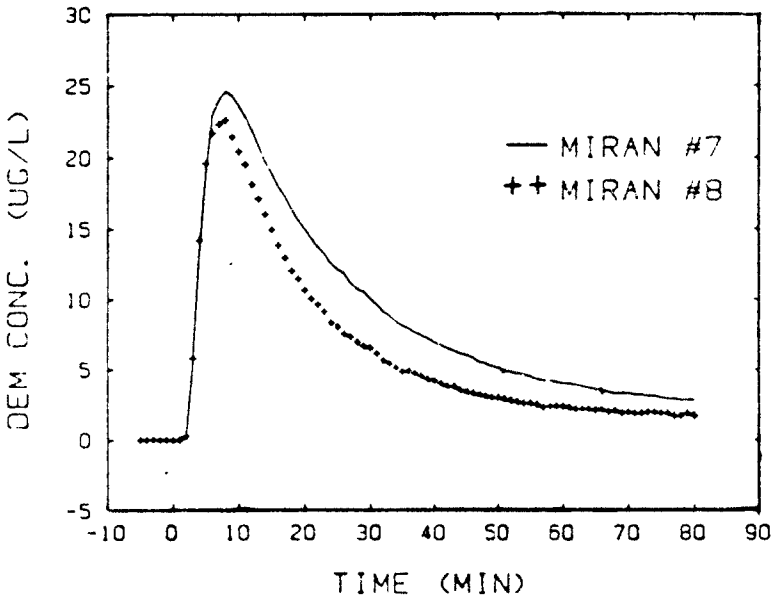


FIGURE 11. Plot of DEM concentration vs time measured by MIRANs for test 6.

are above baseline levels for the second test, so the calibration curve given in the graph has a high degree of uncertainty. Both of these runs were performed using a 4 minute sampling cycle. The sensitivity decreases more dramatically for subsequent runs on days 2 and 3, using the 2 minute sampling cycle. Second, the x-intercept appears to be significantly greater than zero for test 6, run on day 3.

The decrease in sensitivity seen between tests #1 and #2 for day 1 may be due to the lack of sufficient warmup time prior to the start of test #1. It can be seen from Figure 3 that there is a

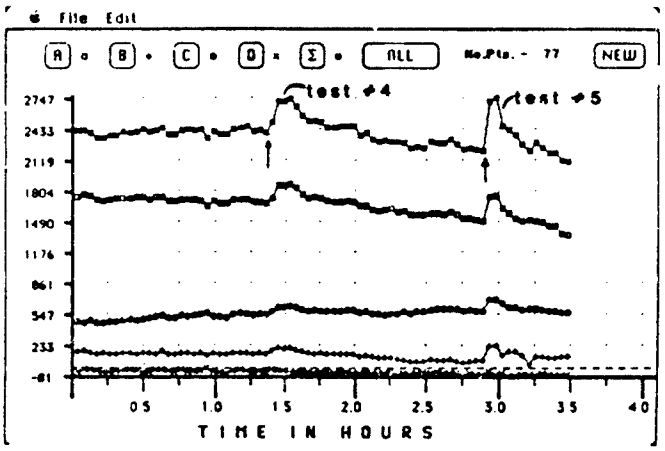


FIGURE 8. Plot of 4-SAW array responses for tests 4 and 5, Day 2.

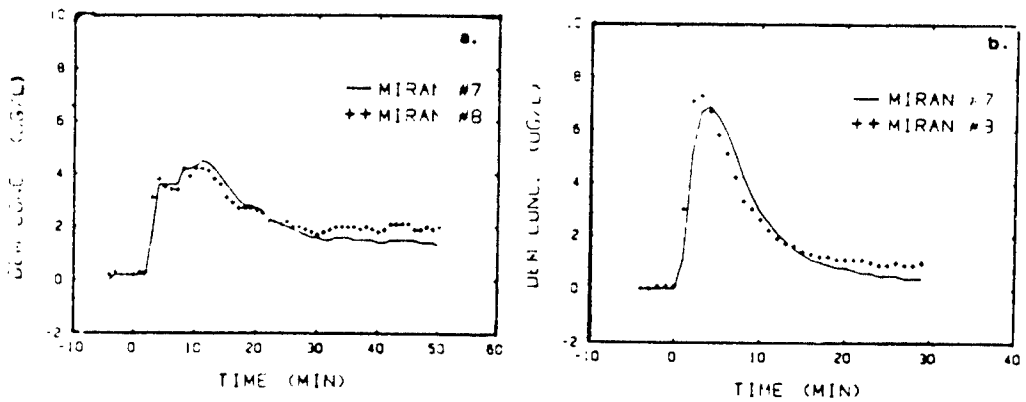


FIGURE 9. Plot of DEM concentration vs time mesured by MIRANs for a) test 4, and b) test 5.

4, 6, 8, and 10 are similar to the shapes of the DEM concentration profiles seen in Figures 5, 7, 9, and 11. This indicates that the SAW sensor array was seeing relatively the same concentration levels as the MIRANs. From the MIRAN data, the DEM concentration range could be estimated, but the exact concentration of simulant at the sensor is not known. This fact, combined with sensor noise and drift, result in a certain amount of error associated with any given data point in these calibrations.

The SAW responses illustrated in Figures 4, 6, 8, and 10 indicate that the FPOL sensor exhibited the greatest sensitivity to the simulant. The FPOL response was calibrated using the MIRAN data, and the resulting calibration curves for the three days of testing are given in Figure 12. There are several features worth noting from this figure. First, the relative sensitivity of the device decreased from the first run on day 1 (seen in curve a) to the final run for the day (seen in curve b). Only 2 data points

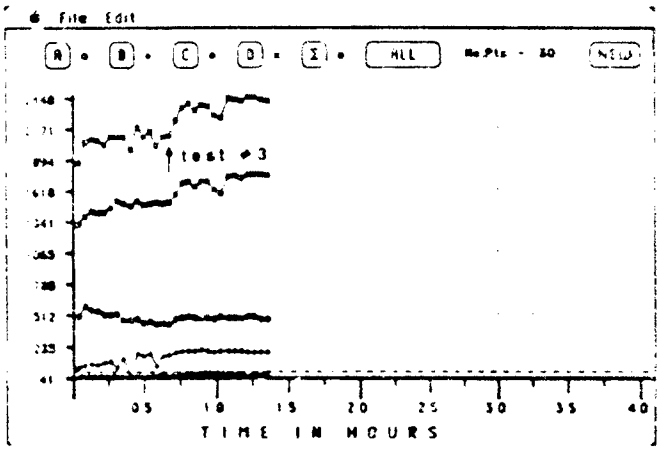


FIGURE 6. Plot of 4-SAW array responses for test 3, Day 2.

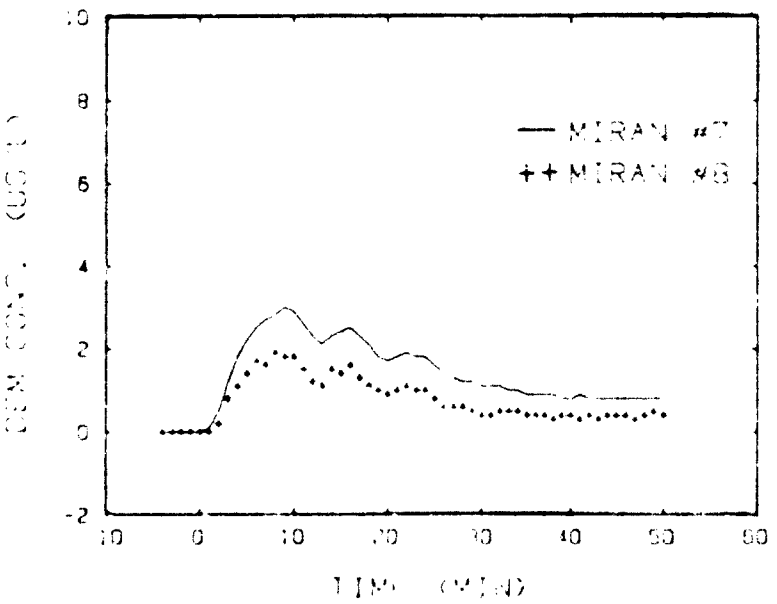


FIGURE 7. Plot of DEM concentration vs time measured by MIRANs for test 3, Day 2.

The MIRAN data were analyzed by Lockheed personnel at the Army/Dugway facility. The data were corrected for baseline drift, and the corrected data were provided to NRL. Copies of the corrected data tables are included as addenda to this report. As noted earlier, only data from MIRAN #7 and MIRAN #8 were of interest, due to their proximity to the 4-SAW array. The DEM concentrations vs. time for these MIRANs for each of the 6 tests are plotted in Figures 5, 7, 9, and 11. These DEM concentrations were used to calibrate the SAW sensor responses in the field. In general, the shapes of the response curves illustrated in Figures

Examples of the sensor array frequency plots for the field tests are given in Figures 4, 6, 8, and 10. The beginning of each test sequence is indicated on these plots with an arrow. A sampling cycle of 4 minutes (2 min. purge/2 min. sample) was used during tests 1 and 2 (seen in Figure 4). It appeared that the raw frequency responses of the sensors during the sampling half of the cycle were fairly rapid, usually reaching an equilibrium response within 1 minute. The subsequent return to baseline during the purge portion of the cycle was also rapid, and reached a steady value within 20-40 seconds after removal of the ambient air stream. Based on these observations, subsequent tests on day 2 and day 3 were performed using a 2 minute cycle (1 min. purge/1 min. sample). An additional factor in using a shorter sampling cycle was the desire for greater response/time resolution. Switching to a 2 minute cycle would generate twice as many data points for comparison with MIRAN data.

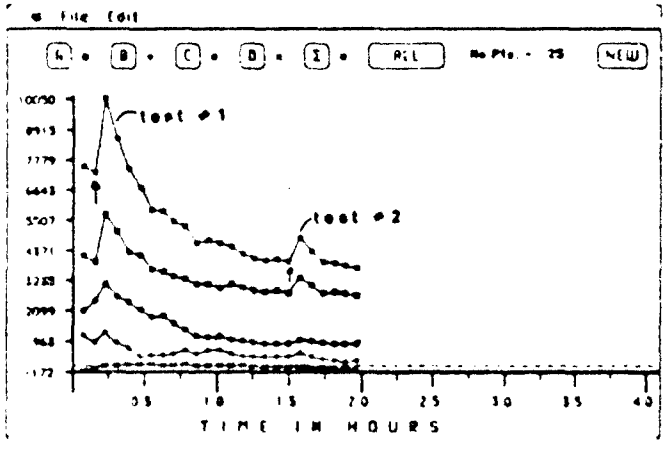


FIGURE 4. Plot of 4-SAW array responses to tests 1 and 2, performed on Day 1. Beginning of each test is indicated on graph with an arrow.

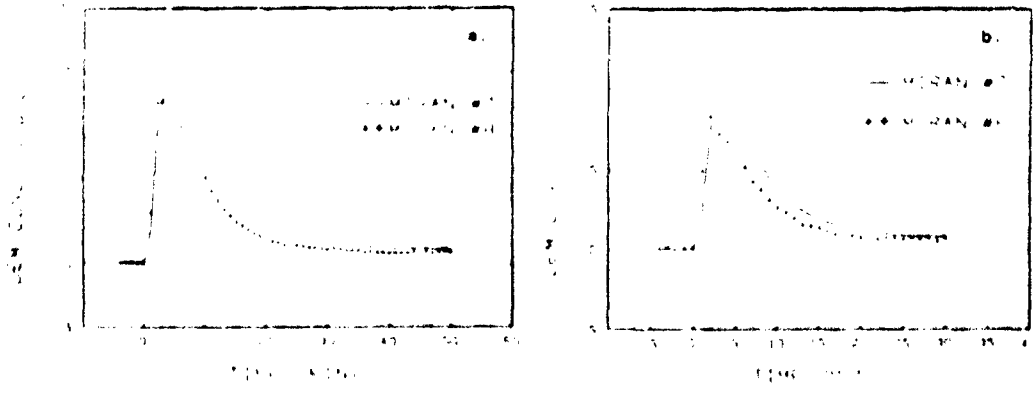


FIGURE 5. Plot of DEM concentration vs time measured by MIRANs for a) test 1, and b) test 2.

B. Results

The frequency shifts of the individual sensors, as well as the cumulative frequency shifts (Σ), were recorded continuously during the tests. During a typical sampling cycle, the SAW frequencies were recorded every 2 seconds as the sensors were exposed to alternating streams of scrubbed air and ambient air. An example of the raw frequency response curve for a two minute cycle is given in Figure 3A (raw data). During the first minute of the cycle, the frequency baseline is established as the sensor is exposed to scrubbed air. During the second half of the sampling cycle the frequency difference increases as the sensor responds to ambient vapors. This frequency difference between scrubbed air and ambient air is represented in the Figure as f(1). At the conclusion of the cycle, the difference between the baseline response and the response to ambient air is calculated, and this difference is recorded and plotted as seen in Figure 3B (plotted data). In part a, two sampling cycles to ambient air are represented. In part b, simulant vapor is added to the ambient background. The increase in frequency response due to the simulant is represented as f(2). The plotted data in Figure 3B represents the difference between the scrubbed air stream and the ambient air stream, with only one data point for every sampling cycle. Shifts in the plotted frequency data thus represent the sensor responses to changes in the concentration or composition of ambient vapors.

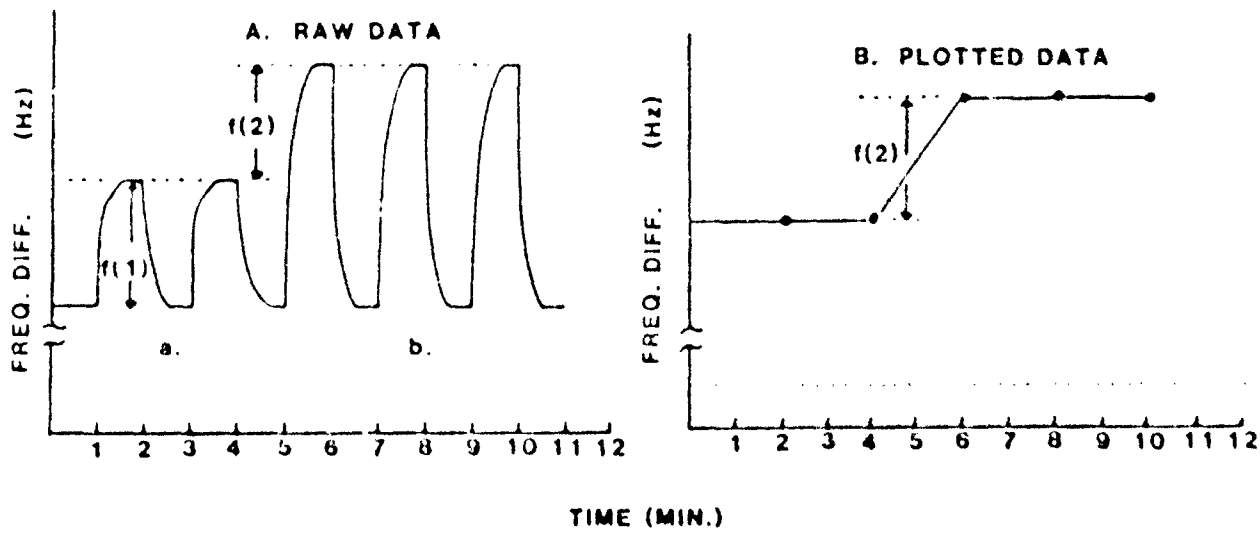


FIGURE 3. Example of data collection during 2 minute sampling cycle. In A, actual frequencies are recorded every 2 seconds during purge and sample portions of the cycle. In part B, the difference frequency between the purge and sample portions of the cycle are plotted. Additional explanation is included in the text.

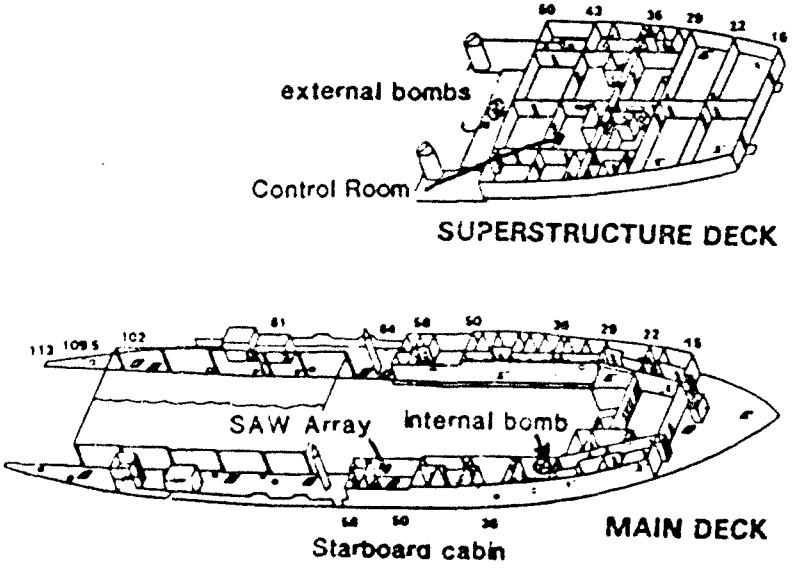


FIGURE 2. Schematic of physical layout of shipboard testing site.

was exploded at internal or external locations, as marked in Figure 2. After detonation, DEM concentrations were monitored as the simulant was dispersed throughout the starboard cabins. When the concentration had decreased sufficiently, usually below 1.0 μg/L, the test was terminated. Ambient temperatures during the tests varied between 18-28 °C, with the cooler temperatures during the morning tests and an average temperture in the starboard cabins of 22-25 °C. The relative humidity was higher in the morning (near 60%) and decreased during the course of the day to below 40%.

TABLE I. TEST SCHEDULES AND CONDITIONS

Test #	Temp. (°C)	Humidity (% RH)	Start Time	Duration (min.)	Sampling Cycle (min.)
1 (5/25)	23-25	58	11:40	50	4
2 (5/25)	25-26	52	13:00	30	4
3 (5/26)	18-21	56	10:40	60	2
4 (5/26)	24-26	41	11:53	54	2
5 (5/26)	25-28	--	13:26	29	2
6 (5/27)	24-27	38	10:10	80	2

* Tests #1-#5 were external bombs with a simulant volume of 500 mL. Test #6 was an internal bomb with a simulant volume of 50 mL.

acquisition of sensor data. Charcoal traps were included in the system to scrub the ambient air to establish a baseline array response. During normal operation, the air stream sent to the sensor alternated between ambient air and purged air that had been passed through the charcoal traps. A more detailed discussion of the sample data collection scheme will be given later. All software for system control, data collection, and algorithms for the reduction of data were developed by MSI.

B. MIRAN IR Detectors

Simulant (diethyl malonate - DEM) concentrations during the field tests were monitored using the Miniature Infra-Red ANalyzer (MIRAN 1A), manufactured by Foxboro Analytical. Simulant detection was achieved by monitoring the IR spectral intensity at a λ of 9.5 μm over a 20.25 meter cell path length. A minimum detectable concentration of 0.05 ppm is achievable with this instrument under optimum conditions (3). These instruments were designed for lab operation, and required special care in setup and calibration for use in the field. All MIRAN data were collected and reduced by Lockheed personnel.

For the purposes of this study, the MIRAN data were used to verify the concentrations of simulant to which the sensor array was exposed. In this manner, the sensitivity and detection limit could be determined for the field tests. Although there were many MIRANS located on board for the tests, only two are of interest. These two instruments, identified as MIRAN #7 and MIRAN #8, were located in the starboard cabins at frames 53 and 55, respectively (see Figure 2). These were in close proximity to the SAW array, which was located at frame 54. Thus the simulant concentrations reported by these two instruments could be used to estimate the concentrations of simulant in the vicinity of the SAW array at a given time during these tests.

FIELD TESTS

A. Physical Layout

All field tests were conducted on board the ex-USS Shadwell during the period of May 25-27, 1988. The layout of the portions of the ship used during these tests is illustrated in Figure 2. The starboard cabins on the main deck had been retro- fitted to meet all necessary power requirements for instrument operation and control, and were sealed off from the remainder of the ship during the conduction of simulant dispersal tests. MIRAN detectors were positioned in the starboard cabins between frames 36 and 58, and on the weather deck at midship. (Note: each frame = 4 ft). MIRAN responses were transmitted to the control room, located on the superstructure deck. The concentration and dispersal of the simulant during the tests were monitored by the MIRANs, and could be observed remotely in real time from the control room.

The testing schedule and pertinent conditions are listed in Table I. Diethyl malonate (DEM) was used as the simulant for all tests. During an average test, a vessel containing the simulant

The 158 MHz dual SAW devices used during this study were provided by Microsensor Systems, Inc., (MSI) of Fairfax, VA (part # SD-158-A). Each device contains two sets of IDTs on the surface of a ST-cut quartz crystal, with each set of IDTs forming an independent delay line. One delay line was coated with a thin polymer film which acted as a semi-selective adsorbent for chemical vapors, while the second delay line remained uncoated to serve as a reference. The individual frequencies of the delay lines were fed into an electronic mixer. The output from the mixer represented the frequency difference between the coated and uncoated delay lines. As the individual sensors were exposed to and adsorbed a given vapor, the frequency difference output for the devices would increase. The magnitude of the observed frequency shift is proportional to the amount of vapor adsorbed into the coating, and hence is a measure of the sensitivity of that coating to that vapor. The coatings used during these tests were fluoropolyol (FPOL - Chan. A), a soluble extract of TENAX-GC (Chan. B), ethyl cellulose (ECEL - Chan. C), and poly(isobutylene) (PIB - Chan. D). It should be emphasized that the TENAX coating represented only a soluble extract of this GC packing material, so that the material actually deposited on the SAW is not well characterized in terms of structure or solubility properties. Coatings were selected based on previously observed reliability and availability. No attempt was made to maximize the sensitivity of the sensors for the specific simulant used in the field tests.

Four coated devices were placed in an array configuration illustrated in Figure 1 (MSI #SAS-158-4). The array was interfaced with an Apple Macintosh microcomputer which controlled the switching of vapor streams, via electrical solenoid valves, and the

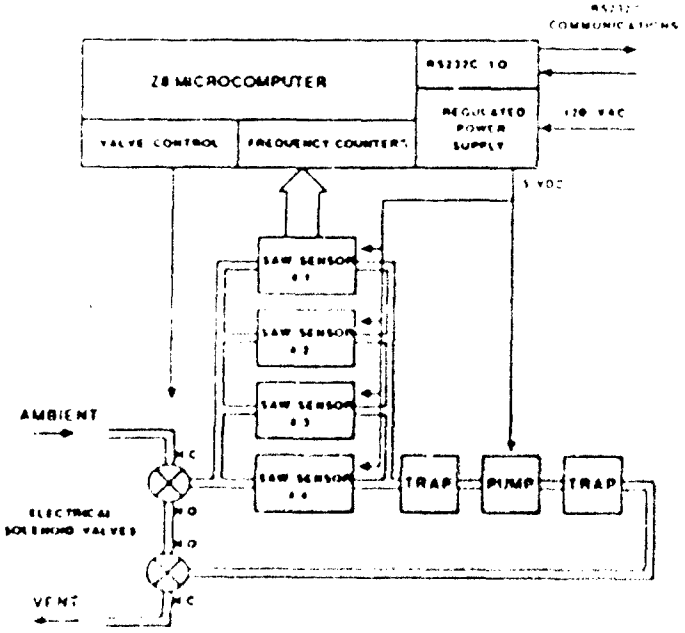


FIGURE 1. Schematic diagram of 4-SAW sensor array configuration, used during field tests.

EVALUATION OF SAW SENSOR ARRAY PERFORMANCE: RESULTS OF FIELD TESTS ON BOARD EX-USS SHADWELL

INTRODUCTION

The Navy's interest in chemical microsensors spans much of the current decade (1980's), with major research programs in the development, testing, and evaluation of various sensor technologies being implemented at the Naval Research Laboratory. Interest in these devices is motivated by their small size, ruggedness, low cost, and potential for rapid and sensitive response. Ultimately, these devices will be used in military environments for such applications as the detection of hazardous materials and the monitoring of decontamination processes. One application of particular interest to the Navy involves the use of these sensors to monitor shipboard environments.

The surface acoustic wave (SAW) device has been the focus of a considerable amount of basic and applied research efforts over the past 7 years. Characterization of the SAW includes determinations of response times, reproducibility, effects of aging, and sensitivity and selectivity of coatings to specific vapors. Until recently, the evaluation of these devices was limited to testing under controlled laboratory conditions. Field tests were needed to verify whether lab results provide an accurate representation of the expected performance of these devices under real shipboard conditions.

Such field tests were recently conducted on board the ex-USS Shadwell. The Shadwell is a decommissioned Navy LSD, currently serving as a training facility under the control of the Navy Technology Center for Safety and Survivability, which is associated with the Combustion and Fuels Branch of the NRL Chemistry Division. It is moored at Little Sand Island in Mobile Bay, Alabama, under an agreement with the US Coast Guard. Additional details regarding the Shadwell testing facility can be found in reference 1. SAW field tests were performed concurrent with simulant dispersal tests by the Lockheed Engineering and Management Services Co., Inc., for the Army/Dugway Proving Grounds, Utah. Results of those field tests and parallel lab studies form the basis of this report.

INSTRUMENTATION

A. SAW Apparatus

The operational principles of the SAW device are described in detail in reference (2). For the purposes of this report, only a brief description of the devices will be included. The SAW consists of a set of interdigital transducers (IDTs) which have been deposited on the surface of a piezoelectric substrate, such as quartz. When a time-varying rf potential is applied to one of the IDTs a Rayleigh wave is established and propagates along the surface of the crystal. The Rayleigh wave velocity depends on the substrate, and the frequency of the wave depends on the geometry of the IDTs. The frequency and velocity of the wave is sensitive to changes occurring on the surface, such as changes in the mass loading or elastic properties of a thin surface film. It is this high degree of sensitivity to surface perturbations that makes the SAW an attractive sensor.

Manuscript approved December 20, 1989

CONTENTS

INTRODUCTION 1

INSTRUMENTATION 1

FIELD TESTS 3

LABORATORY TESTS 11

DISCUSSION 16

RECOMMENDATIONS 18

SUMMARY 19

ACKNOWLEDGEMENTS 19

REFERENCES 20

ADDENDA — Miran Data for Shadwell Field Tests 21

3. DISTRIBUTION/AVAILABILITY OF REPORT

Distribution authorized to U.S. government agencies only; test evaluation; March 1989. Other requests shall be referred to the Commanding Officer, Naval Research Laboratory, Washington, DC 20375-5000.

16. SUPPLEMENTARY NOTATION

*GEO-Centers, Inc., 10903 Indian Head Hwy, Fort Washington, MD 20744.
**Microsensor Systems, Inc., P.O. Box 90, Fairfax, VA 22030.
+Lockhead Engineering Management Services Co. Inc., P.O. Box 217[illegible] D gway, UT 84022-0217.

SECURITY CLASSIFICATION OF THIS PAGE

REPORT DOCUMENTATION PAGE

Form Approved OMB No. 0704-0188

1a REPORT SECURITY CLASSIFICATION: UNCLASSIFIED	1b RESTRICTIVE MARKINGS:
2a SECURITY CLASSIFICATION AUTHORITY:	3 DISTRIBUTION/AVAILABILITY OF REPORT: (See page ii)
2b DECLASSIFICATION/DOWNGRADING SCHEDULE:	
4 PERFORMING ORGANIZATION REPORT NUMBER(S): NRL Memorandum Report 6439	5 MONITORING ORGANIZATION REPORT NUMBER(S):
6a NAME OF PERFORMING ORGANIZATION: Naval Research Laboratory; 6b OFFICE SYMBOL (If applicable): Code 6170	7a NAME OF MONITORING ORGANIZATION:
6c ADDRESS (City, State, and ZIP Code): Washington, DC 20375-5000	7b ADDRESS (City, State, and ZIP Code):
8a NAME OF FUNDING/SPONSORING ORGANIZATION: Air Force, HSD/YAX; 8b OFFICE SYMBOL (If applicable):	9 PROCUREMENT INSTRUMENT IDENTIFICATION NUMBER:
8c ADDRESS (City, State, and ZIP Code): Brooks AFB, TX 78223-5000	10 SOURCE OF FUNDING NUMBERS: PROGRAM ELEMENT NO: 63745F; PROJECT NO: ; TASK NO: ; WORK UNIT ACCESSION NO: DN480-584

11 TITLE (Include Security Classification): Evaluation of SAW Sensor Array Performance: Results of Field Tests on Board EX-USS SHADWELL

12 PERSONAL AUTHOR(S): Ballantine,* D.S., Wohltjen,** H., Thomas,+ R. and Venezky, D.L.

13a TYPE OF REPORT	13b TIME COVERED	14 DATE OF REPORT (Year Month Day)	15 PAGE COUNT
	FROM 5/88 TO 11/88	1989 March 21	43

16 SUPPLEMENTARY NOTATION: (See page ii)

17 COSATI CODES			18 SUBJECT TERMS (Continue on reverse if necessary and identify by block number)
FIELD	GROUP	SUB GROUP	

19 ABSTRACT (Continue on reverse if necessary and identify by block number)

An array of four surface acoustic wave (SAW) devices was subjected to field evaluations on board the ex-USS Shadwell. The sensor array performance was evaluated based on comparison of field data with MIRAN data, and with results of lab tests with the same sensor array. The sensitivity and limit of detection were determined, and recommendations were made for improved performance. The SAW sensor technology demonstrated adequate sensitivity and reliability for use in environmental monitoring applications.

20 DISTRIBUTION/AVAILABILITY OF ABSTRACT	21 ABSTRACT SECURITY CLASSIFICATION
[ ] UNCLASSIFIED/UNLIMITED [X] SAME AS RPT [ ] DTIC USERS	UNCLASSIFIED
22a NAME OF RESPONSIBLE INDIVIDUAL: David L. Venezky	22b TELEPHONE (Include Area Code): (202) 767-3550; 22c OFFICE SYMBOL: Code 6170

DD Form 1473, JUN 86 Previous editions are obsolete SECURITY CLASSIFICATION OF THIS PAGE

S/N 0102-LF-014-6603

Naval Research Laboratory

Washington, DC 20375-5000

NRL Memorandum Report 6439

Evaluation of SAW Sensor Array Performance: Results of Field Tests on Board EX-USS SHADWELL

DAVID S. BALLANTINE

GEO-Centers, Inc.
10903 Indian Head Hwy
Fort Washington, MD 20744

HANK WOHLTJEN

Microsensor Systems, Inc.
P.O. Box 90
Fairfax, VA 22030

ROBERT THOMAS

Lockhead Engineering Management Services Co., Inc.
P.O. Box 217
Dugway, UT 84022-0217

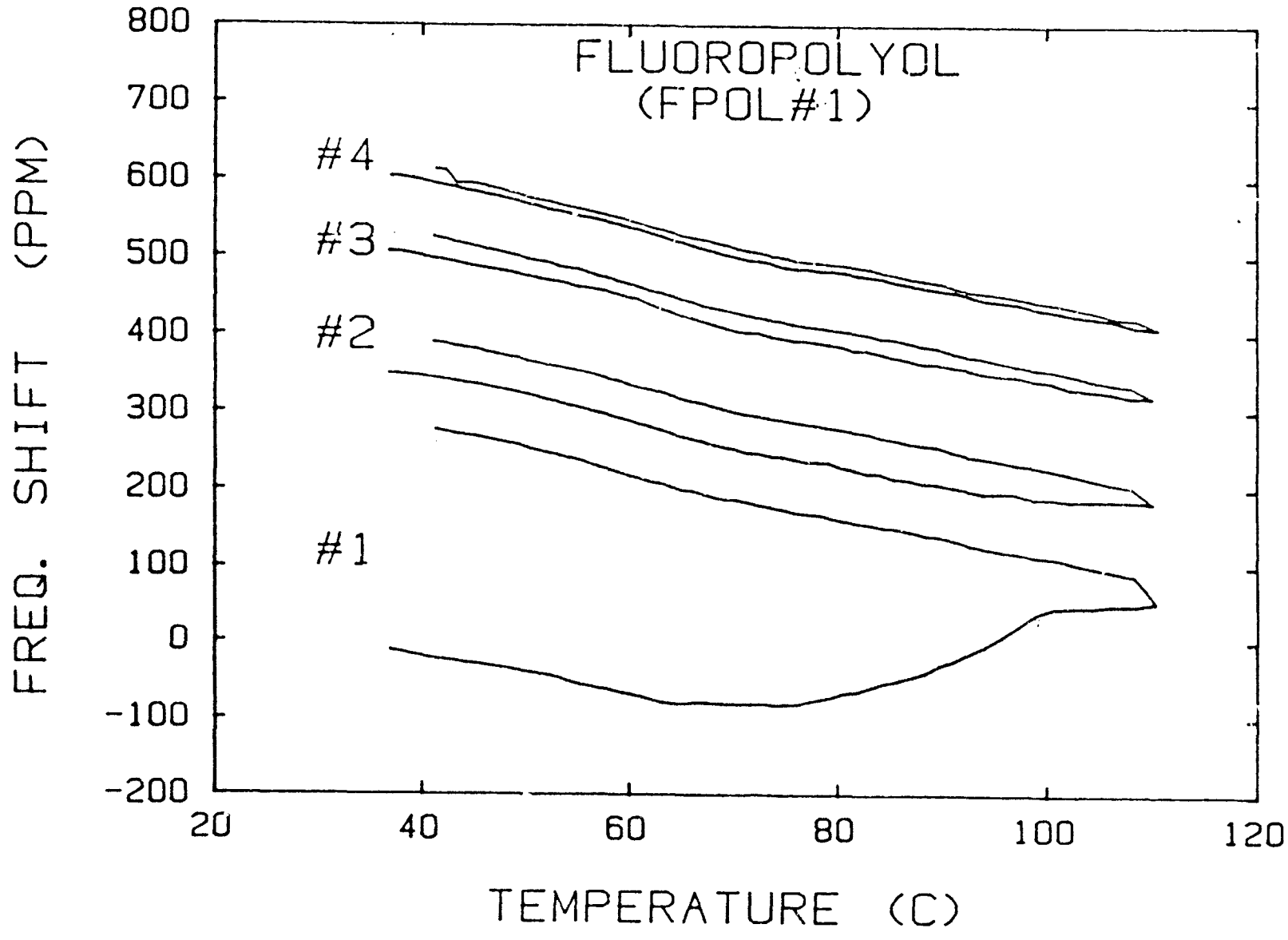
DAVID L. VENEZKY

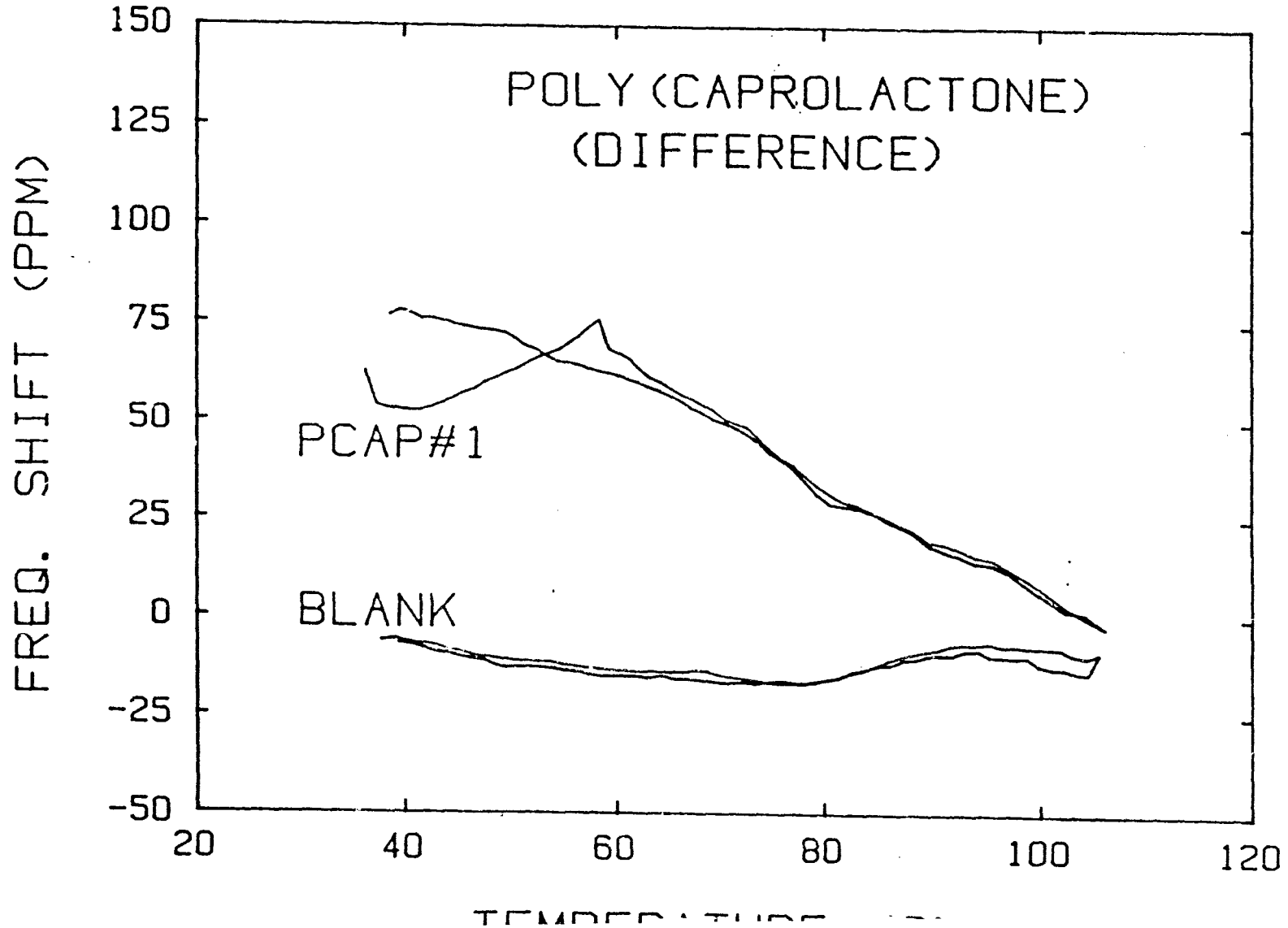
Surface Chemistry Branch
Chemistry Division

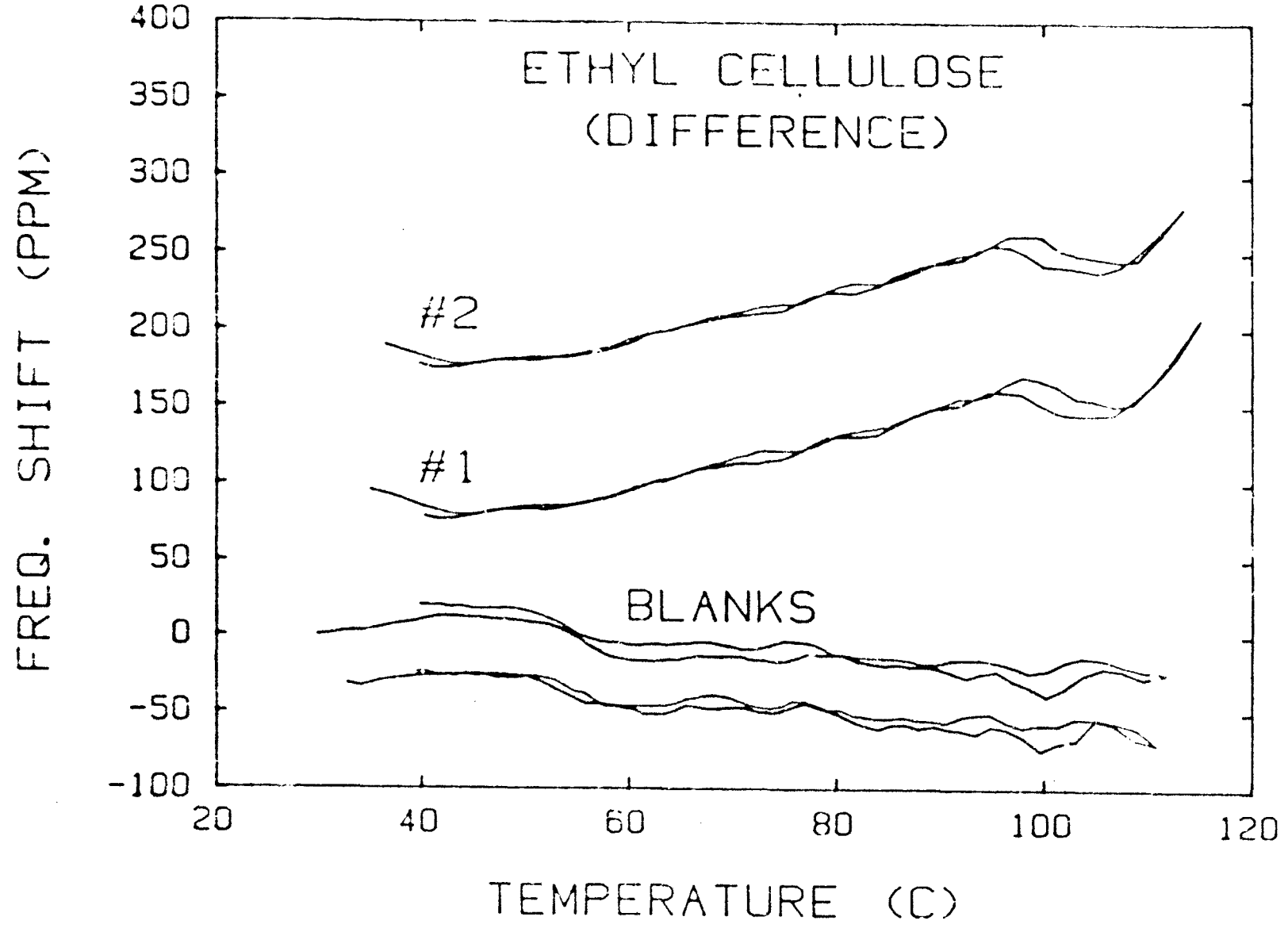
March 21, 1989

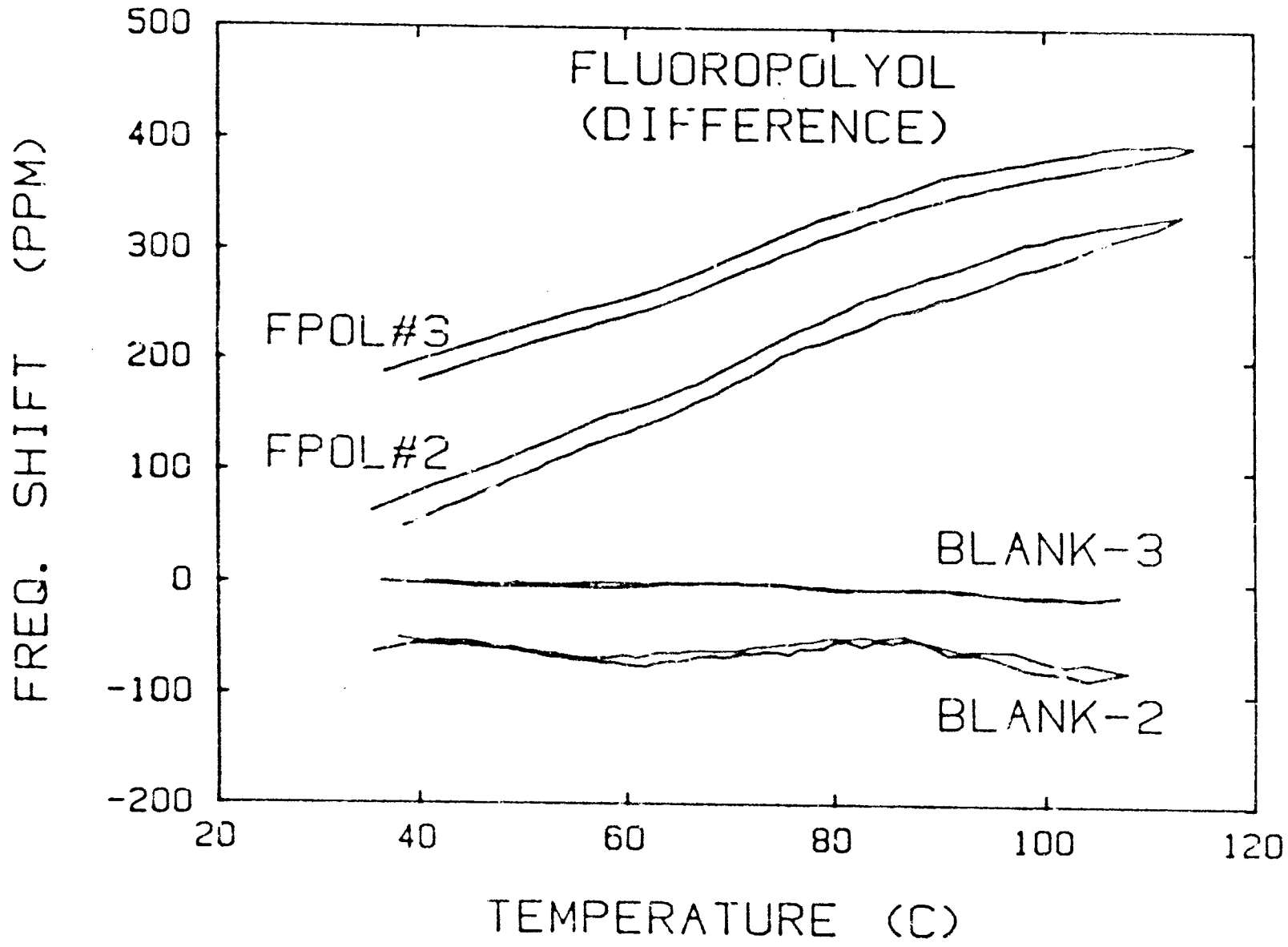
Distribution authorized to U.S. government agencies only; test and evaluation; March 1989. Other requests shall be referred to the Commanding Officer, Naval Research Laboratory, Washington, DC 20375-5000.

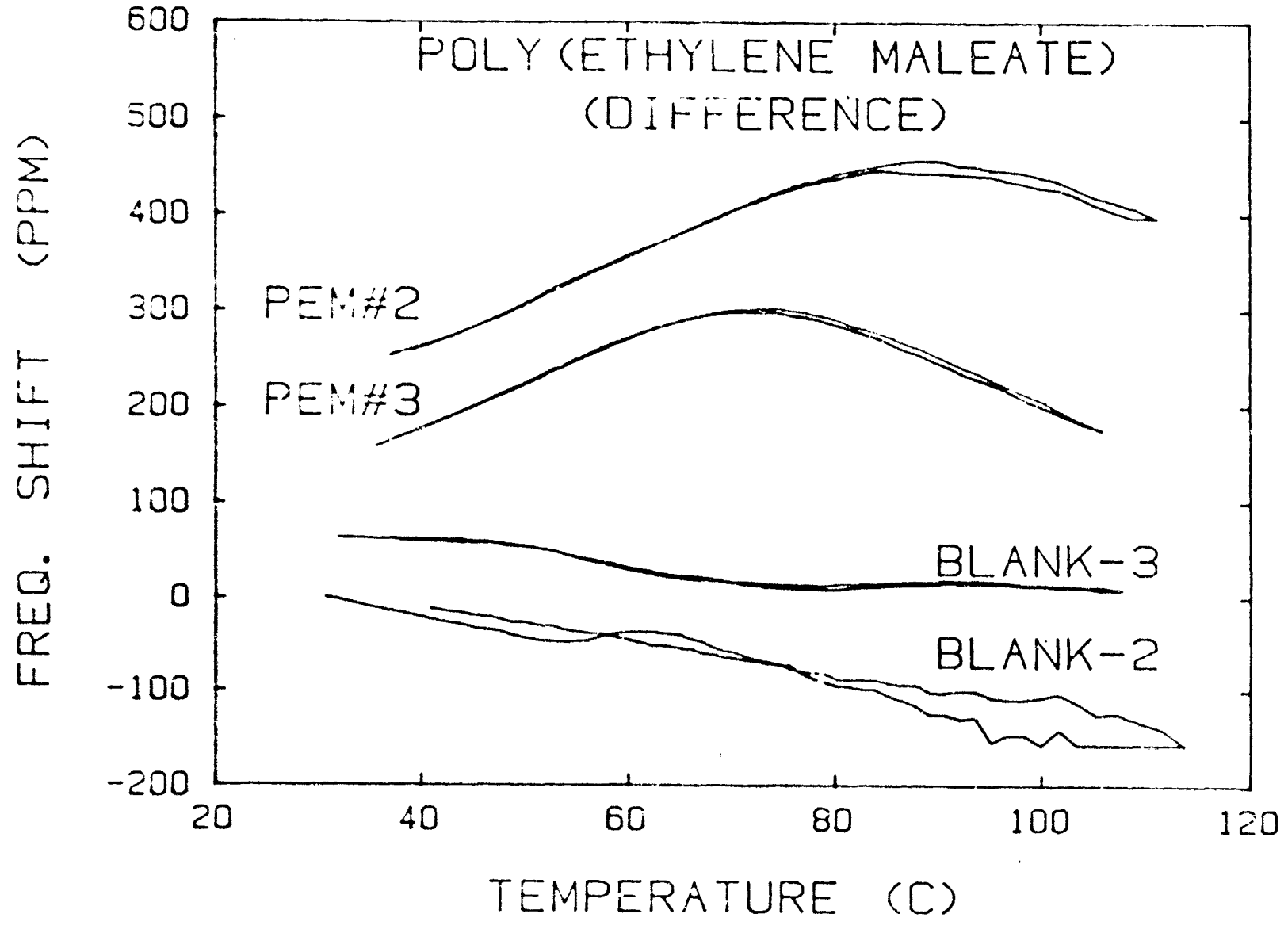
APPENDIX C3

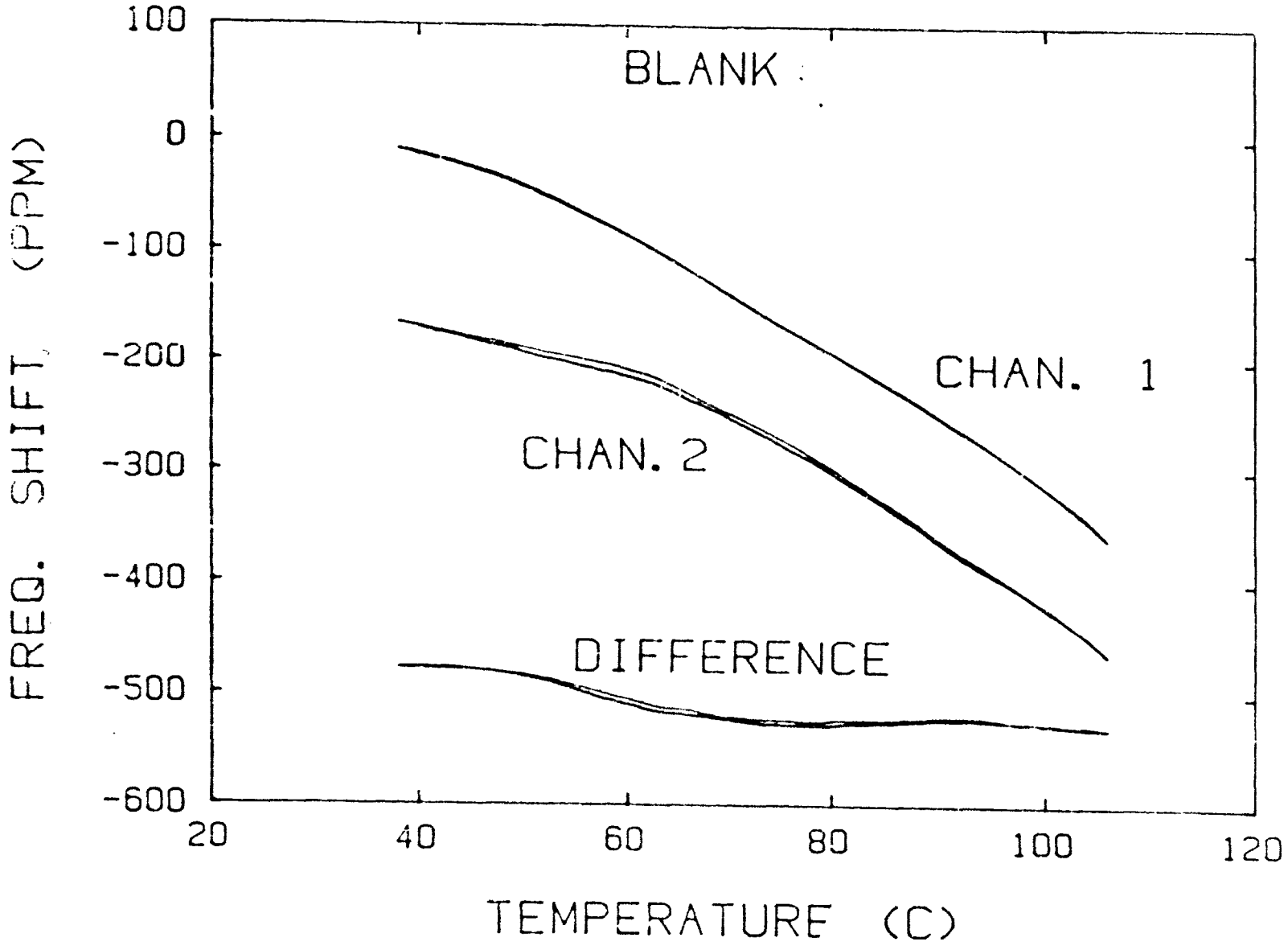

FLUOROPOLYOL
(FPOL#1)
#4
#3
#2
#1
FREQ. SHIFT (PPM)
800
700
600
500
400
300
200
100
0
-100
-200
20
40
60
80
100
120
TEMPERATURE (C)


POLY (CAPROLACTONE)
(DIFFERENCE)
PCAP#1
BLANK
FREQ. SHIFT (PPM)
150
125
100
75
50
25
0
-25
-50
20
40
60
80
100
120

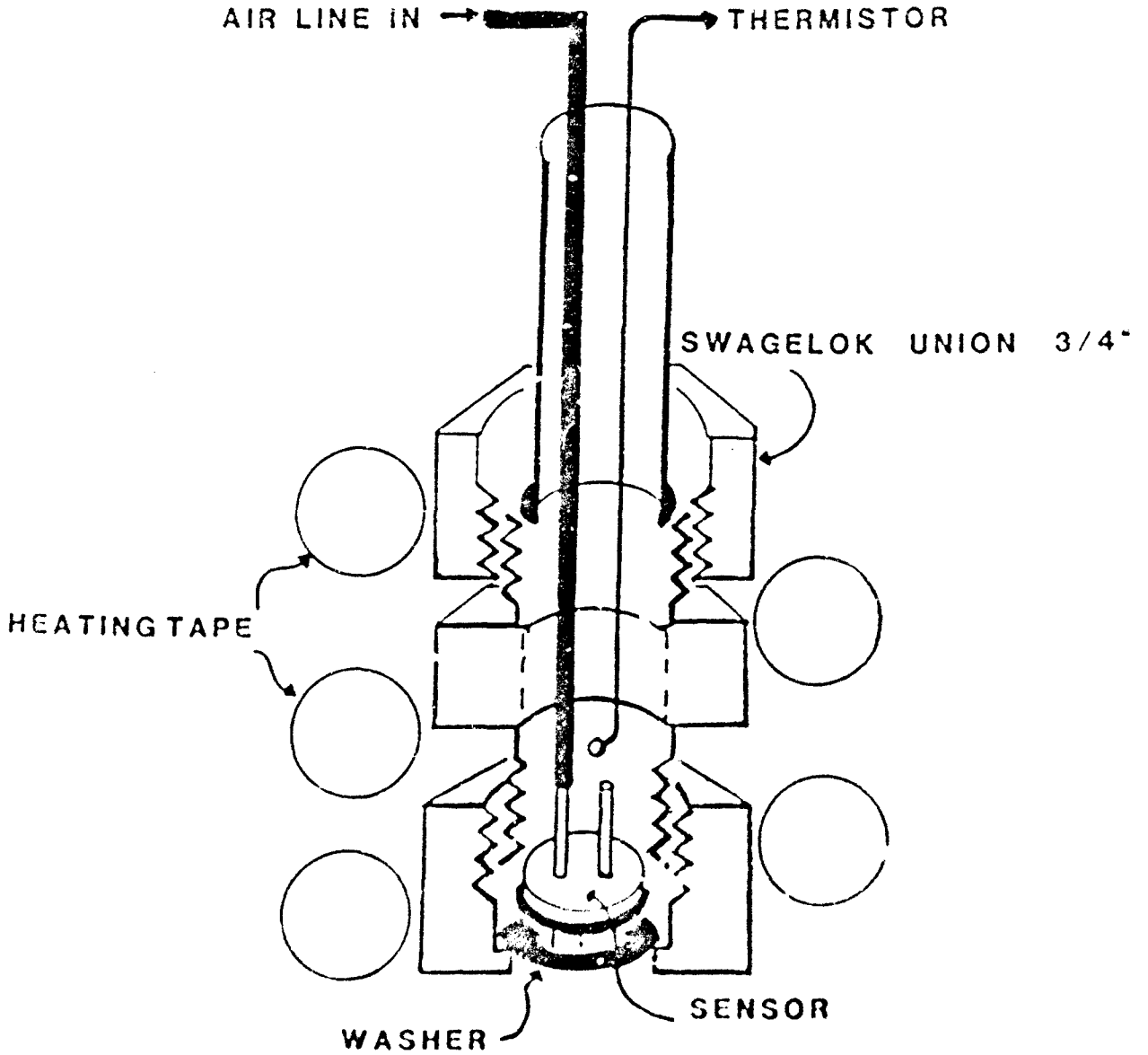

ETHYL CELLULOSE
(DIFFERENCE)
FREQ. SHIFT (PPM)
400
350
300
250
200
150
100
50
0
-50
-100
#2
#1
BLANKS
20
40
60
80
100
120
TEMPERATURE (C)


FLUOROPOLYOL
(DIFFERENCE)
FPOL#3
FPOL#2
BLANK-3
BLANK-2
FREQ. SHIFT (PPM)
500
400
300
200
100
0
-100
-200
20
40
60
80
100
120
TEMPERATURE (C)

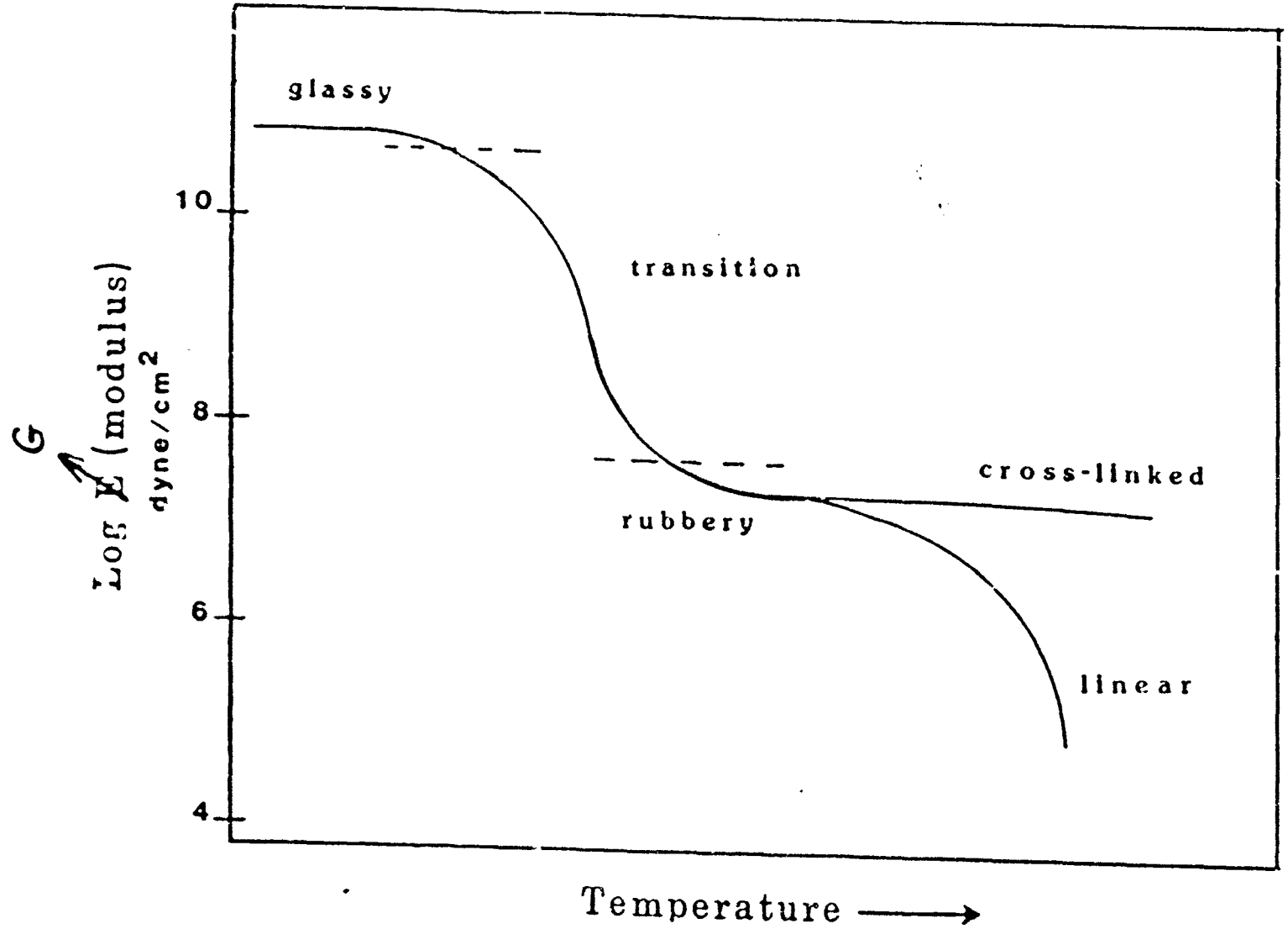

POLY(ETHYLENE MALEATE)
(DIFFERENCE)
FREQ. SHIFT (PPM)
600
500
400
300
200
100
0
-100
-200
20
40
60
80
100
120
TEMPERATURE (C)
PEM#2
PEM#3
BLANK-3
BLANK-2


100
0
-100
-200
-300
-400
-500
-600
FREQ. SHIFT (PPM)
BLANK
CHAN. 1
CHAN. 2
DIFFERENCE
20
40
60
80
100
120
TEMPERATURE (C)

SAW HEATING CHAMBER



IDEALIZED MODULUS/TEMPERATURE CURVE



LIST OF FIGURES

FIGURE 1. Idealized Modulus/Temperature Curves for Visco Elastic Polymers.

FIGURE 2. SAW Heati_ _ Chamber.

FIGURE 3. Frequency-Temperature Curves for Uncoated SAW Device.

FIGURE 4. Frequency-Temperature Curves for two PEM-Coated SAW Devices, and Corresponding Blanks.

FIGURE 5. Frequency-Temperature Curves for Two FPOL-Coated SAW Devices, and Corresponding Blanks.

FIGURE 6. Frequency-Temperature Curves for Successive Heating/Cooling Cycles for and ECEL-Coated SAW Device, and Blank.

FIGURE 7. Frequency-Temperature Curve for PCAP-Coated Device and Corresponding Blank.

FIGURE 8. Frequency-Temperature Curves for Four Successive Heating/Cooling Cycles of a FPOL-Coated SAW Device.

Literature Cited

1. Ballantine, D. S., Jr.; Rose, S. L.; Grate, J. W.; Wohltjen, H. Anal. Chem. 1986, 58, 3058.
2. Wohltjen, H. Sens. Actuators 1984, 5, 307.
3. White, R. M. Proc. IEEE 1970, 58(8), 1238.
4. Ricco, A. J.; Martin, S. J.; Zipperian, T. E. Sens. Actuators 1985, 8, 319.
5. Grate, J. W.; Snow, A.; Ballantine, D. S., Jr.; Wohltjen, H.; Abraham, M. H.; McGill, A.; Sasson, P. Anal. Chem. 1988, 60, 869.
6. Ferry, J. D. In Visco-Elastic Properties of Polymers; J. Wiley & Sons: New York, 1961; Chapter 4.
7. Armeniades, C. D.; Baer, E. In Introduction to Polymer Science and Technology: An SPE Textbook; Kaufman, H. S.; Falcetta, J. J.; Eds.; J. Wiley & Sons: New York, 1977; Chapter 6.
8. Williams, M. L.; Landel, R. F.; Ferry, J. D. J. Am. Chem. Soc. 1955, 77, 3701.
9. Wohltjen, H.; Dessy, R. Anal. Chem. 1979, 51(9), 1470.

ΔH is the thermal activation energy (7). An external oscillating stress will induce conformational changes associated with the relaxation when the frequency (ω) corresponds to the relaxation frequency, or when $\Delta = 1/\tau$. Thus, the thermal activation energy for the relaxation process can be determined by plotting the T_g vs frequency over a broad frequency range. The slope of the resulting curve will correspond to the ωH for that relaxation. This method can be used not only for relaxations at T_g, but for secondary relaxations that occur below the T_g.

Elastic Modulus Determinations. The data presented here are limited due to a lack of information regarding the moduli values for polymers used during this work. The SAW could potentially be used for the determination of such values for glassy polymers. Before such determinations are possible, however, the SAW must be calibrated using well characterized polymer systems. The mass sensitivity of the SAW can be calculated from the first term in Equation 1, and calibrated using rubbery films of known mass so that the modulus effects are negligible. The modulus of glassy materials can then be determined as the difference between the observed frequency shift for a given film and the expected shift due to the mass of the film.

Plasticization Effects. Many polymers undergo plasticization, or softening, when exposed to certain vapors. The effects of plasticization are seen as a decrease in the T_g and an expansion of the rubbery region. By determining the T_g of the polymer films in the presence and absences of a given vapor, the plasticization effects of that vapor can be studied.

Summary

To conclude, the SAW device has great potential for use in the characterization of polymeric materials. It has several advantages over existing methods, including small sample requirements (1 μg or less), great sensitivity, versatility, and low cost. It must be stressed that these SAW data were collected during studies using very thin films. The ability to extrapolate from thin film data to determine the properties of bulk materials must be verified by studying well characterized materials.

In sensor applications, greater care should be taken in the selection and application of polymer films to minimized modulus effects. The effect of elastic properties of the coating materials must be taken into consideration in the interpretation of SAW sensor data. In addition, the sensor community might take advantage of the SAW sensitivity to elastic properties to devise more sensitive sensors, and to expand the applications of these sensors.

Acknowledgements

The work described here was supported by Navy contract N-00014-88-C-2247, and was performed at the Naval Research Laboratory. The authors wish to thank Dr. A. Snow (Code 6120), Dr. D. Venezky and Dr. J. W. Grate (Code 6170) from the Chemistry Division of NRL, and Dr. R. Ting of the NRL/USRD facility for insightful discussions.

range, this is equivalent to a shift of only 4.5 ppm/°C, and becomes comparable to the frequency shifts observed for the bare devices as well as for shifts associated with thermal expansion of the coatings. If the transition occurs over a larger temperature range, such a frequency shift would not be easily identified. In such a case, identification of Tg as a change in the slope of the curve may be a more definitive method.

Future Applications

These preliminary data demonstrate the sensitivity of the SAW device to the elastic properties of polymers. The SAW device has tremendous potential for use in the characterization of these materials. In addition to sensitivity, the SAW also represents a versatile and inexpensive alternative to existing methods. Some of the parameters which could be studied using the SAW are discussed below.

Thermal Expansion Coefficients. The data presented indicate that the thermal expansion of the coatings is translated into a steady decrease in frequency. The slope of this frequency curve should be proportional to the thermal expansion coefficient. The T_g of polymeric materials can be identified by the change in the thermal expansion coefficient at the T_g. To verify the effect of surface coating coverage on observed SAW frequency-temperature response behavior, the results for airbrush film studied here must be compared with results obtained from contiguous films of known thickness.

T_g and T_m. By taking advantage of the large modulus changes that occur at the T_g and T_m, the SAW can be utilized in the identification of these transition temperatures for polymeric materials. Our results have indicated, however, that there are limitations on the applicability of the SAW for these determinations. For example, if the modulus of the initial glassy material is less than 10^{10} dyne/cm^2, then the frequency shift observed at transition will be correspondingly decreased. Also, sharp transitions occurring over small temperature ranges will be more easily identified than gradual transitions spanning large temperature ranges. The use of contiguous films, rather than the dispersed droplet films studied here, should eliminate the gradual drift associated with thermal expansion of the coating and facilitate the identification of T_g. Also, for glassy materials with a modulus below 10^{10} dyne/cm^2, the T_g still may be determined using the thermal expansion technique described previously.

The identification of T_g and T_m for semi-crystalline materials poses a challenge. If there is a high degree of crystallinity, there may be not be a sufficient amount of amorphous glassy polymer for a facile determination of T_g.

Thermal Activation Energies. The relaxation that occurs as the polymer passes from the glassy state to the elastomeric state can be described using an Arrhenius type equation,

$$\tau = \tau_0 \exp(\Delta H/kT) \qquad (3)$$

where τ_0 is the relaxation time at the reference temperature, T_0, and

The shear modulus is a complex term, and is the combined result of both loss and storage components. For a periodic or oscillatory stress, the polymer chain will tend to rearrange into conformations of lower energy to relieve this induced strain. There is a lag between the stress and the strain due to the visco-elastic nature of the polymer. In terms of modulus, the storage modulus is the component that is in phase with the strain and represents the amount of energy stored in the polymer. The amount of energy dissipated during the deformation process is called the loss modulus, and is usually 90° out of phase with the strain (7). For this reason, we would expect to see a localized minimum in the frequency curves corresponding to a maximum in the energy loss in the vicinity of the T_g (or the T_m).

The T_g can reasonably be expected to increase by 3-10 °C for each decade increase in the frequency . Thus, for 158 MHz SAW devices used during this study, the polymer films may exhibit increases in T_g of 25-80 °C. From the parameters given in Table I, the T_g for FPOL, PEM, and ECEL would be expected to fall within the temperature range of our experiments. For PCAP, the T_g is still probably below the temperature range studied, although the T_m would be within the experimental range.

For PCAP and ECEL, there appear to be localized frequency difference maxima in the frequency-temperature curves. (NOTE: these localized maxima correspond to localized frequency minima in the frequency-temperature curves of the individual coated delay lines.) This maxima occurs between 55-60 °C for PCAP, which corresponds to the T_m given in Table I. The maxima is not seen in the cooling portion of the curve but reappears in successive heating cycles. For ECEL, the maxima occurs between 95-100 °C, which is 52-57 °C above the T_g listed in Table I, and well below the T_m. This maxima is seen in both the heating and cooling portions of the curve, and falls within the temperature range that would be expected for the T_g of ECEL on the SAW device. An additional point of interest is that, while the T_g is associated with a relaxation phenomenon and increases with frequency, the T_m represents a change of phase (from the crystalline to the liquid or amorphous state) which does not exhibit a frequency dependence.

The curves for PEM are difficult to interpret. The elevated T_g would be expected to fall between 15-70 °C based on the T_g in Table I. The curves in Figure 4 exhibit a maxima between 75-90 °C which is most likely not the T_g. It is possible that the T_g occurs in the lower end of the expected temperature range, and thus would fall outside the range of our experiments.

For FPOL, the T_g would be expected to fall within the range of 35-90 °C. No frequency difference maxima are observed in this range. Close inspection of the curves in Figure 8 reveal an increase in the slope of the curve between 65-70 °C, which may correspond to the T_g. Since the thermal expansion coefficient increases significantly at the T_g, the rate of coating expansion can be observed as a frequency shift as discussed previously, and would be expected to increase in the region of the T_g.

There are several reasons why a dramatic frequency shift may not be seen at the T_g for the FPOL curves. As noted earlier, a SAW coated with a glassy material having a modulus value of 10^{10} dyne/cm^2 would exhibit a frequency shift of the order of 35 kHz. If the glassy modulus is only 10^9 dyne/cm^2, however, the expected shift decreases to 3.5 kHz or less. If the transition occurs over a 5 degree temperature

subtracting the frequency curve for the blank delay line. It appears that there is a non-recoverable frequency shift during the course of a heating/cooling cycle. This effect decreases with successive cycles. FPOL is a viscous material and would be expected to flow as the temperature increased; over several cycles the flow would gradually diminish as the film spread to its limit. Beyond this point, further increases in surface coverage would be limited to thermal expansion only, and the heating and cooling portions of the curves would become superimposed.

Determination of T_g and T_m. In addition to frequency shifts due to expansion of the film noted in the preceding discussion, the frequency should decrease even further as the film approaches the T_g (or the T_m). To determine the magnitude of the expected shift, we refer again to Equation 1. Typical values for the parameters in Equation 1 are listed in Table II. Solving the equation for a rubbery film (where $\mu = 10^7$ dyne/cm^2) yields an expected frequency shift from mass loading of -335 kHz, and a shift from the modulus contribution of only -35 Hz. For a rubbery film the effects of elastic properties on the observed frequency response can be considered negligible. If, however, the film is glassy, with $\mu = 10^{10}$ dyne/cm^2, the effect of the modulus will be -35 kHz, or greater than 10%. A change in modulus at T_g from 10^{10} dyne/cm^2 to 10^7 dyne/cm^2 would produce a decrease in the observed frequency of 35 kHz. If the modulus change occurs over a 5 degree temperature range, which is reasonable for many polymers, then a decrease of 45 ppm/°C would be expected. (NOTE: 1 ppm = 158 Hz). This should be easily observed over and above the frequency shifts discussed previously.

TABLE II. TYPICAL PARAMETER VALUES*

parameter	description	value (units)
k_1	material constant	-9.33×10^{-8} m^{2}s/kg
k_2	" "	-4.16×10^{-8} " "
V_R	Rayleigh wave velocity	3159.3 m/s
ρ	density of polymer film	1000 kg/m^3
h	film thickness	1×10^{-6} m
f_o	SAW resonant frequency	158 MHz
μ	shear modulus (glass)	10^{10} dyne/cm^2
	" " (rubber)	10^7 " "
$(\lambda + \mu/\lambda + 2\mu)$	.....	0.85 (typical value)

*Values for k_1, k_2, and V_R are for X-Y quartz, taken from reference (2).

ACKNOWLEDGEMENT

We would like to thank Kristen Hafterson, Catherine Pollock and John Wegand of Geo-Centers, Inc. for assistance with the hardness, friction and wear studies; Bill Sproul (BIRL) and Tom Thorpe (NRL) for providing TiN films; and DARPA for partial financial support.

REFERENCES

1. R.F. Bunshah et al, Deposition Technologies for Films and Coatings, Noyes, Park Ridge, N.J., 1982.
2. W.D. Sproul, J.E. Greene and J.A. Thornton (eds), Physics and Chemistry of Protective Coatings (CP no. 149), AIP, New York, 1986.
3. J.K. Hirvonen (ed), Ion Implantation, Academic Press, New York, 1980.
4. G.K. Hubler, O.W. Holland, C.R. Clayton and C.W. White (eds), Ion Implantation and Ion Beam Processing of Materials, North-Holland, NY, 1984.
5. D.M. Mattox, Chapter 3 in Ref. 1.
6. K.R. Padmanabhan, Y.F. Hsieh, J. Chevallier, and G. Sorensen, J. Vac. Sci. Technol. A1 (1983) 279.
7. M. Kohzaki, S. Noda, H. Doi, and O. Kamigaito, Mater. Letts., 6 (1987) 64.
8. J.M.E. Harper, J.J. Cuomo, R.J. Gambino and H.R. Kaufman in in O. Auciello and R. Kelly (eds), Ion Bombardment Modification of Surfaces: Fundamentals and Applications, Elsevier, Amsterdam, 1984, p. 127.
9. P.J. Martin, R.P. Netterfield, W.G. Sainty and C.G.Pacey, J. Vac. Sci. Technol. A2 (1984) 341
10. I.N. Evdokimov and G. Fischer, J. Mater. Sci. 15 (1980) 854.
11. J.S. Colligon, A.E. Hill, and H. Kheyrandish, Vacuum, 34 (1984) 843.
12. R.A. Kant, B.D. Sartwell, I.L. Singer and R.G. Vardiman, Nucl. Instrum. Methods B7/8 (1985) 915.
13. R.A. Kant and B.D. Sartwell, Mat. Sci. & Engineering, 90 (1987) 357.
14. T. Sato, K. Ohata, N. Asahi, Y. Ono, Y. Oka, I. Hashimoto and K. Arimatsu, Nucl. Instrum. Methods, B19/20 (1987) 644.
15. G. Dearnaley, Surf. Coat. Technol., 33 (1987) 453.

16. R.N. Bolster, and I.L. Singer, ASLE Trans., 24 (1981) 526.

17. R.N. Bolster and I.L. Singer in T.R. Shives and M.B. Peterson (eds.), Mechanical Properties, Performance, and Failure Modes of Coatings, Cambridge University Press, Cambridge, 1984, p. 201.

18. W.D. Sproul in Ref. 2, p. 157.

19. J.F. Ziegler, J.P. Biersack and U. Littmark, The Stopping and Range of Ions in Solids, Pergamon Press, NY, 1985, (TRIM Version 2.1).

20. L.R. Doolittle, Nucl. Instrum. and Methods, B9 (1985) 344.

TABLES

Table 1. Range and range straggling values for IBAD TiN films and implanted TiN[19].

ION (Energy)	N^+ (15 keV)		Ti^+ (40 keV)		N^+ (70 keV)
SUBSTRATE	B_4C	TiN	Al_2O_3	TiN	TiN
RANGE(nm)	31	22	23	21	90
RANGE STRAGGLING(nm)	8.2	10	8.2	8.8	31

Table 2. Composite hardness and relative wear resistance of TiN films

	KNOOP HARDNESS* (GPa)	Rel. Wear Resistance (referenced to M2 steel)
(N^+)IBAD	5	0.8
(Ti^+)IBAD	6.4	0.9
Reactive Sputtered	8.5	25

* 0.1-0.2 μm thick films on Ni at 0.15 μm indent depth.

Table 3. Friction coefficients of IBAD and RS films on steel and ceramic substrates.

		FILM TYPE	IBAD					RS	
		ION	N^+	Ti^+	Ti^+	Ti^+	Ti^+	—	—
BALL	PASS No.	SUBSTRATE	52100	52100	B_4C	SiC	Al_2O_3	H2	SiC
52100	1st		0.18	0.16	0.52	0.47	0.35	0.20	—
52100	10th		0.20	0.17	0.16	0.20	0.22	0.18	—
Si_3N_4	1st		0.16	—	0.25	0.26	0.29	0.16	0.63
Si_3N_4	10th		0.16	—	0.24	0.43	0.14	0.15	0.42

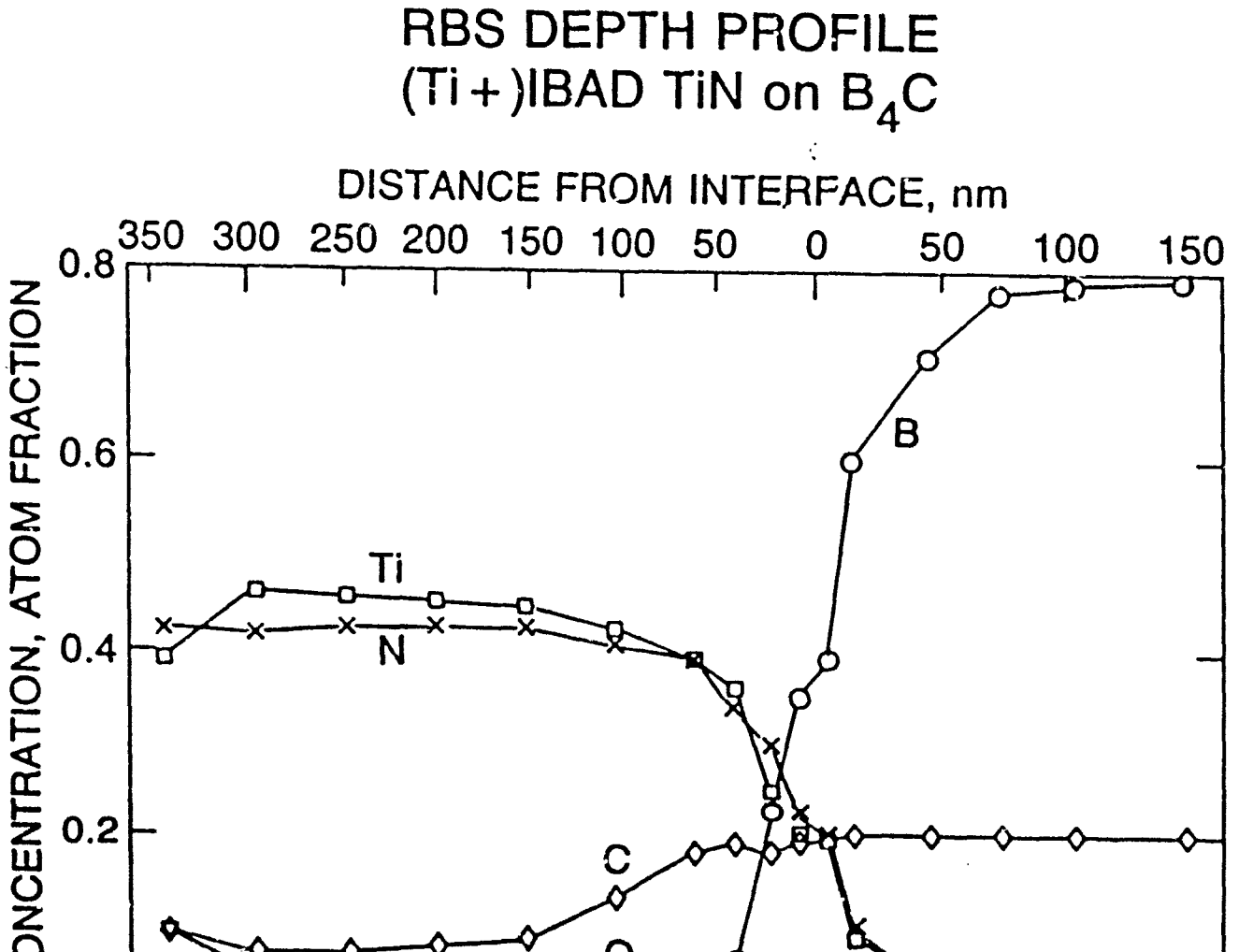


Fig. 1 a. RBS depth profiles of (Ti+)IBAD TiN on B_4C

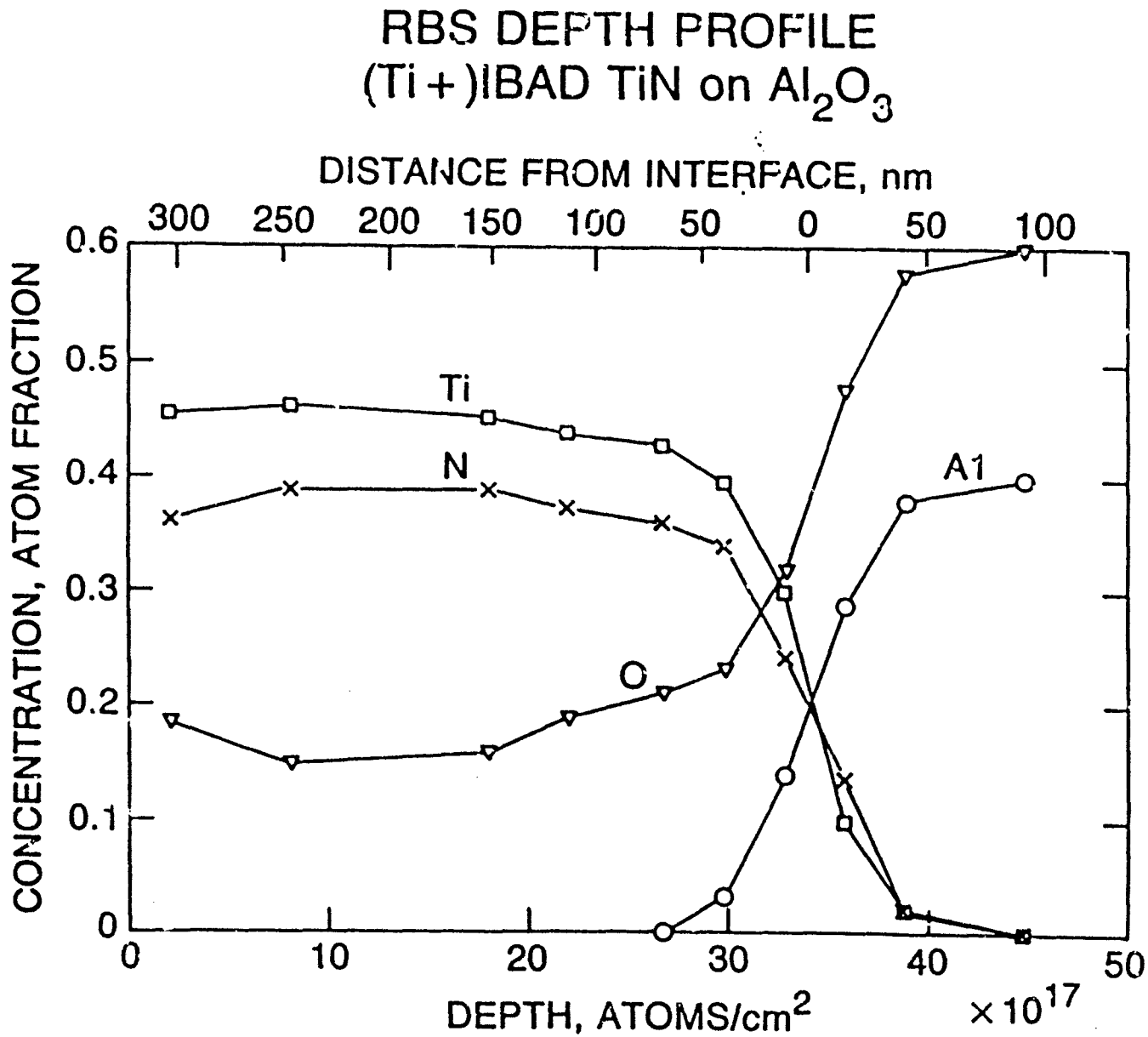


Fig. 1 b. RBS depth profiles of (Ti+)IBAD TiN on Al_2O_3.

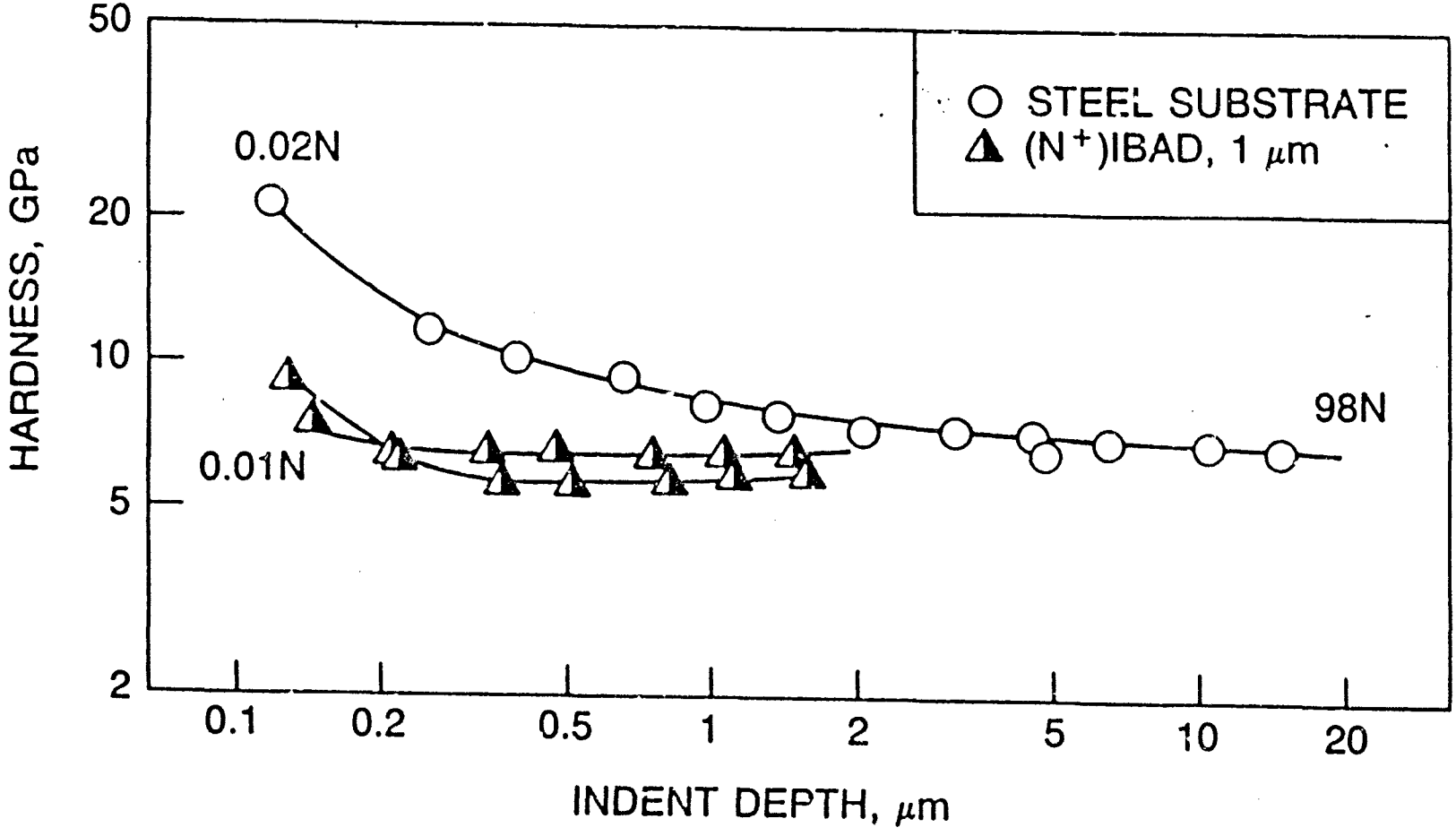


Fig. 2. Composite Knoop hardness vs. indentation depth of thick (N⁺)IBAD TiN films on 52100 steel.

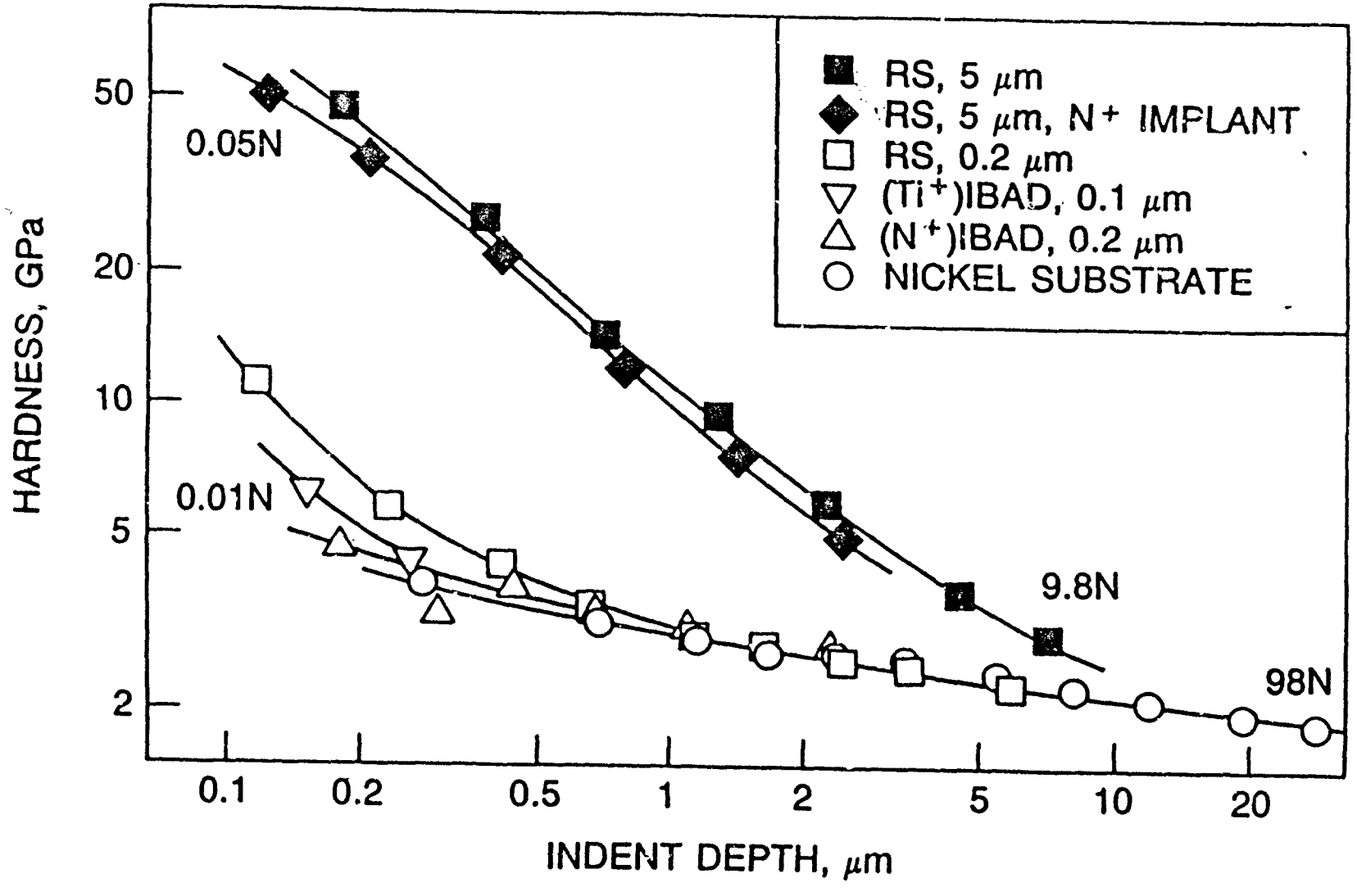


Fig. 3. Composite Knoop hardness vs. indentation depth of IBAD and RS TiN films on nickel.

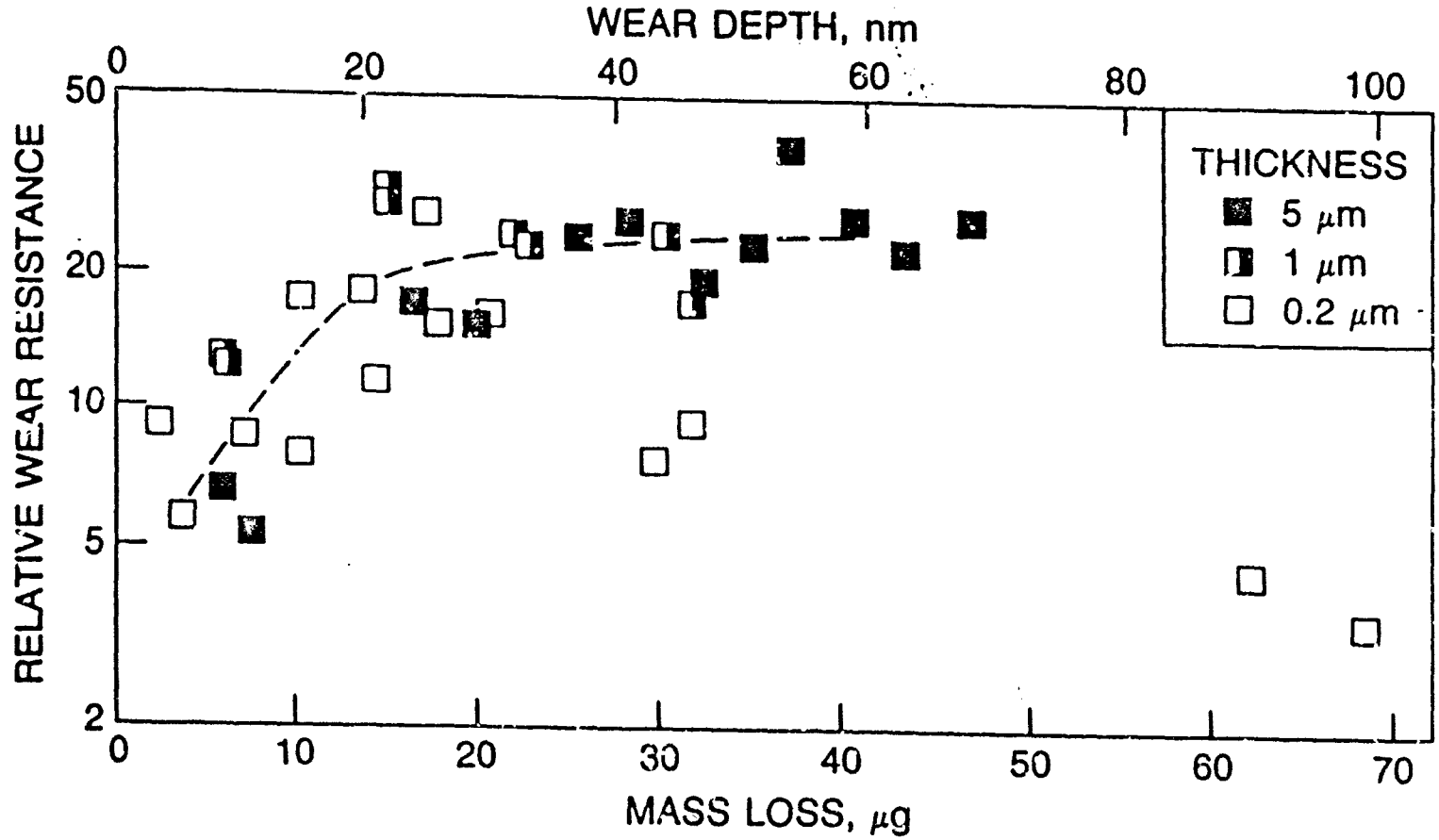
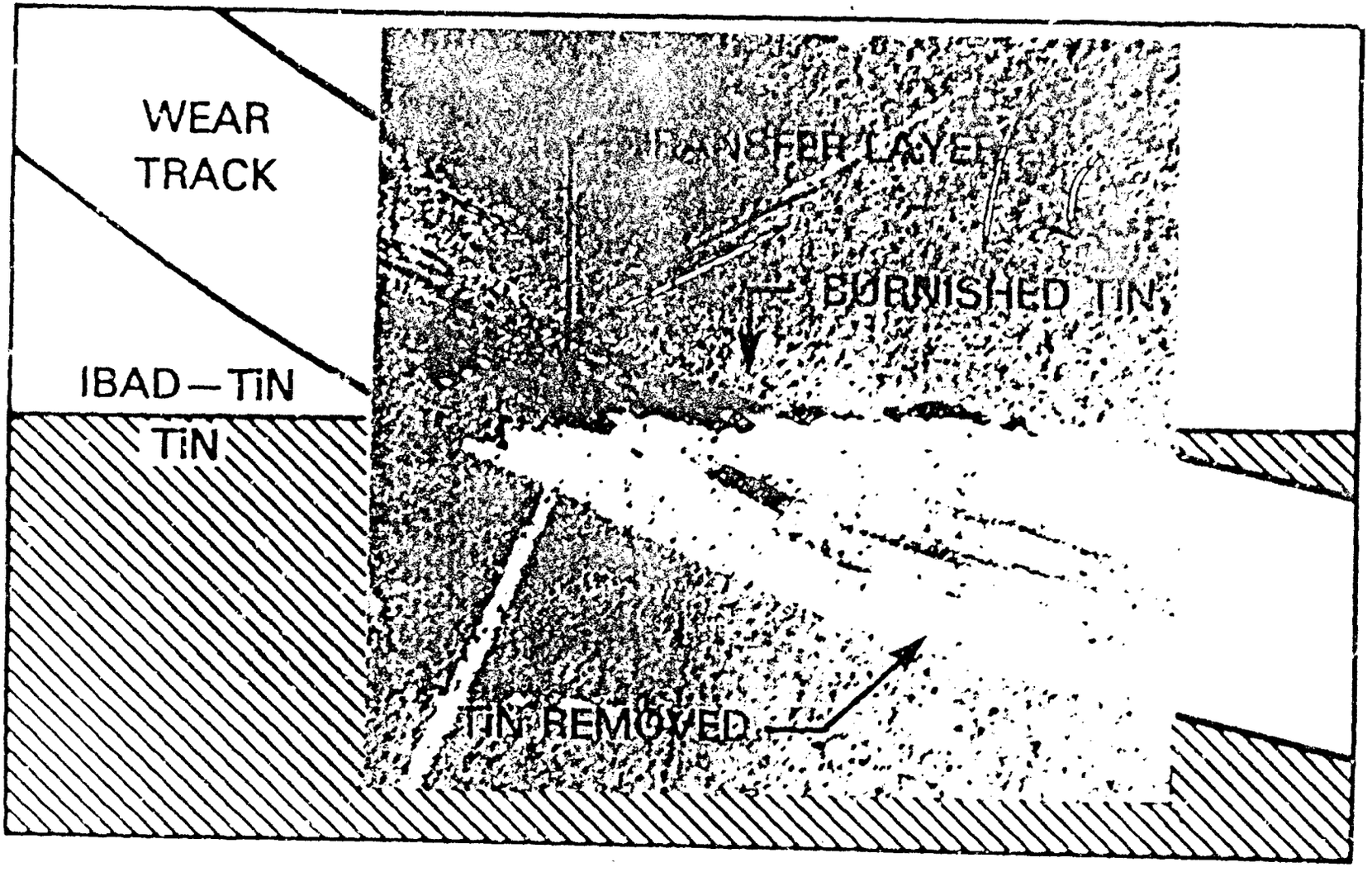


Fig. 4. Relative abrasive wear resistance vs. mass loss of RS TiN films of several thicknesses on nickel substrates referenced to M2 tool steel.

Fig. 5. Ball-on-disk wear track crossing (Ti⁺)IBAD into non-implanted PVD film on SiC substrate (after 240 passes.)



APPENDIX A6

@ June 1988 Gordon Conference

J
A5

FRICTION COEFFICIENTS - HOW LOW CAN THEY GO?

I.L. SINGER, R.N. BOLSTER, J. WEGAND[a], S. FAYEULLE[a,b]
NAVAL RESEARCH LABORATORY. WASHINGTON D.C.
[a] GEO-CENTERS, WASHINGTON D.C.
[b] ECOLE CENTRAL de LYON, ECULLY FRANCE

INTRODUCTION

Friction coefficients of low friction films generally do not obey Amonton's law, which finds that the friction coefficient is independent of load. Investigations of thin films of organic, metallic and dichalcogenide materials tend to show decreasing friction coefficients with increasing loads.

This paper examines the load dependence of the friction coefficients of MoS_2 films. Several explanations for this behavior have been proposed:

a. FRICTION TEXTURING - High loads orient MoS_2 grains with (0002) planes parallel to the substrate;

b. HEATING EFFECTS - High loads generate heat, which drives off moisture (known to increase the friction coefficient);

c. FILM SHEARING UNDER HERTZIAN CONTACT - High loads on elastically deformed substrates result in a friction coefficient, μ, given by:

$$\mu \propto S/L^{\beta},$$

where S is the SHEAR STRENGTH of the film, and $1/3 < \beta < 1/2$, depending on nature of contact (point to line). The above relationship follows directly from the interpretation of friction coefficient as the shearing pressure divided by the normal pressure. For elastic (Hertzian) contact, the normal pressure varies as L^{β}, as seen below.

Data taken from the literature and in our laboratory has been analyzed according to the Hertzian contact model for the friction coefficient of a thin easily sheared film on a hard substrate. Applicability of the model and its implications on the lower limits of friction coefficients are discussed.

DEFORMATION OF METALS BY SPHERICAL INDENTERS (TABOR, 1951)

NOMENCLATURE:

L	load	P_m	mean pressure
a	radius of contact	E	Elastic (Young's) modulus
A	Contact area	S	shear strength
R	Radius of sphere		

THE PRESSURE EXERTED BY A SPHERE ON A FLAT IS GIVEN BY:

$$P_m = L/[\pi a^2] \qquad (1)$$

CONTACT AREA UNDER ELASTIC DEFORMATION:

$$A = \pi a^2 = \pi[(3LR)/(4E)]^{2/3} \qquad (2)$$

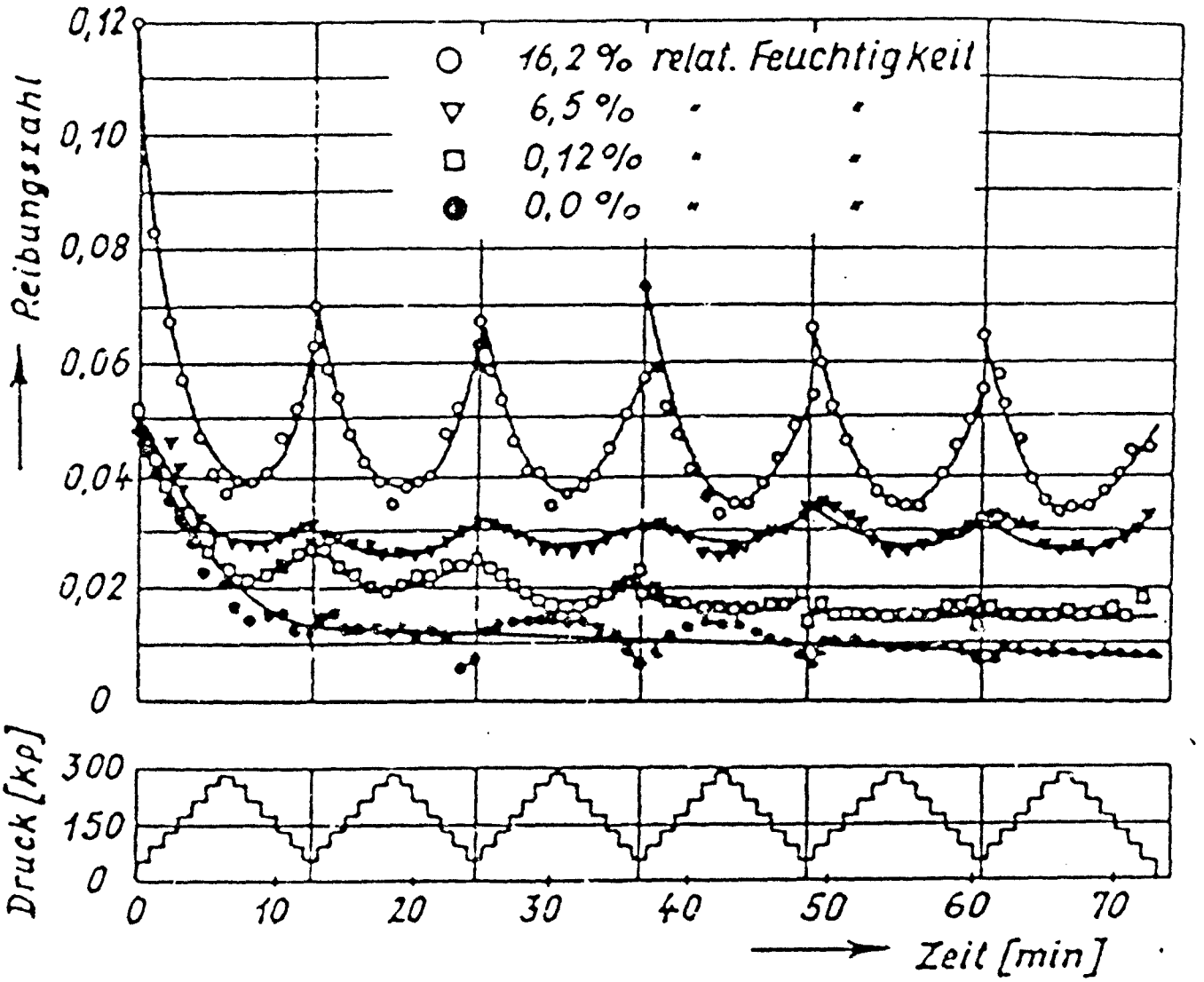
HENCE,

$$P_m = L/[\pi a^2] = 1/\pi * [(4E)/(3R)]^{2/3} * (1/L)^{1/3} \qquad (3)$$

A SIMILAR ANALYSIS FOR CYLINDER VS FLAT GIVES:

$$P_m \propto (1/L)^{1/2} \qquad (4)$$

Gänsheimer (1964)



ild 14: Einfluß von Feuchtigkeit und Belastung auf die Reibungszahl von Molybdändisulfidschichten bei Versuchen mit der LFW-1-Prüfmaschine.

ig 14: Influence de l'humidité et de la charge sur le coefficient de frottement de couches de bisulfure de molybdène lors d'essais faits avec la machine d'essai LFW-1.

14: Influsso dell'umidità e del carico sull'indice d'attrito, negli esperimenti colla macchina di prova LFW-1

Salomon and de Gee (1965)

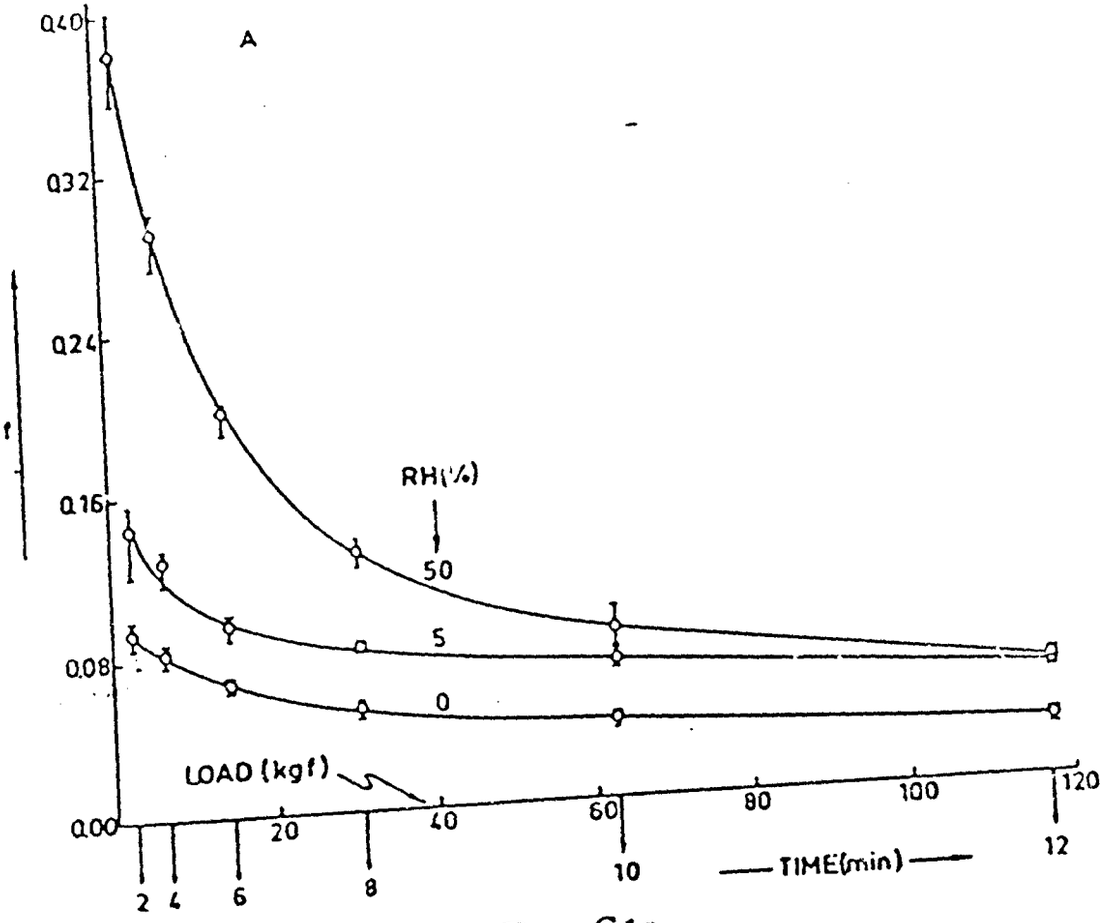
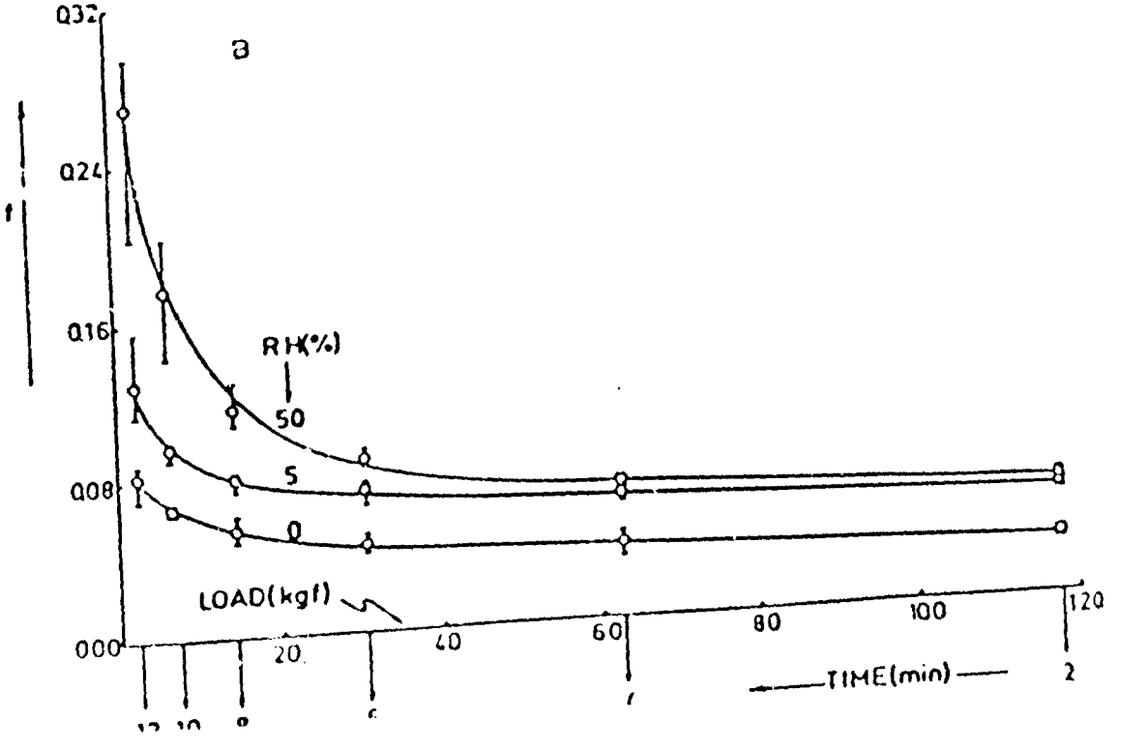
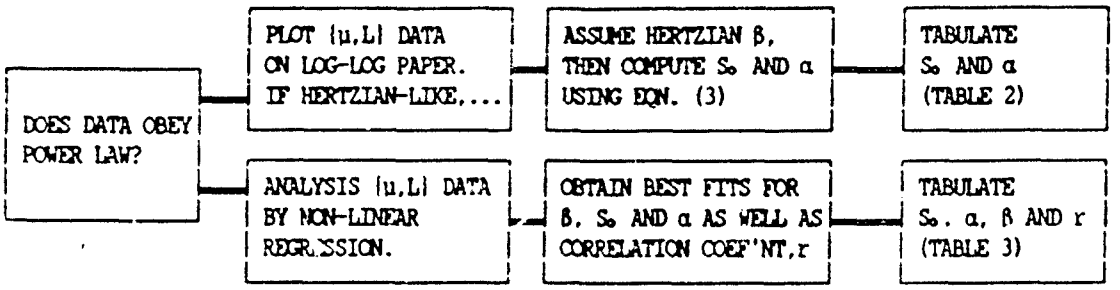
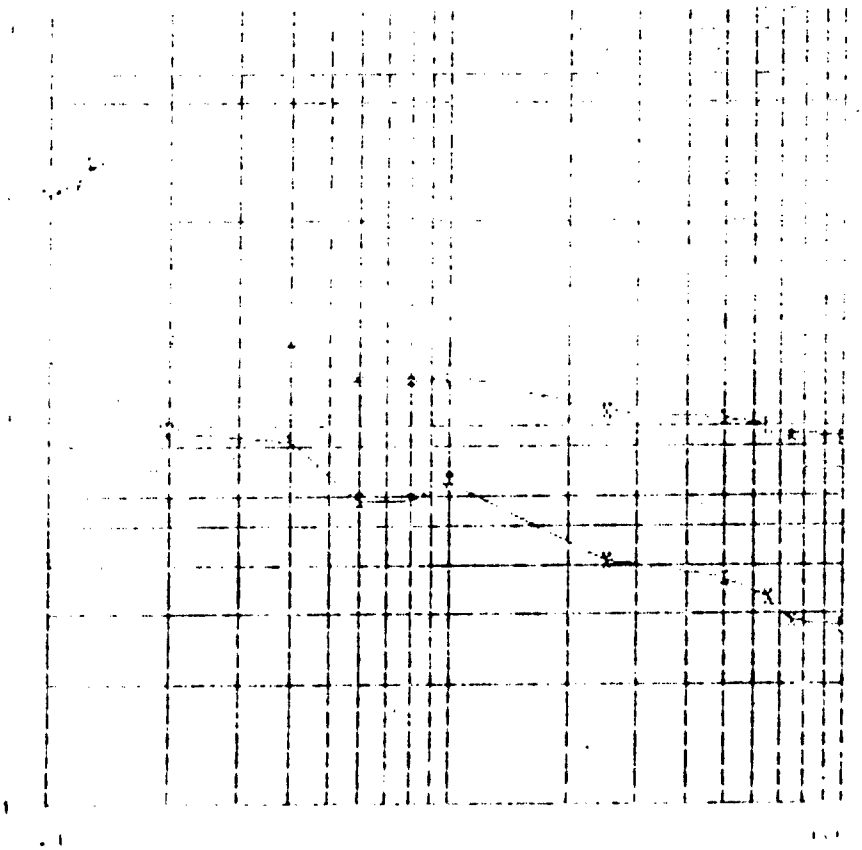


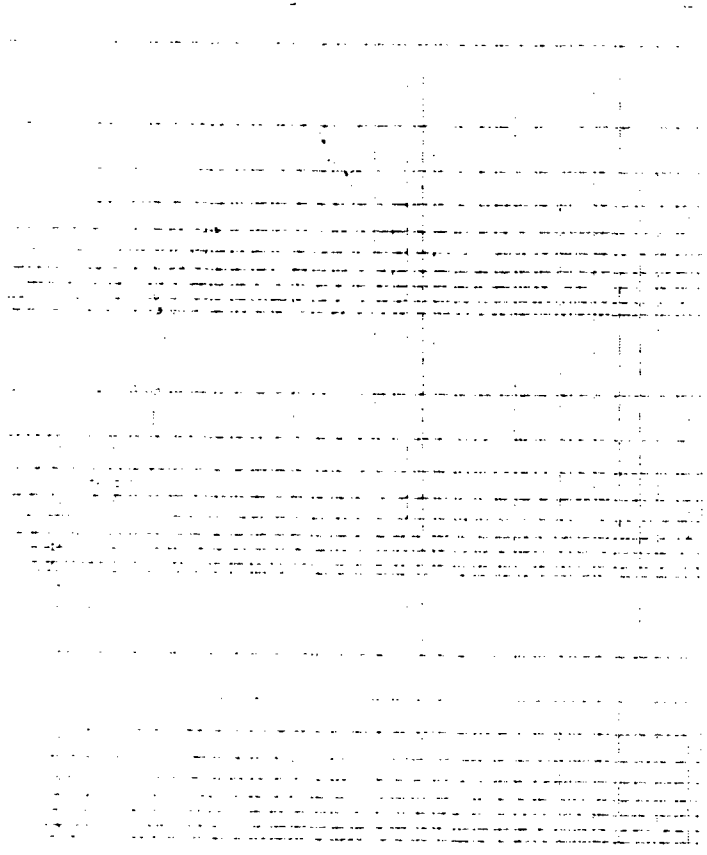
FIG. C1a



ANALYSIS OF μ vs LOAD FOR MoS_2.




=0.0
=0.05



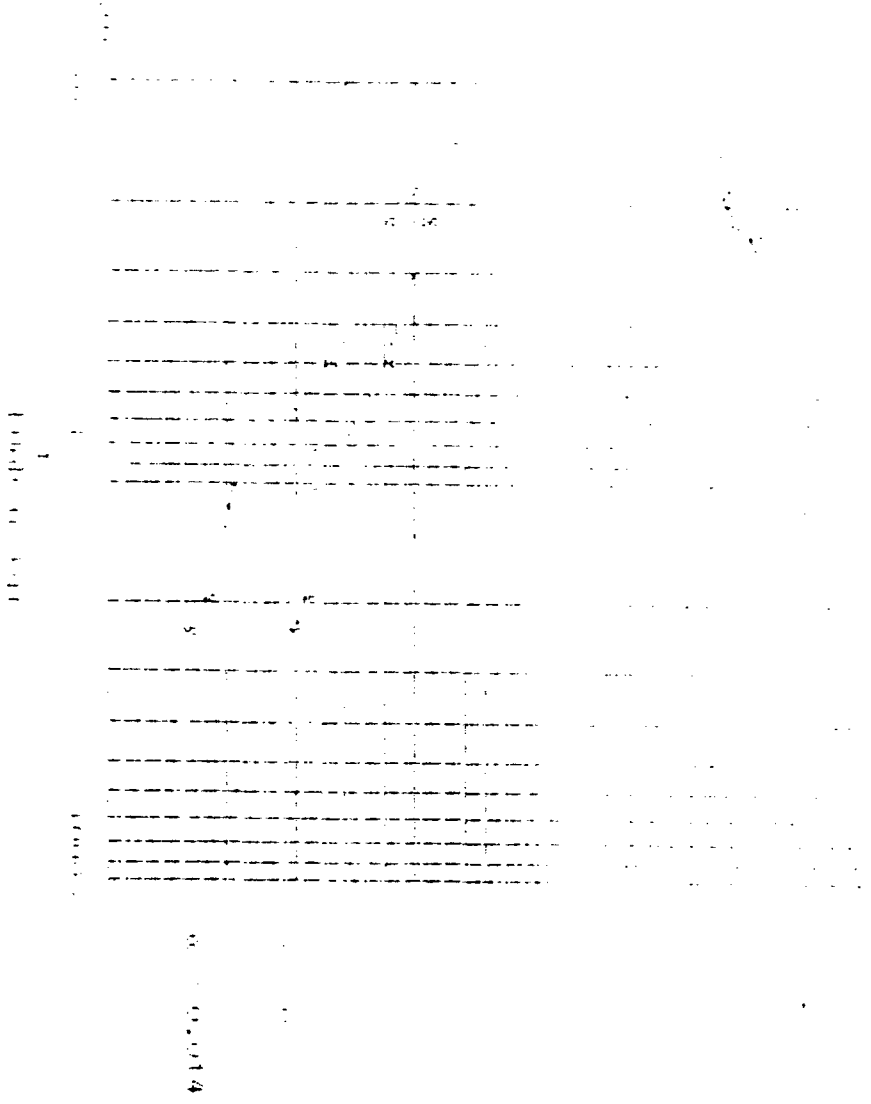


TABLE 3: β, S_o AND α VALUES AND CORRELATION COEFFICIENT BY NON-LINEAR REGRESSION.

INVESTIGATOR	β	α	S_o (MPa)	|r|
GANSHEIMER				
best fit				
RH=16.2	0.002-0.08	-0.3-(-11)	7-100	0.99
RH=6.5	0.001	-4-(-10)	50-100	0.95
α=0 fit				
RH=16.2	0.43-0.50	"0"	10-20	0.98-0.99
RH=6.5	0.12	"0"	10	0.95
KARPE				
best fit	0.2-0.4	0.04-0.07	25-40	0.96-0.99
α=0 fit	-0.15	"0"	60-70	0.95-0.97
SALOMON AND DeGEE				
best fit				
RH=50	0.26	-0.13	20	0.998
RH=5	0.19	-0.02	5	0.990
α=0 fit				
RH=50	0.48	"0"	20	0.992
RH=5	0.23	"0"	5	0.990
ROBERTS				
best fit	0.39	0.001	6.2	0.962
α=0 fit	0.33	"0"	6.6	0.962
NRL				
best fit	0.7	0.22	47	0.988
α=0 fit	0.33	"0"	5	0.985

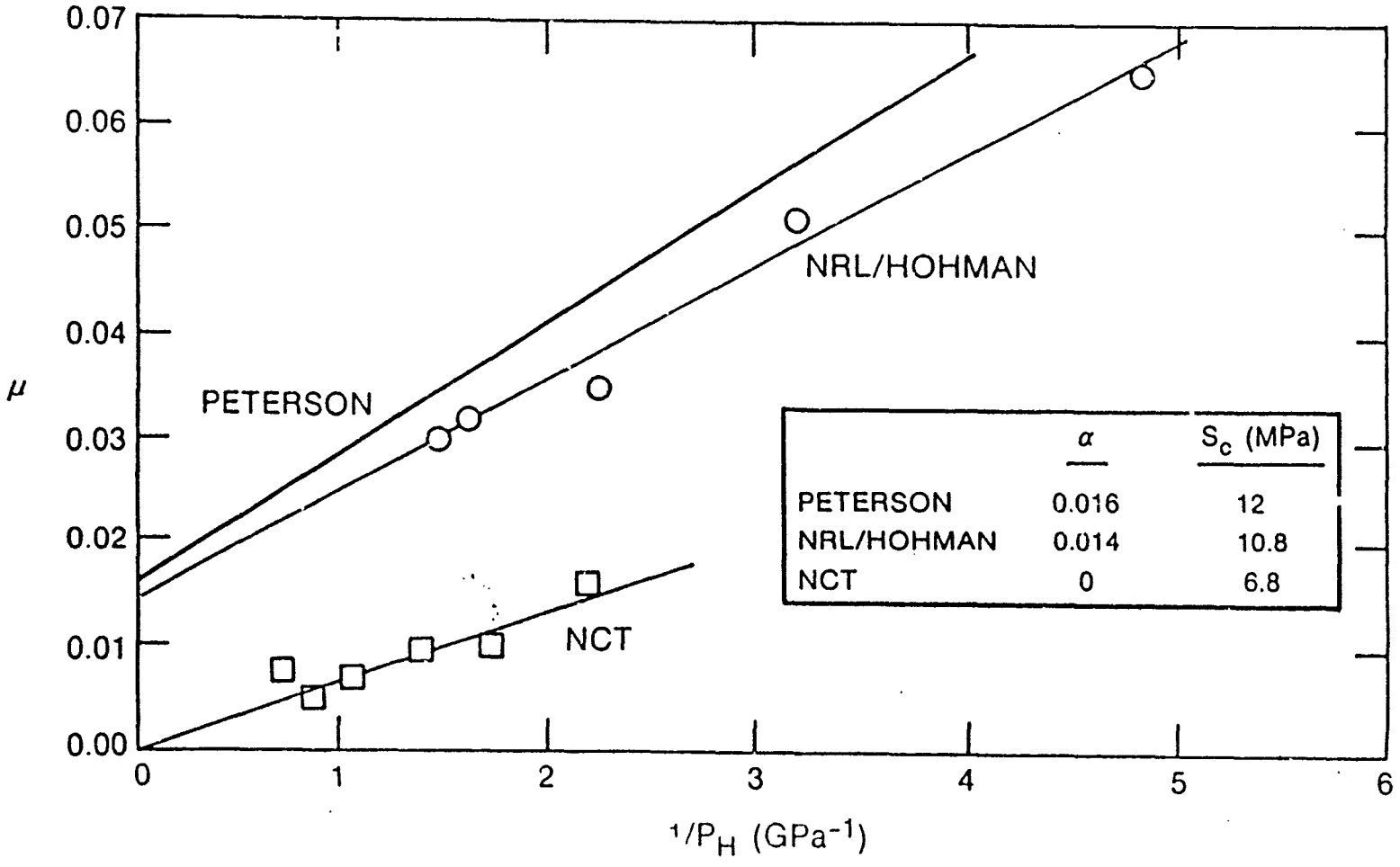
β, α, S_o and r obtained from:

$$\mu = C\, S_o / L^{\beta} + \alpha$$

and C is a geometrical constant.

FRICTION BEHAVIOR OF M_oS_2

$$\mu = \frac{S_o}{P_H} + \alpha$$



	α	S_c (MPa)
PETERSON	0.016	12
NRL/HOHMAN	0.014	10.8
NCT	0	6.8

BIBLIOGRAPHY

1. Kanakia, M.D. and Peterson, M.B., "Literature Review of Solid Lubrication Mechanisms," Interim Report BFLRF No. 213 (AD A185010), Defense Tech Info. Center, Washington DC, November 1986.

2. Gansheimer, J. "Neue Erkenntnisse Uber Dei Wirkungsweise von Molybdandisulfid als Schmierstoffe," Schmiertechnik, 11 (1964) 271-280.

3. Karpe, S.A., "The Effects of Load on the Frictional Properties of Molybdenum Disulfide," Trans. ASLE, 8, (1965) 156-178 .

4. Salomon, G. and DeGee, A.W.J., discussion to Karpe above.

5. Roberts, E.W., "The tribology of sputtered Molybdenum Disulphide films," Proc. Inst. Mech. Eng., Tribology - Friction, Lubrication and Wear, Fifty Years On, Vol. 1, London, (1987) 503-510.

APPENDIX A7

FRICTION & WEAR BEHAVIOUR OF DIAMOND FILMS ON Si

Ian P. Hayward - GeoCenters, Inc.

Irwin L. Singer - Naval Research Lab

13 July 1989

A-1

DIAMOND COATING TRIBOLOGY : Key Issues

How slippery are the coatings (in air and vacuum)?

How hard and tough are the coatings?

How well do the coatings adhere to their substrates?

FRICTION OF DIAMOND AND DLC

	DIAMOND	DLC
IN VACUUM	0.05 TO >1 0.1 (H PRESENT)*	0.005 TO 0.01
IN AIR	0.05	0.1 TO 0.5
TEMPS (<800°C)	0.1	DEGRADES

*I. HAYWARD, CAMBRIDGE UNIV. (1987)

TEST CONFIGURATION

Apparatus	Reciprocating sliding Bidirectional, pin-on-flat.
Pin	Diamond. 200 um radius spherical tip with 100 um diameter wear flat.
Flats	Diamond coated silicon
Load	100 - 300 g (1 - 3 N).
Contact pressure	1 GPa.
Sliding speed	1 mm s^{-1}.
Track lengths	1 mm.
Atmosphere	Air (2% - 70% RH).

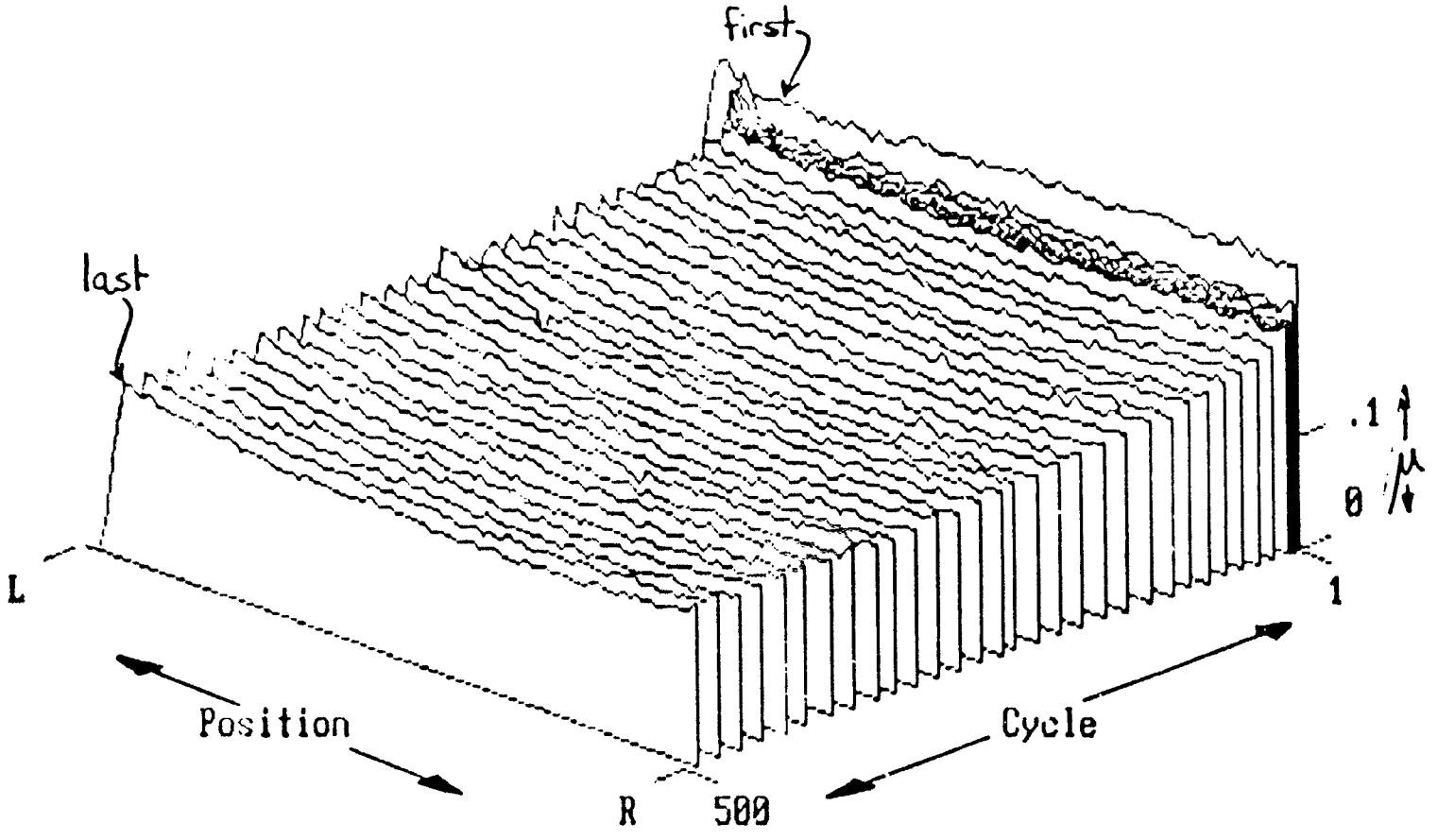
ANALYTICAL TECHNIQUES

Micro Raman.

Infra-red spectroscopy (transmission FTIR).

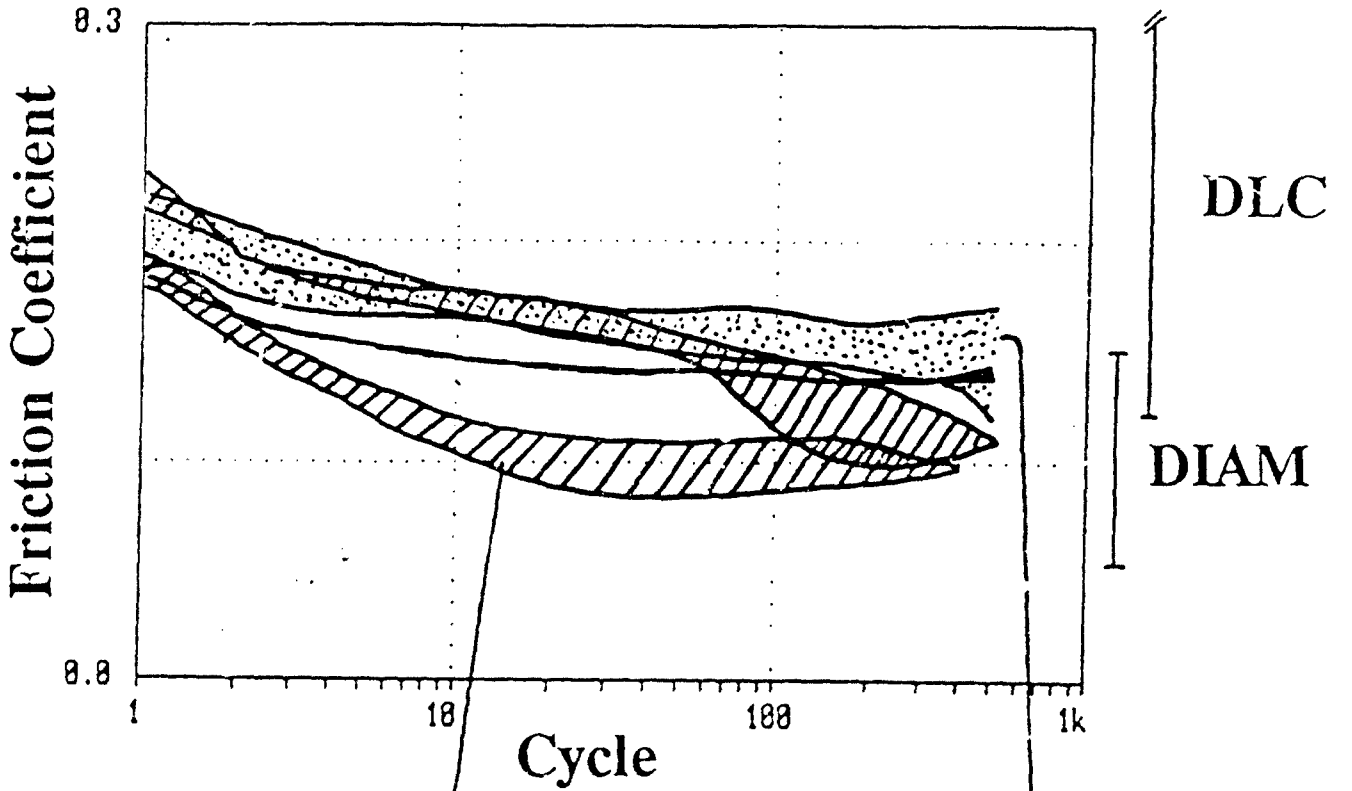
Surface profilometry.

Optical microscopy.



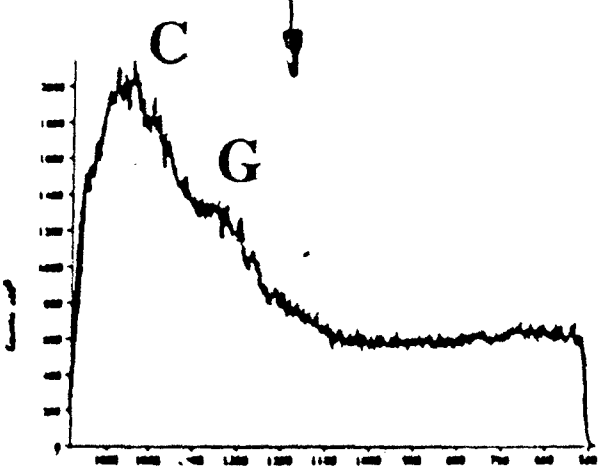
Forward friction coeffic ent (0-100)
XL12B

DIAMOND FILMS DC PLASMA



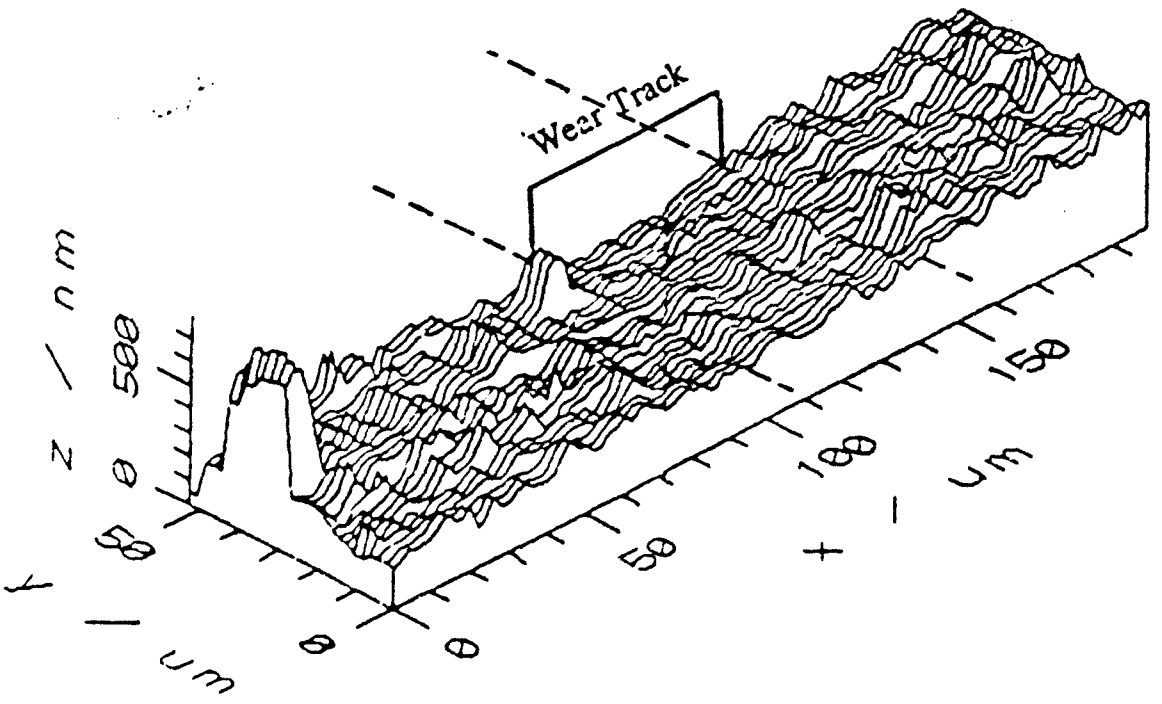
RAMAN





3-D Surface Profile of Crystallume Diamond Film

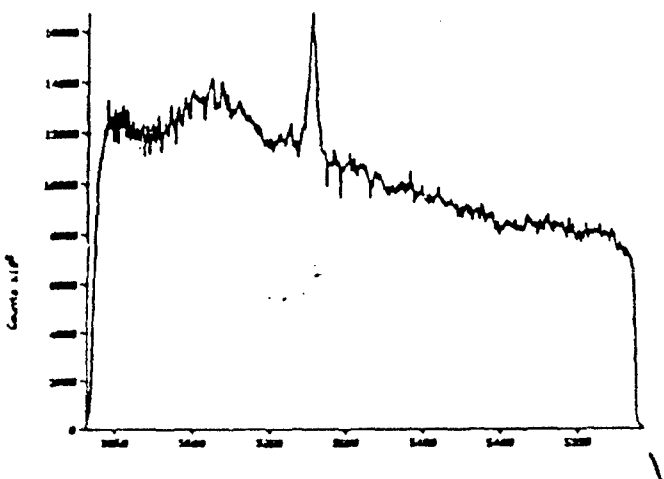
Crystallume specimen 13-Y-2

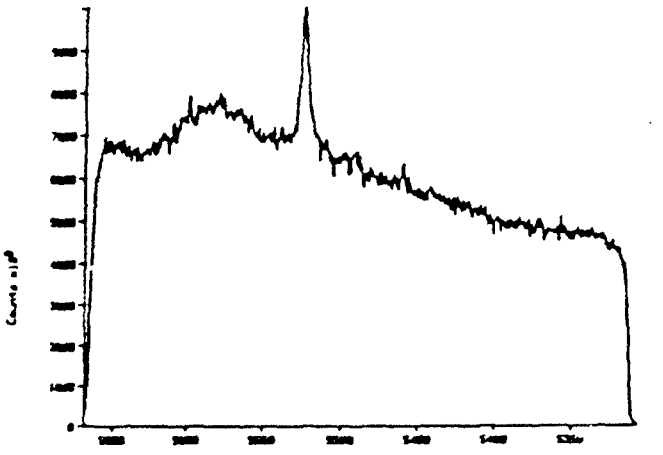


RA 0.07 µm

MICRORAMAN SPECTRA FROM CRYSTALLUME DIAMOND FILM

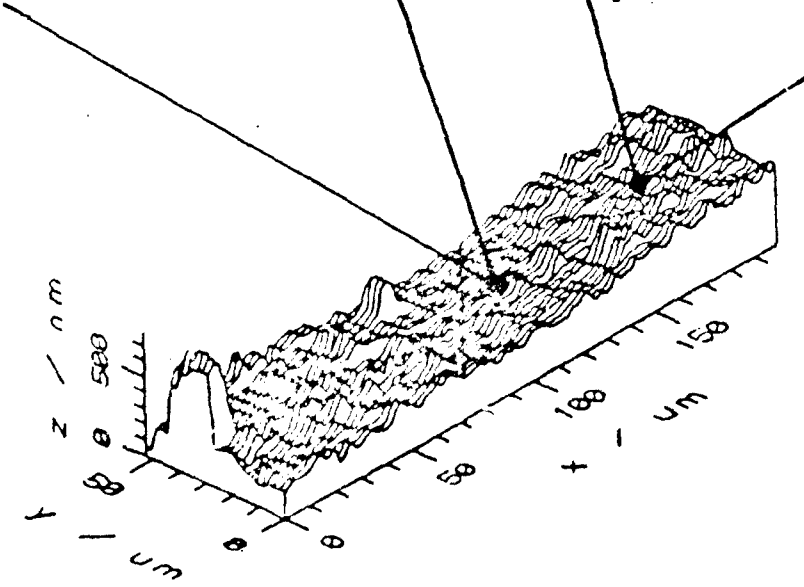
Crystallume specimen 13-Y-2





Spectrum from within wear track

Spectrum from outside wear track



Lower final friction:

- bigger diamond peak in Raman
- less C-H stretching in FTIR
- rougher coating surface before sliding
- rougher wear track (frictional mechanism)

No effect of humidity on friction and wear.

- Diamond friction independent of humidity.
- DLC friction 0.01 at 1% RH or less.

MECHANISM

DIAMOND SLIDING ON (DIAMOND + DLC)

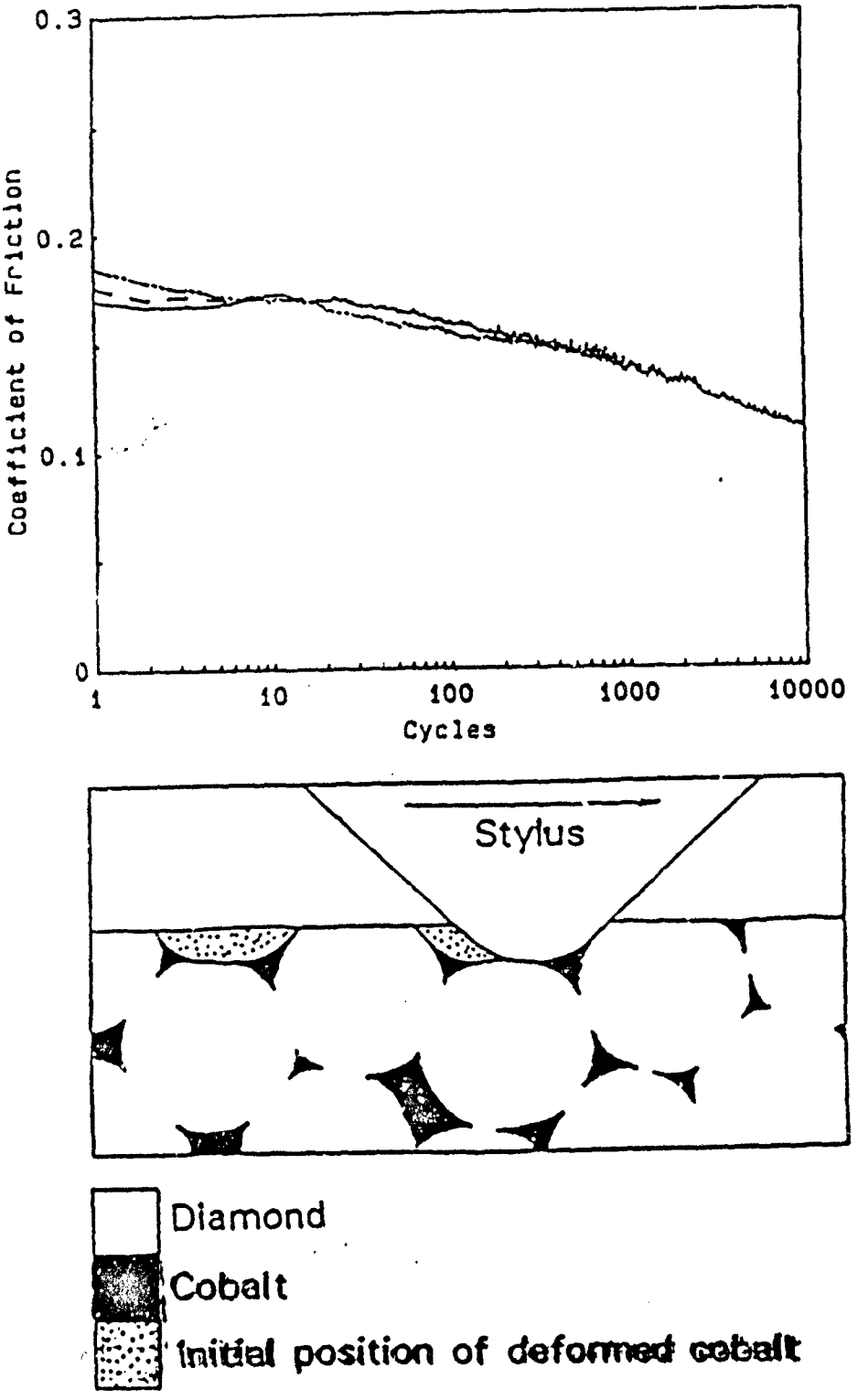
DLC deforms/wears

faster than diamond

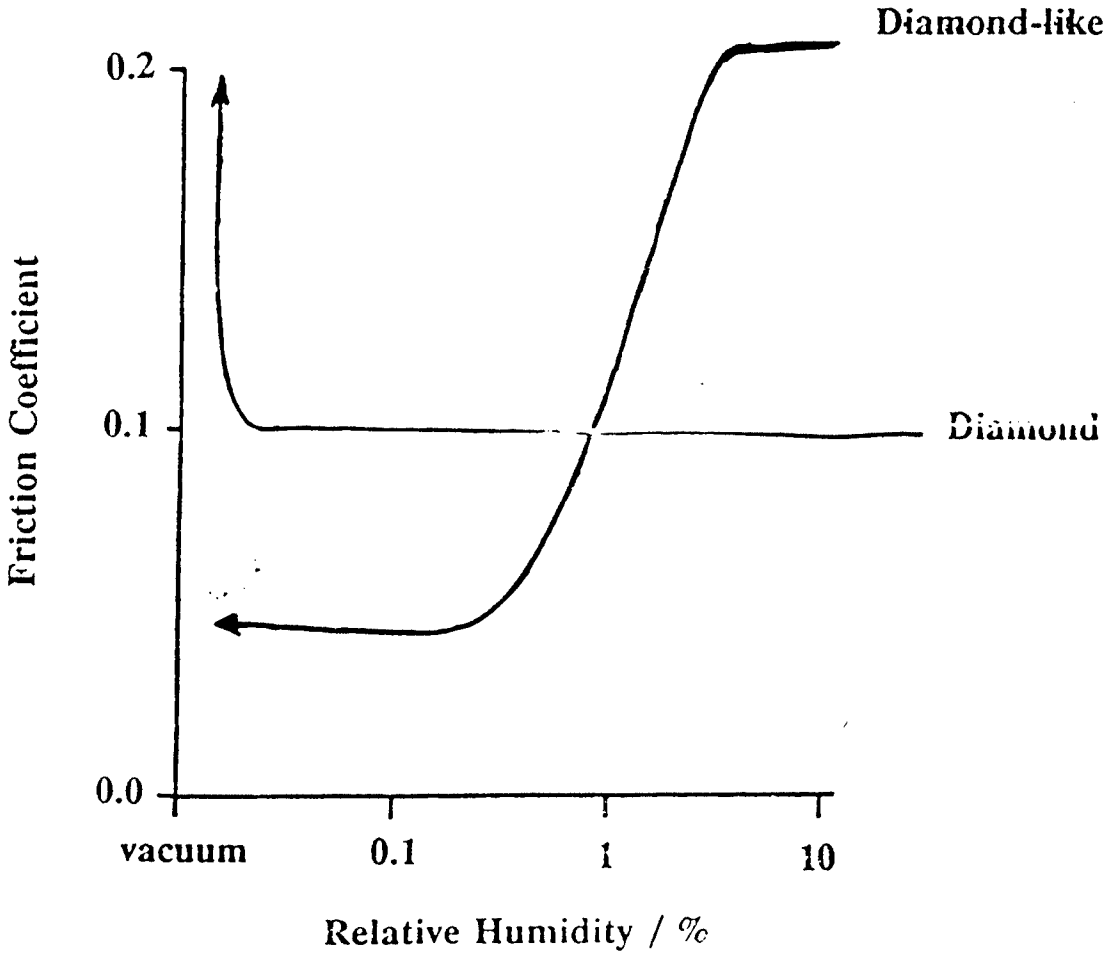
DIAMOND SLIDING ON DIAMOND

DIAMOND SLIDING ON SYNDITE. (Hayward, 1987).

(Small diamond grits sintered in a cobalt matrix).



BENEFICIAL EFFECTS OF DLC

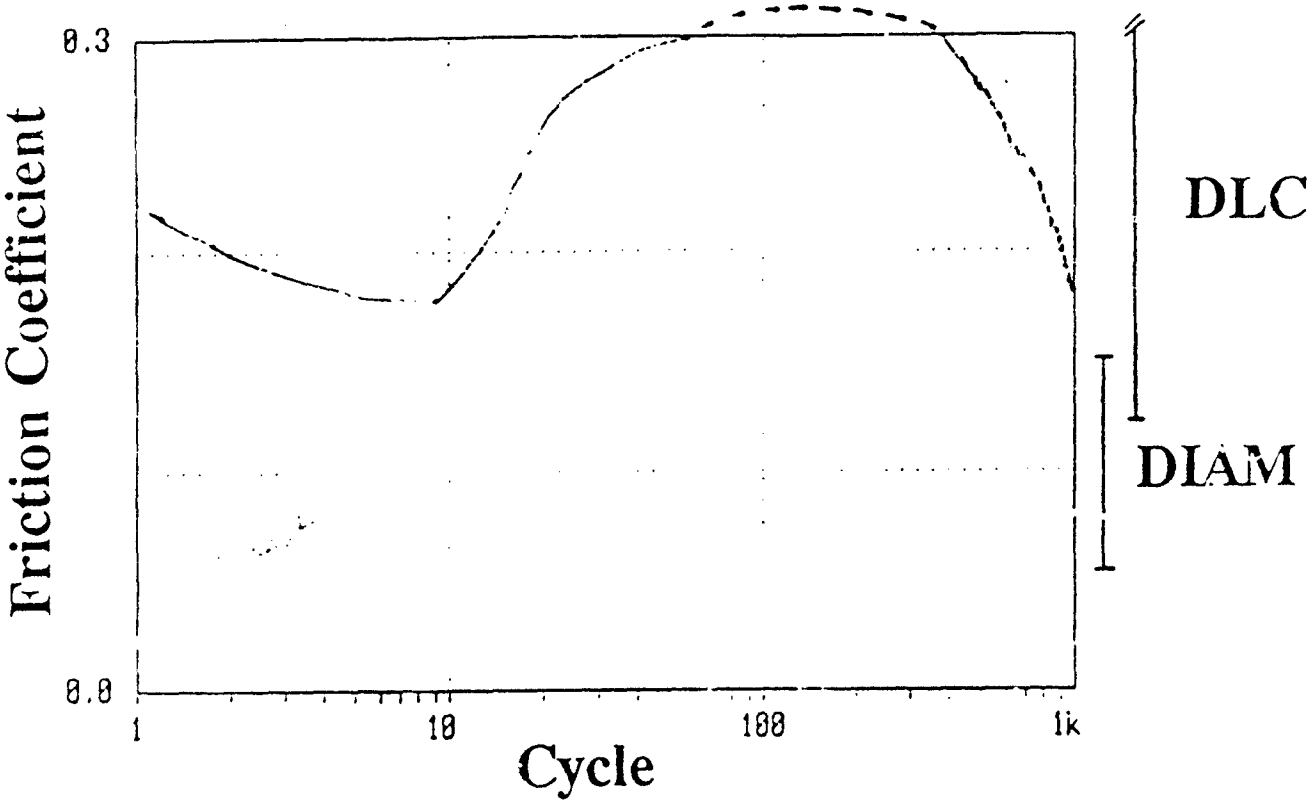


DLC : Weissmantel et al., Thin Solid Films 96, 31 (1982).

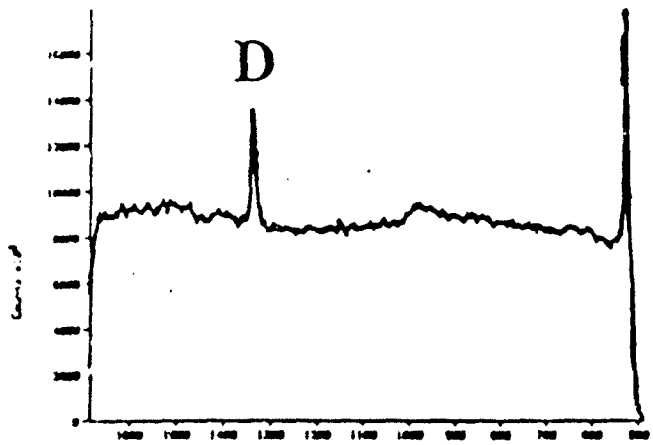
Diamond : Bowden & Hanwell, Proc. R. Soc. A295, (1966).

DIAMOND FILMS

MICROWAVE DEPOSITED



RAMAN



FRICTION OF DIAMOND ON DIAMOND FILMS COATED WITH ORGANIC ACID

Minimum friction coefficient	
without C20 acid	with C20 acid
0.1	0.03

SIGNIFICANCE

If the "proper" surface chemical configuration can be achieved then ultralow friction coefficients are possible on diamond films.

CONCLUSIONS

- Tribological behaviour correlates with Raman and FTIR.

  More diamond... lower final friction.

- Coatings need "running in" to achieve lowest friction values.

- Microwave deposited films appear to have a lower cohesive strength than DC plasma films.

- Surface chemistry modifications may allow very low friction coefficients to be achieved.

PLANS

- FTIR studies of wear tracks.
- Extend studies to harder substrates / higher contact pressures.
- Vacuum Tribotester.
  - Testing in simulated space conditions.
  - Surface analytical techniques (Scanning Auger etc.).
- Non-diamond styli.

DIAMOND FILM TRIBOLOGY (NRL)

- Correlation of friction coefficient with % diamond in film
- Evidence for reduced friction of diamond films with "proper" surface treatment
- Potential of Diamond-like carbon (DLC) components in space applications (vacuum environments)

APPENDIX B1

P^

CHEMICAL
RESEARCH,
DEVELOPMENT &
ENGINEERING
CENTER

CRDEC-TR-045

THE DYNAMIC BEHAVIOR OF WATER VAPOR ON ACTIVATED CARBON

John J. Mahle
RESEARCH DIRECTORATE

David K. Friday
GEO-CENTERS, INC.
Ft. Washington, MD 20744

February 1989

U.S. ARMY
ARMAMENT
MUNITIONS
CHEMICAL COMMAND

Aberdeen Proving Ground, Maryland 21010-5423

Disclaimer

The findings in this report are not to be construed as an official Department of the Army position unless so designated by other authorizing documents.

Distribution Statement

Approved for public release; distribution is unlimited.

UNCLASSIFIED
SECURITY CLASSIFICATION OF THIS PAGE

REPORT DOCUMENTATION PAGE

Form Approved
OMB No. 0704-0188

1a. REPORT SECURITY CLASSIFICATION: UNCLASSIFIED	1b. RESTRICTIVE MARKINGS
2a. SECURITY CLASSIFICATION AUTHORITY	3. DISTRIBUTION/AVAILABILITY OF REPORT: Approved for public release; distribution is unlimited.
2b. DECLASSIFICATION/DOWNGRADING SCHEDULE	
4. PERFORMING ORGANIZATION REPORT NUMBER(S): CRDEC-TR-045	5. MONITORING ORGANIZATION REPORT NUMBER(S)
6a. NAME OF PERFORMING ORGANIZATION: See Reverse; 6b. OFFICE SYMBOL (If applicable)	7a. NAME OF MONITORING ORGANIZATION
6c. ADDRESS (City, State, and ZIP Code)	7b. ADDRESS (City, State, and ZIP Code)
8a. NAME OF FUNDING/SPONSORING ORGANIZATION: CRDEC; 8b. OFFICE SYMBOL (If applicable): SMCCR-RSC-A	9. PROCUREMENT INSTRUMENT IDENTIFICATION NUMBER: DAAA15-87-D-0007
8c. ADDRESS (City, State, and ZIP Code): Aberdeen Proving Ground, MD 21010-5423	10. SOURCE OF FUNDING NUMBERS: PROGRAM ELEMENT NO.; PROJECT NO.: 1C161102; TASK NO.: A71A; WORK UNIT ACCESSION NO.

11. TITLE (Include Security Classification)
The Dynamic Behavior of Water Vapor on Activated Carbon

12. PERSONAL AUTHOR(S)
Mahle, John J. (CRDEC); and Friday, David K. (GEO-Centers, Inc.)

13a. TYPE OF REPORT	13b. TIME COVERED	14. DATE OF REPORT (Year, Month, Day)	15. PAGE COUNT
Technical	FROM 87 Feb TO 88 Jul	1989 February	30

16. SUPPLEMENTARY NOTATION

17. COSATI CODES		
FIELD	GROUP	SUB-GROUP
15	06	03

18. SUBJECT TERMS (Continue on reverse if necessary and identify by block number)
Breakthrough; Simulation; Water vapor; Stage model; Activated carbon; Equilibrium theory

19. ABSTRACT (Continue on reverse if necessary and identify by block number)

Water vapor is present, usually in relatively large concentrations, in many adsorption systems of industrial and military irterest. This work develops an approach to predict the dynamic behavior of water vapor on an activated carbon adsorbent. Prior studies have neglected the importance of including the heat balance to account for behavior to high relative humidities.

Water vapor isotherms were measured for BPL carbon at 15, 25, and 35 °C, and the data were correlated using a modified version of the Antoine Equation first suggested by LeVan. Breakthrough experiments were performed using the following initial bed and feed conditions: (1) 50% RH feed to a dry bed, (2) 80% RH feed to a bed initially equilibrated at 50% RH, and (3) 80% RH feed to a dry bed. Two mathematical models were developed to analyze the values predicted using a non-isothermal stage model with a fluid phase mass transfer resistance and an adiabatic equilibrium theory model.

20. DISTRIBUTION/AVAILABILITY OF ABSTRACT	21. ABSTRACT SECURITY CLASSIFICATION
☒ UNCLASSIFIED/UNLIMITED ☐ SAME AS RPT ☐ DTIC USERS	UNCLASSIFIED

22a. NAME OF RESPONSIBLE INDIVIDUAL	22b. TELEPHONE (Include Area Code)	22c. OFFICE SYMBOL
SANDRA J. JOHNSON	(301) 671-2[illegible]4	SMCCR-SPS-T

DD Form 1473, JUN 86 — Previous editions are obsolete. — SECURITY CLASSIFICATION OF THIS PAGE
UNCLASSIFIED

6. NAME AND ADDRESS OF PERFORMING ORGANIZATION (Continued)

U.S. Army Chemical Pesearch, Development and Engineering Center
ATTN: SMCCR-RSC-A
Aberdeen Proving Ground, MD 21010-5423

GEO-Centers, Inc.
10903 Indian Head Highway
Ft. Washington, MD 20744

PREFACE

The work described in this report was authorized under Project No. 1C161102A71A, Research in CW/CB Defense, and Contract No. DAAA15-87-D-0007. This work was started in February 1987 and completed in July 1988.

The use of trade names or manufacturers' names in this report does not constitute an official endorsement of any commercial products. This report may not be cited for purposes of advertisement.

Reproduction of this document in whole or in part is prohibited except with permission of the Commander, U.S. Army Chemical Research, Development and Engineering Center, ATTN: SMCCR-SPS-T, Aberdeen Proving Ground, Maryland 21010-5423. However, the Defense Technical Information Center and the National Technical Information Service are authorized to reproduce the document for U.S. Government purposes.

This report has been approved for release to the public.

Blank

CONTENTS

		Page
1.	INTRODUCTION	7
2.	THEORY	7
2.1	Material and Energy Balances	7
2.2	Stage Model Approach	10
2.3	Equilibrium Theory	11
3.	MATERIALS AND METHODS	13
4.	RESULTS AND DISCUSSION	14
4.1	Water on Activated Carbon	14
4.2	Breakthrough of 50% RH Feed To A Clean Bed	16
4.3	Breakthrough of 80% RH Feed To Bed Equilibrated At 50% RH	18
4.4	Breakthrough of 80% RH Feed To A Clean Bed	18
5.	CONCLUSIONS	19
	NOTATION	21
	LITERATURE CITED	29

LIST OF FIGURES

		Page
1.	Schematic of Breakthrough Apparatus	22
2.	Path In Modified Isotherm Plane 50%RH, 80%RH Feed To Clean Bed And 80%RH Feed to 50%RH Bed of BPL	23
3.	Enlargement of Path In Modified Isotherm Plane 50%RH, 80%RH Feed To Clean Bed Of BPL	24
4.	Breakthrough of Water Vapor On BPL Carbon 50%RH Feed To Clean Bed	25
5.	Breakthrough Of Water Vapor On BPL Carbon 80%RH Feed To Bed Equilibrated To 50%RH	26
6.	Breakthrough Of Water Vapor On BPL Carbon 80%RH Feed To Clean Bed	27

LIST OF TABLES

		Page
1.	Breakthrough Experiment Conditions	15
2.	Heat Capacities	15

THE DYNAMIC BEHAVIOR OF WATER VAPOR ON ACTIVATED CARBON

1. INTRODUCTION

Water adsorption on activated carbon is of particular interest for air purification applications where contaminants must be removed from humid air. Water vapor adsorption can limit filter performance against challenges of light gases by displacing previously adsorbed contaminants or by reducing the available adsorption space. A complete understanding of the single component adsorption behavior of water vapor on activated carbon can serve as a basis to develop a theory for multicomponent behavior. This study considers in detail the adsorption of water on BPL activated carbon.

The adsorption behavior of any vapor on an adsorbent can be understood through the adsorption equilibrium relationship and the material and energy balances. Water adsorption on activated carbon exhibits a pronounced hysteresis that complicates the analysis of desorption. Doong and Yang[1] present a model for multicomponent adsorption of water and hydrocarbons on activated carbon including equilibrium and adsorber dynamics. Their work, however, neglects the energy balance and does not present data on breakthrough runs. The purpose of this paper is to develop and solve the material and energy balance equations so the results can be compared to actual breakthrough experiments. The results presented here for adsorption dynamics can be extended to desorption dynamics. Two approaches to analyzing the water adsorption process on activated carbons are considered. These are the stage model approach and the equilibrium theory approach. In both cases a mathematical model is used to describe the dynamic behavior of water vapor challenging a bed of activated carbon. Three breakthrough experiments are performed that result in three different types of waves. The characteristics of each wave type and their impact on filter performance are discussed.

2. THEORY

2.1 Material and Energy Balances.

The equations to describe water adsorption on activated carbon should include material and energy balances as well as the equilibrium relationship. The easiest way to develop these equations is to describe the bed as consisting of a solid phase and a vapor phase. The stationary(solid) phase consists of the solid porous

particles and the adsorbate. The vapor phase consists of the inert carrier gas and the adsorbable vapor in both the intersticies of the bed and the pores of the particles.

The governing differential equations for the conservation of mass and energy respectively, neglecting dispersion and channeling, of a fixed-bed adsorber can be written as follows:

$$\epsilon\frac{\partial vc}{\partial z} + \epsilon\frac{\partial c}{\partial t} + \rho_b\frac{\partial q}{\partial t} = 0 \tag{1}$$

$$\epsilon\frac{\partial(v\rho_f h_f)}{\partial z} + \epsilon\frac{\partial(\rho_f h_f)}{\partial t} + \rho_b\frac{\partial h_s}{\partial t} = -U\,\Delta T \tag{2}$$

The fluid phase and stationary phase enthalpies are defined by:

$$h_f = c_f(T - T_{ref}) \tag{3}$$

$$h_s = (c_s + c_a q)(T - T_{ref}) - \int_0^q \lambda\, dq \tag{4}$$

Here c is the vapor concentration, q, the adsorbed phase concentration in moles of adsorbate per unit mass of adsorbent, T, the temperature, z, the distance down the tube length, t, the time, ϵ, the void fraction of the bed, and U, the overall heat transfer coefficient of the filter tube.

The rate at which material is transferred from the passing vapor stream to the surface of the carbon is governed by a film mass transfer resistance which can be written as follows:

$$\rho_b\frac{\partial q}{\partial t} = (k_v a)\,(c - c^*) \tag{5}$$

Equation 5 assumes Glueckauf's linear driving force, where c^* is the vapor phase concentration at the surface of the particle.

Dimensionless variables can be introduced to simplify equations 1, 2, 5:

$$\tau = \frac{\epsilon v_o t}{L} \qquad \zeta = \frac{z}{L} \qquad v^* = \frac{v}{v_o} \tag{6,7,8}$$

$$U' = \frac{2\,U\,L}{\epsilon\, v_o\, r_i} \tag{9}$$

$$(k_v a)' = k_v a \frac{L}{\epsilon\, v_o} \tag{10}$$

The choice of the dimensionless parameter τ has special physical significance. It represents the number of superficial column volumes that have been fed to the bed at any given time.

In evaluating solutions, parameters appearing in equations 1, 2, and 5 can be treated as functions of concentration and temperature. However, to simplify the development, several assumptions can be made, namely:

(a) all heat capacities are constant with mean values taken.

(b) the vapor phase is ideal and the effect of composition on the vapor-phase density and velocity is small.

(c) the adsorption process considered here occurs at low gas phase concentrations so that the effect on velocity and density is negligible.

Thus, the dimensionless velocity and the fluid density can be written as:

$$v^* = \frac{T}{T_o} \qquad \rho_f = \rho_{fo} \frac{T_o}{T} \tag{11,12}$$

For adsorption processes involving gases at low to moderate pressures (which would be typical of all air purification applications) the rate of accumulation in the vapor phase is small compared to the accumulation in the solid phase. This leads to the elimination of the second term in equations 1 and 2. The system of governing differential equations may then be expressed as:

$$\frac{\partial(v^* c)}{\partial \zeta} + \rho_b \frac{\partial q}{\partial \tau} = 0 \tag{13}$$

$$\frac{\partial(v^{*}\rho_f h_f)}{\partial \zeta} + \rho_b \frac{\partial h_s}{\partial \tau} = -U'\Delta T \qquad (14)$$

$$\rho_b \frac{\partial q}{\partial \tau} = (k_v a)' (c - c^{*}) \qquad (15)$$

Equations 13, 14, and 15 are three independent equations with four dependent variables (c, c^{*}, q, T). Another equation is required in order to specify the system, namely the adsorption equilibrium relationship:

$$q = f(c^{*}, T) \qquad (16)$$

The solution to equations 13 - 15 wi h 16 requires the imposition of appropriate initial and boundary conditions. For systems considered here the initial bed state and the feed concentration are constant throughout the experiment. Mathematically this can be expressed as:

$$\begin{aligned} c &= c_o \quad \text{and} \quad T = T_o \quad \text{at } \tau = 0 \quad \text{for } 0 < \zeta < 1 \\ c &= c_{feed} \quad \text{and} \quad T = T_{feed} \quad \text{at } \zeta = 0 \quad \text{for all } \tau > 0 \end{aligned} \qquad (17)$$

Two approaches are taken to solve the governing set of differential equations, 13 - 15, with 16: the stage model and equilibrium theory. The stage model is more flexible and can easily treat systems with non-constant initial and boundary conditions. Generally, equilibrium theory is more insightful about the nature of the adsorption waves, however, it cannot be used where mass and heat transfer effects must be considered. Both techniques are presented here in order to gain a complete understanding of the process.

2.2 Stage Model Approach.

Equations 13 - 15 when coupled with the equilibrium relationship 16 can be reduced to a set of ordinary differential equations using a stage model approach.[2,3] Each stage is considered to be well mixed with the effluent concentration and temperature of stage i used as the feed concentration of stage i+1. Friday and LeVan[4] have reported a successful method for reducing the partial differential equations 13 - 15 to ordinary differential equations by writing the spatial derivatives in equations 13 and 14 in finite difference form using backward differences.

$$\frac{dq_i}{d\tau} = \frac{1}{\rho_b \Delta\zeta}\left[(v^* c)_{i-1} - (v^* c)_i\right] \tag{18}$$

$$\frac{dT_i}{d\tau} = \frac{1}{\rho_b(c_s + c_a q_i)}\left\{\frac{\rho_{f_0} c_f}{\Delta\zeta}(T_{i-1} - T_i)\right. \tag{19}$$
$$\left. - \rho_b[c_a(T_i - T_{ref}) - \lambda_i]\frac{dq_i}{d\tau} - U'\Delta T\right\}$$

The resulting equations 18 and 19 are solved using a Runge-Kutta 4th order integration algorithm with twenty stages.

2.3 Equilibrium Theory.

The development of the equilibrium theory solution requires the mass and heat transfer resistances to be negligible. Therefore, the driving force terms on the right side of equations 14 and 15 are set to zero.

The equilibrium theory solution to 13, 14 and 16 requires the use of the method of characteristics that has been presented by numerous authors.[5-10] If concentration of the material in the bed can be expressed as a function of distance and time by,

$$c = f(\zeta, \tau) \tag{20}$$

then the total differential of c can be written as:

$$dc = \frac{\partial c}{\partial \zeta} d\zeta + \frac{\partial c}{\partial \tau} d\tau \tag{21}$$

The solution along regions of constant concentration require that $dc = 0$ so that equation 19 can be rearranged.

$$\frac{d\zeta}{d\tau} = -\frac{\partial c/\partial \tau}{\partial c/\partial \zeta} \tag{22}$$

Now the material balance equation 13 can be rewritten when the equilibrium relationship 16 is substituted for the partial of q with respect to time.

$$\frac{\partial c}{\partial \zeta} + \rho_b \frac{dq}{d(v^* c)} \frac{\partial c}{\partial \tau} = 0 \qquad (23)$$

Equation 23 can be rearranged into a form compatible with the right hand side of equation 22.

$$-\frac{dc/d\tau}{dc/d\zeta} = \frac{1}{\rho_b} \frac{d(v^* c)}{dq} \qquad (24)$$

When equation 24 is substituted into equation 22 the following expression for the characteristic direction is obtained.

$$\frac{d\zeta}{d\tau} = \frac{1}{\rho_b} \frac{d(v^* c)}{dq} \qquad (25)$$

The left hand side of equation 25 represents the speed with which a given concentration travels down the bed, while the right hand side of equation 25 is the slope of the equilibrium relationship.

The energy balance when written without the heat transfer resistance takes the following form:

$$\frac{\partial(v^* \rho_f h_f)}{\partial \zeta} + \rho_b \frac{\partial h_s}{\partial \tau} = 0 \qquad (26)$$

Using the same procedure as for the material balance, the characteristic equation takes the following form:

$$\frac{d\zeta}{d\tau} = \frac{1}{\rho_b} \frac{d(v^* \rho_f h_f)}{dh_s} \qquad (27)$$

The material and energy balances can be combined for the initial value problem to provide:

$$\frac{r}{\varsigma} = \rho_b \frac{dq}{d(v^* c)} = \rho_b \frac{dh_s}{d(v^* \rho_f h_f)} \tag{28}$$

The two enthalpy terms on the right of equation 28 can be written as functions of q and T. Thus equation 28 can be rearranged in terms of the directional derivative dq/dT to take the following form:

$$\left[\frac{\partial(v^* c)}{\partial q}\frac{\partial h_s}{\partial q}\right]\left(\frac{dq}{dT}\right)^2 + \left[\frac{\partial(v^* c)}{\partial q}\frac{\partial h_s}{\partial T} + \frac{\partial(v^* c)}{\partial T}\frac{\partial h_s}{\partial q} - \frac{d(v^* \rho_f h_f)}{dT}\right]\frac{dq}{dT} + \frac{\partial(v^* c)}{\partial T}\frac{\partial h_s}{\partial T} = 0 \tag{29}$$

Equation 29 is a quadratic in dq/dT. The two solutions correspond to the characteristics emanating from a given point of c, q, and T. By starting from the initial and feed conditions the solution to equation 29 is obtained. The resulting slopes are then plotted in the hodograph planes of q versus T and the q versus $v^* c$ until the characteristics intersect. Implementation of equilibrium theory to obtain the breakthrough curves requires adherence to two rules. A wave must be gradual if possible. Slopes in the $v^* c$ plane must increase from initial bed condition to feed condition. If the slope of the characteristic does not increase continuously in going from initial to feed conditions then the larger concentrations would overrun the smaller concentrations. This is an impossible situation. Earlier studies by Devault[11] and Lax[12] showed that these conditions result in the formation of a shock. The shock path must satisfy the material and energy balances as given by the following relationship:

$$\frac{r}{\varsigma} = \rho_b \frac{\Delta q}{\Delta(v^* c)} = \rho_b \frac{\Delta h_s}{\Delta(v^* \rho_f h_f)} \tag{30}$$

This is similar to equation 28 except that here a chord, rather than the slope of the characteristic, is used to determine the speed of the wave in the bed.

3. MATERIALS AND METHODS

The apparatus used for the breakthrough experiments is shown in Figure 1. Air, used as the carrier gas, passes through a molecular sieve dryer and a carbon filter to remove water and organics. The main metering valve regulates the flow. After the clean air passes through the flowmeter, a portion of the stream is

saturated in a water bath. The desired relative humidity is achieved in the following manner. The metering valve and the bypass valve are set such that the ratio of the their flows produces a relative humidity near the desired value. The humidity analyzer and controller (EG&G 911 Digital Humidity Analyzer) measures the relative humidity of the feed stream based on the temperature of the feed stream. If the relative humidity is below the setpoint, the water bath heater is activated. Since, it is a simple on-off controller with no cooling action, the initial setting of the bypass flow must produce a lower than desired RH. The humidified air flows through the carbon bed and the effluent relative humidity is measured by a second EG&G humidity analyzer. Periodically during each breakthrough run the bed was removed from the flowing air stream in order to weigh it.

The carbon sample used was 12x30 mesh BPL Lot #7502. Calgon literature states that the bulk density of the carbon is 480 kg/m^3. The particle diameter is taken to be 0.001 m. The sample for each experiment is dried for at least two days at 110 °C. The carbon is then poured into a 0.0415 m diameter plexiglass tube to give a bed depth of approximately 4 cm. The overall heat transfer coefficient of the plexiglass is taken to be 0.093 kJ/m^2 K s.

4. RESULTS AND DISCUSSION

4.1 Water On Activated Carbon.

The breakthrough concentration and temperature have been measured using the following feed and initial bed conditions: 50% RH feed to a clean bed, 80% RH feed to a bed equilibrated at 50% RH, 80% RH feed to a clean bed. These conditions have been chosen to illustrate the three different wave types that can be formed in an adsorption bed. Rhee et al.[6] describe the three wave types as gradual, abrupt and combined in their equilibrium theory analysis. The important features of each are discussed as each experiment is analyzed. Table 1 is a summary of the operating conditions for each experiment. Table 2 lists the heat capacity values used in this study.

TABLE 1. Breakthrough Experiment Conditions

Experiment	Feed		Initial Bed Conditions			v	T_{amb}
	RH%	T(K)	RH%	T(K)	Carbon(g)	(m/sec)	(K)
1	50	298	0	297.5	23.96	.0616	297.5
2	80	297	50	297	23.96	.0616	297
3	80	298	0	298	25.85	.123	298

TABLE 2. Heat Capacities

c_a	= 1.04 kJ/kg K
c_s	= 2.7 kJ/kg K
c_f	= 0.075 kJ/kg K
T_{ref}	= 298° K

In order to implement the stage model and the equilibrium theory model the form of the equilibrium relationship must be established. It is proposed that a modification to the Hacskaylo-LeVan isotherm[13] would give a reasonable fit to the data. The form of the equation is as follows:

$$\ln(p) = A' - \frac{B'}{C' + T} \tag{31}$$

where

$$A' = A + (K1\theta + 1)\ln(\theta) \quad B' = B \quad C' = C + K2(1 - \theta) \tag{32}$$

and

$$\theta = \frac{q}{q_{sat}} \tag{33}$$

$$\lambda = RT^2 \left[\frac{\partial \ln (p)}{\partial T} \right]_q = RT^2 \frac{B'}{(C' + T)^2} \tag{34}$$

The following values are used for water adsorption on BPL:

$A = 18.3036 \quad B = 3816.44 \quad C = -46.13$

$K1 = 2.56 \quad K2 = 37.9 \quad q_{sat} = 0.0217$

The Antoine parameters, taken from Reid et al.,[14] give the vapor pressure in millimeters of mercury. The isotherms of water on BPL have been measured previously by Mahle and Friday[15] over the temperature range 15 - 35 °C. Only adsorption data is considered here; desorption is not considered. The result of correlating the adsorption data using equations 31 - 33 is presented in Figures 2 and 3 in the modified isotherm plane of q versus $v^* c$. Figure 3 is an enlargement of Figure 2 in the low loading region.

The value of k_v, the mass transfer coefficient, can be calculated using the Sherwood number correlation of Ranz and Marshall.[16] Calgon literature indicates that an appropriate value for a, the surface to volume ratio, is 3400 m^{-1}.

4.2 Breakthrough of 50% RH Feed To A Clean Bed.

The breakthrough results for a challenge of 50% RH(0.628 mol/m^3 at 298 °K) air to clean bed correspond to a region of the isotherm that is unfavorable for adsorption. The effluent concentration and temperature are plotted as a function of time in Figure 4. The effluent concentration versus time curve is typical of a gradual wave. The breakthrough curve is concave downward to the time axis. After a short period of time, an appreciable percentage of the feed concentration is seen in the effluent. The temperature response is also typical of a gradual wave. The temperature quickly rises to a maximum (in this case about 305 °K) and then falls gradually back to the feed temperature.

Construction of solutions using equilibrium theory requires the use of the two rules stated earlier. A wave will be gradual if possible. Slopes in the q versus $v^* c$ plane must increase from initial to feed conditions. There are two sets of characteristics corresponding to two roots of the equation 29. The two

characteristic curves are required in order to obtain the path that connect any initial condition to any feed condition. The 1 wave is the first wave to leave the bed, therefore it must be the wave connected to the initial condition while the 2 wave is connected to the feed.

The slope of the 1 characteristic on the q versus v^*c plane is decreasing from the initial condition, a clean bed. This means there will be a shock path that leaves this point. This is shown as the bottom dotted line in Figure 2 and the upper dotted line in Figure 3 emanating from the origin. The 2 wave that connects the feed condition, 50% RH, has a constantly increasing slope from initial to feed condition corresponding to a gradual wave represented by the bold solid line in Figures 2 and 3. The point where the shock from the initial condition and gradual wave meet can be found by stepping out in temperature along each path using equations 29 and 30 until they intersect. This corresponds to a plateau concentration. Figures 2 and 3 make it easy to visualize how the solution path cuts across isotherms producing a temperature wave.

There is very close agreement between the stage model, the equilibrium theory model, and the data as seen in Figure 4. The equilibrium theory solution does predicts a larger temperature rise than the stage model. This is expected because equilibrium theory assumes adiabatic behavior. The actual recorded temperature does not reach as high as the prediction because during the first minutes of the run the sample tube was periodically taken off line so that the water uptake could be recorded. Note that both the concentration and the temperature wave travel with the same velocity as seen in Figure 4. This is predicted by equilibrium theory using equation 28.

A preliminary study, using only isothermal equilibrium theory, did not fit the data indicating that the effect of temperature is very important to this process. There is a gradual wave associated with the low RH for the isothermal case. However, the shock associated with temperature tends to overrun these gradual wave characteristics in the adiabatic case leading to a shock in temperature and concentration. Note that because the water isotherm is unfavorable at lower RH these low concentrations tend to run out of the column quickly. The large temperature rise associated with the 1 wave has the effect of removing water from the bed that was just adsorbed at the lower temperature. This increases the required time for complete saturation of the bed. It appears that isothermal adsorption would provide a faster means of achieving saturation.

4.3 Breakthrough of 80% RH Feed To Bed Equilibrated At 50% RH.

The water isotherm is favorable between 50% RH(0.628 mol/m^3 at 298°K) and 80% RH(1.001 mol/m^3 at 298°K) as seen in Figure 2. This is the typical shape of an adsorption isotherm, and one could expect the standard S-shaped breakthrough curve. Figure 5 shows the results of an 80% RH feed to a bed initially equilibrated at 50% RH. Although the shape of this curve is not very sharp, the breakthrough behavior does follow an S-shaped pattern.

This S-shaped pattern is called an abrupt wave or a constant pattern wave. This means that at a certain distance into the bed, the shape of the concentration front does not change as the wave is transmitted down the bed. There is also an initial shock characterized primarily by a temperature rise.

Referring back to Figure 2, the 2 characteristic emanating from the feed of 80% RH and the 1 characteristic from the initial concentration of 50% RH both violate the gradual wave criterion. The slopes of these waves decrease from initial to feed conditions, therefore each of these waves must start as a shock. The equilibrium theory solution then requires that equation 30 be solved from both the initial and feed conditions until they intersect, while at each increment checking to see whether the slope of the gradual wave is continuing to violate the gradual wave criterion. The intersection point leads to a plateau condition. This path is close to having a gradual portion because it is so close to the inflection point of the isotherm. However, the adiabatic nature of this system results in the formation of two shocks.

The simulation provided by the stage model and equilibrium theory represent the data well for this run. The resulting breakthrough behavior is shown in Figure 5. Equilibrium theory provides a very accurate measure of the center of both the concentration and temperature waves. The plateau region between the two shock fronts is apparent in the data. Again the temperature rise measured in the experiment is reduced due to sampling of the uptake weight of the bed. The effect of the mass and heat transfer resistances in the stagemodel becomes obvious in the shock portion of the breakthrough curves. These resistances tend to spread out the shock wave in an actual experiment.

4.4 Breakthrough of 80% RH Feed To A Clean Bed.

The water isotherm changes from unfavorable to favorable between 50% RH and 80% RH. The effect of this inflection in the isotherm should be apparent on the breakthrough behavior. Figure 6 shows the breakthrough data measured for 80% RH feed to a clean bed. Notice that the resulting breakthrough curves of both

temperature and concentration are essentially a combination of the first two experiments. The only difference is the faster flow rate (10 l/min as opposed to 5 l/min).

The equilibrium theory solution path is characterized by an initial 1 wave shock as in the run with 50% RH feed to a clean bed, the lower dotted line in Figure 3. There is also a shock emanating from the feed as in the run with 80% RH feed to a bed equilibrated to 50% RH. However there is a third transition. As the isotherm changes from favorable to unfavorable a combined wave is formed that shows both shock and gradual wave behavior, Figure 2. It is possible to identify this as a combined transition because it does not have a plateau region where the two waves unite. There is a portion of the gradual wave for 80% RH feed to clean bed that parallels the shock path for 80% RH feed to a bed equilibrated at 50%RH. The two runs are not identical over the same range of RH. This result only becomes apparent in the adiabatic analysis.

The shape of both the concentration and temperature profiles agrees with the stage model and equilibrium theory predictions. The subtle shape of the combined transition is not obvious from the data. Equilibrium theory allows this combined transition to be identified.

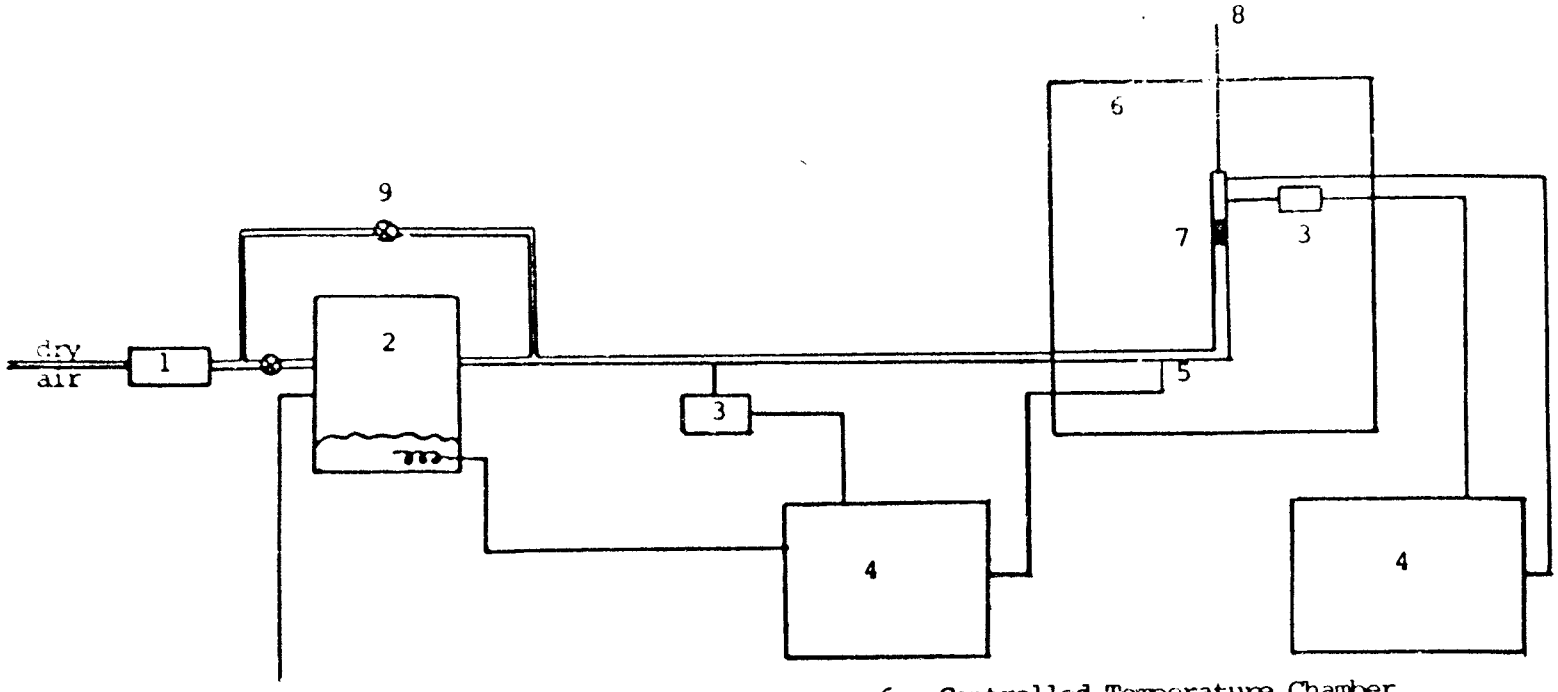
5. CONCLUSIONS

- The three types of waves that can be formed in and passed through an adsorption bed are demonstrated both mathematically and experimentally.
- The stage model seems to fairly represent the breakthrough using correlated equilibrium data and *a priori* calculated rate parameters.
- Equilibrium theory allows the exact nature of the transitions to be explored.
- The inability of equilibrium theory to be used with heat and mass transfer resistances leads to some discrepancy between this method and the experimental results.

Blank

NOTATION

a	= surface to volume ratio(m^{-1})
A, B, C	= Antoine equation parameters(p_{sat} in mm Hg)
c_*	= gas phase concentration of water(mol/m^3)
c	= gas phase concentration of water in the pellet(mol/m^3)
c_a	= heat capacity of adsorbed phase(kJ/kgK)
c_f	= heat capacity of gas phase(kJ/kgK)
c_s	= heat capacity of solid phase(kJ/kgK)
h_f	= enthalpy of gas phase(kJ/kg)
h_s	= enthalpy of solid phase(kJ/kg)
k_v	= mass transfer coefficient(m/s Ref. 16)
K1, K2	= coefficients of water adsorption isotherm, Eq. (32)
L	= length of bed(m)
p	= partial pressure of water(Torr)
q	= solid phase concentration(mol/kg)
q_{sat}	= solid phase concentration at saturation(mol/kg)
r_i	= inner radius of filter tube(m)
R	= gas constant
t	= time
T	= temperature(K)
T_o	= temperature of feed gas(K)
T_{ref}	= heat capacity reference temperature(K)
U	= overall heat transfer coefficient of filter tube(kJ/m^2Ks)
v	= interstitial velocity(m/s)
v_o	= interstitial velocity of feed(m/s)
z	= axial distance coordinate(m)
ϵ	= void fraction of packing
ζ	= dimensionless axial coordinate, Eq. (7)
θ	= fractional saturation of the bed
λ	= heat of adsorption(kJ/mol)
ρ_b	= bulk density of packing(kg/m^3)
ρ_f	= density of gas phase(kg/m^3)
ρ_{fo}	= density of inlet gas (kg/m^3)
τ	= dimensionless time, Eq. (6)



1. Flow meter
2. Water bath
3. Humidity Sensor
4. Humidity Analyzer and Controller
5. Temperature probe
6. Controlled Temperature Chamber
7. Carbon Bed
8. Effluent Air
9. By-pass Valve

Figure 1. Schematic of Breakthrough Apparatus

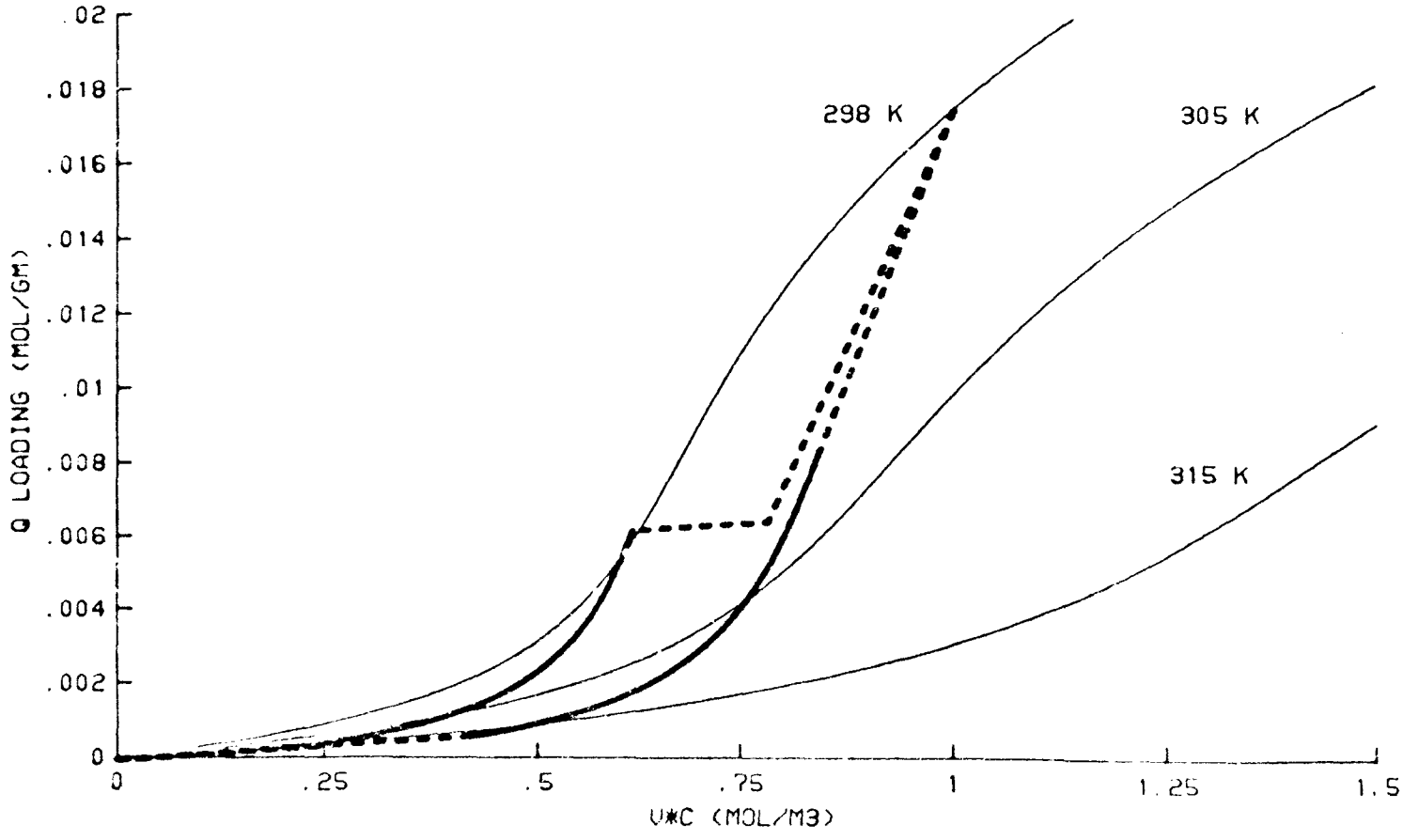


Figure 2. Path In Modified Isotherm Plane
50%RH, 80%RH Feed To Clean Bed
And 80%RH Feed To 50%RH Bed Of BPL

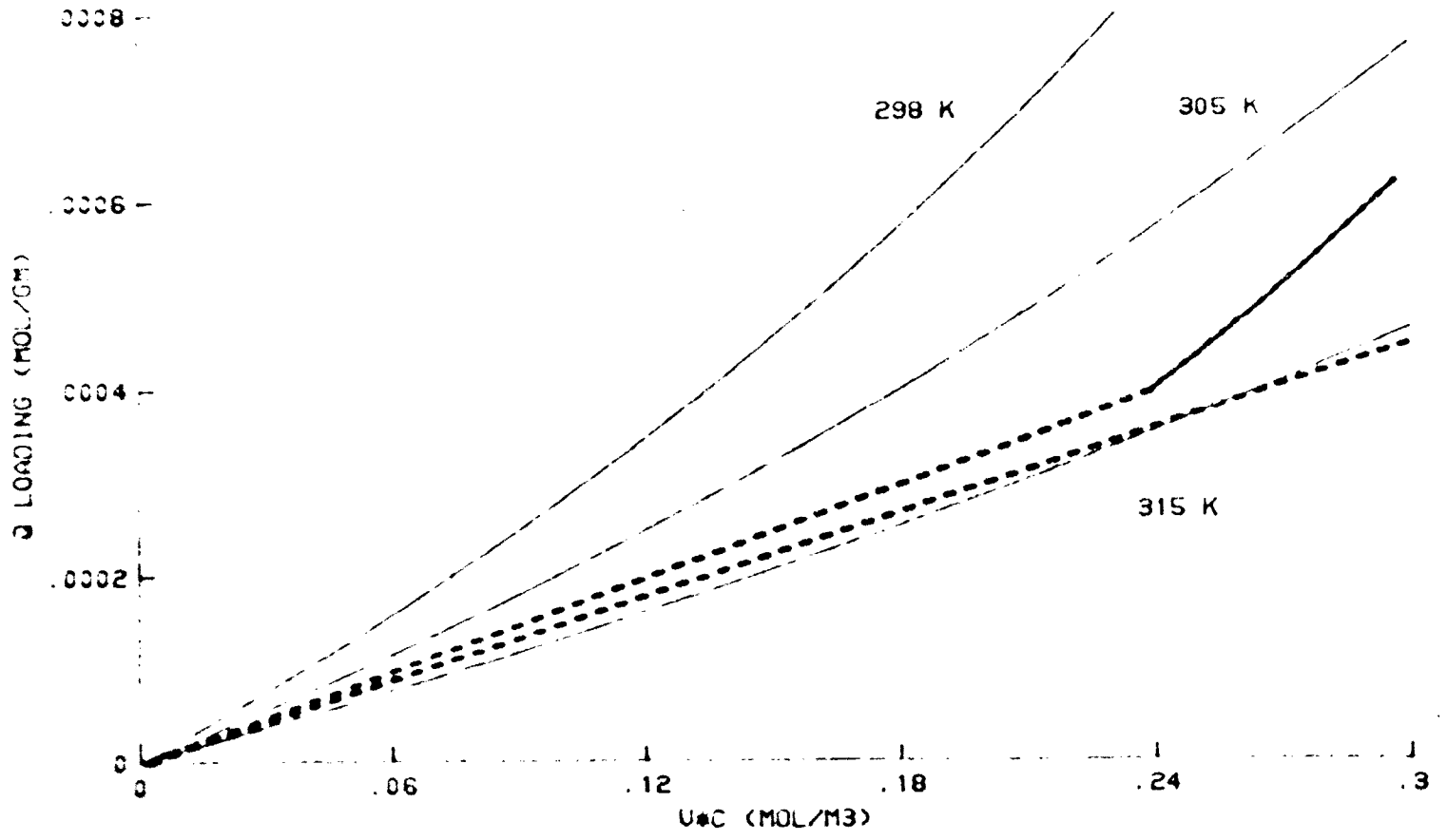


Figure 3. Enlargement Of Path In Modified Isotherm Plane 50%RH, 80%RH Feed To Clean Bed Of BPL

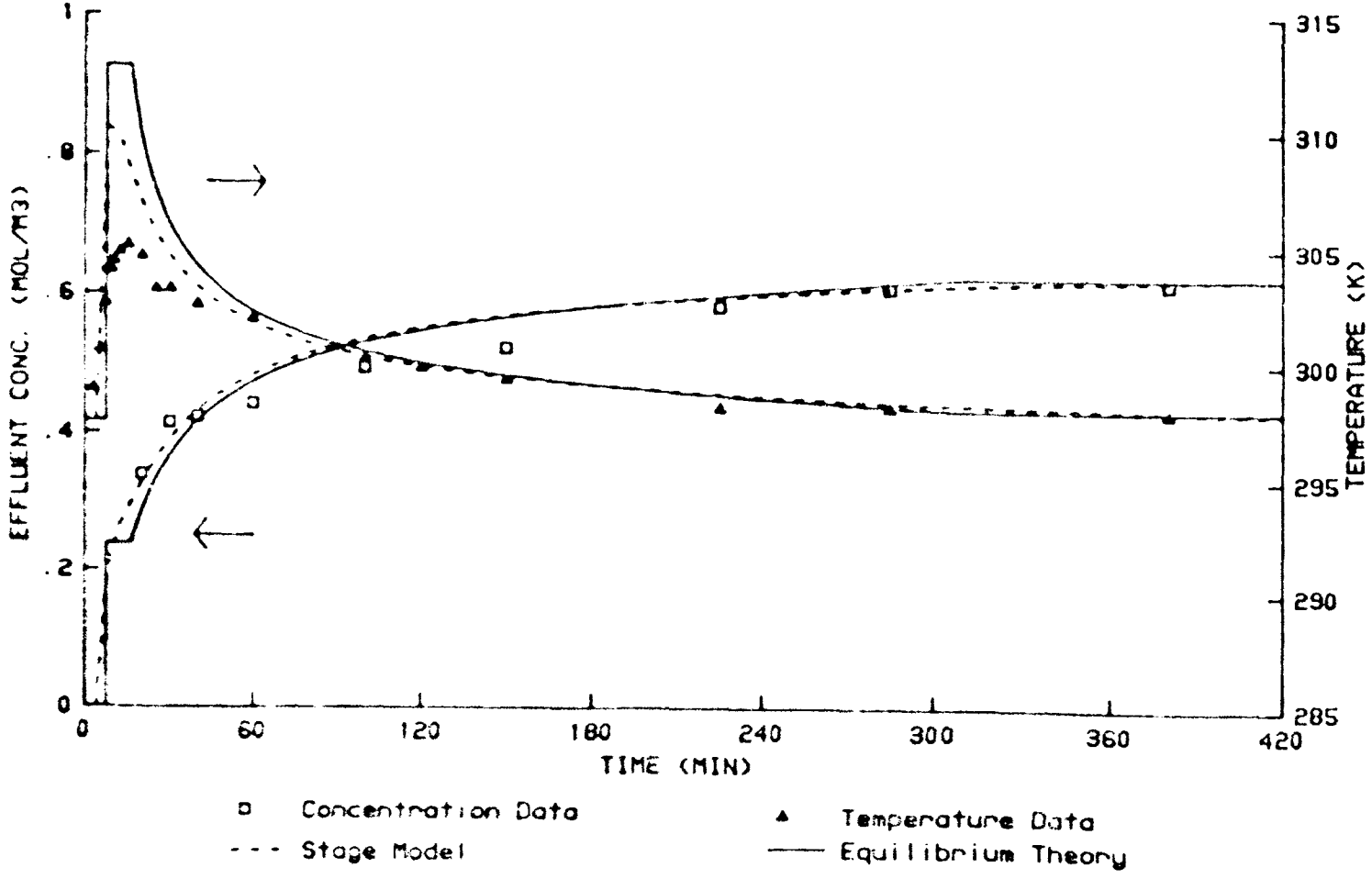


Figure 4. Breakthrough Of Water Vapor On BPL Carbon 50%RH Feed To Clean Bed

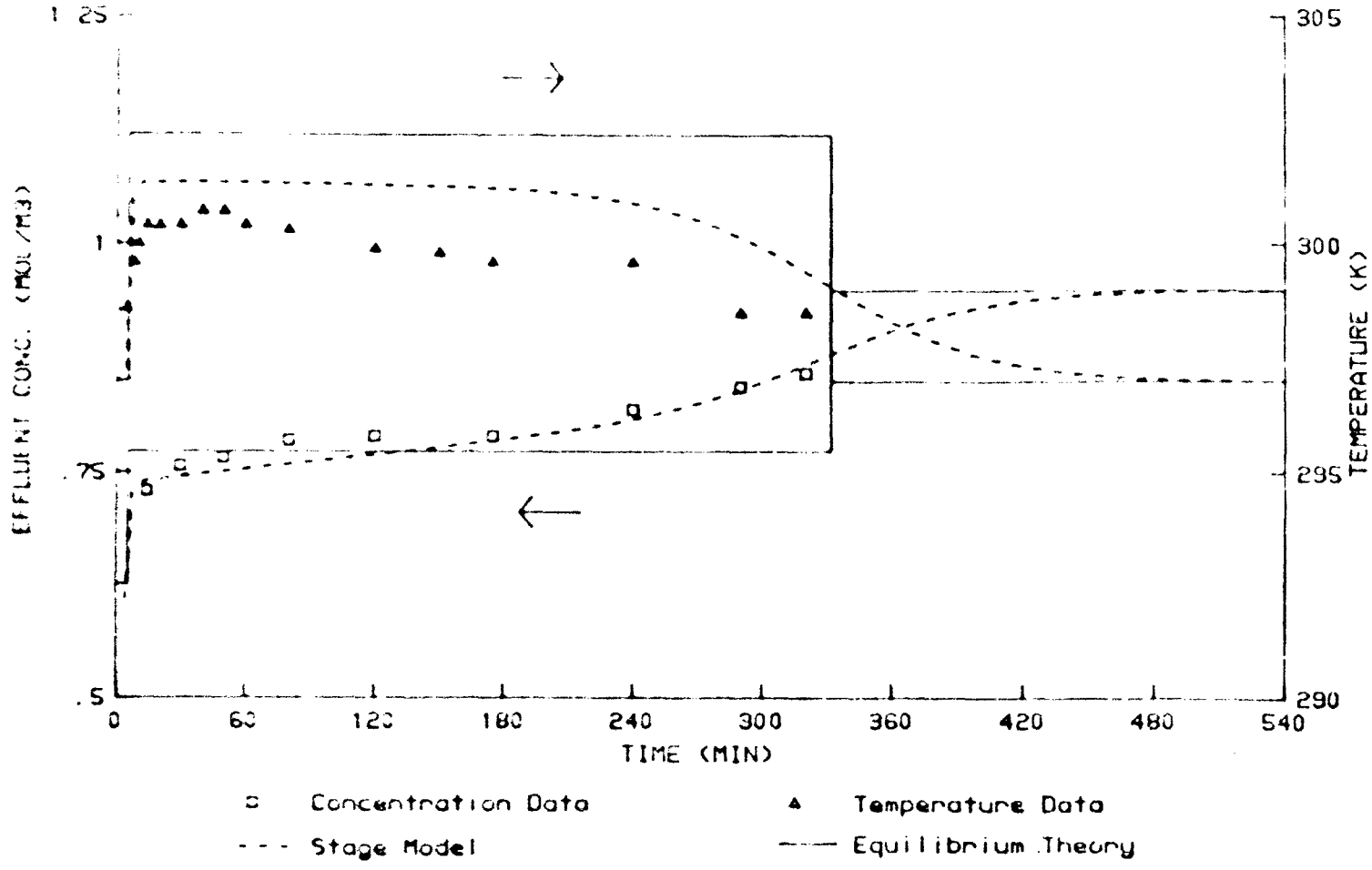


Figure 5. Breakthrough Of Water Vapor On BPL Carbon 80%RH Feed To Bed Equilibrated To 50%RH

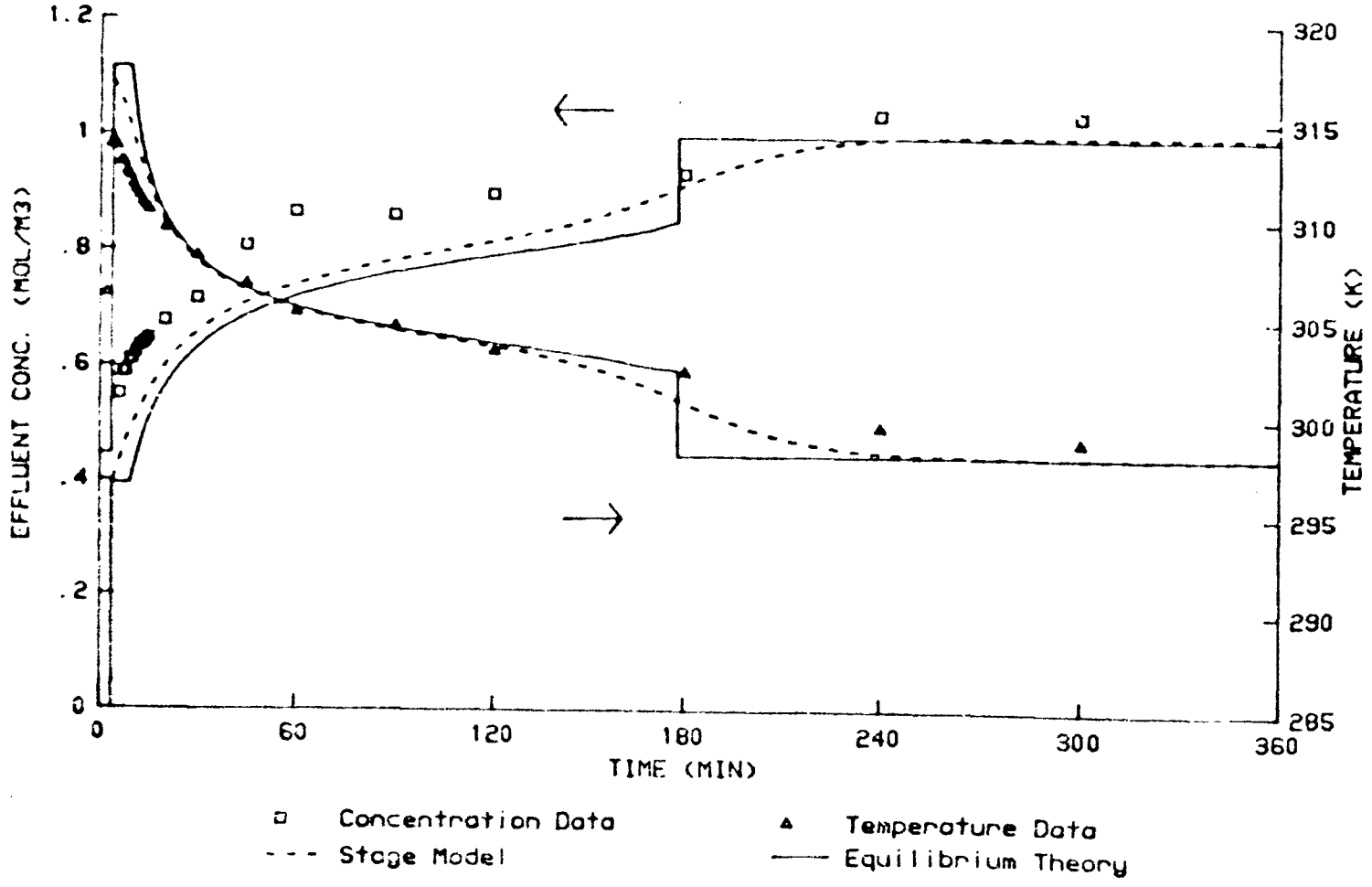


Figure 6. Breakthrough Of Water Vapor On BPL Carbon 80%RH Feed To Clean Bed

Blank

LITERATURE CITED

1. Doong,S.J., and Yang,R.T., "Adsorption of Mixtures of Water Vapor and Hydrocarbons By Activated Carbon Beds: Thermodynamic Model for Adsorption Equilibrium and Adsorber Dynamics," *AIChE Symposium Series: Adsorption and Ion Exchange* vol. 259(83), p. 87 (1987).

2. Rodrigues, A.E. and Beira, E.C., "Staged Approach of Percolation Processes," *AIChE J.* vol. 25, p. 416 (1976).

3. Ikeda, K., "Performance of the Nonisothermal Fixed-Bed Adsorption Column with Nonlinear Isotherms," *Chem. Eng. Sci.* vol. 34, p. 941 (1981).

4. Friday, D.K., and LeVan, D., "Solute Condensation in Adsorption Beds During Thermal Regeneration," *AIChE. J.* vol. 28, p. 86 (1982).

5. Friday, D.K., and LeVan, D., "Thermal Regeneration of Adsorption Beds: Equilibrium Theory for Solute Condensation," *AIChE J.* vol. 30, p. 679 (1984).

6. Acrivos, A., "Method of Characteristics Technique: Application to Heat and Mass Transfer Problems," *Ind. Eng. Chem.* vol. 48, p. 703 (1956).

7. Pan, C. Y., and Basmadjian, D., "Constant Pattern Adiabatic Fixed-Bed Adsorption," *Chem. Eng. Sci.* vol. 22, p. 285 (1967).

8. Pan, C.Y., and Basmadjian, D., "An Analysis of Adiabatic Sorption of Single Solutes in Fixed Beds: Equilibrium Theory," *Chem. Eng. Sci.* vol. 26, p. 45 (1971).

9. Rhee, H.K., Aris, R. and Amundson, N.R., *First Order Partial Differential Equations: Volume I, Theory and Applications of Single Equations*, pp. 188-410, Prentice-Hall, Englewood Cliffs, NJ, 1986.

10. Ruthven, D M., *Principles of Adsorption and Adsorption Processes*, pp. 274-323, John Wiley and Sons, New York, NY 1984.

11. DeVault, D., "The Theory of Chromatography," *J. Amer. Chem. Soc.* vol. 65, p. 532 (1943).

12. Lax, P.D., "The Formation and Decay of Shock Waves," *Amer. Math. Monthly* vol. 79, p. 227 (1972).

13. Hacskaylo, J.J., and LeVan, M.D., "Correlation of Adsorption Equilibrium Data Using a Modified Antoine Equation: A New Approach for Pore-Filling Models," *Langmuir* vol. 1, p. 97 (1987).

14. Reid, R.C., Prausnitz, J.M., and Sherwood,T.K., *The Properties of Gases And Liquids*, 3rd ed., p. 634, McGraw-Hill, New York, NY, 1977.

15. Mahle, J.J., and Friday, D.K., *Water Adsorption Equilibria On Microporous Carbons*, CRDEC-TR-018, U.S. Army Chemical Research, Development and Engineering Center, Aberdeen Proving Ground, MD, November 1988, UNCLASSIFIED REPORT.

16. Ranz, W.E. and Marshall, W.R., "Evaporation From Drops Part II," *Chem. Eng. Prog.* vol. 48, p. 173 (1952).

APPENDIX B2

THE EFFECT OF RELATIVE HUMIDITY ON THE BREAKTHROUGH BEHAVIOR OF EA____ ON ASC-TEDA, PART 1. EXPERIMENTAL STUDIES. (U)

by

Leonard C. Buettner

John J. Mahle

Research Directorate

David K. Friday

GEO - CENTERS Inc.

CONTENTS (U)

		Page
1.	INTRODUCTION	5
2.	MATERIALS AND METHODS	6
2.1	Charcoal Pretreatment and Conditioning	6
2.2	Test Apparatus and Data Collection	7
2.3	Generation of Challenge Gas Concentration ..	7
3.	PROCEDURE	8
4.	RESULTS AND DISCUSSION	9
4.1	Analysis of Breakthrough Data	9
4.2	Related Observations and Additional Experimental Findings.....	11
5.	CONCLUSIONS	12
	LITERATURE CITED	22
	DISTRIBUTION LIST	23

APPENDIX C1

(2) Recent Advances in Capillary Gas Chromatography; Bertsch, W., Jennings, W., Kaiser, R., Eds.; Huthing: Heidelberg, 1981.
(3) White, C.; Houck, R. HRC CC, J. High Resolut. Chromatogr. Chromatogr. Commun. 1986, 9, 4.
(4) Knox, J.; Gilbert, M. J. Chromatogr. 1979, 186, 405.
(5) Mikkers, F.; Everaerts, F.; Verheggen, Th. J. Chromatogr. 1979, 169, 11.
(6) Jorgenson, J.; Lukac, K. Science (Washington, D.C.) 1983, 222, 266.
(7) Jorgenson, J. Science (Washington, D.C.) 1984, 226, 254.
(8) Yeung, E. In Advances in Chromatography; Giddings, J., Ed.; Marcel Dekker: New York, 1984; Vol. 23.
(9) Meyer, V. J. Chromatogr. 1986, 334, 197.
(10) Bornhop, D.; Dovichi, N. Anal. Chem. 1986, 58, 504.
(11) Bornhop, D.; Nolan, T.; Dovichi, N. J. Chromatogr. 1987, 384, 181.
(12) Munk, M. In Liquid Chromatographic Detectors; Vickers, T., Ed.; Marcel Dekker: New York, 1983.
(13) Yeung, Edward In Liquid Chromatography Detectors; Yeung, E., Ed.; Marcel Dekker: New York, 1987.
(14) Woodruff, S.; Yeung, E. J. Chromatogr. 1983, 280, 363.
(15) Bogoslovskii, Y.; Razin, V. Zh. Fiz. Khim. 1971, 40, 1410.
(16) Banerjee, S.; Pack, E., Jr. Anal. Chem. 1982, 54, 326.
(17) Pawliszyn, J. Anal. Chem. 1986, 58, 243.
(18) Pawliszyn, J. Anal. Chem. 1986, 58, 3207.
(19) Pawliszyn, J. J. Liq. Chromatogr. 1987, 10, 3377.
(20) Pawliszyn, J. Rev. Sci. Instrum. 1987, 58, 245.
(21) Sa, A. Principles of Electronic Instrumentation; Arnold: East Kilbridge, Scotland, 1981; p 227.
(22) Lephardt, J. In Transform Techniques in Chemistry; Griffiths, P., Ed.; Plenum: New York, 1979; p 294.
(23) Pawliszyn, J.; Weber, M.; Dignam, M. Rev. Sci. Instrum. 1985, 56, 1740.
(24) Pawliszyn, J. Anal. Chem. 1988, 60, 766.
(25) Ruzicka, J.; Hansen, E. Flow Injection Analysis; Wiley: New York, 1981.
(26) CRC Handbook of Chemistry and Physics, 64th ed.; CRC: Boca Raton, FL, 1985; p E 365.

RECEIVED for review June 13, 1988. Accepted September 13, 1988.

Detection of Hazardous Vapors Including Mixtures Using Pattern Recognition Analysis of Responses from Surface Acoustic Wave Devices

Susan L. Rose-Pehrsson* and Jay W. Grate

Chemistry Division, Naval Research Laboratory, Washington, D.C. 20375-5000

David S. Ballantine, Jr.

GEO-Centers, Inc., 10903 Indian Head Highway, Ft. Washington, Maryland 20744

Peter C. Jurs

152 Davey Laboratory, Pennsylvania State University, University Park, Pennsylvania 16802

Surface acoustic wave (SAW) devices coated with selectively sorbent materials are being investigated as monitors for personnel safety where detection of hazardous vapors is required at sub-part-per-million concentrations in ambient air that can contain interferences at much higher concentrations. A set of ten SAW devices coated with polymer materials designed to interact with different vapor properties has been used to detect hazardous vapors by producing unique fingerprints to represent a given vapor. The coatings were exposed to nine individual vapors and two-component mixtures of the vapors representing different chemical classes and concentrations, and the resulting data matrix was studied by using pattern recognition methods. Four of the coatings were common to a previous study, and their responses to the single vapors were used as a prediction set to test the classification capacity of a linear discriminant developed in that study. All of the vapors were correctly identified, except water. Principal components analysis and clustering methods were applied to the responses of the coatings to all the vapors, including mixtures. The individual vapors cluster into specific regions in space, and the mixtures lie in the areas between the clusters. Supervised learning techniques were used to reduce to eight the number of sensors necessary to identify the hazardous vapors in the presence of mixtures.

INTRODUCTION

Great demands have been placed on toxic vapor detectors because detection of sub-part-per-million concentrations is required in ambient conditions where interferences can be present at much higher concentrations. In addition, field instruments should be small, portable, and inexpensive. It would also be advantageous to have an instrument that could be adapted to many detection problems. Few instruments have the necessary sensitivity and selectivity, while maintaining the small size needed in the field. Microelectronic chemical sensors meet the size requirement, can be very sensitive, and can show 3 to 4 orders of magnitude selectivity between toxic vapors of interest and common interferents. Nevertheless, these capabilities may be insufficient if the interferent concentrations are orders of magnitude greater than the vapor concentrations that must be detected.

Pattern recognition techniques in conjunction with an array of sensors is a promising approach to this type of analytical problem. This approach has been applied to vapor response data from electrochemical sensors (*1*), to the selection of coatings for piezoelectric crystal sensors (*2*), and to the study of coatings and identification of vapors using surface acoustic wave (SAW) devices (*3*). In the latter study, the clustering of vapors demonstrated that vapor solubility properties, such as hydrogen bonding, were important in determining how the sensors respond. In a recent paper by Carey and co-workers, multiple linear regression and partial least-squares calibration techniques were used to measure the concentration of two- and three-component mixtures by an array of nine piezoelectric crystal sensors (*4*). The goal of our present work is the detection of a single vapor or class of vapors in a complex environment, rather than the identification of the different components of the large number of mixtures possible in the environment. Our specific objective is the detection of toxic organophosphorus compounds.

Several research groups are investigating SAW devices for toxic vapor detection because of their small size and excellent sensitivity (*3*, *5*-*21*). These planar microsensors consist of

0003-2700/88/0360-2801$01.50/0 © 1988 American Chemical Society

interdigital transducers that are microfabricated onto the surface of a piezoelectric substrate, such as quartz. The transducers convert an applied radio frequency (rf) voltage into a Rayleigh surface wave when placed in an oscillator circuit. Chemical sensitivity is provided by a thin film coating of a selectively sorbent material. Vapors sorbed into the coating increase its mass and perturb the Rayleigh wave. This perturbation is detected electronically as a shift in the frequency of the oscillator circuit. The principles of operation are described in detail in ref 7. The sensitivity and selectivity of the response are dependent upon the vapor/coating interactions. The sorption of vapors by a SAW sensor coating and the solubility interactions between the vapor and the coating are discussed in detail in ref 5.

An instrument comprised of an array of SAW sensors would be designed with a different coating on each sensor, and each coating would be selected to respond differently to a set of vapors. The combination of sensors selected to interact with different chemical properties would produce a unique fingerprint for each vapor. The sensors encode chemical information about the vapors in a numerical form, which can be analyzed with pattern recognition methods. Each sensor defines an axis in a multidimensional space. Vapors can be represented as points positioned in this space according to sensor responses. Vapors that produce similar responses from the set of coatings will tend to be represented by points that cluster near one another in the multidimensional space. Pattern recognition uses multivariate statistics and numerical analysis to investigate such clustering and to elucidate relationships in multidimensional data sets. By use of supervised learning techniques, a discriminant can be developed to distinguish between toxic vapors of interest and interferents. This type of instrument can be adapted to specific detection problems by the choice of the discriminant developed or by selecting different coatings for the array and developing the appropriate discriminant.

In a previous study conducted in our laboratory, a large data set was generated by using 112-MHz SAW vapor sensors. Pattern recognition techniques were used to analyze the responses of 12 SAW coatings to 11 vapors at various concentrations (3). The vapors were divided into two classes: class 1, vapors of interest; class 2, potential interferences. The number of sensors needed to discriminate between vapors of interest and the interferences was reduced from the original 12 to 4 by pattern recognition data analysis. Several combinations of coatings were successful in the classification.

In the present study, 158-MHz SAW devices were used to generate another large data set. These higher frequency devices have a greater mass sensitivity and are smaller. Each sensor is wire bonded on a conventional 12-pin gold TO-8 header, for ease of handling. Ten coatings were examined, including four used in the previous study. The data set includes exposures to nine single vapors at various concentrations, plus several two-component mixtures of the vapors. The objectives were 2-fold. First, we wanted to test the classification capability of the discriminant generated in the previous study. The responses of the sensors coated with the same materials tested 2 years earlier were used as a prediction set. Second, we wanted to investigate the clustering of sensor responses in a data set including both single vapors and mixtures. These data served as a training set for a new discriminant able to identify hazardous vapors when present in mixtures containing an interference vapor at a much higher concentration.

EXPERIMENTAL SECTION

This study was conducted in two stages: (a) collection of the data and (b) application of pattern recognition analysis methods to the collected data.

Table I. Test Vapors and Mixtures

Class 1
dimethyl methylphosphonate (DMMP)
N,N-dimethylacetamide (DMAC)
mixtures of each class 1 vapor with each class 2 vapor
Class 2
1,2-dichloroethane (DCE)
water
isooctane (ISO)
toluene (TOLN)
diethyl sulfide (DES)
2-butanone (BTN)
1-butanol (BTL)
mixtures of water with each class 2 vapor
isooctane with each class 2 vapor
2-butanone with each class 2 vapor

Table II. Coatings

FPOL	fluoropolyol
PEM	poly(ethylene maleate)
PECH	poly(epichlorohydrin)
PVP	poly(vinylpyrrolidone)
ECEL	ethyl cellulose
PBOH	poly(butadiene) hydroxylated
PEI	poly(ethylenimine)
PEPH	poly(ethylene phthalate)
PFA	poly(isoprene/fluoro alcohol)
PIB	poly(isobutylene)

Materials. The vapors used are listed in Table I. Solvents for the vapor generation were commercial materials of 99% or greater purity, except diethyl sulfide (98%, Aldrich) and dimethyl methylphosphonate (97%, Aldrich).

A list of the coating materials and the abbreviations used in this study is given in Table II. The coating materials poly(epichlorohydrin) and poly(isobutylene) were obtained from Aldrich. Poly(vinylpyrrolidone) was purchased from Alltech. Poly(ethylenimine) and ethyl cellulose were acquired from Polysciences. Poly(ethylene maleate) was prepared as described by Snow and Wohltjen (8). Fluoropolyol was prepared by using methods described by Field (22). Poly(ethylene phthalate) was prepared from phthalic anhydride and ethylene glycol as described in ref 23. The poly(isoprene/fluoro alcohol) was prepared from poly(3,4-isoprene) and excess hexafluoroacetone as described in ref 24, where it is referred to as PIPFA1. Poly(butadiene)-hydroxylated was prepared by hydrolyzing epoxidized poly(butadiene) with aqueous HCl in dioxane. The poly(butadiene) used was from Polysciences.

SAW Sensors. The 158-MHz dual SAW delay lines (Microsensor System, Inc., of Fairfax, VA, part number SD-158-A) have been described (5) and are depicted in Figure 1. The rf electronics modules that operated the devices were described in the same reference. One delay line of each dual device was spray coated with a dilute solution of the coating material in a volatile solvent (usually chloroform, tetrahydrofuran, or a methanol/chloroform mixture) as described in ref 3 and 5. Coating deposition produced frequency shifts of 200–250 kHz, which were recorded and used as a measure of the amount of coating material for normalization and comparison of data (7). The uncoated delay line acted as a reference oscillator to provide compensation for ambient temperature and pressure fluctuations. The low frequency difference signal between the uncoated reference delay line and the coated delay line was monitored during the vapor exposures (3, 5).

Data Collection. Vapor streams were generated by using an automated gas handler system interfaced with an Apple IIe microcomputer. The test vapors were generated from bubblers or permeation tubes and diluted to known concentrations. The gas flow rate to the sensors was 200 mL/min. This experimental system is described in detail in ref 25.

The temperature at the sensors was monitored and was typically 35 ± 2 °C. The sensors were tested in arrays of four connected to the vapor stream in series. Each array included one fluoropolyol-coated sensor and three other coatings. The fluoropolyol-coated sensor provided a check for consistency from one array to another. Each array was exposed to nine single vapors.

Each vapor was measured at four concentrations, with each concentration repeated four times. Two-component mixtures were generated at a single combination of concentrations and the sensor responses were again measured four times. Typical experiments consisted of repeated exposures of air/vapor/air/vapor/air. Sensor exposures were 3 min long with at least 6 min of recovery time between exposures. The difference frequency output was usually recorded every 6 s at 1-Hz resolution. Dimethyl methylphosphonate exposures were repeated periodically throughout each vapor test set to check for consistent sensor performance. Some of the sensors were repeated in more than one array. Poly(vinylpyrrolidone) demonstrated poor reproducibility, and a good data set including mixtures was not generated with that coating. This coating was used only for comparison with the pattern recognition study reported in 1986 (3).

Responses were determined from the equilibrium vapor sorption at the end of the exposure, as described in detail in ref 5. Each sensor was coated with slightly different amounts of material. To enable comparisons of one coating response to another, the responses were normalized for coating thickness by dividing by the kilohertz frequency shift observed when each sensor was coated.

Pattern Recognition. The normalized sensor responses were organized into two data matrices for analysis. The two exposures within a vapor exposure experiment were averaged. A 104 × 4 matrix included data for four coatings exposed to the nine single vapors. The results of all the single vapor exposure experiments at the different concentrations were included. These four coatings were common to our previous study; this matrix was used as a set of unknowns (a prediction set) to test the linear discriminant developed in that study. The second matrix, 172 × 9, included all the coatings tested in this study, except poly(vinylpyrrolidone), tested against both the individual vapors and the mixtures. At least two vapor exposures at each concentration were included in the data set. This matrix was first examined by using the normalized data as collected. It was also examined after correcting for variations observed in the fluoropolyol responses between test arrays.

These data were analyzed on a VAX 11-750 computer using pattern recognition routines included in the ADAPT software system (26). Each row in each matrix is a pattern vector, representing responses of the coatings to a given vapor/concentration experiment. The pattern vectors were normalized by dividing each sensor response by the square root of the sum of the squared sensor responses in a given vapor experiment because dividing the sensor responses by concentration is not possible for a field instrument measuring unknowns. This closure method is pattern normalization as described previously (1). Sensor responses can vary by orders of magnitude; it is important to make them more compatible. Autoscaling, a preprocessing method that scales and normalizes the data, is useful for correcting the imbalance between sensors and does not alter the basic geometry of the clustering (26). Each response for a coating was then autoscaled to a mean of zero and a standard deviation of unity.

Because many of the available sensor coatings encode similar information, collinearities between sensors may cause numerical instabilities in the analysis phase. Multiple linear regression analysis was used to uncover multicollinear relationships among the detector responses in order to identify the smallest set of sensors providing the largest amount of relevant information. Once a set of sensors is found that contributes unique information, pattern recognition techniques for display, mapping, clustering, and classification were employed. the methods used have been described in ref 1 and 3.

RESULTS AND DISCUSSION

SAW Sensor Testing. A schematic diagram of the dual delay line SAW device is given in Figure 1. Sensor response data were collected by monitoring the difference frequency between the coated delay line and the uncoated reference delay line. When the gas stream over the sensor is changed from clean air to vapor-containing air, the frequency of the coated delay line shifts to a lower value. This negative frequency shift is related to the mass of the vapor sorbed by the coating (7). Ideally, the reference signal does not change, and the positive difference signal is also related to the mass of vapor sorbed.

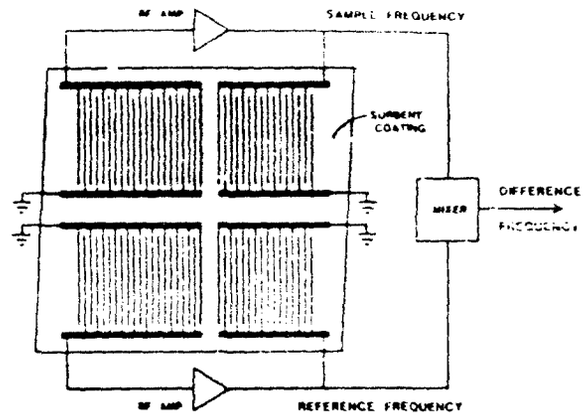


Figure 1. 158-MHz SAW device and associated electronic circuit diagram.

However, in practice, the reference signal can change significantly in response to vapor exposures (5). Therefore, the difference signal accurately represents vapor sorption only when the signal change on the coated side is much greater than the change on the reference side. This condition is true for the sorption of DMMP by fluoropolyol-coated sensors (5), for example, but not for all the vapors and sensor coating materials reported here.

The sensor testing results are presented in Table III as the frequency shift observed divided by the kilohertz of coating on the sensor. Each number is the average of (usually) four measurements at that vapor concentration. Negative difference signals were observed in a minority of cases. These occurred most frequently for the coating poly(isobutylene), which does not sorb most vapors very strongly. The vapor most frequently associated with negative difference signals is water, which can sorb strongly to the glass surface on the reference side.

Our specific objective is the detection of toxic organophosphorus compounds. These strongly hydrogen bond accepting vapors are simulated by using less toxic dimethyl methylphosphonate (DMMP) and *N,N*-dimethylacetamide. DMMP is an organophosphorus compound, and both simulants are strong hydrogen bond acceptors. DMMP vapor streams were generated at low concentrations with a permeation tube, and at higher concentrations with a bubbler. Thus sensors were tested against this vapor over a much wider concentration range than in previous studies (3). The seven vapors that are not simulants represent a variety of potential interferents.

Most coating materials respond similarly to the two simulant vapors and statements about DMMP will usually also apply to *N,N*-dimethylacetamide. The most sensitive coatings for these vapors are fluoropolyol and poly(isoprene/fluoro alcohol). The latter material has been designed to be highly sensitive to these vapors by incorporating the strongly hydrogen bond donating hexafluoro-2-propanol functionality (24, 27, 28). Fluoropolyol has been reported in previous studies (3, 6) and the sorption of vapors by this material has recently been examined in detail (5). Individual fluoropolyol-coated sensors are reproducible for repeated vapor exposures, and separate sensors are comparable to one another. The responses of a single fluoropolyol-coated sensor to repeated exposures of DMMP are reported in Table IV. The range of variation at any given concentration is ca. ±10%. Fluoropolyol-coated sensors were included in each array of four sensors tested simultaneously to provide a check for consistency from one four sensor array to another. The responses of the fluoropolyol sensor in the first test array were used in the data set described here for the pattern recognition analysis.

Table III. Frequency Shifts (dz/kHz)

vapor	concn, μg/L	FPOL	PEM	ECEL	PEI	PEPH	PECH	PFA	PIB	PBOH	PVP
DMAC	81	67.10	9.10	3.97	−0.68	2.60	3.32	158.80	−4.58	2.57	0.47
	40	57.00	7.00	2.97	−0.59	1.26	1.91	124.90	−3.51	1.34	0.29
	20	33.94	3.27	1.54	0.24	0.55	0.93	92.21	−2.74	0.62	0.22
	11	18.83	1.69	0.81	−0.17	0.28	0.54	69.54	−1.96	0.34	0.17
DMMP	2230	257.62	90.66	34.54	−2.64	45.25	44.64	333.92	−8.46	39.53	4.31
	1100	207.58	56.64	25.05	−2.25	24.92	24.07	414.63	−8.24	21.42	2.72
	559	160.90	31.99	14.44	−1.88	14.11	11.48	346.16	−7.97	10.32	1.09
	372	142.23	24.28	10.84	−2.01	11.48	8.01	321.69	−6.09	6.73	0.74
	137	128.81	20.50	8.31	−1.45	7.02	3.90	228.80	−5.95	2.95	1.13
	84	102.79	13.44	5.53	−1.15	4.97	2.32	183.50	−4.90	1.63	1.70
	52	83.89	8.51	4.02	−0.84	3.62	1.53	157.92	−4.27	0.93	0.44
	29	58.70	4.54	2.33	−0.62	2.44	0.80	124.49	−3.18	0.44	0.40
DCE	156000	35.59	56.62	113.18	16.99	47.49	115.79	69.05	52.82	122.03	22.27
	88600	19.35	30.51	72.07	8.05	23.44	55.64	29.07	21.96	54.86	15.50
	45700	8.99	14.34	39.72	3.80	11.03	27.12	11.99	8.86	23.42	7.78
	30500	6.35	9.04	24.75	2.49	7.79	18.45	8.19	5.97	16.54	5.76
DES	137000	8.45	13.02	48.54	5.86	17.02	66.28	133.40	72.88	35.56	5.33
	68700	5.68	6.99	33.45	2.14	8.50	32.46	69.59	32.56	34.51	3.85
	35400	1.83	3.14	18.40	0.85	4.13	15.63	32.91	13.55	14.84	1.85
	23600	0.29	2.31	12.94	0.32	2.80	10.96	22.75	8.39	9.81	1.21
water	7190	2.71	5.23	2.44	35.23	1.99	1.95	20.49	−2.20	1.35	24.44
	3550	4.86	5.41	0.46	12.85	0.32	0.28	7.57	−1.46	0.72	5.79
	1820	2.51	3.63	0.02	4.91	−0.28	−0.01	4.04	−1.20	0.52	−0.40
	1210	1.29	2.93	−0.03	2.86	−0.38	−0.13	1.58	−1.49	0.24	−2.31
LSO	129000	13.43	3.54	7.33	0.82	1.48	21.25	35.17	78.95	25.22	0.54
	64300	5.90	0.98	4.78	0.61	0.74	10.78	14.88	33.49	11.63	1.02
	32100	2.52	0.34	2.67	0.45	0.38	5.10	6.20	13.84	4.30	0.65
	22000	1.77	0.16	1.98	0.13	0.29	3.57	3.76	9.19	3.42	0.56
TOL	57300	23.07	11.73	40.07	3.22	17.94	59.59	56.83	77.31	77.83	4.07
	28400	14.53	7.41	29.92	1.28	8.67	33.95	29.95	37.10	40.68	3.29
	14500	7.68	3.91	17.24	0.53	4.11	16.52	13.32	15.66	17.89	1.95
	9680	5.11	2.64	12.11	0.17	2.91	11.58	7.84	9.38	11.15	1.25
TBTL	8730	31.90	8.09	19.37	3.46	8.92	13.68	104.22	4.10	13.26	7.90
	4390	15.45	3.64	11.29	1.64	5.25	6.71	62.13	4.06	7.01	4.78
	2190	7.46	2.04	6.06	0.91	2.98	4.29	52.67	3.61	5.36	2.61
	1460	5.42	1.50	4.43	0.50	2.37	2.84	29.92	2.04	2.87	2.32
DBTN	149000	195.61	45.37	55.67	10.38	41.18	67.73	325.67	17.58	66.37	11.15
	74600	110.72	22.77	35.06	5.69	19.57	35.52	199.64	5.81	30.60	9.33
	29800	65.53	11.27	18.91	2.80	9.68	15.83	136.41	1.32	15.22	4.48
	22400	45.78	7.51	12.62	1.49	6.88	9.73	111.75	−0.13	10.30	3.81

Table IV. Fluoropolyol Responses to DMMP in Array I

concn, μg/L	response, Hz/kHz						av	% error
137	151	137	130	142	130	117	126	7
	123	134	137	131	122	117		
84	98	91	89	108	100	95	98	12
	94	90	89	107	99	93		
52	77			86	80	74	79	9
	81			85	78	73		
29	53			63	58	52	57	16
	58			68	55	52		

Two common interferents in many environments are water and hydrocarbon fuels. Poly(ethylenimine), a coating material that we have not reported previously, was the most water-sensitive coating in this study (Table III). Poly(vinylpyrrolidone) coated sensors are also water sensitive but were not as sensitive in these tests as had been observed previously (3). Indeed, repeated experiments on this material indicated poor reproducibility from sensor to sensor, and on repeated testing of individual sensors. Data from the most consistently behaved poly(vinylpyrrolidone) coated sensor were selected for use in the prediction set below. Both poly(ethylenimine) functionalities that can interact with water. They are among the most water-sensitive coatings in this data set but are much less sensitive to DMMP than the two DMMP-sensitive coatings noted above. (The DMMP sensitive coatings also respond to water, but their water sensitivities are much less than their DMMP sensitivities.)

The properties of hydrocarbon fuels are represented in the set of vapors by isooctane and toluene. In our previous study, poly(isoprene) was the most sensitive coating material for isooctane. However, the high reactivity of unsaturated hydrocarbon polymers to ozone (29) prompted us to replace it with another elastomeric hydrocarbon polymer, poly(isobutylene). As expected, this material was the most sensitive coating for isooctane among those tested.

The patterns observed in response to DMMP, dimethylacetamide, water, and isooctane are illustrated in Figure 2. These graphs are normalized to the highest response. The patterns for DMMP and dimethylacetamide are quite similar, while those for water and isooctane are strikingly different from them and from each other.

...ve-component mixtures were also included in the sensor test sequence. The vapors in these mixtures and their concentrations are given in Table V. Simulants at low concentrations were mixed with interferents at much higher con-

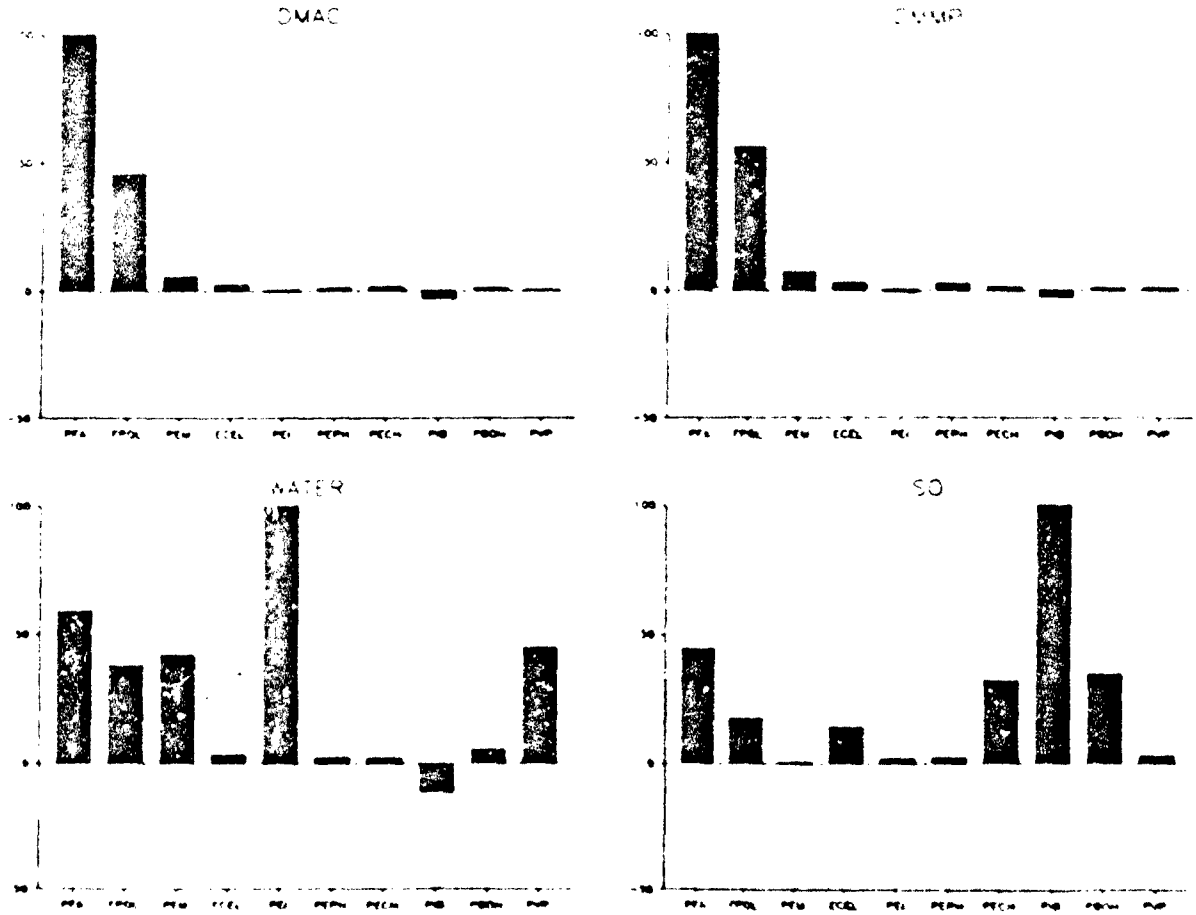


Figure 2. Bar graphs showing relative response patterns using all the coatings tested for four of the test vapors.

Table V. Vapor Mixture Components and Concentrations

		vapor 2 concentration, μg/L							
vapor 1	conen, μg/L	water 1940	ISO 32480	2BTN 35310	DCE 44630	DES 14450	HEPTL 2445	TOL 15330	DMMP B 809
DMMP	46	•	•	•	•	•	•	•	
DMAC	21	•	•	•	•	•	•	•	•
water	1940		•	•	•	•	•	•	•
ISO	32480			•	•	•	•	•	•
2BTN	35310				•	•	•	•	•

mixtures of two components. The observed sensor responses, Δf_{obs}, were examined to see if they were comparable to the responses expected from a linear combination of responses to the single vapors where

$$\Delta f_{calc} = \Delta f_{vapor\,1} + \Delta f_{vapor\,2} \qquad (1)$$

In the vast majority of cases, the observed responses were within 30% of the calculated combination. For nonspecific but reasonably sorbent coatings such as poly(epichlorohydrin) and poly(butadiene) hydroxylated, the agreement was particularly good, typically within 10%. The DMMP sensitive coatings, fluoropolyol and poly(terpene/fluoro alcohol), gave responses to mixtures containing DMMP (at low concentrations) and interferent that ranged from 10% to 30% less than the calculated additive response. In each of these cases, the largest deviations were mixtures of DMMP and 2 butanone. This observation is interesting since these two vapors are both hydrogen bond acceptors and will compete with one another for the hydrogen bond donating sites in the coating material. Notable exceptions to linearly additive responses occurred in quency shift. This result was most frequent with poly(isobutylene) but also occurred for poly(ethylenimine) in response to mixtures of DMMP (low concentration) with toluene, diethyl sulfide, 2 butanone, and 1 butanol. Significantly, responses to mixtures including water, for which poly(ethylenimine) gives important information, were generally within 10–20% of the expected value. Other exceptions to linearly additive responses include the responses of poly(ethylenimine) to mixtures of isooctane and 2 butanone with other interferents and responses of poly(ethylene maleate) to mixtures of water with isooctane, diethyl sulfide, and 1 butanol.

Pattern Recognition Analysis. The vapors and two-component mixtures tested in this study were divided into two classes as shown in Table I. An earlier paper by Stouch and Jurs (*30, 31*) outlined the precautions that should be used to avoid chance or random results when nonparametric classifiers are applied to data. Balanced data sets containing about the same number of observations in each class is one way to minimize chance classifications. Therefore, we collected mixture data for both classes. Class 1 mixtures contain

Table VI. Correlation Matrix for Eight Sensors

	FPOL	PEM	ECEL	PEI	PEPH	PECH	PFA	PIB	PBOH
FPOL	1	-0.134	-0.612	-0.189	-0.444	-0.711	0.601	-0.625	-0.724
PEM		1	0.258	0.705	0.165	0.156	-0.486	-0.241	0.193
ECEL			1	-0.072	0.877	0.917	-0.665	0.456	0.886
PEI				1	-0.185	-0.092	-0.352	-0.181	-0.051
PEPH					1	0.801	-0.427	0.274	0.758
PECH						1	-0.725	0.714	0.989
PFA							1	-0.611	-0.754
PIB								1	0.727
PBOH									1

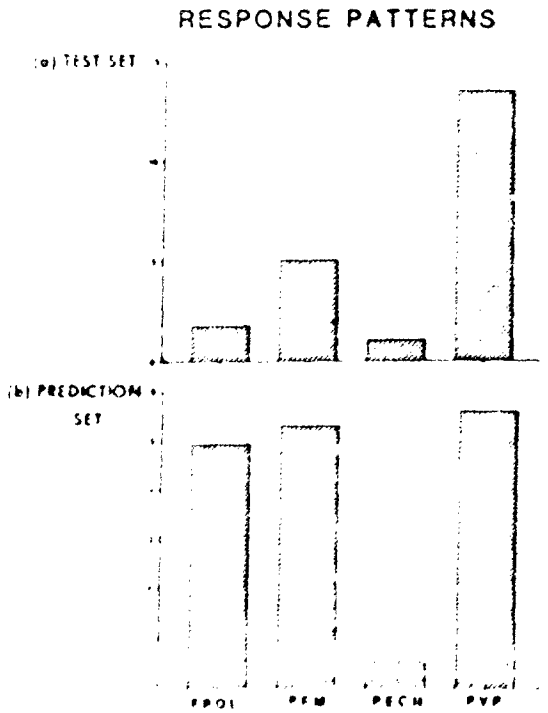


Figure 3. Response patterns for water from (a) the previous test set and (b) the prediction set

Class 2 mixtures contain two interferents.

The responses to the single vapors for the four coatings common to the previous study, fluoropolyol, poly(ethylene maleate), poly(epichlorohydrin), and poly(vinylpyrrolidone), were used as a prediction set. The prediction set measured the ability of the linear discriminant developed in our previous study (3) to classify the vapors in an unknown set into the appropriate classes. All of the vapors in the data matrix (104 × 4) were identified correctly, except water. Figure 3 shows the relative responses to water of the four coatings for both studies. The largest difference is observed from poly(vinylpyrrolidone) (PVP). As noted above, devices coated with poly(vinylpyrrolidone) gave inconsistent responses during the data collection stage. Following the prediction, a supervised learning pattern recognition method called the adaptive least-squares algorithm (37) was employed using the prediction set. A new discriminant, developed from the previous weight vector, produced a completely separable data set. In other words, water was no longer misclassified, and the discriminant recognized the new pattern for water.

The larger data matrix (172 × 9) collected for this study was used as a training set to investigate the clustering of mixtures. Regression analysis revealed a strong pairwise correlation between poly(butadiene) hydroxylated and poly(epichlorohydrin) and some correlation between poly(ethylene phthalate), ethyl cellulose, poly(epichlorohydrin), and poly(butadiene) hydroxylated as shown by the correlation matrix in Table VI. A hierarchical cluster analysis routine using the Euclidean distance metric and flexible fusion (33, 34) was employed to compare the responses of the coatings to all the vapors in the data set. The hierarchical cluster analysis of the coatings demonstrated similar results to the regression analysis. The dendrogram produced from the results of the cluster routine are shown in Figure 4. The y axis on the dendrogram is a measure of dissimilarity; coatings that are fused together lower on the y axis are similar, while coatings fused higher are different. Four large divisions are observed. The coatings correlated in the regression analysis make up one group. Poly(isobutylene) is significantly different from all the other coatings. Poly(ethylene maleate) and poly(ethylenimine) are similar to each other and are very different from all the other coatings. The two DMMP-sensitive coatings, fluoropolyol and poly(isoprene/fluoro alcohol), are similar to one another and significantly different from all the other coatings. Due to the strong correlation with the other coatings, poly(butadiene) hydroxylated was removed from the data set for further analysis.

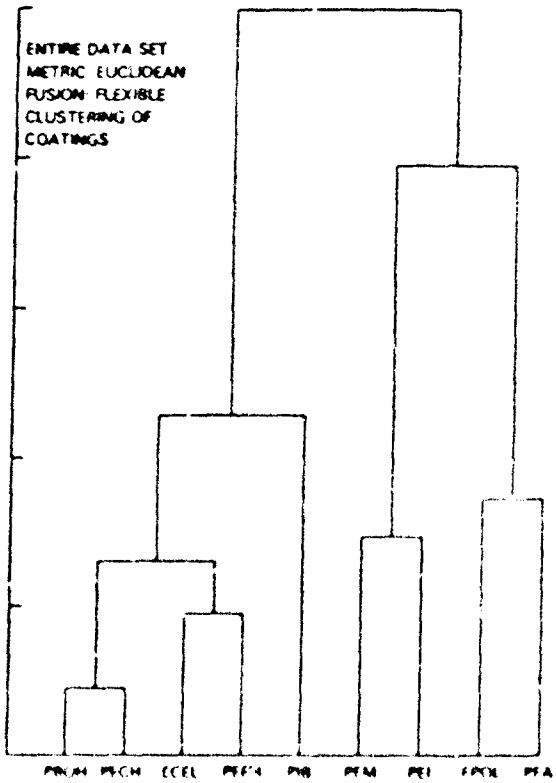


Figure 4. Hierarchical cluster results of coatings based on the responses to nine individual vapors and mixtures.

A graphical means of displaying the large data matrix is through the use of circular profiles. Each pattern vector for a given vapor is drawn in as a polygonal figure, consisting of lines connecting points placed on axes that radiate from the

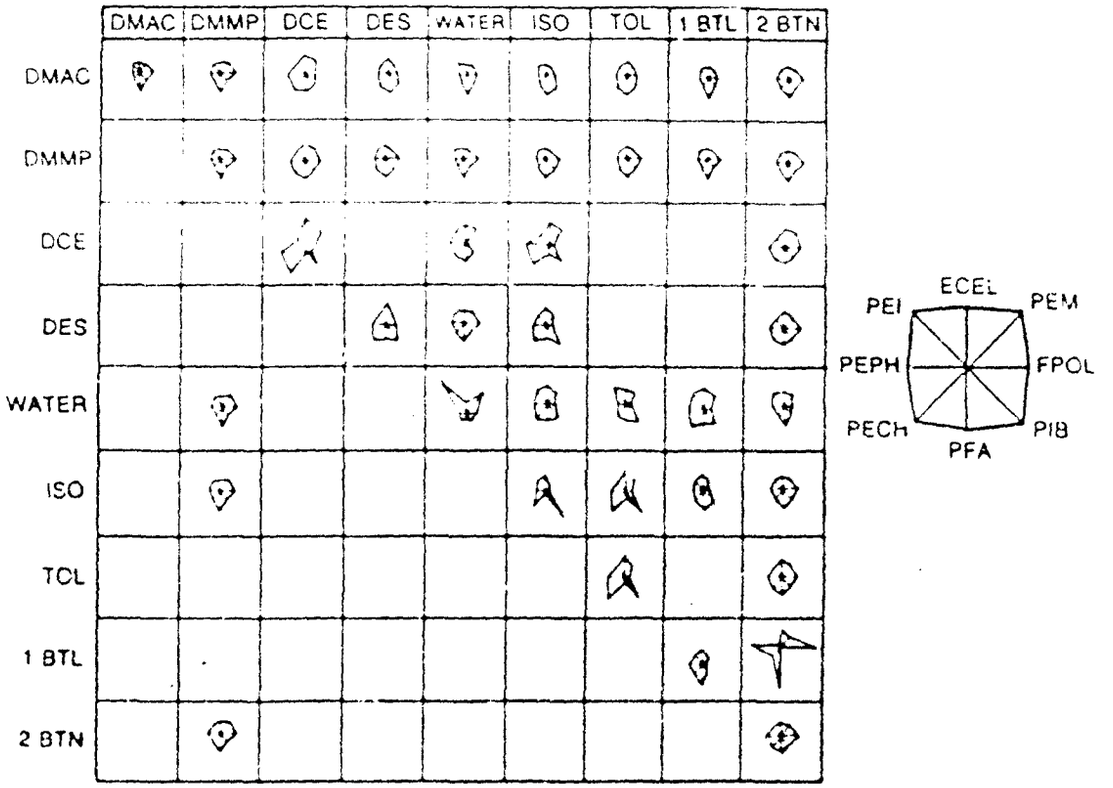


Figure 5. Circular profiles of the individual vapors and each of the mixtures tested and a diagram showing the coating responsible for each of the observed responses.

center like spokes on a wheel. The distance of each point from the center or the length of the spoke depends on the response of the sensor to the vapor. This visual display of the eight sensor responses to each of the vapors and mixtures is shown in Figure 5. A diagram defining the position of each coating represented by each spoke is also drawn. The profiles in each row are the result of the combination of the entry on the left with the vapors listed above each column. For example, the profiles in the top row of the figure are the response of the eight sensors to dimethylacetamide and dimethylacetamide mixed with each of the vapors listed across the columns. The profiles in the second row and in the second column are examples of the responses to DMMP and mixtures containing DMMP. These profiles do change when a class 2 vapor is mixed with the class 1 vapor, although they do maintain a certain character that is not observed among the class 2 vapors. The DMMP in the mixtures listed in the column labeled DMMP was generated from a bubbler and is present at much higher concentrations than in the entries in the row labeled DMMP (generated from a permeation tube).

The first two principal components, found using principal component analysis, were used to initialize a nonlinear mapping routine. The two-principal component plot describes the plane that best represents the data, although misrepresentation of the position of some of the points exists when points are projected from the eight dimensional space of the sensors to 2-space. The nonlinear mapping routine adjusts the position of the points in the two-space defined by the principal component by minimizing an error function so that the resulting plot most closely reflects the relative positions of the points in the 8-space. Thus, the nonlinear mapping routine in combination with principal component analysis transforms a set of points from 8-space to 2-space by maintaining the similarities and dissimilarities between the points. The resulting plot is shown in Figure 6. Only half of the data set [illegible] to reduce its complexity. One example of each concentration for each the vapors is included. A boundary is drawn around each of the single vapors. Most of the data for each individual vapor cluster in discrete sectors. Water, isooctane, toluene, dichloroethane, and diethyl sulfide are well separated from DMMP and dimethylacetamide. All of the mixtures containing a toxic vapor (class 1 vapor) cluster close to the individual class 1 vapors even though the class 2 component is much more concentrated. Butanone and butanol and some of the class 2 mixtures cluster close to the class 1 vapors and could lead to misclassification.

Hierarchical cluster analysis produced similar results. A Euclidean distance metric with flexible fusion (33, 34) was selected to display the data set and the resulting dendrogram is shown in Figure 7. One third of the original data matrix is shown to simplify visualization. Most of the class 2 vapors are grouped together on the right, most of the class 1 vapors are grouped together in the center, and the some of the mixtures are grouped together on the left. The best clustering is among the class 1 vapors and mixtures containing them; these vapors have much similarity as shown by their fusion low on the y axis. Water, isooctane, toluene, dichloroethane, and diethyl sulfide are all located in the block labeled class 2 and they are the least similar to the class 1 vapors. A mixture of dimethylacetamide and dichloroethane clusters with the class 2 vapors. Butanone and butanol and most of the mixtures containing butanone are located on the left side of the dendrogram and appear to be similar to the class 1 vapors because they cluster lower on the y axis.

The data set was [illegible]ided into two classes as defined in Table I. Each class contained 86 vapor experiments for the eight remaining sensors. The data and the correct classification results were given to several supervised learning techniques in the ADAPT software package. The classifiers were designed to generate a discriminant in one classifier and to allow that discriminant to be passed to another. A typical study used a statistically based classifier (35) to generate the

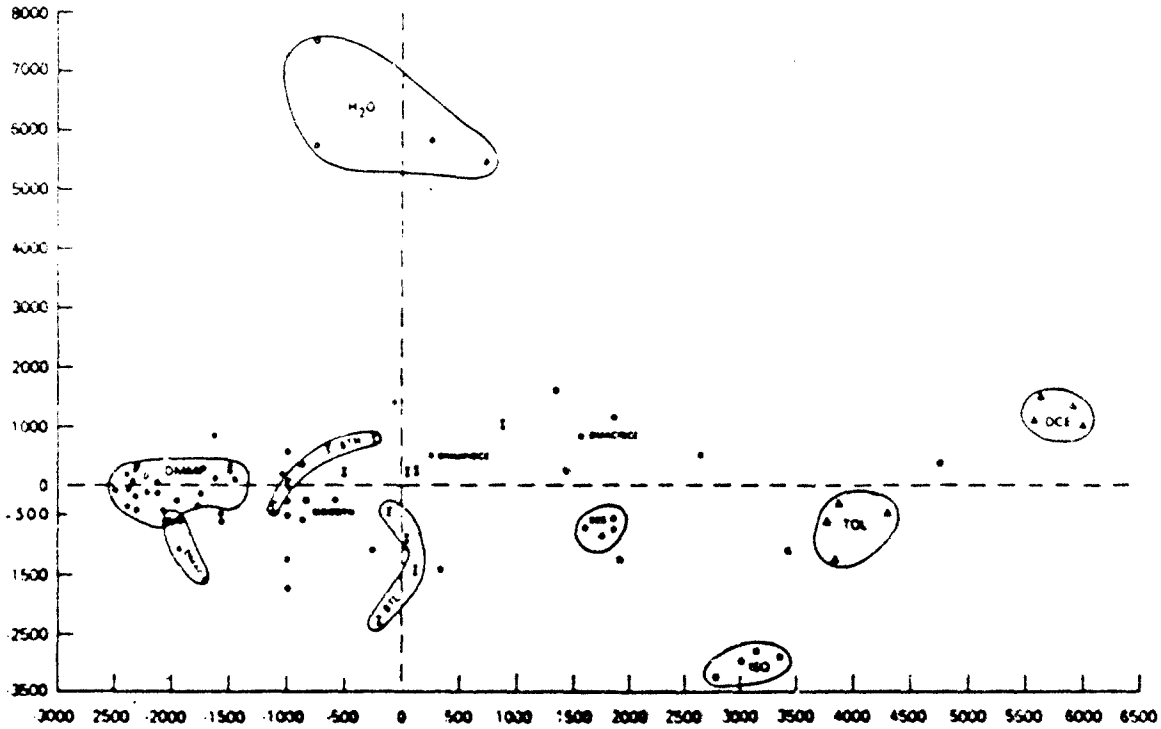


Figure 6. Principal component plot obtained by using results from eight coatings. Each vapor is represented by a symbol. Each of the mixtures is represented by the symbol of vapor 1 in Table V, except the mixtures including DMMP from the bubbler, which have the same symbol as DMMP. The three mixtures misclassified in the discriminate analysis are individually labeled.

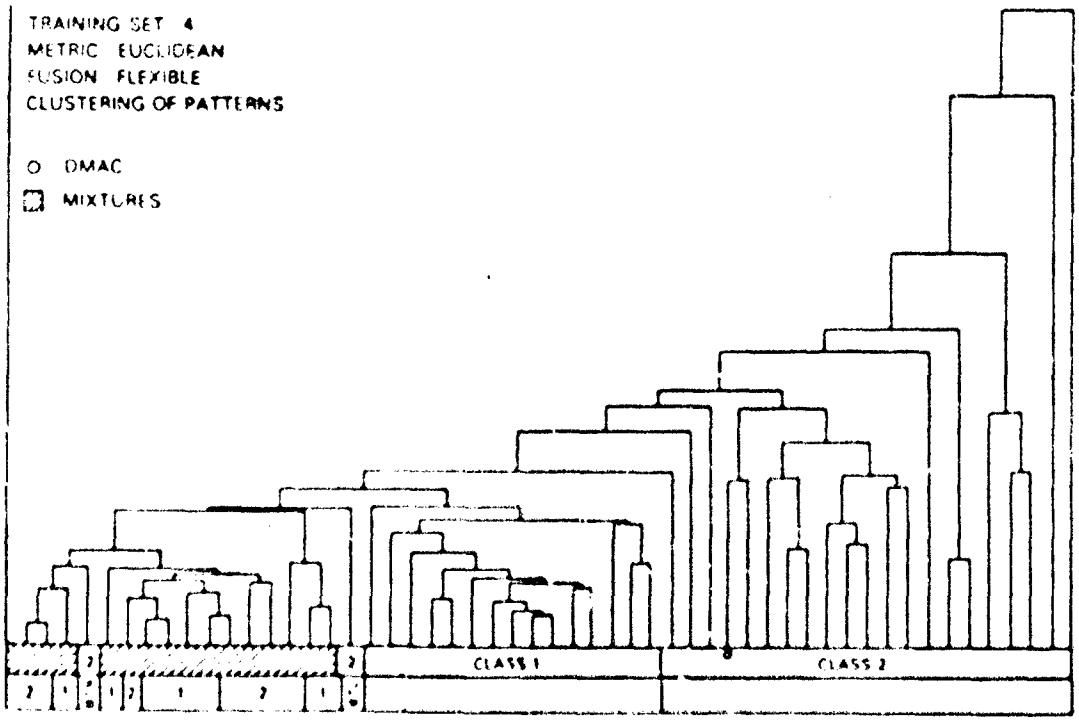


Figure 7. Hierarchical cluster results of the test vapors and mixtures based on eight coatings.

initial discriminant, which was then passed to the adaptive least squares algorithm (J2). Several iterations and several combinations of classifiers were used to train the data set. All of the vapors and mixtures were correctly classified except three mixtures, dimethylacetamide and dichloromethane, DMMP and dichloroethane, and isooctane and butanone. They were consistently misclassified. This is not surprising when the position of these mixtures are identified in the principal-component plot (Figure 7).

The data set was reexamined considering the usually slight variations in the responses of the fluoropolyol-coated sensor in each of the four sensor test arrays. The responses of the fluoropolyol-coated sensor in the first test array served as the standard, and data for each vapor or mixture were examined separately. If the response of the fluoropolyol-coated sensor in a subsequent test array was significantly different from the corresponding response in the first test array (i.e. the difference in the average response between the two test arrays

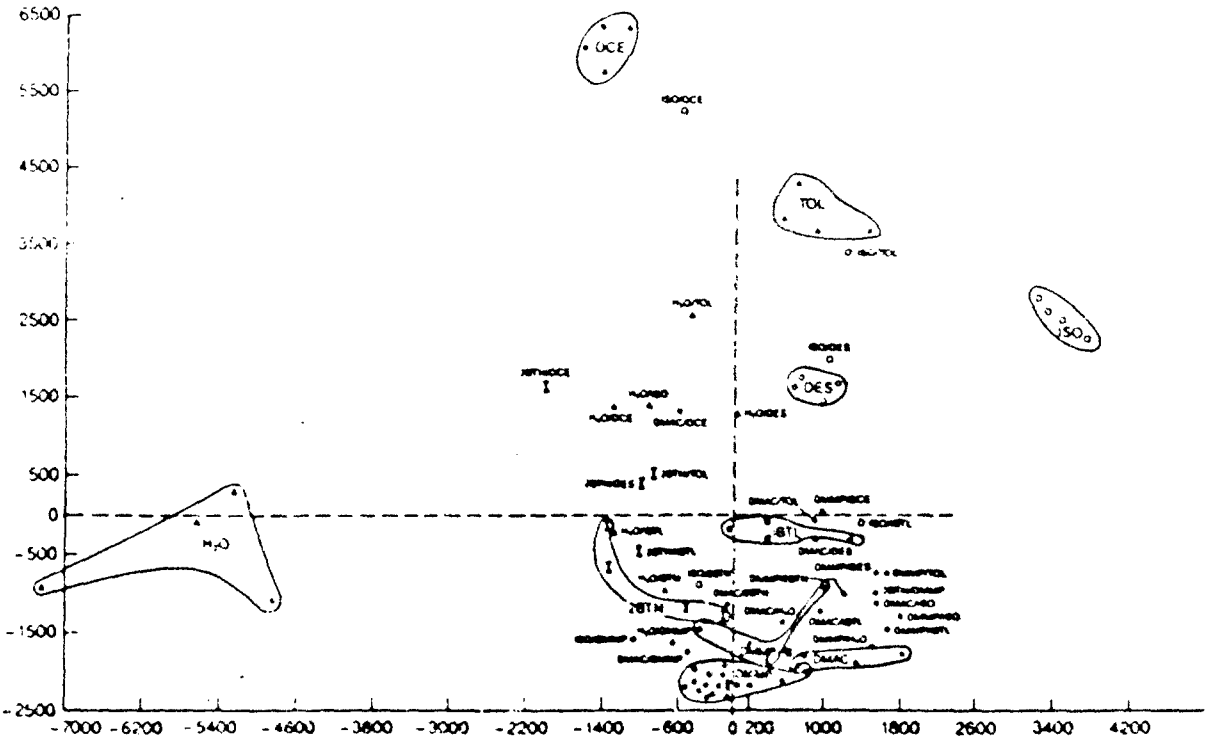


Figure 8. Principal component plot for the corrected data using eight coatings. All of the mixtures are labeled and the individual vapors are enclosed in discrete boundaries.

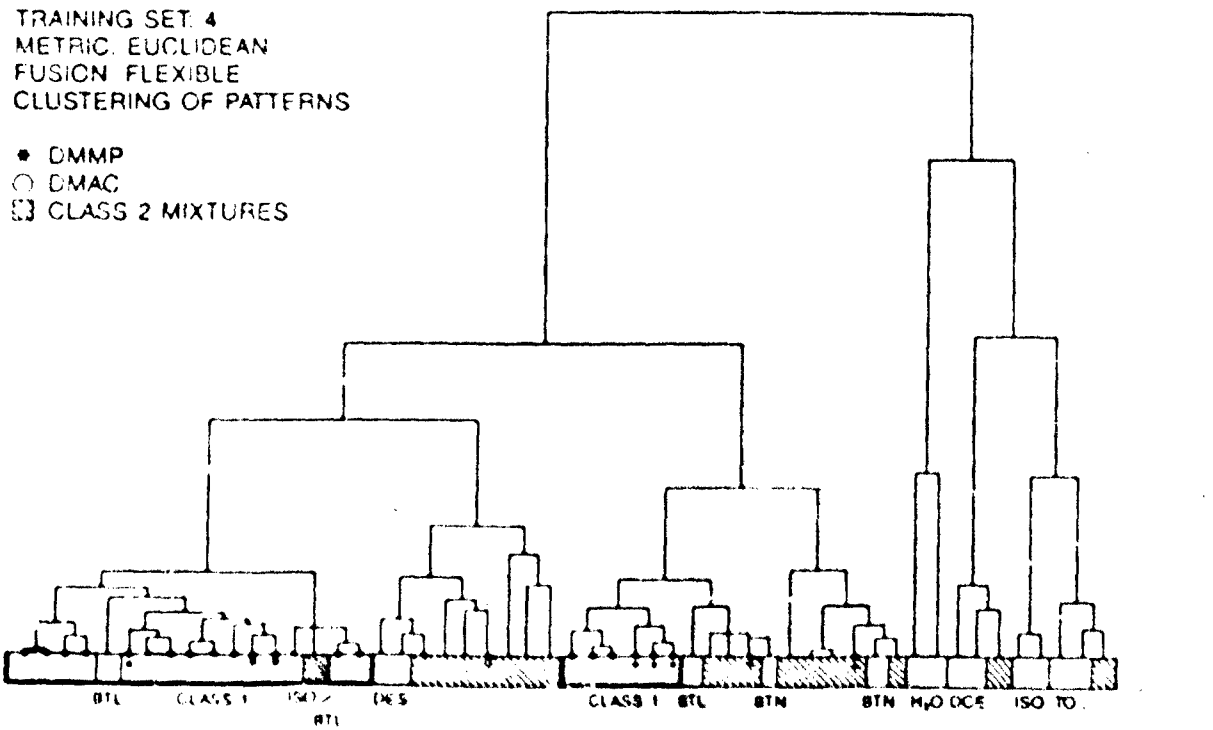


Figure 9. Hierarchical cluster results for the corrected data using eight coatings. The class 2 vapors are labeled, and most of the class 1 vapors are in the bold blocks, the ones that are not are marked.

was greater than the variation in response within the first array), then a linear correction factor was determined. The sensor responses of all the coatings in the subsequent test array to that particular vapor were then multiplied by the correction factor. These factors are given in Table VII.

The regression results indicated the same correlation between the poly(butadiene) hydroxylated and poly(epichlorohydrin) responses. Poly(butadiene) hydroxylated was deleted and the remaining eight coatings were reexamined by using the cluster and display methods. The results of principal component analysis are similar to the uncorrected results for the individual vapors, as shown in Figure 8. The corrected data does improve the clustering of the mixtures. The mixtures do not crowd the class 1 vapors as much as in the previous plot, especially for butanone. The hierarchical cluster analysis supports this observation. As seen in Figure 9, most

Table VII. Correction to the Conditions of the First Array

vapor	FPOL, PEM ECEL	PEI, PEPH	PECH, PFA PIB, PBOH
DMMP	1.00	1.20	1.50
DMAC	1.00	1.30	1.60
DCE	1.00	1.00	1.30
water	1.00	1.50	2.50
ISO	1.00	1.00	1.30
TOL	1.00	1.00	1.30
DES	1.00	1.00	1.30
2BTN	1.00	1.00	1.00
1BTL	1.00	1.00	1.00
DMAC/DCE	1.00	1.00	1.30
DMAC/H_2O	1.00	1.00	1.30
DMAC/ISO	1.00	1.00	1.30
DMAC/TOL	1.00	1.00	1.30
DMAC/DES	1.00	1.00	1.30
DMAC/DMMP	1.00	1.00	1.30
DMAC/2BTN	1.00	1.00	1.30
DMAC/1BTL	1.00	1.00	1.30
DMMP/DCE	1.00	1.00	2.50
DMMP/H_2O	1.00	1.00	2.50
DMMP/ISO	1.00	1.00	2.50
DMMP/TOL	1.00	1.00	2.50
DMMP/DES	1.00	1.00	2.50
DMMP/2BTN	1.00	1.00	2.50
DMMP/1BTL	1.00	1.00	2.50
water/DCE	1.00	1.00	1.30
water/ISO	1.00	1.00	1.30
water/TOL	1.00	1.00	1.30
water/DES	1.00	1.00	1.30
water/DMMP	1.00	1.00	1.30
water/2BTN	1.00	1.00	1.30
water/1BTL	1.00	1.00	1.30
ISO/DCE	1.00	1.10	1.10
ISO/TOL	1.00	1.10	1.10
ISO/DES	1.00	1.10	1.10
ISO/DMMP	1.00	1.10	1.10
ISO/2BTN	1.00	1.10	1.10
ISO/1BTL	1.00	1.10	1.10
2BTN/DCE	1.00	1.10	1.10
2BTN/TOL	1.00	1.10	1.10
2BTN/DES	1.00	1.10	1.10
2BTN/DMMP	1.00	1.10	1.10
2BTN/1BTL	1.00	1.10	1.10

of the class 1 vapors are on the left side of dendrogram and are positioned lower on the y axis relative to the class 2 vapors, indicating less similarity between the two groups. Even the class 1 vapors in the center of the dendrogram are positioned lower on the y axis compared to the class 2 vapors and mixtures containing class 2 vapors. Water, isooctane, toluene, and diethyl sebacate, shown on the right of the dendrogram, are well separated from all the other vapors and are very dissimilar as indicated by the higher level of fusion on the y axis. Most of the class 2 mixtures are closer to the class 1 vapors than the single class 2 vapors, although the mixtures appear in discrete regions in the dendrogram.

The Bayes classifier was used to generate the initial discriminant for the new 172 × 8 data matrix, and the results of that supervised learning technique were used to initialize the adaptive least-squares algorithm. After several iterations, all of the vapors were correctly classified including those mixtures previously misclassified. The resulting discriminant was passed to a classifier called the linear learning machine (35), and the data set was trained further adding thickness to the discriminant hyperplane between the two classes. A deadzone or linear discriminant thickness 200 times greater than the standard generated by the routines was obtained, which indicates that the classes are well separated. A summary of the results is given in Table VIII. The new discriminant was examined by using another routine designed to test the importance of each coating to the classification. In this routine, several classifications were made by using the new discriminant and for each classification one sensor was left out of the analysis. The percentage correctly classified was measured. The lower the percentage correct, the more important the sensor for the discriminant evaluated. The list of sensors is sorted and given in Table VIII from least important to most important. The most important coatings in this linear discriminant are ethyl cellulose, poly(ethylene phthalate), poly(ethylenimine), and poly(isoprene/fluoropolyol). Fluoropolyol is the least important because the removal of this coating from the set would only reduce the classification results to 97%. In the previous study, fluoropolyol was the most important coating based on the classification results. In this study, fluoropolyol has been supplanted by poly(isoprene/fluoro alcohol), which provides much the same information and has greater DMMP sensitivity.

Table VIII. Weight Vector Components for Best Coatings

coating	discriminant function values	no. wrong 1	no. wrong 2	% recognition
	+0.13	0	0	100
FPOL	−0.03	2	3	97
PEM	+0.24	4	7	94
PIB	−0.11	3	7	91
PECH	+0.60	2	15	90
PFA	+0.22	36	15	70
PEI	−0.40	40	17	67
PEPH	−0.32	56	25	53
ECEL	−0.49	72	38	36

CONCLUSIONS

Pattern recognition techniques can readily distinguish between the class 1 vapors and the class 2 vapors when the SAW sensors are exposed to single vapors. The linear discriminant developed in our previous study was 100% successful in distinguishing class 1 from class 2 vapors in the previous data set (3). The same discriminant applied to the single vapors in this data set correctly classified all vapors, except water. This discrepancy arose due to the poor reproducibility of the water-sensitive coating poly(vinylpyrrolidone). A new discriminant was developed to achieve 100% correct classification, and a better water-sensitive, poly(ethylenimine), has been identified.

The single vapors that cluster nearest to DMMP are 2-butanone and 1-butanol. Like DMMP, 2-butanone can accept hydrogen bonds. It differs by being a weaker acceptor and by having a much higher saturation vapor pressure. 1-Butanol is also a hydrogen bond acceptor of comparable strength to 2-butanone, but differs in its ability as a hydrogen bond donor. The saturation vapor pressure of 1-butanol is closer to that of DMMP than that of 2-butanone.

Single vapors could be correctly classified by using as few as four sensors. When two-component mixtures were included in the data set, eight sensors were required to obtain the best classification results. The responses of mixtures were generally close to those expected from a linear combination of the single vapor responses. This result is encouraging because it simplifies the correct classification of mixtures. It is particularly notable in the context of the detection problem discussed here that the responses of the DMMP-sensitive coatings to mixtures containing DMMP were well-behaved.

The clustering results for mixtures were similar to those for single vapors. All of the class 1 mixtures clustered close to the class 1 vapors. The class 2 mixtures clustering closest to the class 1 vapors were usually those containing 2-butanone or 1-butanol. By use of the experimental data as collected, all mixtures could be correctly classified, except three. When correction factors were applied to the data as explained in the

Results, 100% correct classification could be achieved. The mixtures were successfully analyzed even with large concentration differences between the vapors of interest and the potential interferents.

Variations in fluoropolyol-coated sensor responses from one test array to another are likely to arise from three factors. Changes in the actual vapor concentrations generated by the test apparatus will cause linear changes in the responses of the sensors. Variations in the sensor temperature will change sensor response because the sorption of vapors into the coating material varies exponentially with temperature. Hysteresis due to previous vapor exposures might also cause sensor response variations. This is expected to be minimal for sensors whose behavior is based on simple reversible absorption, but it cannot be summarily ruled out.

The ability of pattern recognition techniques to discriminate between vapors is expected to improve as the sensor technology matures and testing procedures are more rigorously controlled. SAW coating materials whose responses are consistent and reproducible, and which provide greater sensitivity, will offer obvious advantages. A set of materials with more widely varying responses to key vapors will enhance the information to be analyzed. Rigorous control of sensor temperature and a truly inert reference on the SAW sensor will improve performance. Finally, it may be useful to examine mixtures where the concentration ratio of the two components is varied.

ACKNOWLEDGMENT

The authors wish to thank Arthur Snow for all his efforts, particularly in materials support and syntheses, Jim Griffith for providing the fluoropolyol, and Hank Wohltjen for his efforts. The authors gratefully acknowledge the support of the coating testing work by Army/CRDEC, Aberdeen Proving Ground, MD, and of the pattern recognition work by HQ RDSX, Brooks Air Force Base, TX.

LITERATURE CITED

(1) Stetter, J.; Jurs, P. P.; Rose, S. L. *Anal. Chem.* **1986**, *58*, 860.
(2) Carey, W. P.; Beebe, K. R.; Kowalski, B. R.; Illman, D. L.; Hirschfeld, T. *Anal. Chem.* **1986**, *58*, 149.
(3) Ballantine, D.; Rose, S. L.; Grate, J. W.; Wohltjen, H. *Anal. Chem.* **1986**, *58*, 3058.
(4) Carey, W. P.; Beebe, K. R.; Kowalski, B. R. *Anal. Chem.* **1987**, *59*, 1529.
(5) Grate, J. W.; Snow, A.; Ballantine, D. S., Jr.; Wohltjen, H.; Abraham, M. H.; McGill, R. A.; Sasson, P. *Anal. Chem.* **1988**, *60*, 869–875.
(6) Wohltjen, H.; Snow, A. W.; Barger, W. R. *Ballantine, D. S. IEEE Trans. Ultrason., Ferroelectrics, Freq. Contr.* **1987**, *UFFC-34*, 172–178.
(7) Wohltjen, H. *Sens. Actuators* **1984**, *5*, 307–325.
(8) Snow, A.; Wohltjen, H. *Anal. Chem.* **1984**, *56*, 1411–1416.
(9) Nieuwenhuizen, M. S.; Nederlof, A. J.; Barendsz, A. W. *Anal. Chem.* **1988**, *60*, 230–235.
(10) Nieuwenhuizen, M. S.; Nederlof, A. J. *Anal. Chem.* **1988**, *60*, 236–240.
(11) Venema, A.; Nieuwkoop, E.; Vellekoop, M. J.; Ghijsen, W. J.; Barendsz, A. W.; Nieuwenhuizen, M. S. *IEEE Trans. Ultrason., Ferroelectrics, Freq. Contr.* **1987**, *UFFC-34*, 148–155.
(12) Nieuwenhuizen, M. S.; Barendsz, A. W. *Sens. Actuators* **1987**, *11*, 45–62.
(13) Nieuwenhuizen, M. S.; Barendsz, A. W.; Nieuwkoop, E.; Vellekoop, M. J.; Venema, A. *Electron. Lett.* **1986**, *22*, 184–185.
(14) Venema, A.; Nieuwkoop, E.; Vellekoop, M. J.; Nieuwenhuizen, M. S.; Barendsz, A. W. *Sens. Actuators* **1986**, *10*, 47–64.
(15) Martin, S. J.; Ricco, A. J.; Niemczyk, T. M.; Frye, G. C. *Sens. Actuators* **1989**, *20*, 253–268.
(16) Ricco, A. J.; Martin, S. J.; Zipperian, T. E. *Sens. Actuators* **1985**, *8*, 319–333.
(17) Martin, S. J.; Schweizer, K. S.; Ricco, A. J.; Zipperian, T. E. *Proceedings of the 3rd Int. Conf. on Solid-State Sensors and Actuators-Transducers*, Philadelphia, PA, June 11–14, 1985; IEEE Cat. No. CH2127-9/85/0000-0066; pp 71–73.
(18) Vetelino, J. F.; Lade, R. K.; Falconer, R. S. *IEEE Trans. Ultrason., Ferroelectrics, Freq. Contr.* **1987**, *UFFC-34*, 156–161.
(19) Bryant, A.; Poirier, M.; Riley, G.; Lee, D. L.; Vetelino, J. F. *Sens. Actuators* **1983**, *4*, 105.
(20) D'Amico, A.; Palma, A.; Verona, E. *Sens. Actuators* **1982/1983**, *3*, 31–39.
(21) Chuang, C. T.; White, R. M.; Bernstein, J. J. *IEEE Electron Device Lett.* **1982**, *EDL-3*, 145–148.
(22) Field, D. E. *J. Paint Technol.* **1976**, *48*, 43.
(23) Snow, A. W.; Ballantine, D. S.; Whitney, T.; Barger, W. R.; Klusty, M.; Wohltjen, H.; Grate, J.; Chaput, D. *Proceedings of the 1986 U.S. Army Chemical Research, Development, and Engineering Center Scientific Conference on Chemical Defense Research*, CRDEC-SP-87008; Reuse, M. D. eds.; U.S. Army, 1987; pp 695–703.
(24) Sprague, L. G.; Snow, A. W.; Sousen, R. L.; Lint, J.; Wohltjen, H.; Ballantine, D. S.; Grate, J. W. *Proceedings of the 1987 U.S. Army Chemical Research, Development and Engineering Center Scientific Conference on Chemical Defense Research*, U.S. Army, in press.
(25) Grate, J. W.; Ballantine, D. S.; Wohltjen, H. *Sens. Actuators* **1987**, *11*, 173.
(26) Stuper, A. J.; Brugger, W. E.; Jurs, P. C. *Computer Assisted Studies of Chemical Structure and Biological Function*; Wiley-Interscience: New York, 1979.
(27) Chang, Y.; Nortyen, J.; Lloyd, D. R.; Barlow, J. W. *Polym. Eng. Sci.* **1987**, *27*, 693.
(28) Barlow, J. W.; Cassidy, P. E.; Lloyd, D. R.; You, C. J.; Chang, Y.; Wong, P. C.; Nortyen, J. *Polym. Eng. Sci.* **1987**, *27*, 703.
(29) Fog, H. M.; Rietz, B. *Anal. Chem.* **1985**, *57*, 2634.
(30) Stouch, T. R.; Jurs, P. C. *J. Chem. Inf. Comput. Sci.* **1985**, *25*, 45.
(31) Stouch, T. R.; Jurs, P. C. *J. Chem. Inf. Comput. Sci.* **1985**, *25*, 92.
(32) Morigaki, I.; Kamatsu, K.; Matsushita, Y. *J. Med. Chem.* **1980**, *23*, 20.
(33) Williams, W. T.; Lance, G. N. *Statistical Methods for Digital Computers*; Enslein, K.; Ralston, A.; Wilf, R., Ed.; Wiley-Interscience: New York, 1975.
(34) Massart, D. L.; Kaufman, L. *The Interpretation of Analytical Chemical Data by the Use of Cluster Analysis*; Wiley: New York, 1983.
(35) Tou, J. T.; Gonzalez, R. C. *Pattern Recognition Principles*; Addison-Wesley: Reading, MA, 1974.

RECEIVED for review April 20, 1988. Accepted July 18, 1988.

APPENDIX C2

INVESTIGATION OF ELASTIC PROPERTIES OF THIN POLYMER FILMS USING SURFACE ACOUSTIC WAVE DEVICES

David S. Ballantine, Jr.[1] and Henry Wohltjen[2]

[1]GEO-CENTERS, Inc., 10903 Indian Head Hwy
Ft. Washington, MD 20744

[2]MicroSensor Systems, Inc., P. O. Box 90
Fairfax, VA 22030

The observed glass transition temperatures (T_g) of several thin polymer films on the surface of SAW devices were increased by 50-60 °C relative to T_g results reported for other methods such as DSC. The increase in the onset of T_g is the result of interaction of the high frequency surface acoustic wave with the polymer film, consistent with the time-temperature superposition principle. The T_g were identified as localized minimum in the frequency curves, or by changes in the slope of the curves, as the coated sensors were heated between 35-110 °C. Potential applications of SAWs for the characterization of polymeric materials and the implication of these findings on the interpretation of SAW sensor data are discussed.

Polymeric materials are being employed in an increasing number of novel applications in our technological society. No doubt, as stronger, more flexible and more durable materials are discovered the demand for these materials will continue to grow. The chemical and physical properties of these materials will determine the types of applications for which they may be employed. Thus, the rapid and reliable characterization of these properties will be crucial.

In the area of chemical sensors, thin polymer films are routinely used as coatings for the semi-selective sorption of chemical vapors. One such sensor technology, the surface acoustic wave (SAW) device, has demonstrated excellent sensitivity as a vapor sensor when coated with films having appropriate solubility properties (1). To date, most sensor applications have taken advantage of the extreme mass sensitivity of the devices. In this paper, we will examine the response mechanisms of the SAW sensor and demonstrate the sensitivity of these devices to changes in elastic properties of the coating

[1]Current address: Department of Chemistry, Northern Illinois University
DeKalb, IL 60115

materials. Finally, we will discuss the significance of these results in terms of current sensor applications, and the applicability and advantages of the SAW for the characterization of polymeric materials.

Background

Since its introduction in the early 1970's, the SAW has seen increasing utilization as a chemical sensor due to its sensitivity, potentially rapid response, and low cost. A brief description of the operating principles of the SAW will aid in understanding the basis of this study and in the interpretation of the results. Typically, a SAW device consists of a set of interdigital transducers which have been microlithographically deposited on the surface of a piezoelectric substrate. The application of a time-varying electric potential to the transducer causes a mechanical deformation of the substrate, resulting in the generation of a surface acoustic wave. The properties of this wave (amplitude, frequency, phase) are sensitive to perturbations occurring on or near the surface of the substrate. A more detailed discussion of the SAW operation can be found in reference (2). The generation of different types of surface waves is possible (3); for the purposes of this work, when we refer to the surface acoustic wave we specifically mean Rayleigh-type surface waves.

In general, the response of the SAW is the combined result of changes in the mass loading, conductivity, or elastic properties of the surface film. Equations describing the effects of changes in these properties on the frequency of the device have been derived previously (2,4). For many sensor studies, non-conducting polymer films are usually employed. One equation, given below, describes the response behavior for a SAW device coated with a thin, lossless, isotropic, non-conducting film,

$$\Delta f = (k_1+k_2)\rho h f_o^2 - k_2 h f_o^2 (4\mu/V_R^2)[(\lambda+\mu)/(\lambda+2\mu)] \qquad (1)$$

where k_1 and k_2 are material constants for the quartz substrate, V_R is the Rayleigh wave velocity, h is the film thickness, ρ is the density, μ is the shear modulus, λ is the Lame constant, and f_o is the fundamental frequency of the device. The first half of the equation yields the frequency shift resulting from mass loading, while the second half describes the effect of changes in the elastic properties of the film on the resonant frequency.

To date, the selection of coatings for vapor sensor applications has been mostly empirical, requiring the screening of a large number of candidate materials to identify coatings with sufficient sensitivity to the vapor of interest. To address this problem, recent work has focused on characterizing the observed sensor responses in terms of solubility interactions (1,5). The sorption of a solute vapor into a solvent coating can be quantitatively defined as a partition coefficient, K. A modified version of Equation 1 has been used to predict the frequency response of coated SAWs to predict the frequency response of these sensors to specific vapors utilizing partition coefficients calculated from GLC data (5). The inherent assumptions in that work are that (1) the polymer coating is a lossless film (that is, there is no significant attenuation of the surface wave resulting from interactions with the surface film), and (2) the contributions to

the observed response from elastic properties of the film are negligible. To justify the second assumption, care was taken to select polymer films that would be above their glass transition temperatures (T_g) at the operating temperature of the device.

In order to assess the validity of the second assumption, a brief discussion of the elastic properties of polymers is needed. The viscoelastic behavior of a polymer is depicted schematically in Figure 1. The parameter of interest in the case of SAWs is the shear modulus, denoted as G in Figure 1 and as μ in Equation 1. Simply stated, the modulus is a measure of the rigidity of the polymer. The regions of interest are the glassy region (where the polymer is a hard, rigid material) and the elastomeric region (where the polymer is a rubber). Rigid, glassy polymers typically have high modulus values on the order of 10^9 - 10^{10} dyne/cm^2. In this region, the polymer chains are locked into the lowest energy conformations and there is insufficient energy in the system to allow free rotation around the polymer backbone. As the temperature increases the polymer becomes an elastomer. In this region, there is sufficient energy in the system for free rotation to occur. This additional rotational freedom is manifested as a 'softening' of the polymer, with a corresponding decrease in the modulus to 10^4 - 10^7 dyne/cm^2. The temperature at which this softening occurs is the T_g. Other changes occur at this temperature that can be monitored experimentally to identify the T_g. These include changes in the specific volume of the polymer, the index of refraction, the gas diffusion coefficient, the thermal expansion coefficient (measured by dilatometry), and specific heat (measured by differential scanning calorimetry (DSC) or by differential thermal analysis (DTA)). Good general discussions of the elastic properties of polymers can be found in references (6,7).

The T_g of a polymer increases as a function of frequency. This phenomenon was first described by Williams, Landel and Ferry in 1955, and became the basis of the time-temperature superposition principle (8). Previous work by Wohltjen and Dessy demonstrated that the SAW could be used to characterize polymeric materials (9). In that work, both thin films and bulk samples were characterized by monitoring changes in the amplitude of the surface wave as the temperature of the polymer samples was increased. Their results indicated that, for thin polymer films, there is significant interaction of the polymer film with the high frequency surface wave, resulting in an increase in the T_g of the polymer. This observation is consistent with the time-temperature superposition principle.

The work to be presented here was motivated by two factors. First, it had been assumed that polymer films used in previous sensor applications were above their T_g at the SAW operating temperature. If the T_g of a given polymer film is significantly increased due to the effects of the high frequency surface wave, then the elastic properties of the film must be taken into consideration when interpreting sensor responses. Second, since the frequency mode of the SAW device represents a more sensitive measurement than the amplitude, these devices have tremendous potential in the area of materials characterization. The following experiments were performed to verify this potential and to investigate the possible effect of elastic properties on sensor responses.

Experimental

The polymer coatings studied are given in Table I, along with pertinent physical parameters. These coatings were selected based on availability, since they are among coatings previously used for chemical sensor studies at NRL. In addition, the transition temperatures (T_g, T_m) are within the range that could be easily investigated using our experimental apparatus. Of these coatings, fluoropolyol (FPOL) and poly(ethylene maleate) (PEM) were provided by the Polymeric Materials Branch, Chemistry Division, of the Naval Research Laboratory in Washington D.C. They are both linear polymers with no observed crystallinity. PEM is a polyester material with a repeating monomer unit of 35-50. FPOL is a highly viscous epoxy pre-polymer with a repeating monomer of 8-10. Densities were measured using a float technique, and T_g were measured by DSC at the NRL Chemistry Division. Additional information regarding the structure and properties of these materials can be found in reference (1).

TABLE I. POLYMER COATINGS AND PHYSICAL PARAMETERS

polymer	T_g (°C)	T_m (°C)	n	ρ (g/cm^3)
fluoropolyol (FPOL)	10	---	8-10	1.653 (25 °C) 1.563 (90 °C)
poly(ethylene maleate) (PEM)	-10	---	35-50	1.353 (25 °C)
ethyl cellulose (ECEL)	43	157-165	---	1.14 (at T_m)
poly(caprolactone)	<-60	60	---	---

Poly(caprolactone) and ethyl cellulose were obtained from Aldrich, and were used as received. They are semi-crystalline materials and would be expected to exhibit localized changes in elastic properties at both T_g and the melting point, T_m. Physical parameters for these polymers were obtained from the Aldrich catalog. No value was available for the T_g of PCAP, the value in Table I is estimated using the relationship

$$T_m = K\,T_g \qquad (2)$$

where $K = 1.4 \pm .2$ (2)

The 158 MHz quartz SAW devices were obtained from MicroSensor Systems, Inc. (MSI part # 08-158A). They consisted of two individual delay lines manufactured on a single quartz chip. Electrical connections to the transducers were established by wire bonding to a T-08 plug-in

package. Additional information regarding the dimensions and geometry of the devices can be obtained from MSI.

Dilute solutions of the coating materials were prepared in chloroform. These solutions were then aspirated using an airbrush to generate a finely dispersed aerosol, which was deposited on one side of the dual SAW device. The other delay line remained uncoated, acting as a reference to correct for frequency deviations due to fluctuations in ambient temperature and pressure.

The coated devices were then placed in the heating chamber illustrated in Figure 2. The chamber consisted of a 3/4" brass Swagelok union fitting which was wrapped with heating tape. The temperature of the heating tape was controlled by a Variac, and the temperature of the chamber was monitored using a YSI Series 400 thermistor. This thermistor was incorporated in a circuit to convert the thermistor resistance into a voltage that could be read directly by the computer-controlled data acquisition system. A dry air stream was heated via a coiled tube located within the chamber prior to introduction to the sensor. A constant flow rate of 40-50 ml/min was maintained during the experiments to minimize the effects of temperature gradients and localized heating near the sensor surface.

The frequencies of the individual delay lines were monitored independently, and the difference frequency of the two sides of the device was obtained as output from an electronic mixer. These frequencies were recorded as the devices were first heated from 35 °C to 110 °C, and as they were subsequently cooled to room temperature. Each device was subjected to repeated heating/cooling cycles, with frequencies being recorded continuously as a function of temperature. The coatings were then removed, as the SAWs were washed in chloroform in an ultrasonic cleaner. The bare devices were once again placed in the heating chamber and subjected to successive heating/cooling cycles. The frequency curves of the bare devices were recorded for use as blanks.

Results and Discussion

Once the effect of temperature on the frequency of a bare device was known, the effect of temperature on the coatings could be determined by subtracting the results for the bare devices from the frequency-temperature curves for the coated devices. The frequency shifts recorded during these temperature studies are reported in parts per million (ppm), which is defined as the observed frequency shift, in Hz, divided by the resonant frequency of the device, in MHz. For the devices used in this study, 1 ppm is equivalent to 158 Hz. In order for several related curves to be easily viewed on the same plot, individual curves are offset from one another by several hundred ppm.

Examples of the frequency-temperature curves for a bare device are given in Figure 3. Channel 1 and channel 2 refer to the two delay lines of the dual device. When used as a sensor, channel 1 would be coated and channel 2 would remain uncoated to act as a reference. The difference curve is the output from the mixer, and represents the frequency difference between the two delay lines.

It is worth noting that there is substantial frequency shift for both delay lines resulting from temperature changes, on the order of 3-6 ppm/°C. This is the result of thermal stresses arising in the

decomposition products and there is no evidence for any triformylated complex present. The impurities did not interfere with the assignments of the resonances (Table II).

The ^{13}C NMR spectrum (Fig.9) also showed evidence of the impurities but the material was clean enough to obtain reliable assignments. As observed in the ^{1}H spectrum, the methyl resonances were reversed in intensity ratio and the formyl resonance was about twice the intensity of the 3-H-$\underline{C}<$ resonance. The assignments in Table II were made with the aid of ^{1}H coupled spectra and a set of spectra taken with short delay times to positively identify the formyl and methine peaks.

^{1}H And ^{13}C NMR Characterization Of [Ru(3-CHO-acac)(acac)$_2$]

^{1}H NMR spectra of the Ru(III) monoformylated derivative (Fig.10) typically revealed little evidence of either free ligand or the diformylated complex as impurities though a few percent of an unidentified paramagnetic complex was apparent (-7.2,-8.9 ppm). The small amount of this impurity had no significant effect on the characterization of the complex by UV-Visible and IR spectroscopy, cyclic voltammetry or elemental analysis. The assignments of the ^{1}H resonances are listed in Table I for comparison with those of the Rh(III) analog. The paramagnetic shifts are quite large with most of the spin density appearing at the 3-$\underline{H}$-C< position, a feature also observed in the parent complex [Ru(acac)$_3$]. The substituted complex displayed a very large splitting of the -C$\underline{H}_3$ resonances, while the methine resonances remained equivalent under C_2 symmetry. The formyl resonance did not display a very large paramagnetic shift.

^{1}H coupled ^{13}C NMR spectra of this derivative (Fig.11) clearly displayed three pairs of >$\underline{C}$=O and -$\underline{C}H_3$ resonances, as expected for C_2 symmetry. The remaining resonances from the >$\underline{C}$-H, >$\underline{C}$-CHO and >C-$\underline{C}$HO nuclei could be assigned by inspection from the J_{CH} coupling patterns and integrated intensities and the assignments are listed below in Table I together with data for the corresponding Rh(III) analog. Unlike the ^{1}H NMR spectrum, the paramagnetic shifts of the ^{13}C methyl nuclei were relatively small. Therefore, the extremely large splitting of the >$\underline{C}$=O resonances was quite surprising. However, the large shifts observed at the 3-H-$\underline{C}<$ and 3-formyl-$\underline{C}<$ positions were to be expected from previous studies of [Ru(acac)$_3$]. As observed in the ^{1}H spectrum, there was only a small paramagnetic shift at the -$\underline{C}$HO nucleus. This was also surprising since the formyl group is attached to a carbon nucleus with a large paramagnetic shift. Although formally in conjugation with the acac$^-$ ring, the small ^{1}H and ^{13}C shifts indicate that this may not be so in the complex.

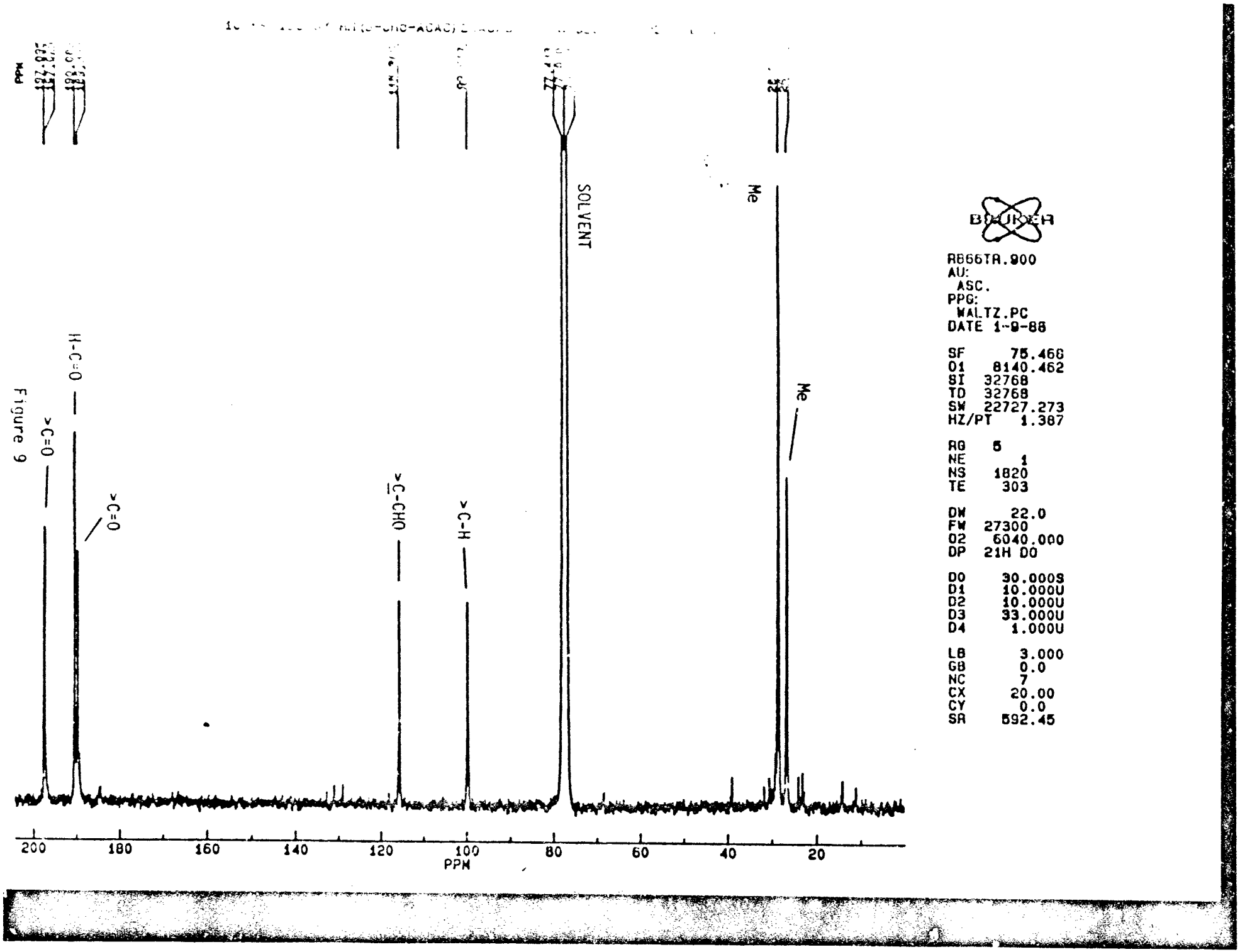

PPM
SOLVENT
Me
Me
O=C<
H-C=O
O=C<
OHC-C<
H-C<
200
180
160
140
120
100
80
60
40
20
PPM
BRUKER
AB66TA.900
AU:
ASC.
PPG:
WALTZ.PC
DATE 1-9-88
SF 75.468
O1 8140.462
SI 32768
TD 32768
SW 22727.273
HZ/PT 1.387
RG 6
NE 1
NS 1820
TE 303
DW 22.0
FW 27300
O2 6040.000
DP 21H D0
D0 30.000S
D1 10.000U
D2 10.000U
D3 33.000U
D4 1.000U
LB 3.000
GB 0.0
NC 7
CX 20.00
CY 0.0
SR 592.45

Figure 9

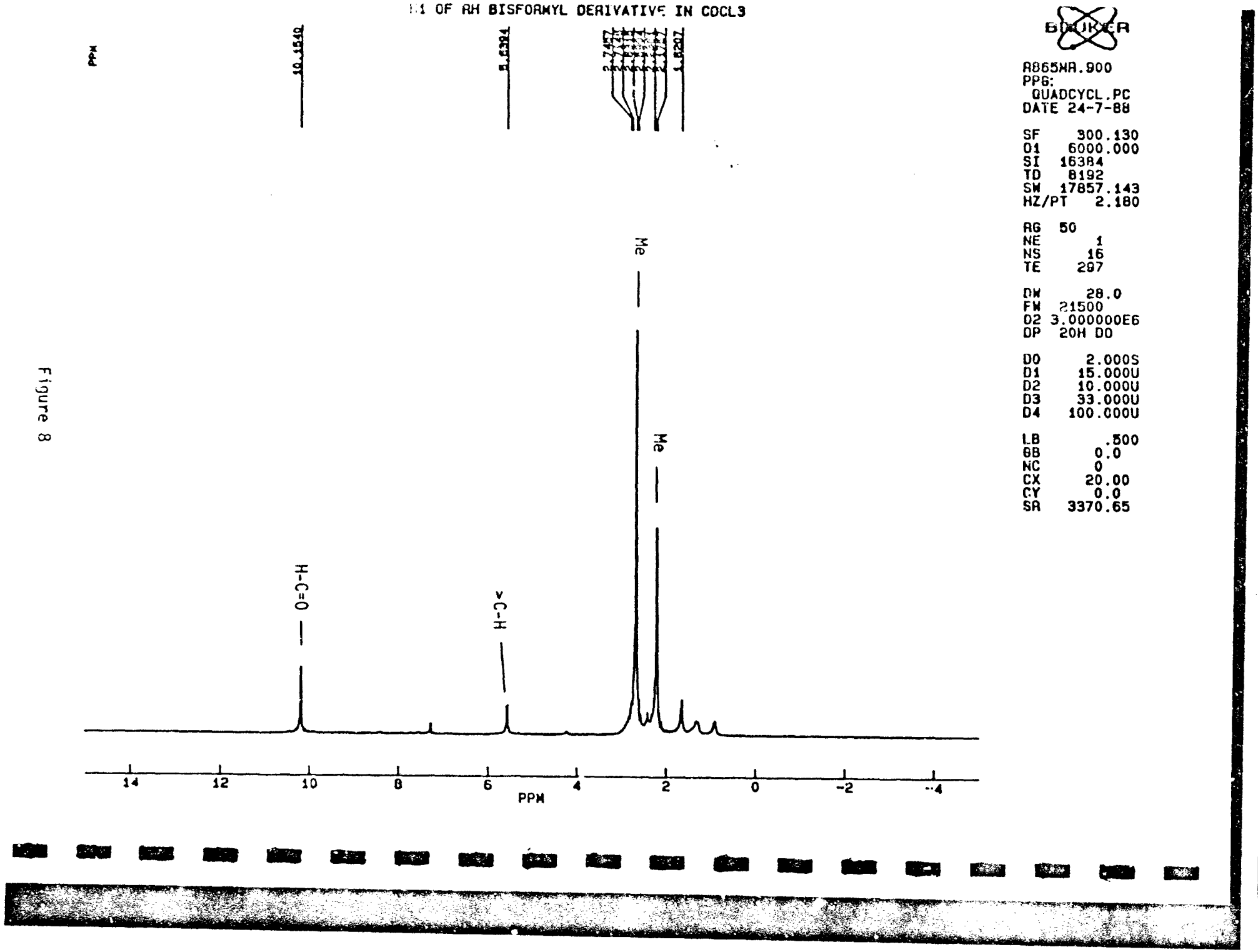

1:1 OF RH BISFORMYL DERIVATIVE IN COCL3
PPM
10.1540
5.6394
2.7457
1.8207
BRUKER
AM665MR.900
PPG:
QUADCYCL.PC
DATE 24-7-88
SF 300.130
O1 6000.000
SI 16384
TD 8192
SW 17857.143
HZ/PT 2.180
RG 50
NE 1
NS 16
TE 297
DW 28.0
FW 21500
D2 3.000000E6
DP 20H D0
D0 2.000S
D1 15.000U
D2 10.000U
D3 33.000U
D4 100.000U
LB .500
GB 0.0
NC 0
CX 20.00
CY 0.0
SR 3370.65
H-C=O
νC-H
Me
Me
14
12
10
8
6
4
2
0
-2
-4
PPM

Figure 8

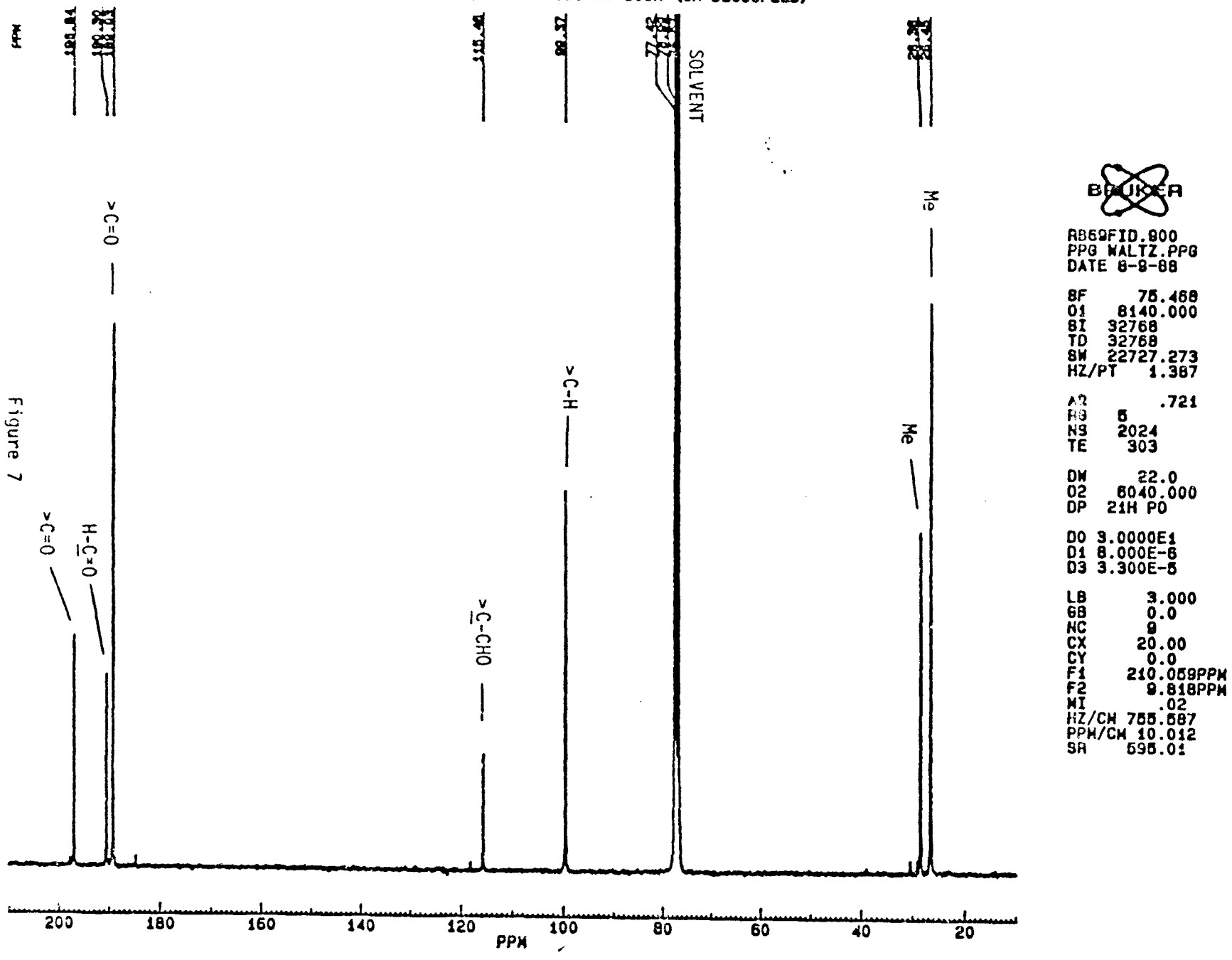

13C OF RH(3-CHO-ACAC)(ACAC)2 IN CDCL3 AT 303K (1H DECOUPLED)
PPM
SOLVENT
O=C<
H-C=O
H-C<
O=C<
OHC-C<
Me
Me
200
180
160
140
120
100
80
60
40
20
PPM
BRUKER
RB69FID.800
PPG WALTZ.PPG
DATE 8-9-88
SF 75.468
O1 8140.000
SI 32768
TD 32768
SW 22727.273
HZ/PT 1.387
AQ .721
RG 6
NS 2024
TE 303
DW 22.0
O2 6040.000
DP 21H PO
D0 3.0000E1
D1 8.000E-6
D3 3.300E-5
LB 3.000
GB 0.0
NC 9
CX 20.00
CY 0.0
F1 210.059PPM
F2 9.818PPM
MI .02
HZ/CM 755.687
PPM/CM 10.012
SR 595.01

Figure 7

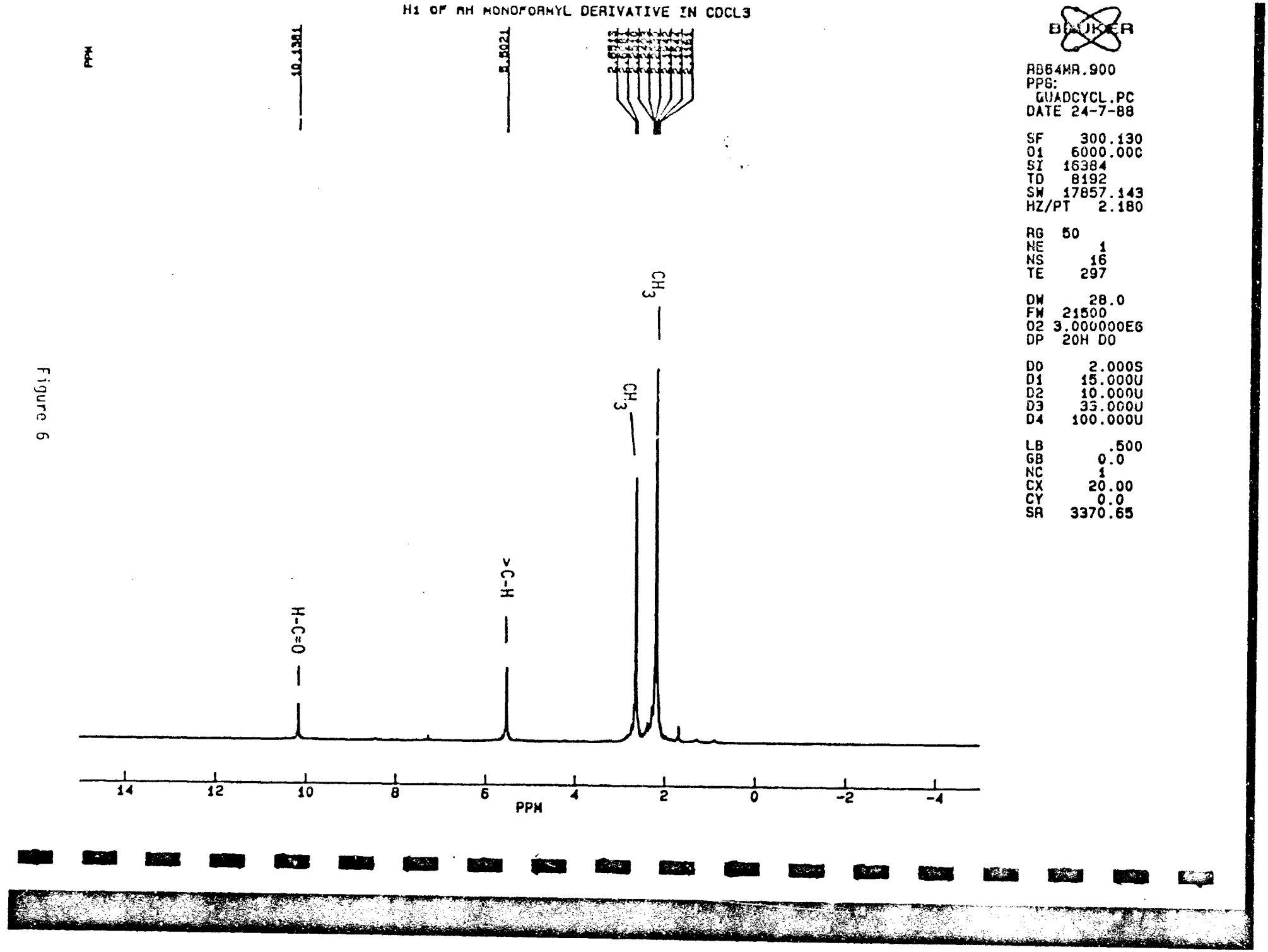

H1 OF AH MONOFORMYL DERIVATIVE IN CDCL3
PPM
10.1381
5.5021
BRUKER
RB64MR.900
PPG:
GUADCYCL.PC
DATE 24-7-88
SF 300.130
O1 6000.00C
SI 16384
TD 8192
SW 17857.143
HZ/PT 2.180
RG 50
NE 1
NS 16
TE 297
DW 28.0
FW 21500
O2 3.000000E6
DP 20H D0
D0 2.000S
D1 15.000U
D2 10.000U
D3 35.000U
D4 100.000U
LB .500
GB 0.0
NC 1
CX 20.00
CY 0.0
SR 3370.65
CH3
CH3
>C-H
H-C=O
14
12
10
8
6
4
2
0
-2
-4
PPM

Figure 6

SOLUTION KINETICS AND MECHANISMS

Part III

NMR Characterization Of The 3-Formyl Derivatives Of [$Ru(acac)_3$] And [$Rh(acac)_3$]

The 3-formyl derivatives of paramagnetic [$Ru(acac)_3$] were prepared for use in electron transfer studies involving a ligand bridged conduction pathway. The Rh(III) analogs were prepared principally as diamagnetic references to measure the paramagnetic shifts of ligand based ^1H and ^{13}C NMR resonances in the paramagnetic Ru(III) complexes. These shifts provide a means of assessing the nature of the low lying π molecular orbital system involved in the conduction of electrons across the ligand. Therefore, some effort was taken to study the paramagnetic shift differences between the Ru(III) and Rh(III) systems.

^1H And ^{13}C NMR Characterization Of [$Rh(3\text{-}CHO\text{-}acac)(acac)_2$]

The monoformylated derivative of [$Rh(acac)_3$] was obtained by chromatographic separation of a mixture of products from the Vilsmeier formylation reaction. TLC plates indicated that this material was pure and the ^1H NMR spectrum (Fig.6) confirmed this with the appearance of two distinct types of methyl peaks (+2.15,+2.61 ppm) as well as single methine (+5.50 ppm) and formyl (+10.14 ppm) resonances.

Owing to the long T_1 relaxation time of the ^{13}C nuclei in this diamagnetic complex, it was necessary to acquire ^{13}C NMR spectra using 30 second delay times between pulses. This procedure resulted in reasonably accurate intensity ratios in ^1H coupled spectra, though NOE enhancements were observed in ^1H decoupled spectra, particularly for the formyl resonance at 190.3 ppm (Fig.7). The sample appeared to be quite clean and there was no difficulty assigning the ^{13}C resonances which are listed below in Table I.

^1H And ^{13}C NMR Characterization Of [$Rh(3\text{-}CHO\text{-}acac)_2(acac)$]

The ^1H NMR spectrum of the diformylated complex (Fig.8) was essentially the same as for the monoformylated derivative above but with opposite intensity ratios for the two types of methyl resonances and with the formyl proton peak being about twice as intense as that for the single 3-$\underline{H}$-C< resonance. Aside from the H_2O and $CHCl_3$ in the deuterated solvent, there were also a few impurity peaks present in this spectrum. These are likely to be ligand

repurified on a separate column. Collman *et alia* had used alumina with a mixture of benzene/CH_2Cl_2 to separate the monoformylated derivative from $[Rh(acac)_3]$.[13] However, $CHCl_3$ seemed to be preferable for separating the two formylated species produced in the modified synthesis. Subsequent ^1H and ^{13}C NMR spectra of these products (*vide infra*) showed that they were the mono- and diformylated complexes, as expected. The samples have been characterized by UV-Visible spectroscopy as well but too little sample remained for elemental analyses.

practically identical but the third appeared to contain a significant amount of $[Rh(acac)_3]$.

Purification: The first two crops were combined and extracted into CH_2Cl_2 and the resulting yellow solution was decanted, leaving behind some oily droplets which were miscible with acetone but not with water. The extract was evaporated to dryness, producing a yellow foam. The procedure was repeated with a mixture of 20 mL of CH_2Cl_2 and 10 mL of hexane producing a fine crystalline material before complete evaporation. The remaining hexane was decanted from the flask and a further addition of 10 mL of hexane was used to wash the flask. The product was recrystallized from 10 mL of CH_2Cl_2 with addition of 10 mL of hexane and cooling in an ice bath. The golden colored material was collected by filtration as above and air dried. A second crop was obtained by concentration of the filtrate. The two samples gave the same UV-Visible spectrum but TLC plates indicated that there were three products in each.

Purification Of $[Rh(3-CHO-acac)(acac)_2]$ and $[Rh(3-CHO-acac)_2(acac)]$

Both samples were purified on silica gel with $CHCl_3$ as the eluant. A single mobile, yellow band was collected leaving behind a gold material at the top of the column and a small amount of another yellow species nearby. The latter was removed with $CHCl_3$ eluant and the gold material was washed off the column with MeOH eluant. The major product, from the first yellow band eluted, was obtained after evaporation to dryness, extraction into CH_2Cl_2, addition of hexane and further rotary evaporation. The minor, gold product obtained from the MeOH eluant was also evaporated to dryness followed by extraction with CH_2Cl_2 (gold solution) and then MeOH (yellow solution).

The major product was characterized by UV-Visible spectroscopy and subsequent ^1H NMR spectra revealed that there were resonances attributable to the formyl substituent. However, the ^{13}C NMR spectrum displayed more resonances than expected and their intensity ratios could not be interpreted in terms of either the monoformylated or diformylated derivatives of $[Rh(acac)_3]$ This was not altogether surprising since alumina TLC plates of the "single band" eluted from a silica gel/$CHCl_3$ column tended to suggest the presence of two species. The difficulty here was discerning any visible difference between the species and the starting material. All species are faintly yellow owing to the tail of a transition in the UV region. The alumina TLC plates were convincing *only* in the light of the NMR spectra.

Consequently, the major product was re-purified by column chromatography using alumina/$CHCl_3$. The first passage partly separated the two species and then each fraction was

Therefore, a Ruthenium analysis was performed using the new Perkin Elmer ICP Atomic Emission instrument at N.R.L. to check these findings. Only [$Ru(acac)_3$], for which plenty of sample was available, was analyzed. Two standard solutions were prepared from $RuCl_3.3H_2O$: one was simply dissolved in H_2O; a second was digested in 2 mL of conc. HNO_3 on a hot plate. The complex was similarly digested. Each sample was diluted with deionized water to ~10 ppm for analysis. The standard prepared without digestion measured ~6% lower than that in HNO_3. Therefore, there is a small matrix effect, even with the ICP technique. The resulting analysis of [$Ru(acac)_3$] *vs* $RuCl_3$ in HNO_3 was 24.93% (expected: 25.37). Given the uncertainty of $RuCl_3.3H_2O$ as a standard this was a good result. Thus, Schwarzkopf's high results were quite erroneous.

Preparation Of [$Rh(3\text{-}CHO\text{-}acac)(acac)_2$] and [$Rh(3\text{-}CHO\text{-}acac)_2(acac)$]

These species were previously reported by Collman *et alia* using the Vilsmeir formylation reaction for [$Rh(acac)_3$] in DMF solution.[13] However, even using a 9 fold excess of $POCl_3$:Rh the yield reported for a 105 min reaction at room temperature was only 7%, the remainder being the starting material. Such a poor yield would have been unacceptable here for obtaining sufficient sample for NMR spectroscopy since only a 1 gram sample of [$Rh(acac)_3$] was available. Furthermore, Dr. Binstead's experience of these reactions suggested that they were *kinetically* controlled so that longer reaction times would be more favorable than a large excess of $POCl_3$ reagent. Side reactions appear to be inevitable so that the crude products must be chromatographed in any case. Therefore, a synthesis was attempted with only a 2 fold excess of $POCl_3$ (as used for the Ru(III) case) but with a reaction time of about 18 hours to ensure more complete reaction and, hopefully, a better yield.

2:1 Preparation: 1 g (2.5 mmol) of 97% [$Rh(acac)_3$] (Aldrich) was dissolved in 15 mL of dry DMF (Aldrich, Sure Seal) with warming. The solution was cooled in an ice bath and stirred magnetically during dropwise addition of a solution of 0.47 mL (5 mmol) of $POCl_3$ in 10 mL of DMF. The reaction mixture was allowed to warm to room temperature and was stirred for 18 hours. The reaction was quenched by addition of 1.1 g of $NaHCO_3$ in ice water (175 mL total volume). This mixture was stirred for 6 hours before a fine precipitate began to form. The mixture was cooled overnight in a refrigerator before collection of the yellow product by filtration followed by washing with water. A second crop was obtained by rotary evaporation of the filtrate and addition of further water (50 mL) to the concentrated DMF solution. The procedure was repeated for a third, sticky crop. After air drying, UV-Visible spectra of the crude samples were obtained in ethanol solution and were compared with the spectrum of the starting material. These indicated that the first two crops were

the diformylated species was repurified on the same silica gel column using a constant 1% $MeOH/CH_2Cl_2$ eluant mixture. TLC plates of the resulting product showed no traces of the minor impurities.

4:1 Preparation: The mono- and diformylated products were separated as a single band from the remaining byproducts on a silica gel column using $CHCl_3$ eluant. Similarly, the 3-4 minor products were collected as a mixture and the brown material at the top of the column was removed using methanol eluant for further investigation. The mono- and diformylated products were separated on a fresh silica gel column using CH_2Cl_2 + (1% → 0.2%) MeOH graded eluant mixtures as described above. The minor products were separated in a similar fashion with a constant 1% $MeOH/CH_2Cl_2$ eluant and the final band was removed with 2% $MeOH/CH_2Cl_2$.

The purified samples of [Ru(3-CHO-acac)(acac)$_2$] and [Ru(3-CHO-acac)$_2$(acac)] were recovered as deep red solids by rotary evaporation from a 50:50 mixture of CH_2Cl_2/*n*-hexane. They were subsequently recrystallized from a 50:50 mixture of CH_2Cl_2/*n*-hexane by slow evaporation, then collected by filtration and washed with *n*-hexane. The samples were dried under high vacuum to remove traces of solvent.

Elemental analyses: Purified samples of [Ru(acac)$_3$], [Ru(3-CHO-acac)(acac)$_2$] and [Ru(3-CHO-acac)$_2$(acac)] produced quite satisfactory C and H analyses. However, Schwarzkopf Laboratories reported very high values for the metal analyses (30-35%) by Atomic Absorption even with a new standard solution and one prepared from $RuCl_3.3H_2O$.

Sample:	% Ru	% C	% H	% O
[Ru(acac)$_3$]				
(theory)	25.37	45.20	5.31	24.10
(found)	24.93	44.89	4.96	---
[Ru(3-CHO-acac)(acac)$_2$]				
(theory)	23.70	45.07	4.96	26.27
(found)	???	45.37	4.93	---
[Ru(3-CHO-acac)$_2$(acac)]				
(theory)	22.24	44.93	4.66	28.17
(found)	???	45.00	4.74	---

Assessment Of Purity: Silica gel TLC plates were used with $CHCl_3$ eluant (0.75% EtOH stabilizer) to ascertain the purity of the crude solid. These indicated that the sample contained mostly diformylated product (brown) and about 10–20% of the monoformylated complex (red). The sample also contained 3–4 *very* minor products (all brown) following the two formylated species and some deep brown decomposition products which did not elute. Therefore, chromatographic separation of the mono- and di-formylated species would most likely lead to a worthwhile amount of the diformylated complex, of which there was only a small amount recovered from the 2:1 scale preparation.

Purification Of [Ru(3-CHO-acac)(acac)$_2$] and [Ru(3-CHO-acac)$_2$(acac)]

Since commercial $CHCl_3$ (0.75% EtOH stabilizer) is ineffective at separation of the formylated derivatives, except at low loadings on high mesh TLC plates, CH_2Cl_2 (Aldrich HPLC) was used in combination with small amounts of methanol (Fisher ACS) on a silica gel column to control the elution rate and to effect improved separation.

2:1 Preparation: The crude product from the formylation reaction was purified by chromatography on silica gel (Aldrich 70–230 mesh) on a 35 cm x 5 cm (i.d.) column using $CHCl_3$ (Fisher ACS) as the eluant. This separated a very small amount of [Ru(acac)$_3$] before the major product band (deep red) which was followed by a number of faint impurity bands and a small amount of brown residue on the top of the column. The resulting deep red band was collected, taken to dryness by rotary evaporation and spot tested on silica gel TLC plates (Baker) for purity using $CHCl_3$ eluant. The product contained both the mono- and diformylated species.

The formylated derivatives were separated on another silica gel column prepared in a mixture of 1% MeOH/CH_2Cl_2. Half of the formylated product was loaded in 0.5% MeOH/CH_2Cl_2 and eluted with this solvent mixture until half way down the column. The eluting strength was gradually reduced to 0.1% MeOH by the time the first, red product (monoformylated derivative) had reached the end of the column. The solvent gradient continued to elute the first red product while the second, brown product (diformylated derivative) became increasingly well retarded. After washing the red product from the column the second band was removed using 2% MeOH/CH_2Cl_2. This resulted in recombination of two faint impurity bands with the brown product. The two separated products were evaporated to dryness and spot tested using TLC plates as above. The red, monoformylated product was *very pure*, while the diformylated product showed the presence of the expected impurity bands washed with it from the column and a tiny amount of monoformylated product. Therefore,

becomes progressively deactivated towards electrophilic attack with the addition of each formyl substituent. Such conditions lead, instead, to total destruction of the complex, probably as a result of acid hydrolysis.

2:1 Preparation: 2 g (5mmol) of [$Ru(acac)_3$] (Aldrich 97%) was dissolved in 25 mL of dry *N,N'*-Dimethylformamide (Aldrich, Sure-Seal) and then cooled in an ice bath. The cold [$Ru(acac)_3$] solution was added dropwise with stirring to a solution of 1.0 mL of $POCl_3$ (10 mmol) in 10 mL of DMF, which was kept cold in an ice bath. The mixture was then allowed to warm to room temperature and was stirred for 6 hours. The reaction was quenched with the addition of 2.12 g of $NaHCO_3$ in a deionized ice water slurry (~150 mL H_2O). The mixture was stirred overnight and then cooled in an ice bath. The resulting product was filtered off and a second crop was obtained by concentration (rotary evaporation) and addition of more deionized water. Both crops were washed with water, air dried and then extracted into $CHCl_3$, filtered to remove inorganic impurities and the deep red filtrate was evaporated to dryness by rotary evaporation. The aqueous residue was evaporated to near dryness and extracted with $CHCl_3$ to obtain a third, impure crop which was discarded. The remaining sticky, brown residue did not contain any further useful product.

Assessment Of Purity: Silica gel TLC plates (Baker) were used with $CHCl_3$ eluant to ascertain the purity of the samples. These indicated that the first two crops contained mostly the monoformylated product and about 20% of the diformylated complex. Otherwise the samples were quite clean and no evidence was found for the starting complex. Therefore, chromatographic separation of the mono- and di-formylated species would most likely lead to two pure species from this preparation.

4:1 Preparation: 2 g (5mmol) of [$Ru(acac)_3$] (Aldrich 97%) was dissolved in 30 mL of dry *N,N'*-Dimethylformamide (Aldrich, Sure-Seal) and then cooled in an ice bath. The cold $Ru(acac)_3$ solution was added dropwise with stirring to a solution of 1.9 mL of $POCl_3$ (~20 mmol) in 20 mL of DMF, which was kept cold in an ice bath. The mixture was then allowed to warm to room temperature and was stirred for about 6 hours. The reaction was quenched with the addition of 4.03 g of $NaHCO_3$ in a deionized ice water slurry (~200 mL H_2O). The mixture was stirred overnight and then cooled in an ice bath. No initial product was obtained so the reaction mixture was concentrated (rotary evaporation), extracted into $CHCl_3$ and filtered through Cellite to remove some oily byproduct. The deep red filtrate was evaporated to near dryness (some DMF remained) and a crude solid was obtained by extraction into CH_2Cl_2 and addition of excess *n*-hexane (Aldrich, Sure-Seal). The solid was collected, washed with *n*-hexane and air dried.

SOLUTION KINETICS AND MECHANISMS

Part II

Preparation and Purification Of The 3-Formyl Derivatives Of [Ru(acac)$_3$] And [Rh(acac)$_3$]

The formylation of [M(acac)$_3$] complexes is commonly undertaken using the Vilsmeier reaction.[13] This scheme uses the DMF solvent as a reagent with $POCl_3$ to produce a reactive intermediate,[14]

$$POCl_3 + DMF \rightarrow [(Me)_2\text{-}CH\text{-}Cl]^+[PO_2Cl_2]^-$$

which then performs an electrophilic attack,

$$M(acac)_3 + [\ \ldots\ ] \rightarrow (3\text{-}X\text{-}acac)_nM(acac)_{3-n}$$

producing the complexed intermediate,

X = 3-(Me)$_2$-CHCl

M = Ru

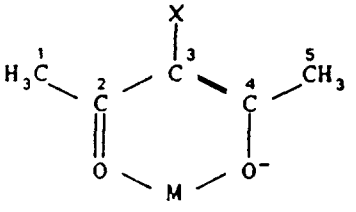


Figure 5

The intermediate can be hydrolysed to the formylated product with the addition of H_2O and stoichiometric $NaHCO_3$ to neutralize the acid so formed, an important consideration given the acid lability of the ligands.

Preparation Of [Ru(3-CHO-acac)(acac)$_2$] and [Ru(3-CHO-acac)$_2$(acac)]

The Vilsmeier formylation reaction was found to be quite effective at derivatizing one acac$^-$ ligand of [Ru(acac)$_3$] but even this required an excess of $POCl_3$ for completion. Typically, the monoformylated derivative required a 2:1 ratio of $POCl_3$:complex though this also produced ~20% of the diformylated derivative as well. In order to produce mostly the diformylated product a 4:1 ratio was required. Even large excesses of $POCl_3$ and long reaction times failed to produce any of the triformylated product and it appears that the complex

2-acetyl-1,3-btdn$^-$

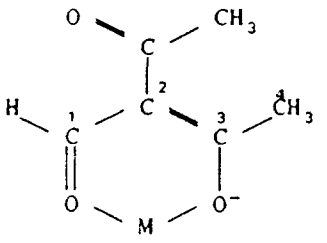


Figure 4

The previous studies on the rates of electron transfer between Ti(III) ion and [Ru(acac)$_2$(3-CHO-acac)] are presumed to be incorrect due to gross impurities in the samples of the Ru(III) complexes. This preliminary reinvestigation has shown that the 3-formyl substituted ligand acts as an excellent electronic conductor. Not only does the monoformyl complex react ~2600 times faster than [Ru(acac)$_3$] with Ti(III) ion but once reduced to the Ru(II) oxidation state it reacts with O_2 quite rapidly and then, of course, consumes further of the excess Ti(III) reductant. The previous workers do not appear to have taken precautions to exclude oxygen from their measurements.

Summary Of The Kinetic Behaviour Of [Ru(acac)$_2$(3-CHO-acac)]

The previous workers observed two exponential decay curves in the reaction of Ti(III) ion with [Ru(acac)$_2$(3-CHO-acac)]. The second, slower reaction appeared to be independent of both [Ti(III)] and [H$^+$]. These workers assumed that the second decay curve could only be ascribed to a scheme where the initial decay produced a bridged intermediate, [Ti^{III}-(ligand)-Ru^{III}], followed by a slower, first order decay with slow electron transfer across the bridging ligand to produce the Ti^{IV}/Ru^{II} redox products.

An alternative explanation for the previous observations can be made based on initial formation of the final [Ru^{II}(3-CHO-acac)(acac)$_2$]$^-$ product followed by a reaction with other Ru(III) contaminant species which do not react as rapidly with Ti(III) by themselves. In this scheme the monoformylated complex would act as a catalyst for the oxidation of the contaminant Ru(III) species by Ti(III) ion. Since they did not vary the initial concentration of the Ru(III) oxidant, such a following reaction would then appear to have a constant observed rate. This explanation could be tested by kinetics measurements with the deliberate addition of suspected Ru(III) contaminants. Finally, this work has demonstrated that the literature precedent for "slow electron transfer" across the 3-formylacac$^-$ bridging ligand is false. A reinvestigation of the kinetics of this reaction will be combined with the ^{1}H and ^{13}C NMR spectroscopy to characterize the electronic conduction pathway across the 3-formylacac$^-$ ligand.

Subsequently, Dr. Robert Binstead (Geo–Centers) was assigned the task of completing this work. During the course of following the previous synthetic procedures, Dr. Binstead discovered that there were a variety of species formed both in the preparation of $[Ru(acac)_3]$ and in the Vilsmeier formylation of $[Ru(acac)_3]$. Most of these impurities could not be removed by the recrystallization methods used in the previous work since they all have very similar solubility properties to the desired products. Indeed, the complexes were quite difficult to purify even by chromatography and required very high ratios of adsorbent:complex mixture for adequate separation with the best eluant choices. The purification procedures required a great deal of time before sufficient sample was available for further work. The purified Ru(III) complexes $[Ru(acac)_3]$, $[Ru(acac)_2(3\text{–}CHO\text{–}acac)]$ and $[Ru(acac)(3\text{–}CHO\text{–}acac)_2]$ were characterized by ^1H and ^{13}C NMR spectroscopies and were of known purity.

While Dr. Berrie did attempt to purify her final 3-formyl product on a silica gel column she used methanol as the eluant which has been shown to result in elution of all species in a single band from the column. Thus, there was effectively no purification of the product. Dr. Binstead's reinvestigation of the kinetics of the reaction between Ti(III) ion and *purified* $[Ru(acac)_2(3\text{–}CHO\text{–}acac)]$ under similar conditions to those used by Berrie and Early revealed NO EVIDENCE OF ANY INTERMEDIATE. The kinetics were clean, displaying a single exponential increase in absorbance at 440 nm corresponding to formation of the Ru(II) product. Under the conditions used { T = 25.5°C, $[Ti(III)] \sim 0.0125$ M, $[H^+] \sim 0.075$ M, I = 1.0 M (NaCl–HCl) } the pseudo-first order rate constant was found to be $k_{obsd} \sim 80\ s^{-1}$ which is about 25% faster than observed by Dr. Berrie for her first decay curve. There was no sign of a subsequent 20 s^{-1} decay. Similar results were obtained at 510 nm. As expected, there were very slow, following absorbance changes due to the rise in turbidity from Ti(IV) polyhydroxo species and the decomposition of $[Ru^{II}(acac)_3]^-$.

Measurements were also made using a 3 month old solution of the monoformylated complex. Interestingly, although the kinetics traces were clean, single exponential decays, the observed rate was slower, $k_{obsd} \sim 40\ s^{-1}$. This result is consistent with the observation of subtle changes in the UV-Visible spectrum of this solution which could be interpreted in terms of a slow isomerization reaction to the thermodynamically favored isomer 2-acetyl-butane-1,3-dionato complex (Fig.4).[10] Thus, the time dependence of the kinetics should be studied over the first few days after dissolution of the 3-formylacac complex to determine the rate constant at zero time since it takes about a day to dissolve $[Ru(3\text{-}CHO\text{-}acac)(acac)_2]$ in aqueous media at 1×10^{-4} M.

the substrate and Ti^{3+} by looking for Deuterium isotope effects on the rate. Comparisons can be drawn from previously published work on *proton coupled electron transfer*.[9]

It should be noted that Early *et alia* had previously found a good linear free energy relationship for reactions between $Ti-OH^{2+}$ and Ru(III) oxidants of the type $[Ru(NH_3)_5(L)]^{n+}$ where L = NH_3, py, Cl^- and OH_2 , none of which can act as a H^+ acceptor in reactions with Ti^{3+} ion. Therefore, it is not surprising that none of these yielded a measurable contribution from a pathway involving Ti^{3+} ion. The $[Ru(acac)_3]$ complex should be considered an extraordinary oxidant being capable of mediating electron and proton transfer with the Ti^{3+} ion as well as normal outer-sphere electron transfer with the $Ti-OH^{2+}$ oxidant. The mechanisms of these reactions are clearly far more complex than envisaged by Early and coworkers and deserve further study.

Kinetic Data For The Reaction Between Ti(III) and $[Ru^{III}(acac)_2(3-CHO-acac)]$

The kinetics of the electron transfer reaction between Ti(III) ion and the monoformylated derivative, $[Ru(3-CHO-acac)(acac)_2]$, were first reported by Berrie and Farly.[2,3]

L = 3-CHO-acac$^-$

M = Ru(III)

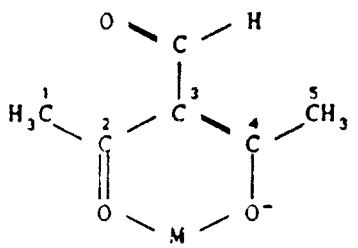


Figure 3

These authors claimed to observe two exponential decays during the reaction, the faster one being dependent on [Ti(III)] and [H^+] while the slower decay (20 s^{-1}) was independent of initial concentrations and appeared to correspond to slow, intramolecular electron transfer within a bridged intermediate formed in the initial, faster decay. This would indeed have been an extraordinary observation since it was out of line with previous measurements of the rates of electron transfer between Ti(III) and Ru(III) complexes via inner-sphere mechanisms.[11,12] Dr. Barbara Berrie studied a similar reaction at N.R.L. where the 3-CHO moiety was further oxidized to the carboxylate group with Tollen's reagent. In this case the same type of behaviour was observed but with a slower decay of the intermediate (~1 s^{-1}). In collaboration with Dr. Robert Kessler, attempts were made to characterize this intermediate using resonance Raman spectroscopy but their work was unsuccessful.

dependence with K_a = 4x10^{-3} for Ti-OH_2^{3+} ⟷ Ti-OH^{2+} + H^+. Clearly, the Table heading referred to reaction (A) while the values for reaction (B) were their raw evaluations of k_{obsd} (s^{-1}). However, these values would then yield second order rate constants of 0.8 M^{-1} s^{-1} and 7 M^{-1} s^{-1}, respectively, somewhat negating the match of the rate constants with a previous linear free energy relationship of log k *vs* ΔG° (V) for $[Ru(NH_3)_5(L)]^{n+}$ type oxidants.[7]

Secondly, even these corrected values could not be reproduced in this laboratory under similar conditions {T=25°C, I=1.0 M (NaCl-HCl), 0.2 mM $[Ru(acac)_3]$, $[Ti(III)]$ ~ 0.0125 M, $[H^+]$ ~ 0.075 M and ~ 0.025 M}. The pseudo-first order rate constants obtained under these conditions were ~0.03 s^{-1} at $[H^+]$ ~ 0.075 M and ~0.15 s^{-1} at $[H^+]$ ~ 0.025 M. After correction for the difference in $[Ti(III)]$ these results are faster by a factor of ~2.3026 ($\log_e 10$). This arose, presumably, from the previous authors' penchant for graphical fits on $\log_{10}$-linear graph paper! The stopped-flow data acquisition program of Dr.J.C.Cooper does, however, evaluate the rate constants correctly. Thus, the second order rate constants are < 2.4 M^{-1} s^{-1} for Ti^{3+} and >12 M^{-1} s^{-1} for Ti-OH^{2+}. The previous authors really wanted the latter value to be ~1 M^{-1} s^{-1} since this was the value they calculated from their previous linear free energy relationship.[7]

The approximation signs on the redetermined rate constants above arise from (a) lack of exact calibration of the Ti(III) concentration (a temporary matter) and (b) in the case of the high acid runs the A_∞ values are subject to error from the following, apparently zero-order decomposition of the Ru(II) product monitored during the reaction (Note: only a tiny fraction of the following reaction was monitored and if followed to completion it would probably appear as a first order exponential decay). In this case, the apparent pseudo-first order rate constants vary with wavelength somewhat (0.026 - 0.034 s^{-1}) being slower where the A_∞ drift is in the same direction as the decay curve and faster where the drift opposes the decay curve. This could be remedied by studies at higher $[Ti(III)]$, to make the redox reaction faster, or through fitting the data to a better model to take into account the following product loss. The low acid runs were not affected by the slow product loss since the rate was 5 times faster than at 0.075 M H^+. These measurements were made both in air saturated and argon bubbled solutions and with both a fresh and 3 month old solutions of $[Ru(acac)_3]$. No differences were observed among these combinations.

In summary, the kinetics of the cross reaction between $[Ru(acac)_3]$ and Ti(III) ion are clean and with a little more work a full pH dependence of the kinetics and electrochemistry could be presented to correct the literature values. In particular, the appearance of a reaction pathway involving Ti^{3+} ought to be studied to determine whether H^+ transfer occurs between

The overall reaction scheme is given by:

pH<2.4

$$Ti^{III}\text{–}OH_2^{3+} + Ru^{III}(acac)_3 \longrightarrow \left\{ \begin{array}{l} Ti^{IV}(O)^{2+} + 2H^+ \\ Ti^{IV}(OH)^{3+} + H^+ \\ Ti^{IV}(OH)_2^{2+} + 2H^+ \end{array} \right\} + Ru^{II}(acac)_3^-$$

An initial outer–sphere electron transfer would produce $Ti^{IV}\text{–}OH_2^{4+}$ which is strongly disfavored even even in highly acidic media. This produces an additional free energy barrier, ΔG_{acid}, for electron transfer which depends on the pH and the pK_a's of the Ti(IV) product. The previous kinetic measurements of Early *et alia* did not extend below pH 1 but there is some suggestion in their data that the rate will fall off further in the range pH<1 so that the kinetic model used by these authors is not strictly correct.[1] A plot of k_{obsd} *vs* pH from the previous work displayed rather imprecise measurements and their limiting rates for the Ti^{3+} and $TiOH^{2+}$ reductants are somewhat unreliable.

The conjugate base $Ti\text{–}OH^{2+}$ has far lower H^+ restrictions on an outer–sphere electron transfer step which should be consequently more rapid than through the Ti^{3+} ion. Rates of cross reactions for $Ti\text{–}OH^{2+}$ follow the Marcus–Hush relationship with a variety of Ru(III) oxidants indicating that this species is "normal" in the free energy sense.[7,8] These include $[Ru(NH_3)_6^{3+}]$, $[Ru(NH_3)_5(py)]^{3+}$, $[Ru(NH_3)_5(H_2O)]^{3+}$ and $[Ru(NH_3)_5(Cl)]^{2+}$. The reason for the well behaved nature of the $Ti\text{–}OH^{2+}$ reductant can be appreciated from the following reaction scheme:

pH>2.4

$$Ti^{III}\text{–}OH^{2+} + Ru^{III}(acac)_3 \longrightarrow \left\{ \begin{array}{l} Ti^{IV}{=}O^{2+} + H^+ \\ Ti^{IV}\text{–}OH^{3+} \\ Ti^{IV}(OH)_2^{2+} + H^+ \end{array} \right\} + Ru^{II}(acac)_3^-$$

Above pH 2.4, where $Ti\text{–}OH^{2+}$ predominates, there would be no *net change* in H^+ composition between reactants and products if Ti(IV) exists as the $Ti\text{–}OH^{3+}$ species (*or this species is not highly disfavoured at least*) resulting in a "normal" outer–sphere electron transfer reaction. Inverse acid dependence would be expected in the region of the pK_a since Ti^{3+} ion would necessarily react more slowly than $Ti\text{–}OH^{2+}$ in an outer–sphere mechanism.

The previous workers presented a table of pseudo–first order rate constants for two reactions with (B) corresponding to the reaction of $[Ru(acac)_3]$ (0.2 mM) with Ti(III) in LiCl–HCl (I=1.0 M, T=25°C) where $[Ti(III)]$ = 0.010 M and $[H^+]$ = 0.004 – 0.080 M.[1] The Table headings list the rate constants as $10^2 k_{obsd}$ (s^{-1}) with numeric values of 0.054 – 0.0096. First, such slow values of k_{obsd} would give second order rate constants in the range 0.054 – 0.0096 M^{-1} s^{-1} while these authors report limiting rate constants of 0.08 M^{-1} s^{-1} (for Ti^{3+}) and 0.7 M^{-1} s^{-1} (for $Ti\text{–}OH^{2+}$), evaluated from a linearized plot for the inverse acid

The "blue" Ti(III) species was able to be prepared in this laboratory bv dissolution of TiH_2 in concentrated HCl under rigorously purged conditions. The color began to turn mauve overnight and after exposure to the atmosphere the color became violet within a few hours. It remains to be established whether the blue species is $TiCl_3$ or some other complex and whether it can be prepared in more dilute HCl media. The speciation of Ti(III) in HCl media is clearly of importance for the kinetic studies with Ru(III) complexes.

Kinetic Data For The Cross Reaction Between Ti(III) Ion And $[Ru^{III}(acac)_3]$

Only a few examples have been reported where Ti^{3+} ion reacts with an outer-sphere oxidant at a measurable rate rather than via initial deprotonation to $Ti\text{-}OH^{2+}$. Most often the H^+ restrictions on the outer-sphere pathway give rise to an infinitesmal rate via Ti^{3+} ion. Those species where a pH independent Ti^{3+} pathway is observed include $[Ru(acac)_3]$. Ti(III) solutions react with $[Ru(acac)_3]$ in HCl media at relatively modest rates and display the expected inverse acid concentration dependence implying that $Ti\text{-}OH^{2+}$ is the effective reductant. However, unlike most outer-sphere reactions with Ru(III) oxidants a slower, "acid independent" pathway involving the Ti^{3+} ion has been reported in kinetic studies by Early *et alia*.[1]

$[Ti(H_2O)_6]^{3+}$ reacts with $[Ru(acac)_3]$ via what *appears to be* an outer-sphere electron transfer pathway owing to the substitution inertness of the Ru(III) complex. However, the actual mechanism may well be more complex, involving H^+ as well as electron transfer steps between Ti^{3+} and the substrate. While $[Ru(acac)_3]$ is kinetically inert to ligand substitution the measured rate constants are not particularly high and there may be the possibility of associative keto-enol isomerization during reaction assisting the necessary removal of a H^+ from Ti^{3+} in the redox step.

Another possibility involves H^+ transfer at the 3-C position of the $acac^-$ ring from Ti^{3+} ion in the associative step prior to electron transfer or concommitant with electron transfer. NMR studies of $[Co(acac)_3]$ in acidic D_2O have demonstrated rapid exchange of the methine proton ascribed to the equilibrium:[6]

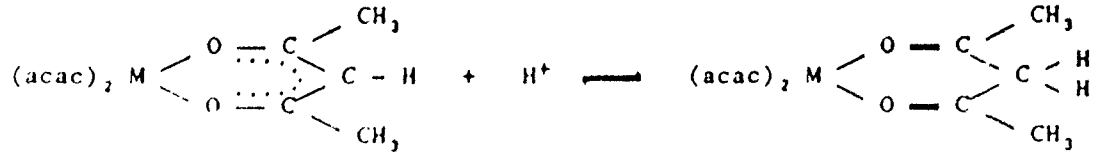


Figure 2

inner-sphere oxidants atom transfer steps provide alternate reaction pathways. Oxidation of Ti(III) at an electrode surface also presumably occurs via $Ti-OH^{2+}$ so that accurate $E_{\frac{1}{2}}$ measurements must rely on rapid equilibration of the H^+ transfer steps before and after electron transfer. This may not always be achieved even in the slow polarographic experiment. It is important to note that dilution of 5 mL of Ti(III) solution in 3 M HCl (15 mmol H^+) into a 0.1 M NaOH solution (10 mmol OH^-) produces a slow color change from mauve to brown followed by a slower return to mauve, as dictated by the final $[H^+]$. Clearly, the electrochemistry of the Ti(IV)/(III) couple needs to be reinvestigated using fast sweep cyclic voltammetry to ascertain whether these redox potentials include a kinetic overpotential term.

The Speciation of Ti(III) In Acidic, Aqueous Media

The UV-Visible spectrum normally associated with violet colored solutions of Ti^{3+} ion in HCl media consists of a slightly split band with $\lambda_{max} \sim 500$ nm ($\epsilon \sim 5\ M^{-1}\ cm^{-1}$) and has been ascribed to the $[Ti(OH_2)_6]^{3+}$ species in such vaunted texts as Cotton & Wilkinson's "Advanced Inorganic Chemistry", where it is used to illustrate the Jahn-Teller splitting of the first d-d transition for this d^1 ion. In an early review article of Intervalence Transfer spectroscopy, Allen and Hush have summarized the known dimerization chemistry for Ti(III)/Ti(IV) mixtures formed by partial oxidation of Ti^{3+} solutions in 11.65 M HCl media.[5] Allen and Hush reported an association constant of 11.7 M^{-1} in 11.65 M HCl for dimerization to form a mixed-valence Ti(III)-Ti(IV) ion. The spectrum of the dimer was rather similar to that reported by Cotton & Wilkinson for $[Ti(OH_2)_6]^{3+}$, though the extinction coefficient of the fully formed dimer was much higher, $\epsilon \sim 90\ M^{-1}\ cm^{-1}$. Furthermore, they reported the spectrum of a blue colored "$TiCl_3$" species having $\lambda_{max} \sim 600$ nm ($\epsilon \sim 5\ M^{-1}\ cm^{-1}$). Thus, it appears that the violet color associated with Ti(III) ion could be due to a mixed-valence ion impurity which absorbs more intensely (~20 fold) than the Ti(III) ion.

It is useful to compare these spectra with those obtained in this laboratory for samples prepared by dissolution of TiH_2 in 3 M HCl under a blanket of argon. This concentrated, violet colored sample, ~0.5 M in 3 M HCl, appeared to have very little of the intense UV absorption attributed to Ti(IV) species, while the visible transition ($\lambda_{max} \sim 500$ nm) appeared similar to the "dimer" spectrum reported by Allen and Hush. On dilution with H_2O the spectrum of this sample was more obviously split but still there was little UV evidence of Ti(IV) being present. This may be due to the speciation of the Ti(IV) oxidation state as a function of $[Cl^-]$. However, it is also likely that the Ti(III) state will exhibit a rich speciation chemistry among various chloro aqua complexes which no doubt would contribute to splitting of the visible absorption band.

Mechanistic Aspects Of Redox Reactions Involving The Ti(III)/Ti(IV) Couple

Solutions of Ti(III) ion at low concentration in HCl media exist principally as the monomeric $[Ti(OH_2)_6]^{3+}$ and $[Ti(OH_2)_5(OH)]^{2+}$ species ($Ti^{3+} \rightleftharpoons TiOH^{2+}$, $K_a \sim 5x10^{-3}$ M) though chloro aqua complexes are probably present also. These Ti(III) species act as both outer-sphere and inner-sphere reductants depending on nature of the oxidant. Where the oxidant contains no ligands capable of acting as an inner-sphere bridge to Ti(III), outer-sphere electron transfer occurs via the $TiOH^{2+}$ species. In basic media Ti(III) appears to exist as polyhydroxo species that are not well characterized. Ti(III) solutions react with O_2 and other oxidants to produce one of a variety of Ti(IV) species including TiO^{2+}, $Ti(O)(OH)^{+}$ and $Ti(OH)_2^{2+}$ and possibly chloro aqua complexes also.

$[Ti(OH_2)_6]^{3+}$ is relatively stable towards reaction with O_2 in 3 M HCl solution owing to large kinetic barriers for outer-sphere electron transfer imposed by changes in the proton composition for the half-reactions,

$$[Ti^{III}(OH_2)_6]^{3+} - e^- \longrightarrow \begin{cases} [Ti^{IV}(OH_2)_5(OH)]^{3+} + H^+ \\ [Ti^{IV}(OH_2)_5(O)]^{2+} + 2H^+ \\ [Ti^{IV}(OH_2)_4(OH)_2]^{2+} + 2H^+ \\ [Ti^{IV}(OH_2)_4(OH)(O)]^{+} + 3H^+ \end{cases}$$

Polarographic electrochemical studies in 1 M Cl^- media by Lee and Early have provided support for the formulation of the Ti(IV) ion as a doubly deprotonated species.[4] The pH dependence of the Ti(IV)/(III) redox couple displays a slope of -120 mV/pH below pH 1 and -60 mV/pH in the pH range 1 to 1.6, consistent with a doubly deprotonated Ti(IV) species in highly acidic media. The apparent change in slope near pH 1 implies that $Ti\text{-}OH^{2+}$ is the dominant form of Ti(III) reacting at the electrode surface for pH>1. Since independent measurements of the pK_a of Ti(III) give values of ~2.4 the electrochemical data appear to be contradictory. Direct reaction of Ti^{3+} with an electrode or an outer-sphere oxidant to form Ti^{4+},

$$[Ti(OH_2)_6]^{3+} \xrightarrow{\text{Outer-Sphere}} [Ti(OH_2)_6]^{4+} + e^-$$

is highly energetically disfavored. Any pathway involving one-electron transfer with Ti(III) would result in an initial outer-sphere Ti(IV) species with the proton composition of the Ti(III) ion so that it is energetically more favorable to deprotonate Ti(III) prior to electron transfer. Thus, most kinetic studies involving Ti(III) with *purely* outer-sphere oxidants show an inverse $[H^+]$ dependence with no detectable reaction via the Ti^{3+} pathway. With O_2 and

L = acac$^-$

M = Ru(III)

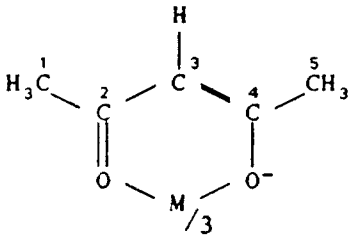


Figure 1

One particularly interesting redox partner is the Ti(III) ion which was studied previously by Early, Bose and Berrie.[1] In aqueous, acid solutions this ion exists principally as a mixture of the hexaaqua complex $[Ti(OH_2)_6]^{3+}$ and its conjugate base $[Ti(OH_2)_5(OH)]^{2+}$. Aqueous HCl solutions of Ti(III) are air oxidized to a polymeric Ti(IV) species only slowly but they are oxidized much more rapidly by many Ru(III) complexes, including $[Ru(acac)_3]$. As expected from previous studies, Early *et alia* observed that $[Ru(acac)_3]$ reacted predominantly with the $Ti(OH)^{2+}$ ion rather than Ti^{3+}. Similar studies by Early and Berrie of the reaction between Ti(III) ion and the monoformylated derivative, $[Ru(acac)_2(3\text{-}CHO\text{-}acac)]$, showed remarkably increased rates of reaction even though the thermodynamic driving force was comparable to that for $[Ru(acac)_3]$.[2,3] However, they observed two exponential decays in their kinetics measurements and ascribed the slower one (20 s^{-1}) to *slow electron transfer across the bridging ligand*, implying the existence of a [Ti–ligand–Ru] intermediate.

Dr. Berrie continued studies on a modified form of this system at N.R.L. and collaborated with Dr. Kessler in trying to characterize the assumed intermediate by resonance Raman spectroscopy. Their lack of success prompted this reinvestigation of the kinetics and mechanism of the reaction between Ti(III) ion and $[Ru(acac)_2(3\text{-}CHO\text{-}acac)]$ by a Geo-Centers scientist in order to determine the rate of electron transfer across the bridging ligand. This study has revealed that the previous work was in error and that the electron transfer across the bridging ligand proceeds rapidly, as expected for a conjugated system. Details of the kinetics measurements and a number of related, fundamental mechanistic issues are presented below.

SOLUTION KINETICS AND MECHANISMS

Part I

Introduction

Electron transfer reactions are elementary, fundamental steps in many chemical processes of interest to the Navy. These include the catalytic reduction of CO_2 and other atmosphere-polluting molecules, the degradation of chemical warfare toxins, the corrosion and passivation of metal surfaces and the modification of surface oxides between metal-metal junctions to improve their electronic conductivity. In each of these processes the design of the chemical system is critical in determining the efficiency of the elementary, electron transfer steps. Funding has not been available for work on the reduction of CO_2 or the deactivation of chemical warfare toxins. Therefore, this report describes recent activities undertaken on some fundamental electron transfer reactions of metal acetylacetonate complexes and an application of electron transfer reactions to the suppression of intermodulation interference (IMI) caused by the poor electronic conductivity of surface oxides in metal-metal junctions.

Fundamental Studies Of Electron Transfer Reactions

A great body of research is available on the kinetics of electron transfer between metal-organic complexes in solution and there is continuing interest in the role of the organic ligand in controlling the rate of electron transfer between metal centers. The electronic conductivity of the organic ligand has an important influence on the kinetics of such redox reactions. Understanding the molecular parameters responsible for facilitating electron transfer between redox centers not only provides deeper insight into biological redox processes but also has importance to a number of device applications, including molecular conductors for IC fabrication and molecular diodes for photonic communications interfaces.

The fundamental studies carried out at N.R.L. in recent years have utilized derivatives of $[Ru^{III}(acac)_3]$, where $acac^-$ = acetylacetonate (or pentane-2,4-dionato) anion. Metal acetylacetonate complexes (Fig.1) are generally easy to prepare and are relatively stable. In the case of Ru(III), the complex can be oxidized or reduced in a facile fashion either electrochemically or using redox reagents. $[Ru(acac)_3]$ is amenable to study in a wide variety of solvents and can be derivatized via substitution reactions at the 3-H position of the ligand. Therefore, this complex provides a good platform for studying the influence of ligand modifications on the rates of electron transfer with a number of redox reagents.

FINAL REPORT

SOLUTION KINETICS AND MECHANISMS

Robert A. Binstead, Ph.D.
GEO-CENTERS, Inc.,
10903 Indian Head Highway,
Fort Washington, MD. 20744

APPENDIX F

```
      CALL AXIPOS(1,0.,390.,450.,1)
      CALL AXISCA(3,INT(XLABEL/XTIC)*NINTX,XMI,XMA,1)
      CALL AXIDRA(1,0,1)
      CALL AXIPOS(1,450.,0.,390.,2)
      CALL AXISCA(3,2*NINTY,YMI,YMA,2)
      CALL AXIDRA(-1,0,2)
      CALL AXIPOS(1,0.,0.,450.,1)
      CALL AXISCA(3,NINTX,XMI,XMA,1)
      CALL AXIDRA(1,1,1)
      CALL AXIPOS(1,0.,0.,390.,2)
      CALL AXISCA(3,NINTY,YMI,YMA,2)
      CALL AXIDRA(-1,-1,2)
      CALL GRAPOL(X,Y,N)
      CALL GRAPOL(X,V,N)
      CALL GRASYM(X(NVIC),Y(NVIC),1,2,0)
      CALL CHAMOD
      READ (5,13) DUMMY
   13 FORMAT (F6.3)
      CALL PICCLE
      CALL DEVEND
      CALL ALFA
      CALL LIB$WAIT(2.)
      RETURN
      END
```

```
C-  DRAW UPPER AND RIGHT LINES.
      CALL MOVTO2(0.,390.)
      CALL LINTO2(450.,390.)
      CALL MOVTO2(450.,0.)
      CALL LINTO2(450.,390.)
      CALL CHASIZ(8.,8.)
C-    DRAW AXES.
      XMI= XMIN
      XMA= XMAX
      YMI= YMIN
      YMA= YMAX
      XD= XMA-XMI
      YD= YMA-YMI
      IF (K .GT. 1) GO TO 7
      XLABEL= 500.
      YLABEL= .5
      XTIC= 100.
      GO TO 8
 7    IF (XD .GE. 1000.) XLABEL = 500.
      IF (XD .GE. 500. .AND. XD .LT. 1000.) XLABEL = 200.
      IF (XD .GE. 200. .AND. XD .LT. 500.) XLABEL = 100.
      IF (XD .GE. 100. .AND. XD .LT. 200.) XLABEL = 50.
      IF (XD .GE. 50. .AND. XD .LT. 100.) XLABEL = 20.
      IF (XD .LT. 50.) XLABEL = 10.
C
      IF (XD .GE. 1000.) XTIC = 100.
      IF (XD .GE. 500. .AND. XD .LT. 1000.) XTIC = 50.
      IF (XD .GE. 300. .AND. XD .LT. 500.) XTIC = 20.
      IF (XD .GE. 50. .AND. XD .LT. 300.) XTIC = 10.
      IF (XD .LT. 50.) XTIC = 5.
C
      IF (YD .GE. 2.) YLABEL = 1.
      IF (YD .GE. 1. .AND. YD .LT. 2.) YLABEL = 0.5
      IF (YD .GE. .5 .AND. YD .LT. 1.) YLABEL = 0.2
      IF (YD .GE. .1 .AND. YD .LT. .5) YLABEL = 0.1
      IF (YD .LT. .1) YLABEL = .02
 8    CALL AXIPOS(1,0.,0.,450.,1)
      XMOD= AMOD(XMIN,XLABEL)
      IF (XLABEL-XMOD .LT. 1E-6 .OR. XMOD .LT. 1E-6) GO TO 11
      NXL= XMIN/XLABEL
      XMI= NXL*XLABEL
      XD= XMA-XMI
 11   NINTX= XD/XLABEL
      IF (ABS(XD-NINTX*XLABEL) .LT. 1E-6) GO TO 9
      NINTX=NINTX+1
      XMA= XMI+NINTX*XLABEL
 9    CALL AXISCA(3,INT(XLABEL/XTIC)*NINTX,XMI,XMA,1)
      CALL AXIDRA(-1,0,1)
      CALL AXIPOS(1,0.,0.,390.,2)
      YMOD= AMOD(YMIN,YLABEL)
      IF (YLABEL-YMOD .LT. 1E-6 .OR. YMOD .LT. 1E-6) GO TO 12
      NYL= YMIN/YLABEL
      YMI= NYL*YLABEL
      YD= YMA-YMI
 12   NINTY= YD/YLABEL
      IF (ABS(YD-NINTY*YLABEL) .LT. 1E-6) GO TO 10
      NINTY=NINTY+1
      YMA= YMI+NINTY*YLABEL
 10   CALL AXISCA(3,2*NINTY,YMI,YMA,2)
      CALL AXIDRA(1,0,2)
```

```
      SUBROUTINE PLPRDG(NVIC)
C-----THIS PROGRAM IS DESIGNED TO PLOT THE TOTAL X-RAY ABSORPTION
C-----COEFFICIENT VS. THE ABSOLUTE X-RAY PHOTON ENERGY.
C
C     *****   EXECUTE PLTEV.FOR,SYS:DRAFT/LIB   *****
C
C-------------------------------------------  ----------------------
C     LATEST REVISION -- JANUARY 1, 1979
C
      DIMENSION EEV(20)
      COMMON /XMDAT/ NSEQ,NPTS,X(1400),Y(1400)
      COMMON /LAB/ LABEL
      COMMON /SQZ/ V(1000),Z(1000)
      CHARACTER LABEL*80,YN*3
C
      EVA = X(1)
      EVB = X(NPTS)
C
      YMIN = MIN(Y(1),V(1))
      YMAX = MAX(Y(1),V(1))
      DO 6 I=2,NPTS
      IF (Y(I).LT.YMIN) YMIN = Y(I)
      IF (V(I).LT.YMIN) YMIN = V(I)
      IF (Y(I).GT.YMAX) YMAX = Y(I)
      IF (V(I).GT.YMAX) YMAX = V(I)
   6  CONTINUE
C-----
      CALL PLOTPG (NPTS,X,Y,V,EVA,EVB,YMIN,YMAX,NVIC,LABEL,2)
C-----
      RETURN
      END
      SUBROUTINE PLOTPG (N,X,Y,V,XMIN,XMAX,YMIN,YMAX,NVIC,LABEL,K)
      REAL X(N),Y(N),V(N)
      CHARACTER LABEL*80,LABEX*82
      CHARACTER*14 TITLE,ITITLE,JTITLE,ATITLE(20),FTITLE
      COMMON /FNAM/ TITLE,JTITLE,ITITLE,ATITLE
C
      CALL VTDTEK
      CALL T4014
      FACT=152.4/511.
      FACT= 2*FACT
      CALL UNITS(FACT)
      CALL PICCLE
      CALL CHAMOD
      CALL LIB$WAIT(2.)
      CALL WINDO2(0.,600.,0.,511.)
      CALL SHIFT2(90.,40.)
      IF (K .GT. 1) GO TO 1
 1    CONTINUE
      CALL CHASIZ(10.,10.)
      CALL MOVTO2(0.,400.)
      LABEX= LABEL//'*.'
      CALL CHASTR(LABEX)
      CALL MOVTO2(270.,400.)
      CALL CHASTR('EXTR.POINT=*.')
      CALL CHAFIX(X(NVIC),8,1)
      FTITLE= TITLE//'*.'
      CALL MOVTO2(330.,370.)
      CALL CHASTR(FTITLE)
      CALL CHAANG(0.)
```

APPENDIX E2

```
      END
      SUBROUTINE PLOTNO (N,X,Y,M,V,W,XMIN,XMAX,YMIN,YMAX,LABEL,D,NODES)
      REAL X(N),Y(N),V(M),W(M),D(4)
      LOGICAL NODES
      CHARACTER LABEL*80,LABEX*82,LEG1*11,LEG2(4)*6,ANS*3
      CHARACTER*14 TITLE,ITITLE,JTITLE,ATITLE(20),FTITLE
      COMMON /FNAM/ TITLE,JTITLE,ITITLE,ATITLE
C
      IF (NODES) THEN
C-  PLOT FIRST FOUR NODES IN EV'S
        LEG1='NODES IN EV'
        DO 1 I=1,4
1       WRITE(UNIT=LEG2(I),FMT='(F6.3)') D(I)
      ENDIF
C
      XMI= XMIN
      XMA= XMAX
      YMI= YMIN
      YMA= YMAX
      XD= XMA-XMI
      YD= YMA-YMI
      XLABEL = XD/8
      YLABEL = YD/10
C  BEGIN PLOTTING
      CALL INIPLT(46,NORMAL,1.0)
      CALL SCALE(XMIN,XMAX,YMIN,YMAX)
      CALL GRAPHBOUNDARY(1500,7500,1400,5600)
      CALL AXIS(XLABEL,'10.0','ENERGY (eV)',2,YLABEL,'10.2',' ',2)
      CALL WRITELEGEND(TITLE,2,9,2,0,9)
      CALL JUSTIFYSTRING(4000,5800,LABEL,0,2,CENTER,BELOW)
      IF (NODES) THEN
        CALL SETLEGEND(8000,6400,0)
        CALL WRITELEGEND(LEG1,2,9,2,0,9)
        DO 237 M1=1,4
              CALL WRITELEGEND(LEG2(M1),2,9,2,0,9)
237     CONTINUE
      ENDIF
      CALL POLYLINE(X,Y,N,3,0,0,0,0)
      CALL POLYLINE(V,W,M,4,0,0,0,1)
      CALL ENDPLT
      CALL SYSTEM('VTRANS PLOT46 1')
      WRITE(6,300)
      READ(5,*) ANS
      IF (ANS(1:1).EQ.'Y'.OR.ANS(1:1).EQ.'y') CALL HARDCOPY('PLOT46')
300   FORMAT(2X,'HARD PLOT? Y/N'/)
      RETURN
      END
```

```
      CALL WRITELEGEND(LEG3,2,9,2,0,9)
      DO 130 I=1,NPL
        DO 120 J=1,400
          X(J)=RA(J,I)
          Y(J)=PHI(J,I)
20      CONTINUE
        CALL POLYLINE(X,Y,400,(I+2),0,0,0,LINE(I))
        CALL WRITELEGEND(LEG4(I),(I+2),9,2,0,LINE(I))
        CALL WRITELEGEND(LEG5(I),(I+2),9,2,0,LINE(I))
30    CONTINUE
      CALL ENDPLT
      CALL SYSTEM('VTRANS PLOT45 1')
      WRITE(6,300)
      READ(5,*) ANS
      IF (ANS(1:1).EQ.'Y'.OR.ANS(1:1).EQ.'y') CALL HARDCOPY('PLOT45')
00    FORMAT(2X,'HARD PLOT? Y/N'/)
      RETURN
      END
      SUBROUTINE PLOTFR(PHI,SM1,WE)
      REAL XLABEL,YLABEL
      CHARACTER*14 TITLE,ITITLE,JTITLE,ATITLE(20),LABEL*80
      COMMON /FNAM/ TITLE,ITITLE,JTITLE,ATITLE
      COMMON /LAB/LABEL
      DIMENSION RA(512),PHI(1024),Y(512)
      CHARACTER*6 SAM,WE1,LEG4*10,LEG5*9,ANS*3

      YMIN=0
      YMAX=0
      XMAX=512
      XMIN=1
      DO 80 J=1,512
      IF (PHI(J).LT.YMIN) YMIN=PHI(J)
      IF (PHI(J).GT.YMAX) YMAX=PHI(J)
      Y(J)=PHI(J)
      RA(J)=J
 80   CONTINUE
      WRITE(UNIT=SAM,FMT='(F6.3)') SM1
      LEG4='SM1='//SAM
      WRITE(UNIT=WE1,FMT='(F6.3)') WE
      LEG5='WE='//WE1
      CALL INIPLT(50,NORMAL,1.0)
      CALL SCALE(XMIN,XMAX,YMIN,YMAX)
      CALL GRAPHBOUNDARY(2000,7500,1400,5600)
      YLABEL=(YMAX-YMIN)/10
      XLABEL=(XMAX-XMIN)/8
      CALL AXIS(XLABEL,'6.0','NH',2,YLABEL,'10.2',' ',2)
      CALL WRITELEGEND(TITLE,2,9,2,0,9)
      CALL JUSTIFYSTRING(2500,5800,LABEL,0,2,CENTER,BELOW)
      CALL SETLEGEND(8000,6400,0)
      CALL POLYLINE(RA,Y,512,2,0,0,0,0)
      CALL WRITELEGEND(LEG4,2,9,2,0,9)
      CALL WRITELEGEND(LEG5,2,9,2,0,9)
30    CONTINUE
      CALL ENDPLT
      CALL SYSTEM('VTRANS PLOT50 1')
      WRITE(6,300)
      READ(5,*) ANS
      IF (ANS(1:1).EQ.'Y'.OR.ANS(1:1).EQ.'y') CALL HARDCOPY('PLOT50')
00    FORMAT(2X,'HARD PLOT? Y/N'/)
      RETURN
```

```
      FMALT = 60.
      PHIMAX = 0.
      DO 160 N=2,NRMAX,NSKP
      ARAY(N-1,J) = (N-1)*DR
      AMG(N-1,J) = FMALT*CABS(FFTINP(N))
      IF (AMG(N-1,J).GT.PHIMAX) PHIMAX = AMG(N-1,J)
  160 CONTINUE
  170 CONTINUE
C
      CALL PLTR(ARAY,AMG,RKMIN,RKMAX,KPOWER,SM1,WE,NPL,SM,WES)
      RETURN
      END
      SUBROUTINE PLTR(RA,PHI,RKMIN,RKMAX,KPOWER,SM1,WE,NPL,SM,WES)
      REAL XLABEL,YLABEL
      CHARACTER*14 TITLE,ITITLE,JTITLE,ATITLE(20)
      COMMON /FNAM/ TITLE,ITITLE,JTITLE,ATITLE
      DIMENSION RA(1002,*),PHI(1002,*),X(401),Y(401),SM(3),WES(3),LINE(3
     Z)
      CHARACTER*6 KMIN,KMAX,SAM(3),WE1(3),KWT*3,LEG1*11,LEG2*11,LEG3*7,
     ZLEG4(3)*10,LEG5(3)*9,ANS*3
C
      LINE(1)=0
      LINE(2)=1
      LINE(3)=4
      YMIN=0
      YMAX=0
      XMAX=8
      XMIN=0
      DO 90 I=1,NPL
      DO 80 J=1,400
      IF (PHI(J,I).LT.YMIN) YMIN=PHI(J,I)
      IF (PHI(J,I).GT.YMAX) YMAX=PHI(J,I)
   80 CONTINUE
   90 CONTINUE
      WRITE(UNIT=KMIN,FMT='(F6.3)') RKMIN
      LEG1='KMIN='//KMIN
      WRITE(UNIT=KMAX,FMT='(F6.3)') RKMAX
      LEG2='KMAX='//KMAX
      WRITE(UNIT=KWT,FMT='(I3)') KPOWER
      LEG3='KWT='//KWT
      IF (NPL.EQ.1) THEN
        SM(1)=SM1
        WES(1)=WE
      ENDIF
      DO 100 I=1,NPL
        WRITE(UNIT=SAM(I),FMT='(F6.3)') SM(I)
        LEG4(I)='SM1='//SAM(I)
        WRITE(UNIT=WE1(I),FMT='(F6.3)') WES(I)
        LEG5(I)='WE='//WE1(I)
  100 CONTINUE
      CALL INIPLT(45,NORMAL,1.0)
      CALL SCALE(XMIN,XMAX,YMIN,YMAX)
      CALL GRAPHBOUNDARY(2000,7500,1400,5600)
      YLABEL=(YMAX-YMIN)/10
      XLABEL=INT((XMAX-XMIN)/8)
      CALL AXIS(XLABEL,'10.2','K',2,YLABEL,'10.2',' ',2)
      CALL WRITELEGEND(TITLE,2,9,2,0,9)
      CALL SETLEGEND(8000,6400,0)
      CALL WRITELEGEND(LEG1,2,9,2,0,9)
      CALL WRITELEGEND(LEG2,2,9,2,0,9)
```

```
      COMPLEX FFTINP(4096),FF(4096)
      INTEGER IWK(14)

      DO 170 J=1,NPL
      DO 10 I=1,MM
      AK(I)= AKN(I,J)
10    CHI(I)= CHIN(I,J)
      NCHI = MM
      PI = 3.1415926
      MARRAY = 4096
      FCUT = 0.02

      RMAX = 8.0
      DR = 0.02

      RCUT = FCUT*FLOAT(MARRAY)
      DK = PI/RCUT
      I=2
      IF (RKMIN.LE.AK(1)) GOTO 100
      I=0
90    I=I+1
      IF (AK(I).LT.RKMIN) GOTO 90
00    NMIN=I-1
10    I=I+1
      IF (I.GE.NCHI) GOTO 120
      IF (AK(I).LT.RKMAX) GOTO 110
20    NMAX=I
      IMIN=NMIN+NLO-1
      IMAX=NMAX+NLO-1
      AKLO = AK(NMIN)
      AKHI = AK(NMAX)

      CALL TRANIN (CHI,AK,FFTINP,AKLO,DK,KPOWER,FHANN,
     1             NMIN,NMAX,NCHI,NPTS1)

----THERE ARE THREE STEPS TO GET FOURIER TRANSFORM BY FFT2 ROUTINE.
----1. CONJUGATE THE COMPLEX BEFORE GETTING INTO FFT2.
----2. DEVICE THE DATA BY MARRAY AFTER FFT2.
----3. THEN REORDER THE DATA FROM REVERSE BINARY ORDER BY SBRT SHUFF.
      DO 140 I=1,4096
40    FFTINP(I) = CONJG(FFTINP(I))

      M = 12
      CALL FFT2 (FFTINP,M,IWK)

      DO 150 I=1,4096
      FFTINP(I) = FFTINP(I)/4096.
      FF(I) = FFTINP(I)
50    CONTINUE

      CALL SHUFF (FFTINP,FF,4096)

      NFFT = AKLO/DK
      XMIN = DK*NFFT
      XMAX = XMIN+DK*FLOAT(NCHI-1)
      NSKP = DR/FCUT+0.000001
      NRMAX = MARRAY*RMAX/RCUT+1.000001

----FMALT IS THE CONSTANT TO GET THE SAME VALUES AS TRAPEZOIDAL
----INTEGRATION.
```

```
      CHARACTER TIX*1,TIY*10,LEG(2)*10,ANS*3
      DATA TIX1/'K'/
      DATA TIY/'    CHI    '/
      LEG(1)='NICE '
      LEG(2)='RAW CHI-BK'
      XMIN= 0.
      XMAX=AK(M)
C
      YMIN=0.
      YMAX=0.
      DO 151 I=1,2
      DO 150 J=1,M
       IF (CHI(J,I).LT.YMIN) YMIN=CHI(J,I)
       IF (CHI(J,I).GT.YMAX) YMAX=CHI(J,I)
 150  CONTINUE
 151  CONTINUE
      WRITE (6,310) YMIN,YMAX
      READ (5,*) OP
      IF (OP.EQ.0) GO TO 152
      WRITE (6,320)
      READ (5,*) YMIN,YMAX
 152  RX(1)=XMIN
      RX(2)=XMAX
      RY(1)=0.
      RY(2)=0.
      XLAB= (XMAX-XMIN)/8
      YLABEL= (YMAX-YMIN)/10
      CALL SYSTEM('DEL PLOT52.DAT')
      CALL INIPLT(52,NORMAL,1.0)
      CALL SCALE(XMIN,XMAX,YMIN,YMAX)
      CALL GRAPHBOUNDARY(2000,7500,1400,5600)
      CALL AXIS(XLAB,'10.0',TIX1,2,YLABEL,'10.3',TIY,2)
      CALL JUSTIFYSTRING (4500,6400,LABEL,0,2,CENTER,BELOW)
      DO 160 I=1,2
       DO 155 J=1,M
         Y(J)=CHI(J,I)
 155   CONTINUE
         CALL POLYLINE(AK,Y,M,(I+1),9,0,0,(I-1))
         CALL WRITELEGEND(LEG(I),(I+1),9,2,0,(I-1))
 160  CONTINUE
      CALL POLYLINE(RX,RY,2,2,9,0.0,0)
      CALL ENDPLT
      CALL SYSTEM('VTRANS PLOT52 1')
      WRITE(6,300)
      READ(5,*) ANS
       IF (ANS(1:1).EQ.'Y'.OR.ANS(1:1).EQ.'y') CALL HARDCOPY('PLOT52')
 300  FORMAT(2X,'HARD PLOT? Y/N'/)
 310  FORMAT(2X,'DEFAULT YMIN= ',F6.3,' YMAX= ',F6.3/
     1          ' 0: FOR DEFAULT VALUES'/
     2          ' 1: FOR USER DEFINED VALUES'/)
 320   FORMAT(2X,'ENTER YMIN,YMAX:'/)
       RETURN
C
       END

       SUBROUTINE PLOTFT(MM,AKN,CHIN,RKMIN,RKMAX,KPOWER,SM1,WE,NPL,SM,
     1                   WES)
       DIMENSION CHIN(1100,*),AKN(1100,*),ARAY(1002,3),AMG(1002,3),
     1           SM(3),WES(3)
       DIMENSION AMPLIT(1024),AK(1100),CHI(1100)
```

```
      IF (CHI(J)*CHI(J+1) .LE. 0.) THEN
        IF (CHI(J) .EQ. 0.) THEN
          AKNOT= AK(J)
          GO TO 210
        ELSEIF (CHI(J+1) .EQ. 0.) THEN
          IF (J .EQ. M-1) THEN
            AKNOT= AK(J+1)
            GO TO 210
          ENDIF
        ELSE
          IF (ABS(CHI(J)) .LE. ABS(CHI(J+1))) THEN
            L= J
          ELSE
            L= J+1
          ENDIF
          AKNOT = AK(L)
          GO TO 210
        ENDIF
      ENDIF
200   CONTINUE
10    CONTINUE
220   CONTINUE
50    DO 270 J=1,M
      X(J)=AK(J)
      Y(J)=CHI(J)
270   CONTINUE
      YLABEL=(YMAX-YMIN)/10
      CALL SYSTEM('DEL PLOT44.DAT')
      CALL INIPLT(44,NORMAL,1.0)
      CALL SCALE(XMIN,XMAX,YMIN,YMAX)
      CALL GRAPHBOUNDARY(2000,7500,1400,5600)
      CALL AXIS(XLAB,'10.0',TIX(1),2,YLABEL,'10.3',TIY(K),2)
      CALL JUSTIFYSTRING (3500,6000,LABEL,0,2,CENTER,BELOW)
      CALL WRITELEGEND(TITLE,2,9,2,0,9)
      IF (NODES) THEN
        CALL SETLEGEND(7600,6400,0)
        CALL WRITELEGEND('NODE',2,9,2,0,9)
        WRITE(UNIT=ZERO,FMT='(F6.3)') AKNOT
        CALL WRITELEGEND(ZERO,2,9,2,0,9)
      ENDIF
      CALL POLYLINE(X,Y,M,K+1,0,0,0,0)
      CALL POLYLINE(RX,RY,2,K+2,0,0,0,0)
      CALL ENDPLT
      CALL SYSTEM('VTRANS PLOT44 1')
      WRITE(6,300)
      READ(5,*) ANS
      IF (ANS(1:1).EQ.'Y'.OR.ANS(1:1).EQ.'y') CALL HARDCOPY('PLOT44')
)0    FORMAT(2X,'HARD PLOT? Y/N'/)
      DO 280 J=1,M
:80   CHI(J)= RCHI(J)
      RETURN

      END
      SUBROUTINE PLTCH2(AK,CHI,M)
      CHARACTER*14 TITLE,JTITLE,ITITLE,ATITLE(20),LABEL*80
      COMMON /FNAM/ TITLE,JTITLE,ITITLE,ATITLE
      COMMON /LAB/ LABEL
      DIMENSION AK(1100),CHI(1100,2),Y(1100)
      DIMENSION RX(2),RY(2)
      LOGICAL EX
```

```
 17     CALL ENDPLT
        CALL SYSTEM('VTRANS PLOT43 1')
        WRITE(6,100)
        READ(5,*) ANS
        IF (ANS(1:1).EQ.'Y'.OR.ANS(1:1).EQ.'y') CALL HARDCOPY('PLOT43')
 100    FORMAT(2X,'HARD PLOT? Y/N'/)
        RETURN
        END
        SUBROUTINE PLOTCHI(M,AK,CHI,SM1,WE,K)
        CHARACTER*14 TITLE,JTITLE,ITITLE,ATITLE(20),LABEL*80
        COMMON /FNAM/ TITLE,JTITLE,ITITLE,ATITLE
        COMMON /LAB/ LABEL
        DIMENSION AK(1100),CHI(1100),RCHI(1100),X(600),Y(600)
        DIMENSION RX(2),RY(2)
        LOGICAL NODES,EX
        CHARACTER TIX1*1,TIY(0:3)*10,YN*3,ZERO*6,ANS*3
        DATA TIX1/'K'/
        DATA TIY(0)/'    CHI   '/
        DATA TIY(1)/'  CHI X K '/
        DATA TIY(2)/'CHI X K**2'/
        DATA TIY(3)/'CHI X K**3'/
        LABEL='CHI PLOT'
C
        NODES=.FALSE.
        DO 40 J=1,M
   40   RCHI(J)= CHI(J)
C
        IF (K .NE. 0 .AND. K .LE. 3) GO TO 70
        GO TO 130
   70   IF (K .NE. 1) GO TO 90
C
        DO 80 J=1,M
   80   CHI(J) = RCHI(J)*AK(J)
        GO TO 130
C-----
   90   IF (K .NE. 2) GO TO 110
        DO 100 J=1,M
  100   CHI(J) = RCHI(J)*AK(J)**2
        GO TO 130
  110   DO 120 J=1,M
  120   CHI(J) = RCHI(J)*AK(J)**3
  130   CONTINUE
C-----
        XMIN= 0.
        XMAX=AK(M)
C
        YMIN=CHI(1)
        YMAX=CHI(1)
        DO 150 J=1,M
        IF (CHI(J).LT.YMIN) YMIN=CHI(J)
        IF (CHI(J).GT.YMAX) YMAX=CHI(J)
  150   CONTINUE
        RX(1)=XMIN
        RX(2)=XMAX
        XLAB= (XMAX-XMIN)/8
        RY(1)=0.
        RY(2)=0.
        IF (K.NE.0) NODES= .TRUE.
        I=1
  190   DO 200 J=1,M
```

```
      YM= YMAC-YMIC
      DO 15 I=1,N
      Z1(I)=Z(I,1)
   15 YC(I)= (Y(I,1)-YMIC)*YR/YM+YL
   16 XLABEL=5.
      IF (K.LT.2) YTICK = 0.0
      IF (K.GE.2) YTICK = 0.05
      IF (K.EQ.1) YLABEL = YMA
      IF (K.GE.2) YLABEL = YD/5
      IF (NPL.EQ.1) THEN
        SM(1) = SM1
        WES(1) = WE
      ENDIF
      DO 20 I=1,NPL
        WRITE (UNIT=SAM(I),FMT='(F6.3)') SM(I)
        LEG1(I)='SM1='//SAM(I)
        WRITE (UNIT=WE1(I),FMT='(F6.3)') WES(I)
0       LEG2(I)='WE='//WE1(I)
      I=1
      CALL INIPLT(43,NORMAL,1.0)
      CALL SCALE(XMIN,XMAX,YMIN,YMAX)
      CALL GRAPHBOUNDARY(2000,7600,1400,5200)
      IF (K .EQ. 1) THEN
        CALL AXIS(XLABEL,'10.0',TITLX1,2,YLABEL,'10.3',TITLY1,2)
        CALL JUSTIFYSTRING(3500,5600,LABEL,0,2,CENTER,CENTER)
        CALL POLYLINE(X,Y,N,I,0,0,0,LINE(I))
        CALL WRITELEGEND(TITLY1,I,0,2,0,LINE(I))
        CALL SETLEGEND(8000,6400,0)
        CALL WRITELEGEND(LEG1(I),I,9,2,0,9)
        CALL WRITELEGEND(LEG2(I),I,9,2,0,9)
        I=I+1
      ENDIF
      IF (K .EQ. 2) THEN
        CALL AXIS(XLABEL,'10.0',TITLX1,2,YLABEL,'10.3',TITLY2,2)
        CALL JUSTIFYSTRING(3500,5600,LABEL,0,2,CENTER,CENTER)
        CALL POLYLINE(X,Z1,N,I,0,0,0,LINE(I))
        CALL WRITELEGEND(TITLY2,I,0,2,0,LINE(I))
        CALL SETLEGEND(8000,6400,0)
        CALL WRITELEGEND(LEG1(I),I,9,2,0,9)
        CALL WRITELEGEND(LEG2(I),I,9,2,0,9)
        I=I+1
      ENDIF
      IF (K .EQ. 3) THEN
        CALL AXIS(XLABEL,'10.0',TITLX1,2,YLABEL,'10.3',TITLY3,2)
        CALL JUSTIFYSTRING(3500,5600,LABEL,0,2,CENTER,CENTER)
        CALL SETLEGEND(8000,6400,640)
        DO 18 I=1,NPL
        DO 30 J=1,N
         Z1(J)=Z(J,I)
0       CONTINUE
        WRITE (UNIT=NUM,FMT='(I2.0)') I
        CALL POLYLINE(X,Z1,N,I,0,0,0,LINE(I))
        CALL WRITELEGEND((NUM//' '//TITLY3),I,0,2,0,LINE(I))
        CALL WRITELEGEND(LEG1(I),I,9,2,0,9)
3       CALL WRITELEGEND(LEG2(I),I,9,2,0,9)
      ENDIF
      IF (K.NE.2) GO TO 17
      CALL POLYLINE(X,YC,N,I,0,0,0,LINE(I))
      CALL SETLEGEND(2000,6000,640)
      CALL WRITELEGEND(TITLY1,I,0,2,0,LINE(I))
```

```
C
C----- THIS PROGRAM PLOTS THE VARIABLES CHI,BKGND AND DBKGD
C----- AGAINST THE BASE VARIABLE AK ----------------------------------
C
      M = NMAX-NMIN+1
C-----
      XMIN=0.0
      XMAX=AK(M,1)
      GO TO (10,20,30) K
   10 YMAX=AMAX1(ABS(CHIMIN),ABS(CHIMAX))
      YMIN=-YMAX
C-----CALL ON SUBROUTINE PLOTVK,GRAPH CHI VS. AK-----------------------
C-----
      CALL PLOTBK(M,AK,CHI,DBKGD,XMIN,XMAX,YMIN,YMAX,YMIC,YMAC,SM1,WE,K,
     1            NPL,SM,WES)
      RETURN
C-----
C-----
   20 YMAC=AMAX1(ABS(CHIMIN),ABS(CHIMAX))
      YMIC=-YMAC
   30 YMAX=DBKMAX
      YMIN=DBKMIN
C
C
      CALL PLOTBK(M,AK,CHI,DBKGD,XMIN,XMAX,YMIN,YMAX,YMIC,YMAC,SM1,WE,K,
     1            NPL,SM,WES)
      RETURN
      END
C-------------------------------------------------------------------------
C
      SUBROUTINE PLOTBK(N,X,Y,Z,XMIN,XMAX,YMIN,YMAX,YMIC,YMAC,SM1,WE,K,
     1                  NPL,SM,WES)
      DIMENSION X(1100,1),Y(1100,1),Z(1100,3),YC(1100),SM(3),WES(3),Z1
     Z(1100)
      CHARACTER TITLX1*1,TITLY1*3,TITLY2*11,TITLY3*5,LABEL*80,LABEX*82
      CHARACTER*14 TITLE,ITITLE,JTITLE,ATITLE(20),FTITLE,NUM*2
      CHARACTER SAM(3)*6,WE1(3)*6,LEG1(3)*10,LEG2(3)*10,ANS*3
      DIMENSION LINE(6)
      COMMON /LAB/ LABEL
      COMMON /FNAM/ TITLE,JTITLE,ITITLE,ATITLE
      DATA TITLX1/'K'/
      DATA TITLY1/'CHI'/
      DATA TITLY2/'DBKGD & CHI'/
      DATA TITLY3/'DBKGD'/
      LABEL=TITLE//'  '//LABEL
      LINE(1)=0
      LINE(2)=1
      LINE(3)=4
      LINE(4)=7
      LINE(5)=3
      LINE(6)=8
      XMI= XMIN
      XMA= XMAX
      YMI= YMIN
      YMA= YMAX
      XD= XMA-XMI
      YD= YMA-YMI
      IF (K .NE. 2) GO TO 16
      YL= YMI+YD/4
      YR= YD/2
```

```
      XMI= XMIN
      XMA= XMAX
      YMI= YMIN
      YMA= YMAX
      XD= XMA-XMI
      YD= YMA-YMI
7     IF (XD .GE. 1000.) XLABEL = 500.
      IF (XD .GE. 500. .AND. XD .LT. 1000.) XLABEL = 200.
      IF (XD .GE. 200. .AND. XD .LT. 500.) XLABEL = 100.
      IF (XD .GE. 100. .AND. XD .LT. 200.) XLABEL = 50.
      IF (XD .GE. 50. .AND. XD .LT. 100.) XLABEL = 20.
      IF (XD .LT. 50.) XLABEL = 10.
      XLABEL=XD/10

      IF (YD .GE. 2.) YLABEL = 1.
      IF (YD .GE. 1. .AND. YD .LT. 2.) YLABEL = 0.5
      IF (YD .GE. .5 .AND. YD .LT. 1.) YLABEL = 0.2
      IF (YD .GE. .1 .AND. YD .LT. .5) YLABEL = 0.1
      IF (YD .LT. .1) YLABEL = .02
      YLABEL=YD/10
8     CALL INIPLT(42,NORMAL,1.0)
      CALL SCALE(XMIN,XMAX,YMIN,YMAX)
      CALL AXIS(XLABEL,'10.0','ENERGY (eV)',3,YLABEL,'10.3','XMU',3)
      CALL WRITELEGEND(LABEL,2,9,3,0,9)
      CALL POLYLINE(X,Y,N,3,9,0,0,0)
      IF (NOPT .EQ. 1) THEN
        CALL JUSTIFYSTRING(3000,3200,'RETURN, THEN TYPE IN START-ENERGY'
     Z  ,0,2,LEFT,CENTER)
        CALL JUSTIFYSTRING(3800,3000,'FOR BACKGROUND: ',0,2,LEFT,CENTER)
      ELSE
        CALL JUSTIFYSTRING(4000,4000,'RETURN, THEN TYPE IN EVKMAX: ',0,2
     Z  ,LEFT,BELOW)
      ENDIF
      CALL ENDPLT
      CALL SYSTEM('VTRANS PLOT42 1')
      WRITE(6,100)
      READ(5,*) ANS
      IF (ANS(1:1).EQ.'Y'.OR.ANS(1:1).EQ.'y') CALL HARDCOPY('PLOT42')
00    FORMAT(2X,'HARD PLOT? Y/N'/)
      IF (NOPT.EQ.1) THEN
       WRITE(6,105 )
       READ(5,*) EVKM
      ELSE
       WRITE(6,110)
       READ(5,*) EVKM
      ENDIF
05    FORMAT(X,'START ENERGY ?'/)
10    FORMAT(X,'MAX ENERGY ?'/)
      RETURN
      END
      SUBROUTINE PLTBCK(NMIN,NMAX,CHIMAX,CHIMIN,SM1,WE,DBKMAX,
     1                  DBKMIN,AK,CHI,DBKGD,K,NPL,SM,WES)
----------EXECUTE PLTBCK.FOR,SYS:DRAFT/LIB----------

      LATEST REVISION -- DECEMBER 17, 1978

      DIMENSION AK(1100,1),CHI(1100,1),DBKGD(1100,1),SM(3),WES(3)
      DIMENSION XMU(1100)
      CHARACTER LABEL*80
      COMMON /LAB/ LABEL
```

```
      CALL ENDPLT
      CALL SYSTEM('VTRANS PLOT40 1')
      WRITE(6,100)
      READ(5,*) ANS
      IF (ANS(1:1).EQ.'Y'.OR.ANS(1:1).EQ.'y') CALL HARDCOPY('PLOT40')
100   FORMAT(2X,'HARD PLOT? Y/N'/)
      RETURN
      END
      SUBROUTINE PLTMOD (N,X,Y,YY,XMIN,XMAX,YMIN,YMAX,LABEL)
      REAL X(N),Y(N),YY(N),XLABEL,YLABEL
      CHARACTER LABEL*80,LABEX*82,ANS*3
      CHARACTER*14 TITLE,ITITLE,JTITLE,ATITLE(20),FTITLE
      COMMON /FNAM/ TITLE,JTITLE,ITITLE,ATITLE
C
      XMI= XMIN
      XMA= XMAX
      YMI= YMIN
      YMA= YMAX
      XD= XMA-XMI
      YD= YMA-YMI
 7    XLABEL = (XD/10)
C      IF (XD .GE. 1000.) XLABEL = 500.
C      IF (XD .GE. 500. .AND. XD .LT. 1000.) XLABEL = 200.
C      IF (XD .GE. 200. .AND. XD .LT. 500.) XLABEL = 100.
C     IF (XD .GE. 100. .AND. XD .LT. 200.) XLABEL = 50.
C    IF (XD .GE. 50. .AND. XD .LT. 100.) XLABEL = 20.
C      IF (XD .LT. 50.) XLABEL = 10.
C
      YLABEL = (YD/10)
C      IF (YD .GE. 2.) YLABEL = 1.
C      IF (YD .GE. 1. .AND. YD .LT. 2.) YLABEL = 0.2
C      IF (YD .GE. .5 .AND. YD .LT. 1.) YLABEL = 0.1
C      IF (YD .GE. .2 .AND. YD .LT. .5) YLABEL = 0.05
C      IF (YD .GE. .1 .AND. YD .LT. .2) YLABEL = 0.02
C      IF (YD .GE. .05 .AND. YD .LT. .1) YLABEL = 0.01
C      IF (YD .LT. .05) YLABEL = 0.005
 8    CALL INIPLT(41,NORMAL,1.0)
      CALL SCALE(XMIN,XMAX,YMIN,YMAX)
      CALL AXIS(XLABEL,'10.0','ENERGY (eV)',2,YLABEL,'10.3','ABSORPTION'
     Z,2)
      CALL JUSTIFYSTRING(4000,5700,LABEL,0,2,CENTER,BELOW)
      CALL WRITELEGEND(TITLE,2,0,2,0,9)
      CALL POLYLINE(X,Y,N,3,0,0,0,0)
      CALL WRITELEGEND('MODIFIED',3,0,2,0,0)
      CALL POLYLINE(X,YY,N,2,5,1,1,9)
      CALL WRITELEGEND('UN-MODIFIED POINTS',2,5,2,0,9)
      CALL ENDPLT
      CALL SYSTEM('VTRANS PLOT41 1')
      WRITE(6,100)
      READ(5,*) ANS
      IF (ANS(1:1).EQ.'Y'.OR.ANS(1:1).EQ.'y') CALL HARDCOPY('PLOT41')
100   FORMAT(2X,'HARD PLOT? Y/N'/)
      RETURN
      END
      SUBROUTINE PLOTSE(N,X,Y,XMIN,XMAX,YMIN,YMAX,LABEL,NOPT,EVKM)
      REAL X(N),Y(N)
      CHARACTER LABEL*80,LABEX*82,ANS*3
      CHARACTER*14 TITLE,ITITLE,JTITLE,ATITLE(20),FTITLE
      COMMON /FNAM/ TITLE,JTITLE,ITITLE,ATITLE
C
```

```
      CALL WRITELEGEND(LABEL2,2,9,2,0,9)
      CALL JUSTIFYSTRING(4000,5700,LABEL,0,2,CENTER,BELOW)
      CALL WRITELEGEND(TITLE,2,9,2,0,9)
      CALL AXIS(XLABEL,'10.0','ENERGY (eV)',2,YLABEL,'10.3','ABSORPTION'
     Z,2)
      CALL POLYLINE(X,Y,N,3,0,0,0,0)
      CALL POLYLINE(X,V,N,4,0,0,0,1)
      CALL POLYLINE(X(NVC1),Y(NVC1),1,6,3,1,1,9)
      CALL POLYLINE(X(NVIC),Y(NVIC),1,6,3,1,1,9)
      CALL ENDPLT
      CALL SYSTEM('VTRANS PLOT39 1')
      WRITE(6,100)
      READ(5,*) ANS
      IF (ANS(1:1).EQ.'Y'.OR.ANS(1:1).EQ.'y') CALL HARDCOPY('PLOT39')
00    FORMAT(2X,'HARD PLOT? Y/N'/)
38    FORMAT(A)
39    FORMAT(' ROTATION: VERTICAL(1) OR HORIZONTAL(2) ? > ')
40    FORMAT(I1)
      RETURN
      END
      SUBROUTINE PLOTE0(N,X,Y,XMIN,XMAX,YMIN,YMAX,E0,YE0,LABEL,K)
      REAL X(N),Y(N),E0(1),YE0(1)
      CHARACTER LABEL*80,LABEX*82,ENERGY*10,LABEL2*25,ANS*3
      CHARACTER*14 TITLE,ITITLE,JTITLE,ATITLE(20),FTITLE
      COMMON /FNAM/ TITLE,JTITLE,ITITLE,ATITLE
      LABEL2='E0='
      WRITE(UNIT=ENERGY,FMT='(F8.2)') E0
      LABEL2(4:14)=ENERGY
      LABEL=' INNERPOTENTIAL DETERMINATION'
      XMI= XMIN
      XMA= XMAX
      YMI= YMIN
      YMA= YMAX
      XD= XMA-XMI
      YD= YMA-YMI
      XLABEL= XD/8
      YLABEL= YD/10
      XTIC= 100.
      GO TO 8
7     IF (XD .GE. 1000.) XLABEL = 500.
      IF (XD .GE. 500. .AND. XD .LT. 1000.) XLABEL = 200.
      IF (XD .GE. 200. .AND. XD .LT. 500.) XLABEL = 100.
      IF (XD .GE. 100. .AND. XD .LT. 200.) XLABEL = 50.
      IF (XD .GE. 50. .AND. XD .LT. 100.) XLABEL = 20.
      IF (XD .LT. 50.) XLABEL = 10.

      IF (YD .GE. 2.) YLABEL = .5
      IF (YD .GE. 1. .AND. YD .LT. 2.) YLABEL = 0.25
      IF (YD .GE. .5 .AND. YD .LT. 1.) YLABEL = 0.1
      IF (YD .GE. .1 .AND. YD .LT. .5) YLABEL = 0.05
      IF (YD .LT. .1) YLABEL = .01
8     CALL INIPLT(40,NORMAL,1.0)
      CALL SCALE(XMIN,XMAX,YMIN,YMAX)
      CALL WRITELEGEND(LABEL2,2,9,2,0,9)
      CALL WRITELEGEND(TITLE,2,9,2,0,9)
      CALL JUSTIFYSTRING(4000,5600,LABEL,0,2,CENTER,BELOW)
      CALL AXIS(XLABEL,'10.0','ENERGY (eV)',2,YLABEL,'10.3','ABSORPTION'
     Z,2)
      CALL POLYLINE(X,Y,N,3,0,0,0,0)
      CALL POLYLINE(E0,YE0,1,4,4,1,1,9)
```

```
      CHARACTER LABEL*80,YN*3
C
      EVA = X(1)
      EVB = X(NPTS)
C
      YMIN = MIN(Y(1),V(1))
      YMAX = MAX(Y(1),V(1))
      DO 6 I=2,NPTS
      IF (Y(I).LT.YMIN) YMIN = Y(I)
      IF (V(I).LT.YMIN) YMIN = V(I)
      IF (Y(I).GT.YMAX) YMAX = Y(I)
      IF (V(I).GT.YMAX) YMAX = V(I)
    6 CONTINUE
C-----
      CALL PLOTPG (NPTS,X,Y,V,EVA,EVB,YMIN,YMAX,NVIC,N,LABEL,2)
C-----
      RETURN
      END
      SUBROUTINE PLOTPG (N,X,Y,V,XMIN,XMAX,YMIN,YMAX,NVIC,NVC1,LABEL,K)
      REAL X(N),Y(N),V(N)
      INTEGER ROT
      CHARACTER LABEL*80,LABEX*82,EXPNT*9,LABEL2*30,YN*3,ANS*3
      CHARACTER*14 TITLE,ITITLE,JTITLE,ATITLE(20),FTITLE
      COMMON /FNAM/ TITLE,JTITLE,ITITLE,ATITLE
C
      LABEL2='EXTR.PNTS= '
      WRITE(UNIT=EXPNT,FMT='(F8.2)') X(NVC1)
      LABEL2(12:20)=EXPNT
      WRITE (UNIT=EXPNT,FMT=' (F8.2)') X(NVIC)
      LABEL2(21:30)=EXPNT
      XMI= XMIN
      XMA= XMAX
      YMI= YMIN
      YMA= YMAX
      XD= XMA-XMI
      YD= YMA-YMI
      IF (K .GT. 1) GO TO 7
      XLABEL= 500.
      YLABEL= .5
      XTIC= 100.
      GO TO 8
    7 IF (XD .GE. 1000.) XLABEL = 500.
      IF (XD .GE. 500. .AND. XD .LT. 1000.) XLABEL = 200.
      IF (XD .GE. 200. .AND. XD .LT. 500.) XLABEL = 100.
      IF (XD .GE. 100. .AND. XD .LT. 200.) XLABEL = 50.
      IF (XD .GE. 50. .AND. XD .LT. 100.) XLABEL = 20.
      IF (XD .LT. 50.) XLABEL = 10.
C
C
      IF (YD .GE. 2.) YLABEL = 1.
      IF (YD .GE. 1. .AND. YD .LT. 2.) YLABEL = 0.5
      IF (YD .GE. .5 .AND. YD .LT. 1.) YLABEL = 0.2
      IF (YD .GE. .1 .AND. YD .LT. .5) YLABEL = 0.1
      IF (YD .LT. .1) YLABEL = .02
    8 CALL INIPLT(39,NORMAL,1.0)
        XMIN=XMIN-.025*XMIN
        XMAX=XMAX+.025*XMAX
        YMIN=YMIN-.5
        YMAX=YMAX+.5
      CALL SCALE(XMIN,XMAX,YMIN,YMAX)
```

```
     1         '  EV(1)=',F10.2,'  EV(NPTS)=',F10.2/)
24   FORMAT (//' WHICH OPTION DO YOU WANT, TYPE NUMBER'//
     1         '  0: PLOTTING OF WHOLE SPECTRUM'/
     2         '  1: PLOTTING OF AN ENERGY RANGE'/)
26   FORMAT (2X,'TYPE IN EVMIN,EVMAX'/)
27   FORMAT (' DO YOU WANT MORE PLOTS?, TYPE YES, OTHERWISE NO'/)
28   FORMAT (A3)
     END
     SUBROUTINE PLOTEV (N,X,Y,XMIN,XMAX,YMIN,YMAX,LABEL,K)
     REAL X(N),Y(N)
     INTEGER ROT
     CHARACTER LABEL*80,LABEX*82,YN*3,ANS*3
     CHARACTER*14 TITLE,ITITLE,JTITLE,ATITLE(20),FTITLE
     LOGICAL TIT
     COMMON /FNAM/ TITLE,JTITLE,ITITLE,ATITLE
     COMMON /DRTIT/ TIT
     COMMON /XMDAT/ NSEQ,NPTS,XX(1400),YY(1400)

     XMI= XMIN
     XMA= XMAX
     YMI= YMIN
     YMA= YMAX
     XD= XMA-XMI
     YD= YMA-YMI
     IF (K .GT. 1) GO TO 7
     XLABEL= 500.
     YLABEL= .5
     XTIC= 100.
     GO TO 8
     XLABEL = XD/8
     YLABEL = YD/10
     CALL INIPLT(38,NORMAL,1.0)
     CALL SCALE(XMIN,XMAX,YMIN,YMAX)
     CALL AXIS(XLABEL,'10.0','ENERGY (eV)',2,YLABEL,'10.3','ABSORPTION'
    Z,2)
     CALL JUSTIFYSTRING(2500,5800,LABEL,0,2,CENTER,BELOW)
     CALL POLYLINE(X,Y,N,4,9,0,0,0)
     CALL ENDPLT
     CALL SYSTEM('VTRANS PLOT38 1')
     WRITE(6,100)
     READ(5,*) ANS
      IF (ANS(1:1).EQ.'Y'.OR.ANS(1:1).EQ.'y') CALL HARDCOPY('PLOT38')
0    FORMAT(2X,'HARD PLOT? Y/N  /)
9    FORMAT(A)
0    FORMAT(I1)
     RETURN
     END
     SUBROUTINE PLPRDG(NVIC,N)
----THIS PROGRAM IS DESIGNED TO PLOT THE TOTAL X-RAY ABSORPTION
----COEFFICIENT VS. THE ABSOLUTE X-RAY PHOTON ENERGY.

     *****    EXECUTE PLTEV.FOR,SYS:DRAFT/LIB    *****

-------------------------------------------------------------------------
     LATEST REVISION -- JANUARY 1, 1979

     DIMENSION EEV(20)
     COMMON /XMDAT/ NSEQ,NPTS,X(1400),Y(1400)
     COMMON /LAB/ LABEL
     COMMON /SQZ/ V(1000),Z(1000)
```

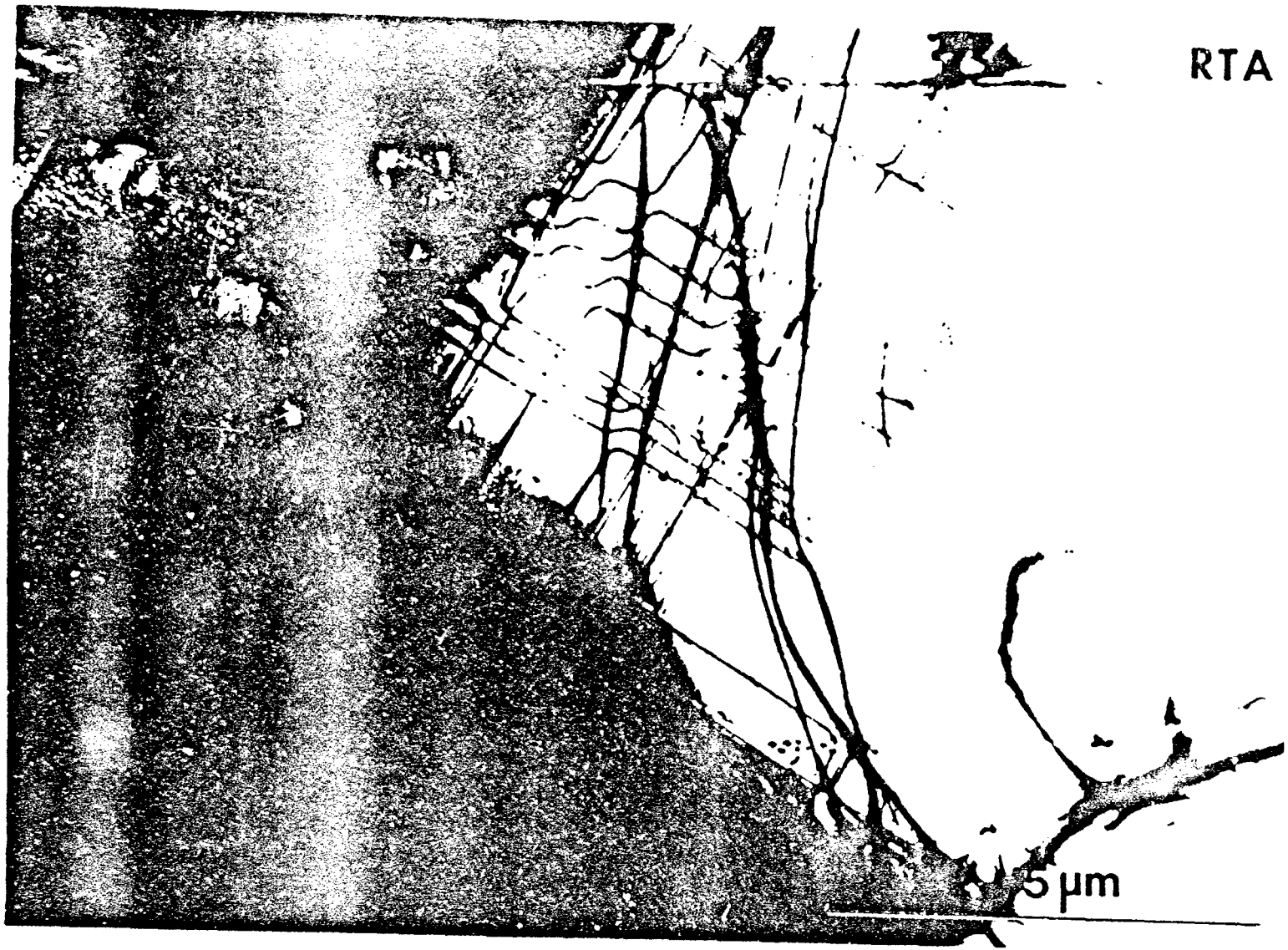
```
        IF (DEF.LT.0.) NGRAPH = NGRAPH+1
      ELSE
        NGRAPH= 0
      ENDIF
C-----
      CALL PLOTEV (NPTS,X,Y,EVA,EVB,YMIN,YMAX,LABEL,2)
C-----
      GO TO 8
    7 CONTINUE
      NGRAPH= 1
      N2= NGRAPH*2
      WRITE (5,26)
      READ(5,*) (EEV(I),I=1,N2)
C
    8 K=1
      IZ=-1
    9 K=K+1
      IF (K-1.LE.NGRAPH) GO TO 15
      IF (II .EQ. 3) THEN
        RETURN
      ELSE
        WRITE (6,27)
        READ (5,28) YN
        IF (YN.EQ.'NO'.OR.YN.EQ.'no'.OR.YN.EQ.'N'.OR.YN.EQ.'n') RETURN
        GO TO 1
      ENDIF
   15 IF (KEYCON.EQ.1) K= 2
      IF (KEYCON.EQ.1) GO TO 11
      IF (K-1.GT.1) GO TO 10
      EVB = EVA
   10 EVA = EVB
      EVB = EVB+250.
      GO TO 12
   11 IZ=IZ+1
      EVA = EEV(IZ*2+1)
      EVB = EEV(IZ*2+2)
   12 J=1
      L=0
      DO 13 I=1,NPTS
      IF (X(I).LT.EVA) J=J+1
      IF (X(I).LE.EVB) L=L+1
   13 CONTINUE
      IF (.NOT. (J .EQ. 1 .AND. L .EQ. 0) .AND. J .LE. NPTS) GO TO 16
      WRITE (6,23) X(1),X(NPTS)
      GO TO 1
C
   16 YMAX = Y(J)
      YMIN = Y(J)
      DO 14 I=J+1,L
      IF (Y(I).GT.YMAX) YMAX = Y(I)
      IF (Y(I).LT.YMIN) YMIN = Y(I)
   14 CONTINUE
      N=L-J+1
C-----
      CALL PLOTEV (N,X(J),Y(J),EVA,EVB,YMIN,YMAX,LABEL,K)
C-----
      GO TO 9
C
   22 FORMAT(I1)
   23 FORMAT (//2X,' EVA AND EVB NOT IN RANGE OF [illegible]'/
```

```
      CALL TRIM(LABEL)
      CALL TRIM(YLAB)
      CALL GRAPHBOUNDARY(2000,8000,1000,5200)
      CALL SCALE(XMIN,XMAX,YMIN,YMAX)
      CALL JUSTIFYSTRING(2000,5600,LABEL,0,2,CENTER,CENTER)
      CALL WRITELEGEND(TITLE,2,9,2,0,9)
      CALL AXIS(XTIC,'10.0','ENERGY (eV)',2,YLABEL,'10.3',YLAB,
     Z2)
      CALL POLYLINE(EV,Y,NPTS,3,9,0,0,0)
      CALL ENDPLT
C END OF HGRAPH ROUTINES
      CALL SYSTEM('VTRANS PLOT37 0')
      WRITE(6,100)
      READ(5,*) ANS
       IF (ANS(1:1).EQ.'Y'.OR.ANS(1:1).EQ.'y') CALL HARDCOPY('PLOT37')
      RETURN
100   FORMAT(2X,'HARD PLOT? Y/N'/)
      END

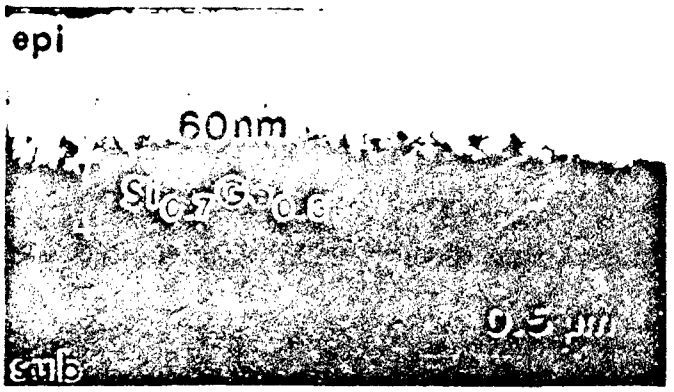
      SUBROUTINE PLTEV(KK)
C-----THIS PROGRAM IS DESIGNED TO PLOT THE TOTAL X-RAY ABSORPTION
C-----COEFFICIENT VS. THE ABSOLUTE X-RAY PHOTON ENERGY.
C
C     *****   EXECUTE PLTEV.FOR,SYS:DRAFT/LIB   *****
C
C-------------------------------------------------------------------------
C     LATEST REVISION -- JANUARY 1, 1979
C
      DIMENSION EEV(20)
      COMMON /XMDAT/ NSEQ,NPTS,X(1400),Y(1400)
      COMMON /LAB/ LABEL
      CHARACTER LABEL*80,YN*3
      COMMON /DRTIT/ TIT
      LOGICAL TIT
C
C-----KEYCON=RETURN, PROGRAM DRAWS EVERY GRAPHS AUTOMATICALLY.
C-----KEYCON=1, PROGRAM DRAWS THE PARTS OF LIMITED EV REGION.
      II= KK
    1 IF (II .EQ. 3) THEN
        KEYCON= 0
        TIT= .FALSE.
      ELSE
        WRITE (6,24)
        READ (5,22) KEYCON
        TIT= .TRUE.
      ENDIF
      IF (KEYCON .NE. 0) GO TO 7
    2 EVA = X(1)
      EVB = X(NPTS)
C
      YMIN = Y(1)
      YMAX = Y(1)
      DO 6 I=2,NPTS
      IF (Y(I).LT.YMIN) YMIN = Y(I)
      IF (Y(I).GT.YMAX) YMAX = Y(I)
    6 CONTINUE
      IF (II .EQ. 3) THEN
        GRAPH = (EVB-EVA)/250.
        NGRAPH = IFIX(GRAPH)
        DEF = NGRAPH-GRAPH
```

```
      SUBROUTINE PLTY0(Y0,Y1,IY)
      DIMENSION Y(1400),Y0(1400),Y1(1400)
      CHARACTER*14 TITLE,ITITLE,JTITLE,ATITLE(20),FTITLE,YLAB
      COMMON /FNAM/ TITLE,JTITLE,ITITLE,ATITLE
      COMMON /XMDAT/ NSEQ.NPTS,EV(1400),XMU(1400)
      COMMON /LAB/ LABEL
      CHARACTER LABEL*80,LABEX*82,ANS*3
      DO 20 I=1,NPTS
      IF (IY.EQ.2) Y(I)= Y0(I)
      IF (IY.EQ.3) Y(I)= Y1(I)
      IF (IY.EQ.4) Y(I)= ALOG(Y0(I)/Y1(I))
      IF (IY.EQ.5) Y(I)= Y1(I)/Y0(I)
   20 CONTINUE
C
      XMIN=EV(1)
      XMAX=EV(1)
      YMIN=Y(1)
      YMAX=Y(1)
C
      DO 50 I=1,NPTS
      IF (EV(I).LT.XMIN) XMIN=EV(I)
      IF (EV(I).GT.XMAX) XMAX=EV(I)
      IF (Y(I).LT.YMIN) YMIN=Y(I)
      IF (Y(I).GT.YMAX) YMAX=Y(I)
   50 CONTINUE
C
C-    DRAW AXES.
      XMI= XMIN
      XMA= XMAX
      YMI= YMIN
      YMA= YMAX
      XD= XMA-XMI
      YD= YMA-YMI
C
    7 IF (XD .GE. 1000.) XTIC = 500.
      IF (XD .GE. 500. .AND. XD .LT. 1000.) XTIC = 200.
      IF (XD .GE. 300. .AND. XD .LT. 500.) XTIC = 100.
      IF (XD .GE. 50. .AND. XD .LT. 300.) XTIC = 50.
      IF (XD .LT. 50.) XTIC = 10.
C
      IF (IY .GT. 3) THEN
        IF (YD .GE. 2.) YLABEL = .5
        IF (YD .GE. 1. .AND. YD .LT. 2.) YLABEL = 0.25
        IF (YD .GE. .5 .AND. YD .LT. 1.) YLABEL = 0.1
        IF (YD .GE. .1 .AND. YD .LT. .5) YLABEL = 0.025
        IF (YD .GE. .05 .AND. YD .LT. .1) YLABEL = 0.01
        IF (YD .GE. .01 .AND. YD .LT. .05) YLABEL = 0.0025
        IF (YD .LT. .01) YLABEL = .001
        YLAB='ABSORPTION'
      ELSE
        YLABEL = INT(YD/10)
        YLAB='DETECTOR DATA'
      ENDIF
        XMIN=XMIN-.025*XMIN
        XMAX=XMAX+.025*XMAX
        YMIN=YMIN-.5
        YMAX=YMAX+.5
C BEGIN CALL OF HGRAPH ROUTINES
      CALL SYSTEM('DEL PLOT37.DAT')
      CALL INIPLT(37,NORMAL,1.0)
```

APPENDIX E1


RTA
5 μm

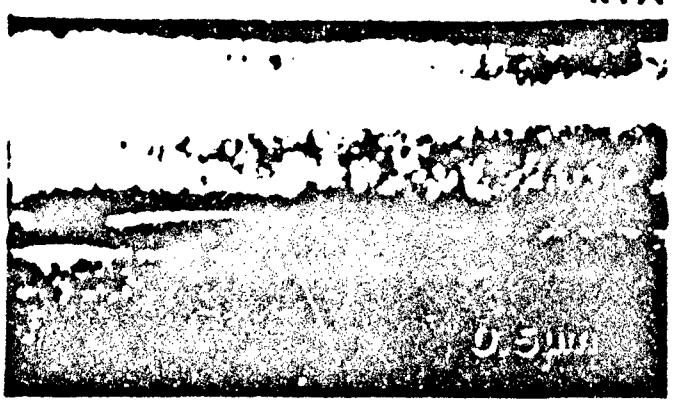
AG

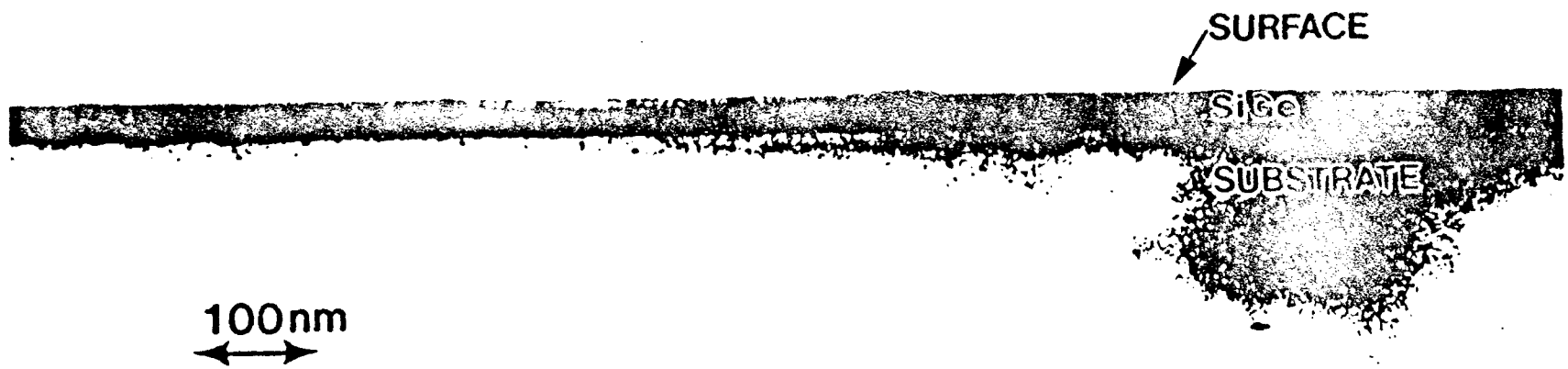


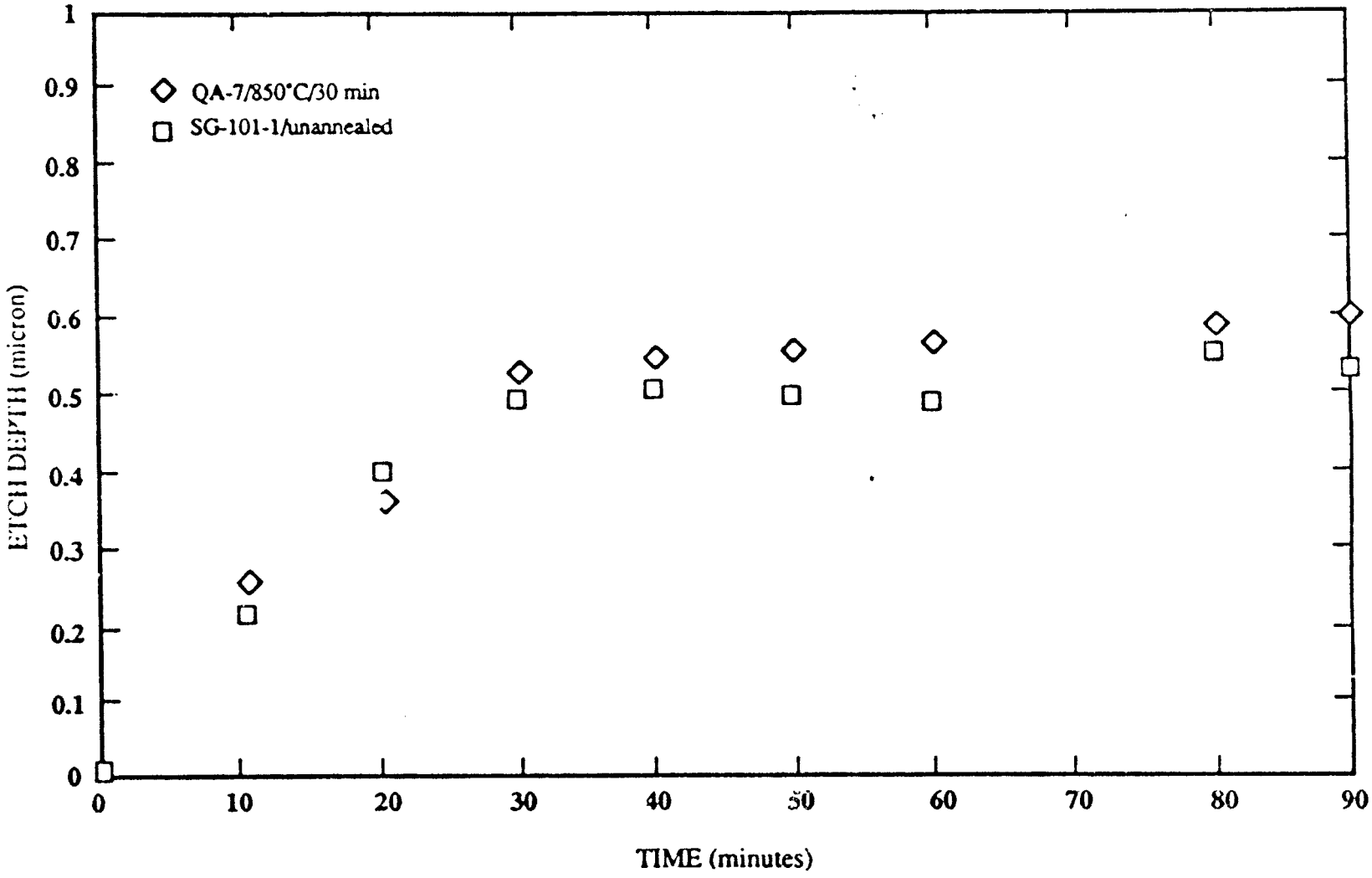
800°C 30min



RTA




SURFACE
SiGe
SUBSTRATE
100nm


QA-7/850°C/30 min
SG-101-1/unannealed
ETCH DEPTH (micron)
TIME (minutes)
0
0.1
0.2
0.3
0.4
0.5
0.6
0.7
0.8
0.9
1
0
10
20
30
40
50
60
70
80
90

Captions for figures

Figure 1: Etching results obtained for as-grown (square), and annealed to 850°C (diamond) $Si/Si_{0.7}Ge_{0.3}$ samples. The $Si_{0.7}Ge_{0.3}$ layer was 60 nm and the epilayer was 500 nm thick.

Figure 2: Cross sectional transmission electron micrograph of a Si/SiGe/substrate sample following thermal treatment to 850°C for 30 minutes, and selective etching through the silicon cap to midway through the $Si_{0.7}Ge_{0.3}$ layer.

Figure 3: Cross-sectional transmission electron micrographs of single $Si_{0.7}Ge_{0.3}$ layer grown on Si(100) with a 500 nm cap layer. Top: as grown; middle: annealed to 800°C for 30 minutes; bottom: rapid thermal anneal to 1200°C for 30 seconds.

Figure 4: Plan view transmission electron micrograph of single $Si_{0.7}Ge_{0.3}$ layer grown on Si(100) with a 500 nm cap after rapid thermal annealing to 1200°C for 30 seconds.

[10] A. Ishizaka and Y. Shiraki. J. Electrochem. Soc., **133**, 666 (1986).

[11] R. Hull, J.C. Bean, F. Cerdeira, A.T. Fiory, and J.M. Gibson. Appl. Phys. Lett., **48**, 56 (1986).

by the Defense Nuclear Agency under NRL contract N00014-87-C-2419.

References

[1] J.C. Sturm. Silicon on insulator and buried metals in semiconductors. Mater. Res. Soc., **107**, 295 (1987).

[2] P.L.F. Hemmet. Silicon on insulator and thin film transistor technology. Mater. Res. Soc., **53**, 207 (1986).

[3] W.P. Maszara, G. Goetz, A. Caviglia, and J.B. McKitterick. J. Appl. Phys., **64**, 4943 (1988).

[4] W.P. Maszara, G. Goetz, A. Caviglia, A. Cserhati, G. Johnson, and J.B. McKitterick. Silicon on insulator and buried metals in semiconductors. Mater. Res. Soc., **107**, 489 (1987).

[5] E.D. Palik, V.M. Bermudez, and O.J. Glembocki. J. Electrochem. Soc., **132**, 135 (1985).

[6] L.J. Palkuti, P. Ling, P. Leonov, H. Kawayoshi, R. Ormond, and J. Yuan. IEEE, **35**, 1653 (1988).

[7] J. Hersener, H.-J Herzog, and L. Csepregi. Microcircuit Engineering, page 309. Academic Press London, 1984.

[8] E. Kasper and J.C. Bean, editors. Silicon Molecular Beam Epitaxy. CRC Press, 1988.

[9] J.F. Gibbons, C.M. Gronet, and K.E. Williams. Appl. Phys. Lett., **47**, 721 (1986).

are confined to the alloy region. This observation is important in that the surface of the device region will be exposed after the etch stop layers are removed. Any dislocations propagating outside the alloy layer would likely cause a degradation in the quality of the SOI layer.

To verify that dislocations do not propagate outside the alloy layer, a plan view specimen of the RTA treated sample was prepared and imaged by TEM. As can be seen in figure 4, the dislocation network is fairly dense, but does not seem to propagate outside the alloy layer. Studies of the thermal stability of strained layer superlattices grown on Si(100) suggest similar results [11]. The containment of these defects in the alloy layers is extremely important for the potential application of SiGe alloys as an etch stop in bonded SOI technology.

The strain relief observed in as-grown material was 4×10^{-5}. Films thermally treated to 800°C, 850°C, and 900°C for 30 minutes, and to 1200 °C for 30 seconds, all experienced strain relief of 2×10^{-4}. None of the thermal treatments fully relaxed the alloy layers, and etching experiments demonstrated that all of the films retained fully functional etch stops.

In summary, a strain sensitive etch has been utilized and characterized for a single alloy etch stop layer composed of 60 nm of $Si_{0.7}Ge_{0.3}$ under a silicon cap layer 500 nm thick. Thermal treatments that are necessary to oxidize and bond this wafer in a bond and etch back process did not destroy the integrity of the etch stop. Misfit dislocations generated in the alloy layer by thermal treatments were found to be contained within this layer.

Acknowledgment

We would like to thank N. Green, A. Krist, and G. Campisi at NRL, and to J. Ngo at ARACOR for their assistance with this project. This work was supported

anneal to 850°C for 30 minutes, and after the wafer was selectively etched for 60 minutes. The 500 nm silicon cap as well as about half of the alloy layer had been removed by the etch. The micrograph shows that good surface uniformity had been obtained.

The stability of the system to thermal treatments that would be encountered during film processing was examined. For bond and etch back, this means that the etch stop and cap layers must be stable to oxidation and bonding temperatures. Samples that had been annealed to 850°C for 30 minutes were characterized by etching experiments as shown in figure 1. The etch rate through the cap layer was unchanged, but the etch rate through the alloy layer increased to 1.7 nm/min. This indicates that strain was only partially relieved by the thermal treatment, and that alloy layers still functioned effectively as an etch stop after thermal treatment. A similar etch rate was obtained for a sample heat treated by RTA at 1200°C for 30 seconds. Therefore, RTA processing does not compromise wafer etching, and may also be used for the bonding process. The demonstrated etch rate and selectivity of this etch stop/etchant system is effective for thinning processes requiring the removal of 2 μm of silicon with a thickness uniformity of 20 nm.

The extent of misfit dislocations arising from strain relief in as-grown and thermally treated samples was examined using (TEM). Figure 3 shows cross sectional images of samples that were as-grown, thermally treated to 800°C for 30 minutes, and treated by RTA to 1200°C for 30 seconds. The as-grown sample shows clean interfaces, and an apparent absence of misfit dislocations. The 800°C annealed sample shows the presence of some dislocations. But the sample subjected to the 1200°C RTA treatment incorporated substantial misfit dislocations, as well as an apparent degradation of the interfacial region.

An important result shown by the cross sectional images is that the dislocations

KOH, 4 g. $K_2Cr_2O_7$, and 100 mL propanol in 400 mL of water at 26°C in a temperature controlled rotary etch system. After cleaning the MBE grown wafers, they were dipped in HF to remove any oxide layers, dried, and immediately placed into the etch bath. Measurement of the etch depth was performed by resistivity profiling of the etched wafers. The change in the position of the buffer/substrate interface marker indicated the amount of silicon material removed from the wafer surface. In this way, the etch depth could be measured with a 20 nm precision. To simulate the selective etching of bonded wafers, etching was done through the 500 nm Si layer instead of through the back face as would be done following bonding of the wafers. Experiments involving bonded wafers that were thinned using precision machining to a nominal 2 μm thickness before selective etching are currently in progress, and will be reported elsewhere.

Etching experiments were performed on a series of samples prepared, and results are shown in figure 1. When an as grown sample was etched, the undoped MBE silicon layer etched at a rate of 17-20 nm/min, and was determined from the initial steep slope observed in figure 1. The as grown $Si_{0.7}Ge_{0.3}$ alloy etched at a rate of 1 nm/min as determined by the less steep part of the curve in figure 1, and this indicates that the selectivity was better than 17:1. For a 60 nm alloy layer, it takes about one hour for breakthrough of the etch stop region.

Etching uniformity was evaluated by resistivity profiling of multiple samples from the same wafer, and samples obtained from several wafers. Uniformity of the etch stop was within the 20 nm precision of the profiling measurement. Local etch uniformity was investigated by Nomarski microscopy and transmission electron microscopy (TEM), and careful inspection indicated a surface free from local step etch artifacts and surface pitting. A TEM cross sectional micrograph was obtained of the etched wafer, as shown in figure 2. The sample was prepared following an

In our process, a strained layer silicon-germanium alloy is grown on a silicon substrate, followed by a silicon cap of variable thickness. This cap is the region where devices will be built following bonding and thinning, hence it is important that the cap is left defect and impurity free. The etch stop can be grown into the seed wafer by techniques such as molecular beam epitaxy or chemical vapor deposition [8,9]. These growth techniques are well developed and generate a sharp silicon/alloy interface. In addition, this etch stop does not leave residual *p*- or *n*-type dopant in the cap layer.

Silicon wafers with an incorporated etch stop were prepared as follows: silicon wafers, *p*- or *n*-doped, were cleaned chemically using a variation of the Shiraki procedure [10]. The cleaned wafers were loaded into a Vacuum Generators V80 MBE system. Following a brief degassing and loading of the wafer into the growth chamber, the chemically grown oxide was removed in-vacuo by heating to 850°C for ten minutes.

A silicon buffer layer was grown at 650°C, between 100-200 nm thick, and at a rate of 1.4 Å/sec. In the buffer layer, gallium was incorporated in a 10 nm layer near the substrate/buffer interface to serve as a marker during etching experiments. The etch stop region was a $Si_{0.7}Ge_{0.3}$ alloy, and was grown at a rate of 2 Å/sec at a temperature of 500°C on the buffer layer. The silicon cap was grown to 500 nm on top of the etch stop at a rate of 2 Å/sec and at 500°C. Following deposition, the wafer was cooled to room temperature and removed from the vacuum system.

Temperature stability studies were performed in a tube furnace under flowing nitrogen. Prepared samples were annealed for 30 minutes at 800-900°C, and samples were also treated by rapid thermal annealing (RTA) to 1200°C for 30 seconds.

Etching was performed using a strain sensitive etchant composed of 100 g.

Silicon on insulator (SOI) substrates are in use for the fabrication of devices that are high speed, resistant to latch up, and are radiation hard [1]. SIMOX has been the most thoroughly studied SOI system to date to replace silicon on sapphire. This material is fabricated by oxygen implantation and annealing to generate a buried oxide [2]. Although SIMOX is a promising technology, threading dislocations generated by the implantation in the active device region limit the performance of the material. In addition, the buried oxide is of poor quality resulting in back channel leakage.

Bond and etch back technology as an alternative to SIMOX for SOI has the advantage of a cleaner oxide/silicon interface at the buried oxide [3,4]. This material is generated by oxidizing the seed and/or handle wafers, followed by bonding the two wafers. The active device region is exposed on the seed wafer by precision machining and etching to the desired film thickness. Although this technology is suitable for the fabrication of 600 nm SOI, the presence of an etch stop is essential to fabricate SOI wafers with a nominal Si film thickness of 250 nm or less. Heavily doped boron regions placed by diffusion or implantation into the silicon have been reported to make an effective etchstop [3,5], and CMOS devices fabricated from these materials display high bulk mobilities and excellent radiation hardness [6]. Silicon membrane technology uses similar boron etch stop with selective etch techniques to fabricate these materials [7]. However, boron incorporated by ion implantation and annealing results in the generation of threading dislocations in the device region, and both diffusion and implantation result in residual p doping. A potential solution to these problems is through the use of an as-grown $Si_{1-x}Ge_x$ alloy strained layer as an etch stop. In this communication we describe a system where defect free, thin film silicon on insulator can be fabricated using such an etch stop.

Office
7/26/89

Submitted APL
7/27

A $Si_{0.7}Ge_{0.3}$ Strained Layer Etch Stop for the Generation of Thin Layer Undoped Silicon

D. Godbey, H. Hughes, and F. Kub
Naval Research Laboratory
Electronics Science and Technology Division
Code 6816
Washington, D.C. 20375-5000

M. Twigg
GEO-Centers Inc.,
10903 Indian Head Highway
Suite 502
Fort Washington, MD 20744

L. Palkuti, P. Leonov, and J. Wang
ARACOR
425 Lakeside Dr.
Sunnyvale, CA 94086

Abstract

The use of a $Si_{0.7}Ge_{0.3}$ strained layer as an etch stop in silicon based materials is reported. The etch rates were characterized through silicon and a 60 nm $Si_{0.7}Ge_{0.3}$ strained layer. The etch rate through undoped silicon was 17-20 nm/min, while the etch rate through the $Si_{0.7}Ge_{0.3}$ layer was 1 nm/min. After annealing the wafer to 850°C for 30 minutes, transmission electron microscopy was used to show that strain in the alloy layer was only partially relieved, and that generated misfit dislocations were confined to the strained $Si_{0.7}Ge_{0.3}$ layer. The etch rate through the strained layer increased to 1.7 nm/min after this treatment, and was still perfectly functional as an etch stop.

APPENDIX D8

TABLE I. X-ray rocking curves for some thin-film semiconductors.

Film/substrate	T_{growth} (°C)	$T_{processed}$ (°C)	Thickness (nm)	FWHM (arcsec)
Ge/Al_2O_3	800	1400	450	317
Ge/Al_2O_3	700	1400	900	400
Ge/Al_2O_3	700	1100	900	575
Si/Al_2O_3[a]	unknown	unknown	390	1200
Si/Al_2O_3[b]	1000	···	630	950

[a] Reference 13.
[b] Reference 14.

could find reported in the literature. The films discussed in Ref. 13 was manufactured by Union Carbide, and had a FWHM of 1200 arcsec for the Si(400) reflection of a 390 nm film. Carey reported that a SOS sample measured gave an x-ray width of 950 arcsec for the Si(400) reflection.[14]

Some of the potential applications for the use of GOS include the development of electronic devices based on germanium where an insulating substrate is necessary. It may also provide a useful substrate on which to grow gallium arsenide since the lattice match between germanium and gallium arsenide is so close. The growth of GaAs on germanium has already been reported.[15]

In summary, crystalline germanium has been grown on $(1\bar{1}02)$ sapphire. The germanium grows with a (110) orientation, and a rocking curve obtained of the (220) reflection gave a full width at half maximum of 317 arcsec for a 500 nm film.

We would like to thank Joseph Pellegrino for many helpful discussions.

[1] J. C. Sturm, *Silicon on Insulator and Buried Metals in Semiconductors* (Materials Research Society, Pittsburgh, PA 1987), Mater. Res. Soc. Proc. Vol. 107, p. 295.
[2] J. C. Sturm, C. K. Chen, L. Pfeiffer, and P. L. F. Hemmett, eds., *Silicon on Insulator and Buried Metals in Semiconductors* (Materials Research Society, Pittsburgh, PA, 1987).
[3] N. V. Gudkova, T. A. Zeveke, T. N. Medvedeva, R. A. Rubtsova, and T. N. Struzheva, Sov. Phys. Crystallogr. 15, 747 (1971).
[4] R. F. Tramposch, J. Electrochem. Soc. 116, 654 (1969).
[5] J. S. Johannessen, Phys. Status Solidi A 10, 569 (1972).
[6] R. F. Tramposch, U.S. patent No. 3 589 936 (1971).
[7] M. S. Abrahams, C. J. Buiocchi, R. T. Smith, J. F. Corboy, J. Blanc, and G. W. Cullen, J. Appl. Phys. 47, 5139 (1976).
[8] J. Blanc and M. S. Abrahams, J. Appl. Phys. 47, 5151 (1976).
[9] M. E. Twigg and E. D. Richmond, J. Appl. Phys. 64, 3037 (1988).
[10] C. C. Chang, J. Vac. Sci. Technol. 8, 500 (1971).
[11] J. G. Pellegrino, E. D. Richmond, and M. E. Twigg, *SOI and Buried Materials* (Materials Research Society, Pittsburgh, PA, 1988), Mater. Res. Soc. Vol. 116, p. 389.
[12] J. C. Bean, Appl. Phys. Lett. 36, 741 (1980).
[13] T. Vreeland, J. Mater. Res. 1, 712 (1986).
[14] K. W. Carey, J. Cryst. Growth, 58, 1 (1982).
[15] Y. Fukuda and Y. Kohama, J. Cryst. Growth 81, 451 (1987).

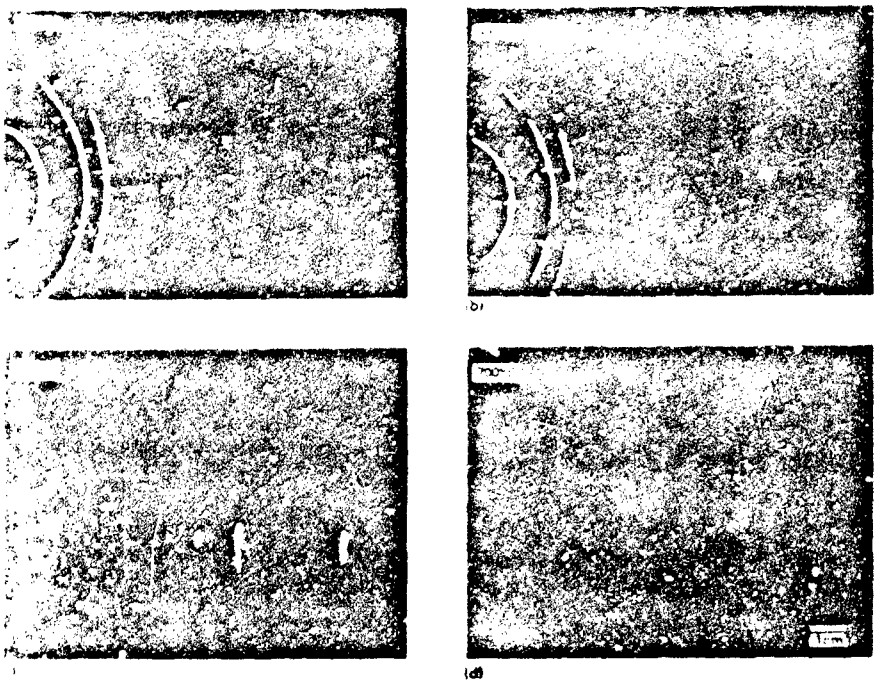


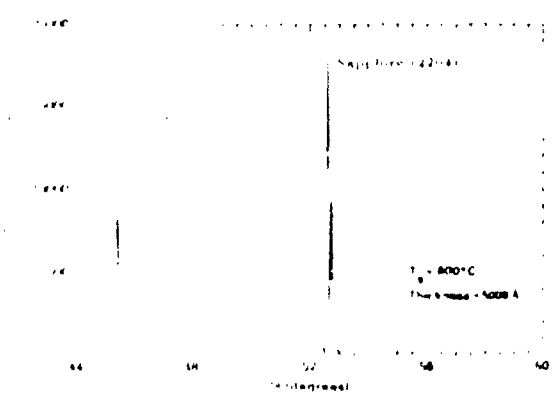
FIG. 1. Read camera diffraction patterns showing crystallinity as a function of substrate temperature for germanium grown on (1102) sapphire. The sapphire substrates were all preannealed at 1400 °C prior to growth, the growth temperatures are shown inset. The camera radius was 5 cm.

sured for a 900 nm film grown at 700 °C, as shown in Fig. 1. Higher temperatures are probably important in growing films because of the increased diffusion rate of germanium across the sapphire surface that is necessary for desorption to occur at the nucleated islands.

Table I also shows that the preanneal temperature is important because for two GOS films grown at 700 °C, the film grown on sapphire preannealed to 1400 °C generated a narrower rocking curve (400 arcsec) than the film grown on sapphire preannealed only to 1100 °C (575 arcsec). One possible explanation for this behavior is that during high-temperature annealing the sapphire surface undergoes reconstruction, resulting in a reduction of surface defects. In addition, it has been demonstated that contaminants such as carbon are effectively removed from the sapphire surface by high-temperature treatments, and perhaps even preferential desorption of oxygen occurs.[10] In a SOS study, Pellegrino *et al.* showed that a higher substrate preanneal temperature resulted in the growth of fewer and larger silicon islands on the sapphire surface, and this is consistent with a reduction in nucleating sites such as carbon and point defects.[11]

Germanium has been grown on sapphire previously,[3–6] but a review of the literature indicates that growing single-crystal GOS has been difficult at best. Apparently some pretreatment such as the preanneal treatment used in these experiments is crucial to the successful growth of this material. This pretreatment also enabled the successful growth of single-crystal silicon on sapphire using MBE by both Pellegrino *et al.*[11] and Bean.[12]

In comparing our GOS films to SOS films, we found that the FWHM of the diffraction peak from the GOS films grown in this laboratory was significantly narrower than the diffraction peaks of several representative SOS films we



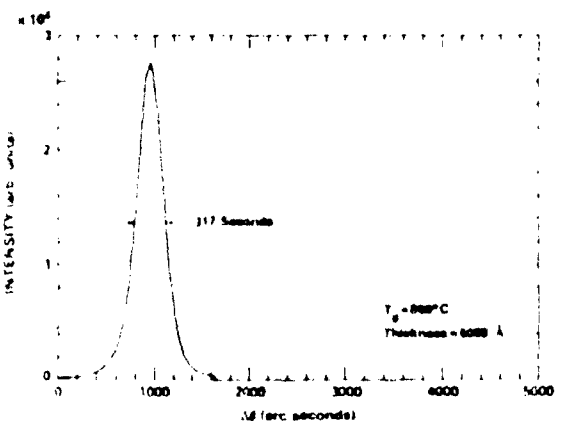


FIG. 3. (220) reflection obtained from Ge grown on (1102) sapphire measured with CuK_{α_1} radiation and a double crystal spectrometer. The first crystal is aligned to diffract the sapphire (2204) reflection. The film was grown at 500 °C on a 1400 °C annealed sapphire substrate to a thickness of 1400 nm.

Single-crystal germanium grown on (1$\bar{1}$02) sapphire by molecular beam epitaxy

D. J. Godbey, S. B. Qadri,[a] M. E. Twigg,[b] and E. D. Richmond
Naval Research Laboratory, Electronics Science and Technology Division Code 6816, Washington, DC 20375-5000

(Received 28 December 1988; accepted for publication 4 April 1989)

Crystalline germanium films have been successfully grown on the (1$\bar{1}$02) sapphire surface using molecular beam epitaxy. Growth at temperatures above 700 °C and after preannealing the sapphire substrates above 1100 °C resulted in germanium films with a (110) orientation. A 500 nm germanium film grown at 800 °C after preannealing the sapphire substrate at 1400 °C gave an x-ray rocking curve width that measured 317 arcsec at half maximum for the (220) reflection.

The growth of crystalline silicon on sapphire (SOS) is well established,[1] and has played an important role in some semiconductor applications.[2] Although the growth of germanium on sapphire (GOS) has been reported in the past,[3–6] to the best of our knowledge single-crystal films have been grown on only the (0001) plane and only after heavily doping the source germanium with arsenic.[4,6] The orientation displayed by these films was not revealed, however. In this letter we report the growth of (110) germanium on the *r* plane (or {1$\bar{1}$02}) of sapphire using molecular beam epitaxy (MBE).

Briefly, the procedure is as follows. The film growth was preceded by chemical cleaning of the sapphire (1$\bar{1}$02) substrates to remove both organic and inorganic contaminants. The wafers were rinsed sequentially in acetone, trichloroethylene, acetone, and methanol, followed by rinsing alternately in hot H_2O:HCl:H_2O_2, 4:1:1, and a 4% HF solution. The wafers were loaded in a Vacuum Generators V80 MBE system equipped with high-purity germanium loaded in an Airco-Temescal single hearth electron gun evaporation source. The sapphire substrates were preannealed between 1100 and 1400 °C, followed by the growth of the germanium films. The growth temperatures ranged from 400 to 800 °C, the growth rate was ~1 Å/s, and the film thicknesses attained were between 400 and 1000 nm.

The grown films were characterized using x-ray diffraction. A series of Read photographs taken as a function of film growth temperature is shown in Fig. 1. All of the films shown were preannealed at 1400 °C. The film grown at 400 °C had a highly reflective mirror-like finish, but the continuous arcs in Fig. 1(a) indicate that the germanium is polycrystalline. The remainder of the spots result from diffraction from the sapphire substrate. As the growth temperature was increased, the degree of polycrystallinity of the grown films decreased as shown in Figs. 1(b) and 1(c). At a growth temperature of 700 °C or above, spots were observed in the Read photos instead of arcs indicating that germanium had a definite preferred orientation [Fig. 1(d)].

The film orientation was determined by x-ray diffraction as shown in Fig. 2. A $\theta/2\theta$ scan of the film grown at 800 °C revealed only the (220) and the (440) reflections of germanium indicating that growth was along the [110] direction. This is in contrast to the (100) orientation that silicon displays when grown on sapphire (1$\bar{1}$02).[7–9] The figure shows the (220) reflection of germanium and the (2$\bar{2}$04) relfection of sapphire.

X-ray measurements were also made from reflecting planes perpendicular to the plane of the substrate. The wafer was cut along the ($\bar{1}$012) plane of sapphire, so that reflections could be observed from the ($\bar{1}$11) plane of germanium and ($\bar{1}$012) plane of sapphire. A cut made perpendicular to the first permitted the measurement of the reflections from the ($\bar{2}\bar{2}$4) plane of germanium, and the (01$\bar{1}$2) plane of the sapphire. This implies a misfit of 6.3% when comparing the interplanar spacings between ($\bar{1}$11) germanium and ($\bar{1}$012) sapphire, and a 0.45% misfit between ($\bar{2}\bar{2}$4) germanium and (03$\bar{3}$6) sapphire. Both the in-plane and perpendicular lattice parameters of germanium were measured to be 5.657 Å, indicating that no significant tetragonal distortion was present.

Transmission electron microscopy (TEM) observations have verified the orientational relationship [i.e., ($\bar{1}$11)/($\bar{1}$012); ($\bar{2}\bar{2}$4)/(01$\bar{1}$2)] between germanium and sapphire that was determined by x-ray diffraction. The presence of a second minor orientation was detected in the thinner films that is symmetrically related to the (110) orientation described above, via the (1$\bar{1}$20) mirror plane of sapphire [i.e, ($\bar{1}$11)/(01$\bar{1}$2); (2$\bar{2}$4)/($\bar{1}$012)]. A small fraction of germanium also assumes the twinned orientations corresponding to the germanium orientations present. This set of crystallographic relationships is identical to that identified by Abrahams *et al.* for (110) silicon islands grown on a (1$\bar{1}$02) sapphire substrate by chemical vapor deposition.[7] Although two orientations were detected in the thinner films by TEM, a single orientation was found to dominate in the germanium films, and x-ray measurements using an oscillating sample (Weissenberg) failed to detect the presence of a second orientation.

The quality of the films was further examined by measuring x-ray rocking curves for the (220) germanium reflections. The rocking curve of the film grown at 800 °C is shown in Fig. 3. The full width at half maximum (FWHM) for this film was 317 arcsec. The thickness of this film was 500 nm, but the width of the x-ray line was narrower than the line

[a] Address: Sachs/Freeman Associates Inc., 1401 McCormack Dr., Landover, MD 20785-5396.
[b] Address: GEO-Centers, Inc., 10903 Indian Head Highway, Suite 502, Fort Washington, MD 20744.

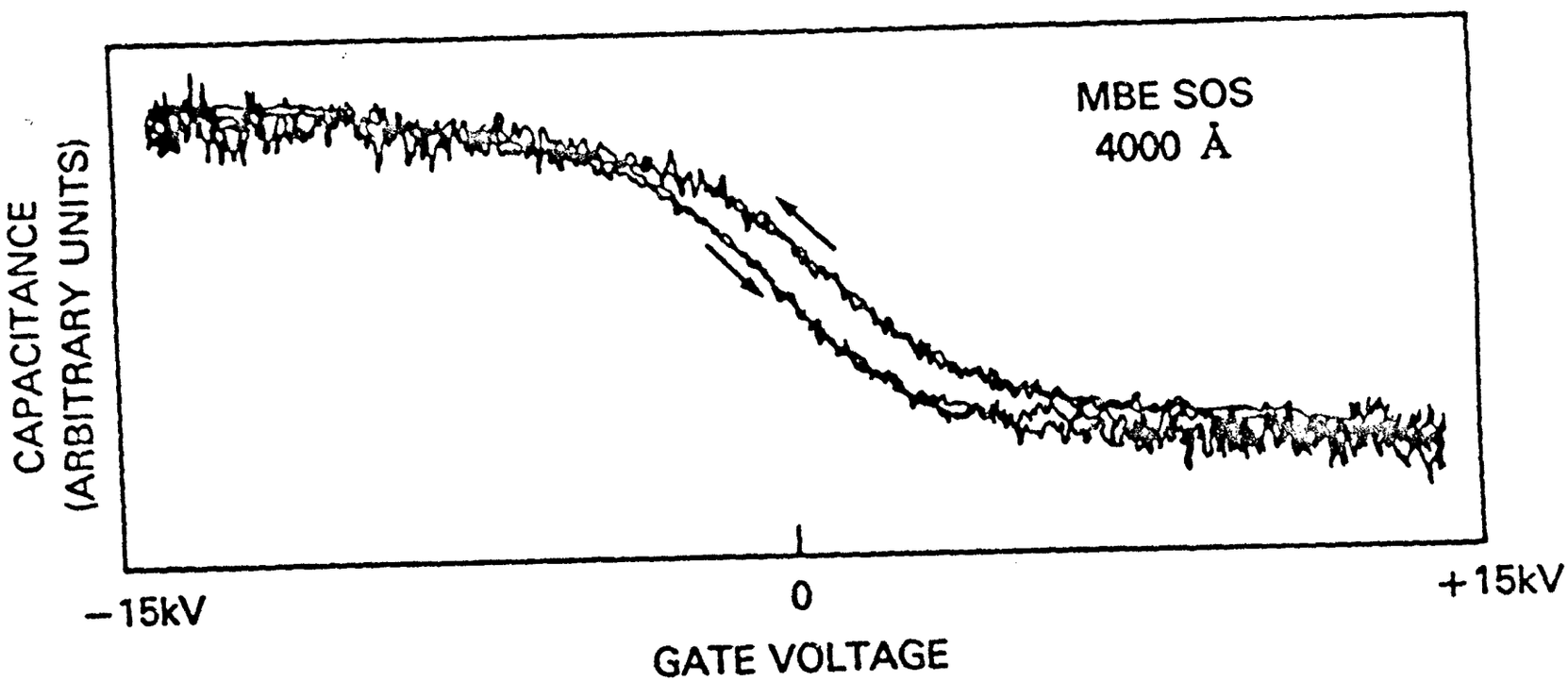
 0003-6951/89/242449-03$01.00 © 1989 American Institute of Physics

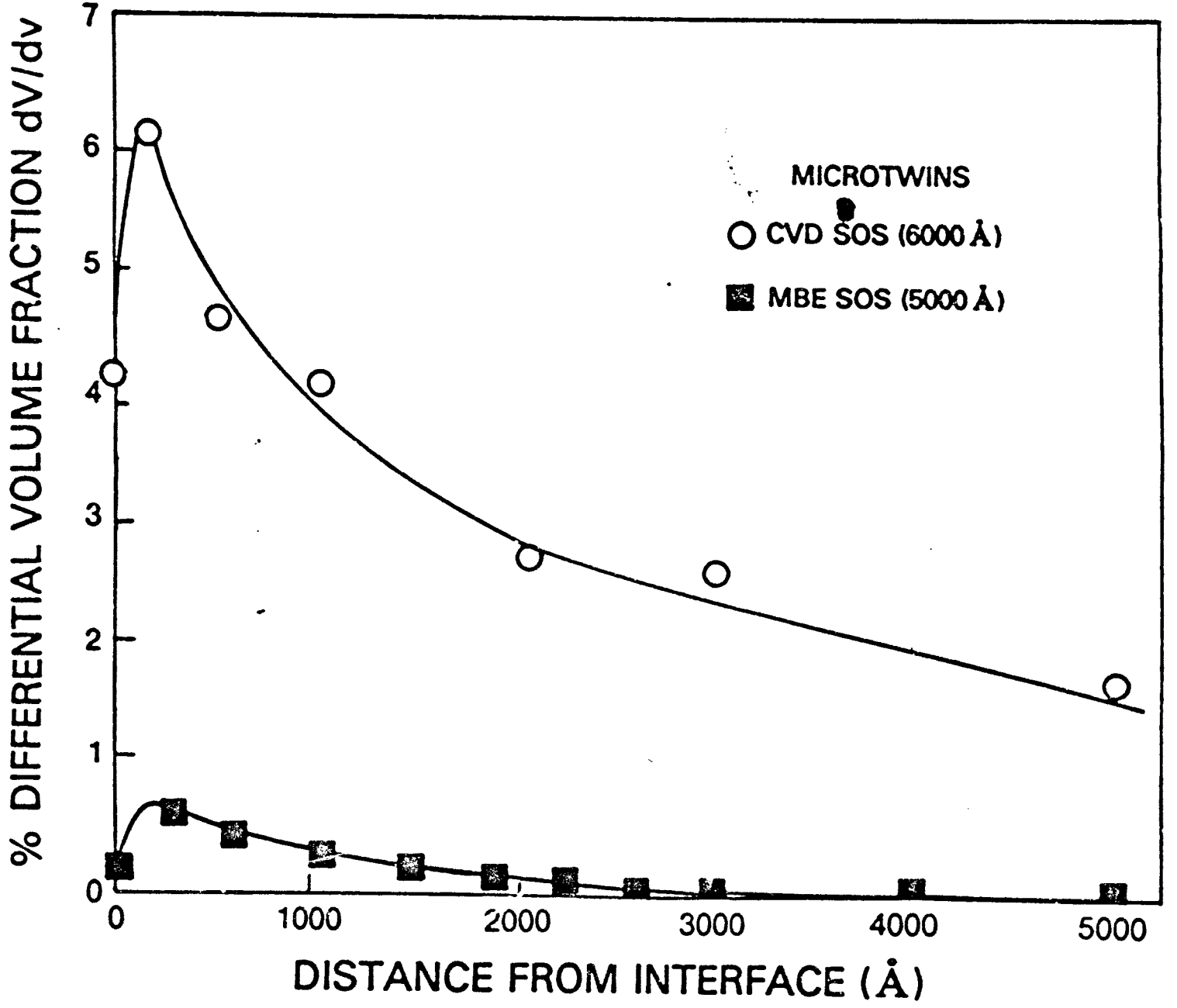
APPENDIX D7

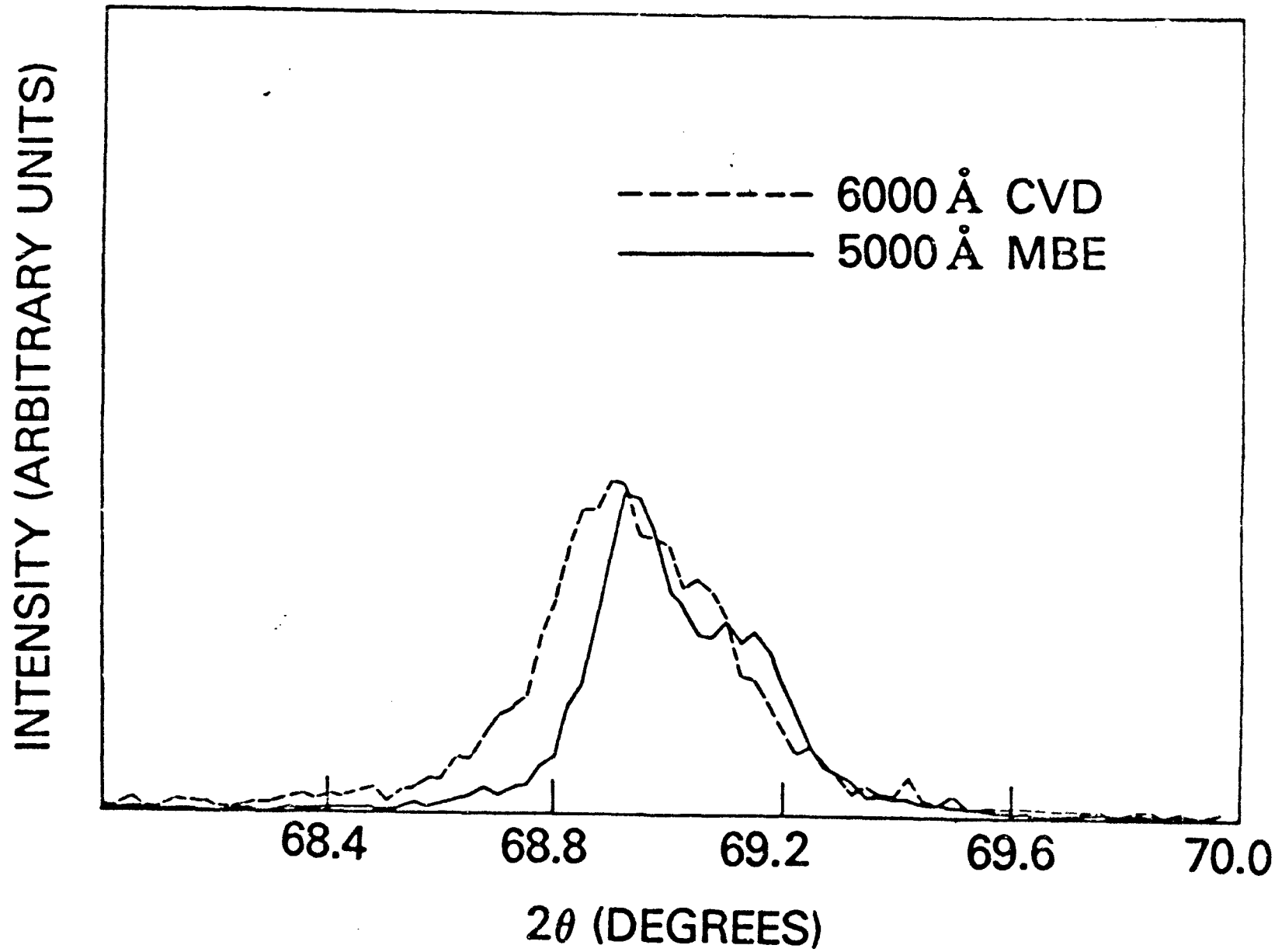
TABLE 1

ELECTRON HALL MOBILITY ($cm^2/V-sec$) AND CARRIER CONCENTRATION (cm^{-3})

T(°K)	MBE		CVD	
	μ_n	n	μ_n	n
300	405	4.5×10^{16}	290	5×10^{15}
77	588	4.2×10^{15}	68	2×10^{14}


MBE SOS
4000 Å
CAPACITANCE
(ARBITRARY UNITS)
−15kV
0
+15kV
GATE VOLTAGE


% DIFFERENTIAL VOLUME FRACTION dV/dv
7
6
5
4
3
2
1
0
0
1000
2000
3000
4000
5000
DISTANCE FROM INTERFACE (Å)
MICROTWINS
CVD SOS (6000 Å)
MBE SOS (5000 Å)


INTENSITY (ARBITRARY UNITS)
6000 Å CVD
5000 Å MBE
68.4
68.8
69.2
69.6
70.0
2θ (DEGREES)

CAPTIONS

1. The theta - 2 theta X-ray diffraction spectra of the (004) Si peak. For bulk Si the peak occurs at 69.17°.

2. The microtwin differential volume fraction for a 600 nm CVD SOS sample and a 500 nm MBE SOS sample.

3. The high voltage CV plot of a 400 nm MBE SOS wafer. The small amount of hysteresis is common to most insulating gate oxides; SiO_2 is an exception.

TABLES

1. The electron Hall mobility and carrier density on a van der Paux structure at room temperature and LN_2 temperatures. Note that the CVD SOS mobility decreases at LN_2 temperatures while the MBE SOS increases dramtically between room temperature and LN_2 temperature. Ther shape factor is .99 and .97 at room temperature and LN_2 temperature respectively.

REFERENCES:

1. H. M. Manasevit and W.I. Simpson, Proc. Am. Phys. Soc., Edmonton, Alberta, Canada, Late News Item (1963); ibid, J. Appl. Phys. 35, 1349 (1964).
2. a) G. W. Cullen, Heteroepitaxial Semiconductors for Electronic Devices, eds. G. Cullen and C. Wang (Springer Verlag, New York, 1978), chapt. 2.; b)P.K. Vasadev, Epitaxial Silicon Technology (Academic Press, New York, 1986), chapt. 4.
3. a) C. T. Naber and J. E. O'Neal, Trans AIME 242, 470 (1968); b) T. Itoh, S. Hasegawa, H. Watanabe, J. Appl. Phys. 39, 479 (1968); c) T. Itoh, S. Hasegawa, N. Kaminaka, J. Appl. Phys. 39, 5310 (1968); d) Y. Yasuda and Y. Ohmura, Japanese J. Appl. Phys. 8, 1098 (1969); e) C.C. Chang, J Vac. Sci. Technol 8, 500 (1971); f) A. G. Cullis and G. R. Booker, Thin Solid Films 31, 53 (1976).
4. a) T. Narusawa, S. Shimizu, and S. Komiya, J. Vac. Sci. Technol. 16, 366 (1979); b) S. Shimizu and S Komiya, J. Vac. Sci. Technol. 17, 489 (1980); c) J. C. Bean, Appl. Phys. Lett. 36, 741 (1980).
5. a) J.G. Pellegrino, M.E. Twigg, E.D. Richmond, SOI and Buried Metals (Materials Research Society, Pittsburgh, 1988), vol. 107, p. 383; b) Joseph G. Pellegrino, Eliezer D. Richmond, Mark E. Twigg, Heteroepitaxy on Silicon: Fundamentals, Structures, and Devices (MaterialsResearch Society, Pittsburgh, 1988), vol. 116, p. 389; c) Joseph Pellegrino, Syed Quadri, Eliezer Richmond, Mark Twigg, and Carl Vold, Heteroepitaxy on Silicon: fundamentals, Structures, and Devices (Materials Research Society, Pittsburgh, 1988), vol. 116, p. 395
6. Eliezer Dovid Richmond, to be published
7. Dave Dumin, Clemson University, private communication.
8. This is a pyrometer with a filter centered at 7.9 um with a pyroelectric detector manufactured by Capintec Instruments, Inc., 6 Arrow Rd. Ramsey, NJ 07446 - sapphire is opaque at this wavelength; previously in the data reported in ref. 5, the substrate temperature was reported to be 750°C determined by an estimate from the Eurotherm controller reading, but for the 1450°C annealed sapphire wafers the temperature is actually closer to 670°C.
9. Jan Maurits, Union Carbide Corporation, private communication
10. M.E. Twigg and E.D. Richmond, J Appl. Phys. 64, 3037 (1988)
11. M. T. Duffy, J.F. Corboy, W.E. Ham, P.J. Zanzucchi, J. Electrochem. Soc. 126, 341C (1979).
12. A.M. Goodman, IEEE Trans Electron Devices ED-21, 753 (1974); ibid, ED-22, 63 (1975).
13. M.E. Twigg, E.D. Richmond, and J. G. Pellegrino, Appl. Phys Lett. 54, 1766 (1989).
14. G. Robertson and P.K. Vasadev, Appl. Surf. Sci. 14 128 (1980)
15. F.T. Morin and J. P. Maita, Phys. Rev. 96, 28 (1954)
16. James L. Repace and Alvin M. Goodman, IEEE Trans Electron devices ED-25, 978 (1978).

positive interface charge in CVD Si/sapphire interfaces.

We would like to acknowledge the help of Dick Soltis in making some of the measurements, and the partial support of the Defense Nuclear Agency.

of other structural and chemical defects. The Hall data for the MBE SOS is indicative of much higher quality silicon epilayers, where phonon scattering dominates to lower temperatures[17] Conversely, in CVD SOS significantly higher defect densities result in electron scattering by charged defects[2b] at these lower temperatures.

The high voltage CV measurements are performed on 400 nm SOS thick samples. A typical CV plot for an MBE sample is shown in Fig. 3. The static Si/sapphire interface states at weak inversion Q_{SSWI} averaged over 3 wafers is -8.0×10^{10} cm^{-2}. Q_{SSWI} for the standard CVD process[18] is about $+2.0 \times 10^{12}$ cm^{-2}.

There are two significant differences between the Q_{SSWI} values for the MBE SOS and the CVD SOS. In the first place, the average interface charge at the Si/sapphire interface for the MBE epilayer is more than an order of magnitude below the interface charge for the CVD material. In the second place, quite striking, is the fact that the sign of the interface charge is negative. This indicates that the chemistry at the Si/sapphire interface for the MBE SOS is significantly different from the standard CVD SOS.

We have shown that the properties of the silicon epilayer are distinctively different between the MBE SOS and the CVD SOS, such that the MBE SOS can not be considered as merely a material improvement of the silicon epilayer of CVD SOS. The microstructural defects have a different morphology having more than an order of magnitude decrease in the microtwin differential volume fraction. In addition, the microtwin differential volume fraction decreases more rapidly for the MBE Si epilayers, decreasing to near the detectable limit at 300nm and below the detectable limit for film thicknesses above 500 nm. Growth at lower substrate temperatures or because of the vacuum annealing, the compressive shear stress of the MBE SOS is reduced. The reduction in defects and stress result in Si epilayers with 40% higher electron Hall mobilities at room temperature. The MBE SOS Hall mobility increases by 50% at LN_2 temperature, relative to its room temperature value, which is more indicative of bulk Si than CVD SOS. The MBE SOS Si/sapphire interface charge is smaller by more than an order of magnitude and is negative compared to the large

epilayers on sapphire, there is a tendency for the one volume fraction of microtwins to decrease with film thickness. For a 500 nm epilayer, one volume of microtwins is an order of magnitude less than for a 150 nm epilayer. For epilayers of 700 nm and thicker, one microtwin volume fraction is sufficiently small that it is difficult to quantify via TEM.[15]

Cross-section TEM micrographs indicate that the microtwins in the MBE epilayer are approximately 30% as wide as the microtwins in the CVD epilayer.

The 400 nm MBE SOS samples are examined by ultraviolet reflectance. The results gives a UVR number of 19, averaged over three wafers. This is compared to a 400nm CVD SOS sample with a UVR number < 22. This technique qualitatively evaluates the quality of the Si epilayer on sapphire. It is largely or completely a measure of the surface morphology of the epitaxial layer[16], as light of this wavelength penetrates only about 100 angstroms into the Si surface. Thus, the surface morphology of the CVD and MBE SOS epilayers is measurably but not drastically different. This result is confirmed by optical Nomarsky interferometry.

The results for the electron Hall mobility are listed in Table 1. The electron Hall mobility is 405 cm^2/V-sec for the 500 nm MBE sample and 290 cm^2/V-sec for the 600 nm CVD sample. This represents a 40% enhancement of the MBE SOS to CVD SOS room temperature mobility. The increase in mobility would be even greater if the film thicknesses were equal. Even more dramatic are the results at LN_2 temperatures. Here the MBE SOS mobility increases to 588 cm^2/V-sec with a carrier concentration of 4.2×10^{15} cm^{-3}. The CVD sample Hall mobility decreased to 68 cm^2/V-sec with a carrier concentration of 2×10^{14} cm^{-3}. We notice in both samples the freeze out of carriers is occurring. The shape factor for these Hall measurements is .99 for the room temperature measurements and .97 for the LN_2 measurements indicating the reliability of the data.

This Hall data for CVD SOS is in reasonable agreement with results obtained elsewhere[2b]. This increase of the MBE SOS mobility is consistent with the decrease in stress and the reduction of the microtwin volume discussed above, as well as the reduction

aluminum.

The (004) X-ray diffraction peak from the 500 nm MBE SOS film is shown in Fig. 1. In addition, the same diffraction peak from a 600 nm CVD SOS film is shown for comparison. The deviation of the peak position from the bulk Si value 0f 69.17° indicates the amount of the elastic strain in the epitaxial layer. We see from Fig. 1 that the deviation of the (004) diffraction peak for the MBE Si epilayer is 21% less than for the thicker CVD Si epilayer. This decrease in the angular position of the (004) peak reflects a decrease in the strain in the Si epilayer. For equivalent thicknesses, we expect this strain reduction to be greater, since the strain reduces with increased thickness[5c]. The reduced strain is felt to result from the lower substrate temperature during deposition or due to some property of the in-situ vacuum anneal.

Fig. 2 shows the microtwin differential volume fraction as a function of the distance from the Si/sapphire interface for a 600 nm CVD SOS and a 500 nm MBE SOS film. First, we note that the maximum microtwin differential volume fraction occurs several hundred angstroms in front of the interface. Thus, the largest volume of microtwins occurs in front of the Si/sapphire interface. The microtwin differential volume fraction is not to be confused with the microtwin density, which is maximum at the interface[10]. This phenomena occurs because the microtwins grow in size reaching a steady state configuration a few hundred angstroms from the interface. At the same time, the microtwins begin to annihilate with distance from the Si/sapphire interface. Therefore, the microtwin differential volume fraction, indicated in Fig. 2, maximizes near, but not at, the interface due to these two competing processes.

Fig. 2 illustrates that, for the 500 nm MBE SOS epilayer, the maximum differential microtwin volume is an order of magnitude or more lower throughout the entire film thickness compared to the CVD epilayer. In addition, the MBE SOS differential microtwin volume fraction decreases more rapidly with distance from the interface than in the CVD sample, effectively going to zero around 300 nm from the Si/sapphire interface. In MBE Si

The microtwin differential volume fraction and microtwin density are quantified by a new transmission electron microscopy (TEM) technique developed at NRL[10]. Prior to developing this technique, a method for quantitatively determining the microtwin volume fraction, as a function of the distance from the Si/sapphire interface, did not exist. The microtwin differential volume fraction represents the percentage of material which is twinned relative to the total amount of material at a given distance from the Si/sapphire interface. The microtwin differential volume fraction is determined from conventional and stereo TEM imaging of plan view samples, as well as from cross-sectional TEM observations.

Ultraviolet reflectometry[11] and Nomarsky microscopy are used to determine the epilayer morphology. The ultraviolet reflectance of the SOS sample and a bulk Si sample is measured at 280 nm. A UVR number is defined which is proportional to the difference in reflectivity.

A single crystal Phillips horizontal diffractometer with a copper target and a 0.5^{o} and 0.2^{o} source and detector slit widths is used to measure the (400) Si X-ray diffraction peak intensities.

The electron Hall mobility is measured. The experimental conditions consist of a magnetic field of 0.205 T, a test voltage of 5.6V, and a test current of 0.1 ma. A van der Pauw configuration is used. The MBE sample is uniformly implanted with phosphorous to give an electron density of 5×10^{16} cm^{-3}. The phosphorous is activated by a rapid thermal anneal at $950^{o}C$ for 5 min. in a N_2 ambient. The CVD sample is doped with phosphorous during growth and has an order of magnitude lower carrier concentration.

The Si/sapphire interface charge is obtained from high voltage capacitance-voltage (CV) plots[12], where the gate voltage varies between +20kV and -20kV, and the sapphire substrate is used as the gate oxide. The samples are prepared by implantation of the Si epilayer with boron prior to metallization. Aluminum dots, 0.8 cm in diameter, are deposited on the back of the sapphire substrate, and the Si side is completely coated with

Epitaxial Si layers on sapphire (SOS) is a technology which originated in 1963 with the work of Manasevits et al.[1] Chemical vapor deposition (CVD) resulted as the dominant deposition technique for SOS[2]. Nonetheless, a number of early experimenters deposited SOS by vacuum techniques[3] where the vacuum ranged from 10^{-11} to 10^{-6} torr, with higher vapor pressures existing during deposition. These films were grown at elevated substrate temperatures (750°C to 1100°C) and high rates (0.2 - 30 nm/sec). The substrate consisted of ither spinel or sapphire of various orientations. With the onset of Si Molecular Beam Epitaxy (MBE), several experimenters have grown epilayers with and without partial ionization[4]. Only in one instance[4c] was a high temperature anneal of 1400°C reported as a substrate pretreatment. In this case the sample was only flashed at this high temperature. Recently, NRL has made a concerted effort to investigate and characterize the growth kinetics and characteristics of Si on (1102) sapphire substrates.[5] In these investigations the substrate is preannealed in-situ at high temperatures for 30 min. The Si is deposited at a deposition rate of 0.05 - 0.10 nm/sec. In this paper the microstructural defects, strain, and electrical properties of MBE SOS are compared and found superior to CVD SOS.

The substrate preparation and deposition were performed in the NRL VG80 Si MBE/Surface-Analytical System.[6] Silicon films are deposited on Union Carbide 3" substrates with a (1102) orientation. The substrates are prepared first by a chemical cleaning procedure[7] followed by an annealing in vacuum at 1450°C for 30 min. After the high temperature anneal, the substrate is immediately transferred to the deposition chamber and a 400 nm or 500 nm epitaxial film is deposited at 0.1 nm/sec. The substrate temperature during deposition was 670°C measured by a specially designed Capintec pyrometer[8] with the emissivity set to 0.93. The base pressure of the system is 2×10^{-11} torr and the deposition pressure is 1×10^{-9} torr. The MBE SOS is compared to CVD SOS of approximately the same thickness. The CVD wafers are grown on (1102) sapphire wafers after a 10 min. anneal in H_2 at 1150°C with the epilayer deposited at a pyrometer measured substrate temperature of 920°C and a deposition rate of 33 nm/sec.[9]

submitted APL

MOLECULAR BEAM EPITAXY VS. CHEMICAL VAPOR DEPOSITION OF SILICON ON SAPPHIRE

Eliezer Dovid Richmond, Joseph G. Pellegrino*, Mark E. Twigg**,

Bernard Mrstik

Naval Research Laboratory, Code 6816, Washington, D.C. 20375-5000

Michael T. Duffy

David Sarnoff Research Center, Princeton, N.J. 08543-5300

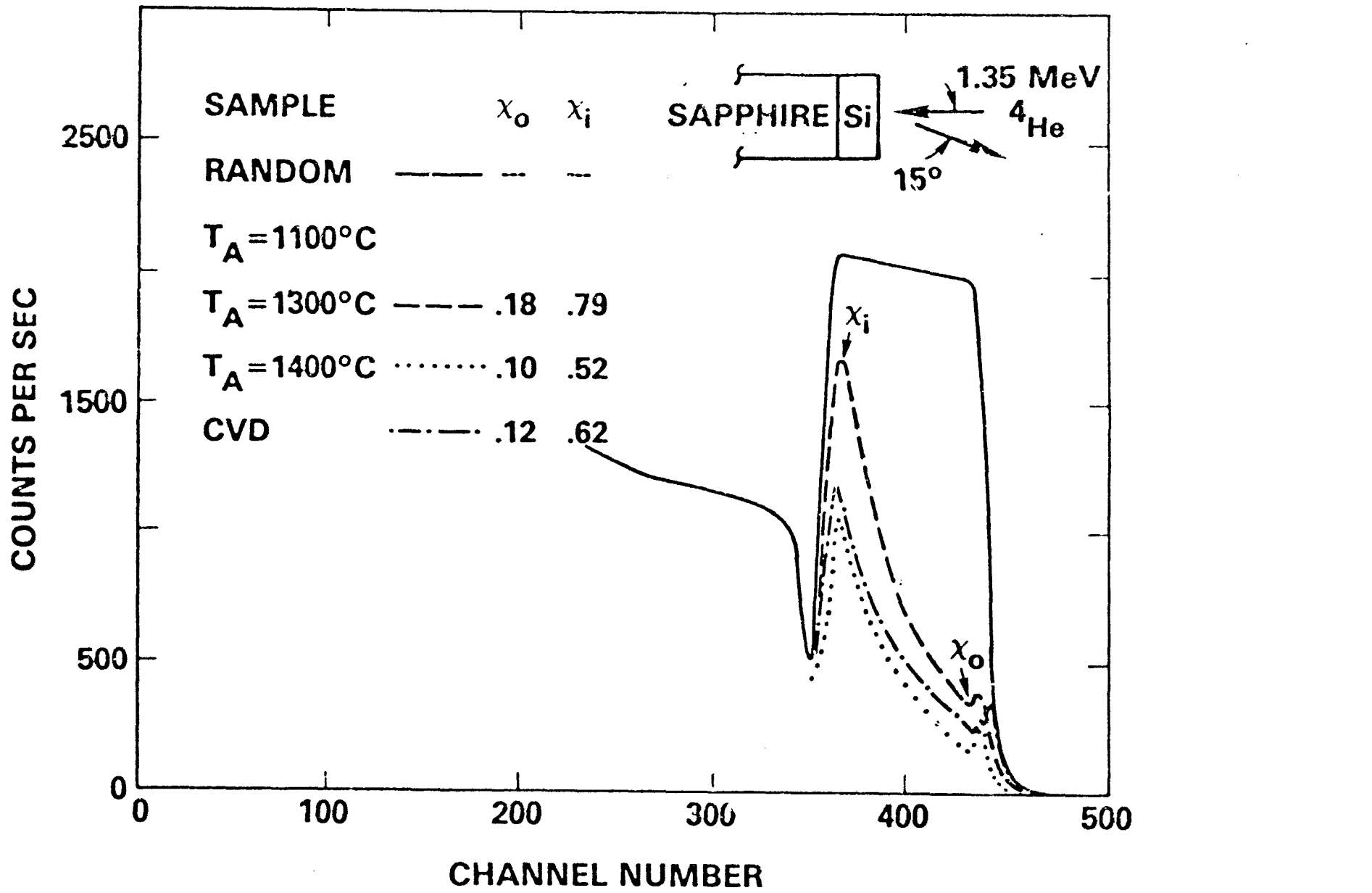
*NIST, Bldg 225, Gaithersburg, Md. 20889

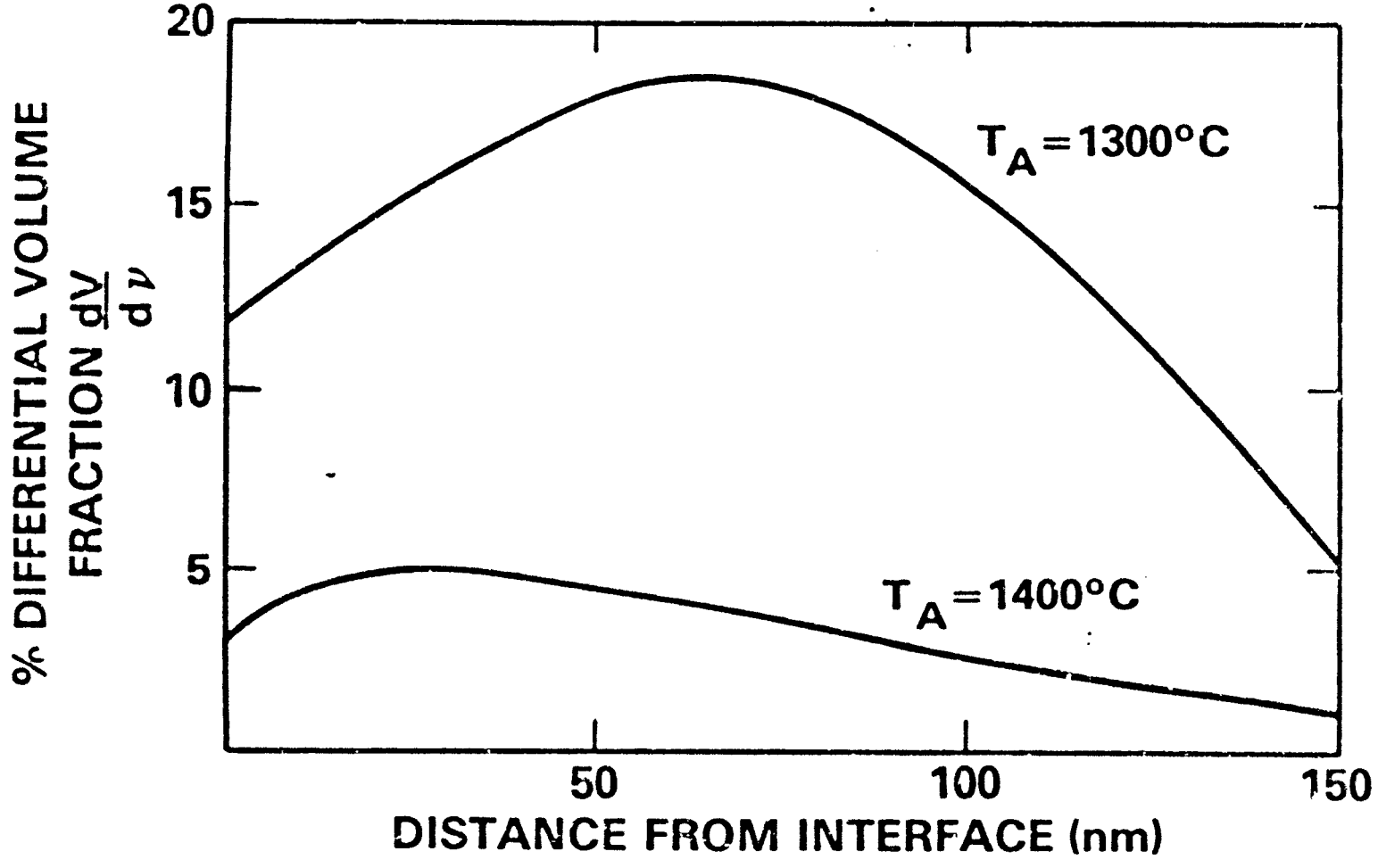
**GEO-Centers, Inc., 10903 Indian Head Highway, Fort Washington, Md. 20744

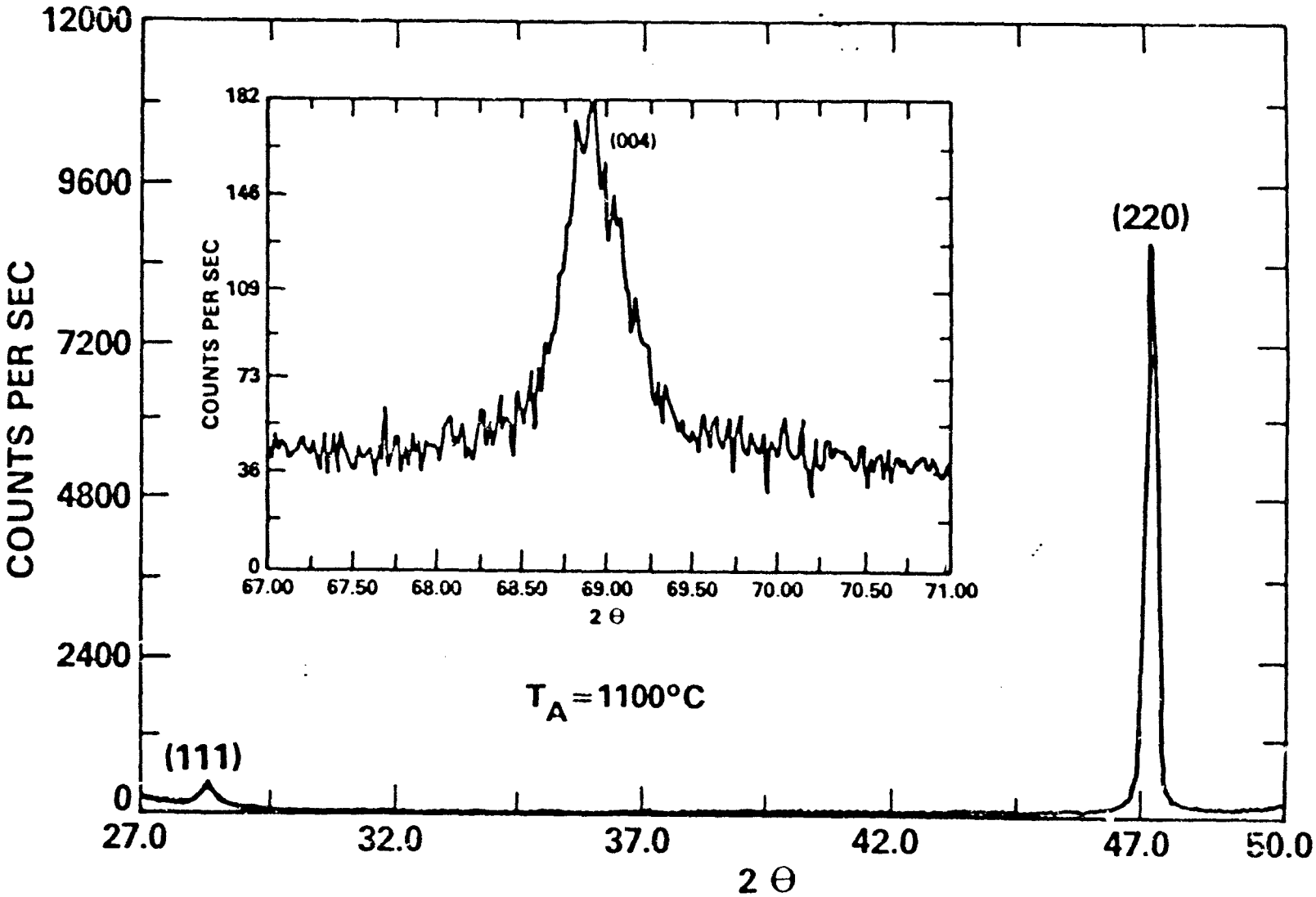
ABSTRACT

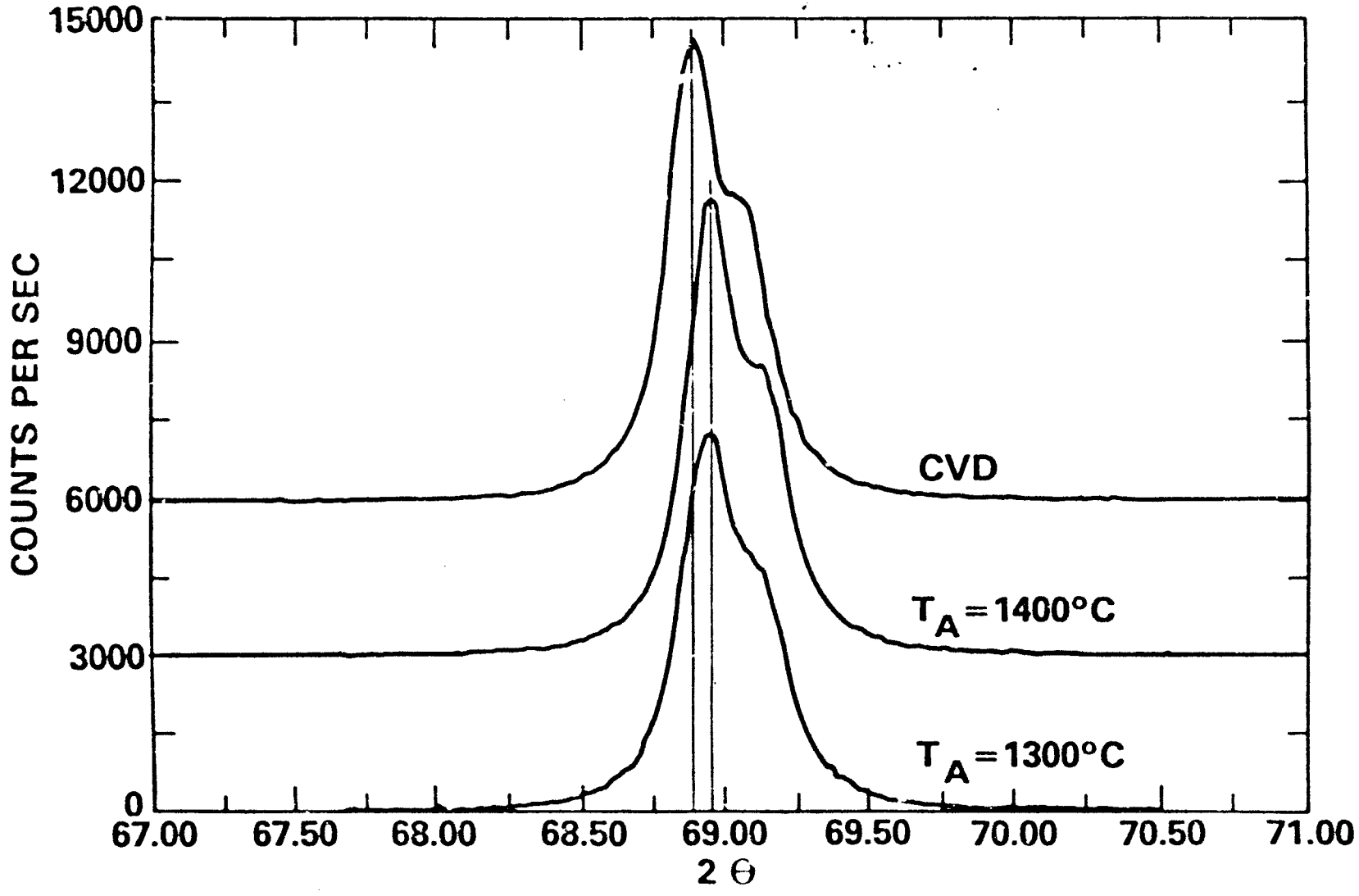
Molecular Beam Epitaxy (MBE) of Si on Sapphire (SOS) has dramatically different and superior properties compared to Chemical Vapor Deposited (CVD) SOS. The strain in the Si epilayer decreases by 21%. A 40% higher electron Hall mobility occurs at room temperature. At LN_2 temperatures the electron mobility increases to a level which is more indicative of bulk Si than of CVD SOS. The microtwin differential volume fraction profile is lower by more than an order of magnitude, and decreases below the detectable limit at 300 nm from the interface. The average Si/sapphire interface charge for MBE SOS is -8.0×10^{10} cm^{-2}, while the interface charge of CVD SOS is 2×10^{12} cm^{-2}.

APPENDIX D6


SAMPLE
χ_o
χ_i
RANDOM
T_A=1100°C
T_A=1300°C .18 .79
T_A=1400°C .10 .52
CVD .12 .62
SAPPHIRE
Si
1.35 MeV
^{4}He
15°
χ_i
χ_o
COUNTS PER SEC
2500
1500
500
0
0
100
200
300
400
500
CHANNEL NUMBER


20
15
10
5
% DIFFERENTIAL VOLUME FRACTION dV/dν
T_A=1300°C
T_A=1400°C
50
100
150
DISTANCE FROM INTERFACE (nm)


12000
9600
7200
4800
2400
0
COUNTS PER SEC
27.0
32.0
37.0
42.0
47.0
50.0
2 Θ
(111)
(220)
$T_A = 1100°C$
182
146
109
73
36
0
COUNTS PER SEC
(004)
67.00
67.50
68.00
68.50
69.00
69.50
70.00
70.50
71.00
2 Θ


15000
12000
9000
6000
3000
0
COUNTS PER SEC
CVD
$T_A = 1400°C$
$T_A = 1300°C$
67.00
67.50
68.00
68.50
69.00
69.50
70.00
70.50
71.00
2 θ

CAPTIONS

1. The X-ray diffraction spectra for the (004) Si peak for a CVD SOS standard and the MBE SOS epilayers grown on substrates annealed in-situ at 1300° C and 1410° C. The (004) peak for bulk Si occurs at $2\theta = 69.128°$. The zero of the different X-ray spectra are offset for clarity.

2. The X-ray diffraction spectrum for the MBE SOS layer grown on a substrate annealed at 1100° C. The layer is polycrystalline with a strong (022) texture.

3. The microtwin differential volume fraction (MDVF) for 0.15μm MBE SOS epilayers grown on substrates at the annealing temperatures indicated. Note that for $T_a = 1300°$ C the mdvf is much greater and the peak occurs further from the Si/sapphire interface.

4. The MeV $^4He^+$ dechanneling. The dechanneling ratio at the surface χ_0 and at the interface χ_i are shown for the different MBE SOS and CVD SOS epilayers. For $T_a = 1100°$, the dechanneling spectrum coincides with the random spectrum.

REFERENCES:

1. C.C. Chang, J. Vac. Sci. and Technol. 8, 500 (1971).
2. T. Narusawa, S. Shimizu, and S. Komiya, J. Vac. Sci. Technol. 16, 366 (1979).
3. Yukio Yasuda and Yamichi Ohmura, Jap. J. Appl. Phys. 8, 1058 (1969).
4. C. T. Naber and J. E. O'Neal, Trans TMS-AIME 242, 470 (1968).
5. J. C. Bean, Appl. Phys. Lett. 36, 741 (1980).
6. a) J.G. Pellegrino, M.E. Twigg, E.D. Richmond, SOI and Buried Metals (Materials Research Society, Pittsburgh, 1988), vol. 107, p. 383; Joseph G. Pellegrino, Eliezer D. Richmond, Mark E. Twigg, Heteroepitaxy on Silicon: Funadamentals, Structues, anmd Devices (Materials Research Society, Pittsburgh, 1988), vol. 116, p. 389; c) Joseph G. Pellegrino, Syed Qadri, Eliezer Richmond, Mark Twigg, and Carl Vold, Heteroepitaxy on Silicon: Funadamentals, Structues, anmd Devices (Materials Research Society, Pittsburgh, 1988), vol. 116, p. 395; d) Eliezer Dovid Richmond, Joseph G. Pellegrino, Mark E. Twigg, and Syed Qadri, submitted for publication and presented at the II International Symposium on Si MBE 30 May - 2 June, 1989, Strasbourg, France.
7. Dave Dumin, Clemson University, private communication.
8. W. Kern and D. A. Polito, RCA Rev. 31, 187 (1970).
9. E.D. Richmond, to be published.
10. M.E. Twigg and E.D. Richmond, J. Appl. Phys. 64, 3037 (1988).
11. T. Vreeland Jr., A. Dommann, C. J. Tsai, and N.A. Nicolet, Thin Films: Stresses and Mechanical Properties (materials research Society, Pittsburgh), vol. 130, p. 3 (1989).
12. T.Vreeland Jr., J. Mater. Res. 1, 712 (1986).
13. Mark Window, Studies of Heteroepitaxial Films Silicon and Cadmium Telluride on Sapphire, Ph.D. Thesis submitted to the University of Liverpool (1989).
14. M.E. Twigg, E.D. Richmond, and J. G. Pellegrino, Appl. Phys. Lett. 54, 1766 (1989).
15. K.A.W. Carey, Silicon on Sapphire: An investigation of the Defect Structure, Ph.D. Thesis submitted to Stanford University (1982).
16. A. Christou, E.D. Richmond, B.R. Wilkins, and A.R. Knudson, Apll. Phys. Lett. 44, 796 (1984).

annealed substrates is superior to CVD SOS. The crystalline quality of the MBE epilayers quickly degrades as the substrate annealing temperature decreases.

We would like to acknowledge the partial support of the Defense Nuclear Agency.

Thus for CVD SOS, one can reasonably interpret the dechanneling in terms of microtwins. For The MBE SOS, especially in the case of the 1410° C sample, we see that while the crystalline quality is only about 20% better as measured by the dechanneling ratio, the expected difference in the twin volume is greater[14] by a factor of 2 to 10. Therefore the dechanneling spectra of the MBE samples is composed of contributions from both planar defects and line defects. The dechanneling spectrum of an MBE SOS sample containing only dislocations is found in Christou et al.[16] This spectrum[16] looks deceivingly like a spectrum resulting only from microtwins, but subsequent cross-section TEM micrographs revealed that the microstructure consisted entirely of dislocations.[17]

SUMMARY:

We have shown that the in-situ vacuum annealing temperature of the sapphire substrate prior to deposition of an epilayer of silicon makes a significant difference in the defect microstructure and crystalline quality of the epilayer. For annealing temperatures above 1100° C, epilayers with a (001) orientation are obtained. At lower temperatures, 1100° C or less, polycrystalline or amorphous layers[8a] are obtained. The MBE SOS epilayers have 24% less tensile strain normal to the epilayer surface relative to the CVD SOS epilayer. The strain in the MBE SOS is independent of substrate annealing temperature and therefore must be a function of the growth kinetics or the chemistry and structure of the sapphire surface. For an annealing temperature of 1100° C the Si film was polycrystalline with a strong (011) texture. The twin volume increases strongly as the substrate annealing temperature decreases. In addition, the peak of the microtwin differential volume fraction shifts to larger distances from the Si/sapphire interface as the substrate annealing temperature decreases. The change occurs principally from the thickening of the microtwins. The X-ray diffraction results and the $^4He^+$ ion MeV dechanneling indicates that the MBE silicon epilayers have higher densities of dislocations than their CVD counterpart. The crystalline quality of the MBE epilayers on 1410° C

microtwins in the epilayers of the lower annealed substrates continue to grow in thickness and width over larger distance from the Si/sapphire interface. This results in the peak occurring further from the interface assuming that the annihilation processes are approximately the same in both epilayers. It should be noted that if the MBE samples analyzed by TEM were 0.3μm thick, then the MDVF would be systematically smaller in both cases.[14]

The microtwin density for the MBE epilayers has the opposite behavior with substrate annealing temperature than the MDVF. The microtwin density increases with increasing substrate annealing temperature. The difference between the 1410° C sample and the 1300° C sample is much less than the difference in the MDVF. Thus, the microtwins in the 1300° C sample are substantially larger, so that the twin volume is larger, but they are fewer in number. On the other hand, when the substrate is heated to a higher temperature, the microtwins are smaller in size and occur more frequently.

The MeV dechanneling results are shown in Fig. 4. Only one random RBS curve is shown for purposes of clarity. But, as noted above the random curve for the four samples analyzed increased in FWHM in approximately 5% intervals from the 1300° C MBE sample to the 1410° C MBE sample to the CVD sample. For the 1100° C MBE sample the MeV dechanneling spectrum is identical to the random spectra indicating a polycrystalline sample, which is consistent with the XRD results shown in Fig. 2. The large dechanneling spectrum of the 1300° C sample indicates that it has the poorest crystalline quality. This is due to the high twin volume in this epilayer. The values of the dechanneling ratio χ_0 at the silicon surface, and χ_i at the silicon/sapphire interface are given in Fig. 4. The best dechanneling spectrum occurs for the 1410° C MBE sample indicating that it has the best crystalline quality. It is interesting to examine what disorder in the Si epilayer contributes to the MeV dechanneling of $^4He^+$ ions. In CVD SOS, the dislocation density[18] is approximately $10^{10}/cm^2$. This represents about the density threshold at which dislocations would make a significant contribution above the crystalline Si axial dechanneling spectrum.

discussed below (Fig. 3), the twin volume of the MBE T_a = 1410° C epilayer is lower than for the T_a = 1300° C epilayer. Therefore one would expect a decrease in the (004) peak intensity for the silicon epilayer on a 1300° C annealed substrate compared to the silicon epilayer on a 1400° C annealed substrate.

This explanation does not address the case of the CVD Si epilayer, in which the twin volume is larger and the (004) intensity greater than the MBE Si epilayer grown on a 1410° C annealed substrate. Part of this increase (≈5%) can be accounted for by the larger thickness of the silicon epilayer of the CVD sample as measured by Rutherford backscattering spectroscopy (RBS). Therefore, we postulate that the MBE epilayers must contain another contribution to the decrease of the XRD intensity. We suggest that the MBE epilayers contain a higher density of dislocations compared to the CVD epilayers. Thus the T_a = 1410° C sample will have a lower (004) XRD intensity than the CVD sample. The dislocations in SOS are being investigated by TEM, but the complexity of the SOS system makes even qualitative evaluation difficult[1,3]. Rocking curves will aid in further understanding of this intensity phenomena.

Fig. 2 shows the XRD results for the sample where the substrate is annealed at 1100° C. Here we find that the Si layer is not epitaxial, but is polycrystalline. The sample is highly textured with a preferred orientation in the <022> direction with an intensity ratio of about 50:1 compared to the (004) and (111) orientations. There is also a (022) contribution to both the T_a = 1410° C and T_a = 1300° C.

The MDVF, Fig. 3, evidences dramatic differences as a function of substrate annealing. The most distinctive feature is that the microtwin volume of the epilayers deposited on lower temperature annealed substrates is dramatically higher. In addition, we find that the peak of the MDVF occurs at a distance of 600Å from the Si/sapphire interface for the 1300° C MBE sample, but peaks closer to the Si/sapphire interface at 200Å for the 1410° C MBE sample. The peak results from the competition of two processes. One is the growth in size of the microtwin, and the second is the annihilation of the microtwins. The

and I = 10 ma for the (024) sapphire peak, V = 40 kV, I = 30 ma for the silicon (004) peak and V = 50 kV, I = 200 ma for the sample with the substrate annealed at 1100° C.

The dechanneling measurements are made on a 3 MeV Tandem Van der Graaff using $^4He^+$ at an energy of 1.35 MeV. The $^4He^+$ beam is incident normal to the sample surface so that channeling occurred along the <100> axis. The backscattered ions are counted using a silicon barrier detector at an angle of 165°. The offset of the detector is near zero.

RESULTS AND DISCUSSION

The XRD results for the (004) Si peak for the T_a = 1410° C and 1300° C samples are shown in Fig. 1. The main peak represents the $K\alpha_1$ contribution. The high angle shoulder results from the $K\alpha_2$ contribution. For bulk Si, 2θ = 69.128°. The (004) Si peak can be interpreted directly as the normal strain of the film[11] Therefore, the Si epilayer is under tensile strain normal to the sample. Consequently, due to tetragonal distortion, the in-plane strain would be compressive as found previously[6,12]. The reduction in strain in the MBE epilayers compared to the CVD epilayer corresponds to a difference $\Delta(2\theta)$ = 0.06°. This corresponds to a decrease of 24% in the tensile strain of the MBE SOS epilayers relative to the CVD SOS epilayers. The strain decrease for the MBE SOS is independent of the in-situ substrate annealing temperature. Therefore we may conclude that the shift in strain is a result of the parameters governing the growth kinetics, such as the growth rate, growth temperature, or ambient. Alternately, there may be some change in the surface chemistry and surface structure above some temperature threshold which causes the reduction in strain, and change in the microstructural defects.

Even though the strain between the MBE SOS and the CVD SOS is independent of the substrate annealing temperature, the peak intensity decreases as we progress from the CVD sample to the T_a = 1410° C MBE sample to the T_a = 1300° C MBE sample. For the MBE samples, this may be explained by the differences in the defect microstructure. As

sample crystallinity is measured by X-ray diffractometry (XRD). The crystalline quality of the silicon epilayer is characterized by MeV $^4He^+$ ion dechanneling.

EXPERIMENT

Silicon films are deposited on Union Carbide 3" wafers with a (1102) orientation. The substrates are first cleaned by a chemical cleaning procedure[7] which is a modification of the RCA clean[8]. The major modifications consist of a substitution of H_2SO_4:H_2O_2 in a ratio of 1:1 instead of the NH_4OH:H_2O_2:H_2O peroxide solution in the RCA clean, and a 30 min. etch in a dilute 1:10 HF:H_2O solution.

Afterwards, the substrate is inserted into the NRL VG80 Si MBE/Surface-Analytical System[4,6]. The sapphire substrates were annealed at 1410° C, 1300° C, and 1100° C. The Si is deposited at 0.5μm to 1.0Å/sec. with an epilayer thickness of 0.15μm or 0.3μm. The thinner films are used for transmission electron microscopy and the thicker films are analyzed by X-ray diffraction and MeV $^4He^+$ ion dechanneling. These results are compared with a 0.3μm thick SOS wafer grown by chemical vapor deposition at Union Carbide Corp.

The microtwin differential volume fraction (MDVF) and microtwin density are quantified by a new TEM technique developed at NRL[10]. Prior to developing this technique, a method for quantitatively determining the microtwin volume fraction, as a function of the distance from the Si/sapphire interface, did not exist. The MDVF represents the percentage of silicon which is twinned relative to the total amount of material in a differential thickness dz at a given distance z' from the Si/sapphire interface. The MDVF is determined from conventional and stereo TEM imaging of plan view samples, as well as from cross-sectional TEM observations.

The X-ray diffraction measurements are performed on a Rigaku SU2000 Rotating Anode with a Cu target. The diffractometer was aligned to the (024) peak of the sapphire substrate before taking spectra. The power settings of the diffractometer were V = 20 kV

INTRODUCTION

Since the inception of the silicon on sapphire (SOS) technology, a number of investigations have pursued the deposition of the silicon epilayer by vapor deposition in a vacuum. Only a limited number of these have used in-situ high temperature annealing of the sapphire substrate as a technique or part of a technique for preparation of the sapphire substrate for silicon deposition. In addition, little attention has been paid to the analysis of the microstructural defects, crystallinity, and crystalline quality of the resulting silicon epilayer. Chang[1] studied the effect of high temperature annealing on the sapphire substrate by AES and LEED. In this case, substrate temperatures up to 1700° C were used. The sapphire substrates were 1 cm square, and heated by depositing a tantalum film on the back of the sample, and then passing a current through the tantalum film. This technique inherently suffers from nonuniform temperature distributions across the sample and stress in the substrate owing to the differences in the linear coefficient of expansion between the sapphire and tantalum and temperature gradients. Chang did not report whether there was any chemical cleaning process before inserting the sample in the vacuum system. Narusuwa et al.[2] annealed samples in-situ up 1100° C for 20 min. and examined the silicon epilayer with RHEED. Yasuda et al.[3] outgassed their samples up to 1100° C for 1 hr. in-situ before growth, and grew at substrate temperatures ranging from 850° C to 1050° C. They examined the films with replica microscopy for defect analysis. Naber et al.[4] annealed the samples at 1200° C and from RHEED results determined that the epilayer crystalline quality was poor. Bean[5] flashed the substrate at 1400° C, showed MeV dechanneling results only for the bare sapphire substrate, but stated that this technique resulted in lower mobilities and poorer crystalline quality.

Recently, NRL has made a concerted effort to investigate and characterize the growth kinetics and characteristics of silicon on (1102) sapphire substrates[6]. In this paper results are reported for substrates annealed in-situ at 1100° C to 1410° C for 30 min. The microstructural defects are characterized by transmission electron microscopy (TEM). The

HE EFFECT OF HIGH TEMPERATURE SUBSTRATE VACUUM ANNEALIN G ON THE MICROSTRUCTURE AND CRYSTALLINE QUALITY OF MBE Si ON SAPPHIRE

E.D. Richmond, M.E. Twigg*, A. R. Knudson, S. Qadri, N. Green**

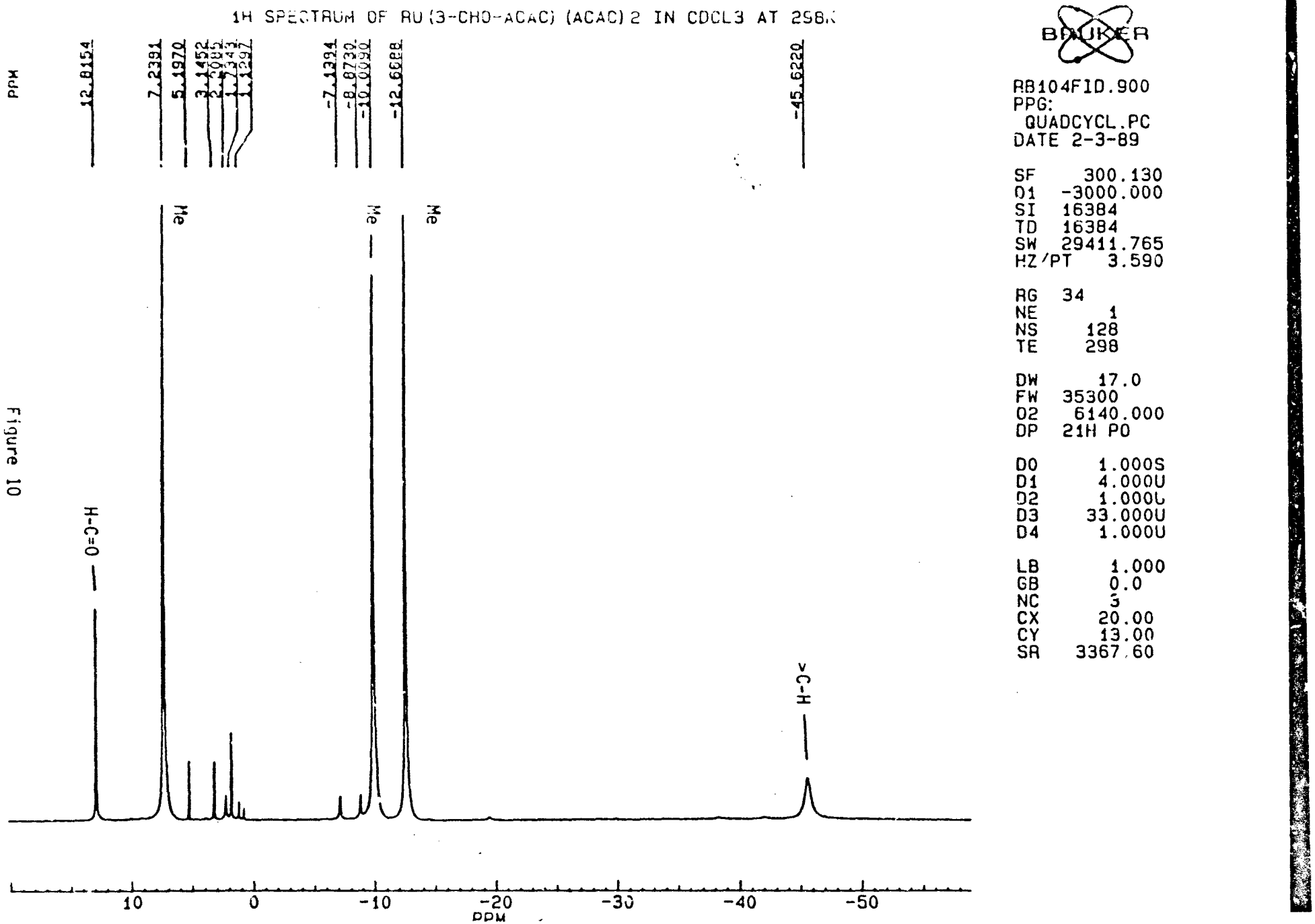
*GEO-Centers, Inc.,10903 Indian Head Highway, Fort Washington, Md. 20744

**Sachs/Freeman Associates,Inc., 1401 McCormick Dr., Landover, Md. 20785

ABSTRACT

We have found that annealing of the sapphire substrate in-situ to very high temperatures (1100° C - 1410° C) has a pronounced effect on the crystalline quality and the microstructure of the resultant epitaxial Si films. The microtwin differential volume fraction peaks further from the interface as the anneal temperature is reduced. Simultaneously, the total amount of twinned material increases as the anneal temperature is reduced. However, the microtwin density (cm^{-2}) decreases with decreasing anneal temperature. This indicates there are fewer but larger microtwins in the epilayers for which the substrate anneals are at lower temperatures. For the lowest anneal temperatures used, the Si layer is polycrystalline with a predominant (011) texture. The (004) Si X-ray diffraction peak occurs at the same angle for substrate anneal temperatures above 1100° C. Therefore, the epilayer strain is independent of the substrate anneal temperature. Thus, the strain must depend on either the growth kinetics or the sapphire surface resulting from the high temperature anneal. The dechanneling o. MeV $^4He^+$ ions reveals that the crystalline quality of the MBE Si epilayer improves substantially with the increasing substrate anneal temperature. For the 1410° C MBE Si epilayer, the value of the dechanneling ratio at the Si surface, $\chi_0 = 0.10$. This is 20% lower than the value of the dechanneling ratio at the surface for chemical vapor deposited silicon on sapphire.

APPENDIX D5


1H SPECTRUM OF RU(3-CHO-ACAC)(ACAC)2 IN CDCL3 AT 298K
PPM
12.8154
7.2391
5.1970
3.1452
-7.1394
-8.8739
-10.0990
-12.6688
-45.6220
Me
Me
Me
H-C=O
H-C<
10
0
-10
-20
-30
-40
-50
PPM
Figure 10
BRUKER
RB104FID.900
PPG:
QUADCYCL.PC
DATE 2-3-89
SF 300.130
O1 -3000.000
SI 16384
TD 16384
SW 29411.765
HZ/PT 3.590
RG 34
NE 1
NS 128
TE 298
DW 17.0
FW 35300
O2 6140.000
DP 21H P0
D0 1.000S
D1 4.000U
D2 1.000U
D3 33.000U
D4 1.000U
LB 1.000
GB 0.0
NC 3
CX 20.00
CY 13.00
SR 3367.60

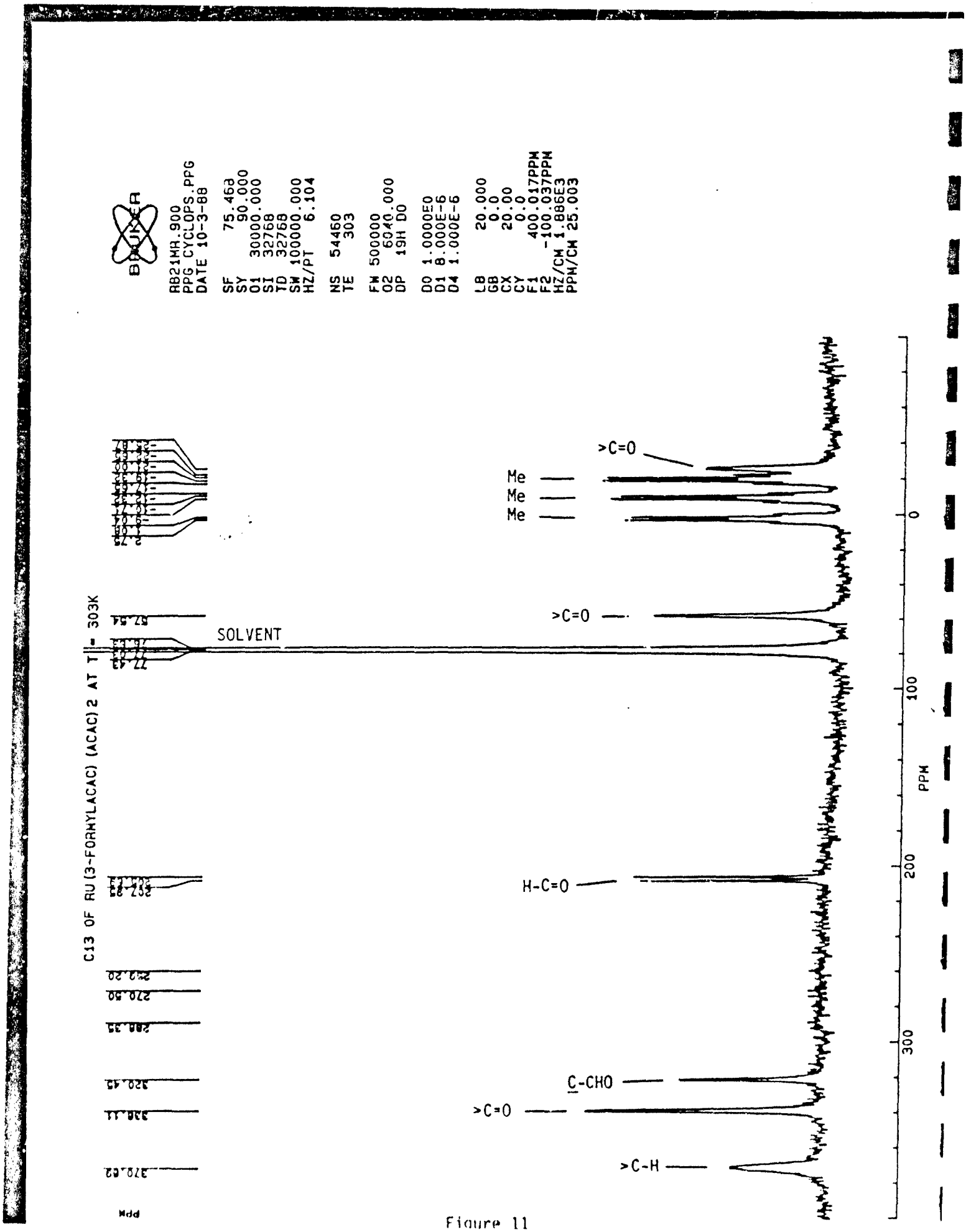

BRUKER
RB21MR.900
PPG CYCLOPS.PPG
DATE 10-3-88
SF 75.463
SY 90.000
O1 30000.000
SI 32768
TD 32768
SW 100000.000
HZ/PT 6.104
NS 54460
TE 303
FW 500000
O2 6040.000
DP 19H D0
D0 1.0000E0
D1 8.000E-6
D4 1.000E-6
LB 20.000
GB 0.0
CX 20.00
CY 0.0
F1 400.017PPM
F2 -100.037PPM
HZ/CM 1.886E3
PPM/CM 25.003
C13 OF RU(3-FORMYLACAC) (ACAC)2 AT T = 303K
SOLVENT
>C=O
Me
Me
Me
>C=O
H-C=O
C-CHO
>C=O
>C-H
PPM
0
100
200
300
Hdd

Figure 11

1H SPECTRUM OF RU(3-CHO-ACAC)2(ACAC) IN CDCL3 AT T = 298K

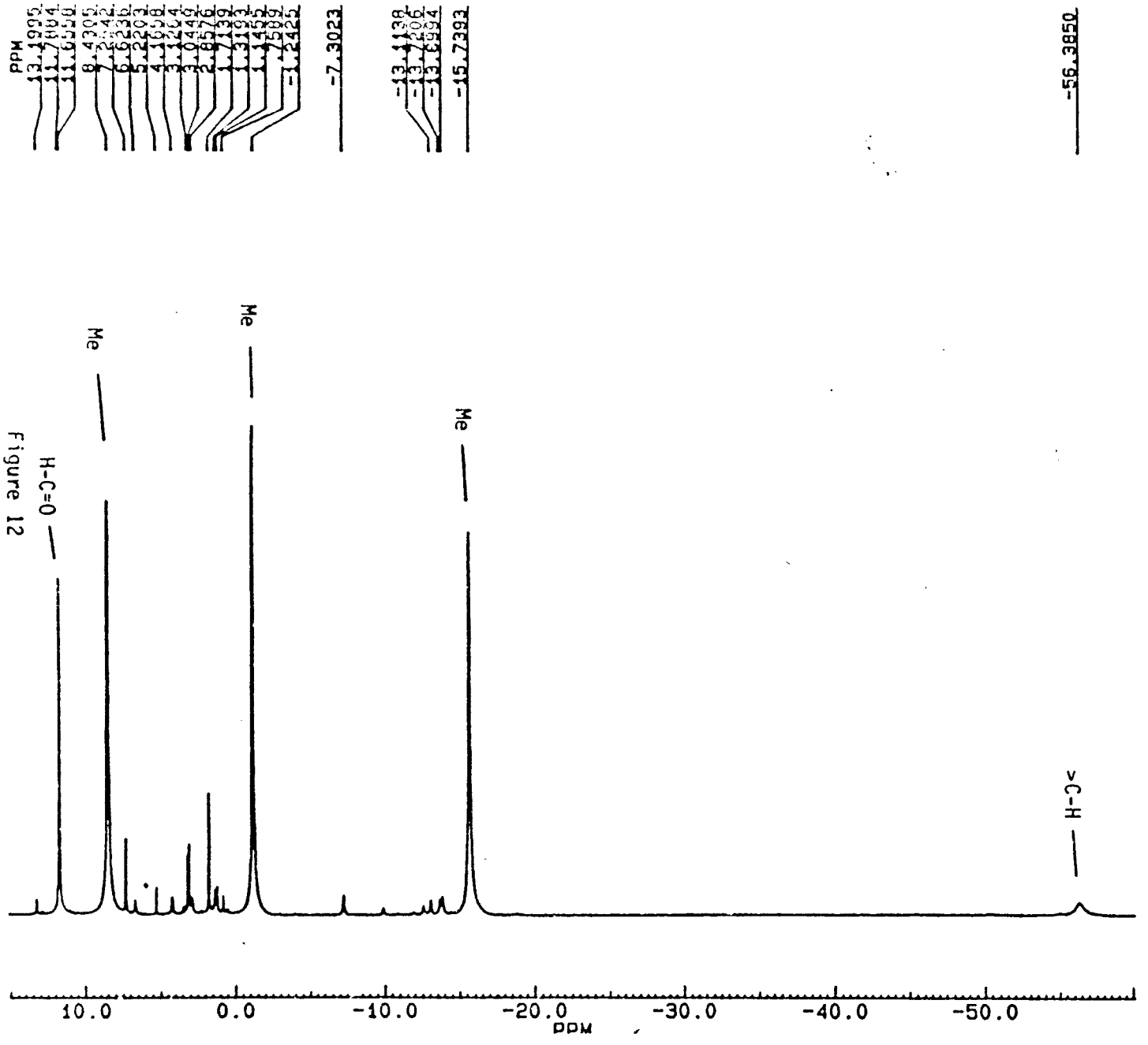


Figure 12

BRUKER

RB121FID.900
PPG:
QUADCYCL.PC
DATE 24-4-89

SF	300.130
O1	-3000.000
SI	16384
TD	16384
SW	29411.765
HZ/PT	3.590
RG	33
NE	1
NS	64
TE	298
DW	17.0
FW	35300
O2	6140.000
DP	20H P0
D0	1.000S
D1	3.000U
D2	1.000U
D3	33.000U
D4	1.000U
LB	1.000
GB	0.0
NC	2
CX	20.00
CY	0.0
SR	3367.88

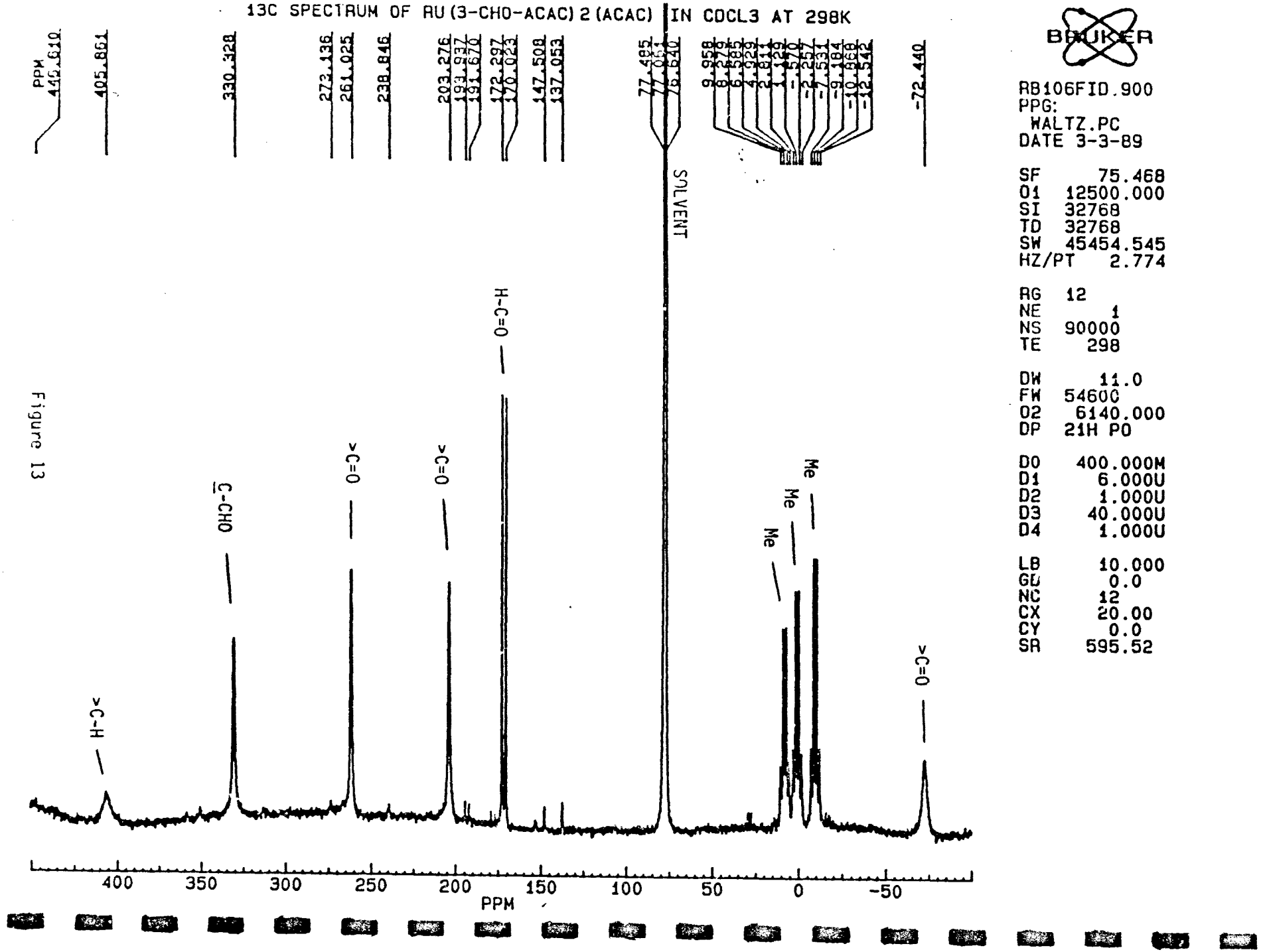

13C SPECTRUM OF RU(3-CHO-ACAC)2(ACAC) IN CDCL3 AT 298K
PPM
446.610
405.861
330.328
273.136
261.025
238.846
203.276
193.937
191.670
172.297
170.023
147.508
137.053
77.485
77.054
76.640
9.958
8.276
8.085
4.929
3.811
1.129
-1.570
-2.257
-7.531
-9.184
-10.968
-12.542
-72.440
SOLVENT
H-C=O
C-CHO
O=C<
O=C<
H-C<
Me
Me
Me
O=C<
400
350
300
250
200
150
100
50
0
-50
PPM
BRUKER
RB106FID.900
PPG:
WALTZ.PC
DATE 3-3-89
SF 75.468
O1 12500.000
SI 32768
TD 32768
SW 45454.545
HZ/PT 2.774
RG 12
NE 1
NS 90000
TE 298
DW 11.0
FW 54600
O2 6140.000
DP 21H PO
D0 400.000M
D1 6.000U
D2 1.000U
D3 40.000U
D4 1.000U
LB 10.000
GB 0.0
NC 12
CX 20.00
CY 0.0
SR 595.52

Figure 13

^{1}H And ^{13}C NMR Characterization Of $[Ru(3-CHO-acac)_2(acac)]$

In the case of the diformylated Ru(III) product, ^{1}H NMR spectra (Fig.12) typically revealed the presence of a trace of the monoformylated species and small amounts of free ligand together with paramagnetic resonances of decomposition products. However, the samples were clean enough for spectroscopic assignments. The methyl resonance of the diformylated complex displayed large splittings while the formyl resonance exhibited only a modest paramagnetic shift. It appears from the 3-$\underline{H}$-C< shifts (Table II) that most of the spin density resides on the unsubstituted $acac^-$ ligand in these complexes.

^{1}H coupled ^{13}C spectra (Fig.13) typically showed the presence of a number of weak resonances attributable to ligand decomposition products but generally the samples were reasonably clean. With the benefit of previous measurements for $[Ru(acac)_3]$ and $[Ru(3-CHO-acac)(acac)_2]$ the ^{13}C spectrum of the diformylated complex could be assigned by inspection for the most part. However, unlike the monoformylated complex it was not possible to assign the >$\underline{C}$=O and >$\underline{C}$-*formyl* resonances uniquely on the basis of intensity ratios. However, the >$\underline{C}$-*formyl* resonance would be expected to lie near the value of +320.45 ppm observed in the monoformylated complex. The assignments resulting from this assumption are listed below in Table II.

Temperature Dependence Of The Paramagnetic Shifts

In order to determine the accuracy of these assignments a temperature dependence study of the ^{13}C spectrum was made for the diformylated complex and the data are summarized in Figure 14, omitting the methyl resonances. These display little temperature dependence. The 3-*formyl* resonance (+171.16 ppm) showed surprisingly little temperature dependence over this limited range. It seems likely that the peak at ~203 ppm is due to a >$\underline{C}$=O resonance since its small temperature dependence is most consistent with a T_∞ limiting value near 190 ppm, a typical diamagnetic >$\underline{C}$=O value. The two remaining resonances at ~261 ppm and ~330 ppm appear to have almost the same slope with temperature so it is not certain which corresponds to the limiting values of ~190 ppm (>$\underline{C}$=O) and ~115 ppm (>$\underline{C}$-formyl). Either assignment places large spin density at these nuclei.

Further support for the assignments of the >$\underline{C}$=O resonances has been provided by complementary measurements of the ^{1}H isotropic shifts *vs* temperature (Fig.15). The latter show that one of the formylated ligand's methyl groups experiences very little shift and consequently it exhibits only a small temperature dependence. The small, negative shift with

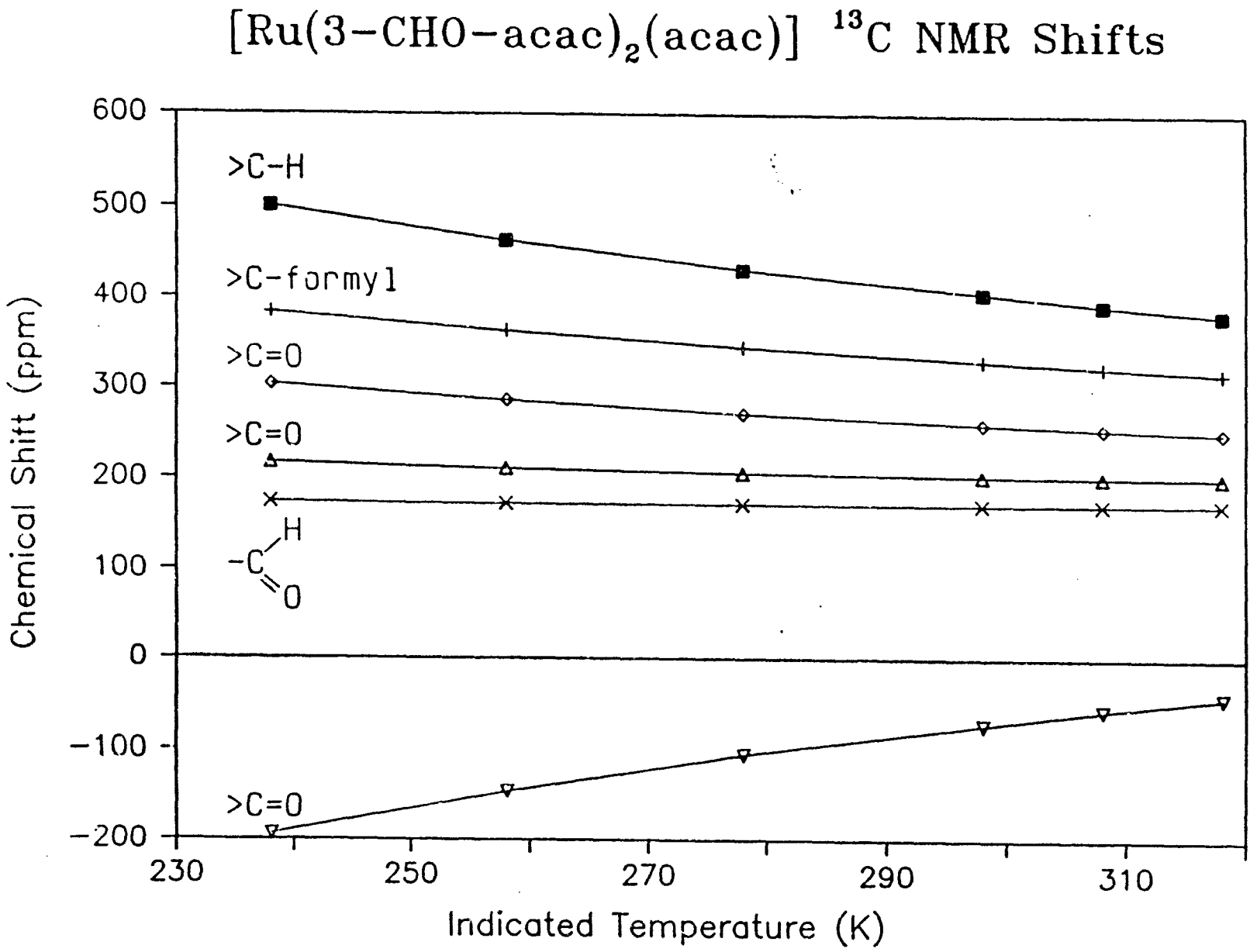

[Ru(3-CHO-acac)2(acac)] 13C NMR Shifts
600
500
400
300
200
100
0
-100
-200
Chemical Shift (ppm)
>C-H
>C-formyl
>C=O
>C=O
>C=O
230
250
270
290
310
Indicated Temperature (K)

Figure 14

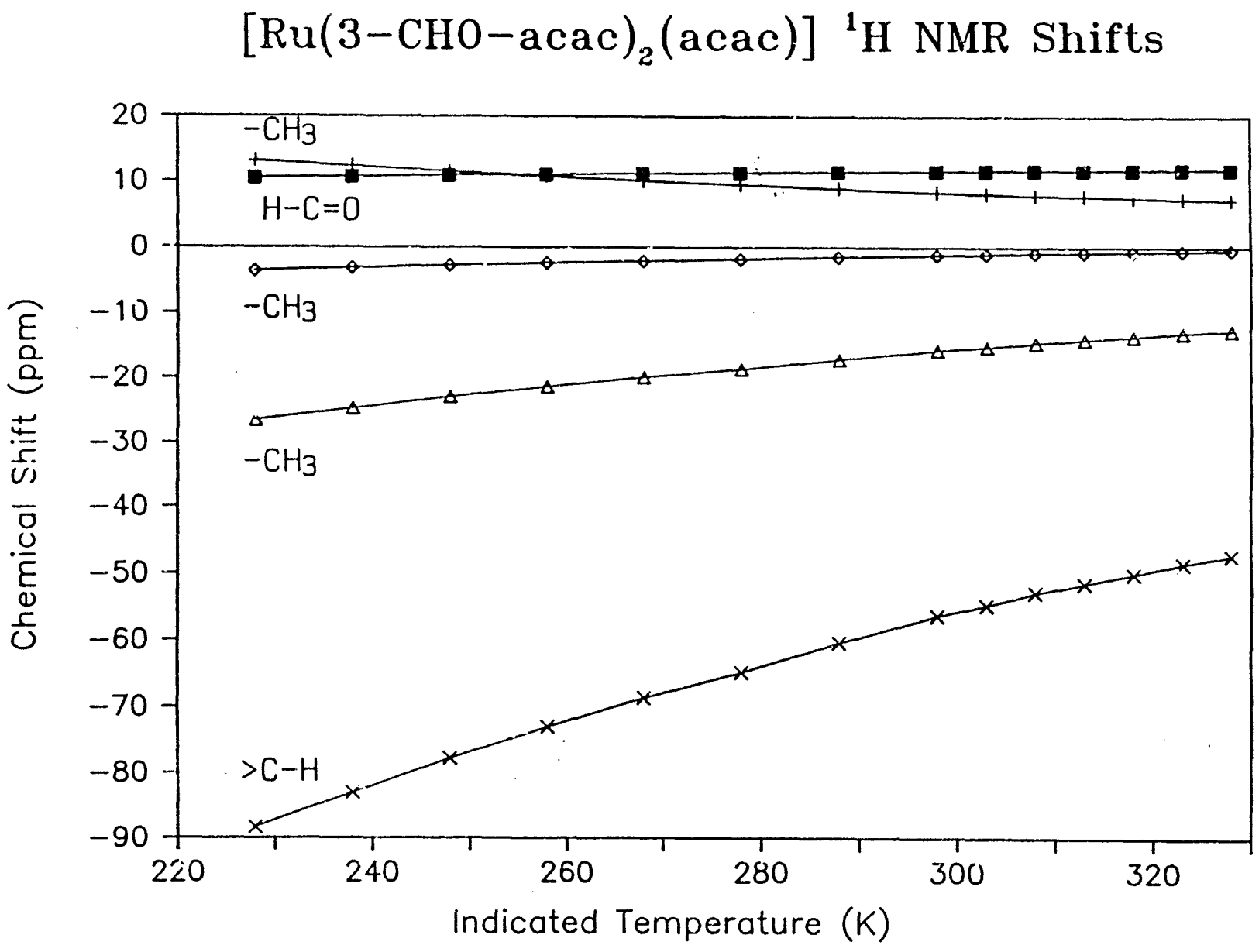

[Ru(3-CHO-acac)2(acac)] 1H NMR Shifts
Chemical Shift (ppm)
Indicated Temperature (K)
20
10
0
-10
-20
-30
-40
-50
-60
-70
-80
-90
220
240
260
280
300
320
-CH3
H-C=O
-CH3
-CH3
>C-H

Figure 15

decreasing temperature (*increasing* χ_M) is consistent with simple through-space dipolar shifts due to the *g*-value anisotropy of the ground state. This implies that the contact shift is nearly zero or just slightly positive at the methyl protons. Together with the ^{13}C data for the neighbouring >C=O group it would appear that one end of the formylated acac$^-$ ligand is depleted of spin density.

This behaviour could arise from a *trans* effect depleting π-electron density from one end of each of the 3-*formyl*-acac$^-$ ligands towards the unsubstituted acac$^-$ ligand. One difficulty with this explanation is the demonstrated electron withdrawing nature of the 3-*formyl* substituent, at least in the σ bonding sense. It would be necessary, therefore, to invoke a compensatory back π bonding effect transferring electron density to the metal and the *trans* ligand system, acac$^-$. It is unlikely that a *trans* effect would completely denude π-electron density from one end of a formally conjugated ligand.

An alternative hypothesis would reverse the assignments of the >C=O groups of the 3-*formyl*-acac$^-$ ligand, with those exhibiting the large +ve isotropic shift being *trans* to the acac$^-$ ligand's >C=O groups (-ve isotropic shifts). Owing to the differences in ligand field stength between the two ligand types the degeneracy of the Ru(III) d^5 t_{2g} orbitals (d_{xy},d_{xz},d_{yz}) will be lifted before any consideration is given to spin-orbit coupling. Although the energy spacing is still small enough to permit rapid electron spin relaxation on the NMR timescale (giving relatively narrow lines) the unpaired spin appears to be restricted mostly to one, unique *d*-orbital whose lobes share the same plane as the acac$^-$ ligand. One coordinated oxygen of each 3-*formyl*-acac$^-$ ligand would interact with this *d*-orbital but with a different orientation of the oxygen lone pair orbitals, which would tend to reduce overlap. The other >C=O group of each 3-*formyl*-acac$^-$ ligand would interact with spin paired metal *d*-orbitals, for the most part, and would thus display very small contact shifts.

All >C=O resonances would display small shifts and line broadening through dipolar coupling to the unpaired electron. Since there is little difference in linewidth for the >C=O resonances attributed to the 3-*formyl*-acac$^-$ ligand it would appear that the dipolar mechanism dominates their linewidths. Only the acac$^-$ ligand displays very large contact shifts and the linewidths are correspondingly broadened with respect to those of the 3-formyl-acac$^-$ ligand. The advantage of this explanation is that it is not necessary to invoke any difference in the nature of the bonding of the acac$^-$ and 3-*formyl*-acac$^-$ ligands. A small difference in their ligand fields probably would be adequate to cause enough splitting of the *d*-orbital degeneracy to give the observed NMR results. The only question remaining is the difference in sign of the shifts for the >C=O resonances on the acac$^-$ and 3-*formyl*-acac$^-$ ligands.

The 3-*formyl* group itself displays no significant temperature dependence in either the ^{13}C or ^{1}H data sets and the absolute shifts are also small *vs* those of the diamagnetic Rh(III) analog. Given the NMR data for the monoformylated complex a small, temperature dependent shift of the formyl substituent would be expected if there was any significant metal $d\pi$ spin density on the ligand. The results suggest that there is little direct interaction of the unpaired metal spin with these substituents in the diformylated complex. Thus, the mechanism of spin transfer to these ligands cannot be the same as for the acac$^-$ ligand (direct filled $p\pi$-$d\pi$ bonding). Rather, the empty ligand π^* orbitals must act as acceptors for the 3-*formyl*-acac$^-$ ligand in the diformylated complex. This would probably account for the change in sign of spin density at the >C=O nuclei *vs* the acac$^-$ ligand. The spin distribution over the ligand may well differ in this case also.

Formally, the same situation must hold for the monoformylated complex. However, in this case the observed NMR data show that a large amount of spin density resides on both of the unsubstituted acac$^-$ ligands. The 3-*formyl*-acac$^-$ ligand experiences larger shifts than in the diformylated complex but again with opposite sign of spin density at the >C=O nuclei. Therefore, it must be assumed that one spin paired *d*-orbital shares the plane of the unique 3-*formyl*-acac$^-$ ligand and that it is somewhat lower in energy than the remaining *d*-orbitals. The latter may well be split by spin-orbit coupling, since there must be a mechanism for rapid electron spin relaxation to explain the narrow NMR linewidths. However, unlike the diformylated complex, this pair of *d*-orbitals must share the unpaired spin. The magnetic inequivalence of the observed >C=O resonances of the acac$^-$ ligands suggests that they are not degenerate but also that they do not differ too much in energy. A consequence of two, nearly degenerate *d*-orbitals sharing the unpaired spin density is a greater interaction of the 3-*formyl*-acac$^-$ ligand with the unpaired spin but not via the direct $p\pi$-$d\pi$ bonding mechanism (L→M charge transfer) that appears to be operative for the acac$^-$ ligands.

In summary, differences in metal t_{2g} *d*-orbital energy caused by 3-*formyl* substituents on acac$^-$ ligands appears to cause preferential overlap of metal centered spin density with the unsubstituted ligand. This requires that the bonded M.O. for the 3-*formyl*-acac$^-$ ligand to be lower in energy than those for the acac$^-$ ligands, a result to be expected given conjugation between the *formyl* group and its acac$^-$ like pseudo-aromatic ring. Furthermore, the opposite behaviour would be predicted for mono- and disubstituted complexes where the substituents raise the energy of the bonded M.O. *vs* acac$^-$.

These considerations may have kinetic consequences for ligand bridged redox events if the substituent effect is such as to reduce the coupling to the hole in the metal t_{2g} orbital set. In the case of the diformylated complex an increase in rate for inner-sphere electron transfer with Ti(III) ion may not be observed. Although there is a greater driving force and a statistical factor in favor of faster reaction compared with the monoformylated complex, there also appears to be less electronic coupling to the hole in the t_{2g} orbital set via the formylated ligand. This would be a true test of whether these systems exhibit non-adiabaticity in the electron transfer event. In all likelihood, these reactions are limited solely by the insertion rate into the coordination sphere of Ti(III) ion and the behaviour of the diformylated complex may just be statistical. This will be tested in due course.

TABLE I

^{1}H And ^{13}C NMR Assignments For

$Rh(3-CHO-acac)(acac)_2$ and $Ru(3-CHO-acac)(acac)_2$

In $CDCl_3$ At T = 303K

Nuclei	Rh(III) δ (ppm)	Ru(III) δ (ppm)	Δ Shift (ppm)
^{1}H:			
$-CH_3$	+2.15	-13.01	-15.16
$-CH_3$	+2.15	-10.30	-12.45
$-CH_3$(f)	+2.61	+7.47	+4.86
O=C-H(f)	+10.14	+12.89	+2.75
>C-H	+5.50	-46.7	-52.2
^{13}C: (^{1}H coupled)			
$-CH_3$	+26.44 (av)	-20.23 (av)	-46.67
$-CH_3$	+26.44 (av)	-9.94 (av)	-36.38
$-CH_3$(f)	+28.40 (av)	+1.87 (av)	-26.53
>C=O	+189.0	-26.48	-215.5
>C=O	+189.0	+57.52	-131.5
>C=O(f)	+196.8	+338.2	+141.4
O=C-H(f)	+190.3 (av)	+206.8 (av)	+16.5
>C-formyl	+115.5	+320.4	+204.9
>C-H	+99.4 (av)	+370.9 (av)	+271.5

TABLE II

^1H And ^{13}C NMR Assignments For

$Rh(3-CHO-acac)_2(acac)$ and $Ru(3-CHO-acac)_2(acac)$

In $CDCl_3$ At T = 298K

Nuclei	Rh(III) δ (ppm)	Ru(III) δ (ppm)	Δ Shift (ppm)
^1H:			
$-CH_3$	+2.18	−15.72	−17.9
$-CH_3(f)$	+2.63	−1.21	−3.84
$-CH_3(f)$	+2.63	+8.48	+5.85
O=C−H(f)	+10.15	+11.69	+1.54
>C−H	+5.54	−56.39	−61.93
^{13}C: (^1H coupled)			
$-CH_3$	+26.38 (av)	−10.03 (av)	−36.41
$-CH_3(f)$	+28.27 (av)	+0 28 (av)	−27.99
$-CH_3(f)$	+28.27 (av)	+7.43 (av)	−20.84
>C=O	+189.4	−72.44	−261.8
>C=O(f)	+197.1	+203.3	+6.2
>C=O(f)	+197.1	+261.0	+63.9
O=C−H(f)	+190.1 (av)	+171.2 (av)	−18.9
>C−formyl	+115.4	+330.3	+214.9
>C−H	+99.52 (av)	+405.9 (av)	+306.4

SOLUTION KINETICS AND MECHANISMS

Part IV

Spectroscopic Characterization Of The 3-Formyl Derivatives Of [Ru(acac)$_3$] and [Rh(acac)$_3$]

Electronic spectroscopy was used to ascertain the degree of π-bonding interaction between the 3-formyl substituent and the acac$^-$ ligand for [Ru(3-CHO-acac)$_n$(acac)$_{3-n}$]. The electronic spectra, redox potentials and NMR spectra were compared with those for the derivatives [Ru(3-X-acac)$_n$(acac)$_{3-n}$] (X = -CH_3,-Br,-I) to illustrate that the formyl substituent does nor interact strongly with the π-electron system of the acac$^-$ ligand. Infrared spectroscopy was also utilized to assess the degree of interaction between the formyl substituent and the acac$^-$ ligand in the complexes.

UV-Visible Spectroscopy Of [Rh(acac)$_3$] And Formylated Derivatives

Ligand absorption tends to dominate the UV-Visible spectra of [M(acac)$_3$] complexes. Endo *et alia* have reported the spectra of a number of substituted [Ru(acac)$_3$] derivatives with somewhat scant data on the free ligands.[15] For acetylacetone in CH_3CN they reported that λ_{max} = 272 nm without an ϵ value, though these are typically ~10^4 M^{-1} cm^{-1} for several related derivatives. No mention was made of splitting due to the presence of keto and enol isomers in this solvent. Akehurst *et alia* have reported a similar value for the 3-formyl-acetylacetone ligand in 0.1 N NaOH (aq.) with λ_{max} = 272 nm (ϵ = 37,140 M^{-1} cm^{-1}) while in EtOH (5% HCl) solution two peaks were observed with λ_{max} = 236 nm (ϵ = 22,190 M^{-1} cm^{-1}) and λ_{max} = 275 nm (ϵ = 19,250 M^{-1} cm^{-1}) due to the presence of both the enol and keto forms of the ligand.[16]

On complexation to a metal the ligand $\pi \rightarrow \pi^*$ and $n \rightarrow \pi^*$ absorptions are shifted appreciably and a set of UV-Visible spectra were obtained over the range 220-800 nm in EtOH solution for the diamagnetic Rh(III) complexes described previously (Fig.16). There is little evidence of metal d-d transitions or low lying M-L charge transfer bands to complicate these spectra so that they reveal mostly the ligand based transitions. The ligand $\pi \rightarrow \pi^*$ transition for [Rh(acac)$_3$] (- ——) occurs below 220 nm. A λ_{max} value of 204 nm (ϵ = 7380 M^{-1} cm^{-1}) was found by Balahura and Lewis in an acidic, aqueous medium for what they believed to be the Cr(III) complex, $[Cr(OH_2)_4(acac)]^{2+}$.[17] Thus, [Rh(acac)$_3$] would be expected to have a similar absorption band with three times the intensity, i.e. ϵ ~ 22,500

Figure 16

Rh(acac)3 & Its Formylated Derivatives In Ethanol Solution
ε x 1E-4 (M-1 CM-1)
Wavelength (nm)
0
.5
1
1.5
2
2.5
3
250
300
350
400
450
500
550
600
650

M^{-1} cm^{-1}. The measured spectrum greatly exceeds this value at 220 nm and it can be inferred that metal based transitions may well interfere with this region. The $n \rightarrow \pi^*$ transition for $[Rh(acac)_3]$ occurs at λ_{max} = 318.0 nm (ϵ = 9857 M^{-1} cm^{-1}) while an unassigned ligand transition is observed at λ_{max} = 258.2 nm (ϵ = 8796 M^{-1} cm^{-1}). By way of comparison, $[Cr(OH_2)_4(acac)]^{2+}$ was found to have transitions at λ_{max} = 326 nm (ϵ = 7880 M^{-1} cm^{-1}) and λ_{max} = 253 nm (ϵ = 4140 M^{-1} cm^{-1}), respectively. The bands are narrower in the Cr(III) species and hence the extinction coefficients do not correlate well with those for $[Rh(acac)_3]$, though presumably the oscillator strengths are similar.

The effect of formylation of $[Rh(acac)_3]$ is also illustrated in Figure 16. A *new* transition is observed at λ_{max} = 256 nm for both the monoformylated (-------) and diformylated (—·—·—) derivatives with an approximate twofold increase in intensity for the latter. Balahura and Lewis observed similar behaviour for $[Cr(OH_2)_4(3\text{-CHO-acac})]^{2+}$.[17] The ring localized transition at 253 nm was observed as a shoulder on the much more intense formyl transition which was split into two peaks at λ_{max} = 244 nm (ϵ = 11,600 M^{-1} cm^{-1}) and λ_{max} = 231 nm (ϵ = 14,100 M^{-1} cm^{-1}). The combined oscillator strengths of these bands would be comparable to that found for $[Rh(3\text{-CHO-acac})(acac)_2]$. Presumably, the splitting in the spectrum of the Cr(III) species is due to a keto ⇌ enol isomerization of the ligand. This must occur at the free aldehyde rather than the coordinated ring >C=O positions since the Cr(III) complex is quite inert towards isomerization to the corresponding 2-acetyl-butanedione linkage isomer, which these authors also prepared. The latter displayed a similar spectrum with λ_{max} = 246 nm (ϵ = 13,150 M^{-1} cm^{-1}) and λ_{max} = 238 nm (ϵ = 12,750 M^{-1} cm^{-1}) for the free ketone group. This complex was similarly inert towards isomerization to the 3-formyl species. Protonation of the free aldehyde group has not been tested yet for the Rh(III) 3-formyl-acac complexes due to their insolubility in aqueous media.

UV-Visible Spectroscopy Of $[Ru(acac)_3]$ And Formylated Derivatives

The UV-Visible spectra of the Ru(III) acetylacetonates are shown in Figures 17-19 in EtOH (ϵ = 24.6, μ = 1.66), CH_3CN (ϵ = 36, μ = 3.53) and CH_2Cl_2 (ϵ = 8.9, μ = 1.14), respectively. The Ru(III) complexes show two extra transitions not observed in the Rh(III) analogs. These are due to the one electron vacancy in the t_{2g}^5 metal orbital set allowing low energy L→M charge transfer bands to appear. For $[Ru(acac)_3]$ (————) these are observed at λ_{max} ~ 505 nm (ave. ϵ ~ 1600 M^{-1} cm^{-1}) and λ_{max} ~ 270 nm (ave. ϵ ~ 17500 M^{-1} cm^{-1}). The ligand centered $\pi \rightarrow \pi^*$ and $n \rightarrow \pi$ transitions are still observed but the latter is significantly red shifted to λ_{max} ~ 347 nm (ave. ϵ ~ 8100 M^{-1} cm^{-1}). This band is slightly split but the oscillator strength should be quite similar to that for $[Rh(acac)_3]$. None of the

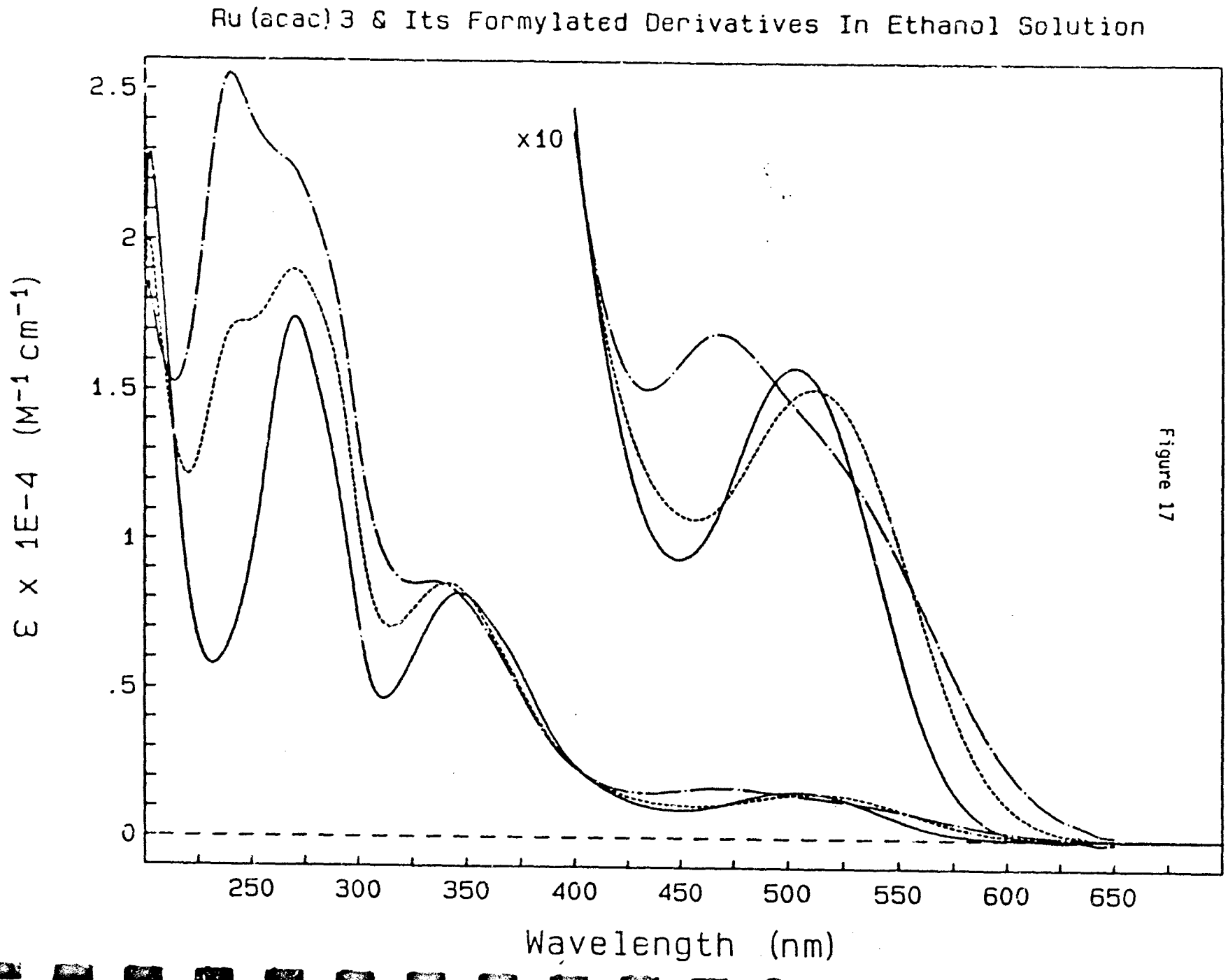

Ru(acac)3 & Its Formylated Derivatives In Ethanol Solution
x10
ε x 1E-4 (M-1 cm-1)
2.5
2
1.5
1
.5
0
250
300
350
400
450
500
550
600
650
Wavelength (nm)

Figure 17

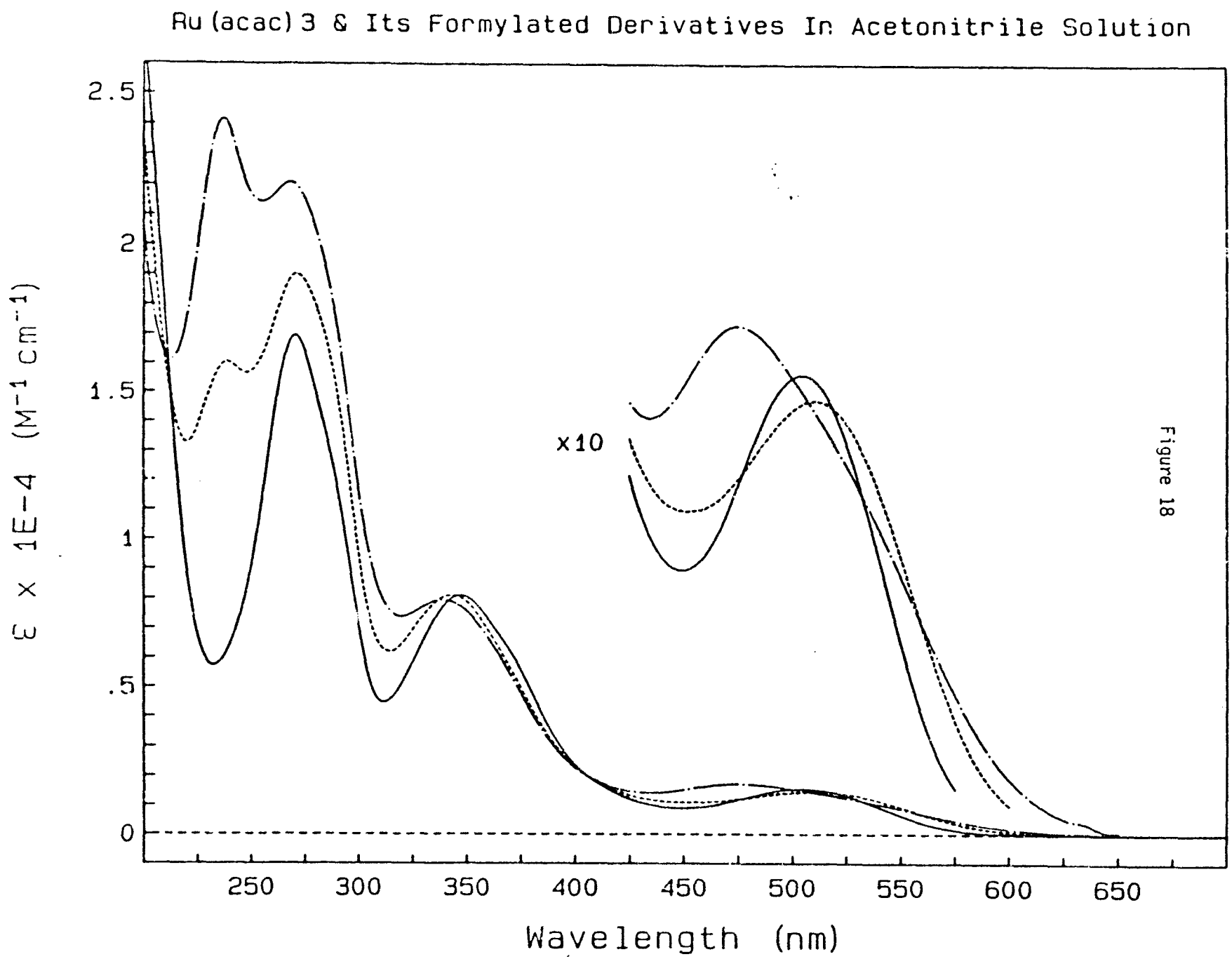

Ru(acac)3 & Its Formylated Derivatives In Acetonitrile Solution
ε x 1E-4 (M-1 cm-1)
2.5
2
1.5
1
.5
0
x10
250
300
350
400
450
500
550
600
650
Wavelength (nm)

Figure 18

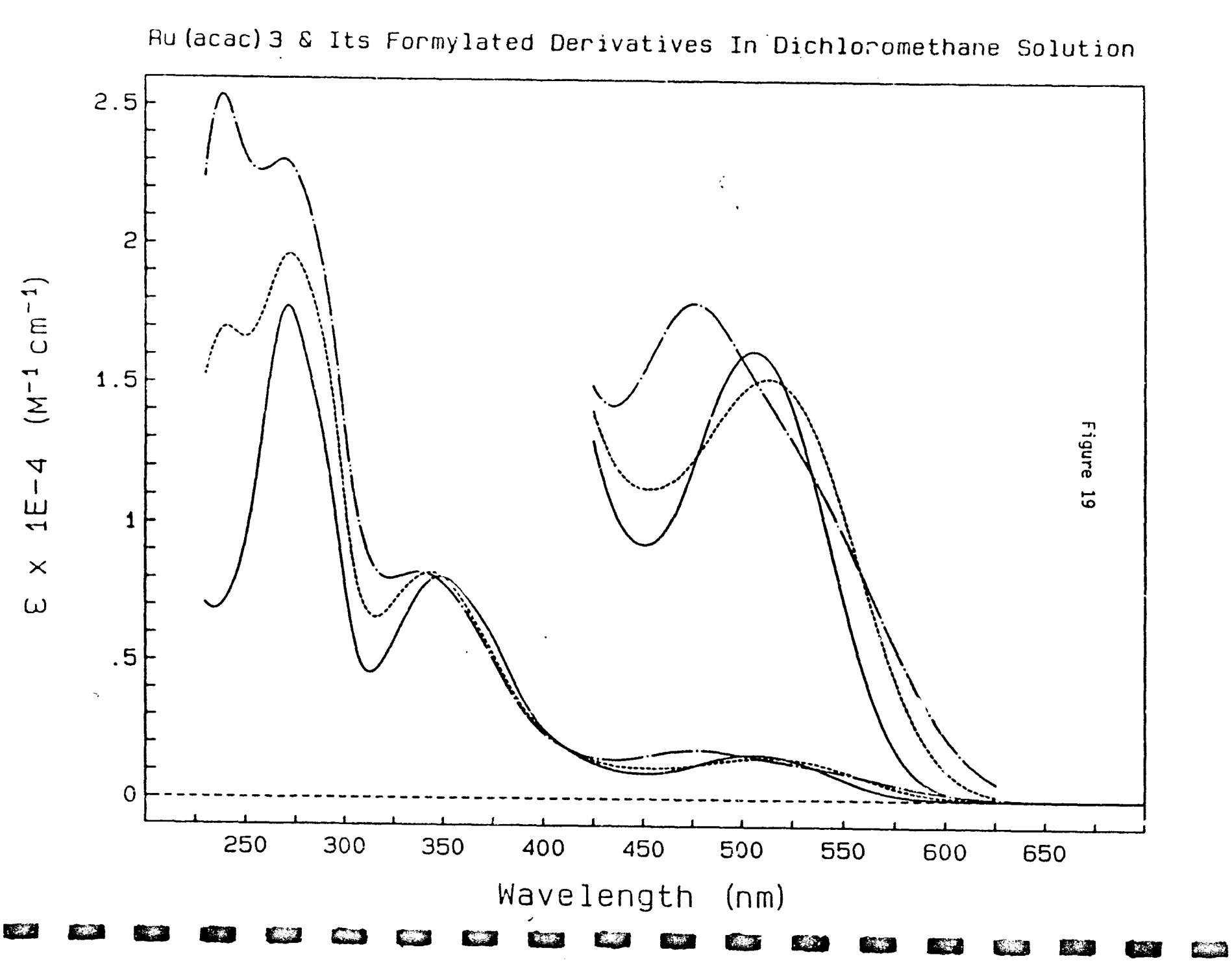

Ru(acac)3 & Its Formylated Derivatives In Dichloromethane Solution
ε x 1E-4 (M-1 cm-1)
2.5
2
1.5
1
.5
0
250
300
350
400
450
500
550
600
650
Wavelength (nm)

Figure 19

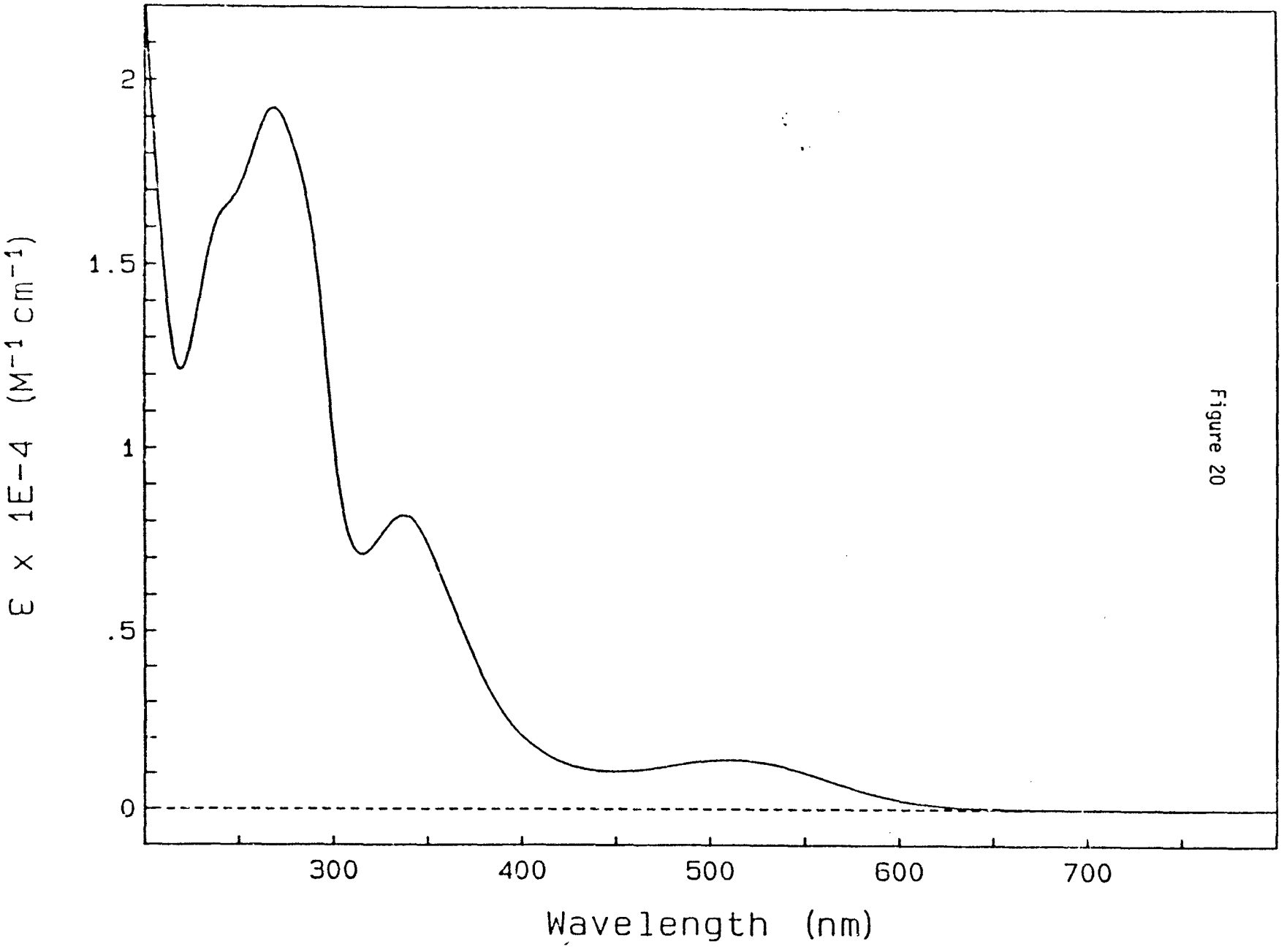

Purified 3-Formylacac Ruthenium(III) Complex In H2O
ε x 1E-4 (M-1 cm-1)
2
1.5
1
.5
0
300
400
500
600
700
Wavelength (nm)

Figure 20

transitions for [Ru(acac)$_3$] display any significant dependence on solvent dielectric constant, ϵ, or the solvent dipole moment, μ. Endo *et alia* have reported the following spectral values for [Ru(acac)$_3$] in CH_3CN solution, λ_{max} nm (ϵ,M^{-1} cm^{-1}): 506 (1550), 349 nm (8710), 272 nm (17380)[15] which differ from those shown in Figure 18: 504.5 (1561), 347.25 (8085), 270.5 (16,950). Since the sample used for the current work has been highly purified and thoroughly characterized by ^1H and ^{13}C NMR spectroscopy the latter values are probably correct.

The monoformylated derivative (-------) displays a similar spectrum to the parent complex with one additional band at λ_{max} ~ 240 nm (ave. ϵ ~ 17,000 M^{-1} cm^{-1}) which varies a little in intensity, position and bandwidth with solvent. These spectra are similar to that obtained in H_2O (Fig.20), where the the formyl transition is rather poorly resolved. The solvent dependence is consistent with specific hydrogen bonding effect at the free aldehyde group. Although separate ligand→metal charge transfer bands would be expected from the acac$^-$ and 3-CHO-acac$^-$ ligands only a single envelope is observed but red shifted to λ_{max} ~ 513 nm (ave. ϵ ~ 1510 M^{-1} cm^{-1}) in the non-aqueous solvents. These measurements contrast rather dramatically with the work of Berrie and Early who reported the following values for λ_{max} nm (ϵ,M^{-1} cm^{-1}): 512 (1050), 338 (6160), 220 (1420).[3] Clearly, these workers did not have pure material!

The diformylated derivative (—·—·—) also displays the free aldehyde transition at λ_{max} ~ 240 nm but at approximately twice the intensity of the monoformylated derivative. Once again, this transition is better resolved in the aprotic solvents. No comparison is available in H_2O owing to insolubility. The ligand→metal charge transfer band is quite obviously split into two components with that due to the 3-CHO-acac$^-$ ligand appearing at λ_{max} = 468-476 nm (ϵ = 1698-1793 M^{-1} cm^{-1}). Note that the splitting of the LMCT band (>= 0.23 eV) parallels the redox potential difference between the parent and diformylated complexes (0.28 eV), as one would expect.

UV-Visible Spectroscopy Of [Ru(3-X-acac)$_n$(acac)$_{3-n}$] (X = -Me,-Br,-I)

The UV-Visible spectra of the 3-bromo- and 3-iodo- substituted complexes were obtained in CH_3CN solution (Fisher, HPLC) and the data are shown in Figures 21-22, respectively. In both cases there is a progressive red-shift of all transitions with increasing numbers of halogen substituents. The lowest energy band is the superposition of LMCT transitions from the individual ligands but, unlike the 3-formyl derivatives, these are not resolved due to the breadth of the overlapping bands.

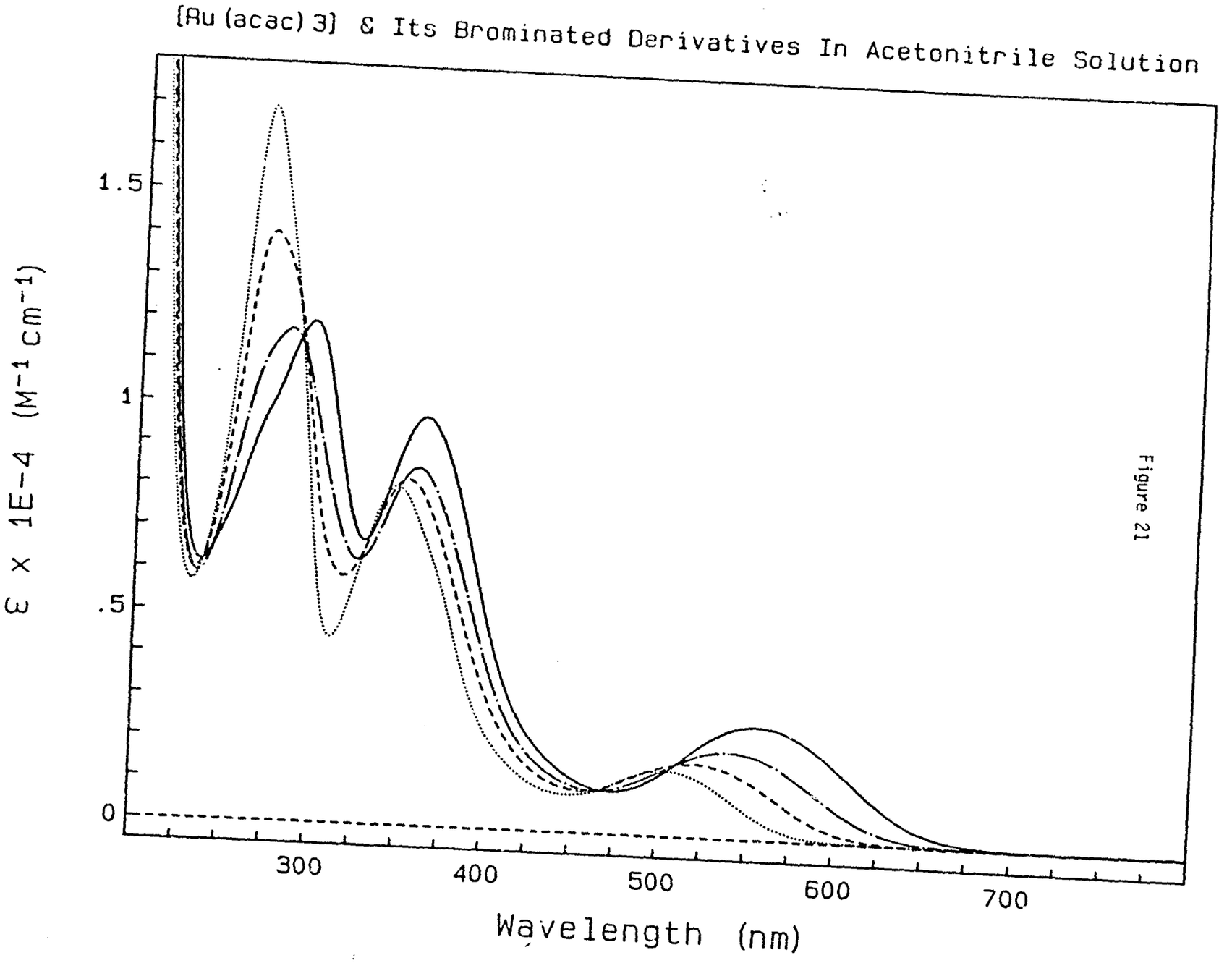

[Ru (acac) 3] & Its Brominated Derivatives In Acetonitrile Solution
ε x 1E-4 (M-1 cm-1)
1.5
1
.5
0
300
400
500
600
700
Wavelength (nm)

Figure 21

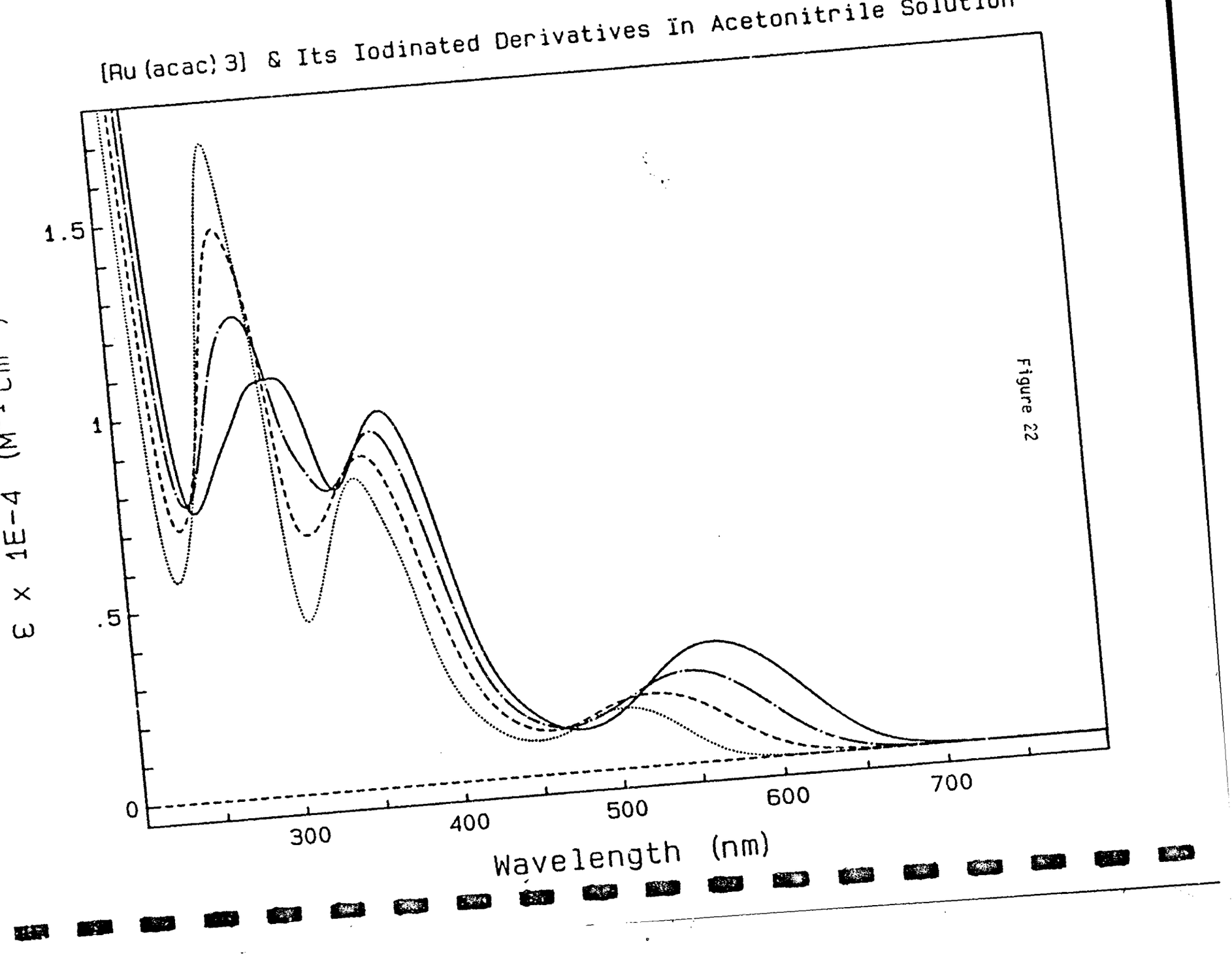

[Ru(acac)3] & Its Iodinated Derivatives In Acetonitrile Solution
ε x 1E-4 (M-1 cm-1)
1.5
1
.5
0
300
400
500
600
700
Wavelength (nm)

Figure 22

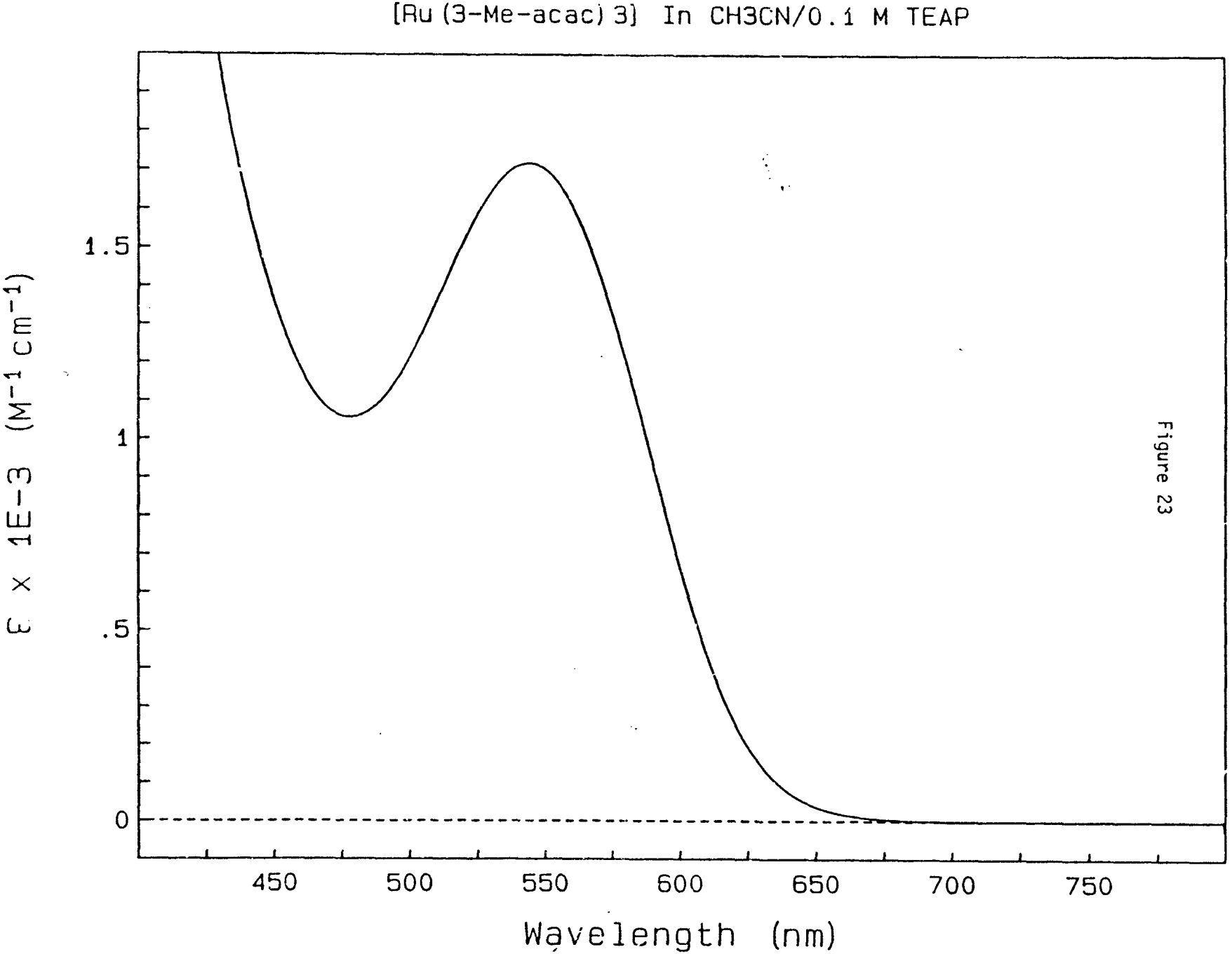

[Ru(3-Me-acac)3] In CH3CN/0.1 M TEAP
ε x 1E-3 (M-1 cm-1)
1.5
1
.5
0
450
500
550
600
650
700
750
Wavelength (nm)

Figure 23

Only the nighest energy transition (ligand $\pi-\pi^*$) displays any significant splitting. The remarkable feature here is the loss of intensity for this ligand centered transition. This indicates that the electron withdrawing substituent interacts strongly with the ligand π system, perhaps via $p\pi-d\pi$(Halogen) ylide bonding. This contrasts sharply with the behaviour of the 3-formyl derivatives whose spectra appeared to be the superposition of $[Ru(acac)_3]$ like transitions with those of the substituent. In this case there appeared to be no significant $p\pi-p\pi$ coupling between the $acac^-$ ring and the formally, conjugated formyl group.

The 3-methyl derivative has not been studied in detail as yet, though the LMCT band (Fig.23) is red-shifted ~50 nm from that of $[Ru(acac)_3]$. This suggests that the 3-methyl group does, as anticipated, behave as an electron withdrawing group which is consistent with its isotropic NMR shifts. Yet electrochemical data (*vide infra*) show the opposite behaviour. Such discrepancies abound when one considers substituents on aromatic or, in this case, pseudo-aromatic rings as nothing more than exogenous appendages. Clearly, the 3-methyl derivative behaves like a benzyl radical with a non-bonding orbital between the π-bonding and π^*-antibonding molecular orbitals. In such a bonding scheme one might well expect to easily remove one electron at a low potential. However, the 3-methyl substituent may still act as an electron withdrawing group *viz à vis* the π and π^* levels. Hence, the various experiments probe different features of the substituent interaction with the pseudo-aromatic ring and none alone suffices. Ultimately, π-M.O. calculations will be required to sort out some of the subtleties in the experimental data.

Infrared Spectroscopy Of $[Ru(acac)_3]$ And Formylated Derivatives

Solution IR measurements were performed on a PE 1710 FTIR (16 scans) in CH_2Cl_2 and CD_2Cl_2 solvents using a single 0.1 mm CsI cell. Solutions were prepared by weighing 10-25 mg samples of the Ru(III) complexes in glass vials to which 0.50 or 1.00 mL of solvent was added via syringe allowing extinction coefficients to be obtained to within 10% precision (solvent evaporation was the largest error). Dichloromethane proved useful for IR measurements since the ν_{CH} and δ_{CH} modes were relatively weak and sharp. However, there are two regions blacked out by the CH_2Cl_2 solvent in 0.1 mm pathlength cells; 1270-1250 cm^{-1} (δ_{CH}) and 760-690 cm^{-1} (ν_{C-Cl}). The former was eliminated by use of CD_2Cl_2, for which the blackout due to δ_{CH} shifts to the 970-940 cm^{-1} region. The ν_{C-Cl} blackout is not so important but does cover up some ring deformation modes.

The solution IR spectrum of $[Ru(acac)_3]$ is shown in Figures 24-25 for the region 2000-450 cm^{-1}. The ring $\nu_{C=O}$ (1545 cm^{-1}) and $\nu_{C=C}$ (1519 cm^{-1}) modes dominate the

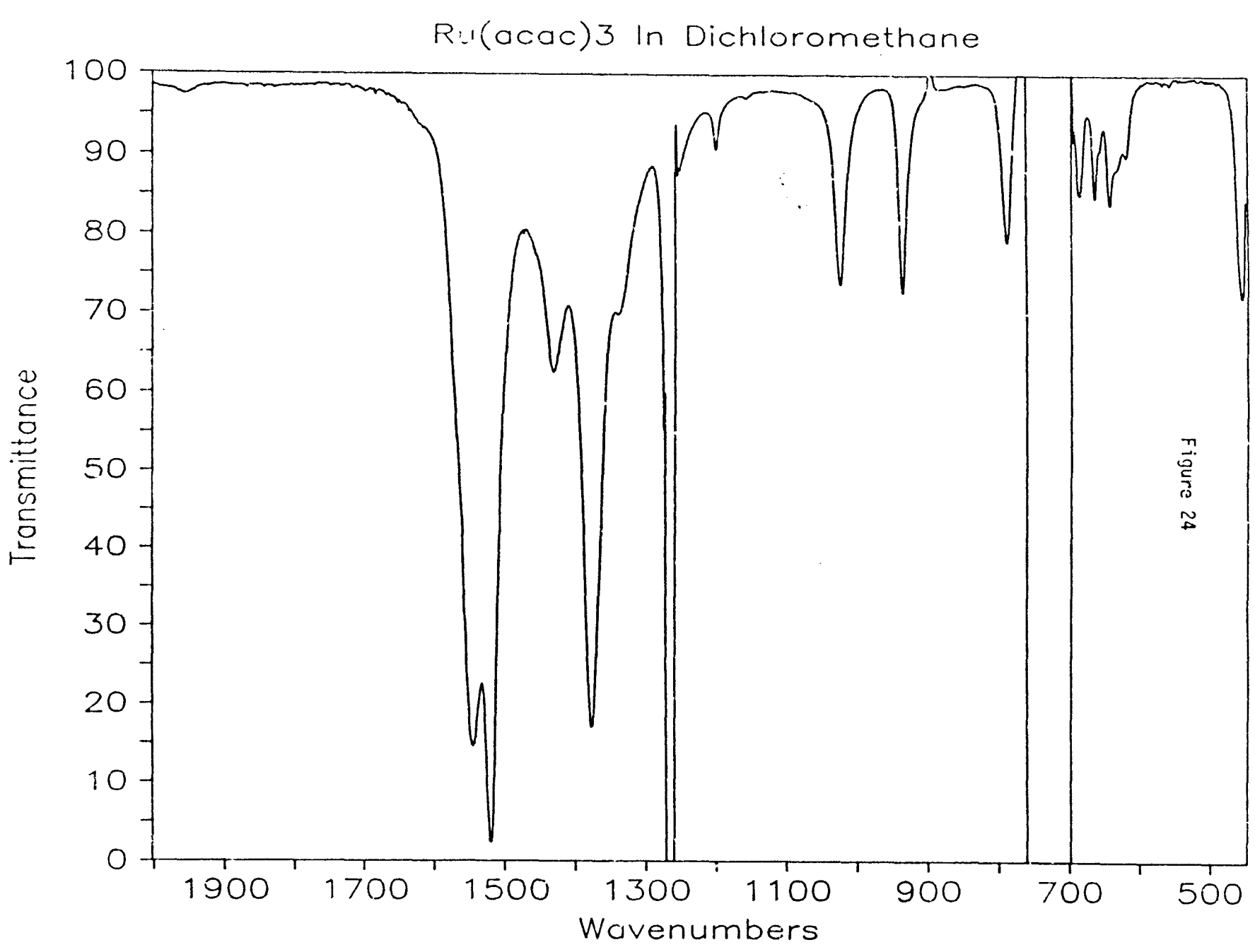

Ru(acac)3 In Dichloromethane
Transmittance
100
90
80
70
60
50
40
30
20
10
0
1900
1700
1500
1300
1100
900
700
500
Wavenumbers

Figure 24

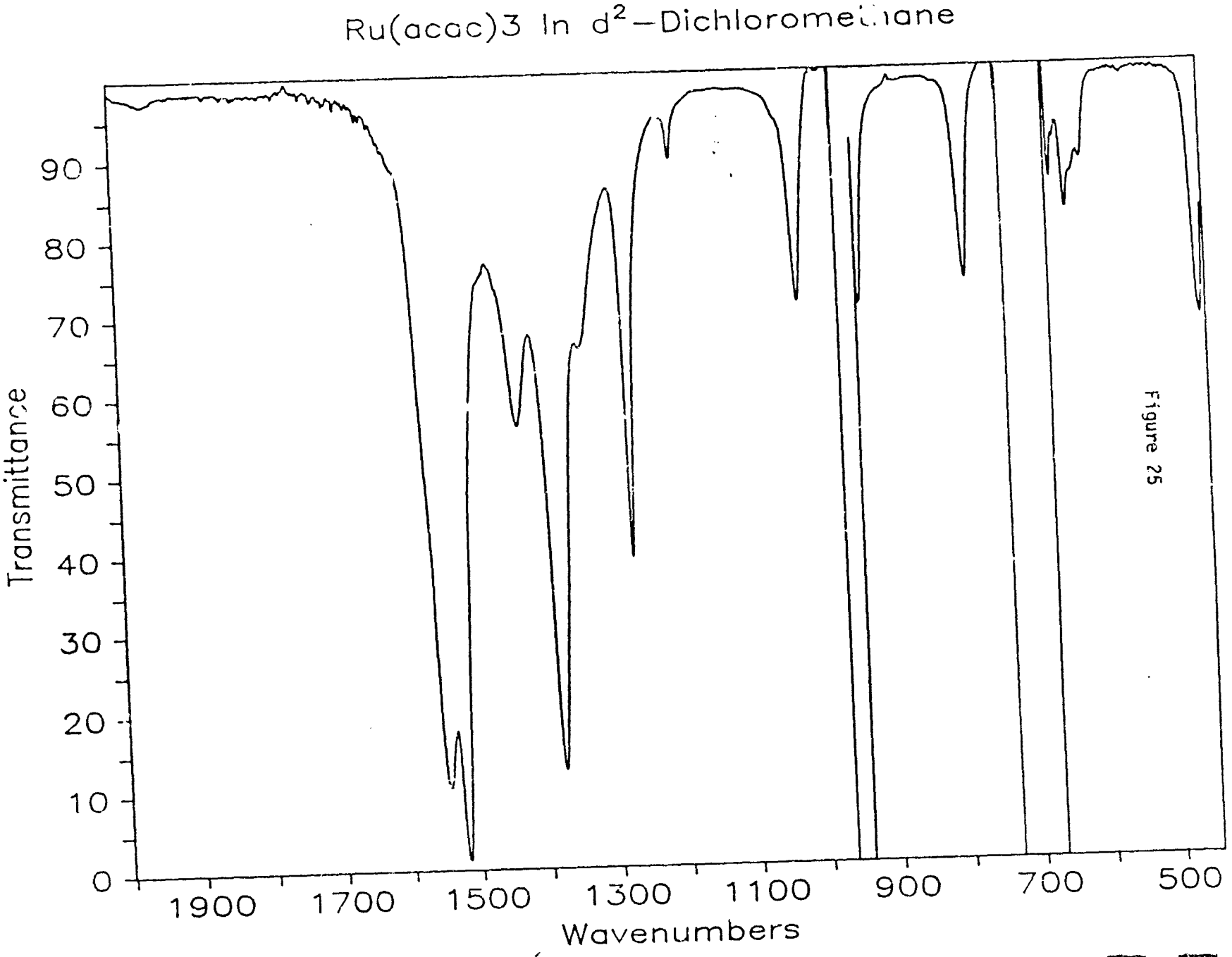

Ru(acac)3 In d2-Dichloromethane
Transmittance
90
80
70
60
50
40
30
20
10
0
1900
1700
1500
1300
1100
900
700
500
Wavenumbers

Figure 25

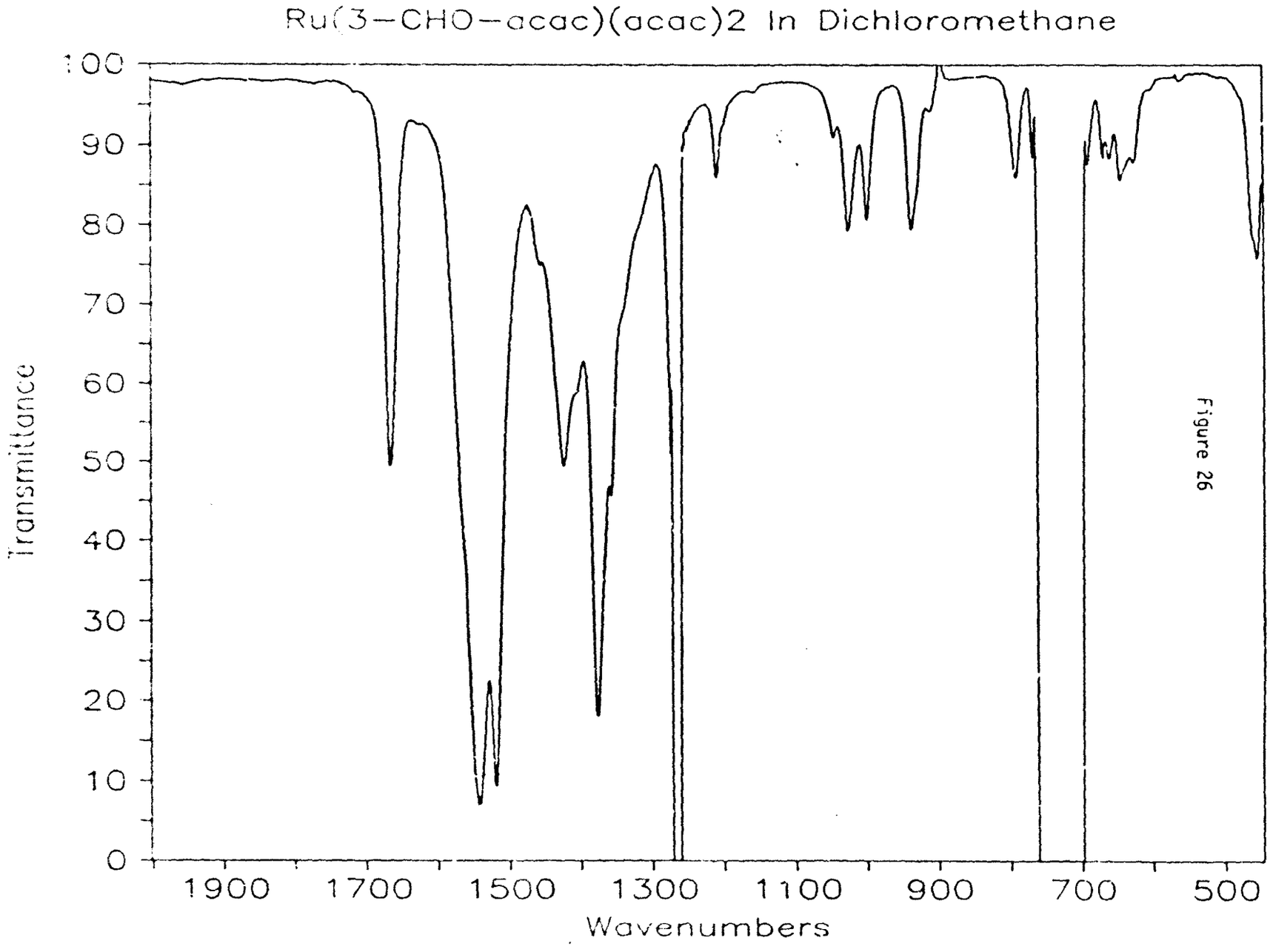

Ru(3-CHO-acac)(acac)2 In Dichloromethane
Transmittance
100
90
80
70
60
50
40
30
20
10
0
1900
1700
1500
1300
1100
900
700
500
Wavenumbers

Figure 26

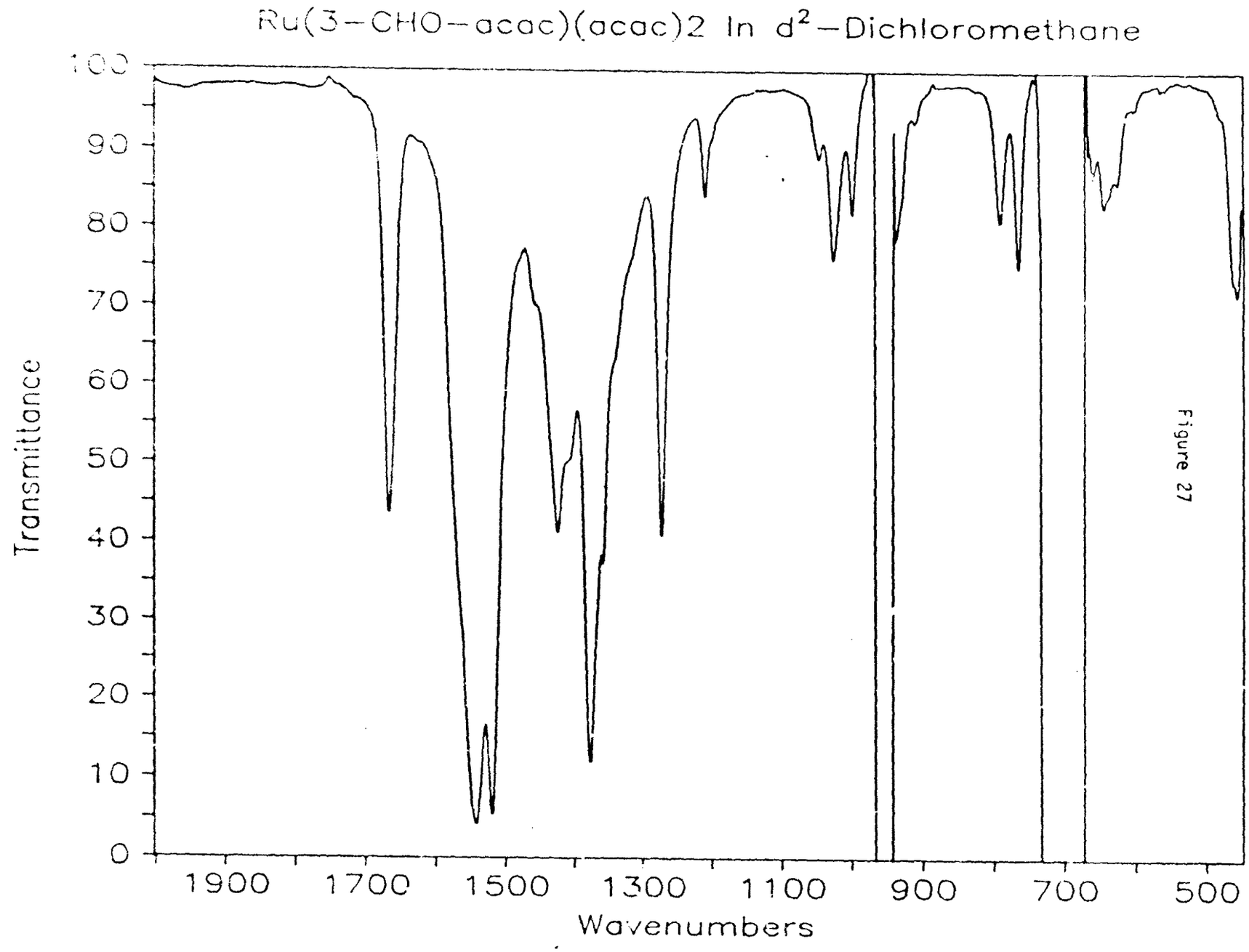

Ru(3-CHO-acac)(acac)2 In d²-Dichloromethane
Transmittance
100
90
80
70
60
50
40
30
20
10
0
1900
1700
1500
1300
1100
900
700
500
Wavenumbers

Figure 27

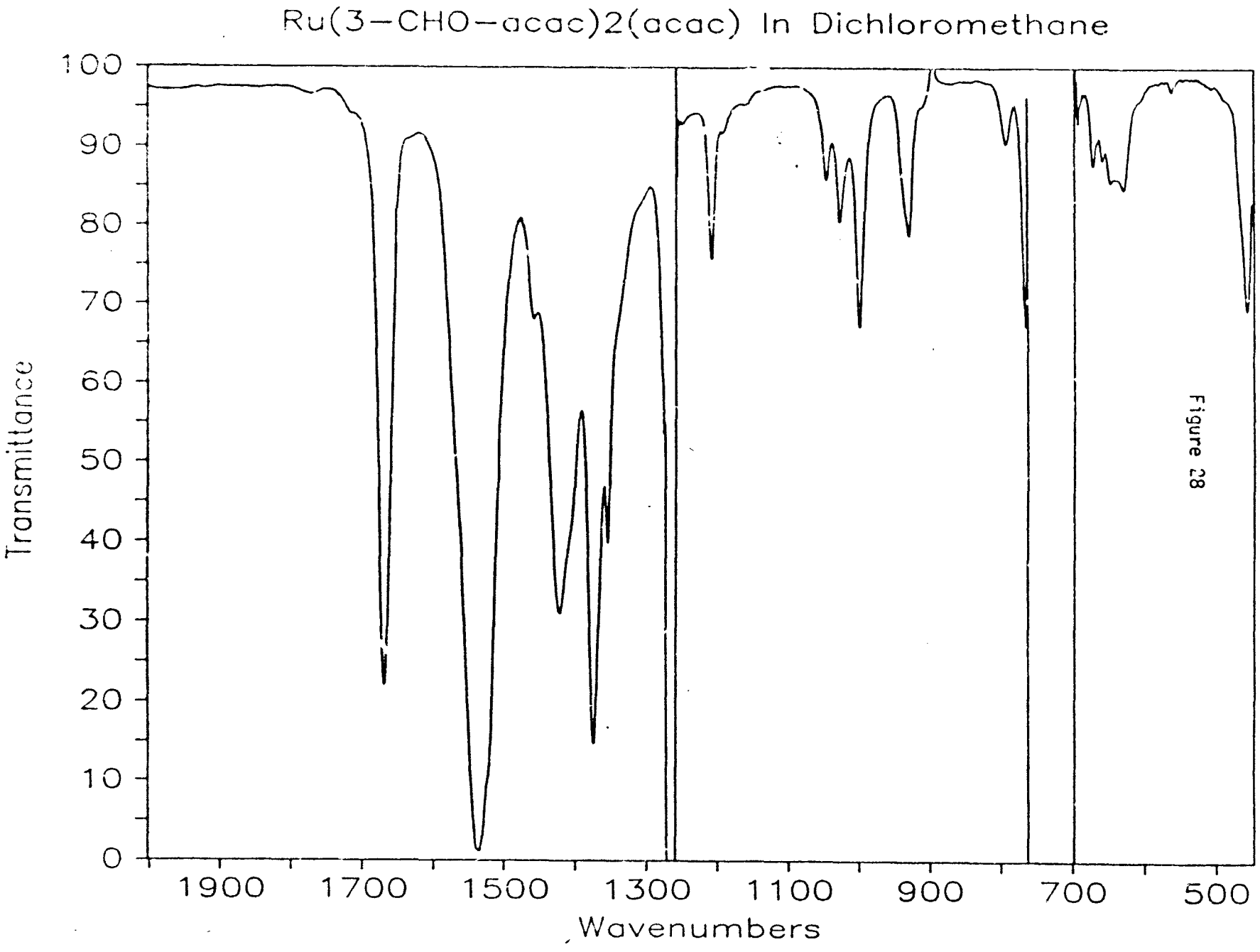

Ru(3-CHO-acac)2(acac) In Dichloromethane
Transmittance
100
90
80
70
60
50
40
30
20
10
0
1900
1700
1500
1300
1100
900
700
500
Wavenumbers

Figure 28

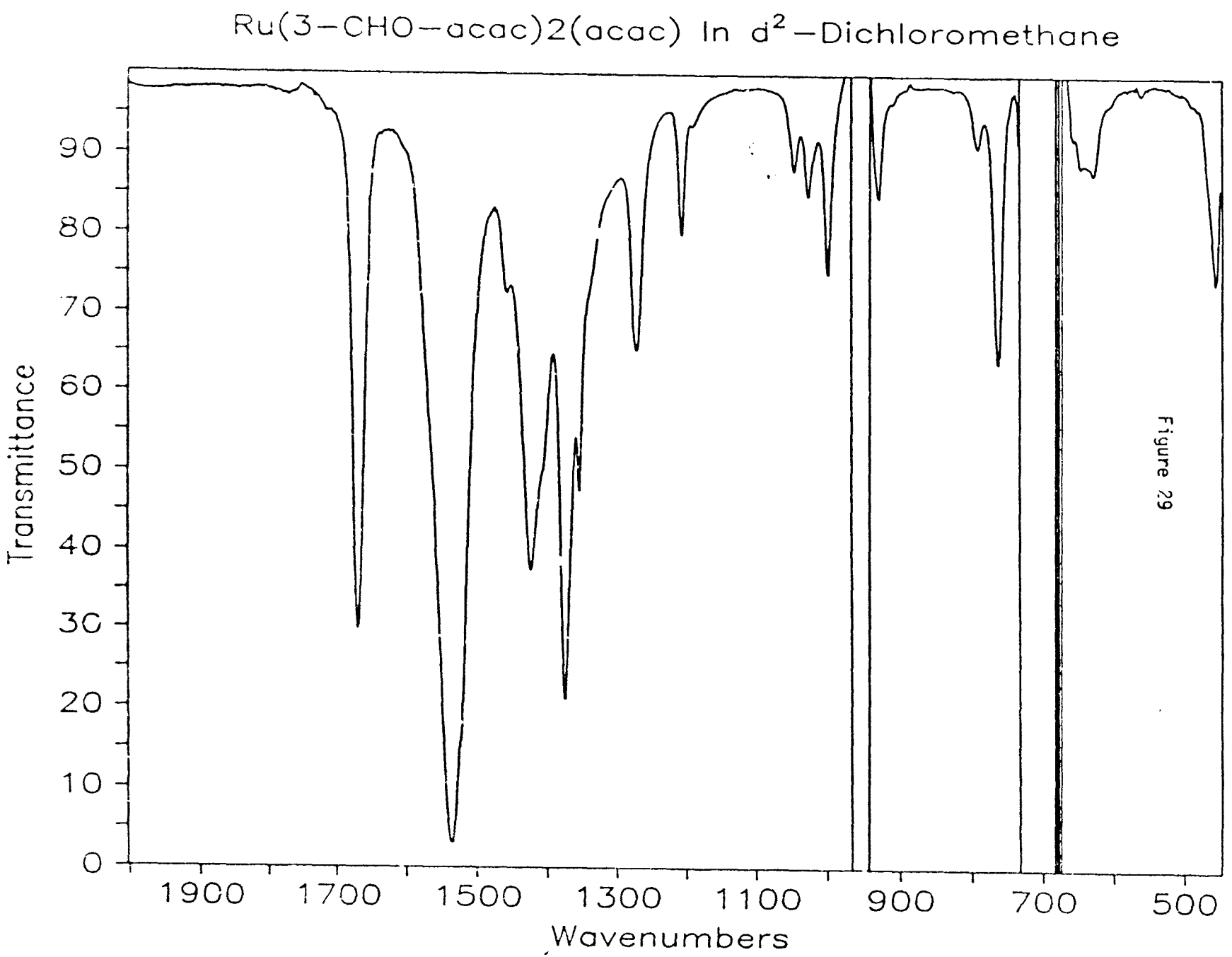

Ru(3-CHO-acac)2(acac) In d²-Dichloromethane
Transmittance
0
10
20
30
40
50
60
70
80
90
1900
1700
1500
1300
1100
900
700
500
Wavenumbers

Figure 29

spectrum. The ordering of these modes was controversial at one time but has been resolved in the literature from ^{18}O and ^{2}D isotopic substitution. Such studies have shown that these modes are coupled, of course, though not to the extent one might think. Shifts in the energies of these vibrational modes have been used as a determinant of relative pseudo-aromatic character in the acac$^-$ ring for different metal ions but these shifts are usually small.

The solution IR spectrum of [Ru(3-CHO-acac)(acac)$_2$] is shown in Figures 26-27. As expected, the free aldehyde $\nu_{C=O}$ mode appears at 1666 cm^{-1} in addition to the normal acac$^-$ ring modes. The spectrum also contains a number of new modes due to the substituted ring and ν_{CH} and δ_{CH} modes of the free aldehyde. The remainder of the spectrum is very similar to the parent complex since there are two unsubstituted ligands. Therefore, the composite rings modes appear at 1543 cm^{-1} ($\nu_{C=O}$) and 1519 cm^{-1} ($\nu_{C=C}$) and no information about the substituted ring is readily extracted from this region of the spectrum.

The solution IR spectrum of [Ru(3-CHO-acac)$_2$(acac)] is shown in Figures 28-29. The free aldehyde band appears at 1669 cm^{-1} and is more intense than in the monoformylated complex. Absorbance mode plots show that the ratio is very close to 2:1, as expected. The ring modes are dominated by the 3-CHO-acac$^-$ ligand in this case and only a single band is observed for $\nu_{C=O}$, $\nu_{C=C}$ at 1534 cm^{-1}, with barely resolvable shoulders for the acac$^-$ ligand mode on either side. Thus, formylation has a dramatic effect on the ring modes! The shifts imply lower bond order for the >C=O groups and higher bond order for the C-C-C fragment of the ring, suggesting a higher degree of pseudo-aromatic character than for the parent acac$^-$ ring. This is the result expected for formylation since, in principle, the resonance delocalization should increase with conjugation to the 3-*formyl* substituent. However, the extent of such electronic coupling is small and the free aldehyde mode is not very different from an aliphatic ketone ($\nu_{C=O}$ ~ 1720 cm^{-1}). The actual extent of the shift will need to be studied experimentally since >C=O modes are very sensitive to solvent H-bonding effects.

A more complete discussion of the vibrational studies will be given at a later date when it is hoped that data will be available for the triformylated derivative. The combination of NMR, UV-Visible and IR spectroscopy on that derivative, if it can be prepared, would be deterministic with regard to the pseudo-aromatic behaviour of the 3-CHO-acac$^-$ ligand on Ru(III) and its role in ligand-bridged electron transfer reactions.

SOLUTION KINETICS AND MECHANISMS

Part V

Electrochemical Characterization Of The Derivatives $[Ru(3\text{-}X\text{-}acac)_n(acac)_{3-n}]$ (X = -CHO,-CH_3,-Br,-I)

Measurements of the redox potentials of $[Ru(acac)_3]$ and its 3-X-acac$^-$ derivatives were used to provide a means of assessing the relative electron-withdrawing ability of the formyl substituent. Since the electronic spectroscopy of these complexes showed that the formyl group does not interact strongly with the acac$^-$ ligand's π-electron system, the electrochemical data below should be interpreted in terms of a σ bonding effect.

Electrochemistry Of $[Ru(3\text{-}CHO\text{-}acac)_n(acac)_{3-n}]$ (n=0,1,2)

Previous electrochemical studies of $[Ru(acac)_3]$ and its monoformylated derivative were performed by Early *et alia* in an aqueous medium of 0.1 HCl/0.9 M LiCl (I = 1.0 M) to match the conditions used in their kinetic measurements.[1] However, these Ru(III)/(II) couples are expected to be pH independent and there is no good reason to perform measurements in strong acid solution. Doing so would almost surely prevent the use of noble metal electrodes due to the onset of hydrogen adsorption and evolution waves. Indeed, the previous workers report the use of a carbon paste working electrode which displays a large overpotential for hydrogen evolution. For initial studies of these systems a medium of 0.1 M NaCl in deionized water was chosen to match the electrolyte in the SSCE reference electrode, to provide low enough solution resistance to avoid potential control errors, to minimize to possibility of Cl$^-$ complexation kinetics in the Ru(II) state and to permit the use of *both* glassy carbon and Au disc working electrodes. The background current from these working electrodes in 0.1 M NaCl was found to be 1.44 $\mu A/mm^2$ for glassy carbon and 0.45 $\mu A/mm^2$ for Au over the range +0.4 to -1.2 V *vs* SSCE. Clearly, the Au disc working electrode is best suited to aqueous studies in this potential range. The situation may well favor glassy carbon in acidic media.

Measurements were obtained for an argon bubble-degassed solution (~7.6×10^{-4} M) of $[Ru(acac)_3]$ in 0.1 M NaCl/H_2O at T = (25 ± 0.1) °C; both the cell and calomel electrode were thermostatted. The Ru(III)/Ru(II) reduction potential was -0.5215 V *vs* SSCE on glassy carbon and -0.518 V *vs* SSCE on gold taken at sweep rates where the ΔE_p was 63-65 mV. The peak splitting was almost constant with sweep rate on gold but broadened on glassy

carbon with increasing sweep rate, indicating slower heterogeneous kinetics on the carbon electrode. These measurements correspond to reduction potentials of −0.286 V (GCE) and −0.282 V (GE) *vs* NHE and compare reasonably well with the value of −0.278 V *vs* NHE reported by Early *et alia*.[1] Junction and reference electrode potential errors are of this order of magnitude. The electrode pretreatment consisted of polishing with 0.05 μ alumina in water slurry on microcloth followed by rinsing in deionized water and methanol with sonication to help remove polishing debris. The origin of slower heterogeneous kinetics on glassy carbon is unknown at present. This observation is somewhat surprising since no H^+ transfer steps are required in the Ru(III)/Ru(II) couple, at least in the overall sense, for which the surface state functional groups would be critical.

Equivalent measurements could not be obtained for the formylated derivatives, which are essentially insoluble in aqueous media. Therefore, electrochemical measurements were obtained in ~5% acetone solutions prepared with the 0.1 M NaCl electrolyte. This solvent system did not display any redox behaviour in the working potential range +0.4 to −0.8 V *vs* SSCE. The solutions were prepared by dilution of 0.5 mL of a nearly saturated solution of each complex in acetone. No precipitation occurred if the dilution was made slowly.

The reduction potential of $[Ru(3\text{-}CHO\text{-}acac)(acac)_2]$ in the above medium was found to be −0.3835 V *vs* SSCE (−0.148 V *vs* NHE) at 25°C on both glassy carbon and gold disc working electrodes (ΔE_p = 65 mV). Once again, unlike the gold electrode glassy carbon displayed increasing peak splitting with increasing sweep rate. These results are in reasonable agreement with the value of −0.16 V *vs* NHE reported by Berrie and Early.[3] After 10 days the aged solution gave a reduction potential of −0.365 V *vs* SSCE on the gold electrode and a quasi-reversible wave near +0.25 V *vs* SSCE. A fresh solution of the monoformylated derivative displayed some irreversible electrochemistry in this region but at a much lower current level so the origin of this behaviour in uncertain at present.

The reduction potential of $[Ru(3\text{-}CHO\text{-}acac)_2(acac)]$ in the same medium was found to be −0.244 V *vs* SSCE (−0.008 V *vs* NHE) on glassy carbon (ΔE_p = 64 mV). No measurement has yet been made for a *fresh* solution on the gold electrode. Aged solutions of the diformylated derivative gave reduction potentials of −0.2305V *vs* SSCE at 1 day (with impurity waves at ~ +0.18 and ~ +0.35 V. After 5 days the reduction appeared at −0.218 V *vs* SSCE but with little evidence of the impurity waves.

It is worth noting that the redox potential for Ti(IV)/Ti(III) in 0.01 F HCl is −0.14 V *vs* NHE, almost the same as the monoformylated derivative. Thus, the redox reaction between Ti(III) and $[Ru(3-CHO-acac)(acac)_2]$ at pH 2 will only go to completion if there is a pseudo-first order excess of one of the reagents; in this case Ti(III) is the only candidate for use in excess. The reactions with $[Ru(3-CHO-acac)_2(acac)]$ and $[Ru(3-CHO-acac)_3]$ may well be more facile since they are easier to reduce than the monoformylated complex. However, these inner-sphere reactions are probably substitution rate limited and may only show a statistical rate increase with the number of formyl groups available.

Electrochemistry Of $[Ru(3-CHO-acac)_n(acac)_{3-n}]$ In CH_3CN/0.1 M TEAP

Since the oxidative electrochemistry was not known for the 3-formyl series, measurements were performed in acetonitrile (Burdick & Jackson) with dried TEAP electrolyte under an argon blanket. The resulting cyclic voltammograms revealed two, reversible one-electron couples ($\Delta E_p \simeq 65$ mV) for each Ru(III) complex within the solvent limits. These are presumed to be the Ru(IV)/Ru(III) and Ru(III)/Ru(II) redox processes. The data are summarized in the Table III below. Both waves shift anodically with increasing numbers of formyl substituents, as expected for electron withdrawing functional groups. In order to provide a comparison for the electron withdrawing power of the formyl group several other 3-X derivatives of $[Ru(acac)_3]$ were prepared via literature routes, purified chromatographically and characterized by ^1H and ^{13}C NMR spectroscopy.

Electrochemistry Of $[Ru(3-X-acac)_n(acac)_{3-n}]$ (n = 1,2,3; X = −Br,−I,−Me)

Cyclic voltammetry of these Ru(III) complexes was performed in dried CH_3CN (Burdick & Jackson) with 0.1 M TEAP electrolyte at 25°C under a blanket of argon (directly from tank). In all cases one oxidative and one reductive wave was observed within the solvent limits and the data are summarized below in Table III.

The iodo- and bromo- derivatives conform to expectation regarding their relative stengths as electron withdrawing substituents. For the bromo- derivatives the Ru(IV)/(III) wave is completely reversible though the Ru(III)/(II) wave appears to be only *quasi*-reversible for the mono- and di-brominated complexes, which may be related to substituent loss in the Ru(II) state. Similar behaviour appears to occur for the iodo series though both waves are *quasi*-reversible for the bisiodinated complex. Susequently, ^1H NMR spectra showed that the iodo- derivatives were contaminated with chloro- derivatives due to the ICl based synthetic route used. The mixed iodo-chloro complexes will differ slightly from the pure iodo-

derivatives in redox potential, so explaining the larger than expected ΔE_p values for this series. Another preparation of the iodo- derivatives will be undertaken in future to obtain more accurate electrochemical and spectroscopic data. However, the trends in the data given in Table III should be valid.

Only the trimethylated derivative, $[Ru(3\text{-}Me\text{-}acac)_3]$, has been prepared so far. However, this is sufficient to show that the methyl group acts as an electron donating substituent in the 3-X-C< position of this complex. Therefore, $[Ru(3\text{-}Me\text{-}acac)_3]$ is significantly easier to oxidize than $[Ru(acac)_3]$. While the Ru(IV)/(III) wave was fully reversible the Ru(III)/(II) wave was broadened, apparently by weak adsorption on the electrode. Repeated cycling through the Ru(III)/(II) wave alone gave very broad waves while a single scan through the Ru(IV)/(III) wave then sharpened up the Ru(III)/(II) wave. This probably points to a solubility problem in the Ru(II) state.

The electrochemical behaviour of the 3-methyl derivative is marked contrast to 3-formyl derivative and this is reflected in their NMR spectra (*vide infra*). While the 3-formyl substituent does not appear to interact strongly with the metal spin density in the π_z molecular orbitals of the 3-CHO-acac$^-$ ligand the 3-methyl substituent displays *very* large isotropic shifts in both ^1H and ^{13}C spectra. Thus, the combination of electrochemical data, UV-visible and NMR spectrospcopy has provided unquestionable evidence for a dramatic lack of π bonding interaction of the 3-formyl substituent in the $[Ru(3\text{-}CHO\text{-}acac)_n(acac)_{3-n}]$ series. However, at the same time the kinetics measurements show that this ligand acts as an effective electronic conduction pathway for the inner-sphere oxidation of Ti(III), which proceeds at nearly the same rate observed for acacH substitution on Ti(III).

Table III

Electrochemical Half-Wave Potentials *vs* SSCE (ν = 100 mV/sec) For $[Ru(3\text{-}X\text{-}acac)_n(acac)_{3-n}]$ in CH_3CN/0.1 M TEAP at T = 25°C

Ru(III) Complex	$E_{\frac{1}{2}}$, V (ΔE_p, mV) Ru(IV)/Ru(III)	$E_{\frac{1}{2}}$, V (ΔE_p, mV) Ru(III)/Ru(II)
$[Ru(3\text{-}Me\text{-}acac)_3]$	+0.706 (64)	-0.930 (76)
$[Ru(acac)_3]$	+0.965 (64)	-0.781 (69)
$[Ru(3\text{-}I\text{-}acac)(acac)_2]$ [a]	+1.016 (69)	-0.665 (76)
$[Ru(3\text{-}I\text{-}acac)_2(acac)]$ [a]	+1.044 (78)	-0.574 (80)
$[Ru(3\text{-}I\text{-}acac)_3]$ [a]	+1.071 (73)	-0.479 (71)
$[Ru(3\text{-}Br\text{-}acac)(acac)_2]$	+1.022 (68)	-0.656 (91)
$[Ru(3\text{-}Br\text{-}acac)_2(acac)]$	+1.083 (68)	-0.552 (83)
$[Ru(3\text{-}Br\text{-}acac)_3]$	+1.133 (66)	-0.451 (69)
$[Ru(3\text{-}CHO\text{-}acac)(acac)_2]$	+1.100 (65)	-0.597 (64)
$[Ru(3\text{-}CHO\text{-}acac)(acac)_2]$	+1.224 (66)	-0.415 (65)

a: These samples were contaminated with mixed iodo-chloro complexes

SOLUTION KINETICS AND MECHANISMS

Part VI

^{1}H AND ^{13}C NMR STUDIES OF PARAMAGNETIC METAL ACETYLACETONATE COMPLEXES

Transition metal complexes of the type $[M(acac)_3]$ ($acac^-$ = pentane-2,4-dionato) were some of the first to be studied by NMR spectroscopy owing to the simplicity of their spectra. The complexes have D_3 symmetry (Fig.30) and therefore the NMR spectra display just two unique ^{1}H resonances ($-C\underline{H}_3$, $>C-\underline{H}$) and three ^{13}C resonances ($-\underline{C}H_3$, $>\underline{C}-H$, $>\underline{C}=O$). The original ^{1}H NMR work on diamagnetic complexes was focused on the question of possible pseudo-aromatic character for the coordinated ligand. Complexes of paramagnetic metals were also among the first to be studied in testing the theoretical predictions of Fermi contact (through bond) and Dipolar coupling (through space) shifts on ^{1}H NMR resonances.[18] These early studies conciuded that there did seem to be some evidence for aromatic character in the bonding of the ligand and indeed the $3-\underline{H}-C<$ position was shown to undergo many of the electrophilic reactions common to aromatic ring systems. When pulsed FT ^{13}C NMR spectroscopy became available the paramagnetic $[M(acac)_3]$ complexes were once again some of the first to be studied in detail.[19]

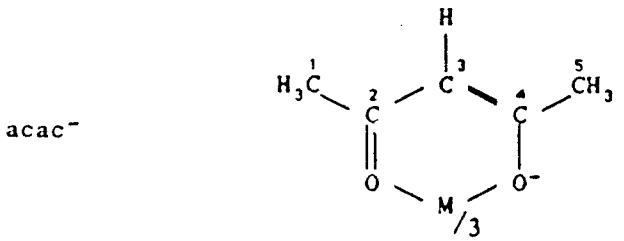


Figure 30

Since the ^{13}C NMR shifts of paramagnetic $[M(acac)_3]$ complexes were quite large, it appeared that this technique would be useful in characterizing the degree of metal character at the $3-\underline{C}<$ position. Electron transfer studies of $[Ru(acac)_2(3-CHO-acac)]$ have demonstrated that the $3-\underline{C}<$ position is the pathway for electronic conduction across the ligand so that ^{13}C NMR spectroscopy, in particular, promised to be a powerful probe of the conduction pathway. Unfortunately, the initial ^{13}C NMR spectra of $[Ru(acac)_3]$ obtained at N.R.L. on a high field NMR instrument demonstated that the early ^{13}C NMR spectra were incorrectly assigned. This discovery raised doubts about *all previous* ^{13}C NMR studies of

paramagnetic [M(acac)$_3$] complexes and the interpretations of the bonding within the ligand framework. Therefore, it became necessary to reinvestigate the ^{13}C NMR spectroscopy of as many additional paramagnetic [M(acac)$_3$] complexes as possible in order to provide an adequate background for the interpretation of paramagnetic shifts in the 3-formyl derivatives used for the kinetics studies.

In the case of [Ru(acac)$_3$] this work has unambiguously identified the 2,4 >C=O and 3 H-C< carbon resonances to be opposite to the previous assignments of Doddrell and Gregson.[19] Therefore, their assignments for [V(acac)$_3$], [Mn(acac)$_3$], [Cr(acac)$_3$] and [Fe(acac)$_3$] were also open to question. These materials were obtained commercially in reagent grade and were used without further purification to reinvestigate their NMR spectra. There was little doubt about the ^1H NMR assignments, although the previous workers did not find the 3-H resonances for [Cr(acac)$_3$] using their CW mode spectrometer. New ^1H NMR spectra were obtained mostly for improved precision, as well as filling in the missing resonances, and these data are summarized in Table IV. Of the paramagnetic complexes reinvestigated (M = V, Cr, Mn, Fe and Ru) the most difficult ^{13}C NMR spectra to obtain were those of [Cr(acac)$_3$], an NMR shift reagent, and [Fe(acac)$_3$] owing to their unfavorable T_{1e} relaxation times, which give rise to extremely broad NMR spectra. The ^{13}C data obtained to date are also summarized in Table IV.

NMR Spectra Of [V(acac)$_3$]

The d^2 complex [V(acac)$_3$] is air sensitive so a fresh sample (packed under nitrogen) was purchased from Aldrich. A saturated solution of [V(acac)$_3$] in $CDCl_3$ was prepared under an inert atmosphere of helium using glove box techniques to fill sealable 5 and 10 mm NMR tubes. In this case, the $CDCl_3$ was dried briefly over P_2O_5, then freeze-pump-thaw degassed and transferred to a sealed vial using vacuum line transfer techniques. This was performed principally to protect the helium filled glove box from moisture. However, this operation was probably beneficial to sample integrity given the known lability of [V(acac)$_3$]. Ligand exchange on V(III) is well known and equimolar mixtures of [V(acac)$_3$] and hexafluoroacetylacetone give complex ^1H NMR spectra due to the presence of all the [V(acac)$_{3-x}$(hfacac)$_x$] species. Another feature of the chemistry of unsymmetrical V(III) acetylacetonates is fairly rapid *cis* $\rightleftharpoons$ *trans* interconversion, which appears to occur via ligand dissociation.

The ^1H NMR spectrum of a helium protected sample of $[V(acac)_3]$ in a 10 mm Young valve sealed tube displayed just the two expected ligand resonances at +45.3 ppm ($-C\underline{H}_3$) and +39.7 ppm ($3-\underline{H}C<$) for T = 303K. The observed ^1H chemical shifts compare well with the values of +45.7 ppm ($C\underline{H}_3$) and +40.1 ppm ($3-\underline{H}-C<$) reported by Eaton.[18] However, Doddrell and Gregson[19] reported somewhat different values of +50 ppm ($C\underline{H}_3$) and +45 ppm ($3-\underline{H}-C<$) *vs* Internal TMS, presumably obtained at a lower temperature.

Some minor peaks due to free ligand also were observed at +2.03 ppm ($C\underline{H}_3$) and +5.48 ppm ($3-\underline{H}-C<$) as well as an unidentified species at +15.5 ppm. However, there was also a large peak at +2.3 ppm whose width (104 Hz) suggested that it might arise from a paramagnetic complex, though its chemical shift was that of a diamagnetic species. However, there was no evidence for a corresponding ^{13}C impurity in the sample so it is reasonable to assign this ^1H impurity to H_2O in the Aldrich sample, broadened and shifted by exchange on V(III). The consequences of this are not severe since the $acac^-$ ligand itself appears to be in the slow exchange region (diamagnetic free ligand peaks are apparent). Therefore, the chemical shifts will be dominated by the paramagnetic V(III) site.

These observations left some doubt about the usefulness of the Aldrich sample of this complex. However, the ^1H decoupled ^{13}C NMR spectrum obtained in a Young valve sealed 10 mm tube under helium contained only the expected number of resonances: +1085 ppm ($>\underline{C}=O$), +55.8 ppm ($3-H\underline{C}<$) and -216.1 ppm ($-\underline{C}H_3$). A ^1H coupled ^{13}C spectrum also was obtained (>100,000 scans) at T = 303K. This clearly revealed the J_{CH} coupling of the methyl resonance at -217.1 ppm (ave.) and the methine resonance at +54.6 ppm (ave.) with the carbonyl resonance remaining as a singlet at +1093 ppm. The small discrepancies are due to differences in sample temperature due to sample heating by the ^1H decoupler.

NMR Spectra Of $[Cr(acac)_3]$

The d^3 complex $[Cr(acac)_3]$ is often used as an NMR shift reagent due to its long T_{1e} value. No difficulty was experienced with the ^1H NMR spectrum but it is easy to appreciate the difficulty of the previous workers in finding the >C-H resonance. The resonances are so broad in this case that they overlap. The apparent peak positions are $-C\underline{H}_3$ = +39.6 ppm (*lit.* +40.2) and >C-H = +29.3 ppm (*no lit. value*). Since Doddrell and Gregson used a CW mode spectrometer for their ^1H spectra they would have been hard pressed to discern the broad, overlapping resonances as separate peaks.[19]

The ^{13}C NMR spectrum was found to be extremely broad in this case and no resonances could be identified with certainty. While Spin-Echo techniques have not yet been attempted it may well prove to be impossible to obtain ^{13}C NMR spectra of this complex so little can be learnt about spin distribution in the ligand framework from NMR data in this case.

NMR Spectra Of [Mn(acac)$_3$]

The d^4 complex [Mn(acac)$_3$] has a favorable T_{1e} value and all three ^{13}C as well as the ^1H resonances have been reported.[19] The ^1H NMR spectrum of [Mn(acac)$_3$] gave resonance positions which agreed well with the literature values; $-C\underline{H}_3$ = +24.8 ppm (*lit.* +25.2) and >C-H = +18.0 ppm (*lit.* +18.1) *vs* internal TMS. There were a number of low intensity peaks present in the ^1H NMR spectrum attributable to free ligand. As well, there is evidence of the resulting paramagnetic Mn(acac)$_2$ hydrolysis product with low intensity peaks near +30 and +15.5 ppm. However, the bulk of the sample is clearly [Mn(acac)$_3$].

The ^1H decoupled ^{13}C NMR spectrum of this sample of [Mn(acac)$_3$] gave shift values of +66.7 ppm ($-\underline{C}H_3$), +507.4 ppm (H-$\underline{C}$<) and +1142 ppm (>$\underline{C}$=O) vs External TMS (Internal TMS = +0.005 ppm) at T = 303K. In order to confirm the assignments another spectrum was obtained without ^1H decoupling. In this case the temperature was unknown (T < 303K) due to breakage of the thermocouple. The resonances were shifted somewhat further from the diamagnetic values (*cf* [Rh(acac)$_3$] in Table IV) due to higher magnetic susceptibility of the sample at the lower probe temperature. Although there was significant paramagnetic broadening, the J_{CH} coupling was discernable on both the 1,5-methyl (+69.5 ppm) and 3-H-$\underline{C}$< (+531 ppm) resonances while the 2,4->$\underline{C}$=O (+1205 ppm) resonance had a single Lorentzian lineshape. Except for the methyl resonance, the values differ markedly from those reported by Doddrell and Gregson; +63.0 ($-\underline{C}H_3$), +395.7 (3-H-$\underline{C}$<) and -293.5 (>$\underline{C}$=O) ppm *vs* Internal TMS.[19] Presumably, their data for the 3-H-$\underline{C}$< and 2,4->$\underline{C}$=O resonances are in error due to foldover aliases. An upper spectral limit of ~ 425 - 450 ppm in the previous work would account for their reported shift values.

NMR Spectra Of [Fe(acac)$_3$]

The d^5 complex [Fe(acac)$_3$] was fairly readily observed by ^1H NMR spectroscopy since the linewidths were not excessive. The observed resonance positions agreed fairly well with the literature values; $-C\underline{H}_3$ = +21.3 ppm (*lit.* +21.8) and >C-H = -29.2 ppm (*lit.* -27.4) *vs* internal TMS. The small discrepancies almost certainly arise from differences in sample temperature.

While the ^{1}H NMR spectrum of this d^5 high-spin complex was easily obtained the ^{13}C NMR spectrum proved to be very elusive. Only one, broad ^{13}C resonance at +598 ppm has been observed to date. Individual spectra of 1656 ppm sweep width (the max'm with the internal digitizer) have been obtained over the range +2146 to -930 ppm without identifying any other features which could be attributed to the missing resonances. Huge sweep width spectra (5500 ppm) were obtained using the fast digitizer mode on the Bruker 300 MSL spectrometer (2048 points max'm, ~30000 scans max'm). However, these did not reveal anything definitive owing to inadequate signal/noise ratio after only 20000 - 30000 scans. It appears that the paramagnetic broadening in this case is just too large to obtain all the ^{13}C chemical shifts by conventional pulsed FT experiments. Doddrell and Gregson reported a single resonance at +279.3 ppm (assigned to $\underline{C}H_3$) for this complex.[19] Presumably this observation was also a foldover alias from use of an insufficient sweep width. The previous assignment of this resonance to the methyl carbon is open to question.

NMR Spectra Of [Ru(acac)$_3$]

The low-spin, d^5 complex [Ru(acac)$_3$] displayed quite narrow NMR lines with ^{1}H resonances at -5.51 ppm (-C$\underline{H}_3$) and -30.5 ppm (3-$\underline{H}$-C<) in agreement with literature values.[18,19] The ^{13}C spectrum yielded just the expected three lines at -23.9 ppm (-$\underline{C}H_3$), +138.3 ppm (>$\underline{C}$=O) and +315.0 (3-H-$\underline{C}$<), the latter being a doublet in ^{1}H coupled spectra. The assignments of the latter pair are the reverse of those reported by Doddrell and Gregson.[19] Their instrument probably lacked sufficient sensitivity to distinguish these correctly. Unfortunately, much of their interpretation of the shifts and linewidths of [Ru(acac)$_3$] is invalidated by this incorrect assignment so a full analysis of this case is presented in the following section.

TABLE IV
^{1}H and ^{13}C NMR Chemical Shifts And Linewidths
For $M(acac)_3$ Complexes *vs* TMS Near Room Temperature

Metal		>C=O	3-HC<	$-CH_3$	3-HC<	$-CH_3$
Rh(III)	ν, ppm [a]	+188.7	+99.3	+26.6	+5.49	+2.16
	($\Delta\nu_{\frac{1}{2}}$,Hz)				(<8)	(<8)
Ru(III)	ν, ppm	+138.3	+315.0	-23.9	-30.5	-5.51
	($\Delta\nu_{\frac{1}{2}}$,Hz)	(78)	(229)	(14)	(111)	(36)
Fe(III)	ν, ppm	___ [b]	+598 [c]	___ [b]	-29.3	+21.2
	($\Delta\nu_{\frac{1}{2}}$,Hz)		(4030)		(2200)	(1200)
Mn(III)	ν, ppm	+1142	+507.4	+66.7	+18.0	+24.8
	($\Delta\nu_{\frac{1}{2}}$,Hz)	(336)	(809)	(100)	(143)	(102)
Cr(III)	ν, ppm	___ [b]	___ [b]	___ [b]	+28.3	+39.6
	($\Delta\nu_{\frac{1}{2}}$,Hz)				(~4000)	(~4000)
V(III)	ν, ppm [c,d]	+1085	+55.8	-216.1	+41.1	+47.0
	($\Delta\nu_{\frac{1}{2}}$,Hz)				(65)	(63)

a: Diamagnetic Reference Complex (similar shifts to $Co(acac)_3$)

b: Unobservable in present work, Spin-Echo measurements required

c: Tentative assignments from incomplete work

d: Impurity present in peak at +2.31 ppm ($\Delta\nu_{\frac{1}{2}}$ ~ 104 Hz)

TABLE V
Selected Literature Data For
^1H and ^2H NMR Chemical Shifts And Linewidths
For $M(acac)_3$ Complexes *vs* TMS Near Room Temperature [a]

Metal	d^n	3-$\underline{H}$C< (ppm)	$\Delta\nu$ (Hz)	-C$\underline{H}_3$ (ppm)	$\Delta\nu$ (Hz)
Ti(III) [b]	1	+32.2		+55.5	140
Ti(III)	1	---		~+55	2000, 4300 [c]
V(III)	2	+40.1		+45.7	25, 45 [c]
Cr(III)	3	---		+38.7	1000, 1400 [c]
Mn(III)	4	+18.1		+25.1	100, 95 [c]
Fe(III)	5	-27.4		+20.7	800, 920 [c]
Co(III)	6	+5.52		+2.22	
Mo(III)	3	+38.3		+124.1	200, 310 [c]
Ru(III)	5	-29.5		-5.4	100, 34 [c]
Rh(III)	6	+5.47		+2.13	

a: Data obtained at 60 MHz unless noted otherwise

b: ^2H data, theoretical $\Delta\nu_H/\Delta\nu_D$ = 42.5

c: Data obtained at 100 MHz

Analysis Of Isotropic Paramagnetic Shifts For $[M(acac)_3]$ Complexes

The paramagnetic shifts of the $[M(acac)_3]$ complexes derive from both Fermi contact and Dipolar magnetic coupling terms. For axially symmetric complexes and $T_{1e} << \tau_c$ these shifts are given as follows:

FERMI CONTACT SHIFTS:

$$\left[\frac{\Delta H}{H}\right]^{con} = \frac{-\beta S'(S'+1)}{9\,\hbar\,\gamma_N\,kT}\,(g_{||}\,A + 2\,g_{\perp}\,B)$$

where,
$A = \frac{1}{2}\,a_N\,g_{s||}$
$B = \frac{1}{2}\,a_N\,g_{s\perp}$

S' is the effective spin (L + S) and a_N is the electron–nucleus hyperfine coupling constant. For a spin–only state, no ZFS and an isotropic g tensor, ($g_{||} = g_{\perp}$, $g_{s||} = g_{s\perp} = 2$).

DIPOLAR COUPLING SHIFTS:

$$\left[\frac{\Delta H}{H}\right]^{dip} = \frac{\beta^2 S'(S'+1)}{9\,kT\,r^3}\,(1 - 3\cos^2\theta)(g_{||}^2 - g_{\perp}^2)$$

These expressions become a little more complex when other terms are included but the forms given above are adequate for illustrating the general features of the effect of unpaired electrons on the chemical shifts of ligand nuclei. Both the Fermi contact and Dipolar terms increase as $S'(S'+1)$ for inceasing numbers of unpaired electrons on the metal. Furthermore, both contributions are dependent on the g–value anisotropy, though only the Dipolar case can become zero. The relative contributions from these terms will vary with the d–electron configuration, deviations from octahedral symmetry and the relative energies of the metal and ligand HOMOs and LUMOs.

LINEWIDTHS:

$$\frac{1}{T_2} = \underbrace{\left[\frac{4\gamma^2 g^2 \beta^2 S(S+1)}{3\,r^6}\right]\tau_c}_{\text{DIPOLAR}} + \underbrace{\left[\frac{A_i^2}{\hbar^2}\,\frac{8\pi^2 S(S+1)}{3}\right]\tau_e}_{\text{FERMI CONTACT}}$$

where A_i are the hyperfine coupling constants, τ_c is the molecular correlation time and τ_e is the electron spin relaxation time. The Dipolar broadening falls off rapidly with distance while the Fermi contact broadening is proportional to the square of the hyperfine coupling constant

and, hence, the square of the paramagnetic shift. Thus, it is useful to compare the ratios of linewidths for contiguous carbon and proton nuclei to determine which mechanism predominates.

Isotropic Paramagnetic Shifts In [Ru(acac)$_3$]

The data in Table VI summarize the paramagnetic shifts which result from the Fermi contact and Dipolar contributions above. The latter would diminish to zero if there were no magnetic anisotropy in this low-spin d^5 Ru(III) complex. However, a magnetically dilute single crystal EPR study by Jarrett has shown three principal g-values (1.28, 1.74 and 2.82) so that the Dipolar contributions to the iostropic shifts will not average to zero.[21]

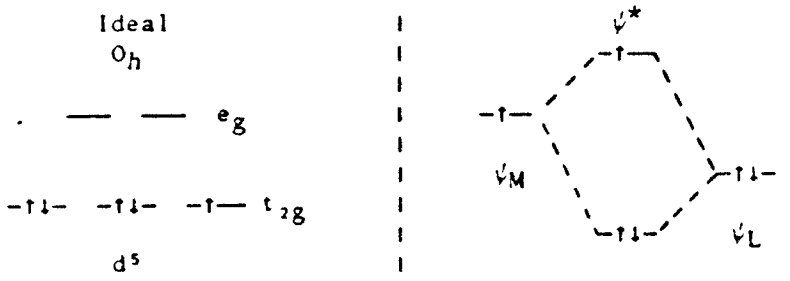


Figure 31

A similar study by Gregson and Mitra, using single crystal magnetic susceptibility, gave g-values in the range 1.5 - 2.5,[22] which fits in better with frozen solution EPR measurements at N.R.L. This confirms that the D_3 ligand field successfully removes the ground state degeneracy and it must also be acknowledged that spin-orbit coupling will further split the states:

Crystal Field Splitting → ^2A, ^2E states

Spin-Orbit Coupling ($\lambda \sim -1200$ cm^{-1}) → closely spaced manifold

The consequence of such a manifold of thermally populated levels is a facile means for rapid T_{1e} electron-spin relaxation which results in narrow NMR lines and relatively broad EPR signals, as observed experimentally. The magnetic anisotropy was used by Doddrell and Gregson to calculate the Dipolar shifts in [Ru(acac)$_3$] assuming the principal magnetic axis coincided with the 3-fold symmetry axis.[19] These corrections to the isotropic NMR shifts (see

TABLE VI

Comparision Of NMR Spectra For

[$Rh(acac)_3$] and [$Ru(acac)_3$] In $CDCl_3$

Nuclei	[$Rh(acac)_3$] δ (ppm)	[$Ru(acac)_3$] δ (ppm)	Δ Shift (ppm)
^1H: *a*			
$-CH_3$	+2.16	-5.51	-7.67
>C-H	+5.49	-30.5	-35.99
^{13}C: (^1H coupled) *b*			
$-CH_3$	+26.6 (av)	-23.9 (av)	-50.5
>C=O	+188.7	+138.3	-50.4
>C-H	+99.3 (av)	+315.0 (av)	+215.7

a: ^1H chemical shifts *vs* TMS

b: ^{13}C chemical shifts *vs* Internal $CDCl_3$ at 77.00 ppm

Table VII) are, however, relatively small so that the bulk of the shift is due to partial delocalization of metal spin density onto the acac⁻ ligands.

The metal spin for a d^5 ion will tend to allign parallel to the applied field in the NMR experiment so that for net Ligand-to-Metal charge transfer (Fig.31) in the expected $d\pi$-$p\pi$ bonding arrangement, (+) spin density should appear at the oxygen nuclei and alternating signs for adjacent atoms in the π-system of the pseudo-aromatic acac⁻ ligand. Negative spin density at the >C=O ^{13}C nuclei would predict a lower average local field and, thus, a lower resonance frequency as observed experimentally (Table VI). {Note that such shifts are denoted curiously as "High Field" shifts since a higher external field would be required to bring the transition into resonance in the original fixed frequency, swept field NMR instruments.} Furthermore, the contiguous ^1H and ^{13}C nuclei at the >CH position display opposite shifts as expected for σ-π_z electron correlation. The observation of large contact shifts at this ring position is the reason behind the companion study of the 3-formyl derivative. It was hoped that the NMR shifts would provide direct evidence for metal spin and electron density at this substituent site which has been found to serve as an efficient bridging ligand in electron transfer reactions (using the π^* orbital).

Sign Of Predicted Spin Density

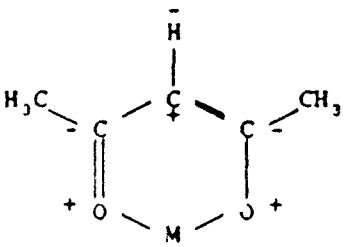


Figure 32

The methyl ^{13}C and ^1H resonances are found to follow the same shift direction as the ring ^{13}C nucleus which might reasonably be ascribed to a hyperconjugation mechanism involving s-p mixing in order to create the same sign of spin density at the methyl C and H nuclei. In reality, there are probably competing σ and π mechanisms involved and the companion studies for the first transition series metals have revealed that the methyl ^1H shifts can go either way.

Analysis Of Linewidths For ^{1}H and ^{13}C NMR Spectra Of $[Ru(acac)_3]$

Although Doddrell and Gregson used incorrect assignments for the ^{13}C resonances in their $[M(acac)_3]$ NMR studies, their work is valuable for pointing out some simple linewidth criteria for confirming the Fermi-contact nature of the isotropic shifts in these species, including $[Ru(acac)_3]$. These authors presented the following simplified forms of the Solomon-Bloembergen linewidth functions for the limiting cases of only Dipolar broadening (DD) and only Hyperfine broadening (HF):

$$(\Delta\nu_{\frac{1}{2}})^{DD} = \frac{(g_e\,\beta_e\,\gamma_N)^2}{15\pi\,r^6}\,S(S+1)\left[\,7\tau_c + \frac{13\tau_c}{1+\omega_s^2\tau_c^2}\,\right]$$

where, r = metal-nucleus distance and τ_c = electron-nuclear interaction time (related to τ_r)

$$(\Delta\nu_{\frac{1}{2}})^{HF} = \frac{a_N^2}{3\pi\,\hbar^2}\,S(S+1)\left[\,\tau_e + \frac{\tau_e}{1+\omega_s^2\tau_e^2}\,\right]$$

where, $a_N = -[3kT\ \gamma_N/\gamma_e\ S(S+1)]\ \sigma_{con}^{N}$ and τ_e = correlation time for hyperfine coupling (electron spin relaxation time). Note the relationship, $1/\tau_c = 1/\tau_e + 1/\tau_r$.

The linewidth ratios for contiguous ^{1}H and ^{13}C nuclei are readily obtained from the equations above in the two limits:

$$\frac{(\Delta\nu_{\frac{1}{2}})_C^{DD}}{(\Delta\nu_{\frac{1}{2}})_H^{DD}} = \frac{\gamma_C^2}{\gamma_H^2}\cdot\frac{r_H^6}{r_C^6}$$

and,

$$\frac{(\Delta\nu_{\frac{1}{2}})_C^{HF}}{(\Delta\nu_{\frac{1}{2}})_H^{HF}} = \frac{\gamma_C^2}{\gamma_H^2}\cdot\left[\,\frac{\sigma_{con}^{C}}{\sigma_{con}^{H}}\,\right]^2$$

where, $(\gamma_C/\gamma_H)^2 = 0.063$. The results of these calculations are summarized in Table VII for the two limiting cases. It is interesting to note that while the isotropic shifts of both the methine H-C< group and methyl H_3C- group appear to be dominated by contact interactions the linewidth ratios suggest that the methyl resonances are predominantly affected by *dipolar broadening*. This may well indicate that the Dipolar correction terms for the isotropic shifts in Table VII are grossly underestimated. However, the ring methine H-C< resonances do behave in the expected manner for a predominantly hyperfine contact interaction at the 3-C position.

TABLE VII
Paramagnetic Shifts And Linewidths
For [R·1(acac)$_3$] In $CDCl_3$

Nucleus	C-H ppm	C-H ppm	CH_3 ppm	CH_3 ppm
δ_{iso}	+209.7	-36.2	-48.2	-7.92
$\delta_{dipolar}$ [a]	-17.2	-7.1	-1.8	-1.6
$\delta_{contact}$	+226.9	-29.1	-46.4	-6.32
$\delta^C_{con}/\delta^H_{con}$	-7.8		+7.3	
$\Delta\nu_{\frac{1}{2}}$ (Hz)	229	111	14	36
$\Delta\nu_{\frac{1}{2}}^C/\Delta\nu_{\frac{1}{2}}^H$ (obsd)	2.1		0.38	
$\Delta\nu_{\frac{1}{2}}^C/\Delta\nu_{\frac{1}{2}}^H$ (calc)^{DD} [b]	0.23		0.22	
$\Delta\nu_{\frac{1}{2}}^C/\Delta\nu_{\frac{1}{2}}^H$ (calc)^{HF}	3.8		3.4	

a: Calculated from anisotropy of $\chi_{\parallel}$ and $\chi_{\perp}$ tensors (Doddrell & Gregson)

b: Calculated for M-C distances of ~4.2 and ~4.4 A, with C-H ~ 1 A

Note that the calculated linewidth ratios in Table VII *do not agree* with those calculated by Doddrell & Gregson (DD = 0.37 & 0.08, HF = 0.3 & 1.0 for H–C< and H_3C–, respectively).[19] Their hyperfine calculations are in error due to the misassignment of the resonances but they also calculated their Dipolar ratios to be very different from one another even though in a following paper[20] they quote the approximate distances used for the calculations in Table VII. There is no $(1 - 3\cos^2\theta)$ dependence in the linewidth ratio equations, so the source of the disagreement is unknown.

Summary Of Isotropic ^1H NMR Shifts For [M(acac)$_3$] Complexes

The literature is replete with ^1H and ^2H NMR studies of the isotropic shifts for paramagnetic [M(acac)$_3$] complexes of all the First Row and several Second Row metals and that data is summarized in Table V. Three features stand out in the literature data.

First, the isotropic shifts gradually decrease across the First Row from Ti(III) to Fe(III) in the opposite behaviour expected from the shift equations above. This has been interpreted as a gradual decrease in the mixing of metal dπ and ligand pπ–orbitals as the increasing nuclear charge affects the orbital extension and energies of the d–orbitals across the First Transition series. Secondly, a number of the metals show a field dependence of their methyl ^1H NMR linewidths, presumably due to electric quadrupolar broadening which has not been included in the linewidth equation above. Thirdly, a change in sign for the isotropic shift occurs for the 3–*H*–C< resonance in Fe(III) which has a half-filled t_{2g}^3 and half-filled e_g^2 configuration. In this case, any covalency leading to Ligand→Metal charge transfer must place β–spin (antiparallel) on the metal, leaving α spin on the ligating atoms which will then cause alternating β–spin (>*C*=O) and α–spin (3–H–*C*<) along the ligand π framework. This would be expected to cause β–spin (antiparallel, shielding) at the 3–*H*–C< nucleus, lowering the resonance frequency (a high–field shift), as is observed experimentally. This would predict, however, that the methyl resonance would also shift to high field (hyperconjugation with >C=O) but this is *not* observed. Rather, it appears that the α–spin in the e_g^* orbitals, which are oriented along the bonding axes, causes an overwhelming σ–shift to low–field. Note that Ru(III) behaves according to expectations since this is a low–spin complex (t_{2g}^5) and the σ–shift term largely vanishes.

Predictions For ^{13}C NMR Shifts

The interpretation of ^{1}H NMR from the literature leads to some simple expectations for spin density at the carbon nuclei in $[M(acac)_3]$ compiexes:

(1) The delocalization pathway for metal electron and spin density is principally a result of $d\pi-p\pi$ overlap since the σ, σ^* orbitals are too far removed in energy from the metal $d\pi$ orbitals for these to interact strongly. While both the t_{2g} and e_g orbitals have the appropriate symmetry to interact with the ligand $p\pi_z$ and $p\pi_z^*$ orbitals the t_{2g} set has the most appropriate spatial orientation for overlap.

(2) For d^1 and d^2 configurations Ligand→Metal charge transfer will probably place α–spin on the metal (maximum spin multiplicity), leaving β–spin on the ligand.

(3) For d^3 and d^4 configurations there is the possibility of Ligand→Metal β–spin transfer into the t_{2g} orbitals or α–spin transfer into the e_g^* set. The most likely event is α–spin into the e_g^* set with β–spin on the ligand to preserve maximum spin multiplicity.

(4) For the high–spin d^5 case there is only one possibility for Ligand→Metal, β–spin transfer to the metal and α–spin on the ligand.

(5) For any configuration, Metal→Ligand charge transfer to unfilled π^* orbitals will transfer α–spin to the ligand.

Experimental Comparisons Of ^{13}C NMR Isotropic Shifts

No ^{13}C NMR data are available at present for the d^1 case, $[Ti(acac)_3]$, but a ^{1}H decoupled spectrum has been obtained for a sample of the d^2 complex, $[V(acac)_3]$. The prediction is for β–spin at the oxygen, α–spin at >C=O and β–spin at 3–H–C<. This corresponds to a +ve shift at >C=O (found: +896 ppm) and a –ve shift at 3–H–C< (found: –43.5 ppm). The methyl carbon appears to be shifted a long way to high–field in this case (–242.7 ppm), which does not match with the observed CH_3 shift (+44.8 ppm).

No strong case can be made for d^3 $[Cr(acac)_3]$ since the ^{13}C spectrum appears to be unobservable. The prediction is for β–spin at the oxygen nuclei, α–spin at >C=O, β–spin at 3–H–C< and α–spin at 3–H–C< (+ve shift). The ^{1}H NMR data display reasonable behaviour with the 3–H–C< resonance shifted +22.5 ppm. The CH_3 resonance is also shifted +37.4

ppm to low field which could be accounted for through hyperconjugation to α–spin at >C=O.

The high–spin d^4 complex, [Mn(acac)$_3$], displays large +ve isotropic NMR shifts for *all* the carbon and proten nuclei. The lack of alternation in the signs of the ^{13}C NMR shifts is bothersome and unexpected. The data appear to be reliable and no simple explanation is apparent and may reflect the σ–shift of the e_g^* electron.

The high–spin d^5 complex, [Fe(acac)$_3$], does display the expected behaviour for ^1H NMR shift at the 3–H–C< nucleus but the presence of e_g^* electrons appears to complicate the behaviour of the CH_3 resonance. There is insufficient ^{13}C data to make any useful observations.

The pattern of isotropic shifts for the low–spin d^5 complex [Ru(acac)$_3$] behaves according to expectations since there are no e_g^* electrons. The ^1H and ^{13}C isotropic shifts are well matched in sign and magnitude to expectations for a predominantly Fermi contact interaction between the metal dπ and ligand pπ orbital systems. This seems to result from direct covalent coupling between the filled ligand pπ and partially filled metal $t_{2g}^5(\pi)$ orbitals.

Low–Spin d^5 Case

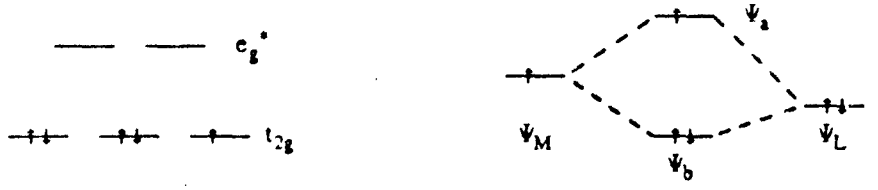


Figure 33

Analysis Of Experimental Linewidths For Other [M(acac)$_3$] Complexes

The linewidth analysis for [Ru(acac)$_3$] presented above suggested that the 3–H–C< position is predominantly Fermi contact shifted while the methyl groups appeared to be dominated by Dipolar coupling.

However, the First Row equivalent, [Fe(acac)$_3$], is a high–spin d^5 species (t_{2g}^3, e_g^2) which produces a more complex interaction between the ligand and the unpaired spin on the metal. The population of the e_g^* levels with unpaired spins should dramatically increase the σ–contact shift component, compared with [Ru(acac)$_3$], since the e_g^* orbitals are oriented along the σ–bonding axes. The effect of e_g^* electrons on metal–ligand bond lengths is well

established and it seems likely that this strong, antibonding interaction will lead to spin ordering along the ligand backbone. Unfortunately, the T_{1e} for the ^6A ground state of [Fe(acac)$_3$] is too long to observe all the ^{13}C NMR resonances which would test the effects of the M-L spin transfer. The assignment of the one observable line at +598 ppm is by no means clear. With a known, long τ_e value [Fe(acac)$_3$] is predominantly Fermi contact broadened. Furthermore, the ^6A ground state is isotropic so that Dipolar shifts should be small. This resonance could be assigned to either the methyl or 3-H-C< position on the basis of the linewidth ratios $\Delta\nu_C/\Delta\nu_H$. If this is the methyl resonance then there is little hope of ever observing the other ^{13}C resonances.

This point is more clearly illustrated in the case of d^4 [Mn(acac)$_3$] since this is also a high-spin species (t_{2g}^3 e_g^1) but with a sufficiently short T_{1e} for observation of all the ^1H and ^{13}C resonances. The observed $\Delta\nu_C/\Delta\nu_H$ ratios are 5.7 for the 3-H-C< and 1.0 for the $-CH_3$ positions. Neither of these corresponds to expectations for purely Fermi contact broadening.

More ^{13}C NMR data are required for further analysis of the nature of the isotropic NMR shifts of these [M(acac)$_3$] complexes. [Fe(acac)$_3$] and [Cr(acac)$_3$] will require use of the Spin-Echo NMR technique for observation of the rapid Free Induction Decay before a meaningful assessment can be made for these complexes. Most of the FID is probably occurring before the start of data acquisition using the conventional 90° pulse experiment.

Analysis Of Isotropic Paramagnetic Shifts In [Ru(3-CHO-acac)(acac)$_2$]

While no independent measurement is available yet for the magnetic anisotopy of the formylated derivatives, the frozen solution EPR spectra suggest that the principal g-values span a relatively narrow range (2.1 - 2.5) so that once again the Dipolar contributions to the observed NMR shifts would be small. Assuming this to be the case the shifts in Table VIII reveal several points of interest. First, the resonances of the unsubstituted ligands retain the same sign of paramagnetic shift though the magnitude is higher, except for the methyl ^{13}C resonances. Secondly, while the magnitudes of the shifts for corresponding resonances are roughly the same for the formylated ligand, the signs do not alternate as expected for a π-system. Thirdly, the paramagnetic shifts of the formyl substituent are relatively small, even though the contiguous ring carbon has a large spin density. The latter observation suggests that the formyl substituent is not well conjugated with the ring π_z system. A plausible explanation for this could be free or restricted rotation of the formyl group, a necessity for magnetic equivalence of the methyl groups.

TABLE VIII

^{1}H And ^{13}C NMR Assignments For

$Rh(3-CHO-acac)(acac)_2$ and $Ru(3-CHO-acac)(acac)_2$

In $CDCl_3$ At T = 298 K

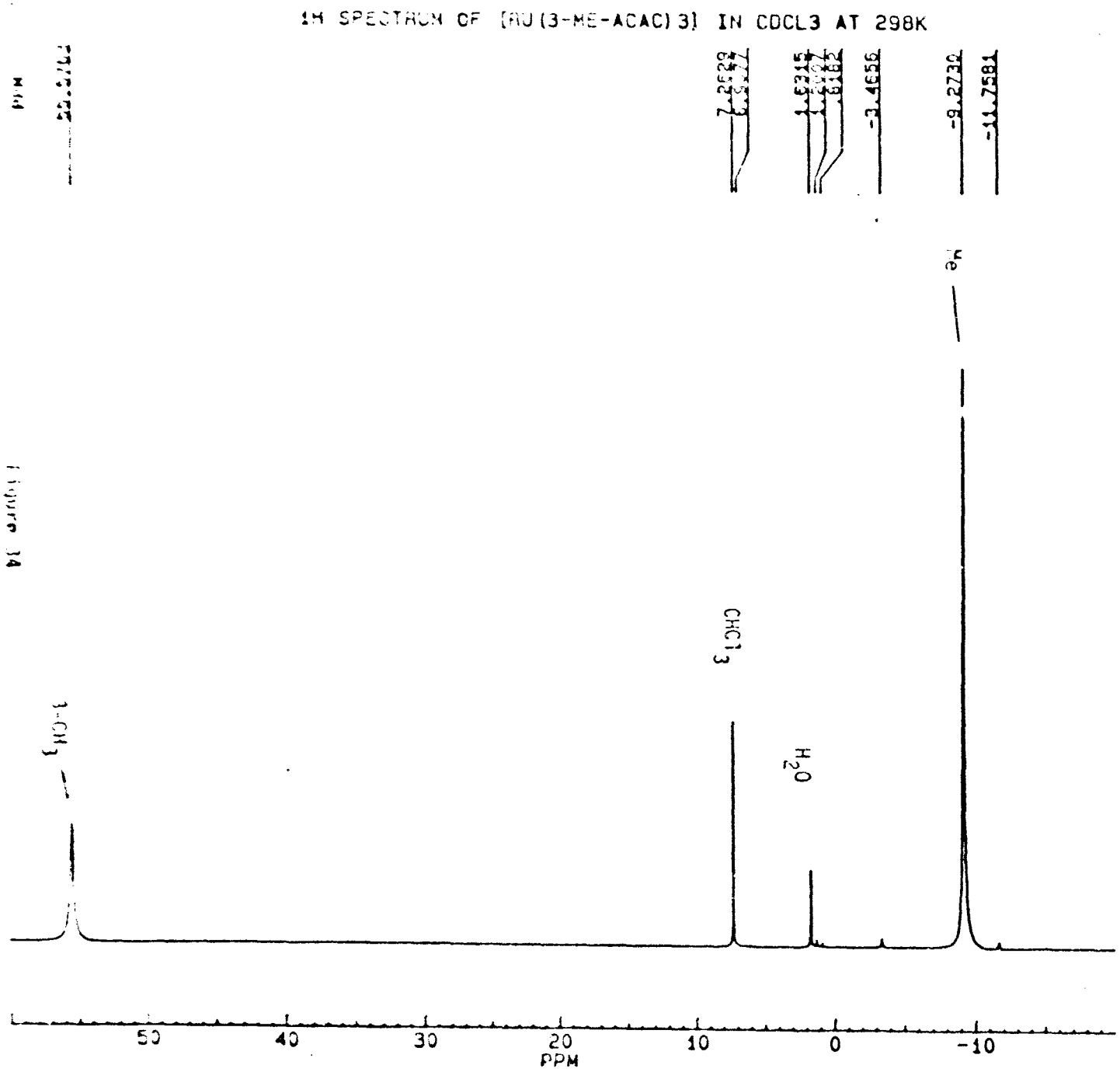
Nuclei	Rh(III) δ (ppm)	Ru(III) δ (ppm)	Δ Shift (ppm)
^{1}H:			
$-CH_3$	+2.15	−13.01	−15.16
$-CH_3$	+2.15	−10.30	−12.45
$-CH_3(f)$	+2.61	+7.47	+4.86
O=C−H(f)	+10.14	+12.89	+2.75
>C−H	+5.50	−46.7	−52.2
^{13}C: (^{1}H coupled)			
$-CH_3$	+26.44 (av)	−20.23 (av)	−46.67
$-CH_3$	+26.44 (av)	−9.94 (av)	−36.38
$-CH_3(f)$	+28.40 (av)	+1.87 (av)	−26.53
>C=O	+189.0	−26.48	−215.5
>C=O	+189.0	+57.52	−131.5
>C=O(f)	+196.8	+338.2	+141.4
O=C−H(f)	+190.3 (av)	+206.8 (av)	+16.5
>C−formyl	+115.5	+320.4	+204.9
>C−H	+99.4 (av)	+370.9 (av)	+271.5

One further cause for concern is the possible Dipolar shift of the 3-formyl-$\underline{C}<$ nucleus caused by the formyl >C=O group itself. This term is probably only partly responsible for the observed chemical shift difference between the 3-formyl-$\underline{C}<$ and 3-H-$\underline{C}<$ nuclei. The largest effect will probably result from the electron withdrawing nature of the formyl substituent. The monoformyl complex is easier to reduce electrochemically by ~0.12 Volts compared with [Ru(acac)$_3$] Presumably, the formylated and unsubstituted ligands have quite an appreciably different pπ-dπ bonding arrangement resulting in differences in the extent of metal electron and spin density in the ligand π systems. It is the differences in the relative energies of the π-donating and π^*-accepting levels of the ligands which result in the magnetic anisotropies responsible for the observed chemical shift differences between the two types of ligands.

Comparisons With The Isotropic Shifts Of [Ru(3-Me-acac)$_3$]

A sensitive test of the extent of π_z interaction with the ring was obtained from the ^{1}H and ^{13}C NMR spectra of the 3-methyl derivative. This species was prepared from the free ligand (Lancaster Synthesis) and $RuCl_3.3H_2O$ (Aldrich) in a similar manner to that described for [Ru(acac)$_3$][1] After recrystallization from $CHCl_3$/n-heptane the complex was almost pure and only some very minor impurity peaks were observed in the ^{1}H NMR spectrum (Fig.34). The chemical shifts of +55.58 ppm (3-C$\underline{H}_3$) and -9.27 ppm (C$\underline{H}$) demonstrated that the 3-C$<$ position was, as usual, a large center of spin density. Furthermore, the sign of shift for the 3-C$\underline{H}_3$ nucleus was opposite that for the 3-$\underline{H}$ nucleus of [Ru(acac)$_3$], the correct prediction for a change from σ-π_z electron correlation to hyperconjugation on methylation. Therefore, it was a great surprise to find that the 3-$\underline{C}H_3$ resonance displayed a -ve shift (Fig.35), the opposite of that predicted by hyperconjugation. This proves that the spin transfer mechanism to the 3-methyl group occurs via σ-π electron correlation (alternating signs through each bond) and substantially weakens the theoretical predictions for hyperconjugation of methyl groups attached to aromatic like rings.

Thus, the lack of any significant paramagnetic shifts for the 3-formyl group in the [Ru(3-CHO acac)$_3$(acac)$_{3-n}$] series is a strong indication that this substituent only interacts with the acac$^-$ ligand in a σ bonding fashion, *i.e.* the formyl group is probably canted out of the plane of the acac$^-$ ring disallowing any σ-π_z electron correlation. Thus, the kinetic behaviour of this complex with Ti(III) ion must be seen to be extraordinary. This opens up new mechanistic questions about the role of formyl group in inner-sphere electron transfer reactions with metal aqua complex ions.



BRUKER

RB139FID.900
PPG:
QUADCYCL.PC
DATE 18-7-89

SF	300.130
O1	10000.000
SI	16384
TD	16384
SW	29411.765
HZ/PT	3.590
RG	35
NE	1
NS	256
TE	298
DW	17.0
FW	35300
O2	6140.000
DP	20H PO
D0	1.000S
D1	3.000U
D2	1.000U
D3	33.000U
D4	1.000U
LB	1.000
GB	0.0
NC	4
CX	20.00
CY	0.0
SR	3367.52

13C SPECTRUM OF [RU(3-ME-ACAC)3] IN COCL3 AT 298K
3-CH3
Me
>C=O
SOLVENT
>C-Me
PPM

Figure 35

SOLUTION KINETICS AND MECHANISMS

Part VII

The Role Of Interfacial Electrochemistry In The Suppression Of IMI From Metal-Oxide-Metal "Rusty-Bolt" Junctions

Intermodulation interference (IMI) is a serious cause of communications problems onboard Navy ships. The sites of this self-generated interference are predominantly the partially conductive junctions formed between pieces of bare metal, which in most cases are steel junctions. Such junctions have nonlinear I-V characteristics from D.C. through to R.F. frequencies. The production of IMI products from these junctions requires them to pass R.F. current and many such junctions are available onboard Navy ships to be excited by the powerful communications transmitters. At some locations these junctions are coupled to unintended but effective natural antennas and these form the bulk of the IMI problems.

The suppression of IMI products from "noisy" junctions can be effected in a number of ways. In some cases it may be possible to decouple the junction from its natural antenna. Alternatively, the junction area may be electrically bypassed with a ground strap. In many instances these methods are not applicable and chemical treatments are being developed to modify the electrical properties of the junctions. The two basic methods which can be applied are (1) to cause additional corrosion in order to make the junction open circuit or (2) to modify the surface oxides in the junction to form a linear, closed circuit path for R.F. current. Neither of these is easy to accomplish in a controlled fashion so that it is vital to understand the basic chemistry in the interface between the metal contacts. A detailed account of the interfacial electrochemistry of Fe-O-Fe junctions is described below and experimental work based these design criteria is in progress at N.R.L.

On The Origin Of Nonlinearity In Fe-O-Fe Junctions

The surfaces of even freshly polished metal rapidly adsorb oxygen from the air and further contaminants are likely to be introduced during rinsing and wiping. However, the junction between two pieces of such very lightly oxidized steel can be considered to conform to the formulation FeO or $Fe(OH)_2$ in humid or moist conditions. The oxide form is known to be non stoichiometric being approximately $FeO_{1.05}$ so that it will have an excess of holes, *i.e. a p-type semiconductor*. The degree of hydration of such dry "Rusty-Bolts" may,

therefore, affect the hole-carrier density in the semiconducting layer. In laboratory tests, the degree of nonlinearity is adjusted by mechanical pressure to lie within a narrow range which is amenable to study. Each of the metal-to-semiconductor interfaces in the Fe-O-Fe junction is expected to display exponential I-V curves according to the Butler-Volmer equation:[23,24]

$$i_{obs} = i_o \left[e^{-\alpha n f \eta} - e^{(1-\alpha) n f \eta} \right]$$

where, i_o = the exchange current density in the semiconductor
α = 0.5 (assuming a symmetrical activation barrier to charge transfer)
n = number of electrons in the rate determining step
f = F/RT = 38.92, V^{-1} at 298K
η = activation overpotential, V (or $[E - E_{eq}]$ where E_{eq} = Fermi level)

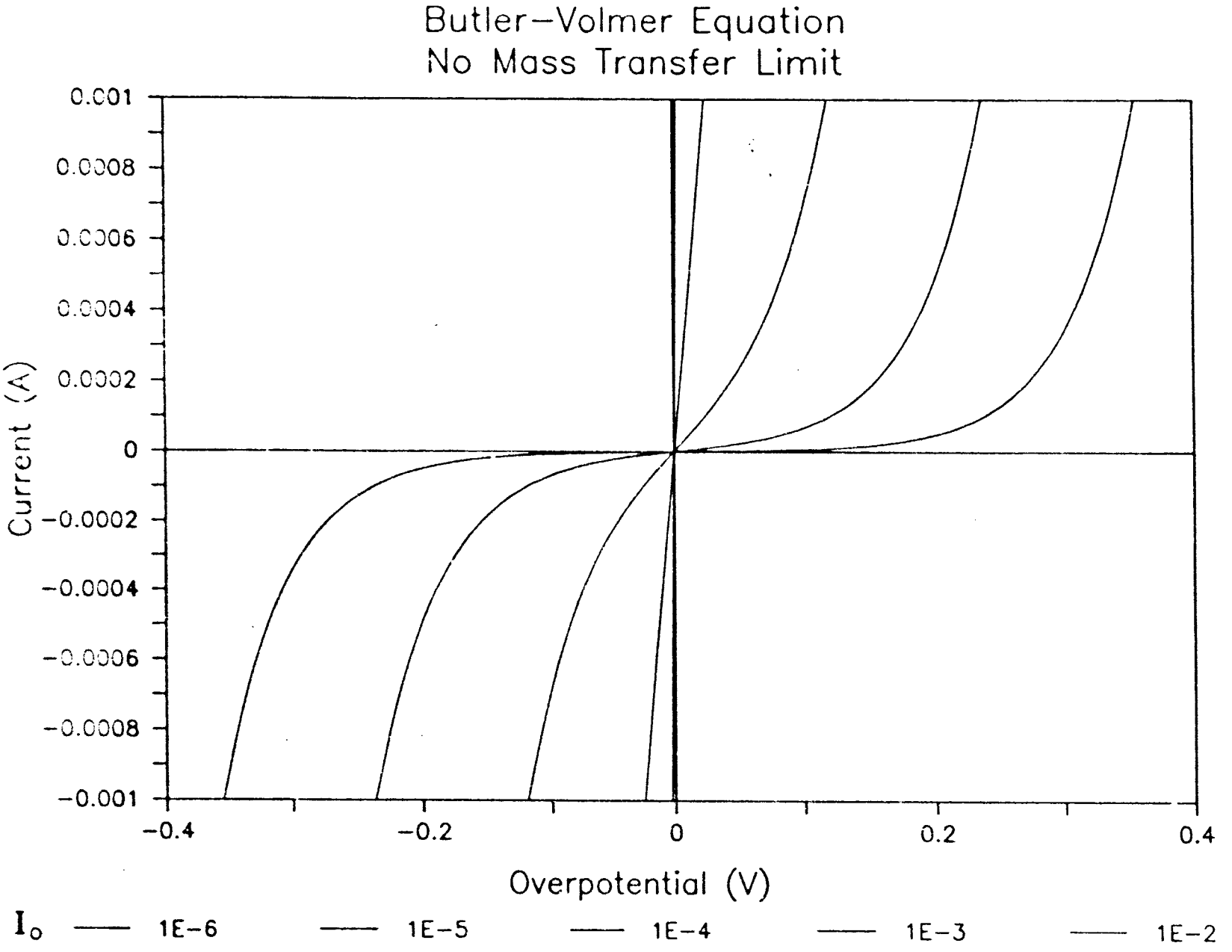
The resulting hyperbolic sine function for charge transfer across each interface is depicted in Figure 36 for 5 values of the exchange current density (i_o = 1E-6,...,1E-2) plotted on a scale of ±1 mA. Although each of these curves is equally non-linear (they differ only by a scale factor), the apparent linearity for *small currents across the interface* is greatly improved with increasing exchange current density, *i.e.* the junction appears to be most nonlinear when the current demand exceeds the current supply in the semiconducting layer.

The experimental I-V curves for the Fe-O-Fe type junctions closely resemble those predicted by the simple Butler-Volmer equation above, which formally applies only to a single interface where mass transport (for systems requiring Faradaic oxidation-reduction or solid-state ion migration) is not a limiting factor. When such factors do limit the charge transfer across the interface then the general i-η equation will describe the behaviour of each interface:[24]

$$i_{obs} = i_o \left[C_{ox}(0,t)/C_{ox}^{\bullet} \, e^{-\alpha n f \eta} - C_{red}(0,t)/C_{red}^{\bullet} \cdot e^{(1-\alpha) n f \eta} \right]$$

where, $C_{ox}^{\bullet}$ = bulk concentration of the oxidized species
$C_{red}^{\bullet}$ = bulk concentration of the reduced species
$C_{ox}(0,t)$ = surface concentration of the oxidized species *vs* time
$C_{red}(0,t)$ = surface concentration of the reduced species *vs* time

The concentration ratio terms limit the maximum current producing characteristic "S-shaped" plateau curves from the modified Butler-Volmer equation. The concentration terms could equally apply to species diffusing to the metal surface to undergo Faradaic redox reactions or


Butler–Volmer Equation
No Mass Transfer Limit
0.001
0.0008
0.0006
0.0004
0.0002
0
−0.0002
−0.0004
−0.0006
−0.0008
−0.001
Current (A)
−0.4
−0.2
0
0.2
0.4
Overpotential (V)
I_o —— 1E−6 —— 1E−5 —— 1E−4 —— 1E−3 —— 1E−2

to ions migrating through the oxide layer under the influence of the extremely high field gradient in the junction (~10^6 V cm^{-1}). Obviously, the general $i-\eta$ curve must be solved *numerically* since the surface concentrations are time dependent. However, such "diffusion limited" I-V curves are observed occasionally during setup of the Fe–O–Fe junctions.

Thus, there is a good physical and chemical basis for the nonlinear I-V properties exhibited by these Fe–O–Fe junctions. Naturally, the type and thickness of the oxide layer between the metal contacts is critical in determining the electronic behaviour of the "Rusty-Bolt" junction. Owing to the technological interest in the passivation and corrosion of metal surfaces there is a vast electrochemical literature on the nature of film growth on metals including the chemical composition, thickness and conductivity of such films. Some of these investigations will be discussed below in relation to the electrical "shorting" effect observed for ethylene glycol solutions containing small amounts of water.

On The Interfacial Electrochemistry Of Iron Surfaces

The electrochemical literature is replete with coulometric, ellipsometric and LEED studies on the nature of oxide film growth on iron surfaces in near neutral water solutions.[25–30] Some studies suggest that *magnetite* [Fe_3O_4 : 2xFe(III), 1xFe(II)] is formed first as a single unit cell layer before further oxidation to haemetite, γ-Fe_2O_3 [Fe(III) only]. Others suggest that $Fe(OH)_2$ and not *magnetite* is the species formed initially. There is no dispute that the final passive layer formed by electrochemical oxidation is γ-Fe_2O_3 and subsequent reduction of this film occurs in two distinct steps. The initial transient observed during anodic polarization has been interpreted as either formation of *maenetite* or oxidation of *adsorbed hydrogen*. While the evidence either way is not convincing it would not be unlikely that both $Fe(OH)_2$ and Fe_3O_4 are formed in the early stages of film growth. The ratio of each would no doubt be strongly influenced by the nature of the buffer solution and the rate of anodization (set by the potential *vs* SCE).

The formation of *magnetite* at the interface is an especially interesting possibility since one would expect this to have much higher conductivity from $Fe^{2+} \rightarrow Fe^{3+}$ electron hopping (*p-type hole conduction*) than for the highly doped Fe(II) oxide, $FeO_{0.95}$, or the final passive layer of the Fe(III) oxide γ-Fe_2O_3. Some literature data on the conductivity of these oxides are summarized below:

Table IX

Electronic Conductivity Of Iron Oxides

Species	Temperature (K)	Conductivity σ (mho/m)	Comment
FeO	873	6.4×10^{3}	High T preparation
Fe_3O_4	293	$\sim 10^{4}$	*hole conduction*
Fe_2O_3	293	3.7×10^{-3}	*n*-type semiconductor

Reference: "The Oxide Handbook", G. V. Samsonov, Plenum, N.Y. (1973)

The high value for the conductivity of FeO is no doubt a result of the high temperature at which it was studied and it would be safe to assume that it is markedly less conductive at room temperature. These values can be converted to specific resistance,

$$R = \rho \cdot l/A$$

where, R = resistance, Ω

$\rho = 1/\kappa$ = specific resistance, $\Omega \cdot$cm

$\kappa = \sigma/100$ = specific conductance, Ω^{-1}/cm

A = cross-sectional area, cm^2

l = length, cm

This yields a value of 0.01Ω for the resistivity for a 1 cm cube of *magnetite* – quite a good electronic conductor! So the formation of this oxide due to the presence of water and oxygen in the Fe–O–Fe interface could be a viable explanation for the increased conductivity of "Rusty-Bolt" junctions. If *magnetite* formation is the predominant source of the increased conductivity of Fe–O–Fe junctions then one would not necessarily expect other Metal–Oxide–Metal junctions to exhibit the same improvement after treatment with hydroxylic solvents. For example, Nickel forms an initial passive oxide surface which is not an electronic conductor.

However, other possibilities exist for conduction across the interface, including the Iron Deposition and Dissolution Reactions for which the following *most probable* electrochemical mechanism has been deduced:

$$Fe + H_2O \underset{k_{-1}}{\overset{k_1}{\rightleftharpoons}} FeOH + H^+ + e^- \quad (1)$$

$$FeOH \xrightarrow{\text{r.d.s}} FeOH^+ + e^- \quad (2)$$

$$FeOH^+ + H^+ \underset{k_{-3}}{\overset{k_3}{\rightleftharpoons}} Fe^{2+} + H_2O \quad (3)$$

This is an example of a multistep mechanism where the Butler-Volmer kinetics expression is modified to apply to a single, rate determining step taking into account the pre- and post-equilibria. After appropriate substitutions the $i-\eta$ function for this scheme is given by:[24]

$$i_{obs} = 2F \left[\overleftarrow{k}\, C_{OH^-}\, e^{(2-\beta)F\Delta\varphi/RT} - \overrightarrow{k}\, C_{OH^-}\, C_{Fe^{2+}}\, e^{-\beta F\Delta\varphi/RT} \right]$$

where,

$\overleftarrow{k} = k_{-2}K_3K_W$

$\overrightarrow{k} = k_2K_1K_W$

$\Delta\varphi$ = interfacial potential, V

β = 0.5 (note the asymmetry in the i *vs* $\Delta\varphi$ function above)

and the other terms have their usual significance. This formulation predicts the correct pH dependence of the corrosion current as well as the Tafel slopes for the corrosion-deposition reaction of Iron in aqueous media near neut pH. Similar expressions can be derived for the diffusion of ions through the oxide layer under the influence of the electric field gradient. Whether a Faradaic or Semiconduction mechanism is responsible for the conductivity of water treated Fe-O-Fe junctions is open to question since the same type of increased exchange current density can result in either case. However, there is little doubt that Water is the active ingredient in providing this increased current carrying capability.

The ultimate formation of γ-Fe_2O_3 and $[Fe(OH)_3]_n$ would not be conducive to maintaining good electrical contact across the interface so that direct treatment of the junction with aerated water would likely lead to eventual failure, although initially such treatment provides a rapid suppression of IMI. Indeed, water treated junctions have been observed to fail after a day or two with large amounts of rust formation in the contact area. However, rust formation can be suppressed with partially dried ethylene glycol. This suggests that a low water content in ethylene glycol is suitable for long term treatment of "Rusty-Bolt" junctions.

On The Role Of Dielectric Constant In The Rusty-Bolt Junction

It had been assumed that the ingress of a high dielectric constant liquid into the "Rusty-Bolt" junction would significantly increase the capacitive coupling between the metal electrodes and so provide an additional, parallel path for R.F. current. Since such a capacitor behaves as a linear circuit element this effect could have been reponsible in part for a reduction in IMI products. In order to test this hypothesis the "Rusty-Bolt" vyce was placed in a plastic box under an atmosphere of dried argon and a deoxygenated solution of the pre-dried ethylene glycol was added via a teflon cannula to a stable, operating nonlinear junction. As expected from similar tests in air, no change in the level of any IMI product frequency was observed for several hours. Since the ethylene glycol must have penetrated the junction area this proves that the dielectric constant of the liquid in the junction has no significant effect on the passage of R.F. signals in the range up to 30 MHz. This implies that the capacitive impedance is large compared with the resistance value (*typ.*~50Ω), *i.e.* $X_c > 1000\Omega$ at 30 MHz. The maximum junction capacitance can then be calculated from the capacitive impedance equation:

$$X_c = \frac{1}{2\pi f C_j} \quad \Omega \qquad \text{where } f \text{ is in Hz, } C_j \text{ in Farads}$$

The calculated capacitance is ~20 pF which is very close to the measured parallel capacitance of dry junctions in this frequency range. Thus, it is fairly certain that the dielectric constant *plays no significant role* in alleviating IMI production in "Rusty-Bolt" junctions.

Summary Of Techniques For IMI Suppression

The ability to modify and control the oxides between metal surfaces is critical for ensuring linear conduction of metal-oxide-metal junctions. By their nature, such junctions are usually depleted of mobile charge carriers and, therefore, exhibit nonlinear I-V behaviour. Through appropriate chemical treatments it is hoped to modify the interfacial oxides to increase the availability of charge carriers, so increasing the exchange current density and alleviating some of the nonlinearity of the junction.

REFERENCES

1: "Nonadiabaticity in Ruthenium(III)–Titanium(III) Outer-Sphere Electron-Transfer Reactions", J.E.Early, R.N.Bose and B.H.Berrie, *Inorg. Chem.* 1983, *22*, 1836.

2: "Measurement of the Rate Constant for Through-bridge Intra-molecular Electron Transfer in the Intermediate of a Ru^{III}–Ti^{III} Redox Reaction involving 3-Formylpentane-2,4-dione as Bridging Ligand", B.H.Berrie and J.E.Early, *J. Chem. Soc. Chem. Commum.* 1982, 471.

3: "Rate-Determining t_{2g}–t_{2g} Electron-Transfer: Reaction of (3-Formylpentane-2,4-dionato) bis(pentane-2,4-dionato)ruthenium(III) with Titanium(III) and Formation of (pentane-2,4-dionato)titanium(III)", B.H.Berrie and J.E.Early, *Inorg. Chem.* 1984, *23*, 774

4: "Thiocyanate Ion as a Bridging Ligand in Reduction of Ruthenium(III) by Titanium(III) and by (*N*-(Hydroxyethyl)ethylenediaminetriacetato)titanium(III)", R.A.Lee and J E.Early, *Inorg. Chem.* 1981, *20*, 1739

5: "Intervalence-Transfer Absorption. Part 1. Qualitative Evidence For Intervalence-Transfer Absorption In Inorganic Systems In Solution And In The Solid State", G.C.Allen and N.S.Hush, *Prog. Inorg. Chem.*, 1967, *8*, 357.

6: "Reduction Studies on Mixed Chelate Complexes", R.J.Balahura and N.A.Lewis *J. Am. Chem. Soc.* 1977, *99*, 4716 and Ref. 19 therein, D.A.Couch, O.W.Howarth and P.Moore, *J. Chem. Soc. Chem. Comm.* 1975, 822

7: "Linear Free Energy Relationship for Outer-Sphere Reduction Of Ruthenium(III) Amine Complexes by Titanium(III)", K.M.Davies and J.E.Early, *Inorg. Chem.* 1978, *17*, 3350

8: "Kinetics of Reduction of $Ru(NH_3)_6^{3+}$ and $Ru(NH_3)_5Cl^{2+}$ by Ti(III)", P.Chalilpoyil, K.M.Davies and J.E.Early, *Inorg. Chem.* 1977, *16*, 3344

9: "H-Atom Transfer between Metal Complex Ions in Solution", Robert A. Binstead and Thomas J. Meyer, *J. Am. Chem. Soc.* 1987, *109*, 3287

10: "Substituent effects in electron transfer reactions. II. The chromium(II) reduction of 2-acetylbutane-1,3-dionatobis(ethylenediamine)cobalt(III) and 3-acetylpentane-2,4-dionatobis(ethylenediamine)cobalt(III)", R.J.Balahura and N.A.Lewis, *Can. J. Chem.* 1979, *57*, 1765

11: "Inner-Sphere Electron Transfer in Some Ruthenium(III)-Titanium(III) Reactions", A.Adegite, J.E.Early and J.F.Ojo *Inorg. Chem.* 1979, *18*, 1535

12: "Kinetics of Aquation of the Tris(acetylacetonate) Complexes of Divalent Chromium, Cobalt and Ruthenium. A Pulse Radiolysis Study", D.Meisel, K.H.Schmidt and D.Meyerstein, *Inorg. Chem.* 1979, *18*, 971

13: "Reactions Of Metal Chelates. III. Nitration And Formylation Of Metal Acetylacetonates", J.P.Collman, R.L.Marshall, W.L.Young III, S.D.Goldby, *Inorg. Chem.*, 1962, *1*, 704.

14: "Advanced Organic Chemistry", J.March, Wiley-Interscience, New York, N.Y. 1989, 3rd Ed., pp 485-486.

15: "A New Synthetic Method For Ruthenium Complexes Of β-Diketonates From 'Ruthenium Blue Solution' And Their Properties", A.Endo, M.Kajitani, M.Mukaida and G.P.Sato, *Inorg. Chim. Acta* 1988, *150*, 25

16: "3-Formylcyclohexanespirocyclopentane-2,4-dione And 2-Formyl-5,5-dimethylcyclohexane-1,3-dione", B.D.Akehurst and J.R.Bartels-Keith, *J. Chem. Soc.* 1957, 4798

17: "Substituent Effects In Electron Transfer Reactions: The Preparation And Chromium(III) Reduction Of 3-Formylpentane-2,4-dionatobis(ethylenediamine)cobalt(III). Preparation Of The Linkage Isomer 2-Acetyl-1,3-butanedionatobis(ethylenediamine)cobalt(III)", R.J.Balahura and N.A.Lewis, *Can. J. Chem.* 1975, *53*, 1154

18: "The Nuclear Magnetic Resonance of Some Paramagnetic Transition Metal Acetylacetonates", D.R.Eaton, *J. Am. Chem. Soc.* 1965, *87*, 3097

19: "Carbon-13 NMR Studies Of Some Paramagnetic Transition Metal Acetylacetonates. Some Linewidth Considerations", D.M.Doddrell and A.K.Gregson, *Chem. Phy. Lett.* 1974, *29*, 512

20: "Temperature-Dependent Isotropic Shifts in Some Paramagnetic Transition Metal Acetylacetonates", A.K.Gregson, D.M.Doddrell and M.R.Bendall, *Aust. J. Chem*, 1979, *32*, 1407

21: "Paramagnetic Resonance In Trivalent Transition Metal Complexes", H.S.Jarrett, *J. Chem. Phys.*, 1957, *27*, 1298.

22: "The Paramagnetic Anisotropy And Axial Ligand Field In Complexes With The $^2T_{2g}$ Cubic Ground Term", A.K.Gregson and S.Mitra, *Chem. Phys. Lett.*, 1969, *3*, 392.

23: "Electrochemical Methods", A. J. Bard and L. R. Faulkner, Wiley, N.Y. (1980) Chapter 3, "Kinetics Of Electrode Reactions"

24: "Modern Electrochemistry", J. O'M. Bockris and A. K. N. Reddy, Plenum, N.Y. (1970) Vol.2, Chapter 8, "Electrodics" Vol.2, Chapter 11, "Some Electrochemical Systems Of Technological Interest" Vol.2, Chapter 9, "Electrodics, More Fundamentals", pp 1080-1092

25: "The Experimental Study Of Passive Materials", J. H. Bartlett, *Electrochim. Acta*, 1971, *16*, 1841

26: "Passivation Of Iron In Borate Buffer Solution", R. P. Frankenthal, *Electrochim. Acta*, 1971, *16*, 1845

27: "The Mechanism Of The Passivation Of Iron In Neutral Solutions: An Ellipsometric And Coulometric Investigation", J. O'M. Bockris, M. A. Genshaw, V. Brusic and H. Wroblowa, *Electrochim. Acta*, 1971, *16*, 1859

28: "The Anodic Oxide Film On Iron In Neutral Solution", N. Sato, K. Kudo and T. Noda, *Electrochim. Acta*, 1971, *16*, 1909

29: "Electronic Conduction Of The Oxide Film On Passive Iron In Neutral Solutions", R. V. Moshtev, *Electrochim. Acta*, 1971, *16*, 2039

30: "Electrode Reactions At Modified Surfaces Dependent On Reaction Site. γ-FeOOH As Example", J. W. Schultze, S. Mohr and M. M. Lohrengel, *J. Electroanal. Chem.* 1983, 57.

APPENDIX G1

Naval Research Laboratory
Washington, DC 20375-5000

NRL Memorandum Report 6229

CARYSPEC

A FORTRAN 77 Program for Spectral Data Acquisition and Control of The Varian CARY 2390 UV-VIS-NIR Spectrophotometer

JOHN C. COOPER

Polymeric Materials Branch
Chemistry Division

ROBERT A. BINSTEAD

GEO-CENTERS, Inc.
10903 Indian Head Highway
Fort Washington, MD 20744

July 14, 1988

Approved for public release; distribution unlimited

UNCLASSIFIED

REPORT DOCUMENTATION PAGE

UNCLASSIFIED	
	Approved for public release; distribution unlimited.
NRL Memorandum Report 6135	
Naval Research Laboratory	Code 6135
Washington, DC 20375-5000	
NAVSEA and NP	
Washington, DC 20362-5101 NAVSEA; 800 N. Quincy St. Arlington, VA 22217 (ONR)	

CARYSPEC - A FORTRAN 77 Program for Spectral Data Acquisition and Control of the Varian CARY 2300-UV/VIS-NIR Spectrophotometer

Stefanski, P.A. and Tasker, P.C.

Interim

Approximately 24 pages

Varian CARY 2300-UV/VIS-NIR spectrophotometer, IEEE-488

CARYSPEC is a FORTRAN 77 program designed for acquisition of UV/VIS/NIR spectra from the CARY 2300 series spectrophotometers via an IEEE-488 interface bus to an external computer system. The program is written to operate on a Hewlett Packard 1000 minicomputer but with very few system dependent features to enable easy conversion for other host systems. The operation of the spectrophotometer is controlled by CARYSPEC using menu displays on the system console to setup instrument parameters, baseline correction, data acquisition and disk file storage. CARYSPEC provides detailed error trapping for inappropriate instrument settings and automatic adjustment of spectral bandwidth and gain level during data acquisition to match the current baseline correction. Spectra are stored in disk files for subsequent use by plotting, scaling and data analysis programs.

CONTENTS

Section	Description	Page
INTRODUCTION		1
IMPLEMENTATION		
1.0	Hardware Interface	2
1.1	System Handshaking	2
1.2	Instrument Commands Format	3
1.3	Instrument Commands Summary	4
1.4	Real Time Transmission Data Format	9
1.5	Illegal Parameter Changes	10
SOFTWARE DESCRIPTION		
2.0	Purpose Of CARYSPEC	11
2.1	Language Features Of CARYSPEC	11
2.2	Structure Of CARYSPEC	12
2.3	BLOCK DATA	22
2.4	SUBROUTINES	24
2.5	FUNCTIONS	31

... cont'd

Section	Description	Page
PROGRAM CODE		
3.0	Source Code Availability	31
3.1	Variable Names And Usage	31
3.2	Program Listing	36

LIST OF TABLES

TABLE	Description	Page
I	ASCII Codes For Touch Panel Keys	6
II	Data File Format	21
III	Glossary Of Integer Variables	32
IV	Glossary Of Real Variables	33
V	Glossary Of Character Variables	34

CARYSPEC

A FORTRAN 77 Program For Spectral Data Acquisition And Control Of The Varian CARY 2390 UV-VIS-NIR Spectrophotometer

INTRODUCTION

The CARY 2300 and 2400 series spectrophotometers are high quality, microprocessor controlled analytical instruments intended for measurements of the UV-Visible and Near IR absorption spectra of solids, liquids and gases. When equipped with an optional IEEE-488 standard interface these instruments and their accessories are programmable by an external computer system enabling acquisition of spectral measurements in digital form. This document describes a fully tested FORTRAN 77 program, CARYSPEC, designed for *single scan* acquisition of spectra from a CARY 2390 instrument using a Hewlett-Packard 1000 minicomputer running the multi-user CI shell and RTE-6/VM operating system. The program uses very few machine specific functions and could be modified easily to run on other host systems supporting the IEEE-488 interface standard.

CARYSPEC implements a large subset of the programmable instrument control functions of the CARY 2390 spectrophotometer in a menu driven format closely resembling the menu displays on the instrument. Therefore, no special training is required for users already familiar with operation of the instrument. Indeed, operation from a computer console has proven to be more convenient than using the clumsy keypad on the instrument. The control functions implemented reproduce the facilities of the spectrophotometer's Instrument Settings, Baseline Setup, Lamp and Detector Modes and Accessory Setup menus, as well as a number of single keypad functions. The program *does not support* the statistics calculation modes, rapid scan setup keys or the automatic sequencer operation for repetitive scans. The latter mode, although useful, is not compatible with reliable IEEE-488 data transmission. A future version of the program may implement this feature using the the single scan mode of CARYSPEC with automatic data file storage and system clock control of the timing of successive scans.

CARYSPEC is a moderately large program and will not run in a single 32K word segment of the Hewlett-Packard 1000 minicomputer. The program has been segmented to run in 5 memory resident nodes of the HP 1000 using the Multi Level Segmentation utility programs SGMTR and MLLDR. The program requires an 88K word memory partition, including 40K words of Extended Memory Addressing (EMA) space for data arrays.

Manuscript approved February 19, 1988

IMPLEMENTATION

1.0 Hardware Interface:

The IEEE-488 interface for the HP 1000 system is implemented with an HP 59310B interface card which utilizes 4 Logical Unit (LU) addresses in the system. The LU addresses are dependent on the computer system and are defined by the system generation. The interface card used by the program, CARYSPEC, occupies LU addresses 35-38 corresponding to card addresses 0-3. Address 0 is a special addressing mode which allows access to low level IEEE-488 bus command sequences for any device number. Addresses 1-3 are predefined automatic READ/WRITE channels which select device numbers 1-3 on the bus. CARYSPEC uses automatic device addressing from channel 3 (LU 38) and consequently the device address of the CARY 2390 has been set to 3. Physical connection between the computer and spectrophotometer consists of 5 metres of IEEE-488 standard cabling. Reliable data transmission was obtained with cable lengths up to 9 metres. With 13 metres of cable commands sent to the CARY 2390 were accepted but data transmissions from the CARY 2390 spectrophotometer were corrupted owing to the limited drive capability of the MC3447L bus transceivers in the CARY 2390. The bus was found to be totally inoperative with a cable length of 17 metres.

1.1 System Handshaking:

The IEEE-488 subsystem of the HP 1000 is operated by the RTE driver DVA37 configured for ASCII Data Record mode. This mode sends and expects to receive an End Of Record (EOR) with data transmission in the form of a Carriage Return/Line Feed (CR/LF) sequence, though Line Feed alone is sufficient. The CARY 2390 accepts commands in this format automatically. However, the instrument must be instructed to send data with the CR/LF trailer using the command "[illegible]", sent as a series of ASCII characters to the instrument. This is the first instrument command in the program CARYSPEC and instructs the CARY 2390 both to insert CR before LF on transmissions and to turn off check sum error detection. Therefore, all commands to the instrument end with a check sum byte of zero. Correctly operating IEEE-488 systems do not require check sum error detection. During real time spectral data transmission the CARY spectrophotometer is the active talker on the bus. The End Of Record character for this mode has been specified as a Line Feed in CARYSPEC - this works without a CR, as expected for IEEE-488 handshaking. Termination of real time transmission is effected by the active controller via a bus level routine which sends the ASCII codes for UNTALK UNLISTEN

1.2 Instrument Commands Format:

Programmable control of the CARY 2300-2400 series spectrophotometers has been implemented by Varian Instruments with a series of *single character* commands in ASCII code, most being accompanied by following characters to select a particular setting for the command selected. The instrument generates similar reply messages to most commands and these character strings must be read by the controller before sending further commands.

Varian's documentation defines the command structure as a sequence of [ASCII] characters in the following format (blanks added for clarity):

[LDI] [MI] [MD] [MQ] [CSM] [EOI]

where,

[LDI] = Logical Device Identifier

ASCII representation of the talk address of the sender - the value is ignored but some character must be sent as a place holder. (NOTE: The correct character for the bus controller at address 0 is "@").

[MI] = Message Identifier

ASCII character C, P or N used to indicate the message type as Command, Positive reply or Negative Reply. (NOTE: This character field is actually INVALID within a command - 'C' will cause a system reset if used).

[MD] = Message Descriptor

ASCII character which specifies the actual command to be executed.

[MQ] = Message Qualifier

A string of characters used to set one or more variables or operating modes.

[CSM] = Check sum

The binary sum of all characters in a particular message - this is always the "0" character since checksum mode is turned off normally.

[EOI] = End Or Identify (actually End Of Record)

A linefeed character is specified as the terminator character to end data transmissions. {NOTE: This is appended automatically by most IEEE-488 drivers during handshaking.}

The [MI] field given in the message structure above is actually invalid within a command and must not be used - otherwise command 'C', system reset, will be executed followed by a bus hang up on the trailing unused command characters. However, the [MI] field is valid in the reply messages from the instrument.

The correct COMMAND format is given by the following fields:

[LDI] [MD] [MQ] [CSM] [LF]

EXAMPLE: Send the Record Trailer Set-up Command '@'

```
      Command="@@20"
      WRITE (UNIT=38,FMT=10) Command
10    FORMAT (A4)
      READ (UNIT=38,FMT=20) Reply
20    FORMAT (A64)
```

where,

@ = [LDI] address of bus controller
@ = [MD] command for record trailer set-up command
2 = [MQ] value to select no check sum (bit 1 = 0), insert CR before LF
0 = [CSM] check sum (off)
LF is sent automatically with WRITE command

All instrument commands sent to the CARY 2390 by an external computer comprise a sequence of ASCII data characters as far as the IEEE-488 bus is concerned. The details of the handshaking, with talk and listen addresses, are transparent to high level languages such as this implementation of FORTRAN 77 where such details are handled automatically by the device driver - in this case DVA37. Unfortunately, Varian Instruments chose to document the software control of the 2300 series instruments for a particular dialect of BASIC used in their proprietary controller, a model DS-15 data station, which appears to operate in a purely binary mode on the IEEE-488 bus. Thus, their examples of the message structure include a line feed character appended to the actual data command message. Furthermore, they confuse this End Of Record character (EOR) with the title of the End Or Identify handshake line of the IEEE-488 bus. The trailing line feed character is omitted from all instrument commands in the program CARYSPEC, this terminator being supplied automatically by the HP 1000 driver routine using the standard FORTRAN output command, WRITE.

While the reply messages generated by the CARY spectrophotometer must be read, only a few require testing for negative replies in a correctly structured program. CARYSPEC utilizes tight error trapping for inappropriate combinations of instrument parameters, diminishing the need for extensive use of the error message numbers from the instrument. In fact, only the Baseline Set Up suoroutine checks for a negative reply and even that is probably superfluous since illegal combinations of operating modes are trapped before calling this routine. Such internal errror trapping provides a smoother user interface compared with taking corrective action after rejection of bad commands by the instrument.

The full range of instrument commands and their reply formats are summarized below in Section 1.3. Some commands can be accessed only using the 'D' command to mimic key pad presses on the instrument. These often involve sequences of key presses to implement a single function. Table I contains the ASCII codes required to send Key Pad entries with the 'D' command. However, full familiarity with the instrument is required to use these effectively. For example, the Baseline Set Up procedure could be implemented by sending a large number of Key Pad sequences but a more efficient means is the 'J' command which includes all of the requested baseline parameters in a single string.

TABLE I

ASCII Codes For Touch Panel Keys

KEY	DECIMAL	ASCII
0	48	'0'
1	49	'1'
2	50	'2'
3	51	'3'
4	52	'4'
5	53	'5'
6	54	'6'
7	55	'7'
8	56	'8'
9	57	'9'
.	58	':'
CLEAR	59	';'
CHANGE	60	'<'
ENTER	61	'='
ABS vs WLNGTH	64	'@'
ABS vs TIME	65	'A'
SEL WLNGTHS	66	'B'
INSTR SETTINGS	67	'C'
LAMPS & DETECTORS	68	'D'
AUTO OP	69	'E'
ACCRY SETTINGS	70	'F'
CALC MODE	71	'G'
BASLN SETUP	72	'H'
TEST FUNCTION	73	'I'
GOTO WLNGTH	74	'J'
LOCK	75	'K'
START	80	'P'
STOP	81	'Q'
RESUME	82	'R'
STANDBY	83	'S'
READY	84	'T'
AUTO BALANCE	85	'U'
CASSETTE	88	'X'
PRINT	89	'Y'
RIGHT CURSOR	104	'h'
LEFT CURSOR	105	'i'
MANUAL SCAN +	106	'j'
MANUAL SCAN -	107	'k'

1.3 Instrument Commands Summary:

'A' Lock or Unlock Keyboard

```
Command = '@AX0'                    where X = 0,1 (Unlock, Lock)
Reply   = '#PAX0'
```

'B' Status Request

```
Command = '@B0'
Reply   = '#PB[ data ]0'            5 bytes of data are returned
```

'C' System Reset

```
Command = '@C0'
No Reply
```

'D' Activate A Touch Panel Key

```
Command = '@DX0'                    where X = ASCII code for Key
Reply   = '#PDX0'
Reply   = '#NDX0'
```

'E' Dump Parameter Table

```
Command = '@E0'
Reply   = '#PE[ no. of data bytes ][ data ]0'
```

'F' Accessory ON/OFF Control

```
Command = '@FXY0'                   where X = 0,1 (Turn Off, On)
                                    where Y = Accessory Number
Reply   = '#PFXY00'                 where 0 before CSM = no error
Reply   = '#NFXY[ error no. ]0'
```

'G' Return Value Of Parameter Or Variable

```
Command = '@G1Y0'                   Y = Index Number Of Parameter
Reply   = '#PG1Y[ string length ][ string ]0'
Command = '@G2Y0'                   Y = Index Number Of Variable
Reply   = '#PG2Y[ value ]0'
Reply   = '#NGXY' error no. ]0'     for X = 1,2
```

'H' Change Value Of A Parameter

Command = '@HXY0' where X = Parameter Number
where Y = Required Index Value

Reply = '#PHXYZ0' where Z = New Index Value

Reply = '#NXY[*error no.*]0'

'I' Change Value Of A Variable

Command = '@IX[*number*]!0' where X = Variable Number

Reply = '#PIX0'

Reply = '#NIX[*error no.*]0'

'J' Set Up A Baseline

Command = '@J[*value 1*]!...[*value 9*]!0'

Reply = '#PJ00' where 0 before CSM = no error

Reply = '#NJ[*error no.*]0'

'K' Request Real Time Data Transmission

Command = '@K1Y0' Interval mode

Command = '@K3Y[*interval*]!0' Continuous mode

where Y = 0-3 specifies delimiter (0, LF, CR, &)

Reply = '#[*data*]!...[*data*]![EOR]#...

Reply = '#NKXY[*error no.*]0' where X = 1,3 (mode)

'L' Display Message On Line 4 Of C.R.T.

Command = '@L1[*message*]0'

Command = '@L00' Turn Off Message Display

Reply = '#PL0' No Negative Reply

'M' Accessory Mode Set Up

Command = '@MX[*value*]'0' where X = Parameter Number

Reply = '#PMX00' where 0 before CSM = no error

Reply = '#NMX[*error no.*]0'

'@' Record Trailer Set Up

Command = '@@Y0' where Y = 0-3 (2 for CR/LF)

No reply

1.4 Real Time Transmission Data Format:

The 'K' command selects one of two real time transmission modes with the CARY spectrophotometer as the active talker on the bus. The continuous mode transmits data at the frequency of the instrument's chopper motor (15 Hz at line frequeny = 60 Hz) in an abbreviated format of Ordinate and Abscissa. The more useful mode, as used in CARYSPEC, is the programmed interval mode which transmits 9 instrument measurements. This increases the overhead for each datum but the extra string processing time has been found to be insignificant for the HP 1000 system. CARYSPEC limits the choice of scan speed and wavelength interval for a maximum transmission rate of 5 Hz. This modest rate is determined by the interrupt service times of the multi-user operating system rather than program processing speed.

The data format for the programmed interval mode varies with the choice of Ordinate and Abscissa modes for the CARY 2390. The data acquisition subroutine ACQUIRE within CARYSPEC supports all 6 choices of Ordinate mode and the 4 choices of Abscissa. However, the main portion of CARYSPEC rejects any choices other than Absorbance or Transmittance *vs* Wavelength which send data in the following formats:

A typical record for Absorbance *vs* Wavelength: (59 characters)

* 0.0012! 2000.00!1!01!128! 2000.00! 0.0! 28.72!-199.83!

A typical record for Transmittance *vs* Wavelength: (58 characters)

* 100.06! 2000.00!1!01!128! 2000.00! 0.0! 28.72!-199.73!

These fields correspond to Ordinate, Abscissa, Cell #, Cycle #, Sample #, Wavelength, Time, Temperature and Gel Scanner Distance. Transmissions from the CARY 2390 are read left-justified into a CHARACTER variable dimensioned to length 64. This is sufficient for all operating modes and makes ACQUIRE a general purpose subroutine for use in other programs. Since the record format is fixed for each choice of Ordinate and Abscissa there is no need to search the data strings for the "!" delimiters. CARYSPEC begins substring extraction at character position 2 and uses arrays XOFF(I) and YOFF(J) to determine the offsets for the first two data fields. The remaining substrings are fixed length and their boundaries are calculated from the sum of the lengths of the first two data fields.

1.5 Illegal Parameter Changes:

Several instrument parameters have been masked off from changes by an external computer, so becoming READ ONLY. The slit height parameters #22 & #26 are not programmable since the slit height is a manual adjustment. The Baseline parameters also are intended to be READ ONLY in order to prevent overwriting the descriptors for a current baseline. Hence, parameters #23 - #26 are updated only when a new Baseline request is sent using the 'J' command. The Baseline status parameter #37 has limited accessibility and can be turned ON or OFF only. CARYSPEC also allows parameter #37 to be set to the RECORD and ON/SETUP states by issuing Key Pad sequences with the 'D' command. However, CARYSPEC does not use these settings to actually record the Baseline. The settings are used only to transfer setup information between the instrument and baseline menu parameters for users accustomed to this feature.

Unfortunately, two setup parameters, DERIV TEMP RANGE (#11) and TEMP ZERO (#13), have also been masked off making it difficult to control the CARY in some operating modes. However, it was discovered that the DERIV TEMP RANGE can be set by using parameter #10, the DERIV RANGE settings for Absorbance and %T. Thus, parameter #11 appears to be an internal table only. Special action has to be taken in selecting the derivative range settings since only the 1,5,10 sequence is valid while a 1,2,5,10 sequence can be selected. CARYSPEC includes an INDEX array variable which holds the valid indices for the derivative modes. This allows derivative spectra to be drawn while the external computer acquires the raw measurements. While CARYSPEC does not allow acquisition with TEMPERATURE as the Ordinate or Abscissa, the functionality of the Temperature setup modes is preserved with one exception. The TEMP ZERO parameter can not be set from the external computer and only the range can be selected from CARYSPEC. Since this is not a feature required for CARYSPEC no attempt has been made to issue a Key Pad sequence for TEMP ZERO.

The CARY 2300 also masks off the %T offset variable (#10) when the 200 %T range is selected. This appears to be designed so that only a 0-200 %T range can be selected. However, if a non-zero offset has already been set for another scale then selection of the 200 %T range will not result in a 0-200 %T scale - it will have the old offset. This illegal mode can be reset by changing to another range and setting the offset to zero before selecting the 200 %T range again.

SOFTWARE DESCRIPTION

2.0 Purpose Of CARYSPEC:

The collection of spectrophotometric data in digitized form provides both a permanent means of storage and the ability to perform more sophisticated analysis. While the instrument obtains spectral measurements as absorbance *vs* wavelength (nm), plotting programs can rescale the raw data into more meaningful units such as molar absorptivity *vs* wavenumber (cm^{-1}). Techniques such as difference spectroscopy no longer need to be performed in real time since data files can be manipulated easily to achieve this function by scaling and subtraction. Noise can be removed from single scan spectra using least squares smoothing while similar functions can be used to generate derivative spectra which are more accurate than those produced in real time by the CARY 2300-2400 series spectrophotometers on their internal pen recorders. Such benefits make it worthwhile to develop software for data transfer between the CARY spectrophotometer and an external computer system, in this case a Hewlett-Packard 1000 minicomputer running the CI shell and RTE-6/VM operating system.

2.1 Language Features Of CARYSPEC:

The program CARYSPEC was written in FORTRAN 77 since this language provides the most complete set of interface and control functions available on the HP 1000. The communication between FORTRAN 77 and the IEEE-488 interface to the CARY 2300 spectrophotometer is completely transparent and standard READ/WRITE statements control the operation of the instrument and the collection of data transmitted by the CARY. Therefore, the program is portable, with some minor alterations, between systems supporting the FORTRAN 77 language and IEEE-488 Input/Output. CARYSPEC uses three machine specific function calls requiring substitution to run on a different host system. The first is CALL FTN77(,29) which changes the free field record length from the default value of 72 to 79. This is used to provide more column space on the console display screen. The second is a call to read the system clock to provide calibrated delay loops. Thus the operation of SUBROUTINE Wait(DELAY) and FUNCTION Time(I) would need to be altered. The third is CALL ABRT(,35,3) which terminates transmission from the CARY by sending UNTALK/UNLISTEN on the IEEE-488 bus. Syntactical differences also appear between various versions of FORTRAN 77, particularly in the READ/WRITE statements. CARYSPEC uses the format READ (1,) and WRITE (1,) for the user's console (defined as LU 1) while Microsoft's compiler uses an * to denote the console unit.

2.2 Structure Of CARYSPEC:

CARYSPEC comprises a large main program unit containing most of the console menu displays, block data for named COMMON variables and a number of subroutines that perform string processing, input validation and communication with the CARY 2390 spectrophotometer. The main program is responsible for all the logic flow and the subroutines execute specific support tasks, which are summarized below:

The main program unit of CARYSPEC comprises 9 distinct segments of code to carry out the the functions of instrument setup, spectral data acquisition and disk file data storage. The code fragments appear under the following assigned labels: MENU, SPECTRUM, BASELINE, ADVANCED, INSTRUMENT, LAMP, ACCESSORY, STORE and EXIT.

MAIN PROGRAM

MENU:

This is the first and main control menu of the program, selecting entry to the remaining instrument control menus, data acquisition, storage and exit routines. The choices are as follows:

'A'.....Acquire Spectrum

This selection branches to label SPECTRUM and performs logical tests for the presence of a valid Baseline in the CARY, valid choices of Abscissa/Ordinate modes and the presence of an unstored spectrum in memory before proceeding with data acquisition. If there is no valid Baseline information in memory the program will branch to label BASELINE. If the Abscissa/Ordinate settings are inappropriate the program will branch to label INSTRUMENT.

'B' Baseline Setup

This selection branches to label BASELINE which reads the current instrument settings and presents the pertinent Baseline parameters in a menu arrangement similar to the equivalent display on the CARY. The user can alter these selections but most will not take effect unless a new Baseline scan is recorded on exit from this menu. Otherwise, an exit is made to the main MENU with the instrument baseline settings intact, a feature of the CARY which prevents inadvertent alterations to the parameters describing the current instrument Baseline.

'I'.....Instrument Settings

This selection branches to label INSTRUMENT, reads the current instrument settings and presents the most important in a menu arrangement similar to the equivalent display on the CARY. The user may alter these instrument settings and any changes are implemented immediately by the instrument. If such changes affect the quality of the Baseline matching for a subsequent acquisition scan then the changes will be overridden automatically, if possible. Otherwise, the user will be directed to record a new Baseline scan with the altered settings, followed by acquisition of the spectrum. In most cases the automatic matching routines will take effect to provide a smooth user interface.

'L'.....Lamps, Detectors/Accessories

This selection branches to label ADVANCED and reads the current instrument settings and presents a number of menu selections for subsidiary functions and operating modes of the CARY. Selection '1' branches to label LAMP and presents a menu which lists the status of the lamp and detector modes, which then may be altered. Selection '2' branches to label ACCESSORY and presents a menu which lists the status of the temperature and printer accessories, which then may be setup as desired. Selection '3' for automatic operations is not yet supported.

'S'.....Store File On Disk

This selection branches to label STORE and prompts the user for entry of pertinent file information before saving a data file to disk. This routine includes standard error checking for File Exists, File Open and disk transfer errors. The user is returned to the main MENU on exit.

'X'.....Exit

This selection branches to label EXIT and checks for the presence of an unstored spectrum which causes a prompt for confirmation before proceeding. The user then has the option of setting the CARY to standby mode, if desired, before the program stops.

SPECTRUM:

This portion of CARYSPEC controls the acquisition of a spectrum from the CARY 2390 spectrophotometer. On entry, this code will check important instrument parameters and status variables and perform conditional branches to BASELINE, INSTRUMENT or MENU if the conditions outlined above are not satisfied. A successful entry will display a request for the wavelength scan limits, which default to the Baseline scan range. New limits may be chosen and are validated for the range 185-3152 nm. (The limits may exceed the Baseline range but this will cause a subsequent call to SUBROUTINE Bline with the new limits and current instrument settings before returning to the data acquisition loop.)

The remaining entry required is the step size interval (0.01-5 nm) during the scan. The instrument is capable of 0.01 nm steps in the UV-VIS region or 0.04 nm in the Near IR. No restrictions are placed on the user in this regard but it is *strongly recommended* that sensible units be chosen, *e.g.* .1, .2, .25, .5 nm. The program will reject combinations of scan rate and step size which would result in the data rate exceeding 5 Hz. This restriction is a result of the rather slow multi-user environment of the HP 1000 rather than a processing speed problem. Either scan rate or step size may be altered to meet this condition. Finally, the wavelength range and step size are used to check the number of data points for the scan. If the request exceeds 10001 points the user is prompted for a new step size.

After satisfying the basic conditions above the program will perform a number of checks on the current operating conditions of the CARY 2390 to determine whether these will match the conditions for the Baseline scan. Mismatched settings of SBW (nm) and GAIN will be reset automatically to smooth over some instrument peculiarities. Other mismatches are assumed to be operator requirements and result in a prompt to record a new Baseline scan. The user may either proceed or abort this operation and return to the main MENU to take corrective action.

Successful traversal of all the matching checks will present a listing of scan parameters and a prompt to Start or Abort the scan. Aborting will return the user to the main MENU and restore the parameter strings describing any previous spectrum in memory. Starting will position the monochromator to the starting wavelength and prompt for Print to Screen during the scan - removal of this I/O overhead helps prevent missed data with several users on the HP 1000. The remainder of the acquisition is automatic, returning to the main MENU after completion.

BASELINE:

The current instrument Baseline parameters are read on entry to this section of CARYSPEC for display in a menu format similar to the Baseline Setup menu on the instrument. This code is responsible for the selection of all relevant parameters for a new Baseline scan. However, since most of these parameters are masked from direct changes by the computer, via SUBROUTINE Select, a number of inappropriate combinations are tested for after each new selection is made. These tests reset the bad parameter requests to the most appropriate selection thereby eliminating the rejection of any parameters in subsequent calls to SUBROUTINE Bline. After validation of the Baseline parameters the program tests whether the operating mode at the start of the scan will be AUTO GAIN (MODE = 1) or AUTO SLIT (MODE = 2). The integer variable MODE then controls the logical operation of the remainder of the program and SUBROUTINE Bline where choices between SBW and GAIN settings are important for determining or controlling the operation of the CARY 2390.

A special exit is made from the BASELINE code for setting the instrument GAIN level if the requested value exceeds the current setting by more than a factor of 10, which can result in misbeaviour of the slit servo system of the CARY 2390. A sudden, large increase in GAIN should just send the instrument closer to zero slit width. However, on *this* CARY 2390, at least, the slit width can overshoot through zero and continue to fully open the slits with high gain, seriously imperilling the detectors! To prevent such a disaster the program will select AUTO SLIT mode and branch to line 490, which is part of the INSTRUMENT code fragment. This subsection resets the current instrument GAIN in factors of 10 until it matches the new Baseline request. The logical variable TRANSFER controls the exit from this routine back to BASELINE.

On exit from the Baseline Setup menu the user may either record a new Baseline or return to the main MENU. Both options read the current instrument parameters before returning to MENU, keeping the program updated. This is performed by re-using part of the code at the start of the BASELINE fragment under the control of logical variable TRANSFER. If a new Baseline is recorded the program will monitor the instrument until completion of the procedure and then issue an AUTO BALANCE command to zero the instrument on the reference material. Subsequent data acquired via the SPECTRUM fragment will therefore produce baseline corrected spectra.

ADVANCED:

This portion of CARYSPEC presents a small menu of subsidiary instrument setup functions that may need to be changed occasionally. The selection are:

'1'.....LAMPS & DETECTORS

This selection will display a further menu which lists the current status of the LAMP POWER, LAMP SELECT and DETECTOR SELECT modes. Normally, both lamps are ON and the lamps and detectors are in AUTO SELECT mode. These settings can be changed to increase the working wavelength range for the individual lamps or detectors. {NOTE: Individual selection of a lamp or detector prevents lamp or detector changes and thereby prevents coverage of part of the wavelength range accessible with AUTO SELECT modes.}

'2'.....ACCESSORY SETTINGS

This selection allows the user to turn on and setup two installed accessories, the TEMPERATURE READOUT and the thermal PRINTER. On entry to this routine both accessories are commanded to an OFF status. If a positive reply is received from the CARY that parameter is reset to ON. If the TEMPERATURE accessory is selected and turned ON a small menu is presented for selection of the TEMPERATURE RANGE. If the PRINTER option is selected and turned ON a subsidiary menu is presented to select the operating mode and interval step size for printer output. The modes supported are Wavelength, Time and Temperature. However, CARYSPEC only acquires data in Wavelength mode.

'3'.....AUTO OPERATIONS

This selection is intended for future expansion for automatic repetitive scans. Currently, it prints an error message and returns for another selection.

'X'.....EXIT TO MENU

This entry returns to the main MENU.

INSTRUMENT

This section of CARYSPEC reads the current wavelength and instrument settings from the CARY and presents the most important functions in a menu format that is very similar to the equivalent display on the instrument. Changes made from this menu are executed by the CARY 2390 immediately. The selections are:

'0' .....WAVELENGTH

This selection allows the monochromator to be repositioned to any valid wavelength for the current selections of Lamp and Detector modes.

'1' .....ORDINATE

Only Absorbance, %T and Temperature are selectable from this menu. However, CARYSPEC will not allow Temperature as a valid ordinate during scans.

'2' .....ABSCISSA

Wavelength, Time and Temperature are selectable from this menu. However, CARYSPEC only allows Wavelength as a valid abscissa during scans.

'3' .....SCAN RATE

The scan rate must be chosen in combination with spectral bandwidth and filter period for accurate recording of bandshape. There is a particular difficulty in the 650 nm region where a Wood's anomaly causes poor baseline correction. The scan rate should not exceed 1 nm/sec per SBW (nm) per second period.

'4' .....CHART DISPLAY

The chart recorder may be used on any setting during data acquisition.

'5' .....REFERENCE MODE

The instrument is normally used in AUTO SELECT mode to allow full wavelength coverage with both lamps and both detectors. However, AUTO GAIN and AUTO SLIT modes may also be used for wavelength scans. The working range for these depends on the detector mode selected. AUTO GAIN may be used above 800 nm with the PM Tube if the UV/VIS detector modes is selected. AUTO SLIT mode can be used for the full instrument range (185-3152 nm). The reference mode for data acquisition must match that used for the Baseline scan. SINGLE BEAM mode is not valid for wavelength scans and is intended only for instrument adjustments.

'6' .....SBW (nm), GAIN

This selection allows setting of *either* the SBW or GAIN depending on whether the CARY is operating in AUTO GAIN or AUTO SLIT mode at the current wavelength. The actual operating mode for AUTO SELECT reference mode is determined by the wavelength and detector select mode. These are checked by CARYSPEC to determine the correct prompt and instrument command.

'7' .....PEN FUNCTION

The pen operates independently of the raw spectrophotometric data sent via the IEEE-488 bus to an external computer and may operate in any valid mode during data acquisition. The Ordinate choice determines which modes are valid and inappropriate selections are masked by CARYSPEC. However, it is perfectly feasible to draw a second derivative spectrum while acquiring data via the IEEE-488 bus.

'8' .....PEN LIMITS

This selection allows for setting the range and offset for all valid Ordinate modes. The NORMAL mode pen limits are selected via the Parameter and Variables Tables. The %T mode has a minor bug for the 200 %T scale. If a previous choice has set a non zero offset this will not be correctly reset to 0 %T as expected since the $\%T_{zero}$ variable is masked off by the CARY on the 200 %T scale. Similarly, the Temperature zero offset parameter *can not be changed* by an external computer, though the setting *is read* by CARYSPEC. A non-zero offset entered from the instrument keypad will be displayed but only one range can be set by CARYSPEC. The Derivative and Log(Abs) mode limits are handled by parameter table selection with special handling of the indexing to prevent use of invalid settings in the CARY firmware table.

'9' .....RESPONSE TIME (sec)

This selection allows the filter period to be set to 0.5, 1, 3 or 10 seconds

During the recording of a Baseline the period should be set to 0.5 seconds for maximum fidelity in the 650 nm region where there is a Wood's anomaly. Failure to observe the scan rate, filter period and SBW limitations will results in improper baseline corrections. Higher period settings can be used on subsequent spectra with little prejudicial effect.

'10'.....BEAM INTERCHANGE

This selection allows the front and rear light beam paths to be interchanged between the sample and reference channels for special applications, such as the diffuse reflectance accessory.

'11'.....SLIT HEIGHT

This selection is not valid - it is a READ ONLY parameter for the manual slit height setting.

'X' .....EXIT Instrument Menu

This selection performs a return to the main MENU.

LAMP:

This subsidiary menu reads and reports the current status of the lamp and detector operating modes. The selections are:

'1' .....LAMP POWER

Normally, the instrument is operated with this parameter set to BOTH ON enabling the complete wavelength range to be covered. However, the UV or VIR/NIR selections may be made to prolong the life of a lamp. CARYSPEC *does not* automatically turn on lamps as required for a particular scan.

'2' .....LAMP SELECT

For complete coverage of the wavelength range 185-3152 nm this parameter must be in the AUTO select mode, which will result in a lamp change at 340 nm. The range covered by the individual lamps may be extended - up to 400 nm for the D_2 lamp (UV) and down to 270 nm for the tungsten lamp (VIS-NIR). However, no lamp change will then be made. CARYSPEC provides error checking for the latter two modes to prevent positioning the monochromator outside the valid wavelength limits since this would result in the instrument turning OFF the current baseline. Recovery from such a state involves repositioning the monochromator and using the ON SETUP selection for Baseline Status in the Baseline Setup menu.

'3' .....EXIT TO MENU

This selection returns to the ADVANCED menu.

ACCESSORY.

The CARY 2390 has two installed accessories programmable by an external computer. The selections are:

"1" .....TEMPERATURE READOUT

This selection should normally be turned ON so that subsequent data files are stored with the correct temperature (a reading of 2.55 is passed by the CARY with the accessory OFF). If this selection is made and turned ON a further menu will be presented for selection of the temperature range. This only affects the pen scaling with TEMPERATURE as the Ordinate or Abscissa - not valid modes for data acquisition in CARYSPEC. Thus, selecting 100 degrees is recommended.

"2" .....PRINTER

This selection allows the user to setup the thermal strip printer to provide instrument readings at selected intervals during a scan (1 point/sec max.). While the selections include WAVELENGTH, TIME and TEMPERATURE the latter two are not valid scan modes in CARYSPEC.

STORE:

This portion of CARYSPEC provides the data file storage routine. On entry to this code CARYSPEC checks that a spectrum has been acquired and has not yet been stored. Otherwise, the program returns to the main MENU. After this validation the program will present a series of prompts for Filename and Directory information, which are then used to build a Pathname and to check that such a file does not already exist in the specified directory. If the filename is valid the user will be prompted for the LABEL, DATE, CONCENTRATION (M) and PATHLENGTH (cm) file descriptors followed by disk file storage. The data file is stored in the following format given in Table II.

EXIT:

This final portion of CARYSPEC checks that any spectrum in memory has been stored and prompts for confirmation before allowing the user to terminate the program. On exit the user may elect to set the CARY 2390 to standby mode if no further spectra will be acquired.

TABLE II

Data File Format

Line	File Variables	Format Type [a]
1	TITLE	CHARACTER (A72)
2	DATE	CHARACTER (A8)
3	XMIN,XMAX,XSTEP,CONC,PATH	REAL (*)
4	ORD,ABSC,CELL,CYCLE,SAMPLE, WAVE,TIMER,TEMP,DIST	REAL (*)
5	J,K,NARRAY	INTEGER (I3,I3,I6)
6-54	PARAM(I)	INTEGER (I2)
55	VARIABLE(I)	REAL (*)
56-/	Y(I)	REAL (*)
/-eof	X(I)	REAL (*)

a: (*) indicates free field format

2.3 BLOCK DATA:

All COMMON variables used by CARYSPEC are held in named COMMON blocks and initialized in BLOCK DATA immediately following the main program unit. The compiler directive /NOALLOCATE/ is used to ensure that only one block of memory is set aside during the multi-level segmentation of CARYSPEC. The variables contained within the COMMON blocks are listed below:

/MODE/ Contains COMMON INTEGER variables

NDATA Number of data points in a scan
Value set in main program
Value used in SUBROUTINE Acquire
Value stored in NARRAY in main program for disk data file

XMODE Specifies abscissa mode for selecting length of data field
Value set in main program
Value used in SUBROUTINE Acquire as index for local array XOFF

YMODE Specifies ordinate mode for selecting length of data field
Value set in main program
Value used in SUBROUTINE Acquire as index for local array YOFF

/CARY/ Contains COMMON REAL variables

ORD, ABSC, CELL, CYCLE, SAMPLE, WAVE, TIMER, TEMP, DIST
Values correspond to the 9 instrument readings sent during scan
Values set in SUBROUTINE Acquire
Values used in main program
Values stored in disk data file

/IP/ Contains COMMON INTEGER arrays

NPAR Specifies the number of settings for each instrument parameter
DIMENSION = 49
Values set in BLOCK DATA
Values used by SUBROUTINE Select for changing instrument settings

OFFSET Species the index offset in the parameter table
DIMENSION = 49
Values set in BLOCK DATA
Values used in SUBROUTINE Select for changing instrument settings

/IS/ Contains COMMON CHARACTER string arrays

Pname Specifies the names of instrument parameters for screen display
DIMENSION = (49)*10 characters
Values set in BLOCK DATA
Values used in SUBROUTINE Select

Vname Specifies the names of instrument variables for screen display
DIMENSION = (49)*8 characters
Values set in BLOCK DATA
Values not used in current version (for future use)

2.4 SUBROUTINES:

CARYSPEC uses subroutines to perform specific tasks which, with one exception, are required more than once. Terminate is setup as a subroutine solely for clarity of main program execution. The purpose and calling sequences are listed below:

Acquire(Inc,PRINT,SINGLE,WAVELENGTH)

Performs real time data acquisition from the CARY 2390 in two modes, single point for updating the current monochromator position and scan mode at Inc (nm) steps. COMMON variables XMODE, YMODE and NDATA select the correct data string format for the Abscissa and Ordinate modes selected by the main program unit and the number of data points required in the scan. The scan mode stores each Abscissa and Ordinate value in EMA COMMON arrays X and Y. COMMON BLOCK /CARY/ returns the final set of readings to the main program unit for data file storage.

/MODE/ INTEGER XMODE,YMODE,NDATA input variables control acquisition

/CARY/ REAL ORD,ABSC,CELL,CYCLE,SAMPLE,WAVE,TIMER,TEMP,DIST output

/DATA/ REAL arrays X,Y hold Abscissa and Ordinate values for output

Inc CHARACTER*4 variable input which specifies the interval (nm)

PRINT LOGICAL variable input which turns screen output on/off during scan

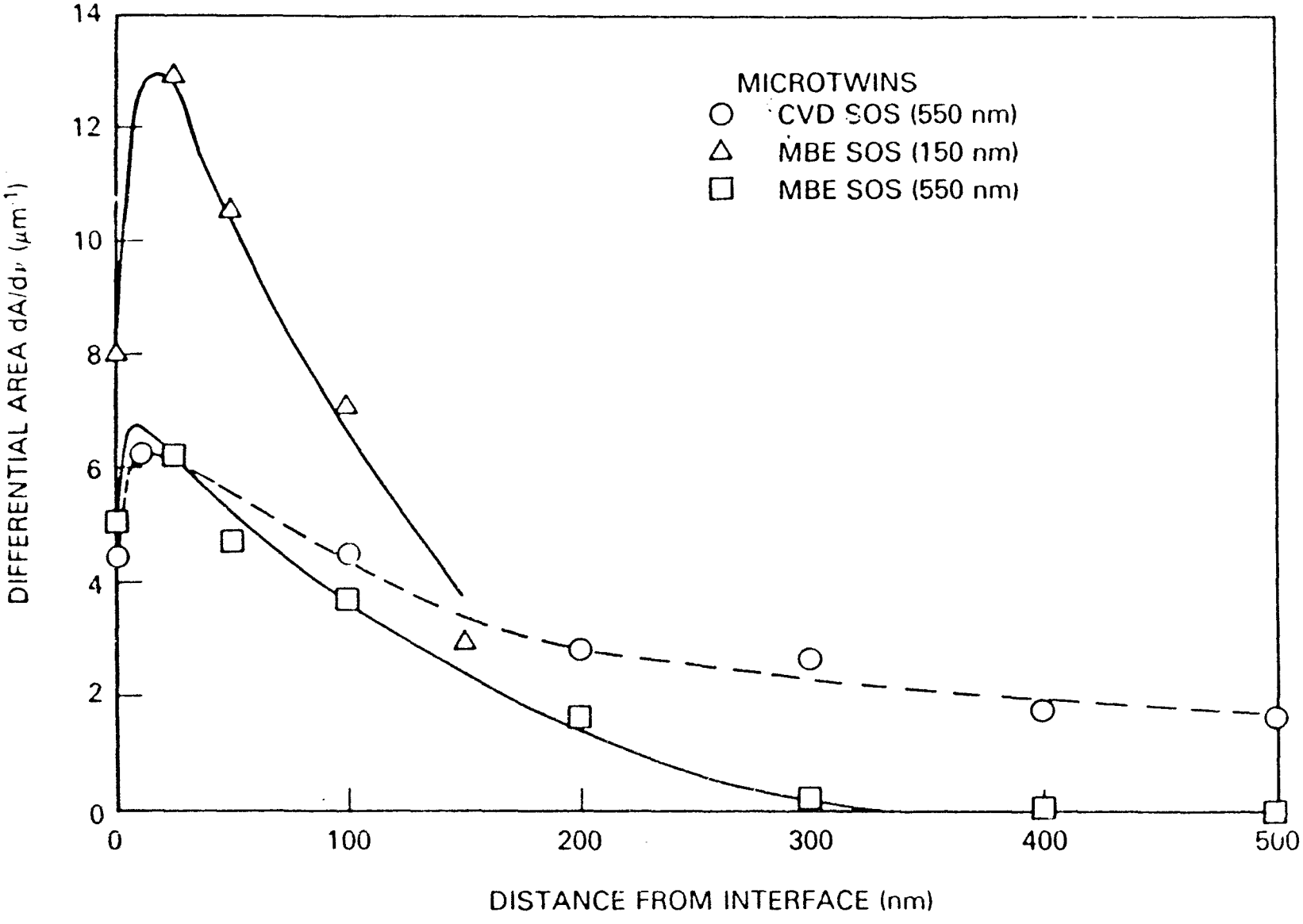
SINGLE LOGICAL variable input which selects single datum or scan mode

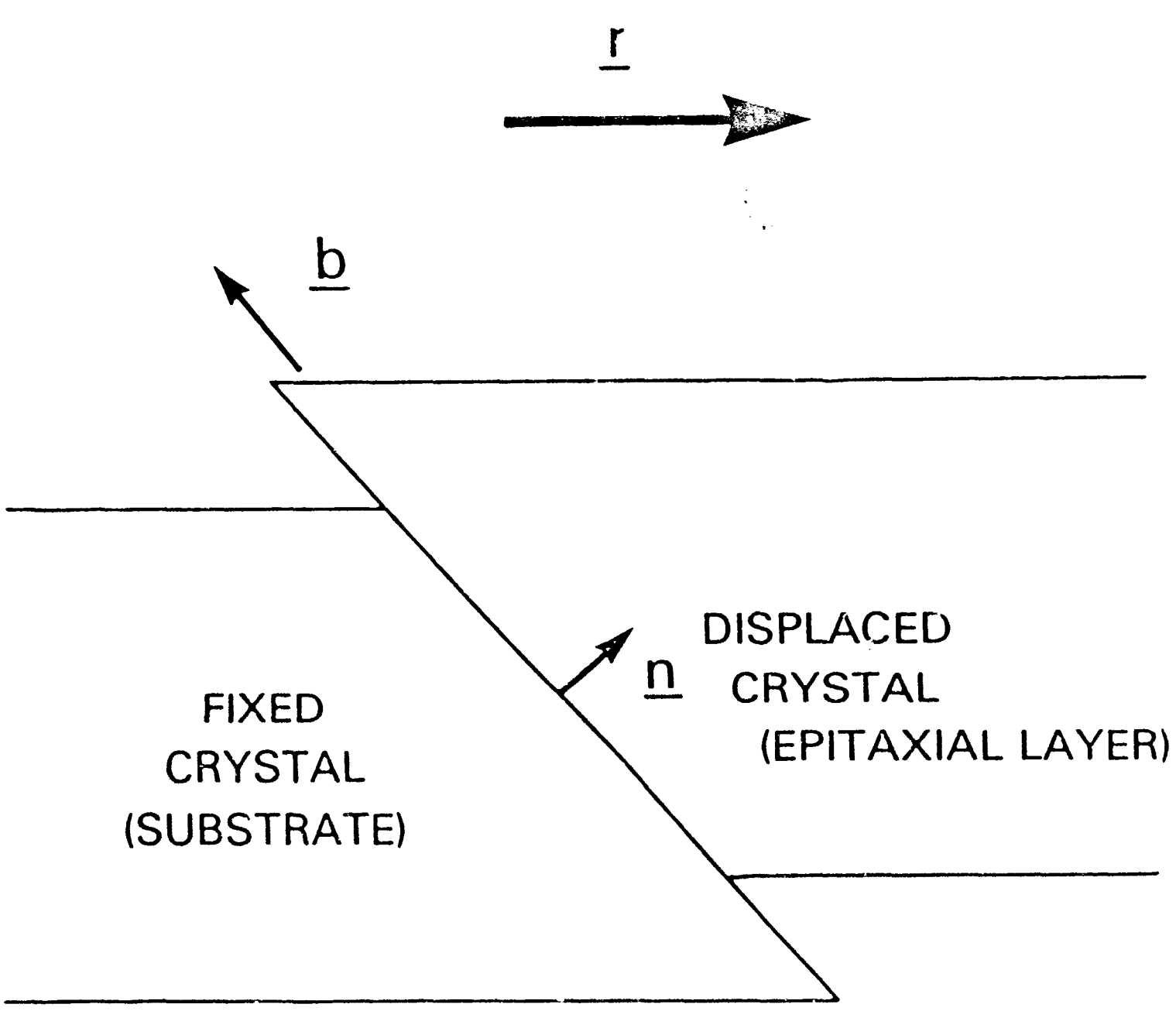
WAVELENGTH

REAL variable output for single datum mode

CALLED BY: Main program unit only

CALLS: SUBROUTINE Val


MICROTWINS
CVD SOS (550 nm)
MBE SOS (150 nm)
MBE SOS (550 nm)
DIFFERENTIAL AREA dA/dν (μm⁻¹)
DISTANCE FROM INTERFACE (nm)
0
2
4
6
8
10
12
14
0
100
200
300
400
500


r
b
n
DISPLACED
CRYSTAL
(EPITAXIAL LAYER)
FIXED
CRYSTAL
(SUBSTRATE)

Bline(WMIN,WMAX,Bdet,Bgain,Blamp,Bperiod,Brate,Bref,Bsbw Bslit,Bscan,Btime, MATCH,MODE)

Performs a Baseline Setup by sending a list of instrument parameter requests to the CARY 2390. Validation of the instrument settings is performed by the main program unit before calling Bline.

WMIN,WMAX	Wavelength limits passed from main program unit
Bdet	CHARACTER*1 variable input to select detector mode
Bgain	CHARACTER*4 variable input to set gain value
Blamp	CHARACTER*1 variable input to select lamp mode
Bperiod	CHARACTER*1 variable input to select period setting
Brate	CHARACTER*1 variable input to select scan rate setting
Bref	CHARACTER*1 variable input to select reference mode
Bsbw	CHARACTER*4 variable input to set SBW value
Bslit	CHARACTER*1 variable input to match physical slit height
Bscan	CHARACTER*14 variable input for screen display of scan rate
Btime	CHARACTER*14 variable input for screen display of period
MATCH	LOGICAL variable .TRUE. on entry and exit unless scan aborted
MODE	INTEGER variable input to specify AUTO GAIN/SLIT mode

Center(TITLE)

Prints a string on the user console centred within a 72 column line.

TITLE CHARACTER*72 string, contents set by calling unit

CALLED BY: Main program unit, SUBROUTINE Select, SUBROUTINE Bline and SUBROUTINE Acquire

CALLS: None

GOTO(Wlength)

Performs the same function as the Key Pad GO TO WLNGTH on the instrument to enable repositioning of the monochromator to a specified wavelength. Error trapping for illegal or inappropriate settings is performed by the main program unit and no negative reply is tested for.

Wlength CHARACTER*7 variable input from the main program unit

CALLED BY: Main program unit only

CALLS: SUBROUTINE Send, SUBROUTINE Instats

EXTENSION: LEN(*string*) function, HP extension to FORTRAN 77

Instats(Slew,...,Windex)

Performs a request for current instrument status from the CARY 2390. Slew is used to determine if the monochromator is still in motion. The other variables are not used in this version. No negative reply is issued by the CARY for this command.

Slew,Model,Ncell,Range,Windex

CHARACTER*1 variables passed back to calling unit

CALLED BY: Main program unit, SUBROUTINE GOTO

CALLS: None

Limits(MIN,MAX)

Reads entries for the wavelength limits from the user console, swaps the entries if necessary and validates the entries against the instrument limits (185 - 3152 nm). The values are then rounded to whole digits.

MIN,MAX REAL variables passed back to main program unit

CALLED BY: Main program unit only
CALLS: None

Line(N)

Prints a line of '-' characters to the user console N columns wide and centred within a 72 column line.

N INTEGER variable input from calling unit

CALLED BY: Main program unit, SUBROUTINE Select, SUBROUTINE Bline and SUBROUTINE Acquire
CALLS: None

Partable(PARAM)

Performs a request to send the parameter table from the CARY 2390 and processes the reply to update the program's list of current instrument settings held in the integer array PARAM. No negative reply is issued by the CARY for this command.

PARAM INTEGER array output which holds the instrument parameter settings DIMENSION = 49, values set by CARY and SUBROUTINE Select

CALLED BY: Main program unit only
CALLS: None

Select(N,PARAM,Pstr)

Performs selection of available instrument settings for parameter N. Calls SUBROUTINE Send(Command) to set new parameter values. Negative replies are not tested since the parameter table values are read again on return to the main program menus calling Select. A special fix has been added for Derivative modes to use only valid selections from PARAM(11) and Pstr(11).

N — INTEGER input value (1 - 49) representing parameters 0 - 48

PARAM — INTEGER array input of current instrument parameter settings
DIMENSION = 4[illegible] used to detect special case indexing for Pstr

Pstr — CHARACTER string array containing all selections for parameters
DIMENSION = (49,16)*14 characters, 41–49 not used in this version

/IP/ — INTEGER arrays NPAR,OFFSET used to select index number for Pstr

/IS/ — CHARACTER array Pname containing the names of each parameter
DIMENSION = (49)*10

INDEX — INTEGER array of valid index values for Derivative modes
DIMENSION = 11, uses local data for indices to PARAM(11)

Send(Command)

Performs an IEEE-488 WRITE to the CARY 2390 to send a string command to the instrument and to read the reply. Negative replies are not checked using this routine. Commands are either validated before calling Send or parameters and variables are read afterwards to check the results from Send.

Command — CHARACTER variable holding an ASCII string command for CARY
DIMENSION = variable, set by calling unit.

CALLED BY: Main program unit, SUBROUTINE Select, SUBROUTINE GOTO

CALLS: None

Str(VALUE,String,PREC)

Performs a conversion from numeric value to a string number for floating point numbers only with up to 12 digits precision. This is more than required by the CARY 2390.

VALUE — REAL variable input to be processed by the routine

String — CHARACTER*14 string output corresponding to VALUE

PREC — INTEGER variable input to set the rounding precision for string

CALLED BY: Main program unit, SUBROUTINE Bline
CALLS: None

Terminate

Performs an IEEE-488 WRITE to UNTALK the CARY 2390 and terminate real time transmission mode.

CALLED BY: Main program unit only
CALLS: ABRT(35,3) an EXTERNAL class system level routine
This function sends the UNTALK/UNLISTEN characters '_?'

Upper(Code)

Performs a check for lower case characters in a string of arbitrary length and converts to upper case if necessary.

Code — CHARACTER variable passed into routine and UPPER case on exit
DIMENSION = arbitrary, set by calling unit

CALLED BY: Main program unit, SUBROUTINE Bline
CALLS: None

Val(String,VALUE)

Performs a conversion from string to numeric value for a string number containing up to 10 digits. This is more than required by the CARY 2390.

String — CHARACTER string input to be processed by routine
DIMENSION = arbitrary, set by calling unit

VALUE — REAL variable output

CALLED BY: Main program unit, SUBROUTINE Vartable, SUBROUTINE Acquire
CALLS: None

Vartable(VARIABLE)

Performs a request to send all 14 instrument variables and processes the replies to update the program's list of current values held in the floating point array VARIABLE. Negative replies from the CARY are not tested in this routine since illegal requests are not issued by Vartable.

VARIABLE — REAL array output which holds the instrument operating variables
DIMENSION = 14, values set by CARY and main program unit

CALLED BY: Main program unit only
CALLS: SUBROUTINE Val

Wait(DELAY)

Performs a loop which tests the system clock until DELAY seconds have elapsed. The routine does not make provision for the special case at the transition to 2400 hours.

DELAY — REAL variable holding the value of the delay period in seconds

CALLED BY: Main program unit and SUBROUTINE Bline
CALLS: FUNCTION Time(I)

2.5 FUNCTIONS:

CARYSPEC uses only one function subprogram that makes an EXEC call to read the system time.

Time(I)

Performs an EXEC call to read the system clock and converts the reading to seconds and centiseconds.

I Dummy argument

CALLED BY: SUBROUTINE Wait only
CALLS: EXEC(ICODE,ITIME) system level command

PROGRAM CODE

3.0 Source Code Availability:

The source code for program CARYSPEC is an 83K ASCII text file available on either a Hewlett-Packard cartridge tape or an IBM 360K format floppy disk. All requests should be accompanied by the blank medium desired. A printed copy of the source code is listed below.

3.1 Variable Names And Usage:

A complete listing of the INTEGER, REAL and CHARACTER variables for the MAIN segment of CARYSPEC is given below in Tables III, IV & V, respectively. The subroutines use the same names as the main program for the same variables. Additional variables in the subroutines and simple integers, I-N, are not documented since their usage is rather obvious. The logical variables MATCH, PRINT, SINGLE and TRANSFER are used within the program to control conditional branching. MATCH is related to BLOCK IF tests for matching of the baseline and spectrum parameters. PRINT controls whether data will be printed to the console screen during data acquisition. SINGLE controls the operation of Acquire to update the wavelength. TRANSFER is used for special branching to reuse portions of code.

Table III

Glossary of INTEGER Variables

Name	Description	Value
ACCESSORY	Assigned Label - Accessory Setup Menu	600
ADVANCED	Assigned Label - Subsidiary Functions	350
BASELINE	Assigned Label - Baseline Setup Menu	200
EXIT	Assigned Label - Terminate Program	900
INSTRUMENT	Assigned Label - Read Cary Settings	390
LAMP	Assigned Label - Lamp & Detector Modes	570
MENU	Assigned Label - Main Control Menu	10
PARAMETERS	Assigned Label - Instrument Setup Menu	400
SPECTRUM	Assigned Label - Acquire Spectrum	90
STORE	Assigned Label - Store Disk File	700
ASCII	ASCII code for a command output	> 48
MODE	Controls the selection of AUTO GAIN/SLIT	0,1
NARRAY	Number of data points in spectrum - file	1-10001
NCOL	Number of screen columns in menu display	50-79
NDATA	Number of data points in spectrum - Acquire	1-10001
PREC	Precision for rounding function in Str	3,4
XMODE	Selects abscissa data format in Acquire	1
YMODE	Selects ordinate data format in Acquire	1,2
NPAR(49)	Number of settings for each parameter	1-16
OFFSET(49)	Index offset for parameter settings	0-11
PARAM(49)	Instrument operating modes table	1-16

Table IV

Glossary of REAL Variables

Name	Description
ORD	Final ordinate value returned by Acquire
ABSC	Final abscissa value returned by Acquire
CELL	Final cell # value returned by Acquire
CYCLE	Final cycle # value returned by Acquire
SAMPLE	Final sample # value returned by Acquire
WAVE	Final wavelength value returned by Acquire
TIMER	Final time valu returned by Acquire
DIST	Final distance value returned by Acquire
BAND	Spectral Bandwidth (nm) - AUTO GAIN mode
CONC	Concentration of sample (M) - file variable
GAIN	Instrument gain - AUTO SLIT mode
NUMBER	General purpose data entry variable
PATH	Pathlength of sample cell (cm) - file variable
PMIN	Pen scale minimum limit
PMAX	Pen scale maximum limit
RATE	Numeric equivalent of scan rate parameter
RATIO	Variable for data rate & slit gain checks
SPECBAND	File variable for SBW (nm) at λ_{min} (nm)
SPECGAIN	File variable for GAIN at λ_{max} (nm)
STEP	Numeric value of step size (nm) interval
WAVELENGTH	Current monochromator position (nm)
WMIN	Requested ending wavelength for scan
WMAX	Requested starting wavelength for scan
XMIN	File variable for WMIN
XMAX	File variable for WMAX
XSTEP	File variable for STEP
ZERO	Pen scale offset variable, %T and Deriv modes
VARIABLE(14)	Instrument operating conditions table
X(10001)	Wavelength array
Y(10001)	Absorbance or %T array

Table V

Glossary Of CHARACTER Variables

Name	Description
Screen Control:	
BELL	CHAR(7) bell character
CLR*2	Clear screen
DOWN*2	Move cursor down 1 line
ESC	CHAR(27) escape character
HOME*2	Move cursor to upper right corner
UP*2	Move cursor up 1 line
Instrument Status:	
Bdet	Baseline detector mode
Bgain*4	Baseline gain setting
Bgbw*4	Baseline SBW or GAIN, depending on mode
Blamp	Baseline lamp mode
Bmin*4	Baseline ending wavelength
Bmax*4	Baseline starting wavelength
Bperiod	Baseline filter setting
Brate	Baseline scan rate
Bsbw*4	Baseline spectral bandwidth
Bslit	Baseline slit height
Odet	Previous spectrum detector mode
Ogain*4	Previous spectrum gain setting
Olamp	Previous spectrum lamp mode
Omin*4	Previous spectrum ending wavelength
Omax*4	Previous spectrum starting wavelength
Operiod	Previous spectrum filter setting
Orate	Previous spectrum scan rate
Osbw*4	Previous spectrum spectral bandwidth
Oslit	Previous spectrum slit height
Sdet	Spectrum detector mode
Sgain*4	Spectrum gain setting
Slamp	Spectrum lamp mode
Smin*4	Spectrum ending wavelength
Smax*4	Spectrum starting wavelength
Speriod	Spectrum filter setting
Srate	Spectrum scan rate
Ssbw*4	Spectrum spectral bandwidth
Sslit	Spectrum slit height

Instrument Control:

Accon*3	Turn accessory on command
Accoff*3	Turn accessory off command
Autobal*4	Perform auto balance to zero reading
Command*44	String of instrument commands to CARY
CSM	Checksum character for data transmission
Bistat*5	Read baseline status parameter command
Instr*4	Recall instrument setup menu display
Key*2	Press key command
Lock*4	Lock keyboard command
Messon*3	Send message to line 4 of CARY display
Messoff*4	Clear message from CARY display
Par*3	Read parameter command
Parset*2	Change parameter command
Ready*4	Release CARY from standby mode
Response*64	String for reply messages from CARY
Setup*4	Record trailer setup command
Standby*4	Place CARY in standby mode
Start*4	Issue a start command
Stop*4	Issue a stop command
String*14	String to pass data to or from subroutines
Unlock*4	Unlock keyboard command
Var*3	Read variable command
Varset*3	Change variable command

Program Control:

Access(5)*4	Accessory status (OFF, ON)
Astat*10	Auto balance status (OFF, SET)
Bscan*14	Scan rate, Baseline screen output
Bstat*10	Baseline status (OFF, ON, ON MATCH)
Btime*14	Filter period, Baseline screen output
Code	Menu selection variable
Icode	Parameter setting in ASCII format
Pcode	Parameter number in ASCII format
Pname(49)*10	Table of names for each parameter
Printer(6)*12	Printer operating mode
Prn(49)*14	Table of names for each parameter setting
Scan*10	Spectrum status (OFF, ACQUIRED, STORED)
TITLE*2	String to be printed to screen
Vname(14)*9	Table of names for each variable
Wlength*7	Wavelength in ASCII format for GOTO

File Storage:

DATE*8	Date in mm/dd/yy format
Directory*40	Directory pathname
Fname*20	Filename and extension
INITIALS*2	User's initials for extension, Sxx
Name*16	Filename without extension
Outfile*63	Complete pathname for file

```
 1 FTN7X,L
 2 $FILES 0,1                          ! * Setup One Disk I/O File
 3 $ALIAS  MODE/,NOALLOCATE            ! * BLOCK DATA Holds Values Of Named
 4 $ALIAS ,CARY/,NOALLOCATE            !   COMMON Variables So Don't Allocate
 5 $ALIAS ,IP ,NOALLOCATE              !   Memory For These Here - SCMTR will
 6 $ALIAS ,IS/,NOALLOCATE              !   Create Memory For These As Required
 7 $EMA ,DATA/                         ! * Use EMA Space For Large Data Arrays
 8 C
 9 C     ******************************************************************
10 C
11       PROGRAM CARYSPEC
12 C
13 C     ******************************************************************
14 C
15 C     This Program Is Designed To Control Data Acquisition From The
16 C     CARY 2390 UV-VIS-NIR Spectrophotometer Via The IEEE-488 Bus.
17 C
18 C     The CARY 2390 Is Addressed As Device #3 On The IEEE-488 Bus.
19 C
20 C     The HP 1000 Is Configured To Operate The IEEE-488 Bus In ASCII
21 C     Data Record Mode With Auto Addressing Enabled. The Bus Occupies
22 C     Logical Unit Addresses 35 - 38 (Device Addresses 0 - 3). LU 38
23 C     Controls The CARY 2390 And LU 35 Is Used To Issue Bus Commands.
24 C
25 C     ------------------------------------------------------------------
26 C
27 C
28 C          AUTHOR:  Dr. Robert A. Binstead,
29 C                   Chemistry Division, Code 6125,
30 C                   Naval Research Laboratory,
31 C                   Washington, D.C. 20375-5000
32 C
33 C
34 C          WRITTEN: December, 1986 - January, 1987
35 C
36 C          VERSION: 1.7
37 C
38 C          REVISED: March, 1987
39 C                                - Modified to store Abscissa (X) array
40 C                                  after Ordinate (Y) values to prevent
41 C                                  data file corruption in the event of
42 C                                  missed data point during multi-user
43 C                                  sessions where the HP 1000 can not
44 C                                  keep up with data transmission rate.
45 C                   May, 1987:
46 C                                - Modified MATCHING criteria between
47 C                                  Spectrum & Baseline to omit checks
48 C                                  on Scan Rate & Period. This allows
49 C                                  the Baseline scan to be taken under
50 C                                  conditions for the best correction
51 C                                  of instrumental artifacts.
52 C                                - On MISMATCHED BASELINE detection the
53 C                                  program will collect a new baseline
54 C                                  with instrument parameters specified
```

```
C                    for the spectrum except for PERIOD
C                    and SCAN RATE which revert to those
C                    for the previous baseline scan.
C                  - Altered data storage routine to use
C                    default or specified cartridge #.
C          June, 1987:
C                  - Modified Filename convention to match
C                    the use of Directory Paths in the
C                    new CI operating system.
C                  - Segmented the program using SGMTR
C                    to fit within CI's smaller boundary.
C          August, 1987:
C                  - Eliminated INQUIRE statement for FILE
C                    EXISTS or FILE OPEN check since this
C                    caused a memory protect error in the
C                    segmented versions if the filename
C                    was already in use. These checks are
C                    made using the IOSTAT number returned
C                    by the OPEN statement instead.
C          November,1987:
C                  - Altered updating of Variables Table
C                    so that SBW at Smin and GAIN at Smax
C                    are stored in Data File.
C          January, 1988:
C                  - Placed All COMMON Variables In Named
C                    COMMON Blocks To Prevent Them From
C                    Being Re-initialized On Calls To Other
C                    Nodes Of The Multi-Level Segmentation
C                  - Explicitly Specified Allocation Of
C                    BLOCK DATA memory Using NOALLOCATE
C                    Compiler Directives.
C                  - Eliminated Overwriting Of Data File
C                    Variables By The Wavelength Reading
C                    Routine. The CALL To Acquire Has
C                    Been Augmented To Bypass The Usual
C                    Spectral COMMON Variables in /CARY/.
C          February,1988:
C                  - Removed Single Beam Operation Since
C                    The Cary Cannot Acquire A Baseline
C                    In This Operating Mode.
C                  - Added Tight Checking For Improper
C                    Combinations Of Baseline Detector,
C                    Lamp and Reference Mode Requests.
C                  - Revised AUTO GAIN vs AUTO SLIT Mode
C                    Selection In Baseline And Instrument
C                    Setup Menus To Utilize Detector Mode
C                    Under AUTO SELECT Reference Selection.
C                  - Added Automatic Adjustment Of SBW And
C                    GAIN Before Scan To Match Baseline.
```

```
C
C       MODES:   All Abscissa & Ordinate Modes (SUBROUTINES)
C                Absorbance or %T vs Wavelength (PROGRAM only)
C
C       MEMORY:  28,000 Words (Max.PATH) + 40,000 Words EMA (DATA)
C                 3,000 Words (MSEG)      + 5 Memory Resident Nodes
C                       - 83 Page Partition Required -
C
C       SEGMENT: This Program Is Too Large To Run Under CI On The
C                HP 1000 - It Must Be Segmented Using SGMTR And
C                MLLDR Loader - A CMD Transfer File SEGMCARY.CMD
C                Contains The Commands To Accomplish This.
C
C     ------------------------------------------------------------
C
      INTEGER ACCESSORY,ADVANCED,BASELINE,EXIT,INSTRUMENT
      INTEGER LAMP,MENU,PARAMETERS,SPECTRUM,STORE
      INTEGER ASCII,MODE,NARRAY,NCOL,NDATA,PREC,XMODE,YMODE
      INTEGER NPAR(49),OFFSET(49),PARAM(49)
      REAL ORD,ABSC,CELL,CYCLE,SAMPLE,WAVE,TIMER,TEMP,DIST,BAND,CONC
      REAL GAIN,NUMBER,PATH,PMIN,PMAX,RATE,RATIO,SPECBAND,SPECGAIN
      REAL STEP,WAVELENGTH,WMIN,WMAX,XMIN,XMAX,XSTEP,ZERO
      REAL VARIABLE(14),X(10001),Y(10001)
      LOGICAL MATCH,PRINT,SINGLE,TRANSFER
C
C         Dimension Screen Control String Variables
C
      CHARACTER BELL,CLR*2,DOWN*2,ERASE*2,ESC,HOME*2,UP*2
C
C         Dimension Instrument Control String Variables
C
      CHARACTER CSM,Lock*4,Unlock*4,Key*2,Accon*3,Accoff*3
      CHARACTER Par*3,Var*3,Parset*2,Varset*2,Messon*3,Messoff*4
      CHARACTER Setup*4,Command*44,Response*64,String*14
C
C         Dimension Specific Key or Function String Variables
C
      CHARACTER Ready*4,Standby*4,Start*4,Stop*4,Instr*4,Autobal*4
C
C         Dimension Program Parameter Variables
C
      CHARACTER Sstat*10,Bstat*10,Astat*10,Wlength*7
      CHARACTER Directory*40,Fname*20,Name*6,Outfile*63
      CHARACTER Smin*4,Smax*4,Sinc*4,Sdet,Sgain*4,Slamp,Sperlod
      CHARACTER Srate,Sref,Sslit,Ssbw*4
      CHARACTER Bmin*4,Bmax*4,Bdet,Bgain*4,Blamp,Bperiod
      CHARACTER Brate,Bref,Bslit,Bsbw*4,Fperiod,Frate
      CHARACTER Omin*4,Omax*4,Oinc*4,Odet,Ogain*4,Olamp,Operiod
      CHARACTER Orate,Oref,Oslit,Osbw*4
C
      CHARACTER DATE*8,INITIALS*2,TITLE*72
      CHARACTER Access(5)*4,Printer(6)*12,Code,Icode,Pcode
      CHARACTER Pname(49)*10,Vname(14)*8,Bscan*14,Btime*14
      CHARACTER Pstr(49,16)*14
```

```
C
C     ---------------------------------------------------------------
C
      COMMON /MODE/NDATA,XMODE,YMODE
      COMMON /CARY/ORD,ABSC,CELL,CYCLE,SAMPLE,WAVE,TIMER,TEMP,DIST
      COMMON /IP/NPAR,OFFSET,/IS/Pname,Vname
      COMMON /DATA/Y,X
C
C         Reference Library IEEE-488 Subroutines
C
      EXTERNAL ABRT
C
C     ---------------------------------------------------------------
C
C         Initialize Cary Command & Status String Variables
C
      DATA CSM,Setup,Lock,Unlock,Key/'0','@@20','@A10','@A00','@D'/
      DATA Accon,Accoff,Par,Var/'@F1','@F0','@G1','@G2'/
      DATA Parset,Varset,Messon,Messoff/'@H','@I','L1','@L00'/
      DATA Ready,Standby,Start/'@DT0','@DS0','@DP0'/
      DATA Stop,Instr,Autobal/'@DQ0','@DC0','@DU0'/
      DATA Sstat,Bstat,Astat/'  OFF','  OFF','  OFF'/
C
C         Initialize Cary Instrument Settings String Arrays
C
      DATA (Pstr(1,I),I=1,6)/'ABSORBANCE','% TRANSMISSION',
     &'TEMPERATURE','% REFLECTANCE','CONCENTRATION','EMISSION'/
      DATA (Pstr(2,I),I=1,4)/'WAVELENGTH','TIME','TEMPERATURE',
     &'DISTANCE'/
      DATA (Pstr(3,I),I=1,11)/'OFF','0.01','0.02','0.05','0.1','0.2',
     &'0.5','1.0','2.0','5.0','10.0'/
      DATA Pstr(4,1)/'OFF'/
      DATA (Pstr(4,I),I=6,15)/'0.2','0.5','1.0','2.0','5.0',
     &'10','20','50','100','200'/
      DATA (Pstr(5,I),I=1,4)/'AUTO SELECT','AUTO GAIN','AUTO SLIT',
     &'SINGLE BEAM'/
      DATA (Pstr(6,I),I=1,5)/'OFF','NORMAL','1ST DERIV','2ND DERIV',
     &'LOG'/
      DATA (Pstr(7,I),I=1,9)/'0.01','0.02','0.05','0.1','0.2','0.5',
     &'1.0','2.0','4.0'/
      DATA (Pstr(8,I),I=10,16)/'2','5','10','20','50','100','200'/
      DATA (Pstr(9,I),I=12,15)/'10','20','50','100'/
      DATA (Pstr(10,I),I=1,5)/'-1.9 TO 0.6','-2.0 TO 0.5',
     &'-2.1 TO 0.4','-2.2 TO 0.3','-2.3 TO 0.2'/
      DATA (Pstr(11,I),I=1,16)/'+/-0.01','+/-0.02','+/-0.05','+/-0.1',
     &'+/-0.2','+/-0.5','+/-1.0','+/-2.0','+/-5.0','+/-10','+/-20',
     &'+/-50','+/-100','+/-200','+/-500','+/-1000'/
      DATA (Pstr(12,I),I=1,16)/'+/-0.01','+/-0.02','+/-0.05','+/-0.1',
     &'+/-0.2','+/-0.5','+/-1.0','+/-2.0','+/-5.0','+/-10','+/-20',
     &'+/-50','+/-100','+/-200','+/-500','+/-1000'/
      DATA (Pstr(13,I),I=1,8)/'+/-0.01','+/-0.02','+/-0.05','+/-0.1',
     &'+/-0.2','+/-0.5','+/-1.0','+/-2.0'/
      DATA (Pstr(14,I),I=1,10)/'0','10','20','30','40','50','60','70',
     &'80','90'/
```

```
212       DATA (Pstr(15,I),I=1,4)/'0.5','1.0','3.0','10'/
213       DATA (Pstr(16,I),I=1,2)/'NORMAL','REVERSE'/
214       DATA (Pstr(17,I),I=1,2)/'OFF','ON'/
215       DATA (Pstr(18,I),I=1,2)/'REPEAT SCAN','SGL/MULTI'/
216       DATA (Pstr(19,I),I=1,2)/'SERIAL','OVERLAY'/
217       DATA (Pstr(20,I),I=1,4)/'BOTH ON','UV ONLY','VIS/NIR ONLY',
218      &'BOTH OFF'/
219       DATA (Pstr(21,I),I=1,3)/'AUTO','UV','VIS/NIR'/
220       DATA (Pstr(22,I),I=1,3)/'AUTO','UV/VIS','NIR'/
221       DATA (Pstr(23,I),I=1,2)/'FULL','1/3'/
222       DATA (Pstr(24,I),I=1,3)/'AUTO','UV/VIS','NIR'/
223       DATA (Pstr(25,I),I=1,3)/'AUTO','UV','VIS/NIR'/
224       DATA (Pstr(26,I),I=1,4)/'AUTO SELECT','AUTO GAIN','AUTO SLIT',
225      &'SINGLE BEAM'/
226       DATA (Pstr(27,I),I=1,2)/'FULL','1/3'/
227       DATA (Pstr(28,I),I=1,6)/'0','1','2','3','4','5'/
228       DATA (Pstr(29,I),I=1,2)/'STANDARDS','UNKNOWNS'/
229       DATA (Pstr(30,I),I=3,6)/'DIRECT','LINEAR','DIRECT-QUAD',
230      &'QUADRATIC'/
231       DATA (Pstr(31,I),I=7,8)/'NORMAL','AVERAGED'/
232       DATA (Pstr(32,I),I=9,13)/'SIGNAL AV','SAMPLE AV','QUICK',
233      &'EXTENDED','FIXED'/
234       DATA (Pstr(33,I),I=1,5)/'DSPL RESULTS','DSPL SETUP','NEXT CONC',
235      &'DELETE SAMPLE','CLEAR RESULTS'/
236       DATA (Pstr(34,I),I=1,2)/'OFF','ON'/
237       DATA (Pstr(35,I),I=1,2)/'1','2'/
238       DATA (Pstr(38,I),I=1,5)/'  OFF','  ON','RECORD',' ','ON/SETUP'/
239       DATA (Pstr(40,I),I=1,2)/'INTERVAL','ACCY-DRIVEN'/
240 C
241       DATA (Printer(I),I=1,3)/'WAVELENGTH','TIME','TEMPERATURE'/
242       DATA (Printer(I),I=4,6)/'DISTANCE','MAX.mm','MIN.mm'/
243 C
244 C         Initialize Screen Control String Variables
245 C
246       BELL=CHAR(7)
247       ESC=CHAR(27)
248       CLR=ESC//'J'
249       HOME=ESC//'h'
250       UP=ESC//'A'
251       DOWN=ESC//'B'
252       ERASE=ESC//'K'
253 C
254 C     ------------------------------------------------------------------
255 C
256 C         Assign Statement Labels
257 C
258 C     ------------------------------------------------------------------
259 C
260       ASSIGN 10  TO MENU
261       ASSIGN 90  TO SPECTRUM
262       ASSIGN 200 TO BASELINE
263       ASSIGN 350 TO ADVANCED
264       ASSIGN 390 TO INSTRUMENT
265       ASSIGN 400 TO PARAMETERS
```

```
      ASSIGN 570 TO LAMP
      ASSIGN 600 TO ACCESSORY
      ASSIGN 700 TO STORE
      ASSIGN 900 TO EXIT
C
C     ---------------------------------------------------------------
C
C         Data Acquisition and Control Menu
C
C     ---------------------------------------------------------------
C
      CALL FFRCL(79)                ! Eliminate Line Wrapping Problems
      CALL Send(Setup)              ! Setup Normal Handshaking With Cary
      CALL Send(Ready)              ! Release Cary From Standby Mode
   10 WRITE (1,*) HOME,CLR
      CALL Send(Instr)              ! Display Instrument Settings On Cary
      CALL Send(Messoff)            ! Turn Off Display Messages On Cary
      CALL Send(Unlock)             ! Unlock Keyboard On Cary
      NCOL=70                       ! Set Display To 70 Columns
      TITLE='Cary 2390'
      CALL Center(TITLE)
      TITLE='Spectral Data Acquisition'
      CALL Center(TITLE)
      WRITE (1,'(T61,A2,A8)') UP,'Rev: 1.7'
      CALL Line(NCOL)
      WRITE (1,20) 'CODE','FUNCTION','STATUS','MIN','MAX','INC'
   20 FORMAT (T4,A4,T14,A8,T34,A7,T50,A3,T58,A3,T66,A3)
      CALL Line(NCOL)
      WRITE (1,30) 'A.....Acquire Spectrum.......',Sstat,Smin,Smax,Sinc
      WRITE (1,40) 'B.....Baseline Setup.........',Bstat,Bmin,Bmax
      WRITE (1,50) 'I.....Instrument Settings....'
      WRITE (1,50) 'L.....Lamps/Detectors/Access.'
      WRITE (1,60) 'S.....Store File on Disk.....',Fname
      WRITE (1,50) 'X.....EXIT Data Acquisition..'
   30 FORMAT (/,T4,A30,T35,A8,T50,A4,T58,A4,T66,A4)
   40 FORMAT (/,T4,A30,T35,A8,T50,A4,T58,A4)
   50 FORMAT (/,T4,A30)
   60 FORMAT (/,T4,A30,T35,A20)
      WRITE (1,*)
      CALL Line(NCOL)
      WRITE (1,*)
   70 WRITE (1,*) UP,ERASE,'_'
      WRITE (1,'(T3,A15,A,A2)') 'Enter the CODE:',BELL,'_'
      READ (1,80) Code
   80 FORMAT (A1)
      CALL Upper(Code)
      IF (Code.EQ.'A') GO TO SPECTRUM
      IF (Code.EQ.'B') GO TO BASELINE
      IF (Code.EQ.'I') GO TO INSTRUMENT
      IF (Code.EQ.'L') GO TO ADVANCED
      IF (Code.EQ.'S') GO TO STORE
      IF (Code.EQ.'X') GO TO EXIT
      GO TO 70
C
```

```
C     ------------------------------------------------------------
C
C         Acquire Spectrum: (Instrument Baseline Must Match)
C
C     ------------------------------------------------------------
C
   90 CALL Partable(PARAM)
      IF ((PARAM(38).NE.1).OR.(Bstat.EQ.'  OFF')) THEN
        WRITE (1,*) UP,ERASE,'_'
        WRITE (1,*) ' Baseline Program Is ABSENT: ',BELL,'_'
        CALL Wait(2.0)
        WRITE (1,*)
        GO TO BASELINE
      END IF
      IF ((PARAM(1).EQ.2).OR.(PARAM(2).NE.0)) THEN
        WRITE (1,*) UP,ERASE,'_'
        WRITE (1,*) ' Ordinate or Abscissa Error: ',BELL,'_'
        CALL Wait(2.0)
        WRITE (1,*)
        GO TO INSTRUMENT
      END IF
      IF (Sstat.EQ.'ACQUIRED') THEN
  100   WRITE (1,*) UP,ERASE,'  SPECTRUM NOT STORED:_'
        WRITE (1,*) ' Proceed With Spectrum (Y or N) ? ',BELL,'_'
        READ (1,80) Code
        CALL Upper(Code)
        IF (Code.EQ.'N') GO TO 70
        IF (Code.NE.'Y') GO TO 100
      END IF
C
C     ------------------------------------------------------------
C
C         Store Previous Spectrum's Parameters For Possible Abort
C
C     ------------------------------------------------------------
C
      Omin=Smin
      Omax=Smax
      Oinc=Sinc
      Odet=Sdet
      Ogain=Sgain
      Olamp=Slamp
      Operiod=Speriod
      Orate=Srate
      Oref=Sref
      Oslit=Sslit
      Osbw=Ssbw
C     ------------------------------------------------------------
      WRITE (1,*) HOME,CLR
      TITLE='Scan Parameters'
      CALL Center(TITLE)
      CALL Line(NCOL)
      WRITE (1,*) DOWN,'  BASELINE:'
      WRITE (1,*) DOWN,'  Scan Limits, (nm): ',Bmin,'/ ',Bmax
```

```
374         CALL Val(Bmin,WMIN)                    ! Default Spectrum To
375         CALL Val(Bmax,WMAX)                    ! Baseline Scan Limits
376         WRITE (1,*) DOWN,DOWN,'  SPECTRUM:'
377         WRITE (1,*) DOWN,'  Scan Limits, (nm): ',Bmin,'/ ',Bmax,
378        &DOWN,DOWN
379     110 WRITE (1,*) UP,ERASE,'  A...Accept, C...Change, X...Exit ? ',
380        &BELL,'_'
381         READ (1,80) Code
382         CALL Upper(Code)
383         IF (Code.EQ.'X') GO TO MENU
384         IF (Code.EQ.'A') GO TO 120
385         IF (Code.NE.'C') GO TO 110
386         CALL Limits(WMIN,WMAX)
387     120 CALL Str(WMIN,String,4)
388         Smin=String(2:5)
389         CALL Str(WMAX,String,4)
390         Smax=String(2:5)
391         WRITE (1,*) UP,ERASE,UP,UP,ERASE,'  Scan Limits, (nm): ',
392        &Smin,'/ ',Smax,DOWN,DOWN
393     130 WRITE (1,*) UP,ERASE,'  Step Size (.01 - 5 nm) : ',BELL,'_'
394         READ (1,*,ERR=130) STEP
395         IF ((STEP.LT.0.01).OR.(STEP.GT.5.0)) GO TO 130
396         CALL Str(STEP,String,4)
397         Sinc=String(2:5)
398     140 CALL Val(Pstr(3,PARAM(3)+1),RATE)
399         RATE=RATE/STEP
400         IF (RATE.GT.5.0) THEN
401           WRITE (1,*) UP,ERASE,'  Data Rate > 5 Hz - _'
402           WRITE (1,*) 'RESET Scan Rate, (Y or N) ? ',
403        &  BELL,'_'
404           READ (1,80) Code
405           CALL Upper(Code)
406           IF (Code.NE.'Y') GO TO 130
407           N=3
408           K=N
409           CALL Select(N,PARAM,Pstr)
410           PARAM(K)=N-1                         ! Update Parameter Table
411           GO TO 140
412         END IF
413         NDATA=INT((WMAX-WMIN)/STEP+.5)+1
414         IF (NDATA.GT.10001) THEN
415           WRITE (1,*) UP,ERASE,'  Too Many Data Points - _'
416           WRITE (1,*) 'Increase Step Size _',BELL
417           CALL Wait(2.0)
418           GO TO 130
419         END IF
420         WRITE (1,*) DOWN,'  Checking Instrument Settings:',BELL
421         CALL GOTO(Bmax)        ! Test Matching At Start Of Baseline Scan
422 C
423 C       ------------------------------------------------------------
424 C
425 C           Set Spectrum Strings to Match Instrument Parameters
426 C
427 C       ------------------------------------------------------------
```

```
C
      Sdet=CHAR(PARAM(22)+48)
      Slamp=CHAR(PARAM(21)+48)
      Speriod=CHAR(PARAM(15)+48)
      Srate=CHAR(PARAM(3)+48)
      Sref=CHAR(PARAM(5)+48)
      Sslit=CHAR(PARAM(23)+48)
      CALL Variable(VARIABLE)              ! Update SBW, GAIN at Bmax
      CALL Str(VARIABLE(10),String,4)
      Ssbw=String(2:5)
      CALL Str(VARIABLE(6),String,4)
      Sgain=String(2:5)
C
C     ---------------------------------------------------------------
C
C         Test For Acceptable Instrument Baseline Matching
C
C     ---------------------------------------------------------------
C
      MATCH=.TRUE.
      IF (WMAX.GT.VARIABLE(3)) MATCH=.FALSE.
      IF (WMIN.LT.VARIABLE(4)) MATCH=.FALSE.
      IF (Sref.NE.Bref) MATCH=.FALSE.
      IF (Slamp.NE.Blamp) MATCH=.FALSE.
      IF (Sdet.NE.Bdet) MATCH=.FALSE.
      IF (Sslit.NE.Bslit) MATCH=.FALSE.
C     ---------------------------------------------------------------
      IF ((MODE.EQ.1).AND.(MATCH)) THEN    ! Exit If Already Failed
        IF (Ssbw.NE.Bsbw) THEN
          WRITE (1,*) UP,ERASE,'  Matching To Baseline SBW:',BELL
          Command=Varset//'9'//Bsbw//'!0'
          CALL Send(Command)
          Ssbw=Bsbw
          CALL Wait(1.0)
        END IF
      END IF
C     ---------------------------------------------------------------
      IF ((MODE.EQ.2).AND.(MATCH)) THEN    ! Exit If Already Failed
        IF (Sgain.NE.Bgain) THEN
          WRITE (1,*) UP,ERASE,'  Matching To Baseline GAIN:',BELL
          Command=Varset//'5'//Bgain//'!0'
          CALL Send(Command)               ! Reset AUTOSLIT Gain Level
          Sgain=Bgain
          CALL Wait(2.0)
        END IF
        IF ((Bref.EQ.'0').AND.(Bdet.EQ.'0').AND.(WMAX.LE.800.0)) THEN
          WRITE (1,*) UP,ERASE,'  Matching To Baseline SBW:',BELL
          Wlength='800 5'
          CALL GOTO(Wlength)               ! Reset To NIR Region
          CALL Wait(1.0)
          Wlength='800 0'
          CALL GOTO(Wlength)               ! Set To Start Of UV/VIS
        END IF                             ! With Matching SBW
      END IF
```

```
      IF (MATCH) GO TO 150
C
C     ------------------------------------------------------------------
C
C        Record New Baseline Using Present Instrument Parameters
C        With Period & Scan Rate From The Previous Baseline Scan
C
C     ------------------------------------------------------------------
C
      WRITE (1,*) DOWN,DOWN
      TITLE='*** NEW BASELINE REQUIRED ***'
      CALL Center(TITLE)
      WRITE (1,*) BELL
      CALL Wait(2.0)
      MATCH=.TRUE.                          ! Baseline Valid Test On Exit
      CALL Bline(WMIN,WMAX,Sdet,Sgain,Slamp,Fperiod,Frate,Sref,Ssbw,
     &Sslit,Bscan,Btime,MATCH,MODE)
      Command=Parset//'>'//Speriod//CSM     ! Reset To Spectrum's Period
      CALL Send(Command)
      Command=Parset//'2'//Srate//CSM       ! Reset To Spectrum's Rate
      CALL Send(Command)
      IF (.NOT.MATCH) THEN
        Sstat='  OFF'                       ! Aborted Scan Exit
        GO TO MENU
      END IF
C
C     ------------------------------------------------------------------
C
C        Update Baseline Parameter Strings
C
C     ------------------------------------------------------------------
C
      Bmin=Smin
      Bmax=Smax
      Bdet=Sdet
      Bgain=Sgain
      Blamp=Slamp
      Bperiod=Fperiod
      Brate=Frate
      Bref=Sref
      Bsbw=Ssbw
      Bslit=Sslit
      Bstat='ON/MATCH'
C     ------------------------------------------------------------------
  150 WRITE (1,*) HOME,CLR
      TITLE='Acquire Spectrum'
      CALL Center(TITLE)
      CALL Line(NCOL)
      WRITE (1,*) DOWN,'  Wavelength Limits, (nm)  ',Smax,'/ ',Smin
      WRITE (1,*) DOWN,'  Step Size, (nm/datum)    ',Sinc
      WRITE (1,*) DOWN,'  Scan Rate, (nm/sec)      '
     &,Pstr(3,PARAM(3)+1)
      WRITE (1,*) DOWN,'  Response Time, (sec)     '
     &,Pstr(15,PARAM(15)+1
```

```
      IF (MODE.EQ.1) THEN
        WRITE (1,*) DOWN,'  Spectral Bandwidth,(nm): ',Ssbw
        GO TO 160
      END IF
      WRITE (1,*) DOWN,'  AUTOSLIT Gain Level     : ',Sgain
  160 WRITE (1,*) DOWN
      WRITE (1,*) DOWN,'  Place Solution Cell In The SAMPLE Beam:'
      WRITE (1,*) DOWN,'       S.....Start Scan'
      WRITE (1,*) DOWN,'       A.....Abort Scan'
      WRITE (1,*) DOWN,'  Enter the CODE: ',BELL,'_'
  170 READ (1,80) Code
      CALL Upper(Code)
C
C     ------------------------------------------------------------
C
C         Restore Old Spectrum's Parameter Strings
C
C     ------------------------------------------------------------
C
      IF (Code.EQ.'A') THEN
        Smin=Omin
        Smax=Omax
        Sinc=Oinc
        Sdet=Odet
        Sgain=Ogain
        Slamp=Olamp
        Speriod=Operiod
        Srate=Orate
        Sref=Oref
        Sslit=Oslit
        Ssbw=Osbw
        GO TO MENU
      END IF
      IF (Code.NE.'S') GO TO 170
C
C     ------------------------------------------------------------
C
C         Set To Starting Wavelength - Check For Instrument Ready
C
C     ------------------------------------------------------------
C
      WRITE (1,*) UP,ERASE,UP,UP,ERASE,UP,UP,ERASE,UP,UP,ERASE,'_'
      WRITE (1,*) ' Slewing to Starting Wavelength:',BELL
      CALL GOTO(Smax)
      SINGLE= FALSE.              ! Scan Mode ON, Single Wavelength OFF
      PRINT= FALSE.               ! Initialize Print Mode To OFF
  180 WRITE (1,*) UP,ERASE,'  Print to Screen, (Y or N) ? ',BELL,'_'
      READ (1,80) Code
      CALL Upper(Code)
      IF (Code.EQ.'Y') THEN
        PRINT= TRUE.
        GO TO 190
      END IF
      IF (Code.NE.'N') GO TO 180
```

```
C
C     ---------------------------------------------------------------
C
C         Select Data String Format For Abscissa & Ordinate In
C         SUBROUTINE Acquire Via COMMON Variables XMODE & YMODE
C
C     ---------------------------------------------------------------
C
  190 YMODE=PARAM(1)+1          ! YMODE = 1 - 6 (Only 1 & 2 Allowed)
      XMODE=PARAM(2)+1          ! XMODE = 1 - 4 (Only 1 Allowed)
      SPECGAIN=VARIABLE(6)      ! Save GAIN Value At Smax For Data File
C
      WRITE (1,*) UP,ERASE,'  Scanning Spectrum:',BELL
C
      CALL Send(Instr)          ! Display Instrument Settings On Cary
      CALL Send(Lock)           ! Lock Keyboard On Cary During Scan
      CALL Wait(1.0)            ! Wait For Cary To Finish Housekeeping
C
C     ---------------------------------------------------------------
C                 *** Data Collection Subroutine ***
C
C         Collects NDATA Readings At Sinc (nm) Steps And
C         Returns Spectrum In Arrays (X),(Y) Via EMA COMMON
C         Final Reading Is Returned Via Named COMMON /CARY/
C
      CALL Acquire(Sinc,PRINT,SINGLE,WAVELENGTH)
C
C     ---------------------------------------------------------------
C
      CALL Terminate            ! UNTALK Cary 2390 From IEEE-488 Bus
      CALL Wait(1.0)            ! Wait For Cary To Finish Housekeeping
      CALL Send(Setup)          ! Re-establish Normal Handshaking
      CALL Send(Stop)           ! STOP Key Issued
      CALL Send(Unlock)         ! UNLOCK Keyboard
      CALL Variable(VARIABLE)   ! Update Instrument Variables To Obtain
      SPECBAND=VARIABLE(10)     ! Value Of Spectral Bandwidth At Smin
      CALL GOTO(Smax)           ! Return To Starting Wavelength
      NARRAY=NDATA              ! Save # Of Data Points In File Variable
      XMIN=WMIN                 ! Save End Of Scan In File Variable
      XMAX=WMAX                 ! Save Start Of Scan In File Variable
      XSTEP=STEP                ! Save Step Size In File Variable
      Sstat='ACQUIRED'
      GO TO MENU
C
C     ---------------------------------------------------------------
C
C         Baseline Call and Status Check
C
C     ---------------------------------------------------------------
C
```

```
640    200 MATCH=.TRUE.
641        TRANSFER=.FALSE.
642    210 WRITE (1,*) UP,ERASE,'  Reading Instrument Baseline: ',BELL,'_'
643        CALL Partable(PARA4)
644        Bstat=Pstr(38,PARAM(38)+1)
645        IF (PARAM(38).GT.1) Bstat=' '//Pstr(38,PARAM(38)+1)
646        CALL Vartable(VARIABLE)
647        WMAX=NINT(VARIABLE(3))
648        WMIN=NINT(VARIABLE(4))
649        BAND=VARIABLE(2)/1000.0      ! Only One Of SBW Or GAIN Is Stored
650        GAIN=VARIABLE(2)/10.0        ! By The Cary For The Baseline Scan
651    220 PREC=4                       ! - Decide Below Which Is Valid.
652        IF (WMAX.LT.1000.0) PREC=3
653        CALL Str(WMAX,String,PREC)
654        Bmax=String(2:5)
655        PREC=4
656        IF (WMIN.LT.1000.0) PREC=3
657        CALL Str(WMIN,String,PREC)
658        Bmin=String(2:5)
659 C      ---------------------------------------------------------------
660        IF (TRANSFER) GO TO MENU     ! EXIT After Return From Bline
661 C      ---------------------------------------------------------------
662        IF (WMAX.GT.900.0) THEN
663          IF (PARAM(24).EQ.1) PARAM(24)=0    ! Bad UV/VIS Detector Mode
664          IF (PARAM(26).EQ.1) PARAM(26)=0    ! Bad AUTO GAIN Ref. Mode
665        END IF
666        IF (WMIN.LT.700.0) THEN
667          IF (PARAM(24).EQ.2) PARAM(24)=0    ! Bad NIR Detector Mode
668        END IF
669        IF (PARAM(24).EQ.2) THEN
670          IF (PARAM(26).EQ.1) PARAM(26)=0    ! Bad NIR Reference Mode
671        END IF
672        IF ((PARAM(24).EQ.0).AND.(PARAM(26).EQ.1)) THEN
673          IF (WMAX.GT.800.0) PARAM(24)=1     ! Bad AUTO Detector Mode
674        END IF
675        IF (WMAX.GT.400.0) THEN
676          IF (PARAM(25).EQ.1) PARAM(25)=0    ! Bad UV Lamp Mode
677        END IF
678        IF (WMIN.LT.270.0) THEN
679          IF (PARAM(25).EQ.2) PARAM(25)=0    ! Bad W Lamp Mode
680        END IF
681 C      ---------------------------------------------------------------
682        Bperiod=CHAR(PARAM(15)+48)
683        Brate=CHAR(PARAM(3)+48)
684        Bdet=CHAR(PARAM(24)+48)
685        Blamp=CHAR(PARAM(25)+48)
686        Bref=CHAR(PARAM(26)+48)
687        Bslit=CHAR(PARAM(27)+48)
688        IF (Bref.EQ.'2') GO TO 230    ! AUTOSLIT Mode On (Both Detectors)
689        IF (Bdet.EQ.'2') GO TO 230    ! NIR Detector  => AUTOSLIT Mode
690        IF (WMAX.GT.900.0) GO TO 230  ! Lamoda > 900  => AUTOSLIT Mode
691        IF (WMAX.GT.800.0) THEN
692          IF (Bdet.EQ.'0') GO TO 230  ! AUTO Detector => AUTOSLIT Mode
693        END IF
```

```
694 C     ------------------------------------------------------------
695       CALL Str(BAND,String,4)
696       Bsbw=String(2:5)              ! SBW Fixed At The Start Of Scan
697       Bgain=' '                     ! Gain Variable During Scan
698       MODE=1
699       GO TO 240
700   230 CALL Str(GAIN,String,4)
701       Bgain=String(2:5)             ! GAIN Fixed At The Start Of Scan
702       Bsbw=' '                      ! SBW Variable During Scan
703       MODE=2
704   240 Command=Key//'HO'             ! Display Baseline Menu On Cary
705       CALL Send(Command)
706       CALL Send(Messoff)            ! Turn Off Any Display Messages
707 C     ------------------------------------------------------------
708       WRITE (1,*) HOME,CLR
709       TITLE='Baseline Setup'
710       CALL Center(TITLE)
711       CALL Line(NCOL)
712       WRITE (1,250) 'INDEX','FUNCTION','SETTING'
713       CALL LINE(NCOL)
714       WRITE (1,*)
715       WRITE (1,260) '0:','.....AUTO BALANCE.....',
716      &Astat
717       WRITE (1,260) '1:','.....BASELINE STATUS.....',
718      &Bstat
719       WRITE (1,280) '2:','.....WAVELENGTH (Max,Min)...',
720      &Bmax,',',Bmin
721       WRITE (1,280) '3:','.....SBW (nm), GAIN.....',
722      &Bsbw,',',Bgain
723       WRITE (1,270) '4:','.....REFERENCE MODE.....',
724      &Pstr(26,PARAM(26)+1)
725       WRITE (1,270) '5:','.....LAMP SELECT.....',
726      &Pstr(25,PARAM(25)+1)
727       WRITE (1,270) '6:','.....DETECTOR SELECT.....',
728      &Pstr(24,PARAM(24)+1)
729       WRITE (1,270) '7:','.....SLIT HEIGHT.....',
730      &Pstr(27,PARAM(27)+1)
731       WRITE (1,270) '8:','.....SCAN RATE (nm/sec).....',
732      &Pstr(3,PARAM(3)+1)
733       WRITE (1,270) '9 ','.....RESPONSE TIME (sec) ..',
734      &Pstr(15,PARAM(15)+1)
735       WRITE (1,260) 'X:','.....EXIT Baseline Menu .....',
736      &' '
737   250 FORMAT (T4,A5,T20,A8,T40,A7)
738   260 FORMAT (T4,A3,T10,A28,A8)
739   270 FORMAT (T4,A3,T10,A28,T40,A14)
740   280 FORMAT (T4,A3,T10,A28,T40,A4,A,A4)
741       WRITE (1,*)
742       CALL Line(NCOL)
743       WRITE (1,*)
744   290 WRITE (1,*) UP,ERASE,'  INDEX Code: ',BELL,'_'
745       READ (1,80) Code
746       CALL Upper(Code)
747       IF (Code.EQ.'X') GO TO 330
```

```
748         N=ICHAR(Code)-48
749         IF ((N.LT.0).OR.(N.GT.9)) GO TO 290
750 C       ------------------------------------------------------------
751         IF (N.EQ.0) THEN
752           CALL Send(Autobal)
753           Astat=' SET'
754           GO TO 220
755         END IF
756         IF (N.EQ.1) N=38
757         IF (N.EQ.2) GO TO 300          ! Update Wavelength Limits
758         IF (N.EQ.3) GO TO 310          ! Update SBW/GAIN
759         IF (N.EQ.4) N=26
760         IF (N.EQ.5) N=25
761         IF (N.EQ.6) N=24
762         IF (N.EQ.7) N=27               ! Slit Control Is Manual Only
763         IF (N.EQ.8) N=3
764         IF (N.EQ.9) N=15
765 C       ------------------------------------------------------------
766         K=N                            ! Instrument Baseline PARAMETERS Are
767         CALL Select(N,PARAM,Pstr)      ! Masked From Direct Changes - The
768         PARAM(K)=N-1                   ! NEW Values Are Only Accepted From
769         IF (K.EQ.38) THEN              ! SUBROUTINE Bline's '@J' Command.
770           WRITE (1,'(T12,A)') '_'
771           GO TO 200
772         END IF
773         GO TO 220
774 C       ------------------------------------------------------------
775   300   CALL Limits(WMIN,WMAX)
776         MATCH=.FALSE.
777         GO TO 220
778   310   WRITE (1,*) UP,ERASE,'_'
779         IF (MODE.EQ.2) GO TO 320
780         WRITE (1,*) ' Spectral Bandwidth (0.04 - 3.60 nm) = ',BELL,'_'
781         READ (1,*,ERR=310) BAND
782         IF ((BAND.LT.0.04).OR.(BAND.GT.3.60)) GO TO 310
783         GO TO 220
784   320   String='(1-1275)'
785         IF (PARAM(24).NE.2) String='(1 - 1000)'
786         WRITE (1,*) ' Gain Level '.String(1:10),' = ',BELL,'_'
787         READ (1,*,ERR=310) NUMBER
788         IF ((NUMBER.LT.1.0).OR.(NUMBER.GT.1275.0)) GO TO 310
789         IF ((NUMBER.GT.1000.0).AND.(PARAM(24).NE.2)) GO TO 310
790         GAIN=VARIABLE(6)
791         RATIO=NUMBER/GAIN
792         IF (RATIO.GT.10.0) THEN
793           WRITE (1,*) UP,ERASE,'_'
794           WRITE (1,*) ' Setting Instrument Gain: ',BELL,'_'
795           CALL Wait(2.0)
796           Command=Parset//'420'              ! Set AUTOSLIT Mode Prior
797           CALL Send(Command)                 ! To Sending New GAIN Level
798           WRITE (1,*)
799           TRANSFER=.TRUE.                    ! Transfer To Instrument
800           GO TO 490                          ! GAIN Setting Routine
801         END IF
```

```
802         GAIN=NUMBER
803         GO TO 220
804 C
805 C       ------------------------------------------------------------
806 C
807 C           Record Baseline Scan In CARY 2390
808 C
809 C       ------------------------------------------------------------
810 C
811     330 WRITE (1,*) UP,ERASE,'_'
812         WRITE (1,*) ' Record NEW Baseline, (Y or N) ? ',BELL,'_'
813         READ (1,80) Code
814         CALL Upper(Code)
815         IF (Code.EQ.'N') GO TO 340
816         IF (Code.NE.'Y') GO TO 330
817         MATCH=.FALSE.
818         I=ICHAR(Brate)-48
819         Bscan=Pstr(3,I+1)
820         I=ICHAR(Bperiod)-48
821         Btime=Pstr(15,I+1)
822         CALL Bline(WMIN,WMAX,Bdet,Bgain,Blamp,Bperiod,Brate,Bref,Bsbw,
823        &Bslit,Bscan,Btime,MATCH,MODE)
824         Fperiod=Bperiod
825         Frate=Brate
826         Astat='  SET'
827     340 TRANSFER=.TRUE. ! Perform An Alternate Return To The Main MENU
828         GO TO 210       ! After Reading Instrument Baseline Parameters
829 C
830 C       ------------------------------------------------------------
831 C
832 C           Menu of Advanced Setup Operations
833 C
834 C       ------------------------------------------------------------
835 C
836     350 WRITE (1,*) HOME,CLR
837         TITLE='Advanced Operations Menus'
838         CALL Center(TITLE)
839         NCOL=50
840         CALL Line(NCOL)
841         WRITE (1,'(T15,A5,T30,A14)') 'INDEX','GROUP FUNCTION'
842         CALL Line(NCOL)
843         WRITE (1,*)
844         WRITE (1,360) '1: .......LAMPS & DETECTORS.......'
845         WRITE (1,360) '2: .......ACCESSORY SETTINGS.......'
846         WRITE (1,360) '3: .......AUTOMATIC OPERATION......'
847         WRITE (1,360) 'X: .......EXIT TO SETUP MENU.......'
848         WRITE (1,*)
849         CALL Line(NCOL)
850     360 FORMAT (T17,A35)
851         WRITE (1,*)
852     370 WRITE (1,'(T15,A2,A2,A9,A,A)') UP,ERASE,'INDEX #: ',BELL,'_'
853         READ (1,80) Code
854         CALL Upper(Code)
855         IF (Code.EQ.'X') GO TO MENU
```

```
      N=ICHAR(Code)-48
      IF (N.EQ.1) GO TO LAMP
      IF (N.EQ.2) GO TO ACCESSORY
      IF (N.EQ.3) GO TO 380
      GO TO 370
  380 WRITE (1,'(T13,A2,A2,A)') UP,ERASE,'_'
      WRITE (1,*) ' Not Supported in Version 1.X ',BELL,'_'
      CALL Wait(2.0)
      GO TO ADVANCED
C
C     ------------------------------------------------------------
C
C         Display and Update Instrument Settings
C
C     ------------------------------------------------------------
C
  390 WRITE (1,*) UP,ERASE,'  Reading Wavelength: ',BELL,'_'
      NDATA=1
      Oinc='1'
      PRINT=.FALSE.                    ! No Display Required
      SINGLE=.TRUE.                    ! Select Wavelength Update Mode
      CALL Partable(PARAM)
      YMODE=PARAM(1)+1                 ! Set Data String Format
      XMODE=2
      Icode=CHAR(PARAM(2)+48)          ! Save Abscissa Mode
      Command=Parset//'110'            ! Set Abscissa = TIME
      CALL Send(Command)
      CALL Send(Setup)
      CALL Wait(0.5)
      CALL Acquire(Oinc,PRINT,SINGLE,WAVELENGTH)
      CALL Terminate
      CALL Wait(0.5)
      CALL Send(Setup)
      CALL Send(Stop)
      Command=Parset//'1'//Icode//CSM
      CALL Send(Command)               ! Restore Abscissa Mode
      WRITE (1,*)
      WRITE (1,*) UP,'_'
  400 WRITE (1,*) ERASE,' Reading Instrument Settings: ',BELL,'_'
      CALL Partable(PARAM)
      CALL Vartable(VARIABLE)
      BAND=VARIABLE(10)                    ! Current SBW (nm)
      GAIN=VARIABLE(6)                     ! Current GAIN Level
      CALL Val(Pstr(8,PARAM(8)+1),PMAX)    ! Pen Limits, %T & %R
      PMIN=VARIABLE(11)
      IF (PARAM(1).EQ.0) THEN              ! Pen Limits, Absorbance
        CALL Val(Pstr(7,PARAM(7)+1),PMAX)
        PMIN=VARIABLE(1)
      END IF
      IF (PARAM(1).EQ.2) THEN              ! Pen Limits, Temperature
        CALL Val(Pstr(9,PARAM(9)+1),PMAX)
        CALL Val(Pstr(14,PARAM(14)+1),PMIN)
      END IF
      PMAX=PMIN+PMAX
```

```
910         I=11                                    ! Index For Deriv. Range
911         IF (PARAM(6).EQ.4) I=10                 ! Index For Log Zero Range
912         String=Pstr(I,PARAM(I)+1)               ! Pen Range Label For Index
913         CALL Send(Instr)                        ! Display Instrument Menu
914 C       ------------------------------------------------------------------
915         WRITE (1,*) HOME,CLR
916         TITLE='Instrument Settings'
917         CALL Center(TITLE)
918         CALL Line(NCOL)
919         WRITE (1,'(T4,A5,T20,A8,T40,A7)') 'INDEX','FUNCTION','SETTING'
920         CALL LINE(NCOL)
921         WRITE (1,*)
922         WRITE (1,410) '0:','.....WAVELENGTH.............',
923        &WAVELENGTH
924         WRITE (1,420) '1:','.....ORDINATE...............',
925        &Pstr(1,PARAM(1)+1)
926         WRITE (1,420) '2:','.....ABSCISSA...............',
927        &Pstr(2,PARAM(2)+1)
928         WRITE (1,420) '3:','.....SCAN RATE (nm/sec).....',
929        &Pstr(3,PARAM(3)+1)
930         WRITE (1,420) '4:','.....CHART DISPLAY (nm/cm)..',
931        &Pstr(4,PARAM(4)+1)
932         WRITE (1,420) '5:','.....REFERENCE MODE.........',
933        &Pstr(5,PARAM(5)+1)
934         WRITE (1,430) '6:','.....SBW (nm), GAIN.........',
935        &BAND,',',GAIN
936         WRITE (1,420) '7:','.....PEN FUNCTION...........',
937        &Pstr(6,PARAM(6)+1)
938         WRITE (1,430) '8:','.....PEN LIMITS (Min,Max)...',
939        &PMIN,',',PMAX
940         IF (PARAM(6).GT.1) WRITE (1,'(T40,A2,A2,A14)') UP,ERASE,String
941         WRITE (1,420) '9:','.....RESPONSE TIME (sec)....',
942        &Pstr(15,PARAM(15)+1)
943         WRITE (1,420) '10:','.....BEAM INTERCHANGE.......',
944        &Pstr(16,PARAM(16)+1)
945         WRITE (1,420) '11:','.....SLIT HEIGHT............',
946        &Pstr(23,PARAM(23)+1)
947         WRITE (1,420) 'X:','.....EXIT Instrument Menu...',' '
948   410 FORMAT (T4,A3,T10,A28,T40,F6.2)
949   420 FORMAT (T4,A3,T10,A28,T40,A14)
950   430 FORMAT (T4,A3,T10,A28,T40,F4.2,A,F5.2)
951         WRITE (1,*)
952         CALL Line(NCOL)
953         WRITE (1,*)
954   440 WRITE (1,*) UP,ERASE,'  INDEX Code: ',BELL,'_'
955         READ (1,'(A2)') Key
956         CALL Upper(Key)
957         IF (Key.EQ.'X') GO TO MENU
958         N=ICHAR(Key(1:1))-48
959         IF (Key(2:2).EQ.' ') GO TO 450
960         N=N*10+ICHAR(Key(2:2))-48
961   450 IF ((N.LT.0).OR.(N.GT.10)) GO TO 440
962 C       ------------------------------------------------------------------
```

```
963         K=N                                   ! Save Index #:
964         IF (N.EQ.0) GO TO 460                 ! Update Wavelength
965         IF (N.EQ.6) GO TO 470                 ! Update SBW/GAIN
966         IF (N.EQ.7) N=6                       ! Pen Function
967         IF (N.EQ.9) N=15
968         IF (N.EQ.10) N=16
969         IF (N.EQ.8) THEN                      ! Update Pen Limits
970           N=I                                 ! Index For Deriv & Log
971           IF (PARAM(6).LE.1) THEN             ! PEN = NORMAL Modes
972             IF (PARAM(1).NE.2) GO TO 520      ! Absorbance & %T Range
973             N=9                               ! Index For Temp. Range
974           END IF
975         END IF
976         CALL Select(N,PARAM,Pstr)             ! Update Parameters
977         IF (K.EQ.5) THEN
978           WRITE (1,'(T12,A)') '_'
979           GO TO 510
980         END IF
981         WRITE (1,'(T13,A2,A)') UP,'_'
982         GO TO PARAMETERS
983 C       ------------------------------------------------------------
984     460 WRITE (1,*) UP,ERASE,'  Wavelength = ',BELL,'_'
985         READ (1,*,ERR=460) NUMBER
986         IF ((NUMBER.LT.185.0).OR.(NUMBER.GT.3152)) GO TO 460
987         IF ((Bdet.EQ.'1').AND.(NUMBER.GT.900.0)) THEN
988           WRITE (1,*) UP,ERASE,'  UV/VIS Detector Limit = 900 nm',BELL
989           CALL Wait(2.0)
990           GO TO 460
991         END IF
992         IF ((Bdet.EQ.'2').AND.(NUMBER.LT.700.0)) THEN
993           WRITE (1,*) UP,ERASE,'  NIR Detector Limit = 700 nm',BELL
994           CALL Wait(2.0)
995           GO TO 460
996         END IF
997         CALL Str(NUMBER,String,6)
998         Wlength=String(2:8)
999         WRITE (1,*) UP,ERASE,'  Slewing to _'
1000        WRITE (1,'(F6.2,A4)') NUMBER,' nm:'
1001        CALL GOTO(Wlength)
1002        GO TO INSTRUMENT
1003 C      ------------------------------------------------------------
1004    470 WRITE (1,*) UP,ERASE,'_'
1005        IF (PARAM(5).EQ.2) GO TO 480     ! AUTOSLIT Mode (Both Detectors)
1006        IF (PARAM(22).EQ.2) GO TO 480    ! NIR Detector  => AUTOSLIT Mode
1007        IF (WAVELENGTH.GT.900.0) THEN
1008          GO TO 480                      ! Lamda >900 nm => AUTOSLIT Mode
1009        END IF
1010        IF (WAVELENGTH.GT.800.0) THEN
1011          IF (PARAM(22).EQ.0) GO TO 480 ! AUTO Detector => AUTOSLIT Mode
1012        END IF
1013        WRITE (1,*) ' Spectral Bandwidth: (0.04 - 3.60 nm) = ',BELL,'_'
1014        READ (1,*,ERR=470) BAND
1015        IF ((BAND.LT.0.04).OR.(BAND.GT.3.60)) GO TO 470
1016        CALL Str(BAND,String,4)
```

```
1017        Command=Varset//'9'//String(2:5)//'!0'
1018        CALL Send(Command)
1019        GO TO 510
1020    480 String='(1 - 1275)'
1021        IF (PARAM(22).NE.2) String='(1 - 1000)'
1022        WRITE (1,*) ' GAIN: ',String(1:10),' = ',BELL,'_'
1023        READ (1,*,ERR=470) NUMBER
1024        IF ((NUMBER.LT.1.0).OR.(NUMBER.GT.1275.0)) GO TO 470
1025        IF ((NUMBER.GT.1000.0).AND.(PARAM(22).NE.2)) GO TO 470
1026        TRANSFER=.FALSE.
1027 C      ********************** SPECIAL ENTRY POINT **********************
1028 C          Baseline GAIN Request > 10*GAIN : Reset GAIN and RETURN
1029 C      *****************************************************************
1030    490 J=0
1031        RATIO=NUMBER/GAIN
1032        DO WHILE (RATIO.GT.10.0)
1033          J=J+1
1034          NUMBER=NUMBER/10.0
1035          RATIO=NUMBER/GAIN
1036        END DO
1037        CALL Str(NUMBER,String,4)
1038        Command=Varset//'5'//String(2:5)//'!0'
1039        CALL Send(Command)
1040        DO 500 I=1,J
1041          NUMBER=NUMBER*10.0
1042          CALL Str(NUMBER,String,4)
1043          CALL Wait(2.0)
1044          Command=Varset//'5'//String(2:5)//'!0'
1045          CALL Send(Command)
1046    500 CONTINUE
1047        IF (TRANSFER) THEN          ! Return to Baseline Setup
1048          GAIN=NUMBER               ! With Instrument GAIN Matched
1049          TRANSFER=.FALSE.          ! To Requested Baseline Gain
1050          GO TO 220
1051        END IF
1052 C      ---------------------------------------------------------------
1053    510 WRITE (1,*) UP,ERASE,'  Waiting for CARY to settle: ',BELL,'_'
1054        CALL Wait(5.0)
1055        WRITE (1,*)
1056        IF (K.EQ.5) WRITE (1,'(T12,A)') '_'
1057        GO TO 560
1058 C      ---------------------------------------------------------------
1059    520 N=8
1060        IF (PARAM(1).EQ.0) N=7
1061        I=N
1062        CALL Select(I,PARAM,Pstr)
1063        I=I+OFFSET(N)
1064        CALL Val(Pstr(N,I),NUMBER)
1065        ZERO=0.0
1066        IF (N.EQ.8) THEN
1067          IF (NUMBER.GT.100.0) GO TO 550
1068          GO TO 530
1069        END IF
```

```
1070        IF (NUMBER.GE.1.0) THEN
1071          NUMBER=4.0-NUMBER
1072          GO TO 530
1073        END IF
1074        NUMBER=3.0
1075    530 WRITE (1,'(T13,A2,A2,A18)') UP,ERASE,'  Zero Suppress: _'
1076        IF (N.EQ.8) THEN
1077          WRITE (1,*) '(0 - 100%) = ',BELL,'_'
1078          GO TO 540
1079        END IF
1080        WRITE (1,'(A9,F4.2,A4,A,A)') '(-0.5 to ',NUMBER,') = ',BELL,'_'
1081    540 READ (1,*,ERR=530) ZERO
1082        IF (N.EQ.8) THEN
1083          IF ((ZERO.LT.0.0).OR.(ZERO.GT.100.0)) GO TO 530
1084          GO TO 550
1085        END IF
1086        IF ((ZERO.LT.-0.5).OR.(ZERO.GT.NUMBER)) GO TO 530
1087    550 CALL Str(ZERO,String,3)
1088        Pcode='0'
1089        IF (N.EQ.8) Pcode=':'
1090        Command=Varset//Pcode//String(1:5)//'!0'
1091        CALL Send(Command)
1092        WRITE (1,'(T12,A)') '_'
1093    560 WRITE (1,*) UP,'_'
1094        GO TO PARAMETERS
1095 C
1096 C       ------------------------------------------------------------
1097 C
1098 C           Lamp and Detector Mode Selection
1099 C
1100 C       ------------------------------------------------------------
1101 C
1102    570 CALL Partable(PARAM)
1103        WRITE (1,*) HOME,CLR
1104        TITLE='Lamp & Detector Modes'
1105        CALL Center(TITLE)
1106        CALL Line(NCOL)
1107        WRITE (1,'(T15,A5,T27,A8,T47,A4)') 'INDEX','FUNCTION','MODE'
1108        CALL Line(NCOL)
1109        WRITE (1,*)
1110        WRITE (1,580) '1: .....LAMP POWER..... ',
1111       &Pstr(20,PARAM(20)+1)
1112        WRITE (1,580) '2: .. ..LAMP SELECT..... ',
1113       &Pstr(21,PARAM(21)+1)
1114        WRITE (1,580) '3: .....DETECTOR SELECT..... ',
1115       &Pstr(22,PARAM(22)+1)
1116        WRITE (1,580) 'X: .....EXIT TO MENU..... ',' '
1117        WRITE (1,*)
1118        CALL LINE(NCOL)
1119    580 FORMAT (T16,A30,A14)
1120        WRITE (1,*)
1121    590 WRITE (1,'(T15,A2,A2,A9,A,A)') UP,ERASE,'INDEX #: ',BELL,'_'
1122        READ (1,80) Code
1123        CALL Upper(Code)
```

```
1124        IF (Code.EQ.'X') GO TO ADVANCED
1125        N=ICHAR(Code)-48
1126        IF ((N.LT.1).OR.(N.GT.3)) GO TO 590
1127        N=(N-1)+20
1128        CALL Select(N,PARAM,Pstr)
1129        GO TO LAMP
1130 C
1131 C       ------------------------------------------------------------------
1132 C
1133 C           Accessory Mode Selection
1134 C
1135 C       ------------------------------------------------------------------
1136 C
1137    600 CALL Partable(PARAM)
1138        DO 610 I=1,2
1139          Access(I)='OFF'
1140          ASCII=(I-1)+48
1141          Pcode=CHAR(ASCII)
1142          Command=Accoff//Pcode//CSM
1143          WRITE (UNIT=38,FMT=*,IOSTAT=N,ERR=999) Command
1144          READ (UNIT=38,FMT=620,IOSTAT=N,ERR=999) Response
1145          IF (Response(2:2).EQ.'P') THEN
1146            Access(I)='ON'
1147            Command=Accon//Pcode//CSM
1148            CALL Send(Command)
1149          END IF
1150    610 CONTINUE
1151    620 FORMAT (A64)
1152    630 WRITE (1,*) HOME,CLR
1153        TITLE='Accessory Control'
1154        CALL Center(TITLE)
1155        CALL Line(NCOL)
1156        WRITE (1,'(T15,A5,T27,A8,T46,A4)') 'INDEX','FUNCTION','MODE'
1157        CALL Line(NCOL)
1158        WRITE (1,*)
1159        WRITE (1,640) '1: ...TEMPERATURE READOUT... ',Access(1)
1160        WRITE (1,640) '2: ...PRINTER..... ',Access(2)
1161        IF (Access(2).EQ.'ON') THEN
1162          WRITE (1,'(T49,A2,A3,A12)') UP,' : ',Printer(IP)
1163        END IF
1164        WRITE (1,640) 'X: ...EXIT TO MENU..... ',' '
1165        WRITE (1,*)
1166        CALL Line(NCOL)
1167    640 FORMAT (T16,A30,A4)
1168        WRITE (1,*)
1169    650 WRITE (1,'(T15,A2,A2,A9,A,A)') UP,ERASE,'INDEX #: ',BELL,'_'
1170        READ (1,80) Code
1171        CALL Upper(Code)
1172        IF (Code.EQ.'X') GO TO ADVANCED
1173        I=ICHAR(Code)-48
1174        IF ((I.LT.1).OR.(I.GT.2)) GO TO 650
1175        ASCII=(I-1)+48
1176        Pcode=CHAR(ASCII)
1177    660 WRITE (1,'(T14,A2,A2,A)') UP,ERASE,'_'
```

```
1178        WRITE (1,*) '(OFF=0, ON=1) ? ',BELL,'_'
1179        READ (1,'(I2)',ERR=660) ASCII
1180        Code=CHAR(ASCII+48)
1181        IF ((Code.NE.'0').AND.(Code.NE.'1')) GO TO 660
1182        Command='@F'//Code//Pcode//CSM
1183        CALL Send(Command)
1184        IF (Code.EQ.'0') GO TO 699
1185        IF (I.EQ.1) THEN
1186          N=9
1187          CALL Select(N,PARAM,Pstr)
1188          GO TO 699
1189        END IF
1190 C      ------------------------------------------------------------------
1191        WRITE (1,*) HOME,CLR
1192        TITLE='Printer Mode'
1193        CALL Center(TITLE)
1194        CALL Line(NCOL)
1195        WRITE (1,'(T15,A5,T27,A8,T46,A4)') 'INDEX','FUNCTION','MODE'
1196        CALL Line(NCOL)
1197        WRITE (1,'(T46,A14)') Pstr(40,PARAM(40))
1198        WRITE (1,670) '1: .....WAVELENGTH..... '
1199        WRITE (1,670) '2: .....TIME..... '
1200        WRITE (1,670) '3: .....TEMPERATURE..... '
1201        WRITE (1,*)
1202        CALL Line(NCOL)
1203   670  FORMAT (T16,A30)
1204        WRITE (1,*)
1205   680  WRITE (1,'(T15,A2,A2,A9,A,A)') UP,ERASE,'INDEX #: ',BELL,'_'
1206        READ (1,'(I2)',ERR=680) IP
1207        IF ((IP.LT.1).OR.(IP.GT.3)) GO TO 680
1208        ASCII=(IP-1)+48
1209        Pcode=CHAR(ASCII)
1210   690  WRITE (1,'(T15,A2,A2,A11,A,A)') UP,ERASE,'INTERVAL = ',BELL,'_'
1211        READ (1,*,ERR=690) NUMBER
1212        CALL Str(NUMBER,String,4)
1213        Command='@M'//Pcode//String(1:5)//'!0'
1214        CALL Send(Command)
1215   699  Command='@DF0'                    ! Update Cary Accessory Display
1216        CALL Send(Command)
1217        GO TO 600
1218 C
```

```
1219 C     ------------------------------------------------------------
1220 C
1221 C         Store Spectrum
1222 C
1223 C     ------------------------------------------------------------
1224 C
1225   700 IF ((Sstat.NE.'ACQUIRED').AND.(Sstat.NE.'STORED')) THEN
1226         WRITE (1,*) UP,ERASE,'  Spectrum is ABSENT: ',BELL,'_'
1227         CALL Wait(2.0)
1228         WRITE (1,*)
1229         GO TO 70
1230       END IF
1231       IF (ABS(XMIN-ABSC).GT.0.5) THEN
1232   710   WRITE (1,*) UP,ERASE,'  SCAN ENDED AT',ABSC,' nm (Expected:',
1233      &  XMIN,'), Proceed (Y or N) ? ',BELL,'_'
1234         READ (1,80) Icode
1235         CALL Upper(Icode)
1236         IF (Icode.EQ.'N') GO TO 70
1237         IF (Icode.NE.'Y') GO TO 710
1238       END IF
1239       TITLE='Store Spectrum'
1240   720 WRITE (1,*) HOME,CLR
1241       CALL Center(TITLE)
1242       CALL Line(NCOL)
1243       WRITE (1,*)
1244       WRITE (1,*) '  Researcher''s Initials, (AA-ZZ) ? ',BELL,'_'
1245       READ (1,'(A2)') INITIALS
1246       CALL Upper(INITIALS)
1247       String='.S'//INITIALS
1248       WRITE (1,*) DOWN
1249       WRITE (1,*) UP,ERASE,'  Filename: (16 chars.) ? ',BELL,'_'
1250       READ (1,'(A16)') Name
1251       CALL Upper(Name)
1252       K=16
1253       DO WHILE (Name(K:K).EQ.' ')
1254         K=K-1
1255       END DO
1256       Fname=Name(1:K)//String(1:4)
1257       WRITE (1,*) DOWN,'  Directory, (Return = /DEFAULT/) ? ',BELL,'_'
1258       READ (1,'(A40)') Directory
1259       IF (Directory.EQ.' ') THEN
1260         Outfile=Fname
1261         GO TO 730
1262       END IF
1263       L=40
1264       DO WHILE (Directory(L:L).EQ.' ')
1265         L=L-1
1266       END DO
1267       IF (Directory(L:L).EQ.'/') L=L-1
1268       Outfile=Directory(1:L)//'/'//Fname
1269   730 L=63
1270       DO WHILE (Outfile(L:L).EQ.' ')
1271         L=L-1
1272       END DO
```

```
1273   740 WRITE (1,*) DOWN,'  Validating: ',Outfile(1:L),' _'
1274       OPEN (UNIT=66,FILE=Outfile(1:L),IOSTAT=N,STATUS='NEW')
1275       WRITE (1,*)
1276       IF (N.NE.0) THEN
1277         N=N-500
1278         WRITE (1,*) UP,ERASE,'_'
1279         IF (N.EQ.2) WRITE (1,*) ' FILE EXISTS: ',BELL,'_'
1280         IF (N.EQ.8) WRITE (1,*) ' FILE OPENED: ',BELL,'_'
1281         IF ((N.NE.2).AND.(N.NE.8)) WRITE (1,*) ' DISK ERROR # ',N,
1282      &  BELL,' _'
1283         CLOSE (UNIT=66,STATUS='DELETE')
1284         CALL Wait(2.0)
1285         GO TO 720
1286       END IF
1287       IF (Code.EQ.'R') GO TO 790
1288       WRITE (1,*) UP,ERASE,'  Validated Filename: ',Fname
1289       WRITE (1,*) DOWN,'  Title, (72 chars):'
1290       WRITE (1,*) '  ',BELL,'_'
1291       READ (1,750) TITLE
1292   750 FORMAT (A72)
1293       WRITE (1,*) DOWN,'  Date, (MM/DD/YY): ',BELL,'_'
1294       READ (1,760) DATE
1295   760 FORMAT (A8)
1296       WRITE (1,*) DOWN
1297   770 WRITE (1,*) UP,ERASE,'  Concentration, (M): ',BELL,'_'
1298       READ (1,*,ERR=770) CONC
1299       IF (CONC.LT.0.0) GO TO 770
1300       WRITE (1,*) DOWN
1301   780 WRITE (1,*) UP,ERASE,'  Pathlength, (cm): ',BELL,'_'
1302       READ (1,*,ERR=780) PATH
1303       IF (PATH.LT.0.0) GO TO 780
1304 C     ------------------------------------------------------------------
1305   790 J=49     ! # of Parameters
1306       K=14     ! # of Variables
1307       VARIABLE(6)=SPECGAIN          ! Store GAIN At Smax
1308       VARIABLE(10)=SPECBAND         ! Store SBW At Smin
1309       WRITE  (1,*) DOWN,'  Storing File: ',Outfile(1:L),BELL
1310       WRITE (66,FMT=750,IOSTAT=N,ERR=820) TITLE
1311       WRITE (66,FMT=760,IOSTAT=N,ERR=820) DATE
1312       WRITE (66,FMT=*,IOSTAT=N,ERR=820) XMIN,XMAX,XSTEP,CONC,PATH
1313       WRITE (66,FMT=*,IOSTAT=N,ERR=820) ORD,ABSC,CELL,CYCLE,SAMPLE,
1314      &WAVE,TIMER,TEMP,DIST
1315       WRITE (66,FMT=800,IOSTAT=N,ERR=820) J,K,NARRAY
1316   800 FORMAT (I3,I3,I6)
1317       WRITE (66,FMT=810,IOSTAT=N,ERR=820) (PARAM(I),I=1,J)
1318   810 FORMAT (I2)
1319       WRITE (66,FMT=*,IOSTAT=N,ERR=820) (VARIABLE(I),I=1,K)
1320       WRITE (66,FMT=*,IOSTAT=N,ERR=820) (Y(I),I=1,NARRAY)
1321       WRITE (66,FMT=*,IOSTAT=N,ERR=820) (X(I),I=1,NARRAY)
1322       CLOSE (UNIT=66,IOSTAT=N,ERR=820,STATUS='KEEP')
1323       Sstat='STORED'
1324       CALL Wait(2.0)
1325       GO TO MENU
1326 C     ------------------------------------------------------------------
```

```
1327   820 WRITE (1,*) UP,ERASE,'  Disk Error #',N,BELL,' :_'
1328       WRITE (1,*) 'R...RESAVE, X ..EXIT to Menu ? ',BELL,'_'
1329       READ (1,80) Code
1330       IF ((Code.NE.'R').AND.(Code.NE.'X')) GO TO 820
1331       WRITE (1,*) UP,ERASE,'  Deleting Old File: ',Outfile(1:L),BELL,
1332      &' _'
1333       CLOSE (UNIT=66,IOSTAT=N,ERR=820,STATUS='DELETE')
1334       CALL Wait(2.0)
1335       IF (Code.EQ.'R') GO TO 720
1336       Fname=' '
1337       Sstat='ACQUIRED'
1338       GO TO MENU
1339 C
1340 C     ---------------------------------------------------------------
1341 C
1342 C         Exit Program
1343 C
1344 C     ---------------------------------------------------------------
1345 C
1346   900 IF (Sstat.EQ.'ACQUIRED') THEN
1347         WRITE (1,*) UP,ERASE,'  SPECTRUM NOT STORED:',
1348      &  '   Exit (Y or N) ? ',BELL,'_'
1349         READ (1,80) Code
1350         CALL Upper(C de)
1351         IF (Code.EQ.'N') GO TO 70
1352         IF (Code.NE.'Y') GO TO 900
1353       END IF
1354   910 WRITE (1,*) UP,ERASE,'  Set To STANDBY, (Y or N) ? ',BELL,'_'
1355       READ (1,80) Code
1356       CALL Upper(Code)
1357       IF (Code.EQ.'N') GO TO 920
1358       IF (Code.NE.'Y') GO TO 910
1359       CALL Send(Standby)
1360   920 WRITE (1,*) UP,ERASE,UP
1361       STOP
1362 C
1363 C     ---------------------------------------------------------------
1364 C
1365 C         IEEE-488 Error Exit
1366 C
1367 C     ---------------------------------------------------------------
1368 C
1369   999 WRITE (1,*) ' Error #',N
1370       STOP
1371       END
```

```
C
C     ********** END OF MAIN PROGRAM **********
C
C         BLOCK DATA FOR NAMED COMMON BLOCK INITIALIZATION
C
C     ****************************************************************
C
$ALIAS /MODE/,NOALLOCATE
$ALIAS /CARY/,NOALLOCATE
$ALIAS /IP/,NOALLOCATE
$ALIAS /IS/,NOALLOCATE
      BLOCK DATA Arrays
      INTEGER NDATA,XMODE,YMODE
      INTEGER NPAR(49),OFFSET(49)
      REAL ORD,ABSC,CELL,CYCLE,SAMPLE,WAVE,TIMER,TEMP,DIST
      CHARACTER Pname(49)*10,Vname(14)*8
      COMMON /MODE/NDATA,XMODE,YMODE
      COMMON /CARY/ORD,ABSC,CELL,CYCLE,SAMPLE,WAVE,TIMER,TEMP,DIST
      COMMON /IP/NPAR,OFFSET
      COMMON /IS/Pname,Vname
C
      DATA NDATA,XMODE,YMODE/0,0,0/
      DATA ORD,ABSC,CELL,CYCLE,SAMPLE,WAVE,TIMER,TEMP,DIST/0.0,0.0,0.0,
     &0.0,0.0,0.0,0.0,0.0,0.0,0.0,0.0/
C
      DATA NPAR/6,4,11,11,4,5,9,7,4,5,11,16,8,10,4,2,2,2,2,4,3,3,2,3,
     &3,3,2,6,2,4,2,5,5,2,2,0,0,5,0,2,0,0,0,0,0,0,0,0,0/
C
      DATA OFFSET/0,0,0,4,0,0,0,9,11,0,0,0,0,0,0,0,0,0,0,0,0,0,0,0,
     &0,0,0,0,2,6,8,0,0,0,0,0,0,0,0,0,0,0,0,0,0,0,0,0,0/
C
      DATA Pname/'Ordinate','Abscissa','Scan Rate','Chart/cm',
     &'Ref.Mode','Pen Functn','A range','%T Range','Temp.Range',
     &'Log Zero','Der.Range','Der.Temp','Kinet.Rnge','Temp.Zero',
     &'Period','Beam Chge','Sequencer','Auto.Op','Chart Op',
     &'Lamp Pwr','Lamp Sel','Det.Sel','Slit Hgt','BLN Det',
     &'BLN Lamp','BLN Ref','BLN Slit','No.cells','Sample',
     &'Curv.Fit','Rec.Prec','Method','Result','Auto Kin',
     &'Samp/Av.',' ',' ',' ','BLN Stat',' ','Printer',' ',' ',
     &'TEST','TEST','TEST','TEST','TEST','TEST','TEST'/
C
      DATA Vname/'A zero','BL SBW/C','BL Wmax','BL Wmin',
     &'Cyc Time','Sel Gain','# cycles','Nwingths','Rec Time',
     &'Sel SBW','%T Zero','SEQ Wmax','SEQ Wmin','Distance'/
C
      END
```

```
C
C     ------------------------------------------------------------------
C
C         Select Mode of Operation for Specific Parameter
C
C     ------------------------------------------------------------------
C
$ALIAS /IP/,NOALLOCATE
$ALIAS /IS/,NOALLOCATE
      SUBROUTINE Select(N,PARAM,Pstr)
      INTEGER ASCII,I,J,K,N,NCOL
      INTEGER NPAR(49),OFFSET(49),PARAM(49),INDEX(11)
      CHARACTER Pname(49)*10,Pstr(49,16)*14,Vname(14)*8
      CHARACTER Command*44,CSM,Icode,Key*2,Pcode,Parset*2,TITLE*72
      CHARACTER BELL,CLR*2,ESC,ERASE*2,DOWN*2,HOME*2,UP*2
      COMMON /IP/NPAR,OFFSET,/IS/Pname,Vname
      DATA CSM,Key,Parset/'0','@D','@H'/
      DATA (INDEX(I),I=1,11)/1,3,4,6,7,9,10,12,13,15,16/
      BELL=CHAR(7)
      ESC=CHAR(27)
      CLR=ESC//'J'
      DOWN=ESC//'B'
      ERASE=ESC//'K'
      HOME=ESC//'h'
      UP=ESC//'A'
      NCOL=50
   10 WRITE (1,*) HOME,CLR
      TITLE='Operating Mode Selection'
      CALL Center(TITLE)
      CALL Line(NCOL)
      WRITE (1,'(T15,A5,T30,A10)') 'Index',Pname(N)
      CALL Line(NCOL)
      WRITE (1,*)
      DO 20 I=1,NPAR(N)
        J=I+OFFSET(N)
        IF ((N.EQ.4).AND.(J.EQ.5)) J=1            ! Chart Index Offset
        IF (N.EQ.11) THEN                         ! Derivative Modes
          J=INDEX(I)                              ! Use Valid Index
          IF ((PARAM(I).NE.0).AND.(I.LE.4)) GO TO 20
        END IF
        WRITE (1,30) I,' .....',Pstr(N,J)
   20 CONTINUE
   30 FORMAT (T16,I2,A10,T30,A14)
      WRITE (1,*)
      CALL Line(NCOL)
      WRITE (1,*)
   40 WRITE (1,'(T15,A2,A2,A9,A,A)') UP,ERASE,'Index #: ',BELL,'_'
      READ (1,'(I2)',ERR=40) K
      IF ((K.LT.1).OR.(K.GT.NPAR(N))) GO TO 40    ! Invalid Index Entry
      IF (PARAM(1).NE.0) THEN
        IF ((K.EQ.5).AND.(N.EQ.6)) GO TO 40       ! Only Log/Abs Valid
        IF ((K.LE.4).AND.(N.EQ.11)) GO TO 40      ! Invalid Deriv Index
      END IF
      IF ((N.EQ.38).AND.(K.GT.2)) GO TO 50        ! Baseline Setup Mode
```

```
1472        IF (N.EQ.11) K=INDEX(K)                          ! Index To Deriv Mode
1473     50 ASCII=(K-1)+OFFSET(N)+48
1474        IF ((N.EQ.4).AND.(K.EQ.1)) ASCII=ASCII-4         ! Chart Index Offset
1475        Icode=CHAR(ASCII)
1476        ASCII=(N-1)+48
1477        Pcode=CHAR(ASCII)
1478        Command=Parset//Pcode//Icode//CSM
1479        CALL Send(Command)
1480        IF ((N.EQ.6).AND.(K.GT.2)) THEN                  ! Special Pen Modes
1481          N=11                                           ! Derivative Modes
1482          IF (K.EQ.5) N=10                               ! Log(Abs) Mode
1483          GO TO 10                                       ! Select Setting
1484        END IF
1485        N=K
1486        RETURN
1487     60 IF (K.EQ.4) GO TO 40
1488        Pcode=CHAR(48+N-1)
1489        Command=Parset//Pcode//'0'//CSM                  ! Set Status To OFF
1490        CALL Send(Command)
1491        Command=Key//'10'                                ! Key = 1
1492        CALL Send(Command)
1493        Command=Key//'=0'                                ! Key = ENTER
1494        CALL Send(Command)
1495        Command=Key//'h0'                                ! Key = RIGHT CURSOR
1496        IF (K.EQ.3) GO TO 70
1497        CALL Send(Command)
1498     70 CALL Send(Command)
1499        CALL Send(Command)
1500        Command=Key//'=0'                                ! Key = ENTER
1501        CALL Send(Command)
1502        N=K
1503        IF (K.EQ.5) N=2
1504        RETURN
1505        END
```

```
1506 C
1507 C     ---------------------------------------------------------------
1508 C
1509 C         Baseline Scan Control
1510 C
1511 C     ---------------------------------------------------------------
1512 C
1513       SUBROUTINE Bline(WMIN,WMAX,Bdet,Bgain,Blamp,Bperiod,Brate,Bref,
1514      &Bsbw,Bslit,Bscan,Btime,MATCH,MODE)
1515       INTEGER INDEX,MODE,N,NCOL
1516       REAL NUMBER,WMIN,WMAX
1517       LOGICAL MATCH,MONITOR
1518       CHARACTER*(*) Bdet,Bgain,Blamp,Bperiod,Brate,Bref
1519       CHARACTER*(*) Bsbw,Bslit,Bscan,Btime
1520       CHARACTER Bgbw*4,BELL,Code,CLR*2,DOWN*2,ERASE*2,Esc,HOME*2,UP*2
1521       CHARACTER Bmin*6,Bmax*6,Command*44,Response*64,String*14
1522       CHARACTER Autobal*4,Blstat*5,Start*4,TITLE*72
1523       DATA Autobal,Blstat,Start/'@DU0','@G1U0','@DP0'/
1524       Esc=CHAR(27)
1525       BELL=CHAR(7)
1526       CLR=Esc//'J'
1527       DOWN=Esc//'B'
1528       ERASE=Esc//'K'
1529       HOME=Esc//'h'
1530       UP=Esc//'A'
1531       MONITOR=.FALSE.                        ! For Testing Routine ONLY
1532       NCOL=70
1533       IF (WMAX.GT.800.0) WMAX=WMAX+0.2       ! * Cary Baseline Bug Fix *
1534       CALL Str(WMAX,String,5)
1535       Bmax=String(2:7)
1536       IF (WMIN.GT.800.0) WMIN=WMIN-0.2       ! * Cary Baseline Bug Fix *
1537       CALL Str(WMIN,String,5)
1538       Bmin=String(2:7)
1539       Bgbw=Bsbw                              ! Only One Of SBW Or GAIN Is
1540       IF (MODE.EQ.2) Bgbw=Bgain              ! Stored By Cary For Baseli
1541 C     ---------------------------------------------------------------
1542       WRITE (1,*) HOME,CLR
1543       TITLE='Baseline Scan Control'
1544       CALL Center(TITLE)
1545       CALL Line(NCOL)
1546       WRITE (1,10) DOWN,'  Wavelength Limits, (nm): ',WMAX,' / ',WMIN
1547    10 FORMAT (T2,A2,A27,F4.1,A3,F4.1)
1548       WRITE (1,*) DOWN,'  Scan Rate, (nm/sec)     : ',Bscan
1549       WRITE (1,*) DOWN,'  Response Time, (sec)    : ',Btime
1550       IF (MODE.EQ.1) THEN
1551         WRITE (1,*) DOWN,'  Spectral Bandwidth,(nm): ',Bsbw
1552         GO TO 20
1553       END IF
1554       WRITE (1,*) DOWN,'  AUTOSLIT Gain Level     : ',Bgain
1555    20 WRITE (1,*) DOWN
1556       WRITE (1,*) DOWN,'  Place Solvent Cells In BOTH Beams:'
1557       WRITE (1,*) DOWN,'       S.....Start Scan'
1558       WRITE (1,*) DOWN,'       A.....Abort Scan'
1559       WRITE (1,*) DOWN,'  Enter the CODE: ',BELL,'_'
```

```
1560     30 READ (1,'(A1)') Code
1561        CALL Upper(Code)
1562        IF (Code.EQ.'A') THEN
1563          MATCH=.FALSE.
1564          RETURN
1565        END IF
1566        IF (Code.NE.'S') GO TO 30
1567        WRITE (1,*) UP,ERASE,UP,UP,ERASE,UP,UP,ERASE,UP,UP,ERASE,'_'
1568        WRITE (1,*) ' Sending Baseline Parameters: ',BELL
1569        Command='@J'//Bmax//'!'//Bmin//'!'//Bgbw//'!'//Bref//'!'//
1570       &Blamp//'!'//Bdet//'!'//Bslit//'!'//Brate//'!'//Bperiod//'!0'
1571        WRITE (UNIT=38,FMT=*,IOSTAT=N,ERR=999) Command
1572        READ (UNIT=38,FMT=40,IOSTAT=N,ERR=999) Response
1573     40 FORMAT (A64)
1574        IF (Response(2:2).EQ.'N') THEN
1575          INDEX=ICHAR(Response(4:4))-48
1576          WRITE (1,*) UP,ERASE,'  Parameter Error: ',INDEX,BELL
1577          CALL Wait(2.0)
1578          MATCH=.FALSE.
1579          RETURN
1580        END IF
1581        WRITE (1,*) UP,ERASE,'  Recording Baseline:',BELL
1582        CALL Send(Start)
1583     50 Command=Blstat
1584        IF (MONITOR) WRITE (1,*) ' Command - ',Command
1585        WRITE (UNIT=38,FMT=*,IOSTAT=N,ERR=999) Command
1586        READ (UNIT=38,FMT=40,IOSTAT=N,ERR=999) Response
1587        IF (MONITOR) WRITE (1,*) ' Response - ',Response
1588        INDEX=ICHAR(Response(6:6))-48
1589        IF (INDEX.NE.1) GO TO 50
1590        WRITE (1,*) UP,ERASE,'  Performing Auto Balance:',BELL
1591        CALL Send(Autobal)
1592        CALL Wait(2.0)
1593        RETURN
1594    999 WRITE (1,*) ' Error #',N,' in SUBROUTINE Bline'
1595        STOP
1596        END
```

```
C
C     ------------------------------------------------------------------
C
C         Go To Specified Wavelength
C
C     ------------------------------------------------------------------
C
      SUBROUTINE GOTO(Wlength)
      INTEGER LENSTR
      CHARACTER Ascii,CSM,Slew,Model,Ncell,Range,Windex
      CHARACTER Command*4,Key*2
      CHARACTER*(*) Wlength
      CSM='0'
      Key='@D'
      Command=Key//'J'//CSM              ! Key = GOTO WAVELENGTH
      CALL Send(Command)
      LENSTR=LEN(Wlength)
      DO 10 I=1,LENSTR
        Ascii=Wlength(I:I)
        IF (Ascii.EQ.' ') GO TO 10
        IF (Ascii.EQ.'.') Ascii=':'
        Command=Key//Ascii//CSM          ! Key = NUMBER (0-9)
        CALL Send(Command)
   10 CONTINUE
      Command=Key//'='//CSM              ! Key = ENTER
      CALL Send(Command)
   20 CALL Instats(Slew,Model,Ncell,Range,Windex)
      IF (Slew.NE.'0') GO TO 20
      RETURN
      END
C
C     ------------------------------------------------------------------
C
C         Instrument Status Test
C
C     ------------------------------------------------------------------
C
      SUBROUTINE Instats(Slew,Model,Ncell,Range,Windex)
      INTEGER N
      CHARACTER Slew,Model,Ncell,Range,Windex
      CHARACTER Stats*3,Data*12
      Stats='@B0'
   10 WRITE (UNIT=38,FMT=*,IOSTAT=N,ERR=999) Stats
      READ (UNIT=38,FMT=20,IOSTAT=N,ERR=999) Data
   20 FORMAT (A12)
      Slew=Data(4:4)
      Model=Data(5:5)
      Ncell=Data(6:6)
      Range=Data(7:7)
      Windex=Data(8:8)
      RETURN
  999 WRITE (1,*) ' Error #',N,' in SUBROUTINE Instats'
      STOP
      END
```

```
C
C     ------------------------------------------------------------
C
C         Read Parameter Table From CARY 2390
C
C     ------------------------------------------------------------
C
      SUBROUTINE Partable(PARAM)
      INTEGER LENSTR,N,INDEX,PARAM(49)
      LOGICAL TEST
      CHARACTER Command*3,Response*64,Ascii
      TEST=.FALSE.
      Command='@E0'
      WRITE (UNIT=38,FMT=*,IOSTAT=N,ERR=999) Command
      READ (UNIT=38,FMT=10,IOSTAT=N,ERR=999) Response
   10 FORMAT (A64)
      IF (TEST) WRITE (1,*) ' RESPONSE - ',Response
      Ascii=Response(4:4)
      LENSTR=ICHAR(Ascii)-48
      IF (TEST) WRITE (1,*) ' String Length   =',LENSTR
      DO 20 I=1,LENSTR
        J=I+4
        Ascii=Response(J:J)
        IF (TEST) WRITE (1,*) ' ASCII Character = ',Ascii
        INDEX=ICHAR(Ascii)-48
        PARAM(I)=INDEX
        IF (TEST) WRITE (1,*) ' Parameter Index =',PARAM(I)
   20 CONTINUE
      RETURN
  999 WRITE (1,*) ' Error #',N,' in SUBROUTINE Partable'
      STOP
      END
C
C     ------------------------------------------------------------
C
C         Read Variable Table From CARY 2390
C
C     ------------------------------------------------------------
C
      SUBROUTINE Vartable(VARIABLE)
      INTEGER LENSTR(14),N
      REAL NUMBER,VARIABLE(14)
      LOGICAL TEST
      CHARACTER Ascii,CSM,Command*5,Response*64,String*14,Varout*3
      DATA (LENSTR(I),I=1,14)/14,11,11,11,10,10,8,8,8,11,11,11,11,11/
      TEST=.FALSE.
      CSM='0'
      Varout='@G2'
      DO 10 I=1,14
        J=I-1
        Ascii=CHAR(J+48)
        Command=Varout//Ascii//CSM
        IF (TEST) WRITE (1,*) ' Command  - ',Command
        WRITE (UNIT=38,FMT=*,IOSTAT=N,ERR=999) Command
```

```
1705          READ (UNIT=38,FMT=20,IOSTAT=N,ERR=999) Response
1706          IF (TEST) WRITE (1,*) ' Response - ',Response
1707          String=Response(6:6+LENSTR(I))
1708          IF (TEST) WRITE (1,*) ' String = ',String
1709          CALL Val(String,NUMBER)
1710          VARIABLE(I)=NUMBER
1711          IF (TEST) WRITE (1,*) ' VALUE  =',VARIABLE(I)
1712       10 CONTINUE
1713       20 FORMAT (A64)
1714          RETURN
1715      999 WRITE (1,*) ' Error #',N,' in SUBROUTINE Vartable'
1716          STOP
1717          END
1718 C
1719 C     ------------------------------------------------------------
1720 C
1721 C         Print a TITLE Centered in 72 columns
1722 C
1723 C     ------------------------------------------------------------
1724 C
1725          SUBROUTINE Center(TITLE)
1726          INTEGER I,J,N
1727          CHARACTER TITLE*72,BLANK*36
1728          BLANK='                                    '
1729          I=72
1730          J=0
1731          DO WHILE (ICHAR(TITLE(I:I)).EQ.32)
1732            J=J+1
1733            I=72-J
1734          END DO
1735          N=J/2
1736          WRITE (1,*) BLANK(1:N),TITLE(1:I)
1737          RETURN
1738          END
1739 C
1740 C     ------------------------------------------------------------
1741 C
1742 C         Print a line of N '-' characters (72 columns max)
1743 C
1744 C     ------------------------------------------------------------
1745 C
1746          SUBROUTINE Line(N)
1747          INTEGER I,N
1748          CHARACTER BLANK*72,DLINE*72,SPACE*36
1749          SPACE='                                    '
1750          BLANK=SPACE//SPACE
1751          SPACE='------------------------------------'
1752          DLINE=SPACE//SPACE
1753          IF (N.GT.72) N=72
1754          I=(72-N)/2
1755          WRITE (1,*) BLANK(1:I),DLINE(1:N)
1756          RETURN
1757          END
```

```
C
C     ---------------------------------------------------------------
C
C         Enter and Validate Wavelength Limits
C
C     ---------------------------------------------------------------
C
      SUBROUTINE Limits(MIN,MAX)
      REAL MIN,MAX,SWAP
      CHARACTER BELL,ERASE*2,ESC,UP*2
      BELL=CHAR(7)
      ESC=CHAR(27)
      ERASE=ESC//'K'
      UP=ESC//'A'
   10 WRITE (1,*) UP,ERASE,'_'
      WRITE (1,*) ' Wavelength Limits: (Min,Max) ',ERASE,BELL,'_'
      READ (1,*,ERR=10) MIN,MAX
      MIN=ABS(MIN)
      MAX=ABS(MAX)
      IF (MIN.LT.MAX) GO TO 20
      SWAP=MIN
      MIN=MAX
      MAX=SWAP
   20 MIN=INT(MIN+.5)
      MAX=INT(MAX+.5)
      IF (MIN.LT.185) GO TO 10
      IF (MAX.GT.3152) GO TO 10
      RETURN
      END
C
C     ---------------------------------------------------------------
C
C         Convert String Entry To Uppercase If Required
C
C     ---------------------------------------------------------------
C
      SUBROUTINE Upper(Code)
      INTEGER LENSTR,N
      CHARACTER*(*) Code
      LENSTR=LEN(Code)
      DO 10 I=1,LENSTR
        N=ICHAR(Code(I:I))
        IF (N.GT.96) Code(I:I)=CHAR(N-32)
   10 CONTINUE
      RETURN
      END
```

```
C
C     ------------------------------------------------------------------
C
C         Read Data In Real Time (INTERVAL) Mode From CARY 2390
C
C     ------------------------------------------------------------------
C
$EMA/DATA/
      SUBROUTINE Acquire(Inc,PRINT,SINGLE,WAVELENGTH)
      INTEGER N,NCOL,NDATA,XMODE,YMODE,XOFF(4),YOFF(6)
      REAL ORD,ABSC,CELL,CYCLE,SAMPLE,WAVE,TIMER,TEMP,DIST
      REAL X(10001),Y(10001),WAVELENGTH
      CHARACTER Command*10,Data*64,Inc*4,Esc,DOWN*2,ERASE*2,UP*2
      CHARACTER S1*8,S2*8,S3,S4,S5*3,S6*8,S7*6,S8*6,S9*7
      LOGICAL CHECK,PRINT,SINGLE,TEST
      COMMON /MODE/NDATA,XMODE,YMODE
      COMMON /CARY/ORD,ABSC,CELL,CYCLE,SAMPLE,WAVE,TIMER,TEMP,DIST
      COMMON /DATA/Y,X
      DATA (XOFF(I),I=1,4)/7,5,5,6/
      DATA (YOFF(I),I=1,6)/7,6,5,6,11,6/
      Esc=CHAR(27)
      UP=Esc//'A'
      DOWN=Esc//'B'
      ERASE=Esc//'K'
      CHECK=.FALSE.              ! Only Used For Testing Routine
      TEST=.FALSE.               ! Only Used For Testing Routine
      J=2+YOFF(YMODE)            ! The First Two Fields In Data String
      K=J+2                      ! Vary In Length With Choice Of Abscissa
      L=K+XOFF(XMODE)            ! And Ordinate - XMODE & YMODE Select
      M=L+2                      ! The Correct Offsets From XOFF/YOFF
      NCOL=70
      IF (.NOT.PRINT) GO TO 20
      CALL Line(NCOL)
      WRITE (1,10) 'Ordinate','Abscissa','Cell','Cycle','Sample',
     &'Wlength','Time','Temp,C','Dist'
   10 FORMAT (A10,A10,A5,A6,A7,A10,A8,A8,A8)
      CALL Line(NCOL)
      WRITE (1,*) DOWN
   20 Command='@K11'//Inc//'!0'
      IF (TEST) WRITE (1,*) ' Command  - ',Command
      WRITE (UNIT=38,FMT=*,IOSTAT=N,ERR=999  Command
      IF (SINGLE) THEN
        READ (UNIT=38,FMT=30,IOSTAT=N,ERR=999) Data
        S6=Data(M+9:M+16)
        CALL Val(S6,WAVELENGTH)
        RETURN
      END IF
   30 FORMAT (A64)
      DO 100 I=1,NDATA
        READ (UNIT=38,FMT=30,IOSTAT=N,ERR=999) Data
C       IF (CHECK) WRITE (1,30) Data
        S1=Data(2:J)             ! Ordinate - Variable Length Field
        S2=Data(K:L)             ! Abscissa - Variable Length Field
        S3=Data(M:M)             ! Remaining Fields Are Fixed Length
```

```
1858          S4=Data(M+2:M+3)
1859          S5=Data(M+5:M+7)
1860          S6=Data(M+9:M+16)
1861          S7=Data(M+18:M+23)
1862          S8=Data(M+25:M+30)
1863          S9=Data(M+32:M+38)
1864 C        IF (CHECK) WRITE (1,*) S1,S2,S3,S4,S5,S6,S7,S8,S9
1865          CALL Val(S1,ORD)
1866          CALL Val(S2,ABSC)
1867          CALL Val(S3,CELL)
1868          CALL Val(S4,CYCLE)
1869          CALL Val(S5,SAMPLE)
1870          CALL Val(S6,WAVE)
1871          CALL Val(S7,TIMER)
1872          CALL Val(S8,TEMP)
1873          CALL Val(S9,DIST)
1874          Y(I)=ORD                ! Ordinate And Abscissa Stored In Arrays
1875          X(I)=ABSC               ! /CARY/ Variables Return Final Reading
1876        IF (.NOT.PRINT) GO TO 100
1877        WRITE (1,*) UP,ERASE,UP
1878        WRITE (1,40) ORD,ABSC,CELL,CYCLE,SAMPLE,WAVE,TIMER,TEMP,DIST
1879     40 FORMAT (F10.4,F10.2,F5.1,F6.1,F7.1,F10.2,F8.1,F8.2,F8.2)
1880    100 CONTINUE
1881        RETURN
1882    999 WRITE (1,*) 'Error #',N,' in SUBROUTINE Acquire'
1883        RETURN
1884        END
```

```
C
C     ------------------------------------------------------------------
C
C         Convert ASCII String To Numeric Value (10 Digits Max'm)
C
C     ------------------------------------------------------------------
C
      SUBROUTINE Val(String,VALUE)
      INTEGER DECPT,EXPON,LENSTR,N,NUM(10)
      REAL VALUE
      DOUBLE PRECISION MULT,SIGN,TEN,DECIMAL
      CHARACTER Ascii
      CHARACTER*(*) String
      LOGICAL INTEGER,TEST
      INTEGER=.TRUE.
      TEST=.FALSE.              ! Only Used For Testing The Routine
      J=1
      K=0
      DECPT=0
      SIGN=1.0
      TEN=10.0
      DECIMAL=0.0
      LENSTR=LEN(String)
      IF (TEST) WRITE (1,*) ' String Number = ',String
      IF (TEST) WRITE (1,*) ' String Length =',LENSTR
      DO 100 I=1,LENSTR
        Ascii=String(I:I)
        N=ICHAR(Ascii)
        IF ((N.GE.48).AND.(N.LE.57)) GO TO 20
        IF (N.EQ.46) INTEGER=.FALSE.
        IF (N.EQ.46) DECPT=K
        IF (N.EQ.45) SIGN=-1.0
        GO TO 100
   20 NUM(J)=N-48
      K=J
      J=J+1
  100 CONTINUE
      IF ((DECPT.EQ.0).AND.(INTEGER)) DECPT=K
      DO 200 J=1,K
        EXPON=DECPT-J
        MULT=TEN**EXPON
        DECIMAL=DECIMAL+NUM(J)*MULT
  200 CONTINUE
      VALUE=SIGN*DECIMAL
      IF (TEST) WRITE (1,*) ' Value =',VALUE
      RETURN
      END
```

```
C
C     ---------------------------------------------------------------
C
C         Convert Number To ASCII String
C
C     ---------------------------------------------------------------
C
      SUBROUTINE Str(VALUE,String,PREC)
      INTEGER ASCII,DECPT,I,J,LENSTR,NDICIT,NUMBER,PREC
      REAL VALUE
      DOUBLE PRECISION DECIMAL,FRACTION,TEN
      CHARACTER Concat*14,Digit(12),Sign,String*14
      LOGICAL INTEGER,TEST
      INTEGER=.TRUE.
      TEST=.FALSE.              ! Only Used For Testing The Routine
      DECPT=0
      J=0
      TEN=10.0
      Sign=' '
      Concat=' '
      IF (TEST) WRITE (1,*) ' Value Entered = ',VALUE
      IF (VALUE.LT.0.0) Sign='-'
      IF (VALUE.EQ.0.0) GO TO 100
      DECIMAL=ABS(VALUE)
      DO WHILE (DECIMAL.GE.1.0)
        DECIMAL=DECIMAL/TEN
        J=J+1
      END DO
      DECPT=J
      IF (TEST) WRITE (1,*) ' # of Whole Digits: ',DECPT
      IF (DECPT.EQ.0) GO TO 30
      DO 20 J=1,DECPT
        DECIMAL=DECIMAL*TEN
        NUMBER=INT(DECIMAL)
        ASCII=NUMBER+48
        Digit(J)=CHAR(ASCII)
        FRACTION=DECIMAL-NUMBER
        DECIMAL=DINT(FRACTION*TEN**(PREC-J)+.5)/TEN**(PREC-J)
   20 CONTINUE
      IF (.NOT.TEST) GO TO 30
      WRITE (1,*) ' The Whole Digits = ',(Digit(I), I=1,DECPT)
   30 J=DECPT
      IF (TEST) WRITE (1,*) ' Decimal Fraction = ',DECIMAL
      IF (DECIMAL.NE.0.0) INTEGER=.FALSE.
      IF (DECPT.GE.12) GO TO 40
      DO WHILE (DECIMAL.NE.0.0)
        J=J+1
        DECIMAL=DECIMAL*TEN
        NUMBER=INT(DECIMAL)
        ASCII=NUMBER+48
        Digit(J)=CHAR(ASCII)
        FRACTION=DECIMAL-NUMBER
        DECIMAL=DINT(FRACTION*TEN**(PREC-J)+.5)/TEN**(PREC-J)
```

```
1985          IF (DECIMAL.EQ.1.0) THEN
1986            DIGIT(J)=CHAR(ASCII+1)
1987            DECIMAL=0.0
1988          END IF
1989          IF (J.GE.12) DECIMAL=0.0
1990        END DO
1991     40 NDIGIT=J
1992        IF (.NOT.TEST) GO TO 50
1993        WRITE (1,*) ' The Characters  = ',(Digit(I), I=1,NDIGIT)
1994     50 IF (NDIGIT.GT.12) GO TO 200
1995        DO 60 I=1,NDIGIT
1996          Concat(I:I)=Digit(I)
1997     60 CONTINUE
1998        IF (INTEGER) GO TO 80
1999        IF (DECPT.EQ.0) GO TO 70
2000        String=Sign//Concat(1:DECPT)//'.'//Concat(DECPT+1:14)
2001        RETURN
2002     70 String=Sign//'.'//Concat
2003        RETURN
2004     80 String=Sign//Concat
2005        RETURN
2006    100 String=' 0.0'
2007        RETURN
2008    200 WRITE (1,*) ' Error in data: (too many digits)'
2009        STOP
2010        END
```

```
C
C     ---------------------------------------------------------------
C
C         Send a Command String To CARY 2390
C
C     ---------------------------------------------------------------
C
      SUBROUTINE Send(Command)
      INTEGER N
      CHARACTER*(*) Command
      CHARACTER Response*64
      LOGICAL TEST
      TEST=.FALSE.              ! Only Used For Testing The Routine
      IF (TEST) WRITE (1,*) ' Command  - ',Command
      WRITE(UNIT=38,FMT=*,IOSTAT=N,ERR=999) Command
      READ (UNIT=38,FMT=10,IOSTAT=N,ERR=999) Response
   10 FORMAT (A64)
      IF (TEST) WRITE (1,*) ' Response - ',Response
      RETURN
  999 WRITE (1,*) 'Error #',N,' in SUBROUTINE Send'
      RETURN
      END
C
C     ---------------------------------------------------------------
C
C         TERMINATE Real Time Transmission from CARY 2390
C
C     ---------------------------------------------------------------
C
C     Send UNTALK/UNLISTEN = '_?' to IEEE-488 Bus
C
      SUBROUTINE Terminate
C     CALL CMDW(35,'_?',0)  ! CMDW occasionally fails to UNADDRESS
      CALL ABRT(35,3)       ! The ABRT command sends '_?' reliably
      RETURN
      END
C
C     ---------------------------------------------------------------
C
C         Wait Specified Delay (sec)
C
C     ---------------------------------------------------------------
C
      SUBROUTINE Wait(DELAY)
      REAL DELAY,PERIOD,Tzero,Time
      PERIOD=0.0
      Tzero=Time(1)
      DO WHILE (PERIOD.LT.DELAY)
        PERIOD=Time(1)-Tzero
      END DO
      RETURN
      END
```

```
2063 C
2064 C     ------------------------------------------------------------
2065 C
2066 C         Read Time (sec) from the HP 1000's RTE-6 Operating System
2067 C
2068 C         Note: I is a dummy argument, no values are passed
2069 C
2070 C     ------------------------------------------------------------
2071 C
2072       REAL FUNCTION Time(I)
2073       INTEGER ICODE,ITIME(5)
2074       ICODE=11
2075       CALL EXEC(ICODE,ITIME)
2076       Time=FLOAT(ITIME(1))/100.0+FLOAT(ITIME(2))+FLOAT(ITIME(3))*60.0
2077      &+FLOAT(ITIME(4))*3600.0
2078       RETURN
2079       END
```

APPENDIX G2

Naval Research Laboratory
Washington, DC 20375-5000

G2

NRL Memorandum Report 6351

EDITSPEC

A FORTRAN 77 Program for Editing and Manipulating Spectral Data from the Varian CARY 2390 UV-VIS-NIR Spectrophotometer

R. A. BINSTEAD

GEO-CENTERS, Inc.
10903 Indian Head Highway,
Fort Washington, MD 20744

J. C. COOPER

Polymeric Materials Branch
Chemistry Division

October 19, 1988

Approved for public release; distribution unlimited.

SECURITY CLASSIFICATION OF THIS PAGE

REPORT DOCUMENTATION PAGE

Form Approved OMB No 0704-0188

1a REPORT SECURITY CLASSIFICATION: UNCLASSIFIED	1b RESTRICTIVE MARKINGS
2a SECURITY CLASSIFICATION AUTHORITY	3 DISTRIBUTION/AVAILABILITY OF REPORT: Approved for public release; distribution unlimited.
2b DECLASSIFICATION/DOWNGRADING SCHEDULE	
4 PERFORMING ORGANIZATION REPORT NUMBER(S): NRL Memorandum Report 6351	5 MONITORING ORGANIZATION REPORT NUMBER(S)
6a NAME OF PERFORMING ORGANIZATION: Naval Research Laboratory; 6b OFFICE SYMBOL (If applicable): Code 6125	7a NAME OF MONITORING ORGANIZATION
6c ADDRESS (City, State, and ZIP Code): Washington, DC 20375-5000	7b ADDRESS (City, State, and ZIP Code)
8a NAME OF FUNDING/SPONSORING ORGANIZATION: SDIO and ONR; 8b OFFICE SYMBOL (If applicable)	9 PROCUREMENT INSTRUMENT IDENTIFICATION NUMBER
8c ADDRESS (City, State, and ZIP Code): Washington, DC	10 SOURCE OF FUNDING NUMBERS: PROGRAM ELEMENT NO 61153N 63224C; PROJECT NO RR011-01-44; TASK NO; WORK UNIT ACCESSION NO

11 TITLE (Include Security Classification) EDITSPEC - A FORTRAN 77 Program for Editing and Manipulating Spectral Data from the Varian CARY 2390 UV-VIS-NIR Spectrophotometer

12 PERSONAL AUTHOR(S): Binstead,* R.A. and Cooper, J.C.

13a TYPE OF REPORT	13b TIME COVERED	14 DATE OF REPORT (Year, Month, Day)	15 PAGE COUNT
Interim	FROM 10/87 TO present	1988 October 19	70

16 SUPPLEMENTARY NOTATION: *GEO-CENTERS, Inc., 10903 Indian Head Highway, Fort Washington, MD 20744

17 COSATI CODES			18 SUBJECT TERMS (Continue on reverse if necessary and identify by block number)	
FIELD	GROUP	SUB-GROUP	UV-VIS-NIR	FORTRAN
			Editing	CARY

19 ABSTRACT (Continue on reverse if necessary and identify by block number)

EDITSPEC is a FORTRAN 77 program designed to provide a number of editing features for UV-VIS-NIR spectral data obtained from the CARY 2300 - 2400 series spectrophotometers. The program is written to operate on a Hewlett-Packard 1000 computer system but with very few system dependent features to enable easy conversion for operation on other host systems. EDITSPEC provides facilities for correction of experimental artifacts and incorrect file descriptors and also includes calculation routines for smoothed, first derivative and second derivative spectra. The program produces new disk files in either the Cary format or in simple ASCII X,Y format for export to curve fitting programs.

20 DISTRIBUTION/AVAILABILITY OF ABSTRACT	21 ABSTRACT SECURITY CLASSIFICATION
☐ UNCLASSIFIED/UNLIMITED ☑ SAME AS RPT ☐ DTIC USERS	UNCLASSIFIED
22a NAME OF RESPONSIBLE INDIVIDUAL: John C. Cooper	22b TELEPHONE (Include Area Code): (202) 767-3115; 22c OFFICE SYMBOL: Code 6125

DD Form 1473, JUN 86 Previous editions are obsolete SECURITY CLASSIFICATION OF THIS PAGE

S/N 0102-LF-014-6603

CONTENTS

Section	Description	Page
INTRODUCTION		1
SOFTWARE DESCRIPTION		
1.0	Purpose Of EDITSPEC	2
1.1	Smoothing And Derivative Spectra	4
1.2	Numerical Least Squares Procedures	5
IMPLEMENTATION		
2.0	Program Structure	6
2.1	File Editing Menu Commands	11
2.2	Data Editing Menu Commands	12
2.3	COMMON DATA	15
2.4	SUBROUTINES	16
2.5	FUNCTIONS	19
2.6	SPECIAL SYSTEM CALL	19

... cont'd

Section	Description	Page
PROGRAM CODE		
3.0	Source Code Availability	20
3.1	Variable Names And Usage	20
3.2	Program Listing	26
APPENDIX I	Sample Smoothed Spectra	58
APPENDIX II	Sample Derivative Spectra	61

LIST OF TABLES

TABLE	Description	Page
I	Data File Format	8
II	Glossary Of Integer Variables	21
III	Glossary Of Real Variables	22
IV	Glossary Of Real Array Variables	23
V	Glossary Of Character Variables	24

EDITSPEC

A FORTRAN 77 Program For Editing And Manipulating Spectral Data From The Varian CARY 2390 UV-VIS-NIR Spectrophotometer

INTRODUCTION

Spectral data acquisition from the CARY 2300 and 2400 series spectrophotometers has been implemented successfully with a Hewlett-Packard 1000 minicomputer system using the FORTRAN 77 program, CARYSPEC, and its companion plotting program, PLOTSPEC, which are described in separate reports. The ability to acquire high quality UV-VIS-NIR spectra must be complemented with flexible analytical software to make full use of the spectroscopic data. This report describes a fully tested FORTRAN 77 program, EDITSPEC, which fulfills the data editing and manipulation requirements of most users in a simple to use menu driven environment. The program reads and manipulates disk data files in Absorbance or % Transmission modes *vs* Wavelength (nm) and stores the edited data in the same format or in a simple ASCII X,Y format for use by curve fitting programs.

The editing facilities provided in EDITSPEC allow for easy corrections to both inaccurate file descriptors and anomalies in the spectral data. Single data points may be altered to remove a glitch or a segment of a spectrum may be offset to produce exact matching between regions obtained using different photodetectors or lamp sources. Nonlinearity of Near IR data from the PbS detector can be corrected in cases where the data extend below 800 nm in AUTOSELECT mode. The absorbance offset between the Photomultiplier and PbS detectors at 800 nm is used to rescale the Near IR region assuming that the PM tube response is perfect. The Cary 2300 series instruments can benefit most from this rescaling routine. The Cary 2400 series instruments already provide nonlinearity correction for the standard PbS detector though this feature is bypassed for the reflectance accessory which suffers badly from nonlinearity. EDITSPEC also provides quartic polynomial least squares calculation routines to produce Smoothed, First Derivative and Second Derivative spectra.

EDITSPEC has been developed for use with an HP 1000 minicomputer system running the RTE-6/VM operating system and CI shell. The program resides in a single 32K word memory segment and utilizes 98K words of Extended Memory Addressing (EMA) area for the large data arrays. Since EDITSPEC makes use of very few special features of the HP 1000 computer system the program could be modified easily to run on other host systems supporting the FORTRAN 77 language.

SOFTWARE DESCRIPTION

1.0 Purpose Of EDITSPEC:

The data acquisition program CARYSPEC was designed to store only *baseline corrected* UV-VIS-NIR spectra in disk files which should, hopefully, be free of all instrumental artifacts. In practice, some small irregularities can still occur at grating, lamp or detector change over points and EDITSPEC provides the user with both single datum and region offset commands to remove such artifacts *albeit* in an arbitrary fashion. Discretion is left to the user for determining which spectral region is likely to have been incorrectly recorded by the particular instrument. The Cary 2400 and upgraded 2300 series spectrophotometers are less likely to require such manipulation since these instruments have more reproducible mechanical positioning for the photodetectors.

The data files produced by CARYSPEC include a number of file description strings and numeric variables to provide permanent, internal documentation for the spectrum. Occasionally, important information, such as solute concentration, is not known at the time of data collection and EDITSPEC provides an easy means of displaying and updating the file descriptors. Since EDITSPEC also provides a number of data transformation routines, the edited spectrum can be stored on disk only with a new filename. This prevents inadvertent loss of the original data.

EDITSPEC supports such file operations as file size reduction, nonlinearity correction for Near IR data and numerical procedures for smoothing of experimental noise and calculation of derivative spectra. The file size reduction operation allows new wavelength limits and data step size to be set, which is useful for matching spectra to be used in the difference spectrum mode of PLOTSPEC. Near IR data often suffer from nonlinearity of the photoconductive PbS detectors used in the Cary 2300 series spectrophotometers. Corrections for such nonlinearity are dependent on *both* the light flux and the absorbance level. The Cary 2400 and upgraded 2300 series instruments provide appropriate correction in the Near IR region for the standard PbS detector. However, detectors on external modules, such as the Diffuse Reflectance accessory, are not corrected. Reflectance spectra often show discontinuities between the PbS and PM tube detectors at 800 nm and EDITSPEC provides a simple rescaling procedure to produce detector matching in these cases. This is not meant to be a panacea but it does provide a more realistic result than the raw data.

Experimental noise is not often a problem with UV-Visible spectra from the Cary spectrophotometers. However, the Near IR region is more noise prone, particularly with the Diffuse Reflectance accessory, due to the poorer signal to noise ratio of PbS detectors and the low efficiency of the rather small integrating sphere. In such cases it may be desirable to use the quartic polynomial least squares smoothing routines in EDITSPEC. This standard procedure has been specially modified to suit the large data redundancy in most UV-VIS-NIR spectra and can be used to remove both *random* noise and *spurious* artifacts from solvent overtone bands in the Near IR region.

The polynomial least squares procedure is also utilized in EDITSPEC to calculate First and Second Derivative spectra with a higher degree of precision than the analog versions which the Cary spectrophotometers produce on their internal pen recorders. These routines can provide useful information in regions of overlapping absorption bands. The resulting First and Second derivative spectra are arbitrarily scaled by factors of x10 and x100, respectively, to facilitate subsequent plotting using the program PLOTSPEC.

EDITSPEC also supports the creation of simple ASCII X,Y text files for exporting data to general purpose curve fitting software. In this mode the abscissa values are converted from Wavelength (nm) to Energy units (cm^{-1}) on output with approximately even Wavenumber spacing between points. The user may select either Absorbance or Extinction Coefficient (M^{-1} cm^{-1}) units for the ordinate and the program will automatically rescale % Transmission data to the selected ordinate, if required.

Finally, EDITSPEC provides a facility for subtraction of a reference *baseline* spectrum for cases in which the pure solvent (in transmittance mode) or reflectance standard does not provide a suitable baseline for the sample under study. For example, thin films on substrates or matrix isolated materials will usually require correction for the absorption or reflectivity loss of the substrate. The *baseline* data file may cover the same or a larger wavelength range than the file to be corrected but both must have the same data interval size, ordinate scale and reference beam modes. These restrictions are intended to ensure that such *baseline* corrections are carried out under closely matched instrumental conditions.

The combination of facilities offered by EDITSPEC should satisfy the needs of most users for producing high quality spectra free from instrumental and sample handling artifacts. The operation of each facility will be discussed separately in more detail below.

1.1 Smoothing And Derivative Spectra:

The numerical procedures used in EDITSPEC for smoothing experimental noise and for calculating derivative spectra are based on standard polynomial least squares regression. The method relies on fitting a high order polynomial, $(a_0 + a_1 x + a_2 x^2 + a_3 x^3 + a_4 x^4 + \ldots)$ to small data segments, $(-x,\ldots,+x)$, replacing the centre point $(x = 0)$ with the fitted values of a_0 (smoothing), a_1 (first derivative), $2a_2$ (second derivative) ... *etc.* The data segment is stepped consecutively across the spectrum to complete the procedure. EDITSPEC uses a quartic polynomial routine with choices of 7, 11, 15, 21 and 25 point segments to provide increasing levels of *local* averaging. The procedure is illustrated below for a 7 point segment:



Smoothing:

The data interval $(-3,\ldots,+3)$ is fitted to a quartic polynomial to calculate a new centre point a_0 denoted by ●. The complete spectrum is smoothed by stepping the 7 point segment consecutively across the spectrum but the procedure obviously can not smooth the first or last 3 points. The smoothing procedure may be repeated as many times as desired and may be limited to just a small region of the complete spectrum.

Derivatives:

An obvious extension to the polynomial regression technique is the easy calculation of derivative spectra with replacement of the centre point by the fitted values of a_1, $2a_2$, ... $n!a_n$ *etc.* for the first, second and higher derivatives.

The technique can only average noise (in the least squares sense) within the width of the selected interval so that with closely spaced data even the 25 point fit may be ineffective. For example, Near IR spectra often display the effects of significant 1/f noise with an effective noise period of 20 nm or more underlying a higher level of more random noise. A naive implementation of the smoothing procedure will fail to deal with very low frequency noise, removing only the more rapid fluctuations. EDITSPEC allows the user to span an arbitrarily wide wavelength range for each fitted segment by evenly spacing the fitted points with an integral number of data points. This results in vastly superior *global* averaging.

1.2 Numerical Least Squares Procedures:

The quartic polynomial regression equations can be written in matrix form as follows:

$$\begin{bmatrix} N & \sum_{1}^{N} x & \sum_{1}^{N} x^2 & \sum_{1}^{N} x^3 & \sum_{1}^{N} x^4 \\ \sum_{1}^{N} x & \sum_{1}^{N} x^2 & \sum_{1}^{N} x^3 & \sum_{1}^{N} x^4 & \sum_{1}^{N} x^5 \\ \sum_{1}^{N} x^2 & \sum_{1}^{N} x^3 & \sum_{1}^{N} x^4 & \sum_{1}^{N} x^5 & \sum_{1}^{N} x^6 \\ \sum_{1}^{N} x^3 & \sum_{1}^{N} x^4 & \sum_{1}^{N} x^5 & \sum_{1}^{N} x^6 & \sum_{1}^{N} x^7 \\ \sum_{1}^{N} x^4 & \sum_{1}^{N} x^5 & \sum_{1}^{N} x^6 & \sum_{1}^{N} x^7 & \sum_{1}^{N} x^8 \end{bmatrix} \cdot \begin{bmatrix} k_0 \\ k_1 \\ k_2 \\ k_3 \\ k_4 \end{bmatrix} = \begin{bmatrix} \sum_{1}^{N} y \\ \sum_{1}^{N} xy \\ \sum_{1}^{N} x^2y \\ \sum_{1}^{N} x^3y \\ \sum_{1}^{N} x^4y \end{bmatrix}$$

or in matrix notation as $\underline{\underline{C}} \cdot \underline{K} = \underline{B}$, where $k_n = n!a_n$, for which the solution vector is given by $\underline{K} = \underline{\underline{C}}^{-1} \cdot \underline{B}$. Evaluation of the the inverse coefficient matrix is simplified using the range of index values $(-x,\ldots,-1,0,+1,\ldots,+x)$ to represent the data interval to be fitted to the polynomial since all the summations for odd powers of x are zero. The resulting solution vector simplifies to a set of known coefficients times $\underline{B}$ which needs to be evaluated for each data segment. EDITSPEC requires the elements of just the first three rows of $\underline{\underline{C}}^{-1}$, comprising 8 non–zero elements of which 7 are unique. A full pivoting Gaussian elimination matrix inversion program was used to solve for the coefficients and these appear as Double Precision DATA for array CC(I,J) in EDITSPEC for the 5 different fitting algorithms provided.

The general solutions for the smoothing and derivative calculations in EDITSPEC are summarized below:

SMOOTHING: $k_0 = \underline{\underline{C}}^{-1}_{(1,1)} \cdot \Sigma y + \underline{\underline{C}}^{-1}_{(1,3)} \cdot \Sigma x^2y + \underline{\underline{C}}^{-1}_{(1,5)} \cdot \Sigma x^4y$

DERIVATIVE 1: $k_1 = \underline{\underline{C}}^{-1}_{(2,2)} \cdot \Sigma xy + \underline{\underline{C}}^{-1}_{(2,4)} \cdot \Sigma x^3y$

DERIVATIVE 2: $k_2 = \underline{\underline{C}}^{-1}_{(3,1)} \cdot \Sigma y + \underline{\underline{C}}^{-1}_{(3,3)} \cdot \Sigma x^2y + \underline{\underline{C}}^{-1}_{(3,5)} \cdot \Sigma x^4y$

IMPLEMENTATION

:.0 Program Structure:

EDITSPEC comprises a large main program unit containing the console menu displays nd string data for the instrument settings variables. A number of subroutines perform input alidation and string processing commands absent from the FORTRAN 77 language. The main rogram unit of EDITSPEC comprises 6 distinct segments of code to carry out the the unctions of disk file data retrieval, instrument settings display, editing of file descriptors and pectral data, data file storage and file creation for exporting ASCII X,Y data to curve fitting rograms *etc.* The code fragments appear under the following assigned labels: MENU, READ, ETTINGS, EDIT, STORE, CURFILE and EXIT.

MAIN PROGRAM

MENU:

This is the first and main control menu of the program, selecting entry to the data retrieval, instrument settings, editing, data file storage and exit routines. The choices are as follows:

'R' .....Read Spectrum

This command causes a branch to label READ and the program performs a logical test for the presence of a valid spectrum in memory before allowing previous data to be overwritten by a new file. If a spectrum is already present in memory the user may elect to overwrite the old data, subtract a baseline reference file or return to the main menu. The data file format is listed below in Table I. Spectra are read into the data arrays X,Y while baseline files are stored in the arrays XB,YB before subtraction takes place.

'I' .....Instrument Settings

This option branches to label SETTINGS and performs logical tests for the presence of spectrum and baseline data files in memory. This routine allows for display of the most important operating conditions of the Cary 2390 spectrophotometer during acquisition of the selected data file to provide an on-line reference when comparing data files.

'E' .....Edit Spectrum

Entry of this command causes a branch to label EDIT. The program then performs a logical test for the presence of a valid spectrum in memory before presenting a sub-menu of editing options. All the data manipulations are performed from these sub-menus.

'S' .....Store Spectrum

This command transfers control to label STORE where logical tests are performed for the presence of a spectrum in memory and whether the data file to be created is an edited or smoothed spectrum. The data files are stored in the Cary format for subsequent use by the plotting program PLOTSPEC.

'D' .....Store Derivative Spectrum

This command also branches to label STORE but in this case the program also checks for the presence of a derivative array in memory before proceeding. First and second derivative spectra are also stored in the Cary format but are scaled arbitrarily x10 and x100, respectively, to simplify subsequent plotting.

'C' .....Store Curve Fitting File

This option allows for creation of simple ASCII X,Y data files from Cary spectra. The program branches to label CURFILE and prompts for entry of the wavelength range in the new data file and the number of data points required (10 - 500). The abscissa values are converted from Wavelength (nm) to Energy units (cm^{-1}) and the program selects data points to be spaced evenly in cm^{-1}. The ordinate data can be Absorbance or Extinction Coefficients only and automatic rescaling is provided for % Transmission data.

'X' .....Exit

The final option causes a branch to the label EXIT which checks whether the spectrum in memory has been saved to disk before allowing the program to terminate.

TABLE I

Data File Format

Line	File Variables [a]	Format Type [b]
1	LABEL(2)	CHARACTER (A72)
2	DATE(2)	CHARACTER (A8)
3	XMIN(2),XMAX(2),XSTEP(2),CONC(2), PATH(2)	REAL (*)
4	ORD(2),ABSC(2),CELL(2),CYCLE(2), SAMPLE(2),WAVE(2),TIMER(2), TEMP(2),DIST(2)	REAL (*)
5	NP,NV,ND(2)	INTEGER (I3,I3,I6)
6-54	PARAM(2,I)	INTEGER (I2)
55	VARIABLE(2,I)	REAL (*)
56-/	Y(I) or YB(I)	REAL (*)
/-eof	X(I) or XB(I)	REAL (*)

a: Disk data files are read into either half of the data arrays

b: (*) indicates free field format

READ:

This section of EDITSPEC opens a disk file previously stored by the data acquisition program CARYSPEC. The data are stored in ASCII code and contain a complete description of the instrument parameter settings as well as the spectral data. The format of the data file is listed above in Table I. The program prompts the user for both the filename and subdirectory. The filename may be up to 16 characters with the extension ".Sxx", where xx are the researcher's initials. The subdirectory defaults to the user's directory if only a RETURN character is entered. If a directory name is given the program builds a complete CI pathname for use in the OPEN statement. If the file cannot be found or the file is already open the program displays an error message and then returns to the main MENU. Otherwise, the file is read and the file descriptors are displayed on the console while the remainder of the data are being transferred. The program then returns to the main MENU.

SETTINGS:

This section of code displays a list of the most important instrument settings of the Cary 2390 spectrophotometer during acquisition of the specified data file. The program includes a large amount of string data for the various settings in the CHARACTER array Pstr. The INTEGER array PARAM is used as an index to this string data while numeric data for the table are obtained from the REAL array VARIABLE. If both a Spectrum and Baseline are present in memory the program will prompt for which settings to display.

EDIT:

This section of code contains two sub-menu displays for performing all the data and file manipulations within EDITSPEC. The first sub-menu allows for alterations to the file descriptors comprising the variables *Concentration (M)*, *Date (MM/DD/YY)*, *Label (72 chars)* and *Pathlength (cm)* using single letter command entries. The remaining choices select entry to the data editing menu or an exit to the main MENU. The data editing menu supports the following functions: *List Data Segment*, *Edit Single Datum*, *Offset Segment*, *Near IR Rescale*, *Smooth Segment* and *Deriv. Spectra*. The operation of these functions is straightforward and each is described in detail below (Sections 2.1-2.2).

STORE:

This section of EDITSPEC provides the data storage routine for edited, smoothed and derivative spectra. On entry to this routine the program checks if a spectrum is present in memory. Otherwise, an error message is displayed before returning to the main MENU. If the *Store Derivative Spectrum* command has been used to enter this routine then a check is also made for the presence of a valid derivative array. If the data file to be stored is a smoothed or a derivative spectrum then the file description label is altered to include the number of smoothing passes (SMxx: ...) or the degree of the derivative calculation (FD: ... or SD: ...). The user is only prompted for initials, filename and subdirectory information before the file is written to a disk file. Standard I/O error checking for a FILE EXISTS or a FILE OPEN error is performed during file creation. The program then returns to the main MENU with the new filename and file status variables for the edited spectrum.

CURFILE:

This section of code provides a simple means of exporting spectral data to curve fitting programs *etc.* The files are created in an ASCII X,Y format with no other information except the end-of-file marker. The abscissa values are converted from Wavelength to linear Energy units (cm^{-1}) and the program selects data so that the spacing between abscissa values is nearly even in cm^{-1} units. The program provides an arbitrary range of 10 - 500 data points for such files which should suit the needs of most ancillary programs. The ordinate mode can be selected as *Absorbance* or *Extinction Coefficient* only and if the original data were collected in % Transmission mode then automatic rescaling is performed during the data storage loop. Standard I/O error checking is performed for a FILE EXISTS or a FILE OPEN error during file creation. The program then returns to the main MENU with an updated status variable for the *Store Curve Fitting File* command.

EXIT:

The final portion of EDITSPEC checks whether a valid spectrum in memory has been stored to disk before allowing the user to terminate the program. The routine does not check the status of Derivative arrays or Curve Fitting files since these can be easily recreated from the stored spectral data file.

2.1 File Editing Menu Commands:

The first editing sub-menu is designed to allow for easy alterations to the file descriptors. The operations are invoked using single letter commands as follows:

'C' .....Concentration, (M)

The Concentration variable is used to scale experimental absorbance values from solution spectra into Molar Extinction Coefficients (absorptivity) units and may need to be altered if the value was unknown at the time of data collection.

'D' .....Date, (MM/DD/YY)

The Date variable is set manually within the data collection program, CARYSPEC, and may need to be altered if it has been entered incorrectly. Only 8 character positions are provided for this entry.

'L' .....Label, (72 chars)

This variable provides descriptive text to document the nature of the spectrum. The maximum text length is 72 characters and the character field is delimited on the console screen by arrow heads under the text entry line.

'P' .....Pathlength, (cm)

This variable is also used in the calculation of Extinction Coefficient values for solution spectra. In other types of spectra this variable can be set to zero.

The data entry routine is arranged in such a way that the current value of a variable is printed to the console screen with the cursor placed over the first character of the old value. Entry of only a RETURN character will keep the old value intact. If any other characters are entered they are treated as the new value. Thus, a complete line must be entered to update the previous data correctly. Cursor control keys should not be used in editing such line entries - the backspace key is the only editing function permitted.

The remaining command entries 'S' and 'X' are used to enter the data editing sub-menu or to exit to the main MENU.

2.2 Data Editing Menu Commands:

The spectral data editing sub-menu provides access to all the array manipulation functions available in EDITSPEC. In common with the other menus, single letter commands are used to select the desired operations given below:

'L' .....List Data Segment

This command provides a means of inspecting the data between any two selected wavelength limits. The data are displayed in pages of 10 points until completion. If the original data were acquired in Absorbance mode this routine lists both the Absorbance and Extinction Coefficient values *vs* Wavelength (nm). In % Transmission mode only the raw data are presented.

'E' .....Edit Single Datum

This command is used to display and update Absorbance or % Transmission data at a single wavelength. The current value is printed on the screen with the cursor positioned over its first character. Entry of only a RETURN character will keep the current value intact. Otherwise, a new entry is assumed for any other characters read from the keyboard. New entries are validated to lie within the range −0.5 to 4.5 for Absorbance mode and 0 to 200 for % Transmission mode. The latter also covers the case of % Reflectance spectra.

'O' .....Offset Segment

The offset command enables corrections to be made for misalignment between regions of a spectrum obtained using different detectors, gratings or source lamps. The routine provides a simple (±) algebraic offset, selected by the user, between the desired wavelength limits without regard to the ordinate mode.

'N' .....Near IR Rescale

This command is used to align the Near IR region of a spectrum with data obtained from the photomultiplier detector in the Visible region. The data must, therefore, have been collected in AUTOSELECT mode so that the detector change is made at 800 nm. The routine inspects the last point obtained with the PbS detector and the first point from PM tube to obtain a default offset value. The default value is written to the console display with the cursor positioned over its first character and entry of just a RETURN character will commence rescaling with this offset.

This routine is most often used to align noisy, high absorbance Near IR data with a noise free Visible region so that it proves more useful to plot the data first to obtain a better estimate for the offset before rescaling. The rescaling procedure is multiplicative for both Absorbance and % Transmission modes. Ideally, the latter should be converted to Absorbance before rescaling but this is not likely to cause any serious errors.

'R' .....Reduce File Size

This command is used to change the size of a data file by reducing the wavelength range or by increasing the step size (nm) between data points. This is most useful in providing matched data files for the spectral subtraction mode of the plotting program, PLOTSPEC. It may also be useful for eliminating excess data from very large files. The reduced file overwrites the current spectrum and recovery is possible only by reading the old data from disk.

'S' .....Smooth Segment

The quartic polynomial smoothing routine in EDITSPEC is provided with data for calculations with 5 different levels of *local* averaging using data segments with 7, 11, 15, 21 or 25 points (-XX,...,0,...,+XX) in the least squares fits. These are selectable from the smoothing algorithm menu which is presented on entry to the routine. The program then displays the wavelength range of the fitted segments with a default integer step size of two points. The user may increase or decrease the wavelength range of the fitted segments by altering the step size variable. Larger values of the step size produce improved *global* averaging, an important feature for removing non-random solvent overtone artifacts. The smoothing routine may be applied over the whole wavelength range or just within a small segment. However, the routine can not smooth the first or last XX data points in the spectrum. The program prints the actual range smoothed on the console screen before prompting for the number of smoothing passes. There is nothing to be gained by performing a large number of smoothing passes with the same algorithm. Rather, it is preferable to select several different fitting intervals, by choice of algorithm and step size, to improve the averaging of low frequency, non-random noise. In general, it is wise to finish a smoothing procedure with the integer step size set to 1 data point to suppress a tendency to produce periodic oscillations in the data with the polynomial regression procedure.

Some examples of smoothed spectra appear as an appendix to this report.

.....Derivative Spectra

The polynomial regression technique in EDITSPEC is also used to calculate first and second derivative spectra. Smoothing may be performed prior to the derivative calculations in order to reduce the noise level, particularly for the second derivative. Selection of the fitting algorithm is identical to the procedure for smoothing. However, the procedure can be performed only once and must encompass the entire wavelength range, less the first and last XX data points. The latter are set equal to the first and last fitted points, respectively. It is most beneficial to provide wide *global* averaging for the derivative functions with fitted intervals on the order of 20–50 nm. If the fitted interval is too narrow then the result is a measure of the point to point noise level and *not* the derivative of the spectrum *per se*.

Some examples of derivative spectra appear as an appendix to this report.

2.3 COMMON DATA:

All COMMON array variables used by EDITSPEC are held in a named COMMON block, /DATA/. The arrays contained within the COMMON block are listed below:

/DATA/ Contains EMA REAL Arrays of spectroscopic data

X
Array containing the spectrum's Wavelength data (nm)
Values read from disk data file
Values used in main program unit

Y
Array containing the spectrum's Absorbance or %T data
Values read from disk data file
Values used in main program unit

XB
Array containing the baseline's Wavelength data (nm)
Values read from disk data file
Values used in main program unit

YB
Array containing the baseline's Absorbance or %T data
Values read from disk data file
Values used in main program unit

Z
Array containing the derivative spectrum's Absorbance or %T data
Values calculated in main program unit
Values stored to disk data file

All the data arrays are dimensioned for 10001 data points maximum in single precision and are specified to reside in EMA memory requiring 98K words of system available memory. These memory demands could be reduced if required since few UV-VIS-NIR spectra have more than a few thousand data points.

2.4 SUBROUTINES:

EDITSPEC uses subroutines to perform specific tasks which are required more than once, including several types of string manipulation and input validation. The purpose and calling sequences are listed below:

Center(TITLE)

Prints a string on the user console centred within a 72 column line.

TITLE CHARACTER*72 string, contents set by calling unit

CALLED BY: Main program unit
CALLS: None

Line(N)

Prints a line of '-' characters to the user console N columns wide and centred within a 72 column line.

N INTEGER variable input from calling unit

CALLED BY: Main program unit
CALLS: None

Klimits(MIN,MAX)

Performs an absolute value function on the input arguments
Validates the resulting arguments so that MIN < MAX

MIN,MAX REAL variables input and output with order swapped if required

CALLED BY: Main program unit
CALLS: None

Ylimits(MIN,MAX)

Validates the input arguments so that MIN < MAX

MIN,MAX REAL variables input and output with order swapped if required

CALLED BY: Main program unit
CALLS: None

Upper(Code)

Performs a check for lower case characters in a string of arbitrary length and converts to upper case if necessary.

Code CHARACTER*(*) variable passed into routine and UPPER case on exit
DIMENSION is set by the calling unit

CALLED BY: Main program unit
CALLS: None
EXTENSION: LEN(*string*) function, an HP extension to FORTRAN 77

Str(VALUE,String,PREC)

Performs a conversion from numeric value to a string number for floating point numbers only with up to 12 digits precision.

VALUE REAL variable input to be processed by the routine

String CHARACTER*14 string output corresponding to VALUE

PREC INTEGER variable input to set the rounding precision for string

CALLED BY: Main program unit
CALLS: None

'al(String,VALUE)

Performs a conversion from string to numeric value for a string number containing up to 10 digits with or without an exponent.

String — CHARACTER*(*) string input to be processed by routine
DIMENSION is set by calling unit

VALUE — REAL variable output

ALLED BY: Main program unit
ALLS: None

/ait(DELAY)

Performs a loop which tests the system clock until DELAY seconds have elapsed. The routine does not make provision for the special case at the transition to 2400 hours.

DELAY — REAL variable holding the value of the delay period in seconds

ALLED BY: Main program unit
ALLS: FUNCTION Time(I)

2.5 FUNCTIONS:

EDITSPEC uses only one function subprogram that makes an EXEC call to read the system time.

Time(I)

Performs an EXEC call to read the system clock and converts the reading to seconds and centiseconds.

I Dummy argument

CALLED BY: SUBROUTINE Wait only
CALLS: EXEC(ICODE,ITIME) system level command

2.6 SPECIAL SYSTEM CALL:

EDITSPEC makes use of a system subroutine call to alter the width of data fields sent to the system console. The record length is changed from the default value of 72 columns to a more useful value of 79 in order to prevent inadvertent screen wrap around.

FFRCL(I)

Alters the column width for standard output

I Default value = 72, EDITSPEC value = 79

CALLED BY: Main program unit only
CALLS: None, system level subroutine call, syntax CALL FFRCL(I)

PROGRAM CODE

.0 Source Code Availability:

The source code for the program EDITSPEC is a 65K ASCII text file available on either Hewlett-Packard cartridge, 9 track tape or an IBM 360K format floppy disk. All requests ıould be accompanied by the blank medium desired. A printed copy of the source code is sted below.

.1 Variable Names And Usage:

A complete listing of the INTEGER, REAL, REAL Array and CHARACTER variables ır the MAIN segment of EDITSPEC is given below in Tables II, III, IV & V, respectively. he subroutines use the same names as the main program for the same variables. Additional ıriables in the subroutines and simple integers, I-N, are not documented since their usage is ıther obvious. The logical variable MATCH is used within the program when comparing two ›ectra for the baseline reference subtraction mode. The logical variable DERIV controls the peration of the smoothing routine in order to re-use the algorithm selection menu and then ranch back to the derivative calculation routine.

Table II

Glossary of INTEGER Variables

Name	Description	Value
CURFILE	Assigned Label - Curve Fitting File	2000
EDIT	Assigned Label - Editing Sub-menus	400
EXIT	Assigned Label - Terminate Program	9999
MENU	Assigned Label - Main Control Menu	10
READ	Assigned Label - Read Spectrum, Baseline	100
SETTINGS	Assigned Label - Scan Conditions	300
STORE	Assigned Label - Store Spectrum	1000
ASCII	ASCII equivalent of digits in Str	48-57
COUNT	Number of smoothing cycles performed	>=0
FINISH	Index of final abscissa value to edit	1-10001
IS	Step size in smoothing or derivatives	1-ITEST
ITEST	Maximum step size for selected algorithm	see text
NCOL	Number of screen columns in menu display	50-70
NDATA	Number of data points in spectrum	1-10001
NFIT	Number of points in curve fitting file	10-500
NPASS	Number of smoothing passes to execute	>=1
NP	Number of parameters to read from file	49
NV	Number of variables to read from file	14
START	Index of first abscissa value to edit	1-10001
XOFF	Index offset at start & end of spectrum	see text
XX	Linear convolution values in least squares	see text
ND(2)	Number of data points read from disk file	1-10001
NPTS(5)	Number of points in least squares fit	7-25
PARAM(2,49)	Instrument operating modes table	1-16

Table III

Glossary of REAL Variables

Name	Description
BAND	Spectral Bandwidth (nm) - AUTO GAIN mode
EC	Extinction Coefficient
FIRST	Starting wavenumber value in X,Y file
GAIN	Instrument gain - AUTO SLIT mode
LAST	Ending wavenumber value in X,Y file
NUMBER	General purpose data entry variable
PMIN	Pen scale minimum limit
PMAX	Pen scale maximum limit
RANGE	Wavelength span for least squares fit
SPACE	Approximate wavenumber steps in X,Y file
STEP	Step size (nm) interval, editing mode
W	Wavenumber loop counter in X,Y file creation
WL	Wavelength to be edited or displayed *etc.*
WMIN,WMAX	Wavelength limits for spectrum in memory
WN,WX	Current wavelength limits for editing
WOFF	Wavelength offsets for smoothing & derivatives
Y1,Y2	Ordinate values at Near IR, Visible change over
YOFF	Absorbance or %T offset, editing mode
ZM	Multiplier for 1st & 2nd derivatives

Table IV

Glossary of REAL Array Variables

Name	Description
ORD(2)	Final ordinate value in file
ABSC(2)	Final abscissa value in file
CELL(2)	Final cell # value in file
CYCLE(2)	Final cycle # value in file
SAMPLE(2)	Final sample # value in file
WAVE(2)	Final wavelength value in file
TIMER(2)	Final time value in file
DIST(2)	Final distance value in file
CONC(2)	Concentration of sample (M), from data file
PATH(2)	Pathlength of sample cell (cm), from data file
VARIABLE(2,14)	Instrument operating conditions table
XMAX(2)	Starting wavelength of scan (nm)
XMIN(2)	Ending wavelength of scan (nm)
XSTEP(2)	Step size (nm), from data file
X(10001)	Wavelength array - spectrum
XB(10001)	Wavelength array - baseline
Y(10001)	Absorbance, %T array - spectrum
YB(10001)	Absorbance, %T array - baseline
Z(10001)	δ(Abs), δ(%T) array - derivative spectrum

Table V

Glossary Of CHARACTER Variables

Name	Description
Screen Control:	
BELL	CHAR(7) bell character
CLR*2	Clear screen
DOWN*2	Move cursor down 1 line
ESC	CHAR(27) escape character
HOME*2	Move cursor to upper left corner
UP*2	Move cursor up 1 line
File Status:	
Cstat*10	Curve fitting file status (STORED)
Dstat*10	Derivative spectrum status (STORED)
DATE(2)*8	Date (mm/dd/yy)
Fstat*10	Edited spectrum status (VALID, STORED)
LABEL(2)*72	Descriptor of spectrum
Pstr(49,16)*14	Table of parameter setting names
Einc*4	Step size interval (nm) - edited spectrum
Emax*4	Starting wavelength (nm) - edited spectrum
Emin*4	Ending wavelength (nm) - edited spectrum
Sinc*4	Step size interval (nm)
Smax*4	Spectrum starting wavelength (nm)
Smin*4	Spectrum ending wavelength (nm)
Sname(2)*20	Spectrum pathname, CI convention
Sstat(2)*10	Spectrum status (VALID, INVALID)

/...

...cont'd

Program Control:

C	Literal comma ','
Code	Menu selection, valid until reset
Directory*40	User directory name, CI convention
Dtype	Type of derivative spectrum (F or S)
Filespec*63	Full pathname for file retrieval or storage
Fit(5)*2	Number of points used by fitting algorithm
Fname*20	Filename entry for building Filespec
Icode	General purpose selection key entry
HEADER*72	Combined file label for data storage
Pfit*10	Literal 'POINTS FIT'
String*14	String to pass data to or from subroutines
TITLE*72	String to be printed to screen
Ymode	Disk file ordinate mode - (A or T)

```
 1 FTN7X,L
 2 $FILES 0,1
 3 $EMA/DATA/
 4       PROGRAM EDITSPEC
 5 C     ------------------------------------------------------------------
 6 C
 7 C     This Program Is Designed To Edit Spectral Data Acquired From
 8 C     The CARY 2390 UV-VIS-NIR Spectrophotometer With CARYSPEC.RUN
 9 C
10 C     The Program Provides Essential Features For Removing Artifacts
11 C     From Experimental Data With Commands For Editing Single Points,
12 C     Offsetting Large Wavelength Regions And Rescaling Near IR Data
13 C     To Correct Mismatch Between The PbS And PM Tube Detectors. The
14 C     Program Also Provides Least Squares Routines For Calculation Of
15 C     Smoothed, First Derivative And Second Derivative Spectra.
16 C
17 C     ------------------------------------------------------------------
18 C
19 C         AUTHOR:  Dr. Robert A. Binstead,
20 C                  Chemistry Division, Code 6125,
21 C                  Naval Research Laboratory,
22 C                  Washington. D.C. 20375
23 C                  U.S.A.
24 C
25 C         WRITTEN: March, 1987
26 C
27 C         VERSION: 1.8
28 C
29 C         REVISED: April, 1987  - Improved Smoothing Routine To Allow
30 C                                 For Multiple Data Steps Between The
31 C                                 Abscissa Points In Each Fit.
32 C                               - Added First And Second Derivative
33 C                                 Spectrum Routines Based On The Same
34 C                                 Quadratic Polynomial Routine.
35 C
36 C                  May,   1987  - Added File Size Reduction Routine
37 C                                 To Enable Exact Matching Of Spectra
38 C                                 For Difference Plotting Mode In The
39 C                                 Program PLOTSPEC
40 C
41 C                  June,  1987  - Modified File Name Convention To
42 C                                 Match The Use Of Directories By
43 C                                 The CI Operating System
44 C
45 C                  August,1987  - Added Data File Creation Routine
46 C                                 For BANDPLOT Curve Fitting Of
47 C                                 Multiple Gaussians To Spectrum
48 C
49 C                  October,1987 - Added Baseline Correction Routine
50 C                                 For Point By Point Subtraction Of
51 C                                 A Second File
52 C                               - Added A NIR Scaling Routine To
53 C                                 Match Reflectance Data From The PbS
```

```
C                                And PM Tube Detectors At 800 nm
C
C                     January,1988 - Added Upper Case Conversion Routine
C                                    To Permit Case Insensitive Input
C
C                     May, 1988    - Revised Data File Creation Routine
C                                    To Use The Simpler (X,Y) Format
C                                    Required By BANDFIT, An Interactive
C                                    Version Of The Old BANDPLOT Program
C                                  - Removed Unused Block Data & Arrays
C                                    Removed Unused Variables & Trimmed
C                                    Down String Data Arrays
C                                  - Added Facility To Edit Data Files
C                                    Collected In % Transmission Mode
C
C                     June, 1988   - Added 25 Point Algorithm To The
C                                    Smoothing & Derivative Routines
C
C          Y-AXIS:  Absorbance
C
C          X-AXIS:  Wavelength
C
C          MEMORY:  30,000 Words (PROGRAM) + 98,000 Words EMA (DATA)
C
C     ------------------------------------------------------------------
C
      INTEGER COUNT,CURFILE,EDIT,EXIT,FINISH,IS,ITEST,MENU
      INTEGER NCOL,NDATA,NFIT,NPASS,ND(2),NPTS(5),NP,NV,PARAM(2,49)
      INTEGER READ,SETTINGS,START,STORE,XOFF,XX
      REAL*8 CC(5,7),SS(5),YY
      REAL BAND,EC,FIRST,GAIN,LAST,NUMBER,PMIN,PMAX,RANGE
      REAL SPACE,STEP,VARIABLE(2,14),W,WL,WN,WX,WOFF,Y1,Y2,YOFF,ZM
      REAL ABSC(2),CELL(2),CONC(2),CYCLE(2),DIST(2),ORD(2),PATH(2)
      REAL SAMPLE(2),TIMER(2),TEMP(2),WAVE(2),XMIN(2),XMAX(2),XSTEP(2)
      REAL X(10001),Y(10001),XB(10001),YB(10001),Z(10001)
      LOGICAL DERIV,MATCH
C
C         Dimension Screen Control String Variables
C
      CHARACTER BELL,CLR*2,DOWN*2,ERASE*2,ESC,HOME*2,UP*2
C
C         Dimension Program Parameter Variables
C
      CHARACTER Cstat*10,Dstat*10,Fstat*10,Sstat(2)*10
      CHARACTER Directory*40,Filespec*63,Fname*20,Sname(2)*20
      CHARACTER Smin*4,Smax*4,Sinc*4,Emin*4,Emax*4,Einc*4
      CHARACTER C,Code,DATE(2)*8,Dtype,Fit(5)*2,HEADER*72,Icode
      CHARACTER INITIALS*2,LABEL(2)*72,Pcode*2,Pfit*10,Pstr(49,16)*14
      CHARACTER String*14,TITLE*72,Ymode
C
C     ------------------------------------------------------------------
C
      COMMON /DATA/X,Y,XB,YB,Z
```

```
C
C     ---------------------------------------------------------------
C
C         Smoothing & Derivative Routine Constants For Quartic Fit
C
C         Smoothing      : J = 1,3,5
C         1st Derivative : J = 2,4
C         2nd Derivative : J = 3,6,7
C
C         I : Segment Size : Abscissa Range : Steps : Data Range
C                                             (MIN=1)
C         1          7          -3,...,+3        X     -3X,...,+3X
C         2         11          -5,...,+5        X     -5X,...,+5X
C         3         15          -7,...,+7        X     -7X,...,+7X
C         4         21         -10,...,+10       X    -10X,...,+10X
C         5         25         -12,...,+12       X    -12X,...,+12X
C
C         Smoothing Of Experimental Spectra Is Almost Universally
C         Performed Using A Polynomial Least Squares Approximation
C         Within Small Data Intervals, Stepped Consecutively Across
C         The Spectrum. The Technique Must Be Applied Intelligently
C         Since No Significant Smoothing Will Occur If The Size Of
C         The Smoothing Segments Is Smaller Than The Period Of The
C         Noise. This Is A Particular Danger With Spectra From The
C         Cary 2390, Where Data Are Often Acquired In Small Steps.
C
C         This Program Utilizes Two Complementary Approaches To
C         Increase The Wavelength Interval Of The Fitted Segments.
C         The First Includes More Data Points Within The Segment With
C         Choices Of 7,11,15,21 & 25 Point Quartic Polynomial Fits To
C         Provide Increasing Levels Of LOCAL Averaging. The Second
C         Method Utilizes Multiple Data Steps Between Each Point In
C         The Fitted Segments, Allowing For Arbitrarily Wide GLOBAL
C         Averaging.
C
C         Random Noise Of Shorter Period Than The Fitted Segments Is
C         Well Filtered By The Smoothing Routine. However, Non-Random
C         Noise Can Produce Sinusoidal Smoothed Spectra. One Means Of
C         Suppressing These Anomalies Is To Apply Several Cycles Of
C         Smoothing, Each With A Different Segment Size Or With A
C         Different Number Of Data Points In The Fits. Small Regions
C         Of Non-Random Artifacts Are Best Removed Using A Large Step
C         Size And Large Number Of Fitted Points For Just That Region
C         Followed By Smoothing The Whole Spectrum With Unit Step Size.
C
C         The Use Of Polynomial Curve Fitting For First & Second
C         Derivative Spectra Is Subject To Digitizing Noise With
C         Data Segments Which Cover Only A Small Wavelength Range.
C
C         The 7,11,15,21 & 25 Point Algorithms Provide Increasing
C         Levels Of Smoothing At The Expense Of Spectral Resolution.
C         This Should Not Be A Problem As Data Are Usually Acquired
C         At Very Small Increments (Large Redundancy). However, The
```

```
C         Larger Range Algorithms Tend To Produce A Sinusoidal Fit,
C         Resulting In Very Strange Second Derivative Spectra. This
C         Can Be Largely Eliminated By Use Of A Minimum Of 2 Data
C         Points Between Fitting Points, While Stepping The Routine
C         1 Data Point At A Time Across The Spectrum.
C
C         A Benefit Of Increased Spacing Between Abscissa Values Is
C         Better Averaging - This Also Reduces Spectral Resolution
C         But Is Still Far Better Than ANALOG Derivative Spectra.
C
C         It Is Recommended That Smoothed, First & Second Derivative
C         Spectra Be Obtained With Increasing Step Size, e.g. 2:4:8,
C         Since Greater Averaging Is Required For The Derivatives.
C
C         A Typical Broad Solution Spectrum Will Require A Fitting
C         Segment Of 25 nm To Be Effective For Second Derivatives.
C         The User Must Decide Which Algorithm & Step Multiple Is
C         Most Appropriate For The Particular Spectrum But A General
C         Guideline Is To Select A Fitting Interval In Which There
C         Is A Significant Change In Absorbance Or Slope.
C
C     ------------------------------------------------------------
      DATA (NPTS(I),I=1,5)/7,11,15,21,25/
      DATA (CC(1,J),J=1,7)/5.6709956709957D-1,2.6256613756614D-1,
     &-2.6515151515151D-1,-3.2407407407407D-2,2.2727272727273D-2,
     &2.1433080808081D-1,-2.1148989898990D-2/
C     ------------------------------------------------------------
      DATA (CC(2,J),J=1,7)/3.33333333333333D-1,6.0379435379435D-2,
     &-5.5361305361305D-2,-2.8813778813779D-3,1.7482517482517D-3,
     &1.6341297591298D-2,-6.0703185703186D-4/
C     ------------------------------------------------------------
      DATA (CC(3,J),J=1,7)/2.395159020546D-1,2.3045899271389D-2,
     &-2.0648855788175D-2,-5.8306798502877D-4,3.4099027907077D-4,
     &3.1838914869101D-3,-6.2206670178806D-5/
C     ------------------------------------------------------------
      DATA (CC(4,J),J=1,7)/1.6923254427629D-1,8.2485070089952D-3,
     &-7.3024633194239D-3,-1.0562014757286D-4,6.0573428456051D-5,
     &5.6541148461326D-4,-5.5661610043088D-6/
C     ------------------------------------------------------------
      DATA (CC(5,J),J=1,7)/1.4169580127478D-1,4.8623545000357D-3,
     &-4.2895207765503D-3,-4.3823594548232D-5,2.4987497756926D-5,
     &2.3322878661008D-4,-1.6138972424588D-6/
C
C     ------------------------------------------------------------
C
C         Initialize String Variables
C
C     ------------------------------------------------------------
C
      DATA (Pstr(1,I),I=1,6)/'ABSORBANCE','% TRANSMISSION',
     &'TEMPERATURE','% REFLECTANCE','CONCENTRATION','EMISSION'/
      DATA (Pstr(2,I),I=1,4)/'WAVELENGTH','TIME','TEMPERATURE',
     &'DISTANCE'/
```

```
213       DATA (Pstr(3,I),I=1,11)/'OFF','0.01','0.02','0.05','0.1','0.2',
214      &'0.5','1.0','2.0','5.0','10.0'/
215       DATA Pstr(4,1)/'OFF'/
216       DATA (Pstr(4,I),I=6,15)/'0.2','0.5','1.0','2.0','5.0',
217      &'10','20','50','100','200'/
218       DATA (Pstr(5,I),I=1,4)/'AUTO SELECT','AUTO GAIN','AUTO SLIT',
219      &'SINGLE BEAM'/
220       DATA (Pstr(6,I),I=1,5)/'OFF','NORMAL','1ST DERIV','2ND DERIV',
221      &'LOG'/
222       DATA (Pstr(7,I),I=1,9)/'0.01','0.02','0.05','0.1','0.2','0.5',
223      &'1.0','2.0','4.0'/
224       DATA (Pstr(8,I),I=10,16)/'2','5','10','20','50','100','200'/
225       DATA (Pstr(9,I),I=12,15)/'10','20','50','100'/
226       DATA (Pstr(10,I),I=1,5)/'-1.9 TO 0.6','-2.0 TO 0.5',
227      &'-2.1 TO 0.4','-2.2 TO 0.3','-2.3 TO 0.2'/
228       DATA (Pstr(11,I),I=1,16)/'+/-0.01','+/-0.02','+/-0.05','+/-0.1',
229      &'+/-0.2','+/-0.5','+/-1.0','+/-2.0','+/-5.0','+/-10','+/-20',
230      &'+/-50','+/-100','+/-200','+/-500','+/-1000'/
231       DATA (Pstr(12,I),I=1,16)/'+/-0.01','+/-0.02','+/-0.05','+/-0.1',
232      &'+/-0.2','+/-0.5','+/-1.0','+/-2.0','+/-5.0','+/-10','+/-20',
233      &'+/-50','+/-100','+/-200','+/-500','+/-1000'/
234       DATA (Pstr(13,I),I=1,8)/'+/-0.01','+/-0.02','+/-0.05','+/-0.1',
235      &'+/-0.2','+/-0.5','+/-1.0','+/-2.0'/
236       DATA (Pstr(14,I),I=1,10)/'0','10','20','30','40','50','60','70',
237      &'80','90'/
238       DATA (Pstr(15,I),I=1,4)/'0.5','1.0','3.0','10'/
239       DATA (Pstr(16,I),I=1,2)/'NORMAL','REVERSE'/
240       DATA (Pstr(17,I),I=1,2)/'OFF','ON'/
241       DATA (Pstr(18,I),I=1,2)/'REPEAT SCAN','SGL/MULTI'/
242       DATA (Pstr(19,I),I=1,2)/'SERIAL','OVERLAY'/
243       DATA (Pstr(20,I),I=1,4)/'BOTH ON','UV ONLY','VIS/NIR ONLY',
244      &'BOTH OFF'/
245       DATA (Pstr(21,I),I=1,3)/'AUTO','UV','VIS/NIR'/
246       DATA (Pstr(22,I),I=1,3)/'AUTO','UV','VIS/NIR'/
247       DATA (Pstr(23,I),I=1,2)/'FULL','1/3'/
248       DATA (Pstr(24,I),I=1,3)/'AUTO','UV/VIS','NIR'/
249       DATA (Pstr(25,I),I=1,3)/'AUTO','UV','VIS/NIR'/
250       DATA (Pstr(26,I),I=1,4)/'AUTO SELECT','AUTO GAIN','AUTO SLIT',
251      &'SINGLE BEAM'/
252       DATA (Pstr(27,I),I=1,2)/'FULL','1/3'/
253       DATA (Pstr(28,I),I=1,6)/'0','1','2','3','4','5'/
254       DATA (Pstr(29,I),I=1,2)/'STANDARDS','UNKNOWNS'/
255       DATA (Pstr(30,I),I=3,6)/'DIRECT','LINEAR','DIRECT-QUAD',
256      &'QUADRATIC'/
257       DATA (Pstr(31,I),I=7,8)/'NORMAL','AVERAGED'/
258       DATA (Pstr(32,I),I=9,13)/'SIGNAL AV','SAMPLE AV','QUICK',
259      &'EXTENDED','FIXED'/
260       DATA (Pstr(33,I),I=1,5)/'DSPL RESULTS','DSPL SETUP','NEXT CONC',
261      &'DELETE SAMPLE','CLEAR RESULTS'/
262       DATA (Pstr(34,I),I=1,2)/'OFF','ON'/
263       DATA (Pstr(35,I),I=1,2)/'1','2'/
264       DATA (Pstr(38,I),I=1,5)/'  OFF','  ON','RECORD',' ','ON/SETUP'/
265       DATA (Pstr(40,I),I=1,2)/'INTERVAL','ACCY-DRIVEN'/
```

```
C
      DATA (Fit(I),I=1,5)/' 7','11','15','21','25'/
C
      Pfit=' POINT FIT'
      BELL=CHAR(7)
      ESC=CHAR(27)
      CLR=ESC//'J'
      HOME=ESC//'h'
      UP=ESC//'A'
      DOWN=ESC//'B'
      ERASE=ESC//'K'
C
C     ---------------------------------------------------------------
C
C         Assign Statement Labels
C
C     ---------------------------------------------------------------
C
      ASSIGN 10  TO MENU
      ASSIGN 100 TO READ
      ASSIGN 300 TO SETTINGS
      ASSIGN 400 TO EDIT
      ASSIGN 1000 TO STORE
      ASSIGN 2000 TO CURFILE
      ASSIGN 9999 TO EXIT
C
C     ---------------------------------------------------------------
C
C         Data Transfer And Edit Control Menu
C
C     ---------------------------------------------------------------
C
      CALL FFRCL(79)                          ! Eliminate Line Wrap
   10 WRITE (1,*) HOME,CLR,'_'
      NCOL=70
      TITLE='Cary 2390'
      CALL Center(TITLE)
      TITLE='Spectral Data Editing'
      CALL Center(TITLE)
      WRITE (1,'(T61,A2,A8)') UP,'Rev: 1.8'
      CALL Line(NCOL)
      WRITE (1,20) 'CODE','FUNCTION','STATUS','MIN','MAX','INC'
   20 FORMAT (T4,A4,T18,A8,T38,A7,T50,A3,T58,A3,T66,A3)
      CALL Line(NCOL)
      WRITE (1,30) 'R','.....Read Spectrum.....',Sstat(1),
     &Smin,Smax,Sinc
      WRITE (1,40) 'I','.....Instrument Setti..gs.....',Sname(1)
      WRITE (1,30) 'E','.....Edit Spectrum.....',Fname,
     &Emin,Emax,Einc
      WRITE (1,50) 'S','.....Store Spectrum.....',Fstat
      WRITE (1,50) 'D','.....Store Derivative.....',Dstat
      WRITE (1,50) 'C','.....Store Curve Fit File....',Cstat
      WRITE (1,60) 'X','.....EXIT Menu.....'
```

```
319     30 FORMAT (/,T6,A,T7,A30,T39,A10,T50,A4,T58,A4,T66,A4)
320     40 FORMAT (/,T6,A,T7,A30,T39,A20)
321     50 FORMAT (/,T6,A,T7,A30,T39,A10)
322     60 FORMAT (/,T6,A,T7,A30)
323        WRITE (1,*)
324        CALL Line(NCOL)
325        WRITE (1,*)
326     70 WRITE (1,*) UP,ERASE,'_'
327        WRITE (1,'(T3,A15,A,A2)') 'Enter the CODE:',BELL,'_'
328        READ (1,80) Code
329        CALL Upper(Code)
330        IF (Code.EQ.'R') GO TO READ
331        IF (Code.EQ.'I') GO TO SETTINGS
332        IF (Code.EQ.'E') GO TO EDIT
333        IF (Code.EQ.'S') GO TO STORE
334        IF (Code.EQ.'D') GO TO STORE
335        IF (Code.EQ.'C') GO TO CURFILE
336        IF (Code.EQ.'X') GO TO EXIT
337        GO TO 70
338     80 FORMAT (A1)
339     90 FORMAT (A14)
340 C
341 C      ---------------------------------------------------------------
342 C
343 C          Read Spectrum
344 C
345 C      ---------------------------------------------------------------
346 C
347    100 TITLE='Read Spectrum'
348        J=1
349        IF (Sstat(1).NE.'VALID') GO TO 120
350    110 WRITE (1,*) UP,ERASE,'  Spectrum is PRESENT: ',
351       &'N...New Spectrum, B...Baseline, Q...Quit ? ',BELL,'_'
352        READ (1,80) Icode
353        CALL Upper(Icode)
354        IF (Icode.EQ.'Q') GO TO 70
355        IF (Icode.EQ.'N') GO TO 120
356        IF (Icode.NE.'B') GO TO 110
357        IF (Sstat(2).EQ.'VALID') THEN
358          WRITE (1,*) UP,ERASE,'  Baseline SUBTRACTED: ',BELL
359          CALL Wait (2.0)
360          GO TO 110
361        END IF
362        TITLE='Subtract Baseline'
363        J=2
364    120 WRITE (1,*) HOME,CLR,'_'
365        CALL Center(TITLE)
366        CALL Line(NCOL)
367        WRITE (1,*) DOWN,'  Enter Filename: ',BELL,'_'
368        READ (1,'(A20)') Sname(J)
369        WRITE (1,*) DOWN,'  Directory, (RETURN = /DEFAULT/): ',BELL,'_'
370        READ (1,'(A40)') Directory
```

```
371       IF (Directory.EQ.' ') THEN
372         Filespec=Sname(J)
373         GO TO 130
374       END IF
375       K=40
376       DO WHILE (Directory(K:K).EQ.' ')
377         K=K-1
378       END DO
379       Filespec=Directory(1:K)//'/'//Sname(J)
380   130 K=63
381       DO WHILE (Filespec(K:K).EQ.' ')
382         K=K-1
383       END DO
384       WRITE (1,*) UP,ERASE,'  Validating: ',Filespec(1:K),' _'
385       CALL Wait(1.0)
386       OPEN (UNIT=66,FILE=Filespec(1:K),IOSTAT=N,STATUS='OLD')
387       WRITE (1,*)
388       IF (N.NE.0) THEN
389         N=N-500
390         WRITE (1,*) UP,ERASE,'_'
391         IF (N.EQ.6) WRITE (1,*) ' File does NOT EXIST: ',BELL,'_'
392         IF (N.EQ.8) WRITE (1,*) ' File is already OPEN: ',BELL,'_'
393         IF ((N.NE.6).AND.(N.NE.8)) WRITE (1,*) ' Disk Error # ',N,
394      &  BELL,'_'
395         CALL Wait(2.0)
396         WRITE (1,*)
397         IF (J.EQ.1) Sstat(J)='INVALID'
398         GO TO MENU
399       END IF
400       Fname=' '                    ! New File Opened So Erase Any
401       Emin=' '                     ! Previous Descriptors For
402       Emax=' '                     ! A Valid Edited Spectrum
403       Einc=' '
404       Sstat(2)=' '
405       WRITE  (1,*) UP,ERASE,'  Reading File: ',Filespec(1:K),BELL
406       READ (66,FMT=140,IOSTAT=N,ERR=230) LABEL(J)
407   140 FORMAT (A72)
408       WRITE (1,*) DOWN,'  Title: '
409       WRITE (1,*) '  ',LABEL(J)
410       READ (66,FMT=150,IOSTAT=N,ERR=230) DATE(J)
411   150 FORMAT (A8)
412       WRITE (1,*) DOWN,'  Date: ',DATE(J)
413       READ (66,*,IOSTAT=N,ERR=230) XMIN(J),XMAX(J),XSTEP(J),CONC(J),
414      &PATH(J)
415       READ (66,*,IOSTAT=N,ERR=230) ORD(J),ABSC(J),CELL(J),CYCLE(J),
416      &SAMPLE(J),WAVE(J),TIMER(J),TEMP(J),DIST(J)
417       WRITE (1,160) DOWN,'Scan Range: ',XMAX(J),' to ',XMIN(J),
418      &' nm at ',XSTEP(J),' nm steps'
419       WRITE (1,'(T4,A2,A12,2X,G9.4)') DOWN,'Conc. (M) : ',CONC(J)
420       WRITE (1,170) DOWN,'Path (cm) : ',PATH(J)
421       WRITE (1,170) DOWN,'Temp. (C) : ',TEMP(J)
422   160 FORMAT (T4,A2,A12,F6.2,A4,F6.2,A7,F4.2,A9)
423   170 FORMAT (T4,A2,A12,F6.2)
```

```
      READ (66,FMT=180,IOSTAT=N,ERR=230) NP,NV,ND(J)
  180 FORMAT (I3,I3,I6)
      IF ((NP.NE.49).OR.(NV.NE.14)) GO TO 220     ! Data Format Error
      WRITE (1,*)
      IF (ABS(XMIN(J)-WAVE(J)).GT.0.2) THEN
        WRITE (1,*) '  Scan ended at',WAVE(J),' nm',BELL
        CALL Wait(2.0)
        WRITE (1,*) UP,ERASE,UP,UP
      END IF
      WRITE (1,*) HOME,'_'
      TITLE='### READING DATAFILE ###'
      CALL Center(TITLE)
      READ (66,FMT=190,IOSTAT=N,ERR=230) (PARAM(J,K),K=1,NP)
  190 FORMAT (I2)
      READ (66,*,IOSTAT=N,ERR=230) (VARIABLE(J,K),K=1,NV)
      NDATA=ND(1)
      IF (J.EQ.1) THEN
        READ (66,*,IOSTAT=N,ERR=230) (Y(I),I=1,NDATA)
        READ (66,*,IOSTAT=N,ERR=230) (X(I),I=1,NDATA)
        WMIN=XMIN(J)
        WMAX=XMAX(J)
        STEP=XSTEP(J)
        CALL Str(WMIN,String,4)
        Smin=String(2:5)
        CALL Str(WMAX,String,4)
        Smax=String(2:5)
        CALL Str(STEP,String,4)
        Sinc=String(2:5)
        Sstat(J)='VALID'
        IF (PARAM(1,1).EQ.0) THEN
          Ymode='A'                 ! Ordinate Mode = ABSORBANCE
        ELSE
          Ymode='T'                 ! Ordinate Mode = TRANSMISSION
        END IF
        GO TO 210                   ! Close Spectrum File
      END IF
C     ------------------------------------------------------------
C         Test For Baseline Matching
C     ------------------------------------------------------------
      MATCH=.TRUE.
      IF (XMIN(1).LT.XMIN(2)) MATCH=.FALSE.
      IF (XMAX(1).GT.XMAX(2)) MATCH=.FALSE.
      IF (XSTEP(1).NE.XSTEP(2)) MATCH=.FALSE.
      IF (PARAM(1,1).NE.PARAM(2,1)) MATCH=.FALSE.
      IF (PARAM(1,5).NE.PARAM(2,5)) MATCH=.FALSE.
      IF (PARAM(1,16).NE.PARAM(2,16)) MATCH=.FALSE.
      IF (PARAM(1,21).NE.PARAM(2,21)) MATCH=.FALSE.
      IF (PARAM(1,22).NE.PARAM(2,22)) MATCH=.FALSE.
      IF (PARAM(1,23).NE.PARAM(2,23)) MATCH=.FALSE.
      IF (PARAM(1,38).NE.PARAM(2,38)) MATCH=.FALSE.
      IF (.NOT.MATCH) GO TO 240
C     ------------------------------------------------------------
C         Read Entire Baseline File
```

```
C     ------------------------------------------------------------
      READ (66,*,IOSTAT=N,ERR=230) (YB(I), I=1,ND(2))
      READ (66,*,IOSTAT=N,ERR=230) (XB(I), I=1,ND(2))
C     ------------------------------------------------------------
C         Match Baseline Index To Starting Wavelength Of Spectrum
C     ------------------------------------------------------------
      START=0
      IF (WMAX.LT.XMAX(2)) THEN
        START=NINT((XMAX(2)-WMAX)/XSTEP(2))
      END IF
      DO 200 I=1,NDATA                  ! Subtract Relevant Wavelength
        K=I+START                       ! Region Of Baseline File :-
        IF (Ymode.EQ.'A') THEN          ! Absorbance Mode
          Y(I)=Y(I)-YB(K)               !   SUBTRACT BASELINE DATA
        ELSE                            ! Transmission Mode
          Y(I)=(Y(I)/YB(K))*100.0       !   RATIO TO BASELINE DATA
        END IF                          ! NB: You Can't READ & SUBTRACT
  200 CONTINUE                          ! With The Implied DO LOOP FORM
      Sstat(J)='VALID'                  ! Set Baseline To VALID
  210 CLOSE (UNIT=66,IOSTAT=N,ERR=230)
      COUNT=0                           ! Zero Smoothing Cycle Counter
      J=1                               ! Select Spectrum Mode Before
      GO TO MENU                        ! Returning To Main Menu
C     ------------------------------------------------------------
  220 WRITE (1,*) UP,ERASE,'  Data Format Error: ',BELL,'_'
      Sstat(J)='ABORTED'
      GO TO 250
  230 WRITE (1,*) UP,ERASE,'  Disk Error #',N,BELL,' _'
      Sstat(J)='INVALID'
      GO TO 250
  240 WRITE (1,*) UP,ERASE,'  Baseline Mismatch Error: ',BELL,'_'
  250 CALL Wait(2.0)
      WRITE (1,*)
      GO TO 210
  260 WRITE (1,*) UP,ERASE,'  Spectrum is ABSENT: ',BELL,'_'
      CALL Wait(2.0)
      WRITE (1,*)
      GO TO 70
C
C     ------------------------------------------------------------
C
C         Display Instrument Settings
C
C     ------------------------------------------------------------
C
  300 IF (Sstat(1).NE.'VALID') GO TO 260
      IF (Sstat(2).EQ.'VALID') THEN
        WRITE (1,*) UP,ERASE,'  S...Spectrum or B...Baseline ? ',
     &  BELL,'_'
        READ (1,80) Icode
        CALL Upper(Icode)
        J=1
        IF (Icode.EQ.'B') J=2
```

```
530       END IF
531       BAND=VARIABLE(J,10)
532       GAIN=VARIABLE(J,6)
533       CALL Val(Pstr(7,PARAM(J,7)+1),PMAX)
534       PMIN=VARIABLE(J,1)
535       IF (PARAM(J,1).NE.0) THEN
536         CALL Val(Pstr(8,PARAM(J,8)+1),PMAX)
537         PMIN=VARIABLE(J,11)
538       END IF
539       PMAX=PMIN+PMAX
540       K=11
541       IF (PARAM(J,6).EQ.4) K=10
542       String=Pstr(K,PARAM(J,K)+1)
543       WRITE (1,*) HOME,CLR,'_'
544       TITLE='Instrument Settings'
545       CALL Center(TITLE)
546       CALL Line(50)
547       WRITE (1,'(T20,A8,T40,A7)') 'FUNCTION','SETTING'
548       CALL LINE(50)
549       WRITE (1,*)
550       WRITE (1,320) 'WAVELENGTH LIMITS.....',
551      &XMIN(J),',',XMAX(J)
552       WRITE (1,330) 'ORDINATE..............',
553      &Pstr(1,PARAM(J,1)+1)
554       WRITE (1,330) 'ABSCISSA..............',
555      &Pstr(2,PARAM(J,2)+1)
556       WRITE (1,330) 'SCAN RATE (nm/sec).....',
557      &Pstr(3,PARAM(J,3)+1)
558       WRITE (1,330) 'CHART DISPLAY (nm/cm)..',
559      &Pstr(4,PARAM(J,4)+1)
560       WRITE (1,330) 'REFERENCE MODE.........',
561      &Pstr(5,PARAM(J,5)+1)
562       WRITE (1,340) 'SBW (nm), GAIN.........',
563      &BAND,',',GAIN
564       WRITE (1,330) 'PEN FUNCTION...........',
565      &Pstr(6,PARAM(J,6)+1)
566       WRITE (1,340) 'PEN LIMITS (Min,Max)...',
567      &PMIN,',',PMAX
568       IF (PARAM(J,6).GT.1) WRITE (1,350) UP,ERASE,String
569       WRITE (1,330) 'RESPONSE TIME (sec)....',
570      &Pstr(15,PARAM(J,15)+1)
571       WRITE (1,330) 'BEAM INTERCHANGE.......',
572      &Pstr(16,PARAM(J,16)+1)
573       WRITE (1,330) 'SLIT HEIGHT... ........',
574      &Pstr(23,PARAM(J,23)+1)
575       WRITE (1,330) 'LAMP SELECT............',
576      &Pstr(21,PARAM(J,21)+1)
577       WRITE (1,330) 'DETECTOR SELECT........',
578      &Pstr(22,PARAM(J,22)+1)
579   320 FORMAT (T15,A23,T40,F5.2,A,F5.2)
580   330 FORMAT (T15,A23,T40,A14)
581   340 FORMAT (T15,A23,T40,F4.2,A,F5.2)
582   350 FORMAT (T40,A2,A2,A14)
```

```
583         WRITE (1,*)
584         CALL Line(50)
585         WRITE (1,*)
586    360  WRITE (1,'(T14,A2,A2,A23,A,A)') UP,ERASE,
587        &'Press RETURN for MENU: ',BELL,'_'
588         READ (1,80) Icode
589         CALL Upper(Icode)
590         IF (Icode.NE.' ') GO TO 360
591         GO TO MENU
592 C
593 C       ---------------------------------------------------------------
594 C
595 C           Edit Spectral File Parameters
596 C
597 C       ---------------------------------------------------------------
598 C
599    400  IF (Sstat(1).NE.'VALID') GO TO 260
600         WRITE (1,*) HOME,CLR,'_'
601         TITLE='Edit Spectral Parameters'
602         CALL Center(TITLE)
603         CALL Line(40)
604         WRITE (1,*)
605         WRITE (1,410) 'C .....Concentration, (M)'
606         WRITE (1,410) 'D .....Date, (MM/DD/YY)   '
607         WRITE (1,410) 'L .....Label, (72 chars) '
608         WRITE (1,410) 'P .....Pathlength, (cm)   '
609         WRITE (1,410) 'S .....Spectral Data      '
610         WRITE (1,410) 'X .....EXIT to Menu       '
611    410  FORMAT (T24,A25,/)
612         CALL Line(40)
613         WRITE (1,*)
614    420  WRITE (1,430) UP,ERASE,'_'
615    430  FORMAT (T19,A2,A2,A)
616         WRITE (1,'(A17,A,A)') ' Enter the CODE: ',BELL,'_'
617         READ (1,80) Icode
618         CALL Upper(Icode)
619         IF (Icode.EQ.'C') GO TO 440
620         IF (Icode.EQ.'D') GO TO 460
621         IF (Icode.EQ.'L') GO TO 470
622         IF (Icode.EQ.'P') GO TO 480
623         IF (Icode.EQ.'S') GO TO 500
624         IF (Icode.EQ.'X') GO TO MENU
625         GO TO 420
626 C       ---------------------------------------------------------------
627    440  WRITE (1,430) UP,ERASE,'_'
628         WRITE (1,*) 'Concentration,(M):  ',CONC(1)
629         WRITE (1,450) UP,BELL
630    450  FORMAT (T39,A2,A,'? _')
631         READ (1,90) String
632         IF (String.EQ.' ') GO TO 420
633         CALL Val(String,CONC(1))
634         CONC(1)=ABS(CONC(1))
635         GO TO 420
```

```
C     ------------------------------------------------------------------
  460 WRITE (1,430) UP,ERASE,'_'
      WRITE (1,*) 'Date, (MM/DD/YY):     ',DATE(1)
      WRITE (1,450) UP,BELL
      READ (1,150) String
      IF (String.EQ.' ') GO TO 420
      DATE(1)=String(1:8)
      GO TO 420
C     ------------------------------------------------------------------
  470 WRITE (1,*) UP,ERASE,'Label:',DOWN
      WRITE (1,'(A3,A72)') '   ',LABEL(1)
      WRITE (1,'(T4,A,T75,A)') '↑','↑'
      WRITE (1,*) UP,UP,BELL,'? _'
      READ (1,140) TITLE
      WRITE (1,*) ERASE,UP,ERASE,UP,UP,ERASE
      IF (TITLE.EQ.' ') GO TO 420
      LABEL(1)=TITLE
      GO TO 420
C     ------------------------------------------------------------------
  480 WRITE (1,430) UP,ERASE,'_'
      WRITE (1,490) 'Pathlength, (cm):   ',PATH(1)
  490 FORMAT (X,A20,X,F5.4)
      WRITE (1,450) UP,BELL
      READ (1,90) String
      IF (String.EQ.' ') GO TO 420
      CALL Val(String,PATH(1))
      PATH(1)=ABS(PATH(1))
      GO TO 420
C     ------------------------------------------------------------------
  500 TITLE='Edit Spectral Data'
      WRITE (1,*) HOME,CLR,'_'
      CALL Center(TITLE)
      CALL Line(40)
      WRITE (1,*)
      WRITE (1,510) 'L .....List Data Segment'
      WRITE (1,510) 'E .....Edit Single Datum'
      WRITE (1,510) 'O .....Offset Segment   '
      WRITE (1,510) 'N .....Near IR Rescale  '
      WRITE (1,510) 'R .....Reduce File Size '
      WRITE (1,510) 'S .....Smooth Segment   '
      WRITE (1,510) 'D .....Deriv. Spectra   '
      WRITE (1,510) 'X .....EXIT Data Editing'
  510 FORMAT (T26,A24,/)
      CALL Line(40)
      WRITE (1,*)
  520 WRITE (1,530) UP,ERASE,'_'
  530 FORMAT (T19,A2,A2,A)
      WRITE (1,540) ' Enter the CODE: ',BELL,'_'
  540 FORMAT (A17,A,A)
      READ (1,80) Code
      CALL Upper(Code)
      WRITE (',*) UP,ERASE,UP
```

```
      IF (Code.EQ.'L') GO TO 550
      IF (Code.EQ.'E') GO TO 630
      IF (Code.EQ.'O') GO TO 660
      IF (Code.EQ.'N') GO TO 660
      IF (Code.EQ.'R') GO TO 660
      IF (Code.EQ.'S') GO TO 740
      IF (Code.EQ.'D') GO TO 740
      IF (Code.NE.'X') THEN
        WRITE (1,*)
        GO TO 520
      END IF
      CALL Str(WMIN,String,4)
      Emin=String(2:5)
      CALL Str(WMAX,String,4)
      Emax=String(2:5)
      CALL Str(STEP,String,4)
      Einc=String(2:5)
      Fname='VALID'
      GO TO 400
C     ------------------------------------------------------------------
  550 WRITE (1,*) '  Scan Range: ',WMIN,' to',WMAX,' nm at',
     &STEP,' nm steps',DOWN,DOWN
  560 WRITE (1,*) UP,ERASE,'  DISPLAY Range: (MIN,MAX) ? ',BELL,'_'
      READ (1,*,ERR=560) WN,WX
      WN=ABS(WN)
      WX=ABS(WX)
      CALL Xlimits(WN,WX)
      IF ((WN.LT.WMIN).OR.(WN.GT.WMAX)) GO TO 560
      IF ((WX.LT.WMIN).OR.(WX.GT.WMAX)) GO TO 560
      START=NINT((WMAX-WX)/STEP)+1
      FINISH=NINT(NDATA-(WN-WMIN)/STEP)
      IF (Ymode.EQ.'A') THEN
        TITLE='Wavelength    Absorbance    Ext.Coeff. (/M/cm)'
      ELSE
        TITLE='Wavelength         % Transmission'
      END IF
      WRITE (1,*) HOME,CLR,'_'
      CALL Center(TITLE)
      CALL Line(50)
      L=1
      DO 580 I=START,FINISH
        WL=(WMAX-FLOAT(I-1)*STEP)          ! Calculated Wavelength
        EC=Y(I)/CONC(1)/PATH(1)            ! Extinction Coefficient
        WRITE (1,*)
        IF (Ymode.EQ.'A') THEN
          WRITE (1,590) X(I),Y(I),EC
        ELSE
          WRITE (1,600) X(I),Y(I)
        END IF
        L=L+1
        IF (L.EQ.10) THEN
          WRITE (1,*) DOWN
  570     WRITE (1,610) UP,ERASE,'Press RETURN to Continue ',BELL,'_'
```

```
741           READ (1,80) Icode
742           CALL Upper(Icode)
743           IF (Icode.NE.' ') GO TO 570
744           WRITE (1,*) HOME,CLR,'_'
745           CALL Center(TITLE)
746           CALL Line(50)
747           L=1
748         END IF
749   580 CONTINUE
750   590 FORMAT (T16,F7.2,T30,F7.4,T45,G10.4)
751   600 FORMAT (T22,F7.2,T41,F7.2)
752   610 FORMAT (T15,A2,A2,A25,A,A)
753       WRITE (1,*) DOWN
754   620 WRITE (1,610) UP,ERASE,'Press RETURN for MENU    ',BELL,'_'
755       READ (1,80) Icode
756       CALL Upper(Icode)
757       IF (Icode.NE.' ') GO TO 620
758       GO TO 500
759 C     ---------------------------------------------------------------
760   630 WRITE (1,*) '  Scan Range: ',WMIN,' to',WMAX,' nm at',
761      &STEP,' nm steps',DOWN,DOWN
762   640 WRITE (1,*) UP,ERASE,'  EDIT Wavelength: ? ',BELL,'_'
763       READ (1,*,ERR=640) WL
764       WL=ABS(WL)
765       IF ((WL.LT.WMIN).OR.(WL.GT.WMAX)) GO TO 640
766       I=NINT((WMAX-WL)/STEP)+1
767       WRITE (1,*) UP,ERASE,UP,UP,ERASE,'   Wavelength: ',X(I),' nm _'
768       WRITE (1,*) '(Expected:',(WMAX-FLOAT(I-1)*STEP),' nm)'
769       IF (Ymode.EQ.'A') THEN
770         String='ABSORBANCE:  _'
771       ELSE
772         String='% T or % R:  _'
773       END IF
774       WRITE (1,'(T5,A2,A14)') DOWN,String
775       WRITE (1,*) Y(I)
776   650 WRITE (1,'(T18,A2,A,A3)') UP,BELL,'? _'
777       READ (1,90) String
778       IF (String.EQ.' ') GO TO 500
779       CALL Val(String,NUMBER)
780       IF (Ymode.EQ.'A') THEN
781         IF ((NUMBER.LT.-0.5).OR.(NUMBER.GT.4.5)) GO TO 650
782       ELSE
783         IF ((NUMBER.LT.0.0).OR.(NUMBER.GT.200.0)) GO TO 650
784       END IF
785       Y(I)=NUMBER
786       GO TO 500
787 C     ---------------------------------------------------------------
788   660 WRITE (1,*) '  Scan Range: ',WMIN,' to',WMAX,' nm at',
789      &STEP,' nm steps',DOWN,DOWN
790       String='OFFSET'
791       K=6
792       IF (Code.EQ.'N') GO TO 700
```

```
      IF (Code.EQ.'R') THEN
        String='FILE'
        K=4
      END IF
  670 WRITE (1,*) UP,ERASE,'  ',String(1:K),' Range: (MIN,MAX) ? ',
     &BELL,'_'
      READ (1,*,ERR=670) WN,WX
      WN=ABS(WN)
      WX=ABS(WX)
      CALL Xlimits(WN,WX)
      IF ((WN.LT.WMIN).OR.(WN.GT.WMAX)) GO TO 670
      IF ((WX.LT.WMIN).OR.(WX.GT.WMAX)) GO TO 670
      START=NINT((WMAX-WX)/STEP)+1
      FINISH=NINT(NDATA-(WN-WMIN)/STEP)
      IS=1
C     ------------------------------------------------------------------
      IF (Code.EQ.'O') GO TO 700
  680 WRITE (1,*) UP,ERASE,'  STEP Multiplier: ? ',IS
      WRITE (1,'(T24,A2,A,A)') UP,BELL,'_'
      READ (1,90) String
      IF (String.NE.' ') THEN
        CALL Val(String,NUMBER)
        IS=NINT(NUMBER)
        IF (IS.GE.NDATA) GO TO 680
      END IF
      J=1
      DO 690 I=START,FINISH,IS
        X(J)=X(I)                          ! Reduced File Begins At
        Y(J)=Y(I)                          ! INDEX=1 - Old File Data
        J=J+1                              ! Is Written Over
  690 CONTINUE
      WAVE=X(FINISH)                       ! Update File Parameters
      ABSC=WAVE                            ! To Match Reduced File
      NDATA=(FINISH-START)/IS+1
      ND(1)=NDATA
      STEP=STEP*FLOAT(IS)
      WMAX=ANINT(X(1))
      WMIN=ANINT(X(NDATA))
      GO TO 500
C     ------------------------------------------------------------------
  700 YOFF=0.0
      IF (Code.EQ.'O') THEN
        String='Absorbance'
        IF (Ymode.EQ.'T') THEN
          String='% T or % R'
        END IF
        GO TO 710
      END IF
      IF ((PARAM(1,5).NE.0).OR.(WMIN.GE.800.0).OR.(WMAX.LE.800.0)) THEN
        WRITE (1,*) UP,ERASE,'  NIR/VIS Change Not Used: ',BELL,'_'
        CALL Wait(2.0)
        GO TO 500
      END IF
```

```
      String='NIR Region'
      START=1
      FINISH=NINT((WMAX-800.0)/STEP)+1
      YOFF=Y(FINISH+1)-Y(FINISH)  ! Offset At 800 nm Detector Change
  710 WRITE (1,720) UP,ERASE,String(1:10),' OFFSET:   ',YOFF
  720 FORMAT (T4,A2,A2,A10,A11,F7.4)
      WRITE (1,'(T24,A2,A,A3)') UP,BELL,'? _'
      READ (1,90) String
      IF (String.NE.' ') THEN
        CALL Val(String,YOFF)
      END IF
      IF (YOFF.EQ.0.0) GO TO 500
      IF (Code.EQ.'N') THEN
        Y2=Y(FINISH+1)              ! First Datum In Visible Region
        Y1=Y2-YOFF                  ! Final Datum In Near IR Region
      END IF
      DO 730 I=START,FINISH
        IF (Code.EQ.'O') Y(I)=Y(I)+YOFF
        IF (Code.EQ.'N') Y(I)=Y(I)*Y2/Y1
  730 CONTINUE
      GO TO 500
C
C     ---------------------------------------------------------------
C
C         Smooth Spectrum
C
C     ---------------------------------------------------------------
C
  740 TITLE='Smooth Spectrum'
      DERIV=.FALSE.
      IF (Code.EQ.'D') GO TO 880      ! Transfer To Derivative Setup
C     ---------------------------------------------------------------
  750 WRITE (1,*) HOME,CLR,'_'
      CALL Center(TITLE)
      CALL Line(NCOL)
      WRITE (1,*) DOWN,'  Select ALGORITHM:',DOWN
      DO 760 I=1,5
        WRITE (1,770) I,'.....',Fit(I),Pfit
  760 CONTINUE
  770 FORMAT (T25,I1,X,A5,X,A2,A10,/)
      I=6
      WRITE (1,'(T25,I1,X,A18)') I,'..... EXIT to Menu'
      WRITE (1,*) DOWN
  780 WRITE (1,790) UP,ERASE,'Enter the CODE # :  ',BELL,'_'
  790 FORMAT (T5,A2,A2,A20,A,A)
      READ (1,80) Icode
      L=ICHAR(Icode)-48
      IF ((L.LT.1).OR.(L.GT.6)) GO TO 780
      IF (L.EQ.6) GO TO 500
      WRITE (1,*) UP,ERASE,UP,UP,ERASE,UP,UP,ERASE,UP,UP,ERASE,UP,UP,
     &ERASE,UP,UP,ERASE,UP,UP,ERASE,UP,UP,ERASE
      WRITE (1,*) UP,'  ALGORITHM: ',Fit(L),Pfit,' (Quartic)'
```

```
C     ------------------------------------------------------------
C
C         Step Multiple Defaults To 2 For Improved Smoothing:
C
C         - The Smoothing Routine Increments 1 Datum Per Fit.
C         - If The Noise Is Non-Random, Increasing The Step Size May
C           Produce A Sinusoidal Approximation, Which Creates Very
C           Poor Second Derivative Spectra. Smooth Those Regions With
C           A Large Step Size To Average The Noise And Then With The
C           Step Size Reduced To 1 Datum To Eliminate Any Ripples.
C         - In General, Higher Multiples Of The Data Step Size Produce
C           Better Smoothing & MUCH BETTER Derivatives.
C
C     ------------------------------------------------------------
      IS=2
      RANGE=FLOAT(NPTS(L)-1)*STEP*FLOAT(IS)
      WRITE (1,*) DOWN,'  Default SEGMENT Size:',RANGE,' nm'
      WRITE (1,*) DOWN
      WRITE (1,*) UP,ERASE,'_'
      WRITE (1,'(X,A20,I1)') ' STEP Multiplier:    ',IS
      WRITE (1,'(T21,A2,A,A3)') UP,BELL,'? _'
      READ (1,90) String
      IF (String.EQ.' ') GO TO 800
      CALL Val(String,NUMBER)
      IS=NINT(NUMBER)
      IF (IS.LT.1) IS=1
      ITEST=(NDATA-1)/(NPTS(L)-1)
      IF (IS.GT.ITEST) IS=ITEST
  800 RANGE=FLOAT(NPTS(L)-1)*STEP*FLOAT(IS)
      WRITE (1,*) UP,ERASE,UP,UP,ERASE,'  Fitted SEGMENT Size:',
     &RANGE,' nm'
C
C     ------------------------------------------------------------
C
C                         LEAST SQUARES SMOOTHING
C                             OF DATA SEGMENT
C
C                         QUARTIC POLYNOMIAL FITS
C
C         X-INDEX:   -XX,...,0,...,+XX Allows For Simplification Of
C                    Least Squares Summations - Odd Powers = Zero
C
C         OFFSETS:   The Algorithm Can NOT Smooth The First Or Last
C                    (XX*IS) Number Of Points In The Spectrum
C
C         X-STEPS:   The Effectiveness Of The Smoothing Can Be Improved
C                    By Widening The Wavelength Interval Used By The
C                    Routine (Range =  IS*XX*STEP nm), Reducing The
C                    Spectral Resolution. The User Must Judge Which
C                    Algorithm & Step Multiplier (IS) Is Best Suited
C                    For The Particular Spectrum. The Minimum Step
C                    Size Is 1 Datum. This Is Adequate For Smoothing
C                    But NOT For Derivative Spectra.
```

```
C
C     ---------------------------------------------------------------
C
      WOFF=STEP*FLOAT(IS*(NPTS(L)-1)/2)          ! Wavelength Offset
      XOFF=(NPTS(L)+1)/2                         ! X-Index Offset+1
C     ---------------------------------------------------------------
      WRITE (1,*) DOWN,'  Scan Range: ',WMIN,' to',WMAX,' nm at',
     &STEP,' nm steps'
      WRITE (1,*) DOWN
      IF (DERIV) GO TO 910              ! Re-enter Derivative Routine
C     ---------------------------------------------------------------
  810 WRITE (1,*) UP,ERASE,'  SMOOTHING Range: (MIN,MAX) ',BELL,'_'
      READ (1,*,ERR=810) WN,WX
      WN=ABS(WN)
      WX=ABS(WX)
      CALL Xlimits(WN,WX)
      IF (WN.LT.WMIN+WOFF) WN=WMIN+WOFF
      IF (WX.GT.WMAX-WOFF) WX=WMAX-WOFF
      START=NINT((WMAX-WX)/STEP)+1
      FINISH=NINT(NDATA-(WN-WMIN)/STEP)
      WRITE (1,*) UP,ERASE,'  SMOOTHING Range: ',WN,' to',WX,' nm',
     &DOWN,DOWN
  820 WRITE (1,*) UP,ERASE,'  Total # of Smoothing PASSES: ',BELL,'_'
      READ (1,*,ERR=820) NPASS
      IF (NPASS.LT.1) GO TO 820
C     ---------------------------------------------------------------
      WRITE (1,*) DOWN
      DO 870 N=1,NPASS
        WRITE (1,*) UP,ERASE,'  Pass #',N,' in PROGRESS:',BELL
        DO 850 I=START,FINISH
          DO 830 J=1,5
            SS(J)=0.0                        ! Zero Summations Array
  830     CONTINUE
          DO 840 K=1,NPTS(L)
            XX=K-XOFF                        ! Segment Is (-XX,+XX):
            YY=DBLE(Y(I+XX*IS))              ! Step Size Is IS*STEP
            SS(1)=SS(1)+YY                   ! Calculate Summations
            SS(3)=SS(3)+YY*DBLE(XX**2)       ! For Least Squares Fit
            SS(5)=SS(5) YY*DBLE(XX**4)       ! Within Segment:
  840     CONTINUE
C     ---------------------------------------------------------------
C         Array CC Holds Known Least Squares Coefficients
C     ---------------------------------------------------------------
          YY=CC(L,1)*SS(1)+CC(L,3)*SS(3)+CC(L,5)*SS(5)
          Z(I)=SNGL(YY)                      ! Z(I) Is Smoothed Segment
  850   CONTINUE                             ! For Range Requested Only
        DO 860 I=START,FINISH
          Y(I)=Z(I)                          ! Update Y(I) With Z(I)
  860   CONTINUE
        COUNT=COUNT+1                        ! Update Total # Of Passes
  870 CONTINUE
      WRITE (1,*) UP,ERASE,'  Smoothing FINISHED: ',BELL,'_'
      CALL Wait(2.0)
```

```
1004        Fstat='SMOOTHED'
1005        IF (Code.EQ.'D') GO TO 900
1006        GO TO 500
1007 C
1008 C     ---------------------------------------------------------------
1009 C
1010 C         Derivative Spectrum Routine
1011 C
1012 C     ---------------------------------------------------------------
1013 C
1014    880 WRITE (1,*) HOME,CLR,'_'
1015        TITLE='Derivative Spectrum'
1016        CALL Center(TITLE)
1017        CALL Line(NCOL)
1018        WRITE (1,*) DOWN
1019    890 WRITE (1,*) UP,ERASE,'  SMOOTH Spectrum First, (Y or N) ? ',
1020       &BELL,'_'
1021        READ (1,80) Icode
1022        CALL Upper(Icode)
1023        IF (Icode.EQ.'Y') THEN
1024          DERIV=.FALSE.
1025          TITLE='Smooth Spectrum'
1026          GO TO 750
1027        END IF
1028        IF (Icode.NE.'N') GO TO 890
1029 C     ---------------------------------------------------------------
1030 C         1st Re-entry Point After Performing Smoothing Algorithm
1031 C     ---------------------------------------------------------------
1032    900 DERIV=.TRUE.
1033        TITLE='Derivative Spectrum'
1034        GO TO 750
1035 C     ---------------------------------------------------------------
1036 C         2nd Re-entry Point After Selecting Derivative Algorithm
1037 C     ---------------------------------------------------------------
1038    910 WN=WMIN+WOFF                        ! Set Limits For Calculation
1039        WX=WMAX-WOFF                        ! Of Derivative Spectrum
1040        START=NINT((WMAX-WX)/STEP)+1
1041        FINISH=NINT(NDATA-(WN-WMIN)/STEP)
1042    920 WRITE (1,*) UP,ERASE,'  FIRST or SECOND Derivative: (F or S) ?',
1043       &BELL,' _'
1044        READ (1,80) Icode
1045        CALL Upper(Icode)
1046        IF (Icode.EQ.'F') THEN
1047          String='FIRST'
1048          M=5
1049          ZM=10.0                           ! 1st Derivative Multiplier
1050          GO TO 930
1051        END IF
1052        IF (Icode.NE.'S') GO TO 920
1053        String='SECOND'
1054        M=6
1055        ZM=100.0                          ! 2nd Derivative Multiplier
1056 C     ---------------------------------------------------------------
```

```
1057    930 WRITE (1,*) UP,ERASE,'  Calculating ',String(1:M),' Derivative:',
1058       &BELL
1059 C      ------------------------------------------------------------------
1060         DO 970 I=START,FINISH
1061           DO 940 J=1,5
1062             SS(J)=0.0                          ! Zero Summations Array
1063    940    CONTINUE
1064           DO 950 K=1,NPTS(L)
1065             XX=K-XOFF                          ! Segment Is (-XX,+XX):
1066             YY=DBLE(Y(I+XX*IS))                ! Step Size Is IS*STEP
1067             SS(1)=SS(1)+YY
1068             SS(2)=SS(2)+YY*DBLE(XX)            ! Calculate Summations
1069             SS(3)=SS(3)+YY*DBLE(XX**2)         ! For Least Squares Fit
1070             SS(4)=SS(4)+YY*DBLE(XX**3)         ! Within Segment:
1071             SS(5)=SS(5)+YY*DBLE(XX**4)
1072    950    CONTINUE
1073 C      ------------------------------------------------------------------
1074 C          Array CC Holds Known Least Squares Coefficients
1075 C      ------------------------------------------------------------------
1076           IF (Icode.EQ.'F') THEN
1077             YY=CC(L,2)*SS(2)+CC(L,4)*SS(4)
1078             GO TO 960
1079           END IF
1080           YY=2.0D0*(CC(L,3)*SS(1)+CC(L,6)*SS(3)+CC(L,7)*SS(5))
1081    960    Z(I)=SNGL(YY)/STEP/FLOAT(IS)*ZM    ! Z(I) Is Derivative Spectrum
1082    970 CONTINUE                               ! Rescaled x10(F) or x100(S)
1083         DO 980 I=1,START-1
1084           Z(I)=Z(START)                      ! Set First XX*IS Points
1085    980 CONTINUE
1086         DO 990 I=FINISH+1,NDATA
1087           Z(I)=Z(FINISH)                     ! Set Last XX*IS Points
1088    990 CONTINUE
1089         WRITE (1,*) UP,ERASE,'  Derivative FINISHED: ',BELL,'_'
1090         CALL Wait(1.0)
1091         Dstat='VALID'
1092         Dtype=Icode
1093         DERIV=.FALSE.
1094         GO TO 500
1095 C
1096 C      ------------------------------------------------------------------
1097 C
1098 C          Store Edited Or Derivative Spectrum
1099 C
1100 C      ------------------------------------------------------------------
1101 C
1102   1000 IF (Sstat(1).NE.'VALID') GO TO 260
1103         IF ((Code.EQ.'D').AND.(Dstat.NE.'VALID')) GO TO 200
1104         IF (ABS(WMIN-WAVE(1)).GT.0.2) THEN
1105   1010    WRITE (1,*) UP,ERASE,'  SCAN ENDED AT',WAVE(1),
1106        &  ' nm (Expected:',WMIN,'), Proceed (Y or N) ? ',BELL,'_'
1107           READ (1,80) Icode
1108           CALL Upper(Icode)
1109           IF (Icode.EQ.'N') GO TO 70
```

```
1110          IF (Icode.NE.'Y') GO TO 1010
1111        END IF
1112        HEADER=LABEL(1)
1113        IF (COUNT.GT.0) THEN
1114          NUMBER=FLOAT(COUNT)
1115          CALL Str(NUMBER,String,2)
1116          HEADER='SM'//String(2:3)//':'//LABEL(1)
1117        END IF
1118        String='Edited'
1119        M=6
1120        IF (Code.EQ.'D') THEN
1121          String='Derivative'
1122          M=10
1123          HEADER=Dtype//'D:'//LABEL(1)
1124        END IF
1125        TITLE='Store '//String(1:M)//' Spectrum'
1126  1020  WRITE (1,*) HOME,CLR,'_'
1127        CALL Center(TITLE)
1128        CALL Line(NCOL)
1129        WRITE (1,*)
1130        WRITE (1,*) '  Researcher''s Initials, (AA-ZZ): ',BELL,'_'
1131        READ (1,'(A2)') INITIALS
1132        WRITE (1,*) DOWN
1133        WRITE (1,*) UP,ERASE,'  Filename, (16 chars.): ',BELL,'_'
1134        READ (1,'(A16)') Fname
1135        L=16
1136        DO WHILE (Fname(L:L).EQ.' ')
1137          L=L-1
1138        END DO
1139        Directory=Fname(1:L)//'.S'//INITIALS
1140        Fname=Directory(1:L+4)
1141        WRITE (1,*) DOWN,'  Directory, (RETURN = /DEFAULT/): ',BELL,'_'
1142        READ (1,'(A40)') Directory
1143        IF (Directory.EQ.' ') THEN
1144          Filespec=Fname
1145          GO TO 1030
1146        END IF
1147        K=40
1148        DO WHILE (Directory(K:K).EQ.' ')
1149          K=K-1
1150        END DO
1151        IF (Directory(K:K).EQ.'/') K=K-1
1152        Filespec=Directory(1:K)//'/'//Fname
1153  1030  K=63
1154        DO WHILE (Filespec(K:K).EQ.' ')
1155          K=K-1
1156        END DO
1157        WRITE (1,*) UP,ERASE,'  Validating: ',Filespec(1:K),' _'
1158        OPEN (UNIT=66,FILE=Filespec(1:K),IOSTAT=N,STATUS='NEW')
1159        WRITE (1,*)
1160        IF (N.NE.0) THEN
1161          N=N-500
1162          WRITE (1,*) UP,ERASE,'_'
```

```
1163          IF (N.EQ.2) WRITE (1,*) ' FILE EXISTS: ',BELL,'_'
1164          IF (N.EQ.8) WRITE (1,*) ' FILE OPENED: ',BELL,'_'
1165          CLOSE (66,IOSTAT=N,ERR=1070)
1166          CALL Wait(2.0)
1167          GO TO 1020
1168        END IF
1169        IF (Icode.EQ.'R') GO TO 1050
1170        WRITE (1,*) DOWN,'  Title: '
1171        WRITE (1,*) '  ',HEADER
1172        WRITE (1,*) DOWN,'  Date: ',DATE(1)
1173        WRITE (1,*) DOWN,'  Concentration, (M): ',CONC(1)
1174        WRITE (1,*) DOWN,'  Pathlength, (cm): ',PATH(1)
1175 C      ------------------------------------------------------------
1176  1050  WRITE (1,*) DOWN,'  Storing File: ',Filespec(1:K),BELL
1177        WRITE (66,FMT=140,IOSTAT=N,ERR=1070) HEADER
1178        WRITE (66,FMT=150,IOSTAT=N,ERR=1070) DATE(1)
1179        WRITE (66,FMT=*,IOSTAT=N,ERR=1070) WMIN,WMAX,STEP,CONC(1),PATH(1)
1180        WRITE (66,FMT=*,IOSTAT=N,ERR=1070) ORD(1),ABSC(1),CELL(1),
1181       &CYCLE(1),SAMPLE(1),WAVE(1),TIMER(1),TEMP(1),DIST(1)
1182        WRITE (66,FMT=180,IOSTAT=N,ERR=1070) NP,NV,NDATA
1183        WRITE (66,FMT=190,IOSTAT=N,ERR=1070) (PARAM(1,I),I=1,NP)
1184        WRITE (66,FMT=*,IOSTAT=N,ERR=1070) (VARIABLE(1,I),I=1,NV)
1185        IF (Code.EQ.'D') THEN
1186          WRITE (66,FMT=*,IOSTAT=N,ERR=1070) (Z(I),I=1,NDATA)
1187          GO TO 1060
1188        END IF
1189        WRITE (66,FMT=*,IOSTAT=N,ERR=1070) (Y(I),I=1,NDATA)
1190  1060  WRITE (66,FMT=*,IOSTAT=N,ERR=1070) (X(I),I=1,NDATA)
1191        CLOSE (UNIT=66,IOSTAT=N,ERR=1070,STATUS='KEEP')
1192        IF (Code.EQ.'D') Dstat='STORED'
1193        IF (Code.EQ.'S') Fstat='STORED'
1194        CALL Wait(2.0)
1195        GO TO MENU
1196 C      ------------------------------------------------------------
1197  1070  WRITE (1,*) UP,ERASE,'  Disk Error #',N,BELL,' :_'
1198        WRITE (1,*) 'R...Resave, X...EXIT to Menu ? ',BELL,'_'
1199        READ (1,80) Icode
1200        CALL Upper(Icode)
1201        IF ((Icode.NE.'R').AND.(Icode.NE.'X')) GO TO 1070
1202        WRITE (1,*) UP,ERASE,'  Deleting Old File: ',Filespec(1:K),BELL,
1203       &' _'
1204        CLOSE (UNIT=66,IOSTAT=N,ERR=1070,STATUS='DELETE')
1205        CALL Wait(2.0)
1206        IF (Icode.EQ.'R') GO TO 1020
1207        Fname=' '
1208        Fstat=' '
1209        GO TO MENU
```

```
1210 C
1211 C     ------------------------------------------------------------------
1212 C
1213 C         Store Curve Fitting File
1214 C
1215 C     ------------------------------------------------------------------
1216 C
1217  2000 WRITE (1,*) HOME,CLR,'_'
1218       TITLE='Curve Fitting File'
1219       CALL Center(TITLE)
1220       CALL Line(NCOL)
1221       WRITE (1,*) DOWN,'  Scan Range: ',WMAX,' to',WMIN,' nm',DOWN,
1222      &DOWN
1223  2010 WRITE (1,*) UP,ERASE,'  File Range: (MIN,MAX) ? ',BELL,'_'
1224       READ (1,*,ERR=2010) WN,WX
1225       WN=ABS(WN)
1226       WX=ABS(WX)
1227       CALL Xlimits(WN,WX)
1228       IF ((WN.LT.WMIN).OR.(WN.GT.WMAX)) GO TO 2010
1229       IF ((WX.LT.WMIN).OR.(WX.GT.WMAX)) GO TO 2010
1230 C     ------------------------------------------------------------------
1231       T7=1.0E7
1232       WRITE (1,*) DOWN
1233  2020 WRITE (1,*) UP,ERASE,'  # Of Data Points: (10-500) ? ',BELL,'_'
1234       READ (1,'(I3)',ERR=2020) NFIT
1235       IF ((NFIT.LT.10).OR.(NFIT.GT.500)) GO TO 2020
1236       IF (NFIT.GT.NDATA) THEN
1237         WRITE (1,*) UP,ERASE,'  File Has Insufficient # Of Points: ',
1238      &  BELL,'_'
1239         CALL Wait(2.0)
1240         GO TO 2020
1241       END IF
1242       FIRST=T7/WX
1243       LAST=T7/WN
1244       SPACE=ANINT((LAST-FIRST)/FLOAT(NFIT-1))
1245  2030 LAST=FIRST+FLOAT(NFIT-1)*SPACE
1246       IF (T7/LAST.LT.WMIN) THEN
1247         SPACE=SPACE-1.0
1248         GO TO 2030
1249       END IF
1250       WRITE (1,*) UP,ERASE,UP,UP,ERASE,'_'
1251       WRITE (1,*) ' File Range: ',FIRST,' to',LAST,' at',SPACE,
1252      &' cm-1 steps',DOWN,DOWN
1253       EMULT=1.0
1254  2040 WRITE (1,*) UP,ERASE,'  Y-scale:  (A...Absorbance, ',
1255      &'E...Ext.Coeff.) ? ',BELL,'_'
1256       READ (1,80) Icode
1257       CALL Upper(Icode)
1258       IF (Icode.EQ.'E') THEN
1259         EMULT=1.0/(CONC(1)*PATH(1))
1260         WRITE (1,*) UP,ERASE,'  Ext.Coeff. vs cm-1'
1261         GO TO 2050
1262       END IF
```

```
1263        IF (Icode.NE.'A') GO TO 2040
1264        WRITE (1,*) UP,ERASE,'  Absorbance vs cm-1'
1265 C      ------------------------------------------------------------
1266   2050 WRITE (1,*) DOWN
1267        IF (Ymode.EQ.'T') THEN
1268          WRITE (1,*) UP,ERASE,'  %T Data -> Absorbance'
1269          WRITE (1,*) DOWN
1270        END IF
1271   2060 WRITE (1,*) UP,ERASE,'  Filename: ? ',BELL,'_'
1272        READ (1,'(A20)') Fname
1273        OPEN (UNIT=66,FILE=Fname,IOSTAT=N,STATUS='NEW')
1274        IF (N.NE.0) THEN
1275          N=N-500
1276          WRITE (1,*) UP,ERASE,'_'
1277          IF (N.EQ.2) WRITE (1,*) ' FILE EXISTS: ',BELL
1278          IF (N.EQ.8) WRITE (1,*) ' FILE OPENED: ',BELL
1279          CLOSE (66,IOSTAT=N,ERR=2999)
1280          CALL Wait(2.0)
1281          GO TO 2060
1282        END IF
1283        WRITE (1,*) UP,ERASE,'  Writing File: ',Fname,BELL
1284 C      ------------------------------------------------------------
1285        DO 2070 W=FIRST,LAST,SPACE
1286          WL=ANINT(T7/W/STEP)*STEP        ! Nearest Wavelength
1287          I=NINT((WMAX-WL)/STEP)+1        ! Index Value
1288          Xval=T7/X(I)                    ! Nearest Wavenumber
1289          IF (Ymode.EQ.'A') THEN
1290            Yval=Y(I)*EMULT               ! Absorbance/Ext.Coeff. Value
1291          ELSE
1292            Yval=ALOG10(100.0/Y(I))*EMULT
1293          END IF
1294          WRITE (66,*) Xval,Yval
1295   2070 CONTINUE
1296 C      ------------------------------------------------------------
1297        CLOSE (66,IOSTAT=N,ERR=2999,STATUS='KEEP')
1298        Cstat='STORED'
1299        GO TO MENU
1300 C      ------------------------------------------------------------
1301   2999 WRITE (1,*) '  Disk Error #',N
1302        CALL Wait(2.0)
1303        Cstat='INVALID'
1304        GO TO MENU
1305 C
1306 C      ------------------------------------------------------------
1307 C
1308 C          Exit Program
1309 C
1310 C      ------------------------------------------------------------
1311 C
1312   9999 IF ((Sstat.EQ.'VALID').AND.(Fstat.NE.'STORED')) THEN
1313          WRITE (1,*) UP,ERASE,'_'
1314          WRITE (1,*) ' Spectrum NOT STORED: Exit, (Y or N) ? ',BELL,'_'
1315          READ (1,80) Icode
```

```
1316            CALL Upper(Icode)
1317            IF (Icode.EQ.'N') GO TO 70
1318            IF (Icode.NE.'Y') GO TO 9999
1319          END IF
1320          WRITE (1,*) UP,ERASE,UP
1321          STOP
1322          END
1323 C
1324 C     ********** END OF MAIN PROGRAM **********
1325 C
1326 C         Print a TITLE Centered in 72 columns
1327 C
1328 C     ****************************************************************
1329 C
1330          SUBROUTINE Center(TITLE)
1331          INTEGER I,J,N
1332          CHARACTER TITLE*72,BLANK*36
1333          BLANK='
1334          I=72
1335          J=0
1336          DO WHILE (TITLE(I:I).EQ.' ')
1337            J=J+1
1338            I=72-J
1339          END DO
1340          N=J/2
1341          WRITE (1,*) BLANK(1:N),TITLE(1:I)
1342          RETURN
1343          END
1344 C
1345 C     ----------------------------------------------------------------
1346 C
1347 C         Print a line of N '-' characters (72 columns max)
1348 C
1349 C     ----------------------------------------------------------------
1350 C
1351          SUBROUTINE Line(N)
1352          INTEGER I,N
1353          CHARACTER BLANK*72,DLINE*72,SPACE*36
1354          SPACE='
1355          BLANK=SPACE//SPACE
1356          SPACE='------------------------------------'
1357          DLINE=SPACE//SPACE
1358          IF (N.GT.72) N=72
1359          I=(72-N)/2
1360          WRITE (1,*) BLANK(1:I),DLINE(1:N)
1361          RETURN
1362          END
```

```
C
C     ------------------------------------------------------------------
C
C         Validate Abscissa Limits
C
C     ------------------------------------------------------------------
C
      SUBROUTINE Xlimits(MIN,MAX)
      REAL MIN,MAX,SWAP
      MIN=ABS(MIN)
      MAX=ABS(MAX)
      IF (MIN.LT.MAX) GO TO 10
      SWAP=MIN
      MIN=MAX
      MAX=SWAP
   10 RETURN
      END
C
C     ------------------------------------------------------------------
C
C         Validate Ordinate Limits
C
C     ------------------------------------------------------------------
C
      SUBROUTINE Ylimits(MIN,MAX)
      REAL MIN,MAX,SWAP
      IF (MIN.LT.MAX) GO TO 10
      SWAP=MIN
      MIN=MAX
      MAX=SWAP
   10 RETURN
      END
C
C     ------------------------------------------------------------------
C
C         Convert String Entry To Upper Case If Required
C
C     ------------------------------------------------------------------
C
      SUBROUTINE Upper(Code)
      INTEGER LENSTR,N
      CHARACTER*(*) Code
      LENSTR=LEN(Code)
      DO 10 I=1,LENSTR
        N=ICHAR(Code(I:I))
        IF (N.GT.96) Code(I:I)=CHAR(N-32)
   10 CONTINUE
      RETURN
      END
```

```
1412 C
1413 C     ------------------------------------------------------------------
1414 C
1415 C         Convert ASCII String To Numeric Value (10 Digits Max'm)
1416 C
1417 C     ------------------------------------------------------------------
1418 C
1419        SUBROUTINE Val(String,VALUE)
1420        INTEGER DECPT,EXPON,LENSTR,M,N,NUM(12),EX(3)
1421        REAL VALUE
1422        DOUBLE PRECISION ESIGN,MULT,SIGN,TEN,DECIMAL
1423        CHARACTER Ascii
1424        CHARACTER*(*) String
1425        LOGICAL EXPONENT,INTEGER,TEST
1426        EXPONENT=.FALSE.
1427        INTEGER=.TRUE.
1428 C      TEST=.FALSE.
1429        J=1
1430        K=0
1431        M=0
1432        DECPT=0
1433        ESIGN=1.0
1434        SIGN=1.0
1435        TEN=10.0
1436        DECIMAL=0.0
1437        LENSTR=LEN(String)
1438 C      IF (TEST) WRITE (1,*) ' String Number = ',String
1439 C      IF (TEST) WRITE (1,*) ' String Length =',LENSTR
1440        DO 100 I=1,LENSTR
1441          Ascii=String(I:I)
1442          N=ICHAR(Ascii)
1443          IF (N.EQ.69) THEN
1444            EXPONENT=.TRUE.
1445            IPOS=I
1446            GO TO 100
1447          END IF
1448          IF (EXPONENT) GO TO 30
1449          IF ((N.GE.48).AND.(N.LE.57)) GO TO 20
1450          IF (N.EQ.46) INTEGER=.FALSE.
1451          IF (N.EQ.46) DECPT=K
1452          IF (N.EQ.45) SIGN=-1.0
1453          GO TO 100
1454       20 NUM(J)=N-48
1455          K=J
1456          J=J+1
1457          GO TO 100
1458       30 IF (N.EQ.45) ESIGN=-1.0
1459          IF ((N.LT.48).OR.(N.GT.57)) GO TO 100
1460          EX(I-IPOS)=N-48
1461          M=M+1
1462      100 CONTINUE
1463          IF ((DECPT.EQ.0).AND.(INTEGER)) DECPT=K
```

```
      DO 200 J=1,K
        EXPON=DECPT-J
        MULT=TEN**EXPON
        DECIMAL=DECIMAL+NUM(J)*MULT
  200 CONTINUE
      DECIMAL=SIGN*DECIMAL
      MULT=0.0
      IF (ESIGN.EQ.-1.0) M=M+1
      DO 300 I=1,M
        MULT=MULT+DBLE(EX(I))*TEN**(M-I)
  300 CONTINUE
      VALUE=DECIMAL*TEN**(ESIGN*MULT)
C     IF (TEST) WRITE (1,*) ' Value =',VALUE
      RETURN
      END
```

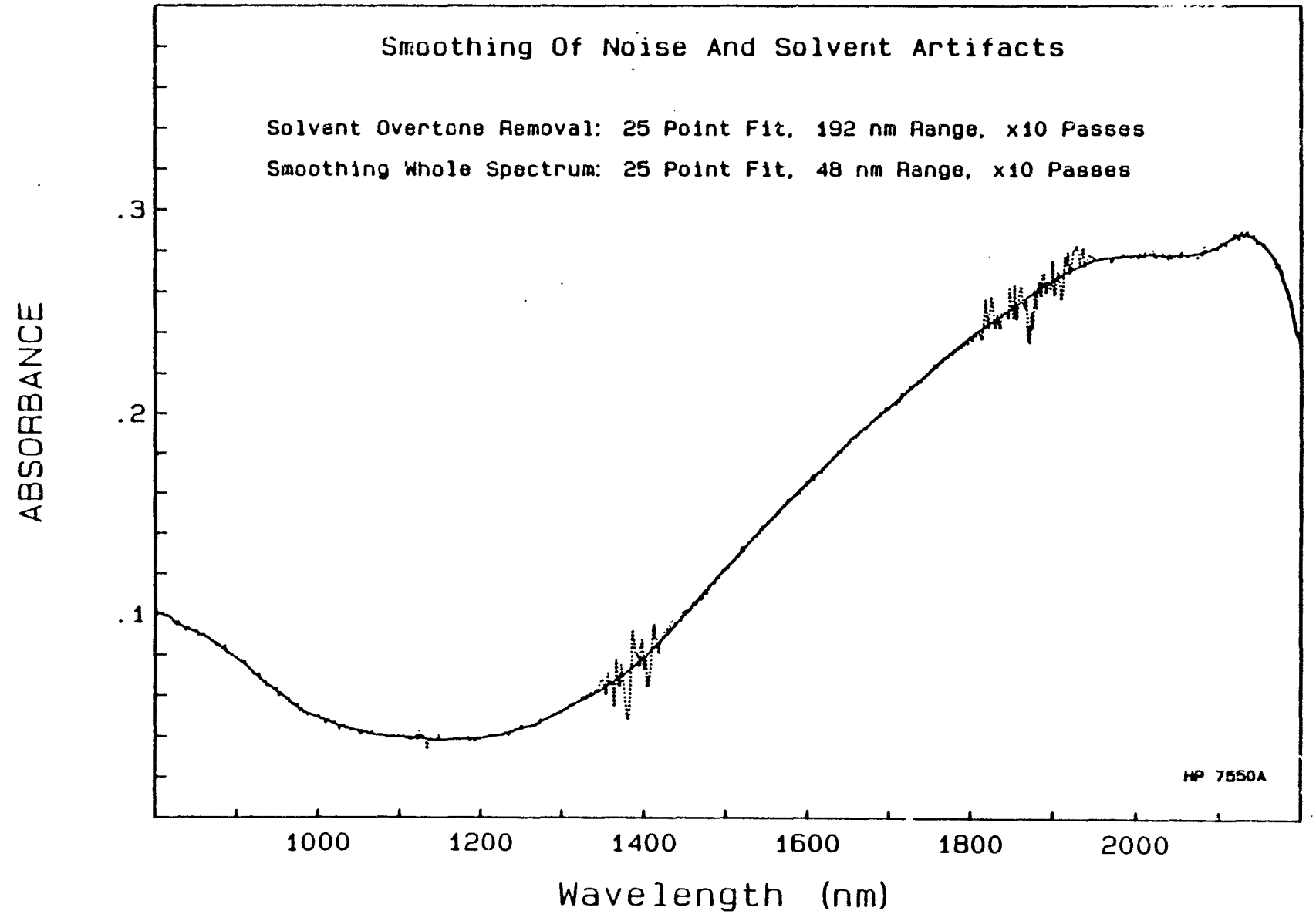
```
1479 C
1480 C     ------------------------------------------------------------------
1481 C
1482 C         Convert Number To ASCII String
1483 C
1484 C     ------------------------------------------------------------------
1485 C
1486       SUBROUTINE Str(VALUE,String,PREC)
1487       INTEGER ASCII,DECPT,I,J,LENSTR,NDIGIT,NUMBER,PREC
1488       REAL VALUE
1489       DOUBLE PRECISION DECIMAL,FRACTION,TEN
1490       CHARACTER Concat*14,Digit(12),Sign,String*14
1491       LOGICAL INTEGER,TEST
1492       INTEGER=.TRUE.
1493 C     TEST=.FALSE.
1494       DECPT=0
1495       J=0
1496       TEN=10.0
1497       Sign=' '
1498       Concat=' '
1499 C     IF (TEST) WRITE (1,*) ' Value Entered = ',VALUE
1500       IF (VALUE.LT.0.0) Sign='-'
1501       IF (VALUE.EQ.0.0) GO TO 100
1502       DECIMAL=ABS(VALUE)
1503       DO WHILE (DECIMAL.GE.1.0)
1504         DECIMAL=DECIMAL/TEN
1505         J=J+1
1506       END DO
1507       DECPT=J
1508 C     IF (TEST) WRITE (1,*) ' # of Whole Digits: ',DECPT
1509       IF (DECPT.EQ.0) GO TO 30
1510       DO 20 J=1,DECPT
1511         DECIMAL=DECIMAL*TEN
1512         NUMBER=INT(DECIMAL)
1513         ASCII=NUMBER+48
1514         Digit(J)=CHAR(ASCII)
1515         FRACTION=DECIMAL-NUMBER
1516         DECIMAL=DINT(FRACTION*TEN**(PREC-J)+.5)/TEN**(PREC-J)
1517    20 CONTINUE
1518 C     IF (.NOT.TEST) GO TO 30
1519 C     WRITE (1,*) ' The Whole Digits = ',(Digit(I), I=1,DECPT)
1520    30 J=DECPT
1521 C     IF (TEST) WRITE (1,*) ' Decimal Fraction = ',DECIMAL
1522       IF (DECIMAL.NE.0.0) INTEGER=.FALSE.
1523       IF (DECPT.GE.12) GO TO 40
1524       DO WHILE (DECIMAL.NE.0.0)
1525         J=J+1
1526         DECIMAL=DECIMAL*TEN
1527         NUMBER=INT(DECIMAL)
1528         ASCII=NUMBER+48
1529         Digit(J)=CHAR(ASCII)
1530         FRACTION=DECIMAL-NUMBER
1531         DECIMAL=DINT(FRACTION*TEN**(PREC-J)+.5)/TEN**(PREC-J)
```

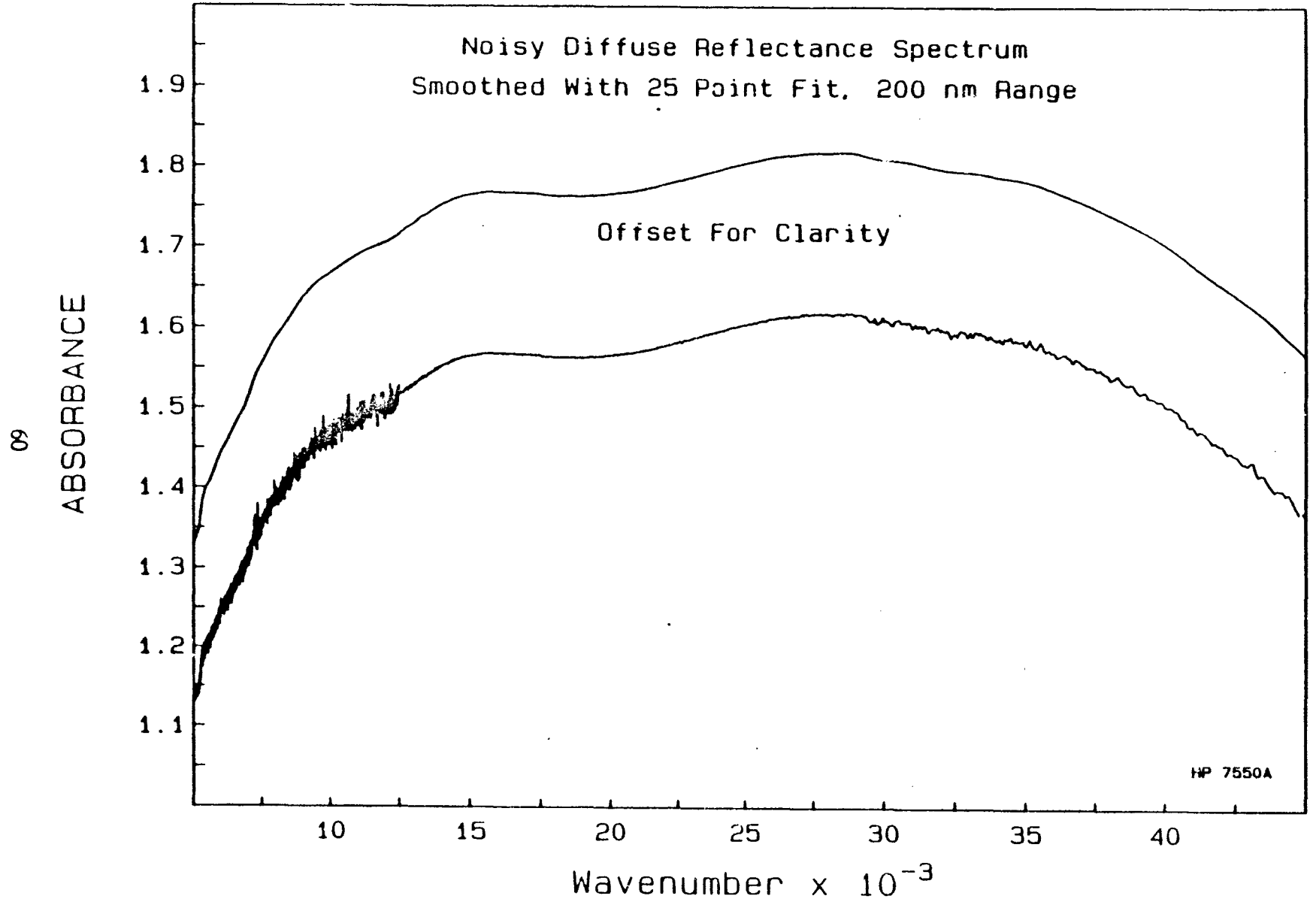
```
1532          IF (DECIMAL.EQ.1.0) THEN
1533            DIGIT(J)=CHAR(ASCII+1)
1534            DECIMAL=0.0
1535          END IF
1536          IF (J.GE.12) DECIMAL=0.0
1537        END DO
1538     40 NDIGIT=J
1539 C      IF (.NOT.TEST) GO TO 50
1540 C      WRITE (1,*) ' The Characters  = ',(Digit(I), I=1,NDIGIT)
1541     50 IF (NDIGIT.GT.12) GO TO 200
1542        DO 60 I=1,NDIGIT
1543          Concat(I:I)=Digit(I)
1544     60 CONTINUE
1545        IF (INTEGER) GO TO 80
1546        IF (DECPT.EQ.0) GO TO 70
1547        String=Sign//Concat(1:DECPT)//'.'//Concat(DECPT+1:14)
1548        RETURN
1549     70 String=Sign//'.'//Concat
1550        RETURN
1551     80 String=Sign//Concat
1552        RETURN
1553    100 String=' 0.0'
1554        RETURN
1555    200 WRITE (1,*) ' Error in data: (too many digits)'
1556        STOP
1557        END
```

```
1558 C
1559 C     ------------------------------------------------------------------
1560 C
1561 C         Wait Specified Delay (sec)
1562 C
1563 C     ------------------------------------------------------------------
1564 C
1565       SUBROUTINE Wait(DELAY)
1566       REAL DELAY,PERIOD,Tzero,Time
1567       PERIOD=0.0
1568       Tzero=Time(I)
1569       DO WHILE (PERIOD.LT.DELAY)
1570         PERIOD=Time(I)-Tzero
1571       END DO
1572       RETURN
1573       END
1574 C
1575 C     ------------------------------------------------------------------
1576 C
1577 C         Read Time (sec) from the HP 1000's RTE-6 Operating System
1578 C
1579 C         Note: I is a dummy argument, no values are passed
1580 C
1581 C     ------------------------------------------------------------------
1582 C
1583       REAL FUNCTION Time(I)
1584       INTEGER ICODE,ITIME(5)
1585       ICODE=11
1586       CALL EXEC(ICODE,ITIME)
1587       Time=FLOAT(ITIME(1))/100.0+FLOAT(ITIME(2))+FLOAT(ITIME(3))*60.0
1588      &+FLOAT(ITIME(4))*3600.0
1589       RETURN
1590       END
```

Appendix I

Sample Smoothed Spectra


Smoothing Of Noise And Solvent Artifacts
Solvent Overtone Removal: 25 Point Fit, 192 nm Range, x10 Passes
Smoothing Whole Spectrum: 25 Point Fit, 48 nm Range, x10 Passes
ABSORBANCE
.3
.2
.1
HP 7550A
1000
1200
1400
1600
1800
2000
Wavelength (nm)

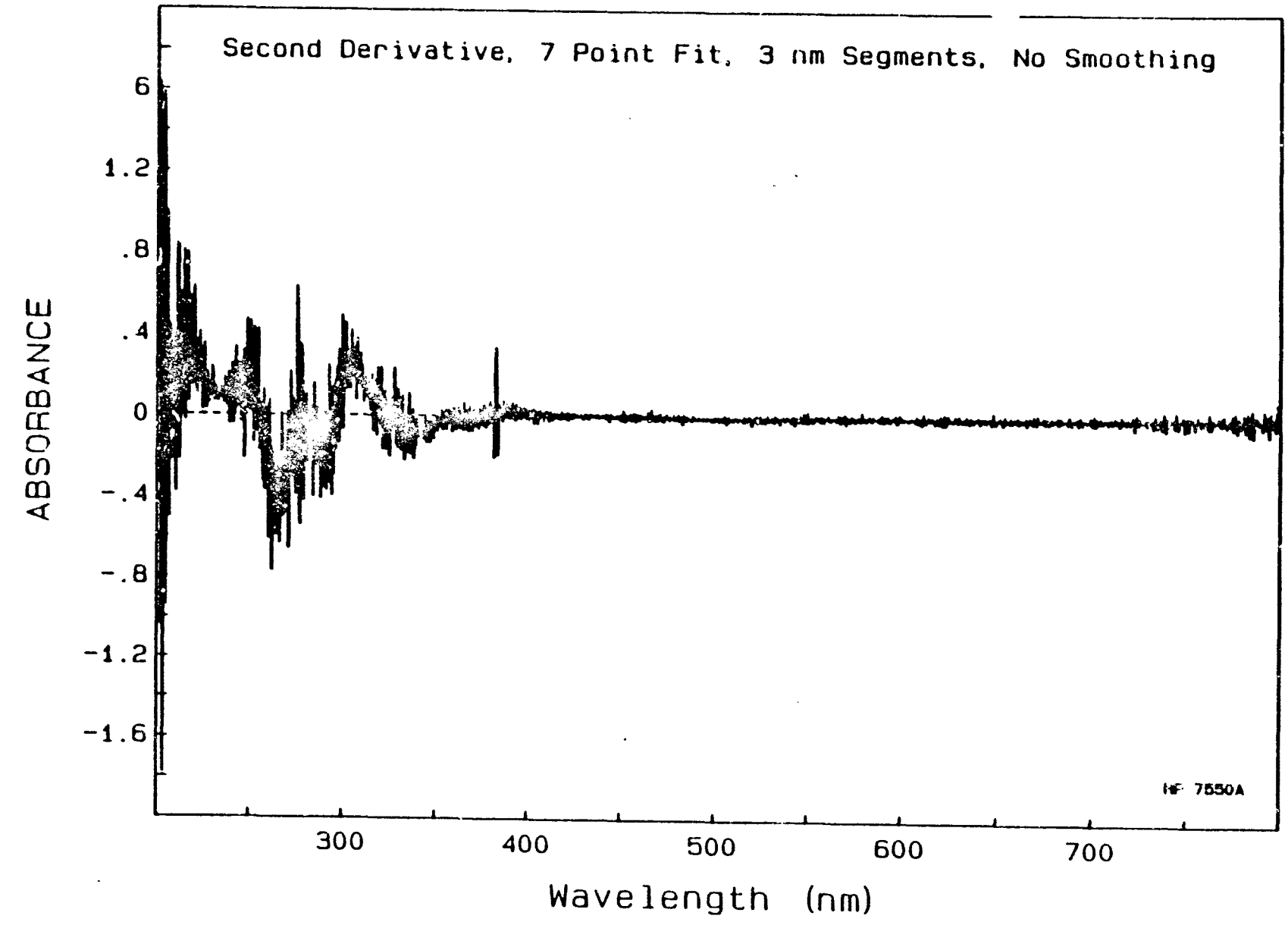

Noisy Diffuse Reflectance Spectrum
Smoothed With 25 Point Fit, 200 nm Range
Offset For Clarity
HP 7550A
ABSORBANCE
1.9
1.8
1.7
1.6
1.5
1.4
1.3
1.2
1.1
10
15
20
25
30
35
40
Wavenumber x 10^{-3}

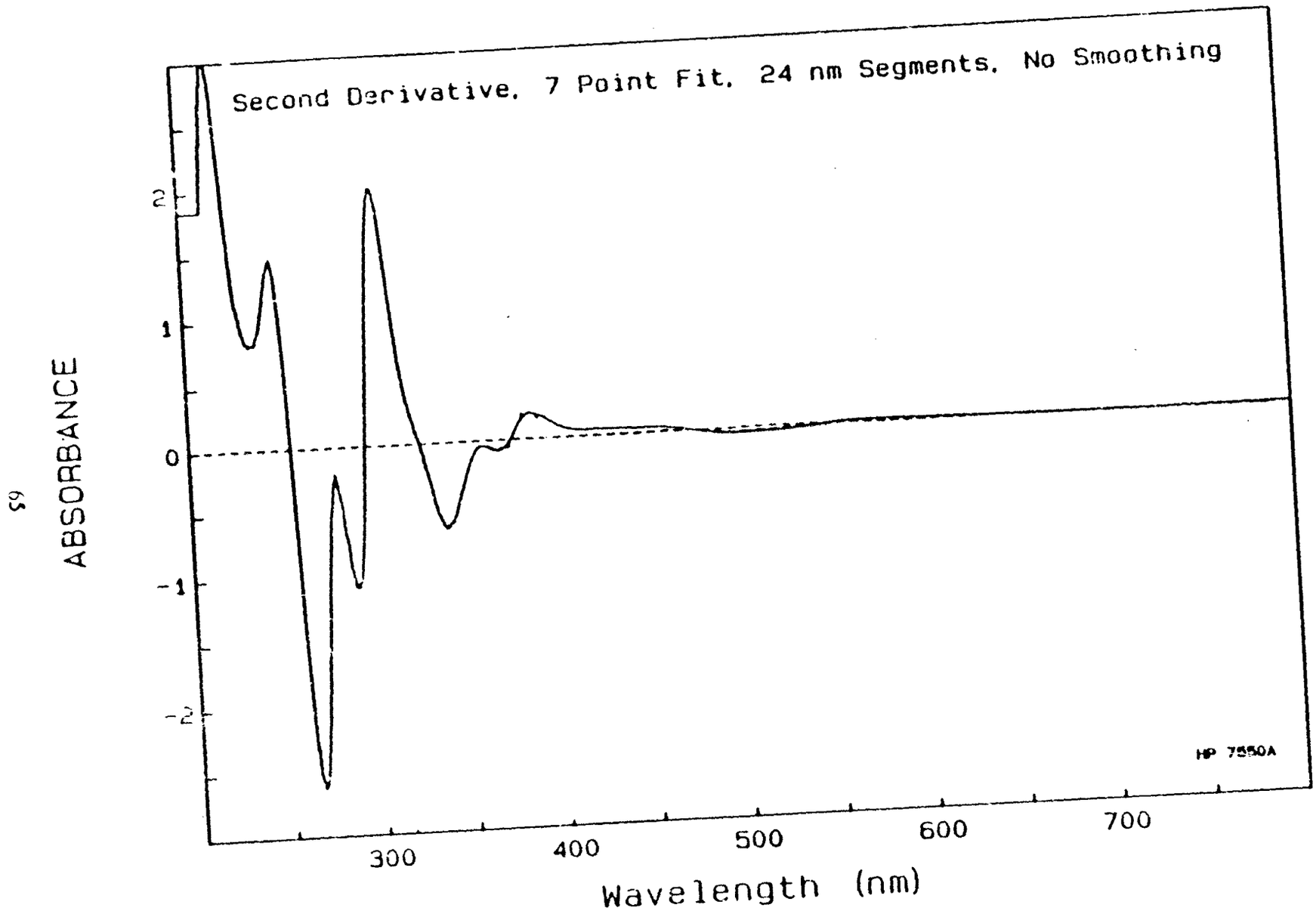
Appendix II

Sample Derivative Spectra

First Derivative, 7 Point Fit, 3 nm Segments, No Smoothing
HP 7550A
ABSORBANCE
.8
.6
.4
.2
0
-.2
-.4
-.6
-.8
300
400
500
600
700
Wavelength (nm)

First Derivative, 7 Point Fit, 24 nm Segments, No Smoothing
HP 7550A
ABSORBANCE
.8
.6
.4
.2
0
-.2
-.4
-.6
300
400
500
600
700
Wavelength (nm)


Second Derivative, 7 Point Fit, 3 nm Segments, No Smoothing
ABSORBANCE
6
1.2
.8
.4
0
-.4
-.8
-1.2
-1.6
300
400
500
600
700
Wavelength (nm)
HP 7550A


Second Derivative, 7 Point Fit, 24 nm Segments, No Smoothing
ABSORBANCE
2
1
0
-1
-2
300
400
500
600
700
Wavelength (nm)
HP 7550A

APPENDIX G3

Naval Research Laboratory

Washington, DC 20375-5000



NRL Memorandum Report 6362

PLOTSPEC

A FORTRAN 77 Program for Plotting Spectral Data from The Varian CARY 2390 UV-VIS-NIR Spectrophotometer

R. A. BINSTEAD

GEO-CENTERS, Inc.,
10903 Indian Head Highway
Fort Washington, MD 20744

J. C. COOPER

Polymeric Materials Branch
Chemistry Division

October 20, 1988

Approved for public release, distribution unlimited.

SECURITY CLASSIFICATION OF THIS PAGE

REPORT DOCUMENTATION PAGE

Form Approved OMB No. 0704-0188

1a REPORT SECURITY CLASSIFICATION: UNCLASSIFIED	1b RESTRICTIVE MARKINGS
2a SECURITY CLASSIFICATION AUTHORITY	3 DISTRIBUTION/AVAILABILITY OF REPORT: Approved for public release; distribution unlimited.
2b DECLASSIFICATION/DOWNGRADING SCHEDULE	
4 PERFORMING ORGANIZATION REPORT NUMBER(S): NRL Memorandum Report 6362	5 MONITORING ORGANIZATION REPORT NUMBER(S)
6a NAME OF PERFORMING ORGANIZATION: Naval Research Laboratory; 6b OFFICE SYMBOL (If applicable): Code 6125	7a NAME OF MONITORING ORGANIZATION
6c ADDRESS (City, State, and ZIP Code): Washington, DC 20375-5000	7b ADDRESS (City, State, and ZIP Code)
8a NAME OF FUNDING/SPONSORING ORGANIZATION: SDIO, ONR; 8b OFFICE SYMBOL (If applicable)	9 PROCUREMENT INSTRUMENT IDENTIFICATION NUMBER
8c ADDRESS (City, State, and ZIP Code): Washington, DC	10 SOURCE OF FUNDING NUMBERS: PROGRAM ELEMENT NO 61153N 53224C; PROJECT NO RR011-01-41; TASK NO; WORK UNIT ACCESSION NO

11 TITLE (Include Security Classification) PLOTSPEC - A FORTRAN 77 Program for Plotting Spectral Data from the Varian CARY 2390 UV-VIS-NIR Spectrophotometer

12 PERSONAL AUTHOR(S): Binstead,* R.A. and Cooper, J.C.

13a TYPE OF REPORT	13b TIME COVERED	14 DATE OF REPORT (Year Month Day)	15 PAGE COUNT
Interim	FROM 10/87 TO present	1988 October 20	78

16 SUPPLEMENTARY NOTATION: *GEO-CENTERS, Inc., 10903 Indian Head Highway, Fort Washington, MD 20744

17 COSATI CODES			18 SUBJECT TERMS (Continue on reverse if necessary and identify by block number)	
FIELD	GROUP	SUB GROUP	UV-VIS-NIR	FORTRAN
			Plotting	CARY

19 ABSTRACT (Continue on reverse if necessary and identify by block number)

PLOTSPEC is a FORTRAN 77 program designed to plot UV-VIS-NIR spectra using data obtained from the CARY 2300 - 2400 series spectrophotometers. The program is written to operate on a Hewlett-Packard 1000 computer system but with very few system dependent features to enable easy conversion for operation on other host systems. PLOTSPEC supports a wide range of Hewlett-Packard digital plotters using the HP-GL command language. The program uses a menu driven environment with automatic scaling and axes setup in the

(Continues)

20 DISTRIBUTION/AVAILABILITY OF ABSTRACT: ☒ UNCLASSIFIED/UNLIMITED ☐ SAME AS RPT ☐ DTIC USERS	21 ABSTRACT SECURITY CLASSIFICATION: UNCLASSIFIED
22a NAME OF RESPONSIBLE INDIVIDUAL: John C. Cooper	22b TELEPHONE (Include Area Code): (202) 767-3115; 22c OFFICE SYMBOL: Code 6125

DD Form 1473, JUN 86 Previous editions are obsolete

S/N 0102-LF-014-6603

19. ABSTRACTS (Continued)

ordinate and abscissa modes of choice. PLOTSPEC offers abscissa choices of Wavelength (nm) or Wavenumbers x 10^{-3} and ordinate choices of Absorbance, Extinction Coefficient, % Reflectance or % Transmission. Annotation and digitizing facilities are also included for easy labelling and peak determinations.

CONTENTS

Section	Description	Page
INTRODUCTION		1
IMPLEMENTATION		
1.0	Hardware Interface	2
1.1	System Handshaking	2
1.2	HP-GL Software Control Of HP Plotters	3
1.3	HP-GL Commands Summary	4
1.4	Default Plotting Parameters	6
SOFTWARE DESCRIPTION		
2.0	Purpose Of PLOTSPEC	7
2.1	Program Structure	8
2.2	Plotting Menu Commands	13
2.3	COMMON DATA	16
2.4	SUBROUTINES	18
2.5	FUNCTIONS	23

... cont'd

Section	Description	Page
PROGRAM CODE		
3.0	Source Code Availability	23
3.1	Variable Names And Usage	23
3.2	Program Listing	29
APPENDIX	Sample Plots	68

LIST OF TABLES

TABLE	Description	Page
I	Data File Format	10
II	Glossary Of Integer Variables	24
III	Glossary Of Real Variables	25
IV	Glossary Of Real Array Variables	26
V	Glossary Of Character Variables	27

PLOTSPEC
A FORTRAN 77 Program For Plotting Spectral Data From The Varian CARY 2390 UV-VIS-NIR Spectrophotometer

INTRODUCTION

Spectral data acquisition from the CARY 2300 and 2400 series spectrophotometers has been implemented successfully using a Hewlett-Packard 1000 minicomputer system using the FORTRAN 77 program CARYSPEC, which is described in a separate report. The ability to acquire high quality UV-VIS-NIR spectra must be complemented with flexible data analysis and plotting software to make full use of the spectroscopic data. This report describes a fully tested FORTRAN 77 program PLOTSPEC which fulfills the plotting requirements of most users in a simple to use menu driven environment. The program supports Absorbance, Extinction Coefficient, % Transmission and % Reflectance ordinates *vs* linear Wavelength (nm) or Energy (cm^{-1}) abscissa. Automatic *data rescaling* is provided between Absorbance units and % Transmission so that either type of data file from CARYSPEC may be plotted in the ordinate of choice. PLOTSPEC supports two concurrent spectra, of up to 10001 data points each, allowing difference spectra to be obtained with automatic scaling for differences in concentration and pathlength. This mode is only valid for Absorbance of Extinction Coefficient ordinate choices and % Transmission data files will be automatically rescaled before plotting. Data treatment in the % Reflectance mode is identical to % Transmission with only the plotting label altered to match the use of this measurement technique. The abscissa axis scaling is bidirectional to suit individual preferences for the direction of increasing wavelength or energy units.

PLOTSPEC has been developed for use with an HP 1000 minicomputer system running the RTE-6/VM operating system and CI shell. In this environment the program communicates with Hewlett-Packard model 9872A and 7550A digital plotters via the IEEE-488 and RS-232C I/O subsytems, respectively. These communication functions are transparent to high level languages on the HP 1000 enabling simple READ/WRITE statements from FORTRAN to control the external plotting operations. The program resides in a single 32K word memory segment and utilizes 79 pages of Extended Memory Addressing (EMA) memory for the large data arrays. Since PLOTSPEC makes use of very few special features of the HP 1000 computer system the program could be modified easily to run on other host systems supporting the FORTRAN 77 language and either the IEEE-488 or RS-232C interface standards.

Manuscript approved August 9, 1988.

IMPLEMENTATION

1.0 Hardware Interface:

The IEEE-488 interface for the HP 1000 system is implemented with an HP 59310B interface card which utilizes 4 Logical Unit (LU) addresses in the system. The LU addresses used within the program are system dependent and are defined during the system generation. The interface card accessed by PLOTSPEC occupies LU addresses 31-34, corresponding to card addresses 0-3. Address 0 enables a special addressing mode for sending low level bus command sequences. Addresses 1-3 are predefined automatic READ/WRITE channels which select device numbers 1-3 on the bus. PLOTSPEC uses LU 33 to automatically address device #2 on the bus (HP 9872A plotter). To simplify alterations to the plotter address the program uses the INTEGER variable PU for the unit number in all READ/WRITE operations with the plotter.

The RS-232C interface to the HP 7550A plotter is implemented via a standard HP 1000 8 channel multiplexer card (MUX) operating at 9600 baud with 8 data bits and XON/XOFF software handshaking protocol. PLOTSPEC does not send device control commands to set these communications parameters within the HP 7550A since these are easy to select from the front panel control of the plotter. In this application the HP 7550A plotter is operated in the STANDALONE mode with DIRECT connection to the MUX output of the HP 1000.

1.1 System Handshaking:

The IEEE-488 subsystem of the HP 1000 is operated by the RTE driver DVA37 configured for ASCII Data Record mode, enabling automatic ASCII $\longleftrightarrow$ NUMERIC conversion on I/O. This mode sends and expects to receive an End Of Record (EOR) with data transmission in the form of a Carriage Return/Line Feed (CR/LF) sequence which matches the requirements of Hewlett-Packard digital plotters.

The RS-232C subsystem is operated by the RTE driver DDV00 which also performs automatic ASCII $\longleftrightarrow$ NUMERIC conversions for FORTRAN I/O statements. This allows PLOTSPEC to control either plotter without regard for differences in the handshaking protocols. Character labelling mode on these plotters requires a special terminator character and PLOTSPEC issues the default Etx character, ASCII 3.

1.2 HP-GL Software Control Of HP Plotters:

PLOTSPEC uses a subset of the Hewlett-Packard Graphics Language (HP-GL) to control the operations of the HP 9872A and HP 7550A digital plotters. The early generation of HP plotters often only allow scaling and plotting commands to use integer units which restricts the utility of the automatic scaling command 'SC' in these plotters. This lack of utility is so severe that the operating manual for the HP 9872A plotter does not even document the existence of the 'SC' command in the HP-GL syntax. However, PLOTSPEC utilizes a general scaling procedure with the 'SC' command which functions on *all models* of HP plotters, maintaining a 0-10000 unit scale on each axis at all times. The 'SC' command has the advantage of automatically mapping these user units onto the scaling points P1 (lower left) and P2 (upper right). In order to map the real user units onto this 10000 x 10000 unit grid the program only needs to use a multiplier (XMULT,YMULT) for the data on each axis. For example, a % Transmission range of 0-100% would require YMULT = 100 for correct scaling of the user's data. This technique maintains software resolution at 1 in 10000 units regardless of the range of the user's MIN,MAX values.

PLOTSPEC also supports *bidirectional* plotting on the X-axis even though the 'SC' scaling command of early HP plotters does not permit setting Xmin > Xmax, *i.e.* numbers increasing towards the left. In order to accomplish this task in a general manner the program uses two Xmin,Xmax ranges, 0 - +10000 (increasing to the right) and -10000 - 0 (increasing to the left). The change in sign has the effect of reversing the direction of plotting. This scheme is known to work on HP 9872A, 7225A, 7470A, 7475A and 7550A model plotters.

The HP-GL commands used within PLOTSPEC are summarized below together with their syntax and parameter types. The type labels INTEGER and DECIMAL should be interpreted as their ASCII representations. All data sent to or received from the plotters is in ASCII code. Therefore, where the command syntax below indicates a program variable, a parameter value enclosed within literal string delimiters is equally applicable. The HP 1000 computer system performs the conversion between numeric and ASCII representations automatically on I/O operations allowing liberal mixtures of literal string and numeric variables to appear in HP-GL instructions, with a few exceptions. For example, the character plot instruction 'CP' fails on receipt of the value 0.0 from a program variable but happily accepts the literal '0.0'. Where HP-GL commands are known fail to function correctly for valid ranges of parameters PLOTSPEC first converts the values to their string representation before sending them to the plotters.

1.3 HP-GL Commands Summary:

'AP' Automatic Pen Pickup

Syntax = 'AP;'

'CP' Character Plot...moves the pen in units of character width, height

Syntax = 'CP',X,',',Y,';'

DECIMAL X,Y

'DF' Default Settings...sets the plotter to default parameters

Syntax = 'DF;'

'DI' Direction...sets the labeling direction

Syntax = 'DI',X,',',Y,';' where X,Y = cos(θ),sin(θ)

DECIMAL X,Y DEFAULT = 1,0

'IP' Input P1,P2 Scaling Points...sets the size of the plot

Syntax = 'IP',X1,',',Y1,',',X2,',',Y2,';'

where (X1,Y1) = lower left scaling coordinate (plotter units)

where (X2,Y2) = upper right scaling coordinate (plotter units)

INTEGER X1,Y1,X2,Y2

'IW' Input Window...sets the size of the plotting window

Syntax = 'IW',X1,',',Y1,',',X2,',',Y2,';'

where (X1,Y1) = lower left soft clip coordinate (plotter units)

where (X2,Y2) = upper right soft clip coordinate (plotter units)

INTEGER X1,Y1,X2,Y2

'LB' Label...draws the following literal characters

Syntax = 'LB',*string*,Etx where Etx = CHAR(3) terminates LB

ASCII *string*

'LT' Line Type...solid or broken lines styles

Syntax = 'LT',PN,',',PL,';' where PN = Pattern number (1-6)

INTEGER PN, DECIMAL PL where PL = Pattern length (0-100%)

'OA' Output Actual Pen Position...sends the current coordinate position

Syntax = 'OA;' followed by READ (...) X,Y,Z

where (X,Y) = current position (plotter units)

where Z = 0 or 1 for pen status (up/down)

INTEGER X,Y,Z

'OP' Output Scaling Points P1,P2...sends the coordinates of plot limits

Syntax = 'OP;' followed by READ (...) X1,Y1,X2,Y2

where (X1,Y1) = lower left scaling point

where (X2,Y2) = upper right scaling point

INTEGER X1,Y1,X2,Y2

'PA' Plot Absolute...moves the pen to an absolute coordinate

Syntax = 'PA',X,',',Y,';' where X,Y = coordinates (plotter units)

HP 9872A: INTEGER X,Y

HP 7550A: INTEGER X,Y or DECIMAL X,Y if user scaling is on

'PD' Pen Down...sets the pen on the plotting surface

Syntax = 'PD;'

'PU' Pen Up...picks up the pen from the plotting surface

Syntax = 'PU;'

'SC' Scale Plot...maps user units for X,Y axes onto P1,P2 scaling points

Syntax = 'SC',X1,',',X2,',',Y1,',',Y2,';'

where (X1,Y1) = coordinate of scaling point P1 (user units)

where (X2,Y2) = coordinate of scaling point P2 (user units)

HP 9872A: INTEGER X1,Y1,X2,Y2

HP 7550A: DECIMAL X1,Y1,X2,Y2

'SR' Size Relative...sets the character size in proportion to axes scaling

Syntax = 'SR',WIDTH,',',HEIGHT,';'

DECIMAL WIDTH,HEIGHT

'SP' Select Pen...picks up the pen from selected stall or carousel position

Syntax = 'SP',X,';' where X = pen number (0-8)

INTEGER X

'TL' Tick Length...sets the length of positive tick marks for axes

Syntax = 'TL',X,';' where X = % of full scale (0-100)

DECIMAL X

'VS' Velocity Select....sets the pen down speed

Syntax = 'VS',X,';' where X = velocity (cm/sec)

INTEGER X

'XT' X-tick...draws a vertical tick mark at the current pen position

Syntax = 'XT;'

'YT' Y-tick...draws a horizontal tick mark at the current pen position

Syntax = 'YT;'

1.4 Default Plotting Parameters:

PLOTSPEC initializes the HP plotters using the 'DF' default parameters command and then sets up the following plotting style:

LABELS The initial label direction is set to horizontal with nominal character fields of 1 x 2 cm and the size relative option is selected.

PEN Pen #1 is selected with automatic pen pickup and set to the UP state. The pen down velocity is set to 5 cm/sec for best line quality with felt tip pens on graphics paper.

SCALE Initial scaling coordinates for the HP 9872A plotter are (1350,1000) and (8500,7000) corresponding to the NOTEBOOK size plot on A-size paper while the plotting window is set to the hard clip limits.

TICKS Tick marks are set to +1% of full scale.

2.0 Purpose Of PLOTSPEC:

This program is intended to provide a flexible plotting facility for spectral data acquired from the Cary 2390 spectrophotometer using the program CARYSPEC, which is described in a separate report. The HP 1000 computer system provides a large EMA area to hold data arrays and PLOTSPEC makes use of this feature to access two concurrent spectra of up to 10001 points each. This allow for difference spectra to be plotted with relative ease compared with the experimental difficulties incurred with real time subtraction. While the raw data from the spectrophotometer consists of Absorbance or % Transmission measurements *vs* Wavelength (nm), PLOTSPEC allows for presentation of the data in more meaningful units as well. The abscissa may be scaled in Wavelength (nm) or Wavenumbers x 10^{-3} with increasing values towards the left or right. The ordinate may be presented in Absorbance, Extinction Coefficient (Molar Absorptivity), % Transmission or % Reflectance. PLOTSPEC automatically rescales the original ordinate data to match the choice of plotting ordinate. Furthermore, automatic range, tick and label position selection is provided for fast and efficient setup of a neat and tidy plot. However, the user can easily alter the default selections in the menu driven plotting environment.

PLOTSPEC also provides some useful annotation facilities for documenting the plot and for producing presentation material. A digitizing routine is interwoven with the annotation commands to enable semi-automatic labelling of peak maxima with the ease of a *point and shoot* technique. More accurate determinations of peak maxima can also be made using a page scrolling data listing routine, though the digitizing facility seems to be perfectly adequate in most cases. The default plotting mode produces a small NOTEBOOK size plot on A-size paper, together with a list of spectral parameters for documentation purposes. A FULL size plotting mode can also be selected to produce a larger plot on A-size paper without a parameter list. Both modes include sufficient space for a centered title over the plot. Additionally, the program provides a USER SET plotting size with default boundaries suited for a full size plot on B-size paper. This mode is ideal for producing poster presentation material. PLOTSPEC supports output to two generic types of Hewlett-Packard digital plotters, the older HP 9872A and the more recent HP 7550A model. However, PLOTSPEC is designed to function with all generations of HP plotters with only minor differences in the position of the plotting origin.

2.1 Program Structure:

PLOTSPEC comprises a large main program unit containing the console menu displays, string data for the instrument settings variables and a number of subroutines that perform string processing, input validation and communication with the HP 9872A and HP 7550A digital plotters. The main program unit is responsible for all the logic flow and the subroutines execute specific support tasks, which are summarized below:

The main program unit of PLOTSPEC comprises 6 distinct segments of code to carry out the the functions of disk file data retrieval, instrument settings display, plotting mode setup and actual plotting operations. The code fragments appear under the following assigned labels: MENU, READ, SETTINGS, DIFF, PLOT and EXIT.

MAIN PROGRAM

MENU:

This is the first and main control menu of the program, selecting entry to the data retrieval, instrument settings, plotting mode and exit routines. The choices are as follows:

'R1' . .....Read Spectrum #1

This command branches to label READ and the program performs logical tests for the presence of a valid spectrum in memory before allowing previous data to be overwritten by a new file. The data file format is listed below in Table I. Files are read into the first dimension of the data arrays and may be plotted using the 'P1' command.

'R2' .....Read Spectrum #2

This command performs the same operation as 'R1' but the file is read into the second dimension of the data arrays. The second spectrum can be plotted independently of the first or used for difference spectroscopy.

'IS' .....Instrument Settings

This option branches to label SETTINGS and prompts for the number of the spectrum. This routine allows for display of the most important operating conditions of the Cary 2390 spectrophotometer during acquisition of the selected spectrum. This provides an on-line reference when comparing a number of spectra.

'PS' .....Plotter Selection

This option allows the user to select either the HP 9872A (default) or HP 7550A plotter as the output device. Digitizing is more convenient with the older HP 9872A plotter but output quality and plotting speed are much improved with the HP 7550A.

'P1' .....Plot Spectrum #1

Selection of this command branches to label PLOT which performs a check for the presence of a valid file in memory. The routine then starts the plotting mode setup for the first spectrum with selection of the abscissa and ordinate scaling modes. The user has a choice of *Nanometres* and *Wavenumbers* for the abscissa and a choice of *ABSORBANCE*, *Extinction Coefficient*, *% Transmission* and *% Reflectance* for the ordinate. The program then proceeds to scale the data and set default plotter operating modes before presenting a menu of plotting options. The original data file may have been recorded in either Absorbance or % Transmission units so the data will be rescaled if the choice of plotting ordinate differs from the file ordinate.

'P2' .....Plot Spectrum #2

This command performs the same operations as 'P1' but uses data residing in the second dimension of the data arrays.

'DS' .....Difference Spectrum (1-2)

Selection of this option causes a branch to label DIFF which first checks for the presence of two valid spectra in memory and then tests for matching of their wavelength range and step size (nm). If the spectra are matched the program continues to label PLOT in the normal fashion. In this case, however, all plotting operations will use the scaled difference between the two data sets. The data from the second spectrum are scaled for differences in concentration or pathlength before subtraction during plotting.

'EX' .....Exit

The final option causes an unconditional branch to the label EXIT which terminates the program.

TABLE I

Data File Format

Line	File Variables [a]	Format Type [b]
1	TITLE(2)	CHARACTER (A72)
2	DATE(2)	CHARACTER (A8)
3	FMIN(2),FMAX(2),FSTEP(2),CONC(2), PATH(2)	REAL (*)
4	ORD(2),ABSC(2),CELL(2),CYCLE(2), SAMPLE(2),WAVE(2),TIMER(2), TEMP(2),DIST(2)	REAL (*)
5	J,K,NDATA(2,I)	INTEGER (I3,I3,I6)
6-54	PARAM(2,I)	INTEGER (I2)
55	VARIABLE(2,I)	REAL (*)
56-/	A(2,I)	REAL (*)
/-eof	W(2,I)	REAL (*)

a: Disk data files are read into either half of the data arrays

b: (*) indicates free field format

READ:

This section of PLOTSPEC opens a disk file previously stored by the data acquisition program CARYSPEC. The data are stored in ASCII code and contain a complete description of the instrument parameter settings as well as the spectral data. The format of the data file is listed above in Table I. The program prompts the user for both the filename and subdirectory. The latter defaults to the user's directory if only a RETURN character is entered. If a directory name is given the program builds a complete CI pathname for use in the OPEN statement. If the file cannot be found or the file is already open the program displays an error message and then returns to the main MENU. Otherwise, the file is read and the file descriptors are displayed on the console while the remainder of the data are being transferred. After completion of the data transfer the program prompts for changes to the concentration or pathlength variables. This feature allows for on-line corrections to the file variables before plotting, though permanent corrections should be made using the file editing program EDITSPEC. The program then returns to the main MENU.

SETTINGS:

This section of code displays a list of the most important instrument settings of the Cary 2390 spectrophotometer during acquisition of the specified spectrum. The program includes a large amount of string data for the various settings in the CHARACTER array Pstr. The INTEGER array PARAM is used as an index to this string data while numeric data for the table are obtained from the REAL array VARIABLES.

DIFF:

Entry into this section of code is made prior to plotting in order to verify that the data in memory are suitable for difference spectral plots. The program first checks that there are two spectra present and proceeds to test for exact matching of the wavelength limits and step size. The editing program EDITSPEC includes routines for preparing subset data files to support the difference plotting mode of PLOTSPEC.

PLOT:

This section of PLOTSPEC allows the user to set up the axes scaling to suit the type of data to be plotted. If the selected spectrum is not present in memory an error message is displayed and the program returns to the main MENU. Otherwise, a prompt is displayed for the choice of abscissa. PLOTSPEC supports two abscissa modes, Wavelength (nm) and Wavenumbers x 10^{-3}. After this selection the program sets a number of X-axis plotting variables and calls Subroutine Xaxis to setup the default tick and label positioning. The abscissa is *bidirectional* allowing the user to select the direction of increasing values. However, the default direction is for values to increase towards the right.

The following prompt is for the choice of ordinate mode. Data may be plotted in a choice of ABSORBANCE, Extinction Coefficient, % Transmission and % Reflectance. The latter pair are identical except for the label on the Y-axis. Data files from the CARYSPEC program may contain either Absorbance or % Transmission values so that rescaling is provided automatically to suit the user's choice of plotting ordinate. If the Difference Spectrum mode has been invoked only the Absorbance and Extinction Coefficient ordinates are valid. If the plotting ordinate uses Absorbance data the program will search the data array for the maximum value to provide automatic ranging on the Y-axis. If Extinction Coefficient mode is specified the program also calculates a suitable Y-axis exponent. Otherwise, the Y-axis defaults to 0-100% limits. The default tick and label positions are then set by calling Subroutine Yaxis.

The user is then prompted to check that the selected plotter is connected and turned on before proceeding to send plotter commands. Finally, the user is presented with the plotting menu with default settings for axis and label sizes, line type, pen velocity, the location of tick marks and axis labels and the command interface for plotting, annotating and digitizing.

EXIT:

The final portion of PLOTSPEC issue an erase command line instruction and then terminates the program unconditionally.

2.2 Plotting Menu Commands:

The interactive plotting control menu is designed both for flexibility and ease of use in setting quite a large number of plotting parameters. On most occasions, the default limits and spacing between tick marks and labels will be perfectly satisfactory. However, the user has complete control over these parameters to suit individual preferences. The various command selections are listed below:

'PL' .....Plot Limits

This command sets the actual range of the data file to be plotted. The default value is the full scan range. If the plotting scale is made smaller than the scan range the plot limits are reduced to match in order to prevent attempts to plot off scale data. If the plotting scale is made larger than the scan range the plot limits are set to the actual scan limits.

'XS' .....X-scale

The range of the X-axis plotting scale defaults to the scan range of the spectrum but may be made larger or smaller than the scan limits. The XMIN,XMAX values may be entered in reverse order to produce a plot with values increasing towards the left. These limits are passed to Subroutine Xaxis to reset the plot limits, tick marks and label positions automatically.

'XT' .....X-tick Spacing

This option allows for customizing the X-axis tick mark spacing with prompts for First, Last and Space. The limits are validated to lie within the current X-scale range and the label positions are automatically reset to match the tick positions.

'XL' .....X-label Spacing

This option allows the user to reset the automatic label positioning. The entries for First, Last and Space are treated in a similar manner to the tick marks.

'YS' .....Y-scale

The range of the Y-axis plotting scale defaults to the MIN,MAX scale appropriate for the selected ordinate. For %R and %T scales the default scale is 0-100%. For Absorbance and Extinction Coefficient ordinates autoranging is used to fit the entire spectrum on scale. The scale range is passed to Subroutine Yaxis to reset the plot limits, tick marks and label positions automatically.

'YT' .....Y-tick Spacing

This option allows for customizing the Y-axis tick mark spacing with prompts for First, Last and Space. The label positions are automatically reset to match the tick marks. No input validation is provided for the limits as it is assumed the user can read the updated console display before plotting.

'YL' .....Y-label Spacing

This option allows the user to reset the automatic label positioning. The entries for First, Last and Space are treated in a similar manner to the tick marks.

'CS' .....Char.Size

The size of character labels can be altered to suit individual preferences. However, the size should not be made much larger than the default fields (1x2 cm) when using the NOTEBOOK or FULL size axes definitions since the labels may not fit within the hard lip limits of the plotters.

'PV' .....Pen Velocity

Plotting quality is very dependent on the pen speed, the type of pen and plotting medium chosen. The program uses a default pen speed of 5 cm/sec for both the axes and spectrum plots. The user can alter these within the range 1-36 cm/sec. While the manual for the HP 7550A plotter *recommends* a speed of 50 cm/sec for the combination of felt tip pen and graphics paper there is no doubt that this is determined more by the quest for throughput than quality. Roller ball pens also work well at the 5 cm/sec pen speed. Thus, there is little need to alter the default values in most cases though transparency plots can benefit from a higher speed (10 cm/sec).

'LT' .....Line Type

The plotters have 6 inbuilt line type functions. The default value specifies a SOLID line. Since PLOTSPEC can plot multiple spectra on the same graph the BROKEN line type function is quite useful. The various patterns can be found by reference to the plotter manuals. The length of the patterns is entered as a % of full scale and a useful guide is to select the same length as the pattern number.

'AX' .....Axes Size

The program includes three, predefined plot types NOTEBOOK, FULL and USER SET. The plotting boundaries vary to suit different functions and paper sizes. The default NOTEBOOK size is a small, A-size plot which allows room for labelling a list of spectral file parameters on the right hand margin. The FULL size plot nicely fills the plotting area of A-size paper with sufficient space for a centered Title over the plot. The USER SET size allows for custom size plots up the the limits of B-size paper. This mode has predefined limits which produce a FULL size plot on B-size paper but the scaling coordinates can be easily altered by the user to suit individual needs.

'AN' .....Annotate Plot

This command allows the use to enter, move and plot Labels, a list of spectral Parameters or a centered Title. The Title defaults to the data file descriptor but the user can enter a new Title if required. The Parameters option is only valid for the NOTEBOOK size plot which allocates room for these descriptors in the right hand margin. The Labelling options allows for entry of descriptive text (up to 40 chars.) which may be positioned and drawn anywhere on the plotting surface. The character size and labelling direction are selectable while the plotting mode supports centered, left and right justification. The character size for labels defaults to 0.6*Normal plot size.

'PA' .....Plot Axes

This command draws the axes grid according to the selected tick and label positions listed in the plotting menu.

'PS' .....Plot Spectrum

Before proceding with the plot this command pauses for the possible entry of a step multiplier. This allows the user to speed plotting for very large data files.

'DD' .....Digitize/Display Data

The program supports manual use of the plotters for digitizing peak positions from the plot. This routine will allow the user to annotate the plot at these positions with either the X coordinate, the Y coordinate or Both. Labels are drawn with small characters in the vertical direction and may be plotted in centered, left or right justified format. In this case, the annotation routine provides offsets to avoid writing over the spectrum.

2.3 COMMON DATA:

All COMMON variables used by PLOTSPEC are held in named COMMON blocks. The variables contained within the COMMON blocks are listed below:

/DATA/ Contains EMA REAL Arrays of spectroscopic data

A — Array containing the Absorbance or %T data
Values read from disk data file
Values used in main program unit

W — Array containing the wavelength data (nm)
Values read from disk data file
Values used in main program unit

/DIGIT/ Contains REAL and INTEGER variables for scaling digitized data

FACTOR — REAL variable for scaling absorbance to extinction coefficient units
Values set in main program unit (from data file variables)
Values used in main program unit and Subroutine Digitize

XMIN, XMAX — REAL variables containing the current X-axis limits
Values set in main program unit
Values used in main program unit, Subroutine Digitize, Subroutine Order and Subroutine Xaxis

YOFF, YSCALE — REAL variables containing the current Y-axis offset & scale length
Values set in main program unit
Values used in main program unit, Subroutine Digitize, Subroutine Order and Subroutine Yaxis

IX,IY — INTEGER variables containing the coordinates of the digitized point

X1,Y1 — INTEGER variables containing the coordinates of the scaling points P1,P2

X2,Y2 — Values set in main program unit and Subroutine Digitize
Values used in main program unit and Subroutine Digitize

/XPARAM/ Contains REAL variables for plotting control

LMIN, LMAX	Current X-axis plotting limits for validation of Tick or Label entries
WN,WX	Current plotting limits for Wavelength o Wavenumber scale
Xtick,	X-axis tick mark spacing
FXT,LXT	First and Last X-axis tick marks
Xlabel,	X-axis label spacing
FXL,LXL	First and Last X-axis labels
	Values set in Subroutine Xaxis
	Values used in main program unit

/YPARAM/ Contains REAL variables for plotting control

Ytick,	Y-axis tick mark spacing
FYT,LYT	First and Last Y-axis tick marks
Ylabel	Y-axis label spacing
FYL,LYL	First and Last Y-axis labels
	Values set in Subroutine Yaxis
	Values used in main program unit

2.4 SUBROUTINES:

PLOTSPEC uses subroutines to perform specific tasks which are required more than once, including string manipulations, input validation, digitizing and data rescaling. The purpose and calling sequences are listed below:

Center(TITLE)

Prints a string on the user console centred within a 72 column line.

TITLE — CHARACTER*72 string, contents set by calling unit

CALLED BY: Main program unit
CALLS: None

Coeff(E,String,K)

Converts a numeric extinction coefficient into a rounded string with exponent, if required. Special handling is executed for 0.0000 and 1.0000 values.

E — REAL variable input from calling unit

String — CHARACTER*(*) output containing floating point string
DIMENSION is set by the calling unit

K — INTEGER variable input from calling unit specifying the number of digits of precision required in string. Output value returns the number of characters in string to the calling unit.

CALLED BY: SUBROUTINE Digitize
CALLS: SUBROUTINE Str

Digitize(X,Xcode,Y,Ext,K)

Reads the current pen position from the plotter and converts the coordinates to the user's units. The routine also converts the Y-coordinate to extinction coefficient format. The main program determines whether the latter value is valid for the ordinate mode in use.

X	REAL variable output containing the abscissa value in user units
Xcode	CHARACTER variable input used to select scaling of the abscissa units
Y	REAL variable output containing the ordinate value in user units
Ext	CHARACTER*(*) output string containing the extinction coefficient DIMENSION is set by the calling unit
K	INTEGER variable input to specify the number of digits precision in Ext Output value contains the number of characters in the returned string

CALLED BY: Main program unit
CALLS: SUBROUTINE Coeff

Exponent(N,Mult)

Converts the scale factor (power of 10) for extinction coefficient mode into string exponents for labelling the Y-axis in the screen menu and on the plotted graph (*e.g.* '1E-3' or '1 ...').

N	REAL variable input, power of 10
Mult	CHARACTER*(*) output string containing multiplier DIMENSION is set by the calling unit

CALLED BY: Main program unit
CALLS: SUBROUTINE Str

Line(N)

Prints a line of '-' characters to the user console N columns wide and centred within a 72 column line.

N INTEGER variable input from calling unit

CALLED BY: Main program unit
CALLS: None

Order(MIN,MAX)

Validates the input arguments so that MIN < MAX

MIN,MAX REAL variables input and output with order swapped if required

CALLED BY: Main program unit
CALLS: None

Rescale(J,K,ND)

Converts ordinate data array between Absorbance units and % Transmission. The data array A(J,I) is accessed from EMA COMMON.

J INTEGER variable input (1 or 2) to specify the spectrum

K INTEGER variable input (0 or 1) to specify the scaling procedure. The original value for K is obtained from PARAM(J,1) in the data file. On return to the main program unit the latter parameter is altered to reflect the current data format.

ND INTEGER variable input containing the number of data points in A(J,I)

CALLED BY: Main program unit
CALLS: None

Str(VALUE,String,PREC)

Performs a conversion from numeric value to a string number for floating point numbers only with up to 12 digits precision.

VALUE — REAL variable input to be processed by the routine

String — CHARACTER*14 string output corresponding to VALUE

PREC — INTEGER variable input to set the rounding precision for string

CALLED BY: Main program unit, SUBROUTINE Coeff, SUBROUTINE Exponent
CALLS: None

Upper(Code)

Performs a check for lower case characters in a string of arbitrary length and converts to upper case if necessary.

Code — CHARACTER*(*) variable passed into routine and UPPER case on exit
DIMENSION is set by the calling unit

CALLED BY: Main program unit
CALLS: None
EXTENSION: LEN(*string*) function, an HP extension to FORTRAN 77

Val(String,VALUE)

Performs a conversion from string to numeric value for a string number containing up to 10 digits. This is more than required by PLOTSPEC.

String — CHARACTER*(*) string input to be processed by routine
DIMENSION is set by calling unit

VALUE — REAL variable output

CALLED BY: Main program unit
CALLS: None

Wait(DELAY)

Performs a loop whic tests the system clock until DELAY seconds have elapsed. The routine does not make provision for the special case at the transition to 2400 hours.

DELAY REAL variable holding the value of the delay period in seconds

CALLED BY: Main program unit
CALLS: FUNCTION Time(I)

Xaxis(XL,XH)

Performs both limits settin~ for the X-axis range variables and selection of the default Tick and Label positions. The routine starts with Xtick set to 1/10 of the full scale range and then compares this with a table of preferred values. If the range is anomalously small or large the Tick and Label positions are based on the 1/10 scale spacing. Otherwise, a neat and tidy spacing is selected from the table values with a label at every other tick position.

Yaxis(YSCALE)

Performs Tick and Label position selection using preferred table values, if possible. The routine start with Ytick equal to 1/10 of YSCALE. If the ordinate uses Extinction Coefficient scaling or the range is anomalously small or large the Tick and Label positions are based on the 1/10 scale spacing. Otherwise, a neat and tidy spacing is selected from the table values with a label at every other tick position.

2.5 FUNCTIONS:

PLOTSPEC uses only one function subprogram that makes an EXEC call to read the system time.

Time(I)

Performs an EXEC call to read the system clock and converts the reading to seconds and centisecords.

I Dummy argument

CALLED BY: SUBROUTINE Wait only
CALLS: EXEC(ICODE,ITIME) system level command

PROGRAM CODE

3.0 Source Code Availability:

The source code for program PLOTSPEC is a 73K ASCII text file available on either a Hewlett-Packard cartridge, 9 track tape or an IBM 360K format floppy disk. All requests should be accompanied by the blank medium desired. A printed copy of the source code is listed below.

3.1 Variable Names And Usage:

A complete listing of the INTEGER, REAL, REAL Array and CHARACTER variables for the MAIN segment of PLOTSPEC is given below in Tables II, III, IV & V, respectively. The subroutines use the same names as the main program for the same variables. Additional variables in the subroutines and simple integers, I-N, are not documented since their usage is rather obvious. The logical variable MATCH is used within the program when comparing two spectra for the difference spectrum mode.

Table II

Glossary of INTEGER Variables

Name	Description	Value
DIFF	Assigned Label - Difference Spectrum	370
EXIT	Assigned Label - Terminate Program	9000
MENU	Assigned Label - Main Control Menu	10
PLOT	Assigned Label - Plot Spectrum, 1 or 2	400
READ	Assigned Label - Read Spectrum, 1 or 2	570
SETTINGS	Assigned Label - Scan Conditions, 1 or 2	300
ASCII	ASCII equivalent of digits in Str	48-57
FINISH	Index of final abscissa value to plot	1-10001
IX,IY,IZ	Plotter position variables READ/WRITE	0-16000
NCOL	Number of screen columns in menu display	50-70
ND	Number of data points in plotted spectrum	1-10001
NP	Number of parameters to read from file	49
NV	Number of variables to read from file	14
PREC	Precision for rounding function in Str	3,4
PN	Plotter model selection number	1,2
PU	Plotter Logical Unit #, READ/WRITE	17,33
PXOFF	Plotter X-zero position offset	0,200
PYOFF	Plotter Y-zero position offset	0,100
START	Index of first abscissa value to plot	1-10001
UX1,UX2	Absolute Plotter scaling coordinates,	0-16000
UY1,UY2	USER size plot dimensions	0-10100
X1,X2	Plotter X & Y coordinates for reading	0-16000
Y1,Y2	soft clip windowing points	0-10100
XP1,XP2	Absolute Plotter scaling coordinates,	0-16000
YP1,YP2	for WRITE to plotter	0-10100
NDATA(2)	Number of data points in spectrum	1-10001
PARAM(2,49)	Instrument operating modes table	1-16

Table III

Glossary of REAL Variables

Name	Description
BAND	Spectral Bandwidth (nm) - AUTO GAIN mode
BHEIGHT	Large label character height
BWIDTH	Large label character width
COFF	Character offset variable, labelling mode
ESCALE	Y-axis scale length, Ext. Coeff. mode
EMULT	Power of 10 for scaling, Ext. Coeff. mode
EOFF	Y-axis offset, Ext. Coeff. mode
FXL,LXL	First & last X-axis labels
FXT,LXT	First & last X-axis tick marks
FYL,LYL	First & last Y-axis labels
FYT,LYT	First & last Y-axis tick marks
GAIN	Instrument gain - AUTO SLIT mode
HEIGHT	Normal label character height
LHEIGHT	Small label character height
LWIDTH	Small label character width
LMIN	Current X-axis lower limit, data entry check
LMAX	Current X-axis upper limit, data entry check
NUMBER	General purpose data entry variable
PMIN	Pen scale minimum limit
PMAX	Pen scale maximum limit
RATIO	General purpose scaling variable
STEP	Step size (nm) interval, plotting mode
T1,...,T4	Powers of 10 (10,...,1E4)
WIDTH	Normal label character width
WN,WX	Current plot limits, default = WMIN,WMAX
WMIN,XMAX	Absolute scan limits (nm) or (kK)
X,Y	General purpose plotting variables
Xlabel	X-axis label spacing
XMIN,XMAX	Left & Right edges of X-scale on plot
XMULT	Multiplier to scale user X-scale to 10000 units
XOFF	Offset to user X-scale units to set min'm at 0
Xtick	X-axis tick spacing
XN,XX	Data entry variables for X-scale, ticks & labels
YN,YX	Data entry variables for Y-scale, ticks & labels
Ylabel	Y-axis label spacing
YMULT	Scales Y-axis data & labels for Ext. Coeff. mode
YOFF	Offset variable on current Y-axis scale
YSCALE	Current Y-axis scale length
Ytick	Y-axis tick spacing

Table IV

Glossary of REAL Array Variables

Name	Description
ORD(2)	Final ordinate value in file
ABSC(2)	Final abscissa value in file
CELL(2)	Final cell # value in file
CYCLE(2)	Final cycle # value in file
SAMPLE(2)	Final sample # value in file
WAVE(2)	Final wavelength value in file
TIMER(2)	Final time value in file
DIST(2)	Final distance value in file
A(2,10001)	Absorbance or %T array
CONC(2)	Concentration of sample (M), from data file
FACTOR(2)	Concentration * Pathlength for scaling spectra
FMAX(2)	Starting wavelength of scan (nm)
FMIN(2)	Ending wavelength of scan (nm)
FSTEP(2)	Step size (nm), from data file
PATH(2)	Pathlength of sample cell (cm), from data file
VARIABLE(2,14)	Instrument operating conditions table
W(2,10001)	Wavelength array

Table V

Glossary Of CHARACTER Variables

Name	Description
Screen Control:	
BELL	CHAR(7) bell character
CLR*2	Clear screen
DOWN*2	Move cursor down 1 line
ESC	CHAR(27) escape character
HOME*2	Move cursor to upper left corner
UP*2	Move cursor up 1 line
File Status:	
DATE(2)*8	Date (mm/dd/yy)
Fname(2)*20	Filename, CI convention
LABEL(2)*72	Descriptor of spectrum
Pstr(23,16)*14	Table of parameter setting names
Smin(2)*4	Spectrum ending wavelength (nm)
Smax(2)*4	Spectrum starting wavelength (nm)
Sinc(2)*4	Step size interval (nm)
Sstat(2)*10	Spectrum status (VALID, INVALID)
Program Control:	
C	Literal comma ','
Code*2	Main menu selection, valid until reset
Directory*40	User directory name, CI convention
Ext*14	Extinction Coefficient, digitize & label modes
Filespec*63	Full pathname, CI convention
Icode	General purpose selection key entry
Mult*5	Y-axis multiplier label, Ext. Coeff. mode
Pcode*2	Plotting menu option, valid until reset
Psize*8	Screen label for axes type selected
Size	Select type of plotted axes, 'N', 'F' or 'U'
String*14	String to pass data to or from subroutines
Text*40	General purpose string for labelling plot
TITLE*72	String to be printed to screen
Xcode	Selects X-axis scale, (nm) or (kK)
Xord*7	X-axis label (nm) or (cm^{-1}), digitize mode
Ycode	Selects Y-axis scale, 'A', 'E', 'R' or 'T'

...cont'd

Plotter Control:

CR	CHAR(13), carriage return
Etx	CHAR(3), Terminator for label mode on plotter
LF	CHAR(10), line feed
Length*6	Broken line style pattern length (%)
Lmode*8	Line type mode (SOLID or BROKEN)
Pattern*6	Broken line type number
Plotter*10	Literal 'HP 9872A' or 'HP 7550A' identifier
Vaxes*2	Pen velocity (cm/sec), axes vectors
Vspec*2	Pen velocity (cm/sec), spectrum
Xleft*6	Literal '0' or '-10000', for scale command SC
Xright*6	Literal '10000' or '0', for scale command SC
Xstring*15	X-axis label, plotter output
Ylow*6	Literal '0'
Ystring*15	Y-axis label, screen and plotter output
Ytop*6	Literal '10000'

```
 1 FTN7X,L
 2 $FILES 0,1
 3 $EMA/DATA/
 4       PROGRAM PLOTSPEC
 5 C     ------------------------------------------------------------------
 6 C
 7 C     This Program Is Designed To Plot Spectral Data Acquired From
 8 C     The CARY 2390 UV-VIS-NIR Spectrophotometer With CARYSPEC.RUN
 9 C
10 C     The Program Supports Output To HP 9872A And HP 7550A Plotters
11 C     The HP 9872A Is Plotter #1 At Address LU 33 (IEEE-488 Device #2)
12 C     The HP 7550A Is Plotter #2 At Address LU 17 (RS-232C Device)
13 C
14 C     ------------------------------------------------------------------
15 C
16 C         AUTHOR:  Dr. Robert A. Binstead,
17 C                  Chemistry Division, Code 6125,
18 C                  Naval Research Laboratory,
19 C                  Washington, D.C. 20375-5000
20 C
21 C         WRITTEN: February, 1987
22 C
23 C         VERSION: 1.72
24 C
25 C         REVISED: March, 1987:
26 C                              - Debugged plotting DO loops
27 C                              - Added Ordinate/Abscissa mode checks
28 C                              - Added ending wavelength check
29 C
30 C                  April, 1987:
31 C                              - Altered to use expt'l X-values
32 C                              - Added screen display routine
33 C                              - Removed rounding from SUB Xlimits
34 C                              - Altered rounding to use NINT function
35 C
36 C                  May, 1987:
37 C                              - Altered annotation mode to support
38 C                                Title, Parameters & Labels on plot
39 C                              - Altered AXES selection to provide
40 C                                default USER values & easy updates
41 C                              - Changed FFRCL to 79 characters to
42 C                                prevent unwanted line wrapping
43 C
44 C                  June, 1987:
45 C                              - Altered Filename convention to match
46 C                                the directory structure of the new CI
47 C                                operating syst..m
48 C                              - The program had to be stripped down
49 C                                to run under the CI operating system
50 C                                by eliminating most I/O error checks
51 C
52 C                  July, 1987:
53 C                              - SEGMENTED versions of the full size
```

```
C                    program failed with Memory Protect
C                    errors at the INQUIRE statement if
C                    the file existed already
C
C          August, 1987:
C                  - Eliminated INQUIRE statement for file
C                    exists or open check to avoid system
C                    crash in the segmented version of the
C                    program. The error checks are now made
C                    using error numbers returned in the
C                    OPEN statement.
C
C          April, 1988:
C                  - Removed needless DATA for Pstr, unused
C                    arrays and most I/O error checks on
C                    WRITE to allow room for the complete
C                    program in a single 32K word segment.
C                  - Added Uppercase string conversion
C                    routine for all string entries.
C                  - Subroutines Xlimits & Ylimits were
C                    replaced by Subroutine Order(MIN,MAX)
C                  - Subroutine Xaxis was added to avoid
C                    duplication in setting X-axis Limits,
C                    Xtick and Xlabel spacing.
C                  - Subroutine Yaxis was added to avoid
C                    duplication in setting Y-axis Limits,
C                    Ytick and Ylabel spacing.
C                  - Altered Annotation Mode For Labels Up
C                    To 40 Characters In Centered, Left &
C                    Right Justified Formats. Positioning
C                    & Character Size Commands Were Added.
C                  - The Pen Position Digitizing Routine
C                    Was Rewritten In Subroutine Form And
C                    A Labelling Command Added To The Menu.
C                  - The Annotation Routine Was Augmented
C                    To Support Peak Position Labels In
C                    Centered, Left & Right Justified Modes
C                    With Special Offset Features To Avoid
C                    Writing Over The Spectrum.
C                  - % Transmission & % Reflectance Modes
C                    Were Added To The Y-scale Selections.
C                  - Re-scaling Between %T & Absorbance
C                    Was Added To Support Both Plotting
C                    Modes From Either Type Of Data File.
C                  - Rounding Functions Were Altered To
C                    Use ANINT (Whole Number) Command To
C                    Avoid Integer Overflow With %T & %R
C                    Labelling.
C                  - Added Automatic Tick & Label Routines
C                    To Select Preferred Values Based On
C                    X & Y Scale Ranges. Defaults To 1/10
C                    Of Scale For Entry Of An Anomalously
C                    Small Or Large Range.
```

```
C                              - Added Code For Selection Of Plotter
C                                Type (HP 9872A / HP 7550A) And Made
C                                Adjustments To The P1,P2 Scaling
C                                Points To Fit Output Within The Hard
C                                Clip Limits Of Both Plotters.
C
C       Y-AXIS:  Absorbance or Extinction Coefficient
C
C       X-AXIS:  Wavelength or Wavenumbers x 1E-3
C
C       MEMORY:  30,000 Words (PROGRAM) + 80,000 Words EMA (DATA)
C
C     ------------------------------------------------------------------
C
      INTEGER DIFF,EXIT,MENU,PLOT,READ,SETTINGS,PARAM(2,49)
      INTEGER FINISH,IX,IY,IZ,NCOL,ND,NDATA(2),NP,NV,PN,PU,PXOFF,PYOFF
      INTEGER START,UX1,UX2,UY1,UY2,X1,X2,Y1,Y2,XP1,XP2,YP1,YP2
      REAL BAND,COFF,ESCALE,EMULT,EOFF,GAIN,LMIN,LMAX,NUMBER
      REAL PMIN,PMAX,RATIO,SCALE,STEP,V,WN,WX,WMIN,WMAX
      REAL XMIN,XMAX,XMULT,XOFF,X,XN,XX,Y,YN,YX,YMULT,YOFF,YSCALE
      REAL Xtick,FXT,LXT,Ytick,FYT,LYT,Xlabel,FXL,LXL,Ylabel,FYL,LYL
      REAL T1,T2,T3,T4,LWIDTH,WIDTH,BWIDTH,LHEIGHT,HEIGHT,BHEIGHT
      REAL ABSC(2),CELL(2),CONC(2),CYCLE(2),DIST(2),ORD(2),PATH(2)
      REAL SAMPLE(2),TIMER(2),TEMP(2),WAVE(2),FMIN(2),FMAX(2),FSTEP(2)
      REAL FACTOR(2),VARIABLE(2,14),A(2,10001),W(2,10001)
      LOGICAL MATCH
C
C       Dimension Screen Control String Variables
C
      CHARACTER BELL,CLR*2,DOWN*2,ERASE*2,ESC,HOME*2,UP*2
C
C       Dimension Program Parameter Variables
C
      CHARACTER DATE(2)*8,Fname(2)*20,LABEL(2)*72,Plotter(2)*10
      CHARACTER Smin(2)*4,Smax(2)*4,Sinc(2)*4,Sstat(2)*10
      CHARACTER C,CR,Code*2,Directory*40,Etx,Ext*14,Filespec*63
      CHARACTER Icode,Length*6,LF,Lmode*8,Mult*5,Pcode*2,Pattern*6
      CHARACTER Psize*8,Size,String*14,Text*40,TITLE*72,Vaxes*2
      CHARACTER Vspec*2,Xcode,Xlef*6,Xord*7,Xright*6,Xstring*15
      CHARACTER Ycode,Ylow*6,Ystring*15,Ytop*6,Pstr(23,16)*14
C
C     ------------------------------------------------------------------
C
      COMMON /DATA/A,W
      COMMON /XPARAM/LMIN,LMAX,WN,WX,Xtick,FXT,LXT,Xlabel,FXL,LXL
      COMMON /YPARAM/Ytick,FYT,LYT,Ylabel,FYL,LYL
      COMMON /DIGIT/FACTOR,XMIN,XMAX,YOFF,YSCALE,IX,IY,J,PU,X1,X2,Y1,Y2
C
C     ------------------------------------------------------------------
C
C       Define Rounding Functions Using Nearest Integer Commands
C
      RO(X)=NINT(X)                        ! Type = INTEGER
```

```
160         R1(X)=ANINT(X*10.0)/10.0          ! Type = REAL
161         R2(X)=ANINT(X*100.0)/100.0        ! Type = REAL
162         R3(X)=ANINT(X*1.0E3)/1.0E3        ! Type = REAL
163 C
164 C       ------------------------------------------------------------------
165 C
166 C           Initialize String Variables
167 C
168         DATA (Plotter(I),I=1,2)/'HP 9872A  ','HP 7550A  '/
169         DATA (Pstr(1,I),I=1,6)/'ABSORBANCE','% TRANSMISSION',
170        &'TEMPERATURE','% REFLECTANCE','CONCENTRATION','EMISSION'/
171         DATA (Pstr(2,I),I=1,4)/'WAVELENGTH','TIME','TEMPERATURE',
172        &'DISTANCE'/
173         DATA (Pstr(3,I),I=1,11)/'OFF','0.01','0.02','0.05','0.1','0.2',
174        &'0.5','1.0','2.0','5.0','10.0'/
175         DATA Pstr(4,1)/'OFF'/
176         DATA (Pstr(4,I),I=6,15)/'0.2','0.5','1.0','2.0','5.0',
177        &'10','20','50','100','200'/
178         DATA (Pstr(5,I),I=1,4)/'AUTO SELECT','AUTO GAIN','AUTO SLIT',
179        &'SINGLE BEAM'/
180         DATA (Pstr(6,I),I=1,5)/'OFF','NORMAL','1ST DERIV','2ND DERIV',
181        &'LOG'/
182         DATA (Pstr(7,I),I=1,9)/'0.01','0.02','0.05','0.1','0.2','0.5',
183        &'1.0','2.0','4.0'/
184         DATA (Pstr(8,I),I=10,16)/'2','5','10','20','50','100','200'/
185         DATA (Pstr(9,I),I=12,15)/'10','20','50','100'/
186         DATA (Pstr(10,I),I=1,5)/'-1.9 TO 0.6','-2.0 TO 0.5',
187        &'-2.1 TO 0.4','-2.2 TO 0.3','-2.3 TO 0.2'/
188         DATA (Pstr(11,I),I=1,16)/'+/-0.01','+/-0.02','+/-0.05','+/-0.1',
189        &'+/-0.2','+/-0.5','+/-1.0','+/-2.0','+/-5.0','+/-10','+/-20',
190        &'+/-50','+/-100','+/-200','+/-500','+/-1000'/
191         DATA (Pstr(12,I),I=1,16)/'+/-0.01','+/-0.02','+/-0.05','+/-0.1',
192        &'+/-0.2','+/-0.5','+/-1.0','+/-2.0','+/-5.0','+/-10','+/-20',
193        &'+/-50','+/-100','+/-200','+/-500','+/-1000'/
194         DATA (Pstr(14,I),I=1,10)/'0','10','20','30','40','50','60','70',
195        &'80','90'/
196         DATA (Pstr(15,I),I=1,4)/'0.5','1.0','3.0','10'/
197         DATA (Pstr(16,I),I=1,2)/'NORMAL','REVERSE'/
198         DATA (Pstr(17,I),I=1,2)/'OFF','ON'/
199         DATA (Pstr(18,I),I=1,2)/'REPEAT SCAN','SGL/MULTI'/
200         DATA (Pstr(19,I),I=1,2)/'SERIAL','OVERLAY'/
201         DATA (Pstr(20,I),I=1,4)/'BOTH ON','UV ONLY','VIS/NIR ONLY',
202        &'BOTH OFF'/
203         DATA (Pstr(21,I),I=1,3)/'AUTO','UV','VIS/NIR'/
204         DATA (Pstr(22,I),I=1,3)/'AUTO','UV/VIS','NIR'/
205         DATA (Pstr(23,I),I=1,2)/'FULL','1/3'/
206 C
207         BELL=CHAR(7)
208         ESC=CHAR(27)
209         CLR=ESC//'J'
210         HOME=ESC//'h'
211         UP=ESC//'A'
212         DOWN=ESC//'B'
213         ERASE=ESC//'K'
```

```
214 C
215       PN=1                          ! Select Plotter #1 (HP 9872A)
216       T1=10.0
217       T2=100.0
218       T3=1000.0
219       T4=10000.0
220 C
221 C     ---------------------------------------------------------------
222 C
223 C         Assign Statement Labels
224 C
225 C     ---------------------------------------------------------------
226 C
227       ASSIGN 10  TO MENU
228       ASSIGN 100 TO READ
229       ASSIGN 300 TO SETTINGS
230       ASSIGN 370 TO PLOT
231       ASSIGN 390 TO DIFF
232       ASSIGN 9000 TO EXIT
233 C
234 C     ---------------------------------------------------------------
235 C
236 C         Data Transfer and Plot Control Menu
237 C
238 C     ---------------------------------------------------------------
239 C
240       CALL FFRCL(79)                ! Set Fields to 79 Characters
241    10 WRITE (1,*) HOME,CLR,'_'
242       NCOL=70
243       TITLE='Cary 2390 Spectral Data Plotting'
244       CALL Center(TITLE)
245       WRITE (1,'(T61,A2,A9)') UP,'Rev: 1.72'
246       CALL Line(NCOL)
247       WRITE (1,20) 'CODE','FUNCTION','STATUS','MIN','MAX','INC'
248    20 FORMAT (T4,A4,T18,A8,T38,A7,T50,A3,T58,A3,T66,A3)
249       CALL Line(NCOL)
250       WRITE (1,30) 'R1','.....Read Spectrum #1........',Sstat(1),
251      &Smin(1),Smax(1),Sinc(1)
252       WRITE (1,30) 'R2','.....Read Spectrum #2........',Sstat(2),
253      &Smin(2),Smax(2),Sinc(2)
254       WRITE (1,50) 'IS','.....Instrument Settings.....'
255       WRITE (1,30) 'PS','.....Plotter Selection.......',Plotter(PN)
256       WRITE (1,40) 'P1','.....Plot Spectrum #1........',Fname(1)
257       WRITE (1,40) 'P2','.....Plot Spectrum #2........',Fname(2)
258       WRITE (1,50) 'DS','.....Difference Spectrum.....'
259       WRITE (1,50) 'EX','.....EXIT Menu...............'
260    30 FORMAT (/,T5,A2,T7,A30,T39,A10,T50,A4,T58,A4,T66,A4)
261    40 FORMAT (/,T5,A2,T7,A30,T39,A16)
262    50 FORMAT (/,T5,A2,T7,A30)
263       WRITE (1,*)
264       CALL Line(NCOL)
265       WRITE (1,*)
266    70 WRITE (1,*) UP,ERASE,'_'
```

```
267         WRITE (1,'(T3,A15,A,A2)') 'Enter the CODE:',BELL,'_'
268         READ (1,80) Code
269      80 FORMAT (A2)
270         CALL Upper(Code)
271 C       ------------------------------------------------------------------
272         IF ((Code.EQ.'R1').OR.(Code.EQ.'R2')) THEN
273             J=ICHAR(Code(2:2))-48
274             GO TO READ
275         END IF
276         IF (Code.EQ.'IS') GO TO SETTINGS
277         IF (Code.EQ.'PS') THEN
278      90     WRITE (1,*) UP,ERASE,'  Select: 1...HP 9872A,',
279        &    '  2...HP 7550A ? ',BELL,'_'
280             READ (1,99) Icode
281             IF ((Icode.NE.'1').AND.(Icode.NE.'2')) THEN
282                 GO TO 90
283             END IF
284             PN=ICHAR(Icode)-48
285             GO TO MENU
286         END IF
287         IF ((Code.EQ.'P1').OR.(Code.EQ.'P2')) THEN
288             J=ICHAR(Code(2:2))-48
289             GO TO PLOT
290         END IF
291         IF (Code.EQ.'DS') THEN
292             J=1
293             GO TO DIFF
294         END IF
295         IF (Code.EQ.'EX') GO TO EXIT
296         GO TO 70
297 C
298 C       ------------------------------------------------------------------
299 C
300 C           Read Spectrum: (J = 1 or 2)
301 C
302 C       ------------------------------------------------------------------
303 C
304      99 FORMAT (A1)
305     100 IF (Sstat(J).EQ.'VALID') THEN
306           WRITE (1,*) UP,ERASE,'  Spectrum is PRESENT: ',
307        &  'Proceed (Y or N) ? ',BELL,'_'
308           READ (1,99) Icode
309           CALL Upper(Icode)
310           IF (Icode.EQ.'N') GO TO 70
311           IF (Icode.NE.'Y') GO TO 100
312         END IF
313         WRITE (1,*) HOME,CLR,'_'
314         TITLE='Read Spectrum #'//Code(2:2)
315         CALL Center(TITLE)
316         CALL Line(NCOL)
317         WRITE (1,*) DOWN,'  Enter Filename: ',BELL,'_'
318         READ (1,'(A20)') Fname(J)
319         CALL Upper(Fname(J))
```

```
      WRITE (1,*) DOWN,'  Directory, (Return = /DEFAULT/) ',BELL,'_'
      READ (1,'(A40)') Directory
      IF (Directory.EQ.' ') THEN
        Filespec=Fname(J)
        GO TO 110
      END IF
      K=40
      DO WHILE (Directory(K:K).EQ.' ')
        K=K-1
      END DO
      IF (Directory(K:K).EQ.'/') K=K-1
      Filespec=Directory(1:K)//'/'//Fname(J)
  110 K=63
      DO WHILE (Filespec(K:K).EQ.' ')
        K=K-1
      END DO
      WRITE (1,*) UP,ERASE,'  Validating: ',Filespec(1:K),' _'
      CALL Wait(1.0)
      OPEN (UNIT=66,FILE=Filespec(1:K),IOSTAT=N,STATUS='OLD')
      WRITE (1,*)
      IF (N.NE.0) THEN
        WRITE (1,*) UP,ERASE,'_'
        N=N-500
        IF (N.EQ.6) WRITE (1,*) ' File does NOT EXIST: ',BELL,'_'
        IF (N.EQ.8) WRITE (1,*) ' File is already OPEN: ',BELL,'_'
        IF ((N.NE.6).AND.(N.NE.8)) WRITE (1,*) ' Disk Error # ',N,
     &  BELL,' _'
        CLOSE (UNIT=66,STATUS='DELETE')
        CALL Wait(2.0)
        WRITE (1,*)
        Sstat(J)='INVALID'
        GO TO MENU
      END IF
      WRITE (1,*) UP,ERASE,'  Reading File: ',Filespec(1:K)
      READ (66,FMT=120,IOSTAT=N,ERR=210) LABEL(J)
  120 FORMAT (A72)
      WRITE (1,*) DOWN,'  Title:'
      WRITE (1,*) '  ',LABEL(J)
      READ (66,FMT=130) DATE(J)
  130 FORMAT (A8)
      WRITE (1,*) DOWN,'  Date: ',DATE(J)
      READ (66,*) FMIN(J),FMAX(J),FSTEP(J),
     &CONC(J),PATH(J)
      READ (66,*) ORD(J),ABSC(J),CELL(J),CYCLE(J),
     &SAMPLE(J),WAVE(J),TIMER(J),TEMP(J),DIST(J)
      WRITE (1,140) DOWN,'Scan Range: ',FMAX(J),' to ',FMIN(J),
     &' nm at ',FSTEP(J),' nm steps'
      WRITE (1,'(T4,A2,A12,2X,G9.4)') DOWN,'Conc. (M) : ',CONC(J)
      WRITE (1,150) DOWN,'Path (cm) : ',PATH(J)
      WRITE (1,150) DOWN,'Temp. (C) : ',TEMP(J)
  140 FORMAT (T4,A2,A12,F6.2,A4,F6.2,A7 F4.2,A9)
  150 FORMAT (T4,A2,A12,F6.2)
```

```
372         CALL Str(FMIN(J),String,4)
373         Smin(J)=String(2:5)
374         CALL Str(FMAX(J),String,4)
375         Smax(J)=String(2:5)
376         CALL Str(FSTEP(J),String,4)
377         Sinc(J)=String(2:5)
378         READ (66,FMT=160,IOSTAT=N,ERR=210) NP,NV,NDATA(J)
379     160 FORMAT (I3,I3,I6)
380         IF ((NP.NE.49).OR.(NV.NE.14)) GO TO 200
381         IF (ABS(FMIN(J)-WAVE(J)).GT.0.1) THEN
382           WRITE (1,*) DOWN,'  Warning! Scan ended at',WAVE(J),' nm',BELL
383           CALL Wait(2.0)
384         END IF
385         WRITE (1,*)
386         TITLE='**** READING SPECTRUM ****'
387         WRITE (1,*) HOME,'_'
388         CALL Center(TITLE)
389         READ (66,FMT=170) (PARAM(J,K),K=1,NP)
390     170 FORMAT (I2)
391         READ (66,*) (VARIABLE(J,K),K=1,NV)
392         READ (66,*) (A(J,K),K=1,NDATA(J))
393         READ (66,*) (W(J,K),K=1,NDATA(J))
394         Sstat(J)='VALID'
395     180 CLOSE (UNIT=66,IOSTAT=N,ERR=210)
396         IF (Sstat(J).NE.'VALID') GO TO MENU
397     190 WRITE (1,*) UP,ERASE,'  EDIT Conc./Path: (Y or N) ? ',BELL,'_'
398         READ (1,99) Icode
399         CALL Upper(Icode)
400         IF (Icode.EQ.'Y') GO TO 230
401         IF (Icode.NE.'N') GO TO 190
402         GO TO MENU
403 C       ------------------------------------------------------------------
404     200 WRITE (1,*) UP,ERASE,'  Data Format Error ',BELL,'_'
405         Sstat(J)='ABORTED'
406         GO TO 240
407     210 WRITE (1,*) UP,ERASE,'  Disk Error #',N,BELL,' _'
408         Sstat(J)='INVALID'
409     220 CALL Wait(2.0)
410         WRITE (1,*)
411         GO TO 180
412 C       ------------------------------------------------------------------
413     230 WRITE (1,*) UP,ERASE,'  (C...Conc , P...Path) ? ',BELL,'_'
414         READ (1,99) Icode
415         CALL Upper(Icode)
416         IF (Icode.EQ.'P') GO TO 250
417         IF (Icode.NE.'C') GO TO 230
418     240 WRITE (1,*) UP,ERASE,'  Concentration, (M) : ',BELL,'_'
419         READ (1,*,ERR=240) CONC(J)
420         GO TO 190
421     250 WRITE (1,*) UP,ERASE,'  Pathlength, (cm)  ',BELL,'_'
422         READ (1,*,ERR=250) PATH(J)
423         GO TO 190
```

```
C
C     ---------------------------------------------------------------
C
C         Error Messages & Returns To Menu
C
C     ---------------------------------------------------------------
C
  250 TITLE='  Conc  or Path = 0.0 '
      GO TO 290
  270 TITLE='  Spectra are MISMATCHED: '
      GO TO 290
  280 TITLE='  Spectrum is ABSENT: '
  290 WRITE (1,*) UP,ERASE,TITLE(1:26),BELL,'_'
      CALL Wait(2.0)
      WRITE (1,*)
      GO TO 70
C
C     ---------------------------------------------------------------
C
C         Display Instrument Settings
C
C     ---------------------------------------------------------------
C
  300 IF ((Sstat(1).NE.'VALID').AND.(Sstat(2).NE.'VALID')) GO TO 280
  310 WRITE (1,*) UP,ERASE,'  Spectrum #, (1 or 2): ',BELL,'_'
      READ (1,'(I2)',ERR=310) J
      IF ((J.NE.1).AND.(J.NE.2)) GO TO 310
      IF (Sstat(J).NE.'VALID') GO TO 280
      BAND=VARIABLE(J,10)
      GAIN=VARIABLE(J,6)
      String=Pstr(7,PARAM(J,7)+1)
      K=1
      IF (PARAM(J,1).NE.0) THEN
        String=Pstr(8,PARAM(J,8)+1)
        K=11
      END IF
      CALL Val(String,PMAX)
      PMIN=VARIABLE(J,K)
      PMAX=PMIN+PMAX
      K=11
      IF (PARAM(J,6).EQ.4) K=10
      String=Pstr(K,PARAM(J,K)+1)
      WRITE (1,* ) HOME,CLR,'_'
      TITLE='Instrument Settings'
      CALL Center(TITLE)
      CALL Line(50)
      WRITE (1,'(T20,A8,T40,A7)') 'FUNCTION','SETTING'
      CALL LINE(50)
      WRITE (1,*)
      WRITE (1,320) 'WAVELENGTH LIMITS      ',PMIN(J),' - ',PMAX(J)
      WRITE (1,330) 'ORDINATE               ',Pstr(1,PARAM(J,1)+1)
      WRITE (1,330) 'ABSCISSA               ',Pstr(2,PARAM(J,2)+1)
      WRITE (1,330) 'SCAN RATE (nm/sec)     ',Pstr(3,PARAM(J,3)+1)
```

```
      WRITE (1,330) 'CHART DISPLAY (nm/cm)..',Pstr(4,PARAM(J,4)+1)
      WRITE (1,330) 'REFERENCE MODE.........',Pstr(5,PARAM(J,5)+1)
      WRITE (1,340) 'SBW (nm), GAIN.........',BAND,',',GAIN
      WRITE (1,330) 'PEN FUNCTION...........',Pstr(6,PARAM(J,6)+1)
      WRITE (1,340) 'PEN LIMITS (Min,Max)...',PMIN,',',PMAX
      IF (PARAM(J,6).GT.1) WRITE (1,350) UP,ERASE,String
      WRITE (1,330) 'RESPONSE TIME (sec)....',Pstr(15,PARAM(J,15)+1
      WRITE (1,330) 'BEAM INTERCHANGE.......',Pstr(16,PARAM(J,16)+1
      WRITE (1,330) 'SLIT HEIGHT............',Pstr(23,PARAM(J,23)+1)
      WRITE (1,330) 'LAMP SELECT............',Pstr(21,PARAM(J,21)+1)
      WRITE (1,330) 'DETECTOR SELECT........',Pstr(22,PARAM(J,22)+1)
  320 FORMAT (T15,A23,T40,F5.2,A,F5.2)
  330 FORMAT (T15,A23,T40,A14)
  340 FORMAT (T15,A23,T40,F4.2,A,F5.2)
  350 FORMAT (T40,A2,A2,A14)
      WRITE (1,*)
      CALL Line(50)
      WRITE (1,*)
  360 WRITE (1,'(T14,A2,A2,A23,A,A)') UP,ERASE,
     &'Press RETURN for MENU: ',BELL,'_'
      READ (1,99) Icode
      IF (Icode.NE.' ') GO TO 360
      GO TO MENU
C
C     ---------------------------------------------------------------
C
C         Plot Mode Setup
C
C     ---------------------------------------------------------------
C
  370 IF (Sstat(J).NE.'VALID') GO TO 280
      GO TO 400
  390 IF ((Sstat(1).NE.'VALID').OR.(Sstat(2).NE.'VALID')) GO TO 280
      MATCH=.TRUE.
      IF (FSTEP(1).NE.FSTEP(2)) MATCH=.FALSE.
      IF (FMIN(1).NE.FMIN(2)) MATCH=.FALSE.
      IF (FMAX(1).NE.FMAX(2)) MATCH=.FALSE.
      IF (MATCH) GO TO 400
      GO TO 270
C     ---------------------------------------------------------------
  400 TITLE='Plot Spectrum #'//CHAR(J+48)
      FACTOR(1)=CONC(1)*PATH(1)
      FACTOR(2)=CONC(2)*PATH(2)
      IF (Code.EQ.'DS') THEN
        IF ((FACTOR(1).EQ.0.0).OR.(FACTOR(2).EQ.0.0)) GO TO 260
        RATIO=FACTOR(1)/FACTOR(2)          ! Temporary Scaling Factor
        TITLE='Difference Spectrum Plot'
      END IF
      IF (FACTOR(J).EQ.0.0) FACTOR(J)=1.0 ! Avoid Division By Zero
      WRITE (1,*) HOME,CLR,'_'
      CALL Center(TITLE)
      CALL Line(NCOL)
      WRITE (1,*) DOWN,DOWN
```

```
      WRITE (1,'(T10,A32)') 'X-scale units:  N.....Nanometres'
      WRITE (1,*)
      WRITE (1,'(T26,A17)') 'W.....Wavenumbers'
      WRITE (1,*) DOWN
410   WRITE (1,420) UP,ERASE,'Code:    ',BELL,'_'
420   FORMAT (T19,A2,A2,A7,A,A)
      READ (1,99) Xcode
      CALL Upper(Xcode)
      IF (Xcode.EQ.'W') THEN
        WRITE (1,*) UP,ERASE,UP,UP,ERASE,UP,UP
        WRITE (1,'(T26,A2,A2,A11)') UP,ERASE,'Wavenumbers'
        Xord=' (cm-1)'
        WMAX=R2(T4/FMIN(J))
        WMIN=R2(T4/FMAX(J))
        GO TO 430
      END IF
      IF (Xcode.NE.'N') GO TO 410
      WRITE (1,*) UP,ERASE,UP,UP,ERASE,UP,UP
      WRITE (1,'(T26,A2,A2,A10)') UP,ERASE,'Nanometres'
      Xord=' (nm)'
      WMAX=R1(FMAX(J))
      WMIN=R1(FMIN(J))
430   ND=NDATA(J)                    ! Number Of Data Points
      STEP=FSTEP(J)                  ! Step Size (nm)
      XMIN=WMIN                      ! X-scale MIN/MAX = Scan Limits
      XMAX=WMAX
      CALL Xaxis(XMIN,XMAX)          ! Set Limits, Tick & Label Spacing
C     ---------------------------------------------------------------
      WRITE (1,*) DOWN,DOWN
      WRITE (1,'(T10,A32)') 'Y-scale units:  A.....Absorbance'
      WRITE (1,*)
      WRITE (1,'(T26,A28)') 'E.....Extinction Coefficient'
      WRITE (1,*)
      WRITE (1,'(T26,A19)') 'R.....% Reflectance'
      WRITE (1,*)
      WRITE (1,'(T26,A20)') 'T.....% Transmission'
      WRITE (1,*) DOWN
440   WRITE (1,420) UP,ERASE,'Code:    ',BELL,'_'
      READ (1,99) Ycode
      CALL Upper(Ycode)
      Text=UP//ERASE//UP//UP//ERASE//UP//UP//ERASE//UP//UP//ERASE//UP
C     ---------------------------------------------------------------
      IF (Code.EQ.'DS') THEN
        IF ((Ycode.EQ.'R').OR.(Ycode.EQ.'T')) GO TO 440
      END IF
C     ---------------------------------------------------------------
      IF (Ycode.EQ.'A') THEN
          Ystring='ABSORBANCE'       ! Select Y-axis Label For Plot
          K=0                        ! Ordinate Mode = Absorbance
      ELSE IF (Ycode.EQ.'E') THEN
          K=0                        ! Ordinate Mode = Absorbance
      ELSE IF (Ycode.EQ.'R') THEN
          Ystring='% Reflectance'
          K=1                        ! Ordinate Mode = % Transmission
```

```
584         ELSE IF (Ycode.EQ.'T') THEN
585             Ystring='% Transmission'
586             K=1                         ! Ordinate Mode = % Transmission
587         ELSE
588             GO TO 440
589         END IF
590 C       ---------------------------------------------------------------
591         IF (PARAM(J,1).NE.K) THEN       ! Test Ordinate Mode Of Spectrum #J
592           CALL Rescale(J,K,ND)          ! Rescale Between Absorbance & %T
593           PARAM(J,1)=K                  ! Reset Ordinate Variable To Match
594         END IF
595         IF (Code.EQ.'DS') THEN          ! Difference Spectrum Mode
596           K=0                           ! Only Absorbance Mode Allowed
597           IF (PARAM(2,1).NE.K) THEN     ! Test Ordinate Mode Of Spectrum #2
598             CALL Rescale(2,K,ND)        ! Rescale To Absorbance If Required
599             PARAM(2,1)=K                ! Reset Ordinate Variable To Match
600           END IF
601         END IF
602 C       ---------------------------------------------------------------
603         IF (Ycode.NE.'E') THEN
604           WRITE (1,*) Text(1:24),UP     ! Erase Unwanted Labels
605           WRITE (1,'(T26,A2,A2,A15)') UP,ERASE,Ystring
606           YMULT=1.0                     ! YMULT Scales Ext.Coeff. Mode
607           IF (Ycode.EQ.'A') GO TO 450
608           YOFF=0.0
609           YSCALE=100.0
610           CALL Yaxis(YSCALE,Ycode)
611           GO TO 460
612         END IF
613 C       ---------------------------------------------------------------
614         IF (FACTOR(J).EQ.0.0) THEN
615           WRITE (1,'(T19,A2,A2,T30,A19,A,A)') UP,ERASE,
616        &  'Conc. or Path = 0.0',BELL,'_'
617           CALL Wait(2.0)
618           WRITE (1,*)
619           GO TO 440
620         END IF
621         WRITE (1,*) Text(1:24),UP     ! Erase Unwanted Labels
622         WRITE (1,'(T26,A2,A2,A22)') UP,ERASE,'Extinction Coefficient'
623 C       ---------------------------------------------------------------
624     450 K=1
625         PMAX=0.0
626         DO WHILE (K.LE.ND)            ! Find Maximum Absorbance
627           NUMBER=A(J,K)
628           IF (Code.EQ.'DS') THEN
629             NUMBER=ABS(A(1,K)-A(2,K)*RATIO)
630           END IF
631           IF (PMAX.LT.NUMBER) PMAX=NUMBER
632           K=K+1
633         END DO
634         SCALE=R3(PMAX+0.001)          ! Round Up Absorbance Max'm
635         IF (PMAX.GT.0.01) SCALE=R2(PMAX+0.01)
636         IF (PMAX.GT.0.10) SCALE=R1(PMAX+0.10)
```

```
637         YOFF=0.0                        ! Initial Y-scale Min'm
638         YSCALE=SCALE                    ! Initial Y-scale Max'm
639         ESCALE=SCALE                    ! Initial E-scale Max'm
640         IF (Code.EQ.'DS') THEN
641           YSCALE=2.0*SCALE              ! 2 x Y-scale for +/- Max'm Range
642           YOFF=SCALE                    ! Set Zero Position At Half Y-scale
643         END IF
644         CALL Yaxis(YSCALE,Ycode)        ! Set Tick & Label Spacing
645         IF (Ycode.EQ.'A') GO TO 460
646 C
647 C       ---------------------------------------------------------------
648 C
649 C           Scale YMULT for Extinction Coefficient Mode
650 C
651 C       ---------------------------------------------------------------
652 C
653         DO WHILE (ESCALE/FACTOR(J).LT.1.0)
654           ESCALE=ESCALE*10.0
655         END DO
656         DO WHILE (ESCALE/FACTOR(J).GT.10.0)
657           ESCALE=ESCALE/10.0
658         END DO
659         RATIO=ESCALE/SCALE              ! Power Of 10 For Exponent
660         YMULT=RATIO/FACTOR(J)           ! Scaling Factor For Ext. Coeff.
661         CALL Exponent(RATIO,Mult)       ! Convert Exponent To String
662 C
663 C       ---------------- ----------------------------------------------
664 C
665 C           Plotting Routine: HP 9872A & HP 7550A
666 C
667 C       ---------------------------------------------------------------
668 C
669     460 PU=33                           ! Plotter Logical Unit # (HP 9872A)
670         PXOFF=0                         ! X-zero Position Offset (HP 9872A)
671         PYOFF=0                         ! Y-zero Position Offset (HP 9872A)
672         IF (PN.EQ.2) THEN
673           PU=17                         ! Plotter Logical Unit # (HP 7550A)
674           PXOFF=200                     ! X-zero Position Offset (HP 7550A)
675           PYOFF=100                     ! Y-zero Position Offset (HP 7550A)
676         END IF
677         WIDTH=1.0                       ! Character Field Width (cm)
678         HEIGHT=2.0                      ! Character Field Height (cm)
679         Lmode='SOLID'                   ! Solid Line Type ON
680         Pattern=' '                     ! Broken Line Type OFF
681         Length=' '                      ! Not Used For Solid Pattern
682         LF=CHAR(10)                     ! Linefeed Character
683         CR=CHAR(13)                     ! Carriage Return Character
684         C=','                           ! Data Separator In HP-GL Commands
685         Etx=CHAR(3)                     ! Label Mode Terminator (HP Default)
686         Size='N'                        ! Plot Size Default Is NOTEBOOK
687         Vaxes='5'                       ! Pen Speed (cm/sec) For Axes Vectors
688         Vspec='5'                       ! Pen Speed (cm/sec) For Spectrum
689 C       ---------------------------------------------------------------
```

```
690         WRITE (1,*) DOWN,DOWN,DOWN
691     470 WRITE (1,480) UP,ERASE,'Press RETURN if plotter is ON: ',BELL,'_'
692     480 FORMAT (T10,A2,A2,A31,A,A)
693         READ (1,99) Icode
694         IF (Icode.NE.' ') GO TO 470
695         WRITE (1,'(T10,A2,A2,A21)') UP,ERASE,'Initializing Plotter:'
696         WRITE (PU,*,IOSTAT=N,ERR=9999) 'DF;'
697         UX1=1300
698         UX2=15500                 ! Default User Set Plotting Boundaries
699         UY1=1200                  ! P1 = (1300,1200) & P2 = (15500,9500)
700         UY2=9500                  ! For B-size Paper On HP 7550A Plotter
701     490 IF (Size.EQ.'F') THEN
702           Psize='FULL'
703           XP1=1350-PXOFF
704           XP2=10000-PXOFF         ! FULL A-size Paper Plotting Boundaries
705           YP1=1000-PYOFF          ! P1 = (1350,1000) & P2 = (10000,7500)
706           YP2=7500-PYOFF          ! Offset P1,P2 For HP 7550A Plotter
707           GO TO 500
708         END IF
709         Psize='NOTEBOOK'
710         XP1=1350-PXOFF
711         XP2=8500-PXOFF            ! NOTEBOOK Size Plotting Boundaries
712         YP1=1000-PYOFF            ! P1 = (1350,1000) & P2 = (8500,7000)
713         YP2=7000-PYOFF            ! Offset P1,P2 For HP 7550A Plotter
714 C       ------- ------------------------------------------------------------
715 C           LU #33 is Device #2 on ISEE-488 interface #1
716 C           LU #17 is serial device on HP MUX (9600 Baud, XON/XOFF)
717 C       ------------------------------------------------------------------
718     500 WRITE (PU,FMT=510)
719     510 FORMAT ('SP1;PU;AP;TL1;DI1,0;IW;')
720         WRITE (PU,*) 'IP',XP1,C,YP1,C,XP2,C,YP2,';'
721         Xleft='0'
722         Xright='10000'
723         XOFF=XMIN
724         IF (XMIN.GT.XMAX) THEN
725           Xleft='-10000'
726           Xright='0'
727           XOFF=XMAX
728         END IF
729         XMULT=14/(XMAX-XMIN)          ! Scales User Units To 0-10000 Range
730         Ylow='0'                      ! YMULT Is Set In Y-scale Routines
731         Ytop='10000'                  ! For A Scaled Range Of 0-10000 Units
732         WRITE (PU,*) 'SC',Xleft,',',Xright,',',Ylow,',',Ytop,';'
733         RATIO=0.6
734         LWIDTH=WIDTH*RATIO            ! LITTLE Size Characters Default To
735         LHEIGHT=HEIGHT*RATIO          ! 0.6 Of The User Set Character Size
736         RATIO=4.0/3.0
737         BWIDTH=WIDTH*RATIO            ! BIG Size Characters Are Kept In
738         BHEIGHT=HEIGHT*RATIO          ! Proportion To The User Set Size
739         WRITE (PU,*) 'SR',WIDTH,',',HEIGHT,';VS',Vaxes,';'
740 C       ------------------------------------------------------------------
741     520 WRITE (1,*) HOME,CLR,'_'
742         CALL Line(NCOL)
```

```
      WRITE (1,530) 'CODE','FUNCTION','MIN','MAX','INC'
  530 FORMAT (T4,A4,T18,A8,T40,A3,T50,A3,T60,A3)
      CALL Line(NCOL)
      WRITE (1,540) 'PL','.....Plot Limits.....',WN,WX
      WRITE (1,540) 'XS','.....X-scale.....',XMIN,XMAX
      IF (Xcode.EQ.'N') WRITE (1,'(T20,A2,A5)') UP,' (nm)'
      IF (Xcode.EQ.'W') WRITE (1,'(T20,A2,A14)') UP,' (cm-1) x 1E-3'
      WRITE (1,550) 'XT','.....X-tick Spacing.....',FXT,LXT,Xtick
      WRITE (1,550) 'XL','.....X-label Spacing.....',FXL,LXL,Xlabel
      WRITE (1,*)
      WRITE (1,560) 'YS','.....Y-scale.....',
     &(-YOFF*YMULT),(YSCALE-YOFF)*YMULT
      IF (Ycode.EQ.'E') WRITE (1,'(T20,A2,A9,A5)') UP,' (Ext) x ',Mult
      WRITE (1,570) 'YT','.....Y-tick Spacing.....',
     &(FYT-YOFF)*YMULT,(LYT-YOFF)*YMULT,Ytick*YMULT
      WRITE (1 570) 'YL','.....Y-label Spacing.....',
     &(FYL-YOFF)*YMULT,(LYL-YOFF)*YMULT,Ylabel*YMULT
      WRITE (1,*)
      WRITE (1,580) 'CS','.....Char.Size (Width,Height)',WIDTH,HEIGHT
      WRITE (1,600) 'PV','.....Pen Velocity (Axes,Spec)',Vaxes,Vspec
      WRITE (1,590) 'LT','.....Line Type.....',Lmode,Pattern,
     &Length
      WRITE (1,590) 'AX','.....Axes Size.....',Psize,' ',' '
      WRITE (1,610) 'AN','.....Annotate Plot.....'
      WRITE (1,610) 'PA','.....PLOT AXES.....'
      WRITE (1,610) 'PS','.....PLOT SPECTRUM .....'
      WRITE (1,610) 'DD','.....DIGITIZE/DISPLAY DATA...'
      WRITE (1,610) 'EX','.....EXIT PLOTTING MODE.....'
  540 FORMAT (T5,A2,T7,A30,T40,F4.1,T50,F4.1)
  550 FORMAT (T5,A2,T7,A30,T40,F4.2,T50,F4.2,T60,F4.2)
  560 FORMAT (T5,A2,T7,A30,T40,F5.3,T50,F5.3)
  570 FORMAT (T5,A2,T7,A30,T40,F5.3,T50,F5.3,T60,F4.3)
  580 FORMAT (T5,A2,T7,A30,T40,F4.2,T50,F4.2)
  590 FORMAT (T5,A2,T7,A30,T40,A8,T50,A6,T60,A6)
  600 FORMAT (T5,A2,T7,A30,T40,A2,T50,A2)
  610 FORMAT (T5,A2,T7,A30)
      CALL Line(NCOL)
      WRITE (1,*)
  620 WRITE (1,*) UP,ERASE,'_'
      WRITE (1,'(T3,A15,A,A2)') 'Enter the CODE ',BELL,'_'
      READ (1,80) Pcode
      CALL Upper(Pcode)
C     ------------------------------------------------------------------
      IF (Pcode.EQ.'PL') GO TO 700
      IF (Pcode.EQ.'XS') GO TO 720
      IF (Pcode.EQ.'XT') GO TO 730
      IF (Pcode.EQ.'XL') GO TO 740
      IF (Pcode.EQ.'YS') GO TO 760
      IF (Pcode.EQ.'YT') GO TO 810
      IF (Pcode.EQ.'YL') GO TO 820
      IF (Pcode.EQ.'CS') GO TO 840
      IF (Pcode.EQ.'PV') GO TO 850
      IF (Pcode.EQ.'LT') GO TO 860
```

```
796         IF (Pcode.EQ.'AX') GO TO 890
797         IF (Pcode.EQ.'EX') GO TO 980
798         IF (Pcode.EQ.'PA') GO TO 1000
799         IF (Pcode.EQ.'AN') GO TO 1100
800         IF (Pcode.EQ.'PS') GO TO 2000
801         IF (Pcode.EQ.'DD') GO TO 3000
802         GO TO 500
803 C       ------------------------------------------------------------------
804     700 WRITE (1,*) UP,ERASE,'  Plot Limits: (Min,Max) ',BELL,'_'
805         READ (1,*,ERR=700) WN,WX
806         CALL Order(WN,WX)
807     710 IF ((WN.LT.WMIN).OR.(WN.GT.WMAX)) WN=WMIN
808         IF ((WX.LT.WMIN).OR.(WX.GT.WMAX)) WX=WMAX
809         GO TO 500
810 C       ------------------------------------------------------------------
811     720 WRITE (1,*) UP,ERASE,'  X-scale: (Min,Max) ',BELL,'_'
812         READ (1,*,ERR=720) XMIN,XMAX
813         XN=XMIN                         ! X-axis Is Bidirectional So Only
814         XX=XMAX                         ! XN,XX Are Ordered For Tick & Label
815         CALL Order(XN,XX)
816         CALL Xaxis(XN,XX)               ! Set Limits, Tick & Label Spacing
817         GO TO 710
818 C       ------------------------------------------------------------------
819     730 WRITE (1,*) UP,ERASE,'  X-tick: (First,Last,Space) ',BELL,'_'
820         READ (1,*,ERR=730) XN,XX,Xtick
821         CALL Order(XN,XX)
822         IF ((XN.LT.LMIN).OR.(XX.GT.LMAX)) GO TO 730
823         Xtick=ABS(Xtick)
824         FXT=XN
825         LXT=XX
826         Xlabel=Xtick
827         GO TO 750
828 C       ------------------------------------------------------------------
829     740 WRITE (1,*) UP,ERASE,'  X-label: (First,Last,Space) ',BELL,'_'
830         READ (1,*,ERR=740) XN,XX,Xlabel
831         CALL Order(XN,XX)
832         IF ((XN.LT.LMIN).OR.(XX.GT.LMAX)) GO TO 740
833         Xlabel=ABS(Xlabel)
834     750 FXL=XN
835         LXL=XX
836         GO TO 500
837 C       ------------------------------------------------------------------
838     760 WRITE (1,*) UP,ERASE,'  Y-scale: (Min,Max) ',BELL,'_'
839         READ (1,*,ERR=760) YN,YX
840         CALL Order(YN,YX)               ! Y-scale Is Unidirectional
841         EOFF=-YN
842         IF (Ycode.NE.'E') GO TO 800
843     770 WRITE (1,780) UP,ERASE,'  Ext.Coeff.Scale: ',Mult,
844        &': (U...UP / D...Down / A...Accept) ? ',BELL,'_'
845     780 FORMAT (A2,A2,A20,A6,A37,A,A)
846         READ (1,99) Icode
847         CALL Upper(Icode)
848         IF (Icode.EQ.'A') GO TO 800
```

```
849         IF (Icode.EQ.'U') THEN
850           EMULT=10.0
851           GO TO 790
852         END IF
853         IF (Icode.EQ.'D') THEN
854           EMULT=0.1
855           GO TO 790
856         END IF
857         GO TO 770
858    790  ESCALE=ESCALE*EMULT          ! Update Ext. Coeff. Scale
859         RATIO=ESCALE/SCALE           ! Power Of 10 For Exponent
860         YMULT=RATIO/FACTOR(J)        ! Scaling Factor For Ext. Coeff.
861         CALL Exponent(RATIO,Mult)    ! Convert Exponent To String
862         GO TO 770
863    800  YSCALE=(YX-YN)/YMULT         ! YMULT Alters Scaling For The
864         YOFF=EOFF/YMULT              ! Extinction Coefficient Mode
865         CALL Yaxis(YSCALE,Ycode)     ! Set Tick & Label Spacing
866         GO TO 500
867  C      ------------------------------------------------------------------
868    810  WRITE (1,*) UP,ERASE,'  Y-tick: (First,Last,Space) ',BELL,'_'
869         READ (1,*,ERR=810) YN,YX,Ytick
870         CALL Order(YN,YX)
871         Ytick=ABS(Ytick)/YMULT
872         FYT=(YN+EOFF)/YMULT
873         LYT=(YX+EOFF)/YMULT
874         Ylabel=Ytick
875         GO TO 830
876  C      ------------------------------------------------------------------
877    820  WRITE (1,*) UP,ERASE,'  Y-label: (First,Last,Space) ',BELL,'_'
878         READ (1,*,ERR=820) YN,YX,Ylabel
879         CALL Order(YN,YX)
880         Ylabel=ABS(Ylabel)/YMULT
881    830  FYL=(YN+EOFF)/YMULT
882         LYL=(YX+EOFF)/YMULT
883         GO TO 500
884  C      ------------------------------------------------------------------
885    840  WRITE (1,*) UP,ERASE,'  Char.size: (Width,Height) ',BELL,'_'
886         READ (1,*,ERR=840) WIDTH,HEIGHT
887         IF (Pcode.EQ.'AN') GO TO 1140   ! Return To Annotation Mode
888         GO TO 500
889  C      ------------------------------------------------------------------
890    850  WRITE (1,*) UP,ERASE,'  Pen Velocity, (Axes,Spectrum): ',BELL,'_'
891         READ (1,*,ERR=850) X,Y
892         IF ((X.LT.1.0).OR.(X.GT.36.0)) GO TO 850
893         IF ((Y.LT.1.0).OR.(Y.GT.36.0)) GO TO 850
894         CALL Str(X,String,2)
895         Vaxes=String(2:3)
896         CALL Str(Y,String,2)
897         Vspec=String(2:3)
898         GO TO 500
899  C      ------------------------------------------------------------------
```

```
900   860 WRITE (1,*) UP,ERASE,'  Line Type: (S.....Solid, B.....Broken) ',
901      &BELL,'_'
902       READ (1,99) Icode
903       CALL Upper(Icode)
904       IF (Icode.EQ.'S') THEN
905         Lmode='SOLID'
906         Pattern=' '
907         Length=' '
908         WRITE (PU,*) 'LT;'
909         GO TO 500
910       END IF
911       IF (Icode.NE.'B') GO TO 860
912       Lmode='PATTERN'
913   870 WRITE (1,*) UP,ERASE,'  Pattern #: (1-6) ',BELL,'_'
914       READ (1,'(I2)',ERR=870) N
915       IF ((N.LT.1).OR.(N.GT.6)) GO TO 870
916       NUMBER=FLOAT(N)
917       CALL Str(NUMBER,String,1)
918       Pattern(1:1)='#'
919       Pattern(3:3)=String(2:2)
920   880 WRITE (1,*) UP,ERASE,'  Pattern Length: (0-10)% ',BELL,'_'
921       READ (1,*,ERR=880) NUMBER
922       IF ((NUMBER.LT.0.0).OR.(NUMBER.GT.10.0)) GO TO 880
923       CALL Str(NUMBER,String,2)
924       K=2
925       DO WHILE (String(K:K).NE.' ')
926         K=K+1
927       END DO
928       Length=String(2:K)
929       WRITE (PU,*) 'LT',Pattern(3:3),',',Length,';'
930       Length(K:K)='%'
931       GO TO 500
932 C     ------------------------------------------------------------------
933   890 WRITE (1,*) UP,ERASE,'  F...FULL, N...NOTEBOOK, U...USER SET ? ',
934      &BELL,'_'
935       READ (1,99) Size
936       CALL Upper(Size)
937       IF (Size.EQ.'F') GO TO 490
938       IF (Size.EQ.'N') GO TO 490
939       IF (Size.NE.'U') GO TO 890
940       Psize='USER SET'
941   900 WRITE (1,*) UP,ERASE,'  Lower Left (X,Y)  =  '
942       WRITE (1,910) UX1,',',UY1,BELL,'_'
943   910 FORMAT (I5,A,I5,' : A...Alter or RETURN ? ',A,A)
944       READ (1,99) Icode
945       CALL Upper(Icode)
946       IF (Icode.EQ.' ') GO TO 940
947       IF (Icode.NE.'A') GO TO 900
948   920 WRITE (1,930) UP,ERASE,BELL,'?  '
949   930 FORMAT (T23,A2,A2,A,A3)
950       READ (1,*,ERR=920) UX1,UY1
951       UX1=ABS(UX1)
952       UY1=ABS(UY1)
```

```
940 XP1=UX1
    YP1=UY1
    IF (XP1.GT.16000) GO TO 920
    IF (YP1.GT.11400) GO TO 920
950 WRITE (1,*) UP,ERASE,'  Upper Right: (X,Y) =  '
    WRITE (1,910) UX2,',',UY2,BELL,'_'
    READ (1,99) Icode
    CALL Upper(icode)
    IF (Icode.EQ.' ') GO TO 970
    IF (Icode.NE.'A') GO TO 950
960 WRITE (1,930) UP,ERASE,BELL,'?  '
    READ (1,*,ERR=960) UX2,UY2
    UX2=ABS(UX2)
    UY2=ABS(UY2)
970 XP2=UX2
    YP2=UY2
    IF (XP2.GT.16000) GO TO 960
    IF (YP2.GT.10100) GO TO 960
    IF ((XP1.GE.XP2).OR.(YP1.GE.YP2)) GO TO 900
    IF ((XP2-XP1).LT.1000) GO TO 900
    IF ((YP2-YP1).LT.1000) GO TO 900
    GO TO 500
C   ------------------------------------------------------------------
980 WRITE (PU,*) 'SP0;'
    CLOSE (PU,IOSTAT=N,ERR=9999)
    GO TO MENU
C
C   ------------------------------------------------------------------
C
C                       AXES PLOTTING ROUTINE
C
C       - Scaling is ON -
C
C           Y-axis: 0-10000 user units
C           X-axis: 0-10000 user units (increasing -> right)
C                   -10000-0 user units (decreasing -> right)
C
C       - Only integral position values are sent in PA commands
C         for compatibility with early model HP plotters.
C
C       - XMULT & YMULT variables scale data to 10000 digits
C         for full scale, ensuring that no round-off errors
C         affect plotting resolution on early model HP plotters
C         which do not accept decimal fractions in SC or PA.
C
C       - Real & Integer values are sent within the HP-GL commands
C         as appropriate - some computers send extra nulls in these
C         modes causing errors on early HP plotters.  In such
C         cases the values must be converted to string literals
C         first.  The present form works correctly on the HP1000.
C
C   ------------------------------------------------------------------
C
```

```
1006  1000 WRITE (1,*) UP,ERASE,'  Plotting Axes: ',BELL,'_'
1007       WRITE (PU,*) 'VS',Vaxes,';LT;PA',Xleft,C,Ylow,';PD;'
1008       WRITE (PU,*) 'PA',Xright,C,Ylow,C,Xright,C,Ytop,C,Xleft,C,Ytop,C,
1009      &Xleft,C,Ylow,';PU;'
1010       DX=1E-5*ABS(XMAX)            ! Delta X & Y ensure completion of
1011       DY=1E-5*ABS(YSCALE)          ! DO loops with fractional steps
1012 C     ------------------------------------------------------------------
1013       DO 1010 V=FXT,LXT+DX,Xtick
1014         I=R0((V-XOFF)*XMULT)
1015         WRITE (PU,*) 'PA',I,',',Ylow,';XT;'
1016  1010 CONTINUE
1017 C     ------------------------------------------------------------------
1018       DO 1020 V=FXL,LXL+DX,Xlabel
1019         I=R0((V-XOFF)*XMULT)
1020         WRITE (PU,*) 'PA',I,',',Ylow,';'
1021         X=R2(V)
1022         CALL Str(X,String,4)
1023 C
1024 C          Find # of digits in string, ignoring sign & trailing blanks
1025 C
1026         K=2
1027         DO WHILE (String(K:K).NE.' ')
1028           K=K+1
1029         END DO
1030         X=(FLOAT(K-2)-0.33)/2.0
1031         WRITE (PU,*) 'CP',-X,',-1;LB',String(2:K-1),Etx
1032  1020 CONTINUE
1033 C     ------------------------------------------------------------------
1034       IF (Xcode.EQ.'N') THEN
1035         Xstring='Wavelength (nm)'
1036         COFF=7.5-0.33
1037       END IF
1038       IF (Xcode.EQ.'W') THEN
1039         Xstring='Wavenumber x 10'
1040         COFF=7.5+0.75-0.33
1041       END IF
1042       String=' 5000'
1043       IF (XMULT.LT.0.0) String='-5000'
1044       WRITE (PU,*) 'PA',String(1:5),',',Ylow,';SR',BWIDTH,C,BHEIGHT,';'
1045       WRITE (PU,*) 'CP',-COFF,',-2;LB',Xstring,Etx,
1046      &'SR',WIDTH,',',HEIGHT,';'
1047       IF (Xcode.EQ.'N') GO TO 1030
1048       WRITE (PU,*) 'CP0,.5;LB-3',Etx
1049 C     ------------------------------------------------------------------
1050  1030 DO 1040 V=FYT,LYT+DY,Ytick
1051         I=R0(V*T4/YSCALE)
1052         WRITE (PU,*) 'PA',Xleft,',',I,';YT;'
1053  1040 CONTINUE
1054 C     ------------------------------------------------------------------
1055       DO 1050 V=FYL,LYL+DY,Ylabel
1056         Y=R3(V-YOFF)
1057         IF (Ycode.EQ.'E') THEN
1058           Y=R2((V-YOFF)*ESCALE/FACTOR(J)/SCALE)
1059         END IF
```

```
1060          I=R0(V*T4/YSCALE)
1061          WRITE (PU,*) 'PA',Xleft,',',I,';'
1062          CALL Str(Y,String,4)
1063          IF (String.EQ.' 0.0') String=' 0'
1064 C
1065 C           Find # of digits in string, ignoring sign & trailing blanks
1066 C
1067          K=2
1068          DO WHILE (String(K:K).NE.' ')
1069            K=K+1
1070          END DO
1071          Y=FLOAT(K-1)+.33
1072          WRITE (PU,*) 'CP',-Y,',-.25;LB',String(1:K-1),Etx
1073  1050 CONTINUE
1074 C     ------------------------------------------------------------------
1075        WRITE (PU,*) 'PA',Xleft,',5000;SR',BWIDTH,',',BHEIGHT,
1076       &';CP-5,0;DI0,1;'
1077        IF (Ycode.EQ.'E') THEN
1078          K=5
1079          IF (Mult(5:5).EQ.' ') K=4
1080          IF (Mult(5:5).EQ.'.') K=1
1081          Ystring='  x '//Mult(1:K)
1082          COFF=(FLOAT(K)+13.5)/2.0-1.5
1083          IF (K.EQ.1) COFF=COFF-0.5
1084          WRITE (PU,*) 'CP',-COFF,',0;CP-.33,.5;DR0,-1;LB3',Etx
1085          WRITE (PU,*) 'DR0,1;CP.33,-.5;LB',Ystring(1:K+4),' (M',Etx
1086          WRITE (PU,*) 'CP0,.25;SR',WIDTH,',',HEIGHT,';LB-1',Etx
1087          WRITE (PU,*) 'SR',BWIDTH,',',BHEIGHT,';CP.5,-.25;LBcm',Etx
1088          WRITE (PU,*) 'CP0,.25;SR',WIDTH,',',HEIGHT,';LB-1',Etx
1089          WRITE (PU,*) 'SR',BWIDTH,',',BHEIGHT,';'
1090          WRITE (PU,*) 'CP0,-.25;LB)',Etx,';DI1,0;'
1091          GO TO 1060
1092        END IF
1093        IF (Ycode.EQ.'A') K=10
1094        IF (Ycode.EQ.'R') K=13
1095        IF (Ycode.EQ.'T') K=14
1096        COFF=FLOAT(K)/2.0-0.167
1097        WRITE (PU,*) 'CP',-COFF,',0;LB',Ystring(1:K),Etx,';DI1,0;'
1098  1060 WRITE (1,*)
1099        IF (YOFF.EQ.0.0) GO TO 1090
1100 C     ------------------------------------------ ----------------------
1101  1070 WRITE (1,*) UP,ERASE,'  Plot a dashed baseline, (Y or N) ? ',
1102       &BELL,'_'
1103        READ (1,99) Icode
1104        CALL Upper(Icode)
1105        IF (Icode.EQ.'N') GO TO 1090
1106        IF (Icode.NE.'Y') GO TO 1070
1107  1080 WRITE (1,*) UP,ERASE,'  Dash Length: (1-5)% ',BELL,'_'
1108        READ (1,*) X
1109        IF ((X.LT.1.0).OR.(X.GT.5.0)) GO TO 1080
1110        IX=R0(X)
1111        IZ=R0(YOFF*T4/YSCALE)
```

```
1112        WRITE (PU,*) 'LT2,',IX,';PA',Xright,',',IZ,';PD;PA',Xleft,
1113       &',',IZ,';PU;LT;'
1114   1090 IF (Psize.EQ.'NOTEBOOK') GO TO 1200
1115        GO TO 2080
1116 C
1117 C      ------------------------------------------------------------
1118 C
1119 C          Annotation - Labels, Parameters, Title
1120 C
1121 C      ------------------------------------------------------------
1122 C
1123   1100 WRITE (1,*) UP,ERASE,'  L...Labels,  P...Parameters,  T...Title',
1124       &',  X...Exit ? ',BELL,'_'
1125        READ (1,99) Icode
1126        CALL Upper(Icode)
1127        IF (Icode.EQ.'T') GO TO 1110
1128        IF (Icode.EQ.'L') GO TO 1120
1129        IF (Icode.EQ.'P') GO TO 1200
1130        IF (Icode.EQ.'X') GO TO 2080
1131        GO TO 1100
1132 C      ------------------------------------------------------------
1133   1110 TITLE=LABEL(J)
1134        WRITE (1,'(A2,A2,A4,A72,T76,A)') UP,ERASE,' ? <',TITLE,'>'
1135        WRITE (1,'(T3,A2,A,A)') UP,BELL,'_'
1136        READ (1,120) TITLE
1137        IF (TITLE.EQ.' ') TITLE=LABEL(J)
1138        WRITE (1,*) UP,ERASE,'  Plotting Title:',BELL
1139        K=72
1140        DO WHILE (TITLE(K:K).EQ.' ')
1141          K=K-1
1142        END DO
1143        CENT=FLOAT(K)/2.0
1144        IX=5000
1145        IF (CENT.LT.1.0) IX=-5000
1146        IY=1
1147        IF (Psize.EQ.'NOTEBOOK') IY=2
1148        WRITE (PU,*) 'PA',IX,',',Ytop,';SR1.2;CP',-CENT,',',IY,';'
1149        WRITE (PU,*) 'LB',TITLE(1:K),Etx
1150        GO TO 1100
1151 C      ------------------------------------------------------------
1152   1120 WRITE (1,'(A2,A2,A13,T58,A)') UP,ERASE,'  Label  ? <','>'
1153        WRITE (1,'(T14,A2,A,A)') UP,BELL,'_'
1154        READ (1,'(A40)') Text
1155        IF (Text.EQ.' ') GO TO 1100
1156        K=40
1157        DO WHILE (Text(K:K).EQ.' ')
1158          K=K-1
1159        END DO
1160   1130 WRITE (1,*) UP,ERASE,'  Label  ',Text(1:K),'  OK (Y or N) ',
1161       &BELL,'_'
1162        READ (1,99) Icode
1163        CALL Upper(Icode)
1164        IF (Icode.EQ.'N') GO TO 1120
1165        IF (Icode.NE.'Y') GO TO 1130
```

```
1140 WRITE (1,*) UP,ERASE,'  C...Char.size,  M...Move,  P...Plot,  ',
     &'V...Vplot,  X...Exit ? ',BELL,'_'
      READ (1,99) Icode
      CALL Upper(Icode)
      IF (Icode.EQ.'C') GO TO 1150
      IF (Icode.EQ.'M') GO TO 1160
      IF (Icode.EQ.'V') GO TO 1170
      IF (Icode.EQ.'P') GO TO 1180
      IF (Icode.NE.'X') GO TO 1140
      GO TO 1100
C     ------------------------------------------------------------------
1150 WRITE (1,*) UP,ERASE,'  Char.Size (Width,Height) ? ',BELL,'_'
      READ (1,*,ERR=1150) LWIDTH,LHEIGHT
      GO TO 1140
C     ------------------------------------------------------------------
1160 WRITE (1,*) UP,ERASE,'  Coordinate, 0-100%: (X,Y) ? ',BELL,'_'
      READ (1,*,ERR=1160) X,Y
      IX=RO(X*100.0+(XMIN-XOFF)*XMULT)
      IY=RO(Y*100.0)
      WRITE (PU,*) 'PA',IX,',',IY,';'
      GO TO 1140
C     ------------------------------------------------------------------
C         Special Entry Point From Digitize Routine (Pcode.EQ.'DD')
C         Special Offset Controls Are Used For Digitize Mode Labels
C     ------------------------------------------------------------------
1170 WRITE (PU,*) 'DI0,1;'          ! Rotate Labelling Axis 0 Degrees
1180 WRITE (1,*) UP,ERASE,   C...Centered,  L...Left Justified,  ',
     &'R...Right Justified ? ',BELL,'_'
      READ (1,99) Icode
      CALL Upper(Icode)
      IF (Icode.EQ.'C') THEN
        X=-FLOAT(K)/2.0
        IF (Pcode.EQ.'DD') THEN
          X=X-0.5                   ! Alter Centering For Leading Blank
          IF (K.GT.8) THEN          ! Alter Centering For Labelling Both
            I=2                     ! X & Y Coordinates In Digitize Mode
            DO WHILE (Text(I:I).NE.' ')
              I=I+1
            END DO                  ! Find Space Between X & Y Labels
            X=X-FLOAT(I+1)
          END IF
        END IF
        GO TO 1190
      END IF
      IF (Icode.EQ.'R') THEN
        X=-FLOAT(K)
        IF (Pcode.EQ.'DD') THEN
          X=X-2.0                   ! Alter Right Justification To Stop
        END IF                      ! Peak Label Writing Over Spectrum
        GO TO 1190
      END IF
      IF (Icode.NE.'L') GO TO 1180
      X=0.0                         ! Convert X=0.0 To '0.0' With Str
```

```
1219        IF (Pcode.EQ.'DD') THEN
1220          X=1.0                          ! Alter Left Justification To Stop
1221        END IF                           ! Peak Label Writing Over Spectrum
1222 C      ------------------------------------------------------------------
1223  1190  CALL Str(X,String,4)
1224        WRITE (1,*) UP,ERASE,'  Plotting Label:',BELL
1225        WRITE (PU,*) 'SR',LWIDTH,',',LHEIGHT,';CP',String,1.5,',-.25,'
1226        WRITE (PU,*) 'LB',Text(1:K),Etx,';CP0,.25;DI1,0;'
1227        IF (Pcode.EQ.'DD') THEN
1228          IX=NINT(T4*FLOAT(IX-X1)/FLOAT(X2-X1)+(XMIN-XOFF)*XMULT)
1229          IY=NINT(T4*FLOAT(IY-Y1)/FLOAT(Y2-Y1))
1230          WRITE (PU,*) 'PA',IX,',',IY,';PU;'
1231          GO TO 3000                     ! Return To Digitize Routine
1232        END IF
1233        GO TO 1100
1234 C      ------------------------------------------------------------------
1235  1200  IF (Psize.EQ.'FULL') GO TO 1300
1236  1210  WRITE (1,*) UP,ERASE,'  Plot Parameters, (Y or N) ? ',BELL,'_'
1237        READ (1,99) Icode
1238        CALL Upper(Icode)
1239        IF (Icode.EQ.'N') GO TO 1100
1240        IF (Icode.NE.'Y') GO TO 1210
1241        WRITE (1,*) UP,ERASE,'  Plotting Parameters:',BELL
1242        WRITE (PU,*) 'PA',Xright,C,Ytop,';'
1243        WRITE (PU,*) 'SR,.75,2;CP0,-.5;LB',LF,LF,' File: ',Fname(J),
1244       &CR,LF,LF,Etx
1245        WRITE (PU,*) 'LB Date: ',DATE(J),CR,LF,LF,Etx
1246        WRITE (PU,*) 'LB Conc.(M):',CONC(J),CR,LF,LF,Etx
1247        WRITE (PU,*) 'LB Path (cm):',PATH(J),CR,LF,LF,Etx
1248        WRITE (PU,*) 'LB Rate (nm/sec): ',
1249       &Pstr(3,PARAM(J,3)+1),CR,LF,LF,Etx
1250        WRITE (PU,*) 'LB Period (sec): ',
1251       &Pstr(15,PARAM(J,15)+1),CR,LF,LF,Etx
1252        WRITE (PU,*) 'LB Ref. Mode: ',
1253       &Pstr(5,PARAM(J,5)+1),CR,LF,LF,Etx
1254        WRITE (PU,*) 'LB Beam Mode: ',
1255       &Pstr(16,PARAM(J,16)+1),CR,LF,LF,Etx
1256        WRITE (PU,*) 'LB SBW (nm) : ',VARIABLE(J,10),CR,LF,LF,Etx
1257        WRITE (PU,*) 'LB Slit Gain: ',VARIABLE(J,6),,CR,LF,LF,Etx
1258        WRITE (PU,*) 'LB Slit Height: ',
1259       &Pstr(23,PARAM(J,23)+1),Etx
1260        GO TO 1100
1261 C
1262 C      ********************* END OF AXES PLOTTING ************************
1263 C
1264 C                          SPECTRUM PLOTTING ROUTINE
1265 C
1266 C          - Velocity Select = 5 cm/sec (Paper), 10 cm/sec (Acetate)
1267 C          - Real variables are used in 'VS' commands
1268 C          - Scaling in ON with Absorbance x 1E4 to match axes
1269 C          - Both Integer and String Numbers are used in 'PA' commands
1270 C          - HP I/O Subsystem Performs Binary <---> ASCII Conversions
1271 C
1272 C      ------------------------------------------------------------------
```

```
1273 C
1274  2000 M=1
1275       WRITE (1,*) UP,ERASE,'  Increase step size, (Y or N) ? ',BELL,'_'
1276       READ (1,99) Icode
1277       CALL Upper(Icode)
1278       IF (Icode.EQ.'N') GO TO 2020
1279       IF (Icode.NE.'Y') GO TO 2000
1280  2010 WRITE (1,*) UP,ERASE,'  Step Multiplier, (>=1): ',BELL,'_'
1281       READ (1,'(I3)',ERR=2010) M
1282       IF (M.LT.1) M=1
1283  2020 X=STEP*FLOAT(M)
1284       CALL Str(X,String,4)
1285 C
1286 C          Find # of digits, ignoring sign & trailing blanks
1287 C
1288       K=2
1289       DO WHILE (String(K:K).NE.' ')
1290         K=K+1
1291       END DO
1292       WRITE (1,*) UP,ERASE,'  Plotting Spectrum @ ',String(2:K-1),
1293      &' nm steps: ',BELL,'_'
1294 C
1295 C     ---------------------------------------------------------------
1296 C
1297 C                          WINDOW SETTING ROUTINE
1298 C
1299 C          - Soft clip limits are set to P1 & P2 scaling coordinates
1300 C            so that off scale data do not plot on graph. This should
1301 C            not happen normally since the plot boundaries are made to
1302 C            match the X-scale limits automatically if the latter are
1303 C            smaller than the scan range.
1304 C          - Plotter sends output parameters as A,B,C,D,CR,LF
1305 C            where (A-D) are string integers (ASCII), which are read
1306 C            into integer variables (ASCII translation is automatic)
1307 C          - Some computers handshake on CR leaving LF in buffer
1308 C            In these cases use READ A,B,C,D,E (N.B. CHARACTER E*1)
1309 C            to clear plotter buffer before the next READ cycle.
1310 C
1311 C     ---------------------------------------------------------------
1312 C
1313  2030 WRITE (PU,*) 'VS',Vspec,';OP;'
1314       READ (PU,*) X1,Y1,X2,Y2
1315       WRITE (PU,*) 'IW',X1,',',Y1,',',X2,',',Y2,';'
1316       IF (Xcode.EQ.'N') THEN
1317         START=RO((WMAX-WX)/STEP)+1
1318         FINISH=RO(FLOAT(ND)-(WN-WMIN)/STEP)
1319         GO TO 2040
1320       END IF
1321       START=RO((T4/WMIN-T4/WN)/STEP)+1
1322       FINISH=RO(FLOAT(ND)-(T4/WX-T4/WMAX)/STEP)
1323 C     ---------------------------------------------------------------
1324  2040 I=0
1325       RATIO=FACTOR(1)/FACTOR(2)
```

```
1326        DO 2070 K=START,FINISH,M
1327          X=W(J,K)                    ! Acquired Wavelength
1328          IF (Xcode.EQ.'N') THEN
1329 C          X=WX-FLOAT(I)*STEP       ! Calculated Wavelength
1330            IX=RO((X-XOFF)*XMULT)
1331            GO TO 2050
1332          END IF
1333 C        X=T4/WN-FLOAT(I)*STEP       ! Calculated Wavelength
1334          IX=RO((T4/X-XOFF)*XMULT)
1335  2050    IF (Code.EQ.'DS') THEN
1336            IY=RO(((A(1,K)-A(2,K)*RATIO)+YOFF)*T4/YSCALE)
1337            GO TO 2060
1338          END IF
1339          IY=RO((A(J,K)+YOFF)*T4/YSCALE)
1340  2060    WRITE (PU,*) 'PA',IX,C,IY,';PD;'
1341          I=I+M
1342  2070  CONTINUE
1343 C      ------------------------------------------------------------------
1344  2080  WRITE (PU,*) 'PU;LT;'
1345        Lmode='SOLID'
1346        Pattern=' '
1347        Length=' '
1348        GO TO 500
1349 C
1350 C      ------------------------------------------------------------------
1351 C
1352 C                      PLOTTER DIGITIZING ROUTINE
1353 C
1354 C          - HP-GL command 'OA' provides pen position without using
1355 C            the clumsy ENTER key on the plotter.
1356 C          - The 'DP' & 'OD' commands are used with ENTER in cases
1357 C            where the plotter is remote from the keyboard.
1358 C
1359 C      ------------------------------------------------------------------
1360 C
1361  3000  WRITE (1,*) HOME,CLR,'_'
1362        TITLE='Digitize Pen Position'
1363        CALL Center(TITLE)
1364        CALL Line(NCOL)
1365        CALL Digitize(X,Xcode,Y,Ext,K)
1366        WRITE (1,3010) 'X-position = ',X,Xord
1367        String=' Absorbance = '
1368        IF (Ycode.EQ.'R') String=' % Reflect. = '
1369        IF (Ycode.EQ.'T') String=' % Transmit. = '
1370        WRITE (1,3020) String,Y
1371        IF ((Ycode.EQ.'A').OR.(Ycode.EQ.'E')) THEN
1372          WRITE (1,3030) 'Ext.Coeff. = '
1373          WRITE (1,*) Ext(I,K),' /M/cm'
1374        END IF
1375  3010  FORMAT (/,T5,A14,T20,F5.3,A7)
1376  3020  FORMAT (/,T5,A14,T20,F6.4)
1377  3030  FORMAT (/,T5,A14)
1378        WRITE (1,*) DOWN
```

```
      WRITE (1,3040) 'D.....Digitize Position'
      WRITE (1,3040) 'L.....Label At Position'
      WRITE (1,3040) 'S.....Segment Display  '
      WRITE (1,3040) 'X.....EXIT To Plotting '
3040  FORMAT (/,T16,A23)
      WRITE (1,*) DOWN,DOWN
3050  WRITE (1,'(T10,A2,A2,A6,A,A)') UP,ERASE,'Code: ',BELL,'_'
      READ (1,99) Icode
      CALL Upper(Icode)
      IF (Icode.EQ.'X') GO TO 500
      IF (Icode.EQ.'D') GO TO 3000
      IF (Icode.EQ.'S') GO TO 4000
      IF (Icode.NE.'L') GO TO 3050
3060  WRITE (1,*) UP,ERASE,'    Place PEN In Stall #1,  ',
     &'Then Press RETURN ',BELL,'_'
      READ (1,99) Icode
      IF (Icode.NE.' ') GO TO 3060
      WRITE (PU,*) 'PU;SP1;'
      CALL Digitize(X,Xcode,Y,Ext,K)
3070  WRITE (1,*) UP,ERASE,'    X...X-label,  Y...Y-label,  B...Both',
     &'  Q...Quit  ? ',BELL,'_'
      READ (1,99) Icode
      CALL Upper(Icode)
      IF (Icode.EQ.'Q') GO TO 3000
      IF (Icode.EQ.'Y') GO TO 3080
      IF ((Icode.NE.'X').AND.(Icode.NE.'B')) GO TO 3070
      CALL Str(X,String,5)
      Text=String                    ! String*14, Text*40 And TITLE*72
      K=40                           ! Are Reuseable String Variables
      DO WHILE (Text(K:K).EQ.' ')
        K=K-1                        ! Find Start Of Trailing Blanks
      END DO
      IF (Icode.EQ.'X') GO TO 3110
C     ------------------------------------------------------------------
3080  IF (Ycode.EQ.'E') THEN
        String=Ext
        GO TO 3090
      END IF
      CALL Str(Y,String,5)
3090  IF (Icode.EQ.'B') THEN
        TITLE=Text(1:K)//'  '//String
        Text=TITLE(1:40)
        GO TO 3100
      END IF
      Text=String
3100  K=40
      DO WHILE (Text(K:K).EQ.' ')
        K=K-1                        ! Find Start Of Trailing Blanks
      END DO
      IF (Icode.EQ.'B') THEN
        Text(K+1:K+2)='  '
        K=K+2
      END IF
3110  GO TO 1170                     ! Transfer To Vertical Label Routine
```

```
1433 C
1434 C     ------------------------------------------------------------
1435 C
1436 C         Display Segment Of Spectrum
1437 C
1438 C     ------------------------------------------------------------
1439 C
1440  4000 String=' (nm)
1441       IF (Xcode.EQ.'W') String=  (cm-1) x 1E-3'
1442       WRITE (1,*) UP,ERASE,'  Scan Range: ',WMIN,' to',WMAX,'_'
1443       WRITE (1,*) String,DOWN,DOWN
1444  4010 WRITE (1,*) UP,ERASE,'  DISPLAY Range: (MIN,MAX) ? ',BELL,'_'
1445       READ (1,*,ERR=4010) W1,W2
1446       CALL Order(W1,W2)
1447       IF ((W1.LT.WMIN).OR.(W1.GT.WMAX)) GO TO 4010
1448       IF ((W2.LT.WMIN).OR.(W2.GT.WMAX)) GO TO 4010
1449       IF (Xcode.EQ.'N') THEN
1450         START=R0((WMAX-W2)/STEP)+1
1451         FINISH=R0(FLOAT(ND)-(W1-WMIN)/STEP)
1452         GO TO 4020
1453       END IF
1454       START=R0((T4/WMIN-T4/W1)/STEP)+1
1455       FINISH=R0(FLOAT(ND)-(T4/W2-T4/WMAX)/STEP)
1456  4020 IF ((Ycode.EQ.'R').OR.(Ycode.EQ.'T')) THEN
1457         Text=Ystring
1458         IF (Ycode.EQ.'R') Text=' '//Ystring
1459         TITLE='Energy        Wavelength        '//Text(1:15)
1460         GO TO 4030
1461       END IF
1462       TITLE='Energy    Wavelength    Absorbance    Ext.Coeff. (/M/cm)'
1463  4030 WRITE (1,*) HOME,CLR,'_'
1464       CALL Center(TITLE)
1465       CALL Line(60)
1466       L=1
1467       DO 4050 I=START,FINISH
1468         X=T4/W(J,I)
1469         Y=A(J,I)
1470         IF (Code.EQ.'DS') Y=A(1,I)-A(2,I)*FACTOR(1)/FACTOR(2)
1471         WRITE (1,*)
1472         IF ((Ycode.EQ.'A').OR.(Ycode.EQ.'E')) THEN
1473             WRITE (1,4060) X,W(J,I),Y,Y/FACTOR(J)
1474         ELSE
1475             WRITE (1,4070) X,W(J,I),Y
1476         END IF
1477         L=L+1
1478         IF (L.EQ.10) THEN
1479           WRITE (1,*) DOWN
1480  4040     WRITE (1,4080) UP,ERASE,'Press RETURN to Continue ',BELL,'_'
1481           READ (1,99) Icode
1482           IF (Icode.NE.' ') GO TO 4040
1483           WRITE (1,*) HOME,CLR,'_'
1484           CALL Center(TITLE)
1485           CALL Line(60)
1486           L=1
```

```
1487          END IF
1488   4050 CONTINUE
1489   4060 FORMAT (T9,F7.3,T21,F7.2,T35,F7.4,T49,G10.4)
1490   4070 FORMAT (T14,F7.3,T30,F7.2,T47,F7.2)
1491   4080 FORMAT (T10,A2,A2,A25,A,A)
1492        WRITE (1,*) DOWN
1493   4090 WRITE (1,4080) UP,ERASE,'Press RETURN for MENU     ',BELL '_'
1494        READ (1,99) Icode
1495        IF (Icode.NE.' ') GO TO 4090
1496        GO TO 3000
1497 C
1498 C       ------------------------------------------------------------
1499 C
1500 C           Exit Program
1501 C
1502 C       ------------------------------------------------------------
1503 C
1504    9000 WRITE (1,*) UP,ERASE,UP
1505        STOP
1506 C
1507 C       ------------------------------------------------------------
1508 C
1509 C           IEEE-488 Error Exit
1510 C
1511 C       ------------------------------------------------------------
1512 C
1513    9999 WRITE (1,*) ' Error #',N
1514        STOP
1515        END
1516 C
1517 C       ********************** END OF MAIN PROGRAM *** **** ************
1518 C
1519 C           Print a TITLE Centered in 72 columns
1520 C
1521 C       ************************************************************ *******
1522 C
1523        SUBROUTINE Center(TITLE)
1524        INTEGER I,J,N
1525        CHARACTER TITLE*72,BLANK*36
1526        BLANK=' '
1527        I=72
1528        J=0
1529        DO WHILE (ICHAR(TITLE(I:I)) EQ.32)
1530          J=J+1
1531          I=72-J
1532        END DO
1533        N=J/2
1534        WRITE (1,*) BLANK(1:N),TITLE(1:I)
1535        RETURN
1536        END
```

```
C
C     ---------------------------------------------------------------
C
C         Extinction Coefficient Rounding
C
C     ---------------------------------------------------------------
C
      SUBROUTINE Coeff(E,String,K)
      INTEGER F,K,M
      REAL E,S
      CHARACTER*(*)String
      CHARACTER Mult*3
      F=0
      S=1.0
      IF (E.LT.0.0) S=-1.0
      E=ABS(E)
      IF ((E.NE.0.0).AND.(E.NE.1.0)) GO TO 10
      String=' 0.0000'
      IF (E.EQ.1.0) String=' 1.0000'
      K=7
      GO TO 50
   10 IF ((E.GT.1.0).AND.(E.LT.10.0)) THEN
        K=K+1
        GO TO 30
      END IF
      IF (E.GE.10.0) GO TO 20
      DO WHILE (E.LT.1.0)
        E=E*10.0
        F=F-1
      END DO
      GO TO 30
   20 DO WHILE (E.GE.10.0)
        E=E/10.0
        F=F+1
      END DO
   30 E=E*S
      CALL Str(E,String,K)
   40 K=2
      DO WHILE (String(K:K).NE.' ')
        K=K+1
      END DO
      IF (F.EQ.0) GO TO 50
      E=FLOAT(F)
      CALL Str(E,Mult,2)
      IF (Mult(1:1).EQ.' ') Mult(1:1)='+'
      M=3
      IF (Mult(3:3).EQ.' ') M=2
      String(K:K+M)='E'//Mult(1:M)
      K=K+M
   50 RETURN
      END
```

```
1588 C
1589 C     ------------------------------------------------------------
1590 C
1591 C         Digitize Pen Position
1592 C
1593 C     ------------------------------------------------------------
1594 C
1595       SUBROUTINE Digitize(X,Xcode,Y,Ext,K)
1596       INTEGER IX,IY,IZ,J,K,PU,X1,X2,Y1,Y2
1597       REAL FACTOR(2),NUMBER,XMIN,XMAX,YOFF,YSCALE,X,Y
1598       CHARACTER*(*) Ext,Xcode
1599       COMMON /DIGIT/FACTOR,XMIN,XMAX,YOFF,YSCALE,IX,IY,J,PU,X1,X2,Y1,Y2
1600       WRITE (PU,*) 'OP;'
1601       READ (PU,*) X1,Y1,X2,Y2
1602       WRITE (PU,*) 'OA;'
1603       READ (PU,*) IX,IY,IZ
1604       X=(XMAX-XMIN)*FLOAT(IX-X1)/FLOAT(X2-X1)+XMIN
1605       IF (Xcode.EQ.'W') THEN
1606         X=ANINT(X*1000.0)
1607         GO TO 10
1608       END IF
1609       X=ANINT(X*10.0)/10.0
1610    10 Y=YSCALE*FLOAT(IY-Y')/FLOAT(Y2-Y1)-YOFF
1611       K=4                              ! K = # Of Digits Precision
1612       NUMBER=Y/FACTOR(J)
1613       CALL Coeff(NUMBER,Ext,K)     ! K = # Of Characters In String
1614       RETURN
1615       END
1616 C
1617 C     ------------------------------------------------------------
1618 C
1619 C         Extinction Coefficient Scale Multiplier
1620 C
1621 C     ------------------------------------------------------------
1622 C
1623       SUBROUTINE Exponent(N,Mult)
1624       INTEGER I
1625       REAL M,N
1626       CHARACTER String*14
1627       CHARACTER*(*) Mult
1628       M=0.0
1629       N=ABS(N)
1630       I=INT(N+.5)
1631       IF (I.EQ.1) THEN
1632         Mult='1   '
1633         GO TO 20
1634       END IF
1635       IF (I.GT.1) GO TO 10
1636       DO WHILE (I.LT.1)
1637         N=N*10.0
1638         M=M-1.0
1639         I=INT(N+.5)
1640       END DO
```

```
      CALL Str(M,String,2)
      Mult='1E-'//String(2:3)
      GO TO 20
   10 DO WHILE (I.GT.1)
        N=N/10.0
        M=M+1.0
        I=INT(N+.5)
      END DO
      CALL Str(M,String,2)
      Mult='1E+'//String(2:3)
   20 RETURN
      END
C
C     ------------------------------------------------------------
C
C         Print a line of N '-' characters (72 columns max)
C
C     ------------------------------------------------------------
C
      SUBROUTINE Line(N)
      INTEGER I,N
      CHARACTER BLANK*72,DLINE*72,SPACE*36
      SPACE='
      BLANK=SPACE//SPACE
      SPACE='------------------------------------'
      DLINE=SPACE//SPACE
      IF (N.GT.72) N=72
      I=(72-N)/2
      WRITE (1,*) BLANK(1:I),DLINE(1:N)
      RETURN
      END
C
C     ------------------------------------------------------------
C
C         Order MIN,MAX Entries If Required
C
C     ------------------------------------------------------------
C
      SUBROUTINE Order(MIN,MAX)
      REAL MIN,MAX,SWAP
      IF (MIN.LT.MAX) GO TO 10
      SWAP=MIN
      MIN=MAX
      MAX=SWAP
   10 RETURN
      END
```

```
1687 C
1688 C     ------------------------------------------------------------------
1689 C
1690 C         Rescale Data Array Between Absorbance And Transmission
1691 C
1692 C     ------------------------------------------------------------------
1693 C
1694 $EMA/DATA/
1695       SUBROUTINE Rescale(J,K,ND)
1696       INTEGER J,K,ND
1697       REAL A(2,10001)
1698       COMMON /DATA/A
1699       IF (K.EQ.1) GO TO 20
1700       DO 10 I=1,ND
1701         A(J,I)=ALOG10(100.0/A(J,I))
1702    10 CONTINUE
1703       RETURN
1704    20 DO 30 I=1,ND
1705         A(J,I)=100.0/10.0**(A(J,I))
1706    30 CONTINUE
1707       RETURN
1708       END
1709 C
1710 C     ------------------------------------------------------------------
1711 C
1712 C         Convert Number To ASCII String
1713 C
1714 C     ------------------------------------------------------------------
1715 C
1716       SUBROUTINE Str(VALUE,String,PREC)
1717       INTEGER ASCII,DECPT,I,J,LENSTR,NDIGIT,NUMBER,PREC
1718       REAL VALUE
1719       DOUBLE PRECISION DECIMAL,FRACTION,TEN
1720       CHARACTER Concat*14,Digit(12),Sign,String*14
1721       LOGICAL INTEGER
1722 C     LOGICAL TEST
1723       INTEGER=.TRUE.
1724 C     TEST=.FALSE.
1725       DECPT=0
1726       J=0
1727       TEN=10.0
1728       Sign=' '
1729       Concat=' '
1730 C     IF (TEST) WRITE (1,*) ' Value Entered = ',VALUE
1731       IF (VALUE.LT.0.0) Sign='-'
1732       IF (VALUE.EQ.0.0) GO TO 100
1733       DECIMAL=ABS(VALUE)
1734       DO WHILE (DECIMAL.GE.1.0)
1735         DECIMAL=DECIMAL/TEN
1736         J=J+1
1737       END DO
1738       DECPT=J
1739 C     IF (TEST) WRITE (1,*) ' # of Whole Digits: ',DECPT
```

```
1740        IF (DECPT.EQ.0) GO TO 30
1741        DO 20 J=1,DECPT
1742          DECIMAL=DECIMAL*TEN
1743          NUMBER=INT(DECIMAL)
1744          ASCII=NUMBER+48
1745          Digit(J)=CHAR(ASCII)
1746          FRACTION=DECIMAL-NUMBER
1747          DECIMAL=DINT(FRACTION*TEN**(PREC-J)+.5)/TEN**(PREC-J)
1748     20 CONTINUE
1749 C      IF (.NOT.TEST) GO TO 30
1750 C      WRITE (1,*) ' The Whole Digits = ',(Digit(I), I=1,DECPT)
1751     30 J=DECPT
1752 C      IF (TEST) WRITE (1,*) ' Decimal Fraction = ',DECIMAL
1753        IF (DECIMAL.NE.0.0) INTEGER=.FALSE.
1754        IF (DECPT.GE.12) GO TO 40
1755        DO WHILE (DECIMAL.NE.0.0)
1756          J=J+1
1757          DECIMAL=DECIMAL*TEN
1758          NUMBER=INT(DECIMAL)
1759          ASCII=NUMBER+48
1760          Digit(J)=CHAR(ASCII)
1761          FRACTION=DECIMAL-NUMBER
1762          DECIMAL=DINT(FRACTION*TEN**(PREC-J)+.5)/TEN**(PREC-J)
1763          IF (DECIMAL.EQ.1.0) THEN
1764            DIGIT(J)=CHAR(ASCII+1)
1765            DECIMAL=0.0
1766          END IF
1767          IF (J.GE.12) DECIMAL=0.0
1768        END DO
1769     40 NDIGIT=J
1770 C      IF (.NOT.TEST) GO TO 50
1771 C      WRITE (1,*) ' The Characters  = ',(Digit(I), I=1,NDIGIT)
1772     50 IF (NDIGIT.GT.12) GO TO 200
1773        DO 60 I=1,NDIGIT
1774          Concat(I:I)=Digit(I)
1775     60 CONTINUE
1776        IF (INTEGER) GO TO 80
1777        IF (DECPT.EQ.0) GO TO 70
1778        String=Sign//Concat(1:DECPT)//'.'//Concat(DECPT+1:14)
1779        RETURN
1780     70 String=Sign//' '//Concat
1781        RETURN
1782     80 String=Sign//Concat
1783        RETURN
1784    100 String=' 0.0'
1785        RETURN
1786    200 WRITE (1,*) ' Error in data: (too many digits)'
1787        STOP
1788        END
```

```
1789 C
1790 C     ------------------------------------------------------------
1791 C
1792 C         Convert String Entry To Uppercase If Required
1793 C
1794 C     ------------------------------------------------------------
1795 C
1796       SUBROUTINE Upper(Code)
1797       INTEGER LENSTR,N
1798       CHARACTER*(*) Code
1799       LENSTR=LEN(Code)
1800       DO 10 I=1,LENSTR
1801         N=ICHAR(Code(I:I))
1802         IF (N.GT.96) Code(I:I)=CHAR(N-32)
1803    10 CONTINUE
1804       RETURN
1805       END
```

```
1806 C
1807 C     ------------------------------------------------------------
1808 C
1809 C         Convert ASCII String To Numeric Value (10 Digits Max'm)
1810 C
1811 C     ------------------------------------------------------------
1812 C
1813       SUBROUTINE Val(String,VALUE)
1814       INTEGER DECPT,EXPON,LENSTR,N,NUM(10)
1815       REAL VALUE
1816       DOUBLE PRECISION MULT,SIGN,TEN,DECIMAL
1817       CHARACTER Ascii
1818       CHARACTER*(*) String
1819       LOGICAL INTEGER
1820 C     LOGICAL TEST
1821       INTEGER=.TRUE.
1822 C     TEST=.FALSE.
1823       J=1
1824       K=0
1825       DECPT=0
1826       SIGN=1.0
1827       TEN=10.0
1828       DECIMAL=0.0
1829       LENSTR=LEN(String)
1830 C     IF (TEST) WRITE (1,*) ' String Number = ',String
1831 C     IF (TEST) WRITE (1,*) ' String Length =',LENSTR
1832       DO 100 I=1,LENSTR
1833         Ascii=String(I:I)
1834         N=ICHAR(Ascii)
1835         IF ((N.GE.48).AND.(N.LE.57)) GO TO 20
1836         IF (N.EQ.46) INTEGER=.FALSE.
1837         IF (N.EQ.46) DECPT=K
1838         IF (N.EQ.45) SIGN=-1.0
1839         GO TO 100
1840    20 NUM(J)=N-48
1841       K=J
1842       J=J+1
1843   100 CONTINUE
1844       IF ((DECPT.EQ.0).AND.(INTEGER)) DECPT=K
1845       DO 200 J=1,K
1846         EXPON=DECPT-J
1847         MULT=TEN**EXPON
1848         DECIMAL=DECIMAL+NUM(J)*MULT
1849   200 CONTINUE
1850       VALUE=SIGN*DECIMAL
1851 C     IF (TEST) WRITE (1,*) ' Value =',VALUE
1852       RETURN
1853       END
```

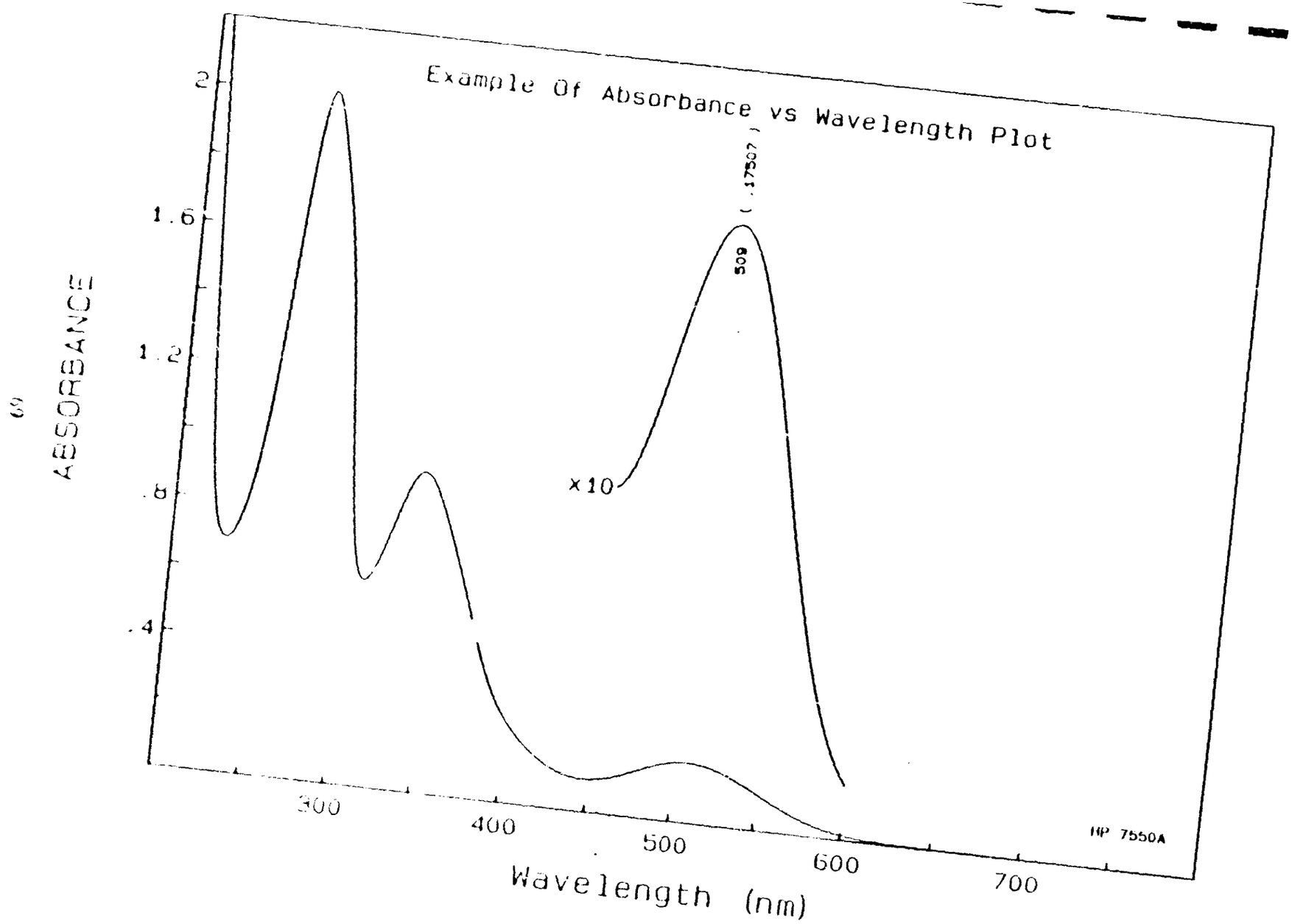
```
1854 C
1855 C     ---------------------------------------------------------------
1856 C
1857 C         Set X-axis Plotting Parameters
1858 C
1859 C     ---------------------------------------------------------------
1860 C
1861       SUBROUTINE Xaxis(XL,XH)
1862       REAL LMIN,LMAX,WN,WX,Xtick,FXT,LXT,Xlabel,FXL,LXL,XH,XL,XS(17)
1863       COMMON /XPARAM/LMIN,LMAX,WN,WX,Ytick,FXT,LXT,Xlabel,FXL,LXL
1864       DATA (XS(I),I=1,17)/.05,.1,.2,.25,.5,1.,2.,2.5,5.,10.,20.,25.,
1865      &50.,100.,200.,250.,500./
1866       LMIN=XL                          ! Set Limits To X-scale Range
1867       LMAX=XH                          ! Defined By XL,XH Arguments
1868       WN=XL
1869       WX=XH
1870 C     ---------------------------------------------------------------
1871       Xtick=0.1*(XH-XL)                ! Set Xtick To 1/10 X-scale
1872       IF ((Xtick.LT.XS(2)).OR.(Xtick.GT.XS(17))) THEN
1873         FXT=XL+Xtick                   ! Test For Xtick Outside The
1874         LXT=XH-Xtick                   ! Preferred Interval Range
1875         Xlabel=Xtick
1876         FXL=FXT
1877         LXL=LXT
1878         GO TO 10                       ! Use Default 1/10 Interval
1879       END IF
1880 C     ---------------------------------------------------------------
1881       I=1
1882       DO WHILE (Xtick.GT.XS(I))        ! Compare 1/10 Scale Xtick Value
1883         I=I+1                          ! To Find The Nearest Preferred
1884       END DO                           ! Interval < 1/10 Of X-scale
1885       Xtick=XS(I-1)
1886 C     ---------------------------------------------------------------
1887       FXT=Xtick*AINT(XL/Xtick)+Xtick   ! Truncate -> FXT <= XL (+Xtick)
1888       LXT=Xtick*AINT(XH/Xtick)         ! Truncate -> LXT <= XH
1889       IF (ABS(XH-LXT).LT.0.01) THEN
1890         LXT=LXT-Xtick                  ! Decrement If LXT = XH
1891       END IF
1892       Xlabel=Xtick*2.0                 ! Truncate -> FXL <= XL (+Xlabel)
1893       FXL=Xlabel*AINT(XL/Xlabel)+Xlabel
1894       LXL=Xlabel*AINT(XH/Xlabel)       ! Truncate -> LXL <= XH
1895       IF (ABS(XH-LXL).LT.0.01) THEN
1896         LXL=LXL-Xlabel                 ! Decrement If LXL = XH
1897       END IF
1898    10 RETURN
1899       END
```

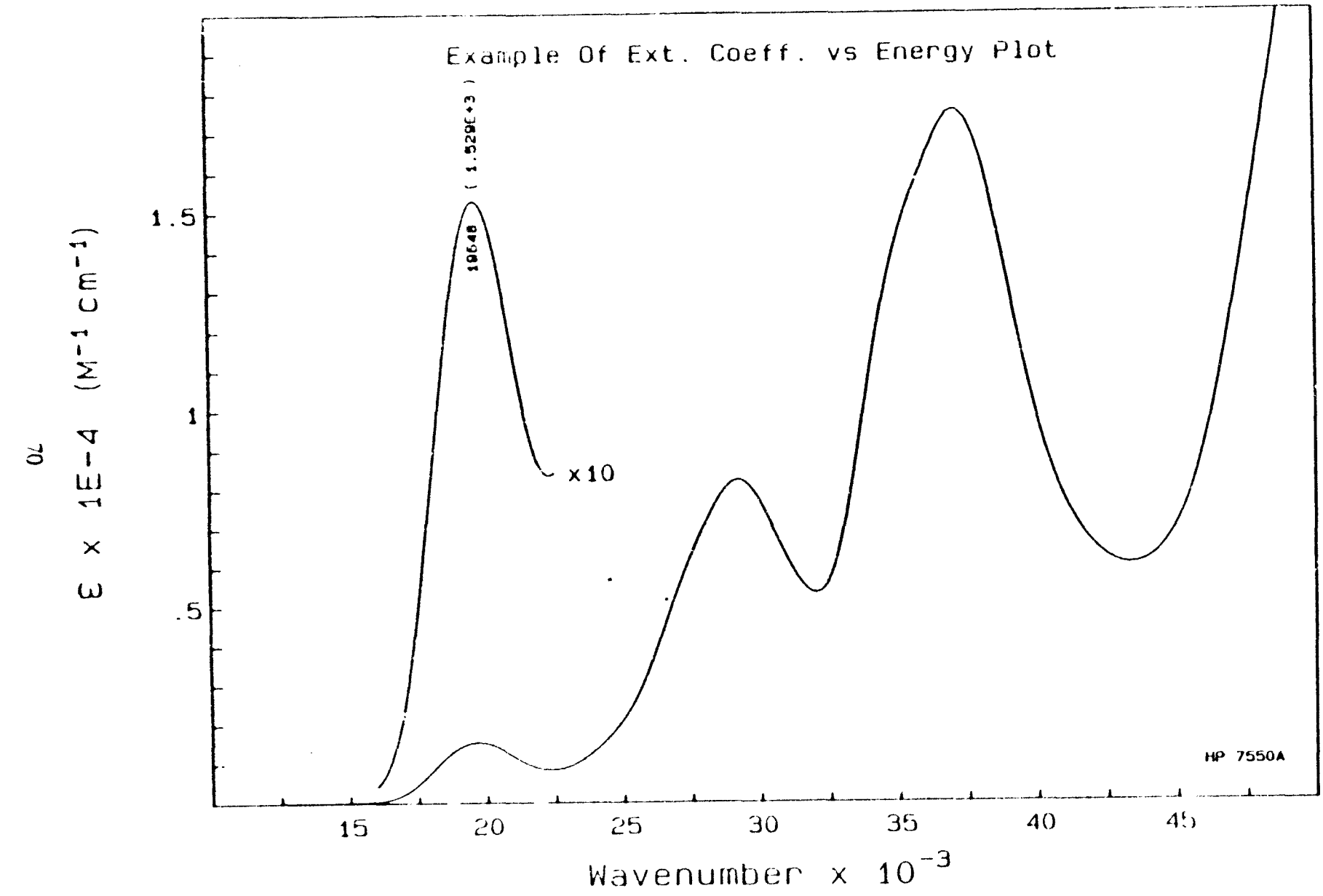
```
1900 C
1901 C     ------------------------------------------------------------
1902 C
1903 C         Set Y-axis Plotting Parameters
1904 C
1905 C     ------------------------------------------------------------
1906 C
1907       SUBROUTINE Yaxis(YSCALE,Ycode)
1908       REAL Ytick,FYT,LYT,Ylabel,FYL,LYL,YSCALE,YS(17)
1909       CHARACTER Ycode
1910       COMMON /YPARAM/Ytick,FYT,LYT,Ylabel,FYL,LYL
1911       DATA (YS(I),I=1,17)/.0005,.001,.002,.005,.01,.02,.05,.1,.2,.5,
1912      &1.,2.,5.,10.,20.,50.,100./
1913       Ytick=0.1*YSCALE
1914       IF ((Ytick.LT.YS(2)).OR.(Ytick.GT.YS(17)).OR.(Ycode.EQ.'E')) THEN
1915         FYT=Ytick
1916         LYT=YSCALE-Ytick
1917         Ylabel=Ytick
1918         FYL=FYT
1919         LYL=LYT
1920         GO TO 10
1921       END IF
1922 C     ------------------------------------------------------------
1923       I=1
1924       DO WHILE (Ytick.GT.YS(I))        ! Compare 1/10 Scale Ytick Value
1925         I=I+1                          ! To Find The Nearest Preferred
1926       END DO                           ! Interval < 1/10 YSCALE
1927       Ytick=YS(I-1)
1928       FYT=Ytick
1929       LYT=Ytick*AINT(YSCALE/Ytick)         ! Truncate -> LYT <= YSCALE
1930       IF (ABS(YSCALE-LYT).LT.1E-4) THEN    ! Decrement If LYT = YS
1931         LYT=LYT-Ytick
1932       END IF
1933       Ylabel=Ytick*2.0
1934       FYL=Ylabel
1935       LYL=Ylabel*AINT(YSCALE/Ylabel)       ! Truncate -> LYL <= YSCALE
1936       IF (ABS(YSCALE-LYL).LT.1E-4) THEN    ! Decrement If LYL = YSCALE
1937         LYL=LYL-Ylabel
1938       END IF
1939    10 RETURN
1940       END
```

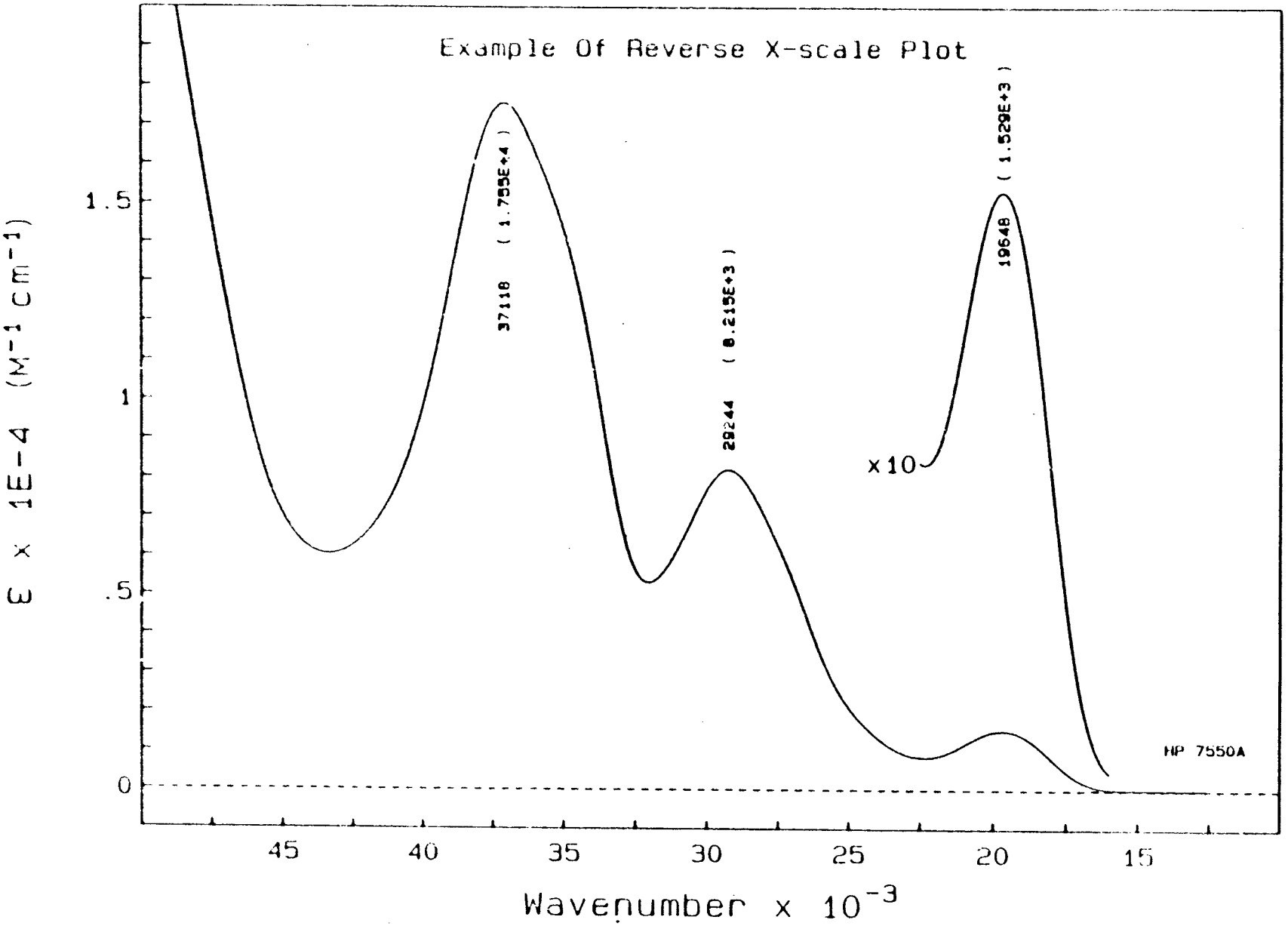
```
1941 C
1942 C     ------------------------------------------------------------
1943 C
1944 C         Wait Specified Delay (sec)
1945 C
1946 C     ------------------------------------------------------------
1947 C
1948       SUBROUTINE Wait(DELAY)
1949       REAL DELAY,PERIOD,Tzero,Time
1950       PERIOD=0.0
1951       Tzero=Time(I)
1952       DO WHILE (PERIOD.LT.DELAY)
1953         PERIOD=Time(I)-Tzero
1954       END DO
1955       RETURN
1956       END
1957 C
1958 C     ------------------------------------------------------------
1959 C
1960 C         Read Time (sec) from the HP 1000's RTE-6 Operating System
1961 C
1962 C         Note: I is a dummy argument, no values are passed
1963 C
1964 C     ------------------------------------------------------------
1965 C
1966       REAL FUNCTION Time(I)
1967       INTEGER ICODE,ITIME(5)
1968       ICODE=11
1969       CALL EXEC(ICODE,ITIME)
1970       Time=FLOAT(ITIME(1))/100.0+FLOAT(ITIME(2))+FLOAT(ITIME(3))*60.0
1971      &+FLOAT(ITIME(4))*3600.0
1972       RETURN
1973       END
```

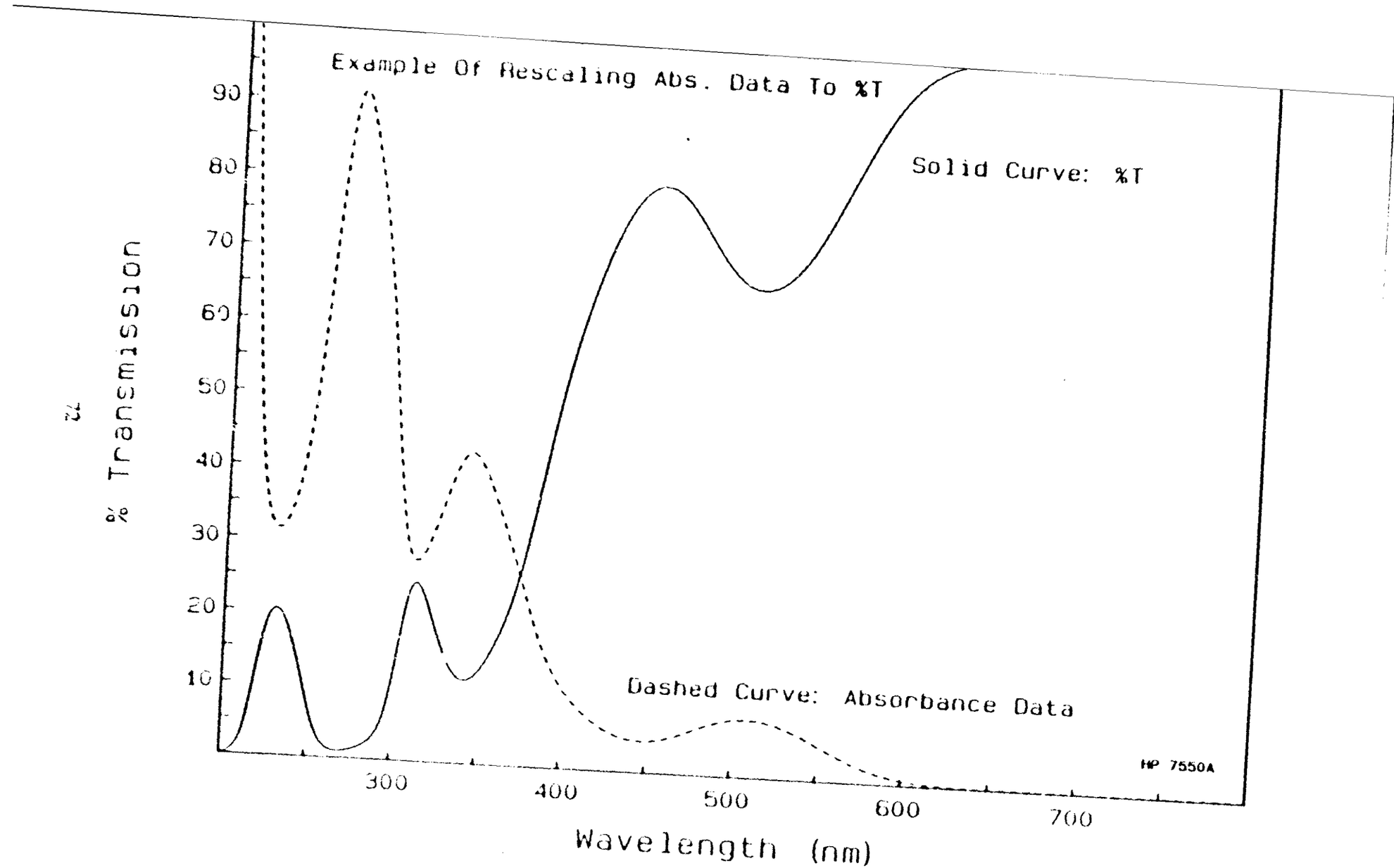
Appendix

Sample Plots


Example Of Absorbance vs Wavelength Plot
ABSORBANCE
2
1.6
1.2
.8
.4
x10
509
300
400
500
600
700
Wavelength (nm)
HP 7550A


Example Of Ext. Coeff. vs Energy Plot
(1.529E+3)
19648
x10
HP 7550A
ε x 1E-4 (M-1 cm-1)
1.5
1
.5
15
20
25
30
35
40
45
Wavenumber x 10-3


Example Of Reverse X-scale Plot
ε x 1E-4 (M-1 cm-1)
1.5
1
.5
0
37118 (1.755E+4)
29244 (8.215E+3)
19648 (1.529E+3)
x10
HP 7550A
45
40
35
30
25
20
15
Wavenumber x 10-3


Example Of Rescaling Abs. Data To %T
Solid Curve: %T
Dashed Curve: Absorbance Data
% Transmission
90
80
70
60
50
40
30
20
10
300
400
500
600
700
Wavelength (nm)
HP 7550A

THE END